Nanoscience and Technology

Hassan Raza *Editor*

Graphene Nanoelectronics

Metrology, Synthesis, Properties and Applications

Springer

NanoScience and Technology

NanoScience and Technology

The series NanoScience and Technology is focused on the fascinating nano-world, mesoscopic physics, analysis with atomic resolution, nano and quantum-effect devices, nanomechanics and atomic-scale processes. All the basic aspects and technology-oriented developments in this emerging discipline are covered by comprehensive and timely books. The series constitutes a survey of the relevant special topics, which are presented by leading experts in the field. These books will appeal to researchers, engineers, and advanced students.

Please view available titles in *NanoScience and Technology* on series homepage
http://www.springer.com/series/3705/

Hassan Raza

Editor

Graphene Nanoelectronics

Metrology, Synthesis, Properties and Applications

With 202 Figures

Springer

Editor

Hassan Raza
University of Iowa
Electrical and Computer Engineering
IATL 116
52246 Iowa City, USA
E-mail: hraza@engineering.uiowa.edu

Series Editors:

Professor Dr. Phaedon Avouris
IBM Research Division
Nanometer Scale Science & Technology
Thomas J. Watson Research Center
P.O. Box 218
Yorktown Heights, NY 10598, USA

Professor Dr. Bharat Bhushan
Ohio State University
Nanotribology Laboratory
for Information Storage
and MEMS/NEMS (NLIM)
Suite 255, Ackerman Road 650
Columbus, Ohio 43210, USA

Professor Dr. Dieter Bimberg
TU Berlin, Fakutät Mathematik/
Naturwissenschaften
Institut für Festkörperphyisk
Hardenbergstr. 36
10623 Berlin, Germany

Professor Dr., Dres. h.c. Klaus von Klitzing
Max-Planck-Institut
für Festkörperforschung
Heisenbergstr. 1
70569 Stuttgart, Germany

Professor Hiroyuki Sakaki
University of Tokyo
Institute of Industrial Science
4-6-1 Komaba, Meguro-ku
Tokyo 153-8505, Japan

Professor Dr. Roland Wiesendanger
Institut für Angewandte Physik
Universität Hamburg
Jungiusstr. 11
20355 Hamburg, Germany

NanoScience and Technology ISSN 1434-4904
ISBN 978-3-642-20467-8 e-ISBN 978-3-642-22984-8
DOI 10.1007/978-3-642-22984-8
Springer Heidelberg Dordrecht London New York

Library of Congress Control Number: 2012932061

Dedicated to our families and the global heritage of science, which binds us together.

In memory of L. Landau, E. Fermi, R. Feynman, A. Salam and R. Smalley for their contributions towards education.

Preface

The modern era of graphene "gold-rush" started around 2004–2005, when it became possible to fabricate samples with the toddler's best friend – the Scotch tape. Since then, the publication trends in this area have been nearly exponential – with more than 10,000 publications in the past seven years with over 3,000 publications in just 2010!

Although many excellent tutorial and review articles exist on various aspects of graphene nanoelectronics to help out newcomers in this area, a unified collection of such articles or chapters on most, if not all, aspects of metrology, synthesis, properties, and applications simply do not exist. When I started my tenure-track position at the University of Iowa in the summer of 2009, I was immediately facing such a group of newcomers. After consulting with some colleagues, I was convinced that such a monograph on these topics would be extremely helpful not only to the graduate students but also equally to experts who wish to get a jump-start in this area. About 10 months into the development of this book project, the 2010 Nobel Prize was announced "for groundbreaking experiments regarding the two-dimensional material graphene," which made this project even more timely and important.

The boundary conditions defined for the contributing authors were to cover theory, experiments, spectroscopy, and applications, as well as to have tutorial-like and/or review-like aspects. The contributors were also encouraged to be inclusive while planning the list of authors to have a wider representation of the community. Within these requirements, the contributing authors have done a remarkable job to integrate various chapters into a unified monograph. Readers are encouraged to look for such cross-referencing among the chapters to enhance the learning experience.

Here, I would like to take time to thank all the contributing authors for their excellent chapters as well as reviewers for their help toward this project. This enthusiastic contribution by the authors and the reviewers also reflects the above-mentioned positive consensus about the imperative need for such a book at this time. I would like to thank M.S. Dresselhaus personally for not only an excellent chapter, but also raising the overall-all morale and spirit by her presence on the project team.

I would also like to acknowledge the keen efforts of K. Horn and S. Adam toward this project.

I would also like to thank my wife Tehseen and son Ahmer. Without their understanding and support toward endless weekend and late-night hours, this book would have not been a reality. Furthermore, I would also like to thank Tehseen for improving the content of the book by providing a non-expert newcomer point of view. Extensive readings by my graduate students, Umair and Ali, also helped to improve the contents of the book for suitability to a general graduate student audience. I would finally like to thank my colleagues at Iowa, D. Andersen, M. Wohlegenannt, and M. Flatté, for weekly hallway discussions about the book.

While this book is focused on tutorial-like and/or review-like aspects of graphene nanoelectronics, we anticipate that in the next 10 years, this research field would have matured enough, leading to novel and innovative applications. At which point, another monograph covering advanced topics should follow up. Finally, I would like to thank Springer Verlag for their help on this project.

Iowa City *Hassan Raza*

Contents

Contributors

Shaffique Adam Center for Nanoscale Science and Technology, National Institute of Standards and Technology, Gaithersburg, MD 20899-6202, USA

Eva Y. Andrei Department of Physics & Astronomy, Rutgers University, Piscataway, NJ 08854, USA

Michael L. Bolen School of Electrical and Computer Engineering and Birck Nanotechnology Center Purdue University, West Lafayette, IN 47907, USA

Luis Brey Instituto de Ciencia de Materiales de Madrid (CSIC), Catoblanco, 28049 Madrid, Spain

Luiz G. Cancado Departamento de Física, Universidade Federal de Minas Gerais, Belo Horizonte- MG, 30123-970, Brazil

Michael Capano School of Electrical and Computer Engineering and Birck Nanotechnology Center Purdue University, West Lafayette, IN 47907, USA

Yuriy Dedkov Fritz-Haber-Institut der Max-Planck-Gesellschaft and SPECS Surface Nano Analysis GmbH, Berlin, Germany

Gene Dresselhaus Massachusetts Institute of Technology, Cambridge, MA 02139-4307, USA

Mildred S. Dresselhaus Department of Physics, Department of Electrical Engineering and Computer Science, Massachusetts Institute of Technology, Cambridge, MA 02139-4307, USA

Herbert A. Fertig Department of Physics, Indiana University, Bloomington, IN 47401, USA

Mikhail Fonin University of Konstanz, Germany

Avik W. Ghosh Charles L Brown School of Electrical and Computer Engineering, University of Virginia, Charlottesville, VA 22901, USA

Karsten Horn Fritz-Haber-Institut der Max-Planck-Gesellschaft and SPECS Surface Nano Analysis GmbH, Berlin, Germany

Siarhei Ihnatsenka Department of Physics, Simon Fraser University, Burnaby, BC, Canada

Ado Jorio Departamento de Física, Universidade Federal de Minas Gerais, Belo Horizonte- MG, 30123-970, Brazil

George Kirczenow Department of Physics, Simon Fraser University, Burnaby, BC, Canada

Kai-Tak Lam Department of Electrical and Computer Engineering, National University of Singapore, Singapore 117576, Republic of Singapore

Guohong Li Department of Physics & Astronomy, Rutgers University, Piscataway, NJ 08854, USA

Gengchiau Liang Department of Electrical and Computer Engineering, National University of Singapore, Singapore 117576, Republic of Singapore

Tony Low Network for Computational Nanoelectronics, Hall for Discovery Learning Research, Purdue University, West Lafayette, IN 47907, USA, and Nanometer Scale Science and Technology, IBM Research Division, IBM T.J. Watson Research Center, Yorktown Heights, NY 10598, USA

Edward McCann Department of Physics, Lancaster University, Lancaster, LA1 4YB, UK

K. Andre Mkhoyan Department of Chemical Engineering and Materials Science, University of Minnesota, Minneapolis, MN 55455, USA

Hongki Min Center for Nanoscale Science and Technology, National Institute of Standards and Technology, Gaithersburg, MD 20899-6202, USA; Maryland NanoCenter, University of Maryland, College Park, MD 20742, USA; Department of Physics and Astronomy, Seoul National University, Seoul 151-747, Korea

Alexei Preobrajenski MAX-Lab, Lund University, Lund, Sweden

Hassan Raza Department of Electrical and Computer Engineering, University of Iowa, Iowa City, IA 52242, USA

Eli Rotenberg The Advanced Light Source, Ernest Orlando Lawrence Berkeley National Laboratory, Berkeley, CA 94720, USA

Riichiro Saito Department of Physics, Tohoku University, Sendai 980-8578, Japan

Thomas Seyller Friedrich-Alexander-Universität Erlangen-Nürnberg, Lehrstuhl für Technische Physik, Erwin-Rommel-Str. 1, 91058 Erlangen, Germany

Tian Shen School of Electrical and Computer Engineering and Birck Nanotechnology Center Purdue University, West Lafayette, IN 47907, USA

Mircea R. Stan Charles L Brown School of Electrical and Computer Engineering, University of Virginia, Charlottesville, VA 22901, USA

Derek A. Stewart Cornell Nanoscale Facility, Cornell University, Ithaca, NY 14853, USA

Frank Tseng Charles L Brown School of Electrical and Computer Engineering, University of Virginia, Charlottesville, VA 22901, USA

Dincer Unluer Charles L Brown School of Electrical and Computer Engineering, University of Virginia, Charlottesville, VA 22901, USA

Katsunori Wakabayashi National Institute for Materials Science (NIMS), Tsukuba 305-0044, Japan

Yanqing Wu School of Electrical and Computer Engineering and Birck Nanotechnology Center Purdue University, West Lafayette, IN 47907, USA

Peide D. Ye School of Electrical and Computer Engineering and Birck Nanotechnology Center Purdue University, West Lafayette, IN 47907, USA

Chapter 1
Introduction

Hassan Raza

Abstract This chapter serves as a *glue* for the contributed chapters in this monograph. Here, we try to summarize the multi- and inter-disciplinary topics covered in various chapters. All chapters are written in a tutorial and review fashion, to serve not only as the state-of-the-art reference for practitioners but also as a useful tutorial for incoming researchers. Each chapter leads the reader from introduction to advanced topics and relates to the topics covered in other chapters wherever applicable. We start with a brief introduction to the atomic and electronic structure of graphene and its various nanostructures, leaving a more detailed discussion to later chapters. We then discuss the historical development of graphene research in *post-2004* era and relate it to the efforts in *pre-2004* time frame. Finally, we focus on the metrology, synthesis, properties and applications of graphene nanomembranes and nanostructures, which relates to the contributed chapters divided into three sections. This chapter is not a review of graphene nanoscience and nanotechnology research and the history of graphene in any way.

1.1 Overview

Graphene is a two-dimensional single-atom thick membrane of carbon atoms arranged in a honeycomb crystal [1–4]. It is a perfect example of a two-dimensional electron system for a physicist, an elegant form of a two-dimensional organic macromolecule consisting of benzene rings for a chemist and a material with immense possibilities for an engineer due to its excellent electrical, magnetic, thermal, optical and mechanical properties. Bilayer graphene is also an important

H. Raza (✉)
Department of Electrical and Computer Engineering, University of Iowa,
Iowa City, IA 52242, USA
e-mail: hraza@engineering.uiowa.edu

H. Raza (ed.), *Graphene Nanoelectronics*, NanoScience and Technology,
DOI 10.1007/978-3-642-22984-8_1, © Springer-Verlag Berlin Heidelberg 2012

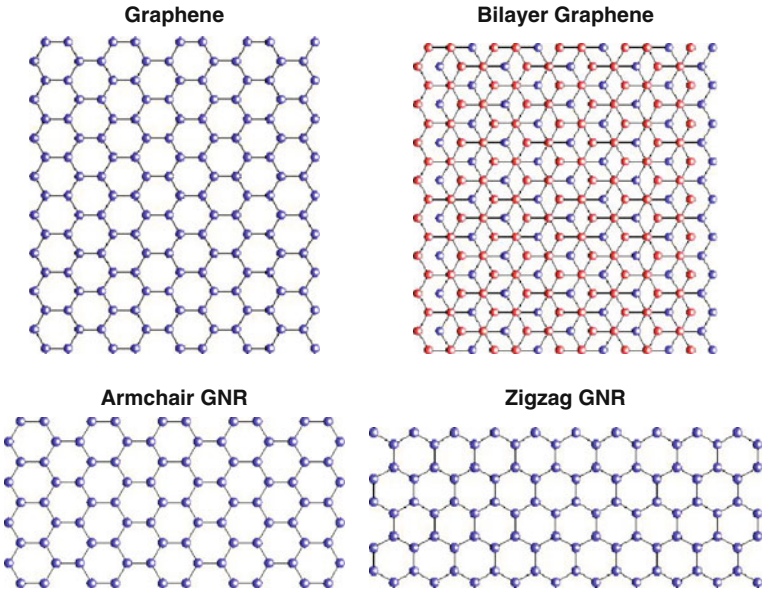

Fig. 1.1 Graphene and its nanostructures. Two graphene membranes with Bernal stacking order form bilayer graphene. One-dimensional nanoribbons with armchair and zigzag edges conceptually extracted from the two-dimensional graphene are shown. Atomic visualization was done using Hückel-NV [17]

material as shown in Fig. 1.1 and has very unique electronic structure and transport properties [5–7].

Another direction is of nanopatterned graphene structures, most notably graphene nanoribbons [8–16] consisting of one-dimensional stripes of the honeycomb arrangement, which lead to bandgap opening, edge functionalization, etc. Depending on the edge shape, two important nanoribbons are armchair graphene nanoribbons and zigzag graphene nanoribbons shown in Fig. 1.1. Finally, when multiple graphene layers are stacked, one obtains graphitic materials, and multiple nanoribbons stacking leads to multilayer graphene nanoribbons.

Historically, the word *graphene* comes from the Greek word *graphein*, which means *to write* – one of the earliest uses of this material. In the 1800s, the name *graphite* was given to the bulk material used in pencils by the German chemist Wagner. For some time, graphite was mistakenly thought to be a form of lead. The confusion of *lead pencils* comes from that misunderstanding. Nonetheless, graphene and graphite have been of immense use to mankind both in physical sciences and in technology as well as in the art form. The inspiring arrangement of carbon atoms leads to the artistic and architectural lattice shell structures – most notable perhaps is Bucky ball by Buckminster Fuller.

The most important historical application of graphite was in the molds to make cannon balls. It was truly a strategic material. In fact, the British crown imposed

embargo on graphite during the Napoleonic wars. Other historical uses of graphite include crucibles due to its refractory nature, lubrication because graphene planes can slide against each other with ease, electrodes and motor/generator brushes due to high conductivity, and materials processing e.g. steel and alloy making. The intercalation compounds of graphite were first reported in the 1840s and have been extensively studied since the 1930s [18]. In recent history, the use of graphite as a neutron moderator to thermalize high energy neutrons in nuclear reactors has been of great significance. The fundamental breakthroughs towards the physical understanding of graphene and graphite were routed in the 1940s and 1950s. Modern derivatives also include carbon nanofibres (with diameters less than 10 nm) prepared and studied extensively in the 1970s and 1980s [2, 19]. Graphene can also be conceptually thought of as a mother material for Bucky ball molecules and carbon nanotubes. Their discoverers in the 1980s (by R. F. Curl Jr, H. W. Kroto, R. E. Smalley, J. R. Heath and co-workers) and 1990s (by S. Iijima), respectively, formed the basis of not only new fundamental research areas, but also exciting new set of applications [19–21].

Since graphene is just an atomic plane of graphite, it was known to humans in the form of graphite deposits around the globe at least for few centuries and was effectively discovered since the invention of X-ray crystallography. It was important to isolate this atomic plane and, much more important, to show that this is a unique material worth further studying. Initial theoretical effort to study its 2D electronic structure was made by P. R. Wallace in 1947 [1] followed by its extension to the electronic structure of 3D graphite by D. F. Johnston, J. W. McClure and M. Yamazaki [22–24]. J. W. McClure also emphasized that the quasiparticles were Dirac-like, which was re-iterated by G. Semenoff [25].

In a nutshell, the results suggested that graphene is a semi-metal, i.e. it has zero bandgap, with linear dispersion around the chemical potential leading to cones in two-dimensional reciprocal space. This was quite a surprising result because most of the matter waves have quadratic dispersions following Schrödinger equation, which is first order in time and second order in space. In the simplest model, it leads to the following dispersion for the conduction and valence bands, respectively:

$$E_{\mathrm{S}}(\boldsymbol{k}) = E_{\mathrm{c,v}} + \frac{\hbar^2|\boldsymbol{k}|^2}{2m_{\mathrm{c,v}}} \tag{1.1}$$

where $E_{\mathrm{c,v}}$ are the conduction and valence band edges and $m_{\mathrm{c,v}}$ are the effective masses of electrons in conduction band and holes in valence band, respectively (m_v is negative, S $\equiv$ *Schrödinger*). One gets zero bandgap for $E_c = E_v$; however, the dispersion still remains quadratic.

In contrast to the Schrödinger equation, the dispersion for the Dirac equation is

$$E_{\mathrm{D}}(\boldsymbol{k}) = \pm\sqrt{m^2c^4 + \hbar^2c^2|\boldsymbol{k}|^2}\,, \tag{1.2}$$

where c is the speed of light and m is the relativistic mass (D $\equiv$ *Dirac*). The positive and negative dispersion plots are shown in Fig. 1.2, which give rise to a

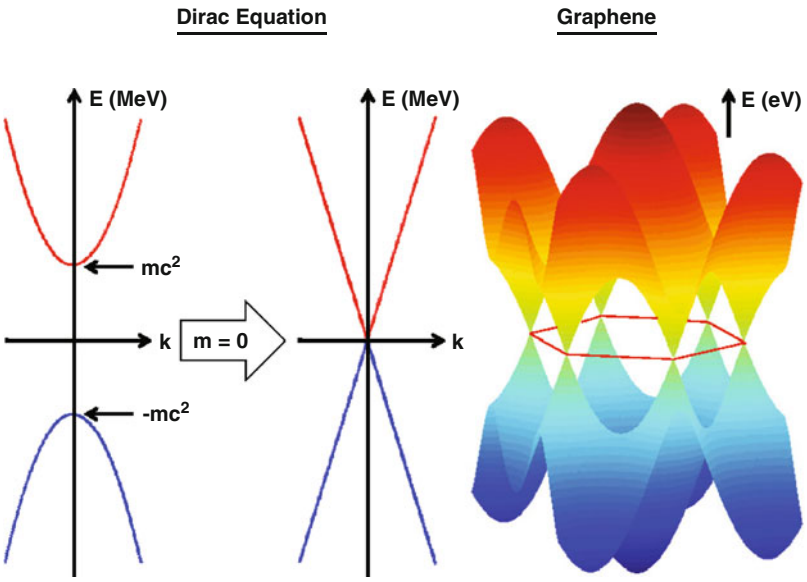

Fig. 1.2 Graphene band structure. Dirac dispersions with $2mc^2$ gap are shown. In the limit of $m = 0$, the gap becomes zero with a linear dispersion, where the energy scale is on the order of MeV. In analogy, the graphene band structure also has a linear dispersion with zero gap around the Dirac point, albeit with the energy in eV range

mass-dependent gap of $2mc^2$ between the positive energy of matter (electron in this case) and the negative energy of anti-matter (positron) – the mc^2 product for an electron is about 0.512 MeV. In the limiting case of m $= 0$, clearly the gap becomes zero. Furthermore, (1.2) becomes

$$E_{\mathrm{D}}(\boldsymbol{k}) = \pm\hbar c|\boldsymbol{k}| \tag{1.3}$$

which is plotted in Fig. 1.2 depicting the linear dispersion with zero bandgap, the energy scale on the order of MeV and the speed equal to that of light.

As a reference, the band structure of graphene is shown in Fig. 1.2, which follows the following equation based on tight-binding description [2]:

$$E_{\mathrm{G}}(\boldsymbol{k}) = \pm t\sqrt{1 + 4\cos\left(\frac{3k_x a_{\mathrm{cc}}}{2}\right)\cos\left(\frac{\sqrt{3}k_y a_{\mathrm{cc}}}{2}\right) + 4\cos^2\left(\frac{\sqrt{3}k_y a_{\mathrm{cc}}}{2}\right)}, \tag{1.4}$$

where $a_{\mathrm{cc}} = 1.42$ Å is the C–C bond length and t is the first nearest-neighbour tight-binding parameter (G $\equiv$ *graphene*). Clearly the bandgap is zero and dispersion is linear around the points where conduction and valence bands meet with a renormalized velocity v resulting in

$$E_{\mathrm{G}}(\boldsymbol{k}) = \pm\hbar v|\boldsymbol{k}| \tag{1.5}$$

similar to the dispersion of Dirac's in (1.3). Readers are encouraged to see Chap. 8 for more discussion about the electronic structure in detail.

This analogy led to the suggestion that electrons and holes act like Dirac fermions in graphene with zero mass and hence zero gap. In other words, charge carriers are mass-less relativistic Dirac fermions with point of intersection between conduction and valence bands labelled as Dirac point and the dispersion cones usually referred to as Dirac cones. Based on this analogy, sometimes phrases like *quantum relativity in our pencils* have been used. Furthermore, there are six points over the Brillouin zone where the conduction and the valence bands meet as shown in Fig. 1.2. Although, one may think that there are six Dirac points, with careful analysis, one concludes that only two points are inequivalent. Moreover, these two points are also related by the time-inversion symmetry.

There have been several efforts geared towards graphene synthesis. H. P. Boehm et al. [27] observed ultra-thin graphitic samples using electron microscopy in 1962. A. J. van Bommel et al. [28] studied thin graphitic fragments on the basal faces of SiC in 1975 by using graphitization of SiC pioneered by E. Acheson in the 1890s [29]. Since the fundamental understanding of photoelectric effect provided by A. Einstein, it has been well known that adsorbates severely affect surface properties. Carbon deposition on metal substrates has been well studied since the 1960s, see e.g. the literature review in [30]. In the surface science community, sometimes graphitic features were observed on metal surfaces, see e.g. [31]. With the discovery of scanning tunnelling microscopy (STM) in the early 1980s [32], visualizing graphite substrates became a routine practice to obtain atomic resolution images. Around the turn of the century, efforts were started to manipulate graphite samples to obtain graphene [33–36].

It is quite interesting that the sample preparation for STM involves pealing graphite samples using scotch tape to expose fresh basal planes of graphene. Understandably, researchers used to throw away the scotch tape with graphitic flakes on it. In 2004, instead of throwing away the tape, Manchester group transfered some of the flakes on a silicon substrate with 300 nm of silicon oxide film and isolated graphene to study the field effect [37]. With the right thickness of the silicon oxide film, it was not only possible to image graphene using an optical microscope but also possible to determine the number of layers from the colour difference or reflection variations as shown in Fig. 1.3. This ground-breaking discovery of transferring graphene onto an arbitrary substrate from graphite led to an immense interest in this material system. The ambipolar field effect in graphene and few layer graphene was demonstrated [37,38] and at the same time very high electronic quality was observed despite its atomic thickness and being placed on atomically rough substrate and covered with all sorts of adsorbates. No one could have predicted that the material could be so good electronically given the common wisdom that the thinner the film the worse its quality. The present day graphene boom is precisely due to this excellent electronic quality. In comparison, monolayer dichalchogenides also

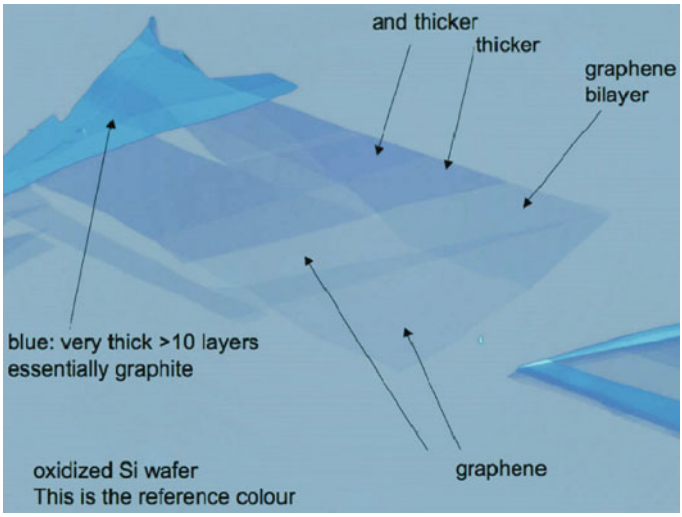

Fig. 1.3 Scotch tape method of graphene synthesis. Multiple layers can be distinguished under visible light (Courtesy of Peter Blake, Graphene Industries [26])

show field effect but with poor electronic quality and hence not as attractive for nanoelectronics [38].

The important breakthrough that propelled graphene research to its heights was the publication of back-to-back papers from the Manchester and Columbia groups [5,39,40] that demonstrated an unusual quantum Hall effect in monolayer graphene. This put to rest any doubts about reproducibility of the previous Manchester results and, from this point, the research community has eagerly embraced the paradigm of one atom thick experimental system with exceptionally high crystal and electronic quality and exotic electron transport properties. Shortly, the field effect in few layer thin epitaxial graphitic layers on SiC was also reported, although the effect was small and the resistance changed by less than 1% because screening becomes important in multilayer devices and does not allow change the carrier concentration across the whole device's thickness [41]. For these groundbreaking experiments, 2010 Physics Nobel prize was awarded to Geim and Novoselov (from Manchester group).

Although seemingly low-tech and humble, the Scotch tape method has allowed researchers to obtain graphene in sufficient quantities for studying fundamental physics and making proof-of-concept devices, which has proved invaluable for advancing graphene research. However, the isolation method is not scalable to be useful in any technology. Therefore, novel synthesis methods are required for large-scale synthesis of graphene membranes. Since the initial discovery, the community has scaled the thin film growth methods of graphite to mono- and multilayer graphene. As of today, epitaxial growth of graphene on SiC by thermal decomposition [42–44], chemical vapour deposition method of graphene synthesis

on metal substrates [45–48] and chemical methods of graphene synthesis have been achieved [49]. All these methods hold great promise for enabling future integrated circuits using graphene-based nanoelectronic devices. However, it is still a long way to achieve the goal of producing high quality wafer scale graphene reproducibly with defect densities on the order of today's state-of-the-art silicon processing.

1.2 Book Summary

This book covers key topics related to graphene nanoelectronics from science and technology perspectives. The contents of most of these chapters are multi- and inter-disciplinary, which makes the integration challenging in a monograph form. However, the distinguished contributing authors have worked closely to make the book coherent and wherever applicable, have cross-referenced the material presented in other chapters. Furthermore, the contributed authors have not only tried to make this book a good reference by providing a review of the state of the art in their respective area of expertise but also presented the material in a tutorial form to make it a good starting point for the newcomers.

In this collection, the topics range from metrology and synthesis to physical properties as well as device applications. For the sake of clarity, we have divided the book into three parts as described below. However, one should be careful that many chapters discuss topics listed in other parts as well. In the next few sections, we outline the three parts of the book and discuss the topics covered briefly to relate them to various chapters.

Part I: Metrology and Synthesis

In this part, the contributed authors discuss metrology and characterization of graphene samples as well as graphene synthesis and device fabrication. This part starts with the introduction and application of Raman spectroscopy in Chap. 2, which has been an extremely valuable tool for studying and characterizing carbon-based nanomaterials for over 40 years. Raman spectra give quantitative information to various physical properties of graphene, e.g. defects, edges, number of layers and doping. Electronic structure and other physical processes contribute to the Raman spectra, which are discussed in detail. The discussion about the Raman spectroscopy of graphene would be concluded with the near-field optics and coherent phonon spectroscopy.

Chapter 3 discusses scanning tunnelling microscopy (STM) and spectroscopy (STS), which is an extremely valuable and versatile tool for probing local properties of graphene and its various nanostructures and edges. Discussion will be provided about the use of STM and STS to experimentally study and characterize the atomic structure, electronic structure, Landau level spectroscopy, defects, edge

states, interactions, substrate effects, localization, dislocations and misalignments in graphene, multilayer graphene, nanoribbons, etc. Another useful avenue is STM-based nanolithography of graphene to form nanostructures.

ARPES (angle-resolved photoemission spectroscopy) has been widely used to study the band structures of graphene and multilayer graphene. Chapter 4 starts with an introduction and a review of ARPES for various graphene structures. It further discusses the effect of adsorbates on graphene and multilayer graphene. Adsorbates are an important consideration in graphene, which are also conceptually related to intercalation graphitic compounds. Unintentional adsorbates can undesirably change the properties and band structure. Whereas, a controlled deposition of adsorbates can lead to systematic effects, e.g. doping, and magnetism.

The next three chapters mainly discuss graphene synthesis and device fabrication. Chapter 5 starts the discussion along these lines with an introduction to graphitization of SiC(0001) surface to form graphene in a historical perspective. The science and technology discussed in this chapter may lead to large-scale fabrication of graphene nanoelectronic devices [41,42,44]. The next chapter carries on the discussion along the same lines, i.e. the fabrication of electronic and spintronic devices using the state-of-the-art tools, starting with epitaxial graphene on SiC. Chapter 6 provides details about the electrical characterization of graphene electronic and spintronic devices. In short, these chapters take a reader through steps of growth, material characterization, device fabrication, atomic layer deposition dielectric growth and finally transport characterization.

Although epitaxial growth is a viable candidate for both large-scale fabrication of electronic and spintronic devices, another growth method holds promise for the same application, notably for spintronics. Chapter 7 discusses this alternate fabrication method, i.e. chemical vapour deposition (CVD) of graphene on metallic substrates. This chapters discusses the growth mechanism, characterization and magnetic effects.

Part II: Electronic Structure and Transport Properties

This part of the book begins with Chap. 8, which provides a thorough introduction to the tight-binding model of graphene and bilayer graphene. Furthermore, the connection of the tight-binding model to the Dirac-like Hamiltonian is discussed. Advanced concepts related to these material systems are explained in a tutorial manner, e.g. chirality, pseudospin, Berry phases, trigonal warping (γ_3), Lifshitz transition, Landau level spectrum, quantum Hall effect and gate-induced bandgap opening, etc.

With the introduction to the electronic structure of the *two-dimensional* graphene and bilayer graphene, Chap. 9 discusses the effect of quantization and edge shapes on the electronic spectrum and the transport properties of the *one-dimensional* graphene nanoribbons. Interesting features like edge localization in zigzag nanoribbons near the equilibrium chemical potential and their absence in the

armchair graphene nanoribbons are discussed. Furthermore, the effect of disorder and impurity scattering is discussed in detail. The chapter concludes with the effect of edge shape on zero conductance Fano resonance in graphene nanojunctions.

Chapter 10 builds on the discussion provided in the previous two chapters to study the electronic structure of quantum rings and superlattices made out of graphene to introduce periodicity in nanoconstricted graphene via boundary conditions and explicit potential, respectively. With properly engineered rings, an *effective* magnetic flux through the rings leads to unique features in the energy spectrum and a persistent current through the ring. On the other hand, a superlattice structure leads to new Dirac points at equilibrium chemical potential, which gives rise to conductance resonances in the quantum transport through these systems.

Chapter 11 extends the discussion in Chap. 8 by providing analysis of the electronic structure of arbitrarily stacked multilayer graphene with and without a magnetic field. The energy band structure, Landau-level spectrum and low-energy effective theory of multilayer graphene are discussed. This chapter concludes with the discussion about the quantum Hall effect, optical conductivity and electrical conductivity.

Chapter 12 reports the state of the art in the macroscopic semi-classical transport through graphene in the presence of disorder and impurities and compare it with the quantum transport theory of graphene and recent experiments. The main topics covered in this context are graphene screening within the random phase approximation (RPA), the self-consistent approximation for ground state properties and effective medium theory for the charge transport.

At the nanoscale, one needs the quantum transport theory. Chapter 13 along with Chaps. 15–18 in Part III provides a set of quantum transport theoretical framework based on Green's function formalism. In this context, Chap. 13 starts with the discussion about conductance quantization of e^2/h per channel per spin in graphene nanoribbons and the effect of edge disorder, dislocations, adsorbates and impurities on the electrical conduction through nanoribbons. The topic of localization discussed in this chapter also relates to the discussion in Chap. 3.

Chapter 14 is a unique chapter about the graphene oxide. This chapter discusses comprehensively the synthesis, fabrication, characterization, ab initio analysis of the bonding and electronic structures. A detailed discussion about its applications is further provided. This chapter relates potential applications with graphene oxide to some of the other topics discussed in the book as a whole.

Part III: From Physics and Chemistry of Graphene to Device Applications

This part of the book is about device applications utilizing graphene and its various nanostructures. However, they also complement the electronic structure and transport discussion of the second part of the book. Nonetheless, the emphasis on device physics makes the chapters in this part very unique. These chapters are

mostly theoretical in nature, but experimental results are comprehensively discussed wherever applicable.

A PN junction diode is the most basic device which is formed by metallurgically joining p-type and n-type semiconducting regions. While graphene is in fact a semimetal, it is still possible to make PN junction devices. Chapter 14 discusses the transport properties of such PN junctions based on graphene. It further discusses the angular selective nature of transmission and Klein tunnelling. Magneto-transport through these junctions is also discussed in the context of snake orbits, edge effects, disorder and strain. Finally, details about the numerical modelling of the quantum transport are provided.

The next chapter is about field effect transistors (FETs) using monolayer and bilayer graphene nanoribbons with armchair and zigzag edges. FETs are the work horse of today's integrated circuits. This chapter discusses the performance analysis of Schottky barrier field effect transistor using armchair-edged and doped zigzag edged bilayer graphene nanoribbons. Finally, nanoelectromechanical switches are discussed for memory applications.

Chapter 17 discusses the electric field modulation in graphene nanostructures. Bandgap opening in bilayer and multilayer graphene has already been discussed in Chaps. 8 and 11. This chapter extends the discussion along these lines in the presence of misalignments and strain as well as provides a review of the modulation effects in armchair and zigzag nanoribbons with and without edge roughness. Device applications for these material systems are also discussed in detail.

The final (Chap. 18) takes the reader from device characteristics to the integration of individual devices into integrated circuits for scalable applications. In particular, discussion about graphene inverter characteristics is provided. With this, the book concludes with an overarching theme of a unique source of review and tutorial material for graphene nanoelectronics research from basic and applied perspectives.

1.3 Outlook

The area of graphene research is progressing by leaps and bounds. Everyday, new discoveries are being made. Given the exponential growth trend, we anticipate that another monograph within 5–10 years will cover the more advanced topics in graphene nanoelectronics, once the facts of graphene *gold rush* have been established on solid footings.

We also anticipate that once the basic science of graphene is established on a more solid footing, novel applications in very diverse areas [50–52] utilizing this exceptional material will follow suit.

Acknowledgements We thank A. K. Geim for a critical review and helpful discussions. We also thank all the contributing authors (especially K. Horn and S. Adam) in this book for useful discussions. Their feedback to make this chapter serve as a cohesive foundation for other chapters has been invaluable. This work was supported by the University of Iowa Presidential Faculty Fellowship.

References

1. P.R. Wallace, Phys. Rev. **71**, 622 (1947).
2. R. Saito, G. Dresselhaus, and M.S. Dresselhaus, *Physical Properties of Carbon Nanotubes*, (Imperial College Press, London, UK, 1998).
3. A.K. Geim and K.S. Novoselov, Nat. Mater. **6**, 183 (2007).
4. A.H. Castro Neto, F. Guinea, N.M. R. Peres, K.S. Novoselov, and A.K. Geim, Rev. Mod. Phys. **81**, 109, 2009.
5. K.S. Novoselov, E. McCann, S.V. Morozov, V.I. Fal'ko, M.I. Katsnelson, U. Zeitler, D. Jiang, F. Schedin and A.K. Geim, Nature Physics **2**, 177 (2006).
6. E. McCann and V.I. Fal'ko Phys. Rev. Lett. **96**, 086805 (2006).
7. E. McCann, Phys. Rev. B **74**, R161403 (2006).
8. K. Nakada, M. Fujita, G. Dresselhaus and M.S. Dresselhaus, Phys. Rev. B **54**, 17954 (1996).
9. M. Fujita, K. Wakabayashi, K. Nakada and K. Kusakabe, J. Phys. Soc. of Japan **65**, 1920 (1996).
10. K. Wakabayashi, M. Fujita, H. Ajiki and M. Sigrist, Phys. Rev. B. **59** 8271 (1999).
11. T. Kawai, Y. Miyamoto, O. Sugino and Y. Koga, Phys. Rev. B **62**, R16349 (2000).
12. V. Barone, O. Hod and G.E. Scuseria, Nano. Lett. **6**, 2748 (2006).
13. Z. Chen, Y.-M. Lina, M.J. Rooksa and P. Avouris, Physica E: Low-dimensional Systems and Nanostructures **40**, 228 (2007).
14. L. Brey and H.A. Fertig, Phys. Rev. B **73**, 235411 (2006).
15. M.Y. Han, B. Ozyilmaz, Y. Zhang and P. Kim, Phys. Rev. Lett. **98**, 206805 (2007).
16. X. Li, X. Wang, L. Zhang, S. Lee, H. Dai, Science **319**, 1229 (2008).
17. L. Oetting, T.Z. Raza, H. Raza, in preparation.
18. M.S. Dresselhausa; G. Dresselhaus, Advances in Physics **30**, 139 (1981).
19. M.S. Dresselhausa; G. Dresselhaus, P. Avouris, *Carbon Nanotubes: Synthesis, Structure, Properties and Applications*, (Springer, Berlin Heidelberg New York, 2001).
20. M.S. Dresselhausa; G. Dresselhaus, P.C. Eklund, *Science of Fullerenes and Carbon Nanotubes: Their Properties and Applications*, (Academic Press, San Diego, California, 1996)
21. A. Jorio, M.S. Dresselhausa; G. Dresselhaus, *Carbon Nanotubes: Advanced Topics in the Synthesis, Structure, Properties and Applications*, (Springer, Berlin Heidelberg New York, 2008).
22. D.F. Johnston, Proc. R. Soc. A, **227**, 349 (1955).
23. J.W. McClure, Phys. Rev. **108**, 612 (1957).
24. M. Yamazaki, J. Chem. Phys. **26**, 930 (1957).
25. G.W. Semenoff, Phys. Rev. Lett. **53**, 2449 (1984).
26. http://grapheneindustries.com/
27. H.P. Boehm et al. Z. Naturforschung **17b**, 150 (1962).
28. A.J. van Bommel, J.E. Crombeen, A. van Tooren. Surf. Sci. **48**, 463 (1975).
29. http://web.mit.edu/invent/iow/acheson.html
30. C. Oshima and A. Nagashima, J. Phys.: Condens. Matter **9**, 1 (1997).
31. J.T. Grant, T.W. Haas, Surface Science, **21**, 76 (1970).
32. C. Bai, *Scanning Tunneling Microscopy and Its Application*, 2nd edn. (Springer, Berlin Heidelberg New York, 2000).
33. K. Seibert, G.C. Cho, W. Kütt, H. Kurz, D.H. Reitze, J.I. Dadap, H. Ahn, M.C. Downer, A.M. Malvezzi, Phys. Rev. B **42**, 2842 (1990).
34. T.W. Ebbesen and H. Hiura, Advanced Materials, **7**, 582 (1995).
35. X. Lu, M. Yu, H. Huang, R.S. Ruoff. Nanotechnology, **10**, 269 (1999).
36. R.B. Little, J. Cluster Sci. **14**, 135 (2003).
37. K.S. Novoselov, A.K. Geim, S.V. Morozov, D. Jiang, Y. Zhang, S.V. Dubonos, I.V. Grigorieva, and A.A. Firsov, Science **306** 666 (2004).
38. K.S. Novoselov, D. Jiang, F. Schedin, T. Booth, V.V. Khotkevich, S.V. Morozov and A.K. Geim, Proc. Natl. Acad. Sci. **102**, 10451 (2005).

39. K.S. Novoselov, A.K. Geim, S.V. Morozov, D. Jiang, M.I. Katsnelson, I.V. Grigorieva, S.V. Dubonos and A.A. Firsov, Nature **438**, 197 (2005).
40. Y. Zhang, Y.-W. Tan, H.L. Stormer and P. Kim, Nature **438**, 201 (2005).
41. C. Berger, Z. Song, T. Li, X. Li, A.Y. Ogbazghi, R. Feng, Z. Dai, A.N. Marchenkov, E.H. Conrad, P.N. First and W.A. de Heer, J. Phys. Chem. B **108**, 19912 (2004).
42. C. Berger, Z. Song, X. Li, X. Wu, N. Brown, C. Naud, D. Mayou, T. Li, J. Hass, A.N. Marchenkov, E.H. Conrad, P.N. First and W.A. de Heer, Science **312** 1191 (2006).
43. Y.Q. Wu, P.D. Ye, M.A. Capano, Y. Xuan, Y. Sui, M. Qi, J.A. Cooper, T. Shen, D. Pandey, G. Prakash and R. Reifenberger, Appl. Phys. Lett. **92**, 092102 (2008).
44. K.V. Emtsev, A. Bostwick, K. Horn, J. Jobst, G.L. Kellogg, L. Ley, J.L. McChesney, T. Ohta, S.A. Reshanov, J. Röhrl, E. Rotenberg, A.K. Schmid, D. Waldmann, H.B. Weber and T. Seyller, Nature Materials **8**, 203 (2009).
45. Q. Yu, J. Lian, S. Siriponglert, H. Li, Y.P. Chen and S.-S. Pei, Appl. Phys. Lett. **93**, 113103 (2008).
46. A. Reina, X. Jia, J. Ho, D. Nezich, H. Son, V. Bulovic, M.S. Dresselhaus and J. Kong, Nano Lett. **9**, 30 (2008).
47. K.S. Kim, Y. Zhao, H. Jang, S.Y. Lee, J.M. Kim, K.S. Kim, J.-H. Ahn, P. Kim, J.-Y. Choi and B.H. Hong, Nature **457**, 706 (2009).
48. X. Li, W. Cai, J. An, S. Kim, J. Nah, D. Yang, R. Piner, A. Velamakanni, I. Jung, E. Tutuc, S.K. Banerjee, L. Colombo, R.S. Ruoff, Science **324**, 1312 (2009).
49. S. Stankovich, D.A. Dikin, R.D. Piner, K.A. Kohlhaas, A. Kleinhammes, Y. Jia, Y. Wu, S.T. Nguyen, R.S. Ruoff, Carbon **45**, 1558 (2007).
50. A.K. Geim, Science **324**, 1530 (2009).
51. V.I. Fal'ko, Nature Phys. **3**, 151 (2007).
52. F. Schwierz, Nature Nanotechnology **5**, 487 (2010).

Part I
Metrology and Synthesis

Chapter 2
Raman Spectroscopy: Characterization of Edges, Defects, and the Fermi Energy of Graphene and sp^2 Carbons

M.S. Dresselhaus, A. Jorio, L.G. Cançado, G. Dresselhaus, and R. Saito

Abstract From the basic physical concepts relating to the Raman spectra of graphene, we can develop characterization methods for point defects and the edge structure. Furthermore, the Fermi energy can be studied by the phonon softening phenomena of the Raman spectra. Finally, we also discuss recent progress on near-field optics.

2.1 Introduction to the Resonance Raman Spectra of Graphene

Raman spectroscopy has been widely used to characterize sp^2 carbon systems, from graphite to carbon nanotubes. Especially interesting is the richness of the Raman spectral response to lattice symmetry breaking and to changes in the Fermi level. These two aspects are very important when moving from bulk 3D materials down to nanomaterials, where single defects, edges, and interactions with the environment become frequent and important. In this scenario, two-dimensional (2D) graphene becomes an important prototype system to study such effects, as we discuss in this chapter. We start by giving, in this section, introductory material with the basic concepts behind the Raman spectroscopy of sp^2 carbon systems.

M.S. Dresselhaus (✉)
Department of Physics, Department of Electrical Engineering and Computer Science, Massachusetts Institute of Technology, Cambridge, MA 02139-4307, USA
e-mail: millie@mgm.mit.edu

A. Jorio · L.G. Cançado
Departamento de Física, Universidade Federal de Minas Gerais, Belo Horizonte - MG, 30123-970, Brazil

G. Dresselhaus
Massachusetts Institute of Technology, Cambridge, MA 02139-4307, USA

R. Saito
Department of Physics, Tohoku University, Sendai 980-8578, Japan

H. Raza (ed.), *Graphene Nanoelectronics*, NanoScience and Technology,
DOI 10.1007/978-3-642-22984-8_2,

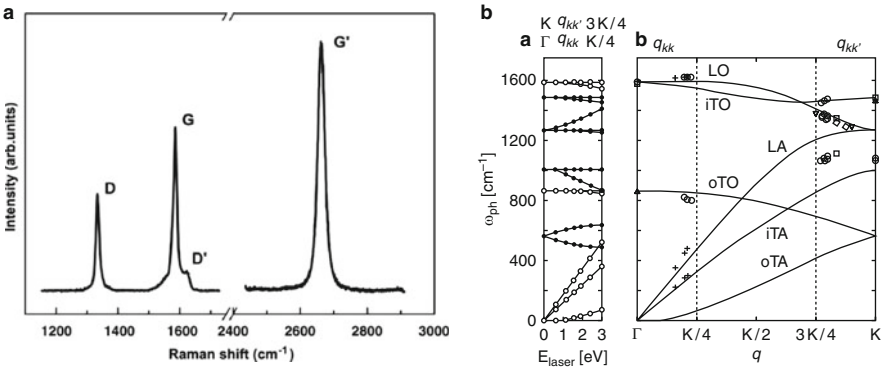

Fig. 2.1 (**a**) Raman spectrum of a graphene edge, showing the main Raman features, the D, G, D', and G' bands taken with a laser excitation energy of 2.41 eV [1]. (**b**) On the *left* are the calculated Raman frequencies for the double-resonance condition in graphene as a function of E_{laser} (bottom horizontal axis) and the corresponding q vector along the K (top horizontal axis). *Solid and open circles* correspond to phonon modes around the K and Γ points, respectively. The q_{KK} vectors from Γ to $K/4$ are shown by *open circles* and the q_{KK} vectors from $3K/4$ to K are shown by *solid circles*. The six calculated phonon dispersion curves (*lines*) and experimental Raman observations (*symbols*) are plotted and shown to be consistent with double resonance theory [16]

2.1.1 The Raman Spectra of sp^2 Carbons

The Raman spectrum of crystalline graphite is characterized by the presence of two strong symmetry-allowed peaks at 1,580 and 2,700 cm^{-1}, the G and G' bands, respectively, where the G label refers to spectral features[1] originating from graphene (see Fig. 2.1). The G band is a spectral feature shown in Fig. 2.1a near 1,600 cm^{-1}, while Fig. 2.1b shows that the G band phonon has a very small wave vector q often approximated as $q = 0$ [2, 3], i.e. a first-order Raman feature originating from the zone-centered, in-plane optical-phonon modes [2, 3]. Because graphene is a zero-gap semiconductor, there is a strong electron–phonon interaction. We will see in Sect. 2.1.4 that because of this strong electron-phonon interaction near $q = 0$, the G-band phonon frequency, intensity, and lineshape are strongly dependent upon doping. The G' band is a second-order, two-phonon feature that is specially strong in sp^2 carbons. The G' band is important for many reasons, due to the fact that the G'-band feature depends upon the phonon wave vector q and allows study of the electronic structure of sp^2 carbons through study of their phonons [4, 5]. Many of the unusual properties of the G' band arise from the mechanism responsible for the large intensity of the G' band, which is a multiple resonance process. These topics are further clarified in Section 2.1.3.

[1] In this chapter, we frequently use the word "feature" to refer to spectral features. For example, "The first-order Raman feature" means that the Raman spectral line originates from a first-order Raman scattering process.

Disorder-induced symmetry-breaking effects are important in the determination of several material properties, such as transport properties and the relaxation of photoexcited carriers [6, 7]. This applies specially to sp^2 carbons, which have high symmetry and, consequently, are highly sensitive to symmetry-breaking defects. Raman spectroscopy is particularly sensitive to symmetry-breaking phenomena in sp^2 carbons. Thus Raman spectroscopy is widely used to identify the presence of defects and disorder in sp^2 networks of different carbon structures, such as diamond-like carbon, amorphous carbon, and nanostructured carbon, as well as carbon nanofibers, nanotubes, nanohorns and most recently graphene [1, 8–11].

In the Raman spectra obtained from graphene and other sp^2 carbon samples containing defects, several additional symmetry-breaking features are found. The feature with highest intensity is the D band which occurs near 1,350 cm^{-1} for laser excitation energies of 2.41 eV (a commonly used laser excitation energy), being associated with near-K point phonons. Another common symmetry-breaking feature in the first-order spectrum is the D' band near 1,620 cm^{-1}, associated with near-Γ ($q \neq 0$) point phonons, where q refers to the phonon wave vector. The D and D' bands can also give rise to overtones and combination modes, thereby resulting in additional symmetry-breaking modes in the Raman spectra. Now we give a brief description of the wave vectors for these modes.

The D band is associated with a breathing-like motion of the carbon atoms located in carbon hexagons that becomes Raman active due to the loss of the lattice symmetry [2, 3]. The most common reasons for symmetry breaking are the presence of vacancies and interstitial or substitutional atoms which can also be introduced intentionally as for example by ion implantation [12] or by introducing interfaces at the borders of crystalline areas [2, 3]. The frequency of the D band is roughly about half of the second-order G' frequency ($\omega_{G'}/2$). The mechanism involved in the G'-band process is a symmetry-allowed two-phonon process that is also present in ideally crystalline graphene. However, the $\sim$1,350 cm^{-1} D-band peak is only observed in the presence of defects or at the edge of a graphene sample in an otherwise perfect infinite graphene structure. The intensity of the D band is proportional to the amount of disorder (as, for example, at a point defect or at a crystallite boundary) in the sample. The ratio between the intensities of the disorder-induced D band and the first-order graphite G band (I_D/I_G) provides a parameter that can be used for quantifying the amount of disorder.

Tuinstra and Koenig showed in 1970 that the I_D/I_G intensity ratio [2, 3] is correlated with the crystallite size L_a by the relation $I_D/I_G = A/L_a$, where A is a constant for a fixed laser excitation energy E_{laser}.[2] This means that the I_D/I_G intensity ratio depends on the laser excitation energy E_{laser} [13]. The Tuinstra and Koenig relationship has been frequently used to characterize carbon sp^2 crystallites large enough to have a well-established graphene-like structure. On the other hand, Lucchese et al. showed recently that in the limit of amorphization, the ratio I_D/I_G

[2]This means that A changes for different E_{laser} and we cannot directly compare the I_D/I_G values of two different samples observed by two different values of E_{laser}.

decreases as the crystallite size goes down to very small L_a values, such as 2nm [14]. In this limit, the sp^2 carbon hexagonal crystal structure for graphene is not well defined.

The so-called D' band, centered at 1,620 cm^{-1}, is usually observed in the Raman spectra of graphene and other disordered sp^2 carbon materials, although the D' band has a weaker intensity when compared to the D band. The D' band feature, reported in 1978 by Tsu et al. [15], also depends on L_a and E_{laser} [9] but involves a different scattering process. The D band involves an intervalley scattering process, as explained below, while the D' band involves an intravalley scattering process [16].

Vidano et al. showed in 1981 [17] that the D and G' bands are dispersive, i.e., their Raman shift frequencies change with E_{laser} according to the relations $\Delta\omega_D/\Delta E_{\mathrm{laser}} \sim 50\,\mathrm{cm}^{-1}/\mathrm{eV}$ and $\Delta\omega_{G'}/\Delta E_{\mathrm{laser}} \sim 100\,\mathrm{cm}^{-1}/\mathrm{eV}$. The out-of-plane stacking order has also been shown to affect the G'-band Raman lineshape and intensity [18–20]. The explanation for the exceptionally large dispersive behavior of both the D band and G' band as well as the large G'-band intensity came in 2000, through the work of Thomsen and Reich [21], and their model described in Section 2.1.3 was extended by Saito et al. to explain the mechanism behind many other dispersive Raman peaks observed in the Raman spectra of sp^2 carbon materials [16, 22]. Characterization of defects by Raman spectroscopy and their related theory is discussed in Sect. 2.2.

2.1.2 Edge Structure of Graphene

In the characterization of defects of graphene, the edges are usually the dominant source of defect-related features in the Raman spectra. There are two symmetrical edge structures, namely armchair and zigzag edges (see Fig. 2.2). The general structure of edges is random but we can treat the general edge as a mixture of zigzag and armchair edges. When we heat a graphene sample to more than 2,000°C in an electron microscope in the presence of the electron beam, the armchair and zigzag edge structures become increasingly dominant and especially the zigzag edges are observed predominately at the highest heat treatment temperatures [23]. In such samples, the more general chiral edges tend to break up into small segments of zigzag and chiral edges [24, 25]. Characterization of the edge structure by Raman spectroscopy and the related theory is discussed in Sect. 2.3.

2.1.3 The Multiple-Resonance Raman Scattering Process

Both the D band and the D' band are double-resonance processes, as briefly described below, except that the D band involves an intervalley scattering process from the K point to the K' point in the Brillouin zone, whereas the D' band is

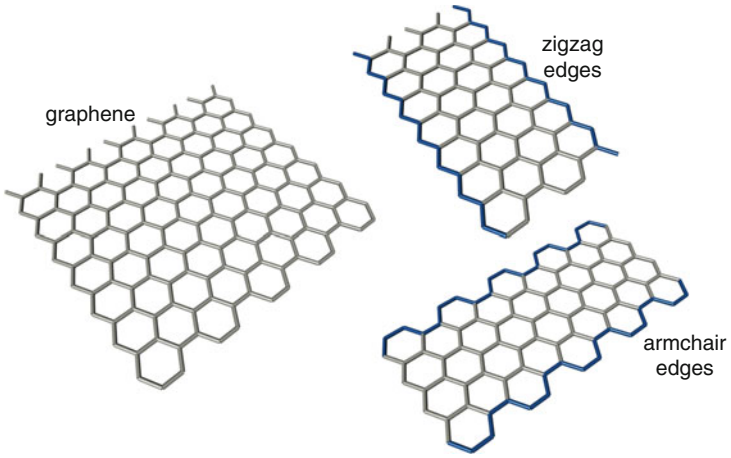

Fig. 2.2 Zigzag and armchair edges in monolayer graphene nanoribbons. The geometrical edge structure and the number of atomic rows of carbon atoms normal to the ribbon axis determine the electronic structure and ribbon properties (Images courtesy of M. Hofmann, MIT.)

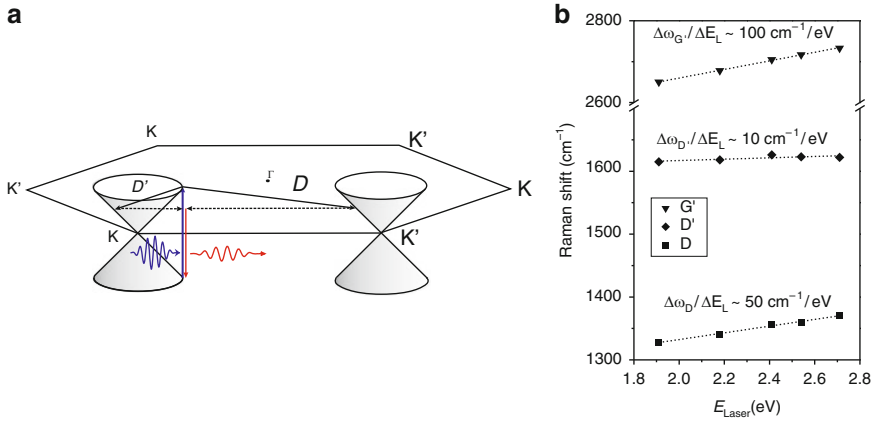

Fig. 2.3 (**a**) Schematics showing the electronic dispersion near the Fermi level at the K and K' points in the hexagonal Brillouin zone of graphene. The light-induced electron–hole formation is indicated by a *blue arrow*. The two resonant electron–phonon scattering processes associated with the D (intervalley) band and the D' (intravalley) band are indicated by *black arrows*. The *dashed arrows* indicate elastic scattering induced by defects. (**b**) Laser energy dependence or dispersion of the frequencies of the D, D', and G' bands which are all dispersive with E_{laser}, but each has a different slope, the smallest slope for the D' band and the largest slope being for the G' band [9]

an intravalley scattering process involving wave vectors q located near the same K point or the same K' point in reciprocal space [see Figs. 2.1b and 2.3a].

Defects in the solid are expressed in terms of an impurity potential $V_{\text{imp}}(q)$ which couples two electron wave functions with the wave vectors k and $k+q$ to each other. Thus the wave vector k is no longer a good quantum number of an electron, which

implies that phonons in the interior of the Brillouin zone ($q \neq 0$) can contribute to the Raman spectra as a higher-order Raman process. This is the origin of disorder-induced Raman spectra. On the other hand, when we consider the multiple-resonance Raman scattering process, phonons with specific $q \neq 0$ can be observed. The intensities of the D band and the D' band $I(\omega, E_{\text{laser}})$ in sp^2 carbons are all enhanced by the double-resonance processes described in Fig. 2.3a [16, 22] (the G' band has a similar process, replacing the electron-defect scattering (dashed line) by another electron-phonon scattering process (solid line)). This resonance produces strong coupling between real electronic states. More specifically, the denominators in the expression for the resonance Raman intensity (or cross section) become small by introducing two real states in the resonance denominators of $I(\omega, E_{\text{laser}})$ which are given in (2.1) [11]:

$$I(\omega, E_{\text{laser}}) = \sum_i \left| \sum_{a,b,c,\omega_{\text{ph}}} \frac{M_{\text{op}}(k, ic) M_{\text{d}}(-q, cb) M_{\text{ep}}(q, ba) M_{\text{op}}(k, ai)}{\Delta E_{ai} (\Delta E_{ai} - \hbar\omega_{\text{ph}})(\Delta E_{bi} - \hbar\omega_{\text{ph}})} \right|^2 , \quad (2.1)$$

then the intensity $I(\omega, E_{\text{laser}})$ can become very large. Here ΔE_{ai} in each of the resonance denominators is given by

$$\Delta E_{ai} = (E_{\text{laser}} - (E_a - E_i) - i\gamma_r), \quad (2.2)$$

where γ_r denotes a broadening factor. In (2.1) the subscripts i, a, b, and c, respectively, denote the initial state, the excited state, the first scattered state of an electron by a phonon, and the second scattered state of an electron by a defect. In this double-resonance process, an electron at wave vector k near the K point is first excited to the conduction band state a by a photon absorption process involving the matrix element $M_{\text{op}}(k, ai)$ [see Fig. 2.3 and (2.1)]. Next a phonon scatters the electron from a to b with the wave vector q in a crystal momentum-conserving process involving matrix element $M_{\text{ep}}(q, ba)$, after which the electron at b near the K' point in reciprocal space is elastically scattered by a defect back to c near the K point with the wave vector $-q$ by the matrix element $M_{\text{d}}(-q, cb)$. Finally the excited electron emits a photon and returns to the valence band to complete the D-band process, which is seen to include a phonon emission process and an inelastic defect scattering process. The symbols M_{op}, M_{ep} and M_{d} denote the electron–photon, electron–phonon and electron-defect scattering matrix elements, respectively. In this double-resonance process, two of three factors in the denominator becomes almost zero (double resonance), which enhances the intensity significantly, resulting in a process with an intensity close to that of a first-order process. The phonon scattering process and the defect scattering process can occur in either order, thereby resulting in a broadening of the Raman linewidth. When these processes are resonant as described above, they enhance the scattering amplitude much more than for nonresonant processes, so that the observed Raman spectra are dominated by the double-resonance D and D'-band scattering processes, both processes fulfilling energy and momentum conservation. Momentum conservation in the presence of disorder can thus be satisfied through an elastic scattering process by a defect, represented by dashed arrows in Fig. 2.3a

in addition to the electron–phonon scattering process for the D and D' bands, each of which involves phonons with very different wave vectors, which are known as intervalley and intravalley wave vectors, respectively [22]. In contrast, the G' band only involves two-phonon processes with intervalley wave vectors q and $-q$.

In Fig. 2.3b, the dispersions (or slopes) of the frequencies of the D, D', and G' bands are plotted as a function of E_{laser}, whose dependencies are well explained by the double-resonance model [16, 21, 22]. The slope or dispersion associated with the G' band is about $100\,\text{cm}^{-1}/\text{eV}$ and it is two times larger than the slope of the D band ($50\,\text{cm}^{-1}/\text{eV}$). The D' band also exhibits a weakly dispersive behavior, the slope being $\sim 10\,\text{cm}^{-1}/\text{eV}$ [9].

When we consider the double-resonance Raman scattering processes, the D and D' bands are not the only disorder-induced one-phonon peaks in the Raman spectra for disordered sp^2 materials. Any combination or overtone of the six dispersive phonon energy branches in sp^2 carbons can occur and disorder-induced Raman frequencies can be related to any of the six phonon branches of graphene with the appropriate wave vector which fulfills the double-resonance condition and with nonzero electron–phonon matrix elements [16]. The intravalley and intervalley double-resonance processes involve phonons near the Γ and K (or K') points, respectively, and we can vary both the resonant wave vector k and q values for electrons and phonons, respectively, by changing E_{laser}, as determined by conservation of energy and momentum requirements [22, 26, 27]. Thus by using electronic band structure information, we can determine the phonon dispersion relations around the K and the Γ points, by considering intervalley and intravalley processes, respectively. This approach has been used for obtaining the graphene phonon dispersion relations (see Fig. 2.1b) using Raman spectroscopy [16, 26].

2.1.4 Concept of the Kohn Anomaly

The Kohn anomaly refers to the softening of phonon frequencies due to electron–phonon coupling and this effect is very important for describing the G band for graphene and metallic carbon nanotubes. According to this effect, a phonon can bring an electron from the valence band to the conduction band, thus creating an electron–hole pair. This process thus renormalizes the phonon energies and lowers the phonon lifetime [28–31]. This phonon effect is dominant near the Γ and K points of the graphene Brillouin zone, thus generating a highly dispersive phonon branch. These phonons are mainly responsible for the G, G', D, and D' band signals, therefore making the Raman spectra from graphene highly sensitive to the Kohn anomaly phenomena. Interestingly, the Kohn anomaly effect can be suppressed by changing the Fermi level, since the electrons or holes that are occupied by doping suppress the electron–phonon interaction, causing a strong dependence of the G-band frequency upon doping (see Sect. 2.4 for details).

This effect is specially interesting in carbon nanotubes [32]. The fundamental difference between metallic carbon nanotubes and semiconducting nanotubes is

the presence of a band gap in semiconducting nanotubes and the absence of a band gap in metallic nanotubes, as well as the carrier concentration in metallic nanotubes at the Fermi energy, leading to a greater importance of the electron–phonon interaction as a phonon scattering process. In practice, the Kohn anomaly is important in modifying the phonon dispersion for metallic nanotubes near the Γ and K (K') points in the Brillouin zone, resulting in both a substantial lowering (by tens of cm^{-1}) of the LO phonon frequency relative to the TO phonon frequency and a broadening in the LO phonon Raman linewidths.

2.1.5 Introduction to Near-Field Raman Spectroscopy

Before ending this introductory section, we mention a technique that has strong potential to provide information about local effects in nanostructures, i.e., the near-field technique. Raman spectroscopy will become an even more powerful tool to characterize disorder in sp^2 materials when we learn how to relate specific defects to their corresponding disordering processes and how to obtain quantitative information about the amount of each type of lattice defect. Some important progress has been achieved in this area, as discussed in this chapter, but substantial achievements will come from single-defect spectroscopy. In this sense, near-field Raman spectroscopy is important in providing more spectroscopic information at a smaller length scale Δx than the diffraction limit of $\lambda_{\text{laser}}/2$, where λ_{laser} is the wavelength of the laser. Near-field Raman spectra of sp^2 carbons, such as SWNTs and graphene, have been taken with the help of a sharp tip which enhances the near-field signal [10] and allows detection of localized defects on a length scale of 30 nm or smaller when looking at G-band or D-band spectra. Of particular interest would be the study of localized defect features in the vicinity of graphene edges, ion-implanted defects [14], and dopant atom impurities [8]. In the world of sp^2 carbons, near-field Raman spectroscopy has been highly informative for high spatial resolution studies of one-dimensional carbon nanotubes, and high expectations are in place for the use of near-field Raman spectroscopy to study edges and defects in graphene (see further details in Sect. 2.5).

2.2 Characterization of Defects

Accurate defect quantification has been a hard task in the field of sp^2 carbons. To achieve a really accurate quantitative description of defect phenomena, Raman spectroscopy has to be combined with microscopy experiments of the structure. Transmission electron microscopy (TEM) or scanning tunneling microscopy (STM) can characterize structural disorder of the crystal in r-space by probing the local surface density of electronic states, with atomic level resolution. Simultaneous in situ TEM and Raman measurements are, in principle, possible. However, a special experimental setup and special sample preparation methods would be needed

for such an experiment. Usually, STM and Raman spectroscopy cannot be easily correlated with each other, since optical spectroscopy probes a volume that is limited by the light penetration depth, while STM is mostly sensitive to surfaces. In this context, the possibility of exfoliating graphite to pull out a single graphene sheet provides an ideal situation in which microscopy and spectroscopy can be correlated to probe disorder effects in both r-space and k-space for the same sample. We describe here some early examples of such work.

There are two different major classes of defects in sp^2 carbon systems that have been largely used to study the Raman signature of disorder. One can be said to have point (or zero-dimensional) defects, and this is the case of the point defects produced by ion bombardment. The other system is composed of small graphitic crystallites, where the disorder is actually related mostly to the graphite borders or edges and, therefore, this disorder relates to a one-dimensional defect. This difference in the "dimensionality" of the defect causes differences in the defect behaviors, as discussed below.

2.2.1 Point Defects Induced by Ion Bombardment

There are different ways of introducing point defects in a crystalline lattice, but the use of ion implantation to study defects in graphite is a well-established technique [12]. These experiments are normally carried out as a function of ion dose and for different ion species and different ion energies. Low mass ions at low ion fluence introduce point defects. Increasing the ion dose causes an increasing density of point defects and eventually causes the damaged regions to overlap as discussed for ion-bombarded HOPG and graphene [8, 12, 14, 33, 34]. The work on graphite brings in the complicated aspect of ion damage depending on penetration depth and cascade effects. Cascade effects are effects whereby a scattered C atom with a large amount of energy hits and perturbs another C atom iteratively, similar to the chain reaction of dominoes.

Raman spectroscopy of monolayer graphene, which is intentionally damaged by Ar^+ ion bombardment, is normally performed so that the energy of the ion is kept low to avoid cascade effects [14, 33]. The ion doses range from very low, so that only a few lattice atoms are perturbed, up to ion doses so high as to come close to full lattice disorder. More specifically for Ar^+ ions this corresponds to ion doses varying from 10^{11} to $10^{15} Ar^+/cm^2$, which correspond, respectively, to one defect per 4×10^4 C atoms for the lower limit and to the onset of full disorder in graphene for the upper limit. The defect density in real space was monitored by STM (scanning tunneling microscopy) images which allowed the extraction of the defect density or alternatively values of the average distances between defects [14].

In Fig. 2.4a we show the Raman spectra of a graphene monolayer subjected to different ion bombardment intensities. From Fig. 2.4a it is clear that the Raman spectra for graphene, mildly disordered graphene, and very highly disordered graphene (close to amorphization) are distinctly different from one another. From the pristine sample (bottom spectrum) to the lowest bombardment dose in Fig. 2.4a

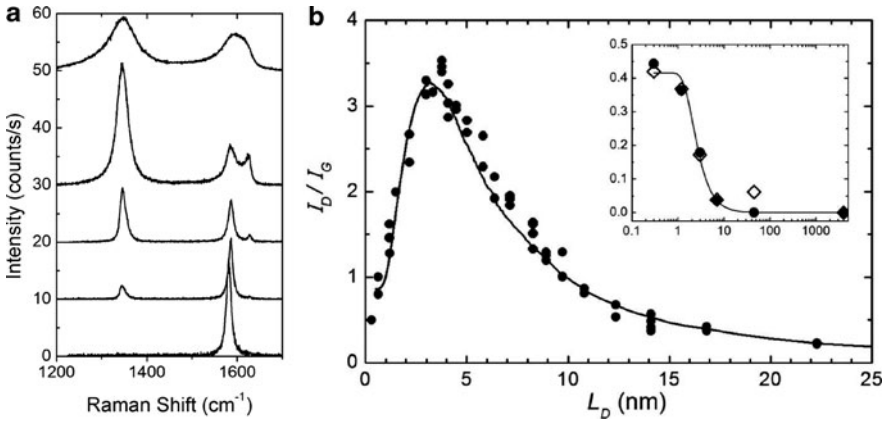

Fig. 2.4 (**a**) Evolution of the first-order Raman spectra (using a $\lambda = 514\,\text{nm}$ laser (2.41 eV)) taken from a graphene monolayer sample deposited on an SiO_2 substrate, subjected to Ar^+ ion bombardment. The ion doses are from the bottom to the top, 10^{10}, 10^{11}, 10^{12}, 10^{13}, and 10^{14} Ar^+/cm^2 [14]. (**b**) The I_D/I_G data points from three different monolayer graphene samples as a function of the average distance L_D between defects. The *solid line* is a modeling of the experimental data using (2.3). The *inset* shows a plot of I_D/I_G vs. L_D on a log scale for L_D for two samples: (i) *open points* for a ∼50-layer graphene sample and *solid circles* are for a small piece of HOPG near a graphene piece. (ii) *solid diamond points*, for a 2 mm-thick bulk HOPG sample, whose measured values are here scaled by $(I_D/I_G) \times 3.5$ [14]

(10^{11} Ar^+/cm^2), the D-band process is activated, showing a very small intensity relative to the G peak (I_D/I_G). Within the bombardment dose range 10^{11}–10^{13} Ar^+/cm^2, the intensities of the disorder-induced peaks increase in intensity. The second disorder-induced peak around $\sim 1,620\,\text{cm}^{-1}$ (the D′ band) also becomes evident within this bombardment dose range. However, above 10^{13} Ar^+/cm^2, the graphene Raman spectra start to broaden significantly and end up exhibiting a profile similar to the graphene phonon density of states (PDOS) for the highest ion dose of 10^{14} Ar^+/cm^2 [14].

In Fig. 2.4b we plot the I_D/I_G ratio as a function of the average distance between defects L_D, through which we can quantify the degree of disorder. As seen in this figure, the I_D/I_G ratio has a nonmonotonic dependence on L_D, increasing initially with increasing L_D up to $L_D \sim 3\,\text{nm}$, where I_D/I_G in Fig. 2.4b has a peak value, and then decreasing for $L_D > 3\,\text{nm}$. Such a behavior suggests the existence of two disorder-induced competing mechanisms contributing to the Raman D-band intensity, which we describe next.

2.2.2 *Model for the D-Band Activated Region*

To explain the I_D/I_G dependence on L_D, the so-called D-band activation model in Fig. 2.5 was proposed [14]. This model assumes that a single impact of an ion on the

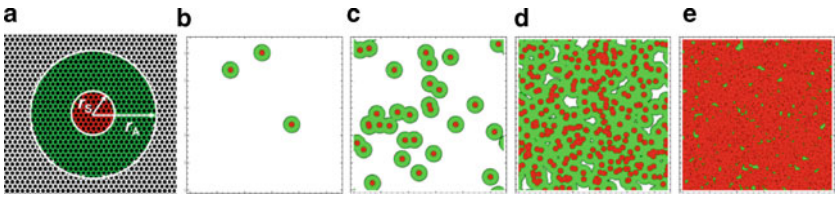

Fig. 2.5 (**a**) Definition of the "activated" A-region (*green*) and "structurally disordered" S-region (*red*). The radii are measured from the ion impact point which is chosen randomly in our simulation. (**b–e**) shows 55 nm×55 nm portions of the graphene simulation cell, with snapshots of the structural evolution of the graphene sheet for different defect concentrations: (**b**) 10^{11} Ar^+/cm^2; (**c**) 10^{12} Ar^+/cm^2; (**d**) 10^{13} Ar^+/cm^2; (**e**) 10^{14} Ar^+/cm^2, like the spectra in Fig. 2.4a [14]

graphene sheet causes modifications on two length scales, here denoted by r_A and r_S (with $r_A > r_S$), which are, respectively, the radii of two circular areas measured from the ion impact point (see Fig. 2.5). Within the shorter radius r_S, a structurally disordered S-region occurs relative to the point of impact. For distances larger than r_S but shorter than r_A, the lattice structure is preserved, but the Raman D band is activated. We call this the activated or A-region. In qualitative terms, an electron–hole excitation will only be able to "see" the structural defect if the electron–hole pair is created sufficiently close to the defect site and if the excited electron (or hole) lives long enough for the defective region to be probed by Raman spectroscopy.

For understanding this model, stochastic simulations were performed for each disorder level shown in Fig. 2.5b–e [14]. Snapshots of each disorder concentration are shown in Fig. 2.5b–e for the same argon ion concentrations as in Fig. 2.4a. In the stochastic simulations of the bombardment process, we randomly chose the impact points for the ions, combined with (2.3) and we select the parameters $r_A = 3\,\text{nm}$ and $r_S = 1\,\text{nm}$, which give the full line curve in Fig. 2.4b. The calculated result is in excellent agreement with the experimental results (points) in this figure [14]. The length scale $r_S = 1\,\text{nm}$, which defines the structurally disordered area, is in excellent agreement with the average size of the disordered structures seen in the STM images. This parameter should, however, not be universal, but it should be specific to the bombardment process, the ion bombardment conditions, and the specific ions used for the ion bombardment [14]. The Raman relaxation length ℓ for the defect-induced resonant Raman scattering in graphene for $E_{\text{laser}} = 2.41\,\text{eV}$ (514 nm) is here defined as $\ell = r_A - r_S = 2\,\text{nm}$.

It is important to have an equation relating I_D/I_G to L_D. Such an equation can be obtained by solving the rate equations for the bombardment process. The entire regime ($0 < L_D < \infty$) can be fitted using

$$\frac{I_D}{I_G} = C_A \frac{r_A^2 - r_S^2}{r_A^2 - 2r_S^2}\left[\exp\left(\frac{-\pi r_S^2}{L_D^2}\right) - \exp\left(\frac{-\pi(r_A^2 - r_S^2)}{L_D^2}\right)\right] + C_S\left[1 - \exp\left(\frac{-\pi r_S^2}{L_D^2}\right)\right], \tag{2.3}$$

where the fitted parameters are $C_A = (4.2 \pm 0.1)$, $C_S = (0.87 \pm 0.05)$, $r_A = (3.00 \pm 0.03)$ nm and $r_S = (1.00 \pm 0.04)$ nm [14]. The C_A parameter is a measure of the maximum possible value of the I_D/I_G ratio in graphene, which would occur in a hypothetical situation in which K–K′ wave vector mixing would be allowed everywhere, but no damage would be made to the hexagonal network of carbon atoms. C_A should then be defined by the electron–phonon matrix elements, and the value $C_A = 4.2$ is then in rough agreement with the ratio between the electron–phonon coupling for the iTO phonons evaluated between the Γ and K points in the Brillouin zone [35]. The C_S parameter is then the value of the I_D/I_G ratio in the highly disordered limit, which has not yet been addressed theoretically. For large values of L_D ($L_D > 6$ nm), a much simpler formula can be used, i.e., $I_D/I_G = A/L_D^2$, where $A = (102 \pm 2)$ nm^2 fit the data.

This model has been extended to account also for the evolution of the D'- and G'-band intensities [33]. Ferreira et al. [33] also described carefully the evolution of the frequencies, intensities, and full-width at half maximum intensity for all the observed peaks in the Raman spectra of graphene, as a function of ion induced disordering and the number of graphene layers. Finally, I_D/I_G depends also on the excitation laser energy (E_{laser}). The results given here apply for $E_{\text{laser}} = 2.41$ eV, and the E_{laser} dependence will be discussed in the next section.

2.2.3 Line Defects at the Edges of Nanographene

Now we turn into the other class of defects, i.e., the one-dimensional defects represented by the graphene borders or edges. By scanning the focused laser light of an optical microscope on a graphite nanocrystallite or graphene, we can observe Raman signals as a function of position, using a technique for known as confocal Raman imaging. The G-band intensity is uniform over the whole graphene surface, while the D-band intensity is localized where the crystalline structure is not perfect, mostly at the edges of the crystallite. We therefore expect to see elastic scattering events at the edges which contribute to the D-band intensity [36, 38]. Notice also that the D-band intensity varies from edge to edge, and this D-band intensity is dependent on the light polarization direction and on the atomic structure at the edge, as discussed later in this chapter.

As pointed in the introduction, the intensity ratio of the D band to the G band, I_D/I_G, is frequently used for the evaluation of crystallite dimensions L_a [2, 40]. The model described for point defects in Sect. 2.2.2 also applies to the edges after several additional effects are taken into account [8]. When we consider a square of crystallite size L_a, the intensity of the G band will vary as $I_G \propto L_a^2$. The intensity of the D band will, however, depend on the width δ of the "border" (of around 2–3 nm) where the D band is activated by the symmetry-breaking border, and this intensity is given by $I_D \propto L_a^2 - (L_a - 2\delta)^2$ consistent with the findings in Sect. 2.2.2. Therefore, for $L_a > 2\delta$, the intensity ratio will then be given by

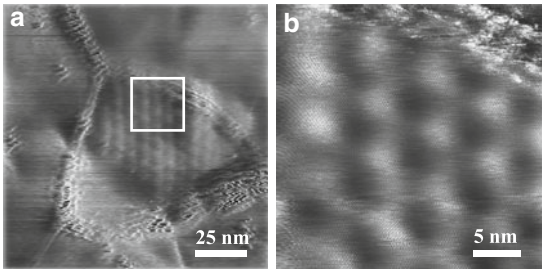

Fig. 2.6 Scanning tunneling microscopy (STM) images with atomic resolution obtained from the surface of a nanographite crystallite of a sample with $L_a = 65$ nm. (**a**) A Moire pattern at the crystallite surface is observed. (**b**) Magnification of the region delineated by the *white square* in part (**a**) [39]

$$\frac{I_D}{I_G} = \alpha \left[4 \left(\frac{\delta}{L_\mathrm{a}} - \frac{\delta^2}{L_\mathrm{a}^2} \right) \right], \tag{2.4}$$

where the scaling factor α is dependent on the appropriate matrix elements [8].

When we take the limit $L_\mathrm{a} \gg \delta$, where the crystallite size is large compared to the heavy damage range, (2.4) can be simplified to yield the Tuinstra–Koenig relation [2]

$$\frac{I_D}{I_G} = C(E_\mathrm{laser})/L_\mathrm{a}, \tag{2.5}$$

in which the value of the empirical constant $C(E_\mathrm{laser})$ depends on E_laser. One could then expect that, once the relaxation length and matrix element ratio were measured for the D-band scattering in ion-bombarded graphene (Sect. 2.2.2), these values could just be used to obtain α and δ. However, the relaxation length and matrix element ratio depend on the structurally disordered area (S-region) shown in Fig. 2.5, which is not well defined for nano-graphite. Figure 2.6 shows two scanning tunneling microscopy (STM) images with atomic resolution obtained from the surface of a crystallite in a nanographite sample with $L_a \simeq 65$ nm. The atomic arrangement of the carbon atoms observed in these images indicates that the samples are formed by nanographitic crystallites, with a disordered grain boundary between crystallites [39]. Variability associated with grain boundaries such as in Fig. 2.6 may also be responsible for the different I_D/I_G vs. L_a results obtained by different research groups, as reported in the literature. However, I_D/I_G also depends on E_laser, the laser excitation energy.

This important fact that the constant $C(E_\mathrm{laser})$ depends on E_laser is known since 1984 [13], but $C(E_\mathrm{laser})$ has been quantitatively determined only more recently [40], using experimental results from nanographites with different L_a values prepared from diamond-like carbon (DLC) films heat treated at different temperatures T_htt [40]. In Fig. 2.7a Raman spectra for the $T_\mathrm{htt} = 2{,}000$°C sample ($L_a = 35$ nm) for five different E_laser values are shown. The spectra are normalized to the G-band intensity, and clearly the ratio (I_D/I_G) increases with decreasing E_laser. To clarify

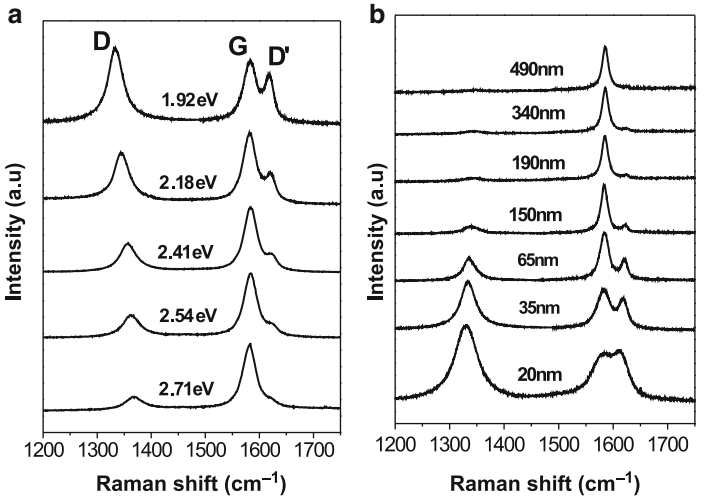

Fig. 2.7 The Raman spectra of (**a**) a nanographite sample heat treated at 2,000°C ($L_a = 35$ nm), for five different laser excitation energies (1.92 eV, 2.18 eV, 2.41 eV, 2.54 eV, and 2.71 eV). (**b**) Nanographite samples with different crystallite sizes L_a using 1.92 eV laser excitation energy [40]

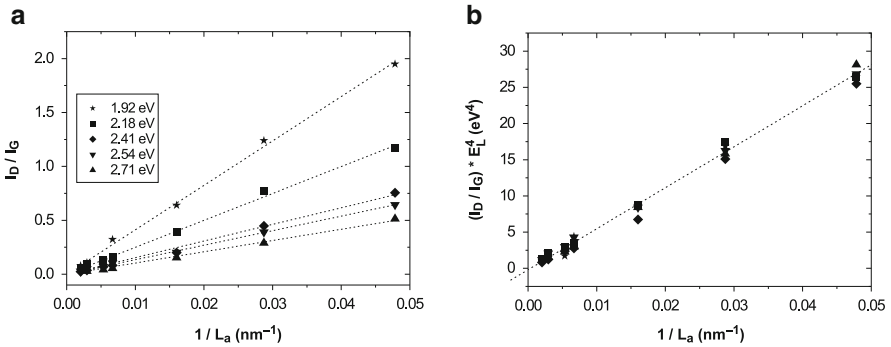

Fig. 2.8 (**a**) The intensity ratio I_D/I_G for nanographite samples is plotted vs. $1/L_a$ using five different laser excitation energies (see text). (**b**) All curves shown in part (**a**) collapse onto the same curve in the $(I_D/I_G)E_L^4$ vs. $(1/L_a)$ plot where E_L denotes the laser excitation energy [40]

this point, we show in Fig. 2.7b, the Raman spectra for different crystallite sizes L_a using the same excitation laser energy $E_{laser} = 1.92$ eV [40], where the L_a sizes were determined by using both STM and X-ray measurements. These L_a values were thus correlated with the I_D/I_G intensity ratios measured at different laser energies leading to a general equation for determining L_a as a function of both the laser excitation energy and the (I_D/I_G) intensity ratio [40].

Figure 2.8a shows a plot of (I_D/I_G) vs. $1/L_a$ for all samples shown in Fig. 2.7. It is clear in Fig. 2.8b that I_D/I_G for a given sample can be scaled by E_{laser} as

$(I_D/I_G)E^4_{\text{laser}}$ vs. L_a. From this relation we can estimate L_a using any laser line in the visible range [40]:

$$L_a(\text{nm}) = \frac{560}{E^4_{\text{laser}}}\left(\frac{I_D}{I_G}\right)^{-1} = (2.4\times 10^{-10})\lambda^4_{\text{laser}}\left(\frac{I_D}{I_G}\right)^{-1}, \tag{2.6}$$

where the laser excitation energy is given in terms of both E_{laser} (eV) and the corresponding wavelength λ_{laser} (nm). This behavior is consistent with D-band intensity calculations [36]. A similar analysis has also been made for carbon foams [41]. In the literature, the (I_D/I_G) ratio is often reported at 2.41 eV, where the I_D/I_G ratio is relatively low in comparison to spectra taken at lower values of energy. Finally, the E^4_{laser} dependence applies also to point defects in graphene, as discussed in detail in Ref. [42].

2.3 Characterization of Edges

As discussed in Sect. 2.1.2, finite size graphene can have two high symmetry edge structures which are known as zigzag and armchair edges [43]. Unlike single wall carbon nanotubes where no edge structures exist along the walls of the nanotubes, experiments show that armchair and zigzag edges of heat-treated graphene nanoribbons are stable and dominant [23]. Here we discuss how to characterize the edge structures of graphene by Raman spectroscopy.

2.3.1 Overview of Graphene Edges

The electron and phonon states exhibit edge-specific properties for armchair or zigzag edges of graphene nanoribbons which can be observed by Raman spectroscopy. A graphene nanoribbon is defined as a one-dimensional graphene strip with edges at both sides and with a fixed width whose structure is specified by a vector in the direction of the ribbon width, similar to the chiral vector of single wall carbon nanotubes [43, 44]. A graphene nanoribbon is obtained either by (1) unrolling nanotubes by heating [45,46], (2) by cutting a graphene sheet by electron-beam lithography [47], or by (3) heating nanodiamond [24, 37].

In the case of the zigzag edge, localized electron states which are called edge states appear and form a flat energy band at the Fermi energy from the K point to the M point in the two-dimensional Brillouin zone [43, 44]. Since the edge states are partially occupied by π electrons, the magnetic properties of edge states show ferromagnetic behavior because of the exchange interaction between spins in the flat energy band structure [48]. Another important fact about the edge state is that the amplitude of the wave function has a large value only on one of the two sublattices of graphene. This fact enhances the electron–phonon interaction [49, 50] only near the zigzag edge. The fact that the wave function has a large value only on one sublattice

corresponds to the pseudospin polarized state of graphene [50]. Here the pseudospin of graphene is defined by the two component wave function of π electrons [51]. Using this fact, possible superconductivity may appear at these edges [52,53]. Igami et al. discussed the possible phonon edge states of graphene nanoribbons with zigzag edges [54]. Similar edge phonon modes are observed at the tube edges in a single wall carbon nanotube (SWNT) with finite length [55].

For the armchair edges of nanoribbons, double-resonance theory (see Sect. 2.1.3) tells us that the D band is strong for the armchair edges since the scattering at the armchair edge corresponds to the intervalley scattering which is relevant to the D-band Raman intensity, while the scattering at the zigzag edge corresponds to intravalley scattering and is very weak [38]. Further, edge-localized phonon modes are observed for thin graphene nanoribbons [56]. Combined with the phonon-softening phenomena of the G band (see Sect. 2.4), the polarization dependence of the Raman signal characterizes the signal of the LO and TO phonon modes for the G band [57], and we can use these polarization techniques to characterize and to distinguish between the different edge structures by Raman spectroscopy. Hereafter we discuss each subject one by one.

2.3.2 *The Characterization of Graphene Edges from Their D-Band Scattering*

In nanographitic samples formed by aggregates of small crystallites, the crystallite borders form defects in real space. Since the crystallites have different sizes and their boundaries are randomly oriented, the defect wave vectors exhibit all possible directions and values. Therefore, the existence of a defect with momentum exactly opposite to the phonon momentum is always possible, giving rise to double-resonance processes [16, 21] connecting any pair of points (electron wave vectors) around the K and K' points in the first Brillouin zone of graphite or graphene. In this case, the intensity of the D band is isotropic and does not depend on the light polarization direction. However, in the case of edges, the D-band intensity is anisotropic because the double-resonance process cannot occur for any arbitrary pair of k points [38]. Since, in real space, the edge defect is well localized in the direction perpendicular to the edge, so that this defect is completely delocalized in this direction in reciprocal space and, therefore, the wave vector of such a defect assumes all possible values perpendicular to the edge. Hence, the defect associated with an edge has a one-dimensional character and it is only able to transfer momentum in the direction perpendicular to the edge.

Here we show that the disorder-induced D band obtained from graphene edges provides useful information about the atomic structure of these edges. The D-band scattering is strongly anisotropic and depends on the orientation of the carbon hexagons with respect to the edge, in the armchair or zigzag arrangements [38]. This anisotropy can be used to define the local degree of order of the atomic structure at the edge. The physics leading to this structurally selective effect is explained on

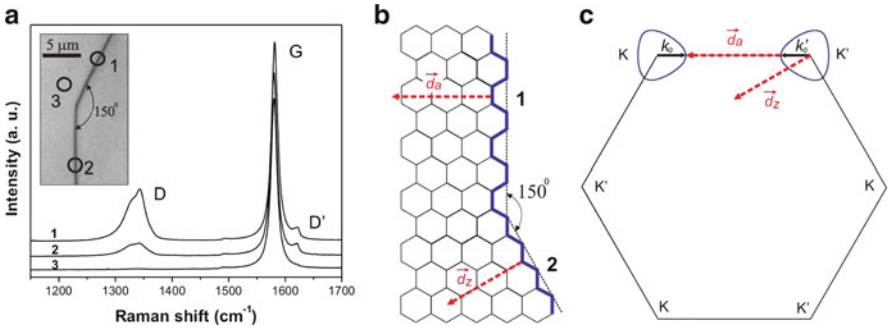

Fig. 2.9 (**a**) Raman spectra at different regions of a highly oriented pyrolytic graphite (HOPG) sample. The *inset* shows an optical image of the sample. Regions 1 and 2 are at HOPG edges, while region 3 is on the flat HOPG surface. (**b**) Idealized structure of the edges shown in the *inset* to part (**a**). The *bold lines* highlight the edge structures, armchair for edge 1 and zigzag for edge 2. The wave vectors of the defects associated with these edges are represented by $\boldsymbol{d}_a$ for armchair and $\boldsymbol{d}_z$ for the zigzag edges. (**c**) The first Brillouin zone of graphene oriented according to the lattice in the real space shown in part (**b**). Note that only the armchair $\boldsymbol{d}_a$ vector is able to connect points belonging to equienergy contours surrounding two inequivalent K and K' points (Adapted from Ref. [38].)

the basis of the well-established double-resonance effect [16, 21] applied to a semi-infinite crystal bounded by a one-dimensional defect.

In Fig. 2.9a, we show three Raman spectra at three different regions of a highly oriented pyrolytic graphite (HOPG) sample [38]. The inset to Fig. 2.9a shows an optical image of the sample. Regions 1 and 2 are at HOPG step edges, while region 3 is taken at an interior point of the HOPG sample. In all spectra, the light propagation is perpendicular to the HOPG basal plane and the polarization of the incident light is parallel to the edge direction in spectra 1 and 2. The G band (centered at approximately 1,580 cm^{-1}) is present in all spectra with the same intensity. The Raman features at approximately 1,340 and 1,620 cm^{-1} are the disorder-induced D and D' bands, respectively. The disorder-induced D and D' bands are observed in spectra 1 and 2, but not in spectrum 3, since spectrum 3 was taken at an interior region of the HOPG with a crystalline order (see inset to Fig. 2.9a). As shown in Fig. 2.9a, the D band is about four times less intense in spectrum 2 compared to spectrum 1, whereas the D'-band intensity remains almost constant for both spectra. The different intensities observed for the D band in spectra 1 and 2 indicate that the D-band intensity depends on the structure of the edges.

High resolution STM images of the edges revealed that edge 1 shown in Fig. 2.9a has an armchair structure, whereas edge 2 has a zigzag structure. To clarify this picture, Fig. 2.9b shows the idealized structure of the edges [38]. The bold blue lines highlight the edge structures, armchair for edge 1 and zigzag for edge 2. The wave vectors of the defects associated with these edges are represented by $\boldsymbol{d}_a$ for armchair and $\boldsymbol{d}_z$ for the zigzag edge. Figure 2.9c shows the first Brillouin zone of graphene oriented according to the lattice in the real space shown in Fig. 2.9b. Note

that only the armchair $\boldsymbol{d}_a$ vector is able to connect points belonging to equienergy contours surrounding two inequivalent K and K' points. An important fact is the change of the wave vector by scattering at the zigzag edges d_z does not connect K and K' points but instead connects K and K or $K'$and K', which means intravalley scattering is occurring. This means that the intervalley double-resonance process associated with this defect cannot occur for a zigzag edge, thereby explaining why the D band is much less intense in the spectra obtained in zigzag edge 2. On the other hand, the D' band is given by an intravalley process, which connects points belonging to the same equienergy contour around the K (or K') point [16]. In this case, momentum conservation can be satisfied by both $\boldsymbol{d}_a$ and $\boldsymbol{d}_z$ vectors[3] and, therefore, the observation of the D' band must be independent of the edge structure though the relative intensity might be different. This conclusion is confirmed by the experimental result shown in Fig. 2.9a, where the D′ band has a similar intensity in both spectra 1 and 2, with armchair and zigzag structures, respectively. It is important to note the observation of a weak D band in spectrum 2, where it should be absent. This weak D band is related to the actual atomic structure of the edge, allowing the scattering of the electron by phonons and defects with wave vectors not perpendicular to the edge. Similar measurements performed on different closely related armchair and zigzag graphene edges also show different D-band intensity ratios, indicating different degrees of disorder for the local atomic arrangement at the different edges [58–60].

We now turn our attention to the dependence of the D-band scattering intensity on the polarization of the incident light relative to the edge direction. Figure 2.10a shows the topographic image of a single graphene layer on a glass substrate. Figure 2.10b–d shows the corresponding Raman intensity images showing the G, G' and D-band intensities, respectively. Notice that the G-band intensity is roughly uniform along the graphene surface. A similar situation occurs for the G' band, which is the overtone of the D band but does not require a disorder-induced process to become Raman active, since momentum conservation is guaranteed in two-phonon Raman processes occurring for the G' band [16]. On the other hand, the D band can be detected only near the graphene edges. Figure 2.10e shows Raman scattering spectra acquired at two different locations (indicated in Fig. 2.10a). The upper spectrum was acquired near the edge of the graphene layer whereas the lower spectrum was recorded $\approx$ 1 μm from the edge. The D band appears only in the spectrum acquired near the edge, indicating that the graphene sheet is essentially free of structural defects. The Raman scattering spectra also reveal that the G' band is composed of a single peak, which confirms that the sample is a *single* monolayer graphene sheet [62]. All confocal Raman images shown in Fig. 2.10b–d were recorded with the polarization vector $\boldsymbol{P}$ of the excitation laser beam oriented parallel to the graphene edge (y direction in Fig. 2.10b). Notice that the D-band intensity associated with the top edge in Fig. 2.10d is weaker than that obtained from the side edges, as we explain below.

[3] It is noted that $\boldsymbol{d}_a$ connects two k points on a constant energy contour.

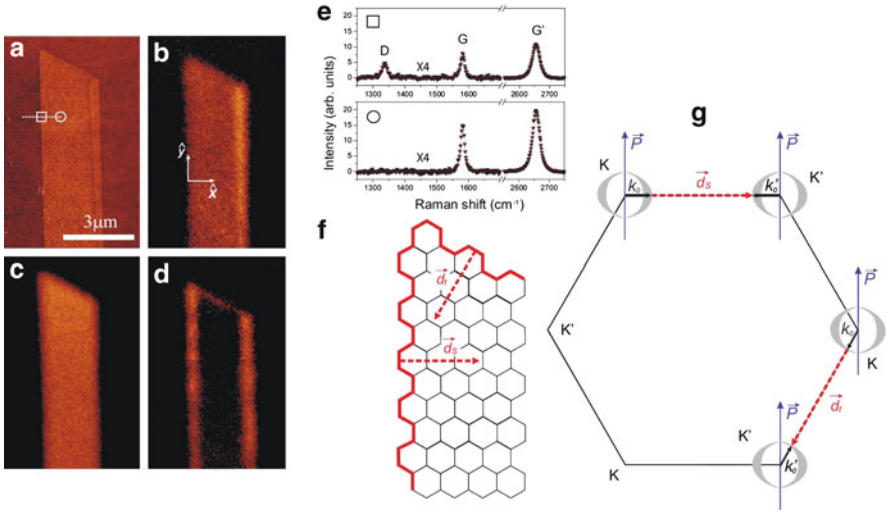

Fig. 2.10 (**a**) Topographic image of a single graphene layer on a glass substrate. (**b**)–(**d**) Corresponding Raman intensity images showing the G-, G'- and D-band intensities, respectively. (**e**) Raman scattering spectra acquired at two different locations of the graphene layer shown in part (**a**). The upper spectrum was acquired near the edge of the graphene layer [position indicated by the *white square* in panel (**a**)] whereas the lower spectrum was recorded $\approx 1\,\mu$m from the edge [position indicated by the *white circle* in panel (**a**)]. (**f**) The idealized structure of the edges of the graphene layer shown in panel (**a**). The wave vectors of the defects associated with these edges are represented by $\boldsymbol{d}_s$ for the left side edge and $\boldsymbol{d}_t$ for the top edge. Notice that both edges have the same symmetry, which based on the strong D-band scattering intensity from the side edges, we suppose to be armchair. (**g**) The first Brillouin zone of graphene oriented according to the lattice in real space shown in part (**f**). $\boldsymbol{P}$ is the polarization vector of the incident light according to the experiment that is responsible for the images shown in parts (**b**)–(**d**). The thickness of the gray region around the K and K' points illustrates the anisotropy in the optical absorption relative to $\boldsymbol{P}$. Note that the light absorption (emission) has a maximum for electrons with wave vectors perpendicular to $\boldsymbol{P}$, and it is null for electrons with wave vectors parallel to $\boldsymbol{P}$

In 2003, Grüneis et al. predicted an anisotropy in the optical absorption coefficient of graphene given by $W_{\text{abs}} \propto |\boldsymbol{P} \times \boldsymbol{k}|^2$, where $\boldsymbol{P}$ is the polarization of the incident (scattered) light for the absorption process, and $\boldsymbol{k}$ is the wave vector of the electron measured from the K or K' point [63]. The thickness of the gray region around the K and K' points at the corners of the first Brillouin zone of graphene shown in Fig. 2.10g illustrates this anisotropy in the optical absorption relative to the vector $\boldsymbol{P}$. Note that the light absorption has a maximum efficiency for electrons with wave vectors perpendicular to $\boldsymbol{P}$, and the efficiency is null for electrons with wave vectors parallel to $\boldsymbol{P}$. A singularity in the density of phonons that participates in the one-dimensional double-resonance intervalley process gives rise to the D band. This singularity in the phonon density of states [63] restricts the wave vector of the electron to the direction perpendicular to the armchair edge ($\boldsymbol{k}_0$ and $\boldsymbol{k}'_0$ in Fig. 2.10g). However, as pointed out before, such electrons will only absorb light efficiently if the polarization vector of the incident light is perpendicular to the

electron wave vector, and therefore a strong double-resonance process will occur only if the polarization vector of the incident light is parallel to the edge. As shown in Fig. 2.10g, this is the case for D-band scattering that originates from the side edges of the graphene piece shown in Fig. 2.10a, which generate defects whose wave vector $\boldsymbol{d}_s$ (see dashed arrow in Fig. 2.10f) connects electron wave vectors $\boldsymbol{k}_0$ and $\boldsymbol{k}'_0$ that are located at maxima in the light absorption efficiency around the K and K' points, respectively. On the other hand, the top edge in Fig. 2.10a generates defects whose wave vectors $\boldsymbol{d}_t$ (see dashed arrow in Fig. 2.10f) connect electron wave vectors $\boldsymbol{k}_0$ and $\boldsymbol{k}'_0$ which are located near nodes in the light absorption efficiency around the K and K' points, respectively (see Fig. 2.10g). This is the reason why the intensity of the D-band signal obtained from the top edge in Fig. 2.10d (forming a relative angle of $\sim 60°$ with $\boldsymbol{P}$) is weaker than that obtained from the side edges. Notice that if the incident light polarization vector is perpendicular to the edge, the D-band Raman scattering cannot be observed even for armchair edges [38, 58, 59].

2.3.3 *Mode assignments of the Raman Spectra of Graphene Nanoribbons*

Next we discuss Raman-active phonon modes of graphene ribbons within nonresonance Raman theory [64]. In the case of graphene, since we always satisfy the resonance condition for Raman spectra, the relative Raman intensity is directly determined by the Raman tensor. Thus a nonresonance Raman calculation can give reasonably reliable information. In Fig. 2.11, we show the unit cell of a graphene ribbon with (a) armchair and (b) zigzag edges. The graphene ribbons lie in the xy plane in which the edges (or the 1D periodicity direction) lie along the x direction,

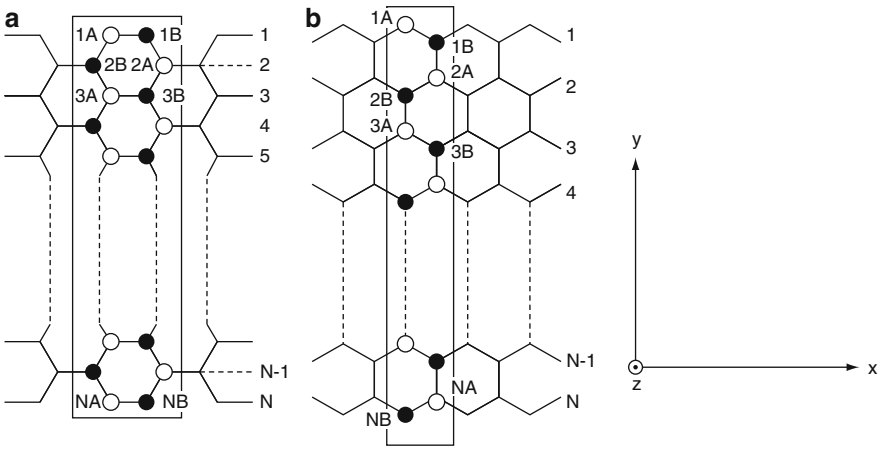

Fig. 2.11 The unit cell of an (**a**) armchair and (**b**) zigzag nanoribbon. The graphene ribbon lies in the xy plane and the edge (periodic) direction is along x [64]

which is also called the quantum confinement direction. The direction of the incident and scattered light is selected as the z (y) direction for the XX, XY, and YY (ZZ) polarizations. Here we should mention that the in-plane and out-of-plane bond polarizabilities need not be the same, which has been shown for boron nitride BN [65]. Thus we cannot always compare the Raman intensities for ZZ and the in-plane polarization, but we can discuss the relative intensities within the ZZ configuration.

The ribbon width N is defined from the number of C–C lines parallel to the ribbon direction, and the corresponding numbers of carbon atoms in the unit cell of the armchair and zigzag nanoribbons are $2N$ for both cases (see Fig. 2.11). Here, we consider, for simplicity, only N = odd for armchair (zigzag) nanoribbons in which the corresponding point group symmetry is D_{2h} (C_{2v}). The case N = even for armchair (zigzag) nanoribbons corresponds to C_{2v} (D_{2h}) symmetry. Further, in the special case of the zigzag nanoribbons with N = half integer, a different type of edge (the so-called the Klein edge) appears [48]. As far as we discuss edge phonons, we did not find any odd–even dependence of N on the phonon properties.

The scattering geometry is specified by the symbols $iISs$ ($i, s = x, y, z$ and $I, S = X, Y, Z$) in which i and s (I and S) denote propagating (polarization) directions of the incident and scattered light, respectively. In bond polarization theory, we cannot specify the propagating direction but we can only specify the polarization direction, because the electromagnetic wave propagations i and I (or s and S) should be perpendicular to each other. Here we consider the following four back-scattering geometries $zXX\bar{z}$, $zXY\bar{z}$, $zYY\bar{z}$, and $yZZ\bar{y}$ in which the overlines $\bar{z}$ and $\bar{y}$ refer to the negative z and negative y directions, respectively.

The Raman-active modes belong to irreducible representations of the D_{2h} point group: (A_g, x^2, y^2, z^2), (B_{1g}, xy), (B_{2g}, xz), and (B_{3g}, yz); C_{2v}: (A_1, x^2, y^2, z^2), (A_2, xy), (B_1, xz), (B_2, yz). In particular, for the scattering geometries $zXX\bar{z}$ and $zYY\bar{z}$, the A_g (A_1) mode is Raman active, while for $zXY\bar{z}$ and $zYX\bar{z}$, the B_{1g} (A_2) mode is Raman active for D_{2h} (C_{2v}).

In Fig. 2.12, calculated results of the Raman spectra are shown for four different geometries of the polarization directions. Here RBLM (RBLM3), EDGE, LO and TO denote, respectively, the radial breathing-like phonon mode (its third harmonic), the edge phonon modes, the longitudinal optical and the in-plane transverse optical phonon modes, whose vibration amplitudes are illustrated in Fig. 2.13. It is noted that the out-of-plane optical phonon mode is not a Raman-active mode. The LO, RBLM (RBM3), and edge modes belong to A_g symmetry, while the TO belongs to B_{1g} (xy) symmetry, which are all Raman active. The TO and LO modes are related to the Raman G band of sp^2 carbon materials whose vibrational amplitudes are perpendicular and parallel, respectively, to the armchair edge and are homogeneous in the interior region of the nanoribbon. In the RBLM, the ribbon width is vibrating, which is similar to the radial breathing mode of a single wall carbon nanotube [65]. The RBLM mode appears at relatively lower ($300\,\mathrm{cm}^{-1}$) frequency regions and the frequency is inversely proportional to the ribbon width. In the experimental situation, the observation of the RBLM is possible only when a fixed ribbon width is made. Further we should consider the interaction of the nano ribbon with the substrate which modifies the RBLM frequency.

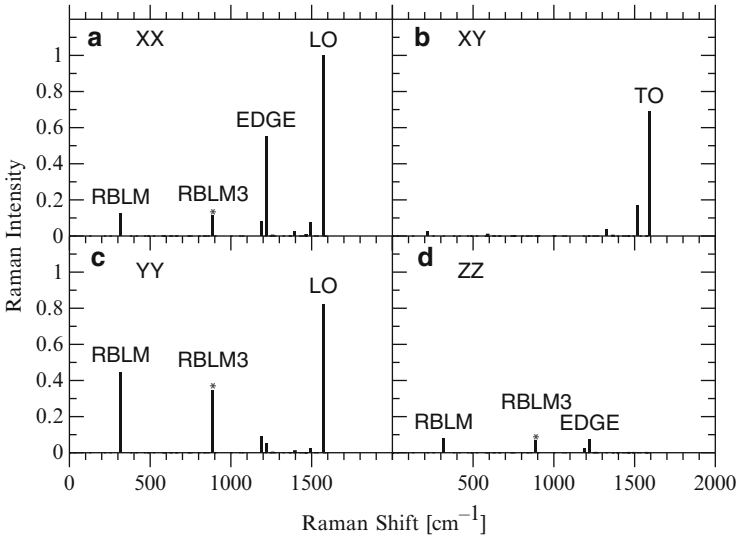

Fig. 2.12 The nonresonance Raman spectra of an $N = 9$ armchair nanoribbon for the scattering geometries of (**a**) $zXX\bar{z}$, (**b**) $zXY\bar{z}$, (**c**) $zYY\bar{z}$, and (**d**) $yZZ\bar{y}$. The Raman intensity is normalized to the one for the largest Raman signal for the four geometries shown [64]

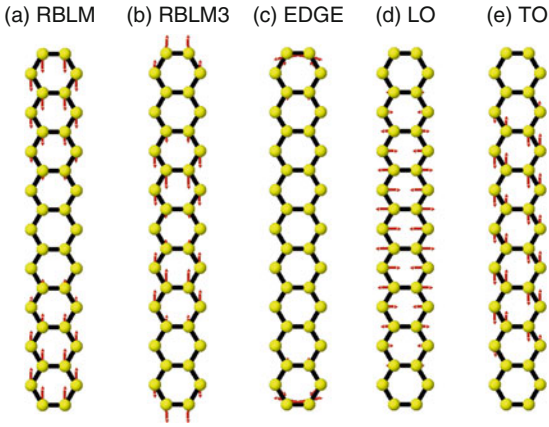

Fig. 2.13 Phonon eigenvectors of an $N = 19$ armchair nanoribbon for (**a**) RBLM, (**b**) RBLM3, (**c**) EDGE (**d**) LO, and (**e**) TO phonon modes [64]

The frequencies of the edge phonon modes are around 1,250 cm^{-1} if we used the force constant set for sp^2 carbon. However, around the armchair edges without any termination, the C–C bond at the edge becomes triple bonds and thus the calculated edge phonon frequency by first principles calculations becomes relatively high (around 2,200 cm^{-1}). When the dangling bond is terminated by H atoms, then the edge phonon modes of armchair edges are downshifted to 1,530 cm^{-1}, which is consistent with the recent Raman measurements on very thin nanographene ribbons [58]. The amplitude of the edge phonon mode is localized only near the armchair edge and its vibrating direction is parallel to the edge. Thus, the Raman intensity

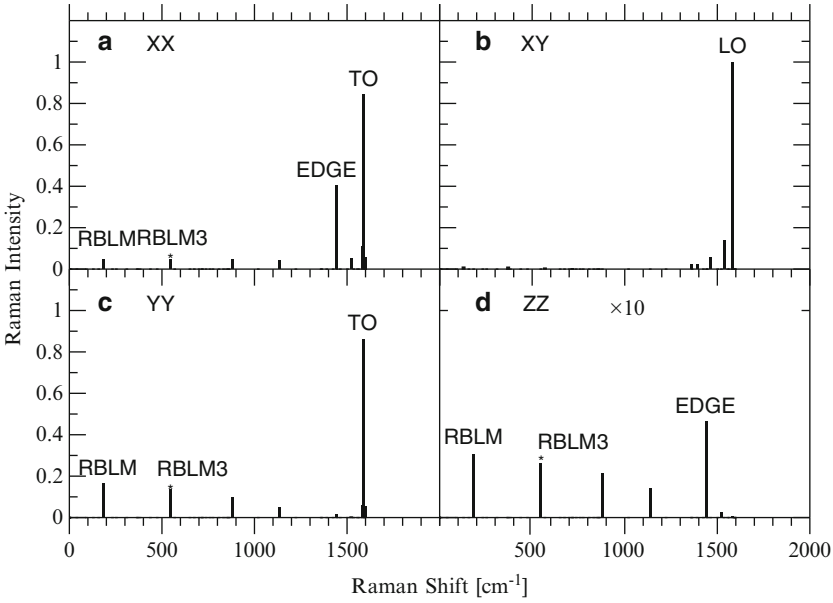

Fig. 2.14 The nonresonance Raman spectra of an $N = 9$ zigzag nanoribbon for the scattering geometries of (**a**) $zXX\bar{z}$, (**b**) $zXY\bar{z}$, (**c**) $zYY\bar{z}$, and (**d**) $yZZ\bar{y}$. The Raman intensity in each spectrum is normalized to the one for the largest Raman signal for the four indicated scattering geometries. The ZZ signals in (**d**) are 10 times enlarged relative to the other geometries [64]

for the edge mode is large for the XX polarization geometry compared with the YY geometry. The TO phonon modes have a large Raman intensity for the XY geometry since TO belongs to B_{1g} symmetry. The RBLM mode has a significant Raman intensity for all XX, YY, and ZZ geometries which are common to A_g symmetry modes [66, 67].

In the ZZ geometry, the G-band modes (TO and LO) disappear and only weak signals of RBLM (RBLM3) and edge phonon modes can be seen. A relatively strong peak at 889 cm^{-1}, which can be seen also in the XX and YY geometries, belongs to a higher frequency RBLM mode with three nodes of vibration (RBLM3). Although the wavelength of the three node mode is one third of the fundamental RBLM (317 cm^{-1}), the corresponding phonon frequency (880 cm^{-1}) is slightly smaller than three times RBLM. This is because the longitudinal acoustic phonon energy dispersion deviates from a linear energy dispersion near the zone boundary region of the Brillouin zone.

In Fig. 2.14, the Raman intensity for an $N = 9$ zigzag nanoribbon is plotted for the scattering geometries of (a) $zXX\bar{z}$, (b) $zXY\bar{z}$, (c) $zYY\bar{z}$, and (d) $yZZ\bar{y}$ [64]. The Raman signal for the ZZ geometry is 10 times enlarged relative to that for the XX, XY, and YY geometries. The vibrational directions of the RBLM, RBLM3, EDGE, TO, and LO phonon modes are illustrated in Fig. 2.15. In the case of zigzag nanotubes, the TO, RBLM (RBLM3), and edge modes belong to A_1 symmetry while

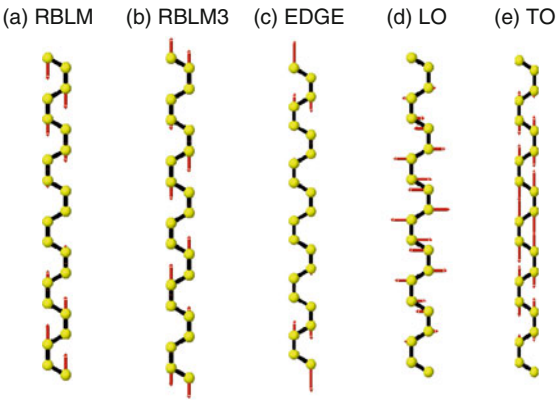

Fig. 2.15 Phonon eigenvectors of an $N = 11$ zigzag nanoribbon for (**a**) RBLM, (**b**) RBLM3, (**c**) Edge, (**d**) LO, and (**e**) TO phonon modes [64]

the LO mode belongs to A_2 symmetry. Thus the TO, RBLM, (RBLM3) and edge phonon modes can be seen in the XX, YY, and ZZ geometries, while the LO phonon mode can be seen in the XY geometry. Generally we cannot distinguish between LO and TO phonon modes from these experiments. However, we will show in the following section that only LO phonon modes show phonon-softening phenomena (the Kohn anomaly in Sect. 2.4) and in this way we can assign LO and TO for graphene edges [69].

The vibrational direction of the edge states for a zigzag nanoribbon is perpendicular to the zigzag edge direction, while that for the armchair nanoribbon is parallel to the armchair edge. This difference of the vibrational direction can be enhanced by terminating the dangling bond by some other heavy element, such as an F atoms. The edge phonon frequency of the zigzag edge is around 1,450 cm^{-1}, which is consistent with previous calculations [68] and experiments [56]. Two intermediate frequency spectra show higher RBLM modes with five and seven nodes.

2.3.4 *Polarization Dependence of the Raman Intensity*

To discuss the Raman intensity as a function of the polarization dependence and the edge dependence, we need to calculate the electron-optical transition amplitude. In Fig. 2.16, the square of calculated optical matrix elements $|M^{\mathrm{opt}}(\mathbf{A})|^2$ for the electromagnetic interaction of an electron in an optical field which depends on both the vector potential $\mathbf{A}$ and the direction of the polarization of the laser light H, is plotted as a function of the angle Θ relative to the edge of the nanoribbon [69].

Here, $\Theta = 0$ corresponds to the polarization of $\mathbf{A}$ (or electric field) being parallel to the edge. In this case, the amplitude $M^{\mathrm{opt}}(\mathbf{A})$ (or the dipole vector in reference [63]) is given by [69]

$$M^{\mathrm{opt}}(\mathbf{A}) = \langle \Psi_{\mathbf{k}}^{\mathrm{c}} | H_{\mathrm{K}}^{\mathrm{em}} | \Psi_{\mathbf{k}}^{\mathrm{v}} \rangle, \tag{2.7}$$

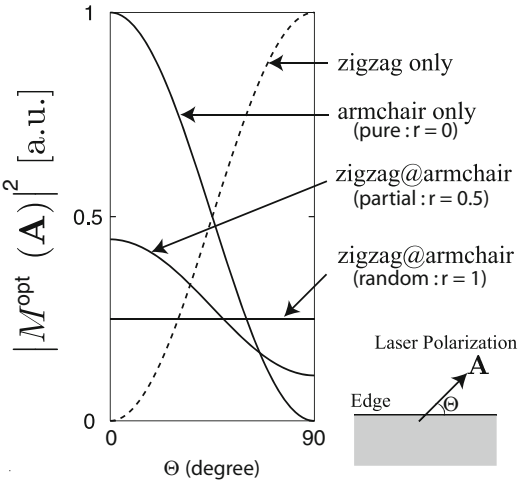

Fig. 2.16 The polarization dependence of the square of the optical transition amplitude ($|M^{\text{opt}}(\mathbf{A})|^2$) is plotted as a function of the angle of laser polarization (Θ) with respect to the orientation of the edge. For a pure zigzag (armchair) edge, as shown by the *dotted* (*solid*) line at the top) the intensity is a maximum when the laser polarization is perpendicular (parallel) to the edge. "zigzag@armchair" denotes the case when a small fraction of zigzag edges is introduced into part of a perfect armchair edge. Here the parameter of r means randomness with $r = 0$ (armchair only), $r = 0.5$ (partial), and $r = 1$ (random: a mixture of zigzag and armchair edges) [69]

where $\Psi^{\text{v}}_{\mathbf{k}}(\mathbf{r})$ is the wave function in the valence energy band, which is related to that in the conduction energy band $\Psi^{\text{c}}_{\mathbf{k}}(\mathbf{r})$ via $\Psi^{\text{v}}_{\mathbf{k}}(\mathbf{r}) = \sigma_z \Psi^{\text{c}}_{\mathbf{k}}(\mathbf{r})$ and $H^{\text{em}}_{\text{K}} = -v_{\text{F}} e\sigma \cdot \mathbf{A}$. Here the vector potential $\mathbf{A}$ enters the perturbation Hamiltonian of the optical dipole transition H^{em}_{K} and v_{F} and σ are, respectively, the Fermi velocity of graphene and the Pauli matrix which operates on the wave functions at the edges [69]. Using the wave functions at zigzag and armchair edges which consist of incident and reflecting waves at each edge, we can obtain the polarization (Θ) dependence of $M^{\text{opt}}(\mathbf{A})$.

In the case of pure zigzag edges (dotted line at the top of Fig. 2.16), the Raman intensity is proportional to $|M^{\text{opt}}(\mathbf{A})|^2 \propto \sin^2\Theta$, while for the pure armchair edges (solid line), $|M^{\text{opt}}(\mathbf{A})|^2 \propto \cos^2\Theta$. In the case of a general graphene ribbon, the edge consists of short segments of zigzag and armchair edges. Here we introduce a randomness factor r into the components of zigzag edges in the armchair edges (zigzag@armchair) in which $r = 0$ corresponds to the pure armchair edges and $r = 1$ is a completely random mixture of zigzag and armchair edges. In Fig. 2.16, we show $|M^{\text{opt}}(\mathbf{A})|^2$ vs. Θ for three different r values. It is clear that there is no angle Θ dependence for $r = 1$, since in this case the dependence would be the sum of $\cos^2\Theta + \sin^2\Theta$ which is unity. In an actual measurement of this polarization dependence, we can get results for intermediate polarization dependencies such as $r = 0.5$, which is consistent with recent experiments [70, 71].

For distinguishing between LO and TO phonon modes, the phonon softening effects observed for the LO mode in graphene (the Kohn anomaly) can be used.

Table 2.1 Dependencies of the Raman intensities and Kohn anomalies on the Γ point optical phonon modes. The symbols ◯ and × for the Raman intensity and the Kohn anomaly represent "occurrence" and "absence," respectively. There is asymmetry between the Raman intensity and the Kohn anomaly; that is, the Kohn anomaly occurs only for the LO mode, while the mode with a strong Raman intensity changes according to the edge shape. The Raman intensity is enhanced when the polarization of the incident laser light is parallel (LO) to the armchair edge or when it is perpendicular (TO) to the zigzag edge [69]

Position	Mode	Raman	Kohn	Polarization
Zigzag	LO	×	◯	×
	TO	◯	×	◯
Armchair	LO	◯	◯	◯
	TO	×	×	×
Bulk	LO	◯	◯	◯
	TO	◯	◯	◯

Depending on the intravalley and intervalley scattering at the armchair or zigzag edges, the occurrence of the Kohn anomaly shows clear edge differences. In Table 2.1, we show a list of the expected Raman signal, the occurrence of the Kohn anomaly, and the polarization effect for zigzag edges, armchair edges, and the interior region of graphene. The detailed derivation of this calculation is discussed in [69]. From Table 2.1, if we get a G-band signal without phonon softening, we can say that the Raman spectra comes from the TO phonon modes at zigzag edges, while the phonon softening (around 30 cm^{-1}) that occurs in the Raman spectra comes from the LO phonon modes at armchair edges. These pure phonon mode behaviors are predicted for a spatial graphene sample with two edges that differ by an angle of 30° between them [57].

2.4 The Fermi Energy Dependence: The Kohn Anomaly

Next we discuss the effect of doping on the G band of single-layer graphene in Sect. 2.4.1, and the corresponding effect of doping on the G band of double-layer graphene is explicitly considered in Sect. 2.4.2.

2.4.1 Effect of Gate Doping on the G-Band of Single-Layer Graphene

In Fig. 2.17, the G-band spectra of single-layer graphene as a function of gate voltage is shown [72]. For achieving high doping levels, electrochemical doping is often used. The G-band frequency is upshifted ((a) and (b)) and the spectral width decreases (see (c)) by doping, as predicted by time-dependent perturbation theory in which the phonon frequency downshifts as a result of the electron–phonon interaction. This effect is known as the Kohn anomaly [28, 29, 57, 73]. In the

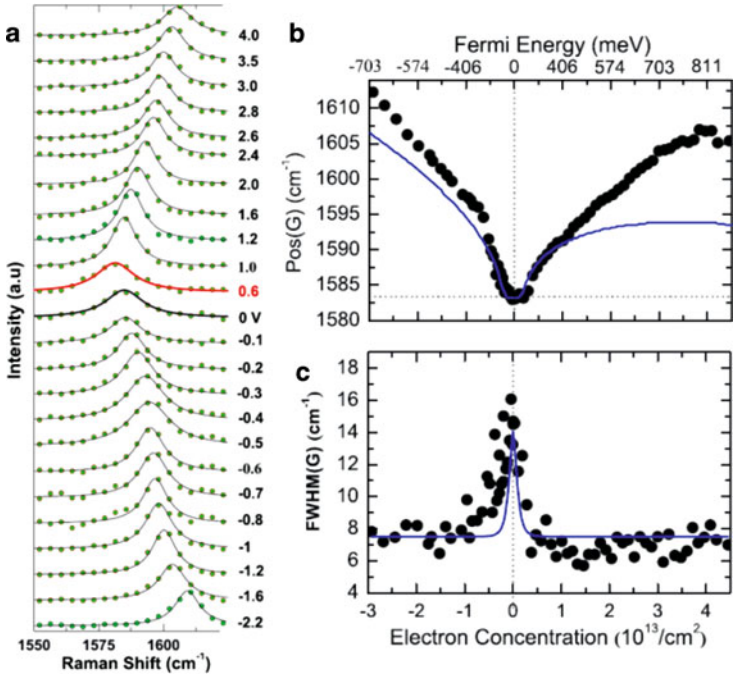

Fig. 2.17 The Raman G peak of doped monolayer graphene. (**a**) The G-band spectra observed at 295 K for many values of the gate voltage V_g. The redish spectrum corresponds to the undoped case. (**b**) The G peak position (frequency) and (**c**) the linewidth as a function of Fermi energy and electron concentration are deduced from the applied gate voltage data. *Black circles*: measurements; *solid line*: finite-temperature non-adiabatic calculation (Adapted from [72].)

electron–phonon interaction, an electron–hole pair is virtually excited by a phonon near the Fermi energy. The gate voltage dependence of the Raman frequency in Fig. 2.17 comes from the fact that either the initial (or final) states for electron–hole pair excitation becomes empty (or occupied) for hole (electron) doping and that the corresponding perturbation processes are suppressed. The lower (higher) energy excitation of the electron–hole pair below (above) $\hbar\omega_G/2$, where ω_G is the G-band phonon frequency, contributes to phonon hardening (softening). Thus the phonon softening becomes a maximum when the Fermi energy is located at $\hbar\omega_G/2$ from the Dirac point energy. The two anomalies at $\pm\hbar\omega_G/2$ are not clearly seen in this experiment due to temperature-induced broadening. However, a gate voltage dependence for the G-band frequency ω_G was measured at $T = 12\,\mathrm{K}$ [74], where phonon anomalies at $E_g = \pm\hbar\omega_G/2$ could be clearly distinguished. The 12 K experiment was, however, carried out on bilayer graphene [74], where another interesting effect occurs, as described in Sect. 2.4.2. The broadening of the Raman spectra comes from the shortening of the lifetime of the G-band phonon by the electron–phonon interaction, and thus the broadening should be a maximum around the Dirac point energy, as is confirmed experimentally in Fig. 2.17c.

Using the pseudospin and the field for the pseudospin [50, 51], Sasaki et al. gave an analytic formula for the electron–phonon interaction for the LO and TO phonon modes for carbon nanotubes [32] and graphene [57]. Although we do not here go into detail regarding this theory, this theoretical analysis will be useful for gaining a general understanding of both the Raman spectra and the physical properties of graphene.

2.4.2 *Effect of Gate Doping on the G Band of Double-Layer Graphene*

The gate doping of double-layer graphene in particular has been investigated by many groups. Part of the interest focuses on the fact that double-layer graphene may exhibit an energy gap under the application of an electric field perpendicular to the graphene surface, which can be used to vary the Fermi level. This effect is important for the application of double-layer graphene for semiconductor devices. Thus the characterization of the Raman spectra of gated double-layer graphene has become an important research topic.

In bilayer or double-layer graphene, the unit cell has four C atoms which gives two π and two π^* energy bands at the K point (see Fig. 2.18). In this case, there will be more than two Kohn anomalies in the G band depending on how the two π bands are occupied by doping (see the right-hand side of Fig. 2.18) [72, 74]. When the Fermi energy reaches $\pm\hbar\omega_G/2$, the $\pi-\pi^*$ transition shown in Fig. 2.18(I) is no longer allowed, as it is in single-layer graphene, but the transition from the now filled lowest energy π^* band to the higher energy π^* band, shown in Fig. 2.18(II), is possible. When the gate voltage rises further and reaches the second π^* band, another singular behavior now occurs in the renormalization process, as shown in Fig. 2.18(III). These effects are seen in the G-band frequency and linewidth of bilayer graphene (of Fig. 2.18), where a distinctly different behavior with respect to the monolayer case (see Fig. 2.17) is clearly observed for both the frequency and linewidth. Therefore, when discussing graphene systems above, we see that the renormalization effect changes significantly in going from single to bilayer graphene, and it would change further by increasing the number of layers, although the renormalization effect will become less and less evident with increasing layer number.

In the case of double-layer graphene, the G-band phonon is split into symmetric (S) and antisymmetric (AS) components corresponding to the symmetry between the upper and lower graphene layers, as shown in Fig. 2.19b [75]. An important point is that the electron-hole excitations for the S and AS G-band phonons are different for the two π^* energy bands [75, 76] (see Fig. 2.20). For electron and hole pair creation by a phonon that couples the π_1 and π_1^* energy bands, only the S symmetry component of the G band is coupled by the electron–phonon interaction (Fig. 2.20a), while for hole doping (Fig. 2.20b) both the S and AS (anti-symmetric) G-band phonons are coupled. Thus an asymmetric behavior in the phonon softening effect appears for electron and hole doping, as shown in Fig. 2.19a.

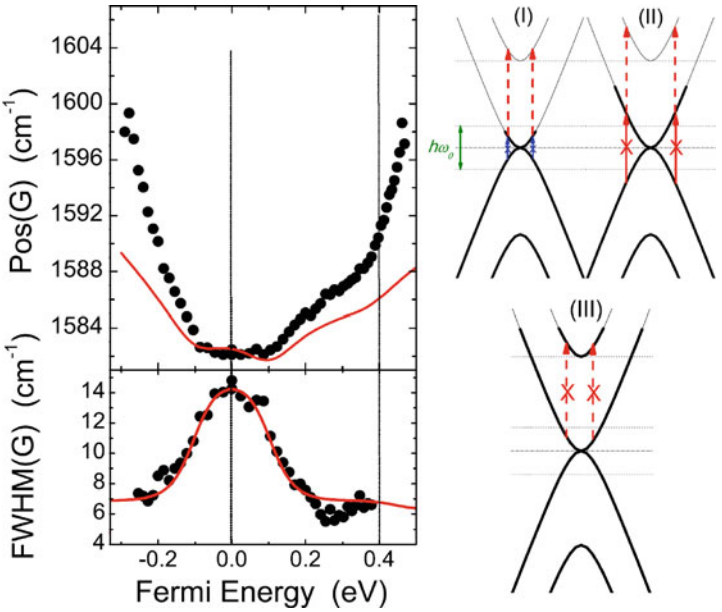

Fig. 2.18 Position of the peak frequency [Pos(G)] and the linewidth [FWHM(G)] measured at full width half maximum intensity for the Raman *G*-band feature of doped bilayer graphene. *Black circles*: measurements; *thin line*: finite-temperature nonadiabatic calculation. On the *right*, schematics of the electron–phonon coupling at three different doping levels, as indicated by the *thicker lines* on the electronic bands (Adapted from [73].)

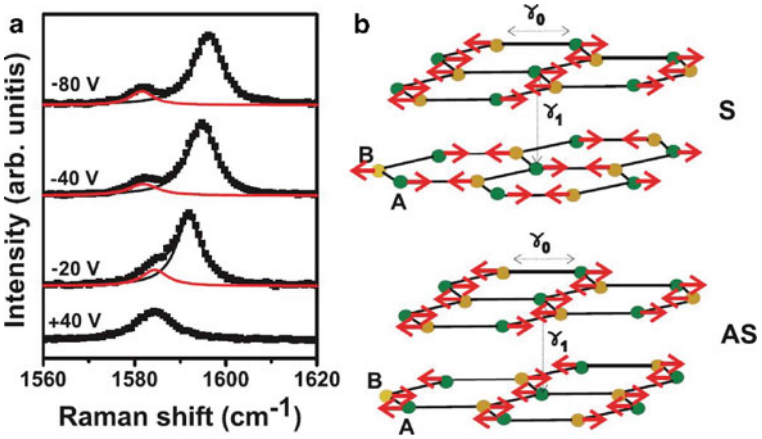

Fig. 2.19 (**a**) Raman *G* band of bilayer graphene for –80 V, –40 V, –20 V and +40 V gate voltages. Two Lorentzian curves (corresponding to the different displacements of the carbon atoms in (**b**)) are needed to fit the *G* band for –80 V, –40 V, and –20 V. (**B**) displacement of the atoms for the S and AS symmetry phonon modes in bilayer graphene [75]

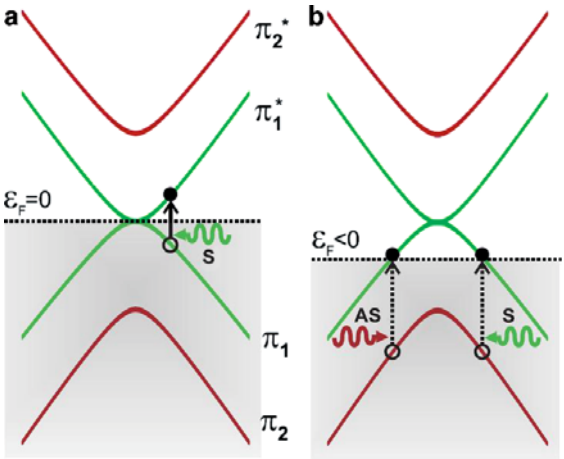

Fig. 2.20 Parabolic band structure of bilayer graphene near the K point where the Fermi level is indicated by the *dotted horizontal line*. The *vertical arrows* illustrate the possible transitions induced by symmetric (*green*) and antisymmetric (*red*) $q \neq 0$ phonons for (**a**) interband electron–hole pair creation and (**b**) intraband electron–hole pair creation. The gap opening in bilayer graphene is not considered in this diagram [75]

2.5 Near-Field Raman Spectroscopy

The last subject of this chapter is near-field Raman spectroscopy. The investigation of sp^2 carbons via conventional Raman spectroscopy has usually been limited by the spatial resolution of usual confocal systems. The spatial resolution Δx of a standard optical microscope is limited by diffraction to roughly the Abbé criterion [77]:

$$\Delta x = \frac{0.61\lambda}{\mathrm{NA}}, \tag{2.8}$$

where λ is the wavelength of light and NA is the numerical aperture of the objective lens. Although the NA can be optimized by performing experiments in a medium with a large index of refraction n that surrounds the sample, or by engineering objectives with large collection angles, conventional microscopes can only achieve resolutions on the order of $\lambda/2$ ($\geq$200 nm). As a consequence, the investigation of structural details at the mesoscopic level becomes a difficult task for Raman spectroscopists.

Tip-enhanced near-field Raman spectroscopy (TERS) [78] has, however, provided an alternative way to overcome this barrier by performing spectroscopic imaging with ultrahigh spatial resolution. TERS studies on sp^2 carbons have been limited mostly to carbon nanotubes until now [77,79–87], while strong enhancement effects in two-dimensional systems are unlikely. However, the use of TERS to study disorder in carbon nanotubes, as discussed in this section, has been largely successful. For this reason, we here discuss the basics for the TERS approach in one-dimensional systems, and some interesting results on carbon nanotubes are presented.

2.5.1 The Spatial Resolution in Optical Microscopes

In general, conventional optical systems are not able to collect the whole spectrum of spatial frequencies associated with optical fields generated by a light source located at a distance sufficiently far from the detector (far-field regime). The angular spectrum representation of a scattered electric field E_s in a plane $z = \text{const.}$ far from the light source is given by [77]

$$E_s(x, y, z) = \int \int_{-\infty}^{\infty} \hat{E}_s(k_x, k_y; 0) e^{i(k_x x + k_y y)} e^{\mp i k_z z} dk_x dk_y, \tag{2.9}$$

where k_x, k_y, and k_z are the spatial frequencies related to the Cartesian coordinates x, y, and z, respectively, and $\hat{E}_s(k_x, k_y; 0)$ are the Fourier amplitudes of the electric field at $z = 0$.

The exponential term $e^{\mp i k_z z}$ in (2.9) influences the propagation of the electric field E_s along the z-axis. The k-vector (k_x, k_y, k_z) and the frequency $\omega = 2\pi c/\lambda$ are related by the free-space dispersion relation, and hence k_z is given by [77]

$$k_z = \sqrt{(2\pi n/\lambda)^2 - k_{\parallel}^2}, \tag{2.10}$$

where we have defined $k_{\parallel}^2 = k_x^2 + k_y^2$. According to (2.9) and (2.10), for $k_{\parallel} \leq 2\pi n/\lambda$, the wave vector k_z is a real number. In this case, the electric field E_s propagates along the z-axis oscillating with $e^{\mp i k_z z}$, giving rise to the far-field component of the optical field. On the other hand, if $k_{\parallel} > 2\pi n/\lambda$, the wave vector k_z becomes an imaginary number, and the electric field E_s decays exponentially along the z direction. If the image plane at $z = \text{const.}$ is sufficiently well separated from the source at $z = 0$, the contribution from this decaying part (evanescent waves) will be lost. Therefore, there is always a loss of information between the near-field and the far-field optical limits.

2.5.2 The Principle of TERS

The goal of tip-enhanced Raman spectroscopy (TERS) is to obtain the spectral response from nanoscopic structures with an optical resolution beyond the diffraction limit. For this purpose, a sharp metal tip is placed sufficiently near the sample surface [88,89]. The tip provides a channel through which the near-field components of the scattered light (evanescent waves) become propagating waves in the far zone. In other words, by using a confined source field with a large bandwidth of spatial frequencies, the high spatial frequencies generated by the sample become accessible in the far field, and the spatial resolution is defined by the diameter of the tip apex [78]. However, there is a fundamental issue involved in such an experiment, which is the fact that the signal generated by the near-field and far-field components of the

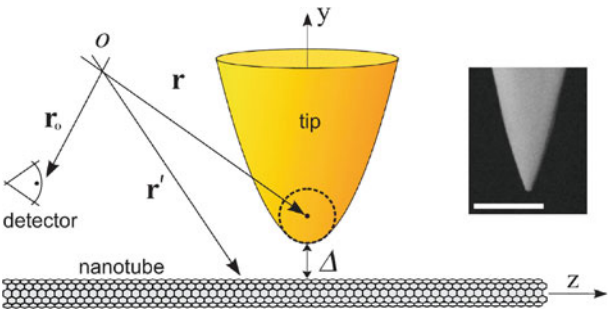

Fig. 2.21 Schematics for the spatially resolved Raman scattering by a carbon nanotube. The position vectors $\mathbf{r}$, $\mathbf{r}'$, and $\mathbf{r}_o$ denote the location of the center of the tip apex, the location of the Raman dipole moment $\mathbf{p}$, and the detector, respectively. The *dashed circumference* represents a small sphere of radius r_{tip} centered at the tip apex, and Δ is the distance between the tip and the nanotube. The *inset* depicts an SEM image of the gold tip used in the experiment, where the scale bar denotes 200 nm [90]

scattered light will be intermixed in the far zone. To solve this issue, the tip might be able to perform its secondary function, which is to enhance the optical fields generated in the near-field regime.

2.5.3 Mechanism of Near-Field Enhancement

This section provides a brief analytical theory for local field enhancement. The theory is given in terms of one-dimensional (1D) systems, which can be directly applied to the well-studied carbon nanotubes [90].

Figure 2.21 shows the experimental configuration and the coordinates used in the theoretical analysis. The electric field $\mathbf{E}$ near the laser-irradiated gold tip is axially symmetric and interacts locally with a single wall carbon nanotube (SWNT) at frequency ω. The induced dipole $\mathbf{p}$ per unit length at the Raman frequency ω_s and at location $\mathbf{r}'$ can be represented as [90]

$$\mathbf{p}(\mathbf{r}', \omega_s) = \boldsymbol{\alpha}^R(\mathbf{r}'; \omega_s, \omega)\, \mathbf{E}_{tot}(\mathbf{r}' - \mathbf{r}; \omega), \tag{2.11}$$

where $\mathbf{r}$ denotes the position of the center of the tip apex, $\boldsymbol{\alpha}^R$ is the Raman polarizability (per unit length), and $\mathbf{E}_{tot}$ is the total electric field interacting with the electron density at $\mathbf{r}'$ in the carbon nanotube.

The analysis that we discuss here applies to one-phonon Raman processes involving vibrations belonging to the totally symmetric A_{1g} irreducible representation which could describe the radial breathing mode (RBM) and the lower and upper components G^- and G^+ of the G band[4]. In this case, the Raman polarizability

[4]The G band in carbon nanotubes splits due to the curvature along the tube circumference.

tensor $\boldsymbol{\alpha}^{\mathrm{R}}$ is written as [90]

$$\boldsymbol{\alpha}_q^{\mathrm{R}} = \begin{bmatrix} \alpha_{\perp,q}^{\mathrm{R}} & 0 & 0 \\ 0 & \alpha_{\perp,q}^{\mathrm{R}} & 0 \\ 0 & 0 & \alpha_{\parallel,q}^{\mathrm{R}} \end{bmatrix}, \quad q \in \{\mathrm{RBM}, \mathrm{G}^+, \mathrm{G}^-\}. \tag{2.12}$$

The field $\mathbf{E}_{\mathrm{tot}}$ in (2.11) is the sum of the external driving field $\mathbf{E}$ and screening fields due to neighboring charges, where the depolarization effect has to be considered. The external driving field $\mathbf{E}$ corresponds to the superposition of the incident laser field $\mathbf{E}_{\mathrm{o}}$ and the localized field generated by the gold tip acting as an optical antenna. Close to the tip apex, the external driving field $\mathbf{E}(\mathbf{r}';\omega)$ resembles the field of an induced dipole $\boldsymbol{\mu}$ located at the center of a small sphere of radius r_{tip} (location $\mathbf{r}$ in Fig. 2.21).

Analysis of the above fields lead to an expression for determining the near-field enhancement as a function of the tip–sample distance Δ. Considering that near-field (NF) and far-field (FF) components are always intermixed, the relative intensity of the scattered signal is given by the sum of these two contributions, i.e., $I/I_{\mathrm{max}} = (I_{\mathrm{FF}} + I_{\mathrm{NF}})/I_{\mathrm{max}}$. Crossterms originating from the interference between the FF and NF components can be neglected. The ratio $I_{\mathrm{max}}/I_{\mathrm{FF}}$ corresponds to the maximum Raman enhancement factor M, which allows us to represent the relative intensity of the scattered signal as [90]

$$\frac{I}{I_{\mathrm{max}}} = \frac{1}{M} + \frac{C}{(\Delta + r_{\mathrm{tip}})^{10}}. \tag{2.13}$$

The M, C, and r_{tip} parameters are to be determined by fitting experimental data, while r_{tip} has to be related to the tip geometry. What is remarkable here is that theory predicts that near-field Raman intensity is inversely proportional to the 10th power of the tip–sample distance, thereby providing a huge enhancement of spatial details [90].

2.5.4 Application to Carbon Nanotubes

Advances in the science of carbon nanotubes generated by tip-enhanced Raman measurements include the detection of local defects, chirality changes, and local dopants [84–87]. The technique of tip-enhanced Raman spectroscopy can be readily applied to study nanostructured features appearing in monolayer or bilayer graphene or at the edges of graphene nanoribbons.

Figure 2.22a shows a large-scale confocal Raman image of a self-organized carbon nanotube serpentine [90, 91]. The contrast (color scale) in the image renders the intensity of the graphitic (C–C stretching) G band ($\sim$1,580 cm^{-1}). Figure 2.22b shows the near-field Raman image corresponding to the G-band intensity acquired in the boxed area in Fig. 2.22a. The resulting resolution of 25 nm is defined by the tip

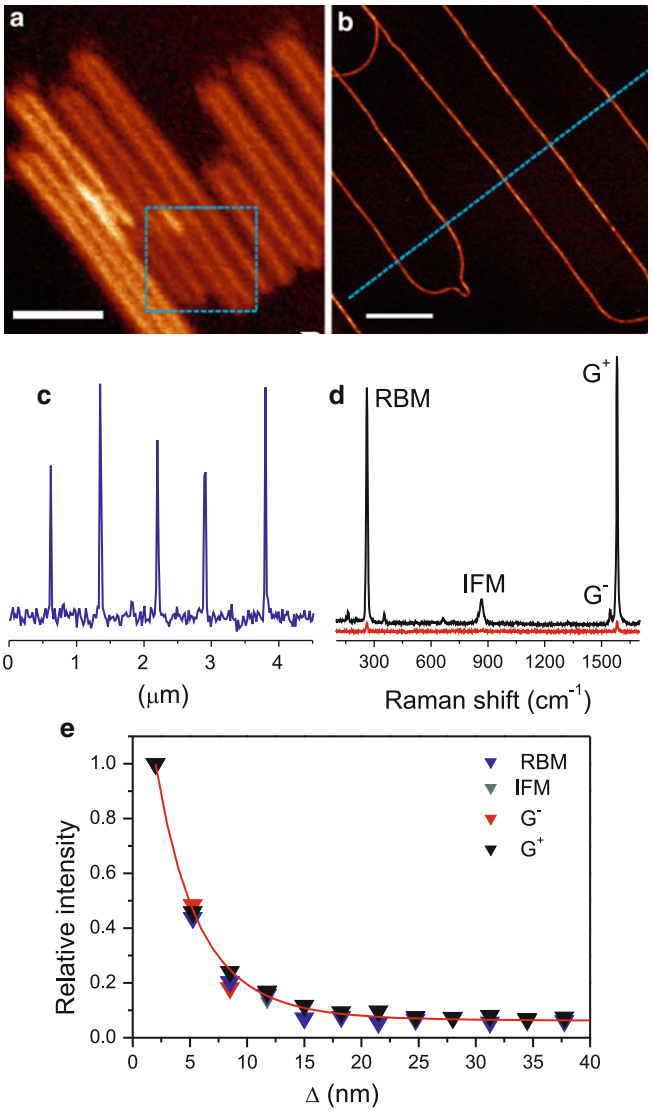

Fig. 2.22 **(a)** Conforcal Raman image corresponding to the G-band intensity of a semiconducting nanotube. The scale bar denotes 6 micrometers. **(b)** Near-field Raman image corresponding to the G-band intensity recorded in the boxed area in (a). The scale bar denote 800 nm. (**c**) Intensity profile obtained along the *dashed line* in panel (**c**). (**d**) Far-field Raman spectrum (*red curve*) and near-field Raman spectrum (*black curve*) recorded at the largest (∼38 nm) and smallest (∼2 nm) tip–sample separation, respectively. (**e**) Approach curves for the intensity of the RBM, IFM, G^- and G^+ phonon bands vs. Δ in Fig. 2.22 [90]

radius. A linecut along the dashed line in image Fig. 2.22b is depicted in Fig. 2.22c. Figure 2.22d shows the corresponding Raman spectra for the smallest (∼2 nm) and largest (∼38 nm) tip–sample separations. The two spectra are offset for clarity. It is evident that near-field imaging not only improves the resolution but also improves the signal-to-noise ratio for the Raman spectra.

The radial breathing mode (RBM) frequency $\omega_{\mathrm{RBM}} = 262\,\mathrm{cm}^{-1}$ identifies the sample as a semiconducting tube whose energy gap for the second $E_{22\mu} \rightarrow E_{22\mu}$ optical transition is in resonance with the incident laser energy. The near-field spectrum also clearly features the intermediate frequency mode (IFM) occurring at $865\,\mathrm{cm}^{-1}$, and the G^- and G^+ peaks occurring at $1{,}545\,\mathrm{cm}^{-1}$ and $1{,}585\,\mathrm{cm}^{-1}$, respectively. Notice that the disorder-induced D band ($\sim 1{,}350\,\mathrm{cm}^{-1}$) is so weak that it cannot be observed, indicating that the serpentine nanotube has a very low defect density. Within the experimental resolution, no differences in the lineshape and resonant frequency of any phonon bands are observed for the far-field and near-field Raman spectra.

Figure 2.22e shows the intensities (integrated areas) of several Raman peaks as a function of the tip–sample separation Δ. All Raman intensities are normalized to the corresponding values at shortest separation ($\Delta \sim 2\,\mathrm{nm}$). The red curve in Fig. 2.22e is a fit to the experimental data according to Eq. (2.13). It can be seen from Fig. 2.22e that the theoretical predictions from [90] are in good agreement with the experimental data. The fitting parameters obtained were $M = 16$, $C = 4.5{\times}10^{15}\,\mathrm{nm}^{10}$, and $r_{\mathrm{tip}} = 35\,\mathrm{nm}$.

2.6 Summary and Perspective

In summary, recent studies on graphene and sp^2 carbons and defects in these systems have significantly advanced our understanding of how Raman spectroscopy can be used to characterize these materials systems. Powerful new experimental techniques such as near-field Raman spectroscopy have become available and have been applied to these materials, and at the same time new theoretical works using the pseudospins of graphene have pushed graphene research in new directions. Especially important also has been the advances in the fabrication and processing of graphene ribbons and their subsequent annealing to form well-defined and stable armchair and zigzag edge structures. Because of the well-defined edge structures that can now be prepared, the theoretical investigation of electron–phonon and electron–photon interactions at the edges can be formulated much better analytically, and theoretical results can now be compared directly with experiments.

Near-field measurements of the Raman spectra of carbon nanotubes have greatly enhanced the spatial resolution which can now be achieved, reaching resolutions much smaller than the wavelength of light. This means that a scanning Raman image can now be directly compared with observations made with other high spatial resolution techniques, such as transmission electron microscopy, scanning probe microscopy (SPM), and x-ray photo emission spectroscopy (XPS) imaging. Since

we now know much more about the physics of the electron–phonon interaction, we can now tune the electron–phonon interaction by varying the Fermi energy. This can be accomplished reliably using electrochemical doping, which now becomes a new parameter that can be varied controllably during Raman spectroscopy experiments. Varying the gate voltage using back gates or top gates or both at once in taking the Raman spectra is now allowing researchers to obtain a better understanding of the Raman spectral width and phonon softening phenomena associated with the Kohn anomaly in both graphene and metallic carbon nanotubes. These techniques are also important for characterizing the Fermi energy position in graphene devices. In the future, we can imagine a possible application of using a Raman signal as a sensor for monitoring the behavior of devices as a function of the gate voltage.

An essential factor in the Raman spectroscopy of carbon nanotubes is the resonance condition for the optical transition energies which can be used to specify the geometrical (n, m) structure of a SWNT through their one-dimensional van Hove singularities. The Raman intensity of SWNTs is determined by how close the optical transition energies are to the laser light energy $\hbar\omega$, while the resonance width in the Raman excitation profile provides an important parameter for observing the Raman signal of a SWNT for a given laser excitation energy even though the Raman intensity (through the exciton–photon and exciton–phonon interactions) is strongly chirality dependent.

On the other hand, in the case of graphene, there are no one-dimensional van Hove singularities for optical transitions except for the case of a very narrow graphene ribbon which would be denoted as a graphene nanoribbon. Such graphene nanoribbons can be considered as a one-dimensional system with properties somewhat analogous to a carbon nanotube except that the graphene nanoribbon has edges which have interesting properties as described elsewhere [25]. The effective resonance condition of an infinite graphene sheet is satisfied for any value of the laser excitation energy. Thus, although the Raman signal of single layer graphene is not as strong as that for SWNTs, we can always get a Raman signal for any number of layers of graphene and for any laser energy that promotes an electron from an occupied state to an empty state. In this sense, the relative Raman intensity depends not on the resonance condition but primarily on the Raman tensor and the electron–phonon interaction. Since the electron–phonon interaction is known to be anisotropic in k space, especially around the K point in the two dimensional Brillouin zone, the analysis of this anisotropy of the electron–phonon interaction can be used to determine the edge direction relative to the polarization of the light, and in particular to distinguish between armchair and zigzag edges. Enhancement of the Raman intensity for graphene is needed for carrying out quick measurements of the Raman spectra, and in such cases tip-enhanced and/or interference-enhanced Raman spectra can now be used to enhance the spatial resolution of pertinent Raman features.

An important issue for discussing the difference between SWNTs and graphene is the dimensionality of the materials because the effect of the Coulomb interaction plays a different role in 2D graphene relative to 1D SWNTs. For example, in SWNTs, the exciton is essential for describing the photoexcited electron and

hole pair, [1] whereas an electron and hole are freely moving in graphene and therefore localization effects are less important. Nevertheless, it is expected that the Coulomb interaction in graphene will be studied in detail in the near future through investigation of the photo-current and electronic transport near the Fermi energy, and the origin of the asymmetric lineshapes observed in the Raman spectra (known as Breit–Wigner–Fano lineshapes) should then be further elucidated.

Ion bombardment measurements have provided us with important information about the area of the Raman-active spatial regions that are associated with the D-band Raman signal. This spatial region is closely related to the phase coherence length (or area) for an electron in which the electron retains its information about the phase of the wave function throughout the elastic scattering events experienced by the electron in the D-band scattering processes [14]. In fact, an interference effect between the incident and scattered electrons at a graphene edge gives selective Raman signals for LO and TO phonon modes, which allows one to distinguish between armchair and zigzag edges by applying theoretical considerations to the interpretation of such Raman spectra. Microscopic analysis of the elastic scattering will become more important in the future in the study of the D-band spectra for different nanostructures containing defects originating from different types of defects (interstitial atoms, impurity atoms, line defects vs. point defects, etc.). The systematic generation of specific types of defects should provide a key approach for obtaining defect type-related information in the Raman spectra through, for example, joint Raman and TEM studies. We can therefore expect that in the future we will be doing more systematic studies on point defects in graphene as a function of ion species of different atomic species, different isotopes of ions with the same atomic number, ions with different energies, etc. The present studies, as described above, of defects in graphene associated with point defects caused by ion implantation already constitute a broad subject. But this is only the beginning. There are many different kinds of defects that can be produced in graphene and carbon nanotubes such as vacancies, divacancies, interstitial atoms of the same or different species, and complexes of impurity/vacancy pairs. Systematic studies of such effects by Raman spectroscopy can teach us a lot about graphene and carbon nanotubes as well as the potential of what Raman spectroscopy can teach about each of these types of defects as they occur in a simple well-characterized system like graphene.

Also in the realm of future work are major opportunities to use the controlled and systematic introduction of defects, such as by ion implantation, into bilayer graphene, for Raman characterization studies, as has been discussed above for monolayer graphene. For bilayer graphene, for example, it would be interesting also to study Raman spectra comparatively from the sample face exposed to the ion beam and from the back side of the sample. The major differences in the electronic structure of monolayer graphene, with its linear $E(k)$ relation, and of bilayer graphene, with its quadratic dispersion relation, could show different behaviors of interest with regard to the modifications of these electronic structures through the introduction of defects.

Another area for future work would be a systematic Raman study of the controlled defects introduced into graphene nanoribbons by ion implantation where the defects could be confined, for example by the use of masks, to the interior of the ribbons or to the edges, including such studies on both zigzag and armchair edges. Graphene nanoribbons are important as a means for introducing band gaps into graphene, with electronic and transport properties that depend on the width of the ribbon as well as on the crystalline orientation and the quality of the structure established at each of the edges. [25] Combined transport, Raman, and electron microscopy measurements would likely prove highly informative for such studies. Thus many research opportunities remain open for exploration in the systematic study of defects, edges, and the defect/edge combination in monolayer and bilayer graphenes. The exploration of the special properties of trilayer graphene including different layer stacking arrangements, is presently a largely unexplored arena.

Raman spectroscopy has been used successfully for characterizing carbon materials for many years both in research laboratories and industrially. Thus we expect that Raman spectroscopy and graphene will become increasingly important as more industrial applications of graphene and sp^2 carbons are found. As more industrial applications are found, the demands for developing standards for describing the quality of graphene materials will increase. Making a thin graphene ribbon with a small width introduces an energy gap. Therefore we can expect graphene ribbons to become more important for applications just because the use of ribbons with narrow widths introduce an energy gap. Furthermore controlling the edge structure of the graphene ribbon so that the edge is atomically smooth allows the introduction of well-defined armchair and zigzag edges [25] with well-defined electronic properties. Thus we can expect increasing attention to be given to Joule heating techniques for increasing the structural perfection of edges and we can expect more use to be made of enhanced edge passivation by functionalization. We can also expect to see more use of multiple measurement techniques including Raman spectroscopy for the characterization of graphene and sp^2 carbon materials based on promising work that has already been carried out using multiple characterization techniques. Many applications would like to combine the exceptional properties of graphene with the special properties of a semiconducting material with a band gap, and for this reason we can expect thin narrow graphene ribbons and graphene/semiconductor substrate interactions to receive increasing attention.

Even within the scope of what is discussed in this chapter, many topics relevant to defects in graphene and carbon nanotubes that have already been studied and documented in the literature have not been discussed here. For example, we did not describe time-dependent phenomena relevant to Raman spectroscopy in graphene, or in other carbon nanostructures, nor did we discuss coherent phonon measurements in which the transmission of the probe light is vibrating at frequencies where phonons are excited coherently. This is a large research field with many interesting regimes depending on the pulse length and pulse intensity. Combining the polarization dependence measurements with coherent phonon measurements should yield important information about the defect type and its special characteristics, but such studies remain as work for the future. Further, we did not mention

measurements that have been made on the stress and temperature dependence of the Raman signal which are also very promising probes that can be used for characterizing the local physical properties of graphene and carbon nanotubes.

Acknowledgements AJ and LGC acknowledge MCTI-CNPq and the AFOSR/SOARD Project (Award No. FA9550-08-1-0236). MSD acknowledges NSF Grant No. DMR-10-04147. R.S. Acknowledges MEXT Grant No. 20241023.

References

1. R. Saito, M. Hofmann, G. Dresselhaus, A. Jorio, M.S. Dresselhaus, Advances in Physics **60**(3), 413 (2011)
2. F. Tuinstra, J.L. Koenig, J. Phys. Chem. **53**, 1126 (1970)
3. F. Tuinstra, J.L. Koenig, J. Compos. Mater. **4**, 492 (1970)
4. R.J. Nemanich, S.A. Solin, Solid State Comm. **23**, 417 (1977)
5. R.J. Nemanich, S.A. Solin, Phys. Rev. B **20**, 392 (1979)
6. C. Kittel, in *Introduction to Solid State Physics*, 6th edn. (Wiley, New York, 1986)
7. N.W. Ashcroft, N.D. Merman, in *Solid State Physics*, (Holt Rinehart and Winston, New York, 1976)
8. A. Jorio, R. Saito, M.S. Dresselhaus, G. Dresselhaus, *Raman Spectroscopy in Graphene Related Systems* (Wiley, WeinHeim, 2011)
9. M.A. Pimenta, G. Dresselhaus, M.S. Dresselhaus, L.G. Cançado, A. Jorio, R. Saito, Phys. Chem. Chem. Phys. **9**, 1276 (2007)
10. A. Jorio, M.S. Dresselhaus, G. Dresselhaus, *Carbon Nanotubes: Advanced Topics in the Synthesis, Structure, Properties and Applications. Springer Series on Topics in Applied Physics* (Springer, Berlin, 2008), vol. 111
11. M.S. Dresselhaus, G. Dresselhaus, R. Saito, A. Jorio, Phys. Rep. **409**, 47 (2005).
12. M.S. Dresselhaus, R. Kalish, *Ion Implantation in Diamond, Graphite and Related Materials. Springer Series in Materials Science* (Springer, Berlin, 1992), vol. 22
13. T.P. Mernagh, R.P. Cooney, R.A. Johnson, Carbon **22**, 39 (1984)
14. M.M. Lucchese, F. Stavale, E.H. Ferriera, C.Vilane, M.V.O. Moutinho, R.B. Capaz, C.A. Achete, A. Jorio, Carbon **48**, 1592 (2010)
15. R. Tsu, J. H. Gonzalez, I.C. Hernandez, Solid State Comm. **27**, 507 (1978)
16. R. Saito, A. Jorio, A.G. Souza Filho, G. Dresselhaus, M.S. Dresselhaus, M.A. Pimenta, Phys. Rev. Lett. **88**, 027401 (2002)
17. R.P. Vidano, D.B. Fishbach, L.J. Willis, T.M. Loehr, Solid State Comm. **39**, 341 (1981)
18. P. Lespade, A. Marchand, M. Couzi, F. Cruege, Carbon **22**, 375 (1984)
19. P. Lespade, R. Al-Jishi, M.S. Dresselhaus, Carbon **20**, 427 (1982)
20. H. Wilhelm, M. Lelausian, E. McRae, B. Humbert, J. Appl. Phys. **84**, 6552 (1998)
21. C. Thomsen, S. Reich, Phys. Rev. Lett. **85**, 5214 (2000)
22. R. Saito, A. Grüneis, Ge.G. Samsonidze, V.W. Brar, G. Dresselhaus, M.S. Dresselhaus, A. Jorio, L.G. Cançado, C. Fantini, M.A. Pimenta, A.G. Souza Filho, New J. Phys. **5**, 157 (2003)
23. X. Jia, M. Hofmann, V. Meunier, B.G. Sumpter, J. Campos-Delgado, J.M. Romo-Herrera, H. Son, Y.-P. Hsieh, A. Reina, J. Kong, M. Terrones, M.S. Dresselhaus, Science **323**, (2009)
24. T. Enoki, Y. Kobayashi, K.-I. Fukui, Int. Rev. Phys. Chem. **26**, 609 (2007)
25. X. Jia, J. Campos-Delgado, M. Terrones, V. Meunier, M.S. Dresselhaus, Nanoscale **3**(3), 1008 (2010)
26. A. Grüneis, R. Saito, T. Kimura, L.G. Cançado, M.A. Pimenta, A. Jorio, A.G. Souza Filho, G. Dresselhaus, M.S. Dresselhaus, Phys. Rev. B **65**, 155405 (2002)

27. J. Jiang, R. Saito, A. Grüneis, S.G. Chou, Ge.G. Samsonidze, A. Jorio, G. Dresselhaus, M.S. Dresselhaus, Phys. Rev. B **71**, 045417 (2005)
28. S. Piscanec, M. Lazzeri, M. Mauri, A.C. Ferrari, J. Robertson, Phys. Rev. Lett. **93**, 185503 (2004)
29. M. Lazzeri, F. Mauri, Phys. Rev. Lett. **97**(26), 266407 (2006)
30. K. Ishikawa, T. Ando, J. Phys. Soc. Jpn. **75**, 84713 (2006)
31. V.N. Popov, P. Lambin, Phys. Rev. B **73**, 085407 (2006)
32. K. Sasaki, R. Saito, G. Dresselhaus, M.S. Dresselhaus, H. Farhat, J. Kong, Phys. Rev. B **77**, 245441 (2008)
33. E.H. Martins Ferreira, Marcus V.O. Moutinho, F. Stavale, M.M. Lucchese, Rodrigo B. Capaz, C.A. Achete, A. Jorio, Phys. Rev. B **82**, 125429 (2010)
34. A. Jorio, M.M. Lucchese, F. Stavale, E.H.M. Ferreira, M.V.O. Moutinho, R.B. Capaz, C.A. Achete, J. Phys. Condens. Matter **22**, 334204 (2010)
35. M. Lazzeri, C. Attaccalite, L. Wirtz, F. Mauri, Phys. Rev. B **78**, 081406R (2008)
36. K. Sato, R. Saito, Y. Oyama, J. Jiang, L.G. Cançado, M.A. Pimenta, A. Jorio, Ge.G. Samsonidze, G. Dresselhaus, M.S. Dresselhaus, Chem. Phys. Lett. **427**, 117 (2006)
37. L.G. Cançado, M.A. Pimenta, R.A. Neves, G. Medeiros-Ribeiro, T. Enoki, Y. Kobayashi, K. Takai, K. Fukui, M.S. Dresselhaus, R. Saito, A. Jorio, Phys. Rev. Lett. **93**, 047403 (2004)
38. L.G. Cançado, M.A. Pimenta, B.R. Neves, M.S. Dantas, A. Jorio, Phys. Rev. Lett. **93**, 247401 (2004)
39. L.G. Cancado, A. Jorio, and M.A. Pimenta, Phys. Rev. B 76, 064304 (2007)
40. L.G. Cancado, K. Takai, T. Enoki, M. Endo, Y.A. Kim, H. Mizusaki, A. Jorio, L.N. Coelho, R. Magalhaes Paniago, M.A. Pimenta, Appl. Phys. Lett. **88**, 3106 (2006)
41. E.B. Barros, N.S. Demir, A.G. Souza Filho, J. Mendes Filho, A. Jorio, G. Dresselhaus, M.S. Dresselhaus, Phys. Rev. B **71**, 165422 (2005)
42. L.G. Cançado, A. Jorio, E.H. Martins Ferreira, F. Stavale, C.A. Achete, R.B. Capaz, M.V.O. Moutinho, A. Lombardo, T.S. Kulmala, A.C. Ferrari, Nano Lett. **11**(8), 3190–3196 (2011)
43. M. Fujita, K. Wakabayashi, K. Nakadw, K. Kusakabe, J. Phys. Soc. Jpn. **65**, 1920 (1996)
44. K. Nakada, M. Fujita, G. Dresselhaus, M.S. Dresselhaus, Phys. Rev. B **54**, 17954 (1996)
45. D.V. Kosynkin, A.L. Higginbotham, A. Sinitskii, J.R. Lomeda, A. Dimiev, B.K. Price, J.M. Tour, Nature **458**(7240), 872 (2009)
46. L. Jiao, L. Zhang, X. Wang, G. Diankov, H. Dai, Nature **458**, 877 (2009)
47. M.Y. Han, B. Özyilmaz, Y. Zhang, P. Kim, Phys. Rev. Lett. **98**, 206805 (2007)
48. K. Kusakabe M. Maruyama, Phys. Rev. B **67**(9), 92406 (2003)
49. L.M. Woods, G.D. Mahan, Phys. Rev. B **61**, 10651 (2000)
50. K. Sasaki, R. Saito, Progr. Theor. Phys. Suppl. **176**, 253 (2008)
51. K. Sasaki, S. Murakami, R. Saito, J. Phys. Soc. Jpn. **75**, 074713 (2006)
52. K. Sasaki, K. Sato, R. Saito, J. Jiang, S. Onari, Y. Tanaka, Phys. Rev. B **75**(23), 235430 (2007)
53. K. Sasaki, J. Jiang, R. Saito, S. Onari, Y. Tanaka, J. Phys. Soc. Jpn. **76**, 033702 (2007)
54. M. Igami, M. Fujita, S. Mizuno, Appl. Surf. Sci. **130–132**, 870 (1998)
55. R. Saito, T. Takeya, T. Kimura, G. Dresselhaus, M.S. Dresselhaus, Phys. Rev. B **59**, 2388 (1999)
56. W. Ren, R. Saito, L. Gao, F. Zheng, Z. Wu, B. Liu, M. Furukawa, J. Zhao, Z. Chen, H.M. Cheng, Phys. Rev. B **81**, 035412 (2010)
57. K. Sasaki, M. Yamamoto, S. Murakami, R. Saito, M.S. Dresselhaus, K. Takai, T. Mori, T. Enoki, K. Wakabayashi, Phys. Rev. B **80**(15), 155450 (2009)
58. Y. You, Z. Ni, T. Yu, Z. Shen, Appl. Phys. Lett. **93**, 163112 (2008)
59. C. Casiraghi, A. Hartschuh, H. Qian, S. Piscanec, C. Georgi, A. Fasoli, K.S. Novoselov, D.M. Basko, A.C. Ferrari, Nano Lett. **9**(4), 1433 (2009)
60. S. Neubeck, Y.M. You, Z.H. Ni, P. Blake, Z.X. Shen, A.K. Geim, K.S. Novoselov, Appl. Phys. Lett. **97**, 053110 (2010)
61. L.G. Cançado, M.A. Pimenta, R. Saito, A. Jorio, L.O. Ladeira, A. Grüneis, A.G. Souza Filho, G. Dresselhaus, M.S. Dresselhaus, Phys. Rev. B **66**, 035415 (2002)

62. L.G. Cançado, A. Reina Cecco, J. Kong, M.S. Dresselhaus, Phys. Rev. B **77**, 245408 (2008)
63. A. Grüneis, R. Saito, Ge.G. Samsonidze, T. Kimura, M.A. Pimenta, A. Jorio, A.G. Souza Filho, G. Dresselhaus, M.S. Dresselhaus, Phys. Rev. B **67**, 165402 (2003)
64. R. Saito, M. Furukawa, G. Dresselhaus, M.S. Dresselhaus, J. Phys. Condens. Matter **22**, 334208 (2010)
65. L. Wirtz, M. Lazzeri, F. Mauri, A. Rubio, Phys. Rev. B **71**, 241402(R) (2005)
66. R. Saito, T. Takeya, T. Kimura, G. Dresselhaus, M.S. Dresselhaus, Phys. Rev. B **57**, 4145 (1998)
67. R. Saito, G. Dresselhaus, M.S. Dresselhaus, *Physical Properties of Carbon Nanotubes* (Imperial College Press, London, 1998)
68. J. Zhou J. Dong, Appl. Phys. Lett. **91**, 173108 (2007)
69. K. Sasaki, R. Saito, K. Wakabayashi, T. Enoki, J. Phys. Soc. Jpn. **79**, 044603 (2010)
70. C. Cong, T. Yu, H. Wang, ACS Nano **6**, 3175 (2010)
71. M. Begliarbekov, O. Sul, S. Kalliakos, E.H. Yang, S. Strauf, Appl. Phys. Lett. **97**, 031908 (2010)
72. A. Das, S. Pisana, B. Chakraborty, S. Piscanec, S.K. Saha, U.V. Waghmare, K.S. Novoselov, H.R. Krishnamurthy, A.K. Geim, A.C. Ferrari, A.K. Sood, Nat. Nanotechnol. **3**, 210 (2008)
73. A. Das, B. Chakraborty, S. Piscanec, S. Pisana, A.K. Sood, and A. C. Ferrari, Phys. Rev. B 79, 155417 (2009)
74. J. Yan, E.A. Henriksen, P. Kim, A. Pinczuk, Phys. Rev. Lett. **101**, 136804 (2008)
75. L.M. Malard, D.C. Elias, E.S. Alves, M.A. Pimenta, Phys. Rev. Lett. **101**, 257401 (2008)
76. T. Ando, J. Phys. Soc. Jpn. **75**, 124701 (2006)
77. L.G. Cançado, A. Hartschuh, L. Novotny, J. Raman Spectrosc. **40**, 1420 (2009)
78. L. Novotny B. Hecht, *Principles of Nano-Optics* (Cambridge University Press, Cambridge, 2006)
79. N. Anderson, A. Hartschuh, L. Novotny, Mater. Today **8**(5), 50 (2005)
80. A. Hartschuh, Angew. Chem. Int. Ed. **47**, 8178 (2008)
81. T. Yano, Y. Inouye, S. Kawata, Nano Lett. **6**(6), 1269 (2006)
82. T. Yano, P. Verma, S. Kawata, Y. Inouye, Appl. Phys. Lett. **88**, 093125 (2006)
83. S.S. Kharintsev, G.G. Hoffmann, P.S. Dorozhkin, G.de With, J. Loos, Nanotechnology **18**, 315502 (2007)
84. A. Hartschuh, E.J. Sánchez, X.S. Xie, L. Novotny, Phys. Rev. Lett. **90**, 095503 (2003)
85. N. Anderson, A. Hartschuh, L. Novotny, J. Am. Chem. Soc. **127**, 2533 (2005)
86. N. Anderson, A. Hartschuh, L. Novotny, Nano Lett. **7**(3), 577 (2007)
87. I.O. Maciel, N. Anderson, M.A. Pimenta, A. Hartschuh, H. Qian, M. Terrones, H. Terrones, J. Campos-Delgado, A.M. Rao, L. Novotny, A. Jorio, Nat. Mater. **7**, 878 (2008)
88. L. Novotny S.J. Stranick, Annu. Rev. Phys. Chem. **57**, 303 (2005)
89. A. Hartschuh, M.R. Beverluis, A. Bouhelier, L. Novotny, Philos. Trans. R. Soc. London A **362**, 807 (2004)
90. L.G. Cançado, A. Jorio, A. Ismach, E. Joselevich, A. Hartschuh, L. Novotny, Phys. Rev. Lett. **103**, 186101 (2009)
91. J.S. Soares, A.P.M. Barboza, P.T. Araujo, N.M. Barbosa Neto, D. Nakabayashi, N. Shadmi, T.S. Yarden, A. Ismach, N. Geblinger, E. Joselevich, C. Vilani, L.G. Cançado, L. Novotny, G. Dresselhaus, M.S. Dresselhaus, B.R.A. Neves, M.S.C. Mazzoni, A. Jorio Nano Lett. **10**(12), 5043 (2010)

Chapter 3
Scanning Tunneling Microscopy and Spectroscopy of Graphene

Guohong Li and Eva Y. Andrei

Abstract Scanning tunneling microscopy (STM) and spectroscopy (STS) are powerful tools that can reveal the intrinsic properties of the masslesss Dirac fermions in graphene. In particular in the presence of a magnetic field STS gives direct access to the unique sequence of quantized Landau levels providing evidence of the chiral nature of the Dirac fermions and their ultrarelativistic spectrum. A twist between graphene layers gives rise to moiré patterns viewed in STM and to Van Hove singularities in the density of states obtained with STS, which enables direct comparison between structure and electronic properties. STM/STS in graphene on SiO_2 provide valuable information about trapped charges, ripples, and other defects. Furthermore, STM can be used to manipulate graphene at nanometer scale.

3.1 Introduction

The electronic properties of graphene [1, 2], a one-atom thick form of crystalline carbon, are unique among all known materials because they are controlled by charge carriers with a conical low energy dispersion which mimics the dynamics of massless Dirac fermions, which carry a Berry phase of π [1, 2]. One of the consequences is a linear and electron–hole symmetric density of states (DOS) that vanishes at the Dirac point allowing for ambipolar gating. In a magnetic field the linear density of states evolves into an unevenly spaced sequence of quantized Landau levels (LL) which includes a level at zero energy that reflects the chirality of the quasiparticles. Owing to the chiral nature of the quasiparticles, backscattering and weak localization are suppressed, resulting in extremely high carrier mobility. Edge states in graphene can carry pure spin currents [3, 4] or exhibit magnetism [5, 6], displaying qualitatively different behavior depending on whether their termination is zigzag or armchair [7]. Ripples, strain, lattice defects,

G. Li (✉) · E.Y. Andrei (✉)
Department of Physics & Astronomy, Rutgers University, Piscataway, New Jersey 08854, USA

H. Raza (ed.), *Graphene Nanoelectronics*, NanoScience and Technology,
DOI 10.1007/978-3-642-22984-8_3,

or atomic substitution endow graphene with unusual properties and can lead to qualitative changes in the band structure giving rise to exotic properties such as gauge fields that are equivalent to ultra-high magnetic fields [8, 9] and atomic collapse [10]. Even more unconventional electronic properties arise in stacks of graphene layers. In Bernal stacked bilayers the quasiparticle excitations become massive chiral fermions, which carry a Berry phase of 2π [1, 2]. Twisting the layers away from Bernal stacking produces new features such as twist-induced saddle points [11] in the band structure, van Hove singularities in the density of states and a low energy spectrum which is restored to that of massless Dirac fermions but with a significantly reduced Fermi velocity at small twist angles [12].

Graphene can exist in various environments. Thus far scanning tunneling microscopy has shown that single layer graphene suspended on the surface of graphite exhibits a perfect honeycomb structure over micrometer length scales and is the flattest and most homogeneous when compared to graphene deposited on other substrates. Furthermore, scanning tunneling spectroscopy revealed that the spectrum of single layer graphene on a graphite substrate is consistent with tight binding calculations and can provide access to many-body effects including electron–phonon and electron–electron interactions. In contrast, graphene deposited on the commonly used SiO_2 substrates produces distorted tunneling spectra reflecting strong perturbations from substrate-induced local doping, ripples, and scattering.

STM and STS are powerful probes which provide direct access to both the structure and the electronic properties of graphene in its various forms. At the same time STM and other scanning probe microscopes (SPM) can modify graphene edges as well as introduce point defects, deposit impurities, and tailor the structure at the nanometer scale.

STM/STS on graphene is a broad and fast moving field making it impossible to cover all the developments. Other aspects of STM/STS works on epitaxial graphene on metals or on SiC are discussed in Chapters 5–7.

3.2 STM/STS Techniques

In STM/STS experiments (Fig. 3.1), one brings a sharp metallic, e.g., Pt–Ir, tip very close to the surface of a sample, with a typical tip–sample distance of $\sim$1 nm. For positive sample bias voltages, electrons tunnel from the tip into empty states in the sample; for negative voltages, electrons tunnel out of the occupied states in the sample into the tip. The tunneling current I is given by [13]

$$I = \frac{4\pi e}{\hbar} \int_{-\infty}^{+\infty} [f(E_F - \mathrm{eV} + \in) - f(E_F + \in)] \rho_s(E_F - \mathrm{eV} + \in) \rho_T(E_F + \in) |M|^2 \, \mathrm{d} \in \tag{3.1}$$

where $-e$ is the electron charge, $\hbar$ Planck's constant over 2π, $f(x)$ is the Fermi function, E_F the Fermi energy, V the sample bias voltage, ρ_s and ρ_T are the density

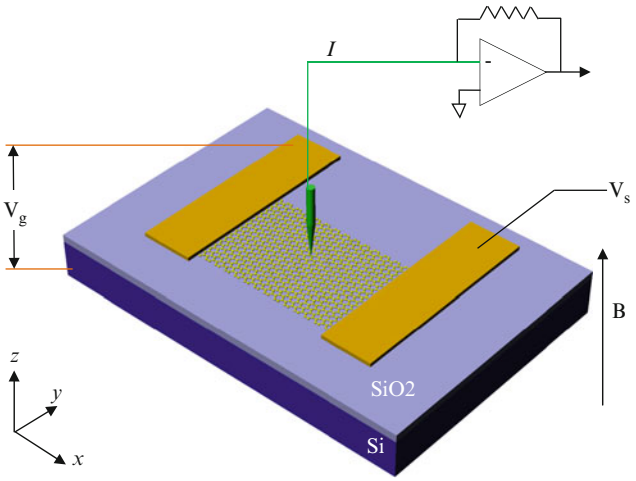

Fig. 3.1 Schematic of STM/STS experiments on graphene. A bias voltage V_s is applied through a metallic contact between a graphene sample and a sharp metallic tip held at ground potential. The tunneling current I is measured by a current amplifier. The tip position is controlled by a piezoelectric tube (not shown) for scanning in the xy plane and for adjusting the tip–sample distance in the z direction when the feedback loop is enabled. The graphene sample can be placed on a SiO_2/Si (heavily doped) substrate so that a gate voltage V_g between Si and graphene can be applied to vary the carrier density of graphene. Importantly a magnetic field B can be applied in the z direction to induce Landau quantization in graphene

of states in the sample and tip, respectively. The tunneling matrix element M depends strongly on the tip–sample distance s, which is usually controlled by a piezoelectric tube. For a given sample bias voltage, as the tip scans above the sample surface, a feedback loop maintains a constant tunneling current by adjusting s to follow the sample surface, therefore producing a topography image. One should note that an STM image not only reflects topography but also contains information about the local density of states of electrons.

In STS measurements, the tip–sample distance is held fixed by turning off the feedback loop. One measures tunneling currents while sweeping the sample bias voltage. Usually one can use a lock-in technique to measure differential conductance directly by applying a small ac modulation to the sample bias voltage. The differential conductance gives a direct measurement of density of states in the sample ($E_F = 0$ in the following)

$$\mathrm{d}I/\mathrm{d}V(V) \propto \rho_S(\varepsilon = eV) \tag{3.2}$$

under the following conditions:

1. zero temperature
2. flat density of states in the tip
3. energy-independent tunneling matrix element

In practice, finite temperatures introduce thermal broadening through the Fermi functions in (3.1), leading to reduced energy resolution in STS. For example, at 4.2K the energy resolution cannot be better than 0.38 meV. Correspondingly, the ac modulation of the sample bias voltage should be comparable to this broadening in order to achieve highest possible resolution. The other two conditions are usually considered satisfied for common tips, such as Pt–Ir, W, and Au tips, as long as sample bias voltage is not too high. Compared to a sharp tip, a blunt tip typically has a flatter density of states. To have reliable STS, one should make sure a good vacuum tunneling is achieved. To this end, one can check the spatial and temporal reproducibility of the spectra and ensure that they are independent of tip–sample distance [14].

For STM/STS measurements on graphene, there are new issues to be considered. First, the STM tip should be as far as possible from the sample surface because graphene is a very flexible material with quite low carrier density. Typical junction resistance should be higher than 5 GΩ (e.g. sample bias voltage 200 mV, tunneling current 20 pA) in order to minimize effects of tip–sample interactions [15]. Second, electrons in graphene are a true two-dimensional system and so their states evolve into LLs in magnetic fields. Therefore, it is useful to apply strong magnetic field normal to graphene layer (Fig. 3.1) in order to fully characterize the massless Dirac fermions. Moreover, the LLs introduce strong peaks in density of states at energies which are not sensitive to the conditions (2) and (3) discussed above. Therefore LL spectroscopy can provide *in situ* calibration of the tip [16], a procedure which usually requires using another material as a calibration standard. Third, the charge carrier density of graphene can be tuned using a back-gate if the sample is on SiO_2/Si (heavily doped) substrate. Thus the back gating is desirable in STM/STS experiments (Fig. 3.1) to access correlation effects in graphene [17].

The size of a typical graphene device on SiO_2 is $\sim$1 μm. It is very difficult for an STM tip to find such a specific device over 1 mm^2 area because STM inherently is a near-sighted microscope. Special arrangements are needed for proper navigation of the STM tip. An optical telescope can help to align the tip to the sample. However, for a low-temperature high-magnetic field STM, optical access usually is difficult. In such case one can navigate the tip by measuring the capacitance between tip and well-designed electrodes around the graphene flake.

To search for decoupled graphene layers on a graphite surface, one can use topography to identify candidate flakes which appear predominantly near large step-like defects. But to know the degree of coupling to the substrate it is crucial to measure STS in a magnetic field because the sequence of LL peaks which appears in this case is a sensitive probe of the degree of coupling to the substrate [18, 19]. In particular, flakes that are completely decoupled are recognized by the appearance of unusually prominent LL peaks arranged in a sequence which follows a unique square root dependence on field and level index.

Since completely decoupled flakes are quite rare, it is necessary to use coarse *xy* positioning stages with travel distances of several millimeters in order to make it possible to carry out an extensive search over a large surface.

3.3 Sample Preparation

Graphene can exist in various environments. It was first isolated for transport measurements by mechanical exfoliation of graphite [20], which consists of stacks of graphene layers weakly coupled by van der Waals forces. Graphite can be easily cleaved in air or under ultrahigh vacuum (UHV). Its fresh surface after cleavage is clean, inert, and atomically flat over large scales. Therefore, soon after the invention of the STM, graphite became a calibration standard and to this day it remains an important substrate for many applications.

Although preparation of graphite surface is simple, the top graphene layer is usually coupled to other layers below. As one will see later, the electronic states in graphene can change dramatically by interlayer coupling. For good graphite crystals, such as Kish graphite, the coherent interlayer coupling results in a three-dimensional band structure. But for highly oriented pyrolitic graphite (HOPG), stacking faults and other detects can effectively reduce the interlayer coupling. Thus one should choose HOPG for the study of decoupled single layer or few layers of graphene.

When single layer graphene is deposited on a SiO_2 substrate by mechanical exfoliation, it is necessary to also deposit metallic electrodes, usually made of Au/Ti or Au/Cr thin films, to carry out STM experiments [21–29]. Table 3.1 lists methods for film deposition and the various cleaning procedures required to carry out a successful STM measurement. One can use a stencil mask [23] to deposit metal films or use microsolder [28] to make electrical connections to avoid using photoresist. However, e-beam lithography is more practical for device fabrications. As can been seen from Table 3.1, the cleaning procedures to remove photoresist residue vary from group to group, and no consensus on the most effective procedure has yet been reached.

Graphene grown by chemical vapor deposition (CVD) is important for applications [30–32]. To study CVD graphene with STM, a suitable sample cleaning procedure is necessary because the transfer process onto different substrates requires chemical methods which usually leave residues. More discussion about CVD graphene can be found in chap. 7.

3.4 Hallmarks of Graphene in STM/STS

Graphene was first considered as a theoretical starting point to understand graphite [33]. A flat infinite size graphene crystal cannot exist in nature because two-dimensional (2d) long range order is not stable at finite temperature [34]. However, the σ bonds between carbon atoms in graphene are strong enough to maintain the atomic network, i.e., the honeycomb lattice, in spite of 3d deformations (ripples) which appear in free standing graphene in vacuum [35]. Once sitting on a substrate, the ripples will be suppressed to some extent but new deformations, which follow

Table 3.1 Methods for making electrodes to graphene and cleaning procedures

Lithography method	Electrodes	Cleaning procedure	Ref.
e-beam Bilayer resist 950 K PMMA/MMA-MAA Developer Methyl isobutyl Ketone /isopropanol (1/3) Remover: acetone	Au (18 nm)/ Cr(1 nm)	Annealing at 280 °C for 6 h in UHV	[21]
e-beam Bilayer resist PMMA/MMA-MAA	Au/Cr	Annealing at 400 °C for 1 h in Ar/H_2 flow flow rate Ar 1,700 mL/min H_2 1,900 mL/min	[22]
e-beam	Au/Ti		[24]
e-beam PMMA	Au/Ti	Annealing at 400 °C for 1 h in Ar/H_2 + 300 °C for 30 min in air	[25]
Lift-off Rinsed in isopropanol and acetone	Au/ Cr(10 nm)	Annealing at 150 °C for 4 h in air +150 °C for 3 h in UHV	[27]
Photolithography	Au	Annealing at 400 °C for 15 min in high oxygen environment	[29]
Stencil mask	Au(30 nm)	Annealing at 400 °C for ∼10 hr in UHV	[23] [26]
Microsolder	In		[28]

the topography of the substrate, can appear due to van der Waals forces between graphene and substrate.

Although the honeycomb lattice has been observed in graphene on various insulating substrates, the electronic states seen on such substrates are heavily distorted by substrate interference. The least disturbed electronic states characteristic of the massless Dirac fermions in single layer graphene [16] were seen using STS on graphene flakes slightly suspended on the surface of graphite that were electronically decoupled from the substrate. Figure 3.2a shows the STM topography of graphene on such a flake. Carbon atoms are located at the six hexagon vertices with an inter-atomic distance 0.142 nm, which is primarily determined by the σ bond. The nearest neighbors, denoted by A and B, belong to different sublattices. In other words, there are two atoms in a unit cell of a triangular Bravais lattice with a lattice constant of $a = 0.245$ nm. The Brillioun zone of the triangular Bravais lattice is a hexagon (Fig. 3.2b). Near the K and K′ corners of the hexagon (Dirac points) the valence and conduction bands touch [1] and the low energy dispersion is conical and electron–hole symmetric

$$E(\vec{k}) = \pm v_F \hbar \vec{k}, \tag{3.3}$$

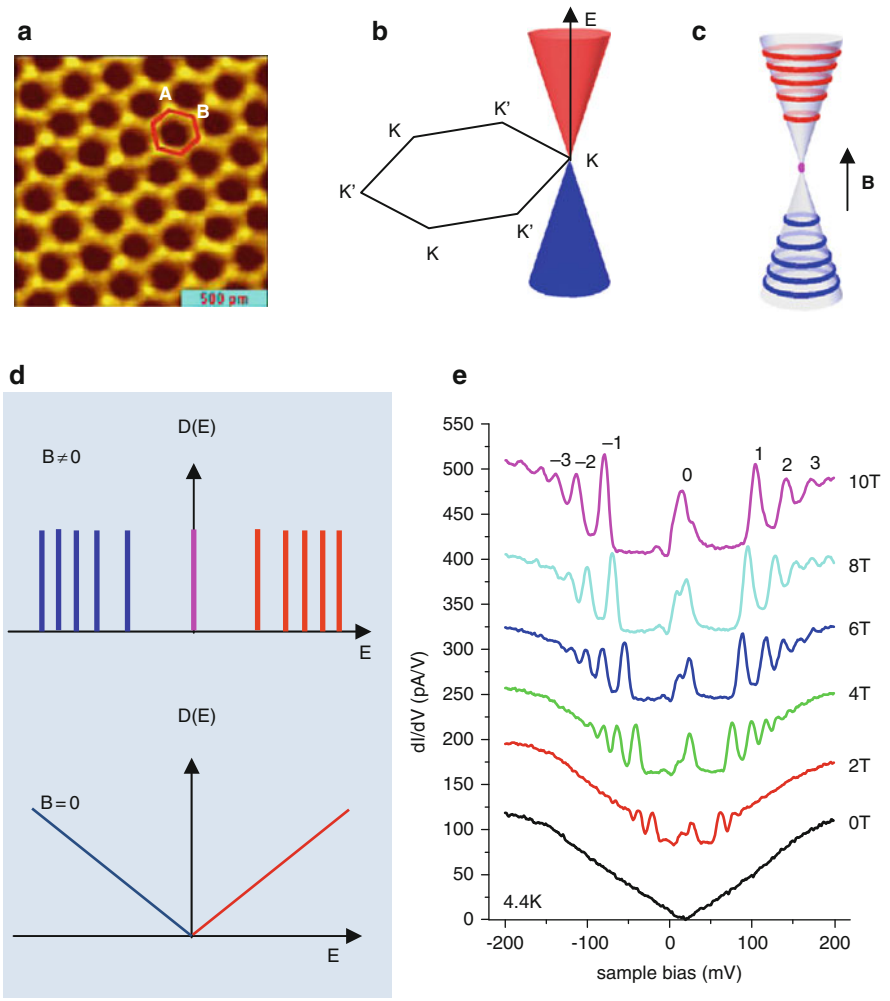

Fig. 3.2 STM/STS on graphene. (**a**) STM image shows the honeycomb structure. A and B atoms belong to different sublattices. (**b**) Brillioun zone showing unequivalent corners K and K′. Near the corners the band structure displays a Dirac cone. (**c**) Landau quantization of the Dirac cone in a magnetic field B. (**d**) Schematic low energy density of states corresponding to (b) and (c). (**e**) STS measurements are generally consistent with (d) but reveal details not expected from a simple tight binding approximation [16]

where v_F is the Fermi velocity, E the energy relative to the Dirac point (DP), $\vec{k}$ the wave vector relative to the K or K′ points in the Brilouin zone, $+/-$ denote electrons and holes. For undoped graphene, the Fermi level sits at the Dirac point. The linear energy–momentum dispersion of (3.3) is the hallmark of ultrarelativistic massless particles akin to (massless) neutrinos or photons. Because of this dispersion the

electron or hole excitations mimic the dynamics of ultrarelativistic charged particles and antiparticles, hence the name massless Dirac fermions. Instead of a scalar, the wave function of the Dirac fermion is a spinor, whose two components denote the amplitudes of Bloch functions on the two sublattices A and B.

The linear dispersion leads to a linear DOS that vanishes at the DP (Fig. 3.2d). When a magnetic field B is applied normal to graphene plane, unusual Landau level sequence appears (Fig. 3.2c):

$$E_n = E_D \pm \sqrt{2e\hbar v_F^2 |n|B}, \tag{3.4}$$

where E_D is the energy at the Dirac point, n is the level index with $n > 0\,(+)$ corresponding to electrons and $n < 0\,(-)$ to holes. The $n = 0$ Landau level is a consequence of the chirality of the Dirac fermions and does not exist in any other known 2d electron system. The field-independent state at the DP together with the square-root dependence on both B and $|n|$ are the hallmarks of massless Dirac fermions. All the Landau levels have the same degeneracy of $4\mathrm{B}/\phi_0$ per unit area, which includes spin (up and down) and valley (K and K′) degeneracy, so that the zero field linear DOS becomes un-evenly spaced δ peaks of the same height in the absence of broadening (Fig. 3.2d).

The theoretical predictions of Fig. 3.2d were confirmed by using STS to measure the quantized LL sequence in magnetic field. Figure 3.2e shows how the evolution of tunneling spectra with magnetic field. In zero field, the spectrum is V-shaped and vanishes at the Dirac point, which is seen ∼16 meV above the Fermi energy, indicating unintentional doping with a concentration of $\sim 2 \times 10^{10}\,\mathrm{cm}^{-2}$ holes. In the presence of a magnetic field, an unevenly spaced sequence of peaks appears flanking on both sides of the $n = 0$ level at the Dirac point. The $n = 0$ level is the only one which does not move with field and only its height increases with field as a result of the increasing flux-line degeneracy. This central peak is a consequence of the chiral symmetry of the massless Dirac fermions and is the hallmark of these quasiparticles. The massless Dirac fermion character is revealed by plotting the peak energies against the reduced variable $(|n|B)^{1/2}$. This scaling procedure collapses all data unto a straight line, as shown in Fig. 3.3. The slope of this curve gives a direct measure of the Fermi velocity obtained according to (3.4). For graphene flakes on graphite that are decoupled from the substrate one notices a reduced Fermi velocity, $v_\mathrm{F} = 0.79 \times 10^6\,\mathrm{m/s}$, the origin of which is discussed below.

Before understanding the tunneling spectra in detail, one may ask how it could be possible to find a decoupled graphene flake on the surface of graphite. If the flake was decoupled, why was it not removed during peeling? Normally cleavage should happen between the least coupled layers. However, partial cleavage could result in a different situation illustrated in Fig. 3.4. Figure 3.4a shows an STM image of HOPG surface. The cross-sectional cut along the line ββ gives an atomic step ∼0.34 nm, close to the interlayer spacing 0.335 nm of graphite, but a cut along the line αα gives a layer separation of ∼0.44 nm, which means the top graphene layer is lifted

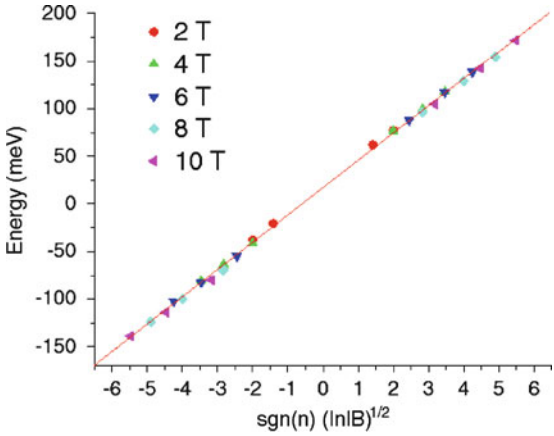

Fig. 3.3 Landau level energies showing square-root dependence on level index and field. Symbols are peaks from Fig. 3.2e and the solid line is a fit to (3.4) (Reprinted figure with permission from [16]. Copyright (2010) by the American Physical Society)

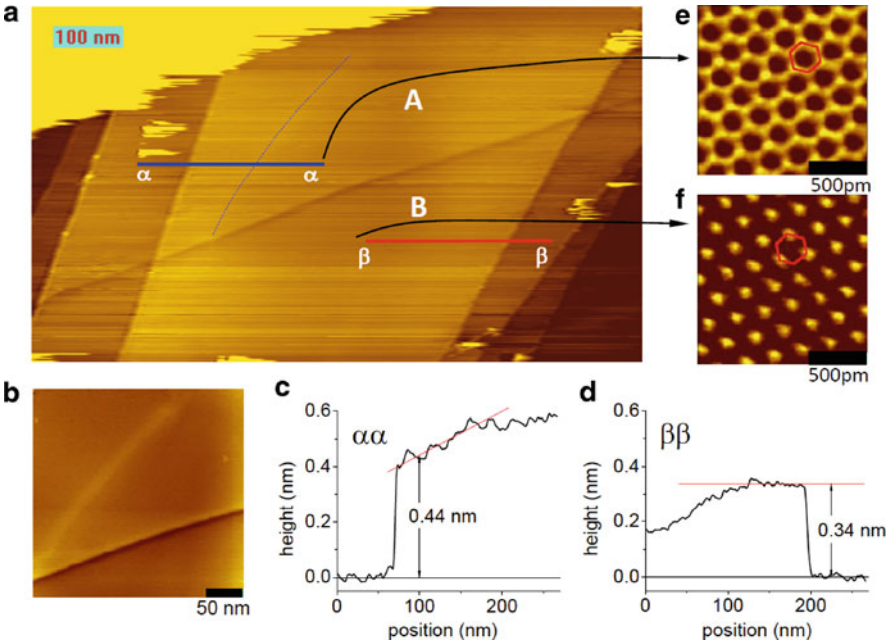

Fig. 3.4 Topography of the graphene layer isolated by extended defects on a graphite surface. (**a**) Large area topography. Two underlying defects are seen: a long ridge that runs diagonally under the top two layers and a fainter one under the first layer (dashed line). (**b**) High resolution image where the fainter ridge is visible. (**c**) Cross-sectional cut along line αα in (**a**). (**d**) Cross-sectional cut along line ββ. (**e, f**) Atomic-resolution image showing honeycomb structure in region A (atoms visible at all six hexagon vertices) and triangular structure in B (atoms seen only at three vertices corresponding to only one visible sublattice). Set sample bias voltage and tunneling current were 300 mV and 9 pA for (**a**), 300 mV and 49 pA for (**b**), 200 mV and 22 pA for (**f**), 300 mV and 55 pA for (**e**) (Reprinted figure with permission from [16]. Copyright (2010) by the American Physical Society)

by ∼30%. A strong ridge serves as a border between regions A and B. Atomic resolution STM image shows a honeycomb structure in region A but a triangular one in region B. The apparent triangular lattice comes from interlayer coupling in Bernal stacked graphite [36] which breaks the sublattice symmetry causing a large reduction in the low-energy density of states on one of the sublattices. As a result only one sublattice is seen in topography measurements taken at low bias voltages. The tunneling spectra in Fig. 3.2e was taken in the center of region A away from any defects. In contrast to region A where both the structure and the Landau level sequence indicate a single graphene layer decoupled from the substrate, in region B both the structure and the more complex sequence of levels indicate coupling to the substrate. A careful study of the Landau level sequence showed that the interlayer coupling in region B near the long ridge was only ∼40 meV, about 10% of that in bulk graphite [18].

3.5 Line Shape of Landau Levels

The region A in Fig. 3.4 is defect free except for a faint hidden ridge. The size of the graphene flake is about 400 nm, much larger than the relevant length scale for Landau level quantization, i.e., the magnetic length, $l_B = \sqrt{e/\hbar B} \sim 25\,nm\Big/\sqrt{B[\mathrm{T}]}$, corresponding to ∼13 nm in 4 T. All the Landau levels have the same degeneracy in an infinite sample. If the sample is finite, the presence of edges will change the degeneracy locally. However, far away from the edges and defects, the local density of states of Landau levels should still be the same, which means that peaks in STS due to Landau levels must have the same area. Figure 3.5 plots such a high

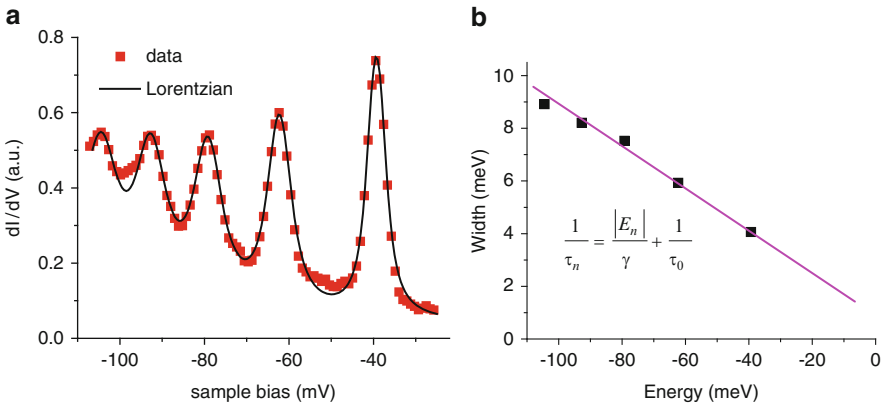

Fig. 3.5 Line shape of Landau levels. (**a**) Tunneling spectroscopy at 4.4 K in 4 T. Symbols are experimental data and the solid line represents a fit with Lorentzian peaks. (**b**) Energy dependence of the peak width [16]

energy resolution STS taken in 4 T, focusing on the hole sector because the Landau levels are closer to the Fermi level in the hole-doped sample. The sharpness and high definition of the Landau level peaks made it possible to extract the energy dependence of the quasiparticle lifetime. The level sequence can be fit with a sum of peak functions centered at the measured peak energies with the line width of each peak and the same peak area as free parameters. The peaks have Lorentzian line shapes instead of Gaussian ones, suggesting intrinsic lifetime rather than impurity broadening. The line width decreases toward the Fermi level, consistent with the fact that interacting quasiparticles have longest lifetime at the Fermi level. It is interesting that the inverse lifetime follows a linear energy dependence

$$\frac{1}{\tau_n} = \frac{|E_n|}{\gamma} + \frac{1}{\tau_0}, \tag{3.5}$$

where E_n is the Landau level energy in units of eV, $\gamma \sim 9\,\mathrm{fs/eV}$ and $\tau_0 \sim 0.5\,\mathrm{ps}$ at the Fermi level. The energy-dependent first term is attributed to the intrinsic lifetime while the second constant term is extrinsic. The latter translates into a mean free path of $l = v_\mathrm{F}\tau_0 \sim 400\,\mathrm{nm}$ which is comparable to the sample size indicating that scattering is primarily due to boundaries so that inside the sample the motion is ballistic. Electron–electron interactions between Dirac fermions are expected to give rise to a linear energy dependence of the inverse lifetime [37]. Theoretical estimates in zero field give $\gamma \sim 20\,\mathrm{fs/eV}$. Since the electron–electron interactions are enhanced in magnetic field, it is possible that the agreement would be even better with calculations made in finite field.

3.6 Electron–phonon Coupling

The basic physics of graphene is captured in a tight-binding model [1]. However, many-body effects are often not negligible. *Ab initio* density functional calculations [38] show that the electron–phonon (e–ph) interactions introduce additional features in the electron self-energy, leading to a renormalized velocity at the Fermi energy $v_F = v_{F0}(1 + \lambda)^{-1}$, where v_{F0} is the un-renormalized velocity and λ is the e–ph coupling constant. Away from the Fermi energy, two dips are predicted in the velocity renormalization factor, $(v_\mathrm{F} - v_{F0})/v_F$, at energies $E_\mathrm{F} \pm \hbar\omega_\mathrm{ph}$, where $\hbar\omega_\mathrm{ph}$ is the characteristic phonon energy. Such dips give rise to shoulders in the zero field DOS at the energy of the relevant phonon and provide a clear signature of the e–ph interactions in STS measurements. In Fig. 3.6a are shown the $\mathrm{d}I/\mathrm{d}V$ spectra measured on a graphene flake decoupled from the graphite substrate. The onset of two shoulder features on both sides of the Dirac point around $\pm 150\,\mathrm{meV}$, and the persistence of the exact same feature over a wide range of junction resistance values, 3.8–50 GΩ, corresponding to a different tip–sample separations, suggests an intrinsic phenomenon consistent with a slow-down of the Fermi velocity due to e–ph interactions.

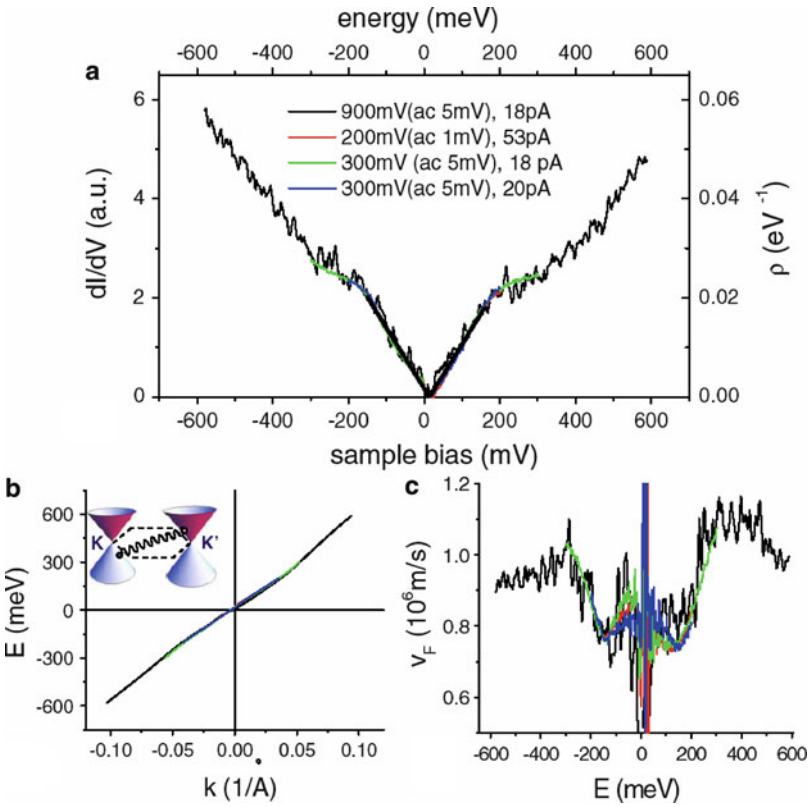

Fig. 3.6 (**a**) Zero field tunneling spectra and density of states. Thick line is the DOS calculated according to Landau levels. Legends show tunneling junction settings [sample bias voltage (bias modulation), tunneling current]. (**b**) Energy–momentum dispersion obtained from the DOS in (**a**). Inset, diagram of inter-valley scattering mediated by A_1' phonon. (**c**) Energy dependence of Fermi velocity (Reprinted figure with permission from [16]. Copyright (2010) by the American Physical Society)

Further analysis requires a calibration of the zero field DOS, which can be accomplished by considering the Landau level spectroscopy in Fig. 3.3. The Landau level sequence provides direct evidence that the quasiparticle excitations in graphene are 2d massless Dirac fermions and allows obtaining the average value of v_F for energies up to 150 meV. Using this fact and the linearity of the DOS we obtain the zero field calibration of the DOS:

$$\rho(E) = \frac{3^{3/2}a^2}{\pi}\frac{|E - E_D|}{\hbar^2 v_F^2} = 0.123\,|E - E_D|\,. \tag{3.6}$$

Comparing to the normalized zero field tunneling spectra in Fig. 3.6a we note that at low energies the measured dI/dV which are linear in energy and vanish at

the Dirac point are remarkably consistent with the expected DOS justifying our assumption that $\mathrm{d}I/\mathrm{d}V \propto$ DOS in the range of -150 meV to 150 meV. Assuming this proportionality remains valid to higher energy range and an isotropic band, one obtains

$$k(E) = \pm \left| \frac{\pi}{A_c} \int_{E_D}^{E} \rho(E')\mathrm{d}E' \right|^{1/2} \tag{3.7}$$

by integrating the measured differential conductance curve, and from it the dispersion relation $E(k)$ shown in Fig. 3.6b. Here A_c is the area of the unit cell. This allows one to calculate the energy dependence of the velocity $v_F = \mathrm{d}E/\mathrm{d}k$, as shown in Fig. 3.6c. Identifying the asymptotic value of the velocity with v_{F0} one can obtain $\lambda \sim 0.26$. The curve bears a striking similarity to that obtained by DFT [38]: it exhibits two dips at the energy of the A_1' phonon $\pm 150(\pm 20)$ meV, suggesting that this phonon, which couples the K and K′ valleys and undergoes a Kohn anomaly, is an important player in the velocity renormalization. Indeed the A_1' phonon has very large line width for single layer graphene, indicating strong e–ph coupling. However, its line width [39, 40] decreases significantly for bilayer graphene and decreases even more for graphite. Therefore e–ph coupling through A_1' is suppressed by interlayer coupling and therefore the e–ph induced velocity renormalization is only observed in single graphene layers that are well decoupled from the substrate. Consequently the Fermi velocity in multilayer graphene should be more close to the un-renormalized value, an expectation which is confirmed by Landau level spectroscopy on multilayers discussed in the next section.

3.7 Coupling Between Graphene Layers

When two graphene layers form a bilayer with Bernal stacking, the band structure is modified due to interlayer coupling, and the Dirac cone structure of the single layer transforms into parabolic bands. The valence and conduction bands still touch at the K and K′ points but the low energy excitations acquire a band mass. It should be emphasized that these massive quasiparticles are different from those in conventional 2d electron systems since, as is the case of the chiral massless Dirac fermions in single layer, they have to be described by spinors instead of scalars to take into account the two inequivalent sublattices. While the massless Dirac fermions in single layer carry a Berry phase [1, 41] of π, the Berry phase carried by the massive chiral fermions in bilayer is 2π. In a magnetic field, as a consequence of the chirality, both systems have a special Landau level at the point where the conduction and valence bands touch which, unlike all other Landau levels, consists of both electron and hole states. The Landau level sequence in the bilayer is

$$E_n = \pm \hbar \omega_c \sqrt{n(n-1)}, \quad n = 0, 1, 2, \ldots, \tag{3.8}$$

where $\omega_c = eB/m^*$ is the cyclotron frequency, m* is the effective band mass, and + and – correspond to electrons and holes, respectively. The energy levels in this sequence are linear in field and the Landau level at zero energy has double the degeneracy of the other Landau levels [42]. The high energy levels, i.e., n»0, are evenly spaced in level index.

For trilayer graphene with Bernal stacking, massless Dirac fermions and massive chiral fermions coexist [43]. As the number of layers increases, the band structure becomes more complex. However, for ten layers or less, the massless Dirac fermions always show up in odd number of layers [44]. Furthermore, changing the stacking sequences away from Bernal can strongly modify the band structure [1,45,46]. More discussions on graphene multilayers can be found in Chap. 11.

Stacking faults and other defects in HOPG cause decoupling of the layers [47, 48]. Therefore, one often can observe strong Landau level spectra in some regions of the surface of HOPG after cleavage [15,48], but usually more than one LL sequence is observed. For example, in Fig. 3.7 we note the coexistence of several sequences: one corresponding to massless Dirac fermions, one to massive chiral fermions, and other sequences. The massive sequence can vary from sample to sample as it is controlled by interlayer coupling [15]. However, the massless sequence is quite robust, showing very weak sample dependence. For graphene multilayers,

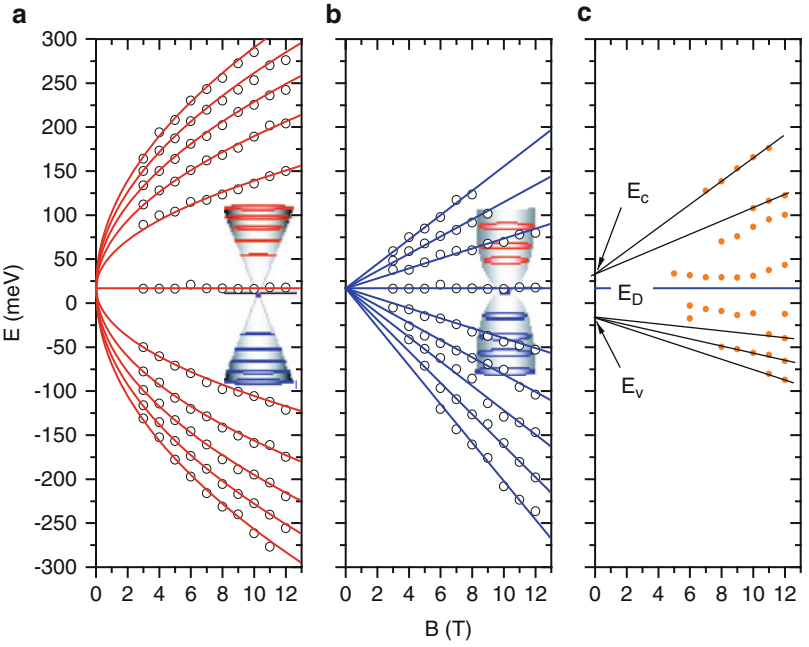

Fig. 3.7 Classification of Landau levels in a multilayer graphene. (**a**)Massless Dirac fermions. (**b**) Massive chiral fermions. (**c**) Unidentified levels (Reprinted by permission from Macmillan Publishers Ltd: Nature Physics [48], copyright (2007))

i.e., when sequences of Landau levels coexist, the massless Dirac fermion sequence gives a Fermi velocity of $v_F = 1.07 \times 10^6$ m/s, which is close to the un-renormalized value. This supports the theoretical expectation that the e–ph coupling through A_1' is suppressed by interlayer coupling as discussed in the previous section.

3.8 Twist Between Graphene Layers

The freedom of stacking between graphene layers is so large that twisting away from the equilibrium Bernal stacking is possible for a wide range of rotation angles. Such a twist generates superstructures, the so-called moiré patterns, which are readily seen in STM topography. Such a pattern is present on the surface of HOPG shown in Fig. 3.8a. This highly ordered pattern shows a period of ~7.7 nm, which

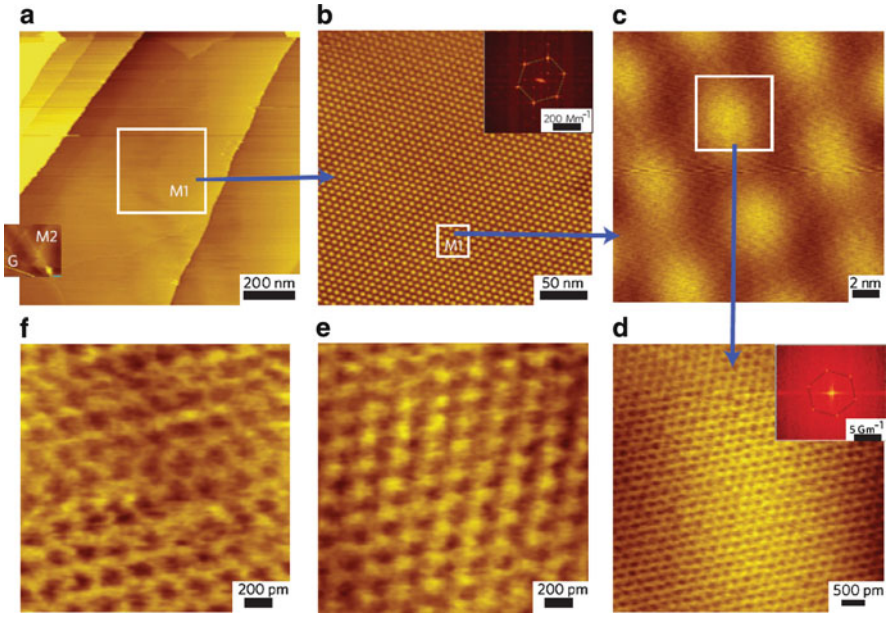

Fig. 3.8 STM of a graphene flake on a freshly cleaved surface of highly oriented pyrolitic graphite revealing a moiré pattern. (**a**) Large-area scan of a graphene flake. Regions M2 and G flank the boundary of the moiré pattern. (**b**) Zoom-in of the frame in a, showing a moiré pattern with period 7.7 ± 0.3 nm. Inset: Fourier transforms of the superstructure. (**c**) Zoom-in to the center of the pattern, region M1. (**d**) Atomic-resolution image of a bright spot. Inset: Fourier transforms of the atomic-resolution image. (**e, f**) Atomic-resolution image on bright and dark regions of the pattern, show a well-ordered triangular lattice within the bright spots (**e**) and a less-ordered honeycomb-like structure in between (**f**). The former indicates Bernal-stacked layers, whereas the latter suggests slipped stacking, resulting from a small-angle rotation between layers. Tunneling current 20 pA, sample bias voltage 300 mV (Reprinted by permission from Macmillan Publishers Ltd: Nature Physics [11], copyright (2010))

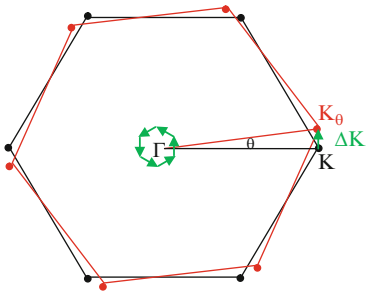

Fig. 3.9 Bragg spots corresponding to two twisted graphene layers with a relative twist angle, θ. The displacement vector ΔK determines the period of the moiré pattern

is much larger than the lattice of constant of graphene, $a = 0.246\,\text{nm}$. Within the moiré pattern, atomic resolution images show different structures on different locations. Zooming into the bright spots of the moiré pattern (Fig. 3.8e) we note that the underlying lattice structure is triangular which indicates graphene layers with Bernal stacking. In between the bright spots there are regions with less-ordered honeycomb-like structure (Fig. 3.8f), which indicates lost registry between layers due to twisting [11].

Moiré patterns on the surface of graphite have been studied by STM for many years [49]. When two graphene layers are rotated relative to each other by an angle θ away from Bernal stacking, the induced moiré pattern has a period L given by

$$L = a/(2\sin(\theta/2)). \tag{3.9}$$

Equation (3.9) can be better understood in terms of the reciprocal space (k-space), i.e., the Fourier transform of the real space. The Fourier transform of the triangular lattice gives Bragg spots at corners of a hexagon as shown in the insets of Figs. 3.8**b** and **d**. When two graphene layers rotate against each other, the two corresponding hexagons in reciprocal space also rotate (Fig. 3.9). The distance between the Bragg spot K and the Γ point in the center of the Brillouin zone is $2\pi/a$. With the rotation, the Bragg spots of the two layers separate by a displacement ΔK:

$$\Delta K = \frac{2\pi}{a} 2\sin(\theta/2). \tag{3.10}$$

These displacement vectors form a new hexagon, which corresponds to the Fourier transform of the moiré pattern. (3.9) can be derived by using $\Delta K = 2\pi/L$. It is worth noting that the new hexagon is rotated by $30° - \theta/2$ relative to the original one, as shown experimentally in Fig. 3.8.

3.8.1 Appearance of Moiré Pattern

Most regions on the surface of HOPG do not exhibit moiré patterns and it is hard to know a priori whether after any given cleavage step they will appear or what

periodicity to expect [50]. To facilitate the formation of moiré patterns, the HOPG surface can be treated in aqueous solutions [51] or organic solvents [52], especially in dichloroethane [53] or 1,2,4-trichlorobenzene [54].

It is important to understand the structure and electronic properties of twisted graphene layers because they appear regularly in two of the most promising methods of graphene synthesis. One is epitaxial graphene layers formed on the C-surface of SiC by thermal decomposition [55]. The other is growth by chemical vapor deposition on catalytic metal surfaces [30–32].

3.8.2 Saddle Point Van Hove Singularities

A rotation between graphene layers causes a shift between the corresponding Dirac points in k-space (Fig. 3.9), so that the Dirac wave vector of the rotated layer is given by $K_\theta = K + \Delta K$. If we use the same origin of the momentum for the two layers, so that a uniform hopping couples states of the same momentum in both layers, the zero energy states do not occur at $k = 0$, but rather at $k = -\Delta K/2$ in layer 1 and $k = \Delta K/2$ in layer 2. Unlike in the Bernal stacked bilayer, there is no direct coupling of the zero energy states in one layer to the zero energy states of the other. As shown in ref. [12], the states near the Dirac cone of each layer couple with amplitudes of order $t_\perp^\theta \approx 0.4 t_\perp$ to states of energy of $\pm\hbar v_\mathrm{F} \Delta K$ in the opposing layer and the linear dispersion is preserved near zero energy. Here, $t_\perp$ is the interlayer hopping for unrotated layers and $v_\mathrm{F} \sim 10^6\,\mathrm{m/s}$ is the Fermi velocity. The two Dirac cones intersect near the center of the superlattice Brillouin zone and hybridize, resulting in a saddle point in the energy dispersion and in two Van Hove singularities which symmetrically flank the Dirac point (Fig. 3.10) [11].The separation between Van Hove singularities is controlled by the twist angle θ. For angles $2° < \theta < 5°$, the separation is given by

$$\Delta E_{VHS} \approx \hbar v_F \Delta K - 2t^\theta \tag{3.11}$$

but curves up at smaller angles (Fig. 3.11).

3.8.3 Single Layer-like Behavior and Velocity Renormalization

As the Van Hove singularities separate from each other with increasing twist angle, the low energy sector of the Dirac cones in each layer is less disturbed. Therefore, for sufficiently low energies electrons in twisted layers can behave like massless Dirac fermions in a single layer graphene [12, 56–63]. However, the slope of the Dirac cone, i.e., Fermi velocity, still reflects the influence of the Van Hove singularities, leading to a renormalized Fermi velocity which depends on twist angle [12]

$$\frac{v_\mathrm{F}(\theta)}{v_\mathrm{F}^0} = 1 - 9\left(\frac{t_\perp^\theta}{\hbar v_F^0 \Delta K}\right)^2. \tag{3.12}$$

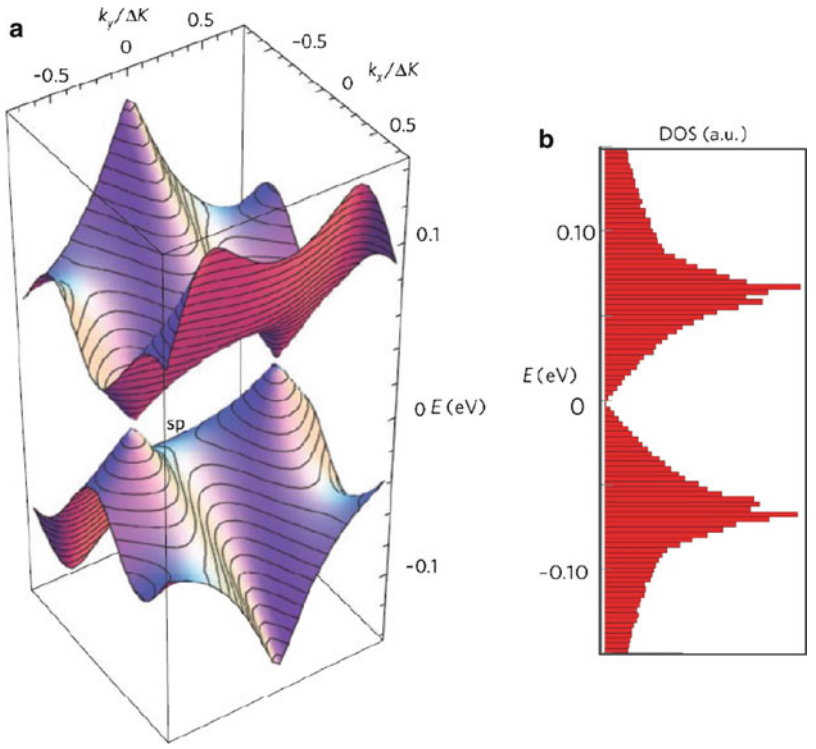

Fig. 3.10 (**a**) Dispersion of lowest energy states for $\theta = 1.79°$, $t_\perp \sim 0.27\,\text{eV}$ of a bilayer. A saddle point (marked "sp") is visible between the two Dirac points in the negative energy band; another one exists in the positive energy band. (**b**) DOS with Van Hove singularities corresponding to the dispersion in (**a**) (Reprinted by permission from Macmillan Publishers Ltd: Nature Physics [11], copyright (2010))

Such velocity renormalization is observed experimentally on CVD graphene films as shown in Fig. 3.12. In region C, a moiré pattern with period of 4.0nm is resolved, while in region B, the pattern is not resolved indicating a much smaller period, which would correspond to a twist angle larger than 10° [30]. In both regions STS in magnetic field show Landau levels of massless Dirac fermions (Fig. 3.12b). However, the spacing between peaks is smaller in region A than that in region B. The corresponding Fermi velocities are $0.87 \times 10^6\,\text{m/s}$ and $1.10 \times 10^6\,\text{m/s}$ for regions C and B, respectively. In zero field, STS performed of large bias sweeps in both regions reveals Van Hove singularities in region C but not in region B even for bias voltages up to $\pm 500\,\text{meV}$ Fig. 3.12d).

Similar Landau levels of massless Dirac fermions have been observed in multilayer graphene grown on SiC substrates [64]. However, it seems that the Landau levels in that case were independent of the moiré patterns, the periods of which correspond to a wide range of twist angles down to $\sim 1.4°$. But the pattern was

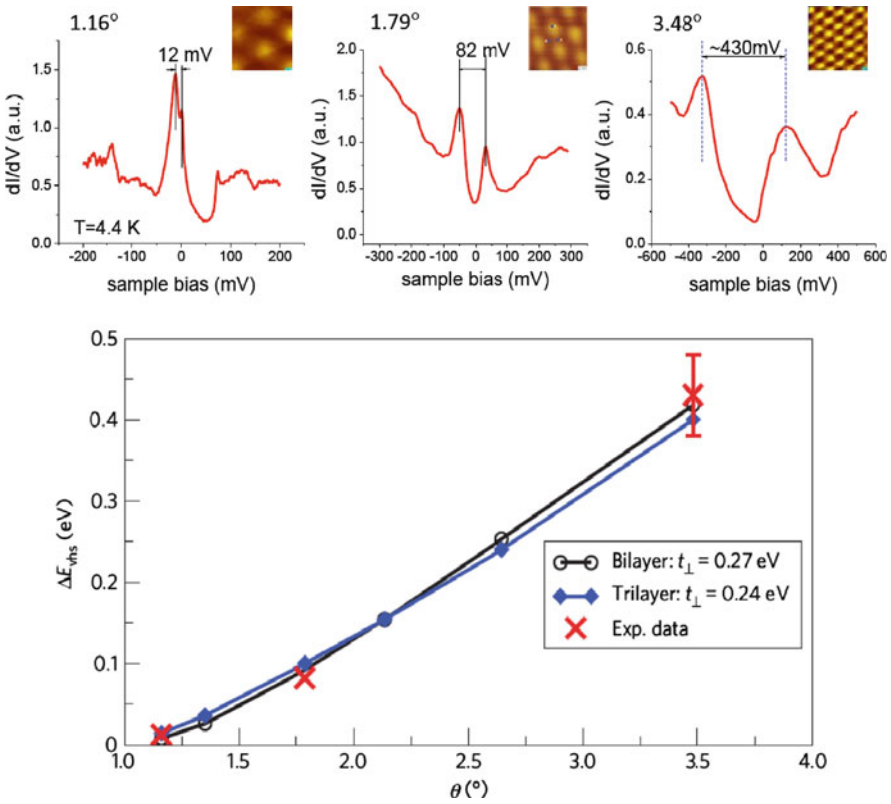

Fig. 3.11 (*top*) Tunneling spectra for different moiré patterns. (*bottom*) Angle dependence of the separation between Van Hove Singularities (Reprinted by permission from Macmillan Publishers Ltd: Nature Physics [11], copyright (2010))

significantly different from that in Fig. 3.8 as it was dominated by a honeycomb structure seen everywhere within the superstructures, which is inconsistent with a simple twist-induced moiré pattern. Later it was shown that the large period superstructure in [64] actually comes from deeper layers, serving as a background to the rotated top layer. The twist angle for the top layer was larger [65] corresponding to a much smaller pattern that was missed in the initial report. The data in [56] provide support for the weak angle dependence of the Fermi velocity at large angles (3.12).

It is important to note that the mechanism of downward velocity renormalization in twisted layers is distinctly different from that in isolated graphene layers discussed in Sect. 3.6. In the twisted layers the renormalization only occurs in the presence of coupling between layers and its magnitude is a sensitive function of the twist angle. By contrast the velocity renormalization observed in the decoupled graphene layer slightly suspended on graphite is due to electron–phonon interaction.

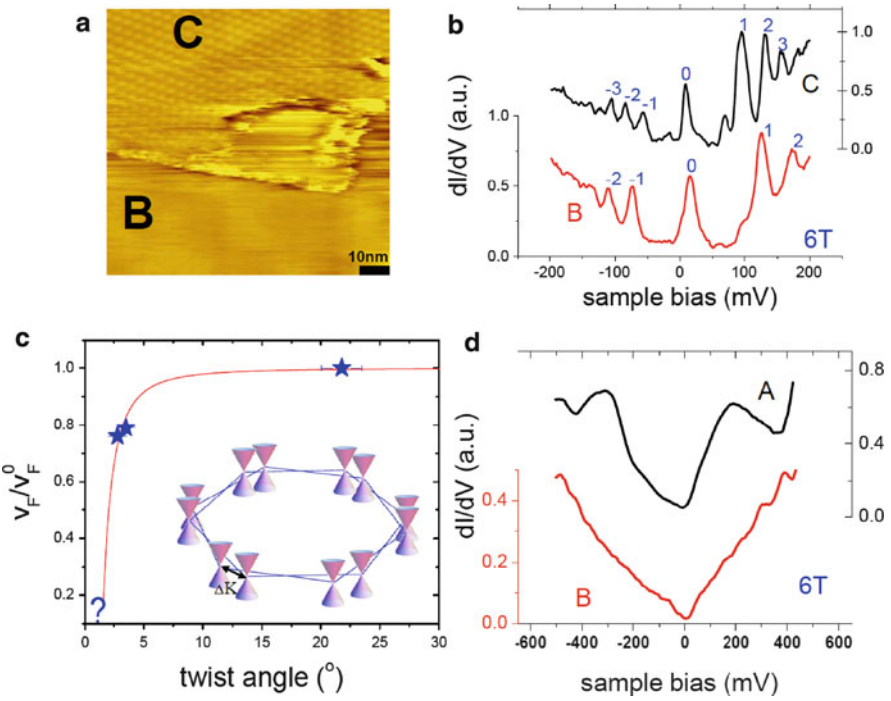

Fig. 3.12 Velocity renormalization. (**a**) Moiré pattern with period of 4.0 nm (region C) and its nearby region B, which is featureless with the same resolution. (**b**) High field (6 T) tunneling spectra taken at locations marked C and B in (**a**). (**c**) Twist angle dependence of velocity renormalization. Line is theoretical prediction according to (3.11). Stars are experimental data. Inset, Dirac cones of twisted layers of graphene. The distance between nearest Dirac cones, ΔK, is controlled by the twist angle. (**d**) Zero field tunneling spectra taken at locations marked C and B in (**a**). Tunneling junction setting: 300 mV and 20 pA for (**a**) and (**b**); 500 mV and 20 pA for (**d**)

This interaction is strongest when the layers are decoupled and tunneling between the top graphene layer and the layers underneath it is completely suppressed as is the case discussed in Sect. 3.6 where the proximity to an atomic step defect causes ∼30% increase in interlayer distance. Furthermore, the zero field tunneling spectra are qualitatively different in the two cases. The twist induced velocity renormalization leads to the appearance of pronounced peaks in the spectra whose separation is proportional to the twist angle, whereas electron–phonon coupling causes shoulder features at an energy controlled by the A_1' phonon. In Sect. 3.7, we showed that the electron-phonon coupling via the A_1' phonon is strongest in decoupled single layer and that it becomes less important as the coupling between layers increases. Here we note that v_F at large twist angles is almost identical to that in multilayers with Bernal stacking, suggesting that electron–phonon coupling via A_1' is also suppressed in twisted layers.

3.9 Graphene on SiO_2

Graphene was first isolated by mechanical exfoliation onto a 300-nm SiO_2 layer supported on n-doped Si [20]. This configuration is convenient because the graphene flakes can be detected by optical microscopy. In addition it is relatively easy to fabricate FET devices which allow ambipolar gating over a wide density range. Such devices were used to study the transport properties of the relativistic carriers and led to the observation of the anomalous quantum Hall effect (QHE) [66, 67] which demonstrated the 2d nature of the carriers in graphene as well as their chiral nature. They are also well suited for building prototypes for nanoelectronics and sensors [68]. However, more sensitive experimental probes revealed that in spite of the fact that the QHE is readily observed in graphene devices deposited on insulating substrates such as SiO_2 and more recently on SiC [69, 70], it is not possible in these devices to approach the Dirac point and probe its unique properties such as ballistic transport [71–73], specular Andreev reflections [74–76] and correlated phenomena such as the fractional QHE [77, 78]. The failure to probe the Dirac point physics in graphene deposited on such substrates was understood following the application of sensitive local probes. Single electron transistor microscopy [79, 80] and STM [21, 22, 81] revealed that the insulating substrates introduce a random potential which creates inhomogeneous local charging leading to electron/hole puddles over a range of densities close to the Dirac point. This makes it impossible to attain the zero carrier density condition at the Dirac point for any applied gate voltage.

3.9.1 Three Types of Corrugations

Similar to the case for graphite substrates [16], STM topography on the SiO_2 surface also shows the honeycomb structure for single layer graphene and a triangular lattice for multilayers [21]. The absence of defects such as interstitials and vacancies in atomic resolution STM images over wide scan ranges confirms the high degree of crystalline order in graphene, despite harsh conditions applied during processing and sample preparation. However, in contrast to graphene on graphite, significant large-scale corrugations [21] are seen in graphene on SiO_2. The correlation length of the corrugation in graphene ($\sim$32 nm) is comparable to that of the SiO_2 substrate ($\sim$23 nm) suggesting that graphene partially conforms to the substrate [22].

On top of the large-scale corrugation, a finer corrugation was observed in some samples [27] with correlation length $\sim$15 nm, as shown in Fig. 3.13. Such short-scale corrugations are believed to be intrinsic to free standing graphene [35, 82]. However, it was noted that the appearance of the small corrugations strongly depends on the sample preparation process, which may suggest that graphene is partially suspended between protrusions in the substrate.

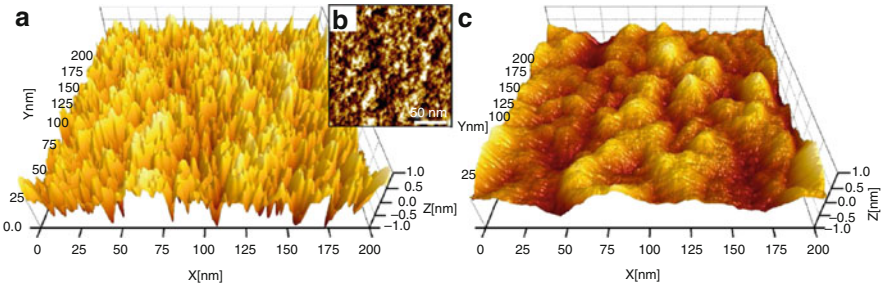

Fig. 3.13 (**a, b**) 3D and 2D constant current STM image of monolayer graphene. (**c**) 3D tapping mode AFM image of the SiO_2 substrate (Reprinted figure with permission from [27]. Copyright (2009) by the American Physical Society)

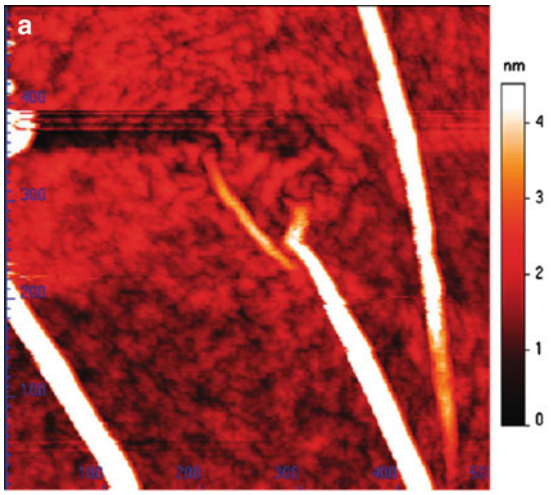

Fig. 3.14 STM topographs of graphene wrinkles (Adapted with permission from [24]. Copyright (2009) American Chemical Society)

During the deposition of graphene with the scotch tape technique, wrinkling is likely to occur especially for large flakes. The wrinkles vary with the precise deposition conditions, forming a third type of corrugation. The wrinkles are more localized in space, for example with a height of $\sim$3 nm over length of $\sim$10 nm as shown in Fig. 3.14 [24]. The wrinkle curvature can provide strong perturbations leading to broken sublattice symmetry which can affect both transport and the STM images leading for example to the appearance of a triangular lattice [22, 24] instead of the honeycomb structure in unperturbed graphene.

The use of atomically flat substrates can significantly reduce the corrugation of graphene. It was found that the roughness of graphene on SiO_2 is significantly larger than that on mica which is comparable to that on Kish graphite [83].

3.9.2 Scanning Tunneling Spectroscopy

Early STS on graphene on SiO_2 reported a gap-like feature within ± 63 meV of Fermi level [23]. The suppression of electronic tunneling near E_F and the concomitant enhancement of tunneling at higher energies were attributed to a phonon-mediated inelastic channel. Thus phonons act as a "floodgate" that controls the flow of the tunneling electrons in graphene. In this scenario, the electrons in the STM tip were assumed to have zero lateral momentum, i.e., at the Γ point in momentum space. Momentum conservation would prevent their direct tunneling into graphene because the Dirac cones are around the K or K′ points. Therefore a third momentum carrying particle, a phonon, would have to be involved to mediate the tunneling event [84]. In other words, only inelastic tunneling processes are allowed. However, such an argument is not valid for an atomically sharp tip because the electron momentum is only restricted by the uncertainty principle, $k \sim \hbar/a_T$ (a_T is the size of the tip) and thus can be sufficiently large to access the K or K′ points. In fact this large gap-like feature was not seen in subsequent STS measurements of either graphene on graphite [16] or graphene on SiC [64] substrates. It is well known that the tunneling spectroscopy of graphene on SiO_2 is spatially nonuniform [25] and gap-like features may be a consequence of local strain induced by ripples, wrinkles, or corrugations [24, 29].

3.9.3 Quantum Interference and Fermi Velocity

In the presence of scattering centers, the electronic wave functions can interfere to form standing wave patterns [85, 86]. These patterns can be observed by measuring the spatial dependence of dI/dV at a fixed sample bias voltage. The Fourier transform of the pattern provides information about the energy and momentum distribution of quasiparticle scattering, which can be used to infer band structure as was demonstrated for bilayer graphene samples [81]. For unperturbed single layer graphene [87], interference patterns are expected to be absent or very weak [88].

However, clear interference patterns are observed for graphene on SiO_2 [26]. Here the main scattering centers are believed to be trapped charges in SiO_2 [89]. Figure 3.15 shows the interference patterns at different sample bias voltages. As the sample bias voltage V_s increases, the structure of the pattern gets finer, and the radius of the Fourier transform ring, $q = 2k$, increases accordingly. Here k is the wave vector of the quasiparticle at energy $E = eV_s$. Plotting the dispersion $E(k)$ against k in Fig. 3.15e gives a linear dispersion from which one obtains $v_F = (1.5 \pm 0.2) \times 10^6$ and $(1.4 \pm 0.2) \times 10^6$ m/s for electron and hole states, respectively. It should be noted that the Fermi velocities in Fig. 3.15e are for states with energies significant away from the Fermi level and the Dirac point. At lower energies, transport measurements yielded $v_F = 1.1 \times 10^6$ m/s [66, 67]. Such velocity renormalization is similar to that discussed in Sect. 3.6.

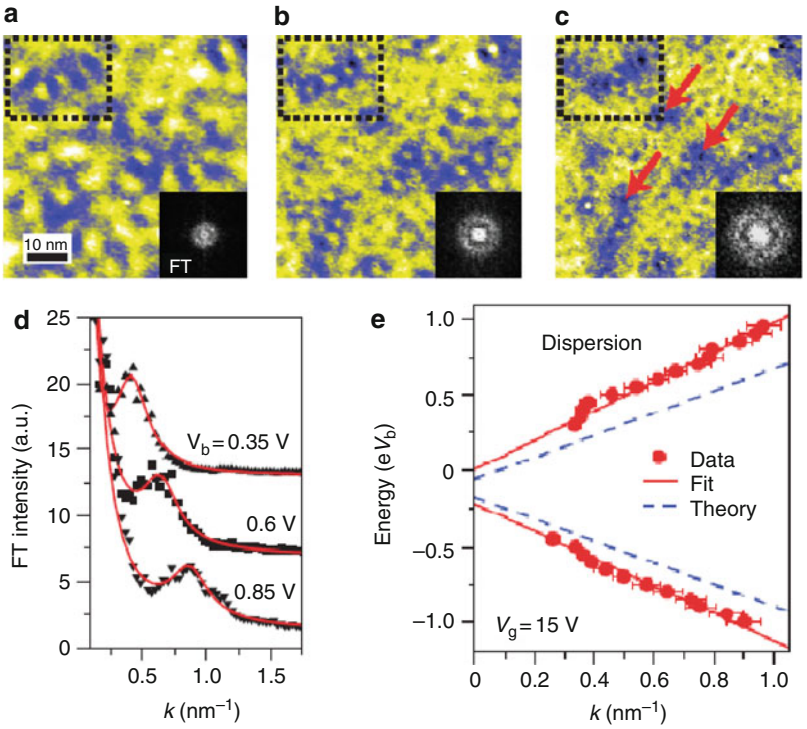

Fig. 3.15 (**a**) Quasiparticle scattering on a graphene surface. (**a–c**) $\mathrm{d}I/\mathrm{d}V$ maps of the same area obtained at sample bias of 0.35, 0.6, and 0.85 V, respectively, at fixed gate voltage of 15 V. Lower right insets: two-dimensional (2D) Fourier transform of each image. Red arrows in (**c**) point to localized scattering centers. (**d**) Radial averaged intensity profiles of the 2D Fourier transforms shown in (**a–c**) plotted as a function of k. Red lines indicate Lorentzian fits. Curves are vertically displaced for clarity (**e**) Quasiparticle energy dispersion above and below the Dirac point ($V_D = -0.2$ V). Each point is extracted from a Fourier analysis as in (**a–d**). Solid red lines show fitted linear curves (Reprinted by permission from Macmillan Publishers Ltd: Nature Physics [26], copyright (2009).)

The renormalization mechanism could be attributed to electron–phonon coupling [16, 38] or to plasmons [90].

3.9.4 Trapped Charges in SiO_2

Individual scattering centers can be identified from the $\mathrm{d}I/\mathrm{d}V$ map taken at energies away from the Dirac point when the electron wave length is small [26]. In Fig. 3.16c, the localized minima in the inhomogenous $\mathrm{d}I/\mathrm{d}V$ map are marked with red arrows as locations of scattering centers. Comparing to the topography in Fig. 3.16a, there are no correlations between corrugations and the scattering centers, suggesting the

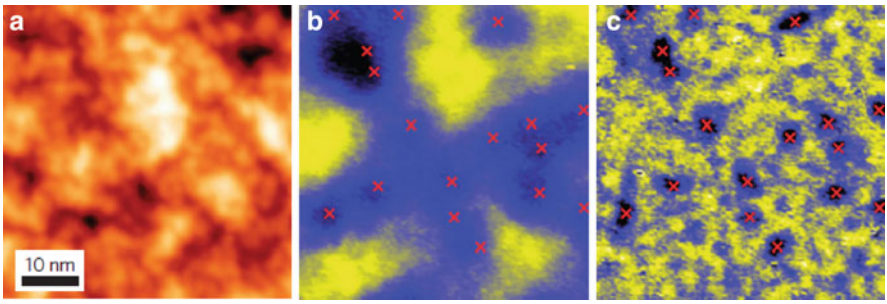

Fig. 3.16 (**a**) STM topography of graphene on SiO_2. (**b**) dI/dV map at a bias near the Dirac point showing electron puddles due to charge fluctuations over the same region of graphene as (**a**). Red crosses indicate the location of quasiparticle scattering centers observed in (**c**). (**c**) dI/dV map of the same area at larger bias revealing impurity scattering centers in electron-rich charge-density puddles (red crosses) (Reprinted by permission from Macmillan Publishers Ltd: Nature Physics [26], copyright (2009).)

latter plays a more important role in the electronic states in graphene. When the sample bias voltage is close to the Dirac point, the electron wave length is so large that it covers many scattering centers. Nowthe dI/dV map in Fig. 3.16b shows coarse structures, arising from the spatial dependence of the Dirac point energy which gives rise to electron–hole puddles across the sample [26, 79].

3.10 Edges, Defects and Magnetism

Magnetic materials usually contain 3d or 4f electrons, such as in Fe, Co, Ni, and rare earth elements/alloys. Magnetic ordering in these materials comes from partially filled d- or f-electron bands. Magnetism is not common for light elements such as carbon which contain only p electrons. However in a bipartite lattice, such as that of grapheme, magnetism can appear in the presence of point defects or edges [5, 6].

Point defects on the graphite surface have been studied with STM for a long time [91, 92]. Recent theoretical work showed that localized electronic states produce strong enhancement of the DOS near the Fermi level [93]. Further analysis based on density functional theory [94] and tight-binding Hubbard model [95] demonstrates that magnetism can appear for a finite concentration of defects due to electron–electron interactions. An STM image of such a defect produced by Ar^+ ion irradiation on the surface of graphite [96] is shown Fig. 3.17. Surrounding the defect one can see an extended threefold $\sqrt{3} \times \sqrt{3}$(R3) pattern. Scanning tunneling spectroscopy on the vacancy reveals a resonance near the Dirac point (Fig. 3.17c) whose intensity exhibits a power law decay with distance away from the vacancy.

Crystallographic edges in graphene can be either zigzag or armchair (Fig. 3.18). A zigzag edge is terminated by atoms belonging to only one sublattice while for armchair the terminations alternate between the two sublattices. (A discussion on

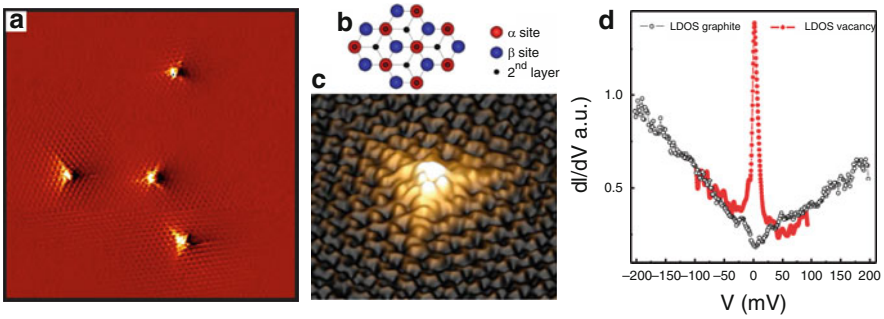

Fig. 3.17 (**a**) $17 \times 17\,\text{nm}^2$ STM topography, measured at 6 K, showing the graphite surface after the Ar^+ ion irradiation. (**b**) Schematic diagram of the graphite structure. (**c**) 3D view of a single isolated vacancy. (**d**) STS measurements of the LDOS induced by the single vacancy on the surface of graphite (Reprinted figure with permission from [96]. Copyright (2009) by the American Physical Society.)

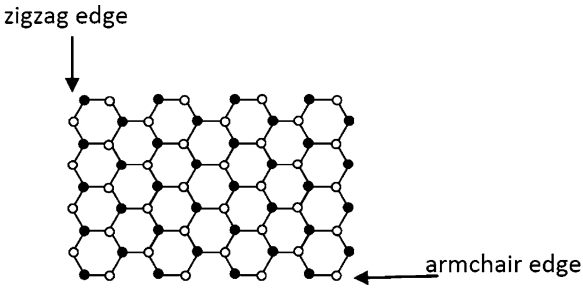

Fig. 3.18 Two types of edges for graphene: zigzag edge and armchair edge. The open and closed circles show the *B*- and *A*-site carbon atoms, respectively

studying graphene edges and defects with Raman spectroscopy can be found in Chap. 2.) On graphite it has been demonstrated that localized states exist near a zigzag edge but not near armchair terminations [97]. The enhanced density of states associated with the zigzag termination has also been seen around grain boundaries in graphite [98].

A localized resonance in the DOS at an edge is a prerequisite for magnetic correlations [5, 6]. Thus far this scenario found support in graphite through comparison between topography, magnetic force microscopy, and electric force microscopy [98].

3.11 SPM-based Nano-lithography

STM and STS are powerful probes that provide direct access to both the structure and the electronic properties of graphene in its various forms. At the same time STM and other scanning probe microscopy tools can modify the surface and the edges, introduce point defects, deposit impurities, and tailor the structure at nanometer

scales [99]. In fact, scanning probe lithography (SPL) has become a leading method in nanolithography [100], together with traditional optical/e-beam lithography and soft lithography. In SPL, a local probe, such as an STM tip, is brought very close to the sample surface so that the tip–sample interaction is strong enough to induce a mechanical or chemical modification. Research in SPL and its hybrid method [100] is a fast moving field with diverse applications. In this section we briefly review developments related to graphene.

3.11.1 Signs of Invasiveness of an STM Tip

An STM tip should be noninvasive if it is used as a probe of the intrinsic surface properties of samples. However, when used in nanolithography the tip has to be sufficiently invasive. Actually the same tip is usually used for *in situ* characterization before and after nanolithography. A natural question is how to define the invasiveness of the STM tip experimentally.

The first signature of an invasive tip is the appearance of distance dependence of the tunneling spectrum [15, 48]. For a sufficiently large tip–sample separation, typically characterized by a tunneling resistance of $\sim$10 GΩ, the spectrum is usually independent of tip–sample distance. As the tip gets closer, a shift in Fermi level appears first and then the spectrum starts to distort, which is accompanied by a decrease of the apparent tunneling barrier height [15].

Another sign of tip invasiveness can be seen in topography. In early STM studies on graphite, one of the most dramatic observations of tip invasiveness was a giant corrugation [101, 102], of order 0.1–0.8 nm, which appeared in the topography of the surface for measurements with low tunneling resistance (20 $-$ 0.5 MΩ). Such corrugation cannot reflect the physical position of the carbon atoms in the honeycomb structure because it is much larger than the interatomic distance. It is now understood that the graphite surface deforms elastically when the tip is very close to it, resulting in the giant corrugation.

For graphene on SiO_2, the force between graphene and substrate can be significantly weaker than that on the graphite surface especially for regions that are corrugated. This could lead to unstable STM images particularly if the tip–surface distance is too small [21].

3.11.2 Folding Graphene Layers

Folding of the top graphene layer on a graphite surface happens occasionally during the cleavage process. An SPM tip can be used to intentionally fold the top layer [103–105]. Such folding was accomplished [105] for STM settings corresponding to a tunneling resistance of $\sim$100 MΩ (100–200 mV sample bias voltage and 1–2 nA tunneling current), in UHV. Folding could also happen during imaging.

To facilitate the folding process [105], the tip was shaken at frequency of 150 Hz at selected edges. Modulating the bias voltage between 50 and 100mV at 250 Hz while scanning the center of the folded region leads to unfolding. Preferred folding directions were found along symmetry axes of graphene.

The mechanism of folding and unfolding was explained as follows [105]. Since the σ bond between carbon atoms is much stronger than the interlayer coupling, an STM tip close to sample surface does not destroy the honeycomb structure when it slowly bends the sample out of plane [102]. A vibrating STM tip generates point-like compression–expansion deformations, which propagate along the graphene layer. The pressure waves are damped at large distances, leaving the layer unharmed. However, at layer edges the pressure waves can interfere with each other and the enhanced vibration amplitude could facilitate the separation of the vibrating layer from its support. Subsequently, the vibrating layer flips over to a new position.

3.11.3 Cutting Graphene Layers

Etching the sample surface by STM tips requires sample bias voltages above a certain threshold, which is much higher than that used in folding. In ultra high vacuum, the threshold voltage depends linearly on the binding energy of the atoms indicating that this process involves sublimation of surface atoms induced by the tunneling electrons [106]. Under ambient conditions Pt–Ir tips were usually used in the etching process. In this case the threshold voltage is independent of the binding energy and the etching process is attributed to a chemical reaction involving water molecules [107–109] at the surface: $C(H_2O) \rightarrow H_2(\uparrow) + C(O)$. Here $C(H_2O)$ represents a water molecule physisorbed on a surface carbon atom and C(O) an oxygen atom chemisorbed on a surface carbon atom. The upward arrow indicates production of a gas molecule. Systematic studies [109] demonstrated that the threshold voltage increased from 1.95 to 3.68 V when the tip scanning speed increased from 0.1 nm/s to 1 mm/s. Such dependence can be understood in terms of the kinetics of the chemical reaction as the reaction time decreases with increasing tip speed. At low scanning speed, the activation energy can be as low as ∼0.9 eV [109].

For fixed tip scanning speed, say 100 nm/s, the results of fabrication depend on the sample bias voltage [109]. Near the threshold voltage, irregular-shaped hillocks, several nanometer in width and 0.1–0.3 nm in height, emerge on the surface. This modification is thought to be due to partial oxidation of the uppermost graphene layer. As shown in Fig. 3.19 the top graphite layer is partially etched at a bias voltage of 3.09 V and etching was completed at 3.19 V, resulting in groves ∼5 nm wide and ∼0.35 nm deep, which is close to the interlayer spacing of graphite layers. The groves become wider and deeper with increasing bias voltage. Above 3.47 V, the surface becomes significantly damaged.

A similar technique was used to cut a nanoribbon on a graphite surface [110,111]. To perform the cutting, a Pt-Ir tip made a single shot scan with tip speed of 1–5 nm/s.

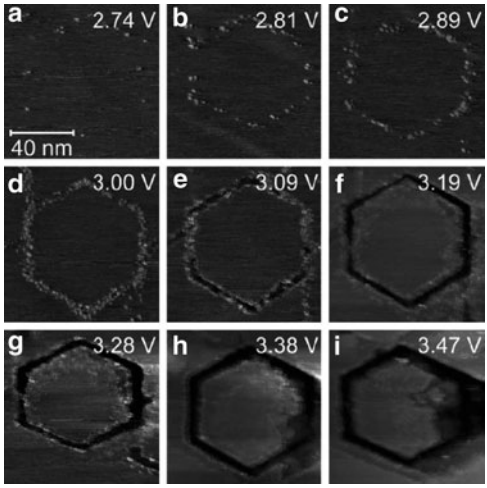

Fig. 3.19 Comparison of STM images of the HOPG surface tailored by STM with various bias voltages: (**a**) 2.72 V, (**b**) 2.81 V, (**c**) 2.89 V, (**d**)3.00 V, (**e**) 3.09 V, (**f**) 3.19 V, (**g**) 3.28 V, (**h**) 3.38 V, and (**i**) 3.47 V. In each tailoring, the STM tip was moved along a regular hexagon with a 40 nm long side (Reprinted from [109], copyright (2004), with permission from Elsevier.)

Depending on the microstructure of tip, the optimal sample bias voltages is in the range 2.2–2.6 V for a tunneling current of 1 nA. An energy gap of ∼0.5 eV was observed in a 10 nm armchair graphene nanoribbon fabricated by this method [110].

In spite of progress in cutting graphene by STM, the details of the cutting process remain to be clarified to achieve reliable fabrication.

3.11.4 Surface Modification

Graphene is chemically inert in air at room temperature. However, atomic hydrogen can bind to graphene to form graphane, which is insulating, if both sides are saturated [112]. When graphene sits on a substrate, its electronic states still change dramatically even though only a single side can be saturated [113]. An STM tip has been used to selectively remove hydrogen atoms via electron stimulated desorption (ESD) in UHV [114]. Such a process is sensitive to the choice of tip. For Pt–Ir tips, desorption occurred under normal imaging conditions. For W tips, the sample surface was not altered with sample bias voltages up to 2 V and tunneling current of 50 pA. When the set point current (50 pA) and tip velocity (75 nm/s) were held constant, desorption events started to occur for bias voltages above +3.5 V. At +4.0 V, a graphene line could be written with an average width of 5–10 nm. At +5.0 V, the line width increased to 15–20 nm [113]. Pristine graphene was recovered after ESD.

Besides hydrogenation, graphene on substrates can be oxidized by Hummers method [115] to form graphene oxide (GO). The resistivity of GO is four orders of magnitude higher than that of the pristine sample [116]. A hybrid SPL techniqu called thermochemical nanolithography (TCNL) has been used to locally reduce the GO [117]. In TCNL, a heated AFM tip [118] is brought into contact with the GO

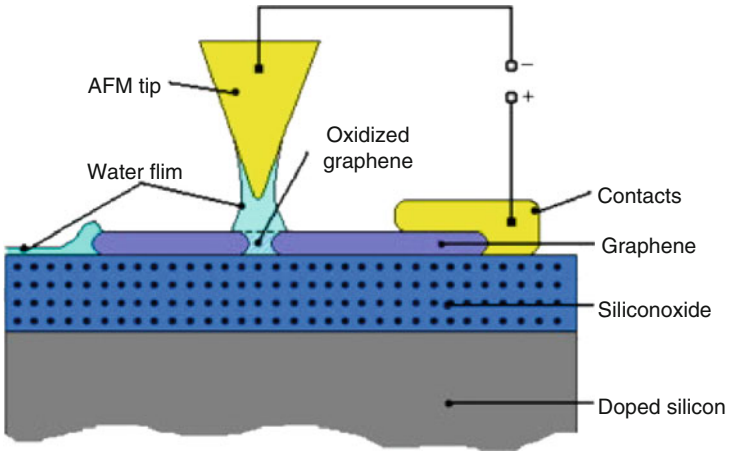

Fig. 3.20 Schematic setup for the local anodic oxidation of graphene. A graphene sheet lies on a silicon oxide substrate and is electrically connected by Au electrodes. A positive bias voltage is applied to the graphene sheet (anode) with the tip of the AFM (cathode) grounded. In a humid environment a water meniscus forms between the AFM and the graphene flake which acts as an electrolyte (Reprinted from [119], copyright (2008), with permission from Elsevier.)

surface with a loading force of 120–230 nN. Nanoscale regions of reduced graphene oxide (rGO) can be patterned down to 12 nm in width at speeds of several mm/s. GO can be reduced with 100% efficiency to recover the resistivity of the pristine sample.

A reverse process was demonstrated by local anodic oxidation (LAO) lithography of graphene [119–121]. Unlike the reduction process, the AFM tip was held at room temperature, working in noncontact mode. A conductive tip was used to apply a large bias voltage, typically 15–35 V, between the tip and the substrate to induce electrochemical oxidation of graphene (Fig. 3.20). A relative humidity of ∼40% was maintained during LAO lithography. The bias voltage could be modulated between zero and the set value with a 100 Hz square wave to help stabilize a water meniscus around the tip [120].

When a constant sample bias voltage was used, LAO lithography fabricated narrow trenches with bump structures on each side of them. The overall line width decreased with increasing tip speed [121]. With a square wave sample bias voltage [120], either trenches or bumps could be fabricated (Fig. 3.21). The formation of trenches was attributed to the oxidation of graphene into volatile carbon oxides under the AFM tip. The bumps were attributed to partial oxidization of graphene into nonvolatile graphene oxide with some oxygen incorporated into the lattice. It was observed that the formation of trenches or bumps could be controlled by the magnitude of the electric fields between tip and sample, high and low fields for the former and latter, respectively [120], which is similar to what is observed in STM lithography [109].

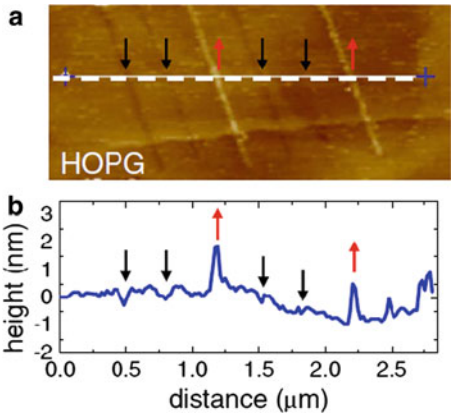

Fig. 3.21 (**a**) AFM images of line patterns created by the LAO technique. (**a**) Trenches or bumps were formed on HOPG surface. Six lines (from left to right) are written with the same tip bias voltage of −20 V while the set point was cycled through 0.3, 0.2, 0.1, 0.3, 0.2, and 0.1 V, corresponding to 15%, 10%, 5%, 15%, 10%, and 5% of the free-oscillation amplitude for an unloaded tip. (**b**) Height profile across the line marked in (**a**) (Reprinted with permission from [120], copyright (2008), American Institute of Physics.)

3.12 Summary and Perspectives

Graphene is a true 2d electron system (DES) with new and exotic electronic properties arising from a unique lattice structure which is particularly well suited for studies by STM/STS. By using STM/STS it is possible to access at the same time both the structure and the electronic properties and to study the interplay between the two. The openness and easy accessibility of the 2DES in graphene distinguishes it from most conventional DES where the carriers are buried deep inside a heterostructure at the interface of two bulk materials, say GaAs/InGaAs. The only other exposed 2DES known, electrons on the surface of liquid helium [122], cannot be studied with STM/STS or any technique such as dc transport that requires contact to the carriers.

In addition to probing the structure of graphene, STM also allows to modify it introducing defects, folds, boundaries, or nanostructures which can profoundly affect its electronic properties. At the same time these electronic properties can be probed in the STS mode to reveal the electronic states and how they are modified in response to external influences including magnetic field, carrier density, substrates, impurities, structural changes, boundaries, and strain.

So far STM/STS and transport measurements were done independently. In the near future we anticipate technical advances combining the two probes *in situ* which will allow correlating transport properties, topography and spectroscopy directly. By combining STM/STS with strong magnetic fields, back gating, and transport measurements it will be possible to explore the properties of correlated electronic

phases such as fractional quantum Hall effect states and skyrmion excitations. Another promising direction is to use SPM lithography to modify graphene devices and to study their properties *in situ* which could provide valuable insight into graphene based nanoelectronics.

Acknowledgements Support for this work was provided by DOE, NSF and Lucent.

References

1. A.H. Castro Neto, F. Guinea, N.M.R. Peres, K.S. Novoselov, A.K. Geim, Rev. Mod. Phys. **81**, 109 (2009)
2. D.S.L. Abergel, V. Apalkov, J. Berashevich, K. Ziegler, T. Chakraborty, Adv. Phys. **59**, 261 (2010)
3. D.A. Abanin, P.A. Lee, L.S. Levitov, Phys. Rev. Lett. **96**, 176803 (2006)
4. M. Wimmer, I. Adagideli, S. Berber, D. Tománek, K. Richter, Phys. Rev. Lett. **100**, 177207 (2008)
5. J.J. Palacios, J. Fernández-Rossier, L. Brey, H.A. Fertig, Semicond. Sci. Technol. **25**, 033003 (2010)
6. O.V. Yazyev, Rep. Prog. Phys. **73**, 056501 (2010)
7. K. Nakada, M. Fujita, G. Dresselhau, M.S. Dresselhaus, Phys. Rev. B **54**17, 954 (1996)
8. V.M. Pereira, A.H. Castro Neto, Phys. Rev. Lett. **103**, 046801 (2009)
9. M.A.H. Vozmediano, M.I. Katsnelson, F. Guinea (2010) arXiv:1003.5179
10. A.V. Shytov, M.I. Katsnelson, L.S. Levitov, Phys. Rev. Lett. **99**, 236801 (2007)
11. G. Li, A. Luican, J.M.B. Lopes dos Santos, A.H. Castro Neto, A. Reina, J. Kong, E.Y. Andrei, Nat. Phys. **6**, 109 (2010)
12. J.M.B. Lopes dos Santos, N.M.R. Peres, A.H. Castro Neto, Phys. Rev. Lett. **99**, 256802 (2007)
13. C.J. Chen, *Introduction to Scanning Tunneling Microscopy*, (Oxford University Press, 2007)
14. O. Fischer, M. Kugler, I. Maggio-Aprile, C. Berthod, C. Renner, Rev. Mod. Phys. **79**, 353 (2007)
15. G. Li, A. Luican, E.Y. Andrei, Physica B **404**, 2673 (2009)
16. G. Li, A. Luican, E.Y. Andrei, Phys. Rev. Lett. **102**, 176804 (2009)
17. V.W. Brar, S. Wickenburg, M. Panlasigui, C.H. Park, T.O. Wehling, Y. Zhang, R. Decker, Ç. Girit, A.V. Balatsky, S.G. Louie, A. Zettl, M.F. Crommie, Phys. Rev. Lett. **104**, 036805 (2010)
18. M. Pereira, F.M. Peeters, P. Vasilopoulos, Phys. Rev. B **76**, 115419 (2007)
19. A. Luican, G. Li, E.Y. Andrei, Solid State Commun. **149**, 1151 (2009)
20. K.S. Novoselov, A.K. Geim, S.V. Morozov, D. Jiang, Y. Zhang, S.V. Dubonos, I.V. Grigorieva, A.A. Firsov, Science **306**, 666 (2004)
21. M. Ishigami, J.J. Chen, W.G. Cullen, M.S. Fuhrer, E.D. Williams, Nano Lett. **7**, 1643 (2007)
22. E. Stolyarova, K.T. Rim, S. Ryu, J. Maultzsch, P. Kim, L.E. Brus, T.F. Heinz, M.S. Hybertsen, G.W. Flynn, Proc. Natl. Acad. Sci. USA **104**, 9209 (2007)
23. Y. Zhang, V.W. Brar, F. Wang, C. Girit, Y. Yayon, M. Panlasigui, A. Zettl, M.F. Crommie, Nat. Phys. **4**, 627 (2008)
24. K. Xu, P.G. Cao, J.R. Heath, Nano Lett. **9**, 4446 (2009)
25. A. Deshpande, W. Bao, F. Miao, C.N. Lau, B.J. LeRoy, Phys. Rev. B **79**, 205411 (2009)
26. Y. Zhang, V.W. Brar, C. Girit, A. Zettl, M.F. Crommie, Nat. Phys. **5**, 722 (2009)
27. V. Geringer, M. Liebmann, T. Echtermeyer, S. Runte, M. Schmidt, R. Rückamp, M.C. Lemme, M. Morgenstern, Phys. Rev. Lett. **102**, 076102 (2009)
28. V. Geringer, D. Subramaniam, A.K. Michel, B. Szafranek, D. Schall, A. Georgi, T. Mashoff, D. Neumaier, M. Liebmann, M. Morgenstern, Appl. Phys. Lett. **96**, 082114 (2010)

29. M.L. Teague, A.P. Lai, J. Velasco, C.R. Hughes, A.D. Beyer, M.W. Bockrath, C.N. Lau, N.C. Yeh, Nano Lett. **9**, 2542 (2009)
30. A. Reina, X. Jia, J. Ho, D. Nezich, H. Son, V. Bulovic, M.S. Dresselhaus, J. Kong, Nano Lett. **9**, 30 (2009)
31. X. Li, W. Cai, J. An, S. Kim, J. Nah, D. Yang, R. Piner, A. Velamakanni, I. Jung, E. Tutuc, S.K. Banerjee, L. Colombo, R.S. Ruoff, Science **324**, 1312 (2009)
32. K.S. Kim, Y. Zhao, H. Jang, S.Y. Lee, J.M. Kim, K.S. Kim, J.H. Ahn, P. Kim, J.Y. Choi, B.H. Hong, Nature **457**, 706 (2009)
33. P.R. Wallace, Phys. Rev. **71**, 622 (1947)
34. N.D. Mermin, Phys. Rev. **176**, 250 (1968)
35. J.C. Meyer, A.K. Geim, M.I. Katsnelson, K.S. Novoselov, T.J. Booth, S. Roth, Nature **446**, 60 (2007)
36. S. Gwo, C.K. Shin, Phys. Rev. B **47**, 13059 (1993)
37. J. Gonzalez, F. Guinea, M.A.H. Vozmediano, Phys. Rev. Lett. **77**, 3589 (1996)
38. C.H. Park, F. Giustino, M.L. Cohen, S.G. Louie, Phys. Rev. Lett. **99**, 086804 (2007)
39. C.H. Park, F. Giustino, M.L. Cohen, S.G. Louie, Nano Lett. **8**, 4229 (2008)
40. J.A. Yan, W.Y. Ruan, M.Y. Chou, Phys. Rev. B **79**, 115443 (2009)
41. D. Xiao, M.C. Chang, Q. Niu, Rev. Mod. Phys. **82**, 1959 (2010)
42. K.S. Novoselov, E. McCann, S.V. Morozov, V.I. Fal′′ko, M.I. Katsnelson, U. Zeitler, D. Jiang, F. Schedin, A.K. Geim, Nat. Phys. **2**, 177–180 (2006)
43. F. Guinea, A.H. Castro Neto, N.M.R. Peres, Phys. Rev. B **73**, 245426 (2006)
44. B. Partoens, F.M. Peeters, Phys. Rev. B **75**, 193402 (2007)
45. S. Latil, L. Henrard, Phys. Rev. Lett. **97**, 036803 (2006)
46. K.F. Mak, J. Shan, T.F. Heinz, Phys. Rev. Lett. **104**, 176404 (2010)
47. T. Mastui, H. Kambara, Y. Niimi, K. Tagami, M. Tsukada, H. Fukuyama, Phys. Rev. Lett. **94**, 226403 (2005)
48. G. Li, E.Y. Andrei, Nat. Phys. **3**, 623 (2007)
49. W.T. Pong, C. Durkan, J. Phys. D **38**, R329 (2005)
50. Z.Y. Rong, Phys. Rev. B **50**, 1839 (1994)
51. P.I. Oden, T. Thundat, L.A. Nagahara, S.M. Lindsay, G.B. Adams, O.F. Sankey, Surf. Sci. **181**, 126 (1987)
52. V.J. Cee, D.L. Patrick, T.P. Beebe Jr., Surf. Sci. **329**, 141 (1995)
53. Y. Wang, Y. Ye, K. Wu, Surf. Sci. **600**, 729 (2006)
54. H.S. Wong, C. Durkan, N. Chandrasekhar, ACS Nano **3**, 3455 (2009)
55. W.A. de Heer, C. Berger, X. Wu, P.N. First, E.H. Conrad, X. Li, T. Li, M. Sprinkle, J. Hass, M.L. Sadowski, M. Potemski, G. Martinez, Solid State Commun. **143**, 92 (2007)
56. J. Hass, F. Varchon, J.E. Millán-Otoya, M. Sprinkle, N. Sharma, W.A. de Heer, C. Berger, P.N. First, L. Magaud, E.H. Conrad, Phys. Rev. Lett. **100**, 125504 (2008)
57. S. Latil, V. Meunier, L. Henrard, Phys. Rev. B **76**, 201402(R) (2007)
58. J.M. Campanera, G. Savini, I. Suarez-Martinez, M.I. Heggie, Phys. Rev. B **75**, 235449 (2007)
59. S. Shallcross, S. Sharma, O.A. Pankratov, Phys. Rev. Lett. **101**, 056803 (2008)
60. G.T. de Laissardière, D. Mayou, L. Magaud, Nano Lett. **10**, 804 (2010)
61. S. Shallcross, S. Sharma, E. Kandelaki, O.A. Pankratov, Phys. Rev. B **81**, 165105 (2010)
62. E.J. Mele, Phys. Rev. B **81**, 161405(R) (2010)
63. R. Bistritzer, A.H. MacDonald, arXiv: 1009.4203
64. D.L. Miller, K.D. Kubista, G.M. Rutter, M. Ruan, W.A. de Heer, P.N. First, J.A. Stroscio, Science **324**, 924 (2009)
65. D.L. Miller, K.D. Kubista, G.M. Rutter, M. Ruan, W.A. de Heer, P.N. First, J.A. Stroscio, Phys. Rev. B **81**, 125427 (2010)
66. K.S. Novoselov, A.K. Geim, S.V. Morozov, D. Jiang, M.I. Katsnelson, I.V. Grigorieva, S.V. Dubonos, A.A. Firsov, Nature **438**, 197 (2005)
67. Y. Zhang, Y.W. Tan, H.L. Stormer, P. Kim, Nature **438**, 201 (2005)
68. A.K. Geim, K.S. Novoselov, Nat. Mater. **6**, 183 (2007)

69. T. Shen, J.J. Gu, M. Xu, Y.Q. Wu, M.L. Bolen, M.A. Capano, L.W. Engel, P.D. Ye, Appl. Phys. Lett. **95**, 172105 (2009)
70. A. Tzalenchuk, S. Lara-Avila, A. Kalaboukhov, S. Paolillo, M. Syväjärvi, R. Yakimova, O. Kazakova, T.J.B.M. Janssen, V. Fal′ko, S. Kubatkin, Nat. Nanotechnol. **5**, 186 (2010)
71. E.H. Hwang, S. Adam, S. Das Sarma, Phys. Rev. Lett. **98**, 186806 (2007)
72. X. Du, I. Skachko, A. Barker, E.Y. Andrei, Nat. Nanotechnol. **3**, 491 (2008)
73. S. Cho, M.S. Fuhrer, Phys. Rev. B **77**, 081402 (2008)
74. C.W.J. Beenakker, Phys. Rev. Lett. **97**, 067007 (2006)
75. J.C. Cuevas, A.L. Yeyati, Phys. Rev. B **74**, 180501 (2006)
76. X. Du, I. Skachko, E.Y. Andrei, Phys. Rev. B **77**, 184507 (2008)
77. X. Du, I. Skachko, F. Duerr, A. Luican, E.Y. Andrei, Nature **462**, 192 (2009)
78. K.I. Bolotin, F. Ghahari, M.D. Shulman, H.L. Stormer, P. Kim, Nature **462**, 196 (2009)
79. J. Martin, N. Akerman, G. Ulbricht, T. Lohmann, J.H. Smet, K. von Klitzing, A. Yacoby, Nat. Phys. **4**, 144 (2008)
80. J. Martin, N. Akerman, G. Ulbricht, T. Lohmann, K. von Klitzing, J.H. Smet, A. Yacoby, Nat. Phys. **5**, 669 (2009)
81. G.M. Rutter, J.N. Crain, N.P. Guisinger, T. Li, P.N. First, J.A. Stroscio, Science **317**, 219 (2007)
82. A. Fasolino, J.H. Los, M.I. Katsnelson, Nat. Mater. **6**, 858 (2007)
83. C.H. Lui, L. Liu, K.F. Mak, G.W. Flynn, T.F. Heinz, Nature **462**, 339 (2009)
84. T.O. Wehling, I. Grigorenko, A.I. Lichtenstein, A.V. Balatsky, Phys. Rev. Lett. **101**, 216803 (2008)
85. M.F. Crommie, C.P. Lutz, D.M. Eigler, Nature **363**, 524 (1993)
86. Y. Hasegawa, P. Avouris, Phys. Rev. Lett. **71**, 1071 (1993)
87. T. Ando, T. Nakanishi, R. Saito, J. Phys. Soc. Jpn. **67**, 2857 (1998)
88. I. Brihuega, P. Mallet, C. Bena, S. Bose, C. Michaelis, L. Vitali, F. Varchon, L. Magaud, K. Kern, J.Y. Veuillen, Phys. Rev. Lett. **101**, 206802 (2008)
89. R. Jayaraman, C.G.A. Sodini, IEEE Trans. Electron Devices **36**, 1773 (1989)
90. A. Bostwick, T. Ohta, T. Seyller, K. Horn, E. Rotenberg, Nat. Phys. **3**, 36 (2007)
91. H.A. Mizes, J.S. Foster, Science **244**, 559 (1989)
92. K. Kelly, N. Halas, Surf. Sci. **416**, L1085 (1998)
93. V.M. Pereira, F. Guinea, J.M.B. Lopes dos Santos, N.M.R. Peres, A.H. Castro Neto, Phys. Rev. Lett. **96**, 036801 (2006)
94. O.V. Yazyev, L. Helm, Phys. Rev. B **75**, 125408 (2007)
95. O.V. Yazyev, Phys. Rev. Lett. **101**, 037203 (2008)
96. M.M. Ugeda, I. Brihuega, F. Guinea, J.M. Gómez-Rodríguez, Phys. Rev. Lett. **104**, 096804 (2010)
97. Y. Niimi, T. Matsui, H. Kambara, K. Tagami, M. Tsukada, H. Fukuyama, Phys. Rev. B **73**, 085421 (2006)
98. J. Cervenka, M.I. Katsnelson, C.F.J. Flipse, Nat. Phys. **5**, 840 (2009)
99. A.A. Tseng, A. Notargiacomo, T.P. Chen, J. Vac. Sci. Technol. B **23**, 877 (2005)
100. H.M. Saavedra, T.J. Mullen, P. Zhang, D.C. Dewey, S.A. Claridge, P.S. Weiss, Rep. Prog. Phys. **73**, 036501 (2010)
101. S. Park, C.F. Quate, Appl. Phys. Lett. **48**, 112 (1986)
102. J.M. Soler, A.M. Baro, N. Garcia, H. Rohrer, Phys. Rev. Lett. **57**, 444 (1986)
103. H. Hiura, T.W. Ebbesen, J. Fujita, K. Tanigaki, T. Takada, Nature **367**, 148 (1994)
104. H.V. Roy, C. Kallinger, K. Sattler, Surf. Sci. **407**, 1 (1998)
105. H.V. Roy, C. Kallinger, B. Marsen, K. Sattler, J. Appl. Phys. **83**, 4695 (1998)
106. S. Kondo, M. Lutwyche, Y. Wada, Appl. Surf. Sci. **75**, 39 (1994)
107. T.R. Albrecht, M.M. Dovek, M.D. Kirk, C.A. Lang, C.F. Quate, D.P.E. Smith, Appl. Phys. Lett. **55**, 1727 (1989)
108. R.L. McCarley, S.A. Hendricks, A.J. Bard, J. Phys. Chem. **96**, 10089 (1992)
109. H.F. Hiura, Appl. Sur. Sci. **222**, 374 (2004)
110. L. Tapaszto, G. Dobrik, P. Lambin, L.P. Biro, Nat. Nanotechnol. **3**, 397 (2008)

111. G. Dobrik, L. Tapasztó, P. Nemes-Incze, P.h. Lambin L.P. Biró, Phys. Status Solidi B **247**, 896 (2010)
112. D.C. Elias, R.R. Nair, T.M.G. Mohiuddin, S.V. Morozov, P. Blake, M.P. Halsall, A.C. Ferrari, D.W. Boukhvalov, M.I. Katsnelson, A.K. Geim, K.S. Novoselov, Science **323**, 610 (2009)
113. P. Sessi, J.R. Guest, M. Bode, N.P. Guisinger, Nano Lett. **9**, 4343 (2009)
114. T.C. Shen, C. Wang, G.C. Abeln, J.R. Tucker, J.W. Lyding, Science **268**, 1590 (1995)
115. W.S. Hummers, R.E. Offeman, J. Am. Chem. Soc. **80**, 1339 (1958)
116. X.S. Wu, M. Sprinkle, X. Li, F. Ming, C. Berger, W.A. de Heer, Phys. Rev. Lett. **101**, 026801 (2008)
117. Z. Wei, D. Wang, S. Kim, S.Y. Kim, Y. Hu, M.K. Yakes, A.R. Laracuente, Z. Dai, S.R. Marder, C. Berger, W.P. King, W.A. de Heer, P.E. Sheehan, E. Riedo, Science **328**, 1373 (2010)
118. J. Lee, T. Beechem, T.L. Wright, B.A. Nelson, S. Graham, W.P. King, J. Microelectromech. Syst. **15**, 1644 (2006)
119. A.J.M. Giesbers, U. Zeitler, S. Neubeck, F. Freitag, K.S. Novoselov, J.C. Maan, Solid State Commun. **147**, 366 (2008)
120. L. Weng, L. Zhang, Y.P. Chen, L.P. Rokhinson, Appl. Phys. Lett. **93**, 093107 (2008)
121. S. Masubuchi, M. Ono, K. Yoshida, K. Hirakawa, T. Machida, Appl. Phys. Lett. **94**, 082107 (2009)
122. E.Y. Andrei, *Two Dimensional Electron Systems on helium and other cryogenic substrates* (Kluwer, 1997)

Chapter 4
The Electronic Properties of Adsorbates on Graphene

Eli Rotenberg

Abstract The impact of atomic and molecular adsorbate atoms on the electronic structure of the graphene lattice is discussed in the context of how they alter, or renormalize, the graphene electronic band structure. This band renormalization is manifested in several ways, including a rigid shift of the electronic bands due to doping, energy gap formation due to breaking of the lattice symmetry, and alteration of the energy dispersion due to changes in electron–electron, electron–phonon, and electron–plasmon interactions. Also, depending on the arrangement of the adsorbates, many exotic states are predicted or have been observed, including ferromagnetism and strong (Anderson) localization regimes. These effects can be observed using the angle-resolved photoemission spectroscopy (ARPES) technique, which is briefly reviewed.

After an overview of electronic and magnetic structure of all atomic adsorbates, we will present results for only three combinations of adatoms: (1) H atoms, (2) K atoms, and (3) mixtures of Ca and K atoms. Experiments with just these three adsorbates reveal diverse physics from Anderson localization, to instability toward Mott and superconducting ground states. These examples involve distinct adsorbate symmetry classes and uncover themes that can be expected to be found generally for adsorbates.

4.1 Introduction: What Are Adsorbates on Graphene Good for?

The many proposed applications for graphene discussed throughout this book have led to an explosion of research into its properties. To enable many of these new technologies, it is necessary to understand and control the interaction of graphene

E. Rotenberg (✉)
The Advanced Light Source, Ernest Orlando Lawrence Berkeley National Laboratory, Berkeley, CA, USA
e-mail: erotenberg@lbl.gov

H. Raza (ed.), *Graphene Nanoelectronics*, NanoScience and Technology,
DOI 10.1007/978-3-642-22984-8_4, © Springer-Verlag Berlin Heidelberg 2012

with adsorbates. This need arises on the one hand because adsorbates can modify the intrinsic properties of graphene, leading to new and useful behaviors, and on the other hand because adsorbates can limit the conductivity of graphene, which can adversely impact electronic devices.

For example, it was recognized early on that the properties of graphene devices fabricated on SiO_2 could be improved by cleaning its surfaces [1], suggesting a clear role for adsorbates in limiting the conduction. Although a role of the substrate to limit mobility was expected, even when freely suspended, mobility was clearly still limited by adsorbates which find their way to the samples during their fabrication. Only when a cleaning process was followed [2] could optimized mobilities be achieved, near 200,000 cm^2/Vs [2, 3] for free-standing graphene membranes. These values were close to the intrinsic mobility limits estimated by the weak electron–phonon coupling in graphene [4, 5].

Yet, we still have a way to go: the highest mobility achieved so far in freestanding graphene was inferred by contactless cyclotron resonance experiments to be in excess of 10,000,000 cm^2/Vs [6]. It is likely that residual adsorbates (and, with related properties, lattice defects) are responsible for limiting synthesized graphene from reaching its potential [7].

Aside from pushing the mobility limits, it is also the control of graphene's properties by means of external modification that will be a key factor to exploiting this material in new device schemes. In this chapter, we discuss how graphene's electronic properties are modified by chemical doping, usually by the sparse adsorption of atoms or molecules.

This topic is of fundamental importance, because by their nature, adsorbates not only can donate electrons or holes to graphene but also can play a role as defects, disrupting the lattice symmetry from which the unique properties of graphene – such as the important pseudospin degree of freedom – are derived.

In situ studies of transport under the influence of a controlled amount of adsorbates have occasionally been conducted [8–10], but such experiments have been relatively rare. One reason is that such adsorption is traditionally the domain of surface science experiments conducted in ultrahigh vacuum (UHV), and there are very few setups which can both conduct such adsorption experiments and measure transport on the same samples.

On the other hand, the fact that graphene can be grown or deposited on a surface allows traditional surface-science probes such as scanning tunneling microscopy (STM) and (ARPES) to be applied to the problem. Both these techniques probe the density of states (DOS) of graphene, the former with spatial, the latter with momentum resolution. Although not directly providing data on mobility, both techniques can reveal crucial information on the energy-dependent scattering properties of adsorbates in a well-controlled way. Furthermore, both techniques probe not only electrons at the Fermi level, but also "hot" carriers, those with energy (relative to the Fermi energy E_F) greater than $k_B T$. Therefore, these tools can also provide information about nonequilibrium properties. ARPES is reviewed in Sect. 4.2, while the use of STM to study graphene is discussed thoroughly in Chap. 3.

Theory has played a key role to understand carbon systems in general, starting well before the actual isolation of graphene crystals. The classic example of this is Wallace, who first calculated graphene's band structure in 1947 as an approximation to graphite [11]. Nevertheless, we must use caution when interpreting theory, especially concerning collective behavior such as magnetism. Such collective behaviors are very sensitive to the assumptions behind the calculations.

As we show in Sect. 4.3, many adatoms are predicted to have a magnetic moment, from which one might infer ferromagnetic behavior. So there has been a large theoretical effort to elucidate the possibility of graphene magnetism in connection with spintronics devices. But to date, neither individual magnetic moments nor collective magnetism has been conclusively observed in any graphene system. The reason stems from the sensitivity of such calculations to the overall symmetry of the adsorbate distribution, and this is discussed in Sect. 4.4.

So, what are adsorbates on graphene actually good for? There are two demonstrated purposes to which theory and experiment can agree: the limitation of carrier lifetime due to scattering and the doping of graphene by chemical interaction.

By their presence, adsorbates add potential terms which can lead to scattering. When adsorbates are charged, they induce a long-range Coulomb potential which can cause a weak carrier scattering [8], but which does not fundamentally alter the Dirac nature of the charge carriers; conversely neutral, covalently bound adsorbates introduce a short-range potential which can have more profound affects [12, 13], possibly inducing insulating behavior [14, 15]. The latter are very similar to lattice defects in this respect, varying only in the relative strength of the short-range potential. These short-range scatterers can introduce quantum corrections to the transport in graphene and are discussed in detail in Sect. 4.5.

By doping the graphene lattice through chemical interaction, adsorbates can achieve a much larger change in Fermi level than can be achieved in devices by external gating. Since the interactions in graphene are *scale free* (more about that in Sect. 4.6), they grow boundlessly with the Fermi level as the charge density increases. This means that certain many-body interactions can be continuously tuned from energy scales from zero to the THz range and beyond, enabling, for example, novel applications in plasmonic devices. This is discussed in detail in Sect. 4.6.

At extreme doping levels, the conical band structure of graphene is no longer a good approximation, and the full lattice must be taken into account. In this condition, the Fermi level can overlap with the saddle points in the band structure at the M points. Then we can expect singularities to arise in the dielectric response function, which can lead to exotic ground states such as superconductivity. There has been one report in the literature showing that such doping densities can be achieved [16], and this is discussed in detail in Sect. 4.7.

If we can control the processes of doping and scattering, then we hope we can control the magnetic and ground state properties (such as metallic, insulating, or superconducting) of graphene with the external influence of heat, chemical environment, or light. This chapter aims to demonstrate the progress in realizing this idea.

4.2 Angle-Resolved Photoemission Spectroscopy

4.2.1 Introduction

This chapter devotes considerable space to examples derived from ARPES data, although many other important tools are being applied to graphene studies. So in this section we will discuss how ARPES works. At the moment, no single reference covers all of the aspects of ARPES, so the reader should be referred separately to Cardona and Ley [17] for a basic introduction to chemical analysis, which is not much discussed in this chapter but is a tool much employed; to Hufner [18, 19] for a discussion of electronic band structure determination; and to Kevan [20] and Damascelli [21, 22] for details on the many-body interpretation of ARPES data.

4.2.2 Band Structure Determination of Graphene

Photoemission is a process that occurs when a soft X-ray photon excites an electron from a bound to an unbound state in a solid. Figure 4.1 illustrates the basic principle.

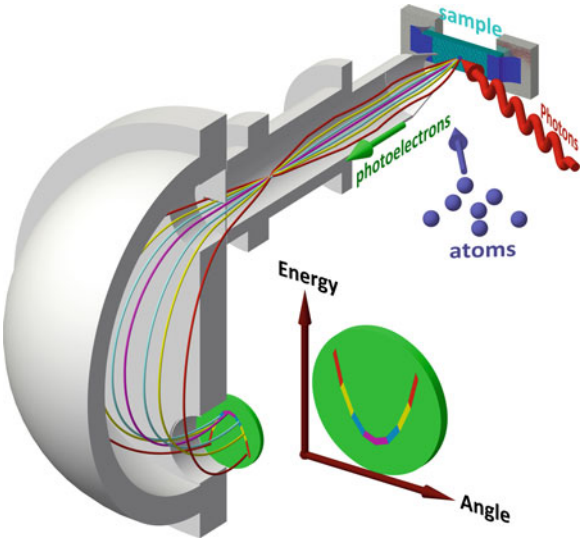

Fig. 4.1 Schematic diagram of the angle-resolved photoemission spectroscopy (ARPES) measurement of graphene. Incident UV or soft X-ray photons (*wavy arrow*) impinge on the graphene target, exciting photoelectrons with a distribution of angles and energies. A planar cut of this distribution is collected by an angular-imaging electron lens (shown in cross section) and dispersed by a nested set of hemispheres held at appropriate potentials. The energy–angle dispersion of the photoelectrons is mapped onto an imaging channel plate. By conducting experiments under a flux of atoms or other adsorbates, doping- and density-dependent studies can be accomplished

A UV or soft X-ray photon impinges on a sample, exciting a distribution of photoelectrons to be emitted into the 2π solid angle in front of the sample. With modern commercial detectors, a single plane of these emitted electrons is collected by a special lens that images the angular distribution onto the entrance slit of an electron spectrometer. The spectrometer consists of two nested hemispheres held at appropriate positive potentials such that the electrons take an approximately circular path, landing onto a two-dimensional imaging plate. Electrons of different kinetic energy are dispersed along one direction, while the angular distribution is preserved in the other direction. Thus, a section of the kinetic energy–angular distribution can be imaged.

The determination of the binding energy–momentum relationship of the electrons proceeds from simple energetic and geometric considerations [20, 22] which are briefly outlined here. The experiment gives us the kinetic energy E_{kin} as a function of photoelectron emission angle θ relative to the sample surface. For electron kinetic energies which are far above E_{F}, we can assume that the escaping electron has a parabolic energy dispersion $E_{\text{kin}} = \hbar^2 k_{\text{out}}^2 / 2m$ where k_{out} is the wavevector of the escaping photoelectron and m is the free electron mass. Therefore, the x, y, and z momentum components and energy of the final state are fully determined.

We can relate the experimental observables to the quantities of interest – the momentum k and energy E of the initial state electron using simple assumptions about the photoemission process. By convention, we assume a simple *three-step model*: (1) excitation of the bound to a high energy state, (2) propagation of the excited state to the vacuum boundary, and (3) passage of the electron from inside to outside the solid. In the last step, we model the vacuum interface by a simple potential step, which is analogous to the change of index of refraction when light passes from inside to outside a prism. The physics is identical for electrons: we find that $k_{\parallel}$, the momentum of the electrons parallel to the surface is conserved, so that

$$k_{||} = k_{\text{out}} \sin\theta. \tag{4.1}$$

We can determine the binding energy E_{bin} relative to E_{F} through energy conservation; we find that

$$E_{\text{bin}} = h\nu - E_{\text{kin}} + \Phi_{\text{W}}. \tag{4.2}$$

Here Φ_{W} is the work function of the material, the energy difference between the states at the vacuum level (just able to escape from the solid) and the Fermi level E_{F}.

Although only a small section of the electron emission from energy bands are counted on the detector, additional parts of momentum space can be measured by rotating the sample or detector to sample different parts of the momentum space. Then, the resulting band structure slices can be stacked and tiled together to form a full sampling of the states in the Brioullin zone. Figure 4.2 shows a comparison of the computed and measured band structure of epitaxial graphene (EG) on SiC(0001) by the ARPES method. Since ARPES by its nature measures only occupied states,

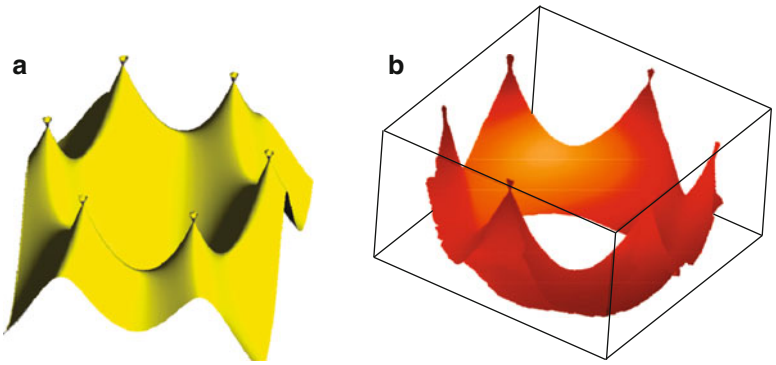

Fig. 4.2 The band structure of n-doped graphene. (**a**) Tight-binding calculation including third-nearest neighbor interactions [26]. (**b**) Three-dimensional rendering of experimental data collected for epitaxial graphene on SiC(0001) [23]

we expect to see the energy bands only from a lower binding energy limit (set by the experimental conditions) up to the Fermi level, which in the case of such EG samples lies just above the charge neutrality point [23, 24].

Thus, ARPES can immediately determine the carrier sign of the graphene, which is negative (electron-like) for n-doping or positive (hole-like) for p-doping. Note that although in some contexts, the sign of the state energies (negative vs. positive) is relative to the Dirac energy E_D, in this chapter we will always use the convention that the sign of the particle energy is relative to the Fermi level E_F. Thus ARPES always measures the negative-energy (hole) states, regardless of how E_F is positioned relative to E_D.

From such data, we can readily determine the model-dependent bandstructure parameters. For example, fitting the data to a single-hopping parameter model ((1.4) in Chap. 1), we find $t = 2.82\,\text{eV}$ [23]. Such parameters are highly dependent on how the fitting is performed [25] and are likely to depend on conditions of the graphene such as doping level and substrate interactions.

In the laboratory, He I radiation (photon energy $h\nu \sim 21\,\text{eV}$) excited in a resonance lamp is commonly employed for ARPES, with counting times of typically 10 min required to acquire band structures with good statistics. Such light sources have limited flux, but extremely good energy resolution. Many of the experiments illustrated in this chapter were instead performed using soft X-ray photons ($\sim$100 eV) generated by the Advanced Light Source, a third generation synchrotron. Such sources have the advantage of significantly higher photon flux and brightness than laboratory sources. The brightness is particularly important because it allows a small focus beam ($\sim$50 m) on the sample, which is useful to probe small or inhomogeneous samples.

Furthermore, imaging electrons emitted from a smaller area greatly improves the momentum resolution [27]. For graphene, the group velocity (in band units where $\hbar = 1$) is large: $v_D = \mathrm{d}E/\mathrm{d}k \approx 7\,\text{eV}{-}\text{Å}$, where E is the electron energy and k is

the momentum expressed in $1/\text{Å}$. A poor momentum resolution, which is around $0.02/\text{Å}$ in a respectable laboratory setup, directly impacts the measured energy resolution. The improved momentum resolution, a factor of 2 or better, available at synchrotrons can therefore overcome the poorer energy resolution ($\sim$10s of meV) of synchrotron sources compared to laboratory sources, which can achieve energy resolution of a few meV. This explains why most published ARPES experiments on graphene are obtained using synchrotron radiation, which has sufficiently high brightness to ensure a small photon beam and therefore high angular resolution.

By adsorbing atoms directly onto the sample during the ARPES measurement, we can acquire "movies" of the band structure as a function of the concentration of adsorbed species. This is arranged by aiming a number of standard sources such as a hot tungsten capillary for atomic hydrogen or Knudsen cell for metallic atoms at the same spot as the photon probe.

We can expect to see a variety of interesting effects in such movies. To begin with, most adsorbates are expected to act as charge donors or acceptors (see Sect. 4.3), so that we expect to see the occupation of the bands change as adsorbates are introduced. This occupation is manifested in the experiments by a change in the Fermi energy, which is accompanied by a change in the size of the Fermi contours compared to the Brillouin zone. Such effects are readily observable, as the experiments discussed in Sects. 4.5–4.7 attest.

Beyond chemical doping, the adsorbates can alter the symmetry of the graphene lattice, leading to a change in the distribution of bands in k-space, and with the possible appearance of energy gaps in the graphene bandstructure, as discussed in more detail in Sect. 4.4. These effects generally require long-range order of the adsorbates, and so are more readily observed in the context of bonding to the substrate in epitaxially grown graphene [28–33]. Although it should be mentioned that in the context of bilayer graphene, symmetry breaking between the two layers can be achieved by adsorption onto one of the layers. This effect also opens a gap observable in ARPES, since long-range order of the adsorbates is not required [34]. This is discussed in greater detail in Chap. 8.

These effects can be readily modeled without considering the interaction between the graphene carriers and each other, or other states in the system such as vibrations or defects. As such, they are considered to be *single-particle* effects. In fact, a proper understanding of the observed band structure requires a full understanding of the many-body interactions. In the next section, we shall explore these interactions and how they renormalize the energy of the electronic states. This renormalization is related to the *self-energy* of the carriers.

4.2.3 Self-energy Determination

If there is sufficient energy and momentum resolution, then the linewidths of the observed spectra are not limited by the instrument but instead reflect the lifetime of the excitations associated with the photoemission process. For sufficiently high

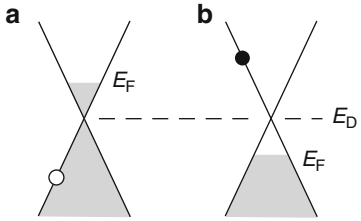

Fig. 4.3 Hot carriers in graphene modeled as excitations in the graphene Fermi sea. (**a**) Hole-like (negative energy states) in n-doped graphene; (**b**) Electron-like (positive energy states) in p-doped graphene. Here the sign of the energy (positive or negative) is relative to the Fermi level (*top* of the *shaded region* representing occupied states). The self energy of the hole in (**a**) and electron (**b**) is the same if particle-hole symmetry is obeyed

photon energies, the outgoing photoelectron has little time to interact with the solid after the photoexcitation process. Therefore to a good approximation, the width of the band structure sheets (see, e.g., Fig. 4.2) in the energy and momentum directions reflects, by an uncertainty principle argument, the inverse scattering time and length, respectively, of the *hole*, or *photohole* left behind when the photoelectron escapes.

In the language of many-body physics, we consider the free carriers in the Fermi sea to be excitations, which can be particle-like (electrons) with positive energy $\hbar\omega$ or antiparticle-like (holes) with negative energy $-\hbar\omega$. (We usually drop the $\hbar$ and speak of ω as the particle energy.) These excitations are illustrated in Fig. 4.3. In an ARPES experiment, we consider the photoemission process to inject a "hot" hole (Fig. 4.3a) for which we determine the energy, momentum, and lifetime. Conversely in a STM experiment we can in principle measure the energy of both holes (Fig. 4.3a) and electrons (Fig. 4.3b), by tunneling electrons into or out of the sample using positive or negative bias.

Because the bands of graphene are linear, with the same slope above and below the Dirac crossing E_D, graphene is said to obey particle-hole symmetry. That is, the lifetime of the hot hole in (Fig. 4.3a) is identical to that of the hot electron in (Fig. 4.3b) if the two systems have the same absolute charge density but opposite character (n vs. p) doping. Thus an ARPES experiment conducted as a function of doping from the p- to the n-doped regimes can determine the lifetime of both the positive and negative energy states.

The many-body interactions of the photoholes are reflected by a renormalization of their energy. As an example, consider a hole interacting with the electron sea through the Coulomb interaction. In the first instance, the appearance of the hole polarizes the local electronic configuration through the screened Coulomb interaction, which can be derived from pristine graphene's band structure. The local fields generated by the hole alter the band structure, which changes the Coulomb interaction, altering the local fields slightly again. The cumulative effect of these interactions results in an energy shift of the hole, called the self-energy. Similar interactions can occur when the lattice is allowed to relax in response to the hole, leading to a self-energy due to electron–phonon interactions, or in magnetic

materials when the spin distribution can interact with the hole, leading to electron–magnon self-energies.

In the absence of such interactions, the photohole has infinite lifetime and is therefore an eigenstate of the system. But in an interacting system, the hole is no longer an eigenstate –it can decay by emitting a phonon for example – and therefore it has a finite lifetime.

The self-energy arises as a fundamental characteristic and accounts for both energy and lifetime renormalization. It is a complex function whose real part contains the screened interaction energy just discussed, and whose imaginary part reflects the finite lifetime of the hole. Because it depends on both the energy and the momentum of the holes, the self-energy is denoted $\Sigma(\mathbf{k}, \omega)$.

The complex self-energy has a familiar analogue when we consider photons passing through a prism. In such a medium, the photons can scatter (or be absorbed) and their velocity is renormalized. Both of these effects are described by a complex function, the index of refraction $n(\omega)$ whose real and imaginary parts describe the velocity renormalization and scattering lifetime, resp. It is well known that the real and imaginary parts of $n(\omega)$ are not independent, but are related to each other by a Kramers–Kronig (KK) transformation to preserve causality. It turns out that the real and imaginary parts of $\Sigma(\mathbf{k}, \omega)$ are similarly related by (KK) transformation for the same reason.

The ARPES experiment is directly connected to $\Sigma(\mathbf{k}, \omega)$ because ARPES measures the single particle spectral function [21, 22]:

$$A(\mathbf{k}, \omega) = -\frac{1}{\pi} \frac{|\mathrm{Im}\Sigma(\mathbf{k}, \omega)|}{(\omega - \omega_\mathrm{b}(\mathbf{k}) - \mathrm{Re}\Sigma(\mathbf{k}, \omega))^2 + (\mathrm{Im}\Sigma(\mathbf{k}, \omega))^2}, \tag{4.3}$$

where $\omega_\mathrm{b}(\mathbf{k})$ is the "bare" band structure (in the absence of many body interactions) that we have been considering until now. $A(\mathbf{k}, \omega)$ has the form of a Lorentzian at energy $\omega = \omega_\mathrm{b}(\mathbf{k}) + \mathrm{Re}\Sigma(\mathbf{k}, \omega)$, whose width is given by $\mathrm{Im}\Sigma(\mathbf{k}, \omega)$.

The self-energy function $\Sigma(\mathbf{k}, \omega)$ arises in any self-consistent theory of the electron gas [35], in particular it can be expressed in perturbation theory as a function of the single-particle Green function propagator G [36]. Thus ARPES can give direct insight to the self-energy function calculated by theories. Unfortunately, since only the negative-energy, $\omega < 0$ (occupied) states are accessed, it cannot give a complete picture of the self-energy.

Now that we have shown how the electronic energy bands can be measured with ARPES (as applied to materials in general), we will approach the problem of adsorbate–graphene interactions. In Sect. 4.3 we will review what properties have been predicted or measured about adsorbates acting in isolation. In Sect. 4.4, we will briefly discuss some issues related specifically to the band structure of graphene. This will be followed by three sections discussing specific experiments, and what could be learned about the adsorbate interactions by ARPES.

4.3 The "Zoology" of Adsorbates

Adsorbates on graphene can be atoms or molecules. In terms of their characteristics, they are comparable to animals in a zoo. Each type of adsorbate could be broadly classified in terms of their species, habitat, and their behavior.

- Species
  - Atom vs. molecule
  - Polar vs. nonpolar molecule
  - Pure system vs. coadsorbates

- Habitat
  - Bonding site: H_6 vs. B_2 vs. T, see Fig. 4.4
  - Disordered vs. ordered arrangement
  - Isolated vs. clustering

- Behavior
  - n vs. p doping
  - Magnetic vs. nonmagnetic
  - Bonding: ionic vs. covalent vs. van der Waals
  - Short vs. long scattering range

Of the many species, we will restrict ourselves to an overview of the habitat and behavior of single atoms, and of these, only a small handful will be discussed in detail. It should also be noted that there are not necessarily clear boundaries between behavior. For example, the distinction between ionic and covalent bonds is not always clear. Furthermore, many calculations use density functional theory (DFT) calculations which do not include effects of van der Waals interaction, which can be an important contribution to the adsorbate bonding [37, 38].

In many cases theory is far ahead of experiment, there being many more adsorbate systems calculated than experimentally tested. In such cases, caution

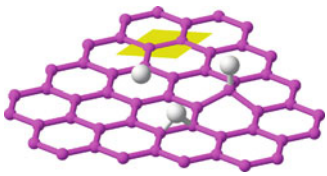

Fig. 4.4 The high-symmetry bonding sites for graphene. H_6 = sixfold hollow site, B_2 = twofold bridge site, T = top site. The T- and B_2-bonding sites are depicted as covalently bonded to one or two C atoms, resp. The top-site C atom is buckled indicating a change from sp^2 to sp^3 hybridization. The *shaded diamond* indicates the graphene unit cell

should be used, since many important predicted quantities such as adsorption energy or magnetic moment can be very sensitive to the details such as calculation method, adsorbate density, and distribution. Also, in some cases calculations and experiments are available only for graphite, which does not necessarily share the exact properties of graphene. Moullet compared the adsorption of Al to graphite and graphene and found no significant difference in the bonding site or energies, suggesting that the adsorption is similar in the two cases [39].

While adsorption of almost every atom in the periodic table has been theoretically considered, the notable exception is that there has been little or no work (experimental or theoretical) on rare-earth (La through Lu) adatoms, which consequently are not reviewed in this chapter. (We are only aware of one prediction that lanthanum adatoms are magnetic [40].) This is surprising considering that their potentially high magnetic moments could lead to interesting magnetic effects and their localized f electrons could lead to interesting effects related to Kondo screening and the Anderson impurity model.

4.3.1 Adsorption of Nontransition-Metal Atoms

Whether an atom dopes graphene as an acceptor (p type) or as a donor (n type) generally depends on the electronegativity of the atom, with the atoms in groups I–III of the periodic table acting as donors with little change to the graphene DOS [37].

Of the group IA atoms (see Table 4.1), hydrogen atoms stand apart, widely agreed to bond covalently to a carbon atom in the T site, converting the carbon lattice locally from sp^2 to sp^3 bonding. At higher coverage (1:1 H–C ratio), a stable covalently bonded sp^3 bonded monolayer has been predicted, called graphane [50, 51]. Hydrogen is discussed extensively in Sect. 4.5.

Table 4.1 Properties of Group IA (alkali) adsorbates on graphene. Items with question marks have not been confirmed experimentally or theoretically, but are reasonably assumed to be true as discussed in the text

Atom	Bonding site T = Top B_2 = Bridge H_6 =Hexagonal	Doping n = Donor p = Acceptor 0 = Neutral	Bonding I = Ionic C = Covalent V = v. d. Waals or physisorbed	Magnetic moment μ_B given
H	T	p [15] n [41]0[42]	C, sp^3	1.0 [42, 43]
Li	H_6 [37, 44]	n [37]	I+V [45]	0 [37]
Na	H_6 [37, 44]	n [37]	I	0 [37]
K	H_6 [37, 44]	n [23, 37, 46]	I	0.17 [37] 0 [46]
Rb	H_6 [44]	n [47]	I	
Cs	H_6 [40, 48] no [44] preference	n [40, 49]	I	0 [40]

The bonding site for the isolated Li, Na, K alkali atoms is the sixfold hollow site H_6 [37, 45]. This represents a general principle that ionically bonded atoms tend to favor the hollow site, where the binding energy can be maximized due to the strongest Coulomb interaction there. The bonding distance to the plane is determined by a balance of this attractive, long-range force, and short-range repulsion by the other electrons [37, 52]. While there is no report for isolated Rb or Cs on graphene, it is reasonable to expect these to sit in the H_6 site as well, since these occur there at higher coverages [48, 53].

With relatively low ionization potential and electronegativity compared to carbon, the alkali atoms are predicted to readily donate their outer *s* electron to graphene. While the free-atom alkalis have partially filled *s* shells and are magnetic, the net magnetic moment is largely quenched for adsorption on graphene, because the unpaired electrons are transferred to the nonmagnetic graphene and become delocalized. A small residual magnetic moment is predicted for Na and K, but as in the case of hydrogen discussed later, these results are very sensitive to the adsorption geometry and calculation method and should be considered with caution [37].

Of the alkali atoms, K adsorption has been extensively studied on monolayer [8, 15, 23], bilayer graphene [54], and graphite [53]. At low coverage, and at low temperature, potassium is distributed dilutely and disordered [55], with large separation between atoms. This suggests that there are long-range repulsive forces between adsorbed K ions, which was confirmed theoretically [56]. At higher temperature ($\sim$100 K), potassium forms a 2×2 ordered layer. It is expected that the charge transfer is reduced in this ordered configuration, because in the layered compound KC_8 (which can be argued is a stack of decoupled K(2×2)-graphene layers [57]) there exists a strong interlayer band associated with *s* electrons retained on the K [58].

Since Li is closest in size to H of the alkali atoms, it appears to have a tendency for covalent bonding at higher coverage. Yang predicted a stable graphane-like layer which is covalently bonded [59] but to the contrary Medeiros has calculated that such a layer is ionically bonded [60]. At lower coverage, Li is predicted to be a donor [37, 61].

There is no experimental report for Rb on graphene, but it forms a similar 2×2 ordered layer as K [47] which has strongly n-doped an epitaxial graphene layer. There is no report for Cs on graphene, but it is known that a small amount Cs reduces the work function of graphite by $\sim$1 eV [49], presumably due to charge transfer from the Cs to the outer graphite layer.

The group IIA alkaline earth atoms (Table 4.2) Mg and Be are not expected to interact with graphene [62] owing to their high ionization potentials: 7.65 and 6.23 eV, respectively, although curiously, Be dimers are predicted to bond strongly [63]. Although having a similar ionization potential (6.1 eV), Ca has been predicted [37, 62] and observed [16] to readily n-dope graphene, because of the additional binding contribution of its *d* electrons which can hybridize with the π^* band of graphene [64]. There is no report so far of Ba or Sr adsorbates on graphene, but on the one hand their low ionization potential and on the other hand the existence of

Table 4.2 Properties of Group IIA (alkaline earth) adsorbates on graphene. For notation, see Table 4.1

Atom	Bonding site	Doping	Bonding	Magnetic moment
Be	None [62, 63]			
Mg	None [62]			
Ca	H_6 [37]	n [16, 37, 62]	I [16]	∼1 [37]
Sr	H_6?	n?	I?	
Ba	H_6 [40]	n [40]	I [40]	0.47 [40]

Table 4.3 Properties of Group IIIA (alkaline earth) adsorbates on graphene. For notation, see Table 4.1

Atom	Bonding site	Doping	Bonding	Magnetic moment
B				
Al	H_6 [37, 70]	n	I	
Ga	H_6 [37, 70]	n	I	
In	H_6 [37, 70]	n	I	
Tl				

Table 4.4 Properties of Group IVA adsorbates on graphene. For notation, see Table 4.1

Atom	Bonding site	Doping	Bonding	Magnetic moment
C	B_2 [38, 70, 73, 74]		C, sp^2 [38]	0.5 [38, 73]
Si	B_2 [70, 74]	n [74]	C, sp^2 [38]	1.59 [38]
Ge	B_2 [70, 74]	n [74]	C, sp^2 [38]	1.76 [38]
Sn	B_2, T [38]		C [38]	1.76 [38]
Pb	B_2, T [38]		V [38]	1.76 [38]

bulk compounds of SrC_6 and BaC_6 [65] suggest that they too should readily adsorb and donate charge to graphene.

Considering the group IIIA atoms (B, Al, Ga, In, and Tl, see Table 4.3), while there has been work on B-doped graphene through substitution [66–69], there have been no predictions or observations of B or Tl adsorption on graphene. Al, Ga, and In have been predicted to adsorb and bond ionically to graphene, donating a significant charge of nearly one electron per atom [37]. A weak preference to adsorb in the H_6 bonding site for these has been predicted [37, 70] as is common for ionic bonding. For Al, experiments indicate to the contrary a preference for top-site bonding [71, 72], consistent with a calculation by Moullet et al. [39].

Of the group IVA atoms (C, Si, Ge, Sn, Pb, see Table 4.4), crystalline C, Si, and Ge have stable diamond structures, and so could be expected to favor sp^3bonding as adatoms. In this scenario we could expect a preference towards the top-site (T, see Fig. 4.4) bonding with little ionic character. Instead, the bridge site (B_2) is favored [38, 70, 73, 74], with a significant change to the occupied DOS that depends on coverage. The bonding is a covalent one, where the bonding C atoms in the graphene have a mixed sp^2–sp^3 hybridization, while the adatom can be largely sp^2-like (see Fig. 4.4). For such a geometry, carbon, Si, and Ge adatoms have been shown to

Table 4.5 Properties of Group VA (pnictogen) adsorbates on graphene. For notation, see Table 4.1

Atom	Bonding site	Doping	Bonding	Magnetic moment
N	B_2 [70,75]	p [75]	I [75]	0.84 [75]
P	B_2 [76]	0 [76]	C [76]	0.86 [76]
As	B_2 [70]			
Sb				
Bi		0 [77]p [78]		

be magnetic with magnetization $\sim$0.5–1.75μ_B [38, 73]. A small but nonnegligible charge transfer is expected for the isolated adatoms [74].

The bonding of Ge, Sn, and Pb is significantly weaker than for the other group IVA atoms, with the T bonding sites nearly equally favored to the B_2 [38]. The charge transfer of Sn and Pb, expected to be small, has not been accurately calculated.

Of the group VA atoms (N, As, P, Sb, Bi, see Table 4.5), nitrogen is predicted to be an acceptor [75], with preferential bonding to the B_2 site [70, 75]. Nitrogen on the edge of graphene nanoribbons has been shown to be a donor, however [79]. Interestingly, an unpaired electron residing on the N atom is predicted to be strongly spin-polarized [75].

Although graphene oxide plays a role to remove As from water [80], there has been little research in the direct interaction of graphene and arsenic other than the prediction of B_2 site bonding [70]. Phosphorous is predicted to be an acceptor, bonded to the B_2 site, forming a magnetic moment [76] at the P atom. This magnetism arises at a localized, minority, midgap state in the electronic band structure.

Antimony adsorption does not appear to have been considered yet; an important limitation to its adsorption is that the Sb surface energy is very low, favoring island formation over atomic adsorption. Various interesting 1D–3D agglomerated structures of Sb on graphite have been observed [81, 82].

Bismuth was shown not to chemisorb and therefore not to strongly dope graphene, and a clustering behavior is predicted [77]. Gierz reported p doping of epitaxial graphene on SiC by antimony and bismuth, but it is likely that this doping results from continuous layers intercalated at the graphene/SiC interface. Thus, the observed p doping falls under the topic of doping by metallization, similar to other metals [84], not chemical doping.

Of the Group VIA atoms (O, S, Se, Te, see Table 4.6), there has been a lot of attention to oxygen adsorbates, due to the technological relevance of graphene and its oxides. As an isolated adsorbate, oxygen was shown to have a strong preference for the B_2 site [70, 75] and to act as an acceptor [75]. The topic of oxygen on graphene is delved in much greater detail in Chap. 14. Although S prefers the same bonding site, it chemically hybridizes with the graphene states near E_F without shifting of the graphene bands to higher or lower energy. Therefore, S appears to be a neutral adsorbate [76]. Both oxygen [75] and sulfur [76] appear to be nonmagnetic.

Table 4.6 Properties of Group VIA (chalcogen) adsorbates on graphene. For notation, see Table 4.1

Atom	Bonding site	Doping	Bonding	Magnetic moment
O	B_2 [70,75]	p [75]		
S	B_2 [76]	0 [76]	C [76]	0 [76]
Se	B_2 [70]			
Te				

Table 4.7 Properties of Group VIIA (halogen) adsorbates on graphene. For notation, see Table 4.1

Group VIIA				
Atom	Bonding site	Doping	Bonding	Magnetic moment
F	T [75]	p [75]	I [75] I+C[83][a]	0 [75]
Cl	B_2 [76]	p [76]	I [76]	0 [76]
Br	B_2 or T [70]			
I				

[a]*On graphite*

Little is known about Se and Te adsorption; Ishii et al. have predicted a stable B_2 bonding site for Se [70].

The halogen atoms (group VIIA, F, Cl, Br, I, see Table 4.7) are interesting because of their strong electronegativity and their potential usage as p dopants in counterpart to the n-doping alkali atoms. However, since atomic halogen sources are a bit harder to come by, there has been much less experimental work with them than the alkalis.

According to predictions, fluorine prefers the T site, acting a strong acceptor, and shows no magnetism as an adsorbate [75]. Chlorine, on the other hand, has been predicted to prefer the B_2 site [76] and to act as a strong acceptor ($\sim$1 electron/atom) indicating a strong ionic bond. No magnetism was predicted. These results are in strong contradiction to the bonding of halogen molecules (Cl_2, F_2) which are mostly van der Waals-bonded [85]. Descending column VIIA of the periodic table, we find that the magnitude of the electronegativity is reduced; this appears to explain the relatively weak bonding of bromine to graphene [70].

4.3.2 Adsorption of Transition Metal Atoms

Transition metal (TM) doping is important at the high coverage limit because such metallization is the basis for making contacts in graphene devices. In this situation the type of doping was predicted to depend on the relative work function of the metal and graphene [84].

At the limit of individual adatom adsorption, interest lies in the potentially large magnetic moment of TM adatoms, which can affect diverse phenomena such as the spin transport [86], superconductivity [87], and Kondo effect [88, 89] in graphene.

Table 4.8 Properties of transition metal adsorbates on graphene. For notation, see Table 4.1. When the bonding sites' binding energies differ by less than 100 meV, then multiple sites are listed

		3*d* transition Metals		
Atom	Bonding site	Doping	Bonding	Magnetic moment
Sc	H_6 [52,70]			2.35 [52]
Ti	H_6 or T [70]H_6 [37,91]	n [9,91]		∼3.3 [37,52,91]
V	H_6 [70]			4.88 [52]
Cr	H_6 [70]no pref. [52]			6 [52]
Mn	H_6 [70,92] not adsorbed [52]		I+V [92]	5.62 [92]
Fe	H_6 [37,70,92]	n [9]	I+V [92]	∼2.1 [37,52,92]
Co	H_6 [52,70,89,92]		I+V [92]	1.1 [92],1.4 [52]
Ni	H_6 or B_2 [70]			0.0 [52]
Cu	B_2 or T [52,70]	n [94]		1.0 [52]
Zn	H_6, B_2, or T [52,70]			0.0 [52]
		4*d* transition metals		
Atom	Bonding site	Doping	Bonding	Magnetic?
Y				
Zr	H_6 [95]	n [95]		
Nb	H_6 [95]	n [95]		
Mo	H_6 [52,70,95]	n [95]		0.0 [52]
Tc	H_6 [95]	n [95]		
Ru	H_6 [95]	n [95]		
Rh	H_6 [95]	n [95]		
Pd	B_2 or T [37,52], B_2 or T or H_6 [95]	n [95]	C [52]	0.00 [37,52]
Ag	B_2 or T [70,93,95] no pref. [52]	n [94,95]	I, V [96,97]	1.0 [52]
Cd				
		5*d* Transition Metals		
Atom	Bonding site	Doping	Bonding	Magnetic?
Hf	H_6 [95]	n [95]		
Ta	H_6 [95]	n [95]		
W	H_6 [95]	n [95]		
Re	H_6 [95]	n [95]		
Os	H_6 [95]	n [95]		
Ir	H_6 [95]	n [95]		
Pt	B_2 or T [95] B_2 [52]	n [9,95]	C [52]	0.0 [52]
Au	B_2 or T [70,95,97] no pref. [37,52]T [46]	n [10,86,95,97] 0 [46] p [94]	I, V [96,97]	−0.15 to −0.17 [97] ∼ 1.0 [37,52,98]
Hg				

What little is known about the adsorption of TM atoms is summarized in Table 4.8. As a whole, calculations are difficult because to account for the adatom *d* electrons, more advanced calculations such as the GGA method should be used instead of LDA [40,95,98]. In general, the TM atoms are relatively strongly bound,

with significant charge transfer to the C atoms, and prefer to be bound to the H_6 hollow site. This is in accord with a general tendency to be ionically bonded, similar to the group I–IIIA atoms. Duffy and Blackman [90] calculate the earlier $3d$ adatoms to prefer the top site, despite their more ionic characters.

The exception is for the more noble atoms (Cu, Ag, Au, Pt, Zn), which are more weakly bound, and for which the binding energy to the different sites varies little. Additional computational difficulty arises in these weakly bound TM atoms, because for these van der Waals interaction becomes a significant contribution to the binding energy. Methods for accurate calculation of this bonding interaction are still under development [99]. Since the binding energy varies little with bonding site, it suggests that these atoms can readily diffuse on the graphene surface, which was shown experimentally for Au [10].

Despite a theoretical consensus about the bonding sites and magnetism of the TM adatoms, so far there has been very little experimental work to confirm these speculations. In an early measurement, silver and gold atoms were observed to adsorb preferentially on top or possibly bridge sites of graphite [71], but otherwise the bonding sites remain largely in the domain of theory. This uncertainty arises not only because the theoretical difficulties were pointed out but also because it is not clear in practice whether TM atoms are well behaved or not. Do TM atoms adsorb into a single preferred site? Do they prefer to sit alone or to collect into islands or clusters? Presently available STM measurements did not achieve atomic resolution of individual TM atoms [100]. The lack of basic information about the growth and arrangement of TM atoms suggests a basic program of exploring the bonding sites as a function of adsorption conditions (flux and temperature) would be very helpful to determine the ideal growth conditions.

The predicted degree of magnetism depends sensitively on the details of the chemical bond between adatom and graphene [52]. For example, electron transfer from adatom d levels to graphene can reduce the magnetic moment from the free atom case, or the d levels of the adatom can be reconfigured due to hybridization. Chromium adatoms have little charge transfer and therefore retain their magnetic moment ($6\,\mu_B$) [52] while Co atoms are strongly hybridized with graphene, leading to a reduction of the magnetic moment from 3 to around 1.1 to $1.4\,\mu_B$ [52, 92]. Platinum's large ground state magnetic moment ($2\,\mu_B$) disappears entirely due to strong covalent bonding to the substrate [52].

Furthermore, an emerging theme is that the local electric field and doping conditions have a strong effect on the distribution of the electrons and hence the magnetic moment of adatoms [40, 98, 100]. This suggests that calculations for adatoms on charge-neutral graphene may not apply to real-world conditions, where the graphene is doped and subject to strong local fields at the graphene/substrate interface.

Upon adsorption, many of the TM adatoms induce midgap states near the Dirac energy. Fe on graphene is an interesting example [92], because there the midgap state is entirely minority spin character and near E_F, while the majority states near E_F show the characteristic Dirac spectrum of graphene and have therefore zero DOS at E_F. Thus, Fe on graphene might be an example of a semi-half-metal [92].

4.4 Adsorbate–Graphene Interactions: General Symmetry Considerations

The interesting features of graphene such as its massless character, Berry's phase, and chiral and pseudospin degree of freedom are ultimately derived from the symmetry of the graphene lattice and the equivalence of the two atoms "A" and "B" in the unit cell shown in Fig. 4.4. Since adsorbates disrupt the local translational symmetry, they share common behaviors which have been extensively discussed and reviewed [101, 102]. The importance of this lattice symmetry to the massless character of graphene can be seen by constructing a Hamiltonian for graphene with and without this equivalence [103]:

$$H = v \begin{pmatrix} \Delta/2 & k_x - \mathrm{i}k_y \\ k_x + \mathrm{i}k_y & -\Delta/2 \end{pmatrix}. \tag{4.4}$$

The eigenstates of this Hamiltonian

$$\Psi = \begin{pmatrix} \psi_\mathrm{A} \\ \psi_\mathrm{B} \end{pmatrix} \tag{4.5}$$

are the amplitudes of p_z-derived tight binding orbitals on the A and B sublattices.

The diagonal elements in (4.4) reflect the on-site potentials at the A and B atoms of the graphene unit cell. Solution of (4.4) for $\Delta = 0$ leads to the familiar gapless spectrum, but for a finite value, a gap of size Δ opens at the Dirac crossing, and the local curvature of the bands there means that a finite effective mass has been introduced.

For $\Delta \neq 0$, this model describes the band structure of a monolayer of hexagonal boron nitride, which has a unit cell containing nonidentical B and N atoms. It can also describe a single graphene layer on hexagonal boron nitride, stacked with its A and B atoms in registry with the B and N atoms [28].

The graphene lattice symmetry can also be broken locally depending on the adsorbate bonding site (Fig. 4.4), which act as defects. For atoms adsorbed in the top, or tetrahedrally bonded site (T), the A–B equivalence is broken, leading to an increase of backscattering which is normally suppressed in graphene. For atoms adsorbed in the bridge site (S_b), the rotational symmetry is broken, while adatoms located in the hexagonal site (H_6) do not break the local mirror or point-group symmetry. These symmetry classes have definite impact on the transport [12, 13, 104] which are discussed elsewhere in this book.

When adsorbates are arranged periodically, the new lattice symmetry can also play a role to induce a band gap. To see why, consider two possible arrangements of adatoms in Fig. 4.5. For adatoms arranged 2×2 lattice atop of the graphene, the Brillouin zone in the reduced-symmetry system is reduced by half in size. Tiling such a Brillouin zone (BZ) shows that the originally inequivalent K and K′ points remain inequivalent in the reduced zone scheme. For adatoms arranged

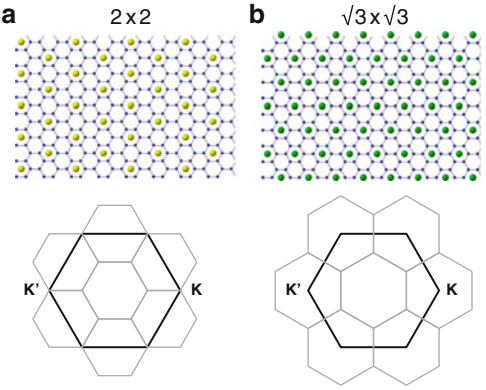

Fig. 4.5 The relationship between real space (*upper panels*) and reciprocal space (*lower panels*) for different arrangements of adatoms. In the lower panels, the *heavy line* is the bare graphene Brillouin zone (BZ), while the *gray lines* are the BZs under the reduced symmetry. (**a**) For 2×2 symmetry, the reduced BZ preserves the nonequivalence of the K and K′ points. No gap is expected to open at E_{D} under such a reconstruction. (**b**) For $\left(\sqrt{3} \times \sqrt{3}\right)$R30° symmetry, the original nonequivalent K and K′ points are both mapped to the ` point of the reduced BZ and therefore become equivalent. A gap is expected to open at E_{D} for such a reconstruction

with $\left(\sqrt{3} \times \sqrt{3}\right)$R30° symmetry, this is not true; the original K and K′ points are mapped onto the center of the new BZ, becoming equivalent. This equivalency translates into the opening of a gap and occurs for any multiple of $\left(\sqrt{3} \times \sqrt{3}\right)$R30° or 3×3 periodicities.

The Hamiltonian in (4.4) is appropriate for modeling crystalline forms of graphene, where each unit cell is identical, but this chapter is concerned with adsorbates that are distributed sparsely and more or less randomly. In this case, it is more appropriate to apply a perturbation potential for each defect [102]

$$\hat{V} = \sum_{i,j} \Psi_i^{\dagger} V_{i,j} \Psi_j \,, \tag{4.6}$$

where i, j sum over atomic sites, and $V_{i,j}$ are 2×2 matrices operating in the A–B sublattice space. For example, a single impurity on top of an A site of the lattice has a potential

$$\hat{V} = \begin{pmatrix} U_A & 0 \\ 0 & 0 \end{pmatrix}. \tag{4.7}$$

Different adsorbates can be modeled simply by changing the impurity potential U_{A}, and the limit $U_{\mathrm{A}} \to \infty$ is used as a model for a vacancy. Seen in this way, top-site adsorbates and vacancy-type defects are symmetry equivalent and differ only in their potential strength.

Even without considering the detailed lattice of graphene, it can be argued that defects will always induce sharp features in the graphene DOS at the Dirac energy E_D[102,105–107], the so-called midgap states. These midgap states appear not only in tight-binding models [108, 109] on extended real-space lattices but also in DFT calculations of adsorbate (and defect) configurations. We will return to the possible existence of the midgap states in the following section.

Furthermore, the distribution of adsorbates, whether periodic or disordered, has a huge influence on the electronic and magnetic properties. As a prototype example of this, we will consider the impact of hydrogen as an adsorbate in Sect. 4.5.

4.5 Hydrogen on Graphene As a Prototype Adsorbate System

4.5.1 Introduction

The hydrogen on graphene problem is important not only for the fundamental issues it raises about graphene. Its importance was realized in the 1970s as a solution to a long-standing question about the cosmos: why is there so much H_2 in the universe? Due to the high density of interstellar ultraviolet radiation in the universe, H_2 molecules should be readily dissociated into free H atoms. Given the low cross section for recombination via two-body collision of H atoms, recombination to H_2 is not favored, and the H/H_2 ratio should be much higher than observed [110].

This problem was discussed by Hollenbach et al. who proposed that H–H recombination could be promoted at the surface of dust particles [111, 112]. Since cosmic dust consists largely of graphitic particles, the interaction of H on graphite surfaces was studied intensely both experimentally and theoretically for both graphite and graphene. Individual H atoms were shown to be stably adsorbed onto the T site. The H–C bond is partially covalent and results in a rehybridization of the C atom from sp^2 to sp^3 configuration as suggested in Fig. 4.4.

The most favorable configuration for recombination of two H atoms into H_2 is when they occupy third-near neighbor (3NN) sites. Upon recombination, the H_2 molecule is not stably bound to the graphite surface and easily devolves back into free space. The favorable cluster configuration can be reached in two ways: first, an incoming second H atom is attracted directly to the second NN site (2NN) [113], after which one atom hops to the 3NN site. Second, the two adatoms, if adsorbed at a larger distance, are attracted to each other and by diffusion can evolve into the favorable 3NN configuration [114, 115]. The sufficiently high probability of these cluster formation is believed to be accountable for the cosmic H_2 distribution.

More recently, the case of graphene highly saturated by H atoms has been considered. In this situation, various arrangements of H atoms have been discussed. One configuration saturates all the A atoms with H on one side of the graphene and the B atoms with H on the other side; this is called *chairlike graphane*

[50, 51, 116]. In *boatlike* graphane, half of the A–B pairs is saturated on each side [116]. Another configuration, *half-graphane* or *graphone* has only the A atoms on one side saturated. Because of the high degree of sp^3 hybridization throughout the lattice, these materials could be considered as two-dimensional analogues of diamond. Detailed calculations predict large gaps at the K points of graphane and half-graphane due to the symmetry breaking within the unit cell [51, 117, 118].

A full understanding of adsorbate systems must go beyond the simple Hamiltonian in (4.4) because of the possibility of unpaired spins leading to magnetism and typically spin-polarized DFT calculations are employed [43, 118, 119]. The electronic and magnetic structure of a periodic arrangement of H on graphene was considered by Duplock et al. [43] for a single H adsorbed to the T site in a 4×4 unit cell of graphene. A gapped band structure emerges with a large band gap of $\sim$1.5 eV. The magnetism emerges in two ways: first by a small exchange splitting of the valence and conduction bands, and second by a flat, spin-polarized band appearing just above the Dirac energy E_{D}. The argument for the large gap arises from on-site coulomb potential, similar to the gap opening in graphane. The flat, spin-polarized band is explained by the localized states near the H atom; these states are formed by p_z orbitals near the H atom [43].

Similar magnetization was predicted by Yazyev [41, 42]. There it was shown that the spin polarization is not localized to the hydrogen atom's T site, but is delocalized over the next 2–3 near neighbors in the C lattice. The spin density has opposite sign for the H in the A vs. B sites.

It would be a mistake to take these theoretical results at face value and conclude that the H-graphene adsorbate system should necessarily be either insulating or magnetic for several reasons. First, because different periodicities other than 4×4 can lead to different results. Garcia-Lastra has shown that a single H atom in a $m \times n$ unit cell will be gapless or nearly gapless for certain periodicities such as when m and n are multiples of 3; this holds true regardless of whether spin is considered [119].

Furthermore, the barrier for migration of covalently bonded impurities is very high, so there can be kinetic obstacles to formation of ordered structures. Therefore, it is unclear if we can expect a real adsorbate system to have H adsorbed only on the A site of the unit cell. Shytov has shown that the long-range interactions favor H atoms randomly distributed over the A and B sites [120] while Cheianov et al. suggested that long-range interactions should tend to preferentially order the H adsorption onto one or the other site [121]. A periodic arrangement with adatoms equally distributed on A and B sites will not always have a gap, and as shown in Yazyev [42], will have a zero net magnetic moment.

Likewise, we have no reason to expect a periodic arrangement of H atoms to be favored during growth, so the distribution of adsorbates need to be carefully considered. Zhou et al. showed that starting from ferromagnetic half-graphane, removal of H atoms suppresses magnetism [117]. On the contrary, Sahin et al. showed that removal of hydrogen atoms from graphane can create magnetism or not, depending on the geometry of the dehydrogenated domains [122].

To complicate things further, graphene samples are not typically flat. Freestanding graphene has been shown to be strongly rippled attributed to instability of two-dimensional crystals [123]. Graphene flakes transferred to SiO_2 have shown to be strongly corrugated due to substrate roughness [124] although this roughness can be alleviated by transfer to flatter substrates [125]. Epitaxially grown graphene on SiC has a small but nonnegligible rippling due to the underlying interface structure [126–128]. Graphene on certain metals such as ruthenium and iridium have shown periodic rippled structures due to lattice mismatch to the substrate [129, 130].

The fact that the graphene may have a finite curvature has strong implications for adsorbate configurations, especially in covalent bonding situations. Positively curved surfaces can encourage clustering of H atoms to NNN positions, since such curvature increases the distance between bonding sites [131]. Such clustering was identified in the graphene on Ir system to open a band gap due to the periodic corrugation potential [32].

While a truly random distribution of H cannot be modeled by DFT, it is possible to apply tight-binding theory to large cluster models with random defect distribution [108, 132–135]. These models use disorder which is modeled by an on-site potential and so can be applied to not only H adatoms, but also other *T*-site located adatoms or carbon vacancies, according to the strength of the on-site potential chosen. (An alternate form of disorder occurs when the hopping parameter between adjacent C atoms varies locally, is called *off-diagonal*, and arises for example due to bond-length variations in the lattice. It is not considered here because it poorly models the influence of H atoms.)

The most important finding is that strong on-site disorder should lead to a metal–insulator transition (MIT) due to the formation of localized states as proposed by Anderson [136]. Such a transition can be expected to occur in three-dimensional materials when scattering from defects is *coherent*, when scattering is minimal between defects, and when the defect density is large enough. Under these conditions localized, nondiffusing states are found between the defects. (In the context of graphene nanoribbons, the Anderson transition is also discussed in Chaps. 9 and 13).

For two-dimensional systems with on-site energy disorder, scaling arguments showed that states are marginally localized [137] regardless of defect density; this calculation was extended to the honeycomb lattice by Schreiber [138]. Whether conduction is impeded in an actual sample with realistic conditions (such as finite size) by localization is very difficult to predict.

4.5.2 Hydrogen on Graphene: Experimental Evidence for Anderson Localization

In the previous section, various theories showed that hydrogen on graphene can display a wide variety of behaviors depending on the distribution of H atoms, with regard to periodicity, sublattice distribution, and clustering. These led to predictions

of band insulating, ferromagnetic, or Anderson-localized behavior. Experimentally, what could actually be observed?

Dosing of hydrogen on graphene cannot be accomplished by exposure to molecular H_2, which has no observable effect on graphite [139], but instead atomic hydrogen sources must be used [139, 140].

As already mentioned, clustering of atomic H into a local graphane-like configuration in the graphene on iridium system was demonstrated [32]. In this work, the insulating character was directly demonstrated by the opening of a significant energy gap in ARPES spectra, and the atomic-scale structure observed on the same samples by STM.

Elias et al. [131] prepared hydrogenated samples of freestanding graphene and graphene on SiO_2 by exposure to H atoms from a microwave plasma source. On the basis of the altered lattice constant of their samples, they could conclude the formation of a half-graphane-like (on SiO_2) and graphane-like (freestanding) compound. On the basis of transport measurements, they concluded that their samples were insulating, since the conductivity vs. temperature followed $\mathrm{d}\sigma/\mathrm{d}T > 0$. The exact nature of this insulating character, however, is not completely clear. They observed variable-range-hopping behavior, i.e., the conductivity of their samples follows the behavior

$$\sigma \propto \mathrm{e}^{-(T_0/T)^{1/3}}. \tag{4.8}$$

The classic example where this behavior is observed is in the Anderson-localized material, but it can also be observed in heterogenous systems. Elias et al. take this view of their samples, which they believe to consist of hydrogen clustered in protruding parts of the sample, separated by metallic graphene regions [131]. The metallic regions cannot conduct through the sample because they are not sufficiently connected to allow transport. This interpretation is admitted by the data but subject to some uncertainty, first because they lacked spatial resolution to confirm the nonpercolative structure, and second because the transport measurements cannot verify if there is a gap in the band structure or the DOS, only whether there is a transport gap.

ARPES experiments combined with transport are informative because they can determine the possible gap or midgap states directly. Data by Bostwick et al. showed qualitatively similar behavior as in the Elias experiments: upon exposing n-doped epitaxial graphene to a slow atomic hydrogen flux, a transition from metallic ($\mathrm{d}\sigma/\mathrm{d}T < 0$) to insulating ($\mathrm{d}\sigma/\mathrm{d}T > 0$) was observed [15]. At the same time, ARPES measurements of the band structure showed a significant reduction in the DOS above the Dirac energy E_D, reflected by the absence of a clear dispersion of the π^* states above E_D, see Fig. 4.6.

But the most intriguing observation is that the circular Fermi surface remains intact, albeit significantly broadened. This broadening near E_F is far more significant than the states below E_D, shown in Fig. 4.6. At the very least this indicates a transition away from Fermi liquid behavior, which is characterized by a long-lived quasiparticle at E_F. This was remarkable behavior since the modest change in diameter of the Fermi surface suggested a density of H atoms only on the order of 0.1 to 1%, assuming each H atom accepts one electron from the graphene.

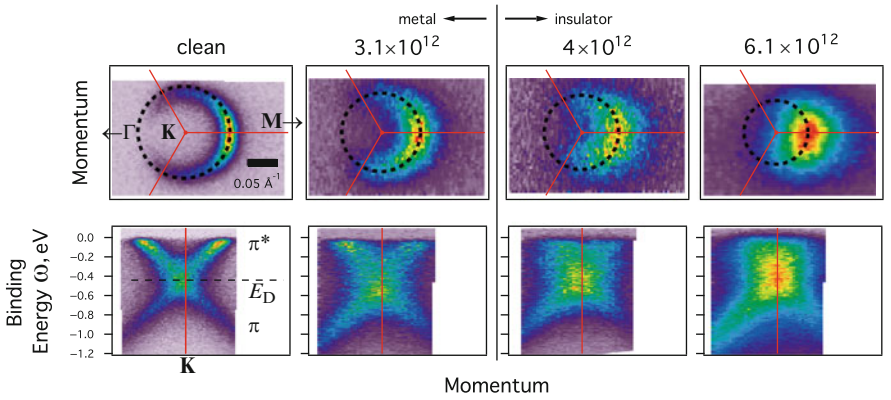

Fig. 4.6 Metal–Insulator transition (MIT) in graphene induced by hydrogen adsorption. (*top*) The Fermi surfaces and (*bottom*) the band structure acquired along a line through the K point, perpendicular to the KM line. The data are acquired for (**a**–**d**) four different doses of H (density in cm^{-2} indicated). The MIT occurs at an H density around $3 \times 10^{12}\,\mathrm{cm}^{-2}$ (Adapted from [15])

Viewed in the time domain, the combination of a reduction of the DOS with the extended linewidth indicates a divergence in the quasiparticle lifetime, or in practical terms, a complete breakdown of the quasiparticle picture. Viewed in the spatial domain, the observation of a mean free path (given by the inverse of the momentum width at E_F) shorter than the Fermi wavelength $1/k_\mathrm{F}$ means that the ordinary conduction of charge carriers becomes meaningless.

Taking these observations together, Bostwick et al. concluded that they had observed a MIT in hydrogen-dosed graphene of the strong (Anderson) localization type [15]. Its appearance is related to a hydrogen-induced state around 200 meV above E_D and 200 meV below E_F. This state was evident in ARPES measurements in regions of momentum space away from the strong graphene bands. Scattering by graphene π electrons from this state induced a mobility gap, which grows until it crosses E_F, at which point the MIT sets in. The abrupt decrease in the DOS above E_D was consistent with predictions by Robinson et al. for atomic hydrogen dosing [141].

The model for Anderson localization does not rely on the details of the chemical interaction between H and graphene but rather on the symmetry breaking character of the adsorbates [12, 13, 104]. So, an important test of whether AL has been achieved in graphene is to find other examples with similar symmetry breaking character but differing in other details of the atomic structure. In particular, carbon vacancies or adsorbates other than hydrogen should equally well induce the Anderson localization (AL) transition. This should be especially true when a significant gain of sp^3 or other hybridization character is present at the defect/adsorbate site. Such rehybridization could lead to an on-site energy for p_z orbitals almost as effective as vacancy formation which prohibits hopping onto the site altogether.

A low level of defects was found to induce AL in carbon nanotubes [142], but the one-dimensional character is an additional factor favoring localization [137], so it is not obvious if similar lattice defects will have the same effect on graphene.

The effect of carbon vacancies on transport was investigated by Fuhrer who prepared their samples by bombardment of graphene flakes exfoliated onto SiO_2. They observed a MIT owing to scattering induced by predicted midgap states, but did not go so far as to claim AL for the MIT [14].

Ozone treatment of graphene has been predicted to generate symmetry-breaking epoxide groups onto graphene [143, 144]. Leconte et al. [144] simulated the effect of 0.1 to 4% coverage of graphene by such groups and concluded that the DOS changes induced by ozone should lead to an AL transition. They went on to conduct experiments on graphene exfoliated onto SiO_2 and confirm the predictions by observing a transition to variable-range-hopping behavior consistent with AL [145].

However their calculation is a bit artificial because they induced symmetry breaking not by breaking the A–B sublattice symmetry but by placing an epoxide group in a single-site, large periodic unit cell. It should be noted that the actual nature of the bonding site was not determined, and that in fact a symmetry-breaking physisorbed state for ozone has also been predicted, which could lead to AL by a different mechanism.

These studies have clearly established that small amounts of disorder can induce a MIT with signatures of AL. The question is whether AL has been conclusively demonstrated or not. Certainly the continuous transition form weak to strong localization with magnetic field by Moser et al. is a step in the right direction [145] to establish this.

The ultimate proof will come by direct observation of wavefunction localization by a real-space probe such as STM. In such an experiment, one hopes to measure the tail of a localized wavefunction, which should be exponential according to Anderson [136]. Such tails have been observed in other localized systems such as matter waves [146], sound waves [147], and light waves [148]. Despite 50 years of research into electron systems, such direct observation of localized states in electronic systems has not been achieved. Graphene offers a new perspective on this problem because it can be attacked so easily with STM and because the structural perfection of the graphene between the defects should easily allow the visualization of the states.

We should conclude this section by discussing the outlook for applications. As pointed out by Leconte et al. [144], it should be possible to find an adsorbate of significant scattering strength to induce AL but of sufficiently weak binding as to reversibly desorb the external species and recover metallic behavior. Hydrogen will not satisfy this because removal of hydrogen by heating is found to etch the graphene, probably leaving carbon vacancies [149]. This was observed by Elias et al. who found that metallicity, but not the original conductivity, was observed upon removal of hydrogen.

If the ideal adsorbate can be found, then one can imagine creating a novel switchable device, which could be triggered reversibly in chemical or electrochemical reactions, or reversed by heat or photons.

4.6 Potassium on Graphene: The Coulomb Interaction in Graphene, Revealed

4.6.1 K Adsorption on Epitaxial Graphene on SiC(0001)

While deposition of a small amount of H atoms [15], epoxide groups [145], and similarly vacancies [14] induces a MIT and dramatic changes to the ARPES spectral function, a similar coverage of K atoms leads only to a modest decrease in mobility [8] and a smooth evolution of the ARPES spectral function [23,150]. This evolution suggests that the Dirac character of the carriers is preserved while at the same time the doping dependence on the band structure and transport properties may be clearly observed.

The first observation [23] of K-doped graphene by ARPES was for epitaxially grown graphene on the SiC(0001) surface (preparation of such graphene surfaces is discussed extensively in Chaps. 5–7). These measurements suggested that, accompanying the expected n-doping of the bands, there was an anomalous feature of the spectral function near the Dirac energy E_D [23] which is reproduced in Fig. 4.7. Namely, the intensity of the graphene π band was weaker than expected near E_D, and furthermore the bands appeared to possess a"kink" there. That is to say, the upper linear π^* bands, when projected downward through E_D, were not aligned with the lower linear π bands but shifted by a doping-dependent value $\acute{}E$. These effects were subtle for the clean graphene (n-doped by substrate interactions) but more clear at higher doses of K.

Since the kink at E_D grows with n, and stays pinned at the K point, it was suggested that its origin was the self-energy of the photohole at E_D due to electron–plasmon coupling. Plasmons are quantized density wave oscillations in the electron gas which are akin to sound waves in elastic media. Since they carry no spin, they are bosons, and since graphene is a two dimensional electron gas, plasmons have a dispersion with wavenumber q [151]:

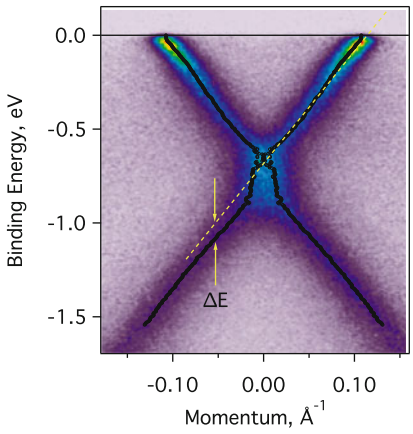

Fig. 4.7 Band structure of K-doped graphene on SiC(0001), for total charge density $n = 5.6 \times 10^{13}\text{cm}^{-2}$. The *closely spaced symbols* are fits to the cuts in the momentum direction to two symmetrical peaks; these indicate the presence of a significant kink, characterized by the energy shift ΔE (Adapted from [23])

$$\omega_{\mathrm{pl}} = \sqrt{4\pi n e^2 q/m^*(1+\epsilon)}. \tag{4.9}$$

Here n is the charge density, m^* is an effective carrier mass, and q plays the role of a momentum loss or gain when the photohole emits or absorbs a plasmon. In order for such scattering to be kinematically allowed, the scattering should also conserve energy, so that in such a decay process, the photohole should absorb or emit an energy equal to that in (4.9).

For zero-rest-mass fermions, $m^* \rightarrow 0$ and (4.9) appears to diverge. Since graphene's carriers are massless, what is the effective mass m^* to be used in (4.9)? Using Einstein's equation $E = mc^2$, we can compute the mass-equivalent of the kinetic energy of the holes:

$$m^* = (E_{\mathrm{F}} - E_{\mathrm{D}})/v_{\mathrm{D}}^2. \tag{4.10}$$

The numerator could be gotten directly from the ARPES measurement, and was compatible with m^* determined independently by transport measurements [152, 153]. We arrive at a small but nonvanishing effective mass around $m^* \sim 0.1m_e$. Using a phenomenological dielectric constant $\epsilon \sim 6$ representative of the substrate, Bostwick et al. were able to show that the elastic electron–plasmon scattering processes contained in (4.9) could well explain the observed kink at E_{D} and energy shift ΔE.

What is more, the scattering of the electron by plasmons at E_{D} was shown to be the only effective scattering channel near E_{D}. This is because conventional electron–electron scattering, the so-called Fermi liquid excitations important for all two-dimensional electron gases [154], does not have a kinematically allowed phase space near E_{D} [23, 155–159]. This follows directly from the linear dispersion and the topology of the bands in momentum space. In nonmagnetic graphene, the only remaining conventional decay channel is electron–phonon scattering, but there too it was shown that such scattering is kinematically forbidden near E_{F} [160–162].

Since the photohole lifetime near E_{D} in n-doped graphene is dominated by electron–plasmon coupling, it suggested some interesting device applications. Namely, if a hot electron carrier population could be pumped in a device, then a population inversion could be established, making conditions right for stimulated emission of plasmons; for example, see the paper by Rana [163]. Such a device would have a wide tunability because of the linear band structure of graphene.

Despite the theoretical support for the plasmon-scattering description, the electron–plasmon scattering mechanism was not the only one proposed to explain the data. Zhou et al. proposed through their own measurements on epitaxial graphene [164] that symmetry breaking of the graphene lattice (of the type illustrated in Fig. 4.5b) could open a gap, leading to reduction of intensity near E_{D}. The possibility of such symmetry breaking rests on the fact that there is a lattice mismatch and 30° rotation of the graphene relative to the SiC(0001) substrate; the net symmetry of the system is $6\sqrt{3} \times 6\sqrt{3}$-R30° which can couple the K and K′ points of the Brillouin zone opening a gap. The energy shift ΔE between lower and upper bands could be ascribed to a self-doping effect.

The appearance of such a symmetry-breaking gap, however, would lead to a breaking of the chiral symmetry, and it was shown that such symmetry breaking was incompatible with ARPES intensity measurements [165, 166]. Later, it was shown directly in transport measurements on SiC(0001) epitaxial graphene that the π Berry's phase shift and Quantum Hall plateaus are preserved [167–169], even down to $n = 5.4 \times 10^{10}\,\mathrm{cm}^{-2}$. This corresponds to a Fermi level only ~30 meV above E_D and clearly shows that any gap due to substrate symmetry breaking must be much smaller than that, or at least that its energy scale is insignificant compared to the observed band structure renormalization [23] and computed interaction strengths [155–159].

It is likely that the observed gap-like feature by Zhou et al. is due to defect scattering in their samples. This can follow from the similarity of their spectra to that of underannealed samples [170] and to the early-stage adsorption of H on graphene discussed in Sect. 4.5. An alternate connection to defect scattering was provided by Benfatto [171], who showed that a purely k-dependent self-energy arising from certain defect scattering can provide an energy gap (and band shift ΔE) without adding any mass, i.e., preserving the Dirac-like linear dispersion. As mentioned above, however, such a gap has been ruled out by direct transport measurements.

Another extrinsic explanation for the anomalies near E_D is the underlying carbon "buffer layer" that lies between the active graphene and the SiC(0001) substrate. These can introduce new band structure features including a gap-like spectrum [128, 172]; however, other features of their calculation including a metallic character of the buffer layer cannot be reproduced by experiment [24, 173] nor can it explain the doping dependence of the observed anomalies in ARPES [23].

4.6.2 K Adsorption on Quasi-free-Standing Epitaxial Graphene on SiC(0001)

Although the argument that the buffer layer causes the anomalous dispersion is weak or inconclusive, its presence is still a complication which we desire to remove. This was accomplished by replacing the complicated buffer layer by a simpler, hydrogen-terminated SiC interface [174,175]. Graphene in such a form has been called "quasi-free-standing" (QFS) due to its subsequent decoupling from the substrate. In one stroke, the sample quality is improved, revealing finer features than were possible before, but also the screening contribution of the substrate, which masks some of the important electron–electron interactions, is greatly reduced, making the signatures of electron–plasmon coupling easier to see [150].

ARPES measurements showed that QFS graphene is p-doped [174, 175], but K adsorption readily converts it to n-type. The ARPES spectral function for such an n-doped sample is shown in Fig. 4.8a [150]. As in Fig. 4.7, an overall offset ΔE between the π and π^* bands is visible, but now it is much larger. And, where before there appeared a stretching of intensity at E_D attributed to a pair of kinked bands,

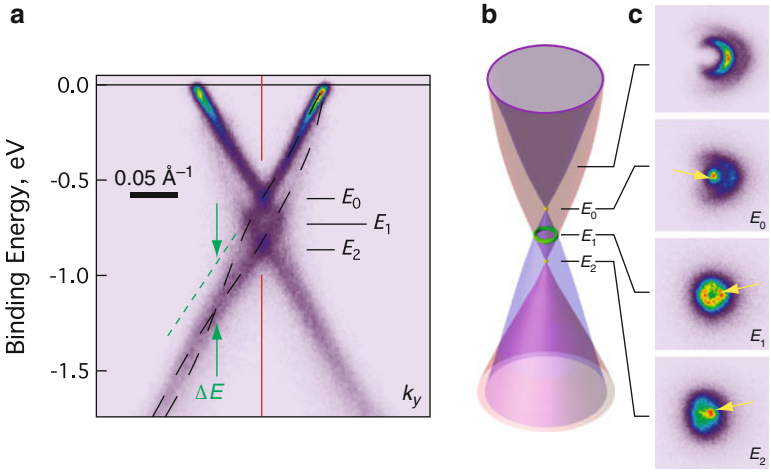

Fig. 4.8 Band structure of K-doped quasi-free-standing graphene in SiC(0001). (**a**) The ARPES measurement of the spectral function shows a prominent splitting of the bands near the Dirac energy $E_D \sim E_0$. (**b**) A schematic model of the reconstructructed band structure. (**c**) Momentum-plane slices of the spectral function at the indicated energies. The Dirac crossings are highlighted by *arrows* (Adapted from [150])

now we can resolve two pairs of bands (one pair highlighted by dashed lines) whose crossings form a diamond shape.

In the full (k_x, k_y) ARPES map, each pair of bands is rotated cylindrically about the K point of the graphene Brillouin zone. Figure 4.8b shows a schematic of the reconstructed band structure. The single Dirac crossing at E_D has been replaced by three crossings: a point-like crossing at energy E_0, a ring-like crossing at E_1, and another point-like crossing at E_2.

Constant-energy planar cuts through the spectral function at four different energies are shown in Fig. 4.8c. The upper panel shows two concentric circular contours, corresponding to the two highlighted (black dashed) bands in Fig. 4.8a, both sharing the same crescent-like intensity distribution. This distribution is a photoelectron interference effect which arises from the interference of emission from the A and B sublattices of graphene [176]. Since such interference arises only when the A and B sublattices are identical, it can be interpreted as a signature of the chiral states of graphene [165, 166], i.e., that both bands are Dirac-like, carrying parallel pseudospin vectors. Thus, the crossings at $E_{0,1,2}$ are between bands of opposite chirality and can be properly called Dirac crossings.

The origin of the band splitting in Fig. 4.8a can be described by GW theory within the random phase approximation $(\text{RPA-GW})_0$ theory [155, 157], which describes the upper of the two bands (closest to E_F) as an ordinary quasiparticle, with a close resemblance to the band in Fig. 4.7. This band is kinked at its Dirac crossing as previously described due to plasmon scattering.

The lower band is a new quasiparticle called a plasmaron [177–179], which is a bound state of a hole and a plasmon propagating in parallel. It arises during the photoemission process itself: The creation of the valence band hole is a sudden perturbation to the system; like the waves generated when a stone is dropped into a pond, the electron gas responds to the core hole by generating plasmon waves. Unlike the stone, though, the hole travels with a finite velocity and can travel in parallel with, and therefore interact with, the plasmon wave.

Not all waves are equally favored for this interaction, however. There is always a single plasmon with the same group velocity as the bare hole, say with momentum q^* and energy Ω^*, such that its group velocity matches the hole's Dirac velocity:

$$\partial\omega_{\mathrm{pl}}/\partial q|_{q=q^*} = v_{\mathrm{D}}. \tag{4.11}$$

Since all the bare holes have the same velocity, they all couple strongly to the same plasmon, leading to the appearance of a discrete excitation – the lower band in Fig. 4.8.

Formally, this process can be described as a resonance in the joint DOS for electron–plasmon scattering [180]. It leads to a strong oscillation in the real part of the self-energy function $\Sigma(\mathbf{k}, \omega)$ that appears in (4.3). When this occurs, in such a way that $\mathrm{Im}\Sigma(\mathbf{k}, \omega)$ is small, a resonance in $A(\mathbf{k}, \omega)$ is observed, describing new propagating entities such as the plasmaron band.

A curious consequence of the linear band structure of graphene is that the Coulomb interaction is *scale-free*. To see what this means, consider the ordinary two-dimensional electron gas, characterized by energy $\omega \propto k^2$. In such a system, the low-temperature behavior is governed by the coupling parameter $r_s = 1/\sqrt{\pi n}$ where n is the charge density and r_s is measured in units of the Bohr radius (see, e.g., [181]). At large r_s, the screening of the Coulomb interaction is weak, electronic correlation is strong, and exotic phases such as the Wigner crystal form. At small r_s, the Coulomb interaction is strongly screened, and the gas behaves as a paramagnet.

In graphene, no such parameter as r_s enters in the Coulomb interaction, and for n-type graphene, there is one unique spectral function that appears for all charge densities. To see why this is so, combine (4.9) and (4.10) using $n \propto \omega_{\mathrm{D}}^2$ and $v_{\mathrm{D}} = (\omega_{\mathrm{D}}/k_{\mathrm{F}})$ appropriate for graphene, and one finds

$$\omega_{\mathrm{pl}}/\omega_{\mathrm{D}} \propto \sqrt{k/k_{\mathrm{F}}}, \tag{4.12}$$

where k_{F} is the Fermi momentum and ω_{D} is the binding energy at the Dirac crossing. This result shows that the plasmon dispersion scales relative to the linear band structure. But the plasmon dispersion occurs at the zeros of the dielectric function $\epsilon(q, \omega)$, which therefore must also be describable in terms of dimensionless coordinates $q/k_{\mathrm{F}}, \omega/\omega_{\mathrm{D}}$. And therefore, the self-energy and ARPES spectral function must also be describable in these same dimensionless units.

This can be directly demonstrated by experiment: Figure 4.9 shows the ARPES spectral function as a function of potassium coverage on QSF graphene. The upper panels are plotted in the physical units ($\mathrm{Å}^{-1}$, eV), while the same data are drawn in normalized coordinates $(k/k_{\mathrm{F}}, \omega/\omega_{\mathrm{D}})$ in the lower panels.

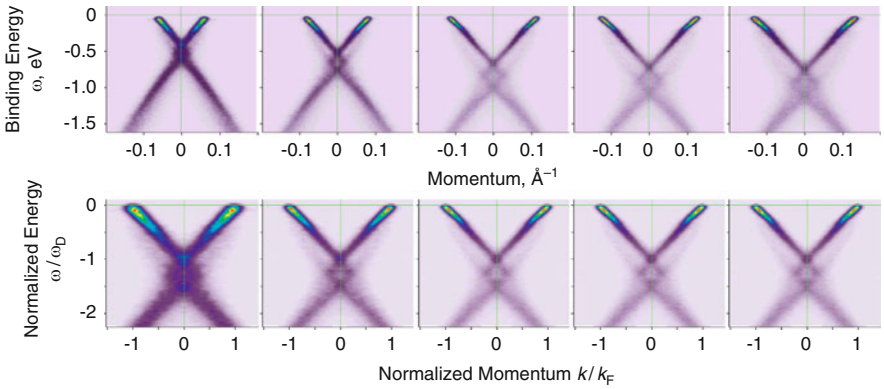

Fig. 4.9 Doping dependence of the plasmaron spectral function observed by adsorption of K atoms on quasi-free-standing graphene. The *upper panels* show the spectral function $A(\mathbf{k}, \omega)$ in physical units (Å^{-1}, eV). From left to right, the potassium dose increases. The *lower panels* show the same data drawn in normalized coordinates ($k/k_F, \omega/\omega_D$). Data are mirror-symmetrized across the K point (Adapted from [150])

The experiment is not free of some fixed scales: there is a pronounced sharpening and small kink of the bands at the fixed energy scale $\omega = -180\,\text{meV}$ [23]. There is also a fixed energy and momentum resolution. Together these effects cause some variation in the normalized spectral functions. Nevertheless, ignoring these effects, it is clear that the plasmon-related parts of the normalized spectral function are invariant with doping, especially with respect to the size of the diamond-shape Dirac crossing region.

Since the spectral function is invariant with doping, the interactions must be described by a single parameter. Recall the vacuum fine structure constant

$$\alpha = \mathrm{e}^2/\hbar c \sim 1/137 \tag{4.13}$$

that describes in quantum electrodynamics (QED) the Coulomb interaction strength in free space. In graphene, the analog of this is the graphene fine structure constant [182]

$$\alpha_G = \mathrm{e}^2/\hbar v_D \times (1/\epsilon) \sim 2.2 \text{ for } \epsilon = 1, \tag{4.14}$$

which is found by making the substitution $c \to v_D$ in (4.13). This large value of α_G indicates a very high degree of correlation, that if achieved, would lead (according to predictions) graphene to be a Mott insulator [183].

In fact, the Coulomb correlations are reduced for graphene on a substrate, whose external screening can be included phenomenologically by the screening parameter ϵ in (4.14). The effect of such a screening parameter was also needed to describe the transport properties of graphene on SiO_2 after adsorption of polarizable water molecules [184].

In general, we can describe the screening constant ϵ to be the average of screening contributions from the semi-infinite space above and below the graphene. For K on graphene, we can neglect the screening contribution for the K atoms, which if fully ionized are hardly polarizable (and too sparse to matter in any case). Comparison of the experimental data in Figs. 4.8 and 4.9 to model calculations [150], Bostwick et al. find a value $\alpha_G^{QFS} \sim 0.5$, so the screening contribution of the H-terminated interface is around $\epsilon^{QFS} \sim 7.8$.

In comparison, the smaller energy shift of the bands ΔE in epitaxial graphene (EG) samples implies a much smaller coupling constant $\alpha_G^{QFS} \sim 0.15$. This means the substrate screening constant ϵ^{EG} could be as high as 30. Such a large polarizability naturally arises from the large number of unsaturated silicon dangling bonds at the buffer layer/SiC interface [128].

To conclude this section, potassium on graphene has played a very different role than hydrogen on graphene in Sect. 4.5. There, the adsorbate was an active player, directly interfering with the carrier transport through strong quantum corrections to the transport. For potassium doping, on the other hand, the quantum corrections to transport due to potassium adatoms are minor [8] but the doping effect is very strong. This difference originates directly from the different symmetry of the bonding sites ($H = T$, $K = H_6$) illustrated in Fig. 4.4.

Unlike hydrogen adatoms, potassium adatoms preserve the A–B lattice symmetry, introducing only a relatively weak long-range Coulomb potential. This allows us to reveal the inherent physics of graphene at high doping. In the next section, we will take this to extremes, going far beyond the Dirac carrier limit to further explore the susceptibility of graphene. There we will show that the electron gas is (conceptually) unstable against a superconducting ground state.

4.7 Calcium Adsorption: Superconducting Instability of Graphene

An early explanation for the high temperature superconductivity in cuprates was the proximity of the Fermi level to a saddle point in the band structure [185, 186] as shown in Fig. 4.10. At extremely high doping levels, graphene's band structure bares a striking similarity, having similar saddle points in a threefold geometry, see Fig. 4.10.

There are three principle arguments for why such a band structure can lead to superconductivity, if the Fermi energy is near the saddle point energy. Together, these arguments comprise the "van Hove scenario" for superconductivity. The first argument is that at such a saddle point, there are present both electron-like and hole-like carriers, thus there is the basis of an attractive interaction necessary for forming Cooper pairs.

The second argument lies in the fact that the DOS has a maximum at the saddle points [101] called a van Hove singularity (VHS). A high DOS is needed because no matter the interaction strength, nothing can happen if there are insufficient carriers.

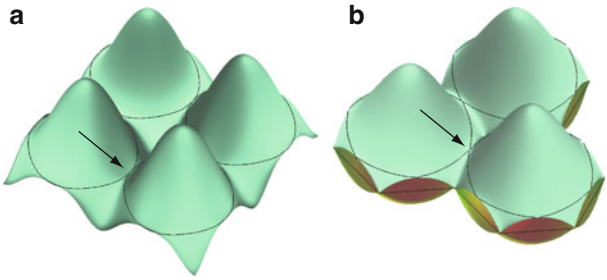

Fig. 4.10 Topology of the band structure of (**a**) High-T_c superconductors and (**b**) graphene. Saddle points in the band structure resulting in van Hove singularities in the density of states are highlighted by *arrows*. Graphene bands were calculated using the tight binding parameters of Reich [26]

The third argument derives from the form of the Lindhard spin and charge susceptibility function:

$$\chi(\mathbf{q},\omega) = -\sum_k \frac{f(\epsilon_\mathbf{k}) - f(\epsilon_{\mathbf{k+q}})}{\epsilon_\mathbf{k} - \epsilon_{\mathbf{k+q}} - \hbar\omega - \mathrm{i}\delta}. \tag{4.15}$$

Because the denominator vanishes at the Fermi edge, it can lead to divergences whose strength depends on the topology of the Fermi surface. At such divergences, $\chi \to \infty$ and the screening becomes essentially perfect at certain wavevectors. Among the consequences of such perfect screening is that Coulomb repulsion (which discourages pairing) is reduced, but also the lattice can become susceptible to distortions. For example, nested, or parallel, sections of the Fermi surface connected by a vector $\mathbf{q}$ will be unstable to forming spin or charge density waves with wavelength $2\pi/\mathbf{q}$, provided that $\mathbf{q}$ does not lie on the reciprocal lattice. This commonly leads to symmetry changes, for example, the Peierls transition in one-dimensional metals [187].

For the topology of graphene's bands in Fig. 4.10b, singularities in the susceptibility will occur at both $\mathbf{q} = 0$ and at those $\mathbf{q}$ which connect any two saddle points. But these $\mathbf{q}$s are all combinations of reciprocal lattice vectors and the various $\overline{\Gamma\mathrm{M}}$ vectors; density excitations on these wavevectors do not lead to symmetry changes. We can conclude that graphene does not have a density wave ground state, so that the ground state will be either ferromagnetic or superconducting.

Some excitement was generated by the discovery of superconducting CaC_6 compounds ($T_c \sim 12\,\mathrm{K}$), consisting of graphene layers intercalated by Ca atoms [188]. Initially, it was proposed that an electron–electron coupling mechanism was responsible, but later the theoretical consensus became that the superconductivity was mainly derived from the electronic states in the Ca layers, not the graphene [189–194]. Also, the doping appears to be far from the VHS energy.

Nevertheless, it is interesting to ask two questions:

1. Can such a high doping level be achieved in graphene?
2. Does the topology of the bands near the saddle point support a superconducting or magnetic instability?

To investigate the first question, McChesney et al. doped graphene using Ca. The aim of Ca doping was to achieve a higher electron transfer per adatom than for potassium. Although that intention was not realized (the computed charge transfer per Ca atom is hardly one electron per adatom [62], not much more than for potassium), it turned out to have a major benefit: deposition of Ca followed by annealing allowed Ca to intercalate under the graphene, leaving the top surface clean for additional chemical dopants to be adsorbed [16].

Figure 4.11 shows the Fermi surfaces and underlying band structures of a variety of doping combinations achieved by this method. The last two panels correspond to doping just below and just above the VHS. The transition between these two – when the closed electron pockets at K and K′ merge to form a single large hole pocket centered at Γ – is called a Lifshitz transition or sometimes an electronic topological transition (ETT). This occurs at a net charge transfer of around 0.18 electrons per unit cell or $3.45 \times 10^{14}\,\mathrm{cm}^{-2}$.

So, the first question is answered that graphene can be readily doped well past the VHS energy.

The answer to the second question depends on the exact shape of the bands. Careful examination of the band structure (Fig. 4.11h, lower panel) near the M point shows that it is extremely flat, indicating that the hole-like states at the VHS have a large (approaching infinite) mass. This suggests that the VHS is particularly strong – having a one-dimensional or *extended* character. Such an extended VHS (eVHS) leads to a square-root divergence in the DOS, whereas an ordinary VHS has a weaker, logarithmic divergence [186].

A comparison of the LDA band structure [26] to the observed band structure is shown in Fig. 4.12. To make this comparison, both the model and the experimental data were fitted to third-near-neighbor tight binding models. The LDA calculation does not capture the flatness of the bands nor the extension of the VHS, suggesting that this eVHS arises by a strong-correlation effect. This is supported by GW calculations, which does capture partially the flatness of the band but not as strongly as the data [195].

Calandra and Mauri showed that such a flat band can occur due to hybridization of Ca $3d$ states with the graphene band [64], but this requires $\sqrt{3} \times \sqrt{3}$ long range order in the Ca or K arrangements which cannot be confirmed in the data (among the associated effects would be a large gap at the Dirac crossings in Fig. 4.11 which is clearly not present).

We have to conclude the presence of an extended VHS in doped graphene, which has probably two origins: a large electron–electron self-energy which depressed the band energy at the graphene M point and second a mass enhancement due to electron–phonon coupling [16]. Support for the influence of many-body interactions

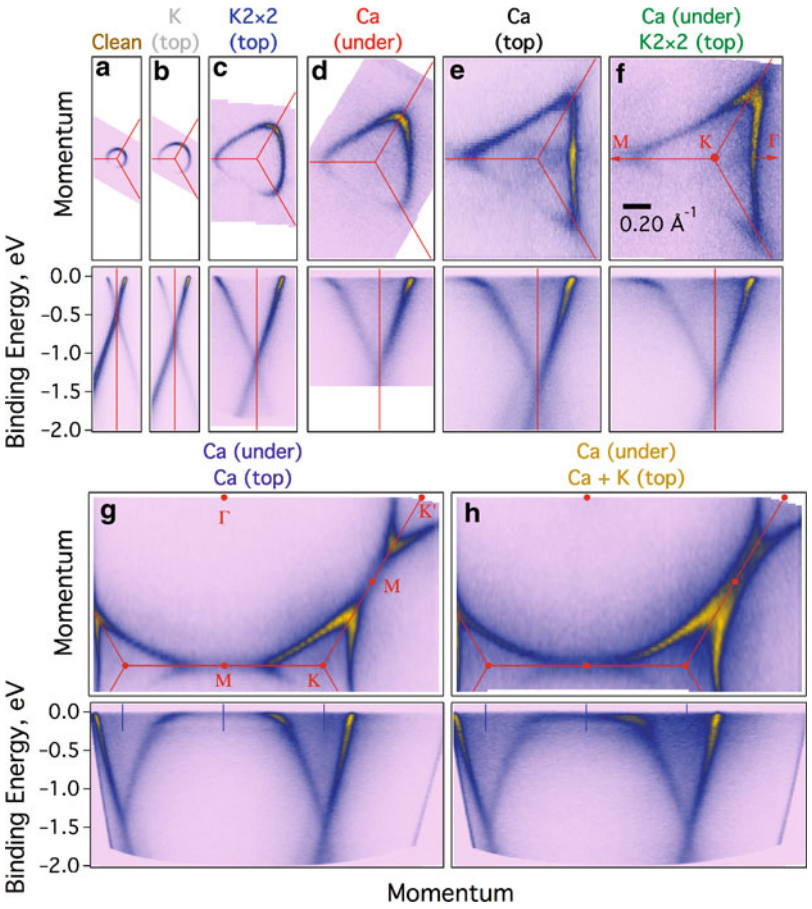

Fig. 4.11 Evolution of the graphene band structure under combinations of potassium and calcium doping both below and above epitaxial graphene on SiC(0001). (**a**) As-grown (clean) epitaxial graphene; (**b**) potassium adatoms on top, at similar coverage as the data in Fig. 4.7; (**c**) saturated, ordered 0.25 ML 2×2 phase of K on graphene; (**d**) saturation dose of Ca under the graphene; (**e**) saturation dose of Ca above the graphene; (**f**) combination of (**d**)+(**c**); (**g**) saturation dose of Ca under the graphene, and some Ca on top; (**h**) same as (**g**) after additional dose of K atoms. Panels (**a**–**f**) share a common momentum scale (see scale bar in (**f**)); the momentum scale in (**g**–**h**) is set by the K-K′ distance, 1.703 Å^{-1} (From [16])

in forming the eVHS is that at the other saddle point *below* E_D, the VHS is of the ordinary type, as predicted by all the models.

Given the detailed shape of the VHS, McChesney et al. went on to calculate the susceptibility $\chi(\mathbf{q})$ and from there to calculate the effective couplings within BCS theory, with on-site Coulomb interaction U as an adjustable parameter. They could show that for any reasonable U, superconductivity induced by the eVHS

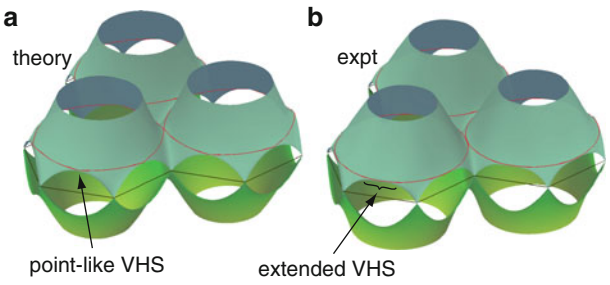

Fig. 4.12 Comparison of (**a**) first-principles LDA calculation [26] and (**b**) experimental band structure for Ca+K doped graphene [16]. The respective bands are represented here by fits to a third-near neighbor tight binding model

would always be favored over a ferromagnetic ground state. Furthermore, they could compute an enhancement of the critical temperature for superconductivity up to two orders of magnitude above what it would be for an ordinary VHS.

This is not to say that the samples investigated were *actually* superconducting – this was not looked for in the experiments – nor that the eVHS scenario explains superconductivity in other carbon systems such as KC_8 and CaC_6. Among other factors, the long-range order and the interlayer coupling of the latter disrupt the band structure, removing the VHS from consideration.

It does suggest that doped graphene can achieve an electronically mediated superconductivity *if* the doping is in the vicinity of the VHS *and* the lattice symmetry is preserved, i.e., the chemical dopants do not introduce new states near the VHS to disrupt the band structure.

4.8 Conclusions and Outlook

Graphene is a remarkable material, and in this chapter we have emphasized its properties in regards to many-body interactions, which can easily be altered and probed by adsorbates. In fact, it is the material *par excellence* for the variety of self-energy phenomena that can be probed on wide energy scales – from meV to 2 eV.

It is not a surprise, then, that it shows hints of such various physics – from Anderson localization, to Mott insulator, to Plasmaronic material (to coin a term), to superconductor – not to mention the massless Dirac character whose elucidation started the rush to further discoveries in 2005.

Considering the zoo of adatoms that can be adsorbed – not to mention molecules, which were not even covered in this chapter, and the very few that have so far been explored as to their effects on graphene – I have come to believe that there is no known phase of condensed matter that will not eventually be realized in graphene: let the animals loose!

Acknowledgements Critical contributions from A. Bostwick, T. Ohta, J. L. McChesney, K. V. Emtsev, F. Speck, S. D. Kevan, Thomas Seyller, and Karsten Horn are gratefully acknowledged. Work was performed at the Advanced, Light Source, E. O. Lawrence Berkeley National Laboratory. The Advanced Light Source is supported by the Director, Office of Science, Office of Basic Energy Sciences of the U.S. Department of Energy under Contract No. DE-AC02-05CH11231.

References

1. J. Moser, A. Barreiro, A. Bachtold, Appl. Phys. Lett. **91**, 163513 (2007)
2. K.I. Bolotin, K.J. Sikes, Z. Jiang, M. Klima, G. Fudenberg, J. Hone, P. Kim, H.L. Stormer, Solid State Comm. **146**(9-10), 351 (2008)
3. X. Du, I. Skachko, A. Barker, E.Y. Andrei, Nat. Nano. **3**(8), 491 (2008)
4. S.V. Morozov, K.S. Novoselov, M.I. Katsnelson, F. Schedin, D.C. Elias, J.A. Jaszczak, A.K. Geim, Phys. Rev. Lett. **100**(1), 016602 (2008)
5. J.H. Chen, C. Jang, S. Xiao, M. Ishigami, M.S. Fuhrer, Nat. Nano. **3**(4), 206 (2008)
6. P. Neugebauer, M. Orlita, C. Faugeras, A.L. Barra, M. Potemski, Phys. Rev. Lett. **103**(13), 136403 (2009)
7. Z. Ni, L. Ponomarenko, R. Nair, R. Yang, S. Anissimova, I. Grigorieva, F. Schedin, P. Blake, Z. Shen, E. Hill, Nano Lett. **10**(10), 3868 (2010). URL http://pubs.acs.org/doi/abs/10.1021/nl101399r
8. J.H. Chen, C. Jang, S. Adam, M.S. Fuhrer, E.D. Williams, M. Ishigami, Nat. Phys. **4**(5), 377 (2008)
9. K. Pi, K.M. McCreary, W. Bao, W. Han, Y.F. Chiang, Y. Li, S.W. Tsai, C.N. Lau, R.K. Kawakami, Phys. Rev. B **80**(7), 075406 (2009)
10. K.M. McCreary, K. Pi, A.G. Swartz, W. Han, W. Bao, C.N. Lau, F. Guinea, M.I. Katsnelson, R.K. Kawakami, Phys. Rev. B **81**(11), 115453 (2010)
11. P.R. Wallace, Phys. Rev. **71**(9), 622 (1947)
12. H. Suzuura, T. Ando, J. Phys. Soc. Jpn. **72**(Suppl. A), 69 (2002)
13. H. Suzuura, T. Ando, Phys. Rev. Lett. **89**(26), 266603 (2002)
14. J.H. Chen, W.G. Cullen, C. Jang, M.S. Fuhrer, E.D. Williams, Phys. Rev. Lett. **102**(23), 236805 (2009)
15. A. Bostwick, J.L. McChesney, K.V. Emtsev, T. Seyller, K. Horn, S.D. Kevan, E. Rotenberg, Phys. Rev. Lett. **103**(5), 056404 (2009)
16. J.L. McChesney, A. Bostwick, T. Ohta, T. Seyller, K. Horn, J. Gonzalez, E. Rotenberg, Phys. Rev. Lett. **104**(13), 136803 (2010)
17. M. Cardona, L. Ley, *Photoemission in Solids I: General Principles*, *Topics in Applied Physics*, vol. 26 (Springer, Berlin, 1978)
18. S. Hufner, *Photoelectron Spectroscopy: Principles and Applications*, 3rd edn. (Springer, Berlin, 2003)
19. S. Hufner, *Very High Resolution Photoelectron Spectroscopy*. Lecture Notes in Physics (Springer, 2007)
20. S.D. Kevan, *Angle-Resolved Photoemission: Theory and Current Applications*, *Studies in Surf. Sci. and Catalysis*, vol. 74 (Elsevier Science Ltd., Amsterdam, 1992)
21. A. Damascelli, Z. Hussain, Z.X. Shen, Review of Modern Physics **75**, 473 (2003)
22. A. Damascelli, Physica Scripta **T109**, 61 (2004)
23. A. Bostwick, T. Ohta, T. Seyller, K. Horn, E. Rotenberg, Nat. Phys. **3**(1), 36 (2007)
24. K.V. Emtsev, F. Speck, T. Seyller, L. Ley, J.D. Riley, Phys. Rev. B **77**(15), 155303 (2008)
25. A. Bostwick, T. Ohta, J.L. McChesney, T. Seyller, K. Horn, E. Rotenberg, Solid State Comm. **143**, 63 (2007)
26. S. Reich, J. Maultzsch, C. Thomsen, P. Ordejon, Phys. Rev. B **66**(3), 035412 (2002)

27. F. Himpsel, Nucl. Instrum. Meth. Phys. Res. **208**(1-3), 753 (1983)
28. G. Giovannetti, P.A. Khomyakov, G. Brocks, P.J. Kelly, J. van den Brink, Phys. Rev. B **76**(7), 073103 (2007)
29. S.Y. Zhou, G.H. Gweon, A.V. Fedorov, P.N. First, W.A. de Heer, D.H. Lee, F. Guinea, A.H. Castro Neto, A. Lanzara, Nat. Mater. **6**, 770 (2007)
30. A. Varykhalov, J. Sanchez-Barriga, A.M. Shikin, C. Biswas, E. Vescovo, A. Rybkin, D. Marchenko, O. Rader, Phys. Rev. Lett. **101**(15), 157601 (2008)
31. T. Brugger, S. Gunther, B. Wang, J.H. Dil, M.L. Bocquet, J. Osterwalder, J. Wintterlin, T. Greber, Phys. Rev. B **79**(4), 045407 (2009)
32. R. Balog, B. Jorgensen, L. Nilsson, M. Andersen, E. Rienks, M. Bianchi, M. Fanetti, E. Laegsgaard, A. Baraldi, S. Lizzit, Z. Sljivancanin, F. Besenbacher, B. Hammer, T.G. Pedersen, P. Hofmann, L. Hornekaer, Nat. Mater. **9**(4), 315 (2010)
33. C. Enderlein, Y. Kim, A. Bostwick, E. Rotenberg, K. Horn, New J. Phys. **12**, 033014 (2010)
34. T. Ohta, A. Bostwick, T. Seyller, K. Horn, E. Rotenberg, Science **313**, 951 (2006)
35. R. Mattuck, *A Guide to Feynman Diagrams in the Many-Body Problem*, 2nd edn. (Dover Publications, New York, 1982)
36. J.S. Zmuidzinas, Phys. Rev. B **2**(11), 4445 (1970)
37. K.T. Chan, J.B. Neaton, M.L. Cohen, Phys. Rev. B **77**(23), 235430 (2008)
38. H. Gao, J. Zhou, M. Lu, W. Fa, Y. Chen, J. Appl. Phys. **107**, 114311 (2010)
39. I. Moullet, Surf. Sci. **331-333**, 697 (1995)
40. J.H. Parq, J. Yu, Y.K. Kwon, G. Kim, Phys. Rev. B **82**(19), 193406 (2010)
41. D.W. Boukhvalov, M.I. Katsnelson, A.I. Lichtenstein, Phys. Rev. B **77**(3), 035427 (2008)
42. O.V. Yazyev, L. Helm, Phys. Rev. B **75**(12), 125408 (2007)
43. E.J. Duplock, M. Scheffler, P.J.D. Lindan, Phys. Rev. Lett. **92**(22), 225502 (2004)
44. L. Qiao, C. Qu, H. Zhang, S. Yu, X. Hu, X. Zhang, D. Bi, Q. Jiang, W. Zheng, Diamond and Related Materials **19**(11), 1377 (2010)
45. M. Khantha, N.A. Cordero, L.M. Molina, J.A. Alonso, L.A. Girifalco, Phys. Rev. B **70**(12), 125422 (2004)
46. H. Pinto, R. Jones, J.P. Goss, P.R. Briddon, Phys. Stat. Sol. (a) **207**(9), 2131 (2010)
47. J. Algdal, T. Balasubramanian, M. Breitholtz, T. Kihlgren, L. Wallden, Surf. Sci. **601**(4), 1167 (2007)
48. Z.P. Hu, J. Li, N.J. Wu, A. Ignatiev, Phys. Rev. B **39**(18), 13201 (1989)
49. S.M. Xu, J. Cao, C.C. Miller, D.A. Mantell, R.J.D. Miller, Y. Gao, Phys. Rev. Lett. **76**(3), 483 (1996)
50. M. Sluiter, Y. Kawazoe, Phys. Rev. B **68**(8), 085410 (2003)
51. J.O. Sofo, A.S. Chaudhari, G.D. Barber, Phys. Rev. B **75**(15), 153401 (2007)
52. L. Hu, X. Hu, X. Wu, C. Du, Y. Dai, J. Deng, Phys. B Condens. Matter **405**(16), 3337 (2010)
53. M. Caragiu, S. Finberg, J. Phys. Condens. Matter **17**(35), R995 (2005)
54. T. Ohta, A. Bostwick, J.L. McChesney, T. Seyller, K. Horn, E. Rotenberg, Phys. Rev. Lett. **98**(20), 206802 (2007)
55. P. Bennich, C. Puglia, P. Bruhwiler, A. Nilsson, A.J. Maxwell, A. Sandell, N. Martensson, P. Rudolf, Phys. Rev. B **59**(12), 8292 (1999)
56. A. Lugo-Solis, I. Vasiliev, Phys. Rev. B **76**(23), 235431 (2007)
57. A. Gruneis, C. Attaccalite, A. Rubio, D.V. Vyalikh, S.L. Molodtsov, J. Fink, R. Follath, W. Eberhardt, B. Buchner, T. Pichler, Phys. Rev. B **80**(7), 075431 (2009)
58. S. Mizuno, H. Hiramoto, K. Nakao, J. Phys. Soc. Jpn. **56**(12), 4466 (1987)
59. C.K. Yang, Appl. Phys. Lett. **94**, 163115 (2009)
60. P. Medeiros, F.d.B. Mota, A.J.S. Mascarenhas, C.M.C.d. Castilho, Nanotechnology **21**(11), 115701 (2010)
61. M. Farjam, H. Rafii-Tabar, Phys. Rev. B **79**(4), 045417 (2009)
62. C. Ataca, E. Akturk, S. Ciraci, Phys. Rev. B **79**(4), 041406 (2009)
63. X. He, Z.X. Chen, Z. Li, Z. Zou, J. Chem. Phys. **133**, 231104 (2010)
64. M. Calandra, F. Mauri, Phys. Rev. B **76**(16), 161406 (2007)

65. T. Enoki, M. Suzuki, M. Endo, *Graphite Intercalation Compounds and Applications* (Oxford University Press, New York, 2003)
66. X. Ma, Q. Wang, L.Q. Chen, W. Cermignani, H.H. Schobert, C.G. Pantano, Carbon **35**(10-11), 1517 (1997)
67. R.H. Miwa, et al., Nanotechnology **19**(15), 155708 (2008)
68. L. Firlej, B. Kuchta, C. Wexler, P. Pfeifer, Adsorption **15**(3), 312 (2009)
69. J. Dai, J. Yuan, P. Giannozzi, Appl. Phys. Lett. **95**(23), 232105 (2009)
70. A. Ishii, et al., J. Phys. Conf. **100**(5), 052087 (2008)
71. E. Ganz, K. Sattler, J. Clarke, Surf. Sci. **219**(1-2), 33 (1989)
72. V. Maurice, P. Marcus, Surf. Sci. **275**(1-2), 65 (1992)
73. P.O. Lehtinen, A.S. Foster, A. Ayuela, A. Krasheninnikov, K. Nordlund, R.M. Nieminen, Phys. Rev. Lett. **91**(1), 017202 (2003)
74. E. Akturk, C. Ataca, S. Ciraci, Appl. Phys. Lett. **96**, 123112 (2010)
75. M. Wu, E.Z. Liu, J.Z. Jiang, Appl. Phys. Lett. **93**, 082504 (2008)
76. Y.G. Zhou, X.T. Zu, F. Gao, H.F. Lv, H.Y. Xiao, Appl. Phys. Lett. **95**, 123119 (2009)
77. O.U. Akturk, M. Tomak, Appl. Phys. Lett. **96**(8), 081914 (2010)
78. I. Gierz, C. Riedl, U. Starke, C.R. Ast, K. Kern, Nano Lett. **8**(12), 4603 (2008)
79. X. Wang, X. Li, L. Zhang, Y. Yoon, P.K. Weber, H. Wang, J. Guo, H. Dai, Science **324**(5928), 768 (2009)
80. V. Chandra, J. Park, Y. Chun, J.W. Lee, I.C. Hwang, K.S. Kim, ACS Nano **4**(7), 3979 (2010)
81. S.A. Scott, S.A. Brown, Eur. Phys. J. Atom. Mol. Opt. Plasma Phys. **39**(3), 433 (2006)
82. Z. Yan, S.S. Kushvaha, W. Xiao, X.S. Wang, Appl. Phys. A **88**(2), 299 (2007)
83. K. Kelly, E. Mickelson, R. Hauge, J. Margrave, N. Halas, Proc. Natl. Acad. Sci. USA **97**(19), 10318 (2000)
84. G. Giovannetti, P.A. Khomyakov, G. Brocks, V.M. Karpan, J. van den Brink, P.J. Kelly, Phys. Rev. Lett. **101**(2), 026803 (2008)
85. A.N. Rudenko, F.J. Keil, M.I. Katsnelson, A.I. Lichtenstein, Phys. Rev. B, 035,427–13 (2010)
86. K. Pi, W. Han, K.M. McCreary, A.G. Swartz, Y. Li, R.K. Kawakami, Phys. Rev. Lett. **104**(18), 187201 (2010)
87. T.O. Wehling, H.P. Dahal, A.I. Lichtenstein, A.V. Balatsky, Phys. Rev. B **78**, 035414 (2008)
88. T.O. Wehling, A.V. Balatsky, M.I. Katsnelson, A.I. Lichtenstein, A. Rosch, Phys. Rev. B, 115427 (6 pp.) (2010)
89. T.O. Wehling, H.P. Dahal, A.I. Lichtenstein, M.I. Katsnelson, H.C. Manoharan, A.V. Balatsky, Phys. Rev. B **81**, 085413 (5 pp.) (2010)
90. D.M. Duffy, J.A. Blackman, Phys. Rev. B **58**(11), 7443 (1998)
91. M.I. Rojas, E.P.M. Leiva, Phys. Rev. B **76**(15), 155415 (2007)
92. Y. Mao, J. Yuan, J. Zhong, J. Phys. Condens. Matter **20**(11), 115209 (2008)
93. D.M. Duffy, J.A. Blackman, Surf. Sci. **415**(3), L1016 (1998)
94. Y. Ren, S. Chen, W. Cai, Y. Zhu, C. Zhu, R.S. Ruoff, Appl. Phys. Lett. **97**(5), 053107 (2010)
95. V. Zólyomi, Á. Rusznyák, J. Koltai, J. Kürti, C. Lambert, physica status solidi (b) **247**(11-12), 2920 (2010)
96. J.P. Jalkanen, M. Halonen, D. FernÃąndez-Torre, K. Laasonen, L. Halonen, The J. Phys. Chem. A **111**(49), 12317 (2007)
97. R. Varns, P. Strange, J. Phys. Condens. Matter **20**(22), 225005 (2008)
98. Y.H. Lu, L. Shi, C. Zhang, Y.P. Feng, Phys. Rev. B **80**(23), 233410 (2009)
99. A. Tkatchenko, L. Romaner, O. Hofmann, E. Zojer et al., MRS Bulletin **35**(June), 435 (2010)
100. V.W. Brar, R. Decker, H.M. Solowan, Y. Wang, L. Maserati, K.T. Chan, H. Lee, Ç.O. Girit, A. Zettl, S.G. Louie, M.L. Cohen, M.F. Crommie, Nat. Phys. (2010)
101. A.H.C. Neto, F. Guinea, N.M.R. Peres, K.S. Novoselov, A.K. Geim, Rev. Mod. Phys. **81**(1), 109 (2009)
102. T.O. Wehling, M.I. Katsnelson, A.I. Lichtenstein, Chem. Phys. Lett. **476**(4-6), 125 (2009)
103. D.P. DiVincenzo, E.J. Mele, Phys. Rev. B **29**(4), 1685 (1984)
104. I.L. Aleiner, K.B. Efetov, Phys. Rev. Lett. **97**(23), 236801 (2006)
105. N. Peres, F. Guinea, A.C. Neto, Phys. Rev. B **73**(12), 125411 (2006)

106. T. Stauber, N.M.R. Peres, F. Guinea, Phys. Rev. B **76**(20), 205423 (2007)
107. V.M. Pereira, J.M.B. Lopes dos Santos, A.H. Castro Neto, Phys. Rev. B **77**(11), 115109 (2008)
108. J. Bang, K.J. Chang, Phys. Rev. B **81**(19) (2010)
109. G. Kirczenow, S. Ihnatsenka, Phys. Rev. B **83**, 245442 (2011)
110. W.D. Watson, Rev. Mod. Phys. **48**(4), 513 (1976)
111. D. Hollenbach, E.E. Salpeter, Astrophys. J. **163**, 155 (1971)
112. D.J. Hollenbach, M.W. Werner, E.E. Salpeter, Astrophys. J. **163**, 165 (1971)
113. C. Mendoza, F. Ruette, Catal. Lett. **3**(1), 89 (1989)
114. L. Hornekaer, Z. Sljivancanin, W. Xu, R. Otero, E. Rauls, I. Stensgaard, E. Laegsgaard, B. Hammer, F. Besenbacher, Phys. Rev. Lett. **96**(15), 156104 (2006)
115. F. Dumont, F. Picaud, C. Ramseyer, C. Girardet, Y. Ferro, A. Allouche, Phys. Rev. B **77**(23), 233401 (2008)
116. M.Z.S. Flores, et al., Nanotechnology **20**(46), 465704 (2009)
117. J. Zhou, M.M. Wu, X. Zhou, Q. Sun, Appl. Phys. Lett. **95**(10), 103108 (2009)
118. J. Zhou, Q. Wang, Q. Sun, X.S. Chen, Y. Kawazoe, P. Jena, Nano Lett. **9**(11), 3867 (2009)
119. J.M. Garcia-Lastra, Phys. Rev. B **82**, 235418 (2010)
120. A.V. Shytov, D.A. Abanin, L.S. Levitov, Phys. Rev. Lett. **103**(1), 016806 (2009)
121. V.V. Cheianov, V.I. Fal'ko, O. Syljuåsen, B.L. Altshuler, Solid State Commun. **149**(37-38), 1501 (2009)
122. H. Sahin, C. Ataca, S. Ciraci, Appl. Phys. Lett. **95**(22), 222510 (2009)
123. J.C. Meyer, A.K. Geim, M.I. Katsnelson, K.S. Novoselov, T.J. Booth, S. Roth, Nature **446**(7131), 60 (2007)
124. E. Stolyarova, K.T. Rim, S. Ryu, J. Maultzsch, P. Kim, L.E. Brus, T.F. Heinz, M.S. Hybertsen, G.W. Flynn, Proc. Nat. Acad. Sci. **104**, 9209 (2007)
125. C.H. Lui, L. Liu, K.F. Mak, G.W. Flynn, T.F. Heinz, Nature **462**(7271), 339 (2009)
126. V. Brar, Y. Zhang, Y. Yayon, A. Bostwick, T. Ohta, J.L. McChesney, K. Horn, E. Rotenberg, M.F. Crommie, Appl. Phys. Lett. **91**(12), 122102 (2007)
127. F. Varchon, P. Mallet, J.Y. Veuillen, L. Magaud, Phys. Rev. B **77**(23), 235412 (2008)
128. S. Kim, J. Ihm, H.J. Choi, Y.W. Son, Phys. Rev. Lett. **100**(17), 176802 (2008)
129. A.B. Preobrajenski, M.L. Ng, A.S. Vinogradov, N. Martensson, Phys. Rev. B **78**(7), 073401 (2008)
130. D. Martoccia, P.R. Willmott, T. Brugger, M. Bjorck, S. Gunther, C.M. Schleputz, A. Cervellino, S.A. Pauli, B.D. Patterson, S. Marchini, J. Wintterlin, W. Moritz, T. Greber, Phys. Rev. Lett. **101**(12), 126102 (2008)
131. D.C. Elias, R.R. Nair, T.M.G. Mohuiddin, S.V. Morosov, P. Blake, M.P. Halsall, A.C. Ferrari, D.W. Boukhvalov, M.I. Katsnelson, A.K. Geim, K.S. Novoselov, Science **323**(5914), 610 (2009)
132. G.G. Naumis, Phys. Rev. B **76**(15), 153403 (2007)
133. S.J. Xiong, Y. Xiong, Phys. Rev. B **76**(21), 214204 (2007)
134. M. Amini, S.A. Jafari, F. Shahbazi, EPL **87**, 37002 (2009)
135. E. Mucciolo, C. Lewenkopf, J. Phys. Condens. Matter **22**, 273201 (2010)
136. P.W. Anderson, Phys. Rev. **109**(5), 1492 (1958)
137. E. Abrahams, P.W. Anderson, D.C. Licciardello, T.V. Ramakrishnan, Phys. Rev. Lett. **42**(10), 673 (1979)
138. M. Schreiber, M. Ottomeier, J. Phys. Condens. Matter **4**(8), 1959 (1992)
139. G.A. Beitel, J. Vac. Sci. Tech. **6**(1), 224 (1969)
140. B. McCarroll, D.W. McKee, Nature **225**(5234), 722 (1970)
141. J.P. Robinson, H. Schomerus, L. Oroszlany, V.I. Fal'ko, Phys. Rev. Lett. **101**(19), 196803 (2008)
142. C. Gomez-Navarro, P.J.D. Pablo, J. Gomez-Herrero, B. Biel, F.J. Garcia-Vidal, A. Rubio, F. Flores, Nat. Mater. **4**(7), 534 (2005)
143. G. Lee, B. Lee, J. Kim, K. Cho, The J. Phys. Chem. C **113**(32), 14225 (2009)

144. N. Leconte, J. Moser, P. Ordejon, H. Tao, A. Lherbier, A. Bachtold, F. Alsina, C.M. Sotomayor Torres, J.C. Charlier, S. Roche, ACS Nano **4**(7), 4033 (2010)
145. J. Moser, H. Tao, S. Roche, F. Alzina, C.M. Sotomayor Torres, A. Bachtold, Phys. Rev. B **81**(20), 205445 (2010)
146. J. Billy, V. Josse, Z. Zuo, A. Bernard, B. Hambrecht, P. Lugan, D. Clement, L. Sanchez-Palencia, P. Bouyer, A. Aspect, Nature **453**(7197), 891 (2008)
147. R.L. Weaver, Wave Motion **12**(2), 129 (1990)
148. D.S. Wiersma, P. Bartolini, A. Lagendijk, R. Righini, Nature **390**(6661), 671 (1997). 10.1038/37757
149. B.J. Wood, H. Wise, J. Phys. Chem. **73**(5), 1348 (1969)
150. A. Bostwick, F. Speck, T. Seyller, K. Horn, M. Polini, R. Asgari, A.H. MacDonald, E. Rotenberg, Science **328**(5981), 999 (2010)
151. F. Stern, Phys. Rev. Lett. **18**(14), 546 (1967)
152. Y. Zhang, Y.W. Tan, H.L. Stormer, P. Kim, Nature **438**, 201 (2005)
153. K.S. Novoselov, E. McCann, S.V. Morosov, V. Fal'ko, M.I. Katsnelson, U. Zeitler, D. Jiang, F. Schedin, A.K. Geim, Nature **438**, 192 (2005)
154. C. Hodges, H. Smith, J.W. Wilkins, Phys. Rev. B **4**(2), 302 (1971)
155. M. Polini, R. Asgari, G. Borghi, Y. Barlas, T. Pereg-Barnea, A.H. MacDonald, Phys. Rev. B **77**(8), 081411 (2008)
156. E.H. Hwang, S. Das Sarma, Phys. Rev. B **75**(20), 205418 (2007)
157. E.H. Hwang, S.D. Sarma, Phys. Rev. B **77**(8), 081412 (2008)
158. C.H. Park, F. Giustino, C.D. Spataru, M.L. Cohen, S.G. Louie, Phys. Rev. Lett. **102**(7), 076803 (2009)
159. C.H. Park, F. Giustino, C.D. Spataru, M.L. Cohen, S.G. Louie, Nano Lett. **9**(12), 4234 (2009)
160. C.H. Park, F. Giustino, M.L. Cohen, S.G. Louie, Phys. Rev. Lett. **99**(8), 086804 (2007)
161. W.K. Tse, S. Das Sarma, Phys. Rev. Lett. **99**(23), 236802 (2007)
162. M. Calandra, F. Mauri, Phys. Rev. B **76**(20), 205411 (2007)
163. F. Rana, IEEE Trans. Nanotechnol. **7**(1), 91 (2008)
164. S.Y. Zhou, D.A. Siegel, A.V. Federov, F. El Gabaly, A.K. Schmid, A.H. Castro Neto, D.H. Lee, A. Lanzara, Nat. Mater. **7**, 259–260 (2008)
165. A. Bostwick, T. Ohta, J.L. McChesney, K.V. Emtsev, T. Seyller, K. Horn, E. Rotenberg, New J. Phys **9**, 385 (2007)
166. M. Mucha-Kruczynski, O. Tsyplyatyev, A. Grishin, E. McCann, V. Fal'ko, A. Bostwick, E. Rotenberg, Phys. Rev. B **77**, 195403 (2008)
167. A. Tzalenchuk, S. Lara-Avila, A. Kalaboukhov, S. Paolillo, M. Syvajarvi, R. Yakimova, O. Kazakova, T.J.B.M. Janssen, V. Fal'ko, S. Kubatkin, Nat. Nano. **5**(3), 186 (2010)
168. J. Jobst, D. Waldmann, F. Speck, R. Hirner, D.K. Maude, T. Seyller, H.B. Webber, Phys. Rev. B **81**, 195434 (2010)
169. T. Shen, J.J. Gu, M. Xu, Y.Q. Wu, M.L. Bolen, M.A. Capano, L.W. Engel, P.D. Ye, Appl. Phys. Lett. **95**, 172105 (2009)
170. E. Rotenberg, A. Bostwick, T. Ohta, J.L. McChesney, T. Seyller, K. Horn, Nat. Mater. **7**, 258 (2008)
171. L. Benfatto, E. Cappelluti, Phys. Rev. B **78**(11), 115434 (2008)
172. Y. Qi, S.H. Rhim, G.F. Sun, M. Weinert, L. Li, Phys. Rev. Lett. **105**(8), 085502 (2010)
173. A. Bostwick, E. Rotenberg, to be published (2011)
174. C. Riedl, C. Coletti, T. Iwasaki, A.A. Zakharov, U. Starke, Phys. Rev. Lett. **103**(24), 246804 (2009)
175. F. Speck, M. Ostler, J. Rßhrl, J. Jobst, D. Waldmann, M. Hundhausen, L. Ley, H.B. Weber, T. Seyller, in *13th International Conference on Silicon Carbide and Related Materials*, *Materials Science Forum*, vol. 645-648 (Nuremberg (Germany), 2009), *Materials Science Forum*, vol. 645-648, pp. 629–632
176. E. Shirley, L. Terminello, A. Santoni, F.J. Himpsel, Phys. Rev. B **51**(19), 13614 (1995)
177. B. Lundqvist, Phys. kondens. Materie **6**(3), 193 (1967)
178. B. Lundqvist, Phys. kondens. Materie **6**(3), 206 (1967)

179. B.I. Lundqvist, Phys. kondens. Materie **7**(2), 117 (1968)
180. P. von Allmen, Phys. Rev. B **46**(20), 13345 (1992)
181. C. Attaccalite, S. Moroni, P. Gori-Giorgi, G.B. Bachelet, Phys. Rev. Lett. **88**(25), 256601 (2002)
182. A.H.C. Neto, Physics **2**, 30 (2009)
183. J.E. Drut, T.A. Lahde, Phys. Rev. Lett. **102**(2), 026802 (2009)
184. C. Jang, S. Adam, J.H. Chen, E.D. Williams, S. Das Sarma, M.S. Fuhrer, Phys. Rev. Lett. **101**(14), 146805 (2008)
185. R.S. Markiewicz, Physica C: Superconductivity **153-155**(Part 3), 1181 (1988)
186. R.S. Markiewicz, J. Phys. Chem. Solid. **58**(8), 1179 (1997)
187. G. Gruner, *Density Waves in Solids* (Addison-Wesley, Reading, PA, 1994)
188. T.E. Weller, M. Ellerby, S.S. Saxena, R.P. Smith, N.T. Skipper, Nat. Phys. **1**, 39 (2005)
189. M. Calandra, F. Mauri, Phys. Rev. Lett. **95**(23), 237002 (2005)
190. M. Calandra, F. Mauri, physica status solidi (b) **243**(13), 3458 (2006)
191. I.I. Mazin, Phys. Rev. Lett. **95**(22), 227001 (2005)
192. J.S. Kim, L. Boeri, R.K. Kremer, F.S. Razavi, Phys. Rev. B **74**(21), 214513 (2006)
193. J.S. Kim, R.K. Kremer, L. Boeri, F.S. Razavi, Phys. Rev. Lett. **96**(21), 217002 (2006)
194. A. Sanna, G. Profeta, A. Floris, A. Marini, E.K.U. Gross, S. Massidda, Phys. Rev. B **75**(2), 020511 (2007)
195. A. Gruneis, C. Attaccalite, L. Wirtz, H. Shiozawa, R. Saito, T. Pichler, A. Rubio, Phys. Rev. B **78**(20), 205425 (2008)

Chapter 5
Epitaxial Graphene on SiC(0001)

Thomas Seyller

Abstract The growth of epitaxial graphene on silicon carbide (SiC) is considered to be a viable route to the development of graphene-based electronic devices. Consequently, much work has been done in the last few years on characterization of this material and on improving its growth and properties. This chapter is devoted to the growth and properties of epitaxial graphene on the hexagonal SiC(0001) surface. The properties of SiC are briefly summarized before the growth of graphene in ultrahigh vacuum (UHV) is described. Next, the electronic and structural properties of the so-called buffer layer are investigated before discussing the band structures of monolayer and bilayer graphene close to the K-point of the hexagonal Brillouin zone. Recent results indicate that growth of graphene in UHV is insufficient for obtaining electronic grade graphene layers. Instead, growth of graphene in Ar atmosphere has been suggested to lead to graphene synthesis on wafer scale and work on this topic is summarized. Then a brief description of transport properties of graphene on SiC(0001) is given. Finally, it will be shown how interface engineering of epitaxial graphene on SiC(0001) may be used to change the properties of the graphene layers.

5.1 Introduction

Graphene, the two-dimensional sheet of carbon atoms in honeycomb arrangement, is one of the most exciting materials currently under investigation. In graphene each carbon atom is bound to three others in a planar geometry. This geometry results from the sp^2-hybridization of the carbon valence orbitals. While the three sp^2-orbitals form strong σ-bonds with the corresponding σ- and σ^*-bands lying far away

T. Seyller (✉)
Friedrich-Alexander-Universität Erlangen-Nürnberg, Lehrstuhl für Technische Physik, Erwin-Rommel-Str. 1, 91058 Erlangen, Germany
e-mail: thomas.seyller@physik.uni-erlangen.de

H. Raza (ed.), *Graphene Nanoelectronics*, NanoScience and Technology,
DOI 10.1007/978-3-642-22984-8_5, © Springer-Verlag Berlin Heidelberg 2012

from the Fermi energy, the remaining p-orbital leads to a delocalized π-bond. The resulting bonding and antibonding π- and π*-bands touch each other only at the K-point of the hexagonal Brillouin zone, as was already calculated by Wallace [1] many years ago. The linear band structure of graphene in the vicinity of the K-point and the fact that the wave function is a two-component wave function similar to a spinor in relativistic quantum mechanics leads to many interesting properties of graphene, which are the topics of individual chapters of this book.

It is probably no understatement to say that the boom of graphene science [2,3] is to a large extent driven by the fact that exfoliation of graphene from HOPG [4] is a relatively easy and cheap method by which samples are obtained for basic research. However clearly, mechanical exfoliation will not enable a technological exploitation of graphene. Alternatively, methods to grow graphene on a substrate need to be developed before electronic applications of graphene have a chance to emerge. In principle, there are two different approaches that are currently under investigation: growth of graphene by chemical vapor deposition on metal substrates [5–9] (see Chap. 7) and epitaxial growth of graphene on the basal plane surfaces of the wide band gap semiconductor silicon carbide (SiC) [10–13]. The latter is the topic of this chapter as well as Chap. 6.

Growing graphene on SiC surfaces is – in principle – a rather simple task. At high enough temperatures, SiC decomposes into silicon and carbon. Silicon atoms sublimate from the surface due to their high vapor pressure. The carbon atoms, however, remain at the surface and form stable C–C bonds in the form of graphite. The graphitization of SiC surfaces is a long known phenomenon and was first observed by Edward G. Acheson, who invented the so-called Acheson process [14] to produce silicon carbide (then called *carborundum*). Later, Acheson [15] observed that heating of silicon carbide to high temperatures leads to the formation of graphite, which was subsequently exploited for the production of artificial graphite (*Acheson graphite*), which was used as a solid lubricant. With increasing interest in SiC for power electronics [16], first systematic studies of its surfaces were carried out. Van Bommel and coworkers [17] investigated the influence of heat treatment on the polar SiC{0001} surfaces using Auger electron spectroscopy and low-energy electron diffraction (LEED) and observed the formation of graphite on the surface. Carbon-rich surface phases were later also studied by other groups (see [18] and references therein). In 2004, the group of Walt de Heer at the Georgia Technical University proposed that proper growth conditions could allow for the production of graphene on top of SiC for electronic applications [10]. This work lead to the development of the field of *epitaxial graphene*. This chapter is devoted to the growth and the properties of epitaxial graphene on SiC surfaces, concentrating on the *silicon* terminated surface.

Since graphene lies conveniently on the surface of the SiC source and substrate material, it can be studied by surface science techniques such as photoelectron spectroscopy, electron diffraction, scanning probe microscopy, etc. In addition, much information can be gained from Raman spectroscopy. Structures such as Hall bars and van der Pauw structures can be easily constructed using standard

lithography in a top-down fashion, which allows access to important transport phenomena.

5.2 Silicon Carbide and Its Polar Surfaces

Silicon carbide comes in a variety of crystalline modifications, the so-called polytypes. Figure 5.1 shows the basic building blocks of SiC polytypes [19]. Due to the sp^3 hybridization of the silicon and carbon s and p valence orbitals, silicon and carbon atoms are bound to four neighbors in a tetrahedral arrangement [see Fig. 5.1a]. The bonds are characterized by a significant degree of ionicity due to the different electronegativities of the two elements [20, 21], which are 1.9 (Si) and 2.55 (C) on the Pauling scale, respectively. So-called bilayers consisting of edge connected Si–C tetrahedra are formed from the individual tetrahedra as shown in Fig. 5.1b.

Bulk crystals of SiC are formed by stacking bilayers on top of each other. Two different stacking arrangements, denoted cubic stacking or hexagonal stacking, are possible which are shown in Fig. 5.1c. Cubic stacking corresponds to the cubic zinc blende structure and hexagonal stacking is found in the hexagonal wurzite structure. In the Ramsdell notation [22], these structures are referred to as 3*C* structure and 2*H* structure, respectively.[1] They are shown in Fig. 5.2. These two different stacking arrangements are mixed in a periodic fashion to form more than 200 known polytypes [23]. Two of them, the hexagonal polytypes 4*H*–SiC and 6*H*–SiC are also shown in Fig. 5.2. Note that in these two polytypes the unit cells contain 4 and 6 bilayers, respectively. All the SiC polytypes are semiconductors with a large band gap, which varies from 2.39 eV for 3*C*–SiC over 3.02 for 6*H*–SiC to 3.27 eV

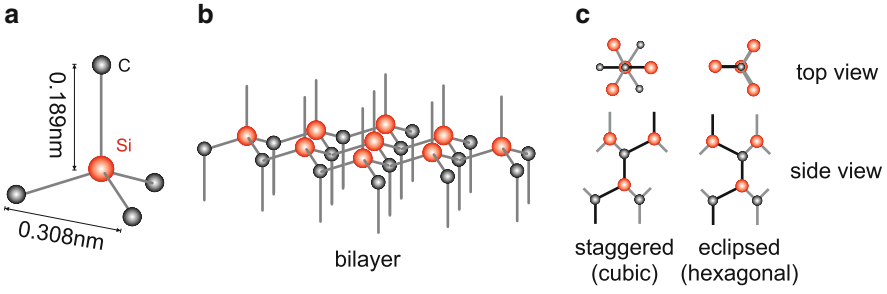

Fig. 5.1 Structural elements of SiC: (**a**) tetrahedral bonding arrangement; (**b**) bilayer; (**c**) the two different stacking arrangements

[1] In the Ramsdell notation the polytypes are characterized by the number of layers which make up the unit cell in c-axis direction and by a letter indicating the nature of the crystal lattice (*C*: cubic, *H*: hexagonal, *R*: rhombohedral).

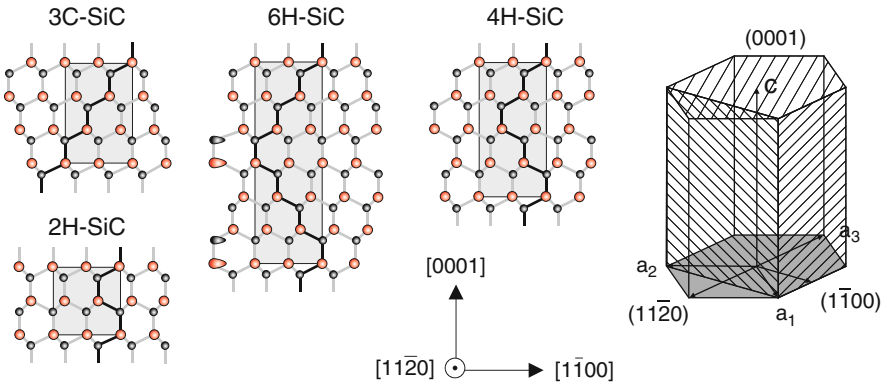

Fig. 5.2 Side view projection onto the (11$\bar{2}$0) plane of the crystal structure of four different polytypes of SiC. Also shown is the hexagonal unit cell indicating the orientation of the (0001), (11$\bar{2}$0), and the (1$\bar{1}$00) planes. The (0001) surface has only Si atoms in the topmost layer and the opposite face only C atoms. The latter is called (000$\bar{1}$) surface

for 4*H*–SiC [24]. Hence, intrinsic or compensated SiC is insulating. This is a clear advantage of SiC as a substrate for graphene: the latter can be directly patterned into devices without prior transfer to another substrate, which is required for graphene grown on metals. Another interesting approach has recently been proposed by Suemitsu et al. [25], who grew cubic silicon carbide on top of Si wafers. Thermally activated growth of graphene on the 3*C*–SiC films may enable the integration of graphene into Si technology.

Due to the importance of SiC surfaces for SiC growth and processing, they have attracted a lot of attention [18, 26–33]. As a consequence, much is known not only about the structural phases of the polar {0001} surfaces of the technologically most important polytypes 6*H*– and 4*H*–SiC, but also about 3C–SiC(111) and 3C–SiC(100) surfaces. Complete phase diagrams for both, the Si-terminated SiC(0001) surface (Si-face) and the C-terminated SiC(000$\bar{1}$) surface (C-face), are given in [18]. The structures observed on these two surface orientations are characterized by a minimization of the number of dangling bonds. Due to symmetry requirements, this can only be achieved in adatom structures of different types and periodicity. One structure, which is of particular importance for epitaxial graphene on SiC(0001), is the carbon-rich $(6\sqrt{3} \times 6\sqrt{3})R30°$ reconstruction, which will be discussed in detail further below.

5.3 Growth of Epitaxial Graphene on SiC(0001) in Ultra-High Vacuum

Many studies of graphene on hexagonal SiC(0001) surfaces have been and are still carried out on layers grown in ultra-high vacuum (UHV). The UHV growth procedure follows the well-known phase diagram [18] as shown schematically in

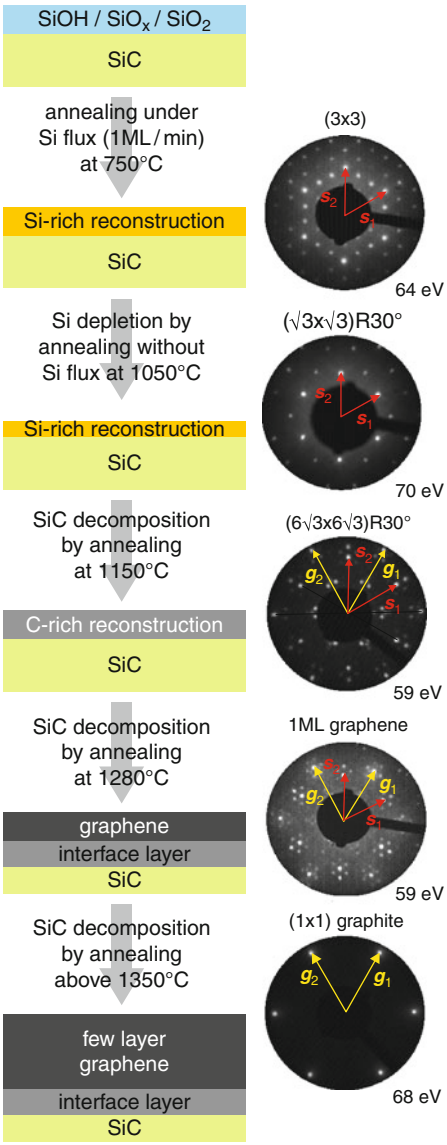

Fig. 5.3 Schematic representation of the preparation procedure for graphene and few-layer graphene on the Si-face. Representative LEED patterns [34] are also shown. The reciprocal lattice vectors of the SiC ($\boldsymbol{s}_1, \boldsymbol{s}_2$) and graphene ($\boldsymbol{g}_1, \boldsymbol{g}_2$) lattices are indicated

Fig. 5.3. After introduction into the UHV chamber, the SiC sample is normally contaminated by oxygen and hydrocarbons from the air. After degassing, the sample is annealed in situ at a temperatures of around 850°C under simultaneous deposition of Si from an evaporator. Typical deposition rates used are of the order of one monolayer per minute (1 ML/min). This treatment results in the formation of an Si-rich (3 × 3) reconstruction [18]. This reconstruction is a rather complicated structure, which consists of an Si adlayer, an Si tetramer and an Si adatom on top

of the tetramer [35]. Excess Si is then gradually removed by subsequent annealing steps. As an intermediate structure, the $(\sqrt{3} \times \sqrt{3})R30°$ reconstruction with one Si adatom per unit cell sitting in a so-called T_4 position [36] is observed after annealing to 1,050°C. Further annealing at 1,150°C leads to desorption of these adatoms and to decomposition of SiC into mainly Si and C. While Si atoms desorb from the surface, C atoms form stable bonds among each other. A C-rich reconstruction with $(6\sqrt{3} \times 6\sqrt{3})R30°$ periodicity is observed. Note that the diffraction pattern shows already spots on a grid belonging to the lattice of graphene. If the temperature is raised to about 1,280°C more Si is lost from the surface and a graphene layer is building up on the surface. The LEED pattern observed at this stage is very similar to the one of the $(6\sqrt{3}\times6\sqrt{3})R30°$ reconstruction. Finally, increasing the temperature even more leads to the formation of additional graphene layers, which form a well-ordered graphite-like stack as is evident from the LEED pattern. Note that the basal plane lattice vectors of the SiC substrate and the growing graphene/graphite stack are rotated against each other by 30 degree.

Another possible pathway for the preparation of graphene on SiC{0001} starts with ex-situ H-etched surfaces. These are usually covered with the silicate adlayer reconstruction [37], which is an ordered monolayer of silicon oxide. Heating such samples in UHV to temperatures close to 1,000°C induces desorption of oxygen and formation of the Si-rich $(\sqrt{3} \times \sqrt{3})R30°$ reconstruction. Upon further annealing, this surface transforms into carbon-rich structures as outlined above [18]. Today, state-of-the art graphene growth is no longer performed in UHV. This will be the topic of Sect. 5.6.

5.4 The $(6\sqrt{3} \times 6\sqrt{3})R30°$ Reconstruction

The carbon-rich $(6\sqrt{3} \times 6\sqrt{3})R30°$ reconstruction deserves special attention. Already van Bommel et al. [17] have realized that the diffraction pattern contains spots at positions corresponding to a graphite lattice. They concluded that the diffraction pattern was due to a graphite layer bound by weak van der Waals interaction to the unreconstructed SiC(1×1) surface. Other groups suggested a similar scenario with a $(\sqrt{3} \times \sqrt{3})R30°$ reconstructed surface below the graphite layer [38–41]. The additional, fractional order spots were interpreted in terms of a moire pattern. The intensity of the fractional order spots is very high, suggesting that there is a considerable buckling in the surface, which is supported by STM images [42].

Further important information comes from ARPES measurements. Figure 5.4a, b shows the valence band dispersion measured for the $(6\sqrt{3} \times 6\sqrt{3})R30°$ reconstruction and a sample with one monolayer graphene along the $\overline{\Gamma K M}$ and $\overline{\Gamma M \Gamma}$ directions of the graphene Brillouin zone, respectively. A striking similarity between the two measurements is that the $(6\sqrt{3} \times 6\sqrt{3})R30°$ reconstruction exhibits clear graphene-like σ-bands which are well developed in band width and periodicity in momentum space. This indicates that the atomic arrangement within the

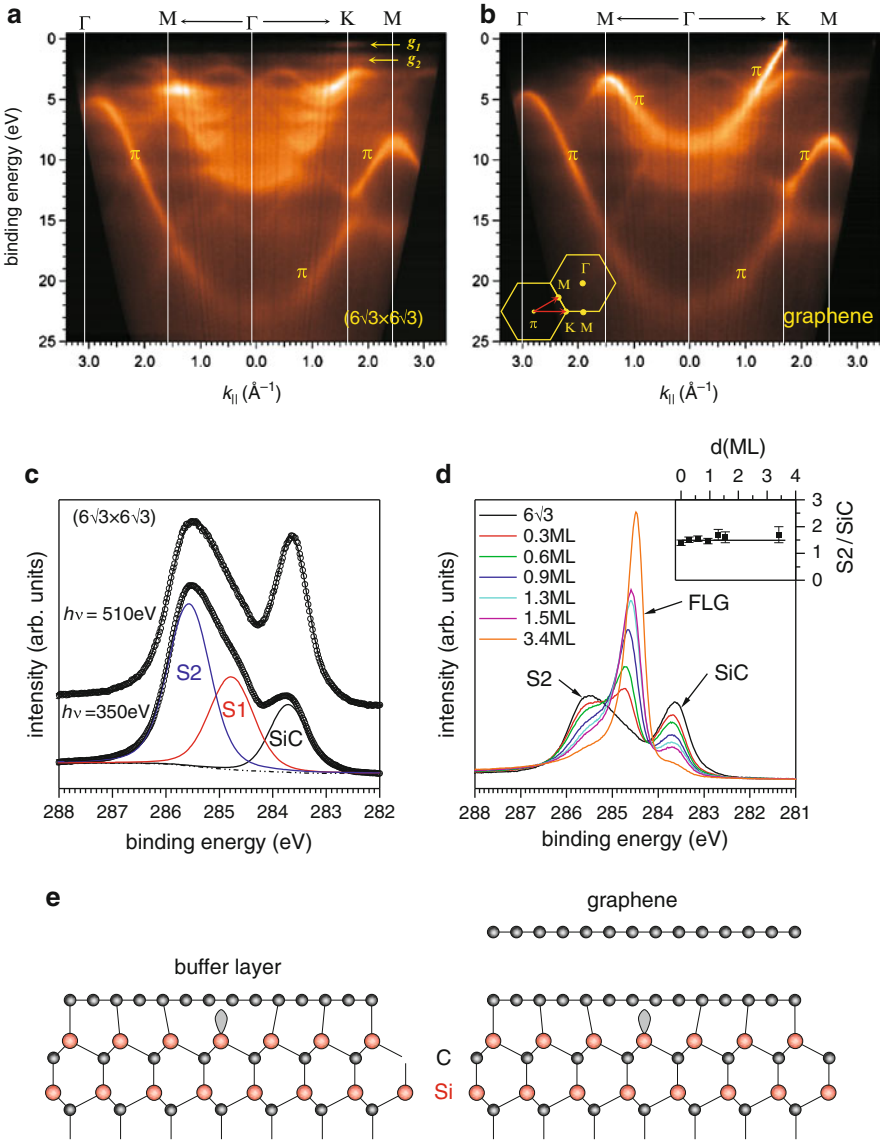

Fig. 5.4 (**a**) and (**b**) Photoelectron intensity map vs. binding energy and parallel electron momentum of SiC(0001)-$(6\sqrt{3} \times 6\sqrt{3})R30°$ and a sample with one monolayer graphene, respectively. The sketch in (**b**) shows the direction of $k_{||}$ within the hexagonal Brillouin zone of graphene. (**c**) C1s core level spectra of the $(6\sqrt{3} \times 6\sqrt{3})R30°$ reconstruction measured with two different photon energies. Also shown is a curve fit using three Voigt profiles. (**d**) C1s core level spectra of the $(6\sqrt{3} \times 6\sqrt{3})R30°$ reconstruction and after growth of graphene. The inset shows the ratio between the intensity of component S2 and the SiC bulk component obtained by curve fitting. Adapted from [34]. (**e**) Model of the buffer layer, i.e. the $(6\sqrt{3} \times 6\sqrt{3})R30°$ reconstruction, and of a monolayer of graphene on top of the buffer layer

$(6\sqrt{3} \times 6\sqrt{3})R30°$-reconstructed layer is topologically identical to that of graphene [34, 43], i.e. that it contains six-membered rings only and no five- or seven-membered rings [44]. Compared to the σ-bands of neutral graphite, the σ-bands of the $(6\sqrt{3} \times 6\sqrt{3})R30°$ reconstruction are shifted by 1.0 ± 0.1 eV toward higher binding energies [34, 43]. For monolayer graphene [Fig. 5.4b], this shift is reduced to 0.4 eV with respect to graphite. The energy shift is due to a partial filling of the π^*-bands by a charge transfer from the substrate, which leads to an effective n-type doping of the graphene layers [34, 43, 45–48].

Interestingly, while there is a well-developed σ-band, the π-band is less developed. Instead, an accumulation of intensity centered around Γ is seen, which has an envelope that is strongly reminiscent of the dispersion of the π-band. This was attributed to band folding caused by the potential of the large unit cell, which affects the delocalized π-states more than the σ-states [34, 43]. The bottom of this band at Γ is located 3.2 eV below the bottom of the π-band of graphene, which points toward a covalent coupling of p_z-orbitals to the substrate [34]. A similar behavior was also observed for graphene on Ni(111) [49–51], where it strongly interacts with the substrate in a commensurate (2×2) structure. The $(6\sqrt{3} \times 6\sqrt{3})R30°$ reconstruction has no states at the Fermi level, i.e. it is insulating with two localized states g_1 and g_2 at binding energies of 0.5 eV and 1.6 eV, respectively. The insulating nature of the $(6\sqrt{3} \times 6\sqrt{3})R30°$ surface is in favor of the conclusion that a strong interaction of at least part of the carbon p_z-orbitals with the substrate exists [34, 43].

This picture is supported by core level spectroscopy. Figure 5.4c shows C1s core level spectra of the $(6\sqrt{3} \times 6\sqrt{3})R30°$ reconstruction. The spectra contain a bulk component (SiC) and two surface components (S1/S2) with an intensity ratio of 1:2. Changing the photon energy and thus the surface sensitivity leaves the intensity ratio almost unchanged [34, 43], which is evidence that the C atoms leading to the two components are in the same plane. From the ARPES spectra, it was concluded that the density of C atoms in the surface layer is the same as in graphite. Using a layer attenuation model, it was estimated that S1 and S2 result from a layer of sp^2-bonded carbon with a thickness of 2.4 ± 0.3 Å which is consistent with a monolayer coverage [34, 43]. It was proposed that one third of the C atoms within this layer is bound covalently to the underlying SiC substrate leading to component S1. The other two thirds visible in the spectrum as component S2 are sp^2-hybridized and connected to C-atoms within the reconstruction layer only [34, 43]. The area density of C-atoms in graphene (3.82×10^{15} cm^{-2}) is close to three times that of Si atoms on the SiC(0001) surface (1.22×10^{15} cm^{-2}). With these numbers, the S1:S2 ratio of 1:2 follows naturally from the above-described bonding scenario.

The conclusion one can draw from the experimental data discussed above is that the $(6\sqrt{3} \times 6\sqrt{3})R30°$ reconstruction is comprised of a graphene layer, which is covalently bound to the substrate. While the σ-bands are fully developed and only shifted in energy due to charge transfer, the π-band are distorted due to covalent bonding to the substrate in such a way that this layer is nonmetallic. Hence, that layer is frequently called "'0th' layer" or "dead layer." Due to the lattice mismatch, the presence of a considerable number of dangling bonds has to be considered.

A schematic ball-and-stick model of the structure is shown in Fig. 5.4e. Several theoretical models [52–56] have been produced, which qualitatively support the above drawn picture of this structure. In particular, STM results are reproduced quite well by calculations [52, 56].

It must be mentioned that other models have been proposed for the buffer layer. A combined STM/DFT [57] study has extended the above model by including defects in the form of five-membered and seven-membered rings, which are arranged in a periodic fashion in order to accommodate the lattice mismatch. Rutter et al. [58] proposed a model with an Si tetramer and an Si adatom in the unit cell located at the interface, which could explain some of the features observed in STM [58], but the presence of these additional Si atoms has not been confirmed by core level spectroscopy [42]. Another model is based on X-ray reflectivity measurements carried out and analyzed by Hass et al. [59]. They concluded that the surface reconstruction is a strongly relaxed SiC bilayer with a dense carbon layer above it. The latter was proposed to contain significant amounts of Si atoms. The apparent discrepancy between photoelectron spectroscopy results and the X-ray reflectivity study is still an open question.

Figure 5.4d depicts C1s spectra of the $(6\sqrt{3} \times 6\sqrt{3})R30°$ reconstruction and of graphene layers grown by annealing this sample stepwise to higher temperatures [34]. Due to the increasing thickness of the stack of graphene layers and the resulting damping of photoelectrons from deeper lying layers, the bulk signal of the SiC substrate is decreasing. A shoulder due to the component S2 is detectable in all C 1s spectra and its intensity decreases as well. Inset of Fig. 5.4d shows that the intensity ratio between the component S2 and the bulk component remains constant during the growth of a thicker stack of graphene layers. This is a clear indication that the $(6\sqrt{3} \times 6\sqrt{3})R30°$ reconstruction remains at the interface between SiC(0001) and FLG [34, 43] as depicted schematically in Fig. 5.4. This is further supported by STM studies [60–63] in which it was observed that at high tunneling bias the graphene layer becomes transparent so that the $(6\sqrt{3} \times 6\sqrt{3})R30°$ reconstructed is imaged. Because of this observation, the $(6\sqrt{3} \times 6\sqrt{3})R30°$ reconstruction is also called "buffer layer" or "interface layer." It was also proposed that the strong bonds between the '0th' layer and the SiC(0001) surface are responsible for the observed alignment between graphene and the SiC lattice on the Si-face [34]. A similar buffer layer is not present at the SiC$((000\bar{1}))$ surface [34]. Here, only a weak bonding between the substrate surface and graphene is observed, which was also made responsible for the observed rotational stacking faults.

5.5 Electronic Structure of Monolayer and Bilayer Graphene at the K-point

The electronic structure near the K-point is most important for the electronic transport properties of graphene. Hence, several groups have investigated the band structure in that region using ARPES [45–48, 64–70]. Figure 5.5a shows ARPES

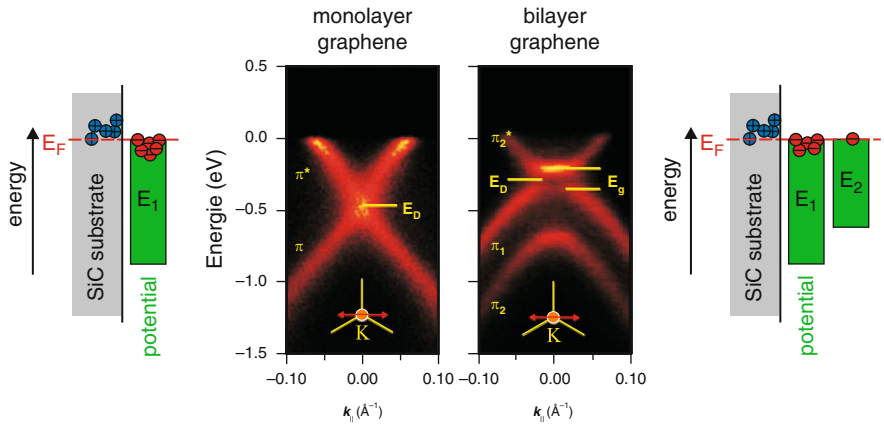

Fig. 5.5 Photoelectron intensity map vs. binding energy and parallel electron momentum of (**a**) monolayer graphene and (**b**) bilayer graphene grown on SiC(0001). The wave vector was varied perpendicular to the $\overline{\Gamma KM}$ direction. The sketch on the *left-hand side* shows how charge is transferred from the substrate surface to the graphene layer. The same is shown for bilayer graphene on the *right-band side*. In this case, the charge is unevenly distributed between the two layers

spectra of monolayer graphene on SiC(0001). The measurements were taken by varying the wave vector perpendicular to the $\overline{\Gamma KM}$ direction. In this direction, both bands are visible and the Dirac crossing can be observed. In the perpendicular direction, only one band is visible due to an interference effect of the emission of the two sublattices of graphene [48, 71, 72]. For monolayer graphene, $E_D - E_F = 450\,\text{meV}$ due to a transfer of charge from the substrate into the graphene layer as indicated in the right-hand sketch in Fig. 5.5. The effect of the charge transfer, which shifts E_D below E_F so that the bottom of the π^*-band becomes visible in ARES, is equivalent to an on-site Coulomb potential E_1. The latter enters the well-known Hamiltonian operator of graphene as diagonal element [48, 73, 74]:

$$H = \begin{pmatrix} E_1 & v_F(k_x - ik_y) \\ v_F(k_x + ik_y) & E_1. \end{pmatrix} \tag{5.1}$$

Here, v_F is the Fermi velocity of graphene. The observed position of E_D relative to E_F corresponds to an excess charge of $n = 1.1 \times 10^{13}\text{cm}^{-2}$. Kopylov et al. [75] have analyzed a theoretical model for the charge transfer assuming either donation of charge from bulk donors or from states in the SiC surface. For both models, they determined the maximum electron density n_{max} induced in monolayer and bilayer graphene. n_{max} is determined by the work function difference and the density of donor states in the bulk or at the surface. Considering the above discussion about the nature of the buffer layer, it seems reasonable to assume that a high density of amphoteric dangling bonds may be present at the interface, which could be a source of the observed excess charge in epitaxial graphene on SiC(0001). That

excess charge is also responsible for the observation that the C1s binding energy of graphene is higher than that of graphite [34,43]. Note that the dispersion deviates from the exact linear behavior of the Hamiltonian in (5.1) due to many body effects [45, 48, 64, 65], which renormalize the measured spectral function as discussed in detail in Chap. 3 of the present book.

The spectrum of the bilayer depicted in Fig. 5.5b exhibits two bonding π-bands. Note that the number of π-bands is increased by one for every layer added to the stack so that counting the number of π-bands seen in ARPES is an efficient tool for determining the number of layers [46]. One of the antibonding π^*-bands is visible as well in Fig. 5.5b because the charge transfer from the substrate surface shifts it below E_F. The second antibonding band is still above E_F and thus not visible.

Closer inspection of the spectra obtained for pristine bilayer graphene on SiC(0001) shows that there is a band gap [46–48], which is caused by the uneven distribution of the charge between the two layers as shown in the sketch on the right-hand side of Fig. 5.5b. In fact, about 95% of the charge sits in the layer closer to the substrate [46]. As a result of the unbalanced charge distribution, the on-site coulomb potential varies between the two layers as shown in Fig. 5.5b. Introducing on-site Coulomb potentials E_1 and E_2 for the two layers into the bilayer Hamiltonian H_{2ML} yields [47, 74, 76–79]

$$H_{2ML} = \begin{pmatrix} E_1 & v_F(k_x - ik_y) & 0 & 0 \\ v_F(k_x + ik_y) & E_1 & \gamma_1 & 0 \\ 0 & \gamma_1 & E_2 & v_F(k_x - ik_y) \\ 0 & 0 & v_F(k_x + ik_y) & E_2 \end{pmatrix}, \tag{5.2}$$

where γ_1 is the hopping term between the B-atoms of the first layer and the A-atoms of the second layer. This equation implies that a band gap of the size $\Delta E = |E_1 - E_2|$ is opened as soon as the two on-site potentials are different. Hence, a tunable band gap can be created by applying an electrostatic field across the bilayer system, which may be used as a switch [47, 80–83]. The first observation of this phenomenon was made, however, using ARPES. The result of the experiment is shown in Fig. 5.6. Ohta et al. [47] doped bilayer graphene on SiC(0001) using potassium. Alkali metal doping is an ancient technique used by surface scientist. Surprisingly enough, that technique still produces new and interesting results as one can see from Chap. 4. Like the electrons from the substrate, which reside in the bottom layer, the electrons donated from the potassium atoms like to sit in the top layer. Hence, the potential E_2 becomes more and more similar to E_1 reducing the band gap. Eventually, $E_2 = E_1$ and the band gap become zero. Finally, more doping of the top layer opens the band gap again because the charge in the top layer is larger than the one in the bottom layer.

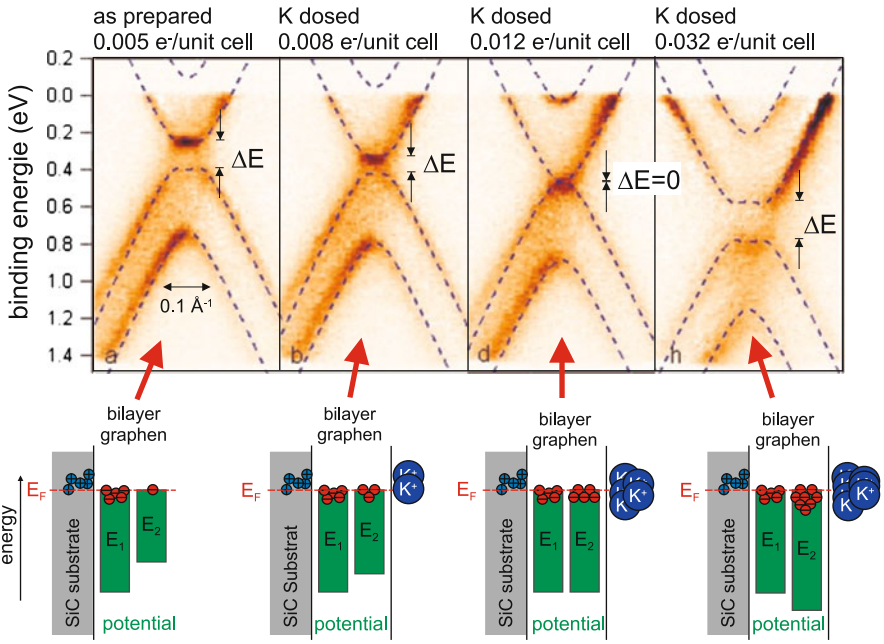

Fig. 5.6 Closing and opening of the band gap in bilayer graphene induced by potassium adsorption [47] on top of the bilayer stack. The *left panel* shows the as-prepared bilayer on SiC(0001). Charge transfer into the bottom layer gives rise to different on-site Coulomb potentials $E_1 < E_2$, which result in a band gap. Doping of the top layer by potassium adsorption on the surface of the bilayer stack reduces the difference between the on-site potentials. If $E_1 = E_2$, the gap is closed ($\Delta E = 0$). Further K dosing increases the potential difference again ($E_1 > E_2$), which reopens the gap. The increasing shift of E_D below E_F is due to the increasing occupation of the π*-bands. Adapted from [47]

5.6 State-of-the Art Graphene Growth in Argon Atmosphere

The growth of graphene on SiC in ultrahigh vacuum has led to very interesting results concerning the basic physics of graphene. Aiming at the development of graphene electronics, one must clarify whether the properties of the layers are sufficiently good for them to be used in devices. Since transport in graphene will suffer from defects and structural imperfections, it is a good idea to first look at the structural properties in more detail. Unfortunately, most surface science methods are not well suited for this task. Electron spectroscopy averages over too large an area and STM is limited mostly to very small dimensions. It turns out that one surface science method is excellently suited to study graphene. This is low-energy electron microscopy (LEEM) and its related techniques [84, 85].

The pioneering LEEM study of epitaxial graphene was carried out by Hibino et al. [86] on graphene grown in UHV. He observed that different areas of the

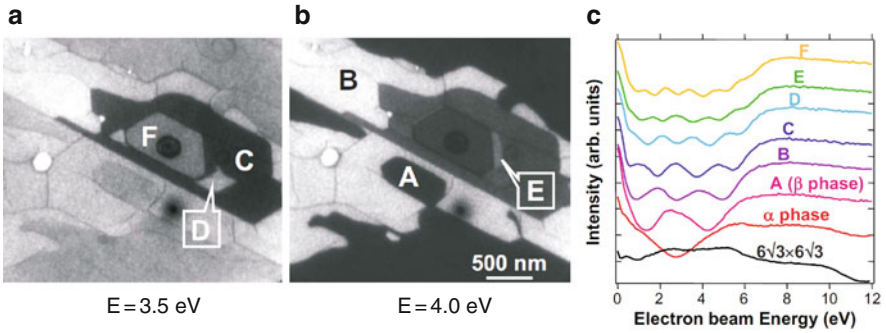

Fig. 5.7 LEEM images of graphene layers grown on SiC(0001) recorded at electron energies of (**a**) 3.5 eV and (**b**) 4.0 eV. The image contrast is caused by a thickness-dependent reflectivity. (**c**) Reflectivity as a function of electron energy for the regions marked in (**a**) and (**b**). The analysis led to the conclusion that the number of minima in the reflectivity spectrum corresponds to the number of graphene layers: α: 1 monolayer; A: 2 monolayers, B: 3 monolayers, etc. Reprinted with permission from [86]. Copyright (2008) by the American Physical Society

sample exhibited different brightness in the bright field[2] LEEM image, i.e. that these areas had a different reflectivity. As an example, two LEEM images are shown in Fig. 5.7a, b. Furthermore, electron reflectivity of these areas displays characteristic oscillations as a function of electron energy as shown in Fig. 5.7c. This behavior is explained by the quantized electronic structure [86] of few-layer graphene films with varying thickness. Resonances with these states allows the impinging electrons to flow into the sample resulting in dips in the reflectivity. The number of dips is a direct measure of the number of layers. Note that the buffer layer has a broad hump in this energy region rather than a dip. Hibino's work has formed the basis of the microscopic thickness determination of epitaxial graphene. Ohta et al. [87] have used LEEM to determine the ratio of the surface area covered by buffer layer, monolayer, and bilayer graphene and correlated the result with ARPES measurements. While ARPES gives the right ratio between monolayer and bilayer, it is basically blind for the buffer layer area. Raman spectroscopy is also capable of determining the number of layers of graphene and few-layer graphene [88–93], but care has to be exercised because the position of Raman peaks is influenced by both strain and charge. In addition, Raman mapping is slower and the spatial resolution is at best of the order of 1/3 of a μm, whereas LEEM has a spatial resolution below 10 nm.

LEEM studies [12, 86, 87] and X-ray diffraction [94] have demonstrated that the thickness distribution on UHV grown samples is rather broad. The films contain many domains of different thicknesses with lateral dimensions of 30–200 nm. The surfaces also show considerable pitting, which increases the number of step edges. This is displayed in Fig. 5.8. Apparently, the SiC surface becomes rough

[2]The bright field mode of LEEM generates an image from the specularly reflected electrons.

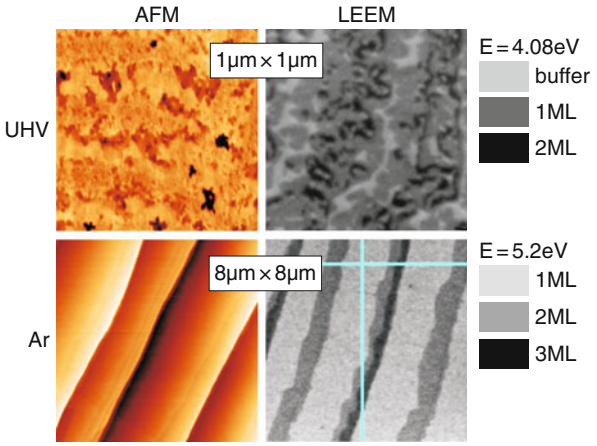

Fig. 5.8 Comparison of AFM (*left*) and LEEM (*right*) images of graphene layers grown on SiC(0001) in UHV (*top*) and Ar atmosphere (*bottom*). Adapted from [12]

during the process of graphene growth. Hannon and Tromp [95] have studied the pitting of SiC(0001) during the formation of the $(6\sqrt{3} \times 6\sqrt{3})R30°$ structure using LEEM. They observed that the pits form because domains of the $(6\sqrt{3} \times 6\sqrt{3})R30°$ reconstruction pin decomposing surface steps and that graphene nucleates in the pits due to the large step density.

The solution to the problem is an increase in the formation temperature of the graphene film. This can be accomplished by carrying out the growth process in an atmosphere of argon [12, 96]. The best results have so far been reported for growth in 1 bar or Ar at $T > 1{,}650°C$. Figure 5.8 shows AFM and LEEM images of graphene grown in such a way [12]. The surface consists now of bunched macro terraces with a width of 2–3 μm and a length of up to 100 μm [12, 96], which are homogeneously covered by monolayer graphene. Only in the vicinity of step edges, which are caused by the unintentional miscut of the SiC(0001) substrate, can one identify the nucleation of additional layers.

But why is the presence of a dense argon atmosphere beneficial for the morphology of the growing graphene film? The answer to this is the significantly higher growth temperature required in Ar (1,550°C at $p_{Ar} = 900$ mbar) compared to UHV (1,280°C). Graphene formation results from SiC decomposition and Si evaporation from the substrate. Si evaporation is, however, slowed down in Ar because the latter acts as a diffusion barrier. In this way an effective Si vapor pressure is build up over the surface, which is not present in UHV. That partial pressure is pushing the chemical equilibrium back to the SiC side. In order to get the graphene growth going, one has to increase the temperature. The higher temperature, on the other hand, enhances diffusion of surface species. Ultimately, this leads to the dramatically improved surface morphology, which appears to be closer to equilibrium. The macro step structure is responsible for the tighter thickness control because nucleation of new graphene layers occurs only at step edges. This suggests that the thickness variations can be further improved by using substrates with a more precise surface orientation. This was verified recently by

the Swedish group [97]. A similar improvement of the graphene film morphology can be obtained by balancing the evaporating Si with an external flux of Si as was reported by Tromp and Hannon [98]. They were able to shift the temperature for graphene growth over several hundred degrees through the addition of disilane into the UHV system.

Ohta et al. [99] have investigated how graphene grows in UHV from samples covered by the buffer layer prepared by Ar-assisted surface graphitization. They showed that the growth morphologies result from cooperative processes of Si sublimation and C diffusion. The growth of high-quality, large-area graphene in a step flow growth mode was observed to arise from etching preexisting triple bilayer SiC steps. Near bilayer steps in the SiC substrate no step flow growth was observed due to instabilities caused by carbon diffusion. Instead, more complex morphologies were observed. They concluded that growing good graphene requires that the buffer layer covered surface has a minimal number of single bilayer SiC steps.

Graphene layers grown in Ar atmosphere were also characterized by XPS, ARPES, and LEED. It was shown that Ar-grown graphene have the same excess carrier concentration as layers grown in UHV. The buffer layer at the interface to the SiC(0001) substrate and the crystallographic relation to the substrate are also independent of the growth environment [12]. Raman spectroscopy, on the other hand, shows a significant reduction of the D peak [12] signaling a reduced density of short range defects. This is probably the reason for the higher carrier mobility observed in Ar grown graphene compared to UHV grown material (see Sect. 5.7). The epitaxial graphene films are under a slight compressive strain [12], which builds up due to the different thermal expansion coefficients of graphene and SiC. Since SiC shrinks more during cooling down from the growth temperature, graphene is compressed [91, 92].

5.7 Transport Properties of Graphene on SiC(0001)

Early measurements of the carrier mobility of graphene on SiC(0001) were presented by Berger et al. [10], who reported a value of around 1,200 cm^2/Vs for a stack of three layers measured at low temperature. Emtsev et al. characterized their Ar grown graphene layers using Hall effect measurements. They observed an unambiguous improvement compared to UHV grown material [12]. However, a clear and strong temperature dependence was also observed so that μ dropped from around 1,850–2,000 cm^2/Vs at 27 K to around 900 cm^2/Vs at 300 K [12, 100]. The reason for this temperature dependence is not very well understood so far. Note that the reported mobility values for epitaxial graphene on SiC(0001) are much lower than those of exfoliated graphene on a substrate, where mobilities of a 10,000–40,000 cm^2/Vs are typically observed [101, 102]. However, these values are usually measured at low carrier concentration close to the Dirac point. In pristine epitaxial graphene on SiC(0001), the carrier concentration is usually close to 1×10^{13} cm^{-2}.

Weingart et al. [103] reported a mobility of 3,130 cm^2/Vs at 1.4 K and 1,640 cm^2/Vs at 300 K for a sample from the same source as that of [12] but with a carrier concentration of 2.6×10^{12} cm^{-2}. In contrast to [12], Weingart et al. [103] did not remove the photo resist after lithography, which is assumed to lead to the observed lowering of the carrier concentration. In a further study, they investigated inertial-ballistic transport in nano-scale cross junctions fabricated from epitaxial graphene on SiC(0001) [104]. Ballistic transport was observed by a negative bend resistance measured in a nonlocal, four-terminal configuration at 4.2 K. Above 80 K, the ballistic transport vanished. The inelastic mean free path determined in this way, fits well to estimates based on carrier mobility measurements using Hall effect. Tedesco et al. [105] have measured the carrier mobility in graphene on SiC(0001) and SiC($(000\bar{1})$) prepared in vacuum. Surprisingly, some samples had excess electrons and some had excess holes. In addition, the concentration of the charge carries varied over a wide range from some 10^{11} to a few 10^{14} cm^{-2}. Although the uncontrolled variation of the carrier concentration is not understood, they observed a clear dependence of the carrier mobility on the carrier density.

Other possibilities to change the carrier concentration are the formation of a top gate by depositing a suitable gate dielectric and through transfer doping by adsorbates. While the former requires rather complicated processing, the latter method can be readily applied to graphene. It has been shown that deposition of 2,3,5,6-tetrafluoro-7,7,8,8-tetracyanoquinodimethane (F4-TCNQ) on top of epitaxial graphene leads to a reduction of the electron concentration [106, 107]. By applying this technique to Hall bars made from epitaxial graphene on SiC(0001), Jobst et al. [100] tuned the carrier concentration to 5×10^{10} cm^{-2} and observed a carrier mobility of 29,000 cm^2/Vs at 27 K. Letting the sample heat up to room temperature reduced again the carrier mobility to around 2,500 cm^2/Vs, while at the same time increasing the concentration to about 5×10^{11} cm^{-2} due to thermal excitation of carriers near E_F. This result suggests that the carrier mobility in epitaxial graphene on SiC(0001) at low temperature can be of the same order of magnitude as that of exfoliated graphene on a SiO_2 substrate. However, apparently the presence of the SiC substrate leads to a strong temperature dependence of the mobility with hitherto unclear origin.

The half-integer quantum Hall effect is the hallmark of graphene and therefore its observation in epitaxial graphene has been very important. Early work by Berger et al. [10] on graphitized SiC(0001) indicated nonlinearities in the Hall resistance R_{xy} as a function of magnetic field H, which coincided with oscillations in the magneto-resistance and which were proposed to be related to the quantum Hall effect. Recently, several studies have reported the observation of the half-integer QHE in epitaxial graphene on SiC(0001) [100, 109, 110], which is typical for graphene [4, 102]. In particular, Tzalenchuk et al. have measured the QHE with very high precision. Their measurements in a large-area epitaxial graphene sample at temperature of 300 mK showed quantum Hall resistance quantization accurate to a few parts in a billion. The work [109] points out the possibility to use epitaxial graphene for quantum metrology, possibly even improve it.

Field effect transistors (FETs) with a top gate have been fabricated by several groups. Kedzierki et al. [111] compared FETs on the Si-face with those prepared on the C-face. In both cases, the number of layers was definitively larger than one. On the former, they observed field effect mobilities of 600–1,200 cm^2/Vs and on the latter up to 5,000 cm^2/Vs. Si-face devices had a higher on/off current ratio than C-face devices probably due to a tighter thickness control. Moon and coworkers [112] demonstrated graphene FETs made from epitaxial graphene on Si-face SiC on a wafer scale using alumina as a gate dielectric. The graphene layer had a mobility of 1,500 cm^2/Vs at a carrier density of 1×10^{13} cm^{-2}. The field effect mobility, however, was much lower (200 cm^2/Vs) due to traps in the gate dielectric. Furthermore, they demonstrated RF device performance and measured a current-gain cutoff frequency (f_T) of 4.4 GHz. Lin et al. fabricated top-gated FETs on 2-inch SiC wafers [108] as shown in Fig. 5.9 with different gate lengths and characterized their electrical parameters. In particular, they determined the cutoff frequency and reported an f_T of 100 GHz for a 240-nm device. FETs produced using waver-scale

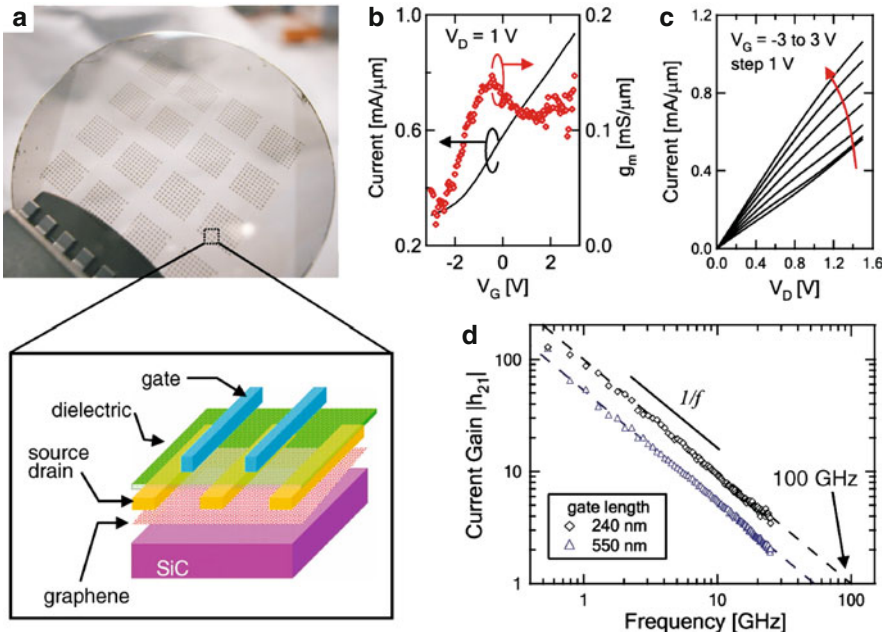

Fig. 5.9 Epitaxial graphene field effect transistors. (**a**) Image of the 2-inch SiC wafer with top-gated epitaxial graphene transistors. (**b**) Drain current I_D and device transconductance g_m of a graphene FET (gate length $L_G = 240$ nm) as a function of gate voltage at drain bias of 1 V with the source electrode grounded. (**c**) Drain current as a function of V_D of a graphene FET ($L_G = 240$ nm) for various gate voltages. (**d**) Small-signal current gain $|h_{21}|$ as a function of frequency f for two FETs with different gate lengths at $V_D = 2.5$ V. The cutoff frequencies were 53 GhZ and 100 GHz for the 550-nm and 240-nm devices, respectively. From [108]. Reprinted with permission of the AAAS

epitaxial graphene synthesis clearly have a high potential for future use in electronic applications.

5.8 Engineering the Interface Between Graphene and SiC(0001) by Hydrogen Intercalation

Recently, there has been some effort to modify the interface between SiC(0001) and epitaxial graphene. There are several reasons to do so. First, the graphene layers on SiC(0001) are typically *n*-type doped due to charge transfer from the substrate surface. Controlling the amount of excess charge would be beneficial for the development of devices such as high frequency transistors. Second, unlike in free-standing graphene [113], there is a strong temperature dependence of the carrier mobility in epitaxial graphene on SiC(0001) as discussed in Sect. 5.7. This strong T-dependence needs to be understood and – if possible – eliminated. Several groups have investigated how to influence the interface between SiC and graphene by intercalation of other elements [114–121]. Here, we shall concentrate on hydrogen intercalation.

Hydrogenation of hexagonal SiC surfaces is a well-established technique [122–130]. The saturation of surface dangling bonds is achieved via annealing of the SiC sample in an atmosphere ($p = 1$ bar) of ultra-pure molecular hydrogen at temperatures above 1,000°C. The so-prepared surfaces are unreconstructed and chemically and electronically passivated. Riedl et al. [42, 116] have subjected SiC samples covered by either the buffer layer or a monolayer graphene on the buffer layer to a similar procedure. Virojanadara et al. [117, 118] have used atomic hydrogen to which they exposed their samples in an UHV environment. Both groups used surface science methods to characterize their samples. Speck et al. [119] and Röhrl et al. [120] also used molecular hydrogen for their studies. In addition to photoelectron spectroscopy, they characterized their samples using Hall effect measurements, Raman spectroscopy, and infrared absorption spectroscopy. However, instead of a saturation of dangling bonds in the buffer layer, a complete transformation of the buffer layer in a quasi-free-standing graphene layer (QFMLG) is observed as schematically shown in Fig. 5.10. Likewise, a sample consisting of a monolayer graphene on the buffer layer (MLG) is transformed into quasi-free-standing bilayer graphene (QFBLG).

Figure 5.11 shows results of several spectroscopic techniques applied to the different systems. The C 1s core level spectra in Fig. 5.11a [119] show the conversion of the buffer layer related peak, which consists of two components S1 and S2 as discussed in Sect. 5.4 into an asymmetric peak due to the resulting graphene layer [116,119]. Note that the relative intensities of the buffer layer-related signals and the bulk signal is different to that shown in Fig. 5.4c due to the different photon energy used in the experiments. Similarly, the C 1s spectrum of MLG shows a graphene-related signal and a shoulder caused by the underlying buffer

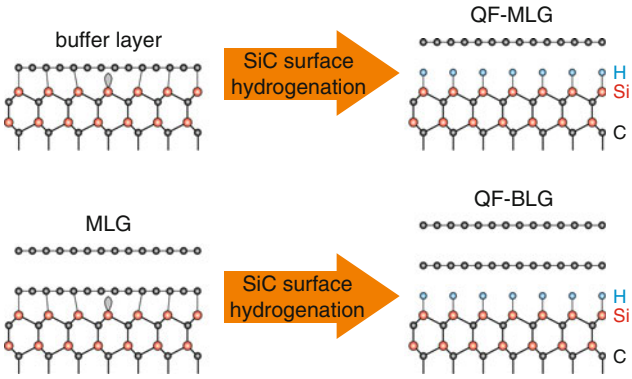

Fig. 5.10 Schematic representation of the conversion (*top*) of the buffer layer into quasi-free-standing monolayer graphene (QFMLG) and (*bottom*) of monolayer graphene (MLG) on the buffer layer into quasi-free-standing bilayer graphene (QFBLG)

layer. Upon annealing in hydrogen that shoulder is removed and an asymmetric line originating from QF-BLG is observed [116, 117, 119]. Comparison of the C 1s binding energies with that of bulk graphite for which the C1s core level is observed at 284.45 eV shows that while MLG is *n*-type doped, the QFMLG and QFBLG layers are p-type doped. The SiC bulk peak is shifted by the surface hydrogenation process due to a change in surface band bending. The magnitude of the surface band bending and the mechanism leading to the observed doping are subject to ongoing investigations. Figure 5.11b depicts ARPES measurements of QFMLG and QFBLG [119]. No buffer layer related states (c.f. Fig. 5.4a, b) are seen in the data. Instead, the measurements clearly reveal the electronic structure of monolayer and bilayer graphene. An ARPES investigation of potassium-doped QFMLG [131] revealed the presence of new quasiparticles, so-called plasmarons, as discussed in Chap. 4.

While photoelectron spectroscopy readily proves the transformation of the buffer layer into quasi-free-standing graphene, it cannot unambiguously ascertain that the surface is saturated by hydrogen. This can be done, however, by Fourier-transform infrared absorption spectroscopy (FTIR) in the attenuated total reflection (ATR) mode as shown in Fig. 5.11c [119]. For both, QF-MLG and QF-BLG a sharp absorption peak due to the Si–H stretch mode is seen. No significant shift is observed compared to the bare H-terminated SiC(0001) surface [124] signaling a weak interaction between the graphene layer and the Si–H entities. The absorption line is virtually absent in s-polarization, which shows that the Si–H bonds are perpendicular to the surface.

Raman spectroscopy was also applied to the transformed layers [119, 120]. Spectra of the 2D line are given in Fig. 5.11d. The line shape analysis of the 2D line supports the formation of QFMLG and QFBLG upon hydrogen treatment of the buffer layer and a graphene monolayer on the buffer layer (MLG), respectively. While the spectrum of QFMLG consists of one narrow line, the signal of QFBLG is made up of four components in agreement with previous results on exfoliated

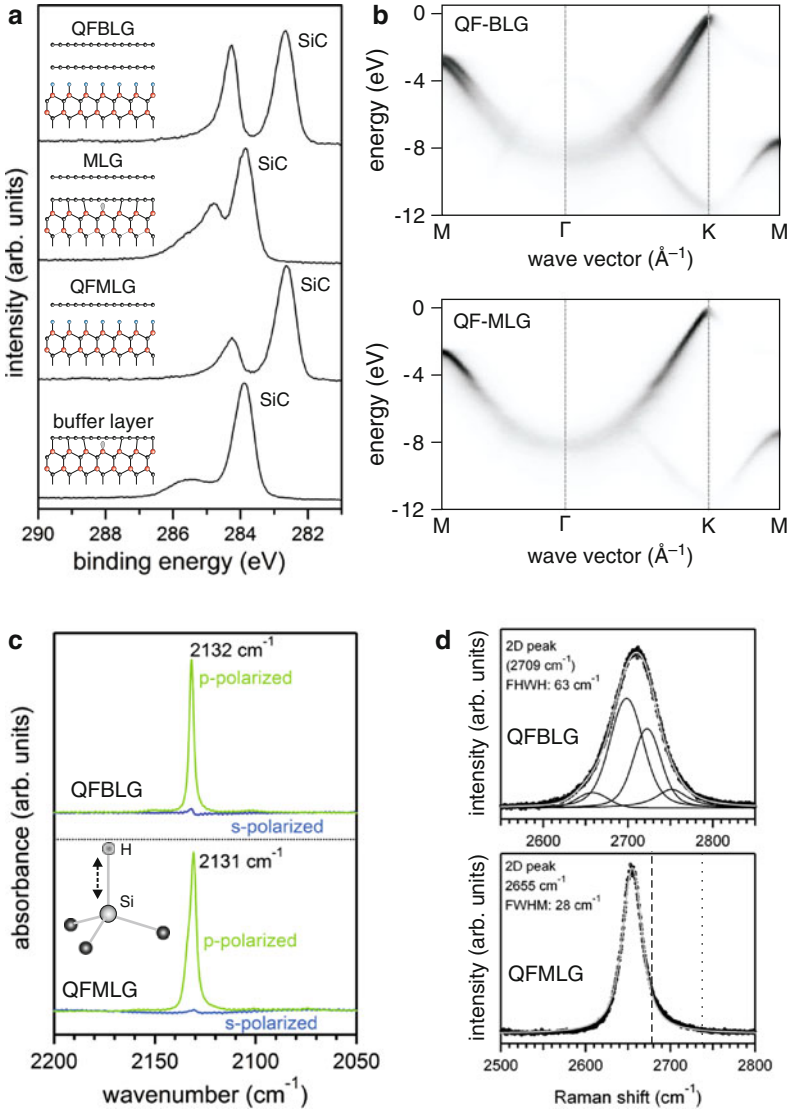

Fig. 5.11 (**a**) C1s core level spectra of the buffer layer, quasi-free-standing monolayer graphene (QFMLG), monolayer graphene on the buffer layer (MLG), and quasi-free-standing bilayer graphene (QFBLG) measured by XPS using Al K_α radiation ($\hbar\omega = 1486.7$ eV). (**b**) Band structure of QFMLG and GFBLQ measured along the high symmetry directions. (**c**) FTIR spectra of the Si–H stretch mode vibration of QFMLG and QFBLG in p- and s-polarization. (**d**) Raman spectra of the 2D-band of QFMLG and QFBLG. The *vertical dashed and dotted lines* indicate the position of the 2D-line observed for exfoliated graphene and for MLG, respectively. Adapted from [119]

graphene [88, 89]. The position of the 2D line of QFMLG with respect to that of exfoliated graphene shows that QFMLG is under slight expansion [119, 120]. In contrast to that, MLG is usually observed to be under compressive strain [91–93, 132, 133] due to the different thermal contraction when the sample is cooled down from growth temperature to room temperature [91, 92, 133]. Compared to MLG [12], there is an increase in the defect related D line (not shown here), which could be a result of the hydrogenation process.

The carrier mobility of QFMLG and QF-BLG was studied using Hall effect measurements by Speck et al. [119] at room temperature and mobility values of 1,250 cm^2/Vs were reported at carrier concentrations of 6×10^{12} cm^{-2}. Recent work on improved samples by the same group [134] showed that the mobility is almost temperature independent and falls from 3,400 cm^2/Vs to 3,100 cm^2/Vs when going from 25 K to 300 K. This demonstrates that successful interface engineering may substantially improve the properties of epitaxial graphene on SiC(0001) with respect to future device applications.

5.9 Conclusion

This chapter has given a brief overview over the properties of epitaxial graphene on SiC(0001). It should serve as a starting point for researchers interested in epitaxial graphene on SiC, a rapidly developing field. In the years since the first proposal of epitaxial graphene on SiC [10], much progress has been made in the understanding of the physical properties of this exciting material system. Atomic and electronic structures as well as vibrational and electronic transport properties have been studied intensively. While exfoliated graphene is expected to lead to many new interesting results, epitaxial graphene has the advantage that it can be prepared on a wafer scale with methods well established in the semiconductor industry. In addition, it also opens many possibilities for fundamental research, which cannot be conducted on the rather small flakes of exfoliated graphene. First studies of electronic devices have been performed using epitaxial graphene, which demonstrate that it holds promise for application in, e.g., high-frequency transistors for analog switching or for improved quantum resistance standards. Other applications such as chemical sensing, micro-mechanical devices, or plasmonic devices are expected to be developed in the future. It is clear that the future of epitaxial graphene is bright.

References

1. P. Wallace, Phys. Rev. **71**, 622 (1947)
2. A.K. Geim, Science **324**(5934), 1530 (2009)
3. A.K. Geim, K. Novolselov, Nat. Mater. **6**, 183 (2007)

4. K.S. Novoselov, D. Jiang, F. Schedin, T.J. Booth, V.V. Khotkevich, S.V. Morozov, A.K. Geim, Proc. Nat. Acad. Sci. U.S.A. **102**, 10451 (2005)
5. Q. Yu, J. Lian, S. Siriponglert, H. Li, Y.P. Chen, S.S. Pei, Appl. Phys. Lett. **93**, 113103 (2008)
6. X. Li, W. Cai, J. An, S. Kim, J. Nah, D. Yang, R. Piner, A. Velamakanni, I. Jung, E. Tutuc, S.K. Banerjee, L. Colombo, R.S. Ruoff, Science **324**, 1312 (2009)
7. X. Li, Y. Zhu, W. Cai, M. Borysiak, B. Han, D. Chen, R.D. Piner, L. Colombo, R.S. Ruoff, Nano Lett. **9**, 4359 (2009)
8. K.S. Kim, Y. Zhao, H. Jang, S.Y. Lee, J.M. Kim, K.S. Kim, J.H. Ahn, P. Kim, J.Y. Choi, B.H. Hong, Nature **457**, 706 (2009)
9. S. Bae, H. Kim, Y. Lee, X. Xu, J.S. Park, Y. Zheng, J. Balakrishnan, T. Lei, H.R. Kim, Y.I. Song, Y.J. Kim, K.S. Kim, B. Ozyilmaz, J.H. Ahn, B.H. Hong, S. Iijima, Nat. Nano. **5**, 574 (2010)
10. C. Berger, Z.M. Song, T.B. Li, X.B. Li, A.Y. Ogbazghi, R. Feng, Z.T. Dai, A.N. Marchenkov, E.H. Conrad, P.N. First, W.A. de Heer, J. Phys. Chem. B **108**, 19912 (2004)
11. C. Berger, Z.M. Song, X.B. Li, X.S. Wu, N. Brown, C. Naud, D. Mayo, T.B. Li, J. Hass, A.N. Marchenkov, E.H. Conrad, P.N. First, W.A. de Heer, Science **312**, 1191 (2006)
12. K.V. Emtsev, A. Bostwick, K. Horn, J. Jobst, G.L. Kellogg, L. Ley, J.L. McChesney, T. Ohta, S.A. Reshanov, J. Roehrl, E. Rotenberg, A.K. Schmid, D. Waldmann, H.B. Weber, T. Seyller, Nat. Mater. **8**, 203 (2009)
13. P.N. First, W.A. de Heer, T. Seyller, C. Berger, J.A. Stroscio, J.S. Moon, MRS Bull. **35**, 296 (2010)
14. E. Acheson, Production of artificial crystalline carbonaceous materials, U.S. Patent 492.767, 28 Feb 1893
15. The Lemelson-MIT Program, Edward Acheson – Carborundum. electronic source http://web.mit.edu/invent/iow/acheson.html. Last accessed on October 3, 2011
16. C. Brandt, R. Clarke, R. Siergiej, J. Casady, S.S.A. Agarwal, in *SiC Materials and Devices*, ed. by Y. Park (Academic Press, New York, 1998), p. 195
17. A.J. Van Bommel, J.E. Crombeen, A. Van Tooren, Surf. Sci. **48**, 463 (1975)
18. U. Starke, in *Recent Major Advances in SiC*, ed. by W. Choyke, H. Matsunami, G. Pensl (Springer Scientific, Berlin, Heidelberg, New York, 2003), p. 281
19. K. Järrendahl, R. Davis, in *SiC Materials and Devices*, *Semiconductors and Semimetals*, vol. 52, ed. by Y. Park (Academic Press, New York, 1998), p. 1
20. M. Sabisch, P. Krüger, J. Pollmann, Phys. Rev. B **51**, 13367 (1995)
21. M. Sabisch, P. Krüger, J. Pollmann, Phys. Rev. B **55**, 10561 (1997)
22. L. Ramsdell, Am. Mineralogist **32**, 64 (1947)
23. N. Jepps, T. Page, Progr. Cryst. Growth Charact. **7**, 259 (1983)
24. G.L. Harris (ed.), *Properties of Silicon Carbide* (INSPEC, Institution of Electrical Engineers, London (UK), 1995)
25. M. Suemitsu, H. Fukidome, J. Phys. D: Appl. Phys. **43**, 374012 (2010)
26. V. Bermudez, Phys. Stat. Sol. (b) **202**, 447 (1997)
27. K. Heinz, J. Bernhardt, J. Schardt, U. Starke, J. Phys.: Cond. Matter **16**, S1705 (2004)
28. U. Starke, J. Schardt, M. Franke, Appl. Phys. A **65**, 587 (1997)
29. P. Martenson, F. Owman, L. Johansson, Phys. Stat. Sol. (b) **202**, 501 (1997)
30. J. Pollmann, P. Krüger, M. Sabisch, Phys. Stat. Sol. (b) **202**, 421 (1997)
31. J. Pollmann, P. Krüger, J. Phys. C: Cond. Matter **16**, S1659 (2004)
32. F. Bechstedt, J. Furthmüller, J. Phys. C: Cond. Matter **16**, S1721 (2004)
33. P. Soukiassian, H. Enriquez, J. Phys. C: Cond. Matter **16**, S1611 (2004)
34. K.V. Emtsev, F. Speck, T. Seyller, J.D. Riley, L. Ley, Phys. Rev. B **77**, 155303 (2008)
35. U. Starke, J. Schardt, J. Bernhardt, M. Franke, K. Reuter H. Wedler, K. Heinz, J. Furthmüller, P. Käckel, F. Bechstedt, Phys. Rev. Lett. **80**, 758 (1998)
36. U. Starke, J. Schardt, J. Bernhardt, M. Franke, K. Heinz, Phys. Rev. Lett. **82**, 2107 (1999)
37. J. Bernhardt, J. Schardt, U. Starke, K. Heinz, Appl. Phys. Lett. **74**, 1084 (1999)
38. I. Forbeaux, J.M. Themlin, J.M. Debever, Phys. Rev. B **58**, 16396 (1998)
39. L. Simon, J.L. Bischoff, L. Kubler, Phys. Rev. B **60**, 11653 (1999)

40. J.E. Northrup, J. Neugebauer, Phys. Rev. B **52**, R17001 (1995)
41. V. Van Elsbergen, T. Kampen, W. Mönch, Surf. Sci. **365**, 443 (1996)
42. C. Riedl, C. Coletti, U. Starke, J. Phys. D: Appl. Phys. **43**, 374009 (2010)
43. K.V. Emtsev, T. Seyller, F. Speck, L. Ley, P. Stojanov, J. Riley, R. Leckey, Mater. Sci. Forum **556–557**, 525 (2007)
44. J.D. Joannopoulos, M.L. Cohen, Phys. Rev. B **7**, 2644 (1973)
45. A. Bostwick, T. Ohta, T. Seyller, K. Horn, E. Rotenberg, Nat. Phys. **3**, 36 (2007)
46. T. Ohta, A. Bostwick, J. McChesney, T. Seyller, K. Horn, E. Rotenberg, Phys. Rev. Lett. **98**, 206802 (2007)
47. T. Ohta, A. Bostwick, T. Seyller, K. Horn, E. Rotenberg, Science **313**, 951 (2006)
48. A. Bostwick, T. Ohta, J.L. McChesney, K.V. Emtsev, T. Seyller, K. Horn, E. Rotenberg, New J. Phys. **9**, 385 (2007)
49. A. Nagashima, N. Tejima, C. Oshima, Phys. Rev. B **50**, 17487 (1994)
50. A.M. Shikin, G.V. Prudnikova, V.K. Adamchuk, F. Moresco, K.H. Rieder, Phys. Rev. B **62**, 13202 (2000)
51. Y.S. Dedkov, M. Fonin, U. Rüdiger, C. Laubschat, Phys. Rev. Lett. **100**, 107602 (2008)
52. F. Varchon, R. Feng, J. Hass, X. Li, B.N. Nguyen, C. Naud, P. Mallet, J.Y. Veuillen, C. Berger, E. Conrad, L. Magaud, Phys. Rev. Lett **99**, 126805 (2007)
53. A. Mattausch, O. Pankratov, Phys. Rev. Lett. **99**, 076802 (2007)
54. A. Mattausch, O. Pankratov, Mater. Sci. Forum **556–557**, 693 (2007)
55. A. Mattausch, O. Pankratov, Phys. Stat. Sol. **245**, 1425 (2008)
56. S. Kim, J. Ihm, H.J. Choi, Y.W. Son, Phys. Rev. Lett. **100**, 176802 (2008)
57. Y. Qi, S.H. Rhim, G.F. Sun, M. Weinert, L. Li, Phys. Rev. Lett. **105**, 085502 (2010)
58. G.M. Rutter, N.P. Guisinger, J.N. Crain, E.A.A. Jarvis, M.D. Stiles, T. Li, P.N. First, J.A. Stroscio, Phys. Rev. B **76**, 235416 (2007)
59. J. Hass, J.E. Millán-Otoya, P.N. First, E.H. Conrad, Phys. Rev. B **78**, 205424 (2008)
60. P. Mallet, F. Varchon, C. Naud, L. Magaud, C. Berger, J.Y. Veuillen, Phys. Rev. B **76**, 041403 (2007)
61. P. Lauffer, K. Emtsev, R. Graupner, T. Seyller, L. Ley, S. Reshanov, H. Weber, Phys. Rev. B **77**, 155426 (2008)
62. C. Riedl, U. Starke, J. Bernhardt, M. Franke, K. Heinz, Phys. Rev. B **76**, 245406 (2007)
63. G.M. Rutter, J.N. Crain, N.P. Guisinger, T. Li, P.N. First, J.A. Stroscio, Science **317**, 219 (2007)
64. A. Bostwick, T. Ohta, J.L. McChesney, T. Seyller, K. Horn, E. Rotenberg, Eur. Phys. J. – Special Topics **148**, 5 (2007)
65. A. Bostwick, T. Ohta, J.L. McChesney, T. Seyller, K. Horn, E. Rotenberg, Solid State Commun. **143**, 63 (2007)
66. C. Riedl, A.A. Zakharov, U. Starke, Appl. Phys. Lett. **93** (2008)
67. S.Y. Zhou, G.H. Gweon, A.V. Fedorov, P.N. First, W.A. de Heer, D.H. Lee, F. Guinea, A.H. Castro Neto, A. Lanzara, Nat. Mater. **6**, 770 (2007)
68. S. Zhou, D. Siegel, A. Fedorov, A. Lanzara, Physica E **40**, 2642 (2008)
69. E. Rotenberg, A. Bostwick, T. Ohta, J.L. McChesney, T. Seyller, K. Horn, Nat. Mater. **7**, 258 (2008)
70. S. Zhou, D. Siegel, A. Fedorov, F.E. Gabaly, A. Schmid, A. Castro Neto, D.H. Lee, A. Lanzara, Nat. Mater. **7**, 259 (2008)
71. E.L. Shirley, L.J. Terminello, A. Santoni, F.J. Himpsel, Phys. Rev. B **51**, 13614 (1995)
72. M. Mucha-Kruczynski, O. Tsyplyatyev, A. Grishin, E. McCann, V.I. Fal'ko, A. Bostwick, E. Rotenberg, Phys. Rev. B **77**, 195403 (2008)
73. V. Fal'ko, Nat. Phys. **3**, 151 (2007)
74. A.H. Castro Neto, F. Guinea, N.M.R. Peres, K.S. Novoselov, A.K. Geim, Rev. Mod. Phys. **81**, 109 (2009)
75. S. Kopylov, A. Tzalenchuk, S. Kubatkin, V.I. Fal'ko, Appl. Phys. Lett. **97**, 112109 (2010)
76. E. McCann, V.I. Fal'ko, Phys. Rev. Lett. **96**, 086805 (2006)
77. E. McCann, Phys. Rev. B **74**, 161403 (2006)

78. F. Guinea, A.H.C. Neto, N.M.R. Peres, Phys. Rev. B **73**, 245426 (2006)
79. E.V. Castro, K.S. Novoselov, S.V. Morozov, N.M.R. Peres, J.M.B.L. dos Santos, J. Nilsson, F. Guinea, A.K. Geim, A.H.C. Neto, J. Phys. Condens. Matter **22**, 175503 (2010)
80. J. Nilsson, A.H. Castro Neto, F. Guinea, N.M.R. Peres, Phys. Rev. B **76**, 165416 (2007)
81. E.V. Castro, K.S. Novoselov, S.V. Morozov, N.M.R. Peres, J.M.B.L. dos Santos, J. Nilsson, F. Guinea, A.K. Geim, A.H.C. Neto, Phys. Rev. Lett. **99**, 216802 (2007)
82. J.B. Oostinga, H.B. Heersche, X. Liu, A.F. Morpurgo, L.M.K. Vandersypen, Nat. Mater. **7**, 151 (2007)
83. A.B. Kuzmenko, E. van Heumen, D. van der Marel, P. Lerch, P. Blake, K.S. Novoselov, A.K. Geim, Phys. Rev. B **79**, 115441 (2009)
84. E. Bauer, Repts. Prog. Phys. **5**, 895 (1994)
85. E. Bauer, Surf. Rev. Lett. **5**, 1275 (1998)
86. H. Hibino, H. Kageshima, F. Maeda, M. Nagase, Y. Kobayashi, H. Yamaguchi, Phys. Rev. B **77**, 075413 (2008)
87. T. Ohta, F. El Gabaly, A. Bostwick, J. McChesney, K.V. Emtsev, A.K. Schmid, T. Seyller, K. Horn, E. Rotenberg, New J. Phys. **10**, 023034 (2008)
88. A.C. Ferrari, J.C. Meyer, V. Scardaci, C. Casiraghi, M. Lazzeri, F. Mauri, S. Piscanec, D. Jiang, K.S. Novoselov, S. Roth, A.K. Geim, Phys. Rev. Lett. **97**, 187401 (2006)
89. D. Graf, F. Molitor, K. Ensslin, C. Stampfer, A. Jungen, C. Hierold, L. Wirtz, Nano Lett. **7**, 238 (2007)
90. C. Stampfer, F. Molitor, D. Graf, K. Ensslin, A. Jungen, C. Hierold, L. Wirtz, Appl. Phys. Lett. **91**, 241907 (2007)
91. J. Röhrl, M. Hundhausen, K. Emtsev, T. Seyller, L. Ley, Mater. Sci. Forum **600–603**, 567 (2009)
92. J. Röhrl, M. Hundhausen, K. Emtsev, T. Seyller, R. Graupner, L. Ley, Appl. Phys. Lett. **92**, 201918 (2008)
93. D.S. Lee, C. Riedl, B. Krauss, K. von Klitzing, U. Starke, J.H. Smet, Nano Lett. **8**, 4320 (2008)
94. J. Hass, R. Feng, T. Li, X. Li, Z. Zong, W.A. de Heer, P.N. First, E.H. Conrad, C.A. Jeffrey, C. Berger, Appl. Phys. Lett. **89**, 143106 (2006)
95. J.B. Hannon, R.M. Tromp, Phys. Rev. B **77** 241404 (2008)
96. C. Virojanadara, M. Syväjarvi, R. Yakimova, L.I. Johansson, A.A. Zakharov, T. Balasubramanian, Phys. Rev. B **78**, 245403 (2008)
97. C. Virojanadara, R. Yakimova, J. Osiecki, M. Syväjärvi, R. Uhrberg, L. Johansson, A. Zakharov, Surf. Sci. **603**, L87 (2009)
98. R.M. Tromp, J.B. Hannon, Phys. Rev. Lett. **102**, 106104 (2009)
99. T. Ohta, N.C. Bartelt, S. Nie, K. Thürmer, G.L. Kellogg, Phys. Rev. B **81**(12), 121411
100. J. Jobst, D. Waldmann, F. Speck, R. Hirner, D.K. Maude, T. Seyller, H.B. Weber, Phys. Rev. B **81**, 195434 (2010)
101. K.S. Novoselov, A.K. Geim, S.V. Morozov, D. Jiang, M.I. Katsnelson, I.V. Grigorieva, S.V. Dubonos, A.A. Firsov, Nature **438**, 197 (2005)
102. Y. Zhang, Y.W. Tan, H.L. Stormer, P. Kim, Nature **438**, 201 (2005)
103. S. Weingart, C. Bock, U. Kunze, K. Emtsev, T. Seyller, L. Ley, Physica E **42**, 687 (2010)
104. S. Weingart, C. Bock, U. Kunze, F. Speck, T. Seyller, L. Ley, App. Phys. Lett. **95**, 262101 (2009)
105. J.L. Tedesco, B.L. VanMil, R.L. Myers-Ward, J.M. McCrate, S.A. Kitt, P.M. Campbell, G.G. Jernigan, J.C. Culbertson, J.C.R. Eddy, D.K. Gaskill, Appl. Phys. Lett. **95**, 122102 (2009)
106. W. Chen, S. Chen, D.C. Qi, X.Y. Gao, A.T.S. Wee, J. Am. Chem. Soc. **129**, 10418 (2007)
107. C. Coletti, C. Riedl, D.S. Lee, B. Krauss, L. Patthey, K. von Klitzing, J.H. Smet, U. Starke, Phys. Rev. B **81**, 235401 (2010)
108. Y.M. Lin, C. Dimitrakopoulos, K.A. Jenkins, D.B. Farmer, H.Y. Chiu, A. Grill, P. Avouris, Science **327**, 662 (2010)

109. A. Tzalenchuk, S. Lara-Avila, A. Kalaboukhov, S. Paolillo, M. Syvajarvi, R. Yakimova, O. Kazakova, T.J.B.M. Janssen, V. Fal'ko, S. Kubatkin, Nat. Nano. **5**, 186 (2010)
110. T. Shen, J.J. Gu, M. Xu, Y.Q. Wu, M.L. Bolen, M.A. Capano, L.W. Engel, P.D. Ye, Appl. Phys. Lett. **95**, 172105 (2009)
111. J. Kedzierski, P.L. Hsu, P. Healey, P.W. Wyatt, C.L. Keast, M. Sprinkle, C. Berger, W.A. de Heer, IEEE Trans. Elec. Dev. **55**, 2078 (2008)
112. J. Moon, D. Curtis, M. Hu, D. Wong, C. McGuire, P. Campbell, G. Jernigan, J. Tedesco, B. VanMil, R. Myers-Ward, C. Eddy, D. Gaskill, IEEE Elec. Dev. Lett. **30**, 650 (2009)
113. K.I. Bolotin, K.J. Sikes, J. Hone, H.L. Stormer, P. Kim, Phys. Rev. Lett. **101**, 096802 (2008)
114. B. Premlal, M. Cranney, F. Vonau, D. Aubel, D. Casterman, M.M. De Souza, L. Simon, Appl. Phys. Lett. **94**, 263115 (2009)
115. I. Gierz, T. Suzuki, R.T. Weitz, D.S. Lee, B. Krauss, C. Riedl, U. Starke, H. Hoechst, J.H. Smet, C.R. Ast, K. Kern, Phys. Rev. B **81**, 235408 (2010)
116. C. Riedl, C. Coletti, T. Iwasaki, A.A. Zakharov, U. Starke, Phys. Rev. Lett. **103**, 246804 (2009)
117. C. Virojanadara, A.A. Zakharov, R. Yakimova, L.I. Johansson, Surf. Sci. **604**, L4 (2010)
118. C. Virojanadara, R. Yakimova, A.A. Zakharov, L.I. Johansson, J. Phys. D – Appl. Phys. **43**, 374010 (2010)
119. F. Speck, M. Ostler, J. Röhrl, J. Jobst, D. Waldmann, M. Hundhausen, H. Weber, T. Seyller, Mater. Sci. Forum **645–648**, 629 (2010)
120. J. Röhrl, M. Hundhausen, F. Speck, T. Seyller, Mater. Sci. Forum **645–648**, 603 (2010)
121. S. Oida, F.R. McFeely, J.B. Hannon, R.M. Tromp, M. Copel, Z. Chen, Y. Sun, D.B. Farmer, J. Yurkas, Phys. Rev. B **82**, 041411 (2010)
122. T. Seyller, Mater. Sci. Forum **483–485**, 535 (2005)
123. T. Seyller, J. Phys.: Cond. Matter **16**, S1755 (2004)
124. N. Sieber, B.F. Mantel, T. Seyller, J. Ristein, L.Ley, T. Heller, D.R. Batchelor, D. Schmeißer, Appl. Phys. Lett. **78**, 1216 (2001)
125. N. Sieber, T. Seyller, L. Ley, D. James, J. Riley, R.L.M. Polcik, Phys. Rev. B **67**, 205304 (2003)
126. N. Sieber, T. Stark, T. Seyller, L. Ley, C. Zorman, M. Mereghany, Appl. Phys. Lett. **80**, 4726 (2002)
127. N. Sieber, T. Stark, T. Seyller, L. Ley, C. Zorman, M. Mereghany, Appl. Phys. Lett. **81**, 1534 (2002)
128. H. Tsuchida, I. Kamata, K. Izumi, J. Appl. Phys. **85**, 3569 (1999)
129. H. Tsuchida, I. Kamata, K. Izumi, Appl. Phys. Lett. **70**, 3072 (1997)
130. H. Tsuchida, I. Kamata, K. Izumi, Jpn. J. Appl. Phys. **36**, L699 (1997)
131. A. Bostwick, F. Speck, T. Seyller, K. Horn, M. Polini, R. Asgari, A.H. MacDonald, E. Rotenberg, Science **328**, 999 (2010)
132. Z.H. Ni, W. Chen, X.F. Fan, J.L. Kuo, T. Yu, A.T.S. Wee, Z.X. Shen, Phys. Rev. B **77**, 115416
133. N. Ferralis, R. Maboudian, C. Carraro, Phys. Rev. Lett. **101**, 156801 (2008)
134. F. Speck, J. Jobst, F. Fromm, M. Ostler, D. Waldmann, M. Hundhausen, H. Weber, T. Seyller, Appl. Phys. Lett. **99**, 122106 (2011)

Chapter 6
Magneto-Transport on Epitaxial Graphene

Peide D. Ye, Michael Capano, Tian Shen, Yanqing Wu, and Michael L. Bolen

6.1 Introduction

Graphene, a monolayer of carbon atoms tightly packed into a two-dimensional (2D) hexagonal lattice, has recently been successfully isolated from highly ordered pyrolytic graphite (HOPG) and shown to be thermodynamically stable and to exhibit astonishing transport properties, such as an electron mobility of $\sim$25,000 cm^2/Vs and velocity of $\sim 10^8$ cm/s at room temperature [1–3]. With the high carrier mobility enabled by its unique electronic structure, graphene has attracted many research efforts recently. Initial works have demonstrated the great potential of graphene for modern electronics applications. These efforts are focused on overcoming the challenges faced to incorporate graphene into microelectronic applications. The three particular challenges are developing a synthesis technique to manufacture graphene over wafer-scale areas, opening an energy bandgap in graphene, and forming a high-quality gate dielectric on the surface of graphene.

An interesting differentiation between the many well-established semiconductor materials in microelectronic industry and graphene is how it was discovered. Most semiconductor materials are created through deposition or melt processes, but the origin of graphene is unique. The first successfully isolated sheet of graphene was formed by Geim and Novoselov through a mechanical exfoliation technique which used cellophane tape to remove and subsequently transfer graphene sheets from HOPG to SiO_2 [2]. This produced graphitic flakes tens of microns in size upon which electronic devices were fabricated. The pioneering work on isolating graphene has been recognized by earning its discoverers the Nobel Prize in Physics for 2010. Since the mechanical exfoliation technique does not require expensive equipment, this approach is still widely used for research purposes. Various alternative methods have been studied and developed to fabricate uniform graphene

P.D. Ye (✉) · M. Capano · T. Shen · Y. Wu · M.L. Bolen
School of Electrical and Computer Engineering and Birck Nanotechnology Center, Purdue University, West Lafayette, IN 47907, USA

H. Raza (ed.), *Graphene Nanoelectronics*, NanoScience and Technology,
DOI 10.1007/978-3-642-22984-8_6,

on a large-scale with controlled layer thickness, including epitaxial graphene grown through the thermal decomposition of SiC [4–9] or chemical vapor deposition (CVD) growth of graphene on metallic substrates, such as copper or nickel [10–13], as described in Chap. 7.

Epitaxial graphene grown on the surface of SiC was first demonstrated three decades ago by Van Bommel [14] and developed further recently by de Heer and Berger et al. [4, 15]. This synthesis technique has proven to be one of the best available to produce high-quality, large-scale graphene. Compared to exfoliated graphene, epitaxial graphene formed by the thermal decomposition of SiC has provided the missing pathway to a viable electronics technology. The electronic band structure of graphene leads to a unique property which is its zero-bandgap. An energy bandgap is essential for typical digital applications as well as most RF applications. Many methods to engineer a bandgap within graphene have been studied such as tailoring nanoribbon structures [16–23] and using bilayer graphene with a displacement field [24–28]. Top gate configuration is a must for any device applications which require high-quality gate dielectric on graphene. Unlike silicon and other conventional semiconductor materials, the unique sp^2 hybridization of graphene provides no chemical bonds on the surface. This lack of bonds makes the surface chemically inert, which is problematic for forming high-quality dielectrics. There are many different solutions being investigated to solve this problem. One such approach is through the use of atomic layer deposition (ALD), the-state-of-the-art dielectric technique developed in Si CMOS technology [29, 30]. It has been found that a surface treatment of NO_2 gas can be used to functionalize the surface of graphene prior to the subsequent ALD of oxide [31]. Also, ultrathin seed layers such as an oxidized Al layer, a commercial NFC 1400–3CP (JSR Micro, Inc.), or perylene-3,4,9,10-tetracarboxylic dianhydride (PTCDA) polymer layers have been investigated [32–35]. Recently, a novel seed layer process using ozone and trimethylaluminum (TMA) as precursors at room temperature was also studied [36]. It is of great importance to provide a high-quality dielectric which does not degrade the channel mobility of graphene transistors. The dielectric should have high phonon energy and low interface trap density to minimize phonon scattering and impurity scattering.

In this chapter, the epitaxial graphene work on SiC performed at Purdue University in the past years is summarized. The summary includes the synthesis process, which uses an Epigress VP508 SiC hot-wall CVD reactor for graphene growth [5, 33, 37–40]. The physical characterization of the epitaxial graphene is discussed from systematic studies by scanning tunneling microscopy (STM), atomic force microscopy (AFM), transmission electron microscopy (TEM), and Raman spectroscopy. Furthermore, the ALD growth mechanism is investigated and ALD high-k/graphene integration is explored. Charge mobility is characterized by Hall mobility measurements and field-effect mobility characterization from top-gated devices. The authors have observed for the first time the half-integer quantum Hall-effect on epitaxial graphene which confirms that epitaxial graphene on SiC shares the same electrical properties as exfoliated graphene [33]. Similar findings were also reported by other groups independently [41–43]. Detailed magneto-transport studies

on monolayer graphene on SiC (0001) are also presented. Ballistic and coherent transport on nanostructured graphene films are also studied as well as spin transport. Related work has also been carried out at the George Institute of Technology, Naval Research Laboratory, Hughes Research Lab, IBM T.J. Watson Research Center, and many other universities.

6.2 Epitaxial Graphene Synthesis

The key to forming epitaxial graphene on SiC relies on controlling the preferential desorption of silicon atoms from the substrate. The first gas phase mass spectrometry studies of the thermal decomposition of SiC occurred in the late 1950s. It was shown that the most prevalent gaseous species sublimating from a thermally decomposing SiC substrate is atomic silicon [44, 45]. This desorption of silicon leaves behind a non-stoichiometric substrate in the form of a carbon rich surface as described in Chap. 5. After self-reconstruction and relaxation, the surface carbon minimizes its free energy through the formation of graphitic bonds. In situ studies using X-ray photoelectron spectroscopy (XPS) as well as Auger electron spectroscopy (AES) have demonstrated the formation of carbon-to-carbon sp^2 bonds [46]. These bonds form the hexagonal, or honeycomb-like, lattice characteristic of graphene. This graphitic film on SiC is generally referred to as epitaxial graphene.

By varying the thermal decomposition conditions, such as growth temperature, growth time, and chamber pressure, the material properties of the epitaxial graphene can be changed. As a simple example, increasing the growth time can increase the thickness of the epitaxial graphene. While true graphene is only a single monolayer thick, epitaxial graphene on SiC can possess the same electrical characteristics despite being multiple atomic layers thick. This is due to the symmetry and rotational stacking sequence of the individual layers within the epitaxial graphene [47]. Rotational stacking faults within epitaxial graphene serve to electronically decouple the individual layers and break the stacking symmetry of Bernal stacked graphite, which is the most common graphitic polytype. Depending on the polar face and growth conditions, uniform films with thicknesses of 1–2 layers or up to tens of layers can be reproducibly and reliably formed over the wafer scale.

The following is the developed process details used to grow high-quality graphene films on SiC. The epitaxial growth starts with a wet cleaning procedure using a Piranha bath and HF dip. Then the samples are transferred into an Epigress VP508 hot-wall CVD reactor for SiC surface preparation, and subsequently, graphene formation. The growth procedure is as follows:

1. A reactive hydrogen environment at 1,500°C is held for 10 min to remove polishing scratches.
2. The chamber is allowed to cool (typically to 700°C or below) while the hydrogen is evacuated.

3. The desired growth environment replaces the hydrogen, either high-vacuum or low-pressure Ar (1–100 mbar).
4. The chamber is brought to 1,100°C and then ramped at 10°C/min to the desired growth temperature (generally 1,350–1,650°C) for a desired length of time (generally 10 min).
5. Allow the chamber to cool naturally.

The growth conditions, film morphology, and electrical properties of the epitaxial graphene films differ markedly between films grown on the C-face (SiC $(000\bar{1})$) and films grown on the Si-face (SiC (0001)). This is because SiC is a polar material. It has been confirmed by several research groups that the graphene film is thicker for C-face grown graphene than Si-face under similar growth conditions [48]. For the C-face, there is only a single silicon-to-carbon sp^3 bond holding the desorbing silicon atom to the surface of the substrate, whereas for the Si-face, there are three bonds holding the silicon atom to the surface.

After growth and cooling, samples are taken out and inspected optically and with AFM. The AFM profilometry micrographs in Fig. 6.1 demonstrate how a growth condition, temperature in this case, affects the surface morphology. The hold time is kept constant at 10 min and a high-vacuum environment is used for this particular set of experiments. Comparing the micrographs, the most drastic change is seen between the 1,450°C and 1,500°C growth temperatures. At temperatures $\geq$ 1,500°C, several-micron large regions of smooth graphene films are obtained

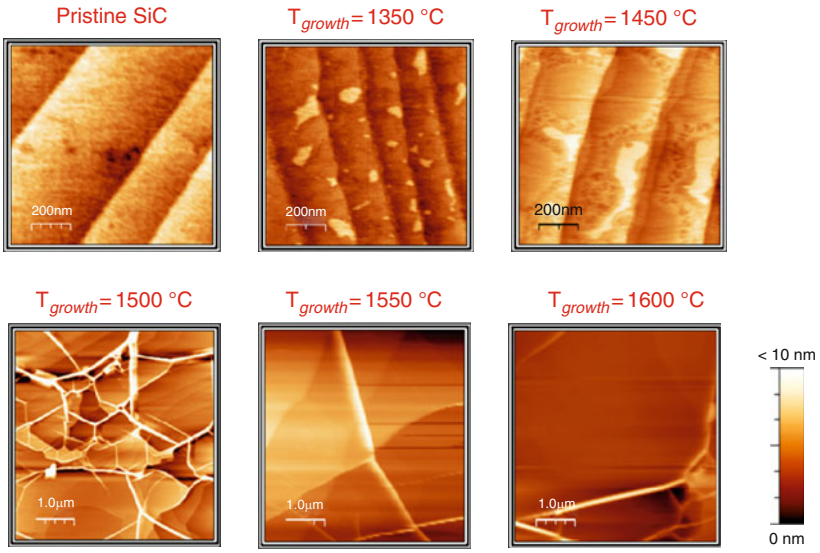

Fig. 6.1 AFM profilometry micrographs of C-face 4H–SiC substrates after H_2 etching and thermal decomposition at 1,350°C, 1,450°C, 1,500°C, 1,550°C, and 1,600°C for 10 min in vacuum (low-10^{-5} mbar). The images were taken by G. Prakash under the guidance of Prof. Reifenberger at Purdue University

which are delineated by ridges that are tens of nanometers high. As determined from angle-resolved XPS, the film itself grows linearly in thickness with increasing temperature. At 1,475°C, it is 1.7 nm thick and it is 5.7 nm thick at 1,600°C. Optimizing the growth conditions allows for thinner films. For example, gaseous argon can be used as a growth ambient as opposed to vacuum. At 1,600°C, using 10 mbar of argon overpressure instead of a vacuum environment is found to decrease the epitaxial graphene thickness by 1.1 nm. The argon overpressure creates an additional kinetic barrier to silicon desorption which can help control epitaxial graphene formation.

Unlike on the C-face, epitaxial graphene formation on the Si-face proceeds in a rate limited manner, which allows for synthesizing more uniform films. The morphology of epitaxial graphene film on the Si-face has a comparatively lower RMS roughness than the C-face due to a lack of ridges, as depicted in Fig. 6.2. Held at 1,550°C under vacuum for 10 min, the Si-face has epitaxial graphene covering approximately 95% of its surface. However, the typical Hall mobility of graphene formed on the Si-face under vacuum is ∼1,300 to 1,600 cm^2/Vs, which is significantly lower than the C-face samples grown at the exact same condition which exhibit a mobility value of ∼5,000 to 6,000 cm^2/Vs.

In addition to AFM, STM has also been used to study the surface of epitaxial graphene. An Omicron ultrahigh-vacuum STM with etched tungsten tips is operated at room temperature in the low 10^{-10} Torr regime. The XY piezocalibration was checked independently by imaging atoms in HOPG. Figure 6.3a shows a three-dimensional representation of epitaxial graphene blanketing the intrinsic terraces of

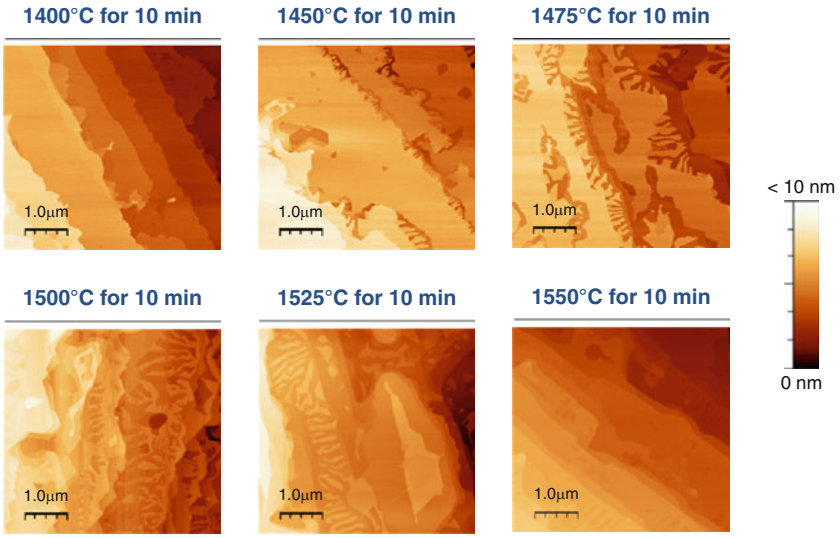

Fig. 6.2 AFM profilometry micrographs of Si-face SiC substrates after H_2 etching and thermal decomposition at 1,400°C, 1,450°C, 1,475°C, 1,500°C, 1,525°C, and 1,550°C for 10 min in vacuum (low-10^{-5} mbar)

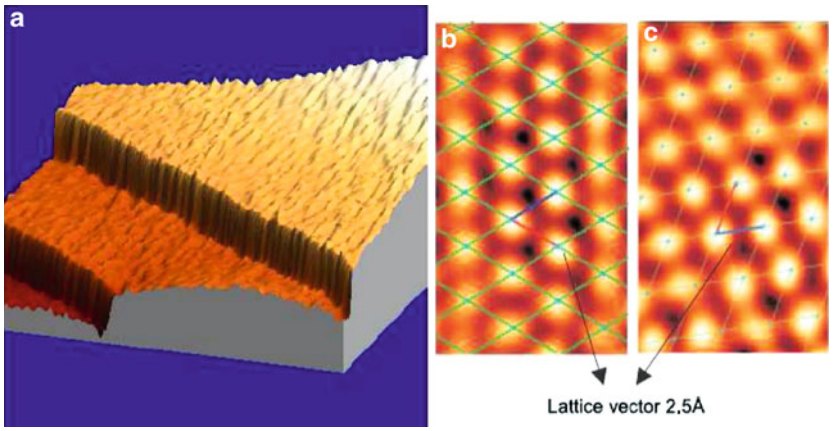

Fig. 6.3 (**a**) STM image of a graphene film formed on a carbon-face on-axis semi-insulating 4H–SiC substrate. The 1.2 or 1.4 nm steps are unit steps in the basal plane of the SiC substrate. (**b**) Atomic resolution STM image of a triangular sublattice of carbon atoms in a graphene film. Due to the offset between two sublattices in a multiple graphene film, only every other surface atom is imaged. The STM work was carried out by Prof. Reifenberger's group at Purdue University

the SiC surface. The local density of states (LDOS) are probed and exhibited in Fig. 6.3b. The measured lattice constant is found to be approximately 2.5 Å which is very close to that of graphene, which is 2.46 Å. Furthermore, the graphene on SiC has the same LDOS as on HOPG. Over atomistic length scales, this is material evidence of the high-quality graphene grown epitaxially on thermally decomposed SiC.

In addition to surface analysis, an atomistic side-view of epitaxial graphene can be obtained through the use of cross-sectional high-resolution TEM (HRTEM). This provides insight into the number of layers formed. Figure 6.4a shows a HRTEM micrograph of graphene layers formed on a Si-face sample held at 1,550°C for 10 min under high-vacuum. The sample is prepared for TEM via focused ion beam (FIB) extraction and then imaged at 300 kV with an FEI Titan 80–300. As can be seen, there is one monolayer of graphene plus a SiC reconstructed buffer layer between the graphene and SiC substrate. Throughout the tens of microns imaged from the extracted sample section, there are typically between 1–2 layers of graphene with a very few regions showing no signs of graphene. This lack of uniformity occurs since graphene formation relies on the pseudo-random process of Si desorption. Figure 6.4b shows another cross-sectional HRTEM image; this time of epitaxial graphene formed on the C-face after thermal decomposition at 1,500°C under vacuum. As previously mentioned, this thickness discrepancy between polar faces is common and thicker films are usually formed on the C-face of SiC under similar growth conditions.

Hall bars are fabricated on epitaxial graphene on both polar faces to understand the quality of the film over a larger length scale than the atomistic views provided by HRTEM and STM. The measured Hall mobility values for both C-face and Si-face devices are presented in Fig. 6.5. The positive correlation between growth pressure

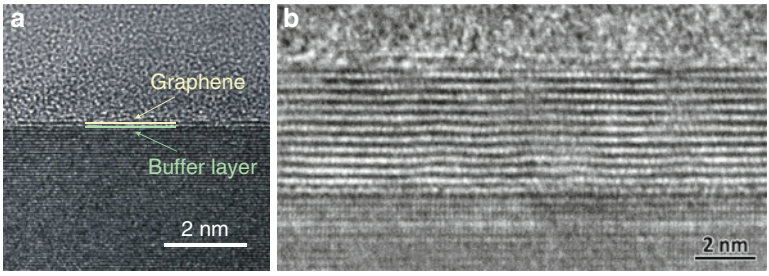

Fig. 6.4 HRTEM micrographs of (**a**) Si-face and (**b**) C-face SiC substrates after 1,550°C and 1,500°C thermal decomposition for 10 min, respectively. The FIB and TEM work was performed by R. Colby under the guidance of Prof. Stach at Purdue University

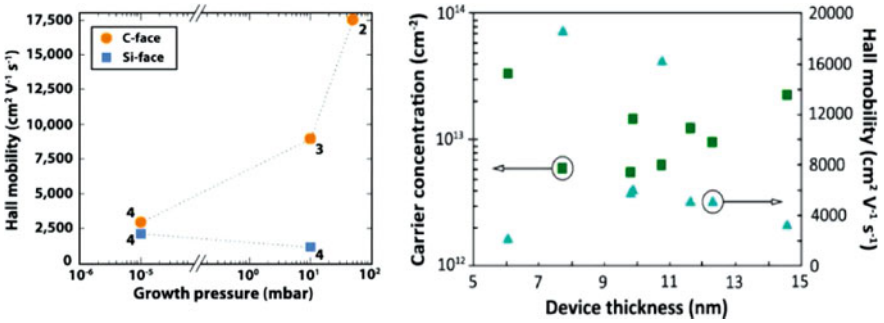

Fig. 6.5 (**a**) Average room-temperature Hall mobility values versus pressure for both C-face and Si-face devices. The graphene coverage is discontinuous at chamber pressures above 50 mbar for the C-face and 10 mbar for the Si-face. The number next to each point represents the number of devices tested, and the *dotted lines* serve as guides to the eye. (**b**) There is no apparent correlation between the thickness of a Hall bar and its measured Hall mobility or carrier concentration. This implies that there is not equal conduction from each graphene layer in the film

and mobility for the C-face is similar to that found by Tedesco et al. [48]. This correlation continues to the point where a large enough Ar overpressure inhibits Si desorption from the SiC sample and epitaxial graphene formation is halted. At 100 mbar (50 mbar) and 10 min growth time, AFM and Raman spectroscopy indicate there is no longer a continuous film of epitaxial graphene on the C-face (Si-face) surface. Instead, on the C-face, isolated patches of epitaxial graphene are found at random locations across the surface. With increased growth time, it is expected, based on previous research, that a continuous film would be achieved at 100 mbar; but for this set of experiments, growth time is held constant at 10 min. There is not a clear increase in Hall mobility values as pressure increases on the Si-face, unlike the trend other groups have observed [49, 50]. This discrepancy could be caused by an increasing density of discontinuities in the epitaxial graphene. As growth pressure increases, so too does the suppression of Si desorption, which leads to a discontinuous epitaxial graphene film. Thus, there is a decrease in the percentage of the surface which is covered by epitaxial graphene as growth pressure increases.

This notion is confirmed via AFM phase contrast imaging. These discontinuities serve as scattering sites, thereby lowering the overall measured Hall mobility.

Figure 6.5b shows an apparent lack of correlation between the thickness of each device and its Hall mobility and carrier concentration value. This is important, because it implies that each graphene layer within the epitaxial graphene does not contribute equally to conduction. If there were equal conduction, then for each additional layer, there would be a monotonic increase in carrier concentration with thickness. Correspondingly, there would be a decrease in the Hall mobility value, since carrier concentration and Hall mobility are inversely related. Instead, neither of these trends are apparent in Fig. 6.5b.

6.3 Dielectric Integration on Epitaxial Graphene

ALD is a thin-film growth technique for depositing uniform and conformal films with atomic precision. ALD is a special modification of the CVD method with the distinctive feature of alternate and cyclic supply of each gaseous precursor to the reactor chamber at relatively low temperature 200–350°C. The alternating pulses of the precursors are chemisorbed on the substrate surface and excesses are removed by a purge step. The key feature of the ALD methods is the saturation of all the reaction and purging steps, which makes film growth self-limiting on the surface. The precision achieved with ALD allows processing of nanometer-scale films in a controlled manner. ALD methods and applications have developed rapidly over the last ten years, particularly for high-k gate oxides. ALD high-k Hf-based oxide has become a manufacturing process to replace SiO_2 in 45 nm node Si complementary metal-oxide semiconductor (CMOS) digital integrated circuits starting in the second half of 2007. It is natural to extend this state-of-the-art CMOS oxide processing technology to graphene. However, the ALD process on graphene is expected to be very different from the deposition on conventional semiconductors or oxides, because the perfect graphene surface is chemically inert [51].

Figure 6.6a shows an AFM topography image of fresh HOPG surface with an atomically smooth (rms = 0.04 nm) carbon surface and atomically sharp step edges created by broken graphene layers. From the line profile (not shown), the step height is measured to be 0.3–0.4 nm, confirming that it is generated by a single graphene layer. Figure 6.6b shows an AFM image of a similar area after 10 cycles, i.e., 1 nm of ALD Al_2O_3 process at 250°C growth temperature. From these images and line profile data (not shown), the graphene surface remains atomically smooth with an rms roughness of 0.04 nm, indicating that no Al_2O_3 films are grown on graphene surface. This demonstrates that conventional H_2O-based ALD process cannot grow two-dimensional, continuous, and isotropic oxide films directly on pristine graphene surfaces. On the other hand, Al_2O_3 nanoribbons with 1.5 nm height and several nanometers wide are clearly observed at step edges, indicating that ALD Al_2O_3 films only grow along the step edges.

It is widely believed that an ultrathin high-k dielectric integration on graphene would be the next major road block toward the realization of high-performance

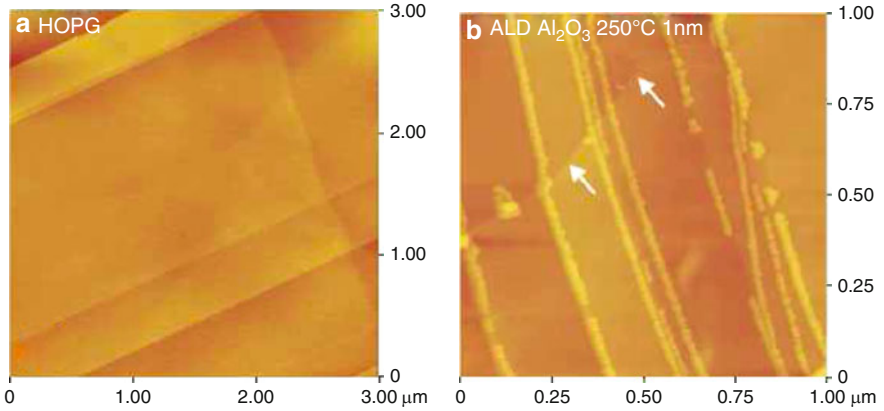

Fig. 6.6 (**a**) AFM images of HOPG surface with graphene terraces and (**b**) similar surface after 1 nm thick ALD Al_2O_3 growth

graphene-based electronic devices. Much research has been carried out in this field using specific seeding or interfacial layers, as has been done with Ge or III–V semiconductors. These research efforts can be categorized as: (1) trimethylaluminum (TMA) + NO_2 seeding layer [31, 51], (2) TMA + O_3 seeding layer [36], (3) a fully oxidized Al seeding layer [32, 33], (4) organic PTCA or PTCDA seeding layer [30, 35], and (5) diluted spin-coated polymer NFC 1400–3CP as a buffered dielectric [34]. Significant additional research is needed to characterize the interface quality and optimize the dielectric formation process at the device level. Our approach is to form ALD high-k gate stack integration on epitaxial graphene films by inserting a 1 nm thick fully oxidized Al film as a seeding layer. The gate stack formation does not degrade the electrical properties of epitaxial graphene films significantly. The half-integer quantum Hall-effect (QHE) is observed in gated epitaxial graphene films on SiC (0001), along with pronounced Shubnikov-de Haas (SdH) oscillations in magneto-transport [33]. The observation of quantum features demonstrates the reasonable success of integration of ALD high-k on epitaxial graphene.

6.4 Top-Gate Graphene Field-Effect Transistors

For most potential graphene applications, it is crucial to have a top gated working transistor that can be integrated into a conventional CMOS process flow, and that enables device scaling. Conventional transistors are made on semiconductors with moderate bandgap (Si $\sim$ 1.12 eV, GaAs $\sim$ 1.4 eV). Bandgap is an important characteristic of the semiconductor that enables the device to turn off and minimizes leakage current at off state. The bandgap energy also influences two performance parameters that tend to offset one another: drive current (mobility) and on–off ratio.

Generally, for narrow bandgap semiconductors, the light effective mass enables high mobility and even ballistic transport. However, in narrow bandgap semiconductors, the off current becomes excessive because band-to-band tunneling current is large. Graphene has very high mobility and room temperature ballistic transport over a few hundred nanometers, which is one of its most attractive properties for device performance. The biggest concern currently for graphene is the poor off-state characteristics. Narrow ribbon widths down to less than 10 nm are required to induce a bandgap and achieve acceptably low off currents. Narrow ribbons of these dimensions are still a challenge, even with modern lithographic techniques [16,17]. The edge roughness of the nanoribbon at 10 nm scale leads to the significant degradation of the intrinsic mobility. Graphene edge surface passivation is another active field currently [52–54].

Because the density of states (DOS) in graphene is linear with respect to the energy level, gate voltage can modulate the DOS linearly to enable modulation of current in the channel. Top-gated transistors have been fabricated and characterized on epitaxial graphene on SiC on both (0001) and $(000\bar{1})$ face of SiC [5]. The device structure of the fabricated graphene FET is shown in Fig. 6.7a. Device isolation of the graphene film was realized by 120 nm deep SF_6-based dry etching with photolithographically defined photoresist as a protection layer. Ti/Au metallization was used to form Ohmic contacts on graphene as source and drain. Physical vapor deposited (PVD) SiO_2 was used as a top gate dielectric. Finally, conventional Ni/Au metals were electron-beam evaporated, followed by lift off to form the gate electrodes. The process requires three levels of lithography (isolation, Ohmic, and gate), all done using a contact mask aligner. PVD dielectrics can be simply applied to graphene devices instead of ALD. However, it is also a challenge to form nanometer thin high-quality dielectric on graphene by the PVD approach.

Figure 6.7a shows the DC output characteristic with a gate bias from 1 to 2.5 V on a device with a fully covered gate. The measured graphene FET has a designed gate length (L_g) of 400 μm and a gate width (L_w) of 50 μm, with a gate oxide of 50 nm SiO_2. The gate leakage current is very low, below 10^{-9} A under the same bias conditions, corresponding to a gate leakage current density of 3×10^{-6} A/cm^2. The drain current can be modulated by approximately 50% with gate bias of a few volts. A reference SiC sample without the graphitization treatment, processed at the same time, shows no current (<40 pA), which confirms conduction through the graphene layers only. Figure 6.7b illustrates the transfer characteristics of this graphene FET at $V_{ds} = 2.0$ V. The drain current or conductance exhibits a region of minimum at $V_{gs} \approx -0.8$ V. This dip in single-graphene layer is well-documented and corresponds to a minimum conductivity of $\sim 4e^2/h$ at the charge neutrality point or Dirac point, where e and h are the electric charge and Planck's constant, respectively. It is the same physical origin here for multilayer graphene films. The device cannot be turned off because graphene or graphite is a semimetal with no bandgap. A finite bandgap can be created by patterning graphene into graphene nanoribbons, but the dimensions of such ribbons press the limits of modern lithography. The slope of the drain current shows that the peak extrinsic transconductance (G_m) is ~1.4 mS/mm, due to its extraordinarily large gate length.

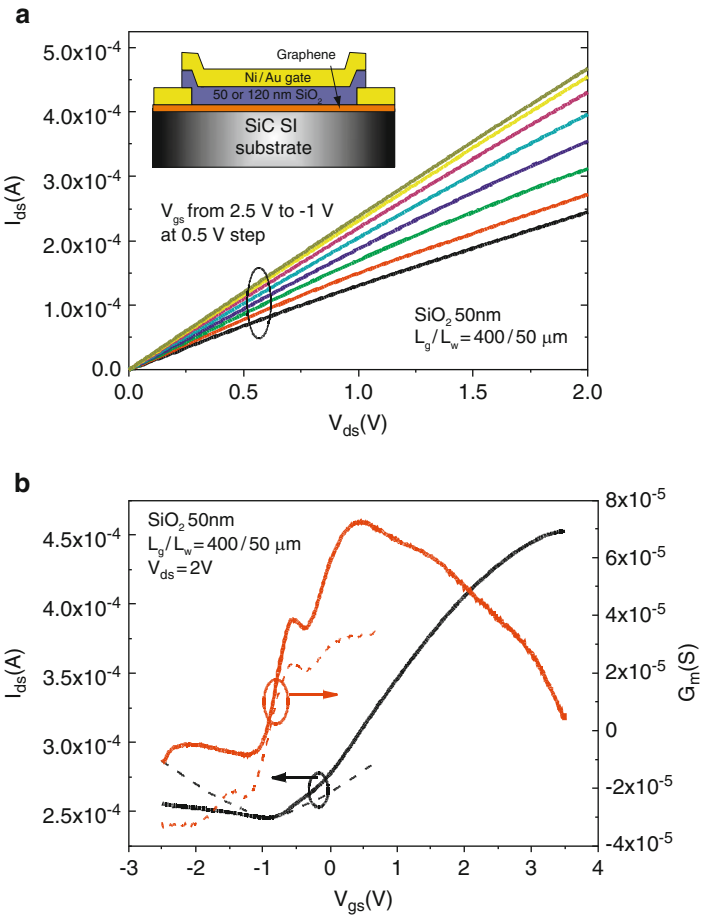

Fig. 6.7 (**a**) I_{ds} vs. V_{ds} as a function of V_{gs} on a few-layer graphene FET measured at room temperature. V_{gs} changes from 2.5 V (*top*) to 1.0 V (*bottom*) in 0.5 V steps. *Inset*: device structure of the top-gate transistor on epitaxial graphene on SiC substrate. (**b**) Transfer characteristics of the same device at $V_{ds} = 2$ V. The *dashed lines* are corrected one around Dirac point after extracting the p–n junction resistance or odd resistance component

The channel mobility can be simply estimated by:

$$\mu = \left[\left(\Delta I_d / V_{ds}\right) / \left(L_w / L_g\right)\right] / C_{ox} \Delta V_{gs} \tag{6.1}$$

using the surface-channel device formula. Here, C_{ox} is determined by $\varepsilon_0 \varepsilon_r A/d$, where ε_0 is the permittivity of free space, ε_r is 3.0 for PVD SiO_2 without annealing, A is the cross-sectional area, and d is the gate oxide thickness. The extracted electron effective mobility is as high as $5,400\,\mathrm{cm}^2/\mathrm{Vs}$. The device characteristics become ambipolar for low charge density near the Dirac point. A simple approach,

proposed by Huard et al., is used to further characterize the sample by extracting the p–n junction resistance [55], as shown by the dashed lines in Fig. 6.7b. The corrected electron mobility drops from 10% to 30% around Dirac point at $V_{gs} = -0.8$ V. Note that this correction is not necessary under unipolar conditions or at high charge density.

6.5 Half-Integer Quantum Hall-Effect in Epitaxial Graphene

Recent reports of large-area epitaxial graphene by thermal decomposition of SiC wafers have provided the missing pathway to a viable electronics technology [4–9]. An interesting question that remains to be addressed is whether the electrical properties of epitaxial graphene on SiC are similar to those in exfoliated graphene films [1–3]. For example, the well-known quantum Hall-effect (QHE), a distinguishing feature or hallmark of a 2D electronic material system, has been observed only very recently in epitaxial graphene on both the Si-face [33, 41, 42] and the C-face [43] of SiC. This question is discussed in this section.

Graphene layers on the Si-face of SiC, with a one-nanometer fully oxidized Al seeding layer grown by ALD to form an Al_2O_3 gate dielectric, were used to examine transport properties. The graphene growth temperature and time were 1,600°C for 10 min in a vacuum of 10^{-5} mbar. Standard Hall-bar devices for magneto-transport measurements were fabricated. Four-point magneto-transport measurements were performed in a variable temperature (0.4 K to 70 K) ^{3}He cryostat in magnetic fields up to 18 T using standard low frequency lock-in techniques. The external magnetic field (B) was applied normal to the graphene plane. Figure 6.8a shows the magneto-resistance R_{xx} and the Hall resistance R_{xy} as a function of magnetic field B from -18 T to 18 T at 0.8 K. From the Hall slope, the electron density is determined to be $1.04 \times 10^{12}/\text{cm}^2$ and Hall mobility of $3{,}580\,\text{cm}^2/\text{Vs}$ at 0.8 K. No significant mobility degradation is observed after ALD gate dielectric. At high magnetic fields, R_{xy} exhibits a plateau while R_{xx} is vanishing, which is the fingerprint of the QHE and SdH oscillations. One well-defined plateau with value $(h/2e^2)$ is observed at $|B| > 15.5$ T, while two higher-order plateaus are developing with values of $(h/6e^2)$ and $(h/10e^2)$, respectively. The pronounced SdH oscillations with at least four distinguishable peaks are also observed at the corresponding magnetic fields. The precision of the plateau is better than 1 part in 10^4 within the instrumental uncertainty. It shows the QHE in epitaxial graphene is also applicable for metrology applications. The R_{xy} quantization in this epitaxial graphene film is in accordance with $[h/(4n+2)e^2]$, where n is the Landau level index, found in exfoliated graphene as a distinguishing feature of Dirac electrons. It is significantly different from conventional Fermi electrons with plateaus of (h/ne^2). The observed well-defined half-integer QHE reproduces the unique features observed in exfoliated single-layer graphene including a Berry phase of π. The observed QHE on this epitaxial graphene confirms that epitaxial graphene on SiC (0001) and exfoliated single-layer

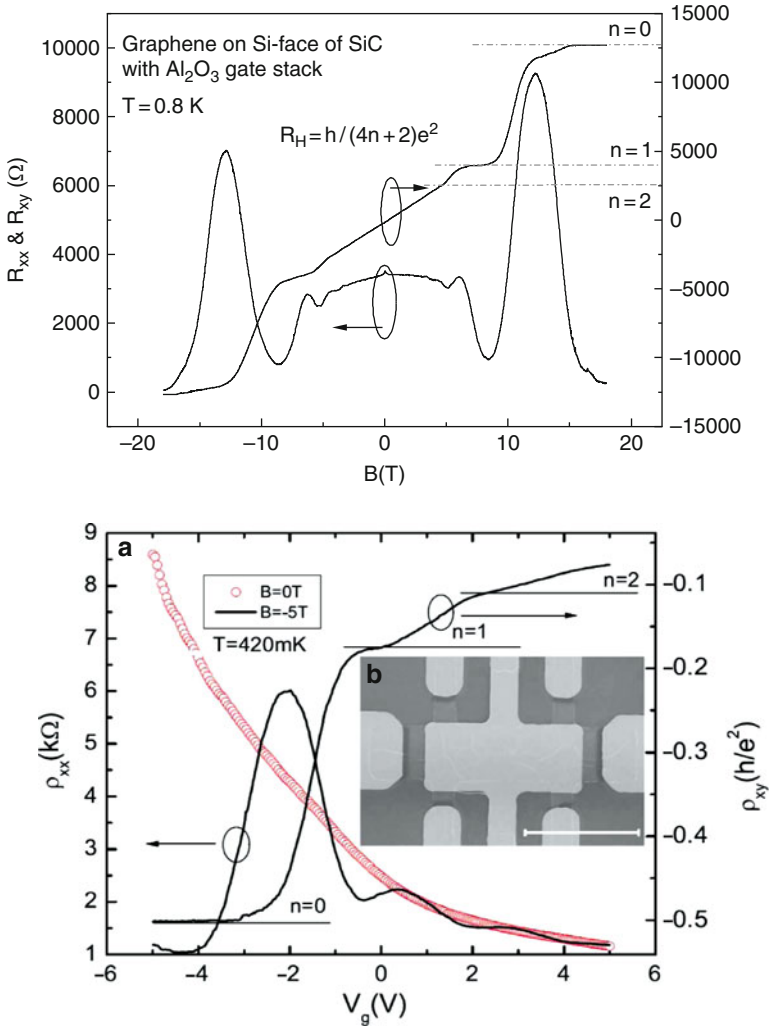

Fig. 6.8 (**a**) Hall resistance and magneto-resistance measured in the device at $T = 0.8\,\mathrm{K}$ and with floating gate bias. The *horizontal dashed lines* corresponding to $h/(4n + 2)e^2$ values. The QHE of the electron gas in epitaxial graphene is shown one quantized plateau and two developing plateau in R_{xy}, with vanishing R_{xx} in the corresponding magnetic field regime. (**b**) Four-terminal resistance as a function of top gate bias (V_g) of the device, grown at 1,600°C in vacuum on SiC (0001), measured at 420 mK with zero magnetic field (*open circles*) and −5 T (*solid lines*). *Inset*: SEM image of a fabricated device. The scale bar is 20 μm

graphene are governed by the same relativistic physics with Dirac particles as transport carries [1–3].

Similar four terminal longitudinal resistivity ρ_{xx} and Hall resistivity ρ_{xy} can also be measured at a constant high magnetic field by changing the carrier density.

Figure 6.8b shows the magneto-transport measurement for a similar device at 420 mK, where the top gate is varied between −5 V and 5 V. At zero magnetic field, ρ_{xx} drops from ∼8.6 kΩ to ∼1.2 kΩ, with an on–off ratio of ∼7. The increase of ρ_{xx} with the decrease of V_g confirms the initial n-type doping of the graphene channel. So far, in this bias range, the Fermi level cannot sweep through the charge neutrality point, due to the heavy doping during the initial graphene growth. At −5 T, most remarkably, ρ_{xy} exhibits clearly quantized plateaus at $h/2e^2$, $h/6e^2$ for electrons accompanied with the minimum in ρ_{xx}, and the higher order plateaus are developing. It leads to the same conclusion as described above that monolayer graphene can be formed on SiC (0001) surface and its electrical property is the same as the exfoliated single-layer graphene governed by the relativistic physics with Dirac fermions as transport carriers.

Applying negative bias can dramatically decrease the carrier density, and makes the low filling factor QHE more easily visible. This approach is exploited by biasing the device at −5 V, which corresponds to an electron density of $2.2 \times 10^{11}/\text{cm}^2$ and mobility of $3,250\,\text{cm}^2/\text{Vs}$ at 420 mK, and measuring the temperature dependence of ρ_{xx} and ρ_{xy} as shown in Fig. 6.9. Note that ρ_{xx} does not fully vanish at high magnetic field even at the lowest temperature. We ascribe this observation to the defect induced scattering that broadens the Landau level and the relatively large contact resistance, which is more than 10 kΩ μm caused by the fabrication process. Nevertheless, the $n = 0$ quantum Hall plateau and the corresponding SdH minimum are still pronounced, even at temperatures as high as 70 K, reaching the liquid nitrogen temperature. More efforts on measuring the same device at room temperature (not shown) reveal the modulation in ρ_{xx} and saturation in ρ_{xy} at 18 T. We believe with further engineering on the device fabrication as well as graphene film growth, it is very possible to observe the $n = 0$ quantum Hall plateau at room temperature and reasonable magnetic field. Room temperature QHE on

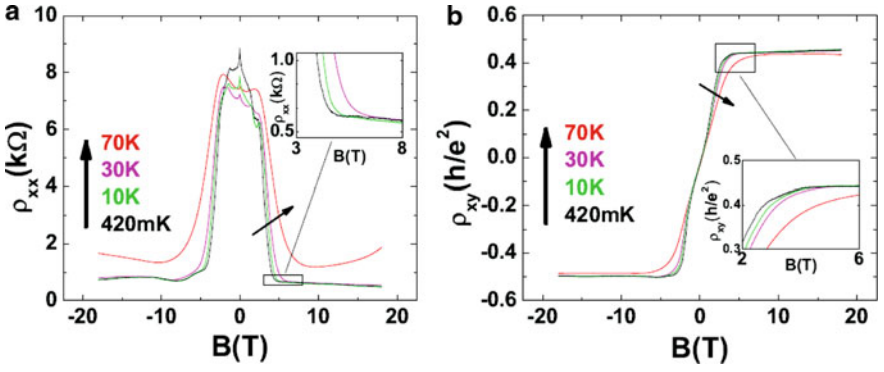

Fig. 6.9 Temperature dependence of ρ_{xx} and ρ_{xy} at $V_g = -5$ V. (**a**) Pronounced SdH minimum remain up to 70 K. (**b**) Pronounced $n = 0$ quantum Hall plateau remains up to 70 K. It is expected to remain up to room temperature

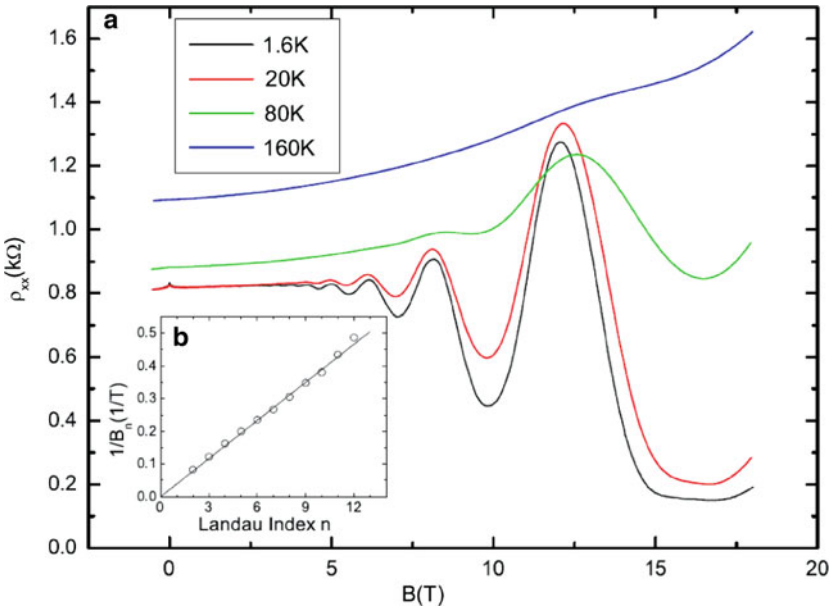

Fig. 6.10 (**a**) Temperature dependence of ρ_{xx} for a device, grown at 1,600°C and 10 mbar argon ambient, at $V_g = 1.8$ V from 1.6 K to 160 K. (**b**) Landau plot of the maximum of the SdH oscillations up to 18 T at 1.6 K. n is the Landau index and B_n is the magnetic field at the corresponding maxima of the oscillations. The *circles* are the experimental data and the *solid line* is the linear fitting. The zero y intercept indicates the Berry's phase of π [3]

epitaxial graphene could be an interesting topic as a quantum resistance standard for metrology applications [42].

To further understand the underlying physics, Landau plot, e.g., the Landau index vs. the inverse of the magnetic field, is investigated as shown in Fig. 6.10b. Here, we start with a sample grown at 1,600°C in a 10 mbar argon ambient, which has a much higher electron density, while more suitable for this purpose due to its more pronounced SdH oscillation peaks, as shown in Fig. 6.10a. The Landau index data are taken at the maximum of the SdH oscillations up to 18 T at 1.6 K. The open circles are the experimental data and the solid line is the linear fitting. The zero y intercept indicates the Berry's phase of π, the hallmark feature for monolayer graphene in electrical transport. From the slope, we can find the carrier density to be $2.46 \times 10^{12}/\text{cm}^2$, consistent with $2.37 \times 10^{12}/\text{cm}^2$ deduced from the Hall slope.

The damping of the SdH oscillations in Fig. 6.10a is caused by thermal broadening of Landau levels. The temperature dependence of the relative peak amplitudes in graphene is given by [56]:

$$A_n(T)/A_n(0) = t_k/\sin ht_k, \tag{6.2}$$

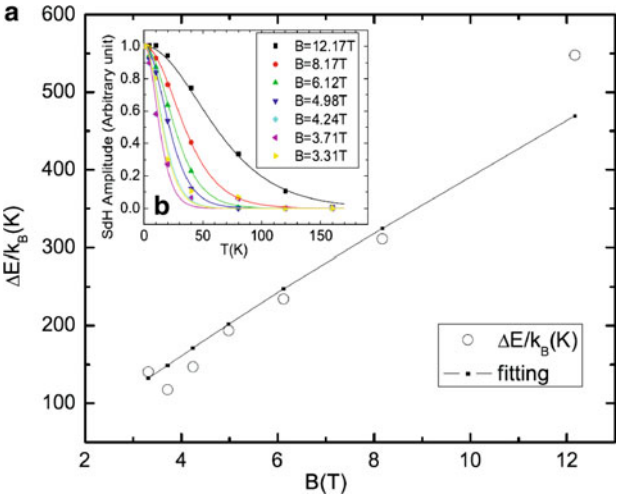

Fig. 6.11 (**a**) Fitting to the Fermi velocity v_F according to the Landau level separation. (**b**) Relative SdH peak fitting according to (6.1) for different temperatures at each peak

where $A_n(T)$ is the relative peak amplitude of the nth SdH peak at temperature T, and $t_k = 2\pi^2 k_B T/\Delta E(B)$ with:

$$\Delta E(B) = E_{n+1}(B) - E_n(B) \tag{6.3}$$

$$= \left(\sqrt{n+1} - \sqrt{n}\right) v_F \sqrt{2eB\hbar} \tag{6.4}$$

the Landau level separation (Fig. 6.11). The experimental value of Landau level separation is determined by fitting the relative SdH peaks according to (6.2) for different temperatures at each peak, as shown in Fig. 6.10b. The relative amplitude is normalized for each peak, for better viewing. The corresponding $\Delta E(B)$ is plotted versus B as the open circles in Fig. 6.10a. The dotted line is the fitting of $\Delta E(B)$ versus B according to (6.4). The fitted v_F is 1.01×10^8 cm/s. Similar analysis were carried out for two other devices grown at 1,600°C SiC (0001) in vacuum, with $v_F = 1.05 \times 10^8$ cm/s and 9.94×10^7 cm/s, respectively. The fitted Fermi velocity agrees remarkably well with the accepted value of $v_F = 1.00 \times 10^8$ cm/s for graphene.

In the center of the impurity broadened Landau level, the localization length ξ, i.e., the spatial extension of the electron wave function, diverges as a power law $\xi \approx (E - E_c)^{-\upsilon}$ with a universal critical exponent υ [57], where E_c is the energy of a Landau level center. Since E_c varies as the B varies, the derivatives $(d\rho_{xy}/dB)^{max}$ between the plateau to plateau transition, and the half-width in ρ_{xx} which is defined as the distance ΔB between the two extreme in $d\rho_{xy}/dB$, provide the experimental measure of the delocalization phenomenon in the integer quantum Hall regime [57]. It has been found that, below a certain characteristic temperature T_{sc}, $(d\rho_{xy}/dB)^{max} \approx T^{-\kappa}$ and $\Delta B \approx T^{\kappa}$, where $\kappa \approx 0.42$ is

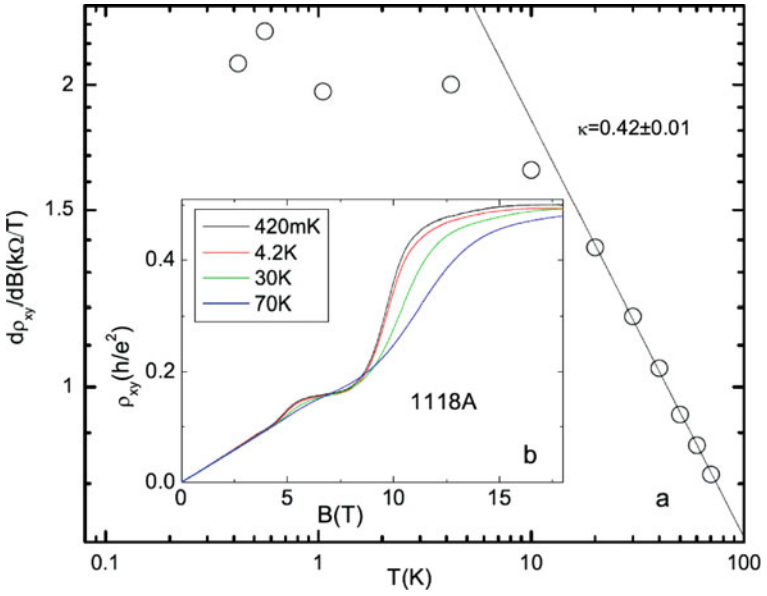

Fig. 6.12 The derivative $(d\rho_{xy}/dB)^{max}$ as a function of temperature for the $n = 1$ plateau to $n = 0$ plateau transition of sample 1,118 A. The *open circles* are the experiment data and the *solid line* is the fitting for the highest 6 temperature points. (**b**) ρ_{xy} of sample 1,118 A from 420 mK to 70 K at $V_g = 0$ V

universal for conventional 2D systems [57–59], and exfoliated graphene [60]. Here, we demonstrate that the universal scaling behavior also holds for epitaxial graphene. Compared to the other conventional 2D systems, graphene T_{sc} is much high than the very low temperature (mK), thus allowing us to probe the same physics at temperatures higher than liquid helium temperature.

Figure 6.12 shows the temperature dependent quantum Hall-effect from 420 mK to 70 K at $V_g = 0$ V for a sample grown at 1,600°C on the Si-face of SiC. Since this specific sample shows the best plateau to plateau transition, it is a good starting point to analyze the scaling behavior. Figure 6.12 shows the temperature dependent derivative $(d\rho_{xy}/dB)^{max}$ for the $n = 1$ plateau to $n = 0$ plateau transition of the same sample. The open circles are the experiment data and the solid line is the fitting for the highest 6 temperature points. As the temperature drops down, $(d\rho_{xy}/dB)^{max}$ starts to saturate, showing that ξ is not dominated by temperature, but rather by an intrinsic length scale, possibly equivalent to the sample size [57–59]. The slope shows $\kappa = 0.42 \pm 0.01$ agrees remarkably well with the accepted universal value of 0.42. We did detailed studies on two devices with B sweeps and another two devices with gate bias sweeps. All four devices show the near universal value of 0.42 on the filling factor 2 to 6 transitions.

6.6 Ballistic and Coherent Transport on Epitaxial Graphene

Antidot arrays are interesting structures to study because of their transport properties in conducting electronic materials. Antidots can be regarded as groups of imposed scattering centers that limit the ballistic transport or the mean free path of carriers [61]. Antidot arrays can also be considered as an ensemble of Aharonov–Bohm (AB) rings connected together [62]. Moreover, antidot arrays are ideal for investigating quantum coherence effects and phase coherence length of carriers. Antidot arrays impose lateral potential barriers that could create a bandgap in graphene [63], similar to the creation of the energy gap by introducing lateral periodic potentials from positive ion cores in a real semiconductor crystal. We have studied the magneto-transport properties of nanostructured antidot arrays in epitaxially grown graphene films on SiC $(000\bar{1})$. Pronounced AB oscillations, weak localization, and commensurability oscillations are observed, directly related to the electrical characteristics of epitaxial graphene films such as mean free path and phase coherence length.

The device structure of the fabricated graphene antidot array is shown in Fig. 6.13a, b. The graphene film for this particular experiment was grown at 1,600°C in vacuum for 10 min on C-face of SiC substrate. Device isolation and antidot formation of the graphene film is realized by O_2 plasma based dry etching with electron-beam-lithography (Vistec VB-6 UHR-EWF) defined HSQ resist as the protection layer. The diameter of the holes is around 40 nm and the defined antidot array period is 80 nm. Ti/Au metallization is used to form the two terminal Ohmic contacts on graphene film. Two-point resistance measurements are performed in a variable temperature (0.4 K to 70 K) ^{3}He cryostat in magnetic fields up to 18 T using low frequency lock-in techniques. The external magnetic field (B) is applied normally to the graphene plane.

Figure 6.13c shows the magneto-conductance $G(B)$ of graphene antidot arrays as a function of perpendicular magnetic field at 0.47 K. The trace is essentially symmetric, $G(B) = G(-B)$, which is the reciprocity relation mandatory for a two-terminal measurement of a stable device. There are three distinguishing features of the measured magneto-conductance. The first is the pronounced weak localization dip around zero magnetic field. The second is distinct conductance minima at ± 4 T and ± 8 T. We attribute these minima to the commensurability between the cyclotron orbits of carriers in certain magnetic fields and the period of artificial holes as illustrated in Fig. 6.13b. There are three distinct types of carriers involved in magneto-transport in antidot arrays: pinned orbits, drifting orbits, and scattering orbits [61]. Pinned orbits remain localized about their orbit centers as shown in Fig. 6.13b and cannot contribute to transport. Pinned orbits play a central role here since they remove a fraction of carriers from the transport process. The magneto-conductance shows minima when the carriers with pinned orbits are trapped in this antidot array. Using the commensurability relation $2R_c = 2\sqrt{\pi N_s}(\hbar/eB) = a$, the carrier density N_s is determined to be $\sim 7.5 \times 10^{12}/\text{cm}^2$ within the right range for graphene films grown on C-face SiC, where R_c is the

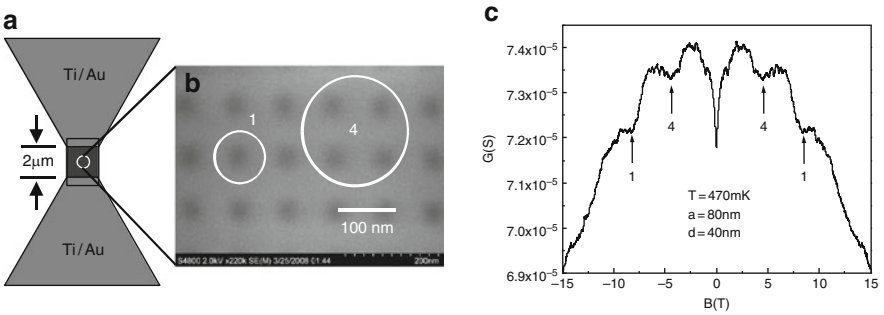

Fig. 6.13 (**a**) The sample layout with $2\,\mu\text{m} \times 2\,\mu\text{m}$ graphene area and two-terminal metal contacts. (**b**) Electron microscopic image of antidote arrays with ∼40 nm holes and ∼80 nm pitches. The commensurate orbits around 1 antidot and 4 antidots are sketched to illustrate the physical origin of Weiss oscillations. (**c**) Magneto-conductance of the graphene antidote arrays measured at $T = 477$ mK. On top of the commensurability oscillations, periodic features are clearly visible as also highlighted in Fig. 6.14a

cyclotron radius, h is the Planck constant, and a is the period of antidot arrays. The elastic mean free path l_e is estimated to be about 220 nm in a reference sample without antidots. The elastic mean free path is $l_e = 2D/v_F$, where the carrier diffusive constant $D = E_F/2N_s e^2\rho$, Fermi energy $E_F = \hbar v_F\sqrt{\pi N_s}$, and ρ is zero-field resistivity of graphene films [4]. The l_e is larger than the circumference of a single antidot (∼125 nm), but slightly smaller than the circumference of the central pinned orbits (∼250 nm). The conclusion from this estimate is that transport is not fully ballistic. The reason for the observation of the second magneto-conductance minima, corresponding to the pinned orbits around four antidots and requiring a much larger l_e, is not clear. Another possibility is magnetic focusing related phenomenon localized with the nanostructures of 40 nm dimension. The third feature is the tiny structures superimposed on the measured trace, for example, between ±2 T and ±7 T. Universal conductance fluctuations are suppressed since the sample size (∼2 μm) is much larger than the phase coherence length. A quantum interference effect is still observable because the antidot size (∼40 nm) is smaller than the phase coherence length. These tiny periodic features are identified as AB oscillations, which are related with each magnetic quantum flux penetrating in one antidot cell. AB oscillations on an exfoliated graphene film have been demonstrated experimentally on a single lithographically defined ring [64].

The black thick curve in Fig. 6.14a shows the measured magneto-conductance between +2 and +12 T with superimposed oscillatory features. By taking the difference of the measured curve and the black baseline curve obtained from smoothing the measured one, a pronounced AB periodically oscillatory curve is exhibited as shown as the grey curve in Fig. 6.14a. The AB oscillation period $\Delta B \approx 0.5$ T in this field range is consistent with the condition that the magnetic flux enclosed within the unit cell of the square antidot lattice changes by a single magnetic flux quantum, i.e., $\Delta B = (h/e)/a^2$ with $a = 80$ nm. The rms amplitude

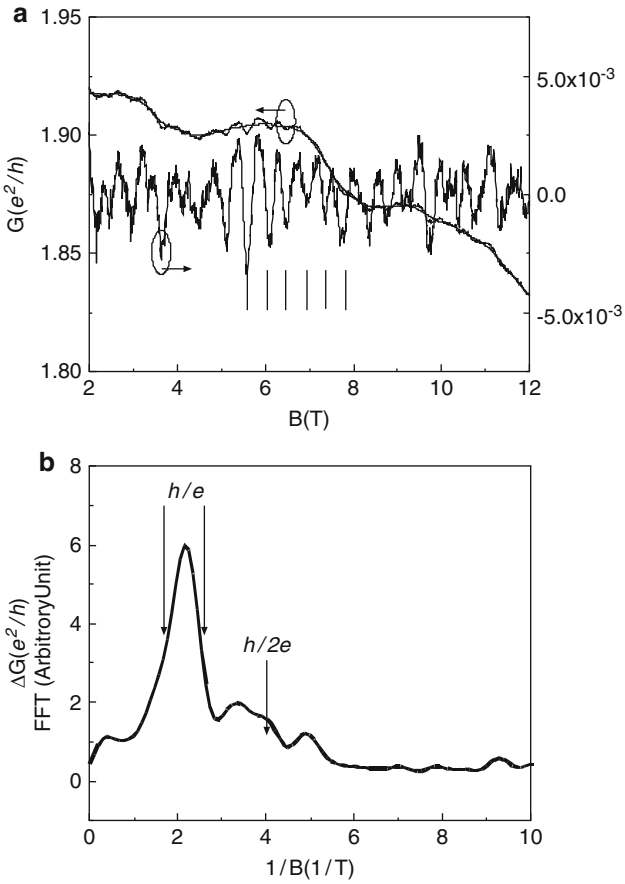

Fig. 6.14 (**a**) The *solid curve* is the measured magneto-conductance. The *thin curve* is the "baseline" after smoothing the original measured curve. The *periodically oscillatory curve* is the subtraction of the two black curves. *Vertical straight lines* are guided by eyes showing periodic B feature of observed AB oscillations. (**b**) Fourier spectrum of the oscillatory *grey curve* between 2 T and 12 T. The *solid curve* is after 6 points smoothing. The two *vertical straight lines* with *arrows* indicate the positions for half-height of the observed h/e peak, as used for the calculation of the inner and outer radii of AB-"ring" structure around one antidot

of AB oscillations is $\sim 0.01e^2/h$. For detailed discussions, Fig. 6.14b illustrates the Fourier power spectrum of Fig. 6.14a with a broad peak centered around 0.47 T, with 0.57 T and 0.40 T as the edge of the half-height width. It corresponds to the inner radius, middle radius, and outer radius of 48 nm, 53 nm, and 57 nm, respectively, if $\Delta B = (h/e)/(\pi r^2)$, where πr^2 is associated with the effective antidot area. It is consistent with the designed geometry well with 40 nm holes and 80 nm pitches. The relatively large inner radius could be related with overdeveloped resist patterns, plasma over-etching, and certain depletion length of graphene edges with

unpassivated dangling bonds. The magnetic length [$l_B = \sqrt{\hbar/eB} = 9.2\,\text{nm}$ at $B = 6\,\text{T}$] or similar edge channels in the quantum Hall regime could also affect the data. The observed AB oscillations demonstrate that the epitaxial graphene on SiC is of high-quality and at least has the quantum coherence length larger than 80–100 nm. The weak peak features around $1/B = 4(1/T)$ could be related to $h/2e$ oscillations [64].

While universal conductance fluctuations are generally observed in small graphene flakes, weak localization correction is strongly reduced compared to the conventional two-dimensional (2D) systems due to suppressed backscattering in graphene loosely coupled to the substrate [65–67]. Short range scattering in epitaxial graphene caused by tight binding to the substrate, short range scattering on the edges of antidots, and warping of the Fermi surface at high densities introduces intervalley scattering [68], which restores weak localization corrections [69]. We observe pronounced negative magneto-resistance at low fields with a sharp cusp at zero field characteristic of weak localization in 2D, as in Fig. 6.15a. Moreover, at higher fields magneto-resistance changes sign, which is expected for the case of strong

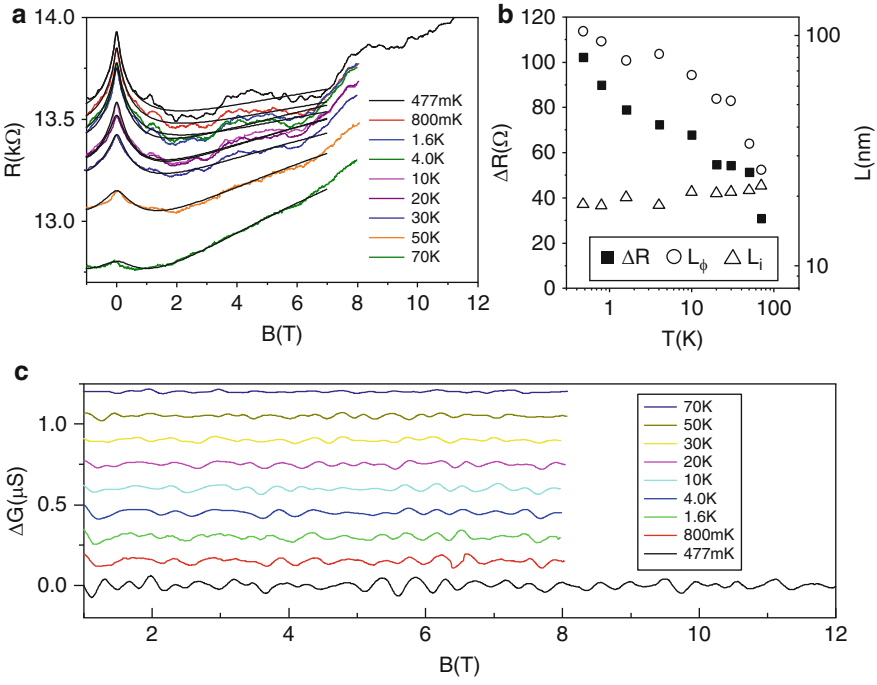

Fig. 6.15 (**a**) Magneto-resistance as a function of the sample temperature from 477 mK up to 70 K. The *solid black curves* are fitted weak localization curves in antidot arrays [70]. (**b**) The coherence length L_Φ and intervalley scattering length L_i of graphene film with antidot arrays versus sample temperatures. (**c**) Temperature dependence of AB oscillations. The traces are vertically shifted for clarity

intervalley scattering [70]. We used the theory developed in [70] to analyze the data and extract both the phase coherence length L_Φ and the intervalley scattering length L_i, shown in Fig. 6.15b. L_i is found to be temperature independent and is approximately equal to the distance between antidots, suggesting that scattering on the antidot edges is the dominant intervalley scattering mechanism in our samples. L_Φ decreases with the increasing temperature, although it does not follow $1/T$ dependence found in unpatterned graphene [68]. We note that the range of field, where weak localization is observed in antidot arrays is much larger than that for unpatterned samples. The temperature dependence of AB oscillations is also plotted in Fig. 6.15c, which is consistent with the data in Fig. 6.15b of weak localization peak fitting.

The intrinsically weak anti-localization of graphene and the restoring of weak localization by defects are of interest to further investigate and unveil the quality of epitaxial graphene. We have studied weak localization on unpatterned epitaxial graphene on SiC (0001). Figure 6.16b shows $\Delta\rho_{xx} = \rho_{xx}(B) - \rho_{xx}(B = 0\,\mathrm{T})$ with $V_g = 1.8\,\mathrm{V}$ at various temperatures for a sample grown at 1,600°C in a 10 mbar argon ambient. At the lowest temperature (e.g., 1.6 K), an overall negative magneto-resistance at low B is observed, typical of weak localization [71]. Although weak

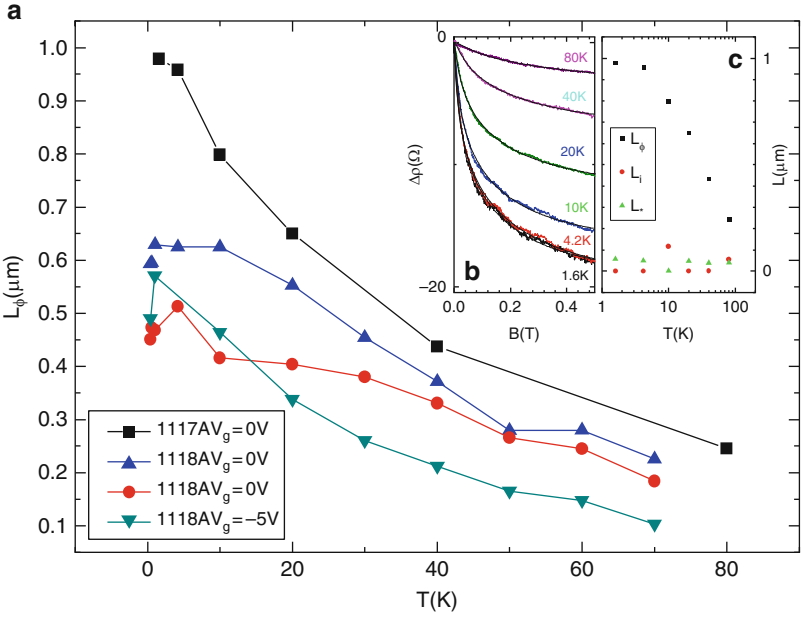

Fig. 6.16 Weak localization. (**a**) Phase coherent length for different devices. The corresponding electron densities are 2.0×10^{11} (bottom), 7.7×10^{11}, 1.0×10^{12}, and $2.4 \times 10^{12}/\mathrm{cm}^2$. (**b**) Magneto-resistance $\Delta\rho_{xx} = \rho_{xx}(B) - \rho_{xx}(B = 0\,\mathrm{T})$ of sample 1,117 A for $V_g = 1.8\,\mathrm{V}$ at various temperatures. The *colored curves* are experiment data, and the *black curves* are the fit. (c) Extracted characteristic lengths from the weak localization as a function of temperature for sample 1,117 A

localization in graphene is usually strongly reduced compared to the conventional 2D systems due to suppressed backscattering, strong intervalley scattering in epitaxial graphene tends to restore weak localization [69, 70, 72, 73]. We have fitted our experimental data using a theory developed by McCann et al. as before [70], and extracted the L_Φ (phase coherence length), L_i (intervalley scattering length), and L_* (intravalley scattering length) for each temperature as shown in Fig. 6.16c. Notice that all three lengths are much smaller than the sample size, indicating the edge is not the dominant scattering source, but rather disorder within the sample dominates scattering. L_Φ increases with decreasing temperature and reaches $\sim$1 μm at 1.6 K, while L_i and L_* are rather temperature insensitive. The extremely short L_i (a few nm) indicates a strong coupling of the single layer graphene to the SiC substrate, significantly different from the case studied in antidot case described in the above paragraphs or in [74], where the multi-layer graphene on the C-face SiC is relatively loosely coupled to the substrate, and the intervalley scattering arose mostly from the shape edges created by the antidot arrays. L_* here is about 40–50 nm, much larger than L_i, indicate moderate amount of other source of disorder larger than atomic scale. Similar analysis was also carried out for other devices grown at 1,600°C in vacuum. They show the similar temperature dependence and the extracted L_Φ are plotted against temperature for all devices as in Fig. 6.16a. They all decrease with the increase of the temperature, and decrease with decreasing carrier density across different samples, due to the effect of enhanced electron–electron interactions [72].

6.7 Spin Transport on Epitaxial Graphene

Spin transport in graphene has attracted intensive interest [75–78] in recent years for potential applications in spintronics due to its weak spin–orbit and hyperfine interactions [79]. In this session, we report on the first SpinFET (spin valve transistor) fabricated on an epitaxial graphene film grown on the C-face of a SiC substrate by high-temperature sublimation. Spin dependent magneto-resistance (MR) is observed from 400 mK to 3 K, showing a maximum spin signal of 0.25% and a maximum spin relaxation length of 200 nm at 400 mK. The multi-layer graphene film investigated here was formed on the C-face SiC at 1,550°C. AFM and SEM inspection confirms that it is possible to have a 2–10 μm domain size atomically smooth graphene films at that growth temperature as described in Sect. 6.2. Figure 6.17a shows the SEM image of one of the fabricated $Ni_{0.80}Fe_{0.20}$/Gr spin valve devices. All patterns were defined by electron-beam lithography. Ti/Au bonding pads were deposited on the graphene film, followed by an oxygen plasma dry etching to isolate the central graphene area with a width (W) of 2 μm and a length of 5 μm. Two $Ni_{0.80}Fe_{0.20}$ electrodes were evaporated for spin injection and detection. They are 400 nm and 1 μm wide, with a separation gap (L) of 400 nm.

Figure 6.17b presents a typical spin dependent MR measured at 400 mK. The magnetic field is applied parallel to the ferromagnetic electrodes and swept firstly from +0.5 T to −0.5 T and then from −0.5 T to +0.5 T. The MR curve exhibits a

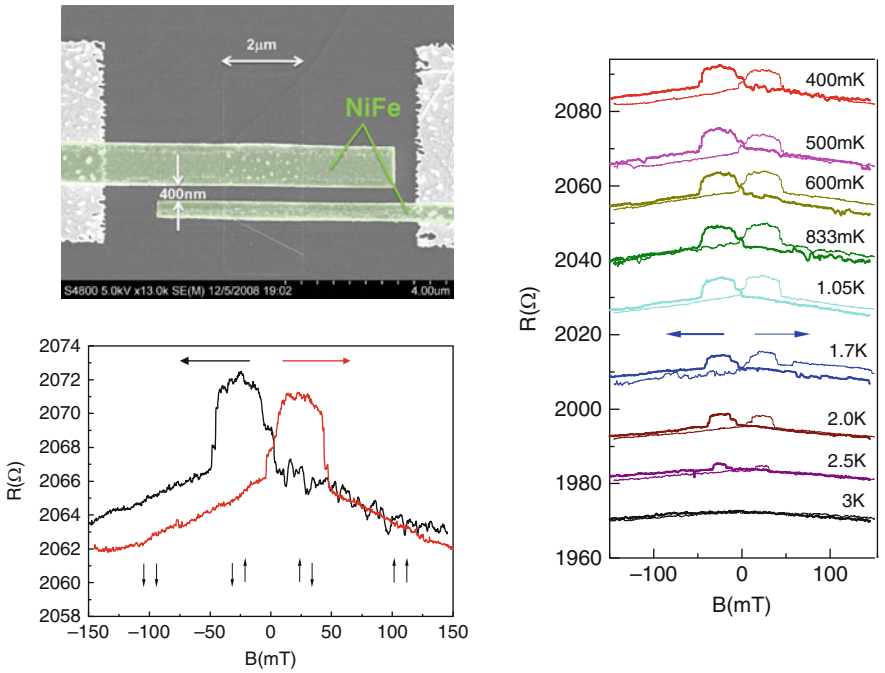

Fig. 6.17 (**a**) SEM image of a SpinFET fabricated on the epitaxial graphene film on SiC. (**b**) MR of the spin valve device measured at 400 mK. The magnetic field is aligned parallel to the ferromagnetic electrodes. The *small vertical arrows* show the magnetization of electrodes at different B fields. *Horizontal arrows* indicate the B field sweep polarity. (**c**) MR of the spin valve device measured at different temperatures from 400 mK to 3 K. The curves are shifted vertically for clarity

clear spin-valve hysteresis loop with a steep change at around ± 5 mT and ∓ 50 mT. The increase of MR is due to the magnetization reversal of the wider ferromagnetic electrode. The switch can occur before the zero-field condition due to multi-domains in the ferromagnetic electrodes, as discussed in [80].

A pronounced temperature dependence of the MR is observed in Fig. 6.17c. The curves are shifted vertically for clarity. As can be seen, both the magnitude and the width of the spin signals decrease as the temperature increases, and eventually disappears at 3 K. The spin relaxation length (λ_{sf}) can be estimated from the magnitude of the spin signals. The graphene sheet resistance (ρ) is estimated to be $\sim 1\,k\Omega/sq$ and $\sim 200\Omega$ in this device. However, the total resistance is $\sim 2\,k\Omega$. The contact resistance is much larger than the spin resistance [81, 82]. The large contact-resistance suggests the $Ni_{0.80}Fe_{0.20}$/graphene junctions could be quasi-tunneling like. XPS studies of the $Ni_{0.80}Fe_{0.20}$/graphite interface indicates that C–O bonds are formed if $Ni_{0.80}Fe_{0.20}$ is deposited on a DI water exposed surface. Assuming that the interfacial C–O bonding leads to tunneling-like spin injection, the spin signal for a local measurement on 2D system can be described simply as,

$R_s = 2P^2\lambda_{sf}\rho e^{-L/\lambda sf}/W$, where the spin polarization P is 0.48 for $Ni_{0.80}Fe_{0.20}$ [81, 82]. The low-limit estimated λ_{sf} versus temperature is 200 nm at 0.4 K and 100 nm at 3 K. The reproducible step-like features are observed on up and down slopes of MR around ± 5 mT and ∓ 50 mT. These may be related with a sequence of mesoscopic domain switching in the ferromagnetic electrodes. The origin of the observed strong temperature-dependent spin effect in graphene is not fully understood. More work are needed on synthesis, process optimization, and physical understanding for an epitaxial graphene SpinFET operating at room temperature.

6.8 Summary

We have systematically studied graphene synthesis on SiC substrates by high-temperature sublimation in vacuum and argon ambient. Monolayer graphene on Si-face of SiC with a room-temperature mobility of 1,500–2,500 cm^2/Vs and multi-layer graphene on C-face of SiC with a mobility of 5,000–18,000 cm^2/Vs are obtained. A high-k gate stack on epitaxial graphene is realized by inserting a fully oxidized nanometer thin aluminum film as a seeding layer followed by an atomic-layer deposition process. The QHE and SdH in epitaxial graphene on SiC (0001) are systematically studied at different temperatures and different top gate bias. This quantum experiment confirms that epitaxial graphene on SiC shares the same relativistic physics as the exfoliated graphene, and the universal scaling in plateau to plateau transition also holds for epitaxial graphene films. Ballistic and coherent transport properties are studied through graphene antidot arrays with the pronounced AB oscillations. SpinFET is also demonstrated at low temperature on epitaxial graphene. All the work shows that epitaxial graphene on SiC provides a platform for future microelectronic and nanoelectronic applications beyond what exfoliated graphene can offer.

Acknowledgements The authors would like to thank the close collaborations with J.A. Cooper, Jr., R. Reifenberger, L.W. Engel, L.P. Rokhinson, E.A. Stach, R.M. Wallace, J. Appenzeller, J.J. Gu, Y. Xuan, M. Xu, K. Xu, and A.T. Neal. The authors also would like to thank G. Jones, T. Murphy, and E. Palm at National High Magnetic Field Laboratory (NHMFL) for experimental assistance. Part of the work on graphene is supported by NRI (Nanoelectronics Research Initiative) through MIND (Midwest Institute of Nano-electronics Discovery), DARPA, and Intel Cooperation. NHMFL is supported by NSF Grant Nos. DMR-0084173 and ECS-0348289, the State of Florida, and DOE.

References

1. A.K. Geim, K.S. Novoselov, Nat. Mater. **6**, 183 (2007)
2. K.S. Novoselov, A.K. Geim, S.V. Morozov, D. Jiang, Y. Zhang, S.V. Dubonos, I.V. Grigorieva, A.A. Firsov, Science **306**, 666 (2004)
3. Y. Zhang, Y.W. Tan, H.L. Stormer, P. Kim, Nature **438**, 201 (2005)

4. C. Berger, Z. Song, X. Li, X. Wu, N. Brown, C. Naud, D. Mayou, T. Li, J. Hass, A.N. Marchenkov, E.H. Conrad, P.N. First, W.A. de Heer, Science **312**, 1191 (2006)
5. Y.Q. Wu, P.D. Ye, M.A. Capano, Y. Xuan, Y. Sui, M. Qi, J.A. Cooper, T. Shen, D. Pandey, G. Prakash, R. Reifenberger, Appl. Phys. Lett. **92**, 092102 (2008)
6. G. Gu, S. Niu, R.M. Feenstra, R.P. Devaty, W.J. Choyke, W.K. Chan, M.G. Kane, Appl. Phys. Lett. **90**, 253507 (2007)
7. J. Kedzierski, P.L. Hsu, P. Healey, P.W. Wyatt, C.L. Keast, M. Springkle, C. Berger, W.A. de Heer, IEEE Trans. Electron Devices **55**, 2078 (2008)
8. J.S. Moon, D. Curtis, M. Hu, D. Wong, C. McGuire, P.M. Campbell, G. Jerigan, J. Tedesco, B. VanMil, R. Myers-Ward, C. Edy Jr., D.K. Gaskill, IEEE Electron Device Lett. **30**, 650 (2009)
9. Y.M. Lin, C. Dimitrakopoulos, K.A. Jenkins, D.B. Farmer, H.Y. Chiu, A. Gill, P. Avouris, Science **327**, 662 (2010)
10. K.S. Kim, Y. Zhao, H. Jang, S.Y. Lee, J.M. Kim, K.S. Kim, J.H. Ahn, P. Kim, J.Y. Choi, B.H. Hong, Nature **457**, 706 (2009)
11. A. Reina, X. Jia, J. Ho, D. Nezich, H. Son, V. Bulovic, M.S. Dresselhaus, J. Kong, Nano Lett. **9**, 30 (2009)
12. Q. Yu, J. Lian, S. Siriponglert, H. Li, Y.P. Chen, S.S. Pei, Appl. Phys. Lett. **93**, 113103 (2008)
13. X. Li, X. Cai, J. An, S. Kim, J. Nah, D. Yang, R. Piner, A. Velamakanni, I. Jung, E. Tutuc, S.K. Banerjee, L. Colombo, R.S. Ruoff, Science **324**, 1312 (2009)
14. A.J. Van Bommel, J.E. Crombeen, A. Van Tooren, Surf. Sci. **48**, 463 (1975)
15. C. Berger et al., J. Phys. Chem. B **108**, 19912 (2004)
16. M.Y. Han, B. Ozyilmaz, Y. Zhang, P. Kim, Phys. Rev. Lett. **98**, 206805 (2007)
17. Z. Chen, Y.M. Lin, M.J. Rooks, P. Avouris, Physica E **40**, 228 (2007)
18. D.V. Kosynkin et al., Nature **458**, 872 (2009)
19. X. Li, X. Wang, L. Zhang, S. Lee, H. Dai, Science **319**, 1229 (2008)
20. X. Wang et al., Phys. Rev. Lett. **100**, 206803 (2008)
21. L. Jiao, L. Zhang, X. Wang, G. Diankov, H. Dai, Nature **458**, 877 (2009)
22. J. Bai, X. Duan, Y. Huang, Nano Lett. **9**, 2083 (2009)
23. X. Wang, H. Dai, Nat. Chem. **2**, 661 (2010)
24. T. Ohta, A. Bostwick, T. Seyller, K. Horn, E. Rotenberg, Science **313**, 951 (2006)
25. E.V. Castro, K.S. Novoselov, S.V. Morozov, N.M.R. Peres, J.M.B. Lopes dos Santos, J. Nilsson, F. Guinea, A.K. Geim, A.H. Castro Neto, Phys. Rev. Lett. **99**, 216902 (2007)
26. J.B. Oostinga, H.B. Heersche, X. Liu, A.F. Morpurgo, L.M.K. Vandersypen, Nat. Mater. **7**, 151 (2008)
27. Y. Zhang, T.T. Tang, C. Girit, Z. Hao, M.C. Martin, A. Zettl, M.F. Crommie, Y.R. Shen, F. Wang, Nature **459**, 820 (2009)
28. F. Xia, D.B. Farmer, Y.M. Lin, P. Avouris, Nano Lett. **10**, 715 (2010)
29. Y. Xuan, Y. Wu, T. Shen, M. Qi, M.A. Capano, J.A. Cooper, P.D. Ye, Appl. Phys. Lett. **92**, 013101 (2008)
30. X. Wang, S.M. Tabakman, H. Dai, J. Am. Chem. Soc. **130**, 8152 (2008)
31. J.R. Williams, L. DiGarlo, C.M. Marcus, Science **317**, 638 (2007)
32. S. Kim, J. Nah, I. Jo, D. Shahrjerdi, L. Colombo, Z. Yao, E. Tutuc, S.K. Banerjee, Appl. Phys. Lett. **94**, 062107 (2008)
33. T. Shen, J.J. Gu, M. Xu, Y.Q. Wu, M.L. Bolen, M.A. Capano, L.W. Engel, P.D. Ye, Appl. Phys. Lett. **95**, 172105 (2009)
34. D.B. Farmer, H.Y. Chiu, Y.M. Lin, K.A. Jenkins, F. Xia, P. Avouris, Nano Lett. **9**, 4474 (2009)
35. Q.H. Wang, M.C. Hersam, Nat. Chem. **1**, 206 (2009)
36. B. Lee, S.Y. Park, H.C. Kim, K.J. Cho, E.M. Vogel, M.J. Kim, R.M. Wallace, J. Kim, Appl. Phys. Lett. **92**, 203102 (2008)
37. L.B. Biedermann, M.L. Bolen, M.A. Capano, D. Zemlyanov, R. Reifenberger, Phys. Rev. B**79**, 125411 (2009)
38. S.E. Harrison, M.A. Capano, R. Reifenberger, Appl. Phys. Lett. **96**, 081905 (2010)
39. M.L. Bolen, S.E. Harrison, L.B. Biedermann, M.A. Capano, Phys. Rev. B **80**, 121411 (2010)

40. M.L. Bolen, T. Shen, J.J. Gu, R. Colby, E.A. Stach, P.D. Ye, M.A. Capano, J. Electron. Mater. **39**, 2696 (2010)
41. J. Jobst, D. Waldmann, F. Speck, R. Hirner, D.K. Maude, T. Seyller, H.B. Weber, Phys. Rev. B **81**, 195434 (2010)
42. A. Tzalenchuk, S. Lara-Avila, A. Kalaboukhov, S. Paolillo, M. Syvajarvi, R. Yakimova, O. Kazalova, T.J.B.M. Janssen, V. Fal'ko, S. Kubatkin, Nat. Nanotechnol. **5**, 186 (2010)
43. X. Wu, Y. Hu, M. Ruan, N.K. Madiomanana, J. Hankinson, M. Sprinkle, C. Berger, W.A. de Heer, Appl. Phys. Lett. **95**, 223108 (2009)
44. J. Drowart, G. de Maria, G. Inghram, J. Chem. Phys. **29**, 1015 (1958)
45. S.G. Davis, D.F. Anthrop, A.W. Searcy, J. Chem. Phys. **34**, 659 (1961)
46. L. Muehlhoff, W.J. Choyke, M.J. Bozack, J.T. Yates, J. Appl. Phys. **60**, 2842 (1986)
47. J. Hass, F. Varchon, J.E. Millán-Otoya, M. Sprinkle, N. Sharma, W.A. de Heer, C. Berger, P.N. First, L. Magaud, E.H. Conrad, Phys. Rev. Lett. **100**, 125504 (2008)
48. J.L. Tedesco, B. VanMil, R.L. Myers-Ward, J. Culbertson, G. Jernigan, P. Campbell, J.M. McCrate, S.A. Kitt,, C. Eddy Jr., D.K. Gaskill, ECS Trans. **19**, 137 (2009)
49. K.V. Emtsev, A. Bostwick, K. Horn, J. Jobst, G.L. Kellogg, L. Ley, J.L. McChesney, T. Ohta, S.A. Reshanov, J. Röhrl, E. Rotenberg, A.K. Schmid, D. Waldmann, H.B. Weber, T. Seyller, Nat. Mater. **8**, 203 (2009)
50. J.L. Tedesco, B.L. VanMil, R.L. Myers-Ward, J.M. McCrate, S.A. Kitt, P.M. Campbell, G.G. Jernigan, J.C. Culbertson, J.C.R. Eddy, D.K. Gaskill, Appl. Phys. Lett. **95**, 122102 (2009)
51. D.B. Farmer, R.G. Gordon, Nano Lett. **6**, 699 (2006)
52. V. Barone, O. Hod, G.E. Scuseria, Nano Lett. **6**, 2748 (2006)
53. Y.W. Son, M.L. Cohen, S.G. Louie, Nature **444**, 347 (2006)
54. K. Xu, P.D. Ye, J. Phys. Chem. C **114**, 10505 (2010)
55. B. Huard, J.A. Sulpizio, N. Stander, K. Todd, B. Yang, D. Goldbaher-Gordon, Phys. Rev. Lett. **98**, 236903 (2007)
56. V.P. Gusynin S.G. Sharapov, Phys. Rev. B **71**, 125124 (2005)
57. H.P. Wei, D.C. Tsui, M.A. Paalanen, A.M.M. Pruisken, Phys. Rev. Lett. **61**, 1294 (1988)
58. W. Li, C.L. Vicente, J.S. Xia, W. Pan, D.C. Tsui, L.N. Pfeiffer, K.W. West, Phys. Rev. Lett. **102**, 216801 (2009)
59. S. Koch, R.J. Haug, K.v. Klitzing, K. Ploog, Phys. Rev. Lett. **67**, 883 (1991)
60. A.J.M. Giesbers, U. Zeitler, L.A. Ponomarenko, R. Yang, K.S. Novoselov, A.K. Geim, J.C. Maan, Phys. Rev. B **80**, 241411 (2009)
61. D. Weiss, M.L. Roukes, A. Menschig, P. Grambow, K. von Klitzing, G. Weimann, Phys. Rev. Lett. **66**, 2790 (1991)
62. D. Weiss, K. Richter, A. Menschig, R. Bergmann, H. Schweizer, K. von Klitzing, G. Weimann, Phys. Rev. Lett. **70**, 4118 (1993)
63. T.G. Pedersen, C. Flindt, J. Pedersen, N.A. Mortensen, A.P. Jauho, K. Pedersen, Phys. Rev. Lett. **100**, 136804 (2008)
64. S. Russo, J.B. Oostinga, D. Wehenkel, H.B. Heersche, S.S. Sobhani, L.M.K. Vandersypen, A.F. Morpurgo, Phys. Rev. B **77**, 85413 (2008)
65. T. Ando, T. Nakanishi, J. Phys. Soc. Jpn 67, 1704 (1998)
66. S.V. Morozov, K.S. Novoselov, M.I. Katsnelson, F. Schedin, L.A. Ponomarenko, D. Jiang, A.K. Geim, Phys. Rev. Lett. **97**, 016801 (2006)
67. H. Suzuura T. Ando Phys. Rev. Lett. **89**, 266603 (2002)
68. A.F. Morpurgo, F. Guinea, Phys. Rev. Lett. **97**, 196804 (2006)
69. F.V. Tikhonenko, D.W. Horsell, R.V. Gorbachev, A.K. Savchenko, Phys. Rev. Lett. **100**, 056802 (2008)
70. E. McCann, K. Kechedzhi, V.I. Fal'ko, H. Suzuura, T. Ando, B.L. Altshuler, Phys. Rev. Lett. **97**, 146805 (2006)
71. C.W.J. Beenakker, H. Vanhouten, Solid State Phys. **44**, 1 (1991)
72. D.K. Ki, D. Jeong, J.H. Choi, H.J. Lee, K.S. Park, Phys. Rev. B **78**, 125409 (2008)
73. X.S. Wu, X.B. Li, Z.M. Song, C. Berger, W.A. de Heer, Phys. Rev. Lett. **98**, 136801 (2007)

74. T. Shen, Y.Q. Wu, M.A. Capano, L.P. Rokhinson, L.W. Engel, P.D. Ye, Appl. Phys. Lett. **93**, 122102 (2008)
75. E.W. Hill, A.K. Geim, K. Novoselov, F. Schedin, P. Blake IEEE Trans. Magnet **42**, 2694–2696 (2006)
76. N. Tombros, C. Jozsa, M. Popinciuc, H.T. Jonkman B.J. van Wees Nature **448**, 571–U4 (2007)
77. H. Goto, A. Kanda, T. Sato, S. Tanaka, Y. ootuka, S. Odaka, H. Muyazaki, K. Tsukagoshi, Y. Aoyagi Appl. Phys. Lett. **92**, 212110 (2008)
78. M. Nishioka A.M. Goldman Appl. Phys. Lett. **90**, 252505 (2007)
79. D. Huertas Hernando, F. Guinea, A. Brataas Phys Rev. B **74**, 155426 (2006)
80. F.J. Jedema, M.S. Nijboer, A.T. Filip, B.J. van Wees Phys. Rev. B **67**, 085319 (2003)
81. C. Jozsa, M. Popinciuc, N. Tombros, H.T. Jonkman, B.J. van Wees Phys. Rev. B **79**, 081402 (R) (2009)
82. S. Takahashi S. Maekawa Phys. Rev. B **67**, 052409 (2003)

Chapter 7
Epitaxial Graphene on Metals

Yuriy Dedkov, Karsten Horn, Alexei Preobrajenski, and Mikhail Fonin

Abstract In this chapter, we review the recent results on graphene films epitaxially grown on $3d - 5d$ transition-metal surfaces focussing mainly on their atomic structure, aspects of chemical interaction both with the substrate and with adsorbates and the electronic structure of graphene at the interface. We discuss a possibility to prepare sandwich-like structures in the form of intercalates as a possible way to controllably tailor the electronic properties of graphene. Recent works on the templated growth of metallic nanostructures on graphene moiré are also reviewed.

7.1 Introduction

Graphene is a flat single layer of carbon atoms arranged in a honeycomb lattice with two crystallographically equivalent atoms (A and B) in its primitive unit cell [1–3] [Fig. 7.1a]. The sp^2 hybridization between one $2s$ orbital and two $2p$ orbitals leads to a trigonal planar structure with a formation of strong σ bonds between carbon atoms that are separated by 1.42 Å. The bonding σ orbitals have a filled shell and, hence, form deeper valence band levels. The $2p_z$ orbitals on the neighboring carbon atoms are perpendicular to the planar structure of the graphene layer and can bind covalently, leading to the formation of a π band. The unique property

Y. Dedkov (✉) · K. Horn
Fritz-Haber-Institut der Max-Planck-Gesellschaft and SPECS Surface Nano Analysis GmbH, Berlin, Germany
e-mail: dedkov@fhi-berlin.mpg.de; horn@fhi-berlin.mpg.de

M. Fonin (✉)
University of Konstanz, Germany
e-mail: mikhail.fonin@uni-konstanz.de

A. Preobrajenski
MAX-lab, Lund University, Sweden
e-mail: alexeip@maxlab.lu.se

H. Raza (ed.), *Graphene Nanoelectronics*, NanoScience and Technology,
DOI 10.1007/978-3-642-22984-8_7,

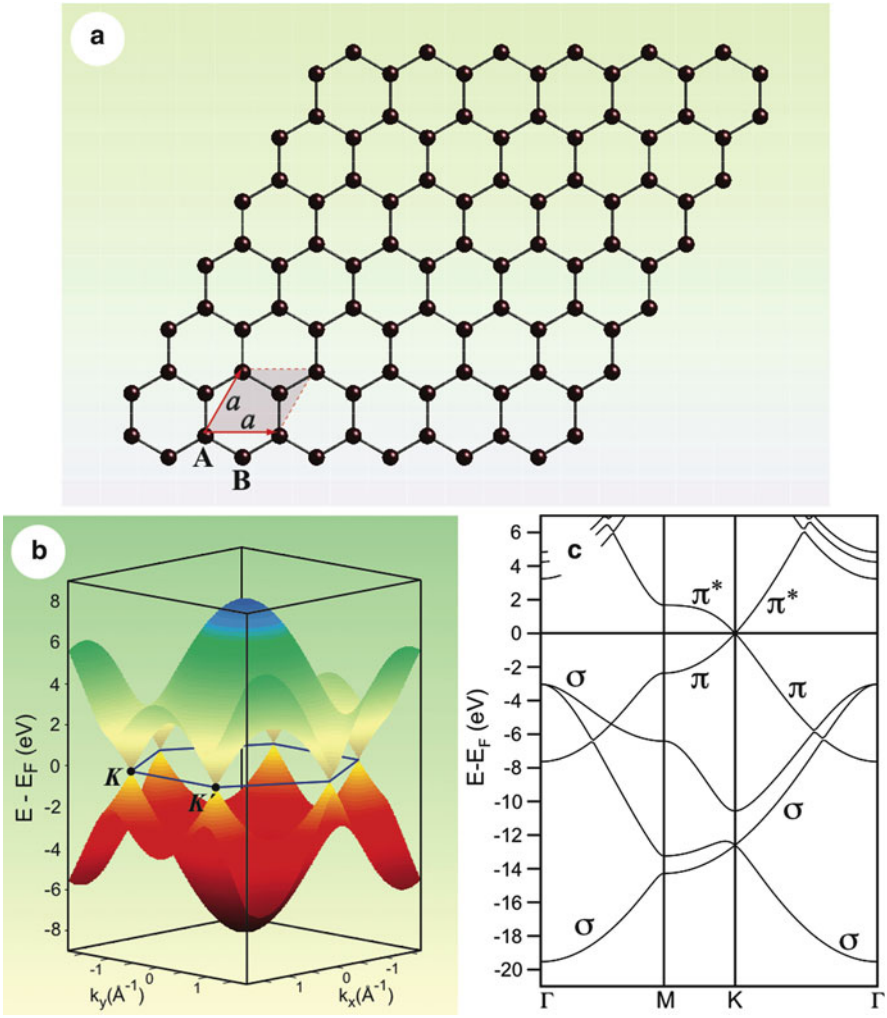

Fig. 7.1 (**a**) Crystal structure of the graphene layer, where carbon atoms are arranged in a honeycomb lattice. The unit cell of graphene with lattice constant a has two carbon atoms per unit cell, A and B. (**b**) Electronic dispersion of π and π^* states in the honeycomb lattice of free-standing graphene obtained in the framework of tight-binding approach. These branches have linear dispersion in the vicinity of the K points of the Brillouin zone of graphene. (**c**) Band structure of free-standing graphene as obtained by means of DFT (σ, π, and π^* bands are marked)

of the electronic structure of graphene is that the π and π^* bands touch at a single point at the Fermi energy (E_F) at the corner of graphene's hexagonal Brillouin zone, and close to this so-called Dirac point the bands display a linear dispersion and form Dirac cones [2] [Fig. 7.1b]. Thus, undoped graphene is a semimetal ("zero-gap semiconductor"). The linear dispersion of the bands mimics the physics of

quasiparticles with zero mass, the so-called massless Dirac fermions [1–3]. The fascinating electronic and transport properties of graphene [1–3] make it to a point of focus not only in fundamental research but also in applied science and technology with a vision to implement graphene in a myriad of electronic devices replacing the existing silicon technology.

However, a widespread implementation of graphene in electronics has been hampered by the two major difficulties: reliable production of high-quality samples, especially in a large-scale fashion and the "zero-gap" electronic structure of graphene, which leads to limitations for direct application of this material in possible electronic devices. As a response to the first challenge, a number of approaches for single layer graphene preparation have been tested, corroborating chemical vapor deposition (CVD) on transition-metal surfaces to be the most promising alternative to micromechanical cleavage for producing macroscopic graphene films. In 2008, mass-production of continuous graphene wafers by the CVD method on polycrystalline Ni or Cu surfaces and its transfer to arbitrary substrates was demonstrated [4–6]. The transferred graphene films show very low sheet resistance of 280 Ω per square, with 80% optical transparency, high electron mobility of 3,700 $cm^2V^{-1}s^{-1}$, and the half-integer quantum Hall effect at low temperatures, indicating that the quality of graphene grown by CVD is as high as that of mechanically cleaved graphene. Further modifications of this method within less than one year led to even more fascinating results, where graphene layers as large as 30 inches were transferred on to a polymer film for the preparation of transparent electrodes [7]. Other recent examples of CVD graphene growth on polycrystalline metal substrates include, for example, Pt [8] and Ru [9] substrates.

Despite the fascinating recent achievements in graphene production, the second problem of controllable doping should be solved prior to being able to implement graphene in any kind of electronic device. Several strategies exist, which allow the modification of the electronic structure of graphene, including (1) fabrication of narrow, straight-edged stripes of graphene, so-called nanoribbons [10, 11], (2) preparation of bi-layer graphene [12, 13], (3) direct chemical doping of graphene by an exchange of a small amount of carbon atoms by nitrogen [14], boron [15] or transition-metal atoms [16]; (4) modification of the electronic structure of the graphene by interaction with substrates [17–21]; (5) intercalation of materials underneath graphene prepared on different substrates [22–27]; (6) deposition of different materials on top of graphene [28–30]. Not surprisingly, the investigation of graphene interaction with supporting or doping materials, which may provide an additional important degree of control of graphene properties has become one of the most important research fields [31–34].

Focusing on the graphene/ferromagnet systems, such hybrid structures may have further intriguing applications. Recent theoretical calculations by Karpan and co-workers [35, 36] for graphene/metal interfaces imply the possibility of an ideal spin filtering in the current-perpendicular-to-the-plane (CPP) configuration for ferromagnet/graphene/ferromagnet sandwich-like structures [Fig. 7.2a]. In this work, the close-packed surfaces of Co and Ni were considered as ferromagnetic (FM) electrodes, which perfectly coincide with graphene from the crystallographic

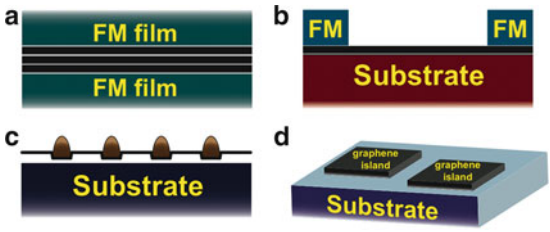

Fig. 7.2 Schematic representations of graphene-based systems, which are of interest for the present graphene/metal studies: (**a**) spin-filtering device, (**b**) graphene-based spin-FET, (**c**) clusters on graphene "nanomesh," and (**d**) graphene islands ("nanodots") on metallic substrates

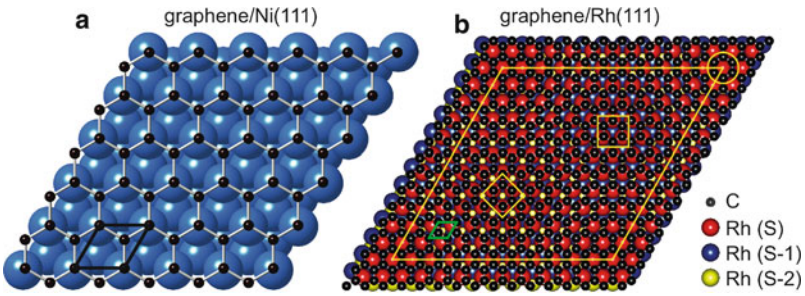

Fig. 7.3 In (**a**), top-view of a simple ball model for the top-fcc graphene/Ni(111) system is shown. Carbon atoms are *small black spheres* and nickel atoms are *big blue spheres*. In (**b**), top-view of a simple ball model for the growth of graphene on Rh(111) is shown. Carbon atoms are *black*, first-layer Rh atoms are *red*, second-layer Rh atoms are *blue*, and third-layer Rh atoms are *yellow spheres*. The *yellow* rhombus outlines the supercell of the moiré structure with four different positions: *atop* (marked by a *circle*), *top-fcc* (marked by a *square*), and *top-hcp* (marked by a *rotated square*)

point of view [Fig. 7.3a]. The spin-filtering effect originates form the unique overlapping of the electronic structures of the graphene monolayer and the close-packed surfaces of ferromagnetic Ni and Co. Graphene is a semimetal with electronic density in the vicinity of E_F at the corners (K points) of the hexagonal Brillouin zone [Fig. 7.1b]. If the Fermi surface projections of ferromagnetic metals, fcc Ni or Co, on the (111) close-packed plane are considered, then in both cases graphene has only a minority electron density around the K points of the surface Brillouin zone. In the absence of any additional factors that lower the symmetry of the system, the preferential transport of only minority electrons and thus perfect spin-filtering will occur in an FM/graphene/FM stack [35, 36]. The interaction between graphene and ferromagnetic materials will, however, change the electronic properties of the interface partially quenching the spin-filtering, but a sizable effect can still be detected by choosing a proper combination of FM materials [37]. The spin-filtering effect is also predicted to increase strongly when multilayer graphene is used in the junctions [35, 36] or when Cu or Mn decouple graphene from FM [36, 37], making these systems highly attractive for possible applications as

spintronic units. Moreover, graphene on its own might be a material of choice for the realization of spintronic devices [38], e. g. the spin-field-effect transistor (spin-FET) [Fig. 7.2b]. Such systems usually require the effective injection of spin-polarized electrons in the conductive channel, which can be made from graphene [39]. Hence, a comprehensive knowledge about the electronic and magnetic properties of graphene/FM interfaces is important for the fabrication of effective graphene-based spintronic units.

Beyond the utilization of its unique electronic properties, graphene may also be exploited for many other applications, for example, using graphene layers as a template for the growth of regular arrays of nanostructures [Fig. 7.2c]. On close-packed noble metal surfaces, such as Ir(111) [40], Rh(111) [41] or Ru(0001) [41–47], graphene forms periodically corrugated moiré patterns with a period of several nanometers [Fig. 7.3b], and such superstructures can act as templates for the preparation of exceptionally well-ordered nanocluster lattices [40, 48–51]. Monodisperse metal cluster arrays on the inert graphene surface can be used in catalysis or magnetic data storage.

In this chapter, we give a comprehensive overview of the recent studies of graphene on metals focussing on such important aspects as morphology and structure of graphene on metals, and the influence of the geometrical arrangement of carbon atoms on the electronic structure of graphene/metal systems. We review results obtained mostly by surface sensitive techniques including scanning tunneling microscopy (STM), core-hole spectroscopies [core-level photoelectron spectroscopy (PES) as well as near-edge X-ray absorption fine-structure spectroscopy (NEXAFS) and X-ray magnetic circular dichroism (XMCD)], and spin- and angle-resolved photoelectron spectrocopies [(SP)ARPES] studies on the graphene overlayers on latice-matched and lattice-mismatched metallic surfaces. We show and discuss how the graphene–metal interaction depends on the metallic substrate and also discuss the possible ways to modify this interaction. Finally, we briefly discuss future developments of this topic with the possible formation of hybrid structures on the basis of graphene and metal.

7.2 Methods of Graphene Preparation on Metal Surfaces

Two common methods of graphene preparation on metallic surfaces exist: (1) elevated temperature segregation of the carbon atoms to the surface of a bulk metallic sample, which was doped with carbon prior to the treatment [Fig. 7.4a] and (2) thermal decomposition of carbon-containing molecules on the surface of transition metals (TMs) [Fig. 7.4b]. In the first method, the transition-metal sample with some amount of carbon impurities or the bulk crystal previously loaded with carbon (via keeping the sample at elevated temperature in the atmosphere of CO or hydrocarbons) is annealed at higher temperatures. This procedure leads to the segregation of carbon atoms to the surface of the metal. Careful control of the temperature and the cooling rate of the sample allows varying the thicknesses of

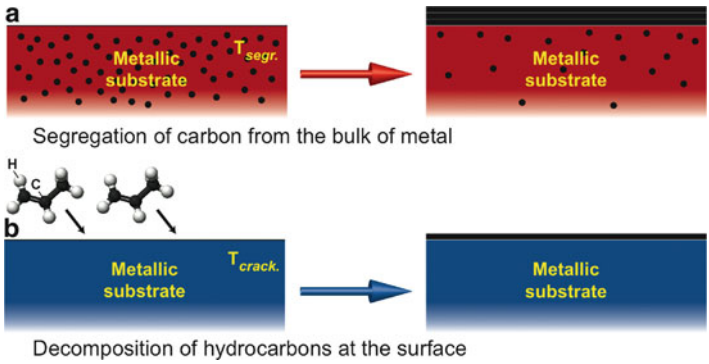

Fig. 7.4 Two ways of the graphene preparation on metal surfaces: (**a**) Segregation of bulk-dissolved carbon atoms to the surface at high temperature T_{segr}; (**b**) Decomposition (cracking) of hydrocarbon molecules at the surface of transition metals at high temperature T_{crack}

the grown graphene layer: monolayer versus multilayer growth. The second method involves the thermal decomposition (cracking) of carbon-containing molecules at a metal surface. Light hydrocarbon molecules, such as ethylene or propene, are commonly used, but the successful decomposition of CO, acetylene, and of heavy hydrocarbon molecules, such as cyclohexane, *n*-heptane, benzene, and toluene, was also demonstrated [17]. Molecules can be adsorbed on a metal surface at room temperature, and then annealing of the sample leads to the decomposition of molecules and hydrogen desorption. Alternatively, the hot sample surface can be directly exposed to precursor molecules, which decompose at the sample surface. Recent experiments demonstrate that both methods, segregation and decomposition, lead to graphene layers of similar quality. In case of segregation, the kinetics of single graphene layer formation is defined by a careful control of the annealing temperature (but multilayers of graphene could also be prepared). In the second method, the graphene thickness is naturally restricted to a single-layer due to the fact that the chemical reaction on the catalytically active metallic surface takes the place. Thus, the speed of hydrocarbon decomposition drops down by several orders of magnitude as soon as the first graphene monolayer is formed [52, 53]. A comprehensive list of metal surfaces, which were used for the preparation of graphene layers is compiled in [17], where preparation methods, the main experimental methods, and the corresponding references are presented for different lattice-matched and mismatched metallic surfaces.

7.3 Experimental Methods

Here, we briefly describe the main microscopic and spectroscopic methods used for the investigation of graphene layers on metal surfaces. For a detailed investigation

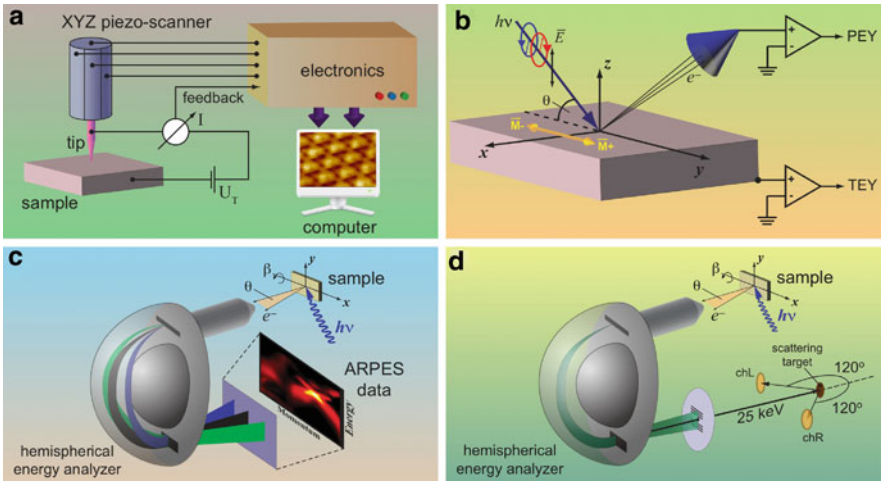

Fig. 7.5 Schematic presentation of the surface science experimental methods mainly referred to in this chapter. (**a**) In STM via keeping the tunneling current constant while scanning, the surface topography can be imaged with atomic resolution. (**b**) In NEXAFS or XMCD experiments, the photon energy of incoming linearly or circularly polarized light, respectively, is tuned over a particular absorption edge and total or partial electron yield is measured. (**c**) In ARPES measurements, the light at a fixed photon energy and polarization is used and photoelectrons are analyzed by their kinetic energy (E_{kin} and emission angle (θ) using a 2D CCD detector allowing to measure the sample electronic structure along a particular direction in the reciprocal space in one shot. Rotation of the sample by an angle β produces the 3D data set of experimental photoemission intensity, $I(E_{\mathrm{kin}}, k_x, k_y)$, where k_x and k_y are in-plane components of the wave-vector calculated from the experimental geometry. (**d**) In spin-resolved PES experiments, 2D CCD detector from (**c**) is replaced by a spin detector (usually classical or mini Mott type) where spin-separation is performed

of surface topography and atomic arrangement, STM is usually implemented (for details, see [54, 55] and Chap. 3). This experimental technique based on vacuum tunneling of electrons, nowadays provides unprecedented insight into atomic structures and local electronic structure at surfaces of low-dimensional nano-objects. In an STM experiment, an atomically sharp tip is positioned by piezoelectric actuators above the surface of an electrically conducting sample at a distance of typically $5 - 15$ Å [Fig. 7.5a]. The application of a small voltage U_{T} between tip and sample results in a quantum tunneling current. By keeping the tunneling current constant while scanning the surface topography can be imaged with atomic resolution. In results presented here, the sign of the bias voltage corresponds to the voltage at the sample. Tunneling parameters are given separately in text for each STM image: U_{T} for tunneling voltage and I_{T} for tunneling current.

In order to obtain information about the unoccupied electronic structure above the Fermi level, the NEXAFS spectroscopy is commonly implemented [Fig. 7.5b]. In this method, the energy of photons generated by a synchrotron light source is tuned over a particular absorption threshold, hence promoting core electrons

to unoccupied states above E_F. In this case, the absorption intensity is roughly proportional to the density of the empty valence band states, although distortions due to final-state effects can be considerable. In order to address the average spatial orientation of selected molecular orbitals (for example π or σ in graphene) at the surface, one can vary the orientation of the sample surface normal with respect to the wave vector of the linearly polarized X-ray light and monitor the absorption intensity. In such an experiment, the absorption intensity associated with a specific molecular orbital final state has a maximum if the electric field vector is aligned parallel to the direction of maximum charge or hole density, i.e. along a molecular orbital, and the intensity vanishes if the electric field vector is perpendicular to the orbital axis. A detailed description of the angular dependence of NEXAFS intensities can be found elsewhere [56, 57]. The XMCD technique is used for the investigation of magnetic properties of materials and allows for a direct determination of spin- and orbital-magnetic moments. In this case, circularly polarized light is used and the absorption coefficient depends on the relative orientation of photon spin and magnetization direction of the sample. The quantitative analysis of the absorption spectra obtained on a magnetic sample with circularly polarized light can be performed with the help of the so-called magneto-optical sum rules for spin- and orbital-magnetic moments [58, 59].

PES represents one of the main experimental tools, which allows to obtain comprehensive information about the electronic structure of solids below E_F (occupied valence band states) including the additional information about many-electron and quasiparticle effects [60–62] (see also Chap. 4). In a photoemission experiment, an electron from an initial state (i) below E_F is excited to some final state (f) above the vacuum level with an incident photon ($h\nu$). By measuring the kinetic energy of the electron in the final state E_f and knowing the incident photon energy ($h\nu$) and the work function (ϕ), the experimenter can trace back to the binding energy of the electron in the initial state E_i. Electrons which stem from the valence band can be found at binding energies of several eV while those from core levels contribute between several tens eV to several thousand eV. Modern electron energy analyzers in ARPES use the so-called 2D CCD detector allowing to obtain the band dispersion of the valence band states in a wide range of emission angles θ in one shot (at a fixed angle β) [Fig. 7.5c]. The emission angle θ can be used for the calculation of wave vector component k_x of electron in solid. A rotation of the sample by angle β produces the 3D data set of experimental photoemission intensity, $I(E_{\text{kin}}, k_x, k_y)$, where E_{kin} is the kinetic energy of electron and k_y is the second in-plane component of the wave-vector calculated from the experimental geometry.

For spin-resolved ARPES experiments, the 2D CCD detector is replaced by a spin-detector [Fig. 7.5d]. Different types of such detectors are described in the literature, but mainly so-called classical-Mott and mini-Mott spin-detectors are used [63]. In these devices, the initially spin-polarized beam of electrons, which passed the energy analyzer is accelerated to high energies and then scattered on a heavy-element target. Scattered electrons are then detected by channeltrons, which are placed at particular scattering angles in order to increase the figure-of-merit of

the detector [chL and chR in Fig. 7.5d]. This allows an effective separation of the spin-polarized electron beam into two channels: spin-up and spin-down electrons. These measurements are performed in the remanence state of the single-domain magnetized sample, and they are usually time consuming due to the fact that back-scattered electrons are detected in the spin-detector.

7.4 Graphene on Lattice-Matched 3*d*-Metal Surfaces

Graphene layers (or monolayers of graphite) on lattice matched $3d$ transition-metal surfaces have been known approximately for three decades. First experiments on graphene/Ni interfaces can be traced back to the mid-1970s [64–68]. In these early experiments segregation of bulk-dissolved carbon on different surfaces of Ni was investigated in order to explore the influence of the graphene layer on their catalytic activity. Structural stability and different growth modes of graphene layers were studied in these works mainly by means of low-energy electron diffraction (LEED) and Auger-electron spectroscopy. Later on, investigations of the atomic structure of graphene on a Ni surface were performed [69, 70]. The so-called $fcc - hcp$ arrangement of carbon atoms above the Ni(111) surface was proposed based on the results of surface extended-energy-loss fine-structure spectroscopy studies [69]. The graphene layer on Ni(111) was found to be flat and slightly expanded compared to bulk graphite (by $\sim$2%). The graphene-Ni distance was estimated to be 2.80 Å, and the Ni(111) substrate was found to remain unchanged. The atomic structure of the graphene/Ni(111) system was also investigated by means of LEED intensity analysis of particular diffraction spots [70]. The results of this study did not support the previous conclusions about the system geometry [69], and *top-fcc* configuration with a slightly buckled graphene layer was found to be the most probable configuration [see Fig. 7.3a for this structure]. This work also predicted a shorter distance of 2.10 Å between the graphene layer and the Ni(111) surface in agreement with the main observations of electron spectroscopy experiments [70].

The electronic structure of the graphene/Ni(111) system was investigated by means of angle-integrated photoemission, electron energy-loss spectroscopy, and ionization-loss spectroscopy methods [69, 72]. The energy bands of graphene were found practically unchanged compared to those of a pure graphite crystal, but an almost rigid shift to higher binding energies of all graphene-derived bands was detected in the experiment, indicating a charge transfer of $0.02e^{-}$/carbon atom from the Ni substrate to the graphene overlayer. Further experiments on graphene/Ni(111) [23, 73] performed by means of angle-resolved PES showed that the energy shift to higher binding energies is different for π- and σ-derived states indicating the different strength of hybridization between Ni $3d$ valence band states and out-of-plane π and in-plane σ valence band states of the graphene layer. The orbital hybridization of the valence band states of graphene and the substrate leads to a considerable interaction between C and Ni atoms, resulting in a rather short distance between graphene and Ni(111), and also to the weakening of the C–C

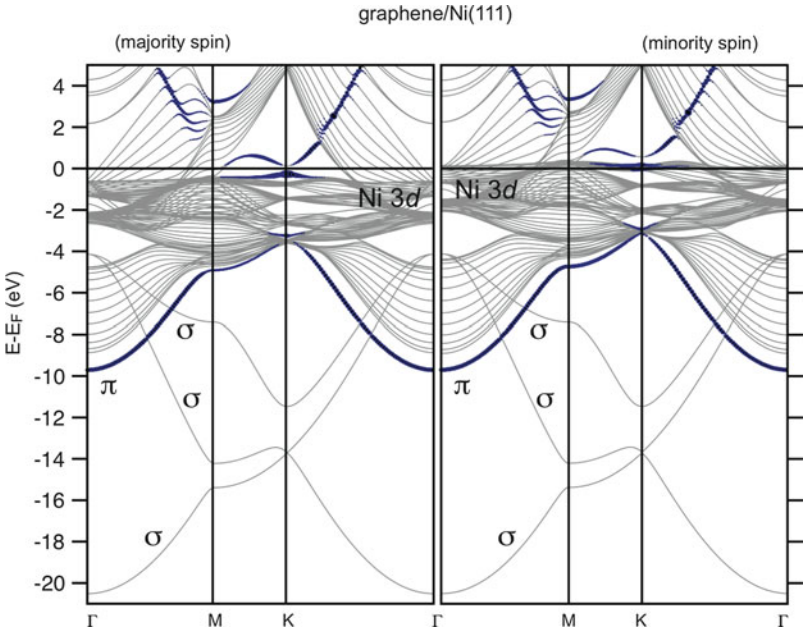

Fig. 7.6 Calculated majority and minority spin band structures for a slab terminated by graphene/Ni(111) interface for a most energetically favorable *top-fcc* configuration. For the *blue (darker) lines*, the carbon p_z character is used as a weighting factor. Data are taken from [71]

in-plane bonds. These results were confirmed by recent experiments [74, 75] and theoretical calculations [35, 36, 71, 76] (Fig. 7.6).

This section presents a detailed analysis of the growth and electronic structure of graphene on lattice-matched $3d$-metal surfaces, focusing mostly on Ni(111). The main experimental observations are presented and discussed in the light of the currently available band-structure calculations.

7.4.1 Atomic Structure of Graphene Layer on Ni(111) and Co(0001)

The STM results presented here were obtained on a graphene layer prepared on thick Ni(111) grown on W(110) [24, 75, 77–79]. Fig. 7.7a shows an STM image of single-layer graphene on Ni(111) after thermal decomposition of propylene. A typical LEED pattern of monolayer graphene on Ni(111) is presented as an inset. The graphene layer is continuous and exhibits a highly ordered crystallographic structure without any visible defects even over large areas. Since Ni(111) and graphene have the nearly similar lattice parameters (the lattice mismatch is of only 1.3 %), graphene forms a hexagonal (1 × 1) structure. A higher magnification STM

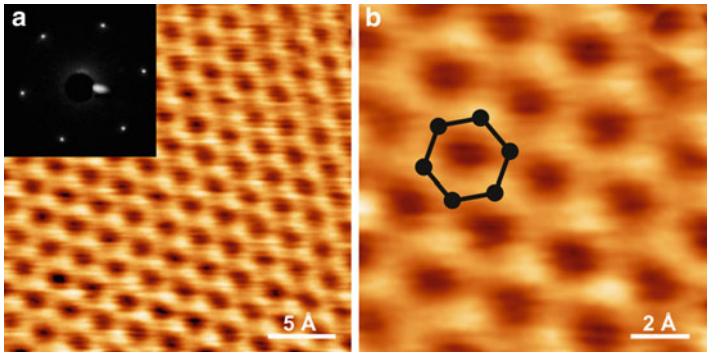

Fig. 7.7 (**a**) A topographic STM image of the high-quality graphene/Ni(111) system. Tunneling parameters: $U_T = 0.002$ V; $I_T = 48$ nA. The inset shows a LEED image obtained at 63 eV. (**b**) Magnified STM image of the perfect graphene lattice. Tunneling parameters: $U_T = 0.002$ V; $I_T = 48$ nA). The graphene honeycomb is marked in (**b**). Data are taken from [75]

image of the graphene surface is shown in Fig. 7.7b with the honeycomb of ideal graphene marked in the image.

So far, several possible atomic configurations were considered for the graphene/Ni(111) interface. Three "high-symmetry" structures are known as *hcp-fcc*, *top-hcp*, and *top-fcc*. In the *top-hcp* configuration, the C atoms are placed directly above the Ni atoms of the first layer (*top* site) and the second layer (*hcp* site) [76]. In *top-fcc*, the C atoms are arranged above the Ni atoms of the first and third (*fcc*) layers [Fig. 7.3a]. In the *hcp-fcc* configuration, the C atoms are placed above *hcp* and *fcc* sites. Three additional configurations were considered recently, which were called *bridge-top*, *bridge-fcc*, and *bridge-hcp*. In these structures, the C atoms are not placed in *hcp-fcc*, *top-hcp*, and *top-fcc* sites but in between [80].

At the moment, no clear consensus exists about which of the above described structures is more energetically stable and which kind of structures are observed in experiments. From the theoretical side, Bertoni et al. [76] used density functional theory (DFT) with the Perdew, Burke, and Ernzerhof generalized gradient approximation (GGA-PBE), which indicated the *top-fcc* to be the most stable atomic configuration at the graphene/Ni(111) interface. DFT-PBE studies were also performed by Kalibaeva et al. [81] reporting that *top-fcc* structure is the lowest energy configuration, whereas *hcp-fcc* has been shown to be unstable. The calculations including three additional "low-symmetry" configurations showed that within DTF with GGA-PBE, none of the structures is stable at the experimentally relevant temperatures; with local-density approximation (LDA), the *bridge-top* configuration was found to be the most energetically favorable one [80]. However, the performed k-point sampling of the Brillouin zone performed in this work seems to be not sufficient for this system (compare [80] and [36]), requiring a further investigations of the graphene/Ni(111) system. From the experimental side, Rosei

et al. [69] and Klink et al. [82] found that the most stable structure is *hcp-fcc*, whereas Gamo et al. [70] found *top-fcc* to be the most favorable configuration.

Graphene terraces (Fig. 7.7) have a peak-to-peak roughness of 0.2 Å and show a honeycomb structure with a lattice constant of 2.4 ± 0.1 Å [Fig. 7.7b], which agrees well with the expected 2.46 Å lattice spacing of graphene [24, 75, 77, 78]. STM images show that within each honeycomb carbon atoms corresponding to different sites appear with a different contrast, which can be attributed to the differences in the local stacking of the graphene sheet and the Ni(111) substrate. Therefore, STM images could be interpreted in the following way: Fig. 7.7 shows a single layer graphene, where one half of carbon atoms are situated on top of nickel atoms and the other half occupy one of the two non-equivalent threefold hollow cites – fcc or hcp. However, it turns to be impossible to directly identify which of the hollow sites is occupied.

The STM experiments performed on the graphene/Co(0001) system also demonstrate the epitaxial growth in the system with one of the carbon atoms in the graphene unit cell situated above Co surface atom [83]. The position of the second carbon atom is not clear and could be obtained only from the comparison of the calculated band structure with experimental structural and spectroscopy data. The recent calculations for this system predict that *top-hcp* and *top-fcc* arrangements at the interface are more favorable with spacing between Co surface and graphene layer of 2.07 Å [83].

7.4.2 *Electronic Structure of Graphene on Lattice-Matched Surfaces*

The lattice matched interface between graphene and Ni(111) is among the most extensively studied graphene/metal systems [23, 69–71, 73, 75–79, 84–87]. A considerable modification of graphene's electronic structure due to the orbital mixing between Ni $3d$ and graphene π states was predicted theoretically [35, 36, 71, 76, 84] and observed recently by NEXAFS spectroscopy [86, 87]. Figure 7.8 shows angle-dependent C $1s$ NEXAFS spectra of graphene on Ni(111) in comparison with the C $1s$ absorption spectrum of highly oriented pyrolytic graphite (HOPG). The spectrum of HOPG is characterized by the C $1s \rightarrow \pi^*$ resonance at 285.3 eV and two C $1s \rightarrow \sigma^*$ resonances around 291.6 eV and 292.7 eV. The shape of this spectrum can be best described including effects of dynamical screening of the core hole [88]. Comparing the C $1s$ NEXAFS spectrum of the graphene/Ni(111) system with the reference graphite spectrum, considerable changes in the spectral shapes are observed, indicating a substantial orbital hybridization between graphene and Ni valence band states at the interface. This is a direct experimental evidence for significant chemical interaction between graphene and Ni(111), in accordance with the relatively high adsorption energy of 125 meV per C atom calculated for this system [89]. A new strong feature at 287.1 eV originates from transitions to the

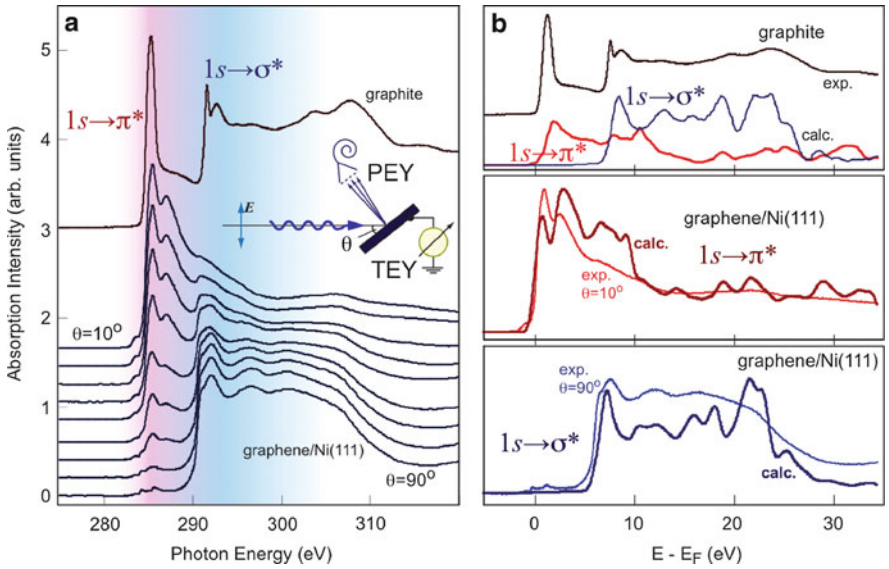

Fig. 7.8 (**a**) Angle-dependent C 1*s* NEXAFS spectra of the graphene/Ni(111) system measured as a function of angle θ, between polarization vector of the incoming linearly polarized light and the surface normal (see inset for exact experimental geometry). The reference spectrum from HOPG is shown in the upper part of the panel. (**b**) Comparison between experimental NEXAFS spectra and calculated EELS of graphite and graphene/Ni(111) for two different incident angles, θ, where transitions from C 1*s* core level on mostly π^*- or σ^*-states occurred. Experimental data are from [75, 86]. Theoretically calculated EELS spectra are taken from [76]

states with π symmetry, as evident by the angle dependence. The characteristic double-peak structure at 285.5 eV and 287.1 eV can be qualitatively understood already with the ground-state DFT calculations [76], while the dynamics of core-hole screening has to be considered for correct reproduction of the spectral profile [87]. In the ground-state approximation, the first π^* resonance can be roughly associated with the unoccupied C $2p$ density of states (DOS) located at the C atoms on top of Ni atoms, while the second π^* peak is mainly due to the C $2p$ DOS on the C atoms located at fcc hollow sites [76, 86, 87]. However, in a real experiment individual contributions are considerably mixed and further affected by the core hole and its dynamical screening. The σ^* resonances are also influenced by the interaction with the substrate: they are visibly broadened and shifted by 0.6 eV to lower energies. The broadening is a result of the increased screening by the substrate electrons. The reduction of the $\pi^* - \sigma^*$ separation reflects the reduced anisotropy of the potential for outgoing electrons due to the slight ripple in the graphene layer on Ni(111) accompanied by a softening of the C–C bonds.

In the following, we would like to compare our NEXAFS results [75, 86] with the recently calculated C K-edge EELS spectra for the graphene/Ni(111) interface [76]. The calculated EELS spectra are found to agree well with the experimental

NEXAFS data [see Fig. 7.8b]: (1) the spectra show the same angle (scattering vector) dependence and (2) the experimentally observed NEXAFS features are well reproduced in the calculated EELS spectra. For example, two peaks in the NEXAFS spectra in the $1s \rightarrow \pi^*$ spectral region at 285.5 eV and 287.1 eV photon energy can be assigned to the double peak structure in the calculated EELS spectrum at 0.8 eV and 3.0 eV above the Fermi level [76]. According to the theoretical calculations [76], the first sharp feature in the NEXAFS spectrum is due to the transition of the electron from the $1s$ core level into the interface state I_4 above the Fermi level (around the K point in the hexagonal Brillouin zone, see Fig. 7.6), which originates from the C p_z–Ni $3d$ hybridization and corresponds to the antibonding orbital between a carbon atom C-top and an interface Ni atom. The second peak in the NEXAFS spectrum is due to the dipole transition of an electron from the $1s$ core level into the interface state I_5 above the Fermi level (around the M-point in the hexagonal Brillouin zone, see Fig. 7.6), which originates from C p_z–Ni $p_x, p_y, 3d$ hybridization and corresponds to a bonding orbital between C-top and C-fcc atoms, involving an Ni interface atom. In the case of the NEXAFS C $1s \rightarrow \sigma^*$, the theory also correctly describes the shape of the absorption spectra [76].

Since the π electrons of graphene are actively involved in the bonding with the Ni substrate, the overall strength of the C–C bonds is considerably decreased. This fact is reflected in the relatively low growth temperature (500°C − 650°C depending on the hydrocarbon flux) and high solubility of carbon in Ni. The growth temperature is significantly lower than that used for graphene formation on more passive metal surfaces (e.g., 850°C − 1,000°C in the case of graphene/Pt or graphene/Ir), where the C–C bonds are not weakened so drastically by the substrate. The metastable equilibrium state of graphene on Ni(111) associated with the permanent formation and re-evaporation of graphene flakes can be reached in the temperature window as low as 650°C − 670°C [79] [Fig. 7.9a, b]. CVD growth is assisted by carbon dissolving in Ni and segregation to the surface, as can be judged from direct monitoring of the growth process with high-resolution C $1s$ PES. Figure 7.9b shows the C $1s$ PE spectra of the final graphene film grown on Ni(111) obtained at different substrate temperatures [79]. In all cases, the main peak at 284.7 eV is asymmetric and can be reliably fitted using a single component with Doniach–Sunjic lineshape. The fit parameters of this peak are comparable with those reported for the C $1s$ line in other graphene/TM systems [41]. The small feature observed at around 283 eV is characteristic of carbon atoms with reduced coordination (as compared to graphene): atomic carbon dissolved in Ni and, possibly, carbon atoms at the borders of graphene flakes. Similar features were observed upon dissociation of CO on Rh nanostructures and were associated with atomic carbon [90, 91]. Since this component results from a disordered phase, its appearance is undesirable. From Fig. 7.9, it is evident that with increasing temperature the signal at 283 eV gradually decreases and vanishes completely close to the equilibrium growth conditions. This implies that all atomic carbon from the substrate is activated at this temperature and participates in graphene formation and/or the contribution from the borders of graphene flakes is reduced due to the reduced nucleation density.

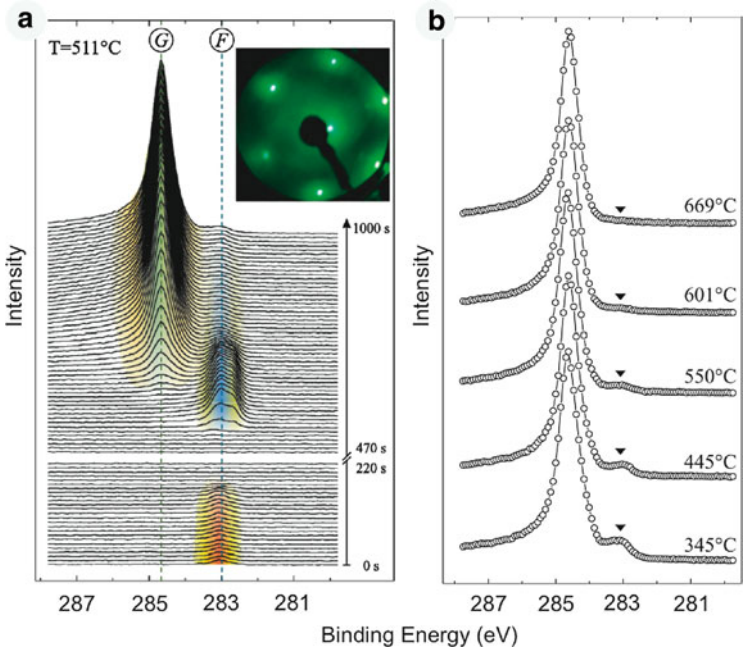

Fig. 7.9 (**a**) Time evolution of the PES intensity in the C 1*s* region during the graphene growth. Individual spectra were recorded every 10 s. *F* and *G* mark the signals from C_3H_6 fragments and graphene, respectively. The inset shows a LEED pattern (primary energy was 80 eV) after growth of graphene. (**b**) C 1*s* PES spectra of the resulting graphene layer obtained at different temperatures. Data are taken from [79]

Figure 7.10 shows two series of ARPES spectra measured along the $\Gamma - K$ direction of the hexagonal Brillouin zone of the graphene/Ni(111) system [75]. Each series is extracted from the 3D sets of data of photoemission intensity $I(E_B, k_x, k_y)$, where E_B is the binding energy and k_x, k_y are the orthogonal components of the in-plane wave vector. The presented photoemission data are in very good agreement with the previously published results [22,23,73,74,78]. In Fig. 7.10, one can clearly discriminate dispersions of the graphene π- and σ-derived states in the region below 2 eV of the binding energy (BE) as well as Ni 3*d*-derived states near E_F. The binding energy of the graphene π states in the center of the Brillouin zone (in the Γ point) equals to 10.1 eV, which is approximately by 2.4 eV larger than the binding energy of these states in pure graphite [77,86]. The shift to larger binding energy is different for σ and π valence band graphene-derived states. This behavior can be explained by the different hybridization strength between these states and Ni 3*d* valence band states, which is larger for the out-of-plane oriented π states compared with the one for the in-plane oriented σ states of the graphene layer. The effect of hybridization between Ni 3*d* and graphene π states can be clearly demonstrated in the region around the *K* point of the Brillouin zone: (1) one of the Ni 3*d* bands at 1.5 eV

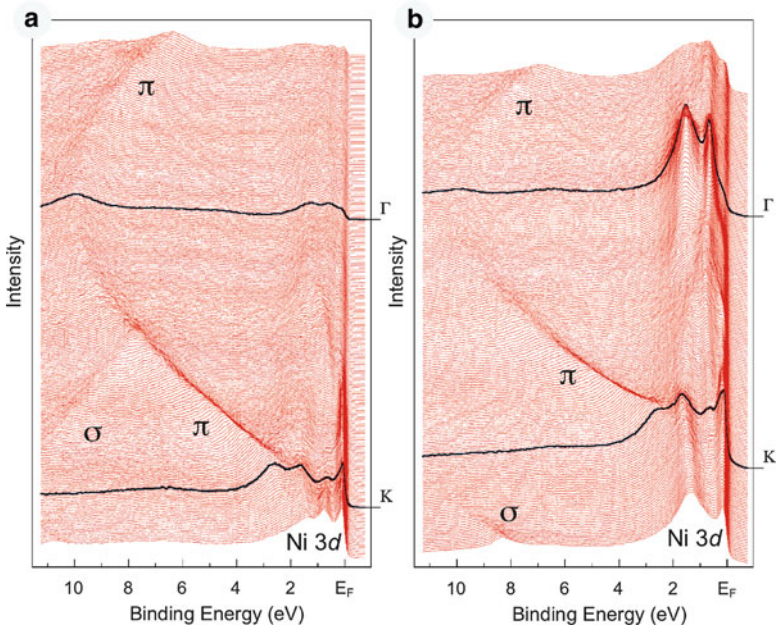

Fig. 7.10 Angle-resolved photoemission spectra of the graphene/Ni(111) system recorded along the $\Gamma - K$ direction of the hexagonal Brillouin zone at (**a**) 70 eV and (**b**) 100 eV of photon energy. Spectra corresponding to Γ and K points are marked by thick black lines. Data are taken from [75]

of BE changes its binding energy by $\approx$ 150 meV to larger BE when approaching the K point; (2) a hybridization shoulder is visible in photoemission spectra, which disperses from approximately 1.6 eV to the binding energy of the graphene π states at the K point. The strong hybridization observed in PES spectra underlines the fact that the π states might become spin-polarized and might gain a non-zero magnetic moment due to the admixture of the Ni $3d$ states into the C π states.

Considering the electronic band structure of the graphene/Ni(111), the region around the K point delivers the most interesting and important information with respect to the possible spin-filtering effects in the graphene/FM or FM/graphene/FM sandwich-like structures. First, the spectral function of the graphene layer on Ni(111) is characterized by the absence of well-ordered structure of the graphene π-bands in the vicinity of the Fermi level and second, the Dirac-cone is not preserved. Both observations can be attributed to a strong interaction between graphene layer and metallic substrate leading to a strong hybridization between the graphene π and the Ni $3d$ valence band states. In the vicinity of the K point, a number of photoemission peaks can be clearly distinguished: (1) a sharp peak about the Fermi level at $0.1 - 0.2$ eV BE, (2) a graphene π-states-related peak at 2.65 eV BE, (3) two peaks at 0.7 eV and 1.65 eV BE.

The analysis of the experimentally obtained electronic structure has recently been performed in [75] relying mainly on two comprehensive sets of electronic

structure calculations currently available for the graphene/Ni(111) system [36, 76]. Calculations by Bertoni et al. [76] predict the existence of three interface states below the Fermi level originating from the strong hybridization between the Ni $3d$ and the graphene π states and corresponding to: (I_1) bonding between C-fcc and interface Ni atoms; (I_2) bonding between C-top and interface Ni atoms; (I_3) antibonding between C-fcc and interface Ni atoms. Karpan et al. [36] performed the band structure calculations of the graphene/Ni(111) system with the major emphasis on the investigation of the spin-dependent transport properties of the Ni/graphene/Ni sandwich structures. Both calculations yielded a quite complicated band structure of the graphene/Ni(111) system around E_F due to the strong hybridization between the graphene and the Ni valence band states.

The interpretation of the experimentally observed photoemission features around the Fermi level could be performed as presented in Ref. [75]. The photoemission peak close to E_F (0.1–0.2 eV BE) could be considered as a combination of the interface state I_3 (both spins) with a large contribution of the graphene π-character and the Ni $3d(\downarrow)$-band. The second peak at 0.7 eV BE could be assigned to the combination of the Ni $3d(\uparrow)$- and Ni $3d(\downarrow)$-bands present in both calculations. The feature at 1.65 eV could be considered as a combination of Ni $3d(\uparrow)$-band and $I_2(\downarrow)$-state with a large graphene π-character. The last photoemission peak (2.65 eV BE) could be assigned to the interface state $I_2(\uparrow)$ with large contribution of the graphene π-character.

In order to check the theoretical predictions concerning the CPP spin-dependent electronic transport properties of the ideal graphene/Ni(111) interface, an analysis of the constant energy photoemission maps close to E_F was performed in [75] (Fig. 7.11). However, flat Ni $3d$ bands, which dominate the photoemission intensity around E_F make the detailed analysis rather difficult. The energy cuts were taken at

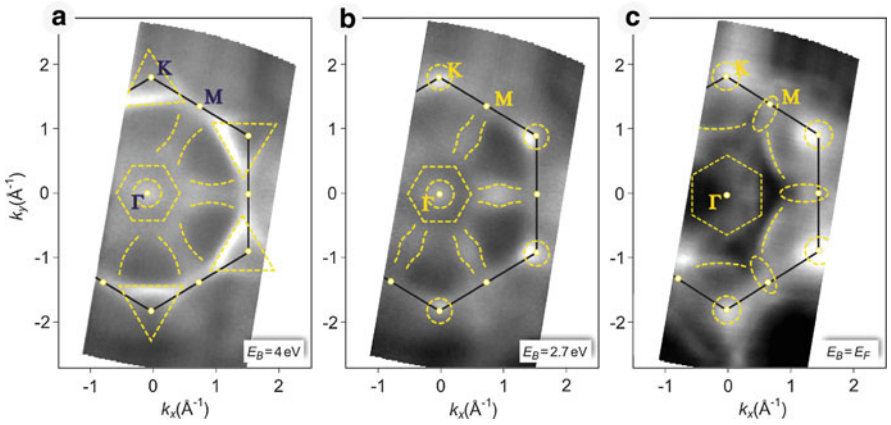

Fig. 7.11 Constant energy cuts of the 3D data sets in the energy-wave vector space, $I(E_B, k_x, k_y)$, obtained through a β-scan from the graphene/Ni(111) system at 100 eV of photon energy. The energy cuts are taken at (**a**) 4 eV and (**b**) 2.7 eV BE as well as at (**c**) E_F. Data are taken from [75]

(a) 4 eV and (b) 2.7 eV of BE as well as at (c) the Fermi level. The energy cut at $E_B = 4$ eV shows characteristic photoemission intensity patterns of the graphene layer, which reflect the symmetry of the system. Below the Dirac point (crossing of straight dispersion lines of π states in free-standing graphene), the graphene π bands are visible in the first Brillouin zone, whereas no bands can be seen in the second one [92]. Additionally, several energy bands are present in the middle of the Brillouin zone (outlined by dashed yellow lines), which also show hexagonal symmetry. These bands originate from the hybridization of the Ni and graphene valence band states. The constant energy cut taken in the region of the minimal binding energy of the graphene π states ($E_B = 2.7$ eV) is shown in Fig. 7.11b. In the case of graphene/Ni(111), the Dirac point is not preserved due to the strong hybridization of Ni $3d$ and graphene π states around the K point. This can also be directly recognized at this energy cut, where graphene π states produce broad intensity spots instead of sharp points in the wave-vector space. As in the previous case, we observe a number of valence band states in the middle part of the Brillouin zone, which again could be assigned to the hybridization-derived states.

The most interesting and important information in view on the spin-dependent transport properties of the graphene/Ni(111) system can be extracted from the constant energy cut obtained at the Fermi energy, which is presented at Fig. 7.11c. Already the analysis of Fig. 7.10a, b shows that the photoemission intensity is increased around the K point and along the $K - M$ direction of the hexagonal Brillouin zone, that correlates with the increased photoemission intensity observed in the energy cut shown in Fig. 7.11c for the Fermi energy. Additionally, a number of arcs surrounding the K points and weak (but distinguished) diamond-shape regions of increased intensity are clearly visible in the middle part and around the M points of the Brillouin zone, respectively. Upon the comparison of the obtained photoemission results for the graphene/Ni(111) system (Figs. 7.10 and 7.11) as well as the Fermi-energy cut with the band structure calculations for this system [35, 36, 71, 76] (Fig. 7.6), we find very good agreement between theory and experiment. Particularly, the region around the Fermi level for the ideal graphene/Ni(111) system is well reproduced in the experiment, confirming the main predictions of the theory. However, more experimental and theoretical efforts are required to determine the spin character of individual bands.

7.4.3 Magnetism of Graphene on the Ni(111) Surface

The earlier discussed hybridization between graphene π and Ni $3d$ valence band states leads also to a partial charge transfer of the spin-polarized electrons from Ni to C. This leads to the appearance of induced effective magnetic moment of carbon atoms, which can be detected in experiments sensitive to the magnetic state of particular elements, such as XMCD. Figure 7.12 shows XMCD spectra of the graphene/Ni(111) system collected at the Ni $L_{2,3}$ (left panel) and C K (right panel) absorption edges in the TEY and PEY modes, respectively [86].

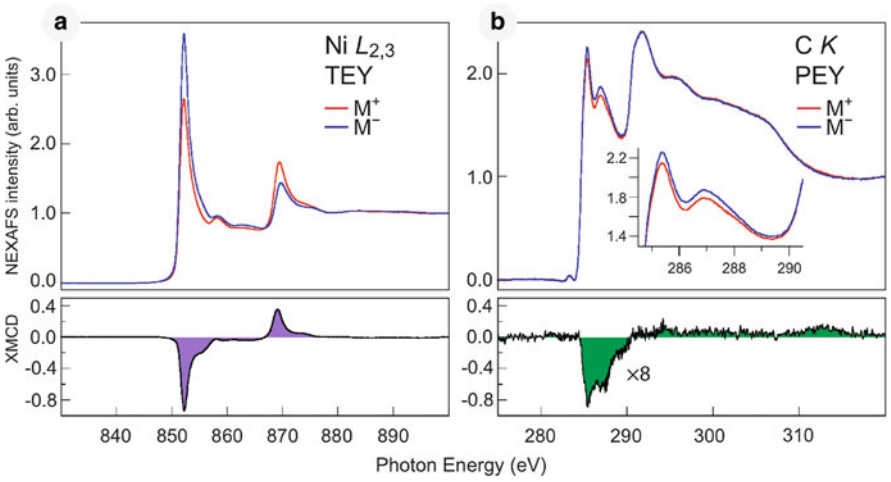

Fig. 7.12 XMCD spectra of the graphene/Ni(111) system measured at the Ni $L_{2,3}$ (**a**) and C K absorption edges (**b**). The corresponding differences reflecting the strength of the dichroic signal are shown in the lower part of the respective figures. Data are taken from [75, 86]

The Ni $L_{2,3}$ XMCD spectrum (white line as well as fine structure behind the absorption edge) is in perfect agreement with the previously published spectroscopic data [93–95] with the extracted values of spin- and orbital-magnetic moments $\mu_S = 0.69\,\mu_B$ and $\mu_L = 0.07\,\mu_B$, respectively, which are in very good agreement with the previously published experimental ones [93, 96]. The experimentally obtained value of the spin-magnetic moment is in agreement with the theoretically calculated one $\mu_S = 0.67\,\mu_B$ for the graphene/Ni(111) system [76]. For the most energetically favorable configuration of carbon atoms on Ni(111), C-*top*–C-*fcc*, calculations predict a reduction of the spin-magnetic moments of Ni interface atoms by 16% till $0.56\,\mu_B$. Experimental data collected in the PEY mode (more surface/interface sensitive) at the Ni $L_{2,3}$ absorption edge also demonstrate slight reduction of spin moment of surface Ni atoms till $\mu_S = 0.63\,\mu_B$ [75, 86] that is consistent with theoretical calculations [76].

The most important and interesting result of these XMCD experiments on the graphene/Ni(111) system is the observation of the relatively large dichroic contrast at the C K absorption edge [Fig. 7.12b]. The C K XMCD spectrum reveals that the major magnetic response stems from transitions of the $1s$ electron onto the π^*-states, while transitions onto the σ^*-states yield very weak (if any) magnetic signal indicating that only the C $2p_z$ orbitals of the graphene layer are magnetically polarized due to the mixing with the Ni $3d$ band. As discussed earlier, the sharp structure at the $1s \rightarrow \pi^*$ absorption edge originates from hybridized C p_z–Ni $3d$ and C p_z–Ni p_x, p_y, $3d$ states (see earlier discussion and [76]).

At the C K absorption edge, the electron transitions occur from the non-spin-orbit split $1s$ initial states to the $2p$ final states and thus, in the analysis of the dichroism effect at the K edge one equation in the "sum" rules is missed. This

means that the XMCD signal at K edges provides the information only on the orbital magnetic moment μ_{orb} [58, 59, 97]. In [75, 86], the value of the C orbital magnetic moment was estimated to be $\mu_{\text{orb}} = 1.8 \pm 0.6 \times 10^{-3}\,\mu_B$. Comparison of the presented results from [75, 86] with recent experimental studies of induced magnetic effects in nonmagnetic materials [98, 99] allows to estimate a value of spin magnetic moment of carbon atoms in graphene/Ni(111) in the range $0.05 - -0.1\,\mu_B$ [75, 86]. An analysis of the calculated spin-resolved electronic structure of graphene/Ni(111) [76] is difficult due to complicated behavior of the majority and minority spin interface states. In [76], the calculated magnetic moment is very small: $-0.01\,\mu_B$ and $0.02\,\mu_B$ for C-top and C-fcc, respectively, although the magnetic splitting of the majority and minority parts of the interface states I_3 and I_4 was found between 0.13 and 0.55 eV, respectively.

The experimentally observed effective magnetic moment of carbon atoms of the graphene layer on Ni(111) is also confirmed by our spin-resolved photoemission study [75]. The main results are presented in Fig. 7.13 showing (a) the spin-resolved spectra and (b) the corresponding spin polarization as a function of the binding energy of Ni(111) and the graphene/Ni(111) system measured in the region of Ni 3d valence band with a photon energy of 65 eV at room temperature in normal emission geometry. The formation of graphene on Ni(111) strongly modifies the valence band spectrum of Ni 3d as a result of the strong interaction between valence band states of graphene and Ni. These considerable modifications of the spin-resolved structure of Ni 3d states as well as a reduction of spin polarization at the Fermi level could

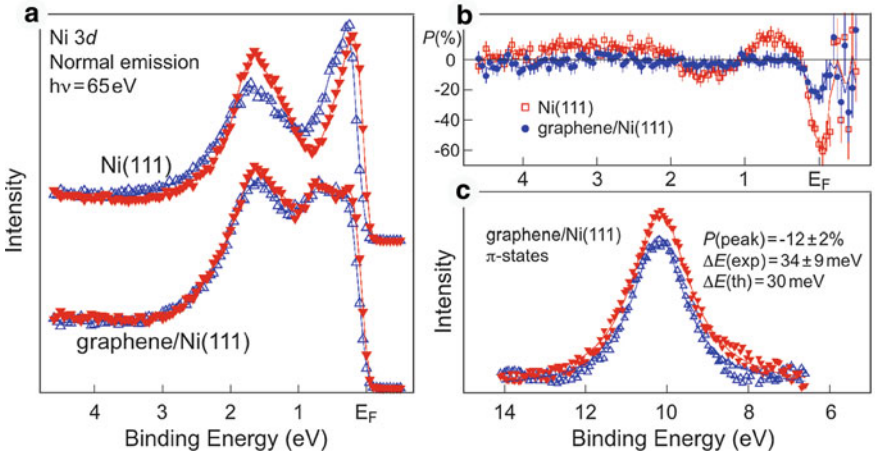

Fig. 7.13 (**a**) Spin-resolved PES spectra and (**b**) corresponding spin polarization of the Ni 3d valence band states as a function of the binding energy for Ni(111) and the graphene/Ni(111) system. (**c**) Spin-resolved photoemission spectra of the π-states of graphene on Ni(111). All spectra were collected in the normal emission geometry with the photon energy of 65 eV. In (**a**) and (**c**), *open and filled triangles* denote spin-up and spin-down electron channels, respectively. Data are taken from [75]

be taken as an indication of the decreasing of magnetic moment of Ni atoms at the interface between graphene and Ni(111), which was predicted by theory [76].

The spin-resolved spectrum of the graphene π states of graphene/Ni(111) measured in normal emission geometry with photon energy of 65 eV is shown in Fig. 7.13c. These results demonstrate a clear spin contrast for the graphene π states with the maximum spin polarization of about $(-12 \pm 2\%)$ and the exchange splitting of about 34 ± 9 meV, which is in rather good agreement with the value extracted from theoretical works [76, 100]. A comparison of these spin-resolved spectra including their sign with the background spin polarization originating from the Ni $3d$ states give an opportunity to conclude that the spin moment of graphene is aligned antiparallel to the magnetization of Ni implying an antiparallel magnetic coupling of graphene to Ni. However, this conclusion is based only on the normal emission spin-resolved measurements and has to be clarified by more intensive spin-resolved PES experiments. Here, we would like to note that the experimental evidence of a pronounced spin polarization at room temperature together with the splitting of the π states in the graphene/Ni(111)system are in contradiction to the results previously reported by Rader et al. [101], where the absence or very small spin polarization of the graphene π states was observed. The origin of this discrepancy is, however, not clear at the moment and further spin-polarized PES investigations of the graphene/Ni(111) system should be undertaken in order to resolve this issue.

7.5 Graphene on Lattice-Mismatched $4d, 5d$-Metal Surfaces

As shown in the previous section, in the case of close lattice parameters between graphene and hexagonally close-packed metal surface, lattice-matched structures are formed, like for graphene on Co(0001) [83] and Ni(111) [53]. However, larger mismatches lead to the formation of superstructures with large periodicity, which were observed on Pt(111) [8, 41, 102–108], Ir(111) [40, 41, 109–114], Pd(111) [41, 115], Rh(111) [33, 41, 51, 116, 117], or Ru(0001) [41–44, 46, 116, 118–121]. Already more than four decades ago, graphene layers were stabilized on noble metal surfaces upon high temperature annealing of Pt and Ru single crystals [102, 103, 116]. After hydrocarbon decomposition or carbon surface segregation on metal surfaces at elevated temperatures sharp satellite spots or segmented rings were observed in LEED [102–104, 109, 116, 119, 122], which were attributed to the formation of graphene layers. However, an extended temperature treatment during the segregation process may lead not only to single layer, but also to multilayers of graphene or even to bulk graphite formation. In the subsequent studies [22, 73, 112, 123, 124], single-layer graphene formation could be discriminated by its characteristic band structure in ARPES (see also previous section). In this section, we will focus on the atomic structure of single-layer graphene on Ir(111), Ru(0001) and Rh(111) surface, as well as on the changes of electronic structure of graphene associated with the bonding to these substrates.

7.5.1 Structure of Graphene on Ir(111), Ru(0001), and Rh(111)

Several growth methods were reported for the preparation of highly ordered graphene monolayers on Ir(111), including pyrolysis of preadsorbed ethylene and graphene growth at elevated temperature, which is also referred to as temperature programmed growth (TPG) and low-pressure CVD of ethylene on hot Ir surface [40, 110, 126]. Upon using high growth temperatures up to 1,320 K, the latter technique allows the preparation of single-layer graphene domains of unprecedented quality. Graphene flakes prepared by this method are dislocation-free and fully coherent over step edges reaching at least micrometers in size [40, 110, 126]. The STM topographic image in Fig. 7.14a shows the perfectly ordered moiré superstructure of single-layer graphene on Ir(111) prepared by high-temperature decomposition of propene [125]. The moiré superstructure was reported to have a periodicity of 25.3 ± 0.4 Å [40, 110, 126, 127], which corresponds to 9.32 Ir lattice constants showing that the structure is incommensurate. Depending on tunneling voltage, the moiré superstructure contrast changes considerably indicating a strong influence

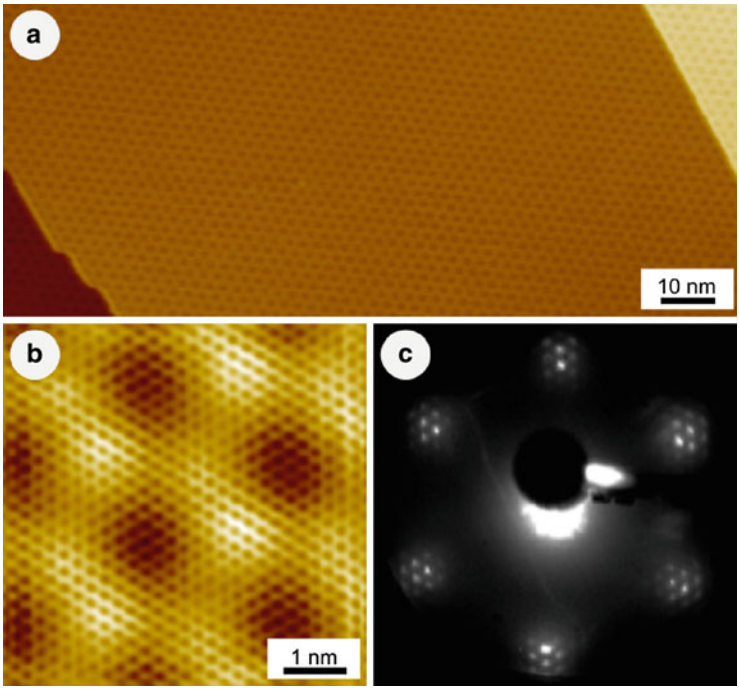

Fig. 7.14 (**a**) Large-scale STM image of an epitaxial graphene layer on the Ir(111) surface. (**b**) Atomically resolved STM image of the moiré structure of the graphene layer on Ir(111). (**c**) LEED image of the graphene layer on Ir(111) taken at a primary electron energy of 70 eV. Tunneling parameters for STM images: (**a**) $U_T = 1.12$ V; $I_T = 0.18$ nA; (**b**) $U_T = 0.01$ V; $I_T = 2.56$ nA. Data are taken from [125]

of the electronic structure in STM [40, 110, 126, 127]. The high-resolution STM image in Fig. 7.14b shows no atomic-scale defects, confirming a high crystalline quality of single layer graphene on the Ir(111) surface [125]. The full graphene honeycomb lattice is clearly visible in all areas of the moiré supercell. The LEED pattern of the graphene/Ir(111) surface is shown in Fig. 7.14c [125]. The pattern shows hexagonal symmetry consisting of a six pairs of iridium and carbon spots surrounded by hexagonally arranged satellites correspond to the superstructure. The LEED measurements yield a value of 25.8 ± 2.0 Å [40, 110, 126, 127] for the periodicity of the superstructure, which coincides with the value extracted from the STM images. Beyond the most abundant graphene moiré structure on Ir(111) described above additional orientations of graphene were reported recently [111]. A combined low-energy electron microscopy (LEEM), selected-area LEED and STM investigation revealed three additional moiré domains, which are rotated by $\sim 14°$, $\sim 18.5°$, and $\sim 30°$ with respect to the most abundant orientation. Along with rotational variants, liner defect structures in graphene sheets were observed by LEEM [111]. STM shows that these defects are wrinkles in the graphene layer, suggesting that the graphene sheets delaminate locally upon substrate contraction during cooling after growth at higher temperatures [111, 128]. Upon temperature cycling, a hysteresis in the appearance and disappearance of the wrinkles was observed [128]. However, for possible applications a controlled graphene growth is highly desirable allowing fabrication of large defect-free well-oriented monolayer graphene sheets. Recent studies show that millimeter-sized graphene films of a single orientation and unprecedented structural perfection can be prepared on Ir(111) by a cyclic growth exploiting the different growth and oxygen etching speeds of the domain variants [129].

On the Ru(0001) surface graphene also forms a moiré structure. A topographic STM image presented in Fig. 7.15a shows large graphene flakes formed on the terraces of the Ru(0001) surface after the carbon segregation at high temperature [42]. Figure 7.15b shows atomically resolved STM image of graphene on Ru(0001) indicating a strong atomic contrast variation within the supercell of the moiré structure. Contrary to the STM data obtained on graphene/Ir(111), here the full graphene honeycomb lattice is only visible at the moiré maxima [9, 42]. At the two nonequivalent minima of the moiré supercell only one of the two carbon sublattices is resolved. The observed atomic contrast across the graphene supercell is assigned to the local variation of the interaction strength between the graphene sheet and the underlying ruthenium surface depending on the atomic registry of carbon atoms with the Ru atoms. The two nonequivalent minima in the graphene unit cell differ with respect to the Ru atoms in the substrate layer. In one region, the carbon atoms occupy *top-hcp* sites, in the other *top-fcc* sites. Recent surface X-ray diffraction (SXRD) investigation [43] showed that contrary to the previously proposed periodicity of approximately (11×11), i.e., with (12×12) graphene unit cells overlaid, the true structure is a (25×25) graphene on (23×23) Ru structure, meaning that the unit cell consists of four moiré subcells. More recently, the graphene/Ru(0001) structure was further refined upon a detailed analysis of the SXRD data [130]. The proposed structure shows an excellent agreement with previous STM studies [9, 42].

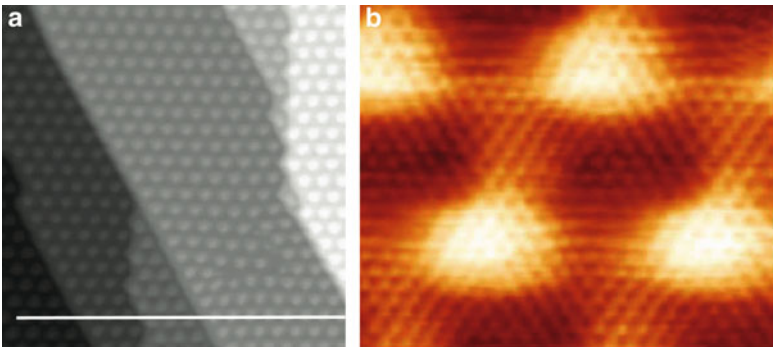

Fig. 7.15 (**a**) 500 Å×500 Å topographic STM image recorded after annealing Ru(0001) sample at 1,470 K. The surface is fully covered by graphene and Ru step edges are aligned along the main directions of the overlayer, indicating a restructuring of the underlying Ru surface. (**b**) 50 Å×50 Å atomically resolved image of the graphene overlayer on Ru(0001). The image shows three different levels of apparent heights, namely four bright maxima, a *dark* minimum in the center between the three maxima on the right hand side, and a *less dark* minimum between the three maxima on the left hand side. Tunneling parameters for STM images: (**a**) $I_T = 1$ nA, $U_T = -0.2$ V; (**b**)$I_T = 1$ nA, $U_T = -0.05$ V. Data are taken from [42]

A pronounced corrugation of both graphene and ruthenium substrate at the interface was found supporting the idea of a chemisorbed graphene layer with significant interaction with the substrate. Moreover, areal chirality in the in-plane movements in graphene layer on Ru(0001) was observed [130].

In the following, we would like to focus on the graphene/Rh(111) system exhibiting a rather complicated moiré pattern. An overview of a graphene layer on the Rh(111) surface is shown in Fig. 7.16a [117]. The graphene domain exhibits a highly ordered moiré structure without any visible defects even over large areas. Rh steps are aligned along the main crystallographic directions of the graphene moiré, which is attributed to the substantial reshaping of the Rh(111) surface during the graphene growth process in order to accommodate the periodicity and orientation of the graphene overlayer. The apparent vertical corrugation of the graphene monolayer is measured to be in the range of 0.5–1.5 Å (peak-to-peak) depending on the tunneling conditions [see inset in Fig. 7.16a]. LEED pattern of the graphene moiré on Rh(111) is presented in Fig. 7.16d. Qualitative analysis of STM and LEED images show that the close-packed directions of graphene and the unit cell vectors of the moiré are parallel to the close-packed $\langle 1\bar{1}0 \rangle$ directions of Rh(111). From the LEED images, a periodicity of 2.90 ± 0.1 nm of the moiré superstructure on Rh(111) was calculated, which is in reasonable agreement with the average distance between the neighboring moiré features measured in STM images and corresponds roughly to 12 times the lattice constant of graphene and 11 times that of Rh(111). A higher magnification STM image of the graphene surface is shown in Fig. 7.16b with the unit cell of the moiré superstructure marked by a rhombus. Four distinctive regions corresponding to different apparent height levels can be

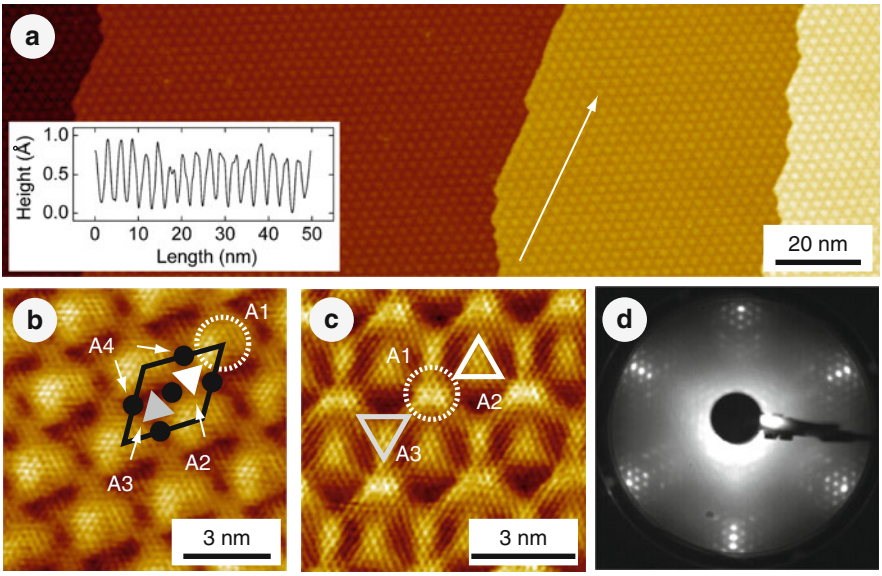

Fig. 7.16 (**a**) Large-scale STM image of an epitaxial graphene layer on the Rh(111) surface. Inset shows a height profile measured along the *white arrow*. (**b**) High magnification image of the unit cell of the moiré structure. The *black rhombus* outlines the supercell of the moiré structure. Main surface features are marked in the image: moiré maximum (A1) by a *circle*, the brighter half-cell (A2) by a *white solid triangle*, the *darker* half-cell (A3) by a *gray solid triangle*, and bridging *black* minima (A4) by *black solid circles*. (**c**) Atomically resolved STM image of the moiré structure of the graphene layer on Rh(111) taken with different tunneling parameters compared with (**b**). (**d**) LEED image of the graphene layer on Rh(111) taken at a primary electron energy of 58 eV. Tunneling parameters for STM images: (**a**) $U_T = 1.12$ V; $I_T = 0.18$ nA; (**b**) $U_T = 0.01$ V; $I_T = 2.56$ nA; (**c**) $U_T = 0.02$ V; $I_T = 30$ nA. Data are taken from [117]

distinguished within the moiré supercell: three maxima of different heights (A1, A2, A3) and black minima (A4). The most prominent maxima (A1) are surrounded by six black minima as well as by three less intense maxima A2 and A3. Each of the less intense maxima (A2, A3) is surrounded by three black minima (A4). The different contrast features within the moiré unit cell can be distinguished much better in the high-resolution STM image in Fig. 7.16c recorded at different tunneling conditions compared to Fig. 7.16b. In most regions of the moiré supercell, the graphene sublattice symmetry is broken and only one of the two carbon sublattices is imaged. We attribute this effect to the strong, covalent interaction between the graphene layer and the Rh(111) substrate.

A more detailed description of the atomic configurations can be carried out on the basis of a simple ball model presented in Fig. 7.3b. Three highly symmetric positions of carbon atoms (or centers of carbon rings) with respect to the underlying Rh lattice can be assigned: hcp-fcc (or *atop*) sites at the corners of the moiré unit cell, *top-fcc* (or hcp) and *top-hcp* (or fcc) sites in the center of the right and left half-cell of the moiré unit cell, respectively. In the STM image [Fig. 7.16c]

hcp-fcc regions appear as the bright maxima of the moiré structure (A1), *top-hcp* and *top-fcc* appear as the two less intense maxima (A2 and A3), exhibiting two different intensity levels (A2 is brighter than A3). In contrast to graphene on Ru(0001) [42, 43, 120], in this present study we observe that bright features (local maxima) are surrounded by dark depressions (A4) present in both halves of the moiré unit cell corresponding to the *bridge-top* areas, which we believe are strongly bonded to the metallic substrate. The full graphene honeycomb lattice is only visible in areas directly on top or adjacent to the A1 maxima (moiré maxima), which we attribute to the weak coupling of these regions of the graphene sheet to the Rh lattice. The atomic structure of other regions is dominated by the strong covalent interaction with the metal substrate, especially within the black minima (A4), where C atoms are placed in *bridge-top* positions. Recent theoretical investigations showed that for graphene on Ni(111) [80] as well as for graphene on Ru(0001) [121] such *bridge* positions are energetically favorable, which might lead to a relatively strong C–Rh bonding in these regions. Especially the *bridge-top* position, which we believe gives rise to the observed black depressions in the STM images, was found to be one of the most energetically stable configurations [80]. Interestingly, the observed pronounced bonding of the *bridge-top* regions is almost completely suppressed in graphene on Ru(0001) [42, 43, 120], where no local height variation within the half-cells of the moiré structure was observed. We also would like to point out that the atomic structure of graphene on Rh(111) also differs from that of the *h*-BN "nanomesh" on Rh(111) [131, 132].

7.5.2 *Electronic Structure of Graphene on Lattice-Mismatched Surfaces*

In a straightforward way, the degree of interfacial hybridization between graphene π and TM d states can be probed in the C 1s X-ray absorption experiment. Figure 7.17a shows C 1s NEXAFS spectra for graphene layer on Pt(111), Ir(111), Rh(111), and Ru(0001) together with the corresponding LEED patterns [41]. The spectra are arranged in such a way that from top to bottom the substrate-induced changes to the original graphite spectrum increase, thus providing a direct evidence for the growing chemical interaction between graphene and metals in the series Pt–Ir–Rh–Ru. Evidently, the 4d and 5d metals fall into two different groups as regards bonding to graphene. In the case of 5d metal substrates, the C 1s NEXAFS spectrum is weakly affected preserving shapes and energies of the distinctive resonant features A, B, and C. On Pt(111), the influence of the substrate is restricted mainly to the appearance of the step-like feature A′ at 284 eV due to the lowering of the Fermi level as a result of the charge transfer at the interface. Very weak chemical bonding of graphene to Pt(111) cannot force the overlayer uniquely in registry with the substrate, as can be judged from the LEED pattern with segmented rings reflecting different domain orientations of graphene [Fig. 7.17a, lower

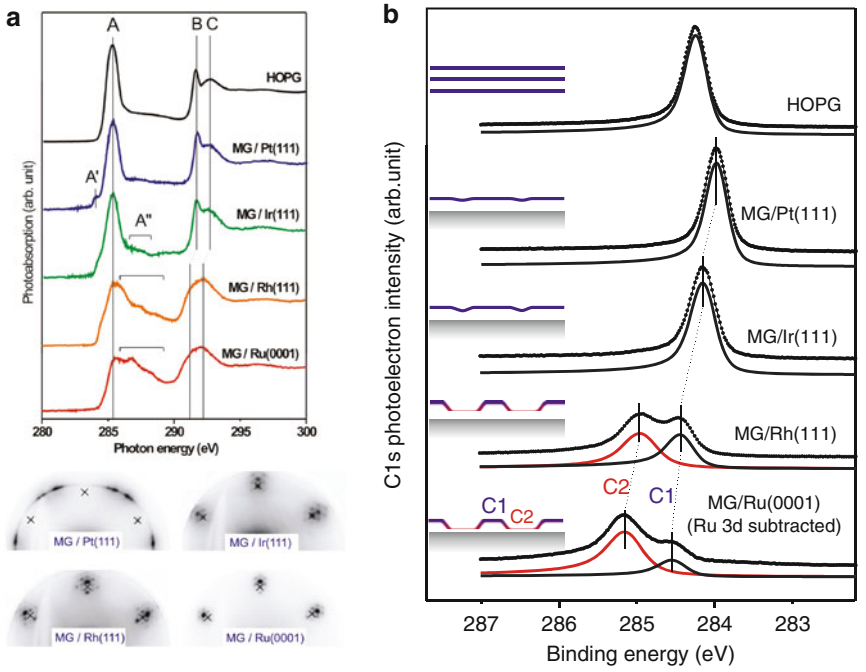

Fig. 7.17 (**a**) C 1*s* NEXAFS spectra from graphene layer adsorbed on several lattice-mismatched TM surfaces. The C 1*s* spectrum from HOPG is shown for comparison. Lower panel shows the corresponding LEED patterns; substrate-related spots are marked with *crosses*. (**b**) C 1*s* photoelectron spectra taken in normal emission from graphene layer adsorbed on several lattice-mismatched TM surfaces. Photon energy is 400 eV. For graphene/Ru(0001), the Ru 3*d* signal is subtracted. Data are taken from [41]

panel] [41, 104, 105, 122, 133, 134]. The detailed structure of possible graphene/Pt moiré patterns has been revealed in a recent combined LEED/LEEM study [107]. On Ir(111), shoulder A′ is already disturbed by weak chemisorption and a new bonding-related π^* feature A″ starts to develop between 286.5 eV and 288 eV. A reduction in the 5*d* occupancy in going from Pt (d^9) to Ir (d^7) is probably the main reason for the growing interaction with graphene, since it causes a depopulation of the antibonding states. A slight increase in the bonding strength (as compared to graphene/Pt) results in the occurrence of one principal domain orientation, as reflected in the mismatch-induced moiré pattern in LEED [Fig. 7.17a, lower panel].

In the case of 4*d* metal substrates (Rh and Ru), the electronic structure of graphene is strongly disturbed, as reflected in the C 1*s* NEXAFS spectra [Fig. 7.17a]. Indeed, the spectra of graphene on Rh(111) and Ru(0001) resemble the C 1*s* spectrum from graphene on Ni(111), which is discussed above (Fig. 7.8). Both π^* and σ^* resonances are strongly reshaped, and the separation between the π^* and σ^* manifolds is visibly reduced. Again, these changes reflect strong TM 4*d* – graphene π orbital mixing and softening of the C–C bonds caused by the

formation of covalent bonds between C atoms and the substrates. The general trends in the strength of interaction between graphene and late TMs are the following: (1) along the row it increases with decreasing occupancy of the d shell and (2) for the same occupation numbers, it is similarly strong for the $3d$ and $4d$ shells, but considerably weaker for the $5d$ shell. The former trend is due to the gradual depopulation of the antibonding states with reducing d shell occupation. The latter effect can be understood in terms of orbital overlap. In going from $4d$ to $5d$ elements, relativistic effects become significant, resulting in contracting the $6s$ orbitals and expanding the $5d$ orbitals. Probably, the overlap of the graphene π states with more diffuse $5d$ orbitals is worse than with more localized $4d$ orbitals.

The co-existence of lowered and elevated graphene areas on lattice-mismatched TM substrates (see previous subsection for the exact surface geometry) can be directly observed in a core-level PE experiment. Figure 7.17b shows C $1s$ PE spectra from graphene on Pt(111), Ir(111), Rh(111), and Ru(0001) compared with the reference spectrum from HOPG. The double-peak structure observed for graphene/Rh and graphene/Ru is due to the strong corrugation of graphene: C1 results from the nonbonding elevated sites, while C2 represents bonding low-lying areas. The peak-fit analysis reveals that C2 is considerably broader than C1 reflecting the effect of gradually varying chemical surrounding of the C atoms across the bonding sites [41]. There is an obvious correlation between the strength of interfacial chemical bonds probed by NEXAFS [Fig. 7.17a] and the size of the area occupied by the bonding sites [Fig. 7.17b]. On the $5d$ metal substrates, the bonding with graphene is weak, and the C2 component is not detected in the C $1s$ PE spectra, thus implying no pronounced "pores" and weak corrugation. With increasing covalent interaction at the graphene/TM interfaces, component C2 grows in the spectrum at the cost of C1, and becomes dominating for the most reactive graphene/Ru interface. Even quantitative information about the effective "pore" sizes for different graphene/TM interfaces can be extracted from the core-level PE spectra if the effects of photoelectron diffraction on the intensity ratio C1/C2 are properly filtered out [41].

In order to gain a detailed insight into the origin of the bonding between graphene and lattice-mismatched noble metal substrates, photoemission studies have been performed, which provide direct information about the electronic structure of the occupied valence band states. An ARPES photoemission intensity map of the graphene/Ir(111) system measured along the $K - \Gamma - K$ direction is shown in Fig. 7.18 [135]. In the ARPES spectra of graphene on Ir(111), the π band with linear dispersion up to E_F and the Dirac cone are clearly visible at the K point [112, 135]. The position of the Dirac point was estimated to be 0.10 ± 0.02 eV above E_F, indicating only a slight p-doping [112, 135]. No sign of hybridization of graphene with the electronic bands of Ir(111) was observed, which is in line with the recent DFT calculations suggesting only a weak bonding [136]. Additionally, Dirac cone replicas and minigaps in the band structure were observed being the consequence of a superperiodic potential imposed by the moiré structure [112, 135].

In the case of strongly interacting graphene/Ru(0001) system, pronounced changes in the electronic structures occur compared with quasi-free-standing

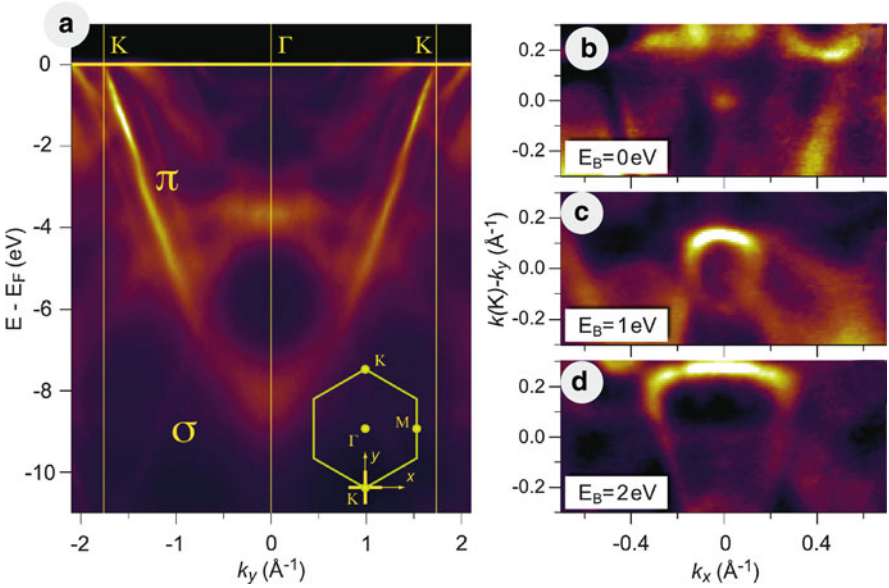

Fig. 7.18 (**a**) Photoemission intensity map along the $K - \Gamma - K$ direction and (**b–d**) the constant energy cuts obtained for the graphene/Ir(111) system at $h\nu = 120$ eV of photon energy. Data are taken from [135]

graphene or graphene/Ir(111). Figure 7.19 shows the measured band structure of graphene/Ru(0001) along the $\Gamma - K$ direction of the surface Brillouin zone [124]. At the K point, the π band reaches a binding energy of 4.6 ± 0.1 eV, which confirms a strong interaction of graphene with the substrate. The experiment is in good agreement with calculations for a 1×1 graphene sheet 2.2 Å above the topmost Ru layer with the *top-hcp* atomic configuration. Similar results were obtained in recent photoemission studies on the strongly bound graphene on Rh(111) [117]. The difference in binding energy of the π states at the Γ point in graphene/Rh(111) and pure graphite amounts to about 2.3 eV, which is close to the value for graphene/Ni(111) and also for graphene/Ru(0001). This shift reflects the effect of hybridization of the graphene π bands with the Rh $4d$ bands and, to a lesser extent, with the Rh $5s$ and $5p$ states. These results indicate that the bonding strength of the graphene layer on top of the Rh(111) surface is comparable to that observed in graphene/Ru(0001). However, a considerable local redistribution of the orbital hybridization in graphene/Rh(111) compared to Ru(0001) or Ir(111) can be deduced from strong contrast variations observed by STM.

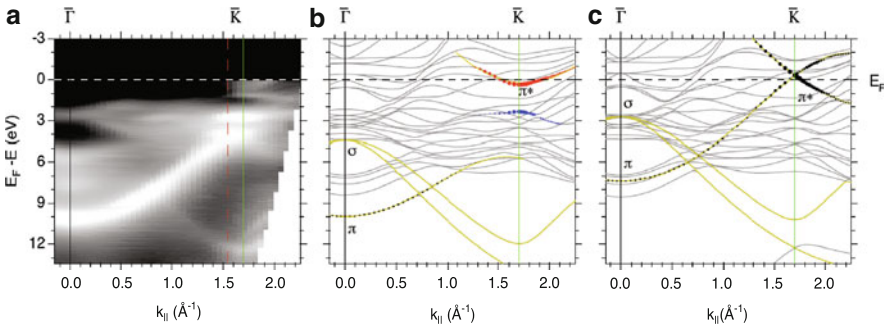

Fig. 7.19 (**a**) Band structure of the graphene/Ru(001) system measured along the $\bar{\Gamma} - \overline{K}$ direction of the hexagonal Brillouin zone. (**b**) and (**c**) DFT of graphene/Ru(0001) for the low $[(C_A,C_B) \sim (top, hcp)]$ and high $[(C_A,C_B) \sim (hcp, fcc)]$ regions, respectively. The *vertical lines* at $\bar{K}$ indicate the boundaries of the 1×1 surface Brillouin zones for Ru (*red dashed*) and graphene (*green solid*). The size of the *filled circles* in (**b**) and (**c**) represents the p_z weight of the adsorbate atoms on the bands, where *blue* describes C_A (*top*) and *red* describes *hollow* site atoms (C_B). *Black circles* depict the average of the two inequivalent adsorbate atoms. *Thick yellow* curves are guides for the eyes. Data are taken from [124]

7.6 Hybrid Structures on the Basis of Graphene Layers on Metal Surfaces

As was shown in previous sections, high-quality graphene layers can be grown on closed packed TM surfaces by means of CVD of hydrocarbons on the surface or segregation of carbon from the bulk. In contrast to the graphite intercalation compounds where the interaction between the graphene layers and the intercalated atoms is dominated by charge transfer, bonding of the graphene layers to the transition metal substrate has a more covalent character due to hybridization of d-orbitals with the π states of graphene layer. In spite of stronger interactions, alkali or noble metals can be intercalated between graphene layer and the metal substrate. The experimental procedure requires the deposition of intercalation material on the graphene-covered surface followed by the subsequent annealing of the system, which results effective intercalation underneath graphene. While in the case of alkali metals, a strong charge transfer into the antibonding π^* states is expected [73], particularly intercalation of noble metals leads to a weakening of the graphene-substrate bonding and the formation of almost isolated graphene layers on the substrate [22, 23, 26, 137–139].

Intercalation of magnetic transition metal atoms such as Co between the graphene overlayer and an e.g. nonmagnetic substrate have still not been reported. Only recent experiments show that at least Fe may be intercalated between a graphene layer and an Ni(111) substrate [24]. In an alternative approach, thin magnetic films may be grown on a nonmagnetic substrate and be covered subsequently by graphene. A possible problem here may be chemical reactions of carbon with the transition

metal substrate induced by the high temperatures needed for the cracking of the propene molecules. For Ni surfaces, respective interactions have not been observed. The situation, however, may change for Co and Fe, where the tendency of carbide formation is much larger than for Ni.

Another interesting scenario is the growth of thin transition metal films on top of a graphene monolayer. If ordered overstructures can be grown without intercalation or destruction of the graphene layer, then even multilayer structures of graphene and transition metals may be synthesized. In fact, carbide formation may be suppressed if the temperature is kept low enough. Such hybrid structures (FM/graphene/FM) were predicted to be a perfect spin filter due to the perfect in-plane lattice constants match and that their electronic structures overlap in reciprocal space for one spin direction only. On the contrary, transition-metal adsorbate may tend to island growth on graphene at low temperatures. In fact, island growth has been reported for Mn, Cr, and V [140], while the formation of a monolayer was achieved for Ru on C(0001) [141].

7.6.1 Intercalation-like Systems

The first attempt to prepare a graphene-based intercalation-like system was reported in the work by Nagashima et al. [73], where intercalation of alkali atoms (Cs, K, Na) underneath graphene layer on Ni(111) was performed. Efficient intercalation of alkali-metals underneath of the graphene layer was observed already at room temperature. Alkali-metal intercalation is accompanied by a modification of dispersion of the valence band states of graphene due to the increasing of the distance between graphene layer and Ni, and consequently, the weakening of the hybridization strength between graphene π and Ni $3d$ valence band states. This effect is reflected in the valence band photoemission spectra of this system by a strong modification of dispersion of the graphene π states around the K point of the Brillouin zone (Fig. 7.20). The electronic structure of the obtained graphene-based intercalation-like system is very similar to the one of the pristine graphite crystal. It was found that intercalation of alkali metals underneath graphene layer is energetically favorable, leading to the weakening of the bonding between graphene and substrate. The main results of these experiments were recently confirmed and refined in work [74]. Similar effects were observed upon intercalation of the divalent rare-earth metals, such as Eu and Yb [142].

Later on, the main interest in the graphene-based intercalation-like systems shifted to the investigation of the possibility to recover the original free-standing graphene-like electronic structure, where the Dirac cone is fully or partially restored. From the electronegativity point of view, it is possible via intercalation of noble metals, such as Cu, Ag, or Au. The earlier studies of Cu- and Au-intercalation underneath graphene on Ni(111) performed by means of ARPES and high-resolution electron-energy-loss spectroscopy (HREELS) demonstrate that it is possible to fully decouple electronic structures of graphene and substrate [22, 23, 137–139]

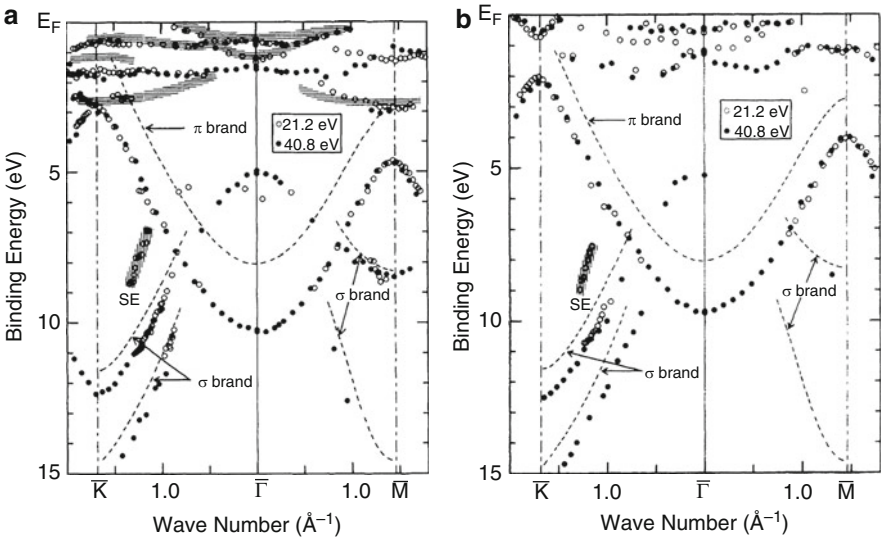

Fig. 7.20 Experimental band dispersion of (**a**) graphene/Ni(111) and (**b**) the graphene/Na/Ni(111) system. *Shaded bands* in (**a**) near E_F indicate the dispersion relations of the Ni 3*d* bands for the clean Ni(111) surface. Experimental dispersions of the bulk graphite are also shown by *broken lines*. Data are taken from [73]

(Fig. 7.21). Valence-band PES spectra taken in normal-emission geometry at 50 eV photon energy are shown in Fig. 7.21a and demonstrate the intercalation of thin layers of Cu (4 Åand 12 Å) underneath graphene layer on Ni(111) [23]. In the energy distribution curves, features originating from the π states of graphene and the 3*d* states of Ni can be readily distinguished. Upon deposition of copper on graphene/Ni(111), the PE intensity of the π graphene-derived states decreases, but remains clearly visible. Annealing of the Cu/graphene/Ni(111) system leads to an increase of intensity of the π states of graphene at the expense of the Cu 3*d* signal and a shift of the π graphene-derived band toward lower binding energies. Thereby, the intensity of the Ni 3*d* emission is almost unaffected by the annealing. The same behavior was observed for the thicker copper pre-deposited layers. Such changes of the intensities of the valence-band features of the studied system were assigned to the intercalation of thin Cu layers in the space between graphene and Ni substrate. The energy shift of the π band is caused by a change of chemical bonding between the graphene layer and the substrate through intercalation of Cu [23]. These observations were confirmed by STM and LEED, where a slight misorientation of the weakly bonded regions of graphene was detected [23].

Energy dispersions of the graphene-derived bands in the Brillouin zone of graphene are plotted in Fig. 7.21b for the graphene/Cu/Ni(111) system (different thicknesses of copper layer are marked in the figure) [23]. It was found that for this intercalation-like graphene-based system the measured energy bands are shifted toward lower binding energies as compared to their location for the

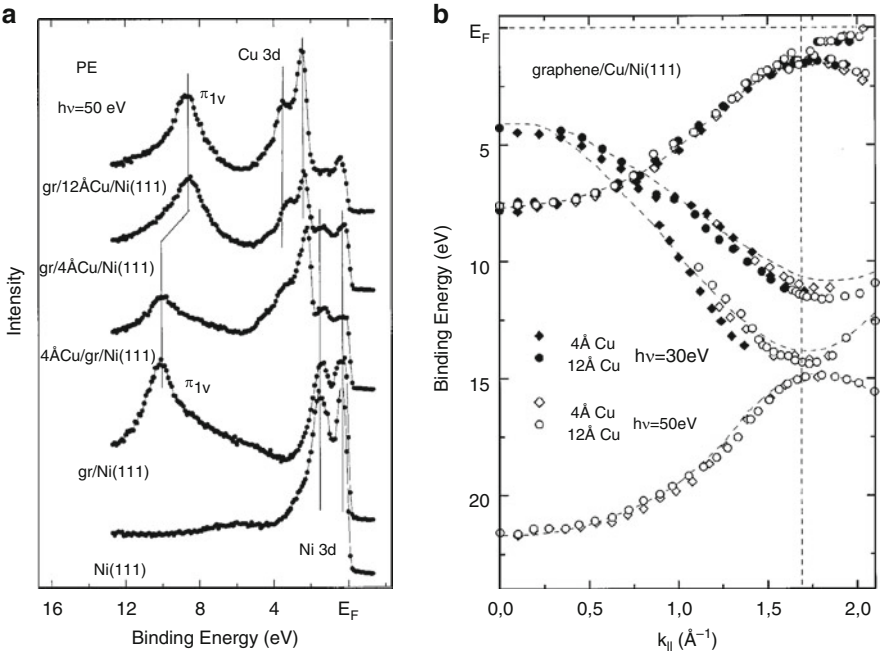

Fig. 7.21 (**a**) Normal emission PE spectra demonstrating the process of 3*d* metal intercalation underneath graphene layer on Ni(111): of the clean Ni(111) surface, a graphene/Ni(111), 4 Å Cu/graphene/Ni(111), as well as the graphene/4 Å Cu/Ni(111) and the graphene/12 Å Cu/Ni(111) systems. (**b**) Experimental band structure of the graphene/Cu/Ni(111) system. For comparison, the band structure of pristine graphite is shown by *dashed lines*. Data are taken from [23]

graphene/Ni(111) system; they approach the energies known for pristine graphite. Only for the graphene/Cu/Ni(111) system a splitting of the π states is observed around the K point: One spectral feature shifts toward higher binding energies for angles corresponding to emission from the second Brillouin zone; a second feature continues to shift up to an energy closest to E_F, but differs from that of the graphene/Ni(111) system. These features can be well defined in the second Brillouin zone, but cannot be distinguished in the first Brillouin zone. The same behavior of the graphene-derived valence-band states was later observed for the system obtained via Ag-intercalation [138].

An interesting case was considered in [22, 26, 139], where intercalation of Au underneath graphene was investigated by means of STM and ARPES. In these works, the amount of intercalated Au was estimated to be 1 ML (ML = monolayer) independent on the thickness of the predeposited metal, which is different from the Cu and Ag intercalation where different thicknesses of pre-deposited metal were intercalated [23, 137, 138]. In [22], an almost complete restoration of the free-standing graphene band structure along the $\Gamma - M$ direction of the Brillouin

zone was observed for the graphene/Ni(111) system after Au-intercalation that was also confirmed by the accompanied HREELS studies. These results were recently confirmed by the more systematic studies of the graphene/Au/Ni(111) system [139], where the full restoring of the Dirac-cone at the Fermi level was observed (within the accuracy of 25 meV).

The systematic studies of the gold intercalation underneath the graphene layer on Ru(0001) were recently performed by means of ARPES [26]. For this system, the Fermi surface appears to be point-like; however, a close look at the dispersion of the graphene-derived π states around the Fermi level [Fig. 7.22a; left-hand side, lower panel] reveals that the Dirac point is $\approx$150 meV above E_F, which is consistent with a small p-doping of the graphene layer in the graphene/Au/Ru(0001) system. A similar p-doping of graphene was recently observed in the case of deposition and annealing of a thin Au layer on the graphene monolayer on SiC(0001) [25]. In order to obtain an information about the Dirac crossing point, the electron doping via deposition of K atoms was performed, and the clear energy gap of about 200 ± 60 meV was observed, which is independent of the amount of deposited K (Fig. 7.22). It was proposed that the band gap in the graphene/Au/Ru(0001) system results from a symmetry breaking of the two carbon sublattices in the graphene layer, which results in a weak breaking of the chiral symmetry, inducing a weak but finite intensity of the left band along the $\Gamma - K$ direction, between the two arrows in Fig. 7.22c [143]. The ratio of the left to right band intensities in Fig. 7.22c is about 35, which agrees with theoretical predictions for the size of a gap of 200 meV [143]. For the 2 ML graphene/Ru(0001), there is no equivalent observable intensity [between the arrows in Fig. 7.22b], consistent with the lack of a gap at the Dirac point.

7.6.2 Growth of Noble Metal Clusters on Graphene Moirè

Highly uniform graphene moiré structures can be used as templates for the growth of uniform cluster arrays with nearly perfect long range order. This idea was first experimentally tested for graphene moiré on the Ir(111) surface allowing the preparation of Ir cluster superlattices [40]. Recently, further experiments with graphene/Ir(111) system were performed aiming to extend the row of superlattice forming materials [128, 144]. Figure 7.23 displays STM topographs recorded on graphene/Ir(111) after deposition 0.2−0.8 ML of various metals at 300 K. Deposited metal clusters are pinned to graphene and the preferred regions of the cluster adsorption at 300 K were identified as hcp areas of the moiré suprecell where the carbon ring center of graphene is located above hcp sites of the underlying Ir(111). During initial deposition, the hcp areas are filled by metal clusters with a relatively uniform size until all moiré unit cells are filled. Upon further deposition, metal clusters start to grow in size, but a narrow size distribution is preserved. LDA calculations showed that sp^2 to sp^3 rehybridization of carbon atoms in the graphene layer underneath Ir clusters is responsible for the cluster adsorption [136]. Carbon atoms were shown to form strong bonds either to Ir surface atoms of the

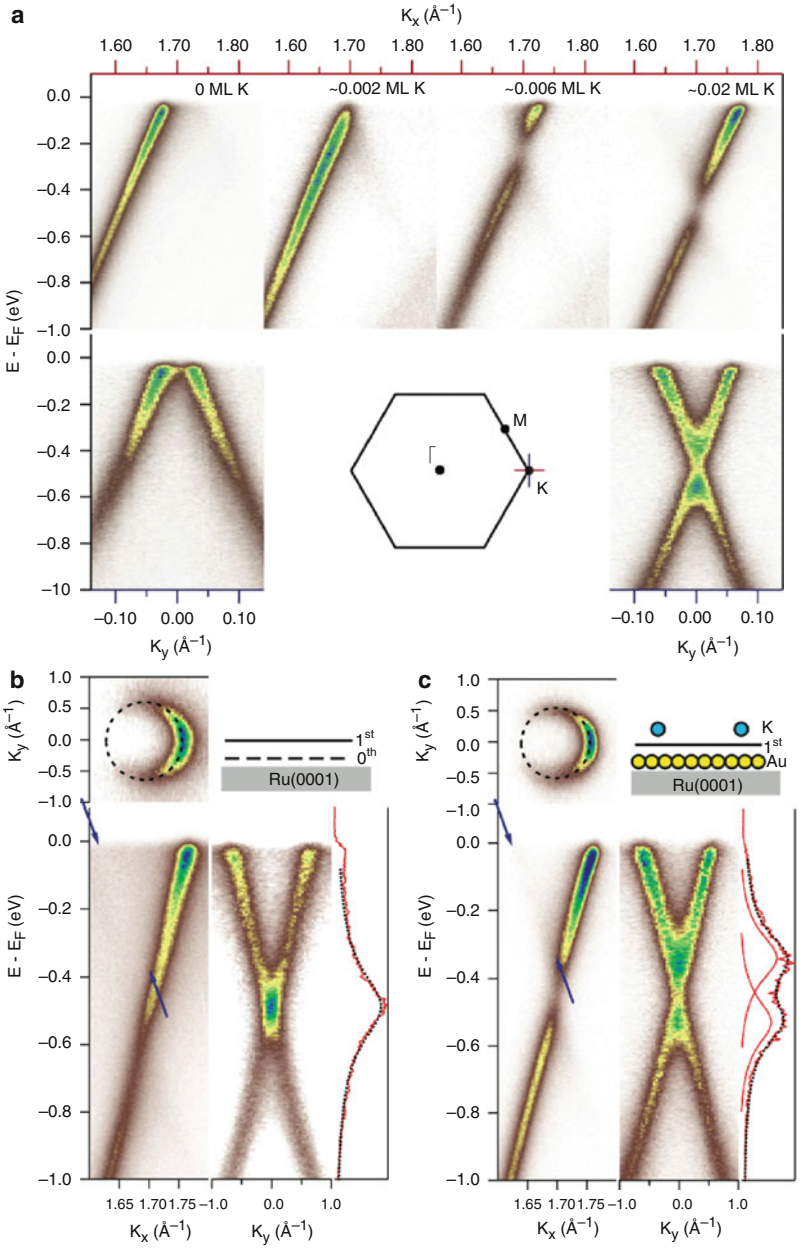

Fig. 7.22 (**a**) A series of photoemission intensity maps around the *K* point of the Brillouin zone of the 1 ML graphene/Au/Ru(0001) system for clean (*left column*) and progressive doping with potassium. The upper and lower rows are taken along the two orthogonal directions in the reciprocal space as indicated by the *red and black lines* at the *K* point in the Brillouin zone (inset). Comparison of the spectral function of (**b**) 2 ML graphene/Ru(0001) and (**c**) graphene/1 ML Au/Ru(0001) is shown in the lower panel together with corresponding PE intensity profiles at the *K* point. Data are taken from [26]

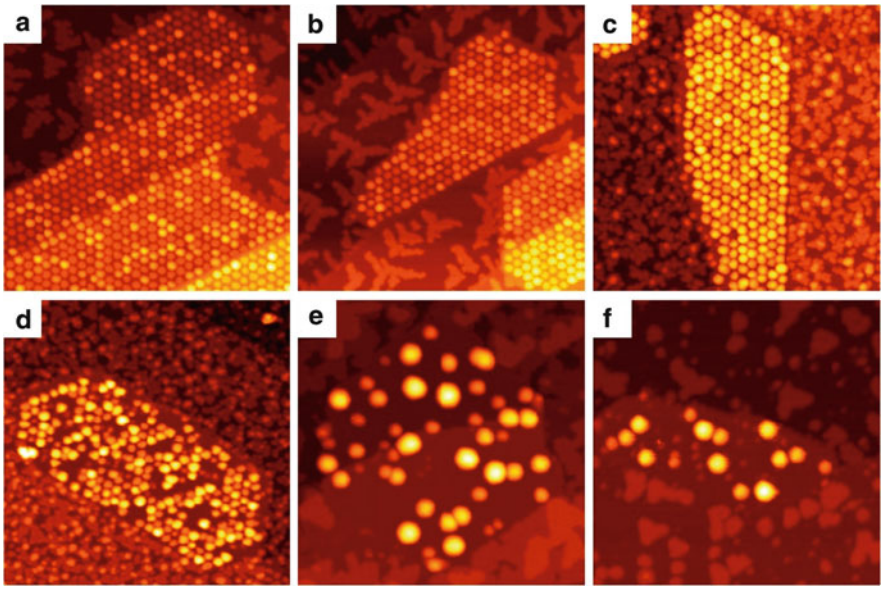

Fig. 7.23 700 Å × 700 Å STM images of the Ir(111) surface covered by graphene flakes after the deposition of various metals at 300 K. (**a**) 0.20 ML Ir, average cluster size $S_{av} = 17$ atoms; (**b**) 0.25 ML Pt, $S_{av} = 22$ atoms; (**c**) 0.44 ML W, $S_{av} = 38$ atoms; (**d**) 0.53 ML Re, $S_{av} = 60$ atoms; (**e**) 0.77 ML Fe, $S_{av} = 420$ atoms; (**f**) 0.25 ML Au, $S_{av} = 100$ atoms. Data are taken from [144].

substrate or to the Ir atoms of the clusters resulting in buckling of the graphene layer. However, as can be seen in the STM images not all metals form a cluster superlattice on graphene/Ir(111). Ir and Pt form superlattices of high perfection [Fig. 7.23a, b], whereas for Fe [Fig. 7.23e] and Au [Fig. 7.23f] no superlattice can be realized at 300 K [144]. In case of Re, Fe, and Au, the superlattice formation can be efficiently improved either by lowering the deposition temperature or cluster-seeding. In the latter case, Ir seed clusters are first created in nearly all moiré unit cells, which act as nucleation centers during further metal deposition at 300 K yielding highly uniform metal cluster superlattices with Ir cores [128]. Most of the investigated metal cluster superlattices on graphene/Ir(111) were found to be stable up to 400 K. More recently, the suitability of the graphene/Ru(0001) moiré for the fabrication of uniform cluster lattices of Pt has been tested [48–50]. Pt clusters were found to preferably occupy locations corresponding to the brighter of the two moiré minima within the moiré unit cell, which are identified as the fcc regions [50]. Upon growth at 140–180 K, Donner et al. [50] prepared highly uniform periodic arrays of monodisperse Pt clusters, which were found to be structurally stable up to room temperature. However, the perfection of the prepared periodic arrays of Pt clusters on graphene/Ru(0001) seems to vary strongly depending on the deposition temperature, Pt deposition rates, as well as deposited amount of Pt [48–50]. Such highly ordered cluster arrays of noble metals are of interest for possible applications in nanocatalysis.

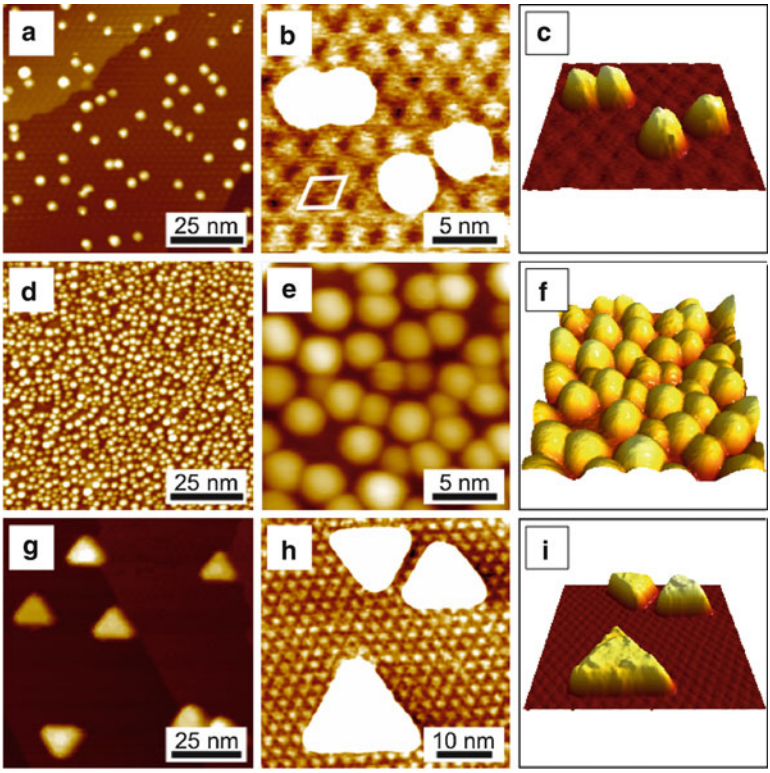

Fig. 7.24 (**a–b**) Topographic STM images obtained after the deposition of nominally 0.25 ML Ni at 150 K on graphene on Rh(111). The moiré superstructure unit cell in (**b**) is outlined by a rhombus. (**c**) Rendered perspective image of the STM topograph presented in (**b**). (**d–e**) Topographic STM images obtained after the deposition of nominally 1.50 ML Ni at 150 K on graphene on Rh(111). (**f**) Rendered perspective image of the STM topograph presented in (**e**). (**g–h**) STM topograph of nominally 0.90 ML Ni on graphene/Rh(111) deposited at room temperature. (**i**) Rendered perspective image of the STM topograph presented in (**h**). Tunneling parameters for STM images: (**a–c**) $U_T = 1.78$ V; $I_T = 0.11$ nA; (**d**) $U_T = 1.20$ V; $I_T = 0.35$ nA; (**e–f**) $U_T = 1.28$ V; $I_T = 1.53$ nA; (**g**) $U_T = 0.90$ V; $I_T = 0.88$ nA; (**h–i**) $U_T = 1.54$ V; $I_T = 1.15$ nA). Data are taken from [51]

7.6.3 Growth of Magnetic Metal Clusters on Graphene Moirè

Fabrication of ordered arrays of magnetic clusters is of a particular interest with respect to possible technological applications in magnetic data storage. Graphene moiré on Rh(111) has recently been used as a template for the growth of Ni clusters [51]. Figure 7.24a, b shows STM topographs of 0.25 ML of Ni deposited on graphene/Rh(111) at 150 K. Large terraces and steps of graphene/Rh(111) covered with Ni nanoclusters (NCs) can be clearly distinguished. The NCs show mostly hemispherical shapes with at least some cluster edges, which appear to be oriented

along the in-plane $<1\bar{1}0>$ direction. The apparent height of the clusters was measured to be 0.85 ± 0.1 nm, which roughly corresponds to four *fcc* (111) planes of Ni. The clusters are loosely bound to the graphene surface at room temperature and could easily be swept away by the STM tip during scanning, which is in row with other reports [50]. The diameter distribution of the clusters is very narrow with the average cluster diameter being 3.1 nm. Most of the Ni clusters were found to be located on the regular grid showing a quite high unit cell occupation probability for the deposited amount. However, the nucleation of NCs obviously occurs at two different regions within the moiré unit cell (*top-fcc* and *top-hcp*). The randomized occupation can be attributed to the fact that the deposition temperature of 150 K is below the optimum temperature. Upon increasing Ni coverage, no visible order of the cluster arrangement can be realized. Figure 7.24d–f shows the surface morphology after the deposition of 1.50 ML of Ni at 150 K. Ni clusters exhibit a distinctly different size distribution compared with that at lower coverages. The lateral size of the clusters is more spread.

Ni deposited at room temperature exhibits a completely different growth mode compared with deposition at 150 K [51]. Instead of small compact NCs, Ni forms triangular-shaped islands with their edges roughly aligned with the close packed $< 1\bar{1}0 >$ directions of the Rh(111) substrate as shown in Fig. 7.24g–i. The existence of large islands nucleated at terraces indicates that Ni atoms are highly mobile on the graphene surface at room temperature. On the other hand, it is remarkable that, in spite of the weak bonding strength between Ni and graphene surface, the moiré structure imposes registration and orientation on the Ni nanostructures. The average apparent height of the islands is 1.8 nm and the size defined by the length of the edges is ranging from about 5 nm to about 18 nm. The surface of the islands is rather flat. The two different orientations can be attributed to the initial nucleation taking place either at a *top-hcp* and *top-fcc* site. The long edges of the islands are not always exactly aligned with the high-symmetry $<1\bar{1}0>$ directions of Rh(111). Some of the islands are oriented with an angle of up to $\pm 10°$ with respect to these high-symmetry directions. Clockwise-rotated and counterclockwise-rotated islands are found to occur with equal probability. Since the magnetic anisotropy depends on shape and size of the cluster, the deposition temperature is the key parameter to play with in order to control the magnetic properties of the nanoclusters.

7.6.4 Chemical Functionalization of Graphene on Transition Metal Surfaces

One of the main routes towards the modification of graphene electronic structure in a controllable way is the chemical functionalization by atoms and molecules, i.e., the process of creating covalent bonds between graphene and adsorbates. The general principles of chemical functionalization of graphene and recent achievements in this field are discussed recently in the review by Boukhvalov and Katsnelson [29].

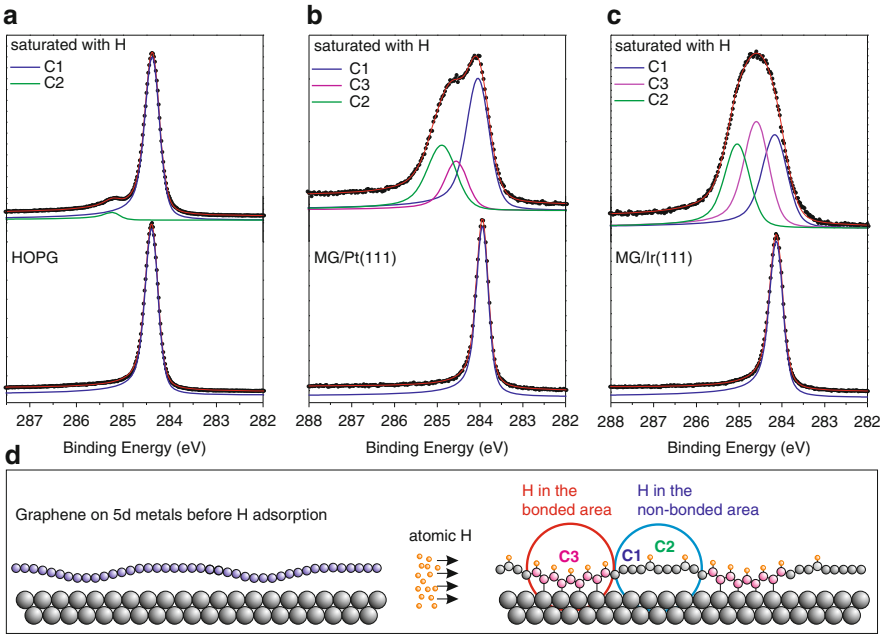

Fig. 7.25 C 1*s* PE spectra taken with $h\nu = 400$ eV from pristine and fully hydrogenated (**a**) graphite and graphene on (**b**) Pt(111) and (**c**) Ir(111). (**d**) Schematic representation of the hydrogenation process for graphene on 5*d* metal surfaces (Ir, Pt). Substrate atoms are shown by *large circles*, C atoms by *middle-size circles*, H atoms by *small circles*. Data are taken from [145]

In comparison with the free-standing graphene, graphene/metal interfaces may be more advantageous for the formation of covalent bonds with atomic and molecular species, since the interaction with the substrate can weaken the lateral C–C bonds and "activate" graphene. This effect can be demonstrated by the example of chemical functionalization of graphene induced by atomic hydrogen. In the graphene/Ir(111) system, a gradual H adsorption has been shown to result in a controllable opening of the band gap due to the sp^2-to-sp^3 transition in the more bonding parts of the graphene/Ir(111) moiré [114].

The influence of the chemical nature of the underlying metal on the ability of graphene to adsorb atomic H has been recently studied for a variety of graphene/metal interfaces [145]. As can be judged from the C 1*s* PE spectra shown in Fig. 7.25a–c, the same H treatment of different graphitic substrates results in very different H uptake values. Here, different spectral components correspond to the C atoms in the flat (sp^2) coordination (C1), directly bonded to H (C2) and directly bonded to the metal substrate in the buckled (sp^3) coordination (C3). Without a reactive substrate, the saturated H coverage is relatively low, while for graphene on a reactive metal substrate, like Pt(111) and Ir(111), the H uptake value can increase significantly. In Fig. 7.25d, the process of H adsorption on a nano-patterned graphene layer weakly bound to a 5*d* substrate is schematically illustrated. The

more bonding graphene patches (pores) are able to achieve 50% H coverage by forming graphene-like structures [146]. This process becomes possible due to the strengthening of the C $2p_z$ – TM $5d$ bonds, which can involve the unpaired electrons released upon breaking the C–C bonds in the course of H adsorption. The total area of more strongly bonding graphene sites (pores) is higher for graphene on Ir than on Pt, thus resulting in the higher H coverage. The nonbonding graphene areas are much more passive, and hydrogenation of these sites is expected to be similar to that of HOPG. For the already strongly bound and lattice matched interfaces (such as graphene/Ni) the mechanism of H adsorption is different, since further strengthening of the C–Ni bonds is impossible. In this case, the unpaired electrons released upon destroying the C–C double bonds by H adsorption are supposed to form dangling bonds on graphene, thus hampering further H adsorption [145].

7.7 Conclusions and Outlook

With all the recent and well-justified excitement about the unusual properties of graphene, it is often forgotten that graphene films on metal surfaces were studied more than forty years ago. Sometimes, they were considered an unavoidable nuisance, for example in the process of cleaning nickel and other transition metal surfaces in ultrahigh vacuum experiments, or an outright problem, in the context of catalyst poisoning through a carbon layer. In the course of such studies, the geometric and electronic structure of these "single layer graphite" films was carefully studied by means of modern surface science techniques, and even the distinction between strongly bound layers and an almost free-standing film, created by intercalation of noble metals between graphene and the transition metal substrate was examined. While the discovery of the unusual electronic and transport properties in graphene in 2005 [147, 148] centered on graphene flakes on insulating (SiO_2) or semiconducting (SiC) surfaces, renewed attention has returned to graphene on metals. Many interesting discoveries have been made, as documented in this chapter. It was shown that graphene films can be grown with unprecedented structural perfection, over micrometers and larger, on substrates such as iridium and rhodium. Bonding of graphene to lattice-matched (Ni, Co) and mismatched (Ru, Rh, Pt, Ir) metals has been analyzed, and the emergence of moiré patterns with large differences in bonding strength in the supercell was observed. The reasons for the large differences in bonding strength of graphene to Ni and Co, on the one hand, and the $5d$ metals, on the other, are still a matter of discussion. As far as fundamental studies of electronic effects are concerned, it is true that the preparation and examination of graphene on metals suffers from a serious disadvantage, in that transport experiments, which are at the center of attention (e.g. the anomalous quantum Hall effect) are not feasible. However, this disadvantage is partly compensated by the recent discovery that graphene growth on metals may be the only viable pathway toward the mass production of large-scale monolayer films for deposition on various substrates, for example as transparent electrodes.

Clearly, much more work is necessary (and in all likelihood, already under way, given the enormous economic stakes involved) to optimize graphene growth and the techniques to lift if off a suitable metal substrate.

The study of graphene on metal substrates has much more to offer, however. The fact that the moiré structure formed by graphene on Ir(111) gives rise to a template for the growth of clusters with a narrow size dispersion, and with perfect ordering across the surface has come as a complete surprise. Such self-organized cluster growth systems lend themselves almost naturally to investigations of size-dependent electronic structure, general physical properties, and adsorption or catalytic behavior; moreover, in $3d$ metal clusters, their magnetic properties promise to be an exciting field of study. Here at least, growth on a metal surface does not inhibit investigations as long as the latter is not ferromagnetic, e.g. in the case of iridium.

This brings us to consider the investigation of graphene-ferromagnet interfaces: theoretical studies predict a few-layer film of graphene on either Ni or Co to act as a highly efficient spin filter, because of the difference in overlap between the minority and majority spin states and the graphene bands at the corners of the Brillouin zone. A physical realization of such systems may bring the elusive spin field effect transistor closer to realization. The properties of spin transport in graphene have received intense interest ever since it was demonstrated that spin coherence lengths are in the micrometer range [39]. Injection and detection of electrons with different spin orientations is important in the context of a recently proposed experiment, in which Cooper pairs from a superconducting electrode are separated into two opposite graphene strips. Ferromagnetic contacts are then attached to the end of these strips, permitting the measurement of the electrons' spin state, thus offering to perform experiments with entangled electron states in a transport experiment.

Last but not least, the study of adsorption, intercalation processes on graphene itself, is a promising field for which only few reports are available at present. Functionalization of graphene is clearly an important issue, also in the context of doping and for sensing applications, but equally exciting is the prospect of using adsorption and self-organization processes of complex organic molecules on metal surfaces to create various "lower-than-two" dimensional graphene-like structures of the wire and dot type. The wealth of molecules with benzene ring segments provided by organic chemistry in ever larger numbers offers the possibility to prepare high-quality graphene "nanoribbons", and first examples have already been described in the literature.

Progress in the field of graphene research, and also in studies of graphene on metals, is so rapid that the present overview can only give a glimpse of the current status, and may have to be updated within a year or so. The rapid pace of progress is a demonstration of the maturity of the way in which the experimental probes and their interpretation are mastered, and it is matched by the theoretical understanding of properties and processes at the surface and interface of graphene. Investigating graphene and carbon-related structures on metals holds great promise for novel and, from a basic science and applications-oriented perspective, exciting discoveries.

Acknowledgements We thank all co-workers and collaborators for their contributions to this work, in particular, M. Weser, S. Böttcher, C. Enderlein, E. Voloshina, E. Goering, M. Sicot, P. Leicht, A. Zusan, O. Zander, A. S. Vinogradov, M. L. Ng, and S. Bouvron. This work has been supported by the European Science Foundation (ESF) under the EUROCORES Programme EuroGRAPHENE (Project "SpinGraph"). Y. D. acknowledges the financial support by the German Research Foundation (DFG) under project DE 1679/2-1. M. F. gratefully acknowledges the financial support by the Research Center "UltraQuantum" (Excellence Initiative), by the German Research Foundation (DFG) via the Collaborative Research Center (SFB) 767, and the Baden-Württemberg Stiftung. A. P. is grateful for the financial support from the Swedish Research Council.

References

1. A.K. Geim, K.S. Novoselov, Nat. Mater. **6**, 183 (2007)
2. A.K. Castro Neto, F. Guinea, N.M.R. Peres, K.S. Novoselov, A.K. Geim, Rev. Mod. Phys. **81**, 109 (2009)
3. A.K. Geim, Science **324**, 1530 (2009)
4. Q. Yu, J. Lian, S. Siriponglert, H. Li, Y.P. Chen, S.-S. Pei, Appl. Phys. Lett. **93**, 113103 (2008)
5. K.S. Kim, Y. Zhao, H. Jang, S.Y. Lee, J.M. Kim, K.S. Kim, J.-H. Ahn, P. Kim, J.-Y. Choi, B.H. Hong, Nature **457**, 706 (2009)
6. X. Li, W. Cai, J. An, S. Kim, J. Nah, D. Yang, R. Piner, A. Velamakanni, I. Jung, E. Tutuc, S.K. Banerjee, L. Colombo, R.S. Ruoff, Science **324**, 1312 (2009)
7. S. Bae, H. Kim, Y. Lee, X. Xu, J.-S. Park, Y. Zheng, J. Balakrishnan, T. Lei, H.R. Kim, Y.I. Song, Y.-J. Kim, K.S. Kim, B. Ozyilmaz, J.-H. Ahn, B.H. Hong, S. Iijima, Nat. Nanotechnol. **5**, 574 (2010)
8. B.J. Kang, J.H. Mun, C. Y. Hwang, B.J. Cho, J. Appl. Phys. **106**, 104309 (2009)
9. E. Sutter, P. Albrecht, P. Sutter, Appl. Phys. Lett. **95**, 133109 (2009)
10. J. Bai, R. Cheng, F. Xiu, L. Liao, M. Wang, A. Shailos, K.L. Wang, Y. Huang, X. Duan, Nat. Nanotechnol. **5**, 655 (2010)
11. J. Cai, P. Ruffieux, R. Jaafar, M. Bieri, T. Braun, S. Blankenburg, M. Muoth, A.P. Seitsonen, M. Saleh, X. Feng, K. Müllen, R. Fasel, Nature **466**, 470 (2010)
12. T. Ohta, A. Bostwick, T. Seyller, K. Horn, E. Rotenberg, Science **313**, 951 (2006)
13. Y. Zhang, T.-T. Tang, C. Girit, Z. Hao, M.C. Martin, A. Zettl, M.F. Crommie, Y.R. Shen, F. Wang, Nature **459**, 820 (2009)
14. X. Wang, X. Li, L. Zhang, Y. Yoon, P.K. Weber, H. Wang, J. Guo, H. Dai, Science **324**, 768 (2009)
15. S. Dutta, S.K. Pati, J. Phys. Chem. B **112**, 1333 (2008)
16. Y. Mao, J. Yuan, J. Zhong, J. Phys.: Condens. Matter **20**, 115209 (2008)
17. J. Wintterlin, M.L. Bocquet, Surf. Sci. **603**, 1841 (2009)
18. P.A. Khomyakov, G. Giovannetti, P.C. Rusu, G. Brocks, J.V.D. Brink, P.J. Kelly, Phys. Rev. B **79**, 195425 (2009)
19. E. Rotenberg, A. Bostwick, T. Ohta, J.L. McChesney, T. Seyller, K. Horn, Nat. Mater. **7**, 258 (2008)
20. S.Y. Zhou, D.A. Siegel, A.V. Fedorov, F.E. Gabaly, A.K. Schmid, A.H.C. Neto, D.H. Lee, A. Lanzara, Nat. Mater. **7**, 259 (2008)
21. G. Giovannetti, P.A. Khomyakov, G. Brocks, P.J. Kelly, J. van den Brink, Phys. Rev. B **76**, 073103 (2007)
22. A. Shikin, G. Prudnikova, V. Adamchuk, F. Moresco, K. Rieder, Phys. Rev. B **62**, 13202 (2000)

23. Y.S. Dedkov, A.M. Shikin, V.K. Adamchuk, S.L. Molodtsov, C. Laubschat, A. Bauer, G. Kaindl, Phys. Rev. B **64**, 035405 (2001)
24. Y.S. Dedkov, M. Fonin, U. Rüdiger, C. Laubschat, Appl. Phys. Lett. **93**, 022509 (2008)
25. I. Gierz, C. Riedl, U. Starke, C. Ast, K. Kern, Nano Lett. **8**, 4603 (2008)
26. C. Enderlein, Y.S. Kim, A. Bostwick, E. Rotenberg, K. Horn, New J. Phys. **12**, 033014 (2010)
27. I. Gierz, T. Suzuki, R.T. Weitz, D.S. Lee, B. Krauss, C. Riedl, U. Starke, H. Hoechst, J.H. Smet, C. R. Ast, K. Kern, Phys. Rev. B **81**, 235408 (2010)
28. K.T. Chan, J.B. Neaton, M.L. Cohen, Phys. Rev. B **77**, 235430 (2008)
29. D. W. Boukhvalov, M.I. Katsnelson, J. Phys.: Condens. Matter. **21**, 344205 (2009)
30. C. Coletti, C. Riedl, D.S. Lee, B. Krauss, L. Patthey, K. von Klitzing, J.H. Smet, U. Starke, Phys. Rev. B **81**, 235401 (2010)
31. E.J.H. Lee, K. Balasubramanian, R.T. Weitz, M. Burghard, K. Kern, Nat. Nanotechnol. **3**, 486 (2008)
32. F. Xia, T. Mueller, R. Golizadeh-Mojarad, M. Freitag, Y.-M. Lin, J. Tsang, V. Perebeinos, P. Avouris, Nano Lett. **9**, 1039 (2009)
33. T. Mueller, F. Xia, M. Freitag, J. Tsang, P. Avouris, Phys. Rev. B **79**, 245430 (2009)
34. B. Huard, N. Stander, J.A. Sulpizio, D. Goldhaber-Gordon, Phys. Rev. B **78**, 121402 (2008)
35. V.M. Karpan, G. Giovannetti, P.A. Khomyakov, M. Talanana, A.A. Starikov, M. Zwierzycki, J. van den Brink, G. Brocks, P.J. Kelly, Phys. Rev. Lett. **99**, 176602 (2007)
36. V.M. Karpan, P.A. Khomyakov, A.A. Starikov, G. Giovannetti, M. Zwierzycki, M. Talanana, G. Brocks, J.V.D. Brink, P.J. Kelly, Phys. Rev. B **78**, 195419 (2008)
37. O.V. Yazyev, A. Pasquarello, Phys. Rev. B **80**, 035408 (2009)
38. O.V. Yazyev, M.I. Katsnelson, Phys. Rev. Lett. **100**, 047209 (2008)
39. N. Tombros, C. Jozsa, M. Popinciuc, H. T. Jonkman, B.J. van Wees, Nature **448**, 571 (2007)
40. A. N'Diaye, S. Bleikamp, P. Feibelman, T. Michely, Phys. Rev. Lett. **97**, 215501 (2006)
41. A.B. Preobrajenski, M.L. Ng, A.S. Vinogradov, N. Mårtensson, Phys. Rev. B **78**, 073401 (2008)
42. S. Marchini, S. Guenther, J. Wintterlin, Phys. Rev. B **76**, 075429 (2007)
43. D. Martoccia, P.R. Willmott, T. Brugger, M. Björck, S. Günther, C.M. Schlepütz, A. Cervellino, S.A. Pauli, B.D. Patterson, S. Marchini, J. Wintterlin, W. Moritz, T. Greber, Phys. Rev. Lett. **101**, 126102 (2008)
44. A.L. Vazquez de Parga, F. Calleja, B. Borca, M.C.G. Passeggi, J.J. Hinarejos, F. Guinea, R. Miranda, Phys. Rev. Lett. **100**, 1 (2008)
45. P.W. Sutter, J.-I. Flege, E.A. Sutter, Nature Mater. **7**, 406 (2008)
46. P. Sutter, M.S. Hybertsen, J.T. Sadowski, E. Sutter, Nano Lett. **9**, 2654 (2009)
47. B. Borca, S. Barja, M. Garnica, J.J. Hinarejos, A.L.V. de Parga, R. Miranda, F. Guinea, Semicond. Sci. Tech. **25**, 034001 (2010)
48. H. Zhang, Q. Fu, Y. Cui, D. Tan, X. Bao, J. Phys. Chem. C **113**, 8296 (2009)
49. Y. Pan, M. Gao, L. Huang, F. Liu, H.J. Gao, Appl. Phys. Lett. **95**, 093106 (2009)
50. K. Donner, P. Jakob, J. Chem. Phys. **131**, 164701 (2009)
51. M. Sicot, S. Bouvron, O. Zander, U. Ruediger, Y.S. Dedkov, M. Fonin, Appl. Phys. Lett. **96**, 093115 (2010)
52. A. Nagashima, H. Itoh, T. Ichinokawa, C. Oshima, S. Otani, Phys. Rev. B **50**, 4756 (1994)
53. C. Oshima, A. Nagashima, J Phys.: Condens. Matter **9**, 1 (1997)
54. S. Hla, J. Vac. Sci. Technol. B **23**, 1351 (2005)
55. D. Fujita and K. Sagisaka, Sci. Technol. Adv. Mater. **9**, 013003 (2008)
56. J. Stöhr and M. Samant, J. Electr. Spectr. Rel. Phenom. **98**, 189 (1999)
57. J. Stöhr, J. Magn. Magn. Mat. **200**, 470 (1999)
58. B. Thole, P. Carra, F. Sette, G. van der Laan, Phys. Rev. Lett. **68**, 1943 (1992)
59. P. Carra, B. Thole, M. Altarelli, X. Wang, Phys. Rev. Lett. **70**, 694 (1993)
60. F. Reinert, S. Hüfner, New J. Phys. **7**, 97 (2005)

61. A. Damascelli, Z. Hussain, Z. Shen, Rev. Mod. Phys. **75**, 473 (2003)
62. A. Damascelli, Phys. Scripta **T109**, 61 (2004)
63. P.D. Johnson, Rep. Prog. Phys. **60**, 1217 (1997)
64. L. Isett, J. Blakely, Surf. Sci. **47**, 645 (1975)
65. L. Isett, J. Blakely, Surf. Sci. **58**, 397 (1976)
66. J. Shelton, H. Patil, J. Blakely, Surf. Sci. **43**, 493 (1974)
67. M. Eizenberg, J. Blakely, Surf. Sci. **82**, 228 (1979)
68. M. Eizenberg, J. Blakely, J. Chem. Phys. **71**, 3467 (1979)
69. R. Rosei, M. Decrescenzi, F. Sette, C. Quaresima, A. Savoia, P. Perfetti, Phys. Rev. B **28**, 1161 (1983)
70. Y. Gamo, A. Nagashima, M. Wakabayashi, M. Terai, C. Oshima, Surf. Sci. **374**, 61 (1997)
71. E.N. Voloshina, Y.S. Dedkov, in *Electronic and Magnetic Properties of the Graphene-Ferromagnet Interfaces: Theory vs Experiment*, ed. by S. Mikhailov. *Physics and Applications of Graphene – Experiments* (INTECH Education and Publishing, Vienna, 2010) ISBN 978-953-307-217-3
72. R. Rosei, S. Modesti, F. Sette, C. Quaresima, A. Savoia, P. Perfetti, Solid State Commun. **46**, 871 (1983)
73. A. Nagashima, N. Tejima, C. Oshima, Phys. Rev. B **50**, 17487 (1994)
74. A. Grüneis, D. Vyalikh, Phys. Rev. B **77**, 193401 (2008)
75. Y.S. Dedkov, M. Fonin, New J. Phys. **12**, 125004 (2010)
76. G. Bertoni, L. Calmels, A. Altibelli, V. Serin, Phys. Rev. B **71**, 075402 (2004)
77. Y.S. Dedkov, M. Fonin, C. Laubschat, Appl. Phys. Lett. **92**, 052506 (2008)
78. Y.S. Dedkov, M. Fonin, U. Rüdiger, C. Laubschat, Phys. Rev. Lett. **100**, 107602 (2008)
79. A. Grueneis, K. Kummer, D.V. Vyalikh, New J. Phys. **11**, 073050 (2009)
80. M. Fuentes-Cabrera, M.I. Baskes, A.V. Melechko, M.L. Simpson, Phys. Rev. B **77**, 035405 (2008)
81. G. Kalibaeva, R. Vuilleumier, S. Meloni, A. Alavi, G. Ciccotti, R. Rosei, J. Phys. Chem. B **110**, 3638 (2006)
82. C. Klink, I. Stensgaard, F. Besenbacher, E. Laegsgaard, Surf. Sci. **342**, 250 (1995)
83. D. Eom, D. Prezzi, K.T. Rim, H. Zhou, M. Lefenfeld, S. Xiao, C. Nuckolls, M.S. Hybertsen, T.F. Heinz, G.W. Flynn, Nano Lett. **9**, 2844 (2009)
84. K. Yamamoto, M. Fukishima, T. Osaka, C. Oshima, Phys. Rev. B **45**, 11358 (1992)
85. Y. Souzu, M. Tsukada, Surf. Sci. **326**, 42 (1995)
86. M. Weser, Y. Rehder, K. Horn, M. Sicot, M. Fonin, A.B. Preobrajenski, E. N. Voloshina, E. Goering, Y.S. Dedkov, Appl. Phys. Lett. **96**, 012504 (2010)
87. J. Rusz, A.B. Preobrajenski, M.L. Ng, N. A. Vinogradov, N. Mårtensson, O. Wessely, B. Sanyal, O. Eriksson, Phys. Rev. B **81**, 073402 (2010)
88. O. Wessely, M. Katsnelson, O. Eriksson, Phys. Rev. Lett. **94**, 167401 (2005)
89. G. Giovannetti, P.A. Khomyakov, G. Brocks, V.M. Karpan, J.V.D. Brink, P.J. Kelly, Phys. Rev. Lett. **101**, 026803 (2008)
90. S. Andersson, M. Frank, A. Sandell, A. Giertz, B. Brena, P. Brühwiler, N. Mårtensson, J. Libuda, M. Baümer, H. Freund, J. Chem. Phys. **108**, 2967 (1998)
91. F. B. de Mongeot, A. Toma, A. Molle, S. Lizzit, L. Petaccia, A. Baraldi, Phys. Rev. Lett. **97**, 056103 (2006)
92. E. Shirley, L. Terminello, A. Santoni, F. Himpsel, Phys. Rev. B **51**, 13614 (1995)
93. P. Srivastava, F. Wilhelm, A. Ney, M. Farle, H. Wende, N. Haack, G. Ceballos, K. Baberschke, Phys. Rev. B **58**, 5701 (1998)
94. S. Dhesi, H. Dürr, G. van der Laan, E. Dudzik, N. Brookes, Phys. Rev. B **60**, 12852 (1999)
95. A. Nesvizhskii, A. Ankudinov, J. Rehr, K. Baberschke, Phys. Rev. B **62**, 15295 (2000)
96. K. Baberschke, Appl. Phys. A **62**, 417 (1996)
97. D. Huang, H. Jeng, C. Chang, G. Guo, J. Chen, W. Wu, S. Chung, S. Shyu, C. Wu, H. Lin, C. Chen, Phys. Rev. B **66**, 174440 (2002)
98. H. Mertins, S. Valencia, W. Gudat, P. Oppeneer, O. Zaharko, H. Grimmer, Europhys. Lett. **66**, 743 (2004)

99. C. Sorg, N. Ponpandian, M. Bernien, K. Baberschke, H. Wende, R.Q. Wu, Phys. Rev. B **73**, 064409 (2006)
100. Z.Y. Li, Z.Q. Yang, S. Qiao, J. Hu, R.Q. Wu, J. Phys.: Condens. Matter **23**, 225502 (2011)
101. O. Rader, A. Varykhalov, J. Sanchez-Barriga, D. Marchenko, A. Rybkin, A.M. Shikin, Phys. Rev. Lett. **102**, 057602 (2009)
102. H. Lyon, G. Somorjai, J. Chem. Phys. **46**, 2539 (1967)
103. A. Morgan, G. Somorjai, Surf. Sci. **12**, 405 (1968)
104. Z. Hu, D. Ogletree, M. van Hove, G. Somorjai, Surf. Sci. **180**, 433 (1987)
105. T. Land, T. Michely, R. Behm, J. Hemminger, G. Comsa, Surf. Sci. **264**, 261 (1992)
106. S. Entani, S. Ikeda, M. Kiguchi, K. Saiki, G. Yoshikawa, I. Nakai, H. Kondoh, T. Ohta, Appl. Phys. Lett. **88**, 153126 (2006)
107. P. Sutter, J. Sadowski, E. Sutter, Phys. Rev. B **80**, 245411 (2009)
108. M. Gao, Y. Pan, C. Zhang, H. Hu, R. Yang, H. Lu, J. Cai, S. Du, F. Liu, H.-J. Gao, Appl. Phys. Lett. **96**, 053109 (2010)
109. B. Nieuwenhuys, D. Hagen, G. Rovida, G. Somorjai, Surf. Sci. **59**, 155 (1976)
110. J. Coraux, A.T. N'Diaye, M. Engler, C. Busse, D. Wall, N. Buckanie, F.-J.M. zu Heringdorf, R. van Gastel, B. Poelsema, T. Michely, New J. Phys. **11**, 023006 (2009)
111. E. Loginova, S. Nie, K. Thuermer, N.C. Bartelt, K.F. McCarty, Phys. Rev. B **80**, 085430 (2009)
112. I. Pletikosić, M. Kralj, P. Pervan, R. Brako, J. Coraux, A. N'Diaye, C. Busse, T. Michely, Phys. Rev. Lett. **102**, 056808 (2009)
113. P. Lacovig, M. Pozzo, D. Alfè, P. Vilmercati, A. Baraldi, S. Lizzit, Phys. Rev. Lett. **103**, 166101 (2009)
114. R. Balog, B. Jorgensen, L. Nilsson, M. Andersen, E. Rienks, M. Bianchi, M. Fanetti, E. Laegsgaard, A. Baraldi, S. Lizzit, Z. Sljivancanin, F. Besenbacher, B. Hammer, T. G. Pedersen, P. Hofmann, L. Hornekaer, Nat. Mater. **9**, 315 (2010)
115. J. Hamilton, J. Blakely, Surf. Sci. **91**, 199 (1980)
116. J. Grant, T. Haas, Surf. Sci. **21**, 76 (1970)
117. M. Fonin, M. Sicot, O. Zander, S. Bouvron, P. Leicht, U. Rudiger, M. Weser, Y.S. Dedkov, K. Horn, Nano Lett. (submitted) (2010)
118. F. Himpsel, K. Christmann, P. Heimann, D. Eastman, P. Feibelman, Surf. Sci. **115**, L159 (1982)
119. M. Wu, Q. Xu, D. Goodman, J .Phys. Chem. **98**, 5104 (1994)
120. B. Wang, M.L. Bocquet, S. Marchini, S. Guenther, J. Wintterlin, Phys. Chem. Chem. Phys. **10**, 3530 (2008)
121. W. Moritz, B. Wang, M.L. Bocquet, T. Brugger, T. Greber, J. Wintterlin, S. Guenther, Phys. Rev. Lett. **104**, 136102 (2010)
122. B. Lang, P. Legare, G. Maire, Surf. Sci. **47**, 89 (1975)
123. C. McConville, D. Woodruff, S. Kevan, M. Weinert, J. Davenport, Phys. Rev. B **34**, 2199 (1986)
124. T. Brugger, S. Guenther, B. Wang, J.H. Dil, M.-L. Bocquet, J. Osterwalder, J. Wintterlin, T. Greber, Phys. Rev. B **79**, 045407 (2009)
125. M. Fonin, unpublished (2010)
126. J. Coraux, A.T. N'Diaye, C. Busse, T. Michely, Nano Lett. **8**, 565 (2008)
127. A.T. N'Diaye, J. Coraux, T. N. Plasa, C. Busse, T. Michely, New J. Phys. **10**, 043033 (2008)
128. A.T. N'Diaye, R. van Gastel, A.J. Martinez-Galera, J. Coraux, H. Hattab, D. Wall, F.-J.M. zu Heringdorf, M.H. von Hoegen, J.M. Gomez-Rodriguez, B. Poelsema, C. Busse, T. Michely, New J. Phys. **11**, 113056 (2009)
129. R. van Gastel, A.T. N'Diaye, D. Wall, J. Coraux, C. Busse, N.M. Buckanie, F.-J.M. zu Heringdorf, M.H. von Hoegen, T. Michely, B. Poelsema, Appl. Phys. Lett. **95**, 121901 (2009)
130. D. Martoccia, M. Bjoerck, C.M. Schlepuetz, T. Brugger, S.A. Pauli, B.D. Patterson, T. Greber, P.R. Willmott, New J. Phys. **12**, 043028 (2010)

131. M. Corso, W. Auwarter, M. Muntwiler, A. Tamai, T. Greber, J. Osterwalder, Science **303**, 217 (2004)
132. H. Dil, J. Lobo-Checa, R. Laskowski, P. Blaha, S. Berner, J. Osterwalder, T. Greber, Science **319**, 1824 (2008)
133. M. Sasaki, Y. Yamada, Y. Ogiwara, S. Yagyu, S. Yamamoto, Phys. Rev. B **61**, 15653 (2000)
134. H. Ueta, M. Saida, C. Nakai, Y. Yamada, M. Sasaki, S. Yamamoto, Surf. Sci. **560**, 183 (2004)
135. Y.S. Dedkov, H. Vita, M. Weser, K. Horn, M. Fonin, unpublished (2010)
136. P.J. Feibelman, Phys. Rev. B **77**, 165419 (2008)
137. D. Farias, A. Shikin, K. Rieder, Y.S. Dedkov, J. Phys.: Condens. Matter. **11**, 8453 (1999)
138. Y.S. Dedkov, M. Poygin, D. Vyalikh, A. Starodubov, A.M. Shikin, V.K. Adamchuk, arXiv:cond-mat/0304575v1 [cond-mat.mtrl-sci] (2003)
139. A. Varykhalov, J. Sanchez-Barriga, A.M. Shikin, C. Biswas, E. Vescovo, A. Rybkin, D. Marchenko, O. Rader, Phys. Rev. Lett. **101**, 157601 (2008)
140. C. Binns, S. Baker, A. Keen, S. Mozley, C. Norris, H. Derbyshire, S. Bayliss, Phys. Rev. B **53**, 7451 (1996)
141. R. Pfandzelter, G. Steierl, C. Rau, Phys. Rev. Lett. **74**, 3467 (1995)
142. A. Shikin, M. Poigin, Y.S. Dedkov, S. Molodtsov, V. Adamchuk, Phys. Solid State **42**, 1170 (2000)
143. A. Bostwick, T. Ohta, J. Mcchesney, K. Emtsev, T. Seyller, K. Horn, E. Rotenberg, New J. Phys. **9**, 385 (2007)
144. A.T. N'Diaye, T. Gerber, C. Busse, J. Myslivecek, J. Coraux, T. Michely, New J. Phys. **11**, 103045 (2009)
145. M.L. Ng, R. Balog, L. Hornekaer, A.B. Preobrajenski, N.A. Vinogradov, N. Mårtensson, K. Schulte, J. Phys. Chem. C **114**, 18559 (2010)
146. J. O. Sofo, A.S. Chaudhari, G.D. Barber, Phys. Rev. B **75**, 153401 (2007)
147. K.S. Novoselov, A.K. Geim, S.V. Morozov, D. Jiang, M.I. Katsnelson, I.V. Grigorieva, S.V. Dubonos, A.A. Firsov, Nature **438**, 197 (2005)
148. Y. Zhang, Y.W. Tan, H.L. Stormer, P. Kim, Nature **438**, 201 (2005)

Part II
Electronic-structure and Transport Properties

Chapter 8
Electronic Properties of Monolayer and Bilayer Graphene

Edward McCann

Abstract The tight-binding model of electrons in graphene is reviewed. We derive low-energy Hamiltonians supporting massless Dirac-like chiral fermions and massive chiral fermions in monolayer and bilayer graphene, respectively, and we describe how their chirality is manifest in the sequencing of plateaus observed in the integer quantum Hall effect. The opening of a tuneable band gap in bilayer graphene in response to a transverse electric field is described, and we explain how Hartree theory may be used to develop a simple analytical model of screening.

8.1 Introduction

More than sixty years ago, Wallace [1] modeled the electronic band structure of graphene. Research into graphene was stimulated by interest in the properties of bulk graphite because, from a theoretical point of view, two-dimensional graphene serves as a building block for the three-dimensional material. Following further work, the tight-binding model of electrons in graphite, which takes into account coupling between layers, became known as the Slonczewski–Weiss–McClure model [2–4]. As well as serving as the basis for models of carbon-based materials including graphite, buckyballs, and carbon nanotubes [5–11], the honeycomb lattice of graphene has been used theoretically to study Dirac fermions in a condensed matter system [12, 13]. Since the experimental isolation of individual graphene flakes [14], and the observation of the integer quantum Hall effect in monolayers [15, 16] and bilayers [17], there has been an explosion of interest in the behavior of chiral electrons in graphene.

This chapter begins in Sect. 8.2 with a description of the crystal structure of monolayer graphene. Sect. 8.3 briefly reviews the tight-binding model of electrons

E. McCann (✉)
Department of Physics, Lancaster University, Lancaster, LA1 4YB, UK
e-mail: ed.mccann@lancaster.ac.uk

H. Raza (ed.), *Graphene Nanoelectronics*, NanoScience and Technology,
DOI 10.1007/978-3-642-22984-8_8, © Springer-Verlag Berlin Heidelberg 2012

in condensed matter materials [11, 18], and Sect. 8.4 describes its application to monolayer graphene [11, 19, 20]. Then in Sect. 8.5, we explain how a Dirac-like Hamiltonian describing massless chiral fermions emerges from the tight-binding model at low energy. The tight-binding model is applied to bilayer graphene in Sect. 8.6, and Sect. 8.7 describes how low-energy electrons in bilayers behave as massive chiral quasiparticles [17, 21]. In Sect. 8.8, we describe how the chiral Hamiltonians of monolayer and bilayer graphene corresponding to Berry's phase π and 2π, respectively, have associated four- and eightfold degenerate zero-energy Landau levels, leading to an unusual sequence of plateaus in the integer quantum Hall effect [15–17].

Section 8.9 discusses an additional contribution to the low-energy Hamiltonians of monolayer and bilayer graphene, known as trigonal warping [4, 9, 21–25] that produces a Liftshitz transition in the band structure of bilayer graphene at low energy. Finally, Sect. 8.10 describes how an external transverse electric field applied to bilayer graphene, due to doping or gates, may open a band gap that can be tuned between zero up to the value of the interlayer coupling, around three to four hundred meV [21, 26, 27]. Hartree theory and the tight-binding model are used to develop a simple model of screening by electrons in bilayer graphene in order to calculate the density dependence of the band gap [28].

8.2 The Crystal Structure of Monolayer Graphene

8.2.1 The Real Space Structure

Monolayer graphene consists of carbon atoms arranged with a two-dimensional honeycomb crystal structure as shown in Fig. 8.1a. The honeycomb structure [11,18] consists of the hexagonal Bravais lattice, Fig. 8.1b, with a basis of two atoms, labeled A and B, at each lattice point.

Throughout this chapter, we use a Cartesian coordinate system with x and y axes in the plane of the graphene crystal, and a z axis perpendicular to the graphene plane. Two-dimensional vectors in the same plane as the graphene are expressed solely in terms of their x and y coordinates, so that, for example, the primitive lattice vectors of the hexagonal Bravais lattice, Fig. 8.1b, are $\mathbf{a}_1$ and $\mathbf{a}_2$, where

$$\mathbf{a}_1 = \left(\frac{a}{2}, \frac{\sqrt{3}a}{2}\right), \qquad \mathbf{a}_2 = \left(\frac{a}{2}, -\frac{\sqrt{3}a}{2}\right), \tag{8.1}$$

and $a = |\mathbf{a}_1| = |\mathbf{a}_2|$ is the lattice constant. In graphene, $a = 2.46\,\text{Å}$ [11]. The lattice constant is the distance between unit cells, whereas the distance between carbon atoms is the carbon–carbon bond length $a_{CC} = a/\sqrt{3} = 1.42\,\text{Å}$. Note that the honeycomb structure is not a Bravais lattice because atomic positions A and B are not equivalent: it is not possible to connect them with a lattice vector

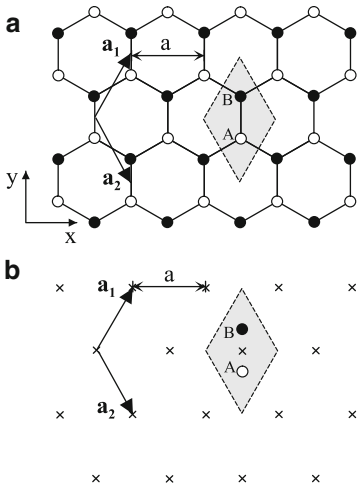

Fig. 8.1 (**a**) The honeycomb crystal structure of monolayer graphene, where white (black) circles indicate carbon atoms on A (B) sites and straight lines indicate σ bonds between them. Vectors $\mathbf{a}_1$ and $\mathbf{a}_2$ are primitive lattice vectors of length equal to the lattice constant a. The shaded rhombus is a unit cell containing two atoms, one A and one B. (**b**) Crosses indicate lattice points of the hexagonal Bravais lattice. The honeycomb structure in (**a**) consists of the hexagonal Bravais lattice [shown in (b)] with a basis of two atoms, one A and one B, at each lattice point

$\mathbf{R} = n_1\mathbf{a}_1 + n_2\mathbf{a}_2$, where n_1 and n_2 are integers. Taken alone, the A atomic positions (or, the B atomic positions) make up an hexagonal Bravais lattice and, in the following, we will often refer to them as the "A sublattice" (or, the "B sublattice").

8.2.2 The Reciprocal Lattice of Graphene

Primitive reciprocal lattice vectors $\mathbf{b}_1$ and $\mathbf{b}_2$ satisfying $\mathbf{a}_1\mathbf{b}_1 = \mathbf{a}_2\mathbf{b}_2 = 2\pi$ and $\mathbf{a}_1\mathbf{b}_2 = \mathbf{a}_2\mathbf{b}_1 = 0$ are given by

$$\mathbf{b}_1 = \left(\frac{2\pi}{a}, \frac{2\pi}{\sqrt{3}a}\right), \qquad \mathbf{b}_2 = \left(\frac{2\pi}{a}, -\frac{2\pi}{\sqrt{3}a}\right). \tag{8.2}$$

The resulting reciprocal lattice is shown in Fig. 8.2, which is an hexagonal Bravais lattice. The first Brillouin zone is hexagonal, as indicated by the shaded region in Fig. 8.2.

8.2.3 The Atomic Orbitals of Graphene

Each carbon atom has six electrons, of which two are core electrons and four are valence electrons. The latter occupy $2s$, $2p_x$, $2p_y$, and $2p_z$ orbitals. In graphene,

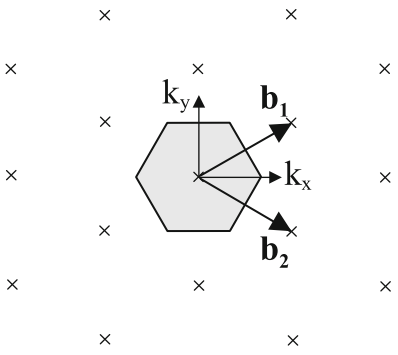

Fig. 8.2 The reciprocal lattice of monolayer graphene, where crosses indicate reciprocal lattice points, and vectors $\mathbf{b}_1$ and $\mathbf{b}_2$ are primitive lattice vectors. The shaded hexagon indicates the first Brillouin zone

the orbitals are sp^2 hybridized, meaning that two of the $2p$ orbitals, the $2p_x$ and $2p_y$ that lie in the graphene plane, mix with the $2s$ orbital to form three sp^2 hybrid orbitals per atom, each lying in the graphene plane and oriented 120° to each other [11]. They form σ bonds with other atoms, shown as straight lines in the honeycomb crystal structure, Fig. 8.1a. The remaining $2p_z$ orbital for each atom lies perpendicular to the plane, and, when combined with the $2p_z$ orbitals on adjacent atoms in graphene, forms a π orbital. Electronic states close to the Fermi level in graphene are described well by a model taking into account only the π orbital, meaning that the tight-binding model can include only one electron per atomic site, in a $2p_z$ orbital.

8.3 The Tight-Binding Model

We begin by presenting a general description of the tight-binding model for a system with n atomic orbitals ϕ_j in the unit cell, labeled by index $j = 1 \ldots n$. Further details may be found in the book by Saito, Dresselhaus, and Dresselhaus [11]. It is assumed that the system has translational invariance. Then the model may be written using n different Bloch functions $\Phi_j(\mathbf{k}, \mathbf{r})$ that depend on the position vector $\mathbf{r}$ and wave vector $\mathbf{k}$. They are given by

$$\Phi_j(\mathbf{k}, \mathbf{r}) = \frac{1}{\sqrt{N}} \sum_{i=1}^{N} e^{i\mathbf{k}.\mathbf{R}_{j,i}} \phi_j \left(\mathbf{r} - \mathbf{R}_{j,i}\right), \tag{8.3}$$

where the sum is over N different unit cells, labeled by index $i = 1 \ldots N$, and $\mathbf{R}_{j,i}$ denotes the position of the jth orbital in the ith unit cell.

In general, an electronic wave function $\Psi_j(\mathbf{k}, \mathbf{r})$ is given by a linear superposition of the n different Bloch functions,

$$\Psi_j(\mathbf{k}, \mathbf{r}) = \sum_{l=1}^{n} c_{j,l}(\mathbf{k})\, \Phi_l(\mathbf{k}, \mathbf{r}), \tag{8.4}$$

where $c_{j,l}$ are coefficients of the expansion. The energy $E_j(\mathbf{k})$ of the jth band is given by

$$E_j(\mathbf{k}) = \frac{\langle \Psi_j | \mathcal{H} | \Psi_j \rangle}{\langle \Psi_j | \Psi_j \rangle}, \tag{8.5}$$

where $\mathcal{H}$ is the Hamiltonian. Substituting the expansion of the wave function (8.4) into the energy gives

$$E_j(\mathbf{k}) = \frac{\sum_{i,l}^{n} c_{ji}^* c_{jl} \langle \Phi_i | \mathcal{H} | \Phi_l \rangle}{\sum_{i,l}^{n} c_{ji}^* c_{jl} \langle \Phi_i | \Phi_l \rangle}, \tag{8.6}$$

$$= \frac{\sum_{i,l}^{n} H_{il} c_{ji}^* c_{jl}}{\sum_{i,l}^{n} S_{il} c_{ji}^* c_{jl}}, \tag{8.7}$$

where transfer integral matrix elements H_{il} and overlap integral matrix elements S_{il} are defined by

$$H_{il} = \langle \Phi_i | \mathcal{H} | \Phi_l \rangle, \qquad S_{il} = \langle \Phi_i | \Phi_l \rangle. \tag{8.8}$$

We minimize the energy E_j with respect to the coefficient c_{jm}^* by calculating the derivative

$$\frac{\partial E_j}{\partial c_{jm}^*} = \frac{\sum_{l}^{n} H_{ml} c_{jl}}{\sum_{i,l}^{n} S_{il} c_{ji}^* c_{jl}} - \frac{\sum_{i,l}^{n} H_{il} c_{ji}^* c_{jl} \sum_{l}^{n} S_{ml} c_{jl}}{\left(\sum_{i,l}^{n} S_{il} c_{ji}^* c_{jl} \right)^2}. \tag{8.9}$$

The second term contains a factor equal to the energy E_j itself, (8.7). Then setting $\partial E_j / \partial c_{jm}^* = 0$ and omitting the common factor $\sum_{i,l}^{n} S_{il} c_{ji}^* c_{jl}$ gives

$$\sum_{l=1}^{n} H_{ml} c_{jl} = E_j \sum_{l=1}^{n} S_{ml} c_{jl}. \tag{8.10}$$

This can be written as a matrix equation. Consider the specific example of two orbitals per unit cell, $n = 2$. Then we can select the possible values of m (either $m = 1$ or $m = 2$) and write out the summation in (8.10) explicitly:

$$m = 1 \quad \Rightarrow \quad H_{11} c_{j1} + H_{12} c_{j2} = E_j \left(S_{11} c_{j1} + S_{12} c_{j2} \right), \tag{8.11}$$

$$m = 2 \quad \Rightarrow \quad H_{21} c_{j1} + H_{22} c_{j2} = E_j \left(S_{21} c_{j1} + S_{22} c_{j2} \right). \tag{8.12}$$

These two equations may be combined into a matrix equation

$$\begin{pmatrix} H_{11} & H_{12} \\ H_{21} & H_{22} \end{pmatrix} \begin{pmatrix} c_{j1} \\ c_{j2} \end{pmatrix} = E_j \begin{pmatrix} S_{11} & S_{12} \\ S_{21} & S_{22} \end{pmatrix} \begin{pmatrix} c_{j1} \\ c_{j2} \end{pmatrix}. \tag{8.13}$$

For general values of n, defining H as the transfer integral matrix, S as the overlap integral matrix, and ψ_j as a column vector,

$$H = \begin{pmatrix} H_{11} & H_{12} & \cdots & H_{1n} \\ H_{21} & H_{22} & \cdots & H_{2n} \\ \vdots & \vdots & \ddots & \vdots \\ H_{n1} & H_{n2} & \cdots & H_{nn} \end{pmatrix}, \; S = \begin{pmatrix} S_{11} & S_{12} & \cdots & S_{1n} \\ S_{21} & S_{22} & \cdots & S_{2n} \\ \vdots & \vdots & \ddots & \vdots \\ S_{n1} & S_{n2} & \cdots & S_{nn} \end{pmatrix}, \; \psi_j = \begin{pmatrix} c_{j1} \\ c_{j2} \\ \vdots \\ c_{jn} \end{pmatrix}, \tag{8.14}$$

allows the relation (8.10) to be expressed as

$$H\psi_j = E_j S\psi_j \,. \tag{8.15}$$

The energies E_j may be determined by solving the secular equation

$$\det\left(H - E_j S\right) = 0 \,, \tag{8.16}$$

once the transfer integral matrix H and the overlap integral matrix S are known. Here, "det" stands for the determinant of the matrix. In the following, we will omit the subscript $j = 1 \ldots n$ in (8.15), (8.16), bearing in mind that the number of solutions is equal to the number of different atomic orbitals per unit cell.

8.4 The Tight-Binding Model of Monolayer Graphene

We apply the tight-binding model described in Sect. 8.3 to monolayer graphene, taking into account one $2p_z$ orbital per atomic site. As there are two atoms in the unit cell of graphene, labeled A and B in Fig. 8.1, the model includes two Bloch functions, $n = 2$. For simplicity, we replace index $j = 1$ with $j = A$, and $j = 2$ with $j = B$. Now we proceed to determine the transfer integral matrix H and the overlap integral matrix S.

8.4.1 Diagonal Matrix Elements

Substituting the expression for the Bloch function (8.3) into the definition of the transfer integral (8.8) allows us to write the diagonal matrix element corresponding to the A sublattice as

$$H_{AA} = \frac{1}{N} \sum_{i=1}^{N} \sum_{j=1}^{N} e^{i\mathbf{k}.\left(\mathbf{R}_{A,j} - \mathbf{R}_{A,i}\right)} \langle \phi_A \left(\mathbf{r} - \mathbf{R}_{A,i}\right) | \mathcal{H} | \phi_A \left(\mathbf{r} - \mathbf{R}_{A,j}\right) \rangle, \tag{8.17}$$

where $\mathbf{k} = (k_x, k_y)$ is the wave vector in the graphene plane. Equation (8.17) includes a double summation over all the A sites of the lattice. If we assume that the

dominant contribution arises from the same site $j = i$ within every unit cell, then:

$$H_{AA} \approx \frac{1}{N} \sum_{i=1}^{N} \langle \phi_A \left(\mathbf{r} - \mathbf{R}_{A,i}\right) | \mathcal{H} | \phi_A \left(\mathbf{r} - \mathbf{R}_{A,i}\right) \rangle . \tag{8.18}$$

The matrix element $\langle \phi_A | \mathcal{H} | \phi_A \rangle$ within the summation has the same value on every A site, i.e. it is independent of the site index i. We set it to be equal to a parameter

$$\epsilon_{2p} = \langle \phi_A \left(\mathbf{r} - \mathbf{R}_{A,i}\right) | \mathcal{H} | \phi_A \left(\mathbf{r} - \mathbf{R}_{A,i}\right) \rangle , \tag{8.19}$$

that is equal to the energy of the $2p_z$ orbital. Then keeping only the same site contribution,

$$H_{AA} \approx \frac{1}{N} \sum_{i=1}^{N} \epsilon_{2p} = \epsilon_{2p} . \tag{8.20}$$

It is possible to take into account the contribution of other terms in the double summation (8.17), such as next-nearest neighbor contributions [29, 30]. They generally have a small effect on the electronic band structure and will not be discussed here. The B sublattice has the same structure as the A sublattice, and the carbon atoms on the two sublattices are chemically identical. This means that the diagonal transfer integral matrix element corresponding to the B sublattice has the same value as that of the A sublattice:

$$H_{BB} = H_{AA} \approx \epsilon_{2p} . \tag{8.21}$$

A calculation of the diagonal elements of the overlap integral matrix proceeds in a similar way as for those of the transfer integral. In this case, the overlap between a $2p_z$ orbital on the same atom is equal to unity,

$$\langle \phi_A \left(\mathbf{r} - \mathbf{R}_{A,i}\right) | \phi_A \left(\mathbf{r} - \mathbf{R}_{A,i}\right) \rangle = 1 . \tag{8.22}$$

Then assuming that the same site contribution dominates,

$$S_{AA} = \frac{1}{N} \sum_{i=1}^{N} \sum_{j=1}^{N} e^{i\mathbf{k}.\left(\mathbf{R}_{A,j} - \mathbf{R}_{A,i}\right)} \langle \phi_A \left(\mathbf{r} - \mathbf{R}_{A,i}\right) | \phi_A \left(\mathbf{r} - \mathbf{R}_{A,j}\right) \rangle , \tag{8.23}$$

$$\approx \frac{1}{N} \sum_{i=1}^{N} \langle \phi_A \left(\mathbf{r} - \mathbf{R}_{A,i}\right) | \phi_A \left(\mathbf{r} - \mathbf{R}_{A,i}\right) \rangle , \tag{8.24}$$

$$= \frac{1}{N} \sum_{i=1}^{N} 1 \tag{8.25}$$

$$= 1 . \tag{8.26}$$

Again, as the B sublattice has the same structure as the A sublattice,

$$S_{BB} = S_{AA} = 1\,. \tag{8.27}$$

8.4.2 Off-Diagonal Matrix Elements

Substituting the expression for the Bloch function (8.3) into the definition of the transfer integral (8.8) allows us to write an off-diagonal matrix element as

$$H_{AB} = \frac{1}{N}\sum_{i=1}^{N}\sum_{j=1}^{N} e^{i\mathbf{k}.\left(\mathbf{R}_{B,j}-\mathbf{R}_{A,i}\right)}\langle\phi_A\left(\mathbf{r}-\mathbf{R}_{A,i}\right)|\mathcal{H}|\phi_B\left(\mathbf{r}-\mathbf{R}_{B,j}\right)\rangle. \tag{8.28}$$

It describes processes of hopping between the A and B sublattices, and contains a summation over all the A sites ($i = 1 \ldots N$) at positions $\mathbf{R}_{A,i}$ and all the B sites ($j = 1 \ldots N$) at $\mathbf{R}_{B,j}$.

In the following, we assume that the dominant contribution to the off-diagonal matrix element (8.28) arises from hopping between nearest neighbors only. If we focus on an individual A atom, i.e. we consider a fixed value of the index i, we see that it has three neighboring B atoms, Fig. 8.3, that we will label with a new index l ($l = 1 \ldots 3$). Each A atom has three such neighbors, so it is possible to write the nearest-neighbors contribution to the off-diagonal matrix element (8.28) as

$$H_{AB} \approx \frac{1}{N}\sum_{i=1}^{N}\sum_{l=1}^{3} e^{i\mathbf{k}.\left(\mathbf{R}_{B,l}-\mathbf{R}_{A,i}\right)}\langle\phi_A\left(\mathbf{r}-\mathbf{R}_{A,i}\right)|\mathcal{H}|\phi_B\left(\mathbf{r}-\mathbf{R}_{B,l}\right)\rangle\,. \tag{8.29}$$

The matrix element between neighboring atoms, $\langle\phi_A|\mathcal{H}|\phi_B\rangle$, has the same value for each neighboring pair, i.e., it is independent of indices i and l. We set it equal to a parameter, $t = \langle\phi_A\left(\mathbf{r}-\mathbf{R}_{A,i}\right)|\mathcal{H}|\phi_B\left(\mathbf{r}-\mathbf{R}_{B,l}\right)\rangle$. Since t is negative [11], it is common practice to express it in terms of a positive parameter $\gamma_0 = -t$, where

$$\gamma_0 = -\langle\phi_A\left(\mathbf{r}-\mathbf{R}_{A,i}\right)|\mathcal{H}|\phi_B\left(\mathbf{r}-\mathbf{R}_{B,l}\right)\rangle\,. \tag{8.30}$$

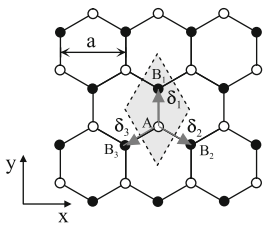

Fig. 8.3 The honeycomb crystal structure of monolayer graphene. In the nearest-neighbor approximation, we consider hopping from an A site (white) to three adjacent B sites (black), labeled B_1, B_2, B_3, with position vectors $\boldsymbol{\delta}_1$, $\boldsymbol{\delta}_2$, $\boldsymbol{\delta}_3$, respectively, relative to the A site

Then we write the off-diagonal transfer integral matrix element as

$$H_{AB} \approx -\frac{1}{N}\sum_{i=1}^{N}\sum_{l=1}^{3} e^{i\mathbf{k}.\left(\mathbf{R}_{B,l}-\mathbf{R}_{A,i}\right)}\gamma_0\,, \tag{8.31}$$

$$= -\frac{\gamma_0}{N}\sum_{i=1}^{N}\sum_{l=1}^{3} e^{i\mathbf{k}.\boldsymbol{\delta}_l} \equiv -\gamma_0 f\left(\mathbf{k}\right)\,, \tag{8.32}$$

$$f\left(\mathbf{k}\right) = \sum_{l=1}^{3} e^{i\mathbf{k}.\boldsymbol{\delta}_l}\,, \tag{8.33}$$

where the position vector of atom B_l relative to the A_i atom is denoted $\boldsymbol{\delta}_l = \mathbf{R}_{B,l} - \mathbf{R}_{A,i}$, and we used the fact that the summation over the three neighboring B atoms is the same for all A_i atoms.

For the three B atoms shown in Fig. 8.3, the three vectors are

$$\boldsymbol{\delta}_1 = \left(0, \frac{a}{\sqrt{3}}\right)\,, \quad \boldsymbol{\delta}_2 = \left(\frac{a}{2}, -\frac{a}{2\sqrt{3}}\right)\,, \quad \boldsymbol{\delta}_3 = \left(-\frac{a}{2}, -\frac{a}{2\sqrt{3}}\right). \tag{8.34}$$

Note that $|\boldsymbol{\delta}_1| = |\boldsymbol{\delta}_2| = |\boldsymbol{\delta}_3| = a/\sqrt{3}$ is the carbon–carbon bond length. Then the function $f\left(\mathbf{k}\right)$ describing nearest-neighbor hopping may be evaluated as

$$f\left(\mathbf{k}\right) = \sum_{l=1}^{3} e^{i\mathbf{k}.\boldsymbol{\delta}_l}\,, \tag{8.35}$$

$$= e^{ik_y a/\sqrt{3}} + e^{ik_x a/2}e^{-ik_y a/2\sqrt{3}} + e^{-ik_x a/2}e^{-ik_y a/2\sqrt{3}}\,, \tag{8.36}$$

$$= e^{ik_y a/\sqrt{3}} + 2e^{-ik_y a/2\sqrt{3}}\cos\left(k_x a/2\right)\,. \tag{8.37}$$

The other off-diagonal matrix element H_{BA} is the complex conjugate of H_{AB}:

$$H_{AB} \approx -\gamma_0 f\left(\mathbf{k}\right)\,, \qquad H_{BA} \approx -\gamma_0 f^*\left(\mathbf{k}\right)\,. \tag{8.38}$$

A calculation of an off-diagonal element of the overlap integral matrix proceeds in a similar way as for the transfer integral:

$$S_{AB} = \frac{1}{N}\sum_{i=1}^{N}\sum_{j=1}^{N} e^{i\mathbf{k}.\left(\mathbf{R}_{B,j}-\mathbf{R}_{A,i}\right)}\langle\phi_A\left(\mathbf{r}-\mathbf{R}_{A,i}\right)|\phi_B\left(\mathbf{r}-\mathbf{R}_{B,j}\right)\rangle, \tag{8.39}$$

$$\approx \frac{1}{N}\sum_{i=1}^{N}\sum_{l=1}^{3} e^{i\mathbf{k}.\left(\mathbf{R}_{B,l}-\mathbf{R}_{A,i}\right)}\langle\phi_A\left(\mathbf{r}-\mathbf{R}_{A,i}\right)|\phi_B\left(\mathbf{r}-\mathbf{R}_{B,l}\right)\rangle\,, \tag{8.40}$$

$$= s_0 f\left(\mathbf{k}\right)\,, \tag{8.41}$$

where the parameter $s_0 = \langle \phi_A(\mathbf{r} - \mathbf{R}_{A,i}) | \phi_B(\mathbf{r} - \mathbf{R}_{B,l}) \rangle$, and $S_{BA} = S_{AB}^* = s_0 f^*(\mathbf{k})$. The presence of nonzero s_0 takes into account the possibility that orbitals on adjacent atomic sites are not strictly orthogonal.

8.4.3 The Low-Energy Electronic Bands of Monolayer Graphene

Summarizing the results of this section, the transfer integral matrix elements (8.21) and (8.38), and the overlap integral matrix elements (8.27) and (8.41) give

$$H_1 = \begin{pmatrix} \epsilon_{2p} & -\gamma_0 f(\mathbf{k}) \\ -\gamma_0 f^*(\mathbf{k}) & \epsilon_{2p} \end{pmatrix}, \qquad S_1 = \begin{pmatrix} 1 & s_0 f(\mathbf{k}) \\ s_0 f^*(\mathbf{k}) & 1 \end{pmatrix}, \quad (8.42)$$

where we use the subscript "1" to stress that these matrices apply to monolayer graphene. The corresponding energy E may be determined by solving the secular equation $\det(H_1 - E S_1) = 0$, (8.16):

$$\det \begin{pmatrix} \epsilon_{2p} - E & -(\gamma_0 + E s_0) f(\mathbf{k}) \\ -(\gamma_0 + E s_0) f^*(\mathbf{k}) & \epsilon_{2p} - E \end{pmatrix} = 0, \quad (8.43)$$

$$\Rightarrow \quad (E - \epsilon_{2p})^2 - \left([E - \epsilon_{2p}] s_0 + \epsilon_{2p} s_0 + \gamma_0 \right)^2 |f(\mathbf{k})|^2 = 0. \quad (8.44)$$

Solving this quadratic equation yields the energy:

$$E_\pm = \frac{\epsilon_{2p} \pm \gamma_0 |f(\mathbf{k})|}{1 \mp s_0 |f(\mathbf{k})|}. \quad (8.45)$$

This expression appears in Saito *et al* [11], where parameter values $\gamma_0 = 3.033\,\text{eV}$, $s_0 = 0.129$, $\epsilon_{2p} = 0$ are quoted. The latter value ($\epsilon_{2p} = 0$) means that the zero of energy is set to be equal to the energy of the $2p_z$ orbital. The resulting band structure $E_\pm$ is shown in Fig. 8.4 in the vicinity of the Brillouin zone. A particular cut through the band structure is shown in Fig. 8.5, where the bands are plotted as a function of wave vector component k_x along the line $k_y = 0$, a line that passes through the center of the Brillouin zone, labeled Γ, and two corners of the Brillouin zone, labeled K_+ and K_- (see the inset of Fig. 8.5). The Fermi level in pristine graphene is located at zero energy. There are two energy bands that we refer to as the conduction band (E_+) and the valence band (E_-). The interesting feature of the band structure is that there is no band gap between the conduction and valence bands. Instead the bands cross at the six corners of the Brillouin zone, Fig. 8.4. The corners of the Brillouin zone are known as K points, and two of them are explicitly labeled K_+ and K_- in Fig. 8.4. Near these points, the dispersion is linear and electronic properties may be described by a Dirac-like Hamiltonian. This will be explored in more detail in the next section. Note also that the band structure displays a large asymmetry between the conduction and valence bands that is most

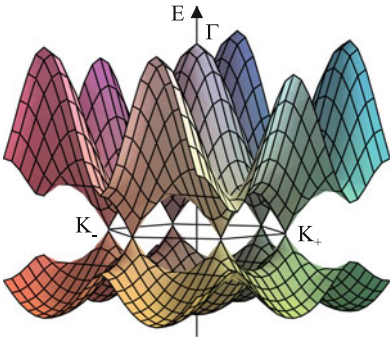

Fig. 8.4 The low-energy band structure of monolayer graphene (8.45) taking into account nearest-neighbor hopping with parameter $\gamma_0 = 3.033$ eV, nearest-neighbor overlap parameter $s_0 = 0.129$, and orbital energy $\epsilon_{2p} = 0$ [11]. The plot shows the bands calculated in the vicinity of the first Brillouin zone, with conduction and valence bands touching at six corners of the Brillouin zone, two of them are labeled K_+ and K_-. Label Γ indicates the center of the Brillouin zone

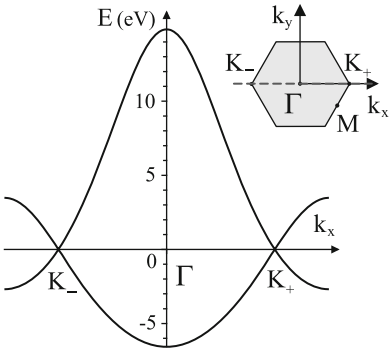

Fig. 8.5 The low-energy band structure of monolayer graphene (8.45) taking into account nearest-neighbor hopping with parameter $\gamma_0 = 3.033$ eV, nearest-neighbor overlap parameter $s_0 = 0.129$, and orbital energy $\epsilon_{2p} = 0$ [11]. The plot shows a cut through the band structure Fig. 8.4, plotted along the k_x axis intersecting points K_-, Γ, and K_+ in the Brillouin zone, shown as the dotted line in the inset

pronounced in the vicinity of the Γ point. This arises from the nonzero overlap parameter s_0 appearing in (8.45).

The tight-binding model described here cannot be used to determine the values of parameters such as γ_0 and s_0. They must be determined either by an alternative theoretical method, such as density-functional theory, or by comparison of the tight-binding model with experiments. Note, however, that the main qualitative features described in this chapter do not depend on the precise values of the parameters quoted.

8.5 Massless Chiral Quasiparticles in Monolayer Graphene

8.5.1 The Dirac-Like Hamiltonian

As described in the previous section, the electronic band structure of monolayer graphene, Figs. 8.4, 8.5, is gapless, with crossing of the bands at points K_+ and K_- located at corners of the Brillouin zone. In this section, we show that electronic properties near these points may be described by a Dirac-like Hamiltonian.

Although the first Brillouin zone has six corners, only two of them are nonequivalent. In this chapter, we choose points K_+ and K_-, Figs. 8.4, 8.5, as a nonequivalent pair. It is possible to connect two of the other corners to K_+ using a reciprocal lattice vector (hence, the other two are equivalent to K_+), and it is possible to connect the remaining two corners to K_- using a reciprocal lattice vector (hence, the remaining two are equivalent to K_-), but it is not possible to connect K_+ and K_- with a reciprocal lattice vector. To distinguish between K_+ and K_-, we will use an index $\xi = \pm 1$. Using the values of the primitive reciprocal lattice vectors $\mathbf{b}_1$ and $\mathbf{b}_2$, (8.2), it can be seen that the wave vector corresponding to point K_ξ is given by

$$\mathbf{K}_\xi = \xi \left(\frac{4\pi}{3a}, 0 \right) . \tag{8.46}$$

Note that the K points are often called "valleys" using nomenclature from semiconductor physics.

In the tight-binding model, coupling between the A and B sublattices is described by the off-diagonal matrix element H_{AB}, (8.38), that is proportional to parameter γ_0 and the function $f(\mathbf{k})$, (8.35). Exactly at the K_ξ point, $\mathbf{k} = \mathbf{K}_\xi$, the latter is equal to

$$f\left(\mathbf{K}_\xi\right) = e^0 + e^{i\xi 2\pi/3} + e^{-i\xi 2\pi/3} = 0 . \tag{8.47}$$

This indicates that there is no coupling between the A and B sublattices exactly at the K_ξ point. Since the two sublattices are both hexagonal Bravais lattices of carbon atoms, they support the same quantum states, leading to a degeneracy point in the spectrum at K_ξ, Figs. 8.4, 8.5.

The exact cancelation of the three factors describing coupling between the A and B sublattices, (8.47), no longer holds when the wave vector is not exactly equal to that of the K_ξ point. We introduce a momentum $\mathbf{p}$ that is measured from the center of the K_ξ point,

$$\mathbf{p} = \hbar\mathbf{k} - \hbar\mathbf{K}_\xi . \tag{8.48}$$

Then the coupling between the A and B sublattices is proportional to

$$f\left(\mathbf{k}\right) = e^{ip_y a/\sqrt{3}\hbar} + 2e^{-ip_y a/2\sqrt{3}\hbar} \cos\left(\frac{2\pi\xi}{3} + \frac{p_x a}{2\hbar} \right) , \tag{8.49}$$

$$\approx \left(1 + \frac{i p_y a}{\sqrt{3}\hbar}\right) + 2\left(1 - \frac{i p_y a}{2\sqrt{3}\hbar}\right)\left(-\frac{1}{2} - \frac{\xi\sqrt{3}p_x a}{4\hbar}\right), \tag{8.50}$$

$$\approx -\frac{\sqrt{3}a}{2\hbar}\left(\xi p_x - i p_y\right), \tag{8.51}$$

where we kept only linear terms in the momentum $\mathbf{p} = \left(p_x, p_y\right)$, an approximation that is valid close to the K_ξ point, i.e. for $pa/\hbar \ll 1$, where $p = |\mathbf{p}| = (p_x^2 + p_y^2)^{1/2}$. Using this approximate expression for the function $f(\mathbf{k})$, the transfer integral matrix (8.42) in the vicinity of point K_ξ becomes

$$H_{1,\xi} = v\begin{pmatrix} 0 & \xi p_x - i p_y \\ \xi p_x + i p_y & 0 \end{pmatrix}. \tag{8.52}$$

Here, we used $\epsilon_{2p} = 0$ [11], which defines the zero of the energy axis to coincide with the energy of the $2p_z$ orbital. The parameters a and γ_0 were combined into a velocity v defined as $v = \sqrt{3}a\gamma_0/(2\hbar)$.

Within the linear-in-momentum approximation for $f(\mathbf{k})$, (8.51), the overlap matrix S_1 may be regarded as a unit matrix, because its off-diagonal elements, proportional to s_0, only contribute quadratic-in-momentum terms to the energy $E_\pm$, (8.45). Since S_1 is approximately equal to a unit matrix, (8.15) becomes $H_1\psi = E\psi$, indicating that H_1, (8.52), is an effective Hamiltonian for monolayer graphene at low-energy. The energy eigenvalues and eigenstates of H_1 are given by

$$E_\pm = \pm v p\,, \qquad \psi_\pm = \frac{1}{\sqrt{2}}\begin{pmatrix} 1 \\ \pm\xi e^{i\xi\varphi} \end{pmatrix} e^{i\mathbf{p}.\mathbf{r}/\hbar}\,, \tag{8.53}$$

where $\pm$ refer to the conduction and valence bands, respectively. Here φ is the polar angle of the momentum in the graphene plane, $\mathbf{p} = \left(p_x, p_y\right) = p\,(\cos\varphi, \sin\varphi)$.

8.5.2 Pseudospin and Chirality in Graphene

The effective Hamiltonian (8.52) and eigenstates (8.53) in the vicinity of the K_ξ point have two components, reminiscent of the components of spin-1/2. Referring back to the original definitions of the components of the column vector ψ, (8.4) and (8.14), shows that this is not the physical spin of the electron, but a degree of freedom related to the relative amplitude of the Bloch function on the A or B sublattice. This degree of freedom is called pseudospin. If all the electronic density was located on the A sublattice, Fig. 8.6a, this could be viewed as a pseudospin "up" state (pointing upwards out of the graphene sheet) $|\uparrow\rangle = (1, 0)^T$, whereas density solely on the B sublattice corresponds to a pseudospin "down" state (pointing downwards out of the graphene sheet) $|\downarrow\rangle = (0, 1)^T$, Fig. 8.6b. In graphene,

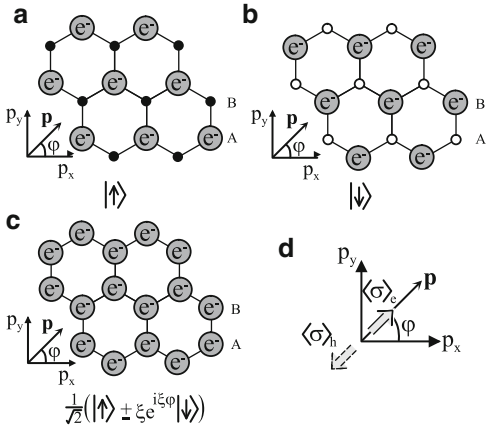

Fig. 8.6 Schematic representation of the pseudospin degree of freedom: (**a**) electronic density solely on the A sublattice can be viewed as a pseudospin "up" state, whereas (**b**) density solely on the B sublattice corresponds to a pseudospin "down" state; (**c**) in graphene, electronic density is usually shared equally between A and B sublattices, so that the pseudospin part of the wave function is a linear combination of "up" and "down," with amplitudes dependent on the direction of the electronic momentum $\mathbf{p}$; (**d**) at valley K_+, the pseudospin $\langle\boldsymbol{\sigma}\rangle_e$ in the conduction band is parallel to the momentum, whereas the pseudospin $\langle\boldsymbol{\sigma}\rangle_h$ in the valence band is anti-parallel to the momentum

electronic density is usually shared equally between A and B sublattices, Fig. 8.6c, so that the pseudospin part of the wave function is a linear combination of "up" and "down," and it lies in the plane of the graphene sheet.

Not only do the electrons possess the pseudospin degree of freedom, but also they are chiral, meaning that the orientation of the pseudospin is related to the direction of the electronic momentum $\mathbf{p}$. This is reflected in the fact that the amplitudes on the A or B sublattice of the eigenstate (8.53) depend on the polar angle φ. It is convenient to use Pauli spin matrices in the A/B sublattice space, σ_i where $i = 1 \ldots 3$, to write the effective Hamiltonian (8.52) as

$$H_{1,\xi} = v\left(\xi\sigma_x p_x + \sigma_y p_y\right) . \tag{8.54}$$

If we define a pseudospin vector as $\boldsymbol{\sigma} = \left(\sigma_x, \sigma_y, \sigma_z\right)$, and a unit vector as $\hat{\mathbf{n}}_1 = (\xi\cos\varphi, \sin\varphi, 0)$, then the Hamiltonian becomes $H_{1,\xi} = vp\,\boldsymbol{\sigma}.\hat{\mathbf{n}}_1$, stressing that the pseudospin $\boldsymbol{\sigma}$ is linked to the direction $\hat{\mathbf{n}}_1$. The chiral operator $\boldsymbol{\sigma}.\hat{\mathbf{n}}_1$ projects the pseudospin onto the direction of quantization $\hat{\mathbf{n}}_1$: eigenstates of the Hamiltonian are also eigenstates of $\boldsymbol{\sigma}.\hat{\mathbf{n}}_1$ with eigenvalues ± 1, $\boldsymbol{\sigma}.\hat{\mathbf{n}}_1\psi_\pm = \pm\psi_\pm$. An alternative way of expressing this chiral property of electrons is to explicitly calculate the expectation value of the pseudospin operator $\langle\boldsymbol{\sigma}\rangle = \left(\langle\sigma_x\rangle, \langle\sigma_y\rangle, \langle\sigma_z\rangle\right)$ with respect to the eigenstate $\psi_\pm$, (8.53). The result, $\langle\boldsymbol{\sigma}\rangle_{e/h} = \pm(\xi\cos\varphi, \sin\varphi, 0)$, shows the link between pseudospin and momentum. For valley K_+, the pseudospin in the

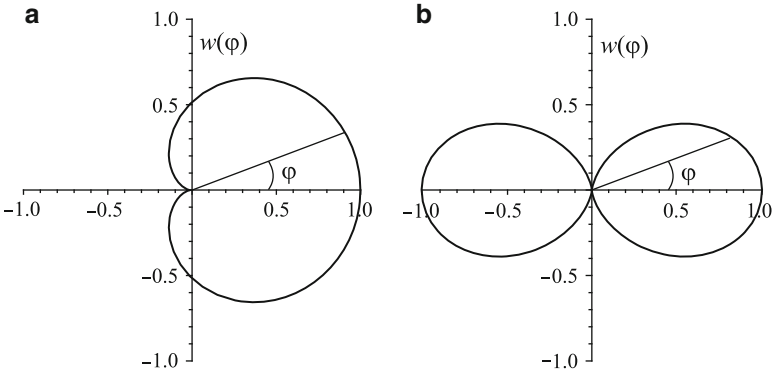

Fig. 8.7 Anisotropic scattering of chiral electrons in graphene: (**a**) angular dependence $w(\varphi) = \cos^2(\varphi/2)$ of the scattering probability off an A-B symmetric potential in monolayer graphene [9, 10, 33] and (**b**) $w(\varphi) = \cos^2(\varphi)$ in bilayer graphene [21, 37]

conduction band $\langle \boldsymbol{\sigma} \rangle_e$ is parallel to the momentum, whereas the pseudospin in the valence band $\langle \boldsymbol{\sigma} \rangle_h$ is antiparallel to it, Fig. 8.6d.

If the electronic momentum $\mathbf{p}$ rotates by angle φ, then adiabatic evolution of the chiral wave function $\psi_\pm$, (8.53), produces a matching rotation of the vector $\hat{\mathbf{n}}_1$ by angle φ. For traversal of a closed contour in momentum space, corresponding to $\varphi = 2\pi$, then the chiral wave function undergoes a phase change of π known as Berry's phase [31, 32]. It can be thought of as arising from the rotation of the pseudospin degree of freedom.

The chiral nature of low-energy electrons in graphene places an additional constraint on their scattering properties. If a given potential does not break the A-B symmetry, then it is unable to influence the pseudospin degree of freedom which must, therefore, be conserved upon scattering. Considering only the pseudospin part of the chiral wave function $\psi_\pm$, (8.53), the probability to scatter in a direction φ, where $\varphi = 0$ is the forward direction, is proportional to $w(\varphi) = |\langle \psi_\pm(\varphi) | \psi_\pm(0) \rangle|^2$. For monolayer graphene, $w(\varphi) = \cos^2(\varphi/2)$, Fig. 8.7a. This is anisotropic, and displays an absence of backscattering $w(\pi) = 0$ [9, 10, 33]: scattering into a state with opposite momentum is prohibited because it requires a reversal of the pseudospin. Such conservation of pseudospin is at the heart of anisotropic scattering at potential barriers in graphene monolayers [34, 35], known as Klein tunneling.

8.6 The Tight-Binding Model of Bilayer Graphene

In this section, we describe the tight-binding model of bilayer graphene. To do so, we use the tight-binding model described in Sect. 8.3 in order to generalize the model for monolayer graphene discussed in Sect. 8.4.

We consider Bernal-stacked bilayer graphene [17,21,36] (also called AB-stacked bilayer graphene). It consists of two parallel layers of carbon atoms, each arranged with a honeycomb arrangement as in a monolayer, that are coupled together, Fig. 8.8. There are four atoms in the unit cell, a pair $A1$, $B1$, from the lower layer and a pair $A2$, $B2$, from the upper layer. In Bernal stacking, the layers are arranged so that two atoms, $B1$ and $A2$, are directly below or above each other, whereas the other two atoms, $A1$ and $B2$, do not have a counterpart in the other layer. The primitive lattice vectors $\mathbf{a}_1$ and $\mathbf{a}_2$, and the lattice constant a are the same as for monolayer graphene, and the unit cell, shown in Fig. 8.8a, has the same area in the x-y plane as in the monolayer. Therefore, the reciprocal lattice and first Brillouin zone are the same as in monolayer graphene, Fig. 8.2. The unit cell of bilayer graphene contains four atoms, and, if the tight-binding model includes one p_z orbital per atomic site, there will be four bands near zero energy, instead of the two bands in monolayer graphene.

Essential features of the low-energy electronic band structure may be described by a minimal tight-binding model including nearest-neighbor coupling γ_0 between $A1$ and $B1$, and $A2$ and $B2$, atoms on each layer, and nearest-neighbor interlayer coupling γ_1 between $B1$ and $A2$ atoms that are directly below or above each other,

$$\gamma_1 = \langle \phi_{A2}\left(\mathbf{r}-\mathbf{R}_{A2}\right)|\mathcal{H}|\phi_{B1}\left(\mathbf{r}-\mathbf{R}_{B1}\right)\rangle\,. \tag{8.55}$$

Then we can generalize the treatment of monolayer graphene, (8.42), to write the transfer and overlap integral matrices of bilayer graphene, in a basis with components $A1$, $B1$, $A2$, $B2$, as

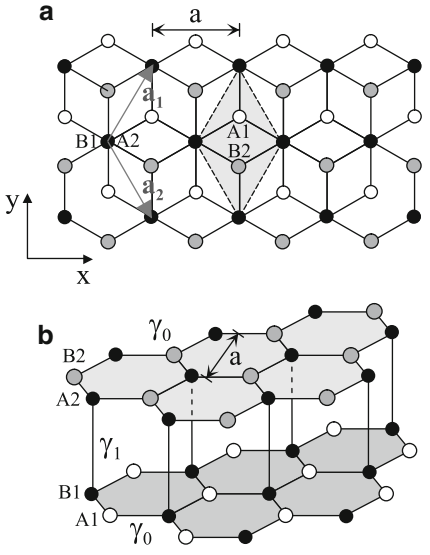

Fig. 8.8 Schematic representation of the crystal structure of AB-stacked bilayer graphene: (**a**) plan view with $A1$ (*white*) and $B1$ atoms (*black*) on the lower layer, $A2$ (*black*) and $B2$ atoms (*gray*) on the upper layer. Vectors $\mathbf{a}_1$ and $\mathbf{a}_2$ are primitive lattice vectors of length equal to the lattice constant a, and the shaded rhombus is a unit cell; (**b**) side view where the parameter γ_0 represents nearest-neighbor coupling within each layer, γ_1 nearest-neighbor coupling between the $B1$ and $A2$ atoms on different layers

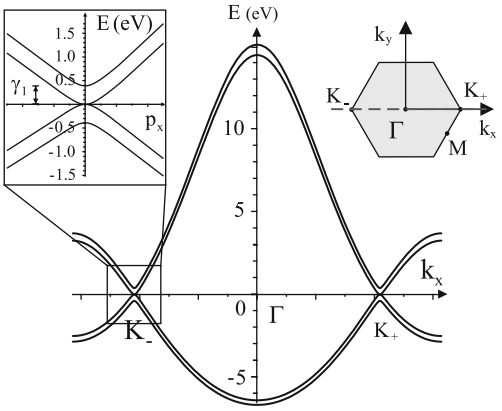

Fig. 8.9 The low-energy band structure of bilayer graphene taking into account nearest-neighbor hopping with parameter $\gamma_0 = 3.033\,\text{eV}$, nearest-neighbor overlap parameter $s_0 = 0.129$, orbital energy $\epsilon_{2p} = 0$ [11], and interlayer coupling $\gamma_1 = 0.39\,\text{eV}$. The plot shows the bands calculated along the k_x axis intersecting points K_-, Γ, and K_+ in the Brillouin zone, shown as the dotted line in the right inset. The left inset shows the band structure in the vicinity of the point K_-

$$H = \begin{pmatrix} \epsilon_{2p} & -\gamma_0 f(\mathbf{k}) & 0 & 0 \\ -\gamma_0 f^*(\mathbf{k}) & \epsilon_{2p} & \gamma_1 & 0 \\ 0 & \gamma_1 & \epsilon_{2p} & -\gamma_0 f(\mathbf{k}) \\ 0 & 0 & -\gamma_0 f^*(\mathbf{k}) & \epsilon_{2p} \end{pmatrix}, \tag{8.56}$$

$$S = \begin{pmatrix} 1 & s_0 f(\mathbf{k}) & 0 & 0 \\ s_0 f^*(\mathbf{k}) & 1 & 0 & 0 \\ 0 & 0 & 1 & s_0 f(\mathbf{k}) \\ 0 & 0 & s_0 f^*(\mathbf{k}) & 1 \end{pmatrix}. \tag{8.57}$$

The upper-left and lower-right 2×2 blocks describe behavior within the lower ($A1/B1$) and upper ($A2/B2$) layers, respectively. The off-diagonal 2×2 blocks, containing parameter γ_1, describe interlayer coupling.

The band structure of bilayer graphene may be determined by solving the secular equation $\det(H - E_j S) = 0$, (8.16). It is plotted in Fig. 8.9 for parameter values $\gamma_0 = 3.033\,\text{eV}$, $s_0 = 0.129$, $\epsilon_{2p} = 0$ [11] and interlayer coupling $\gamma_1 = 0.39\,\text{eV}$. There are four energy bands, two conduction bands and two valence bands. Overall, the band structure is similar to that of monolayer graphene, Fig. 8.5, with each monolayer band split into two by an energy approximately equal to the interlayer coupling γ_1 [36]. The most interesting part of the band structure is in the vicinity of the K points [21], as shown in the left inset of Fig. 8.9, which focuses in on the bands around K_-. At the K point, one of the conduction (valence) bands is split away from zero energy by an amount equal to the interlayer coupling γ_1 ($-\gamma_1$). The split bands originate from atomic sites $B1$ and $A2$ that have a counterpart atom directly above or below them on the other layer. Orbitals on these pairs of

atoms ($B1$ and $A2$) are strongly coupled by the interlayer coupling γ_1 and they form a bonding and anti-bonding pair of bands, split away from zero energy. In the following, we refer to them as "dimer" states, and atomic sites $B1$ and $A2$ are called "dimer" sites. The remaining two bands, one conduction and one valence band, touch at zero energy: as in the monolayer, there is no band gap between the conduction and valence bands. In the vicinity of the K points, the dispersion of the latter bands is quadratic $E_\pm \propto \pm|\mathbf{k} - \mathbf{K}_\xi|^2$, and electronic properties of the low-energy bands may be described by an effective Hamiltonian describing massive chiral particles. This will be explored in more detail in the next section.

8.7 Massive Chiral Quasiparticles in Bilayer Graphene

8.7.1 The Low-Energy Bands of Bilayer Graphene

To begin the description of the low-energy bands in bilayer graphene, we set $s_0 = 0$, thus neglecting the nonorthogonality of orbitals that tends to become important at high energy. Then the overlap matrix S, (8.57), becomes a unit matrix, and H, (8.56), is an effective Hamiltonian for the four bands of bilayer graphene at low energy [21]:

$$H = \begin{pmatrix} 0 & -\gamma_0 f(\mathbf{k}) & 0 & 0 \\ -\gamma_0 f^*(\mathbf{k}) & 0 & \gamma_1 & 0 \\ 0 & \gamma_1 & 0 & -\gamma_0 f(\mathbf{k}) \\ 0 & 0 & -\gamma_0 f^*(\mathbf{k}) & 0 \end{pmatrix}, \tag{8.58}$$

where we used $\epsilon_{2p} = 0$ [11] to define the zero of the energy axis to coincide with the energy of the $2p_z$ orbital. Eigenvalues of the Hamiltonian are given by

$$E_\pm^{(\alpha)} = \pm\frac{\gamma_1}{2}\left(\sqrt{1 + \frac{4\gamma_0^2|f(\mathbf{k})|^2}{\gamma_1^2}} + \alpha\right), \qquad \alpha = \pm 1\,. \tag{8.59}$$

Over most of the Brillouin zone, where $4\gamma_0^2|f(\mathbf{k})|^2 \gg \gamma_1^2$, the energy may be approximated as $E_\pm^{(\alpha)} \approx \pm(\gamma_0|f(\mathbf{k})| + \alpha\gamma_1/2)$, meaning that the $\alpha = \pm 1$ bands are approximately the same as the monolayer bands, (8.45), but they are split by the interlayer coupling γ_1. The eigenvalues $E_\pm^{(1)}$, (8.59), describe two bands that are split away from zero energy by $\pm\gamma_1$ at the K point (where $|f(\mathbf{k})| = 0$) as shown in the left inset of Fig. 8.9. This is because the orbitals on the $A2$ and $B1$ sites form a dimer that is coupled by interlayer hopping γ_1, resulting in a bonding and antibonding pair of states $\pm\gamma_1$.

The remaining two bands are described by $E_\pm^{(-1)}$. Near to the K_ξ point, $pa/\hbar \ll 1$, we replace the factor $\gamma_0|f(\mathbf{k})|$ with vp, (8.51):

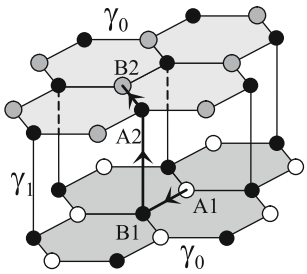

Fig. 8.10 Schematic representation of the crystal structure of AB-stacked bilayer graphene illustrating the processes that contribute to effective coupling between $A1$ (*white*) and $B2$ atoms (*gray*), in the presence of strongly coupled "dimer" sites $B1$ and $A2$ (*black*). The black arrowed line indicates the three-stage process: intralayer hopping between $A1$ and $B1$, followed by an interlayer transition via the dimer sites $B1$ and $A2$, followed by another intralayer hopping between $A2$ and $B2$

$$E_{\pm}^{(-1)} \approx \pm\frac{\gamma_1}{2}\left(\sqrt{1+\frac{4v^2p^2}{\gamma_1^2}}-1\right). \tag{8.60}$$

This formula interpolates between linear dispersion at large momenta ($\gamma_1 \ll vp < \gamma_0$) and quadratic dispersion $E_{\pm}^{(-1)} \approx \pm v^2p^2/\gamma_1$ near zero energy, where the bands touch. These bands arise from effective coupling between the orbitals on sites, $A1$ and $B2$, that do not have a counterpart in the other layer. In the absence of direct coupling between $A1$ and $B2$, the effective coupling is achieved through a three-stage process as indicated in Fig. 8.10. It can be viewed as an intralayer hopping between $A1$ and $B1$, followed by an interlayer transition via the dimer sites $B1$ and $A2$, followed by another intralayer hopping between $A2$ and $B2$. This effective coupling may be succinctly described by an effective low-energy Hamiltonian written in a two-component basis of p_z orbitals on $A1$ and $B2$ sites.

8.7.2 The Two-Component Hamiltonian of Bilayer Graphene

The effective two-component Hamiltonian may be derived from the four-component Hamiltonian, (8.58), using a Schrieffer–Wolff transformation [21,38]. In the present context, a straightforward way to do the transformation is to consider the eigenvalue equation for the four-component Hamiltonian, (8.58), as four simultaneous equations for the wave-function components $c_{A1}, c_{B1}, c_{A2}, c_{B2}$:

$$Ec_{A1} + \gamma_0 f(\mathbf{k})\, c_{B1} = 0\,, \tag{8.61}$$

$$\gamma_0 f^*(\mathbf{k})\, c_{A1} + Ec_{B1} - \gamma_1 c_{A2} = 0\,, \tag{8.62}$$

$$-\gamma_1 c_{B1} + Ec_{A2} + \gamma_0 f(\mathbf{k})\, c_{B2} = 0\,, \tag{8.63}$$

$$\gamma_0 f^*(\mathbf{k})\, c_{A2} + Ec_{B2} = 0\,. \tag{8.64}$$

Using the second and third equations, (8.62) and (8.63), it is possible to express the components on the dimer sites, c_{B1} and c_{A2}, in terms of the other two:

$$c_{B1} = \frac{\gamma_0 f(\mathbf{k})}{\gamma_1 d} c_{B2} + \frac{E\gamma_0 f^*(\mathbf{k})}{\gamma_1^2 d} c_{A1}, \tag{8.65}$$

$$c_{A2} = \frac{E\gamma_0 f(\mathbf{k})}{\gamma_1^2 d} c_{B2} + \frac{\gamma_0 f^*(\mathbf{k})}{\gamma_1 d} c_{A1}, \tag{8.66}$$

where $d = 1 - E^2/\gamma_1^2$. Substituting these expressions into the first and fourth equations, (8.61) and (8.64), produces two equations solely in terms of c_{A1} and c_{B2}. Assuming $|E| \ll |\gamma_1|$ and $|\gamma_0 f(\mathbf{k})| \ll |\gamma_1|$, we use $d \approx 1$ and keep terms up to order $1/\gamma_1$ only:

$$E c_{A1} + \frac{\gamma_0^2 f^2(\mathbf{k})}{\gamma_1} c_{B2} = 0, \tag{8.67}$$

$$\frac{\gamma_0^2 (f^*(\mathbf{k}))^2}{\gamma_1} c_{A1} + E c_{B2} = 0. \tag{8.68}$$

It is possible to express these two equations as a Schrödinger equation, $H_2\psi = E\psi$, with a two-component wave function $\psi = (c_{A1}, c_{B2})^T$ and two-component Hamiltonian

$$H_{2,\xi} = -\frac{1}{2m} \begin{pmatrix} 0 & (\xi p_x - i p_y)^2 \\ (\xi p_x + i p_y)^2 & 0 \end{pmatrix}, \tag{8.69}$$

where we used the approximation $f(\mathbf{k}) \approx -v(\xi p_x - i p_y)/\gamma_0$, (8.51), valid for momentum $pa/\hbar \ll 1$ close to the K_ξ point, and parameters v and γ_1 were combined into a mass $m = \gamma_1/(2v^2)$.

The effective low-energy Hamiltonian of bilayer graphene, (8.69), resembles the Dirac-like Hamiltonian of monolayer graphene, (8.52), but with a quadratic term on the off-diagonal instead of linear. The energy eigenvalues and eigenstates of H_2 are given by

$$E_\pm = \pm \frac{p^2}{2m}, \qquad \psi_\pm = \frac{1}{\sqrt{2}} \begin{pmatrix} 1 \\ \mp e^{i2\xi\varphi} \end{pmatrix} e^{i\mathbf{p}.\mathbf{r}/\hbar}, \tag{8.70}$$

where $\pm$ refer to the conduction and valence bands, respectively. Here, φ is the polar angle of the momentum in the graphene plane, $\mathbf{p} = (p_x, p_y) = p(\cos\varphi, \sin\varphi)$.

8.7.3 Pseudospin and Chirality in Bilayer Graphene

The two-component Hamiltonian (8.69) of bilayer graphene has a pseudospin degree of freedom [17, 21] related to the amplitude of the eigenstates (8.70) on

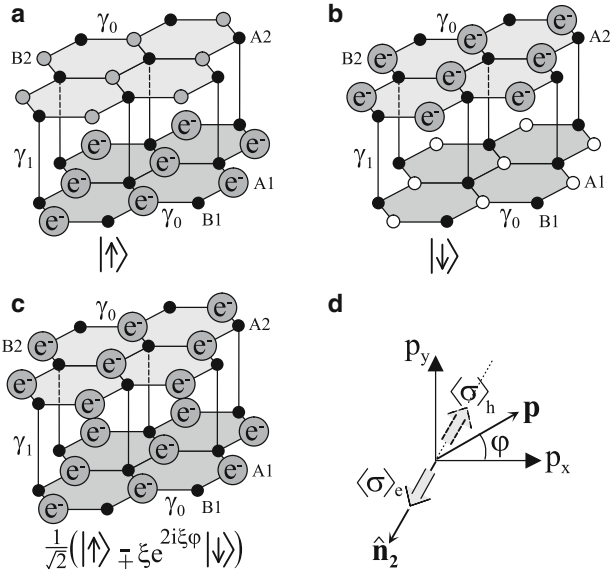

Fig. 8.11 Schematic representation of the pseudospin degree of freedom in bilayer graphene: (**a**) electronic density solely on the $A1$ sublattice on the lower layer can be viewed as a pseudospin "up" state, whereas (**b**) density solely on the $B2$ sublattice on the upper layer corresponds to a pseudospin "down" state; (**c**) in bilayer graphene, electronic density is usually shared equally between $A1$ and $B2$ sublattices, so that the pseudospin part of the wave function is a linear combination of "up" and "down," with amplitudes dependent on the direction of the electronic momentum $\mathbf{p}$; (**d**) at valley K_+, the pseudospin $\langle\boldsymbol{\sigma}\rangle_e$ in the conduction band is parallel to the quantization direction $\hat{\mathbf{n}}_2$, whereas the pseudospin $\langle\boldsymbol{\sigma}\rangle_h$ in the valence band is antiparallel to $\hat{\mathbf{n}}_2$. Direction $\hat{\mathbf{n}}_2$ is related to the direction of momentum $\mathbf{p}$, but turns in the x-y plane twice as quickly as it

the $A1$ and $B2$ sublattice sites, where $A1$ and $B2$ lie on different layers. If all the electronic density was located on the $A1$ sublattice, Fig. 8.11a, this could be viewed as a pseudospin "up" state (pointing upward out of the graphene sheet) $|\uparrow\rangle = (1,0)^T$, whereas density solely on the $B2$ sublattice corresponds to a pseudospin "down" state (pointing downward out of the graphene sheet) $|\downarrow\rangle = (0,1)^T$, Fig. 8.11b. In bilayer graphene, electronic density is usually shared equally between the two sublattices, Fig. 8.11c, so that the pseudospin part of the wave function is a linear combination of "up" and "down," and it lies in the plane of the graphene sheet.

Electrons in bilayer graphene are chiral [17, 21], meaning that the orientation of the pseudospin is related to the direction of the electronic momentum $\mathbf{p}$, but the chirality is different to that in monolayers. As before, we use Pauli spin matrices in the $A1/B2$ sublattice space, σ_i where $i = 1 \ldots 3$, to write the effective Hamiltonian (8.69) as

$$H_{2,\xi} = -\frac{1}{2m}\left[\sigma_x\left(p_x^2 - p_y^2\right) + 2\xi\sigma_y p_x p_y\right]. \tag{8.71}$$

If we define a pseudospin vector as $\boldsymbol{\sigma} = (\sigma_x, \sigma_y, \sigma_z)$, and a unit vector as $\hat{\mathbf{n}}_2 = -(\cos 2\varphi, \xi \sin 2\varphi, 0)$, then the Hamiltonian becomes $H_{2,\xi} = (p^2/2m)\,\boldsymbol{\sigma}.\hat{\mathbf{n}}_2$, stressing that the pseudospin $\boldsymbol{\sigma}$ is linked to the direction $\hat{\mathbf{n}}_2$. The chiral operator $\boldsymbol{\sigma}.\hat{\mathbf{n}}_2$ projects the pseudospin onto the direction of quantization $\hat{\mathbf{n}}_2$: eigenstates of the Hamiltonian are also eigenstates of $\boldsymbol{\sigma}.\hat{\mathbf{n}}_2$ with eigenvalues ± 1, $\boldsymbol{\sigma}.\hat{\mathbf{n}}_2\psi_\pm = \pm\psi_\pm$. In bilayer graphene, the quantization axis $\hat{\mathbf{n}}_2$ is fixed to lie in the graphene plane, but it turns twice as quickly in the plane as the momentum $\mathbf{p}$. If we calculate the expectation value of the pseudospin operator $\langle\boldsymbol{\sigma}\rangle = (\langle\sigma_x\rangle, \langle\sigma_y\rangle, \langle\sigma_z\rangle)$ with respect to the eigenstate $\psi_\pm$, (8.70), then the result $\langle\boldsymbol{\sigma}\rangle_{e/h} = \mp(\cos 2\varphi, \xi \sin 2\varphi, 0)$, illustrates the link between pseudospin and momentum, Fig. 8.11d.

If the momentum $\mathbf{p}$ rotates by angle φ, adiabatic evolution of the chiral wave function $\psi_\pm$, (8.70), produces a matching rotation of the quantization axis $\hat{\mathbf{n}}_2$ by angle 2φ, not φ as in the monolayer, Sect. 8.5.2. Thus, traversal around a closed contour in momentum space results in a Berry's phase [31, 32] change of 2π of the chiral wave function in bilayer graphene [17, 21]. For Berry's phase 2π chiral electrons in bilayer graphene, (8.70), the probability to scatter in a direction φ, where $\varphi = 0$ is the forward direction, is proportional to $w(\varphi) = |\langle\psi_\pm(\varphi)|\psi_\pm(0)\rangle|^2 = \cos^2(\varphi)$ [21, 37] as shown in Fig. 8.7b. This is anisotropic, but, unlike monolayers Fig. 8.7a, does not display an absence of backscattering ($w(\pi) = 1$ in bilayers): scattering into a state with opposite momentum is not prohibited because it does not require a reversal of the pseudospin.

8.8 The Integer Quantum Hall Effect in Graphene

When a perpendicular magnetic field is applied a two-dimensional electron gas, the electrons follow cyclotron orbits, and their allowed energies are quantized into values known as Landau levels [39]. At low magnetic field, the Landau levels give rise to quantum oscillations including the de Haas-van Alphen effect and the Shubnikov-de Haas effect. At higher fields, the discrete Landau level spectrum is manifest in the integer quantum Hall effect [40–42], a quantization of Hall conductivity into integer values of the quantum of conductivity e^2/h. For monolayer graphene, the Landau level spectrum was calculated over fifty years ago by McClure [43], and the integer quantum Hall effect was observed [15, 16] and studied theoretically [13, 30, 45–47] in recent years. The chiral nature of electrons in graphene results in an unusual sequencing of the quantized plateaus of the Hall conductivity. In bilayer graphene, the experimental observation of the integer quantum Hall effect [17] and calculation of the Landau level spectrum [21] revealed further unusual features related to the chirality of electrons.

8.8.1 The Landau Level Spectrum of Monolayer Graphene

We consider a magnetic field perpendicular to the graphene sheet $\mathbf{B} = (0, 0, -B)$, where $B = |\mathbf{B}|$. The Dirac-like Hamiltonian of monolayer graphene (8.52) may be

written as

$$H_{1,K_+} = v\begin{pmatrix} 0 & \pi^\dagger \\ \pi & 0 \end{pmatrix}, \quad H_{1,K_-} = -v\begin{pmatrix} 0 & \pi \\ \pi^\dagger & 0 \end{pmatrix}, \quad \begin{cases} \pi = p_x + ip_y \\ \pi^\dagger = p_x - ip_y \end{cases}, \tag{8.72}$$

in the vicinity of corners of the Brillouin zone K_+ and K_-, respectively. The off-diagonal elements of the Hamiltonian (8.72) contain operators $\pi = p_x + ip_y$ and $\pi^\dagger = p_x - ip_y$, where, in the presence of a magnetic field, the operator $\mathbf{p} = (p_x, p_y) \equiv -i\hbar\nabla + e\mathbf{A}$. Here, $\mathbf{A}$ is the vector potential and the charge of the electron is $-e$.

Using the Landau gauge $\mathbf{A} = (0, -Bx, 0)$ preserves translational invariance in the y direction, so that eigenstates may be written in terms of states that are plane waves in the y direction and harmonic oscillator states in the x direction [41, 42],

$$\phi_\ell(x, y) = A_\ell \mathcal{H}_\ell\left(\frac{x}{\lambda_B} - \frac{p_y\lambda_B}{\hbar}\right)\exp\left[-\frac{1}{2}\left(\frac{x}{\lambda_B} - \frac{p_y\lambda_B}{\hbar}\right)^2 + i\frac{p_y y}{\hbar}\right]. \tag{8.73}$$

Here, $\mathcal{H}_\ell$ are Hermite polynomials of order ℓ, for integer $\ell \geq 0$, and the normalization constant is $A_\ell = 1/\sqrt{2^\ell \ell! \sqrt{\pi}}$. The magnetic length λ_B, and a related energy scale Γ, are defined as

$$\lambda_B = \sqrt{\frac{\hbar}{eB}}, \qquad \Gamma = \frac{\sqrt{2}\hbar v}{\lambda_B} = \sqrt{2\hbar v^2 eB}\,. \tag{8.74}$$

With this choice of vector potential, $\pi = -i\hbar\partial_x + \hbar\partial_y - ieBx$ and $\pi^\dagger = -i\hbar\partial_x - \hbar\partial_y + ieBx$. Acting on the harmonic oscillator states (8.73) gives

$$\pi\phi_\ell = -\frac{\sqrt{2}i\hbar}{\lambda_B}\sqrt{\ell}\,\phi_{\ell-1}\,, \tag{8.75}$$

$$\pi^\dagger\phi_\ell = \frac{\sqrt{2}i\hbar}{\lambda_B}\sqrt{\ell+1}\,\phi_{\ell+1}\,, \tag{8.76}$$

and $\pi\phi_0 = 0$. These equations indicate that operators π and $\pi^\dagger$ are proportional to lowering and raising operators of the harmonic oscillator states ϕ_ℓ. The Landau level spectrum is, therefore, straightforward to calculate [43–45]. At the first valley, K_+, the Landau level energies and eigenstates of H_{1,K_+} are

$$K_+,\ \ell \geq 1: \quad E_{\ell,\pm} = \pm\frac{\sqrt{2}\hbar v}{\lambda_B}\sqrt{\ell}\,, \qquad \psi_{\ell,\pm} = \frac{1}{\sqrt{2}}\begin{pmatrix} \phi_\ell \\ \mp i\phi_{\ell-1} \end{pmatrix}, \tag{8.77}$$

$$K_+,\ \ell = 0: \quad E_0 = 0\,, \qquad \psi_0 = \begin{pmatrix} \phi_0 \\ 0 \end{pmatrix}, \tag{8.78}$$

where $\pm$ refer to the conduction and valence bands, respectively. Equation (8.77) describes an electron (plus sign) and a hole (minus sign) series of energy levels, with prefactor $\Gamma = \sqrt{2}\hbar v/\lambda_B$ (8.74), proportional to the square root of the magnetic field. In addition, there is a special level (8.78) fixed at zero energy that arises from the presence of the lowering operator in the Hamiltonian, $\pi\phi_0 = 0$. The corresponding eigenfunction ψ_0 has nonzero amplitude on the A sublattice, but its amplitude is zero on the B sublattice. The form (8.72) of the Hamiltonian H_{1,K_-} at the second valley, K_-, shows that its spectrum is degenerate with that at K_+, with the role of the A and B sublattices reversed:

$$K_-,\ \ell \geq 1: \quad E_{\ell,\pm} = \pm\frac{\sqrt{2}\hbar v}{\lambda_B}\sqrt{\ell}\,, \qquad \psi_{\ell,\pm} = \frac{1}{\sqrt{2}}\begin{pmatrix} \pm i\,\phi_{\ell-1} \\ \phi_\ell \end{pmatrix}, \tag{8.79}$$

$$K_-,\ \ell = 0: \quad E_0 = 0\,, \qquad \psi_0 = \begin{pmatrix} 0 \\ \phi_0 \end{pmatrix}. \tag{8.80}$$

Thus, the eigenfunction ψ_0 of the zero-energy level has zero amplitude on the B sublattice at valley K_+ and zero amplitude on the A sublattice at K_-. If we take into account electronic spin, which contributes a twofold degeneracy of the energy levels, as well as valley degeneracy, then the Landau level spectrum of monolayer graphene consists of fourfold-degenerate Landau levels.

8.8.2 The Integer Quantum Hall Effect in Monolayer Graphene

In this section, we describe how the Landau level spectrum of graphene is reflected in the dependence of the Hall conductivity $\sigma_{xy}(n)$ on carrier density n. In conventional two-dimensional semiconductor systems, in the absence of any Berry's phase effects, the Landau level spectrum is given by $E_\ell = \hbar\omega_c(\ell + 1/2)$, $\ell \geq 0$, where $\omega_c = eB/m$ is the cyclotron frequency [41, 42]. Here, the lowest state lies at finite energy $E_0 = \hbar\omega_c/2$. If the system has an additional degeneracy g (for example, $g = 2$ for spin), then plateaus [40–42] occur at quantized σ_{xy} values of $N(ge^2/h)$, where N is an integer and e^2/h is the quantum value of conductance, i.e. each step between adjacent plateaus has height ge^2/h, Fig. 8.12a. Each σ_{xy} step coincides with the crossing of a Landau level on the density axis. Since the maximum carrier density per Landau level is gB/φ_0, where $\varphi_0 = h/e$ is the flux quantum, the distance between the σ_{xy} steps on the density axis is gB/φ_0.

As described above, monolayer graphene has fourfold (spin and valley) degenerate Landau levels $E_{\ell,\pm} = \pm\sqrt{2\ell}\hbar v/\lambda_B$ for $\ell \geq 1$ and $E_0 = 0$. The Hall conductivity $\sigma_{xy}(n)$, Fig. 8.12b, displays a series of quantized plateaus separated by steps of size $4e^2/h$, as in the conventional case, but the plateaus occur at half-integer values of $4e^2/h$ rather than integer ones:

$$\sigma_{xy} = -\frac{1}{2}(2N+1)\left(\frac{4e^2}{h}\right), \tag{8.81}$$

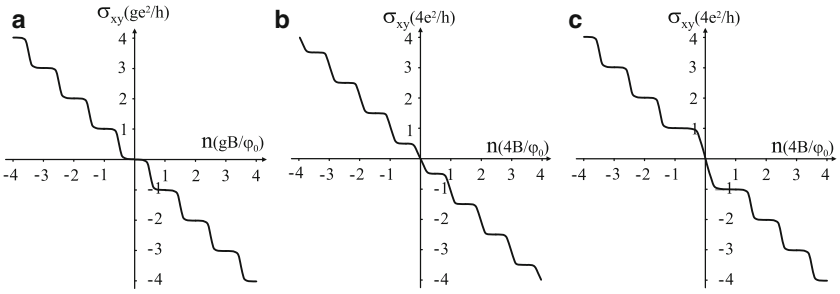

Fig. 8.12 Schematic representation of three types of integer quantum Hall effect, showing the density dependence of the Hall conductivity $\sigma_{xy}(n)$: (**a**) conventional two-dimensional semiconductor systems with additional system degeneracy g; (**b**) monolayer graphene; (**c**) bilayer graphene. Here, B is the magnitude of the magnetic field and $\varphi_0 = h/e$ is the flux quantum

where N is an integer, as observed experimentally [15, 16] and described theoretically [13, 30, 45–47]. This unusual sequencing of σ_{xy} plateaus is explained by the presence of the fourfold-degenerate Landau level E_0 fixed at zero energy. Since it lies at the boundary between the electron and hole gases, it creates a step in σ_{xy} of $4e^2/h$ at zero density. Each Landau level in monolayer graphene is fourfold degenerate, including the zero energy one, so the distance between each σ_{xy} step on the density axis is $4B/\varphi_0$, i.e. the steps occur at densities equal to integer values of $4B/\varphi_0$.

8.8.3 The Landau Level Spectrum of Bilayer Graphene

In the presence of a perpendicular magnetic field, the Hamiltonian (8.69) describing massive chiral electrons in bilayer graphene may be written as

$$H_{2,K_+} = -\frac{1}{2m}\begin{pmatrix} 0 & (\pi^\dagger)^2 \\ \pi^2 & 0 \end{pmatrix}, \qquad H_{2,K_-} = -\frac{1}{2m}\begin{pmatrix} 0 & \pi^2 \\ (\pi^\dagger)^2 & 0 \end{pmatrix}, \tag{8.82}$$

in the vicinity of corners of the Brillouin zone K_+ and K_-, respectively. Using the action of operators π and $\pi^\dagger$ on the harmonic oscillator states ϕ_ℓ, (8.75) and (8.76), the Landau level spectrum of bilayer graphene may be calculated [21]. At the first valley, K_+, the Landau level energies and eigenstates of H_{2,K_+} are

$$K_+,\ \ell \geq 2: \quad E_{\ell,\pm} = \pm\frac{\hbar^2}{m\lambda_B^2}\sqrt{\ell(\ell-1)}\,, \quad \psi_{\ell,\pm} = \frac{1}{\sqrt{2}}\begin{pmatrix} \phi_\ell \\ \pm\phi_{\ell-2} \end{pmatrix}, \tag{8.83}$$

$$K_+,\ \ell = 1: \quad E_1 = 0\,, \qquad \psi_1 = \begin{pmatrix} \phi_1 \\ 0 \end{pmatrix}, \tag{8.84}$$

$$K_+,\ \ell = 0: \quad E_0 = 0\,, \qquad \psi_0 = \begin{pmatrix} \phi_0 \\ 0 \end{pmatrix}, \tag{8.85}$$

where $\pm$ refer to the conduction and valence bands, respectively. Equation (8.83) describes an electron (plus sign) and a hole (minus sign) series of energy levels. The prefactor $\hbar^2/(m\lambda_B^2)$ is proportional to the magnetic field, and it may equivalently be written as Γ^2/γ_1 or as $\hbar\omega_c$ where $\omega_c = eB/m$. For high levels, $\ell \gg 1$, the spectrum consists of approximately equidistant levels with spacing $\hbar\omega_c$. Note, however, that we are considering the low-energy Hamiltonian, so that the above spectrum is only valid for sufficiently small level index and magnetic field $\sqrt{\ell}\Gamma \ll \gamma_1$. As well as the field-dependent levels, there are two special levels, (8.84) and (8.85), fixed at zero energy. There are two zero-energy levels because of the presence of the square of the lowering operator in the Hamiltonian. It may act not only on the oscillator ground state to give zero energy, $\pi^2\phi_0 = 0$, (8.85), but also on the first excited state to give zero energy, $\pi^2\phi_1 = 0$, (8.84). The corresponding eigenfunctions ψ_0 and ψ_1 have nonzero amplitude on the $A1$ sublattice, that lies on the bottom layer, but their amplitude is zero on the $B2$ sublattice.

The form (8.82) of the Hamiltonian H_{2,K_-} at the second valley, K_-, shows that its spectrum is degenerate with that at K_+ with the role of the $A1$ and $B2$ sublattices reversed. It may be expressed as $H_{2,K_-} = \sigma_x H_{2,K_+}\sigma_x$ so that $\psi_{\ell,\pm}(K_-) = \sigma_x\psi_{\ell,\pm}(K_+)$, $\psi_1(K_-) = \sigma_x\psi_1(K_+)$, and $\psi_0(K_-) = \sigma_x\psi_0(K_+)$. Thus, the eigenfunctions ψ_0 and ψ_1 of the zero-energy levels have zero amplitude on the $B2$ sublattice at valley K_+ and zero amplitude on the $A1$ sublattice at K_-. If we take into account electronic spin, which contributes a twofold degeneracy of the energy levels, as well as valley degeneracy, then the Landau level spectrum of bilayer graphene consists of fourfold degenerate Landau levels, except for the zero-energy levels which are eightfold degenerate. This doubling of the degeneracy of the zero-energy levels is reflected in the density dependence of the Hall conductivity.

8.8.4 The Integer Quantum Hall Effect in Bilayer Graphene

The Hall conductivity $\sigma_{xy}(n)$ of bilayer graphene, Fig. 8.12c, displays a series of quantized plateaus occurring at integer values of $4e^2/h$ that is practically the same as in the conventional case, Fig. 8.12a, with degeneracy per level $g = 4$ accounting for spin and valleys. However, there is a step of size $8e^2/h$ in σ_{xy} across zero density in bilayer graphene [17, 21]. This unusual behavior is explained by the eightfold degeneracy of the zero-energy Landau levels. Their presence creates a step in σ_{xy} at zero density, as in monolayer graphene, but owing to the doubled degeneracy as compared to other levels, it requires twice as many carriers to fill them. Thus, the transition between the corresponding plateaus is twice as wide in density, $8B/\varphi_0$ as compared to $4B/\varphi_0$, and the step in σ_{xy} between the plateaus must be twice as high, $8e^2/h$ instead of $4e^2/h$. This demonstrates that although Berry's phase 2π is not reflected in the sequencing of quantum Hall plateaus at high density, it has a consequence in the quantum limit of zero density, as observed experimentally [17].

Here, we showed that the chiral Hamiltonians of monolayer and bilayer graphene corresponding to Berry's phase π and 2π, respectively, have associated four- and

eightfold degenerate zero-energy Landau levels, producing steps of four and eight times the conductance quantum e^2/h in the Hall conductivity across zero density [15–17]. In our discussion, we neglected interaction effects and we assumed that any valley and spin splitting, or splitting of the $\ell = 1$ and $\ell = 0$ levels in bilayer graphene, are negligible as compared to temperature and level broadening.

8.9 Trigonal Warping in Graphene

So far, we have described the tight-binding model of graphene and showed that the low-energy Hamiltonians of monolayer and bilayer graphene support chiral electrons with unusual properties. There are, however, additional contributions to the Hamiltonians that perturb this simple picture. In this section, we focus on one of them, known in the graphite literature as trigonal warping [4, 22–25].

8.9.1 Trigonal Warping in Monolayer Graphene

The band structure of monolayer graphene, shown in Fig. 8.4, is approximately linear in the vicinity of zero energy, but it shows deviations away from linear behavior at higher energy. In deriving the Dirac-like Hamiltonian of monolayer graphene (8.52), we kept only linear terms in the momentum $\mathbf{p} = \hbar\mathbf{k} - \hbar\mathbf{K}_\xi$ measured with respect to the K_ξ point. If we retain quadratic terms in $\mathbf{p}$, then the function $f(\mathbf{k})$, (8.51), describing coupling between the A and B sublattices becomes

$$f(\mathbf{k}) \approx -\frac{\sqrt{3}a}{2\hbar}(\xi p_x - i p_y) + \frac{a^2}{8\hbar^2}(\xi p_x + i p_y)^2, \tag{8.86}$$

where $pa/\hbar \ll 1$. Using this approximate expression, the Dirac-like Hamiltonian (8.52) in the vicinity of point K_ξ is modified [9] as

$$H_{1,\xi} = v\begin{pmatrix} 0 & \xi p_x - i p_y \\ \xi p_x + i p_y & 0 \end{pmatrix} - \mu\begin{pmatrix} 0 & (\xi p_x + i p_y)^2 \\ (\xi p_x - i p_y)^2 & 0 \end{pmatrix}, \tag{8.87}$$

where parameter $\mu = \gamma_0 a^2/(8\hbar^2)$. The corresponding energy eigenvalues are

$$E_\pm = \pm\sqrt{v^2p^2 - 2\xi\mu v p^3 \cos 3\varphi + \mu^2 p^4}. \tag{8.88}$$

For small momentum near the K point, $pa/\hbar \ll 1$, the terms containing parameter μ are a small perturbation because $\mu p^2/(vp) = pa/(4\sqrt{3}\hbar)$. They contribute to a weak triangular deformation of the Fermi circle that becomes stronger as the momentum $\mathbf{p}$ becomes larger. Figure 8.13 shows the trigonal warping of the Fermi

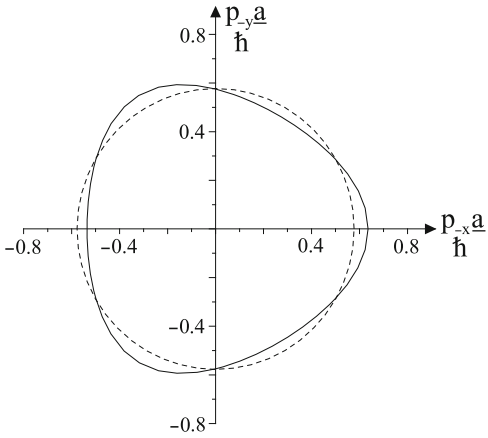

Fig. 8.13 Trigonal warping in monolayer graphene. The solid line shows the isoenergetic line $E = 0.5\gamma_0$ in the vicinity of the valley K_+ using (8.88), the dashed line shows the circular isoenergetic line obtained by neglecting trigonal warping $\mu = 0$

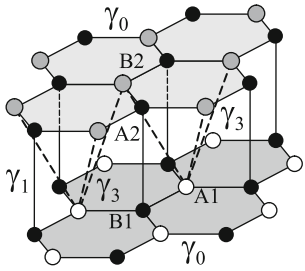

Fig. 8.14 Schematic representation of the crystal structure of AB-stacked bilayer graphene illustrating skew interlayer coupling γ_3 (*dashed lines*) between p_z orbitals on sites $A1$ (*white*) and $B2$ (*gray*)

circle near point K_+, obtained by plotting (8.88) for constant energy $E = 0.5\gamma_0$. The presence of the valley index $\xi = \pm 1$ in the angular term of (8.88) means that the orientation of the trigonal warping at the second valley K_- is reversed.

8.9.2 *Trigonal Warping and Lifshitz Transition in Bilayer Graphene*

In deriving the low-energy Hamiltonian of bilayer graphene (8.69), the linear approximation of $f(\mathbf{k})$ (8.51) in the vicinity of the K point was used. Taking into account quadratic terms in $f(\mathbf{k})$ would produce higher-order in momentum contributions to (8.69), that would tend to be relevant at large momentum $\mathbf{p}$. There is, however, an additional interlayer coupling in bilayer graphene that contributes to trigonal warping and tends to be relevant at small momentum $\mathbf{p}$, i.e. at low energy and very close to the K point.

The additional coupling is a skew interlayer coupling between p_z orbitals on atomic sites $A1$ and $B2$, Fig. 8.14, denoted γ_3. For each $A1$ site, there are three $B2$ sites nearby. A calculation of the matrix element between $A1$ and $B2$ sites in the tight-binding model proceeds in a similar way as that between adjacent A

and B sites in monolayer graphene, as described in Sect. 8.4.2. Then the effective Hamiltonian in a basis with components $A1$, $B1$, $A2$, $B2$, for the four low-energy bands of bilayer graphene (8.58) is [21]:

$$H = \begin{pmatrix} 0 & -\gamma_0 f(\mathbf{k}) & 0 & -\gamma_3 f^*(\mathbf{k}) \\ -\gamma_0 f^*(\mathbf{k}) & 0 & \gamma_1 & 0 \\ 0 & \gamma_1 & 0 & -\gamma_0 f(\mathbf{k}) \\ -\gamma_3 f(\mathbf{k}) & 0 & -\gamma_0 f^*(\mathbf{k}) & 0 \end{pmatrix}, \tag{8.89}$$

where

$$\gamma_3 = -\langle \phi_{A1}(\mathbf{r} - \mathbf{R}_{A1}) | \mathcal{H} | \phi_{B2}(\mathbf{r} - \mathbf{R}_{B2}) \rangle . \tag{8.90}$$

The γ_3 term is relevant at low energy because it is a direct coupling between the $A1$ and $B2$ orbitals that form the two low-energy bands. Thus, using the linear-in-momentum approximation (8.51), terms such as $\gamma_3 f(\mathbf{k}) \approx -v_3 (\xi p_x - i p_y)$ appear in the two-component Hamiltonian written in basis c_{A1}, c_{B2}. Equation (8.69) is modified as [21]

$$H_{2,\xi} = v_3 \begin{pmatrix} 0 & \xi p_x + i p_y \\ \xi p_x - i p_y & 0 \end{pmatrix} - \frac{1}{2m} \begin{pmatrix} 0 & (\xi p_x - i p_y)^2 \\ (\xi p_x + i p_y)^2 & 0 \end{pmatrix}, \tag{8.91}$$

where $v_3 = \sqrt{3} a \gamma_3 / (2\hbar)$ and $m = \gamma_1 / (2v^2)$. Taking into account trigonal warping, the low-energy Hamiltonian of bilayer graphene (8.91) resembles that of monolayer graphene (8.87). The principle difference lies in the magnitude of the parameters. Since $\gamma_3 = 0.315\,\text{eV}$ [4] is an order of magnitude less than $\gamma_0 = 3.033\,\text{eV}$ [11], then $v_3 \ll v$. Thus, the linear term dominates in monolayers and the quadratic term dominates in bilayers over a broad range of energy. The energy eigenvalues of $H_{2,\xi}$, (8.91), are

$$E_\pm = \pm \sqrt{v_3^2 p^2 - \xi \frac{v_3 p^3}{m} \cos 3\varphi + \left(\frac{p^2}{2m} \right)^2}, \tag{8.92}$$

for energies $|E_\pm| \ll \gamma_1$. Over a range of energy, the term independent of v_3 dominates, and the v_3 dependent terms produce trigonal warping of the isoenergetic line in the vicinity of each K point. The effect of trigonal warping increases as the energy is lowered, until, at very low energies $E_L \approx \frac{1}{4}\gamma_1 (v_3/v)^2 \approx 1\,\text{meV}$, it leads to a Lifshitz transition [48]: the isoenergetic line breaks into four parts [4, 21–25, 49, 50]. There is one "central" part, centered on the K point ($p = 0$), that is approximately circular with area $\mathcal{A}_c \approx \pi E^2 / (\hbar v_3)^2$. In addition, there are three "leg" parts that are elliptical with area $\mathcal{A}_\ell \approx \frac{1}{3}\mathcal{A}_c$. Each ellipse has its major axis separated by angle $2\pi/3$ from the major axes of the other leg parts, as measured from the K point, with the ellipse centered on $|p| = \gamma_1 v_3 / v^2$.

Here, we have described the low-energy band structure of monolayer and bilayer graphene within a simple tight-binding model, including a Lifshitz transition in bilayer graphene at very low energy $E_L \approx 1\,\text{meV}$. It is quite possible that electron–electron interactions have a dramatic effect on the band structure of bilayer graphene, producing qualitatively different features at low energy [51–56].

8.10 Tuneable Band Gap in Bilayer Graphene

8.10.1 Asymmetry Gap in the Band Structure of Bilayer Graphene

In graphene monolayers and bilayers, a combination of space and time inversion symmetry [57] guarantees the existence of a gapless band structure exactly at the K point, i.e. the A and B sublattices ($A1$ and $B2$ in bilayers) are identical, leading to degeneracy of the states they support at the K point. Breaking inversion symmetry by, say, fixing the two sublattice sites to be at different energies, would lead to a gap between the conduction and valence bands at the K point. In monolayer graphene, breaking the A/B sublattice symmetry in a controllable way is very difficult: it would require a periodic potential because A and B are adjacent sites on the same layer. In bilayer graphene, however, the $A1$ and $B2$ sublattices lie on different layers and, thus, breaking the symmetry and opening a band gap may be achieved by doping or gating. Band-gap opening in bilayer graphene has recently been studied both theoretically [21, 28, 58–65] and in a range of different experiments [26, 27, 62, 63, 66–74].

If we introduce an asymmetry parameter $\Delta = \epsilon_2 - \epsilon_1$ describing the difference between on-site energies in the two layers, $\epsilon_{A2} = \epsilon_{B2} = \epsilon_2 = \frac{1}{2}\Delta$, $\epsilon_{A1} = \epsilon_{B1} = \epsilon_1 = -\frac{1}{2}\Delta$, then the transfer integral matrix of bilayer graphene (8.56), in a basis with components $A1$, $B1$, $A2$, $B2$, becomes [21, 28, 59]

$$H = \begin{pmatrix} -\frac{1}{2}\Delta & -\gamma_0 f(\mathbf{k}) & 0 & 0 \\ -\gamma_0 f^*(\mathbf{k}) & -\frac{1}{2}\Delta & \gamma_1 & 0 \\ 0 & \gamma_1 & \frac{1}{2}\Delta & -\gamma_0 f(\mathbf{k}) \\ 0 & 0 & -\gamma_0 f^*(\mathbf{k}) & \frac{1}{2}\Delta \end{pmatrix}. \tag{8.93}$$

The band structure may be determined by solving the secular equation $\det(H - E_j S) = 0$ using overlap matrix S, (8.57). It is plotted in Fig. 8.15 for parameter values $\gamma_0 = 3.033\,\text{eV}$, $s_0 = 0.129$ and $\Delta = \gamma_1 = 0.39\,\text{eV}$. A band gap appears between the conduction and valence bands near the K points (left inset in Fig. 8.15).

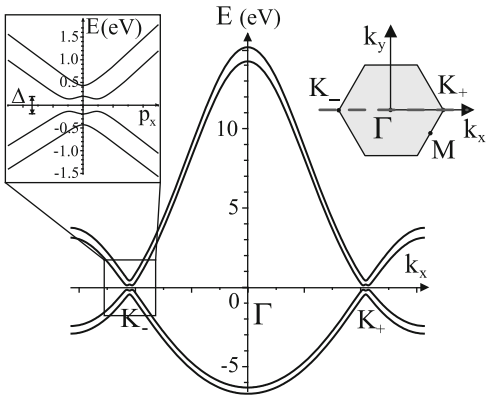

Fig. 8.15 The low-energy band structure of bilayer graphene in the presence of interlayer asymmetry Δ. Parameter values are $\gamma_0 = 3.033\,\text{eV}$, $s_0 = 0.129$, $\Delta = \gamma_1 = 0.39\,\text{eV}$. The plot shows the bands calculated along the k_x axis intersecting points K_-, Γ, and K_+ in the Brillouin zone, shown as the dotted line in the right inset. The left inset shows the band structure in the vicinity of the point K_-

To develop an analytic description of the bands at low energy, we neglect nonorthogonality of the orbitals on adjacent sites, so that the overlap matrix S, (8.57), becomes a unit matrix. Then the bands at low energy are described by Hamiltonian, (8.93), with eigenvalues [21] given by

$$E_{\pm}^{(\alpha)} = \pm\left[\frac{\Delta^2}{4} + v^2p^2 + \frac{\gamma_1^2}{2} + \alpha\frac{\gamma_1^2}{2}\sqrt{1 + \frac{4v^2p^2}{\gamma_1^2} + \frac{4\Delta^2v^2p^2}{\gamma_1^4}}\right]^{1/2}, \quad (8.94)$$

where $\alpha = 1$ for the split bands and $\alpha = -1$ for the low-energy bands. Here, we used the linear approximation $f(\mathbf{k}) \approx -v\left(\xi p_x - i p_y\right)/\gamma_0$, (8.51), so that $\gamma_0|f(\mathbf{k})| \approx vp$. Eigenvalues $E_{\pm}^{(-1)}$ describe the low-energy bands split by a gap. They have a distinctive "Mexican hat" shape, shown in the left inset in Fig. 8.15. The separation between the bands exactly at the K point, $E_+^{(-1)}(p=0) - E_-^{(-1)}(p=0)$, is equal to $|\Delta|$, but the true value of the band gap Δ_g occurs at nonzero value of the momentum p_g away from the K point,

$$p_g = \frac{|\Delta|}{2v}\sqrt{\frac{\Delta^2 + 2\gamma_1^2}{\Delta^2 + \gamma_1^2}}, \quad (8.95)$$

$$\Delta_g = E_+^{(-1)}(p_g) - E_-^{(-1)}(p_g) = \frac{|\Delta|\gamma_1}{\sqrt{\Delta^2 + \gamma_1^2}}. \quad (8.96)$$

For moderate values of the asymmetry parameter, $|\Delta| \ll \gamma_1$, then the band gap $\Delta_g \approx |\Delta|$, but for extremely large values, $|\Delta| \gg \gamma_1$, the gap saturates $\Delta_g \approx \gamma_1$, where γ_1 is of the order of three to four hundred meV. The value of the asymmetry parameter Δ and bandgap Δ_g may be tuned using an external gate potential, but the ability of an external gate to induce a potential asymmetry between the layers of the bilayer depends on screening by the electrons in bilayer graphene, as discussed in the following.

8.10.2 Self-Consistent Model of Screening in Bilayer Graphene

8.10.2.1 Introduction

The influence of screening on band-gap opening in bilayer graphene has been modeled using the tight-binding model and Hartree theory [28, 60, 62, 63, 65], and this simple analytic model is in good qualitative agreement with density functional theory [60,64] and experiments [62,63,67,69,71]. Recently, the tight-binding model and Hartree theory approach has been applied to graphene trilayers and multilayers [75–78]. Here, we review the tight-binding model and Hartree theory approach which provides analytical formulae that serve to illustrate the pertinent physics. We will use the SI system of units throughout, and adopt the convention that the charge of the electron is $-e$ where the quantum of charge $e > 0$.

Using elementary electrostatics, it is possible to relate the asymmetry parameter $\Delta = \epsilon_2 - \epsilon_1$ to the distribution of electronic density over the bilayer system in the presence of external gates, but the density itself depends explicitly on Δ because of the effect Δ has on the band structure, (8.94). Therefore, the problem requires a self-consistent calculation of density and Δ, leading to a determination of the gate-dependence of the gap Δ_g.

The model assumes that bilayer graphene consists of two parallel conducting plates located at $x = -c_0/2$ and $+c_0/2$, where c_0 is the interlayer spacing, as illustrated in Fig. 8.16. The two layers support electron densities n_1, n_2, respectively, corresponding to charge densities $\sigma_1 = -en_1$, $\sigma_2 = -en_2$, and the permittivity of the bilayer interlayer space is ε_r (neglecting the screening effect of π-band electrons that we explicitly take into account here). We consider the combined effect of a back and top gate, with the back (top) gate at $x = -L_b$ ($x = +L_t$), held at potential V_b (V_t), separated from the bilayer by a dielectric medium with relative permittivity ε_b (ε_t). In addition, we include the influence of additional background charge near the bilayer with density n_{b0} on the back-gate side and n_{t0} on the top-gate side, yielding charge densities $\sigma_{b0} = en_{b0}$ and $\sigma_{t0} = en_{t0}$ where n_{b0} and n_{t0}, are positive for positive charge.

8.10.2.2 Electrostatics

Applying Gauss's Law first to a Gaussian surface enclosing cross-sectional area A of both layers of the bilayer and, second, to a Gaussian surface enclosing one layer only yields

$$-\varepsilon_0\varepsilon_b E_b A + \varepsilon_0\varepsilon_t E_t A = -e\left(n_1 + n_2 - n_{b0} - n_{t0}\right) A\,, \tag{8.97}$$

$$-\varepsilon_0\varepsilon_r E A + \varepsilon_0\varepsilon_t E_t A = -e\left(n_2 - n_{t0}\right) A\,. \tag{8.98}$$

The electric fields may be related to potential differences,

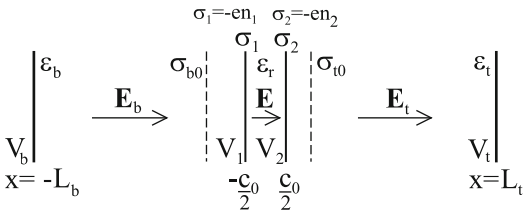

Fig. 8.16 Schematic of bilayer graphene in the presence of back and top gates. Bilayer graphene consists of two parallel conducting plates with respective electron densities n_1, n_2 located at $x = -c_0/2$ and $+c_0/2$, respectively, where c_0 is the interlayer spacing, and ε_r is the permittivity of the bilayer interlayer space. The back (*top*) gate at $x = -L_b$ ($x = +L_t$), held at potential V_b (V_t), is separated from the bilayer by a dielectric medium with relative permittivity ε_b (ε_t). Dashed lines indicate additional background charge near the bilayer with charge densities σ_{b0} and σ_{t0} on the back-gate and top-gate side, respectively

$$E_b \approx V_b/L_b\,, \qquad E_t \approx -V_t/L_t\,, \tag{8.99}$$

$$E \approx (V_1 - V_2)/c_0 \equiv \Delta/(ec_0), \tag{8.100}$$

and, when substituted into (8.97) and (8.98), they give

$$n = n_1 + n_2 = \frac{\varepsilon_0\varepsilon_b V_b}{eL_b} + \frac{\varepsilon_0\varepsilon_t V_t}{eL_t} + n_{b0} + n_{t0}\,, \tag{8.101}$$

$$\Delta = -\frac{\varepsilon_t}{\varepsilon_r}\frac{c_0}{L_t}eV_t + \frac{e^2c_0}{\varepsilon_0\varepsilon_r}(n_2 - n_{t0})\,. \tag{8.102}$$

The first equation, (8.101), relates the total density of π-band electrons $n = n_1 + n_2$ on the bilayer to the gate potentials, generalizing the case of monolayer graphene [14]. The second equation, (8.102), gives the value of the asymmetry parameter. Using (8.101), it may be written in a slightly different way:

$$\Delta = \Delta_{\rm ext} + \Lambda\gamma_1\frac{(n_2 - n_1)}{n_\perp}\,, \tag{8.103}$$

$$\Delta_{\rm ext} = \frac{1}{2}\frac{\varepsilon_b}{\varepsilon_r}\frac{c_0}{L_b}eV_b - \frac{1}{2}\frac{\varepsilon_t}{\varepsilon_r}\frac{c_0}{L_t}eV_t + \Lambda\gamma_1\frac{(n_{b0} - n_{t0})}{n_\perp}\,, \tag{8.104}$$

where parameters $n_\perp$ and Λ are defined as

$$n_\perp = \frac{\gamma_1^2}{\pi\hbar^2v^2}\,, \qquad \Lambda = \frac{c_0e^2\gamma_1}{2\pi\hbar^2v^2\varepsilon_0\varepsilon_r} \equiv \frac{c_0e^2n_\perp}{2\gamma_1\varepsilon_0\varepsilon_r}\,. \tag{8.105}$$

The first term in (8.103) is $\Delta_{\rm ext}$, the value of Δ if screening were negligible, as determined by a difference between the gate potentials, (8.104). Equations (8.101,8.104) show that the effect of the background densities n_{b0} and n_{t0} may be absorbed in a shift of the gate potentials V_b and V_t, respectively.

The second term in (8.103) indicates the influence of screening by electrons on the bilayer, where $n_\perp$ is the characteristic density scale and Λ is a dimensionless parameter indicating the strength of interlayer screening. Using $\gamma_1 = 0.39\text{eV}$ and $v = 1.0 \times 10^6 \text{ms}^{-1}$ gives $n_\perp = 1.1 \times 10^{13}\text{cm}^{-2}$. For interlayer spacing $c_0 = 3.35\text{Å}$ and dielectric constant $\varepsilon_r \approx 1$, then $\Lambda \sim 1$, indicating that screening is an important effect.

8.10.2.3 Layer Densities

Equation (8.103) uses electrostatics to relate Δ to the electronic densities n_1 and n_2 on the individual layers. The second ingredient of the self-consistent analysis are expressions for n_1 and n_2 in terms of Δ, taking into account the electronic band structure of bilayer graphene. The densities are determined by an integral with respect to momentum over the circular Fermi surface

$$n_{1(2)} = \frac{2}{\pi\hbar^2} \int p\, dp \left[|\psi_{A1(2)}(p)|^2 + |\psi_{B1(2)}(p)|^2 \right], \tag{8.106}$$

where a factor of four is included to take into account spin and valley degeneracy. Using the four-component Hamiltonian (8.93), with linear approximation $f(\mathbf{k}) \approx -v\left(\xi p_x - i p_y\right)/\gamma_0$, it is possible to determine the wave function amplitudes on the four atomic sites [28] to find

$$n_{1(2)} = \int dp\, p \left(\frac{E \mp \Delta/2}{\pi\hbar^2 E} \right) \left[\frac{\left(E^2 - \Delta^2/4\right)^2 \mp 2v^2 p^2 E\Delta - v^4 p^4}{\left(E^2 - \Delta^2/4\right)^2 + v^2 p^2 \Delta^2 - v^4 p^4} \right], \tag{8.107}$$

where the minus (plus) sign is for the first (second) layer and E is the band energy.

For simplicity, we consider the Fermi level to lie within the lower conduction band, but above the Mexican hat region, $|\Delta|/2 < E_F \ll \gamma_1$. We approximate the dispersion relation, (8.94), as $E_+^{(-1)} \approx \sqrt{\Delta^2/4 + v^4 p^4/\gamma_1^2}$, which neglects features related to the Mexican hat. Then the contribution to the layer densities from the partially filled conduction band [28, 65] is given by

$$n_{1(2)}^{\text{cb}} \approx \frac{n}{2} \mp \frac{n_\perp \Delta}{4\gamma_1} \ln \left(\frac{2|n|\gamma_1}{n_\perp |\Delta|} + \sqrt{1 + \left(\frac{2n\gamma_1}{n_\perp \Delta} \right)^2} \right), \tag{8.108}$$

where the total density $n = p_F^2/\pi\hbar^2$. In addition, although the filled valence band does not contribute to a change in the total density n, it contributes toward the finite layer polarization in the presence of finite Δ which, to leading order in Δ, is given by

$$n_{1(2)}^{\text{vb}} \approx \pm \frac{n_\perp \Delta}{4\gamma_1} \ln \left(\frac{4\gamma_1}{|\Delta|} \right). \tag{8.109}$$

Then the total layer density, $n_{1(2)} = n_{1(2)}^{\rm cb} + n_{1(2)}^{\rm vb}$, is given by

$$n_{1(2)} \approx \frac{n}{2} \mp \frac{n_\perp \Delta}{4\gamma_1} \ln\left(\frac{|n|}{2n_\perp} + \frac{1}{2}\sqrt{\left(\frac{n}{n_\perp}\right)^2 + \left(\frac{\Delta}{2\gamma_1}\right)^2} \right) . \tag{8.110}$$

8.10.2.4 Self-Consistent Screening

The density-dependence of the asymmetry parameter Δ and band gap Δ_g are determined [28, 65] by substituting the expression for the layer density, (8.110), into (8.103):

$$\Delta\,(n) \approx \Delta_{\rm ext} \left[1 - \frac{\Lambda}{2} \ln\left(\frac{|n|}{2n_\perp} + \frac{1}{2}\sqrt{\left(\frac{n}{n_\perp}\right)^2 + \left(\frac{\Delta}{2\gamma_1}\right)^2} \right) \right]^{-1} , \tag{8.111}$$

with $\Delta_{\rm ext}$ given by (8.104). The logarithmic term describes the influence of screening: when this term is much smaller than unity, screening is negligible and $\Delta \approx \Delta_{\rm ext}$, whereas when the logarithmic term is much larger than unity, screening is strong, $|\Delta| \ll |\Delta_{\rm ext}|$. The magnitude of the logarithmic term is proportional to the screening parameter Λ. As discussed earlier, $\Lambda \sim 1$ in bilayer graphene, so it is necessary to take account of the density dependence of the logarithmic term in (8.111).

To understand the density dependence of Δ, let us consider bilayer graphene in the presence of a single back gate, $V_t = n_{b0} = n_{t0} = 0$. This is a common situation for experiments with exfoliated graphene on a silicon substrate [14–17]. Then the relation between density and gate voltage, (8.101), becomes the same as in monolayer graphene [14], $n = \varepsilon_0 \varepsilon_b V_b/(eL_b)$. The expression for $\Delta_{\rm ext}$, (8.104), reduces to $\Delta_{\rm ext} = \Lambda\gamma_1 n/n_\perp$, and the expression for $\Delta\,(n)$, (8.111), simplifies [28] as

$$\Delta\,(n) \approx \frac{\Lambda\gamma_1 n}{n_\perp} \left[1 - \frac{\Lambda}{2} \ln\left(\frac{|n|}{n_\perp} \right) \right]^{-1} . \tag{8.112}$$

The value of the true band gap $\Delta_g(n)$ may be obtained using (8.96), $\Delta_g = |\Delta|\gamma_1/\sqrt{\Delta^2 + \gamma_1^2}$. Asymmetry parameter $\Delta(n)$ and band gap $\Delta_g(n)$ are plotted in Fig. 8.17 as a function of density n. For large density, $|n| \sim n_\perp$, the logarithmic term in (8.112) is negligible and the asymmetry parameter is approximately linear in density, $\Delta(n) \approx \Lambda\gamma_1 n/n_\perp$. At low density, $|n| \ll n_\perp$, the logarithmic term is large, indicating that screening is strong, and the asymmetry parameter approaches $\Delta(n) \approx 2\gamma_1(n/n_\perp)/\ln(n_\perp/|n|)$. The comparison of $\Delta(n)$ and $\Delta_g(n)$, Fig. 8.17a, shows that, at low density $|n| \ll n_\perp$, $\Delta_g(n) \approx |\Delta(n)|$ and, asymptotically, $\Delta_g(n) \approx 2\gamma_1(|n|/n_\perp)/\ln(n_\perp/|n|)$. This is independent of the screening parameter

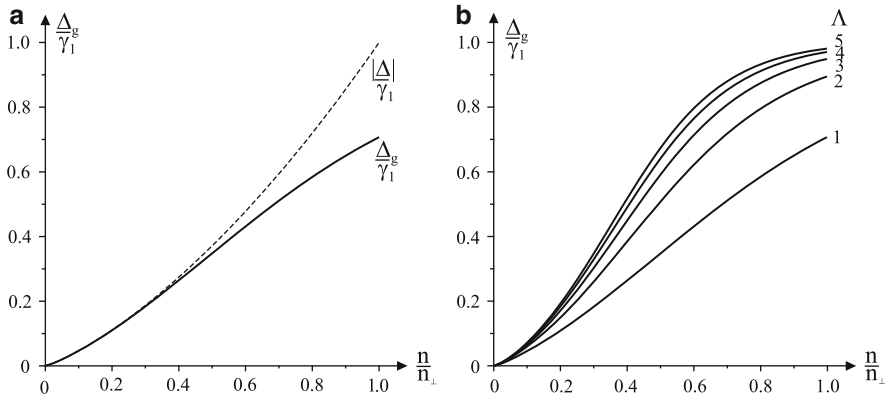

Fig. 8.17 Density-dependence of the band gap Δ_g in bilayer graphene, in the presence of a single back gate: (**a**) asymmetry parameter Δ and gap $\Delta_g = |\Delta|\gamma_1/\sqrt{\Delta^2 + \gamma_1^2}$ for screening parameter $\Lambda = 1$; (**b**) band gap Δ_g for different values of the screening parameter. Plots were made using (8.96) and (8.112)

Λ [see Fig. 8.17b]. The curves for different values of the screening parameter Λ, Fig. 8.17b, illustrate that, even when $|\Delta|$ is very large, $|\Delta| \gg \gamma_1$, Δ_g saturates at the value of γ_1.

In deriving the above expression for $\Delta(n)$, a number of approximations were made including simplifying the band structure [by omitting features related to the Mexican hat or to other possible terms in the Hamiltonian (8.93)], neglecting screening due to other orbitals, and neglecting the effects of disorder and electron–electron exchange and correlation. Nevertheless, it seems to be in good qualitative agreement with density functional theory calculations [60,64] and experiments (see, for example, [62,63,67,69,71]).

8.11 Summary

In this chapter, some of the electronic properties of monolayer and bilayer graphene were described using the tight-binding model. Effective Hamiltonians for low-energy electrons were derived, corresponding to massless chiral fermions in monolayers and massive chiral fermions in bilayers. Chirality in graphene is manifest in many electronic properties, including anisotropic scattering and an unusual sequence of plateaus in the quantum Hall effect. There are a number of additional contributions to the low-energy Hamiltonians of graphene that influence chiral electrons and we focused on one of them, trigonal warping, here.

Comparison with experiments suggest that the tight-binding model generally works very well in graphene. The model contains parameters, corresponding to the energies of atomic orbitals or to matrix elements describing hopping between

atomic sites, that cannot be determined by the model. They must be estimated by an alternative theoretical method, such as density-functional theory, or they can be treated as fitting parameters to be determined by comparison with experiments. The simple model described in this chapter is versatile and it serves as the starting point for a wide range of models encapsulating advanced physical phenomena, including interaction effects. In Chap. 11, the tight-binding model is used to describe the electronic structure of multilayer graphene. Here, we described a different example: the use of the tight-binding model with Hartree theory to develop a simple model of screening by electrons in bilayer graphene in order to calculate the density dependence of the band gap induced by an external electric field.

Acknowledgements The author thanks colleagues for fruitful collaboration in graphene research, in particular V.I. Fal'ko, and EPSRC for financial support.

References

1. P.R. Wallace, Phys. Rev. **71**, 622 (1947)
2. J.C. Slonczewski, P.R. Weiss, Phys. Rev. **109**, 272 (1958)
3. J.W. McClure, Phys. Rev. **108**, 612 (1957)
4. M.S Dresselhaus, G. Dresselhaus, Adv. Phys. **51**, 1 (2002)
5. D.P. DiVincenzo, E.J. Mele, Phys. Rev. B **29**, 1685 (1984)
6. J. González, F. Guinea, M.A.H. Vozmediano, Phys. Rev. Lett. **69**, 172 (1992)
7. H. Ajiki, T. Ando, J. Phys. Soc. Jpn. **62**, 1255 (1993)
8. C.L. Kane, E.J. Mele, Phys. Rev. Lett. **78**, 1932 (1997)
9. T. Ando, T. Nakanishi, R. Saito, J. Phys. Soc. Jpn. **67**, 2857 (1998)
10. P.L. McEuen, M. Bockrath, D.H. Cobden, Y.-G. Yoon, S.G. Louie, Phys. Rev. Lett. **83**, 5098 (1999)
11. R. Saito, M.S. Dresselhaus, G. Dresselhaus *Physical Properties of Carbon Nanotubes*, (Imperial College Press, London, 1998)
12. G.W. Semenoff, Phys. Rev. Lett. **53**, 2449 (1984)
13. F.D.M. Haldane, Phys. Rev. Lett. **61**, 2015 (1988)
14. K.S. Novoselov, A.K. Geim, S.V. Morozov, D. Jiang, Y. Zhang, S.V. Dubonos, I.V. Grigorieva, A.A. Firsov, Science **306**, 666 (2004)
15. K.S. Novoselov, A.K. Geim, S.V. Morozov, D. Jiang, M.I. Katsnelson, I.V. Grigorieva, S.V. Dubonos, A.A. Firsov, Nature **438**, 197 (2005)
16. Y.B. Zhang, Y.W. Tan, H.L. Stormer, P. Kim, Nature **438**, 201 (2005)
17. K.S. Novoselov, E. McCann, S.V. Morozov, I.V. Fal'ko, M.I. Katsnelson, U. Zeitler, D. Jiang, F. Schedin, A.K. Geim, Nature Phys. **2** 177 (2006)
18. N.W. Ashcroft, N.D. Mermin, *Solid-State Physics*, (Brooks/Cole, Belmont, 1976)
19. A.H. Castro Neto, F. Guinea, N.M.R. Peres, K.S. Novoselov, A.K. Geim, Rev. Mod. Phys. **81**, 109 (2009)
20. C. Bena, G. Montambaux, New J. Phys. **11**, 095003 (2009)
21. E. McCann, V.I. Fal'ko, Phys. Rev. Lett. **96**, 086805 (2006)
22. G. Dresselhaus, Phys. Rev. B **10**, 3602 (1974)
23. K. Nakao, J. Phys. Soc. Japan **40**, 761 (1976)
24. M. Inoue, J. Phys. Soc. Japan **17**, 808 (1962)
25. O.P. Gupta, P.R. Wallace, Phys. Status. Solidi. B **54**, 53 (1972)
26. T. Ohta, A. Bostwick, T. Seyller, K. Horn, E. Rotenberg, Science **313**, 951 (2006)

27. J.B. Oostinga, H.B. Heersche, X. Liu, A.F. Morpurgo, L.M.K. Vandersypen, Nature Materials **7**, 151 (2007)
28. E. McCann, Phys. Rev. B **74**, 161403(R) (2006)
29. K. Sasaki, S. Murakami, R. Saito, Appl. Phys. Lett. **88**, 113110 (2006)
30. N.M.R. Peres, F. Guinea, A.H. Castro Neto, Phys. Rev. B **73**, 125411 (2006)
31. S. Pancharatnam, Proc. Indian Acad. Sci. A **44**, 247 (1956)
32. M.V. Berry, Proc. R. Soc. Lond. A **392**, 45 (1984)
33. H. Suzuura, T. Ando, Phys. Rev. Lett. **89**, 266603 (2002)
34. V.V. Cheianov, V.I. Fal'ko, Phys. Rev. B **74**, 041403(R) (2006)
35. M.I. Katsnelson, K.S. Novoselov, A.K. Geim, Nature Phys. **2**, 620 (2006)
36. S.B. Trickey, F. Müller-Plathe, G.H.F. Diercksen, J.C. Boettger, Phys. Rev. B **45**, 4460 (1992)
37. V.I. Fal'ko, K. Kechedzhi, E. McCann, B.L. Altshuler, H. Suzuura, T. Ando, Solid State Comm. **143** 33 (2007)
38. J.R. Schrieffer, P. A. Wolff, Phys. Rev. **149**, 491 (1966)
39. L.D. Landau, Z. Phys. **64**, 629 (1930)
40. K. von Klitzing, G. Dorda, M. Pepper, Phys. Rev. Lett. **45**, 494 (1980)
41. R.E. Prange, S.M. Girvin (eds.), *The Quantum Hall Effect*, (Springer-Verlag, New York, 1986)
42. A.H. MacDonald (ed.), *Quantum Hall Effect: A Perspective*, (Kluwer, Boston, 1989)
43. J.W. McClure, Phys. Rev. **104**, 666 (1956)
44. H.J. Fischbeck, Phys. Status Solidi **38**, 11 (1970)
45. Y. Zheng, T. Ando, Phys. Rev. B **65**, 245420 (2002)
46. V.P. Gusynin, S.G. Sharapov, Phys. Rev. Lett. **95**, 146801 (2005)
47. I.F. Herbut, Phys. Rev. B **75**, 165411 (2007)
48. L.M. Lifshitz, Zh. Exp. Teor. Fiz. **38**, 1565 (1960); [Sov. Phys. JETP **11**, 1130 (1960)]
49. B. Partoens, F.M. Peeters, Phys. Rev. B **74**, 075404 (2006)
50. E. McCann, D.S.L. Abergel, V.I. Fal'ko, Solid State Comm. **143**, 110 (2007)
51. J. Nilsson, A.H. Castro Neto, N.M.R. Peres, F. Guinea, Phys. Rev. B **73**, 214418 (2006)
52. H. Min, G. Borghi, M. Polini, A.H. MacDonald, Phys. Rev. B **77**, 041407(R) (2008)
53. F. Zhang, H. Min, M. Polini, A.H. MacDonald, Phys. Rev. B **81**, 041402(R) (2010)
54. R. Nandkishore, L.S. Levitov, Phys. Rev. Lett. **104**, 156803 (2010)
55. O. Vafek, K. Yang, Phys. Rev. B **81**, 041401(R) (2010)
56. Y. Lemonik, I.L. Aleiner, C. Toke, V.I. Fal'ko, Phys. Rev. B **82**, 201408 (2010)
57. J.L. Manes, F. Guinea, M.A.H. Vozmediano, Phys. Rev. B **75**, 155424 (2007)
58. S. Latil, L. Henrard, Phys. Rev. Lett. **97**, 036803 (2006)
59. F. Guinea, A.H. Castro Neto, N.M.R. Peres, Phys. Rev. B **73**, 245426 (2006)
60. H. Min, B.R. Sahu, S.K. Banerjee, A.H. MacDonald, Phys. Rev. B **75**, 155115 (2007)
61. M. Aoki, H. Amawashi, Solid State Commun. **142**, 123 (2007)
62. E.V. Castro, K.S. Novoselov, S.V. Morozov, N.M.R. Peres, J.M.B. Lopes dos Santos, J. Nilsson, F. Guinea, A.K. Geim, A.H. Castro Neto, Phys. Rev. Lett. **99**, 216802 (2007)
63. L.M. Zhang, Z.Q. Li, D.N. Basov, M.M. Fogler, Z. Hao, M.C. Martin, Phys. Rev. B **78**, 235408 (2008)
64. P. Gava, M. Lazzeri, A.M. Saitta, F. Mauri, Phys. Rev. B **79**, 165431 (2009)
65. M.M. Fogler, E. McCann, Phys. Rev. B **82**, 197401 (2010)
66. E.A. Henriksen, Z. Jiang, L.-C. Tung, M.E. Schwartz, M. Takita, Y.-J. Wang, P. Kim, H.L. Stormer, Phys. Rev. Lett. **100**, 087403 (2008)
67. Z.Q. Li, E.A. Henriksen, Z. Jiang, Z. Hao, M.C. Martin, P. Kim, H.L. Stormer, D.N. Basov, Phys. Rev. Lett. **102**, 037403 (2009)
68. Y. Zhang, T.-T. Tang, C. Girit, Z. Hao, M.C. Martin, A. Zettl, M.F. Crommie, Y.R. Shen, F. Wang, Nature **459**, 820 (2009)
69. K.F. Mak, C.H. Lui, J. Shan, T.F. Heinz, Phys. Rev. Lett. **102**, 256405 (2009)
70. A.B. Kuzmenko, E. van Heumen, D. van der Marel, P. Lerch, P. Blake, K.S. Novoselov, A.K. Geim, Phys. Rev. B **79**, 115441 (2009)
71. A.B. Kuzmenko, I. Crassee, D. van der Marel, P. Blake, K.S. Novoselov, Phys. Rev. B **80**, 165406 (2009)

72. A.B. Kuzmenko, L. Benfatto, E. Cappelluti, I. Crassee, D. van der Marel, P. Blake, K.S. Novoselov, A. K. Geim, Phys. Rev. Lett. **103**, 116804 (2009)
73. Y. Zhao, P. Cadden-Zimansky, Z. Jiang, P. Kim, Phys. Rev. Lett. **104**, 066801 (2010)
74. S. Kim, K. Lee, E. Tutuc, Phys. Rev. Lett. **107**, 016803 (2011)
75. M. Koshino, E. McCann, Phys. Rev. B **79**, 125443 (2009)
76. A.A Avetisyan, B. Partoens, F.M. Peeters, Phys. Rev. B **79**, 035421 (2009)
77. A.A Avetisyan, B. Partoens, F.M. Peeters, Phys. Rev. B **80**, 195401 (2009)
78. M. Koshino, Phys. Rev. B **81**, 125304 (2010)

Chapter 9
Electronic Properties of Graphene Nanoribbons

Katsunori Wakabayashi

Abstract Graphene is a one atomic thickness carbon sheet, where the low-energy electronic states of graphene are described by the massless Dirac Fermions. The orientation of edge in graphene determines energy spectrum of the π-electrons. Zigzag edges possess edge localized states with energies close to the Fermi level. However, armchair edges do not have such localized states. In this chapter, we shall introduce the nanoscale and edge shape effect on electronic properties of graphene. Starting from the basic description of electronic states of graphene nanoribbons on the basis of tight-binding model and massless Dirac equation, we briefly introduce the transport properties of disordered graphene nanoribbons and nanojunctions.

9.1 Introduction

Recently, graphene, a single-layer hexagonal lattice of carbon atoms, has emerged as a fascinating system for fundamental studies in condensed matter physics, as well as the promising candidate material for future application in nanoelectronics and molecular devices [1, 2]. The honeycomb crystal structure of single layer graphene consists of two nonequivalent sublattices and results in a unique band structure for the itinerant π-electrons near the Fermi energy which behave as massless Dirac fermion. The valence and conduction bands touch conically at two nonequivalent Dirac points, called $\boldsymbol{K}_+$ and $\boldsymbol{K}_-$ point, which form a time-reversed pair, i.e., opposite chirality. The chirality and a Berry phase of π at the two Dirac points provide an environment for unconventional and fascinating two-dimensional electronic properties [3–5], such as the half-integer quantum Hall effect [6–8], the absence of backward scattering [4, 9], and π-phase shift of the Shubnikov-de Haas oscillations [10]. Since they have excellent electronic mobility [11] and high thermal

K. Wakabayashi (✉)
National Institute for Materials Science (NIMS), Tsukuba 305-0044, Japan
e-mail: WAKABAYASHI.Katsunori@nims.go.jp

H. Raza (ed.), *Graphene Nanoelectronics*, NanoScience and Technology,
DOI 10.1007/978-3-642-22984-8_9,

conductivity [12], graphene is recognized as one of the key materials to realize the next-generation devices.

The successive miniaturization of the graphene electronic devices inevitably demands the clarification of edge effects on the electronic structures of nanometer-sized graphene. The presence of edges in graphene has strong implications for the low-energy spectrum of the π-electrons [13–15]. There are two basic shapes of edges, *armchair* and *zigzag*, which determine the properties of graphene ribbons. Ribbons with zigzag edges (zigzag ribbon) possess edge localized states with energies close to the Fermi level [13–17]. In contrast, edge states are completely absent for ribbons with armchair edges. Since the zigzag edge can provide strong magnetic response [13, 15, 16, 18, 19], much effort has been devoted to studying the edges in graphitic nanomaterials. Recent experiments using scanning tunneling microscope (STM), spectroscopy (STS) [20–23] and high-resolution angle-resolved photoemission spectroscopy (ARPES) [24] support the evidence of edge localized states. Recently several experimental routes have been realized to synthesize graphene nanoribbons. Use of lithographic patterning of graphene samples [25, 26] can yield graphene nanoribbons; however, the reported ribbons have large widths between 15 and 100 nm with small electronic band gap up to 200 meV due to the significant edge roughness. Second route [27], that use chemical method such as solution-dispersion and sonication, has shown that graphene sheets spontaneously break into ribbons of narrow width and rather smooth edges. Recently carbon nanotubes can be cut along their axis and flattened out to form the graphene nanoribbons [28, 29]. A bottom-up approach can also provide a route for synthesis of linear two-dimensional graphene nanoribbons with lengths of up to 12 nm [30]. Although the control of edge structure which is necessary for the application of nano-graphene to nanoelectronics devices is still difficult, several experimental trials already exist using Joule heating [31], anisotropic etching [32], and chemical synthesis [33]. The combination of these new methods could lead to the design of graphene nanoribbons and nanostructures having edges of controlled orientation and electronic properties.

The electronic transport and magnetic properties of graphene nanoribbons show a number of intriguing phenomena due to their peculiar electronic properties. Graphene nanojunction structures can provide zero-conductance Fano resonances in their low-energy electronic transport [34–37], which can be used for current-controlling switching devices [34–37] or valley filtering device [38]. The novel magnetic properties of zigzag edges [13, 15, 16] can be used for half-metallic conduction [18] and spin Hall effect [39]. Various chemical modifications have been suggested to stabilize the edge spin polarized magnetic states [40–42]. Recently transport measurement for graphene nanoribbons is reported [43–49].

Since the graphene nanoribbons can be viewed as a new class of quantum wires, one might expect that random impurities inevitably cause Anderson localization, i.e., conductance decays exponentially with increasing system length L and eventually vanishes in the limit of $L \to \infty$. However, as we will see in this chapter, it is shown that zigzag nanoribbons with long-ranged impurities possess a perfectly conducting channel (PCC) [50, 51]. This fact is very strong contrast compared with

the quantum wire composed of massive free electrons. The related topic is also presented in Chap. 8.

In this chapter, we will give a brief overview on the electronic and transport properties of graphene nanoribbons. In zigzag nanoribbons, for disorder without inter-valley scattering a single PCC emerges associated with a chiral mode due to edge states, i.e., the absence of the localization. Nano-graphene junctions are shown to have the zero-conductance anti-resonances associated with the edge states. The relation between the condition of the resonances and geometry is discussed.

9.2 Electronic States of Graphene

Before the discussion of the π-electronic states of graphene nanoribbons, we shall briefly review the π-band structure of a graphene sheet [52]. In Figs. 9.1a, b, the lattice structure of graphene and the first Brillouin Zone (BZ) of graphene lattice are shown, respectively. We use a single-orbital nearest-neighbor tight binding model for the π electron network. The Hamiltonian can be written as

$$H = -t \sum_{\boldsymbol{R_B}} \sum_{l=1}^{3} a^{\dagger}_{\boldsymbol{R_B}+\boldsymbol{\tau}_l} b_{\boldsymbol{R_B}} + h.c., \tag{9.1}$$

where $a^{\dagger}_{\boldsymbol{R_A}}$ ($b^{\dagger}_{\boldsymbol{R_B}}$) creates an electron at $\boldsymbol{R_A}$ ($\boldsymbol{R_B}$) on $A(B)$-subblattice. Similarly, $a_{\boldsymbol{R_A}}$ ($b_{\boldsymbol{R_B}}$) annihilates an electron at $\boldsymbol{R_A}$ ($\boldsymbol{R_B}$) on $A(B)$-subblattice. These operators satisfy the Fermion anti-commutation relations:

$$\left\{a_{\boldsymbol{R_A}}, a^{\dagger}_{\boldsymbol{R'_A}}\right\} = \delta_{\boldsymbol{R_A},\boldsymbol{R'_A}}, \left\{b_{\boldsymbol{R_B}}, b^{\dagger}_{\boldsymbol{R'_B}}\right\} = \delta_{\boldsymbol{R_B},\boldsymbol{R'_B}}, \tag{9.2}$$

$$\left\{a_{\boldsymbol{R_A}}, a_{\boldsymbol{R'_A}}\right\} = 0, \left\{b_{\boldsymbol{R_B}}, b_{\boldsymbol{R'_B}}\right\} = 0, \tag{9.3}$$

and others are zero. t is the transfer integral between nearest neighbor carbon sites which is roughly estimated at about 3.0eV in a graphene system. More precise value can be estimated using ARPES discussed in Chap. 4. We apply the following Fourier transformation to this Hamiltonian:

$$a_{\boldsymbol{R_A}} = \frac{1}{\sqrt{L_x L_y}} \sum_k \mathrm{e}^{i\mathbf{k}\mathbf{R_A}} \alpha_{\boldsymbol{k}}, \tag{9.4}$$

$$b_{\boldsymbol{R_B}} = \frac{1}{\sqrt{L_x L_y}} \sum_k \mathrm{e}^{i\mathbf{k}\mathbf{R_B}} \beta_{\boldsymbol{k}}. \tag{9.5}$$

Here $\boldsymbol{k} = (k_x, k_y)$ and $L_x(L_y)$ means the number of unit cell in $x(y)$-direction.

$$H_k = -t \sum_{\boldsymbol{k}} \sum_{l=1}^{3} \mathrm{e}^{-ik\boldsymbol{\tau}_l} \alpha^{\dagger}_{\boldsymbol{k}} \beta_{\boldsymbol{k}} + h.c., \tag{9.6}$$

Here we insert a one-particle state

$$|\Psi(k)\rangle = \left(A\alpha_{\boldsymbol{k}}^{\dagger} + B\beta_{\boldsymbol{k}}^{\dagger}\right)|0\rangle, \tag{9.7}$$

into the Schrödinger equation

$$H_k|\Psi(k)\rangle = E|\Psi(k)\rangle. \tag{9.8}$$

Here $|0\rangle$ means the vacuum state. Note that $\alpha_k|0\rangle = \beta_k|0\rangle = 0$. Thus we have

$$\begin{pmatrix} 0 & f_{AB}^{*}(\boldsymbol{k}) \\ f_{AB}(\boldsymbol{k}) & 0 \end{pmatrix}\begin{pmatrix} A \\ B \end{pmatrix} = E\begin{pmatrix} A \\ B \end{pmatrix} \tag{9.9}$$

with

$$f_{AB}(\boldsymbol{k}) = -t\sum_{l=1}^{3} \mathrm{e}^{-i\boldsymbol{k}\boldsymbol{\tau}_l}. \tag{9.10}$$

Thus, the energy bands are given by

$$E_s(\boldsymbol{k}) = st\sqrt{3 + 2\cos\left(\frac{k_x a}{2} + \frac{\sqrt{3}k_y a}{2}\right) + 2\cos\left(\frac{k_x a}{2} - \frac{\sqrt{3}k_y a}{2}\right) + 2\cos\left(k_x a\right)} \tag{9.11}$$

with $s = \pm$. Since one carbon site has one π-electron on average, only $E_{-}(\mathbf{k})$-band is completely occupied. The density of states (DOS) is calculated by

$$D(E) = -\frac{1}{\pi}\mathrm{Im}\int_{1\mathrm{stBZ}} \mathrm{d}\boldsymbol{k}\frac{1}{E - E(\boldsymbol{k}) + i\eta}, \tag{9.12}$$

where the area of $\boldsymbol{k}$-integration is 1st BZ and η is infinitesimally small real number.

In Figs. 9.1 c, d, the energy dispersion of π-bands in the first Brillouin Zone (BZ) and the corresponding density of states are depicted, respectively. Near the Γ point, both valence and conduction bands have the quadratic form of k_x and k_y, *i.e.* $E_{\boldsymbol{k}} = \pm(3 - 3|\boldsymbol{k}|^2/4)$. At the M points, the middle points of sides of the hexagonal BZ, the saddle point of energy dispersion appears and the density of states diverges logarithmically. Near the K point of the corner of hexagonal first BZ, the energy dispersion is linear in the magnitude of the wave vector, $E_{\mathbf{k}} = \pm\sqrt{3}ta|\boldsymbol{k}|/2$, where the density of states linearly depends on energy. Here $a(= \sqrt{3}|\boldsymbol{\tau}_i|(i = 1, 2, 3))$ is the lattice constant. The Fermi energy is located at the K points and there is no energy gap at these points, since $E_{\mathbf{k}}$ vanishes at these points by the hexagonal symmetry. The electronic states near the **K**-point can be described by massless Dirac equation [4, 5].

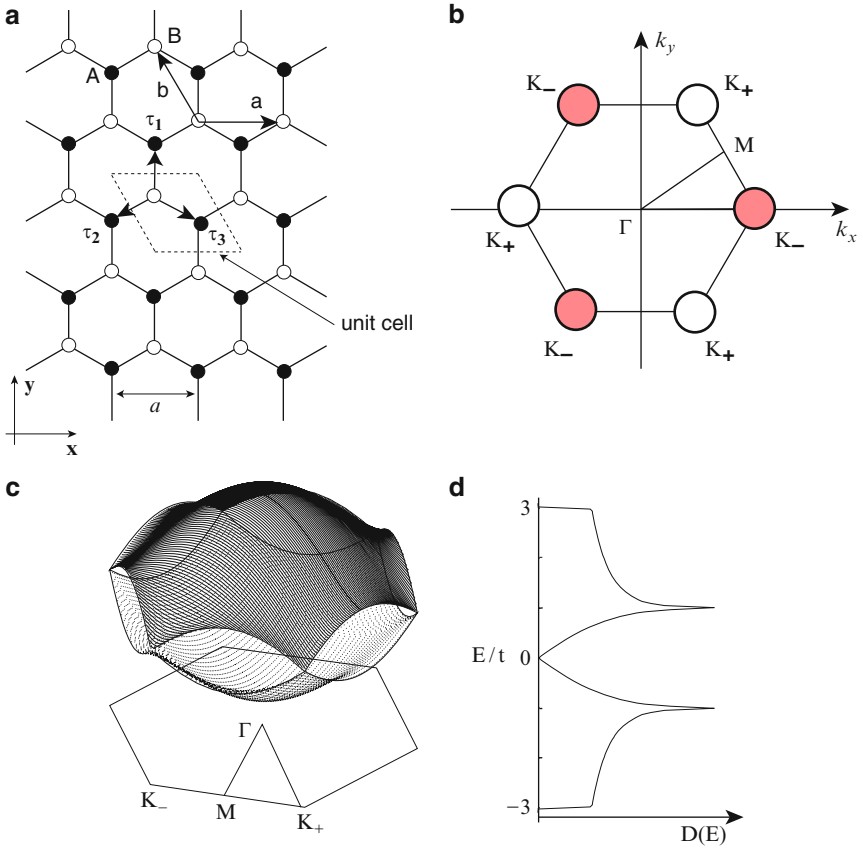

Fig. 9.1 (**a**) Graphene sheet in real space, where the *black* (**white**) *circles* mean the A(B)-sublattice site. a is the lattice constant. $\boldsymbol{a} = (a, 0)$ and $\boldsymbol{b} = (-a/2, \sqrt{3}a/2)$ are the primitive vectors. Here $\boldsymbol{\tau_1} = (0, a/\sqrt{3})$, $\boldsymbol{\tau_2} = (-a/2, -a/2\sqrt{3})$, and $\boldsymbol{\tau_3} = (a/2, -a/2\sqrt{3})$. (**b**) First Brillouin zone of graphene. $\boldsymbol{K_+} = \frac{2\pi}{a}(\frac{1}{3}, \frac{1}{\sqrt{3}})$, $\boldsymbol{K_-} = \frac{2\pi}{a}(\frac{2}{3}, 0)$, $\boldsymbol{\Gamma} = (0, 0)$ (**c**) The π band structure and (d) the density of states of graphene sheet. The valence and conduction bands make contact at the degeneracy point $\boldsymbol{K_\pm}$

9.2.1 Tight-Binding Model and Edge States

There are two typical shapes of a graphene edge, called *armchair* and *zigzag*. The two edges have 30° difference in their cutting direction. Here we show the way that the graphene edges drastically change the π electronic structures [13]. Especially, a zigzag edge provides the localized edge state, while an armchair edge does not show such localized states.

A simple and useful model to study the edge and size effect is one of the graphene ribbon models as shown in Figs. 9.2a, b. We define the width of graphene ribbons as N, where N stands for the number of the dimer (two carbon sites) lines for

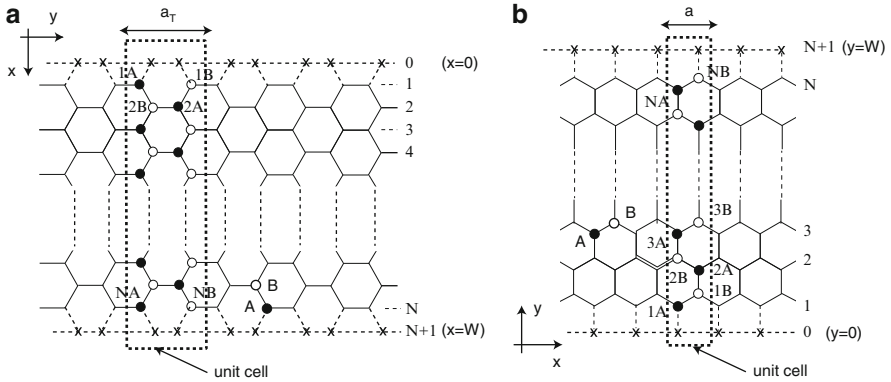

Fig. 9.2 Structure of graphene nanoribbon with (**a**) armchair edges (*armchair ribbon*) and (**b**) zigzag edges (*zigzag ribbon*). The lattice constant is a and N defines the ribbon width. The *circles with dashed line* indicate the missing carbon atoms for the edge boundary condition of massless Dirac equation. a_T is the width of unit cell for armchair nanoribbons

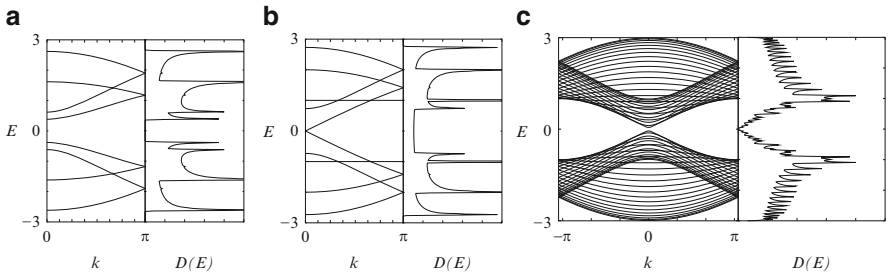

Fig. 9.3 Energy band structure $E(k)$ and density of states $D(E)$ of armchair ribbons of various widths [(**a**) $N = 4$, (**b**) 5 and (**c**) 30]

the armchair ribbon and by the number of the zigzag lines for the zigzag ribbon, respectively. It is assumed that all dangling bonds at graphene edges are terminated by hydrogen atoms, and thus give no contribution to the electronic states near the Fermi level. We use a single-orbital tight binding model for the π electron network.

The energy band structures of armchair ribbons are shown in Figs. 9.3a–c, for three different ribbon widths, together with the density of states. The wave number k is normalized by the length of the primitive translation vector of each graphene nanoribbon, and the energy E is scaled by the transfer integral t. The top of the valence band and the bottom of the conduction band are located at $k = 0$. It should be noted that the ribbon width decides whether the system is metallic or semiconducting. As shown in Fig. 9.3b, the system is metallic when $N = 3j - 1$, where $j = 1, 2, 3, \ldots$. For the semiconducting ribbons, the direct gap decreases with increasing ribbon width and tends to zero in the limit of very large N. For narrow non-doped metallic armchair nanoribbons, the energy gap can acquire due

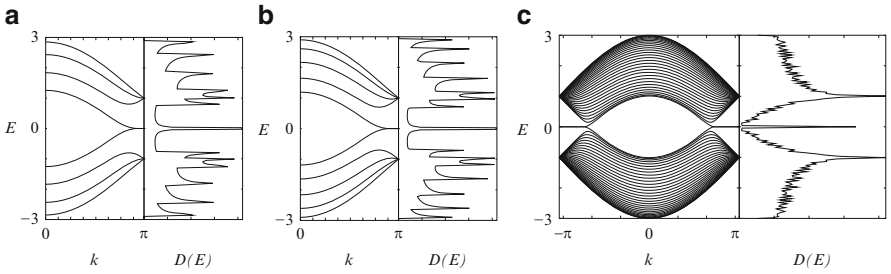

Fig. 9.4 Energy band structure $E(k)$ and density of states $D(E)$ of zigzag ribbons of various widths [(**a**) $N = 4$, (**b**) 5 and (**c**) 30]

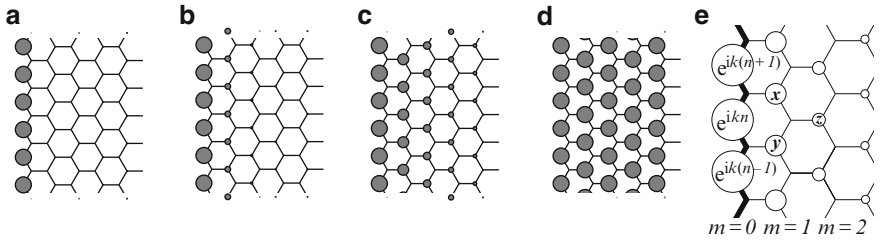

Fig. 9.5 Charge density plot for analytic solution of the edge states in a semi-infinite graphene sheet, when (**a**) $k = \pi$, (**b**) $8\pi/9$, (**c**) $7\pi/9$ and (**d**) $2\pi/3$. (**e**) An analytic form of the edge state for a semi-infinite graphene sheet with a zigzag edge, emphasized by *bold lines*. Each carbon site is specified by a location index n on the zigzag chain and by a chain order index m from the edge. The magnitude of the charge density at each site, such as x, y and z, is obtained analytically (see text). The radius of each circle is proportional to the charge density on each site, and the drawing is made for $k = 7\pi/9$

to Peierls instabilities toward low temperatures [53], which is consistent with the recent density functional theory calculation [19, 54].

For zigzag ribbons, however, a remarkable feature arises in the band structure, as shown in Figs. 9.4a–c. We see that the highest valence band and lowest conduction band are always degenerated at $k = \pi$. It is found that the degeneracy of the center bands at $k = \pi$ does not originate from the intrinsic band structure of graphene sheet. These two special center bands get flatter with increasing ribbon width. A pair of partial flat bands appears within the region of $2\pi/3 \leq |k| \leq \pi$, where the bands sit in the vicinity of the Fermi level.

The electronic state in the partial flat bands of the zigzag ribbons can be understood as the localized state near the zigzag edge via examining the charge density distribution [13–15, 20–22]. The emergence of the edge state can be solved by considering a semi-infinite graphene sheet with a zigzag edge. First to show the analytic form, we depict the distribution of charge density in the flat band states for some wave numbers in Fig. 9.5a–d, where the amplitude is proportional to the radius. The wave function has nonbonding character, i.e., finite amplitudes only on

one of the two sublattices which includes the edge sites. It is completely localized at the edge site when $k = \pi$, and starts to gradually penetrate into the inner sites as k deviates from π reaching the extend state at $k = 2\pi/3$.

Considering the translational symmetry, we can start constructing the analytic solution for the edge state by letting the Bloch components of the linear combination of atomic orbitals (LCAO) wavefunction be ..., $e^{ik(n-1)}$, e^{ikn}, $e^{ik(n+1)}$,... on successive edge sites, where n denotes a site location on the edge. Then the mathematical condition necessary for the wave function to be exact for $E = 0$ is that the total sum of the components of the complex wave function over the nearest-neighbor sites should vanish. In Fig. 9.5e, the above condition is $e^{ik(n+1)} + e^{ikn} + x = 0$, $e^{ikn} + e^{ik(n-1)} + y = 0$ and $x + y + z = 0$. Therefore, the wave function components x, y, and z are found to be $D_k e^{ik(n+1/2)}$, $D_k e^{ik(n-1/2)}$, $D_k^2 e^{ikn}$, respectively. Here $D_k = -2\cos(k/2)$. We can thus see that the charge density is proportional to $D_k^{2(m-1)}$ at each non-nodal site of the m-th zigzag chain from the edge. Then the convergence condition of $|D_k| \leq 1$ is required, for otherwise the wave function would diverge in a semi-infinite graphene sheet. This convergence condition defines the region $2\pi/3 \leq |k| \leq \pi$ where the flat band appears.

The energy spectrum and corresponding wavefunctions can be solved analytically within the nearest neighbor tight-binding model using wave-mechanics approach [15, 55], monomer Green's function approach [56], and transfer matrix approach [57, 58]. For armchair nanoribbons, we can show that the relative phase due to the chirality of pseudo-spin in the wavefunction between sublattice A and B is preserved; however, for zigzag nanoribbons such phase factor due to the pseudo-spin disappears [55, 59]. Such difference in the phase factor of wavefunction makes strong edge orientation dependence in the response of Raman spectroscopy [60, 61], which was recently confirmed experimentally [62–64].

9.2.2 Massless Dirac Equation

The relation between massless Dirac spectrum of graphene and low-energy electronic states of nanoribbons is discussed here. The electronic states near the two nonequivalent Dirac points ($\boldsymbol{K}_{\pm}$) can be described by 4×4 Dirac equation, i.e.,

$$H_{\boldsymbol{k}\cdot\boldsymbol{p}} \boldsymbol{F}(\boldsymbol{r}) = \epsilon \boldsymbol{F}(\boldsymbol{r}) \tag{9.13}$$

with

$$H_{\boldsymbol{k}\cdot\boldsymbol{p}} = \begin{pmatrix} 0 & \gamma(\hat{k}_x - i\hat{k}_y) & 0 & 0 \\ \gamma(\hat{k}_x + i\hat{k}_y) & 0 & 0 & 0 \\ 0 & 0 & 0 & \gamma(\hat{k}_x + i\hat{k}_y) \\ 0 & 0 & \gamma(\hat{k}_x - i\hat{k}_y) & 0 \end{pmatrix} \tag{9.14}$$

and

$$\boldsymbol{F}(\boldsymbol{r}) = \begin{pmatrix} F_A^{\boldsymbol{K}+}(\boldsymbol{r}) \\ F_B^{\boldsymbol{K}+}(\boldsymbol{r}) \\ F_A^{\boldsymbol{K}-}(\boldsymbol{r}) \\ F_B^{\boldsymbol{K}-}(\boldsymbol{r}) \end{pmatrix}. \tag{9.15}$$

Here, $\hat{k}_x(\hat{k}_y)$ is wavevector operator, and can be replaced as $\hat{\boldsymbol{k}} \rightarrow -i\hat{\nabla}$ in the absence of magnetic field. γ is a band parameter which satisfies $\gamma = \sqrt{3}ta/2$. $F_A^{\boldsymbol{K}\pm}(\boldsymbol{r})$ and $F_B^{\boldsymbol{K}\pm}(\boldsymbol{r})$ are the envelope functions near $\boldsymbol{K}_{\pm}$ points for sublattice A and B which slowly vary in the length scale of the lattice constant. We can rewrite the above effective mass Hamiltonian using the Pauli matrices $\tau^{x,y,z}$ for valley space $(\boldsymbol{K}_{\pm})$ as

$$H_{\boldsymbol{k}\cdot\boldsymbol{p}} = \gamma\left[\hat{k}_x(\sigma^x \otimes \tau^0) + \hat{k}_y(\sigma^y \otimes \tau^z)\right]. \tag{9.16}$$

Here, τ^0 is the 2×2 identity matrix. We can easily obtain the linear energy spectrum for graphene as

$$\epsilon = s\gamma|k| \qquad with \qquad s = \pm 1, \tag{9.17}$$

and the corresponding wavefunctions with the definition of $\Phi_{\boldsymbol{K}_{\pm}} = \left[F_{\boldsymbol{K}_{\pm}A}, F_{\boldsymbol{K}_{\pm}B}\right]$ are

$$\Phi_{\boldsymbol{K}_{\pm}} = \frac{1}{\sqrt{2}}\begin{pmatrix} s \\ \mathrm{e}^{\pm i\phi_k} \end{pmatrix}\mathrm{e}^{i\boldsymbol{k}\cdot\boldsymbol{r}} \tag{9.18}$$

Here

$$\mathrm{e}^{\pm i\phi_k} = \frac{k_x \pm ik_y}{|k_x + ik_y|}. \tag{9.19}$$

9.2.2.1 Zigzag Nanoribbons

The low-energy electronic states for zigzag nanoribbons also can be described starting from the Dirac equation [17, 65]. Since the outermost sites along 1^{st} (Nth) zigzag chain are B(A)-sublattice, an imbalance between two sublattices occurs at the zigzag edges leading to the boundary conditions

$$\phi_{\boldsymbol{K}_{\pm}A}(\boldsymbol{r}_{[0]}) = 0, \quad \phi_{\boldsymbol{K}_{\pm}B}(\boldsymbol{r}_{[N+1]}) = 0, \tag{9.20}$$

where $\boldsymbol{r}_{[i]}$ stands for the coordinate at i^{th} zigzag chain. The energy eigenvalue and wavenumber are given by the following relation:

$$\varepsilon = \pm(\eta - k)\mathrm{e}^{\eta W}, \tag{9.21}$$

where $\eta = \sqrt{k^2 - \varepsilon}$. It can be shown that the valley near $k = 3\pi/2a$ in Fig. 9.1b originates from the $\boldsymbol{K}_{+}$-point, the other valley at $k = -3\pi/2a$ from $\boldsymbol{K}_{-}$-point [17, 65].

9.2.2.2 Armchair Nanoribbons

The boundary condition of armchair nanoribbons projects $\boldsymbol{K}_+$ and $\boldsymbol{K}_-$ states into Γ point in the first Brillouin Zone as can be seen in Fig. 9.1b. Thus, the low-energy states for armchair nanoribbons are the superposition of $\boldsymbol{K}_+$ and $\boldsymbol{K}_-$ states. The boundary condition for armchair nanoribbons [65] can be written as

$$[F_A^+(x,y) + F_A^-(x,y)]|_{x=0,W} = 0, \tag{9.22}$$

$$[F_B^+(x,y) - F_B^-(x,y)]|_{x=0,W} = 0. \tag{9.23}$$

If the ribbon width W satisfies the condition of $W = (3/2)(N_w + 1)a$ with $N_w = 0, 1, 2, \ldots$, the system becomes metallic with the linear spectrum. The corresponding energy is given by

$$\epsilon_{n,k,s} = s\gamma\sqrt{\kappa_n^2 + k^2}, \tag{9.24}$$

where $\kappa_n = \frac{2\pi n}{3(N_w+1)a}$, $n = 0, \pm 1, \pm 2, \ldots$ and $s = \pm$. The $n = 0$ mode is the lowest linear subband for metallic armchair ribbons. The energy gap (Δ_s) to first parabolic subband of $n = 1$ is given as

$$\Delta_s = 4\pi\gamma/3(N_w + 1)a, \tag{9.25}$$

which is inversely proportional to ribbon width. It should be noted that small energy gap can be acquired due to the Peierls distortion for half-filling at low temperatures [19, 53], but such effect is not relevant for single-channel transport in the doped energy regime.

9.2.3 Edge Boundary Condition and Intervalley Scattering

The matrix elements of the intervalley scattering term depend on the edge orientation and the range of impurity potential. According to [9], the impurity potential can be included in the massless Dirac equation by adding the following potential term $\hat{U}_{\text{imp}}$ described as

$$\hat{U}_{\text{imp}} = \begin{pmatrix} u_A(\boldsymbol{r}) & 0 & u'_A(\boldsymbol{r}) & 0 \\ 0 & u_B(\boldsymbol{r}) & 0 & -u'_B(\boldsymbol{r}) \\ u'_A(\boldsymbol{r})^* & 0 & u_A(\boldsymbol{r}) & 0 \\ 0 & -u'_B(\boldsymbol{r})^* & 0 & u_B(\boldsymbol{r}) \end{pmatrix}, \tag{9.26}$$

with

$$u_X(\boldsymbol{r}) = \sum_{\boldsymbol{R}_X} g\left(\boldsymbol{r} - \boldsymbol{R}_X\right) \tilde{u}_X\left(\boldsymbol{R}_X\right) , \tag{9.27}$$

$$u'_X(\boldsymbol{r}) = \sum_{\boldsymbol{R}_X} g\left(\boldsymbol{r} - \boldsymbol{R}_X\right) \mathrm{e}^{-\mathrm{i}2\boldsymbol{K}\cdot\boldsymbol{R}_X} \tilde{u}_X\left(\boldsymbol{R}_X\right) , \tag{9.28}$$

where $\tilde{u}_X(\boldsymbol{R}_X)$ is the local potential due to impurities for $X = A$ or B. Here $g(\boldsymbol{R})$ with the normalization condition of $\sum_{\boldsymbol{R}} g(\boldsymbol{R}) = 1$ is a real function which has an appreciable amplitude in the region where $|\boldsymbol{R}|$ is smaller than a few times of the lattice constant, and decays rapidly with increasing $|\boldsymbol{R}|$. For convenience, we distinguish the impurity into two types by the range of the impurity potential: one is long-ranged impurities (LRI) if the range of impurity potential is much larger than the lattice constant, and the other is short-ranged impurity (SRI) if the range of impurity is smaller than the lattice constant.

If only the LRI are present, we can approximate $u_A(\boldsymbol{r}) = u_B(\boldsymbol{r}) \equiv u(\boldsymbol{r})$ and $u'_A(\boldsymbol{r}) = u'_B(\boldsymbol{r}) \equiv u'(\boldsymbol{r})$. In the case of carbon nanotubes and zigzag nanoribbons, $u'_X(\boldsymbol{r})$ vanishes after the summation over $\boldsymbol{R}_X$ in (9.28) since the phase factor $\mathrm{e}^{-\mathrm{i}2\boldsymbol{K}\cdot\boldsymbol{R}_X}$ strongly oscillates in the x-direction. This means that the two valleys are independent and one can only focus on either $\boldsymbol{K}_+$ or $\boldsymbol{K}_-$ valley. *Thus LRIs do not induce the intervalley scattering for zigzag nanoribbons.*

However, this cancelation is not complete in an armchair nanoribbon because the averaging over the x-direction is restricted to the finite width of W. This means that we cannot neglect the contribution from scatterers particularly in the vicinity of the edges to $u'_X(\boldsymbol{r})$. *This means that intervalley scattering does not vanish even in the case of LRI in the armchair nanoribbons.*

9.3 Electronic Transport Properties

We numerically discuss the electronic transport properties of the disordered graphene nanoribbons. In general, electron scattering in a quantum wire is described by the scattering matrix [66]. Through the scattering matrix $\boldsymbol{S}$, the amplitudes of the scattered waves $\boldsymbol{O}$ are related to the incident waves $\boldsymbol{I}$,

$$\begin{pmatrix} \boldsymbol{O}_L \\ \boldsymbol{O}_R \end{pmatrix} = \boldsymbol{S} \begin{pmatrix} \boldsymbol{I}_L \\ \boldsymbol{I}_R \end{pmatrix} = \begin{pmatrix} \boldsymbol{r} & \boldsymbol{t}' \\ \boldsymbol{t} & \boldsymbol{r}' \end{pmatrix} \begin{pmatrix} \boldsymbol{I}_L \\ \boldsymbol{I}_R \end{pmatrix} . \tag{9.29}$$

Here, $\boldsymbol{r}$ and $\boldsymbol{r}'$ are reflection matrices, $\boldsymbol{t}$ and $\boldsymbol{t}'$ are transmission matrices, L and R denote the left and right lead lines. The Landauer-Büttiker formula [67] relates the scattering matrix to the conductance of the sample. The electrical conductance is calculated using the Landauer-Büttiker formula,

$$G(E) = \frac{e^2}{\pi\hbar} \mathrm{Tr}(\boldsymbol{t}\boldsymbol{t}^\dagger) = \frac{e^2}{\pi\hbar} g(E). \tag{9.30}$$

Here the transmission matrix $\boldsymbol{t}(E)$ is calculated by means of the recursive Green function method [34, 68]. For simplicity, throughout this chapter, we evaluate electronic conductance in the unit of quantum conductance ($2e^2/h$), i.e., dimensionless conductance $g(E)$. We would like to mention that recently the edge disorder effect on the electronic transport properties of graphene nanoribbons was studied using similar approach [69–72].

Since the transmission probability is unity in the clean limit, the dimensionless conductance at zero temperature is equal to the number of channels, i.e., the number of subbands across the Fermi energy. Thus the dimensionless conductance is given as

$$g(E) = \begin{cases} n & \text{semiconducting ANR} \\ n+1 & \text{metallic ANR} \\ 2n+1 & \text{ZNR} \end{cases} \tag{9.31}$$

Here, $n = 0, 1, 2, \ldots$.

9.3.1 One-Way Excess Channel System

In this subsection, we consider the conductance of zigzag nanoribbons in the clean limit in detail. As can be seen in Fig. 9.6a, there is always one excess left-going channel in the right valley ($\boldsymbol{K}_+$) within the energy window of $|E| \leq 1$. Analogously, there is one excess right-going channel in the left valley ($\boldsymbol{K}_-$) at the same energy. Although the number of right-going and left-going channels are balanced as a whole system, if we focus on one of two valleys, there is always one excess channel in one direction, i.e., a chiral mode.

Now let us consider to inject electrons from left to right side through the sample. When the chemical potential is changed from $E = 0$ ($E > 0$), the quantization rule of the dimensionless conductance ($g_{\boldsymbol{K}_+}$) in the valley of $\boldsymbol{K}_+$ is given as

$$g_{\boldsymbol{K}_+} = n, \tag{9.32}$$

where $n = 0, 1, 2, \ldots$. The quantization rule in the $\boldsymbol{K}_-$-valley is

$$g_{\boldsymbol{K}_-} = n + 1. \tag{9.33}$$

Thus, conductance quantization of the zigzag nanoribbon in the clean limit near $E = 0$ has the following odd-number quantization, i.e.,

$$g = g_{\boldsymbol{K}_+} + g_{\boldsymbol{K}_-} = 2n + 1. \tag{9.34}$$

Since we have an excess mode in each valley, the scattering matrix has some peculiar features which can be seen when we explicitly write the valley dependence

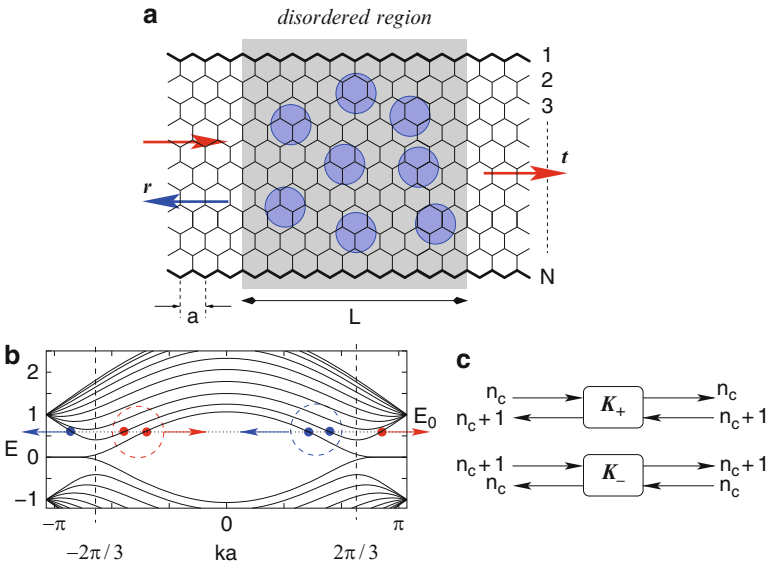

Fig. 9.6 (**a**) Schematic of disordered graphene zigzag nanoribbons. The disordered region with randomly distributed impurities lines in the shaded region and has the length L. Randomly distributed circles schematically represent the long-ranged impurities. (**b**) Energy dispersion of zigzag ribbon with $N = 10$. The valleys in the energy dispersion near $k = 2\pi/3a$ ($k = -2\pi/3a$) originate from the Dirac $\boldsymbol{K}_+(\boldsymbol{K}_-)$-point of graphene. The *red-filled (blue-unfilled) circles* denote the right (*left*)-moving open channel at the energy E_0(*dashed horizontal line*). In the left(*right*) valley, the degeneracy between right and left moving channels is missing due to one excess right(*left*)-going mode. The time-reversal symmetry under the intra-valley scattering is also broken. (**c**) Schematic figure of scattering geometry at $\boldsymbol{K}_+$ and $\boldsymbol{K}_-$ points in zigzag nanoribbons, where a single excess right-going mode exists for $\boldsymbol{K}_-$ point. But a single excess left-going mode exists for $\boldsymbol{K}_-$ point. Here $n_c = 0, 1, 2, \ldots$ (Ref. [51])

in the scattering matrix. By denoting the contribution of the right valley ($\boldsymbol{K}_+$) as $+$, and of the left valley ($\boldsymbol{K}_-$) as $-$, the scattering matrix can be rewritten as

$$\begin{pmatrix} \boldsymbol{O}_L^+ \\ \boldsymbol{O}_L^- \\ \boldsymbol{O}_R^+ \\ \boldsymbol{O}_R^- \end{pmatrix} = \begin{pmatrix} r & t' \\ t & r' \end{pmatrix} \begin{pmatrix} \boldsymbol{I}_L^+ \\ \boldsymbol{I}_L^- \\ \boldsymbol{I}_R^+ \\ \boldsymbol{I}_R^- \end{pmatrix}. \tag{9.35}$$

Here we should note that the dimension of each column vector is not identical. Let us denote the number of the right-going channel in the valley $\boldsymbol{K}_+$ or the left-going channel in the valley $\boldsymbol{K}_-$ as n_c. For example, $n_c = 1$ at $E = E_0$ in Fig. 9.6b. Figure 9.6c shows the schematic figure of scattering geometry for $\boldsymbol{K}_+$ and $\boldsymbol{K}-$ points. Thus the dimension of the column vectors is given as follows:

$$\begin{cases} dim(\boldsymbol{I}_{\boldsymbol{L}}^{+}) = n_c, & dim(\boldsymbol{I}_{\boldsymbol{R}}^{+}) = n_c + 1, \\ dim(\boldsymbol{I}_{\boldsymbol{L}}^{-}) = n_c + 1, & dim(\boldsymbol{I}_{\boldsymbol{R}}^{-}) = n_c, \end{cases} \tag{9.36}$$

and

$$\begin{cases} dim(\boldsymbol{O}_{\boldsymbol{L}}^{+}) = n_c + 1, & dim(\boldsymbol{O}_{\boldsymbol{R}}^{+}) = n_c, \\ dim(\boldsymbol{O}_{\boldsymbol{L}}^{-}) = n_c, & dim(\boldsymbol{O}_{\boldsymbol{R}}^{-}) = n_c + 1. \end{cases} \tag{9.37}$$

Subsequently, the reflection matrices have the following matrix structures:

$$\boldsymbol{r} = \begin{array}{c} \\ n_c + 1 \\ n_c \end{array} \begin{array}{c} \begin{array}{cc} n_c & n_c + 1 \end{array} \\ \begin{pmatrix} \boldsymbol{r}_{++} & \boldsymbol{r}_{+-} \\ \boldsymbol{r}_{-+} & \boldsymbol{r}_{--} \end{pmatrix} \end{array}, \tag{9.38}$$

$$\boldsymbol{r'} = \begin{array}{c} \\ n_c \\ n_c + 1 \end{array} \begin{array}{c} \begin{array}{cc} n_c + 1 & n_c \end{array} \\ \begin{pmatrix} \boldsymbol{r'}_{++} & \boldsymbol{r'}_{+-} \\ \boldsymbol{r'}_{-+} & \boldsymbol{r'}_{--} \end{pmatrix} \end{array}. \tag{9.39}$$

The reflection matrices become nonsquare when the intervalley scattering is suppressed, i.e., the off-diagonal submatrices ($\boldsymbol{r}_{+-}$, $\boldsymbol{r}_{-+}$ and so on) are zero.

When the electrons are injected from the left lead of the sample and the intervalley scattering is suppressed, a system with an excess channel is realized in the $\boldsymbol{K}_{-}$-valley. Thus, for single valley transport, the $\boldsymbol{r}_{--}$ and $\boldsymbol{r'}_{--}$ are $n_c \times (n_c + 1)$ and $(n_c + 1) \times n_c$ matrices, respectively, and $\boldsymbol{t}_{--}$ and $\boldsymbol{t'}_{--}$ are $(n_c + 1) \times (n_c + 1)$ and $n_c \times n_c$ matrices, respectively. Noting the dimensions of $\boldsymbol{r}_{--}$ and $\boldsymbol{r'}_{--}$, we find that ${\boldsymbol{r}_{--}}^{\dagger}\boldsymbol{r}_{--}$ and $\boldsymbol{r'}_{--}{\boldsymbol{r'}^{\dagger}}_{--}$ have a single zero eigenvalue. Combining this property with the flux conservation relation ($\boldsymbol{S}^{\dagger}\boldsymbol{S} = \boldsymbol{S}\boldsymbol{S}^{\dagger} = \boldsymbol{1}$), we arrive at the conclusion that $\boldsymbol{t}_{--}\boldsymbol{t}_{--}^{\dagger}$ has an eigenvalue equal to unity, which indicates the presence of a PCC only in the right-moving channels. Note that $\boldsymbol{t'}_{--}{\boldsymbol{t'}^{\dagger}}_{--}$ does not have such an anomalous eigenvalue. If the set of eigenvalues for $\boldsymbol{t'}_{--}{\boldsymbol{t'}^{\dagger}}_{--}$ is expressed as $\{T_1, T_2, \cdots, T_{n_c}\}$, that for $\boldsymbol{t}_{--}\boldsymbol{t}_{--}^{\dagger}$ is expressed as $\{T_1, T_2, \cdots, T_{n_c}, 1\}$, i.e. a PCC. Thus, the dimensionless conductance g for the right-moving channels is given as

$$g_{\boldsymbol{K}_{-}} = \sum_{i=1}^{n_c+1} T_i = 1 + \sum_{i=1}^{n_c} T_i, \tag{9.40}$$

while that for the left-moving channels is

$$g'_{\boldsymbol{K}_{-}} = \sum_{i=1}^{n_c} T_i. \tag{9.41}$$

We see that $g_{\boldsymbol{K}_{-}} = g'_{\boldsymbol{K}_{-}} + 1$. Since the overall time reversal symmetry (TRS) of the system guarantees the following relation:

$$\begin{aligned} g'_{\boldsymbol{K}_+} &= g_{\boldsymbol{K}_-}, \\ g'_{\boldsymbol{K}_-} &= g_{\boldsymbol{K}_+}, \end{aligned} \tag{9.42}$$

the conductance $g = g_{\boldsymbol{K}_+} + g_{\boldsymbol{K}_-}$ (right-moving) and $g' = g'_{\boldsymbol{K}_+} + g'_{\boldsymbol{K}_-}$ (left-moving) are equivalent. If the probability distribution of $\{T_i\}$ is obtained as a function L, we can describe the statistical properties of g as well as g'. The evolution of the distribution function with increasing L is described by the DMPK (Dorokhov-Mello-Pereyra-Kumar) equation for transmission eigenvalues [73]. The presence of a PCC can cause the breakdown of universal conductance fluctuations unless ribbon width is very large [74].

9.3.2 Model of Impurity Potential

As shown in Fig. 9.6a, the impurities are randomly distributed with a density n_{imp} in the nanoribbons. In our model we assume that the each impurity potential has a Gaussian form of a range d

$$V(\boldsymbol{r}_i) = \sum_{\boldsymbol{r_0}(random)} u \exp\left(-\frac{|\boldsymbol{r}_i - \boldsymbol{r}_0|^2}{d^2}\right) \tag{9.43}$$

where the strength u is uniformly distributed within the range $|u| \leq u_M$. Here u_M satisfies the normalization condition:

$$u_M \sum_{\boldsymbol{r}_i}^{(full\ space)} \exp\left(-\boldsymbol{r}_i^2 d^2\right) / (\sqrt{3}/2) = u_0. \tag{9.44}$$

In this work, we set $n_{\text{imp.}} = 0.1$, $u_0 = 1.0$ and $d/a = 1.5$ for LRI and $d/a = 0.1$ for SRI.

9.3.3 Perfectly Conducting Channel: Absence of Anderson Localization

We focus first on the case of LRI using a potential with $d/a = 1.5$ which is already sufficient to avoid inter-valley scattering. Figure 9.7a shows the averaged dimensionless conductance as a function of L for different incident energies(Fermi energies), averaging over an ensemble of 40,000 samples with different impurity configurations for ribbons of width $N = 10$. The potential strength and impurity density are chosen to be $u_0 = 1.0$ and $n_{imp.} = 0.1$, respectively. As a typical localization effect we observe that $\langle g \rangle$ gradually decreases with growing length L

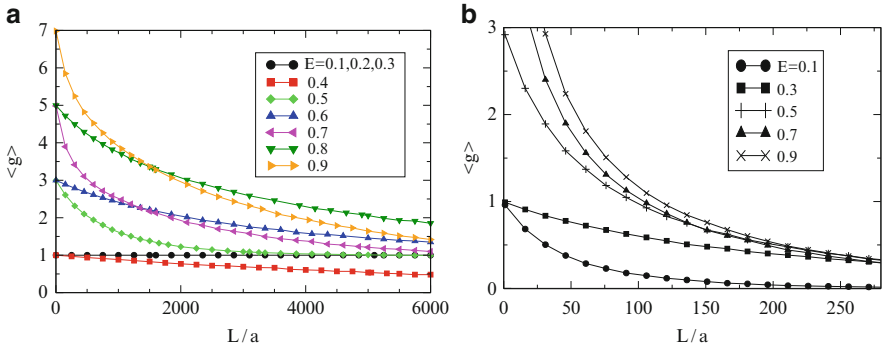

Fig. 9.7 L-dependence of the averaged dimensionless conductance, $\langle g \rangle$ for zigzag nanoribbon with $N = 10$, (**a**) $d/a = 1.5$ (no inter-valley scattering), (**b**) $d/a = 0.1$ (inter-valley scattering). Here $u_0 = 1.0$, and $n_{imp.} = 0.1$. More than 9,000 samples with different impurity configuration are included in the ensemble average (Ref. [51])

(Fig. 9.7). However, $\langle g \rangle$ converges to $\langle g \rangle = 1$ for LRIs (Fig. 9.7a), indicating the presence of a single *perfectly conducting* channel. It can be seen that $\langle g \rangle$ has an exponential behavior as

$$\langle g \rangle - 1 \sim \exp(-L/\xi) \tag{9.45}$$

with ξ as the localization length.

As the effect is connected with the subtle feature of an excess mode in the band structure, it is natural that the result can only be valid for sufficiently weak potentials. For potential strengths comparable to the energy scale of the band structure, e.g. the energy difference between the transverse modes, the result should be qualitatively altered [75]. Deviations from the limit $\langle g \rangle \to 1$ also occur, if the incident energy lies at a value close to the change between $g = 2n - 1$ and $g = 2n + 1$ for the ribbon without disorder. This is for example visible in above calculations for $E = 0.4$ where the limiting value $\langle g \rangle < 1$ (Fig. 9.7a).

Turning to the case of SRI the inter-valley scattering becomes sizable enough to ensure TRS, such that the perfect transport supported by the effective chiral mode in a single valley ceases to exist. In Fig. 9.7b, the nanoribbon length dependence of the averaged conductance for SRIs is shown. Since SRI causes the inter-valley scattering for any incident energy, the electrons tend to be localized and the averaged conductance decays exponentially, $\langle g \rangle \sim \exp(-L/\xi)$, without developing a perfect conduction channel.

In this subsection, we have completely neglected the effect of electron-electron interaction, which may acquire the energy gap for non-doped zigzag nanoribbon at very low-temperatures accompanying with the edge spin polarization [13, 16, 18]. In such situation, small transport gap will appear near $E = 0$. Since the edge states have less Fermi instability for doped regime, the spin polarized states might be less important for doped system. Also, in the low density region near

the Dirac point, the strong density inhomogeneity called puddle might play an important role [77].

9.4 Universality Class

According to random matrix theory, ordinary disordered quantum wires are classified into the standard universality classes, orthogonal, unitary and symplectic. The universality classes describe transport properties which are independent of the microscopic details of disordered wires. These classes can be specified by time-reversal and spin rotation symmetry. The orthogonal class consists of systems having both time-reversal and spin-rotation symmetries, while the unitary class is characterized by the absence of time-reversal symmetry. The systems having time-reversal symmetry without spin-rotation symmetry belong to the symplectic class. These universality classes have been believed to inevitably cause the Anderson localization although typical behaviors are different from class to class.

In the graphene system, the presence or absence of the intervalley scattering affect the time reversal symmetry of the system. If the inter-valley scattering is absent, *i.e.* $u'_X(\boldsymbol{r}) = 0$, the Hamiltonian $\hat{H}_0 + \hat{U}_{\rm imp}$ becomes invariant under the transformation of $\mathcal{S} = -\mathrm{i}\left(\sigma^y \otimes \tau^0\right) C$, where C is the complex-conjugate operator. This operation corresponds to the special time-reversal operation for pseudospins within each valley, and supports that the system has the symplectic symmetry. However, in the presence of inter-valley scattering due to SRI, the invariance under $\mathcal{S}$ is broken. In this case, the time reversal symmetry across two valleys described by the operator $\mathcal{T} = (\sigma^z \otimes \tau^x) C$ becomes relevant, which indicates orthogonal universality class. Thus as noted in [78], graphene with LRI belongs to symplectic symmetry, but that with SRI belongs to orthogonal symmetry.

However, in the zigzag nanoribbons, the boundary conditions which treat the two sublattices asymmetrically leading to edge states give rise to a single special mode in each valley. Considering now one of the two valleys separately, say the one around $k = k_+$, we see that the pseudo TRS is violated in the sense that we find one more left-moving than right-moving mode. Thus, as long as disorder promotes only intra-valley scattering, the system has no time-reversal symmetry. On the other hand, if disorder yields inter-valley scattering, the pseudo TRS disappears but the ordinary TRS is relevant making a complete set of pairs of time-reversed modes across the two valleys. Thus we expect to see qualitative differences in the properties if the range of the impurity potentials is changed.

The presence of one PCC has been recently found in disordered metallic carbon nanotubes with LRI [76]. The PCC in this system originates from the skew-symmetry of the reflection matrix, ${}^t\boldsymbol{r} = -\boldsymbol{r}$ [76], which is special to the symplectic symmetry with odd number of channels. On the other hand, zigzag ribbons without inter-valley scattering are not in the symplectic class, since they break TRS in a

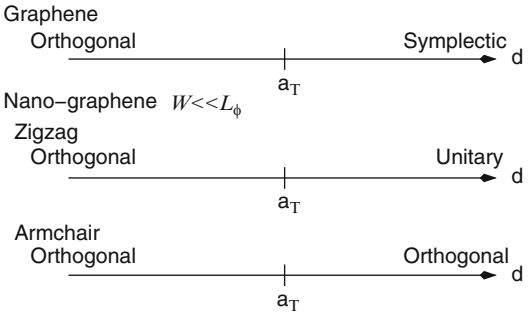

Fig. 9.8 Summary concerning the universality crossover. With increasing the range of the impurity potential, graphene is known to be the orthogonal for SRIs and the symplectic class for LRIs. However, zigzag nanoribbons are unitary class for SRIs. Armchair ribbons are classified into orthogonal class for all the range of the impurity. L_ϕ is the phase coherence length. W is the width of graphene ribbons (Ref. [51])

special way. The decisive feature for a PCC is the presence of one excess mode in each valley as discussed in the previous section (Fig. 9.6b).

In view of this classification, we find that the universality class of the disordered zigzag nanoribbon with long-ranged impurity potential (no inter-valley scattering) is the *unitary* class (no TRS). On the other hand, for short-range impurity potentials with inter-valley scattering, the disordered ribbon belongs to the *orthogonal* class (with overall TRS). Consequently, we can observe a crossover between two universality classes when we change the impurity range continuously.

However, in the disordered armchair nanoribbons, the special time-reversal symmetry within each valley is broken even in the case of LRI. This is because $u'_X(\boldsymbol{r}) \neq 0$ as we have seen in Sect. 9.2.3. Thus, irrespective of the range of impurities, the armchair nanoribbons are classified into orthogonal universality class. *Since the disordered zigzag nanoribbons are classified into unitary class for LRI but orthogonal class for SRI [50], it should be noted that the universality crossover in nanographene system can occur not only due to the range of impurities but also due to the edge boundary conditions.*

9.4.1 Graphene Nanoribbons with Generic Edge Structures

As we have seen, zigzag ribbons with long-ranged impurity potentials retain a single PCC. This PCC originates for the following two reasons: (1) The spectrum contains two valleys (two Dirac $\boldsymbol{K}_\pm$-points) which are well enough separated in momentum space as to suppress intervalley scattering due to the long-ranged impurities, (2) the spectrum in each valley is chiral by possessing a right- and left-moving modes

which differ by one in number, and so scattered electrons can avoid in one channel backscattering.

We extend our analysis to the electronic spectrum of nanoribbons for which the ribbon axis is tilted with respect to the zigzag axis and keep the balance between A- and B-sublattice sites.

In Fig. 9.9a, we show the definitions of coordinates and primitive vectors which specifies the geometry of the ribbon. For this purpose we introduce the two vectors, $\boldsymbol{T} = (m, n) = m\boldsymbol{a_1} + n\boldsymbol{a_2}$ and $\boldsymbol{W} = (0, l) = l\boldsymbol{a_2}$, where l, m, n are integers. The pure zigzag ribbon corresponds to $m = -n$ and the pure armchair edge is given by $m = n$.

Figures 9.9b and c show the energy band structures of ribbons with the general edge structures of $\boldsymbol{W} = (0, 20)$ and (b) $\boldsymbol{T} = (-4, 3)$ and (c) $\boldsymbol{T} = (-6, 5)$. As we expected, the partially flat bands due to localized edge modes appear which break the balance between left- and right-going modes in the two valleys. Both examples are rather close to the zigzag edge so that the two valleys are well separated. In this case PCC can appear. If the geometry of the ribbons deviates more strongly from the zigzag condition, the valley structure will become less favorable for creating a PCC, as the momentum difference between valleys shrinks. It is important to note that the extended unit cell along these generalized ribbons reduces the valley separation drastically through Brillouin zone folding. The length scale is the new effective lattice constant a_T along the ribbon. Under these circumstances, the condition for long-ranged impurity potentials is more stringent, d being larger than a_T and not a.

In the present sample quality of graphene nanoribbons, the edge structures are random and the width of the ribbon fluctuates in the range of 10%. According to the recent tight-binding numerical calculations, it seems that the electronic conduction in disordered zigzag nanoribbons is more robust than that of armchair nanoribbons against edge disorders [79–81]. Such robust conduction in zigzag nanoribbons might be attributed to the presence of PCC due to the special time reversal symmetry breaking for pseudospin.

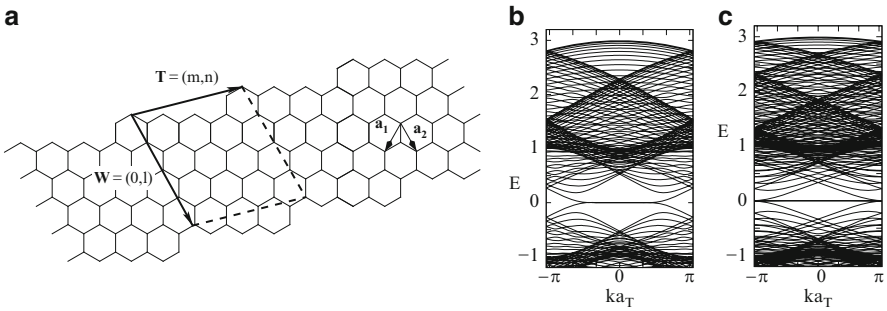

Fig. 9.9 (**a**) The primitive vectors for nanoribbon with the general edge structures. The translational vector is defined as $\boldsymbol{T} = (m, n) = m\boldsymbol{a_1} + n\boldsymbol{a_2}$, and the ribbon width is defined by the vector $\boldsymbol{W} = (0, l) = l\boldsymbol{a_2}$. The number of carbon atoms in the unit cell is $2(l + 1)m$. The corresponding energy band structures of $\boldsymbol{W} = (0, 20)$ for (**b**) $\boldsymbol{T} = (-4, 3)$ and (**c**) $\boldsymbol{T} = (-6, 5)$. Here a_T is the effective lattice constant which is given as $|\boldsymbol{T}|$ (Ref. [51])

9.5 Transport Properties Through Graphene Nanojunction

In this section, we study the electronic transport in graphene nanojunctions. Here, we consider nanojunctions as shown in Figs. 9.10a and b. Nanojunctions are classified into the armchair ribbon with armchair edge junction (AAA-junction), that with zigzag one (AZA-junction), the zigzag ribbon with armchair edge junction (ZAZ-junction) and that with zigzag one (ZZZ-junction). The width of left (right) armchair ribbon is defined by $M_L(M_R)$ while that of zigzag one is by $N_L(N_R)$. Here we note that the armchair ribbon is metallic only for $M_{(L,R)} = 3I - 1$ (I : integer) while the zigzag ribbon is always metallic.

Figures 9.10c and d show the energy dependence of the conductance for armchair and zigzag ribbon junctions, respectively. We set $(M_L, M_R) = (32, 20)$ and $(N_L, N_R) = (30, 20)$. The energy is normalized by $\Delta^L_{s,A}$ ($\Delta^L_{s,Z}$), denoting the end of single-channel energy regime of the left wider armchair (zigzag) ribbon. These energy scales are related to the ribbon width by $\Delta^L_{s,A} \simeq \sqrt{3}\pi\gamma_0 a/2W$ and $\Delta^L_{s,Z} \simeq 3\sqrt{3}\pi\gamma_0 a/8W$, where $W = (M_L + 1)a/2$ and $W = \sqrt{3}(N_L + 1)a/2$ for armchair and zigzag ribbons, respectively. The maximum conductance is limited by the number of channel at the right narrower ribbon (black dotted line in Figs. 9.10c and d).

The behavior of conductance strongly depends on junction structure in the single-channel energy regime ($|E| < \Delta^L_{s,(A,Z)}$), while it does not in the multi-channel one ($|E| > \Delta^L_{s,(A,Z)}$). In the single-channel energy regime, the conductance mostly remains unity in the AAA-junction while the zero conductance dip appears in the AZA-junction at $E = 0$. This zero conductance dip is due to the anti-resonance induced by the coupling between a continuous state at ribbon and a localized state at zigzag edge junction. In addition, the junction region is mainly semiconducting and works as a barrier for low-energy transport in the AZA-junction, since the ribbon width are narrowed as $M_L-1, M_L-2, \ldots$. Hence, by the combination of a resonance and a barrier effect, the width of zero conductance dip in the AZA-junction is rather wide and the FWHM (full width at half maximum) can be roughly estimated as $\Delta^L_{s,A}$. On the other hand, the junction region is always metallic or semiconducting in the AAA-junction since the ribbon width are narrowed as $M_L - 3, M_L - 6, \ldots$.

In the ZAZ-junction, the sharp zero conductance dips appear in the vicinity of the end of single-channel energy regime ($E \simeq \pm\Delta^L_{s,Z}$). In zigzag ribbons, propagating electrons belong to one of two valleys in the single-channel energy regime, while the second channel will be opened in both valleys as the energy of incident electrons increases. Since the group velocity of a second channel is almost zero at the bottom of subband, the second channel in the other valley works as a bound state similar to the zigzag edge state at $E = 0$. The FWHM of dips can be roughly estimated as $\Delta^L_{s,A}/20$ in our numerical simulation performed for several different values of the ribbon width N_L and the width difference $\Delta N = N_L - N_R$ within the range $N_L/3 \leq \Delta N \leq 2N_L/3$.

In the ZZZ-junction, several zero conductance dips appear at nonzero energies. This is due to the energy level splitting induced by the coupling between the

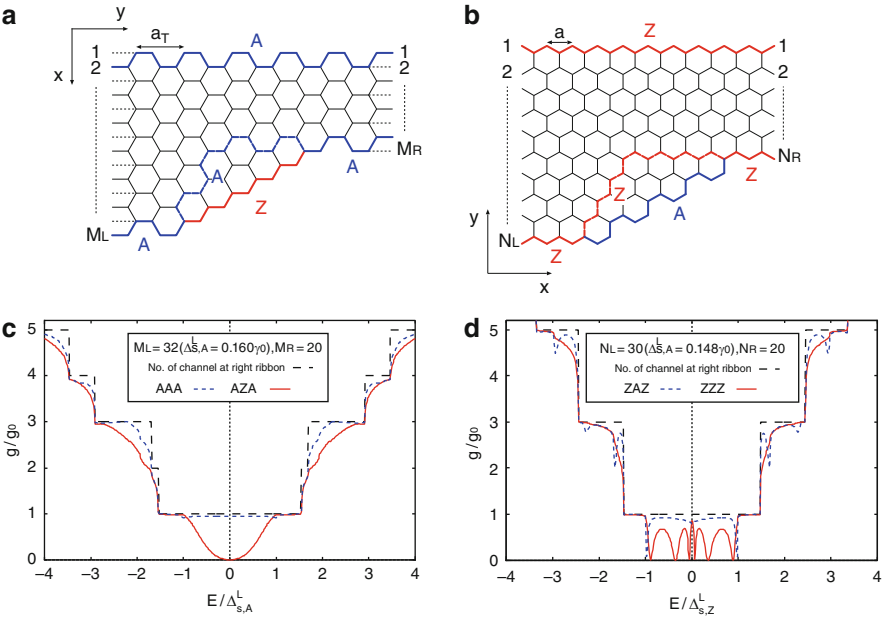

Fig. 9.10 (**a**) Armchair ribbons with armchair junction (AAA-junction, *blue dotted line*) and zigzag junction (AZA-junction, *red solid line*). (**b**) Zigzag ribbons with armchiar junction (ZAZ-junction, *blue solid line*) and zigzag junction (ZZZ-junction, *red dotted line*). (**c**) Conductance as a function of energy in armchair ribbon junctions. The width of left and right ribbons are $M_L = 32$ and $M_R = 20$. Conductance mostly remains unity in the AAA-junction while the zero conductance dip appears in the AZA-junction at $E = 0$ for the single-channel energy regime ($|E| < \Delta^L_{s,A}$). (**d**) Conductance as a function of energy in zigzag ribbon junctions. The width of left and right ribbons are $N_L = 30$ and $N_R = 20$. Conductance mostly remains unity in the ZAZ-junction while several zero conductance dips appear in the ZZZ-junction at nonzero energies for the single-channel energy regime ($|E| < \Delta^L_{s,Z}$) (Ref. [36])

edge-localized state on A-sublattice at ribbon and the edge-localized states on B-sublattice at junction. Moreover, the coupled states have different nodes as the width difference ΔN is getting larger.

9.6 Summary

In this chapter, we have presented a brief overview on the electronic and transport properties of graphene nanoribbons focusing on the effect of edge shapes and impurity scattering. Concerning transport properties for disordered systems, the most important consequence is the presence of a PCC in zigzag nanoribbons, i.e., the absence of Anderson localization which is believed to inevitably occur in the one-dimensional electron system. The origin of this effect lies in the

single-valley transport which is dominated by a chiral mode. On the other hand, large momentum transfer through impurities with short-range potentials involves both valleys, destroying this effect and leading to usual Anderson localization. We have seen that the degree of freedoms with respect to edge structures can be a source of wide variety of electron transport phenomena such as zero-conductance Fano-resonances, which will serve to design the nano-carbon electronics devices.

References

1. K.S. Novoselov, A.K. Geim, S.V. Morozov et. al., Science **306**, 666 (2004)
2. A.K. Geim and K.S. Novoselov, Nat. Mater. **6**, 183 (2007)
3. A.H. Castro Neto, F. Guinea, N.M.R. Peres, K.S. Novoselov, and A.K. Geim, Rev. Mod. Phys. **81**, 109 (2009)
4. T. Ando, J. Phys. Soc. Jpn.**74**, 777 (2005)
5. T. Ando, Prog. Theor. Phys. Suppl. **176**, 203 (2008)
6. K.S. Novoselov, A.K. Geim, S.V. Morozov, et. al., Nature **438**, 197 (2005)
7. Y. Zhang, Y.W. Tan, H.L. Stormer, P. Kim, Nature **438**, 201 (2005)
8. K.S. Novoselov et.al., Nat. Phys. **2**, 177 (2006)
9. T. Ando and T. Nakanishi, J. Phys. Soc. Jpn. **67**, 1704 (1998)
10. I.A. Luk'yanchuk and Y. Kopelevich Y, Phys. Rev. Lett. **93**, 166402 (2004)
11. K.I. Bolotin, K.J. Sikes, Z. Jiang et al., Solid State Comm. **146**, 351 (2008)
12. A.A. Balandin, S.Ghosh, W.Z. Bao, et al., Nano Lett. **8**, 902 (2008)
13. M. Fujita, K. Wakabayashi, K. Nakada, and K. Kusakabe, J. Phys. Soc. Jpn. **65**, 1920 (1996)
14. K. Nakada, M. Fujita, G. Dresselhaus, M.S. Dresselhaus, Phys. Rev. **B54**, 17954 (1996)
15. K. Wakabayashi, M. Fujita, H. Ajiki, M. Sigrist, Phys. Rev. **B59**, 8271 (1999)
16. K. Wakabayashi, M. Sigrist, and M. Fujita, J. Phys. Soc. Jpn. **67**, 2089 (1998)
17. K. Wakabayashi, Dissertation, University of Tsukuba, (2000) http://www.tulips.tsukuba.ac.jp/dspace/handle/2241/2592
18. Y.W. Son, M.L. Cohen, and S.G. Louie, Nature **444**, 347 (2006)
19. Y.W. Son, M.L. Cohen, S.G. Louie, Phys. Rev. Lett. **97**, 216803 (2006)
20. Y. Kobayashi et. al., Phys. Rev.**B71**, 193406 (2005)
21. Y. Kobayashi et. al., Phys. Rev.**B73**, 125415 (2006)
22. Y. Niimi et. al., Phys. Rev.**B73**, 085421 (2006)
23. K.A. Ritter and J.W. Lyding, Nature Mat. **8**, 235 (2009)
24. K. Sugawara, T. Sato, S. Souma et al., Phys. Rev. **B73**, 045124 (2006)
25. M. Y. Han MY et. al., Phys. Rev. Lett. **98**, 206805 (2007)
26. Z. Chen et.al., Physica E **40**, 228 (2007)
27. X. Li et.al., Science **319**, 1229 (2008)
28. L. Jiao et.al., Nature **458**, 877 (2009)
29. D.V. Kosynkin et.al., Nature **458**, 872 (2009)
30. X. Yang et.al., J. Am. Chem. Phys. **130**, 4216 (2008)
31. X. Jia et.al., Science **323**, 1701 (2009)
32. L.C. Campos, V.R. Manfrinato, J.D. Sanchez-Yamgishi, J. Kong and P. Jarillo-Herrero, Nano Lett. **9**, 2600 (2009)
33. J. Cai, P. Ruffieux, R. Jaafar, M. Bieri, T. Braun, S. Blankenburg, M. Muoth, A.P. Seitsonen, M. Saleh, X. Feng, K. Müllen, and R. Fasel, Nature **466**, 470 (2010)
34. K. Wakabayashi, M. Sigrist, Phys. Rev. Lett. **84**, 3390 (2000)
35. K. Wakabayashi, Phys. Rev. **B64**, 125428 (2001)
36. M. Yamamoto and K. Wakabayashi, Appl. Phys. Lett. **95**, 082109 (2009)
37. K. Wakabayashi, T. Aoki, Int. J. Mod. Phys. B **16**, 4897 (2002)

38. A. Rycerz, J. Tworzydlo, C.W.J. Beenakker, Nat. Phys. **3**, 172 (2007)
39. C.L. Kane, E.J. Mele, Phys. Rev. Lett. **95**, 226801 (2005)
40. K. Wakabayashi, J. Phys. Soc. Jpn. **79**, 034706 (2010)
41. S. Dutta, Phys. Rev. Lett. **102**, 096601 (2009)
42. E. Kan, J. Am. Chem. Soc. **130**, 42224 (2008)
43. F. Molitor et.al., Phys. Rev. **B76**, 245426 (2007)
44. X. Wang et.al., Phys. Rev. Lett. **100**, 206803 (2008)
45. L. Tapaszto et.al., Nat. Nanotech **3**, 397 (2008)
46. C. Stampfer et.al., Phys. Rev. Lett. **102**, 056403 (2009)
47. L. Campos et.al., Nano Lett. **9**, 2600 (2009)
48. H. Miyazaki et.al., Appl. Phys. Exp. **1**, 024001 (2008)
49. J. Güttinger et.al., Phys. Rev. Lett. **103**, 046810 (2009)
50. K. Wakabayashi, Y. Takane, M. Sigrist, Phys. Rev. Lett. **99**, 036601 (2007)
51. K. Wakabayashi, Y. Takane, M. Sigrist, Carbon **47**, 124 (2009)
52. P.R. Wallace, Phys. Rev. **71**, 622 (1947)
53. M. Fujita, M. Igami, K. Nakada, J. Phys. Soc. Jpn. **66**, 1864 (1997)
54. O. Hod et.al., Phys. Rev. **B77**, 035411 (2008)
55. K. Wakabayashi, K. Sasaki, T. Nakanishi, T. Enoki, Sci. Tech. Adv. Mat. **11**, 054504 (2010)
56. A. Onipko, Phys. Rev. **B78**, 245412 (2008)
57. S. Compernolle, L. Chibotaru, A. Ceulemans, J. Chem. Phys. **119**, 2854 (2003)
58. K. Sasaki, K. Wakabayashi, T. Enoki, J. Phys. Soc. Jpn. **80**, 054710 (2011)
59. K. Sasaki and K. Wakabayashi, Phys. Rev. **B82**, 035421 (2010)
60. K. Sasaki, M. Yamamoto, S. Murakami, R. Saito, M. S. Dresselhaus, K. Takai, T. Mori, T. Enoki, K. Wakabayashi, Phys. Rev. **B80**, 155450 (2009)
61. K. Sasaki, R. Saito, K. Wakabayashi, T. Enoki, J. Phys. Soc. Jpn. **79**, 044603 (2010)
62. C. Cong, T. Yu, H. Wang, ACS Nano, **4**, 3175 (2010)
63. C. Casiraghi, A. Hartschuh, H. Qian, S. Piscanec, C. Georgi, A. Fasoli, K. S. Novoselov, D. M. Basko and A. C. Ferrari, Nano Lett, **9** 1433 (2009)
64. M. Begliarbekov, O. Sul, S. Kalliakos, E.-H. Yang, S. Strauf, Appl. Phys. Lett. **97**, 031908 (2010)
65. L. Brey, H.A. Fertig, Phys. Rev. **B73**, 235411 (2006)
66. C.W.J. Beenakker, Rev. Mod. Phys. **69**, 731 (1997)
67. M. Büttiker, Y. Imry, R. Landauer, S. Pinhas, Phys. Rev. **B31**, 6207 (1985)
68. T. Ando, Phys. Rev. **B44**, 8017 (1991)
69. T.C. Li, S.P. Lu, Phys. Rev. **B77** 085408 (2008)
70. E. Louis, J.A. Vergés, F. Guinea, G. Chiappe, Phys. Rev. **B75** 085440 (2007)
71. E. R. Mucciolo et.al., Phys. Rev. **B79**, 075407 (2009)
72. S. Ihnatsenka, G. Kirczenow, Phys. Rev. **B80** 201407(R) (2009)
73. Y. Takane, K. Wakabayashi, J. Phys. Soc. Jpn. **76**, 053701 (2007)
74. Y. Takane, K. Wakabayashi, J. Phys. Soc. Jpn. **77**, 054702 (2008)
75. K. Wakabayashi, J. Phys. Soc. Jpn. **71**, 2500 (2002)
76. T. Ando, H. Suzuura, J. Phys. Soc. Jpn. **71**, 2753 (2002)
77. S. Das Sarma, S. Adam, E.H. Hwang, E. Rossi, Rev. Mod. Phys. **83**, 407 (2011)
78. H. Suzuura, T. Ando, Phys. Rev. Lett. **89**, 266603 (2002)
79. D.A. Areshkin, D. Gunlycke, C.T. White, Nano Lett. **7**, 204 (2007)
80. A. Cresti, S. Roche, New J. Phys. **11**, 095004 (2009)
81. A. Cresti, S. Roche, Phys. Rev. **B79**, 233404 (2009)

Chapter 10
Mesoscopics in Graphene: Dirac Points in Periodic Geometries

H.A. Fertig and L. Brey

Abstract We review the interesting physics associated with two possible realizations of mesoscopic graphene systems where periodicity plays an important role: graphene rings, and graphene in a superlattice potential. The electronic spectra of graphene rings contain signatures of "effective time reversal symmetry breaking," which are naturally interpreted in terms of effective magnetic flux contained in the ring, even when no real flux is present. This remarkable behavior arises because the low energy physics of electrons is controlled by a Dirac equation. This also creates unusual effects in a one dimensional superlattice potential, which allows the number of Dirac points at zero energy to be manipulated by the strength and/or period of the potential. The emergence of new Dirac points is accompanied by strong signatures in the conduction properties of the system.

Graphene has many properties that make it an attractive candidate material for small scale electronic devices. Creating such systems will require cutting the system into shapes with useful electronic properties, or application of electric potentials. When such systems become very small – "mesoscopic" – quantum mechanics is known to profoundly affect their properties. Ideally such quantum effects can be exploited to create fast and compact electronic and optical devices.

Mesoscopic physics in semiconductor systems has been studied for over three decades, and the basic physics of how small size affects their electronic properties are at this point well known [1]. In the simplest models, one treats electrons in these systems as non-interacting particles, confined to some region defined by the system

H.A. Fertig (✉)
Department of Physics, Indiana University, Bloomington, IN 47401 USA
e-mail: hfertig@indiana.edu

L. Brey
Instituto de Ciencia de Materiales de Madrid (CSIC), Catoblanco, 28049 Madrid, Spain
e-mail: brey@icmm.csic.es

H. Raza (ed.), *Graphene Nanoelectronics*, NanoScience and Technology,
DOI 10.1007/978-3-642-22984-8_10, © Springer-Verlag Berlin Heidelberg 2012

shape and subject to some effective potential. That the electrons are moving inside a semiconductor environment rather than in a vacuum is well-accounted for by describing the electrons with a Schrödinger equation with an appropriate effective mass.

Remarkably, electrons in graphene cannot be described within this simple paradigm. The honeycomb structure of the carbon network in which electrons in graphene reside instead yields a *Dirac equation* governing the low energy electronic states. The wavefunctions in this equation have two components, which are analogs of the electron spin in the real Dirac equation [2], but in this context represent wavefunction amplitudes on the two Bravais sublattices of the network. The fact that this effective spinor changes direction when the wavefunction changes, and the Berry's phase associated with a changing spinor wavefunction, lead to quantum interference effects with no analog for electrons in standard semiconductors. In graphene, the band structure includes two inequivalent Dirac cones, one at each of the two inequivalent corners of the Brillouin zone, which are referred to as the **K** and **K**′ valleys. When intervalley scattering is negligible, the unusual effects associated with the spinor structure of the wavefunctions become evident.

In this chapter, we discuss two surprising consequences of the spinor structure of the wavefunctions in mesoscopic settings. We will first describe the electronic spectra associated with graphene rings, systems made up of short ribbons that close upon themselves. We shall see that the most natural interpretation of these spectra is in terms of effective magnetic flux quanta passing through the rings. This "effective time-reversal symmetry breaking" is distinct from *real* time reversal symmetry breaking, which would occur if a genuine magnetic field were present. Instead, the effective field points in opposite directions for two classes of wavefunctions which we will describe, so that as a whole the system preserves time-reversal symmetry.

One of the more dramatic effects of the spinor structure of the graphene wavefunctions is known as the Klein paradox [2]. When massless Dirac particles impinge normally upon a sharp potential barrier, rather than reflecting as would be the case for a Schrödinger particle, the particles are transmitted. The simple explanation for this is that reflection involves a 180° rotation of the spinor wavefunction, yielding a state completely orthogonal to the incident one, so that there is no amplitude for backscattering. One can generalize this physics to a series of barriers and wells – a superlattice potential – and reach the expectation that electrons in graphene should pass unimpeded through such a structure. For normal incidence this turns out to be true, and this is reflected in a velocity along the superlattice axis that is the same as if no potential were present. However, *perpendicular* to the superlattice axis, the velocity is degraded as the superlattice potential is turned on, and is even inverted beyond a critical value of the potential. The meaning of this inversion is that new Dirac points are generated. In principle, many such Dirac points can be induced, and we shall see that there is a clear signature in transport for the "birth" of these Dirac points.

10.1 Graphene Ribbons

We begin our discussion of graphene rings with the components from which they are constructed, graphene ribbons. Our first goal in this context is to show that one can understand both the electronic spectra and the wavefunctions produced by microscopic tight-binding calculations using the simpler Dirac equation [3].

10.1.1 Hamiltonian

As mentioned above, the carbon atoms in graphene form a honeycomb structure, whose primitive lattice vectors may be written as $\mathbf{a} = a_0(1, 0)$ and $\mathbf{b} = a_0(1/2, \sqrt{3}/2)$. Each unit cell contains two atoms (the two sublattices), denoted by A and B, located at $(0, 0)$ and at $\mathbf{d} = a_0(0, 1/\sqrt{3})$. In the simplest model, bands formed from the sp^2 orbitals, which create the backbone covalent bonding in graphene, are assumed to be filled and inert. Mobile electron move in the plane by hopping among the p_z orbitals of the carbon atoms. If we allow only nearest neighbor hopping of amplitude t between the p_z orbitals, one obtains an electronic spectrum with Dirac points at the six corners of the Brillouin zone. Only two of these are inequivalent, and their positions in the Brillouin zone may be written as $\mathbf{K} = \frac{2\pi}{a_0}(\frac{1}{3}, \frac{1}{\sqrt{3}})$ and $\mathbf{K}' = \frac{2\pi}{a_0}(-\frac{1}{3}, \frac{1}{\sqrt{3}})$. Because we are interested in the low-energy states near these points, it is appropriate to adopt the $\mathbf{k}\cdot\mathbf{P}$ approximation [4, 5]. In this approach, wavefunctions are expressed in terms of envelope functions $[\psi_A(\mathbf{r}), \psi_B(\mathbf{r})]$ and $[\psi'_A(\mathbf{r}), \psi'_B(\mathbf{r})]$ which multiply the states at the $\mathbf{K}$ and $\mathbf{K}'$ points, respectively. The envelope functions may be combined into a 4-vector $\Psi = (\psi_A, \psi_B, -\psi'_A, -\psi'_B)$ [6], which satisfies a Dirac equation $H\Psi = \varepsilon\Psi$, with

$$H = \gamma a_0 \begin{pmatrix} 0 & -k_x + ik_y & 0 & 0 \\ -k_x - ik_y & 0 & 0 & 0 \\ 0 & 0 & 0 & k_x + ik_y \\ 0 & 0 & k_x - ik_y & 0 \end{pmatrix}, \tag{10.1}$$

where $\gamma = \sqrt{3}t/2$. Note that $\mathbf{k}$ denotes the separation in reciprocal space of the wavefunction from the $\mathbf{K}$ ($\mathbf{K}'$) point in the upper left (lower right) block of the Hamiltonian.

It should be noted that this description is appropriate only at low energies, well below the scale of γa_0, which is of the order of 2 eV. For Fermi energies at this scale, one needs to use the more basic tight-binding description, and the Dirac physics which is crucial to the physics that we discuss below becomes largely irrelevant. For undoped graphene the Fermi energy is well away from these energy scales, and the description in terms of the Dirac Hamiltonian should work relatively well.

The bulk solutions of Hamiltonian (10.1) are well known [4]. The eigenstates retain their valley index as a good quantum number and the wavefunctions, with energies $\varepsilon = \pm\gamma a_0|\mathbf{k}|$, may be written as $[e^{i\mathbf{kr}}e^{-i\theta_\mathbf{k}/2}, \mp e^{i\mathbf{kr}}e^{i\theta_\mathbf{k}/2}, 0, 0]$ for the **K** valley , and $[0, 0, e^{i\mathbf{kr}}e^{i\theta_\mathbf{k}/2}, \pm e^{i\mathbf{kr}}e^{-i\theta_\mathbf{k}/2}]$ for the $\mathbf{K}'$ valley. Here, $\theta_\mathbf{k} = \tan^{-1} k_x/k_y$.

10.1.2 Zigzag Nanoribbons

Zigzag edges of a graphene nanoribbon are illustrated on the top and bottom edges of Fig. 10.1. Notice that the atoms at each edge are of the same sublattice (A on the top edge of Fig. 10.1 and B on the bottom edge). In Fig. 10.1, we also show a unit cell needed in a tight-binding calculation for zigzag ribbons, containing $N/2$ A-type atoms that alternate along the unit cell with $N/2$ B-type atoms. The total width of the nanoribbon is $L = \frac{N}{4}\sqrt{3}\,a_0$. We impose periodic boundary conditions along the direction parallel to the edge, so that in effect our geometry is a short, fat nanotube. To be concrete, we will assume that the edges lie along the $\hat{y}$ direction, so in the discussion of the zigzag nanoribbons, the coordinate axes in Fig. 10.1 are rotated by 90^0, and the eigenstates are proportional to e^{iky}. In Fig. 10.2, we plot an example of the electronic spectrum of a nanoribbon with zigzag edges. These represent confined electrons states of the nanoribbon, with energies near the Dirac point. Figure 10.3 illustrates the energy of the first three of these states, near $k = K_y$, as a function of the nanoribbon width.

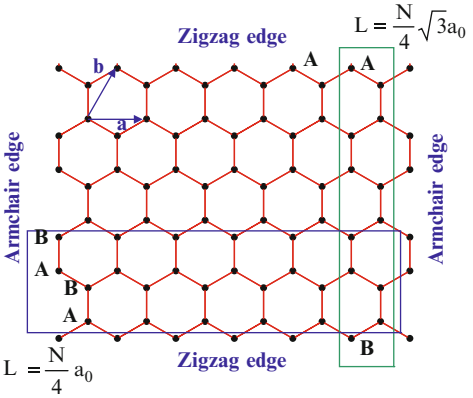

Fig. 10.1 The lattice structure of a graphene sheet. The primitive lattice vectors are denoted by **a** and **b**. Top and bottom are zigzag edges, left and right are armchair edges. Atoms enclosed in the vertical (horizontal) rectangle represent the unit cell used in the calculation of nanoribbons with zigzag (armchair) edges. The length of the nanoribbons, L, as function of the number of atoms, N, in the unit cell is also indicated

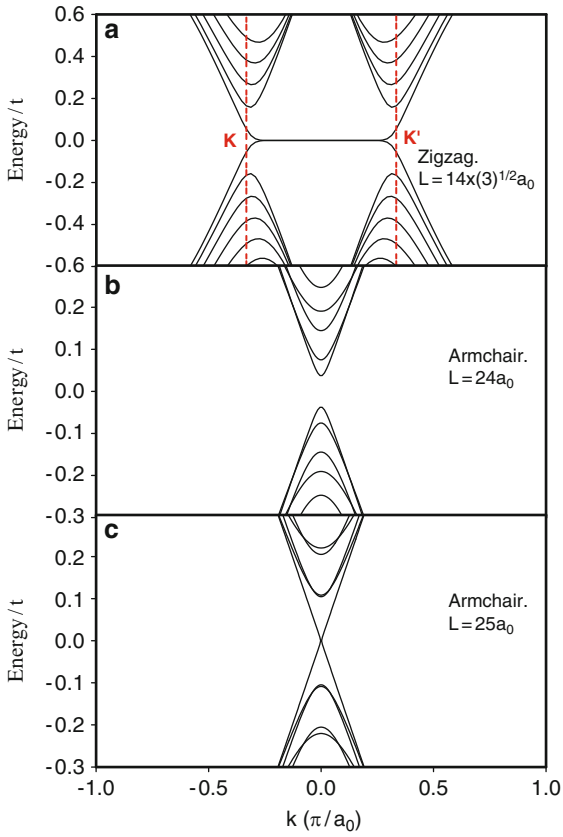

Fig. 10.2 Examples of energy bands for a graphene nanoribbon with periodic boundary conditions in one direction. k is the wavevector parallel to the nanoribbon edge, measured with respect the center of the Brillouin center. (**a**) Ribbon terminated in zigzag edges with 56 atoms in the unit cell. The dispersionless states correspond to confined surface states. The band structures of insulating and metallic armchair nanoribbons are plotted in (**b**) and (**c**) respectively

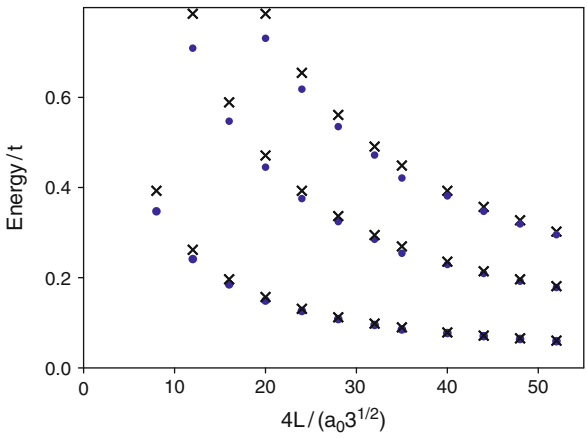

Fig. 10.3 Calculated confined state energies at a Dirac point versus the nanoribbon width, in a zigzag nanoribbon. The dots are tight binding results, and the crosses are the results of the $\mathbf{k} \cdot \mathbf{P}$ approximation

The two bands of nearly dispersionless localized surface states connecting the regions near the K_y and K'_y which are apparent in Fig. 10.2a are a well-known feature of zigzag graphene ribbons [7]. These have a very interesting property that in these electric subbands, near the **K** point we have only $\partial\varepsilon/\partial k_y < 0$ for positive energy states, and near the $\mathbf{K}'$ the derivative has the opposite sign. This means currents in this electric subband are *chiral*: currents in a particular direction along the ribbon are associated with one valley or the other.

The dependence of the electronic states on the width of the nanoribbon may be understood in terms of eigenstates of the Dirac Hamiltonian with appropriate boundary conditions: setting the wavefunction to zero on the A sublattice on one edge, and on the B sublattice for the other. We can understand the lines of vanishing wavefunction to be lattice sites that would lie just beyond the edges if bonds had not been cut to form them.

For the continuum description, we begin by rotating the wavevectors in (10.1), $k_x \to k_y$, $k_y \to -k_x$ so that the zigzag edge lies along the $\hat{y}$, and the domain of the wavefunctions is $0 < x < L$. Translational invariance in the $\hat{y}$ direction guarantees they can be written in the form $\psi_\mu(')(\mathbf{r}) = e^{ik_y y}\phi_\mu(')(x)$. [Note that the primes (′) here and in what follows refers to wavefunctions near the $\mathbf{K}'$ point, not to differentiation of the function.] To find wavefunctions for a system with edges, we make the replacement $k_x \to -i\,\partial_x$ in (10.1) (after the rotation). By acting on the spinor state twice with the Hamiltonian, one easily finds for the **K** ($\mathbf{K}'$) valley that the wavefunctions obey

$$\begin{aligned}\left(-\partial_x^2 + k_y^2\right)\phi_B(') &= \tilde{\varepsilon}^2\phi_A(') \\ \left(-\partial_x^2 + k_y^2\right)\phi_A(') &= \tilde{\varepsilon}^2\phi_B(')\end{aligned} \tag{10.2}$$

with $\tilde{\varepsilon} = \varepsilon/(\gamma a_0)$. The general solutions of (10.2) have the form

$$\phi_\mu(x) = Ae^{zx} + Be^{-zx}\ , \tag{10.3}$$

with $z = \sqrt{k_y^2 - \tilde{\varepsilon}^2}$, which can be real or imaginary.

For the zigzag nanoribbon, we meet the boundary condition for each type of wavefunction separately:

$$\phi_A(x=0) = \phi'_A(x=0) = \phi_B(x=L) = \phi'_B(x=L) = 0\ . \tag{10.4}$$

Notice this means we may obtain solutions for the **K** and $\mathbf{K}'$ valleys separately; the boundary conditions do not introduce valley mixing. These conditions leads to a transcendental equation for the allowed values of z,

$$\frac{k_y - z}{k_y + z} = e^{-2Lz}\ . \tag{10.5}$$

Equation (10.5) supports solutions with real values of $z \equiv k$ for $k_y > k_y^c = 1/L$, which correspond to the surface states. These have energies $\pm\sqrt{k_y^2 - k^2}$, and are linear combinations of states localized on the left and right edges of the ribbon. For large values of k_y, $k \to k_y$ and the surface states become decoupled. For $k_y < 0$, there are no states with real z that can meet the boundary conditions, so surface states are absent. For values of k_y in the range $0 < k_y < k_y^c$, the surface states are so strongly admixed that they are indistinguishable from confined states.

For pure imaginary $z = ik_n$, the transcendental equation becomes

$$k_y = \frac{k_n}{\tan(k_n L)} \ , \tag{10.6}$$

so that each solution k_n has two confined states with energies $\tilde{\varepsilon} = \pm\sqrt{k_n^2 + k_y^2}$ and wavefunctions

$$\begin{pmatrix} \phi_A \\ \phi_B \end{pmatrix} = \begin{pmatrix} \sin(k_n x) \\ \pm\frac{i}{\tilde{\varepsilon}}(-k_n \cos(k_n x) + k_y \sin(k_n x)) \end{pmatrix} \ . \tag{10.7}$$

How quantitative are the results of our Dirac equation analysis when compared with the microscopic tight-binding results? Fig. 10.3 compares the energies of the three lowest confined states of a zigzag nanoribbon as a function of its width, as computed both in the tight-binding approach [8] and using the Dirac equation. It is apparent that the two approaches match quite well, even for rather small widths ($\sim$35Å).

In Fig. 10.4, we plot the squared wavefunction for the lowest energy state of a zigzag nanoribbon as obtained in the tight binding approach. Figure 10.4a corresponds to $k_y = 0$ ($k = -2\pi/3a_0$ with respect the center of the Brillouin zone), and Fig. 10.4b to $k_y = 0.02 \times 2\pi/3a_0$. The first case corresponds to a nodeless confined state, and we find the wavefunction is described nearly perfectly by (10.7), whereas the second case is the expected linear combination of surface state wavefunctions that decay exponentially from the edges as $\exp(-kx)$. Note also that the wavefunctions vary very smoothly on the scale of the lattice constant, indicating that valley mixing is negligible for these wavefunctions [9]. This contrasts strongly with the case of nanoribbons with armchair edges.

10.1.3 Armchair Nanoribbons

The geometry for an armchair edge nanoribbon is illustrated on the left and right edges of Fig. 10.1, along with the unit cell used in the corresponding tight-binding calculations. In this orientation, the width of the nanoribbon is related to the number of atoms in the unit cell through the expression $L = \frac{N}{4}\, a_0$. Here, the edge runs along the $\hat{y}$ direction, and no rotation of the figure is needed to represent our calculations.

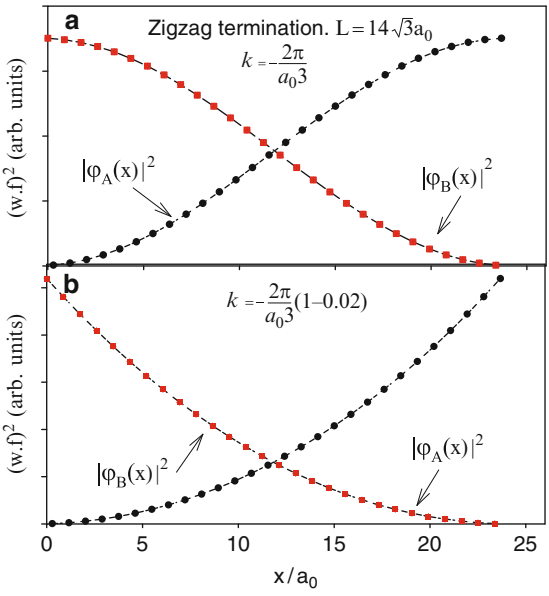

Fig. 10.4 Squared wavefunction for the state closest to zero energy for a zigzag nanoribbon, as obtained from tight binding calculations. The width of the ribbon is $L = 14\sqrt{3}a_0$. (**a**) $k = -2\pi/3a_0$, and (**b**) $k = (-2\pi/3a_0)(1 - 0.02)$. Both are measured from the center of the Brillouin zone

The electronic spectra of armchair nanoribbons have a rather different width dependence than we find in the zigzag case. Figure 10.2b and c illustrates two examples of spectra for armchair nanoribbons of different width. One sees that in the latter figure there is a Dirac point, leading to metallic behavior for an undoped ribbon whereas the former is a band insulator. In general, we find that armchair nanoribbons of width $L = (3M + 1)a_0$, with M integral, are metallic, whereas all the other cases are insulators. The energy of the confined states also behave in a discontinuous way with respect to the width of the ribbon. In Fig. 10.5, we plot the energy of the lowest positive energy confined states at the center of the Brillouin zone as a function of the nanoribbon width. In the inset of this figure, we see that the separation in energy between confined states is also strongly dependent on the number of atoms in the unit cell.

As in the case of the zigzag nanoribbons, this behavior may be understood in terms of eigenstates of the Dirac Hamiltonian with the correct boundary conditions. In Fig. 10.1, one may see that the termination consists of a line of A–B dimers, so it is natural to have the wavefunction amplitude vanish on both sublattices at $x = 0$ and $x = L + a_0/2$. To do this, we must admix valleys, and require

$$\phi_\mu(x = 0) = \phi'_\mu(x = 0)$$

$$\phi_\mu(x = L + a_0/2) = \phi'_\mu(x = L + a_0/2)\, e^{i\Delta K\,(L + \frac{a_0}{2})}\ ,$$

with $\Delta K = \frac{4\pi}{3a_0}$. The $a_0/2$ offset in the boundary condition on the right is appropriate because the two leftmost atoms in the ribbon unit cell are $L + a_0/2$

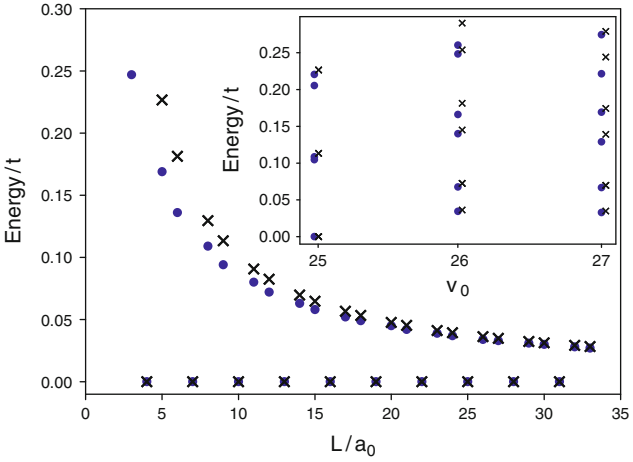

Fig. 10.5 Calculated lowest energy confined states at the center of the Brillouin zone versus the nanoribbon width, for an armchair nanoribbon. The dots correspond to the tight binding results and the crosses are the results of the $\mathbf{k} \cdot \mathbf{P}$ approximation. In the inset, we plot the six lowest energy confined states for three different widths. The Dirac equation results are slightly shifted to the right for clarity. Note that the for $L = 25a_0$ the Dirac equation results are doubly degenerate

to the left of the two rightmost atoms (see Fig. 1.) With these boundary conditions the general solutions of the Dirac equation are plane waves,

$$\phi_B(x) = e^{ik_n x} \quad \text{and} \quad \phi'_B(x) = e^{-ik_n x}. \tag{10.8}$$

The wavevector k_n satisfies the condition

$$e^{2ik_n(L+a_0/2)} = e^{i\Delta K\,(L+a_0/2)}\ , \tag{10.9}$$

so that

$$\left(k_n - \frac{2\pi}{3}\right)(2L + a_0) = 2\pi n \tag{10.10}$$

with n an integer. Thus for armchair nanoribbons the allowed values of k_n are

$$k_n = \frac{2\pi n}{2L + a_0} + \frac{2\pi}{3a_0}, \tag{10.11}$$

with energies $\pm\sqrt{k_n^2 + k_y^2}$. Note that, in contrast to the zigzag nanoribbon case, the allowed values of k_n are independent of k_y. For a width of the form $L = (3M+1)a_0$, the allowed values of k_n, $k_n = \frac{2\pi}{3a_0}\left(\frac{2M+1+n}{2M+1}\right)$, create doubly degenerate states for $|2M + 1 + n| \geq 0$, and allow a zero energy state when $k_y \to 0$. Nanoribbons of widths that are not of this form have nondegenerate states and do not include a zero energy mode. The quality of the Dirac equation approach for describing the electronic states of armchair nanoribbons is reflected in Fig. 10.5 where the energies

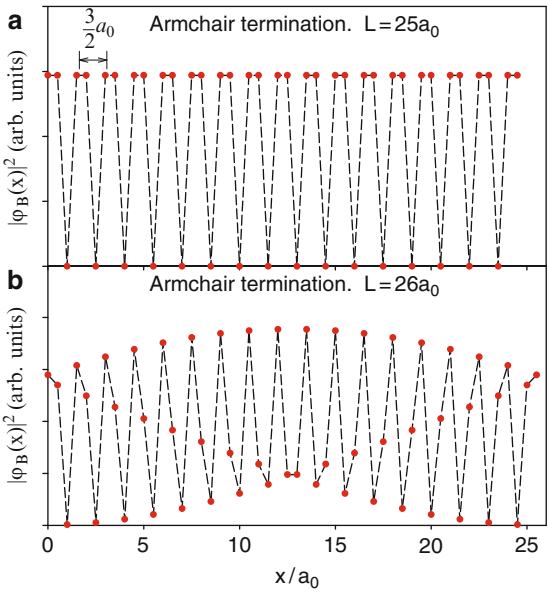

Fig. 10.6 Squared wavefunction of the state with energy closest to zero for an armchair ribbon of width (**a**) $L = 25a_0$ and (**b**) $L = 26a_0$, as obtained from tight binding calculations

of the confined states obtained by diagonalizing the tight binding Hamiltonian and by solving (10.11) are compared. The quantitative agreement is apparent for all but the narrowest ribbons.

The admixing of different valley states to meet the boundary condition means that the wavefunction will oscillate with period $2\pi/\Delta K$ [6]. This behavior can explicitly be seen in Fig. 10.6, which illustrates the squared wavefunction from the tight binding calculation. The short oscillation in the wavefunctions has exactly the period expected for the valley mixing we introduced to meet the boundary conditions.

10.2 Graphene Quantum Rings

Quantum rings of metal or semiconducting materials have been studied over the years as a one of the simplest mesoscopic systems in which quantum effects play an important role [10]. For simple one dimensional rings, since these systems close upon themselves, the wavefunctions must accumulate an integral number of wavelengths as one goes around the ring. For a ring of circumference L, this means the allowed wavefunctions have allowed momenta $p = 2\pi n/L$ (in units where $\hbar = 1$) for n integer, and there are discrete allowed energy states of the form $E_n = (2\pi n)^2/2mL^2$, where m is the electron effective mass. When magnetic flux passes through the ring, this spectrum is shifted to values of the form $E_n(\Phi) = [2\pi(n + \Phi/\Phi_0)]^2/2mL^2$, where $\Phi = BA$ is the magnetic flux

through the ring hole of area A, and $\Phi_0 = hc/e$ is the magnetic flux quantum. Notice for $\Phi = 0$ (or, equivalently, any integer), there is a state of zero energy, but for Φ/Φ_0 noninteger a gap opens between zero energy and the lowest (positive) energy state. The periodicity of the spectrum with respect to enclosed magnetic flux implies that the magnetization of the ring will vary periodically with field, with a period reflecting the area enclosed by the ring. One can learn about the spectra of these systems by measuring this Aharonov–Bohm effect in the magnetic response to an external magnetic field, for a single ring or a collection of them.

In real ring structures, there are many important details not captured by the simple one-dimensional picture, including effects of disorder and interactions, coupling to external degrees of freedom, and effects associated with the shapes of the rings. This more complicated physics has kept this system an active field of study.

Very recently, graphene rings have joined this general area of study. One can imagine forming graphene rings in several ways. For example, graphene ribbons may be closed into very short nanotubes; while relatively simple, the boundaries of these have spectra which depend on how the honeycomb network is terminated at the edges of the tube [11, 12]. Tight-binding descriptions of flat graphene rings involve both different edge terminations and corner geometries [15–18], with results that are sensitive to both. Rather than use a direct tight-binding description, an alternate approach is to employ the Dirac equation and solve for the wavefunctions with an appropriate set of boundary conditions [13]. In such studies, the choice of boundary conditions is crucial in determining the details of the spectrum. The simplest of these involve "infinite mass boundary conditions" [14] or zigzag boundary conditions [3, 6], neither of which involves mixing of valleys, allowing for an interpretation of the spectra in terms of individual Dirac cones [15]. Related problems of graphene rings joined together to form an antidot superlattice have also been considered [19]. Some recent experimental studies have recently been published [20, 21] in which Aharonov–Bohm oscillations in graphene rings are reported. This demonstrates that large enough phase coherence lengths may be reached to allow quantum coherence effects to be observed, although current sample geometries are not sufficiently controlled to allow direct comparison with the theoretical studies of idealized models.

10.2.1 Chirality in Armchair Nanoribbons

In Sect. 10.1.2, we saw that currents in different directions in the lowest subband of a zigzag nanoribbon are associated with different valleys, and are in this sense chiral. Because armchair nanoribbon states involve admixtures of states from different valleys, it is clear that precisely the same effect cannot be present in this type of ribbon. However, as we describe more carefully below, states in the lowest (positive energy) electric subband of metallic armchair ribbons do in fact possess a chirality, although the symmetry involved is more subtle: it involves an interchange of both the sublattice and valley indices of the electrons [22]. The existence of such a

quantum number turns out to have very interesting consequences for graphene rings constructed from armchair nanoribbons.

An important property of armchair ribbons that make them particularly interesting to consider in the context of rings is that 60° corner junctions may be constructed from such ribbons [23] which are perfectly transmitting at low energy. As mentioned in the introduction, such a situation – where there is no backscattering in the ring – in conventional metallic or semiconducting rings would yield a zero energy state in the spectrum. The graphene junctions, however, introduce a phase shift as electrons pass through them, with a resulting spectrum that looks much like magnetic flux has been thread through the ring. This "effective time-reversal symmetry breaking" (ETRSB) is a hallmark of the Dirac equation that governs the electron dynamics at low energy.

The relevant symmetry in this problem can be characterized in terms of a 4×4 matrix,

$$T = \begin{pmatrix} 0 & 0 & 0 & i \\ 0 & 0 & -i & 0 \\ 0 & i & 0 & 0 \\ -i & 0 & 0 & 0 \end{pmatrix}, \tag{10.12}$$

which acts on the electron wavefunctions in the ribbon represented by 4-vectors, $\mathbf{\Psi}_{p_n,p_y} = (\Phi^{A,\mathbf{K}}, \Phi^{B,\mathbf{K}}, \Phi^{A,\mathbf{K}'}, \Phi^{B,\mathbf{K}'})$. (Note that in this discussion it is convenient to define the vectors without a minus sign in the second two entries, as was the case in Sect. 10.1.1.) The quantum number p_n is a transverse momentum characterizing the electron subband, and p_y is the momentum along the ribbon. One may easily confirm that T commutes with the Hamiltonian, and the armchair boundary condition respects this symmetry as well [22]. In general, one must admix wavefunctions with positive and negative values of p_n to construct eigenstates of T; however, the $p_n = 0$ subband is special in that $\mathbf{\Psi}_{p_n=0,p_y}$ is an eigenstate of T. In this case one finds

$$T\mathbf{\Psi}_{0,p_y} = sgn(\varepsilon)sgn(p_y)\mathbf{\Psi}_{0,p_y}, \tag{10.13}$$

where $sgn(\varepsilon)$ is the sign of ε. Thus, for metallic nanoribbons the eigenvalue of T in the lowest subband ($p_n = 0$) is tied to the direction of current $sgn(p_y)$, in a way that is highly analogous to the connection between current direction and valley index for zigzag nanoribbons, with the eigenvalue of T playing the role of valley index.

10.2.2 Phase Jumps at Corner Junctions

Figure 10.7a illustrates a typical armchair graphene ring which implements the interesting properties discussed above. An important property of the corner junctions in this geometry is that, in addition to perfectly transmitting at low energy, they induce a phase jump in the wavefunctions as an electron passes through them. This

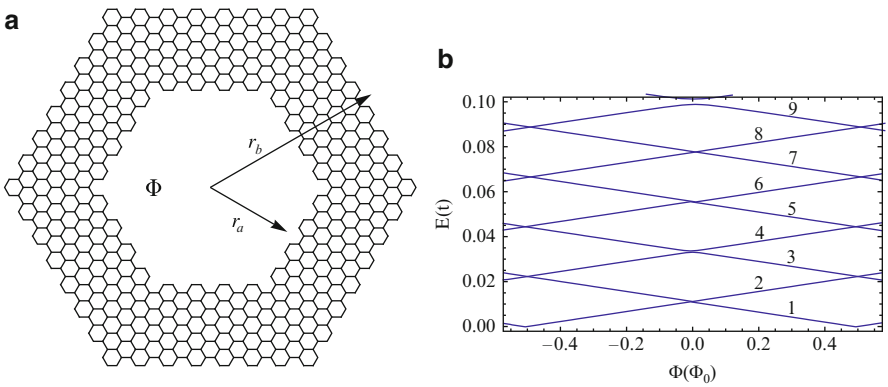

Fig. 10.7 Armchair hexagonal ring. (**a**) Illustration of a ring with inner radius r_a, outer radius r_b, and flux Φ passing through the hole. (**b**) Energy spectrum near $E = 0$ in units of the hopping matrix element t, for $E > 0$. For this ring the spectrum is particle-hole symmetric, and $r_a = 32.5a$, $r_b = 38.5a$. Integers label the energy levels

can be demonstrated explicitly by matching wavefunctions in the lowest subband where two arms of armchair ribbon are joined [22]. The result confirms the unit transmission found previously for these junctions [23], and also demonstrates that the wavefunctions jump by a factor of $\pm i$ as one passes through a junction, with the sign determined by the eigenvalue of the T operator defined above.

This phase shift can also be viewed from the continuum perspective. Consider a long metallic armchair nanoribbon segment with its front and back ends identified to form a cylinder, effectively a short, fat nanotube. We may simulate the phase shift associated with the junction by adding a gauge field. With the convention, we have adopted in this section for our wavefunctions, the Hamiltonian has the form ($\hbar = 1$)

$$H(\mathbf{p}) = v_F \begin{pmatrix} 0 & -p_x + ip_y & 0 & 0 \\ -p_x - ip_y & 0 & 0 & 0 \\ 0 & 0 & 0 & p_x + ip_y \\ 0 & 0 & p_x - ip_y & 0 \end{pmatrix}, \tag{10.14}$$

where $p_{x(y)} = \frac{1}{i}\partial_{x(y)}$. Writing $\Psi_{p_n,p_y} = e^{i\chi}\Psi'_{p_n,p_y}$, we can rewrite the Dirac equation for the wavefunctions in the form $H(\mathbf{p} - \mathbf{A})\Psi'_{p_n,p_y} = \varepsilon\Psi'_{p_n,p_y}$, with $\mathbf{A} = \partial_y\chi\,\hat{y}$ and $\chi = \frac{\pi}{2}T\Theta(y)$, where the junction between ribbons is located at $y = 0$. In this representation, Ψ'_{p_n,p_y} is continuous across the junction, and the phase jump is fully implemented by the $e^{i\chi}$ factor.

The presence of the gauge field can be interpreted as being due to a pair of solenoids carrying magnetic flux in opposite directions, one above the plane of the ribbon, the other below. In this way, one can understand the problem of n-sided rings constructed from metallic armchair ribbons with these corner junctions as being the same (near zero energy) as the problem of a ribbon closed into a cylinder (i.e., a

short nanotube), with $2n$ flux tubes, half threaded through in one direction and half just outside it in the other direction. In this way, the system has properties illustrating ETRSB. It is important to recognize that *real* time reversal symmetry is preserved for the system, because the effective flux runs in opposite directions for different eigenvalues of the operator T. As we shall see in detail below, the low energy spectra of such rings as found from solutions of the tight-binding model behave precisely as if these phase jumps are present. The resulting spectra present properties which may be understood as signaling the ETRSB in graphene.

10.2.3 Numerical Results

The simplest ring system one can study using metallic armchair ribbons and the 60° corner junctions discussed above is the hexagonal ring, as illustrated in Fig. 10.7a. The fact that the junctions are perfectly transmitting in the lowest subband might lead one to think that the low energy spectrum is the same as that of a metallic armchair ribbon closed into an cylinder (i.e., a very short carbon nanotube.) If this were the case, one would expect states at zero energy when no external magnetic flux threads the ring. Our discussion above, however, indicates that one needs to include the effective flux passing through the ring to understand the spectrum.

Figure 10.7b is the spectrum obtained from computing the eigenvalues of the tight-binding model near zero energy, as a function of flux Φ through the ring. Note in these calculations we include only the phase factors in the hopping matrix elements due to a solenoid passing through the hole of ring; magnetic flux through the individual plaquettes of the honeycomb lattice is not included. In general, the spectrum in this case is perfectly particle-hole symmetric, so only positive energy states are displayed.

The form of the spectrum is highly reminiscent of what has been seen previously in hexagonal rings with zigzag edges [15]. In particular, it takes the form of two sets of spectra, each with broken time reversal symmetry such that the energies have a particular sign of slope near $\Phi = 0$. The spectra are effectively time reverses of one another so that the spectrum as a whole has time-reversal symmetry; in particular, the spectrum evolves in the same way whether positive or negative flux is threaded through the hole. In the case of zigzag ribbons, the two sets of spectra are associated with the two valleys. In the present case, they are associated with the two eigenvalues of the matrix T. Note that the crossing of the energy states through zero at $\Phi = \pm\Phi_0/2$ may be understood as resulting from the sum of the effective fluxes due to the corner junctions and that of the real field summing to an integral number of flux quanta.

The phase jumps associated with the corners may be demonstrated explicitly by a careful examination of wavefunctions. Figure 10.8 labels a set of sites around the ring, and Fig. 10.9 illustrates the wavefunctions on one of the sublattices for the four lowest positive energy levels at $\Phi = 0$. The jumps in amplitude associated with passing through the corners of the junctions are quite apparent. The amplitudes

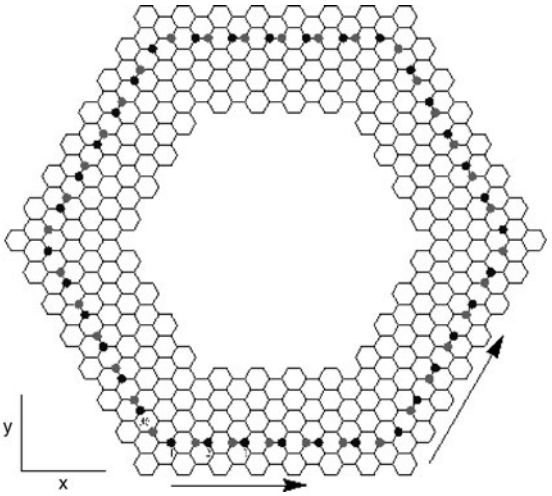

Fig. 10.8 Hexagonal ring illustrating site labels for examination of wavefunction. Black dots indicate sites on A sublattice, gray dots are on B sublattice. The actual ring used in calculations has $r_a = 32.5a$ and $r_b = 38.5a$, with a the lattice constant of the underlying triangular lattice

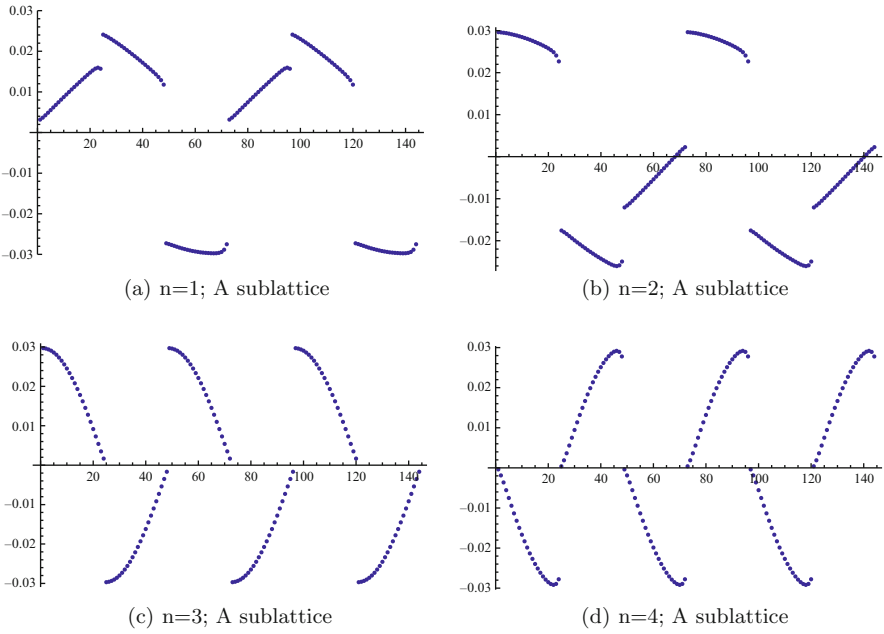

(a) n=1; A sublattice (b) n=2; A sublattice

(c) n=3; A sublattice (d) n=4; A sublattice

Fig. 10.9 Wavefunctions at zero flux Φ for the four lowest eigenstates $n = 1, 2, 3, 4$ illustrated in Fig. 10.7b

in the sides of the ring may be understood as linear combinations of pure plane waves, with momentum $\pm p_y$ along the ribbon directions, yielding purely real wavefunctions. Fits to wavefunctions with well-defined $|p_y|$ and phase jumps of $e^{i\theta_0} = \pm i$ yield excellent results [22]; typical results are presented in Table 10.1,

Table 10.1 Table showing values of p_y, θ_0, and m in formula of form $6(p_y L + \theta_0) = 2\pi m$ used in matching numerically generated wavefunctions with forms expected from wavefunction continuity around a ring (see text)

Energy level	$p_y L$	θ_0	m
1	$\pi/6$	$\pi/2$	2
2	$-\pi/6$	$-\pi/2$	-2
3	$\pi/2$	$\pi/2$	3
4	$-\pi/2$	$-\pi/2$	-3
5	$5\pi/6$	$\pi/2$	4
6	$-5\pi/6$	$-\pi/2$	-4

which shows that the values of p_y may be understood from continuity of the wavefunctions when the phase jumps are included. The results also demonstrate that the sign of the phase jump is determined by the eigenvalue of T.

The presence of six $\pi/2$ phase jumps (due to the six corners of the hexagon) implies that $p_y = 0$ is not an allowed momentum for the electron wavefunction in this type of ring. Thus there is no allowed zero energy state, as would be expected for a metallic ribbon closed into an annulus, and its absence is imposed by the presence of phase factors that are very suggestive of effective magnetic flux threading the ring, as discussed above. Thus the gap in the spectrum around $\varepsilon = 0$ may be interpreted as a signature of ETRSB.

It is interesting to contrast these results with those for a graphene hexagonal ring with zigzag edges [15]. In the latter case, the low energy states are strongly confined to the edges and are highly sensitive to the corner geometry, and there is no apparent analog of the perfect transmission through the corner junctions that one finds in the armchair case [23]. The resulting spectrum near zero energy is gapped, in a way that cannot be closed via magnetic flux through the hole [15]. One can nevertheless understand the spectrum in terms of overlaid spectra from the two valleys. The zigzag ring thus carries some signature for ETRSB, although they are more subtle than in the armchair case discussed here.

One may examine how robust this behavior is with respect to various perturbations of the ring geometry. Figure 10.7b clearly displays level crossings of states with different quantum numbers associated with the sixfold rotational symmetry of the structure. A generic perturbation breaking this symmetry opens small gaps at these crossings, but in most cases does not spoil the basic property that no zero energy state is present when no (real) magnetic flux threads the ring. An important exception is the effect of removing atoms from the corners of the junctions, which in effect introduces a short length of zigzag edge. Such structures induce localized zero energy states [24], which are insensitive to flux (real or effective) through the ring. In general, a collection of rings will have various defects, but one might expect that the energy level statistics of such an ensemble will reflect the tendency for the rings to have a gap at zero energy.

10.3 Graphene in a Periodic Potential

The electronic structure of graphene may also be manipulated by external potentials. Of particular interest are periodic potentials, which in principle allow one to "engineer" the band structure of the system. Moreover, because such potentials can be varied continuously, in principle one can manipulate the system to tailor its conduction properties, opening many possibilities for electronic devices. Much recent work has focused on *pn* junctions as a first realization of such systems [25–28]; some of this is discussed in Chap. 15 below. Periodic potentials may be induced by interaction with a substrate [29–31] or controlled adatom deposition [32]. Recently, the existence of periodic ripples in suspended graphene has been demonstrated [33]; in a perpendicular electric field this would also induce a periodic potential.

A one-dimensional periodic (i.e., superlattice) potential has profound effects on the transport properties of graphene. As described in the introduction, Klein paradox physics dictates that the velocity of electrons along a superlattice axis should be the same as in the absence of the potential, but this is not at all the case perpendicular to it. This creates anisotropy in the electron velocity around the Dirac point which may "collimate" the flow of electrons [34]. The slowing of the electron velocity perpendicular to the superlattice axis, for strong enough potential, or large enough period of the potential, can become so pronounced that the sign of the electron velocity inverts, creating new Dirac points at zero energy in the band structure [35, 36]. The emergence of these new Dirac points turns out to be controlled by the parameter V_0/G_0, where V_0 is the potential amplitude (assumed below to be a cosine below) and $L = 2\pi/G_0$ is the period [35]. The new Dirac points emerge whenever $J_0(\frac{4V_0}{\hbar v_F G_0}) = 0$, where J_0 is a Bessel function and v_F the speed of the Dirac fermions in the absence of the potential. The total number of Dirac points (associated with a single valley and electron spin) is thus $2N+1$, with N the number of zeros of $J_0(x)$, with $|x| < \frac{4V_0}{\hbar v_F G_0}$.

These emerging Dirac points have a clear signature in transport along the superlattice axis: conductance resonances appear at the values of V_0/G_0 where they first appear, as illustrated in Fig. 10.10. Much like undoped graphene, in the limit of large width, the conductance scales as L_y/L_x for most values of V_0/G_0, with L_y the system width and L_x its length. The system behaves diffusively, i.e., is characterized by a conductivity rather than a conductance. This interpretation is consistent with the computed Fano factor, illustrated in Fig. 10.10b. At the resonances, however, the conductance becomes independent of L_x, and the Fano factor indicates a more ballistic-like transport.

10.3.1 Counting Dirac Points

For such periodic structures, one may ascertain analytically how many Dirac points will appear at zero energy. For concreteness, we take our external potential to have

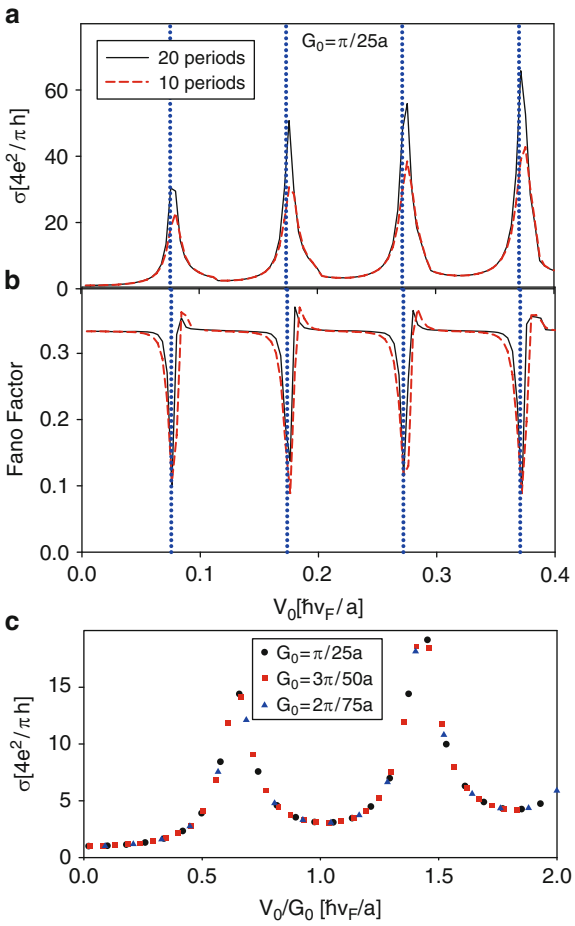

Fig. 10.10 (**a**) Conductivity and (**b**) Fano factor, as function of V_0 and for $G_0 = \pi/25a$, for two different graphene sample lengths containing 10 and 20 periods of the periodic potential $2V_0 \cos G_0 x$. Panel (**c**) shows the conductivity as function of V_0/G_0 as obtained from different superlattices potentials. This result indicates that the conductivity only depends on V_0/G_0

the form $V(x) = 2V_0 \cos G_0 x$. Assuming that $2\pi/G_0$ is large compared to the underlying graphene lattice constant, this potential will be ineffective at mixing valleys, so that we may examine the spectrum for just one of them, and for a single spin species, and recognize that the states coming from the other valley and/or spin will be the same. The massless Dirac Hamiltonian with a potential then takes the form of a 2×2 matrix,

$$H = \hbar v_F(-i\sigma_x \partial_x + k_y \sigma_y) + V(x)\mathcal{I}, \tag{10.15}$$

where $\sigma_{x,y}$ are the Pauli matrices, and $\mathcal{I}$ is the identity matrix. The corresponding wavefunctions which this acts upon has two components, $\Phi_{A,B}$, which we assume has k_y has a good quantum number.

A unitary transformation [35,37] allows the Hamiltonian to be recast in the form

$$H' = \hbar v_F \begin{pmatrix} -i\partial_x & -ik_y e^{i\alpha(x)} \\ ik_y e^{-i\alpha(x)} & i\partial_x \end{pmatrix}, \tag{10.16}$$

where $e^{i\alpha(x)} = \sum_{l=-\infty}^{l=\infty} J_l(\frac{4V_0}{\hbar v_F G_0}) e^{ilG_0 x}$, and J_n is the n-th Bessel function of the first kind. Dirac points at zero energy must satisfy $H'\phi = 0$; such solutions have the property $\phi_A = \phi_B^*$. Writing $\phi_A = |\phi_A| e^{i\chi}$, one obtains equations for χ and $|\phi_A|$ [35]

$$k_y \sin(\alpha - 2\chi) + \partial_x \chi = 0, \tag{10.17}$$

$$|\phi_A| \propto \exp\left\{-k_y \int_{x_0}^{x} \cos[\alpha(x') - 2\chi(x')] dx'\right\}. \tag{10.18}$$

Since ϕ is a Bloch state of the superlattice, it must obey the Bloch relation $\phi_{A,B}(x + L_0) = e^{ik_x L_0} \phi_{A,B}(x)$, with k_x the crystal momentum. For a zero energy state, only $k_x = 0$ is possible. We then require (i) $\chi(x + L_0) = \chi(x) + 2\pi m$ with m an integer, and (ii) $\int_0^{L_0} \cos[\alpha(x) - 2\chi(x)] = 0$. To see whether χ can satisfy these relations, it is helpful to recast (10.17) by writing $\tilde{\chi} = 2\chi - \alpha$, and $x \to t$, so that

$$-\partial_t \tilde{\chi} - \partial_t \alpha + 2k_y \sin\tilde{\chi} = 0. \tag{10.19}$$

This is the equation of motion for the position $\tilde{\chi}$ of an overdamped particle (with unit viscosity), subject to a periodic time-dependent force $\partial_t \alpha$ and a spatially periodic force $2k_y \sin\tilde{\chi}$. Despite the periodicity of the forces involved, the generic solution to this equation is not periodic. However, for certain parameters periodic solutions can be found, which correspond to allowed zero energy solutions of the Dirac equation in a periodic potential.

Equation (10.17) is nonlinear and an analytic solution is not readily available. However, one may generate approximate solutions perturbatively in k_y. Writing $\chi = k_y \chi^{(1)} + k_y^2 \chi^{(2)} + \mathcal{O}(k_y^3)$, one finds

$$\chi^{(1)} = -\int^x dx' \sin\alpha(x') + C^{(1)}$$

and

$$\chi^{(2)} = 2C^{(1)} \int^x dx_1 \cos\alpha(x_1) - 2\int^x dx_1 \cos\alpha(x_1) \int^{x_1} dx_2 \sin\alpha(x_2) + C^{(2)},$$

where $C^{(1,2)}$ are constants of integration. Explicitly performing the integrations for the above two equations, one finds that condition (i) can be satisfied if

$$k_y^2 J_0 \left[2C^{(1)} L_0 - \sum_{\ell\, odd} \frac{J_\ell}{\ell G_0} L_0\right] = 2\pi m. \tag{10.20}$$

Here, J_0 and J_ℓ are Bessel functions evaluated at $4V_0/\hbar v_F G_0$. Since we have employed a small k_y expansion, the only consistent solution is for $m = 0$. In this case (10.20) fixes $C^{(1)}$, and the resulting χ (and the associated $\tilde{\chi}$) is periodic. Condition (*ii*) may then be implemented to fix a the value of k_y at which a zero mode appears,

$$\left(\frac{k_y}{G_0}\right)^2 = -\frac{J_0}{2\sum_{\ell_1,\ell_2\, odd} J_{\ell_1} J_{\ell_2} J_{-\ell_1-\ell_2}/\ell_1\ell_2}. \tag{10.21}$$

Equation (10.21) predicts the presence of a zero mode whenever the right hand side is positive. This turns out to occur for values of $x = \frac{4V_0}{\hbar v_F G_0}$ just above the values of x where $J_0(x) = 0$; the sign of the denominator on the right hand side of (10.21) always works out such that $k_y^2 > 0$ in this situation. With increasing x, the solution moves to larger $|k_y|$ until it diverges where the three Bessel function sum vanishes, which is always prior the next zero of $J_0(x)$. We note that since our approximation is only valid for small k_y, (10.21) cannot accurately predict the location of the zero energy states well away from $k_y = 0$. However, since zero energy states can only annihilate in pairs, once they emerge from the origin they should persist. This expectation is born out by numerical studies, which we describe next.

10.3.2 Numerical Solutions of the Dirac Equation

Our expectations about the new zero energy states can be directly confirmed by numerically solving the Dirac equation in a periodic potential. To accomplish this, we represent the Hamiltonian $H = H_0 + 2V_0 \cos G_0 x$ in a plane wave basis and diagonalize the resulting matrix for momenta (k_x, k_y), with $-G_0/2 < k_x < G_0/2$. In Fig. 10.11 we plot, for different values of V_0, the lowest few energy eigenvalues as a function of k_y for $k_x = 0$ and a superlattice potential of period $50a$, where a is the lattice constant for pure graphene. As V_0 increases the group velocity at the Dirac point decreases to zero, and therafter two zero energy states emerge from $k_y = 0$ as the group velocity of the $k_y = 0$ Dirac point becomes finite again. These are the new zero energy states discussed above; we find that they emerge precisely when $J_0(\frac{4V_0}{\hbar v_F G_0}) = 0$. Upon further increase of V_0, the group velocity along k_x at $k_y = 0$ becomes zero again and a new pair of zero energy states emerge from $k_y = 0$, again precisely at the next zero of $J_0(\frac{4V_0}{\hbar v_F G_0}) = 0$. This pattern continues to repeat itself with increasing V_0. Further studies for different periodicities confirms the prediction that the emergence of these points depends only on the ratio V_0/G_0, precisely as discussed in the previous section.

10.3.3 Conductivity

Using transfer matrices, one may compute the conductivity through a graphene strip of length L_x, containing N_p periods of the superlattice potential. Boundary

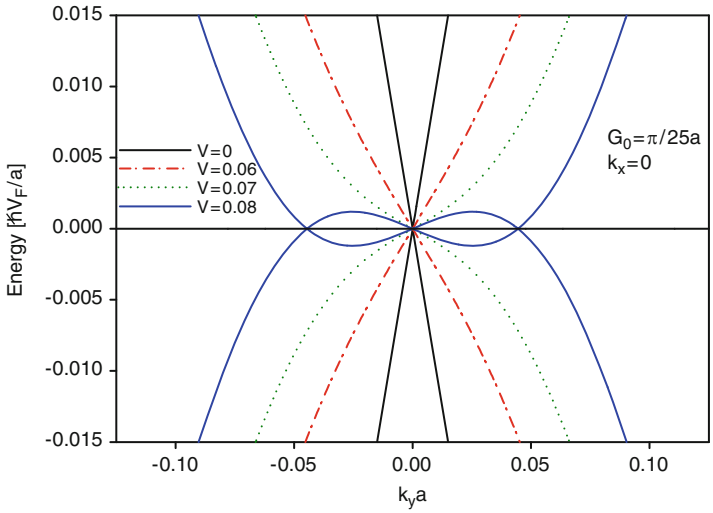

Fig. 10.11 Energy bands of graphene in presence of a superlattice potential $2V_0 \cos G_0 x$, as function of k_y with k_x=0, for several values of V_0 and $G_0 = \pi/25a$

conditions are taken to be periodic in the transverse direction, leading to transverse wavefunctions labeled by a momentum k_y; this is justified when the width of the strip, L_y, is much larger than its length. From the transmission probability of each mode, T_{k_y}, we obtain the conductance G and the Fano factor (ratio of noise power and mean current),

$$G = 4\frac{e^2}{h}\sum_{k_y} T_{k_y}, \quad F = \frac{\sum_{k_y} T_{k_y}(1 - T_{k_y})}{\sum_{k_y} T_{k_y}}, \tag{10.22}$$

where the factor 4 accounts for the spin and valley degeneracy. The conductivity is related to the conductance via geometrical factors, $\sigma = G \times L_y/L_x$. In what follows, we work in the limit $L_y >> L_x$.

For pristine graphene, $V_0 = 0$, the conductivity is independent of L_x and takes the value $\sigma_0 = 4e^2/\pi h$, and the Fano factor takes on the universal value 1/3. This latter value is consistent with the apparent diffusive behavior of pure, undoped graphene [38], as discussed in more detail below in Chap. 13. Figure 10.10 shows the conductivity and the Fano factor as a function of V_0, for two graphene strips, respectively containing 10 and 20 periods of a potential of the form $2V_0 \cos G_0 x$, where $G_0 = \pi/50a$. For finite values of V_0, apart from some resonances, the system behaves diffusively ($F = 1/3$) and the conductivity is well-defined. Interestingly, between the peaks the overall scale increases with V_0, showing that the periodic potential tends to enhance the conductivity.

At certain values of V_0, one observes peaks in the conductance, for which the conductivity is not well-defined and the Fano factor tends to zero. These resonances

occur precisely whenever new zero energy states emerge from the origin in $k-$space, and represent a direct experimental signature of their presence. We believe the resonances occur because the group velocity vanishes when a zero energy state emerges, leading to a strong enhancement of the density of states. A further check that the resonances are associated with the zero energy states is to see that they depend on the ratio V_0/G_0; Fig. 10.10c demonstrates that this is the case not just for the resonances but for the entire conductance curve.

10.4 Conclusion

In this chapter, we have reviewed some recent progress in understanding nanostructured graphene, particularly when those structures involve some form of periodicity. Our first step was to show that the spectra and eigenstates of electrons in graphene nanoribbons can be understood quantitatively from a continuum description, the Dirac equation. The results showed that currents are generically chiral in the lowest positive energy subbands of such systems, with interesting consequences. Graphene quantum rings constructed from armchair ribbons were shown to offer a signature of effective time reversal symmetry breaking that is unique to the low energy physics of graphene: for appropriately chosen corner geometries, the spectra are gapped at zero energy even when the ribbons from which they are constructed themselves are not. This behavior may be naturally understood in terms of effective flux quanta enclosed by the ring, with direction correlated with the direction of current carried by a given wavefunction. Graphene in a periodic superlattice potential offers the possibility of band gap engineering, in an in-principle controllable way: the number of Dirac points at zero energy is controlled by the period and magnitude of the external potential. Appearances of these new Dirac points are accompanied by resonances in the conductance of the system. Clearly, graphene offers a new environment in which electronic properties may be tailored by nanoscale lithography and electric fields, yielding behaviors with no analog in conventional low dimensional electron systems. There is much yet to be explored in this class of problems and systems, with potential for further unique behaviors and device applications.

Acknowledgements The authors would like to thank many colleagues for collaborations and discussions related to this work. These include A.P. Iyengar, Tianhuan Luo, D. Arovas, and K. Ziegler. Funding for the work described here was provided by the MEC-Spain via Grant No. FIS2009-08744 (LB), and by the NSF through Grant No. DMR-0704033 (HAF).

References

1. E. Akkermans, G. Montambaux, *Mesoscopic Physics of Electrons and Photons*, (Cambridge, New York, 2007).
2. F. Schwabl, *Advanced Quantum Mechanics*, (Springer, Heidelberg, 2008)

3. L. Brey, H.A. Fertig, Phys. Rev. B **73**, 235411 (2006)
4. T. Ando, J. Phys. Soc. Jpn. **74**, 777 (2005)
5. D.P. DiVincenzo, E.J. Mele, Phys. Rev. B **29**, 1685 (1984)
6. L. Brey, H.A. Fertig, Phys. Rev. B **73**, 195408 (2006)
7. M. Fujita et al., J. Phys. Soc. Jpn. **65**, 1920 (1996)
8. J.P. Robinson, H. Schomerus, Phys. Rev. B. **76**, 115430 (2007); A. Onipko, Phys. Rev. B **78**, 245412 (2008); L. Malysheva and A. Onipko, Phys. Rev. Lett. **100**, 186806 (2008)
9. A.R. Akhmerov, C.W.J. Beenakker, Phys. Rev. B **77**, 085423 (2008)
10. Y. Imry, *Introduction to Mesoscopic Physics*, (Oxford, New York, 1997)
11. S. Nakamura, K. Wakabayashi, A. Yamashiro, K. Harigaya, Physica E **22**, 684 (2004)
12. H. Yoshioka, S. Higashibata, J. Phys.: Conf. Ser. **150**, 022105 (2009)
13. C. Beenakker, Rev. Mod. Phys. **80**, 1337 (2008)
14. M.V. Berry, R.J. Mondragon, Proc. R. Soc. London, Ser. A **412**, 53 (1987)
15. P. Recher, B. Trauzettel, A. Rycerz, Y. Blanter, C. Beenakker, A. Morpurgo, Phys. Rev. B **76**, 235404 (2007)
16. D. Bahamon, A.L.C. Pereira, P.A. Schulz, Phys. Rev. B **79**, 125414 (2009)
17. J. Wurm, A. Rycerz, I. Adagideli, M. Wimmer, K. Richter, H.U. Baranger, Phys. Rev. Lett. **102**, 056806 (2009)
18. J. Wurm, M. Wimmer, H. Baranger, K. Richter, Semicond. Sci. Technol. **25**, 034003 (2010)
19. J.A. Fuerst et al., N. Journal of Phys. **11**, 095020 (2009); T.G. Pedersen et al., Phys. Rev. Lett. **100**, 136804 (2008)
20. S. Russo, J.B. Oostinga, D. Wehenkel, H.B. Heersche, S.S. Sobhani, L.M.K. Vandersypen, A.F. Morpurgo, Phys. Rev. B **77**, 085413 (2008)
21. F. Molitor, M. Huefner, A. Jacobsen, A. Pioda, C. Stampfer, K. Ensslin, & T. Ihn, New. J. Phys. **12**, 043054 (2010)
22. T. Luo, A. Iyengar, H.A. Fertig, L. Brey, Phys. Rev. B **80**, 165310 (2009)
23. A. Iyengar, T. Luo, H. A. Fertig, L. Brey, Phys. Rev. B **78**, 235411 (2008)
24. J.J. Palacios, J. Fernandez-Rossier, L. Brey, H.A. Fertig, Semiconduct. Sci. Technol. **25**, 033003 (2010)
25. A. Young, P. Kim 2009 Nat. Phys. **5**, 222 (2009)
26. B. Huard, J.A. Sulpizio, N. Stander, K. Todd, B. Yang, D. Goldhaber-Gordon, Phys. Rev. Lett. **98**, 236803 (2007)
27. N. Stander, B. Huard, D. Goldhaber-Gordon, Phys. Rev. Lett. **102**, 026807 (2009)
28. J.R. Williams, L. DiCarlo, C.M. Marcus, Science **317**, 638 (2007)
29. S. Marchini, J. Wintterlin, Phys. Rev. B **76**, 075429 (2007)
30. A.L.V. de Parga, F. Calleja, B. Borca, J.M.C.G. Passeggi, J. Hinarejos, F. Guinea, R. Miranda, *Phys. Rev. Lett.* **100**, 056807 (2008)
31. Y. Pan, N. Jiang, J.T. Sun, D.X. Shi, S.X. Du, F. Liu, & H.-J. Gao, Advanced Materials **21**, 2777 (2009)
32. J.C. Meyer, C.O. Girit, M.F. Crommie, A. Zettl, Appl. Phys. Lett. **92**, 123110 (2008)
33. W. Bao, Feng Miao, Zhen Chen, Hang Zhang, Wanyoung Jang, Chris Dames, Chun Ning Lau, Nat. Nanotech. **4**, 562 (2009)
34. C. Park, Y.-W. Son, L. Yang, M.L. Cohen, S.G. Louie, Nano Lett. **8**, 2920 (2008)
35. L. Brey, H.A. Fertig, Phys. Rev. Lett. **103**, 046809 (2009)
36. C. Park, Y.-W. Son, L. Yang, M.L. Cohen, S.G. Louie, Phys. Rev. Lett. **103**, 046808 (2009)
37. C. Park, L. Yang, Y-W. Son, M.L. Cohen, S.G. Louie, Phys.Rev.Lett. **101**, 126804 (2008)
38. J. Tworzydlo, B. Trauzettel, M. Titov, A. Rycerz, C.W. Beenakker, Phys. Rev. Lett. **96**, 246802 (2006)

Chapter 11
Electronic Properties of Multilayer Graphene

Hongki Min

Abstract In this chapter, we study the electronic structure of arbitrarily stacked multilayer graphene in the absence or presence of magnetic field. The energy band structure and the Landau-level spectrum are obtained using a π-orbital continuum model with nearest-neighbor intralayer and interlayer tunneling terms. Using degenerate state perturbation theory, we analyze the low-energy effective theory and show that the low-energy electronic structure of arbitrarily stacked graphene multilayers consists of chiral pseudospin doublets with a conserved chirality sum. We discuss the implications of this for the quantum Hall effect, optical conductivity, and electrical conductivity.

11.1 Introduction

The recent explosion [1–6] of research on the electronic properties of single layer and stacked multilayer graphene sheets has been driven by advances in material preparation methods [7, 8], by the unusual [9–11] electronic properties of these materials including unusual quantum Hall effects [12, 13], and by hopes that these elegantly tunable systems might be useful electronic materials.

Electronic properties of multilayer graphene strongly depend on the stacking sequence. Periodically stacked multilayer graphene [14–19] and arbitrarily stacked multilayer graphene [20, 21] have been studied theoretically, demonstrating that the low-energy band structure of graphene multilayer consists of a set of independent pseudospin doublets. It was shown that energy gap can be induced by a

H. Min (✉)
Center for Nanoscale Science and Technology, National Institute of Standards and Technology, Gaithersburg, MD 20899-6202, USA

Maryland NanoCenter, University of Maryland, College Park, MD 20742, USA

Department of Physics and Astronomy, Seoul National University, Seoul 151-747, Korea
e-mail: hmin@snu.ac.kr

H. Raza (ed.), *Graphene Nanoelectronics*, NanoScience and Technology,
DOI 10.1007/978-3-642-22984-8_11,

perpendicular external electric field in ABC-stacked multilayer graphene [22, 23]. Furthermore, in ABC stacking electron–electron interactions play more important role than other stacking sequences due to the appearance of relatively flat bands near the Fermi level [23]. Optical properties of multilayer graphene using absorption spectroscopy have been studied experimentally [24] and theoretically [25–28] showing characteristic peak positions in optical conductivity depending on stacking sequences. Transport properties of multilayer graphene have been studied theoretically within the coherent potential approximation for averaged local impurities [29–31] and using Boltzmann transport theory [32,33]. (See Chap. 12 for transport theory in graphene.)

In this chapter, we describe the electronic structure of arbitrarily stacked multilayer graphene and analyze its low-energy spectrum. (Here we are not considering graphene sheets with rotational stacking faults, which typically appear in epitaxial graphene grown on carbon-face SiC substrate and behave as a collection of decoupled monolayer graphene [34–36].) Interestingly, the low-energy effective theory of multilayer graphene is always described by a set of chiral pseudospin doublets with a conserved chirality sum. We discuss implications of this finding for the quantum Hall effect, optical conductivity, and electrical conductivity in multilayer graphene. (See Chap. 8 for electronic properties of monolayer and bilayer graphene.)

11.1.1 Stacking Arrangements

In multilayer graphene, there are three distinct stacking arrangements, labeled A, B, and C, classified by the relative position in two-dimensional (2D) plane, and in each plane the honeycomb lattice of a single sheet has two triangular sublattices, labeled by α and β, as illustrated in Fig. 11.1a. (Here we use α and β for sublattices instead of A and B to avoid any confusion with stacking arrangements, A, B, and C.) Different stacking types are obtained by displacing sublattices along the honeycomb edges or by rotating by $\pm 60°$ about a carbon atom on one of the two sublattices. Special stacking sequences are generated by repeated AB, ABC, and AA stacking, and are called Bernal, rhombohedral, and hexagonal stacking, respectively.

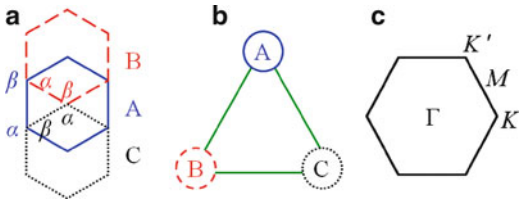

Fig. 11.1 (**a**) Three distinct stacking arrangements A, B and C in multilayer graphene and representative sublattices α and β in the A, B, and C layers. (**b**) The stacking triangle where each added layer cycles around. (**c**) Brillouin zone of the honeycomb lattice

Each added layer cycles around the stacking triangle in either the right-handed or the left-handed sense, or stays at the same position in the triangle, as seen in Fig. 11.1b. For example, Bernal (AB) stacking corresponds to moving with a reversal in direction at every step, and rhombohedral (ABC) stacking corresponds to moving with no reversals in direction, while hexagonal (AA) stacking corresponds to not moving around the triangle at all. As discussed later, the cyclic motion in the stacking triangle is closely related to the chirality of multilayer graphene.

11.1.2 π-Orbital Continuum Model

In graphene, p_z orbitals form low-energy bands near the Fermi energy while sp^2-hybridized s, p_x, and p_y orbitals form high-energy bands. They are also called π-orbitals and σ-orbitals, respectively, from the symmetry of the orbital shape. The π-orbital continuum model for the N-layer graphene Hamiltonian describes energy bands near the hexagonal corners of the Brillouin zone, the K and K' points (Fig. 11.1c):

$$\mathcal{H} = \sum_{\boldsymbol{p}} \Psi_{\boldsymbol{p}}^{\dagger} H(\boldsymbol{p}) \Psi_{\boldsymbol{p}}, \tag{11.1}$$

where $\Psi_{\boldsymbol{p}} = (c_{1,\alpha,\boldsymbol{p}}, c_{1,\beta,\boldsymbol{p}}, \ldots, c_{N,\alpha,\boldsymbol{p}}, c_{N,\beta,\boldsymbol{p}})$ and $c_{l,\mu,\boldsymbol{p}}$ is an electron annihilation operator for layer $l = 1, \cdots, N$, sublattice $\mu = \alpha, \beta$, and 2D momentum $\boldsymbol{p}$ measured from the K or K' point. The K and K' points are often called *valleys*.

The simplest model for a multilayer graphene system allows only nearest-neighbor intralayer hopping t and the nearest-neighbor interlayer hopping $t_\perp$. The monolayer graphene quasiparticle velocity $v \approx 10^6\,\mathrm{m\,s^{-1}}$ is related with t by $\frac{\hbar v}{a} = \frac{\sqrt{3}}{2} t$, where $a = 0.246\,\mathrm{nm}$ is a lattice constant of monolayer graphene. (In this chapter, for simplicity, $t \approx 3\,\mathrm{eV}$ and $t_\perp \approx 0.3\,\mathrm{eV}$ will be used in numerical calculations. See Chap. 8 for discussion of the values of hopping parameters and other neglected remote hopping terms. See also [16].) Although this minimal model is not fully realistic, some aspects of the electronic structure can be easily understood by fully analyzing the properties of this model. We describe limitations of the minimal model later.

11.2 Energy Band Structure

11.2.1 Preliminaries

Before analyzing the energy spectrum of multilayer graphene, let us consider the Hamiltonian of a one-band tight-binding model for a one-dimensional (1D) chain of length N with nearest-neighbor hopping parameter $t_\perp$, as illustrated in Fig. 11.2:

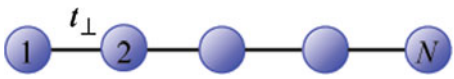

Fig. 11.2 Chain of length N with nearest-neighbor hopping parameter $t_\perp$

$$H = \begin{pmatrix} 0 & t_\perp & 0 & 0 & \\ t_\perp & 0 & t_\perp & 0 & \\ 0 & t_\perp & 0 & t_\perp & \cdots \\ 0 & 0 & t_\perp & 0 & \\ & & \cdots & & \end{pmatrix}. \tag{11.2}$$

This Hamiltonian is important for analyzing the role of interlayer hopping as explained below.

Let $\boldsymbol{a} = (a_1, \ldots, a_N)$ be an eigenvector with an eigenvalue ε. Then the eigenvalue problem reduces to the following difference equation:

$$\varepsilon a_n = t_\perp (a_{n-1} + a_{n+1}), \tag{11.3}$$

with the boundary condition $a_0 = a_{N+1} = 0$. Assuming $a_n \sim \mathrm{e}^{\mathrm{i}n\theta}$, it can be shown that (See for example [37])

$$\begin{aligned} \varepsilon_r &= 2\, t_\perp \cos\theta_r, \\ \boldsymbol{a}_r &= \sqrt{\frac{2}{N+1}} (\sin\theta_r, \sin 2\theta_r, \ldots, \sin N\theta_r) \end{aligned} \tag{11.4}$$

where $r = 1, 2, \ldots, N$ is the chain eigenvalue index and $\theta_r = r\pi/(N+1)$. Note that odd N chains have a zero-energy eigenstate at $r = (N+1)/2$ with an eigenvector that has nonzero constant amplitude on every other positions alternating in sign.

11.2.2 Monolayer Graphene

First, let us briefly review the effective Hamiltonian of monolayer graphene. (See Chap. 8 for detailed discussion of the effective Hamiltonian of monolayer and bilayer graphene.) In the absence of spin–orbit interactions, π-orbitals are decoupled from other orbitals forming low-energy bands near the Fermi energy. The Hamiltonian for the decoupled π-orbitals is given by [38]

$$H(\boldsymbol{k}) = \begin{pmatrix} 0 & (-t) f(\boldsymbol{k}) \\ (-t) f^*(\boldsymbol{k}) & 0 \end{pmatrix}, \tag{11.5}$$

where t is the (positive) nearest neighbor intralayer hopping parameter and

$$f(\boldsymbol{k}) = \mathrm{e}^{\mathrm{i}\frac{k_y a}{\sqrt{3}}} + 2\cos\left(\frac{k_x a}{2}\right)\mathrm{e}^{-\mathrm{i}\frac{k_y a}{2\sqrt{3}}}. \tag{11.6}$$

Here we chose a coordinate system in which the honeycomb Bravais lattice has primitive vectors, $\boldsymbol{a}_1 = a(1,0)$ and $\boldsymbol{a}_2 = a\left(\frac{1}{2}, \frac{\sqrt{3}}{2}\right)$.

At the K and K' points, $f(\boldsymbol{k})$ becomes zero. Among the equivalent K or K' points, we can choose $K = (\frac{4\pi}{3a}, 0)$ and $K' = -K$ for simplicity. If we expand $f(\boldsymbol{k})$ around the K point, the effective Hamiltonian near the K point can be obtained as

$$H^K(\boldsymbol{q}) = \begin{pmatrix} 0 & \hbar v(q_x - iq_y) \\ \hbar v(q_x + iq_y) & 0 \end{pmatrix}, \tag{11.7}$$

where $\frac{\hbar v}{a} = \frac{\sqrt{3}}{2}t$ and $\boldsymbol{q}$ is a wavevector measured from the K point. Similarly, if we expand $f(\boldsymbol{k})$ around the K' point, the effective Hamiltonian near the K' point can be obtained as

$$H^{K'}(\boldsymbol{q}) = \begin{pmatrix} 0 & -\hbar v(q_x + iq_y) \\ -\hbar v(q_x - iq_y) & 0 \end{pmatrix}, \tag{11.8}$$

where $\boldsymbol{q}$ is measured from the K' point.

In a compact form, (11.7) and (11.8) can be combined as

$$H^{K/K'}(\boldsymbol{q}) = \hbar v(\tau_z q_x \sigma_x + q_y \sigma_y), \tag{11.9}$$

where σ_α are Pauli matrices describing the sublattice degrees of freedom, $\tau_z = 1$ for the K point and $\tau_z = -1$ for the K' point, respectively. From now on, for multilayer graphene we will only consider the Hamiltonian near the K point. The Hamiltonian near the K' point can easily be obtained using (11.8).

11.2.3 AA Stacking

In the case of AA stacking, there is vertical hopping between $\alpha - \alpha$ sites and $\beta - \beta$ sites. Thus, the Hamiltonian at K in the $(\alpha_1, \beta_1, \alpha_2, \beta_2, \cdots)$ basis is given by

$$H_{\mathrm{AA}}(\boldsymbol{p}) = \begin{pmatrix} 0 & v\pi^\dagger & t_\perp & 0 & 0 & 0 & \\ v\pi & 0 & 0 & t_\perp & 0 & 0 & \\ t_\perp & 0 & 0 & v\pi^\dagger & t_\perp & 0 & \\ 0 & t_\perp & v\pi & 0 & 0 & t_\perp & \cdots \\ 0 & 0 & t_\perp & 0 & 0 & v\pi^\dagger & \\ 0 & 0 & 0 & t_\perp & v\pi & 0 & \\ & & & \cdots & & & \end{pmatrix}, \tag{11.10}$$

where $\boldsymbol{p} = \hbar \boldsymbol{k}$, $\boldsymbol{k}$ is a wavevector measured from the K point and $\pi = p_x + i p_y$.

For an eigenvector $(a_1, b_1, \ldots, a_N, b_N)$ with an eigenvalue ε and fixed 2D momentum, the difference equations in this case are

$$\begin{aligned} \varepsilon a_n &= t_\perp (a_{n-1} + a_{n+1}) + v\pi^\dagger b_n, \\ \varepsilon b_n &= t_\perp (b_{n-1} + b_{n+1}) + v\pi a_n, \end{aligned} \tag{11.11}$$

with the boundary condition $a_0 = a_{N+1} = b_0 = b_{N+1} = 0$.

Let $c_n \equiv a_n + b_n \mathrm{e}^{-\mathrm{i}\phi}$ and $d_n \equiv a_n - b_n \mathrm{e}^{-\mathrm{i}\phi}$ where $\phi = \tan^{-1}(p_y/p_x)$. Then

$$\begin{aligned} (\varepsilon - v|\boldsymbol{p}|) c_n &= t_\perp (c_{n-1} + c_{n+1}), \\ (\varepsilon + v|\boldsymbol{p}|) d_n &= t_\perp (d_{n-1} + d_{n+1}), \end{aligned} \tag{11.12}$$

with the same boundary condition $c_0 = c_{N+1} = d_0 = d_{N+1} = 0$. Thus, the electronic structure of AA-stacked N-layer graphene can be thought of as consisting of separate 1D chains for each wavevector in the 2D honeycomb lattice Brillouin zone. Then the energy spectrum is given by

$$\varepsilon^{\pm}_{r,\boldsymbol{p}} = \pm v|\boldsymbol{p}| + 2t_\perp \cos\left(\frac{r\pi}{N+1}\right), \tag{11.13}$$

where $r = 1, 2, \ldots, N$. Note that for odd N, the $r = (N+1)/2$ mode provides two zero-energy states at $\boldsymbol{p} = 0$ per spin and valley.

Figure 11.3 shows the band structure of AA-stacked trilayer and tetralayer graphene near the K point. Because of the hybridization between $\alpha - \alpha$ and $\beta - \beta$

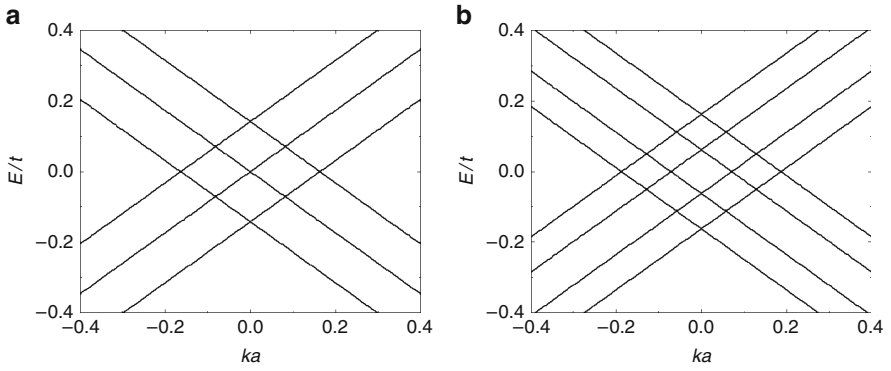

Fig. 11.3 Energy band structure near the K point for AA-stacked (**a**) trilayer and (**b**) tetralayer graphene with nearest-neighbor intralayer hopping $t = 3\,\mathrm{eV}$ and nearest-neighbor interlayer hopping $t_\perp = 0.1t$. k is a wavevector measured from the K point and a is a lattice constant of graphene

sublattices in each layer, additional zero-energy states can occur at momenta that are remote from the K and K' points.

11.2.4 AB Stacking

In the case of AB stacking, there is vertical hopping between $\beta_1 - \alpha_2 - \beta_3 - \alpha_4 - \ldots$ sites from the bottom layer. Thus, the Hamiltonian at K in the $(\alpha_1, \beta_1, \alpha_2, \beta_2, \ldots)$ basis has the following form:

$$H_{\mathrm{AB}}(\boldsymbol{p}) = \begin{pmatrix} 0 & v\pi^\dagger & 0 & 0 & 0 & 0 & \\ v\pi & 0 & t_\perp & 0 & 0 & 0 & \\ 0 & t_\perp & 0 & v\pi^\dagger & 0 & t_\perp & \\ 0 & 0 & v\pi & 0 & 0 & 0 & \cdots \\ 0 & 0 & 0 & 0 & 0 & v\pi^\dagger & \\ 0 & 0 & t_\perp & 0 & v\pi & 0 & \\ & & & \cdots & & & \end{pmatrix}. \tag{11.14}$$

The subtle difference in this Hamiltonian compared to the AA case changes the electronic structure in a qualitative way. To obtain the energy spectrum of AB-stacked N-layer graphene, let us consider corresponding difference equations [15]:

$$\begin{aligned} \varepsilon a_{2n-1} &= (v\pi^\dagger) b_{2n-1}, \\ \varepsilon b_{2n-1} &= t_\perp (a_{2n-2} + a_{2n}) + (v\pi) a_{2n-1}, \\ \varepsilon a_{2n} &= t_\perp (b_{2n-1} + b_{2n+1}) + (v\pi^\dagger) b_{2n}, \\ \varepsilon b_{2n} &= (v\pi) a_{2n} \end{aligned} \tag{11.15}$$

with the boundary condition $a_0 = a_{N+1} = b_0 = b_{N+1} = 0$.

Letting $c_{2n-1} \equiv b_{2n-1}$ and $c_{2n} \equiv a_{2n}$, the difference equations reduce to

$$(\varepsilon - v^2 |\boldsymbol{p}|^2 / \varepsilon) c_n = t_\perp (c_{n-1} + c_{n+1}) \tag{11.16}$$

with the boundary condition $c_0 = c_{N+1} = 0$. Then the energy spectrum is given by

$$\varepsilon - v^2 |\boldsymbol{p}|^2 / \varepsilon = 2 t_\perp \cos\left(\frac{r\pi}{N+1}\right), \tag{11.17}$$

where $r = 1, 2, \cdots, N$. Thus

$$\varepsilon^{\pm}_{r,\boldsymbol{p}} = t_\perp \cos\left(\frac{r\pi}{N+1}\right) \pm \sqrt{v^2 |\boldsymbol{p}|^2 + t_\perp^2 \cos^2\left(\frac{r\pi}{N+1}\right)}. \tag{11.18}$$

Note that the relativistic energy spectrum for a particle with the momentum $\boldsymbol{p}$ and mass m is given by

$$\varepsilon_{\boldsymbol{p}} = \sqrt{|\boldsymbol{p}|^2 c^2 + m^2 c^4}, \tag{11.19}$$

where c is the velocity of light. Thus the effective mass can be identified as $m_r v^2 = \left| t_\perp \cos\left(\frac{r\pi}{N+1}\right)\right|$ for a mode r.

For a massive mode with mass m_r, the low-energy spectrum is given by

$$\varepsilon_{r,\boldsymbol{p}} \approx \begin{cases} +\dfrac{\boldsymbol{p}^2}{2m_r} & \text{if } t_\perp \cos\left(\frac{r\pi}{N+1}\right) < 0, \\ -\dfrac{\boldsymbol{p}^2}{2m_r} & \text{if } t_\perp \cos\left(\frac{r\pi}{N+1}\right) > 0. \end{cases} \tag{11.20}$$

For odd N, the mode with $r = (N+1)/2$ is massless and its energy is given by

$$\varepsilon_{\boldsymbol{p}}^{\pm} = \pm v|\boldsymbol{p}|. \tag{11.21}$$

Therefore, the low-energy spectrum with odd number of layers is a combination of one massless Dirac mode and $N-1$ massive Dirac modes per spin and valley. For even number of layers, all N modes are massive at low energies.

Figure 11.4 shows the band structure of AB-stacked trilayer and tetralayer graphene near the K point. As discussed earlier, the trilayer has one massless mode and two massive modes, while the tetralayer has all massive modes at low energies per spin and valley. Note that at $\boldsymbol{p} = 0$, each massless mode gives two zero energies while each massive mode gives one zero energy. Therefore, for odd N, there are $2+(N-1) = N+1$ zero-energy states, while for even N, there are N zero-energy states per spin and valley.

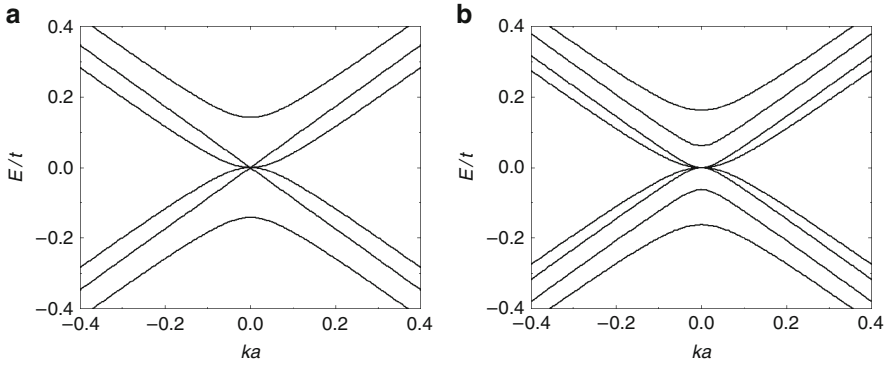

Fig. 11.4 Energy band structure near the K point for AB-stacked (**a**) trilayer and (**b**) tetralayer graphene with $t = 3\,\text{eV}$ and $t_\perp = 0.1t$

11.2.5 ABC Stacking

In the case of ABC stacking, there is vertical hopping between all the lower layer β sites and all the upper layer α sites. Thus, the Hamiltonian at K in the $(\alpha_1, \beta_1, \alpha_2, \beta_2, \cdots)$ basis is given by

$$H_{\mathrm{ABC}}(\boldsymbol{p}) = \begin{pmatrix} 0 & v\pi^\dagger & 0 & 0 & 0 & 0 & \\ v\pi & 0 & t_\perp & 0 & 0 & 0 & \\ 0 & t_\perp & 0 & v\pi^\dagger & 0 & 0 & \\ 0 & 0 & v\pi & 0 & t_\perp & 0 & \cdots \\ 0 & 0 & 0 & t_\perp & 0 & v\pi^\dagger & \\ 0 & 0 & 0 & 0 & v\pi & 0 & \\ & & & \cdots & & & \end{pmatrix}. \tag{11.22}$$

Unfortunately for ABC stacking, there do not exist low-order difference equations with a simple boundary condition, but it is still possible to derive a low-energy effective Hamiltonian.

For $\boldsymbol{p} = 0$ each $\beta - \alpha$ pair forms a symmetric–antisymmetric doublet with energies $\pm t_\perp$, leaving the bottom α_1 and top β_N sites as the only low-energy states. It is possible to construct a 2×2 effective Hamiltonian for the low-energy part of the spectrum using perturbation theory. The same procedure can then be extended to arbitrary stacking sequences. More detailed discussion of the low-energy effective theory is presented in Sect. 11.4.

The simplest example is bilayer graphene. Low and high energy subspaces are identified by finding the spectrum at $\boldsymbol{p} = 0$ and identifying all the zero-energy eigenstates. The intralayer tunneling term, which is proportional to π or $\pi^\dagger$, couples low and high energy states. Using degenerate state perturbation theory, the effective Hamiltonian in the low energy space is given by [39]

$$H_2^{\mathrm{eff}}(\boldsymbol{p}) = -\begin{pmatrix} 0 & \frac{(\pi^\dagger)^2}{2m} \\ \frac{(\pi)^2}{2m} & 0 \end{pmatrix} = -t_\perp \begin{pmatrix} 0 & (\nu^\dagger)^2 \\ (\nu)^2 & 0 \end{pmatrix}, \tag{11.23}$$

where we have used a (α_1, β_2) basis, $m = t_\perp / 2v^2$ and $\nu = v\pi / t_\perp$.

In the same way, the effective Hamiltonian of ABC-stacked N-layer graphene in the (α_1, β_N) basis is

$$H_N^{\mathrm{eff}}(\boldsymbol{p}) = -t_\perp \begin{pmatrix} 0 & (\nu^\dagger)^N \\ (\nu)^N & 0 \end{pmatrix}, \tag{11.24}$$

which turns out to be a pseudospin Hamiltonian with the chirality N, as is discussed in Sect. 11.4. Note that for mathematical convenience, we have chosen a gauge in which a minus sign appears in front of $t_\perp$.

Equation (11.24) can be proven by the mathematical induction method. Imagine that adding one more layer on top of N-layer graphene with ABC stacking. Then the combined Hamiltonian is given by

$$H_{N+1}^{\text{eff}}(\boldsymbol{p}) = -t_\perp \begin{pmatrix} 0 & (\nu^\dagger)^N & 0 & 0 \\ (\nu)^N & 0 & -1 & 0 \\ 0 & -1 & 0 & \nu^\dagger \\ 0 & 0 & \nu & 0 \end{pmatrix}, \tag{11.25}$$

using the $(\alpha_1, \beta_N, \alpha_{N+1}, \beta_{N+1})$ basis.

Let P be a low-energy subspace spanned by (α_1, β_{N+1}) and Q be a high-energy subspace spanned by (α_{N+1}, β_N). Note that the effective Hamiltonian for $v|\boldsymbol{p}| \ll t_\perp$ can be derived using the degenerate state perturbation theory [41],

$$H_{\text{eff}} \approx H_{PP} - H_{PQ} \frac{1}{H_{QQ}} H_{QP}. \tag{11.26}$$

Here the Hamiltonian matrices projected to P and Q subspace are given by

$$H_{QQ}(\boldsymbol{p}) = t_\perp \begin{pmatrix} 0 & 1 \\ 1 & 0 \end{pmatrix}, \; H_{PQ}(\boldsymbol{p}) = -t_\perp \begin{pmatrix} 0 & (\nu^\dagger)^N \\ \nu & 0 \end{pmatrix} \tag{11.27}$$

and $H_{PP}(\boldsymbol{p}) = 0$. Thus,

$$H_{N+1}^{\text{eff}}(\boldsymbol{p}) \approx -t_\perp \begin{pmatrix} 0 & (\nu^\dagger)^{N+1} \\ (\nu)^{N+1} & 0 \end{pmatrix} \tag{11.28}$$

which proves (11.24). The corresponding energy spectrum in (11.24) is given by

$$\varepsilon_{\text{eff},\boldsymbol{p}}^{\pm} = \pm t_\perp \left(\frac{v|\boldsymbol{p}|}{t_\perp} \right)^N. \tag{11.29}$$

Figure 11.5 shows the band structure of ABC-stacked trilayer and tetralayer graphene near the K point. Note that at $\boldsymbol{p} = 0$, there are only two zero energy states per spin and valley no matter how thick the stack is.

11.2.6 Arbitrary Stacking

It is easy to generalize the previous discussion to construct the Hamiltonian for an arbitrarily stacked multilayer graphene system. The intralayer Hamiltonian at K for ith layer is given by

$$H_{ii}(\boldsymbol{p}) = \begin{pmatrix} 0 & v\pi^\dagger \\ v\pi & 0 \end{pmatrix}. \tag{11.30}$$

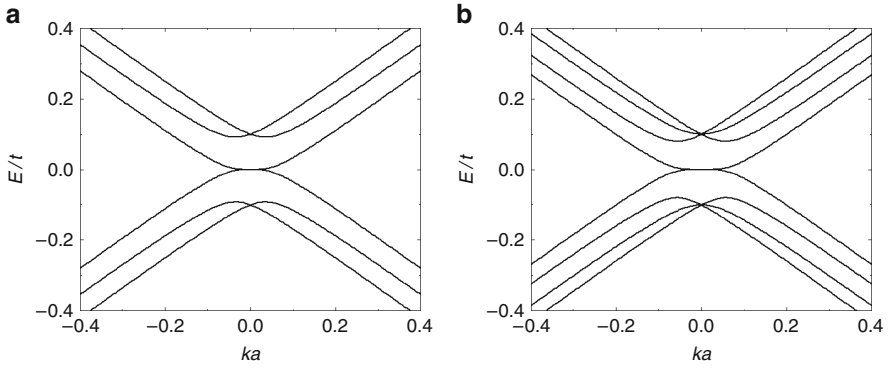

Fig. 11.5 Energy band structure near the K point for ABC-stacked (**a**) trilayer and (**b**) tetralayer graphene with $t = 3\,\mathrm{eV}$ and $t_\perp = 0.1t$

The interlayer Hamiltonian between i and $i+1$ layers is given by

$$H_{i\,i+1}(\boldsymbol{p}) = \begin{cases} H_{\mathrm{AA}}^{\mathrm{inter}} & \text{if AA, BB, or CC stacking,} \\ H_{\mathrm{AB}}^{\mathrm{inter}} & \text{if AB, BC, or CA stacking,} \\ H_{\mathrm{AC}}^{\mathrm{inter}} & \text{if AC, CB, or BA stacking,} \end{cases} \tag{11.31}$$

where

$$H_{\mathrm{AA}}^{\mathrm{inter}}(\boldsymbol{p}) = \begin{pmatrix} t_\perp & 0 \\ 0 & t_\perp \end{pmatrix},\ H_{\mathrm{AB}}^{\mathrm{inter}}(\boldsymbol{p}) = \begin{pmatrix} 0 & 0 \\ t_\perp & 0 \end{pmatrix},\ \text{and}\ H_{\mathrm{AC}}^{\mathrm{inter}}(\boldsymbol{p}) = \begin{pmatrix} 0 & t_\perp \\ 0 & 0 \end{pmatrix}. \tag{11.32}$$

Then the Hamiltonian at K for an arbitrary stacking in the $(\alpha_1, \beta_1, \alpha_2, \beta_2, \cdots)$ basis is given by

$$H(\boldsymbol{p}) = \begin{pmatrix} H_{11} & H_{12} & 0 & 0 & 0 & 0 & \\ H_{21} & H_{22} & H_{23} & 0 & 0 & 0 & \\ 0 & H_{32} & H_{33} & H_{34} & 0 & 0 & \\ 0 & 0 & H_{43} & H_{44} & H_{45} & 0 & \cdots \\ 0 & 0 & 0 & H_{54} & H_{55} & H_{56} & \\ 0 & 0 & 0 & 0 & H_{65} & H_{66} & \\ & & & \cdots & & & \end{pmatrix}, \tag{11.33}$$

where $H_{i+1\,i} = H_{i\,i+1}^{\dagger}$.

Figure 11.6 shows the band structure of ABCB-stacked tetralayer graphene and ABBC-stacked tetralayer graphene near the K point. For ABCB-stacked tetralayer graphene, the low-energy spectrum looks like a superposition of a linear dispersion and a cubic one. For ABBA-stacked tetralayer graphene, zero energies appear not only at the Dirac point but also away from it. A more detailed low-energy spectrum analysis is presented in Sect. 11.4.

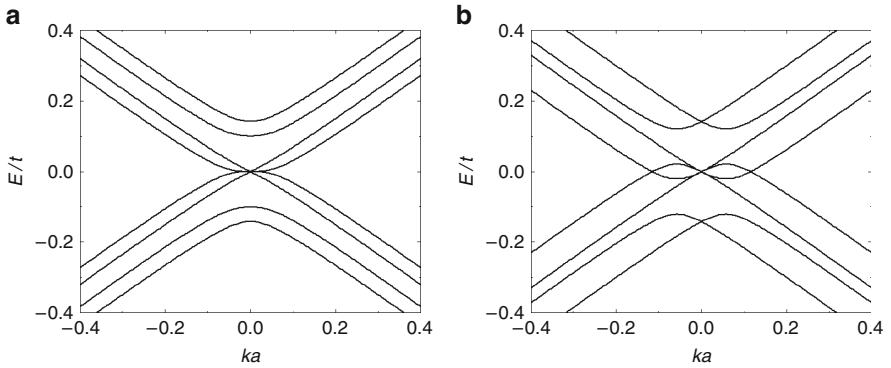

Fig. 11.6 Energy band structure near the K point for (**a**) ABCB-stacked and (**b**) ABBC-stacked tetralayer graphene with $t = 3\,\mathrm{eV}$ and $t_\perp = 0.1t$

11.3 Landau-Level Spectrum

11.3.1 Preliminaries

In the presence of a magnetic field $\boldsymbol{B} = B\hat{z}$, a Hamiltonian is modified by $\boldsymbol{p} \to \boldsymbol{p} + \frac{e}{c}\boldsymbol{A}$, where $\boldsymbol{A}$ is the vector potential with $\boldsymbol{B} = \nabla \times \boldsymbol{A}$. The quantum Hamiltonian is most easily diagonalized by introducing raising and lowering operators, $a = \ell\pi^\dagger/\sqrt{2}\hbar$ and $a^\dagger = \ell\pi/\sqrt{2}\hbar$, where $\ell = \sqrt{\hbar c/e|B|}$, and noting that $[a, a^\dagger] = 1$. Then the wavefunction amplitude on each sublattice of each layer is expanded in terms of parabolic band Landau-level states $|n\rangle$ which are eigenstates of $a^\dagger a$. For many Hamiltonians, including those studied here, the Hamiltonian can be block-diagonalized by fixing the parabolic band Landau-level offset between different sublattices and between different layers.

11.3.2 AA Stacking

In the case of AA stacking, choose the nth Landau-level basis at K as $(\alpha_{1,n-1}, \beta_{1,n}, \cdots, \alpha_{N,n-1}, \beta_{N,n})$. Then (11.10) reduces to

$$H_{\mathrm{AA}}(n) = \begin{pmatrix} 0 & \varepsilon_n & t_\perp & 0 & 0 & 0 \\ \varepsilon_n & 0 & 0 & t_\perp & 0 & 0 \\ t_\perp & 0 & 0 & \varepsilon_n & t_\perp & 0 \\ 0 & t_\perp & \varepsilon_n & 0 & 0 & t_\perp \cdots \\ 0 & 0 & t_\perp & 0 & 0 & \varepsilon_n \\ 0 & 0 & 0 & t_\perp & \varepsilon_n & 0 \\ & & & \cdots & & \end{pmatrix}, \tag{11.34}$$

where $\varepsilon_n = \sqrt{2n}\hbar v/l$. Note that 2D Landau level states with a negative index do not exist so the corresponding basis states and matrix elements are understood as being absent in the matrix block. Thus, $H_{\mathrm{AA}}(n = 0)$ is an $N \times N$ matrix, while $H_{\mathrm{AA}}(n > 0)$ is a $2N \times 2N$ matrix.

Diagonalizing (11.34) using the difference equation method gives the exact Landau level spectrum. For $n > 0$, Landau-levels are

$$\varepsilon_{r,n}^{\pm} = \pm\varepsilon_n + 2t_\perp \cos\left(\frac{r\pi}{N+1}\right), \tag{11.35}$$

where $r = 1, 2, \ldots, N$. Note that for $n = 0$, Landau levels are given by $\varepsilon_{r,0} = 2t_\perp \cos\left(\frac{r\pi}{N+1}\right)$. Thus for odd N, there exists one (B-independent) zero-energy Landau level at $r = (N+1)/2$ per spin and valley.

Figure 11.7 shows the Landau levels of AA-stacked trilayer and tetralayer graphene as a function of magnetic field. For the trilayer, there is one zero-energy Landau level, while for the tetralayer, there is no zero-energy Landau level. Note that there are Landau levels crossing the zero-energy line in AA stacking.

11.3.3 AB Stacking

In the case of AB stacking, a proper choice of the nth Landau-level basis at K is $(\alpha_{1,n-1}, \beta_{1,n}, \alpha_{2,n}, \beta_{2,n+1}, \alpha_{3,n-1}, \beta_{3,n}, \alpha_{4,n}, \beta_{4,n+1}, \ldots)$ such that all the interlayer hopping terms are contained in the nth Landau-level Hamiltonian. Then (11.14) reduces to

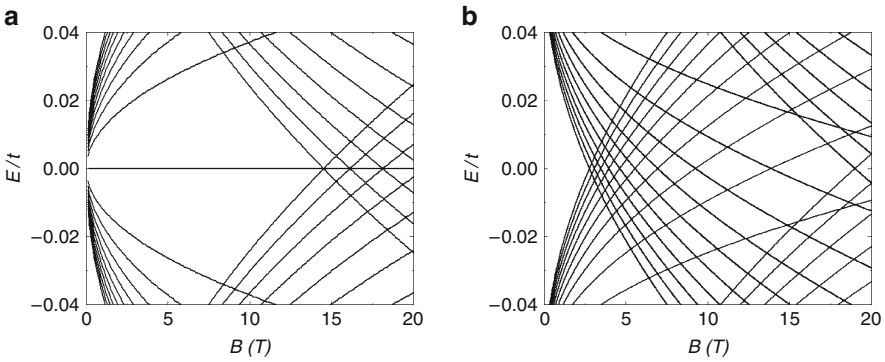

Fig. 11.7 Landau levels of AA-stacked (**a**) trilayer and (**b**) tetralayer graphene with $t = 3$ eV and $t_\perp = 0.1t$. Landau levels are shown up to $n = 10$

$$H_{\mathrm{AB}}(n) = \begin{pmatrix} 0 & \varepsilon_n & 0 & 0 & 0 & 0 & \\ \varepsilon_n & 0 & t_\perp & 0 & 0 & 0 & \\ 0 & t_\perp & 0 & \varepsilon_{n+1} & 0 & t_\perp & \\ 0 & 0 & \varepsilon_{n+1} & 0 & 0 & 0 & \cdots \\ 0 & 0 & 0 & 0 & 0 & \varepsilon_n & \\ 0 & 0 & t_\perp & 0 & \varepsilon_n & 0 & \\ & & & \cdots & & & \end{pmatrix}. \tag{11.36}$$

As discussed in Sect. 11.3.2, special care should be given for states with a negative index.

For the Hamiltonian in (11.36), there do not exist corresponding difference equations with a proper boundary condition, thus cannot be diagonalized analytically. From (11.23), however, the low-energy Landau levels for massive mode with mass m_r can be obtained as

$$\varepsilon_{r,n} \approx \begin{cases} +\hbar\omega_r \sqrt{n(n+1)} & \text{if } t_\perp \cos\left(\frac{r\pi}{N+1}\right) < 0, \\ -\hbar\omega_r \sqrt{n(n+1)} & \text{if } t_\perp \cos\left(\frac{r\pi}{N+1}\right) > 0, \end{cases} \tag{11.37}$$

where $r = 1, 2, \ldots, N$ and $\omega_r = e|B|/m_r c$, which is proportional to B. These equations apply at small B, just as the low-energy dispersions for $B = 0$ applied at small momentum $\boldsymbol{p}$. For the massless mode, from (11.21) Landau levels are given by

$$\varepsilon_n^{\pm} = \pm\varepsilon_n, \tag{11.38}$$

which is proportional to $B^{1/2}$.

Figure 11.8 shows the Landau levels of AB-stacked trilayer and tetralayer graphene as a function of magnetic field. Note that the linear B dependence expected for massive modes applies over a more limited field range when the mass is small. For the trilayer, Landau levels are composed of massless Dirac spectra ($\propto B^{1/2}$) and

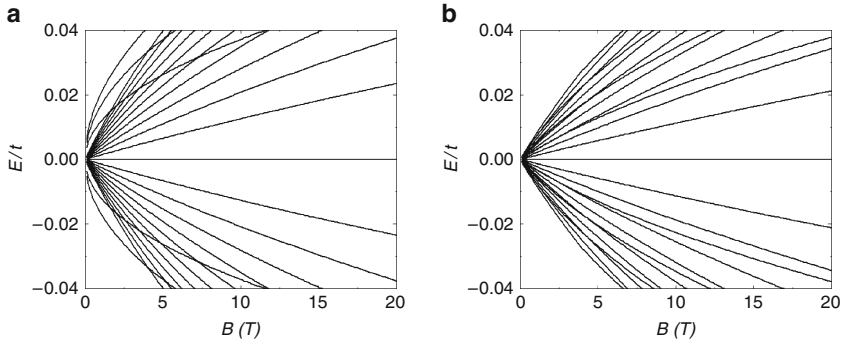

Fig. 11.8 Landau levels of AB-stacked (**a**) trilayer and (**b**) tetralayer graphene with $t = 3\,\mathrm{eV}$ $t_\perp = 0.1t$. Landau levels are shown up to $n = 10$

massive Dirac spectra ($\propto B$), while for the tetralayer, Landau levels are all massive Dirac spectra. This is consistent with the band structure analysis shown in Fig. 11.4.

Note that the massive modes in (11.37) have two zero-energy Landau levels for $n = -1$ and 0, whereas the massless mode in (11.38) has one for $n = 0$. There are therefore N zero-energy Landau levels per spin and valley in both even and odd N AB stacks. This property can also be understood directly from the Hamiltonian in (11.36), by eliminating negative n basis states and rearranging rows to block-diagonalize the matrix.

11.3.4 ABC Stacking

In the case of ABC stacking, a proper choice of the nth Landau-level basis at K is $(\alpha_{1,n-1}, \beta_{1,n}, \alpha_{2,n}, \beta_{2,n+1}, \alpha_{3,n+1}, \beta_{3,n+2}, \cdots)$ such that all the interlayer hopping terms are contained in the nth Landau level Hamiltonian. Then (11.22) reduces to

$$H_{\mathrm{ABC}}(n) = \begin{pmatrix} 0 & \varepsilon_n & 0 & 0 & 0 & 0 & \\ \varepsilon_n & 0 & t_\perp & 0 & 0 & 0 & \\ 0 & t_\perp & 0 & \varepsilon_{n+1} & 0 & 0 & \\ 0 & 0 & \varepsilon_{n+1} & 0 & t_\perp & 0 & \cdots \\ 0 & 0 & 0 & t_\perp & 0 & \varepsilon_{n+2} & \\ 0 & 0 & 0 & 0 & \varepsilon_{n+2} & 0 & \\ & & & \cdots & & & \end{pmatrix}. \tag{11.39}$$

As discussed in Sect. 11.3.2, special care should be given for states with a negative index.

The low-energy spectrum can be obtained from the effective Hamiltonian in (11.24). For $n > 0$, Landau levels are given by

$$\varepsilon_n^{\pm} = \pm\hbar\omega_N \sqrt{n(n+1)\cdots(n+N-1)}, \tag{11.40}$$

where $\hbar\omega_N = t_\perp(\sqrt{2}\hbar v/t_\perp l)^N \propto B^{N/2}$, while for $n = -N+1, -N+2, \ldots, 0$ they are zero. Note that there are N zero-energy Landau levels per spin and valley for ABC-stacked N-layer graphene.

Figure 11.9 shows the Landau levels of ABC-stacked trilayer and tetralayer graphene as a function of magnetic field. For the trilayer, Landau levels are proportional to $B^{3/2}$, while for the tetralayer, Landau levels are proportional to B^2 at low energies.

11.3.5 Arbitrary Stacking

It is straightforward to generalize the previous discussion to construct the Hamiltonian in the Landau level basis for an arbitrarily stacked multilayer graphene

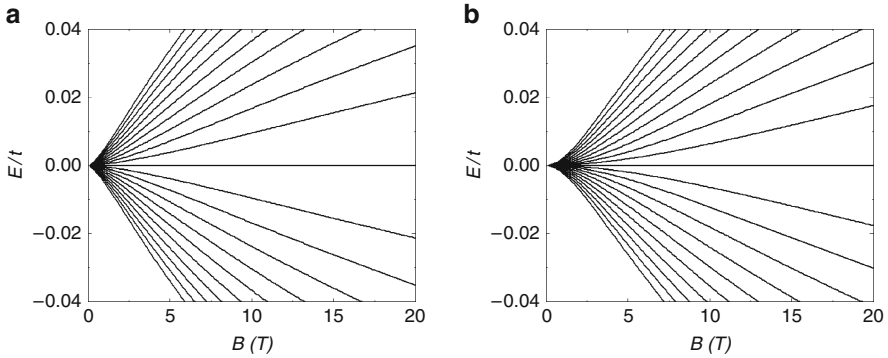

Fig. 11.9 Landau levels of ABC-stacked (**a**) trilayer and (**b**) tetralayer graphene with $t = 3\,\mathrm{eV}$ and $t_\perp = 0.1t$. Landau levels are shown up to $n = 10$

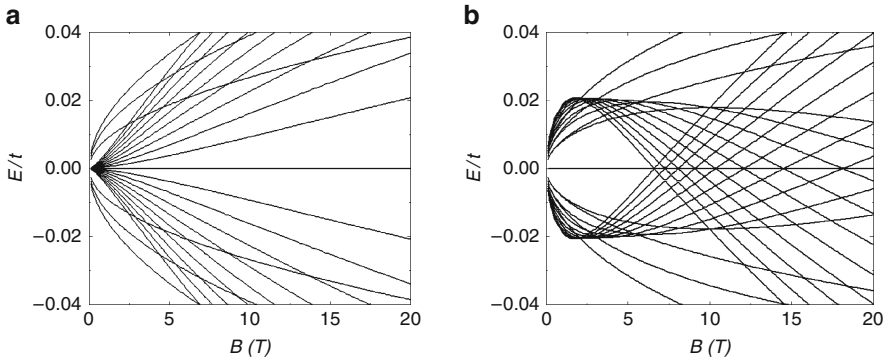

Fig. 11.10 Landau levels of (**a**) ABCB-stacked and (**b**) ABBC-stacked tetralayer graphene with $t = 3\,\mathrm{eV}$ and $t_\perp = 0.1t$. Landau levels are shown up to $n = 10$

system. As seen in (11.34), (11.36) and (11.39), it is possible to make the Hamiltonian block-diagonal by properly choosing the Landau-level basis.

Let us assume that the nth Landau-level basis at K for the ith layer is $(\alpha_{i,n-1}, \beta_{i,n})$. Then the basis for $i+1$th layer is

$$\begin{cases} (\alpha_{i+1,n-1}, \beta_{i+1,n}) & \text{if AA, BB, or CC stacking,} \\ (\alpha_{i+1,n}, \beta_{i+1,n+1}) & \text{if AB, BC, or CA stacking,} \\ (\alpha_{i+1,n-2}, \beta_{i+1,n-1}) & \text{if AC, CB, or BA stacking} \end{cases} \tag{11.41}$$

between i and $i+1$ layers. As discussed in Sect. 11.3.2, special care should be given for states with a negative index.

Figure 11.10 shows Landau levels of ABCB-stacked tetralayer graphene and ABBC-stacked tetralayer graphene. For the ABCB-stacked tetralayer graphene, the

Landau levels at low energies look like a superposition of $B^{1/2}$ and $B^{3/2}$ levels, which is consistent with Fig. 11.6a. For the ABBA-stacked tetralayer graphene, there are Landau levels crossing the zero-energy line, which is consistent with Fig. 11.6b. Detailed low-energy Landau-level spectrum analysis is presented in Sect. 11.4.

11.4 Low-Energy Effective Theory

11.4.1 Introduction

In monolayer graphene, there are two sublattices, α and β in a unit cell and wavefunctions are described by the amplitudes on each sublattice. In bilayer graphene, there are, in addition, top and bottom layer degrees of freedom and wavefunctions at low energies have two components localized on one of the sublattices in each layer. The two component wavefunctions in graphene are very similar to the spinor wavefunctions of real spins and are frequently referred to as a *pseudospin*. *Chirality* is formally defined as a projection of pseudospin on the direction of motion [3]. It is known that monolayer graphene is described by a pseudospin doublet with chirality one while bilayer graphene is described by a pseudospin doublet with chirality two. Below, we consider the meaning of this statement and its natural extension to arbitrarily stacked multilayer graphene.

In this section, we present the low-energy effective theory of arbitrarily stacked multilayer graphene using a degenerate state perturbation theory. We demonstrate an unanticipated low-energy property of graphene multilayers, which follows from an interplay between interlayer tunneling and the chiral properties of low-energy quasiparticles in an isolated graphene sheet. The low-energy band structure of multilayer graphene consists of a set of independent pseudospin doublets and its chirality sum is given by the number of layers [20, 21].

11.4.2 Pseudospin Hamiltonian

First, define a pseudospin Hamiltonian which describes 2D chiral quasiparticles. A pseudospin Hamiltonian with the chirality index J is of the form

$$H_J(\boldsymbol{p}) = t_\perp \begin{pmatrix} 0 & (v_{\boldsymbol{p}}^\dagger)^J \\ (v_{\boldsymbol{p}})^J & 0 \end{pmatrix} \tag{11.42}$$

$$= t_\perp \left(\frac{v^* |\boldsymbol{p}|}{t_\perp} \right)^J [\cos(J\phi_{\boldsymbol{p}})\, \sigma_x + \sin(J\phi_{\boldsymbol{p}})\, \sigma_y],$$

where $v_{\boldsymbol{p}} \equiv v^*|\boldsymbol{p}|e^{i\phi_{\boldsymbol{p}}}/t_\perp$, σ_α is a Pauli matrix acting on the doublet pseudospin and $\phi_{\boldsymbol{p}} = \tan^{-1}(p_y/p_x)$ is the orientation of $\boldsymbol{p}$. v^* is the effective in-plane Fermi velocity (for example, $v^* = v$ for $J = 1$ monolayer and $J = 2$ bilayer graphene, and in general for periodic ABC stacking). Note that quasiparticles described by the pseudospin Hamiltonian with chirality J acquire a Berry phase $J\pi$ upon an adiabatic evolution along a closed orbit, which can be viewed as rotation of the pseudospin by an angle $J\pi$ [39].

The Hamiltonian has a simple energy spectrum given by

$$\varepsilon_{s,\boldsymbol{p}} = st_\perp \left(\frac{v^*|\boldsymbol{p}|}{t_\perp}\right)^J, \tag{11.43}$$

and corresponding eigenfunctions are

$$|s, \boldsymbol{p}\rangle = \frac{1}{\sqrt{2}} \begin{pmatrix} s \\ e^{iJ\phi_{\boldsymbol{p}}} \end{pmatrix} \tag{11.44}$$

where $s = \pm 1$ for positive (negative) energy states, respectively.

11.4.3 Stacking Diagrams

When sheets are stacked to form a multilayer system, there is an energetic preference for an arrangement in which each layer is rotated by 60° with respect to one of the two sublattices of its neighbors [40]. This prescription generates 2^{N-2} ($N > 1$) distinct N-layer sequences if we exclude consecutive stacking (such as AA, BB, or CC). We refer to multilayers in this class as *normal*. For the analysis of low-energy effective theory, we only consider the normal stacking and discuss the effects of the consecutive stacking later.

When a B layer is placed on an A layer, a C layer on a B layer, or an A layer on a C layer, the α sites of the upper layer are above the β sites of the lower layer and therefore linked by the nearest-neighbor interlayer π-orbital hopping amplitude $t_\perp$. For the corresponding anticyclic stacking choices (A on B, B on C, or C on A), it is the β sites of the upper layer and the α sites of the lower layer that are linked. All distinct normal stacking sequences with $N = 3, 4$, and 5 layers are illustrated in Fig. 11.11, in which we have arbitrarily labeled the first two layers starting from the bottom as A and B.

11.4.4 Partitioning Rules

The low-energy band and Landau-level structure can be read off the stacking diagrams illustrated in Fig. 11.11 by partitioning a stack using the following rules, which are justified in the following section:

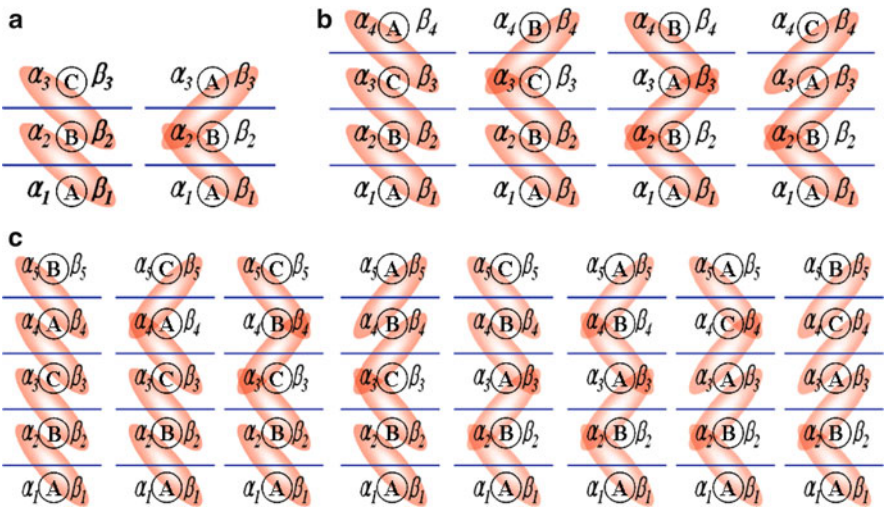

Fig. 11.11 All normal stacking sequences and linkage diagrams for $N = 3, 4$ and 5 layers in (**a**), (**b**), and (**c**), respectively. *Shaded ovals* link α and β nearest-neighbor interlayers

1. Identify the longest nonoverlapping segments within which there are no reversals of stacking sense. When there is ambiguity in the selection of nonoverlapping segments, choose the partitioning which incorporates the largest number of layers. Each segment defines a J-layer partition of the stack and may be associated with a chirality J doublet.
2. Iteratively partition the remaining segments of the stack into smaller J elements, excluding layers contained within previously identified partitions, until all layers are exhausted.

Because each layer is a member of one and only one partition, the partitioning rules imply that the chirality sum in an N-layer stack is given by

$$\sum_{i=1}^{N_{\mathrm{D}}} J_i = N, \tag{11.45}$$

where N_{D} is the number of pseudospin doublets. Note that N_{D} depends on the details of the stacking sequence and is given by half the sum of the number of isolated sites and the number of odd-length chains.

The chirality decompositions which follow from these rules are summarized in Table 11.1. Note that when each added layer cycles around the stacking triangle of Fig. 11.1b in the same rotational sense, the chirality increases. Reversals of the rotational sense tend to increase N_{D}. Although chiralities are decomposed depending on the stacking sequence, the chirality sum is conserved and given by the number of layers.

Table 11.1 Chirality decomposition for $N = 3, 4, 5, 6$ layer stacks

Stacking	Chirality	Stacking	Chirality
ABC	3	ABCABC	6
ABA	2⊕1	ABCABA	5⊕1
		ABCACA	4⊕2
ABCA	4	ABCACB	4⊕2
ABCB	3⊕1	ABCBCA	3⊕3
ABAB	2⊕2	ABCBCB	3⊕2⊕1
ABAC	1⊕3	ABCBAB	3⊕2⊕1
		ABCBAC	3⊕3
ABCAB	5	ABABCA	2⊕4
ABCAC	4⊕1	ABABCB	2⊕3⊕1
ABCBC	3⊕2	ABABAB	2⊕2⊕2
ABCBA	3⊕2	ABABAC	2⊕1⊕3
ABABC	2⊕3	ABACAB	2⊕1⊕3
ABABA	2⊕2⊕1	ABACAC	1⊕3⊕2
ABACA	1⊕3⊕1	ABACBC	1⊕4⊕1
ABACB	1⊕4	ABACBA	1⊕5

In applying these rules, the simplest case is repeated ABC stacking for which there are no stacking sense reversals and therefore a single $J = N$ partition. In the opposite limit, repeated AB stacking, the stacking sense is reversed in every layer and the rules imply $N/2$ partitions with $J = 2$ for even N, and when N is odd a remaining $J = 1$ partition.

Between these two limits, a rich variety of qualitatively distinct low-energy behaviors occur. For example, in the ABCB-stacked tetralayer, ABC is identified as a $J = 3$ doublet and the remaining B layer gives a $J = 1$ doublet. The low-energy band structure and the Landau-level structure of this stack, as illustrated in Figs. 11.6a and 11.10a, have two sets of low-energy bands with $|E| \propto k, k^3$, Landau levels with $|E| \propto B^{1/2}, B^{3/2}$, and four zero-energy Landau levels per spin and valley. All these properties are predicted by the partitioning rules.

11.4.5 Degenerate State Perturbation Theory

This approach starts from the well-known $J = 1$ massless Dirac equation [1,2] $\boldsymbol{k} \cdot \boldsymbol{p}$ model for isolated sheets,

$$H_{\mathrm{MD}}(\boldsymbol{p}) = -\begin{pmatrix} 0 & v\pi^\dagger \\ v\pi & 0 \end{pmatrix}, \tag{11.46}$$

where $\pi = p_x + \mathrm{i}p_y$ and v is the quasiparticle velocity. (For mathematical convenience we have chosen a gauge in which a minus sign appears in the definition.) An N-layer stack has a two-dimensional band structure with $2N$ atoms per unit cell. The Hamiltonian can be written as

$$H = H_\perp + H_\parallel, \tag{11.47}$$

where $H_\perp$ accounts for interlayer tunneling and $H_\parallel$ for intralayer tunneling. $H_\parallel$ is the direct product of massless Dirac model Hamiltonians $H_{\rm MD}$ for the sublattice pseudospin degrees of freedom of each layer. The low-energy Hamiltonian is constructed by first identifying the zero-energy eigenstates of $H_\perp$ and then treating $H_\parallel$ as a perturbation.

Referring to Fig. 11.11, $H_\perp$ is the direct product of a set of finite-length 1D tight-binding chains, as shown in (11.4), and a null matrix with dimension equal to the number of isolated sites. The set of zero-energy eigenstates of $H_\perp$ consists of the states localized on isolated sites and the single zero-energy eigenstates of each odd-length chain.

The low-energy effective Hamiltonian is evaluated by applying leading order degenerate state perturbation theory to the zero-energy subspace. The matrix element of the effective Hamiltonian between degenerate zero-energy states r and r' is given by [41]

$$\langle \Psi_r | H | \Psi_{r'} \rangle = \langle \Psi_r | \, H_\parallel \left[\hat{Q}(-H_\perp^{-1}) \hat{Q} \, H_\parallel \right]^{n-1} | \Psi_{r'} \rangle \,, \tag{11.48}$$

where n is the smallest positive integer for which the matrix element is nonzero, $\hat{P}$ is a projection operator onto the zero-energy subspace and $\hat{Q} = 1 - \hat{P}$.

To understand the structure of this Hamiltonian, let us consider ABC-stacked multilayer graphene and re-derive the low-energy effective Hamiltonian in (11.24). For ABC-stacked N-layer graphene, the zero-energy states are the two isolated site states in bottom and top layers, α_1 and β_N. $N-1$ sets of two-site chains form high-energy states. Because $H_\parallel$ is diagonal in layer index and $H_\perp$ (and hence $H_\perp^{-1}$) can change the layer index by one unit, the lowest order at which α_1 and β_N are coupled is $n = N$.

According to (11.4), the wavefunction of each two-site chain is given by

$$|\Phi_{\sigma_r}\rangle = \frac{1}{\sqrt{2}} \big(|\beta_r\rangle + \sigma_r \, |\alpha_{r+1}\rangle \big) \tag{11.49}$$

with the energy $\varepsilon_r = t_\perp \sigma_r$, where $\sigma_r = \pm 1$ and $r = 1, 2, \ldots, N-1$. From (11.48),

$$\begin{aligned}
\langle \alpha_1 | H | \beta_N \rangle &= \langle \alpha_1 | \, H_\parallel \left[\hat{Q}(-H_\perp^{-1}) \hat{Q} \, H_\parallel \right]^{N-1} | \beta_N \rangle \\
&= \sum_{\{\sigma_r\}} \frac{\langle \alpha_1 | H_\parallel | \Phi_{\sigma_1} \rangle \cdots \langle \Phi_{\sigma_{N-1}} | H_\parallel | \beta_N \rangle}{(-\varepsilon_1) \cdots (-\varepsilon_{N-1})} \\
&= -t_\perp \sum_{\{\sigma_r\}} \frac{(-\sigma_1/2) \ldots (-\sigma_{N-1}/2)}{(-\sigma_1) \cdots (-\sigma_{N-1})} (v^\dagger)^N \\
&= -t_\perp (v^\dagger)^N \sum_{\sigma_1, \ldots, \sigma_{N-1}} \frac{1}{2^{N-1}} \\
&= -t_\perp (v^\dagger)^N ,
\end{aligned} \tag{11.50}$$

where $v = v\pi/t_\perp$. Here $\langle\alpha_1|H_\parallel|\Phi_{\sigma_1}\rangle = -(1/\sqrt{2})t_\perp v^\dagger$, $\langle\Phi_{\sigma_{N-1}}|H_\parallel|\beta_N\rangle = -(\sigma_{N-1}/\sqrt{2})t_\perp v^\dagger$ and $\langle\Phi_{\sigma_r}|H_\parallel|\Phi_{\sigma_{r+1}}\rangle = -(\sigma_r/2)t_\perp v^\dagger$ were used. Thus, the effective Hamiltonian of N-layer graphene with ABC stacking has a single $J = N$ pseudospin doublet given by

$$H_N^{\text{eff}} = -t_\perp \begin{pmatrix} 0 & (v^\dagger)^N \\ (v)^N & 0 \end{pmatrix}. \tag{11.51}$$

A more complex but representative example is realized by placing a single reversed layer on top of ABC-stacked N-layer graphene with $N > 2$. Note that the last chain has three sites, thus it has a zero-energy state β_{N+1}^- defined by

$$|\beta_{N+1}^-\rangle = \frac{1}{\sqrt{2}}\left(|\beta_{N+1}\rangle - |\beta_{N-1}\rangle\right), \tag{11.52}$$

and two high-energy states with energies $\sqrt{2}\sigma_{N-1}t_\perp$ defined by

$$|\Phi_{\sigma_{N-1}}\rangle = \frac{1}{2}|\beta_{N-1}\rangle + \frac{\sigma_{N-1}}{\sqrt{2}}|\alpha_N\rangle + \frac{1}{2}|\beta_{N+1}\rangle, \tag{11.53}$$

where $\sigma_{N-1} = \pm 1$. Then the first-order perturbation theory gives

$$\langle\alpha_{N+1}|H|\beta_{N+1}^-\rangle = -\frac{t_\perp}{\sqrt{2}}v\dagger, \tag{11.54}$$

suggesting the existence of the massless Dirac mode with a *reduced* velocity.

As in (11.50), the result is

$$H_{N+1}^{\text{eff}} = -t_\perp \begin{pmatrix} 0 & \frac{v^\dagger}{\sqrt{2}} & 0 & \frac{(v^\dagger)^2}{2} \\ \frac{v}{\sqrt{2}} & 0 & -\frac{(v)^{N-1}}{\sqrt{2}} & 0 \\ 0 & -\frac{(v^\dagger)^{N-1}}{\sqrt{2}} & 0 & \frac{(v^\dagger)^N}{2} \\ \frac{v^2}{2} & 0 & \frac{(v)^N}{2} & 0 \end{pmatrix}, \tag{11.55}$$

using a $(\alpha_{N+1}, \beta_{N+1}^-, \alpha_1, \beta_N)$ basis. The first 2×2 block in (11.55) gives a $J = 1$ doublet with a reduced velocity. The matrix in (11.55) is not block-diagonal thus the second 2×2 matrix block is not obviously an N-chiral system. The $J = N$ doublet in this instance includes both the (α_1, β_N) subspace contribution and an equal contribution due to perturbative coupling to the $(\alpha_{N+1}, \beta_{N+1}^-)$ subspace. Using a similar perturbation theory shown in (11.26), we can obtain higher order correction by integrating out the massless Dirac mode which forms a higher energy state. Then the final Hamiltonian is reduced to

$$H_{N+1}^{\text{eff}} \approx H_1 \oplus H_N, \tag{11.56}$$

where

$$H_1 = -t_\perp \begin{pmatrix} 0 & v^\dagger/\sqrt{2} \\ v/\sqrt{2} & 0 \end{pmatrix}, \quad H_N = -t_\perp \begin{pmatrix} 0 & (v^\dagger)^N \\ (v)^N & 0 \end{pmatrix}. \tag{11.57}$$

This means that the combined system can be described by a combination of one 1-chiral system with a reduced velocity and one N-chiral system. Note that stacking a layer with an opposite handedness partitions a system into systems with different chiralities.

Similarly, we can extend the degenerate state perturbation theory to arbitrarily stacked multilayer graphene [20, 21]. Then, the effective Hamiltonian of any N-layer graphene is given as follows:

$$H_N^{\text{eff}} \approx H_{J_1} \oplus H_{J_2} \oplus \cdots \oplus H_{J_{N_D}} \tag{11.58}$$

with the chirality sum rule in (11.45).

11.4.6 Limitations of the Minimal Model

The low-energy effective Hamiltonian has been obtained from the minimal model in which only the nearest-neighbor intralayer tunneling and nearest-neighbor interlayer tunneling are included. The result is valid when contributions from the neglected terms are smaller than the terms in the effective Hamiltonian from the minimal model.

For example, in bilayer graphene, if the interlayer tunneling term $\gamma_3 \approx 0.3\,\text{eV}$ from the $\alpha_1 \to \beta_2$ hopping process (called trigonal warping) is included, a term with an energy scale $v_3|\boldsymbol{p}|$ appears in the low-energy effective theory [39], where $\frac{\hbar v_3}{a} = \frac{\sqrt{3}}{2}\gamma_3$. Then the massive-chiral effective Hamiltonian in (11.23) applies at energies larger than the trigonal-warping scale but still smaller than the interlayer hopping scale

$$v_3|\boldsymbol{p}| < \frac{(v|\boldsymbol{p}|)^2}{t_\perp} < t_\perp. \tag{11.59}$$

11.4.7 Effects of the Consecutive Stacking

The analysis presented so far is based on the assumption that stacking one layer directly on top of its neighbor (AA, BB, or CC stacking) is not allowed. We can still apply a similar diagram analysis and identify the zero-energy states at the Dirac point even if a consecutive stacking exists. In this case, however, zero-energy states can appear not only at the Dirac points but also at other points in momentum space. The degenerate state perturbation theory at the Dirac point discussed so far, therefore, cannot completely capture the low-energy states.

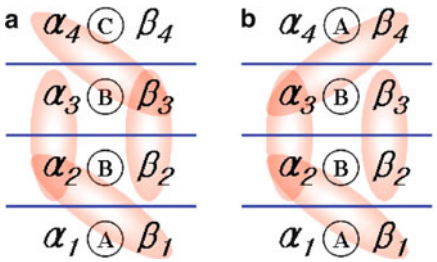

Fig. 11.12 Stacking diagrams for (**a**) ABBC-stacked and (**b**) ABBA-stacked tetralayer graphene. Shaded ovals link nearest-neighbor interlayers

As an example, let us consider ABBC-stacked tetralayer graphene, as illustrated in Fig. 11.12a. Here, in addition to α_1 and β_4, there are two zero-energy states at each three-site chain defined by

$$\left|\tilde{\beta}_1\right\rangle = \frac{1}{\sqrt{2}}\left(|\beta_1\rangle - |\alpha_3\rangle\right),$$
$$|\tilde{\alpha}_4\rangle = \frac{1}{\sqrt{2}}\left(|\alpha_4\rangle - |\beta_2\rangle\right). \tag{11.60}$$

Thus the matrix elements between low-energy states are given by

$$\left\langle\alpha_1|H|\tilde{\beta}_1\right\rangle = \langle\tilde{\alpha}_4|H|\beta_4\rangle = -\frac{t_\perp}{\sqrt{2}}v^\dagger. \tag{11.61}$$

Therefore, the system at the Dirac point can be described by two massless Dirac modes with a reduced velocity, as shown in Figs. 11.6b and 11.10b.

Another example is ABBA-stacked tetralayer graphene, as illustrated in Fig. 11.12b. In this case, there are two zero-energy states at α_1 and α_4. The high-energy states Φ_r and corresponding energies ε_r are given by (11.4) with $N = 4$; thus

$$\langle\alpha_1|H|\alpha_4\rangle = \sum_{r=1}^{4}\frac{\langle\alpha_1|H_\parallel|\Phi_r\rangle\langle\Phi_r|H_\parallel|\alpha_4\rangle}{(-\varepsilon_r)} = -ct_\perp|v|^2, \tag{11.62}$$

where $c = \frac{1}{5}\sum_r \sin\left(\frac{r\pi}{5}\right)\sin\left(\frac{4r\pi}{5}\right)/\cos\left(\frac{r\pi}{5}\right) = -1$. Here the low-energy state is composed of one *non-chiral* massive mode. Note that because of the non-chirality, there are no zero-energy Landau levels.

11.5 Applications

11.5.1 Quantum Hall Conductivity

Applying the Kubo formula to a disorder-free systems gives the conductivity tensor with an external magnetic field along z,

$$\sigma_{ij}(\omega) = -\frac{e^2}{2\pi\hbar l_B^2} \sum_n f_n \Omega_{ij}^n(\omega), \tag{11.63}$$

where f_n is Fermi factor of nth energy state, $i, j = x, y$ and

$$\Omega_{ij}^n(\omega) = \mathrm{i} \sum_{m \neq n} \left[\frac{\langle n|\hbar v_i|m\rangle \langle m|\hbar v_j|n\rangle}{(\varepsilon_n - \varepsilon_m)(\varepsilon_n - \varepsilon_m + \hbar\omega + \mathrm{i}\eta)} - \frac{\langle m|\hbar v_i|n\rangle \langle n|\hbar v_j|m\rangle}{(\varepsilon_n - \varepsilon_m)(\varepsilon_n - \varepsilon_m - \hbar\omega - \mathrm{i}\eta)} \right]. \tag{11.64}$$

Here v_i is a velocity operator obtained by taking a derivative of the Hamiltonian $H(\boldsymbol{p})$ with respect to p_i. Note that in the case of multilayer graphene, the velocity operator is constant, i.e., it does not depend on the Landau-level index.

The appropriate quantized Hall conductivity is obtained by evaluating $\sigma_{\mathrm{H}} = \sigma_{xy}(0)$. In Fig. 11.13, we plot the noninteracting Hall conductivity as a function of Fermi energy for normal tetralayer graphene stacks assuming neutralizing ionized donors spread equally between the four layers. Note that though the positions of jumps in the Hall conductivity are different depending on the stacking sequences, all the normal tetralayers follow the same quantization rule with the large jump between the $\pm(4e^2/h)N/2$ Hall plateaus at $\varepsilon_{\mathrm{F}} = 0$, where $N = 4$ for tetralayers.

It follows from (11.45) that the Hall conductivity of an N-layer stack has strong integer quantum Hall effects with the following quantization rule:

$$\sigma_{xy} = \pm\frac{4e^2}{h}\left(\frac{N}{2} + n\right), \tag{11.65}$$

where n is a non-negative integer.

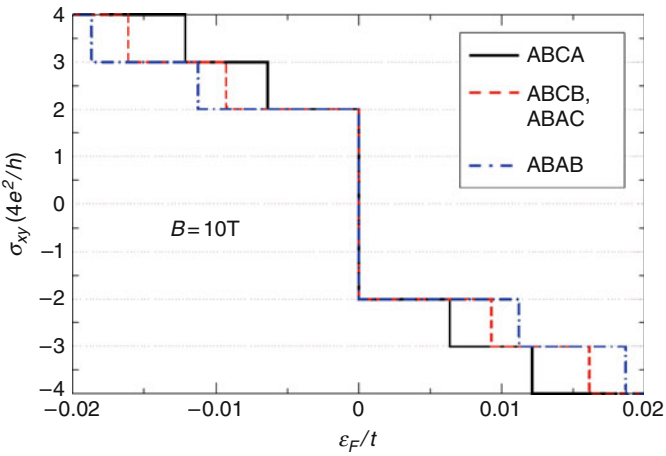

Fig. 11.13 Noninteracting system Hall conductivity as a function of the Fermi energy for all the normal tetralayer graphene stacks when $B = 10\,\mathrm{T}$, $t = 3\,\mathrm{eV}$, and $t_\perp = 0.1t$. The Hall conductivity calculations shown in this figure assume neutralizing ionized donors spread equally between the four layers

Although the minimal model we use includes only the nearest-neighbor intralayer tunneling and nearest-neighbor interlayer tunneling, these results are approximately valid in the broad intermediate magnetic field B range between $\approx$10 and $\approx$100 T, over which the intralayer hopping energy in the field ($\approx\hbar v/\ell$, where $\ell/\sqrt{|B|} = \sqrt{\hbar c/e} \approx 25.7\,\mathrm{nm}/\sqrt{\mathrm{T}}$ defines the magnetic length ℓ) is larger than the distant neighbor interlayer hopping amplitudes that we have neglected but still smaller than $t_\perp$. For example, consider the $\alpha_1 \to \alpha_3$ hopping process in ABA-stacked trilayer with the tunneling term $\gamma_2 \approx -20\,\mathrm{meV}$ [16], then the valid range of magnetic field for the minimal model is given by

$$|\gamma_2| < \frac{(\hbar v/l)^2}{t_\perp} < t_\perp. \tag{11.66}$$

When γ_2 does not play an important role (in $N = 2$ stacks, for example), the lower limit of the validity range is parametrically smaller. The minimum field in bilayers has been estimated to be $\approx$1 T [39], by comparing intralayer hopping with the $\gamma_3 \approx 0.3\,\mathrm{eV}$ interlayer hopping amplitude as in (11.59),

$$\hbar v_3/l < \frac{(\hbar v/l)^2}{t_\perp} < t_\perp. \tag{11.67}$$

Discussion on the effects of disorder and electron–electron interactions can be found in Refs. [20, 21].

11.5.2 Optical Conductivity

One particularly intriguing property of neutral single-layer graphene sheets is the interband optical conductivity [42–45], which is approximately constant over a broad range of frequencies with a value close to

$$\sigma_{\mathrm{uni}} = \frac{\pi}{2}\frac{e^2}{h}, \tag{11.68}$$

dependent only on fundamental constants of nature. Recently, it was also found [46] that for frequencies in the optical range, the conductivity per layer in multilayer graphene sheets is also surprisingly close to σ_{uni}. Here we identify the emergent chiral symmetry of multilayers as a key element of the physics responsible for the ubiquity of σ_{uni} in multilayer graphene systems [28].

The optical conductivity of an N-layer system is expected to approach $N\sigma_{\mathrm{uni}}$ for frequencies that exceed the interlayer-coupling scale but are smaller than the π-bandwidth scale, since the layers then contribute independently and the Dirac model still applies. In the low-energy limit the spectrum separates asymptotically into decoupled pseudospin doublets, each of which has chiral symmetry. The

conductivity of a pseudospin doublet with chirality J is $J\sigma_{\text{uni}}$. It then follows from the chirality sum rule in (11.45) that the conductivity of the ideal model also approaches $N\sigma_{\text{uni}}$ in the $\omega \to 0$ limit. Note that the low-frequency limit of the interband conductivity does not result from independent single-layer contributions but has a completely different origin.

The Kubo formula for the real part of the optical conductivity, $\sigma_{\text{R}}(\omega) \equiv \text{Re}[\sigma_{xx}(\omega)]$, of a 2D electron-gas system is

$$\sigma_{\text{R}}(\omega) = -\frac{\pi e^2}{h} \sum_{n \neq n'} \int \frac{\text{d}^2 k}{2\pi} \frac{f_{n,\boldsymbol{k}} - f_{n',\boldsymbol{k}}}{\varepsilon_{n,\boldsymbol{k}} - \varepsilon_{n',\boldsymbol{k}}} \times \left| \langle n, \boldsymbol{k} | \, \hbar v_x \, | n', \boldsymbol{k} \rangle \right|^2 \delta(\hbar\omega + \varepsilon_{n,\boldsymbol{k}} - \varepsilon_{n',\boldsymbol{k}}), \tag{11.69}$$

where $\varepsilon_{n,\boldsymbol{k}}$ and $|n, \boldsymbol{k}\rangle$ are eigenvalues and eigenvectors of the Hamiltonian matrix H, $f_{n,\boldsymbol{k}}$ is a Fermi occupation factor and $v_a = \partial H/\hbar\partial k_a$ is the velocity operator.

Figure 11.14 shows the optical conductivity for all the normal tetralayer graphene stacks. The rhombohedral ABCA stacking yields a $J = 4$ low-energy chiral doublet and three two-site-chain split-off bands. The optical conductivity has a divergent infrared (IR) feature associated with the $J = 4$ chiral doublet to two-site chain transitions. The onset of this absorption band has an extremum at finite $ka \approx 0.1$, implying a divergent joint density of states. Bernal ABAB stacking yields two $J = 2$ chiral doublets and four-site-chain split-off bands. The optical conductivity shows two jump-discontinuity IR features associated with $\boldsymbol{k} = 0$ transitions between the $J = 2$ doublets and the split-off bands. Intermediate ABCB and ABAC stackings, which are related by inversion symmetry, yield $J = 1$ and $J = 3$ chiral doublets and both two- and three-site-chain split-off bands. The optical conductivity shows strong IR features associated with transitions between the chiral doublets and split-off bands. As shown in this example, the optical conductivity spectrum can provide a convenient qualitative characterization of multilayer graphene stacks [28].

11.5.3 Electrical Conductivity

We can apply the multilayer graphene theory developed so far to the transport properties of multilayer graphene. (See Chap. 12 for transport theory in graphene.) From the Einstein relation, the electrical conductivity is given by

$$\sigma = e^2 \mathcal{D}(\varepsilon_{\text{F}}) D, \tag{11.70}$$

where $\mathcal{D}(\varepsilon_{\text{F}})$ is the density of states at the Fermi energy ε_{F} and D is the diffusion constant. In graphene, $\mathcal{D}(\varepsilon_{\text{F}}) = g_{\text{s}} g_{\text{v}} \rho(\varepsilon_{\text{F}})$ where $g_{\text{s}} = 2$ and $g_{\text{v}} = 2$ are spin and valley degeneracy factors, respectively, and $\rho(\varepsilon_{\text{F}})$ is the density of states per spin

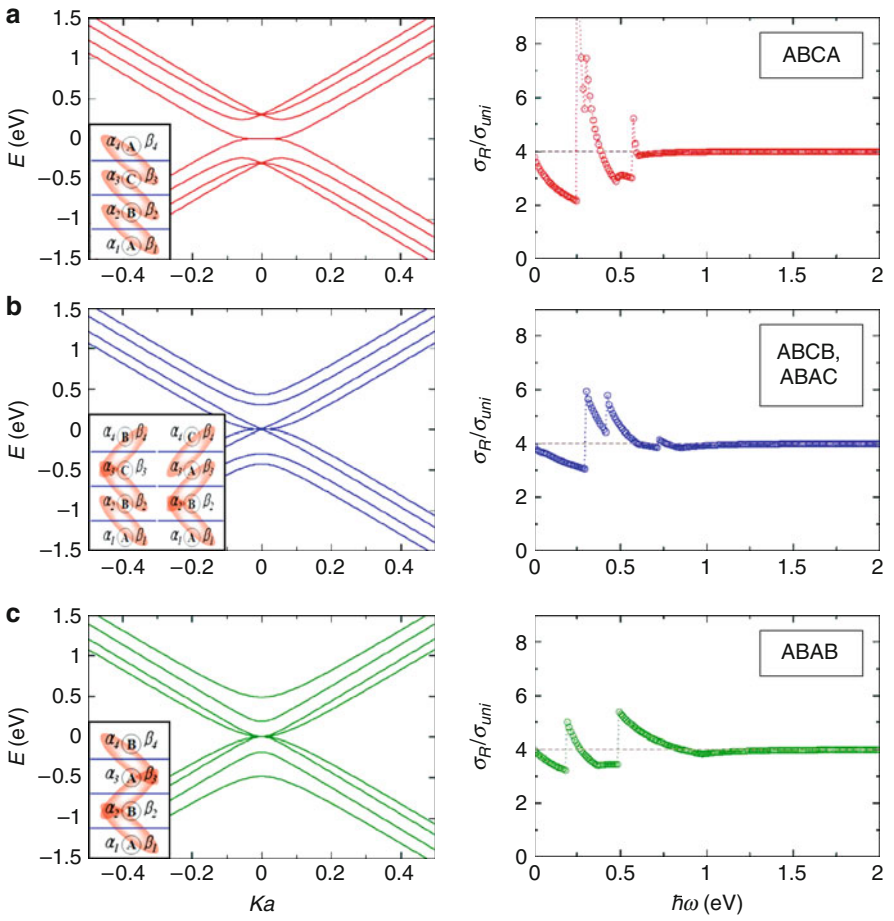

Fig. 11.14 Energy band structure and real part of the conductivity for all the normal tetralayer graphene stacks, ABCA (*top*), ABCB, ABAC (*middle*) and ABAB (*bottom*). The *insets* show stacking diagrams where *shaded ovals* link sublattices α and β to the nearest-neighbor interlayers

and valley. In 2D electron system, the diffusion constant is given by $D = \frac{1}{2} v_{\mathrm{F}}^2 \tau_{\mathrm{F}}$ where v_{F} is the Fermi velocity and τ_{F} is the relaxation time.

For simplicity, assume rotational symmetry in the energy spectrum. Then v_{F} and $\rho(\varepsilon_{\mathrm{F}})$ are given by

$$v_{\mathrm{F}} = \frac{1}{\hbar} \left. \frac{\mathrm{d}\varepsilon}{\mathrm{d}k} \right|_{\varepsilon=\varepsilon_{\mathrm{F}}} \tag{11.71}$$

and

$$\rho(\varepsilon_{\mathrm{F}}) = \frac{k_{\mathrm{F}}}{2\pi \left| \mathrm{d}\varepsilon/\mathrm{d}k \right|_{\varepsilon=\varepsilon_{\mathrm{F}}}} = \frac{k_{\mathrm{F}}}{2\pi\hbar v_{\mathrm{F}}}. \tag{11.72}$$

From Fermi's golden rule, τ_F is given by

$$\frac{1}{\tau_F} = \frac{2\pi}{\hbar} n_I V_I^2 \rho(\varepsilon_F), \tag{11.73}$$

where V_I^2 is the squared effective impurity potential averaged over the azimuthal angle ϕ. In a graphene system, V_I^2 is given by

$$V_I^2 = \frac{1}{2\pi} \int_0^{2\pi} d\phi |V_I(\phi)|^2 F(\phi)(1 - \cos\phi), \tag{11.74}$$

where $V_I(\phi)$ is the matrix element of the impurity potential at ϕ and $F(\phi)$ is the chiral factor at the same band defined by

$$F(\phi) = |\langle k, \phi = 0 | k, \phi \rangle|^2. \tag{11.75}$$

Note that the relaxation time is a weighted average of the collision probability in which forward scattering ($\phi = 0$) receives very little weight.

As an example, consider simple short range scatterers neglecting interband scattering. The short range interaction can be characterized by the effective scattering cross-section length d_{sc} as

$$V_I(\phi) = \frac{2\pi e^2 d_{sc}}{\epsilon}, \tag{11.76}$$

where ϵ is the effective dielectric constant. Note that it is straightforward to extend the transport properties of multilayer graphene to other types of scatterers such as Coulomb interactions by changing the potential type in (11.74).

First, let us consider the general dependence of electrical conductivity σ on the density n for a J-chiral system. From (11.70),

$$\sigma \sim \rho(\varepsilon_F) v_F^2 \tau_F. \tag{11.77}$$

Note that $v_F \sim k_F^{J-1}$, $\tau_F^{-1} \sim n_I V_I^2 \rho(\varepsilon_F)$, $\rho(\varepsilon_F) \sim k_F / v_F \sim k_F^{2-J}$ and $n = k_F^2/\pi$. From (11.76), the short range interaction has $V_I \sim$ constant. Thus, for a J-chiral system with short range scatterers, σ has the following form:

$$\sigma \sim \frac{n^{J-1}}{n_I}. \tag{11.78}$$

From the chiral decomposition of multilayer graphene, arbitrarily stacked multilayer graphene is described by direct products of a set of chiral systems. Thus at low energies, or equivalently at low densities, the electrical conductivity is described by the sum of each chirality contribution.

Figure 11.15 shows the electrical conductivity of all the normal tetralayer graphene for short range interaction neglecting the effect of electron–hole puddles and interband scattering. (See [32] for discussion of the electron-hole puddles,

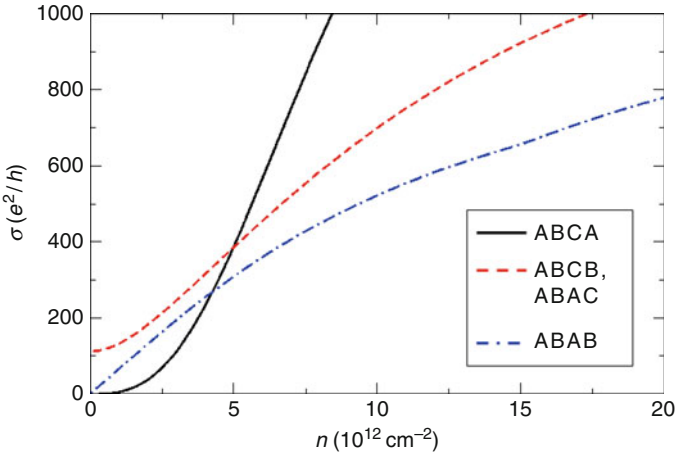

Fig. 11.15 Electrical conductivity of all the normal tetralayer graphene stacks for short range interaction with $\alpha_{gr} = e^2/(\epsilon\hbar v) = 1$ neglecting the effect of electron–hole puddles and interband scattering. The impurity density and effective impurity distance were set as $n_{\rm I} = 10^{12}$ cm^{-2} and $d_{\rm sc} = 0.3$ nm. For the hopping terms, $t = 3$ eV and $t_\perp = 0.1t$ were used, and other terms were neglected

interband scattering and other types of scatters.) At low densities, from (11.78), ABCA stacking, which yields a $J = 4$ chiral doublet, shows n^3 density dependence, while ABAB stacking, which yields two $J = 2$ chiral doublets, shows linear density dependence in the electrical conductivity for short range interaction. Intermediate ABCB and ABAC stackings, which yield $J = 1$ and $J = 3$ chiral doublets, show the density dependence for the superposition of n^0 and n^2. At high densities, however, energy band structure looks like a collection of monolayer graphene, thus the electrical conductivity eventually scales approximately as that of monolayer graphene.

11.6 Conclusions

We have demonstrated how the Hamiltonian of multilayer graphene is constructed using a π-orbital continuum model in the absence and presence of a magnetic field. A low-energy effective theory is derived using degenerate state perturbation theory. The low-energy bands of normal multilayer graphene can be decomposed into $N_{\rm D}$ pseudospin doublets with chirality J_i for ith doublet. Though $N_{\rm D}$ depends on the stacking sequence, $\sum_{i=1}^{N_{\rm D}} J_i = N$ is always satisfied in a normal N-layer graphene stack. Many physical properties of multilayer graphene systems can be understood easily from this chiral decomposition analysis.

Acknowledgements The work has been supported in part by the NIST-CNST/UMD-NanoCenter Cooperative Agreement. The authors thank J.J. McClelland, M.D. Stiles, S. Adam, and B.R. Sahu for their valuable comments.

References

1. A.K. Geim, K.S. Novoselov, Nat. Mater. **6**, 183 (2007)
2. A.K. Geim, A.H. MacDonald, Phys. Today **60**(8), 35 (2007)
3. M.I. Katsnelson, Mater. Today **10**, 20 (2007)
4. A.H. Castro Neto, F. Guinea, N.M.R. Peres, K.S. Novoselov, A.K. Geim, Rev. Mod. Phys. **81**, 109 (2009)
5. N.M.R. Peres, Rev. Mod. Phys. **82**, 2673 (2010)
6. S. Das Sarma, S. Adam, E.H. Hwang, E. Rossi, Rev. Mod. Phys. **83**, 407 (2011)
7. K.S. Novoselov, A.K. Geim, S.V. Morozov, D. Jiang, Y. Zhang, S.V. Dubonos, I.V. Grigorieva, A.A. Firsov, Science **306**, 666 (2004)
8. C. Berger, Z. Song, T. Li, X. Li, A.Y. Ogbazghi, R. Feng, Z. Dai, A.N. Marchenkov, E.H. Conrad, P.N. First, W.A. de Heer, J. Phys. Chem. B **108**, 19912 (2004)
9. T. Ohta, A. Bostwick, T. Seyller, K. Horn, E. Rotenberg, Science **313**, 951 (2006)
10. A. Rycerz, J. Tworzydl, C.W.J. Beenakker, Nat. Phys. **3**, 172 (2007)
11. V.V. Cheianov, V. Fal'ko, B.L. Altshuler, Science **315**, 1252 (2007)
12. K.S. Novoselov, A.K. Geim, S.V. Morozov, D. Jiang, M.I. Katsnelson, I.V. Grigorieva, S.V. Dubonos, A.A. Firsov, Nature **438**, 197 (2005)
13. Y. Zhang, Y.-W. Tan, H.L. Stormer, P. Kim, Nature **438**, 201 (2005)
14. S. Latil, L. Henrard, Phys. Rev. Lett. **97**, 036803 (2006)
15. F. Guinea, A.H. Castro Neto, N.M.R. Peres, Phys. Rev. B **73**, 245426 (2006)
16. B. Partoens, F.M. Peeters, Phys. Rev. B **74**, 075404 (2006)
17. B. Partoens, F.M. Peeters, Phys. Rev. B **75**, 193402 (2007)
18. M. Koshino, T. Ando, Phys. Rev. B **76**, 085425 (2007)
19. M. Koshino, T. Ando, Phys. Rev. B **77**, 115313 (2008)
20. H. Min, A.H. MacDonald, Phys. Rev. B **77**, 155416 (2008)
21. H. Min, A.H. MacDonald, Prog. Theor. Phys. Suppl. 176, 227 (2008)
22. M. Aoki, H. Amawashi, Solid State Commun. **142**, 123 (2007)
23. F. Zhang, B. Sahu, H. Min, A.H. MacDonald, Phys. Rev. B **82**, 035409 (2010)
24. K.F. Mak, J. Shan, T.F. Heinz, Phys. Rev. Lett. **104**, 176404 (2010)
25. C.L. Lu, C.P. Chang, Y.C. Huang, R.B. Chen, M.L. Lin, Phys. Rev. B **73**, 144427 (2006)
26. C.-L. Lu, H.-C. Lin, C.-C. Hwang, J. Wang, M.-F. Lin, C.-P. Chang, Appl. Phys. Lett. **89**, 221910 (2006)
27. M. Koshino, T. Ando, Solid State Commun. **149**, 1123 (2009)
28. H. Min, A.H. MacDonald, Phys. Rev. Lett. **103**, 067402 (2009)
29. J. Nilsson, A.H. Neto, F. Guinea, N.M. Peres, Phys. Rev. Lett. **97**, 266801 (2006)
30. J. Nilsson, A.H. Castro Neto, Phys. Rev. Lett. **98**, 126801 (2007)
31. J. Nilsson, A.H. Castro Neto, F. Guinea, N.M.R. Peres, Phys. Rev. B **78**, 045405 (2008)
32. H. Min, P. Jain, S. Adam, M.D. Stiles, Phys. Rev. B **83**, 195117 (2011)
33. H. Min, E.H. Hwang, S. Das Sarma, Phys. Rev. B **83**, 161404(R) (2011)
34. J.M.B. Lopes dos Santos, N.M.R. Peres, A.H. Castro Neto, Phys. Rev. Lett. **99**, 256802 (2007)
35. J. Hass, F. Varchon, J.E. Millăn-Otoya, M. Sprinkle, N. Sharma, W.A. de Heer, C. Berger, P.N. First, L. Magaud, E.H. Conrad, Phys. Rev. Lett. **100**, 125504 (2008)
36. E.J. Mele, Phys. Rev. B **81**, 161405(R) (2010)
37. P.D. Ritger, N.J. Rose, *Equations with Applications* (McGraw-Hill Book Company, New York, 1968)
38. R. Saito, G. Dresselhaus, M.S. Dresselhaus, *Physical Properties of Carbon Nanotubes* (Imperial College Press, London, 1998)
39. E. McCann, V.I. Falko, Phys. Rev. Lett. **96**, 086805 (2006)
40. J.C. Charlier, J.P. Michenaud, X. Gonze, Phys. Rev. B **46**, 4531 (1992)
41. J.J. Sakurai, *Modern Quantum Mechanics* (Addison Wesley, Reading, 1994)
42. R.R. Nair, P. Blake, A.N. Grigorenko, K.S. Novoselov, T.J. Booth, T. Stauber, N.M.R. Peres, A.K. Geim, Science **320**, 1308 (2008)

43. F. Wang, Y. Zhang, C. Tian, C. Girit, A. Zettl, M. Crommie, Y.R. Shen, Science **320**, 206 (2008)
44. Z.Q. Li, E.A. Henriksen, Z. Jiang, Z. Hao, M.C. Martin, P. Kim, H.L. Stormer, D.N. Basov, Nat. Phy. **4**, 532 (2008)
45. K.F. Mak, M.Y. Sfeir, Y. Wu, C.H. Lui, J.A. Misewich, T.F. Heinz, Phys. Rev. Lett. **101**, 196405 (2008)
46. P.E. Gaskell, C. Rodenchuk, H.S. Skulason, T. Szkope, Appl. Phys. Lett. **94**, 143101 (2009)

Chapter 12
Graphene Carrier Transport Theory

Shaffique Adam

Abstract This chapter describes the theory of carrier transport in two-dimensional graphene sheets. At high carrier density, the conductivity of graphene depends on carrier density, the dielectric constant of the substrate, and the properties of the impurity potential, which all can be treated using the Boltzmann transport formalism. At low carrier density, disorder causes the local random fluctuations in carrier density to exceed the average density. As a consequence, the carrier transport at the Dirac point is highly inhomogeneous. The ensemble-averaged properties of these puddles of electrons and holes are described by a self-consistent theory, and the conductivity of this inhomogeneous medium is given by an effective medium theory. Comparing this transport theory with the results of representative experiments rigorously tests it validity and accuracy.

12.1 Introduction

Graphene has emerged as an exciting new material with remarkable technological promise and fascinating theoretical possibilities. On the materials front, graphene is the strongest measured material [1], has demonstrated superiority over conventional materials for high-frequency applications [2] and has the highest phonon-limited mobility at room-temperature of any known semiconductor [3]. It was recently demonstrated that graphene is a cheap and versatile transparent conductor suitable for touch-screen and solar cell applications [4]. On the theoretical front, among many exciting proposals, graphene's Weyl-Dirac description gives rise to: a quantum critical Dirac point where perfectly clean graphene at zero temperature has no intrinsic length scale (see, e.g., [5]); a topological symmetry that enables graphene

S. Adam (✉)
Center for Nanoscale Science and Technology, National Institute of Standards and Technology, Gaithersburg, MD 20899-6202, USA
e-mail: shaffique.adam@nist.gov

H. Raza (ed.), *Graphene Nanoelectronics*, NanoScience and Technology,
DOI 10.1007/978-3-642-22984-8_12, © Springer-Verlag Berlin Heidelberg 2012

to evade Anderson localization in the absence of a magnetic field [6–8]; and the possibility for the emergence of novel quantum states [9]. But the heart of graphene studies and its subsequent electronic applications is to understand and explain the first measurements [10–13] of carrier transport in these single-atom-thick planer sheets of carbon atoms.

The electronic structure of graphene was discussed in Chap. 8. The subject of this chapter is to understand the transport mechanisms in these 2D graphene sheets. The result is a complex interplay of weak disorder, weak electron–electron interactions, and some quantum mechanics that conspire together to give the constant mobility at high carrier density and the minimum conductivity plateau at low density [14].

The purpose of this chapter is not to be a review of the graphene transport literature; indeed, three such reviews became available recently [15–17], and all of the material covered here can be found in either [15] or [18], which provide the full context, history, and shortcomings of this work as well as a comprehensive comparison with alternative theoretical approaches. Nor is this intended to be a substitute for the original literature; rather, it is a presentation of the main concepts leading up to the calculation of graphene's conductivity in a coherent and pedagogical manner, providing extended details (beyond those available in the terse format of the original articles), so that a motivated graduate student could reproduce the calculations, while simultaneously highlighting with broad strokes the essential insights that motivated those calculations.

Our starting point is to appreciate that theoretical studies [19, 20] anteceding graphene's discovery predicted that graphene should have a universal minimum conductivity at zero carrier density and a density-independent, but disorder dependent conductivity at high density. The first transport experiments in graphene [10–13] completely defied both these expectations: the minimum conductivity, while finite, showed significant sample-to-sample fluctuations, and at high carrier density, the conductivity increased linearly with carrier density.

While some questions still remain, we now more-or-less understand these trends quantitatively. The theory relies on three important concepts that make up the core of this chapter. First, graphene's linear dispersion gives rise to quite unusual screening properties. In Sect. 12.2.1, screening is treated within the Random Phase Approximation (RPA), where one finds [21–24] that graphene behaves like a metal at distances longer than the Fermi wavelength and like an insulator at shorter distances. It is this unusual screening, for example, that results in the inability of graphene to screen out long-range impurity potentials such as charged Coulomb impurities. In this context, the rest of Sect. 12.2 discusses the semiclassical Boltzmann transport theory for different impurity models including screened charged impurities [14, 21, 25, 26], Yukawa potentials [27, 28], screened short-range scatterers [29], and midgap states [30], concluding that charged impurities are likely to be the dominant scattering mechanism in current transport experiments using exfoliated graphene on insulating substrates.

The self-consistent approximation [14] to describe the ground-state properties of graphene close to the Dirac point is presented in Sect. 12.3.1. At low carrier density, the disorder-induced fluctuations in the local carrier density become larger than the

average density. The system breaks up into inhomogeneous regions with varying carrier density, commonly referred to as electron and hole puddles (see Chap. 15 for a discussion of the p-n junctions that form at the interface of these puddles).

For short-range disorder, this gives rise to an effective carrier density that scales as the square-root of the areal density of impurities, while for charged impurities, the problem needs to be solved self-consistently. By mapping the screened potential onto a Gaussian model, we can solve for all statistical properties of the electron and hole puddles including their root-mean-square carrier density and the typical size of a puddle [31]. We show that the predictions of the self-consistent approximation [14] are in good agreement with numerical density functional theory results [32, 33] as well as local spectroscopic probes of graphene [34–37].

In Sect. 12.3.2, we discuss electron transport in this inhomogeneous potential using an effective medium theory [38–40]. This is a systematic technique to obtain the conductivity of an inhomogeneous material by mapping it onto a uniform system with the same conductivity. This allows us to describe the full crossover from the Dirac point, where fluctuations dominate the transport to high carrier density, where these fluctuations are irrelevant. In Sect. 12.3.3, we discuss the transport properties at finite temperature, by including the activated transport in both the electron and hole regimes; and in a finite magnetic field. In Sect. 12.3.4, we study the quantum transport in graphene [7] assuming the Gaussian correlated impurity model. By comparing a fully quantum-mechanical numerical calculation of the conductivity to the semiclassical Boltzmann transport theory, we find that while the two theories are incompatible at weak disorder, they are compatible for strong disorder [41]. This result elucidates why quantum corrections are small and the semiclassical transport theory should dominate in the experimentally relevant regime. By combining these four concepts (i.e., graphene screening, Klein tunneling, the self-consistent approximation, and the effective medium theory), we summarize our results in Sect. 12.3.5 and demonstrate that four distinct features of the graphene transport measurements, namely, (1) the shift of the Dirac point (or charge neutrality point) to a nonzero applied back-gate voltage; (2) the carrier mobility at high density; (3) the value of the minimum conductivity, and (4) the width of the minimum conductivity plateau are all captured by the theory, which depends on only two experimentally tunable parameters (n_{imp}, which is the areal density of charged impurities, and r_s, which is the effective fine structure constant in graphene determined by its dielectric environment).

Finally, in Sect.12.4 we discuss a sample of three representative experiments that confirm the predictions of the theory. The first looks at magnetotransport data taken from the Manchester group [42], where we demonstrate that having fixed n_{imp} from the transport data at zero magnetic field, one gets agreement at weak field for both $\rho_{xx}(B)$ and $\rho_{xy}(B)$ without introducing any additional parameters [43]. We then compare the predictions for $\sigma_{\mathrm{min}}(n_{\mathrm{imp}})$ with several of the early experiments in the literature including data from Columbia group [13], where they found samples with over an order-of-magnitude variation in the sample mobility, and from Maryland group [44], where they directly tuned n_{imp} by adding potassium impurities to graphene in ultra-high vacuum. Finally, we discuss a third experiment, where r_s

was tuned by depositing several monolayers of ice on top of the graphene sheet [28] providing a parameter-free test of the theoretical predictions. Our main conclusion is that these experiments (and others) have shown remarkable agreement with the theoretical predictions discussed in this chapter.

12.2 Graphene Boltzmann Transport

The derivation of the semiclassical Drude–Boltzmann transport formalism can be found in several solid state textbooks [45, 46] and is basically a way of calculating the scattering time τ by accounting for the charge flow into and out of momentum eigenstates of the disorder-free system caused by the scattering potential. The formalism is considered semiclassical because the carrier dynamics are assumed to be a classical diffusion process between scattering centers, but the scattering is assumed to be quantum mechanical (where for weak disorder, for example, is calculated within the Born approximation.[1]) For our purposes, this is equivalent to the the leading order diagrammatic expansion for the current–current correlation function within the Kubo formalism in the limit of either vanishing disorder, or when $k_F\ell \gg 1$, where k_F is the Fermi momentum and $\ell = v_F\tau$ is the mean free path.

The result is often expressed as the Einstein relation $\sigma = e^2\nu(E_F)D$, where $\nu(E_F) = 2_s2_v|E_F|/(2\pi\hbar^2v_F^2)$ is the density of states at the Fermi energy (only electrons close to the Fermi energy are involved in transport), and $D = v_F^2\tau/2$ is the diffusion constant in two dimensions. The "classical" contribution to the conductivity is therefore

$$\sigma = \frac{2_s2_ve^2}{2h}k_F\ell, \tag{12.1}$$

where 2_s accounts for spin degeneracy, and considering the two graphene valleys as decoupled gives 2_v.

The total conductivity, taking into account the next leading order in $k_F\ell$ includes "quantum corrections" $\Delta\sigma = \pm[2_s2_ve^2/(\pi h)]\ln(L/\ell)$ that we discuss in Sect. 12.3.4 below. The Boltzmann transport theory gives the mean free path $\ell = v_F\tau$ as

$$\frac{\hbar}{\tau} = 2\pi n_{\rm imp}\sum_{\mathbf{k}'}\left|\frac{V(q)}{\epsilon(q)}\right|^2 F(\theta)\frac{1-\cos(\theta)}{2}\delta(E_F-\varepsilon_{k'}). \tag{12.2}$$

The derivation of this equation is a straightforward extension of the usual case and will not be done here. Instead, we briefly define all the terms and motivate their

[1]The Born approximation treats the scattering potential to leading order. It is not obvious that attempts to go beyond the approach presented here have provided a more accurate solution (see discussion in [15] and [41]). A critique of the Born approximation can be found in [17] and [47].

origin. $n_{\rm imp}$ is the two-dimensional areal density of impurities. As alluded to above, one can obtain this "classical" limit by considering the case of vanishing impurity concentration, and the leading order term is therefore linear in $n_{\rm imp}$. Built into (12.2) is the assumption that the impurities are uncorrelated and the concentration is dilute enough so that processes involving multiple scattering off the same impurity are smaller than the single scattering process. The δ-function guarantees energy conservation and requires that only the electrons at the Fermi energy participate in the transport, while $q = |\mathbf{k} - \mathbf{k}'|$ is the momentum transfer between incoming plane-waves with wave vector $\mathbf{k}$ and outgoing wavefunctions with wavevector $\mathbf{k}'$. Note, $\mathbf{k}$ and $\mathbf{k}'$ lie on different points of the circular Fermi surface of radius $k_{\rm F}$ thereby defining the scattering angle $\theta = \theta_{kk'}$.

What is different for graphene is the "chirality factor" $F(\theta)$, which arises from the fact that the eigenvectors of the Dirac Hamiltonian are plane waves multiplied by spinors that for momentum states given by k_x and k_y depend only on the angle $\theta_{\mathbf{k}} = \arctan(k_y/k_x)$. Computing the overlap between incoming and outgoing states involves an overlap of the spinor parts of the wavefunction, which gives $F(\theta) = [1 + \cos(\theta)]/2$ for Dirac fermions [21, 25, 26]. A little bit of algebra gives

$$\frac{\hbar}{\tau} = \frac{4}{\pi}\frac{k_{\rm F}}{v_{\rm F}}\int_0^1 d\eta\, \eta^2\sqrt{1-\eta^2}\left|\frac{V(2k_{\rm F}\eta)}{\epsilon(2k_{\rm F}\eta)}\right|^2, \tag{12.3}$$

where $V(q = 2k_{\rm F}\eta)$ is the bare-scattering potential, and $\epsilon(q = 2k_{\rm F}\eta)$ is the static dielectric function that accounts for the screening by electrons. It should be clear from (12.3) that the nature of both the impurity potential and the screening function can have a major impact on graphene conductivity. For example, for unscreened Coulomb scatterers where $V(q) \sim q^{-1}$, we see that $\tau \sim k_{\rm F}$ implying that for fixed impurity concentration, the mean free path gets smaller (and vanishes) as one approaches the Dirac point (i.e., $k_{\rm F} \to 0$), whereas for unscreened delta-correlated scatterers defined here as having $V(q) \sim q^0$, we get $\tau \sim 1/k_{\rm F}$ and the mean free path gets larger (and diverges) as one approaches the Dirac point. This strong dependence on impurity type that follows directly from applying the rules of the semiclassical Drude–Boltzmann formalism to graphene can seem counter-intuitive to those more familiar with transport in conventional 2D systems (the same result is obtained using diagrammatic perturbation theory or Green's functions methods).

The contribution from screening can also seem unusual. As we shall see below, it turns out, by pure coincidence, that for graphene the Thomas–Fermi (TF) result is reproduced in the Random Phase Approximation (RPA) even for $q \neq 0$. (For $q = 0$ the agreement between RPA and Thomas–Fermi is guaranteed by the compressibility sum rule). Within the TF approximation, we have that $\epsilon(q, k_{\rm F})$ depends on the ratio $\eta = q/(2k_{\rm F})$ as

$$\epsilon(\eta) = 1 + V(q = 2k_{\rm F}\eta)\nu(E_{\rm F}) = 1 + 2r_s/\eta, \tag{12.4}$$

where $r_s = e^2/(\kappa\hbar v_F)$ is the gas parameter defined as the ratio of potential energy to kinetic energy, which measures the relative strength of the electron–electron interactions. Equivalently, r_s can be thought of as the effective "fine-structure constant" or coupling constant for interacting Dirac fermions. We note in passing that for a parabolic dispersion $r_s \sim k_F^{-1}$ so that low carrier density heralds the strongly interacting regime, while for graphene's linear dispersion $r_s \approx 2/\kappa \leq 2$, is density independent.[2]

One interesting and perhaps unexpected effect is the opposite role of dielectric screening for Coulomb and short-range impurities. One notices that increasing the dielectric screening of the environment (i.e., increasing κ or decreasing r_s) *decreases the conductivity* for delta-correlated impurities, where $V(q) \sim q^0$. This is because decreasing r_s reduces the electron–electron interactions and therefore the ability of the electron gas to screen the impurity potential, making the disorder potential appear stronger than before. In sharp contrast, for Coulomb scatterers where $V(q) \sim e^2/(\kappa q) \sim r_s/q$, decreasing r_s weakens the impurity potential thereby *increasing the conductivity*.

While the discussion so far has been somewhat qualitative, the goal for the remainder of this section is to be more quantitative. The semiclassical transport result (12.3) depends on the interplay between the impurity potential $V(q)$ and the screening properties of graphene electrons. We will first discuss the calculation of $\epsilon(q)$ within the RPA, followed by the calculation of the conductivity with different choices for the disorder potential $V(q)$.

12.2.1 Screening: Random Phase Approximation (RPA)

In the modern context,[3] the RPA approximation is usually understood in terms of a diagrammatic expansion for the electron gas self-energy (see [45, 46]). Within the RPA, the dielectric function is related to the polarizability as $\epsilon(q) = 1 + V(q)\Pi(q)$ (see right panel of Fig. 12.1), where $\Pi(q)$ (left panel of Fig. 12.1) is the polarizability function (or "pair-bubble"). The goal of this section is to calculate the pair-bubble for graphene. We now know that both the inter-band and intra-band contributions are important. Historically, the inter-band contribution was derived much earlier [48], while the full solution for the graphene polarizability appeared

[2]Here, κ is the average of the dielectric constants of the medium above and below the graphene sheet, and the numerical coefficient ($\max[r_s] \approx 2$) is a material parameter set by the overlap of the carbon π-orbitals in the honeycomb lattice and the separation between the carbon atoms set by the σ-bonds.

[3]Historically, the RPA was introduced by Bohm and Pines when discussing the plasma oscillations of the electron gas in the high density limit. In that context, the approximation corresponds to looking at the Fourier transform of the potential energy and showing that after subtracting the term that was linear in carrier density, the subleading term had sums over the phase of electrons that depended on their position. Averaging over position gave a highly oscillatory summand that would be negligible or equivalent to the vanishing of that sum for random electron phases.

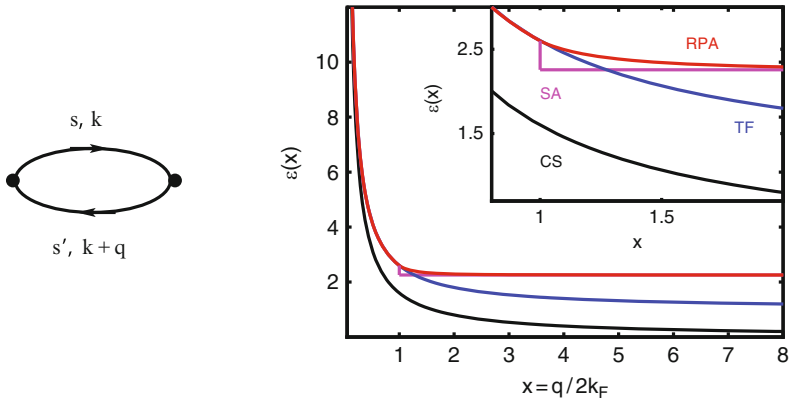

Fig. 12.1 Left panel shows diagrammatic representation of the polarization bubble corresponding to (12.5). The right panel shows different dielectric functions used in the literature, including the "Complete Screening" (CS), "Thomas-Fermi" (TF), and "Random Phase Approximation" (RPA). The inset shows a blow-up at $q = 2k_F$ to show how the "Step Approximation" (SA) given by (12.10) differs from the exact result (12.9)

only after the discovery of graphene [21–24]. Here, we follow the derivation by Hwang and Das Sarma [22].

The polarizability function (see Fig. 12.1) is given by

$$\Pi(q) = \frac{2_s 2_v}{L^2} \sum_{k,s,s'} \frac{f_k^s - f_{k'}^{s'}}{\varepsilon_{s,k} - \varepsilon_{s',k'}} \frac{1 + ss' \cos\theta_{k,k'}}{2}, \tag{12.5}$$

where f_k is the Fermi distribution, and what is different for graphene is the sum over both electron bands ($s = 1$) and hole bands ($s = -1$) and the overlap between the spinor components of the wavefunction (see [21] for more details). Expanding the sum over band-indices s, s', one can group the terms involving f^+ and f^- separately calling the former Π_+ and the later Π_-, where $\Pi(q) = \Pi^+(q) + \Pi^-(q)$. This grouping is especially useful since at zero temperature $f_k^+ = \theta(k_F - k)$ and $f_k^- = 1$. One notices that the term $\Pi^-(q)$ is just the contribution from a completely filled valence band and a completely empty conduction band (which is also called "intrinsic graphene"), while the term $\Pi^+(q)$ is the polarizability of, for example, a partially filled electron band ignoring the valence band. (Particle-hole symmetry means that it is the same for an empty conduction band with a valence band partially filled with holes. For simplicity, we assume that $E_F > 0$, where the corresponding results for $E_F < 0$ are identical). The intrinsic polarizability is given by[4]

[4]The integral can be done by making the substitution $x = |k| - |k + q|$ and noticing that

$$k\,dk = \frac{1}{2} \frac{x^2 - q^2}{x + q\cos\theta_{kq}} \frac{dx}{1 - \cos\theta_{kk'}}. \tag{12.6}$$

$$\Pi^{-}(q) = \frac{2_s 2_v}{\hbar v_{\rm F}} \int \frac{d^2k}{(2\pi)^2} \frac{1-\cos\theta}{|k|+|k+q|} = \frac{2_v 2_s q}{16\hbar v_{\rm F}}. \tag{12.7}$$

Since the intrinsic polarizability is proportional to q, one can immediately see that the dielectric function becomes independent of q, i.e. $\epsilon(q) = 1 + r_s\pi/2$. This result remains correct whenever $q \gg 2k_{\rm F}$, where one can then approximate the graphene polarizability as that of intrinsic graphene. At these large momenta (or small distances), the existence of a completely filled valence band means that graphene screens like a dielectric insulator.

In contrast, the contribution $\Pi^{+}(q)$ is metallic in nature (this is because particle-hole excitations around the Fermi circle are constrained by the compressibility sum rule, and these are bounded by the bottom of the conduction band). To calculate $\Pi^{+}(q)$, one first notices that the terms that involve $f_{k'}^{+}$ are related to those with f_k^{+} by a change of variable, where $\Pi^{+}(q) = \Pi_1^{+}(q) + \Pi_1^{+}(-q)$, and

$$\begin{aligned}\Pi_1^{+}(q) &= \frac{2_s 2_v}{\hbar v_{\rm F}} \int \frac{d^2k}{(2\pi)^2}\theta(k-k_{\rm F}) \frac{|k|+|k+q|\cos\theta_{kk'}}{(|k|+|k+q|)\,(|k|-|k+q|)}, \\ &= \frac{2_s 2_v}{4\hbar v_{\rm F}\pi}\left[1 + \frac{k_{\rm F}}{2\pi}\int_0^{k_{\rm F}} dk \int_0^{2\pi} d\phi \frac{4k^2-q^2}{q^2-2kq\cos\phi}\right]. \end{aligned} \tag{12.8}$$

For $|q| < 2k_{\rm F}$, the integral gives $-\pi|q|/8$ and this contribution to Π^{+} exactly cancels the intrinsic contribution from Π^{-}, so that the Thomas–Fermi result $\Pi(q) = \nu(E_{\rm F}) = 2k_{\rm F}/(\pi\hbar v_{\rm F})$ works beyond the $q \to 0$ limit.[5] Introducing the variable $x = q/2k_{\rm F}$ and putting everything together, the graphene polarizability is

$$\frac{\Pi(q=2k_{\rm F}x)}{\nu(E_{\rm F})} = \begin{cases} 1, & \text{for } x \le 1 \\ 1 + \dfrac{\pi x}{4} - \dfrac{x}{2}\arcsin\left(\dfrac{1}{x}\right) - \dfrac{1}{2x}\sqrt{x^2-1}, & \text{for } x \ge 1. \end{cases} \tag{12.9}$$

This coincidence of $\Pi(q)/\nu(E_{\rm F}) = 1$ for $q \le 2k_{\rm F}$ also holds for the 2D electron gas [49] but it is not universally true, *e.g.* it does not hold for graphene bilayers (see discussion in [15]). Moreover, as we shall see in Sect. 12.3 below, the Thomas–Fermi and RPA screening approximations give quantitatively different results for the disorder-induced potential fluctuations and the resulting graphene minimum conductivity at low carrier density. In this case, we will need the full dielectric function $\epsilon(q) = 1 + V(q)\Pi(q)$, which can readily be obtained from (12.9). However, since in such cases we are typically integrating $\epsilon(q)$ over all q, the

[5] The fact that $\Pi(q) = \nu(E_{\rm F})$ for $q \le 2k_{\rm F}$ implies that for high-density *transport properties*, the Thomas–Fermi approximation and the RPA give the same results (notice that (12.3) only integrates the dielectric function from 0 to $2k_{\rm F}$), where $\epsilon(q \le 2k_{\rm F}) = 1 + V(q)\Pi(q) = 1 + q_{\rm s}/q$.

full RPA result is indistinguishable from the following Step Approximation (SA) for the dielectric function [14]

$$\epsilon(q) = \begin{cases} 1 + \frac{q_s}{q}, & \text{for } q \le 2k_F \\ 1 + \frac{r_s \pi}{2}, & \text{for } q > 2k_F. \end{cases} \tag{12.10}$$

The graphene dielectric function is shown in Fig. 12.1, where we compare the Step Approximation (SA) given by (12.10) with the Thomas–Fermi (TF), RPA, and Complete Screening (CS) approximations. In this context, the CS approximation corresponds to the assumption $\epsilon(q) = q_s/q$, which can be thought of as the TF approximation with the additional assumption that $q_s \gg q$. However, for monolayer graphene since $r_s \le 2$ and $q_s = 4k_F r_s$, the condition $q \sim 2k_F \ll 4k_F r_s$ is never realized.

12.2.2 Coulomb Scatterers

Having established that (12.3) and (12.4) remain valid within the RPA, one can then calculate the transport properties of various scattering potentials. We begin with long-range Coulomb potentials. Taking the 2D Fourier transform of a charged impurity displaced by a distance d from the 2D plane in a medium with dielectric constant κ, we get

$$V(q) = \frac{2\pi e^2}{\kappa} \frac{e^{-qd}}{q}. \tag{12.11}$$

Solving (12.3) gives $\sigma(n, n_{\text{imp}}, r_s, d)$. The effect of increasing d is to slightly increase the conductivity from the $d = 0$ value [26]. For $d \approx 1$ nm, it is sufficient to use the result for $d = 0$, in which case, an analytic solution for $\sigma(n, n_{\text{imp}}, r_s, d = 0)$ can be obtained

$$\sigma = A[r_s] \frac{e^2}{h} \frac{n}{n_{\text{imp}}} = 20 \frac{e^2}{h} \frac{n}{n_{\text{imp}}} \quad \text{for } r_s = 0.8. \tag{12.12}$$

The function $A[r_s]$ is shown in Fig. 12.2. To be consistent with the notation in the original literature, we express $A[r_s] = F_1[x = 2r_s]^{-1}$, and

$$\frac{F_1(x)}{x^2} = \frac{\pi}{4} + 3x - \frac{3x^2\pi}{2} + x(3x^2 - 2)\frac{\arccos[1/x]}{\sqrt{x^2 - 1}}. \tag{12.13}$$

As anticipated in the discussion below (12.4), $A[r_s]$ is a monotonically decreasing function (see Fig. 12.2) implying that increasing the dielectric constant of the substrate would increase the graphene mobility provided the new substrate had a similar number of charge traps. Similarly, for suspended graphene, one "loses" about a factor of 2 from the decrease of $A[r_s]$, but since by current annealing the

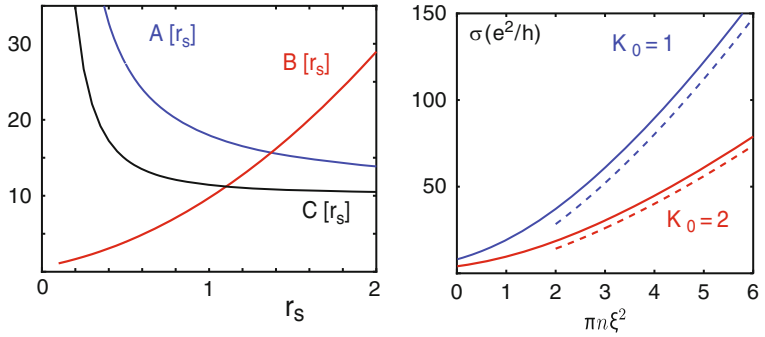

Fig. 12.2 High-density graphene conductivity for different impurity models. Left panel: Dimensionless coefficients that determine the dependence of the high-density conductivity on graphene's effective fine-structure constant r_s (see text for details). For charged impurities, $\sigma = A[r_s](e^2/h)(n/n_{\rm imp})$, while for delta-correlated impurities $\sigma = B[r_s](e^2/h)\sigma_0$. Yukawa-like disorder behaves qualitatively like charged impurities, $\sigma = C[r_s](e^2/h)(n/n_{\rm imp})$, although as seen in the figure, there are quantitative differences. Right panel: Conductivity for the Gaussian correlated impurity model as a function of $\pi n\xi^2$ for $K_0 = 1$ and $K_0 = 2$. Dashed lines are the high density asymptote $\sigma = (2\sqrt{\pi}e^2/K_0h)(2\pi n\xi^2)^{3/2}$

sample, one can reduce the impurity density by more than an order of magnitude, one can still drastically improve the carrier mobility [50, 51].

12.2.3 Gaussian White Noise Disorder

White noise disorder is the most common approximation made when discussing the conductivity of the regular 2D electron gas. One simply assumes that $V(q)$ is a constant (*i.e.*, independent of q). Mathematically, this corresponds to uncorrelated impurities each expressed as a delta-function in real space, *i.e.*, $V_{\rm tot}(r) = u_0 \sum_{i=1}^{N} \delta(r - r_i)$, where the impurities are located at positions r_i with zero range. Physically, this could correspond to atomically sharp defects such as dislocations or missing atoms (although when calculating their effect on the conductivity, here we neglect any intervalley transitions). Solving (12.3), we find $\sigma = B[r_s]\sigma_0$, where σ_0 is a constant proportional to $(n_{\rm imp}u_0^2)^{-1}$ and $B[r_s] = (F_2[x = 2r_s])^{-1}$, where

$$F_2(x) = \frac{\pi}{2} - \frac{16x}{3} + 40x^3 + 6\pi x^2 - 20\pi x^4 + 8x^2(5x^3 - 4x)\frac{\arccos[1/x]}{\sqrt{x^2-1}}. \tag{12.14}$$

The function $B[r_s]$ is shown in Fig. 12.2. We note that as discussed earlier, $B[r_s]$ is a monotonically increasing function of r_s since dielectric screening makes the impurity potential look weaker at larger r_s resulting in a larger conductivity. Also,

the functions $A[r_s]$ and $B[r_s]$ are real and positive for all values of $r_s > 0$ (i.e., the ratio of $\arccos(1/x)$ and $\sqrt{x^2-1}$ is real, even for values of $x < 1$).

12.2.4 Yukawa Potential

In principle, one could calculate the screening properties for any scattering potential. By comparison with experiment where the dielectric environment is changed (see Sect. 12.4 below), one could then establish definitively the nature of the disorder impurity potential. In 3D, the Yukawa potential (in real space) is the Fourier transform of the screened Coulomb potential (in momentum space). However, in 2D we have been unable to obtain a closed-form analytic expression for the screened Coulomb potential in real-space. Instead, one could solve for the Boltzmann conductivity for the phenomenological Yukawa potential, where

$$\frac{V(q)}{\epsilon(q)} = \frac{2\pi e^2}{\kappa}\frac{1}{\sqrt{q^2+q_s^2}}, \tag{12.15}$$

to find $\sigma = C[r_s](e^2/h)(n/n_{\rm imp})$, where $C[r_s] = (F_3[x = 2r_s])^{-1}$ and

$$\frac{F_3(x)}{x^2} = \frac{\pi}{4} + \frac{\pi x^2}{2} - \frac{\pi x}{2}\sqrt{1+x^2}. \tag{12.16}$$

Qualitatively, the Yukawa potential behaves similarly to the screened Coulomb potential, but there are quantitative differences. For example, at $r_s = 0.8$, for the same number of impurities, a graphene sample with Yukawa-like disorder would have about half the mobility compared to the screened Coulomb potential. The experiments along the lines discussed in Sect. 12.4, where $n_{\rm imp}$ or r_s is tuned in a controlled fashion can discriminate between the two models.

12.2.5 Gaussian Correlated Impurities

A very popular choice for impurity potential in graphene is the Gaussian correlated potential, where

$$\langle V(r)V(r')\rangle = K_0\frac{(\hbar v_{\rm F})^2}{2\pi\xi^2}e^{-|\mathbf{r}-\mathbf{r}'|/(2\xi^2)}. \tag{12.17}$$

This potential has two parameters: K_0 is a dimensionless measure of the potential strength and ξ specifies its correlation length. The reason for its wide use is both theoretical and practical. First, by looking at the dependence on ξ, one can study the crossover from short-range to long-range impurity behavior [52]. Second, the limit $n \to 0$ for $\xi = 0$ is somewhat uncontrolled in several respects. Without going into the details, we just point out, as we shall see below, that many physical

quantities (such as the conductivity) depend on the quantity $n\xi^2$ and so keeping a finite ξ allows one to take the limit $n \to 0$. And finally, unlike the long-range Coulomb potential that can introduce spurious divergences in finite sized numerics, a finite ξ makes these computations more convergent. There are also some experimental indications that atomic hydrogen dopants in graphene give changes to the conductivity that are consistent with the predictions of this Gaussian correlated impurity model [53]. We assume here that the values of K_0 and ξ are for a screened impurity potential (see Sect. 12.3.1 below where we give expressions for $K_0[r_s]$ and $\xi[r_s]$ for a particular mapping of the Coulomb potential). Integrating (12.3) for this model, we find [41]

$$\sigma(K_0, x = n\xi^2) = \frac{4e^2}{h} \frac{xe^x}{K_0 I_1(x)}, \tag{12.18}$$

where I_1 is the modified Bessel function. Two points are worth making here: (1) For large carrier density $x \gg 1$, the conductivity is super-linear $\sigma \sim n^{3/2}$; and (2) In the limit $n \to 0$, the conductivity remains finite (see Fig. 12.2), although in Sect. 12.3.4 we argue that this is not the origin of the graphene minimum conductivity even for this choice of impurity potential.

12.2.6 Midgap States

An increasingly popular choice (See, e.g., [17, 30, 54, 55]) for modeling graphene impurities is the so-called midgap states or resonant scatterer model. Unlike the other forms of disorder we have examined, where we assume that the disorder is a small perturbation to the pristine case, these works consider the impurities to be strong enough to generate extra structure in the density of states. In the unitary limit (*i.e.*, assuming that the impurities create a maximal phase-shift of $\pi/2$ between incoming and outgoing wavefunctions), one can show [30, 56]

$$\sigma(n) = \frac{2e^2}{\pi h} \frac{n}{n_{\text{imp}}} \ln^2\left[\sqrt{\pi n} R\right], \tag{12.19}$$

where R is the scattering radius of the impurity and n_{imp} is the concentration of resonant scatterers. As a function of carrier density, the graphene conductivity in the midgap model looks linear at low carrier density, and is sublinear at high density, quite similar to the case when one considers the presence of both Coulomb scatterers and short-range scatterers. Although both of these scenarios have two adjustable parameters, it is nonetheless possible to distinguish them experimentally. Indeed, in experiments on graphene irradiated with ions [57], it appears that the midgap states model better captures the experimentally observed $\sigma(n, n_{\text{imp}})$ than the combination of weak Coulomb and short-range scatterers. Whereas for most other samples, the combination of weak scatterers seems to dominate (see Sect. 12.4).

For the purposes of this chapter, we would like to make three cautionary remarks about this impurity model: (1) In the range between weakly interacting impurities

(i.e., Born approximation) and the case of unitary scatterers is the whole spectrum of strong but not unitary impurities. While the theory of unitary scatterers might be tractable, there is no reason why nature would choose this particular limit. (2) Resonant scatterers typically give a maximal phase-shift at a particular energy (and hence the name), but provide only weak scattering away from this resonant energy. While treating mid-gap states in graphene, it is often assumed that the impurity state is resonant over the entire energy window probed in transport. In principle, it should be possible to extract the width of the resonance by looking for changes in the conductivity as a function of r_s, although this problem has not yet been treated theoretically. (3) There has been only very limited work (e.g., [47, 54, 58] and references therein) connecting these midgap states to the graphene minimum conductivity problem. Although this is the subject of Sect. 12.3 below, it is worth mentioning here that relying exclusively on midgap states, for example, by obtaining a residual carrier density by integrating the density of states including the structure induced by the resonant impurities, cannot explain the graphene minimum conductivity. To get the experimentally observed values of $\sigma_{\min}$ requires an unphysically large number of defects (such as missing atoms). Not only would these large number of defects degrade the mobility far beyond what is observed in the same transport experiments at high carrier density, but these would most certainly be observable in scanning tunneling microscope (STM) studies, which have actually found the opposite case, i.e., a very low concentration of such defects (see e.g., Chap. 3 and [9, 37, 59, 60]).

We would argue that even when samples are deliberately made to have a large number defects (e.g. by ion irradiation), the residual carrier density is still determined by the charged impurity concentration (see e.g., discussion in [57]). In such a case, where one has the combination of resonant scatterers and Coulomb scatterers using the mid-gap model (12.19) is almost indistinguishable from the Coulomb impurity model. This is because the mid-gap model has an additional adjustable parameter R that could be tuned to get the pre-factor of the conductivity to be comparable to $A[r_s] \approx 20$ (see Fig. 12.2). In this case, the only way to distinguish mid-gap states from charged impurities is by controllably changing some parameter such r_s [28], the concentration of charged impurities [44], or the concentration of resonant scatterers [57].

12.3 Transport at Low Carrier Density

One of the biggest puzzles that emerged from the first transport experiments on graphene was the existence of a finite conductivity at zero carrier density. It turns out that well before the discovery of graphene, it was predicted by [19] and others that there should be a universal quantum limited ballistic conductivity in clean graphene $\sigma_{\min} = (4/\pi)e^2/h$. However, the first transport experiments measured values closer to $\sigma_{\min} = 4e^2/h$. Since at that time, the observed value was widely believed to be universal, this unexpected value for the minimum conductivity in graphene was dubbed the "problem of the missing π".

It is the goal of this section to discuss the quantitative theoretical explanation for this problem. The short answer to this mystery is that the minimum conductivity observed in experiments is not universal, but depends on the concentration of charged impurities. For relatively dirty graphene samples, the enhanced conductivity caused by the fluctuations in carrier density induced by the disorder is roughly compensated by the increased scattering caused by those impurities. In this regime, $\sigma_{\min} \approx 4e^2/h$ and depends only weakly on the disorder concentration (although we emphasize that the value is not universal, and even dirtier samples should have a lower conductivity). For samples that are 30 times cleaner, the reduced scattering term wins, giving a *larger* value for the minimum conductivity $\sigma_{\min} = 8e^2/h$.

Indeed, later experiments [13] observed that the minimum conductivity was not universal, but varied from $\sigma_{\min} = 2e^2/h$ to $8e^2/h$ consistent with theoretical predictions [14].

For even cleaner samples, the minimum conductivity would continue to increase until either the mean-free-path becomes comparable to the sample size or the size of the puddles (i.e., carrier density fluctuations) would shrink to fewer than a couple of electrons. Then the semiclassical diffusive transport would cross over to the fully quantum ballistic regime (which we discuss in Sect. 12.3.4).

As alluded to in the introduction to this chapter, the explanation of the graphene minimum conductivity problem is an intricate symphony that brings together the physics of disorder, electron–electron interactions and quantum mechanics. Here, disorder plays a dual role: it is primarily responsible for scattering the electrons that gives rise to the finite conductivity in the first place (recall that the bulk conductivity of any 2D conductor without disorder is infinite) *and* it induces the carrier density fluctuations; so that depending on the amount of disorder, the local carrier density can be quite large, allowing, at least locally, for a nonvanishing conductivity. The relatively weak electron–electron interactions in graphene give the mechanics of how the electrons "see" the disorder potential, which is invariably screened by the quasiparticle cloud, and this applies equally to both roles of disorder, as a scattering center and in inducing the density inhomogeneities. With quantum mechanics comes Klein tunneling, the ability of electrons to transmute to holes across potential barriers – which in our case implies that we do not need to worry about the scattering at the boundary between the electron and hole puddles. The contribution to the total conductivity is dominated by the conductivity *within* the puddles and not *across* them.[6]

We should mention that historically this solution emerged only after carefully comparing the experimental data to the high-density Boltzmann theory discussed in Sect. 12.2 above. That theory is only valid at high density, or more specifically, when $k_F\ell \gg 1$, or $\sigma(n) \gg e^2/h$. Oftentimes, either by serendipity or insight, theories

[6]To fully discuss the role of Klein tunneling in graphene transport would require a larger discussion than is possible here. For the semiclassical calculation presented here, we ignore the additional contribution to the resistance arising from p-n junctions. The validity of this assumption is rigorously tested in Sect. 12.3.4 below. For a more complete discussion on the role of p-n junctions in graphene transport, as well as an explanation for the remarkable property of perfect transmission of carriers at normal incidence, see Chap. 12 and [15].

work well beyond their formal limits of applicability – we have already seen that for graphene and the usual 2D electron gases, the RPA calculation showed explicitly that the Thomas–Fermi screening theory, which is valid formally only at $q \to 0$, actually works well for $q \leq 2k_F$. Similarly, the RPA-Boltzmann theory for the usual 2DEG system continues to work beyond its formal regime of applicability in high mobility n-GaAs systems [61] until new physics such as percolation or localization takes over at even lower carrier densities.

However, when a careful comparison with experiment was done in [26] to see when deviations from this semiclassical theory begin to show up, it revealed two important features that inspired the theoretical ideas presented below. First, the high density theory *did* work better than expected. From (12.12), one would expect the high density theory to work only for $n \gg n_{\text{imp}}$, but in fact, the theory worked for $n \gtrsim n_{\text{imp}}/2$. Second, the minimum conductivity value did not occur at a singular point (i.e., at the Dirac point with precisely zero carrier density), but rather there was a minimum conductivity plateau of width $\Delta n \approx n_{\text{imp}}$. In fact, there was no singularity at all – the plateau smoothly joined up to the high-density Boltzmann result and the value of the conductivity minimum was not universal, but seemed somewhat correlated with the sample quality. It was pointed out already in [26] that for $n \approx n_{\text{imp}}/2$, the fluctuations in carrier density n_{rms} were comparable to the average carrier density implying that understanding the physics of the minimum conductivity was understanding the physics of puddles, i.e., how they are formed and how they conduct carriers, and had nothing to do with the properties of the peculiar Dirac point that was experimentally inaccessible due to the presence of disorder. This was significant since at the time, most attempts to explain the graphene minimum conductivity focused on the singular properties of the conical point in the graphene Dirac spectrum.[7]

12.3.1 Self-Consistent Approximation

Perhaps, the most important result discussed in this chapter is the self-consistent ansatz of [14]. In a nutshell, the self-consistent ansatz is a semianalytic method for calculating the fluctuations in carrier density n_{rms} from the properties of the disorder

[7] To illustrate somewhat simplistically how one could get into trouble at the Dirac point, consider the Einstein relation that was discussed earlier $\sigma = e^2 \nu(E_F) D$. At the Dirac point, $\nu(E_F)$ vanishes but for short-range impurities, $D \to \infty$, which gives rise to a disorder-dependent minimum conductivity at the Dirac point (see Fig. 12.2). Similar cancellation of divergences gives rise to the following puzzle [19]. If one calculated the conductivity by first taking the clean limit while keeping either temperature or frequency finite, one would obtain the universal value $\sigma_{\text{min}} = (\pi/2)e^2/h$. However, taking frequency and temperature to zero first, then taking the clean limit gives $\sigma_{\text{min}} = (4/\pi)e^2/h$. At the time of writing, the crossover between these two universal limits remains an unsolved problem. However, for the purposes of understanding current graphene dc transport experiments, we maintain that none of this "universal" physics is relevant.

potential. By now this ansatz has been rigorously tested against numerical density functional calculations [32] (for the case of interacting electrons) and with a numerical computation of the Landauer formula [41] (for the fully quantum mechanical case). The self-consistent ansatz states that the root-mean-square fluctuations in carrier density ($n_{\rm rms}$) is related to the screened disorder potential at that carrier density.

One can think of the ansatz as follows: If the induced carrier density $n_{\rm rms}$ is small, the disorder potential will be poorly screened thereby inducing a large carrier density. But a large carrier density will better screen the disorder potential resulting in a lower carrier density. This process will reach an equilibrium when the changes in the induced carrier density exactly balance the changes in screening.

12.3.1.1 Formalism

To be more quantitative, let us further assume that the largest contribution to $n_{\rm rms}$ is the Thomas–Fermi contribution i.e. $n_{rms} \approx \sqrt{3}\langle E_{\rm F}^2\rangle/(\pi\hbar^2 v_{\rm F}^2)$, where the angular brackets denote averaging over an ensemble of disorder configurations and the $\sqrt{3}$ factor just comes from the fact that for graphene $n_{\rm rms}$ is the second moment of density and the fourth moment of Fermi energy. In this case, the self-consistent ansatz reads

$$\pi\hbar^2 v_{\rm F}^2 n^* = \langle E_{\rm F}^2\rangle = \langle V_D^2[n^*]\rangle. \tag{12.20}$$

This corresponds to finding a residual carrier density $n^* = n_{\rm rms}/\sqrt{3}$ that satisfies (12.20), where $V_D[n^*]$ is the disorder potential screened by a homogeneous electron gas at carrier density n^*.

It should be apparent from (12.20) that it will be important to calculate the ensemble averaged properties of the screened disorder potential. For example, one can show that by assuming uncorrelated random impurities of concentration $n_{\rm imp}$, where each impurity has a disorder potential $\phi(r,n)$ (with Fourier transform $\tilde{\phi}(q,n)$) then [62]

$$\langle V_D(r)V_D(0)\rangle_c = n_{\rm imp}\int \frac{d^2q}{(2\pi)^2}[\tilde{\phi}(q,n)]^2 e^{-i\mathbf{q}\cdot\mathbf{r}}, \tag{12.21}$$

where the subscript "c" indicates that terms proportional to $\langle V_D(0)\rangle$ have been excluded. To simplify the discussion, we just set $\langle V_D(0)\rangle = 0$. We will discuss the case of finite doping in Sect. 12.3.2 below, but for now, we can imagine that setting $\langle V_D(0)\rangle = 0$ corresponds to tuning the back gate voltage to coincide with the Dirac point, thereby ensuring charge neutrality.

In this case, a more general result states that for any arbitrary disorder potential $\phi(r)$, one has

$$\langle V_D^k\rangle_c = n_{\rm imp}\int d^2r[\phi(r,n)]^k. \tag{12.22}$$

Since knowing all moments of a distribution function is equivalent to knowing the distribution function itself, in principle, after using (12.20) to set $\phi(r,n) = \phi(r,n^*)$, (12.22) then defines the full probability distribution function of the screened disorder potential.

Taking this together with the two-point correlation function (12.21), one then has a complete statistical description of *all* properties of the Dirac point in the presence of disorder. Any physical observable, such as $\sigma_{\min}$ should be a function of the moments in (12.22). In practice, however, since for the screened Coulomb impurity problem, no closed-form analytic expression is available for $\phi(r,n)$, the moments of (12.22) can only be computed numerically, and one needs to truncate the computation after a finite number of moments.

In this vein, it is sometimes useful to consider the mapping to the Gaussian correlated disorder (see (12.17)), which can be accomplished as follows

$$\frac{K_0\hbar^2 v_{\rm F}^2}{2\pi\xi^2} = n_{\rm imp}\int \frac{d^2q}{(2\pi)^2}[\tilde{\phi}(q,n)]^2 = \pi\hbar^2 v_{\rm F}^2 n^*,$$
$$\xi = \sqrt{\frac{2}{\pi}}\frac{\int \frac{dq}{2\pi}[\tilde{\phi}(q,n)]^2}{\int \frac{d^2q}{(2\pi)^2}[\tilde{\phi}(q,n)]^2}. \tag{12.23}$$

While this "Gaussian mapping" can be done for any arbitrary potential $\phi(r,n)$, it will only be a good approximation if higher moments of the impurity potential in (12.22) can be neglected.[8] We also find

$$n_{\rm rms} = n^*\sqrt{3 + \frac{1}{\pi n_{\rm imp}\xi^2}}. \tag{12.24}$$

We now specialize to the case of Coulomb impurities, where from (12.11) we have

$$\tilde{\phi}(q) = \frac{2\pi e^2}{\kappa}\frac{e^{-qd}}{q\epsilon(q)}. \tag{12.25}$$

The dielectric function $\epsilon(q)$ was defined in (12.10). Notice that to calculate $n_{\rm rms}$ the integrals run over all momenta q and so, unlike the transport calculations in Sect. 12.2, the full RPA result will differ from the Thomas–Fermi result.

The integrals above for n^*, K_0 and ξ can all be done analytically, and although simple asymptotic expansions can be made in various limits, we have found,

[8] We have been slightly sloppy with language, using the term Gaussian approximation to refer to both when the disorder potential has Gaussian two-point spatial correlation function (see (12.17)) and when the disorder probability distribution function is determined only from the second moment (see (12.22)). From the context, it should be clear which case we mean, although we should caution that the two approximations can be quite different. For example, (12.24) describes a Gaussian two-point correlation function, but is equivalent to a Gaussian distribution function only in the limit when $n_{\rm imp}\pi\xi^2 \gg 1$.

unfortunately, that the regime relevant to current experiments requires the use of the full functional form. To simplify the notation somewhat, we introduce the auxiliary functions $C_0(z)$ and $D_0(z)$ where for $E_1(x) = \int_x^\infty t^{-1}e^{-t}dt$, we have

$$\begin{aligned} C_0(r_s,z) &= -1 + \frac{4E_1(z)}{(2+\pi r_s)^2} + \frac{2e^{-z}r_s}{1+2r_s} \\ &\quad + (1+2zr_s)e^{2zr_s}(E_1[2zr_s] - E_1[z(1+2r_s)]), \qquad (12.26) \\ D_0(r_s,z) &= 1 - \frac{8r_s z E_1[z]}{(2+\pi r_s)^2} + \frac{8e^{-z}r_s}{(2+\pi r_s)^2} - \frac{2e^{-z}r_s}{1+2r_s} \\ &\quad - 2zr_s e^{2zr_s}(E_1[2zr_s] - E_1[z(1+2r_s)]). \end{aligned}$$

Using these definitions, one finds [31]

$$\left.\begin{aligned} n^* &= 2\,n_{\rm imp}\,r_s^2\,C_0, \\ K_0 &= \frac{1}{4r_s^2}\left(\frac{D_0}{C_0}\right)^2, \\ \xi &= \frac{1}{\sqrt{n_{\rm imp}}}\frac{D_0}{4\pi r_s^2}\,(C_0)^{-3/2}, \end{aligned}\right\} \ \text{RPA} \qquad (12.27)$$

where $z = 4d\sqrt{\pi n^*}$. Notice that given the concentration of charged impurities $n_{\rm imp}$, the dielectric constant of the substrate (which sets r_s) and the distance d of the impurities from the graphene sheet, one can calculate the strength of the screened disorder potential, the size of the electron and hole puddles as well as the number of electrons within each puddle. In particular, we note that to leading order, the overall scale-factor of the puddle size is set by the average distance between the impurities $n_{\rm imp}^{-1/2}$, and is proportional to r_s^{-2}. This allows one to make crude estimates, predicting, for example, that the size of the puddles in suspended graphene are roughly the same as those on a SiO_2 substrate. This is because although suspended graphene has more than an order of magnitude fewer impurities, one only gains as $n_{\rm imp}^{-1/2}$, while suspending graphene more than doubles r_s, which decreases the puddle size as r_s^{-2}.

Notice that for the Complete Screening (CS) limit discussed earlier, the auxiliary functions have very simple asymptotes: $C_0(z \gg 1) \to (2r_s z)^{-2}$ and $D_0(z \gg 1) \to (2r_s z)^{-1}$. In this limit (which is valid only for very dirty samples when $d\sqrt{n^*} \gg 1$), we find

$$\left.\begin{aligned} n^* &= \frac{1}{d}\sqrt{\frac{n_{\rm imp}}{32\pi}}, \\ \xi &= d\sqrt{\tfrac{8}{\pi}}, \\ K_0 &= d\sqrt{8\pi n_{\rm imp}}. \end{aligned}\right\} \ \begin{matrix}\text{Complete} \\ \text{Screening}\end{matrix} \qquad (12.28)$$

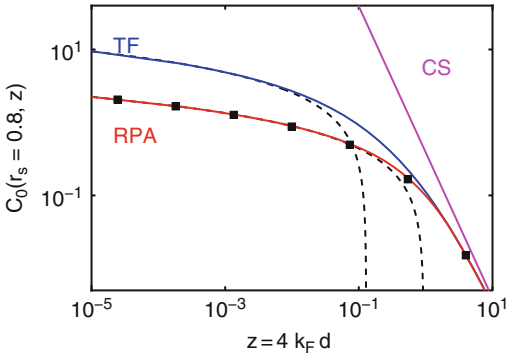

Fig. 12.3 Comparison of the dimensionless voltage fluctuation function $C_0(r_s, z)$ (see (12.26)) using different screening approximations. The Random-Phase-Approximation (RPA) shown in blue is the main approximation used in the present work. The Thomas–Fermi (TF) and Complete Screening (CS) approximations give different results except when $r_s z \gg 1$. Dashed lines are small density analytic asymptotes for the Thomas–Fermi and RPA (see (12.29)) and the squares show the numerical evaluation of (12.22) using the Coulomb potential (12.11) with the exact dielectric function (12.9)

In Fig. 12.3, we show the function $C_0(z)$ for the RPA, Thomas–Fermi (TF) and Complete Screening (CS) approximations. For $z \gg 1$, the RPA and TF results approach the CS results, while in the opposite limit of $z \ll 1$, we have

$$C_0(r_s, z \to 0) = \frac{-1}{2r_s + 1} - \ln\left[\frac{2r_s}{2r_s + 1}\right] - \frac{4\ln(\tilde{\gamma} z)}{(2 + \pi r_s)^2}, \tag{12.29}$$

where $\tilde{\gamma} \approx 1.781$ is Euler's constant. While using this asymptotic expression might be useful for qualitative estimates, we emphasize that in order to make any quantitative predictions, one is forced to use the full expression in (12.26).

12.3.1.2 Results

Having developed the self-consistent formalism above, we are now ready to reap some concrete results. Figure 12.4 captures the central results of the self-consistent approximation. The top panel shows the ensemble averaged two-point correlation function $\langle V(r)V(0)\rangle$. This quantity can be measured experimentally by measuring the density fluctuations at the Dirac point, although at present all the published experimental data lack sufficient resolution to make a detailed comparison. Nevertheless, they are at least consistent [34–37,59] with the theoretical predictions. However, we can compare our results to those obtained using other theoretical approaches. The solid (blue) lines are the evaluation of (12.21) for two values of n_{imp}. The red diamonds are the results of the density function theory (DFT) taken from [32] using the same parameters. One notices that the self-consistent

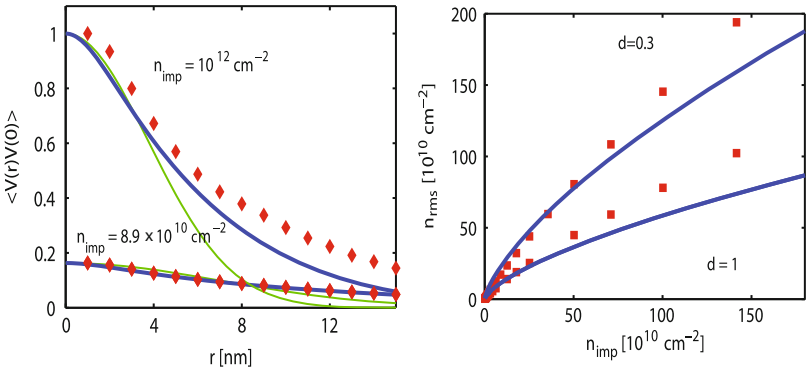

Fig. 12.4 Results of the self-consistent approximation (SCA). *Left panel*: Two-point correlation function of the screened Coulomb disorder potential. Blue line is the SCA result (12.20), while green line is the Gaussian approximation (12.23). The red data points taken from [32] show the same quantity computed from a density functional approach (see also discussion in [18]). *Right panel*: The root-mean-square carrier density at the Dirac point computed using the same approximations – blue line is the SCA (12.24) and red squares are the DFT results ([32])

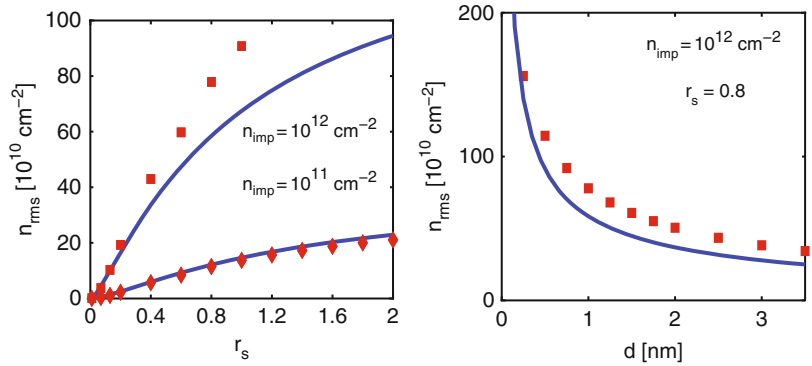

Fig. 12.5 Dependence of the carrier density fluctuations on effective fine structure constant r_s (*left panel*) and distance of the Coulomb impurities from the graphene sheet d (*right panel*). Solid lines are the self-consistent result (12.20) and data points were computed in [32] using a density functional approach

approximation (SCA) agrees quantitatively with the DFT results. The green line shows the Gaussian mapping, which works remarkably well for the cleaner data. The full width at half maximum of $\langle V(r)V(0)\rangle$ (which is related to ξ through the Gaussian mapping) is a measure of the correlation length that sets the size of the puddles.

One of the main goals of developing the SCA was to calculate $n_{\rm rms}$ as a function of disorder parameters. This is shown in the right panel of Fig. 12.4 and Fig. 12.5, and these results also agree well with the DFT results [32]. Finally, in Fig. 12.6 we show the potential strength K_0 and puddle correlation length ξ (related to the puddle

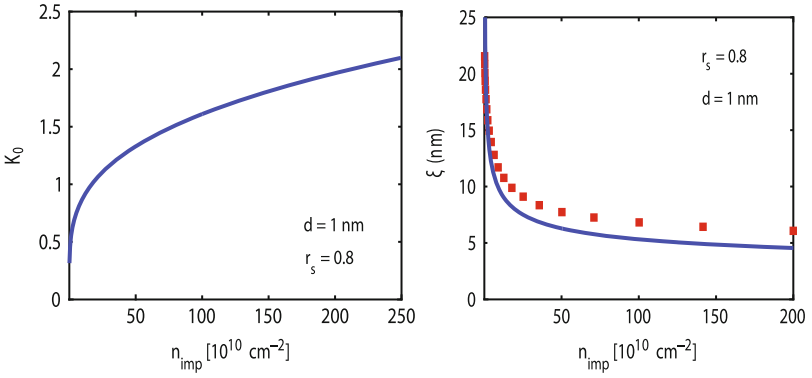

Fig. 12.6 Results for the Gaussian mapping of the Coulomb potential (see (12.23)). Left panel shows the dimensionless disorder strength K_0 as a function of charged impurity density. Right panel shows the Gaussian correlation length ξ, which is related to the average puddle size. Also shown as red squares is the density functional result of [32], where we note that for a Gaussian distribution function, a factor of $2\sqrt{2\ln 2}$ needs to be multiplied by the correlation length ξ to obtain the full width at half maximum (FWHM) that is more commonly used to characterize the graphene puddles (see [18])

size) as a function of n_{imp} obtained by mapping the microscopic Coulomb disorder onto the Gaussian potential.

12.3.2 Effective Medium Theory

In the previous section, we demonstrated that the self-consistent approximation can be used to quantify all the statistical properties of the Dirac point in the presence of disorder. For these dirty samples, the question now arises: given that we can characterize the Dirac point, what is the conductivity through this highly inhomogeneous medium? (See Fig. 12.7). Or in other words, now that we know the size of the puddles and how many carriers are inside the puddles, can we calculate the graphene minimum conductivity? The earliest (and crudest) estimate was simply to say that

$$\sigma \approx \begin{cases} \sigma_B(n^*) & \text{for } n \le n^*, \\ \sigma_B(n) & \text{for } n > n^*, \end{cases} \tag{12.30}$$

where $\sigma_B(x) = 20(e^2/h)(x/n_{\text{imp}})$ [14]. We shall see in this section that this rather fortuitously turns out to be an excellent approximation.

The implication of (12.30) is the following: The disorder potential causes some residual carrier density n^*, which then gives rise to the minimum conductivity. As discussed in Sect. 12.3.1 above, n^* is determined by balancing the role of impurities

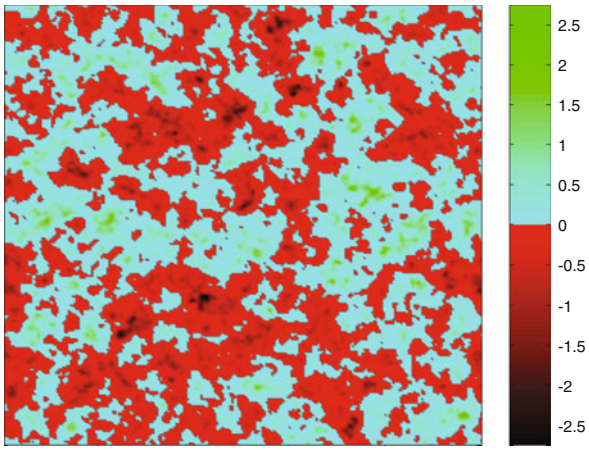

Fig. 12.7 At the Dirac point, disorder breaks the system into puddles of electrons and holes. The figure, taken from [63], is a simulation of a 250 nm by 250 nm square of graphene with typical density of charged impurities. The color scale reflects the local density in units of $10^{12}\,\mathrm{cm}^{-2}$. The goal of this section is to calculate the conductivity of this highly inhomogeneous material

doping graphene and the enhanced screening of doped graphene – but at a very basic level, it should be obvious that increasing the number of impurities increases n^* (see Fig. 12.4); which in turn should *increase* the conductivity. However, increasing n_{imp} also means more scattering, which should *decrease* the conductivity. Therefore, the minimum conductivity emerges as a delicate balance between the dual property of the disorder potential to both induce carriers and scatter carriers.

For the disorder concentrations present in the first experimental samples, these two effects roughly cancel resulting in a minimum conductivity that depends only weakly on disorder – and hence the early belief that the value was universal. For cleaner samples, the Coulomb impurity scattering term wins out, implying that cleaner samples should show stronger variation with disorder and have a larger value for σ_{min}. (See Sect. 12.4 for further discussion of experiments).

Before we turn to the full treatment that validates the use of (12.30), let us look at what is obviously left out in this simple estimate. Since σ_B is the semiclassical Boltzmann conductivity, all quantum interference corrections are neglected. Section 12.3.4 below addresses quantum effects and studies the full crossover from quantum transport to diffusive transport. The approximation also assumes that the total conductivity is given by the conductivity within the puddles and not between puddles. As discussed earlier, this is justified because of the Klein tunneling across the p-n junctions. We refer the reader to [15] for more on the role of the boundary between the electron and hole puddles.

There are two further assumptions in (12.30). While one might buy that $\sigma_{\mathrm{min}} = \sigma_B(n^*)$, and $\sigma(n \gg n_{\mathrm{imp}}) = \sigma_B(n)$, the hard "plateau" with a singularity at $n = n^*$ is highly artificial. Second, even the assumption that $\sigma_{\mathrm{min}} = \sigma_B(n^*)$ ignores the possibility that the minimum conductivity could depend on higher moments of the carrier density – for example, we could have proposed $\sigma_{\mathrm{min}} = \sigma_B(n_{\mathrm{rms}})$ instead. Answering these two questions led to the development of an effective medium theory for graphene transport [38].

The starting point is to assume that locally $\sigma(r) = \sigma_B[n(r)]$. Then taking the continuum approximation and using well-known effective medium theory (EMT) results [64] one finds [38]

$$\int dn P[n] \frac{\sigma(n) - \sigma_{\rm EMT}}{\sigma(n) + \sigma_{\rm EMT}} = 0, \tag{12.31}$$

where $P[n]$ is the carrier density probability distribution function. This integral equation for the conductivity of the inhomogeneous medium is valid so long as there are more than a few electrons inside each puddle. For current experiments on graphene, this is always the case. Theoretical calculations [32, 38] showed that disordered graphene had two kinds of puddles – macroscopically large puddles with low carrier density that contained $\approx$ 500 electrons, and very small puddles with a large carrier density that contained $\approx$ 5 electrons. The statistics of these two regions were such that averaging over the entire sample gave results for the puddle correlation length ξ and $n_{\rm rms}$ that agreed with the self-consistent approximation discussed in the previous section. Making the further assumption that $P[n]$ is a Gaussian distribution with width $n_{\rm rms}$ and mean $n_g = \alpha V_g$, one finds [40]

$$\int_0^\infty \exp\left[\frac{-n^2}{2n_{\rm rms}^2}\right] \cosh\left[\frac{n_g n}{n_{\rm rms}^2}\right] \frac{\sigma(n) - \sigma_{\rm EMT}}{\sigma(n) - \sigma_{\rm EMT}} = 0. \tag{12.32}$$

To find the conductivity at the Dirac point, one sets the density induced by the back-gate voltage $n_g = 0$ giving for charged impurities

$$2ze^{-z^2}\left(\pi \,\mathrm{Erfi}[z] - \mathrm{Ei}[z^2]\right) = \sqrt{\pi}, \tag{12.33}$$

where Erfi is the imaginary error function, Ei is the exponential integral function and $z = \sigma_{\rm EMT}/(\sqrt{2}\sigma_B[n_{\rm rms}]) \approx 0.405$. This gives $\sigma_{\rm EMT} \approx 0.9925\ \sigma_B(n^*)$, implying that the early estimates for the minimum conductivity due to Coulomb scatterers (12.30) were accurate to within 1 % of the effective medium theory result. However, with (12.32) one can now solve the full crossover of graphene conductivity as a function of carrier density from the Dirac point where the conductivity minimum is dominated by the contribution from the fluctuations in carrier density inside the electron and hole puddles to the high-density regime, where the carrier density is uniform and the conductivity is given by the semiclassical Boltzmann results of Sect. 12.2.

Figure 12.8 shows the effective medium theory results $\sigma_{\rm EMT}(n)$ for both Coulomb scatterers and Gaussian correlated impurities, where $n_{\rm rms} = \sqrt{3}n^*$ was obtained from the self-consistent approximation. Figure 12.9 shows the minimum conductivity $\sigma_{\rm min}$ for both Coulomb scatterers and for the Gaussian correlated impurity model. In Sect. 12.4 below, we will compare the Coulomb impurity results (left panel of Fig. 12.9) to several experiments in the literature. Moreover, there has been some

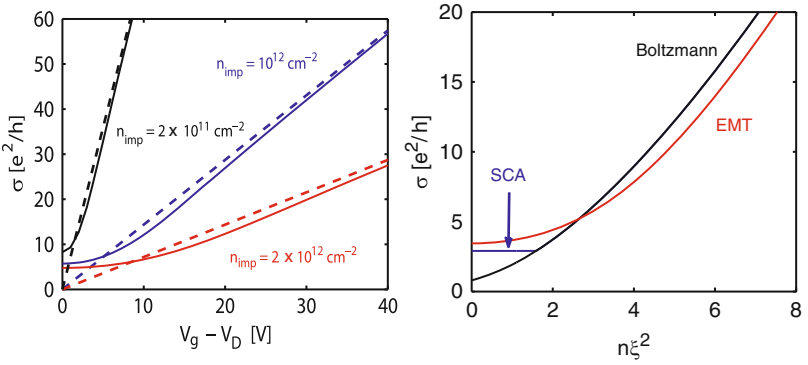

Fig. 12.8 Graphene conductivity as a function of carrier density for charged impurities (*left panel*) and Gaussian correlated impurities (*right panel*). Dashed lines in left panel are the high-density Boltzmann transport result. For Coulomb impurities (*solid lines in left panel*), the effective medium theory (EMT) results agree with the earlier estimate (12.30) to within 1 %. For Gaussian impurities (right panel), the EMT gives slightly larger values for the minimum conductivity than (12.30). Also shown (in black) is the high-density Boltzmann result. The EMT result approaches the Boltzmann result for $n\xi^2 \gg 1$

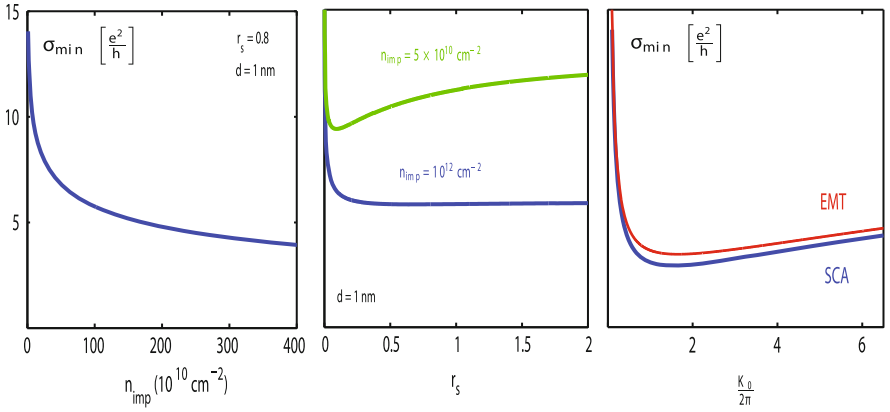

Fig. 12.9 Dependence of graphene minimum conductivity on disorder parameters. All panels have the same scale for $\sigma_{\min}$ on the y-axis. *Left panel*: For charged impurities, $\sigma_{\min}$ decreases monotonically as a function of impurity density. *Center panel*: Samples with large Coulomb disorder (blue curve) show almost no dependence of $\sigma_{\min}$ on the effective fine structure constant r_s; cleaner samples (*green curve*) show the minimum conductivity increasing weakly with r_s. *Right panel*: For the Gaussian correlated impurity model, the effective medium theory result (12.32) is slightly larger (*red curve*) than the analytic result $\sigma_{\min}[x = K_0/2] = 2e^x/xI_1(x)$ shown in blue and derived from (12.30)

recent evidence that the predictions of the Gaussian impurity model (right panel of Fig. 12.9) are relevant for experiments doping graphene with atomic hydrogen [53], although there has been no microscopic theory explaining why hydrogen impurities should have such correlations.

12.3.3 Magneto-Transport and Temperature Dependence of the Minimum Conductivity

One remarkable feature of this RPA-Boltzmann approach to solving the minimum conductivity problem is that the theory can then be generalized (without any further fitting parameters) to other experimental situations. The model makes definitive predictions for a variety of situations that have as yet not been explored theoretically using this technique (for example, the Nerst signal, the thermopower and weak-localization close to the Dirac point all in some way depend on the self-consistent carrier density n^*, which once determined through the dc transport, would then determine these additional properties). While we do not explore all these different experiments in this book chapter, it is relatively straightforward to generalize the formalism presented here to other situations. As an illustration of how such a generalization would work, we consider two cases here.

The first is the semiclassical magnetoresistance in a weak magnetic field, and the second is the temperature dependence of the minimum conductivity.[9] The magneto-transport of graphene at sufficiently large temperatures that the phase-coherent transport is negligible and sufficiently small magnetic fields B such that Landau levels have not developed is given by the semiclassical Drude model. In graphene, the current density in the $\hat{x}$ and $\hat{y}$ directions is [43]

$$J_x = [\sigma_{xx}^{(e)} + \sigma_{xx}^{(h)}]E_x + [\sigma_{xy}^{(e)} + \sigma_{xy}^{(h)}]E_y;\ J_y = [\sigma_{yx}^{(e)} + \sigma_{yx}^{(h)}]E_x + [\sigma_{yy}^{(e)} + \sigma_{yy}^{(h)}]E_y.$$

The superscript $c = (e, h)$ denotes electron and hole carriers. The longitudinal and Hall conductivities are given by

$$\sigma_{xx}^{(c)} = \sigma_{yy}^{(c)} = \frac{\sigma_0^{(c)}}{1 + \left(\sigma_0^{(c)} R_H^{(c)} B\right)^2};\ \sigma_{xy}^{(c)} = -\sigma_{yx}^{(c)} = \frac{\left[-\sigma_0^{(c)}\right]^2 R_H^{(c)} B}{1 + \left(\sigma_0^{(c)} R_H^{(c)} B\right)^2}, \tag{12.34}$$

where $R_H^{(c)} = 1/n_{(c)}e^{(c)}$ and the zero-field electrical conductivity for each carrier is $\sigma_0^{(c)}$. So far, this is general for any two carrier model.[10] Applying the self-consistent

[9] Here, we assume that the temperature dependence arises only from thermal smearing of the Fermi distribution function. While this assumption that the temperature dependence occurs only from this activation-like behavior is an excellent approximation for bilayer graphene (see [40]), for monolayer graphene, additional physics such as the degradation of the conductivity due to phonons in dirty samples, and the crossover to the ballistic regime for suspended samples restrict the temperature range for which this thermal broadening picture dominates the conductivity.

[10] As an aside, we should mention that the two-carrier model above (and assuming Coulomb impurities, (12.12)) relates field-effect mobility to the carrier mobility as

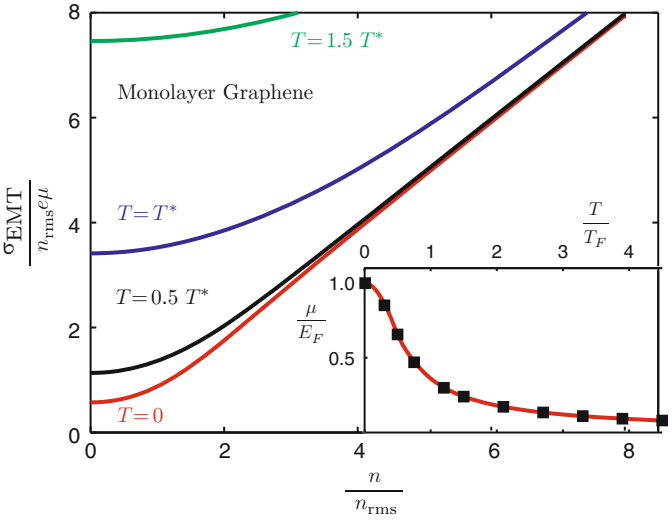

Fig. 12.10 Temperature dependence of graphene conductivity. Left panel shows effective medium theory conductivity for different values of $k_{\rm B}T^* = \hbar v_{\rm F}\sqrt{\pi n_{\rm rms}}$, where $n_{\rm rms}$ is obtained from the self-consistent theory. Inset shows the chemical potential calculated numerically (squares) and the extrapolation function (12.36) used to evaluate the conductivity. Perturbation theory for $t = T/T^* \ll 1$ gives $\sigma(t)/\sigma(0) = 1 + 4\pi^2 t^4 \ln t/(9|\pi - 2|)$

theory simply gives $\sigma_0^{(e)} + \sigma_0^{(h)} = \sigma_{\rm EMT}$, where $\sigma_{\rm EMT}$ is obtained from (12.32). This is an illustration of how the self-consistent theory can easily be generalized to other situations.

The second example we discuss here is the temperature dependence of the minimum conductivity. For simplicity, we assume the presence of only Coulomb scatterers and that the thermal smearing of the Fermi surface is the only source of temperature dependence. In this case, the local conductivity can be written as $\sigma(n,T) = n(T=0)e\mu_c \frac{n_e+n_h}{n_e-n_h}$, where $n_e(T) = \int_0^\infty dE\ \nu(E) f(E,\mu,k_{\rm B}T)$ and $n_h(T) = \int_{-\infty}^0 dE\ \nu(E)[1 - f(E,\mu,k_{\rm B}T)]$, where $f(E,\mu,k_{\rm B}T)$ is the Fermi-Dirac function with $k_{\rm B}$ the Boltzmann constant. The only subtle point is determining the chemical potential μ obtained by solving for $n_g = n_e - n_h$, where n_g is proportional to the applied gate voltage (and determined by the capacitive coupling of graphene to the gate). Data points in the inset of Fig. 12.10 show chemical

$$\mu_H \equiv \frac{\rho_{xy}}{\rho_{xx}B} = \frac{\sigma_{xy}}{\sigma_{xx}B} \approx \frac{A[r_s]}{n_{\rm imp}}\left(\frac{n_e - n_h}{n_e + n_h}\right), \tag{12.35}$$

where only in the very limited carrier density range $n^* \sim n_{\rm imp} \ll n \ll B[r_s]\sigma_0/n$ is the Hall mobility the same as the field-effect mobility $\mu_c = \sigma/ne$ (where the specific boundaries of this window depend on the number of short-range and long-range impurities and the dielectric environment).

potential $\mu(T)$ obtained by the numerical solution of the implicit equation, $1 = 2(T/T_F)^2\{\mathrm{Li}_2[-\exp(\mu/k_BT)]-\mathrm{Li}_2[-\exp(-\mu/k_BT)]\}$, as well as the interpolation function

$$F_\mu(x) = \mu(T/T_F)/E_F = g(x)(1-\pi^2x^2/6) + \bar{g}(x)/(4\ln 2x), \tag{12.36}$$

where E_F is the Fermi energy, and $g(x) + \bar{g}(x) = 1$ are a choice of complementary functions, e.g. we use $g(x) = (1 + \mathrm{Erf}[10(x-1/2)])/2$ and $\bar{g}(x) = \mathrm{Erfc}[10(x-1/2)]/2$ [65]. From the inset, one finds that the interpolation function adequately describes the evolution of the chemical potential with temperature (see [40] for more details).

Applying the EMT formalism then gives the results shown in the left panel of Fig. 12.10. Since n_{rms} is obtained from the self-consistent approximation, this result gives a parameter free prediction for the effects of thermal broadening on the minimum conductivity.

12.3.4 Quantum to Classical Crossover

After the discovery of graphene, two parallel approaches developed to understand the conductivity of graphene. The first was the fully quantum-mechanical approach based on the Landauer formalism [66, 67], where graphene was found to have a universal quantum-limited conductivity of $\sigma_{min} = 4e^2/(\pi h)$, a value that was considerably lower than what was observed experimentally.[11] While this formalism fully captures the quantum mechanics of graphene electrons, it ignores electron-interaction effects such as screening (discussed in Sect. 12.2.1 above). The natural question arises: can the discrepancy between the universal quantum-limited value and the value observed in experiments be caused by disorder? Early numerical work [25] suggested that this might be the case. At the time of writing this chapter, there has not been any convincing (or generally accepted) analytical model that addresses the role of disorder on the quantum-limited graphene conductivity at the charge neutrality point (see [15] for details). However, there have been (at least) five numerical studies [7, 16, 41, 68, 69] that have established that so long as the disorder is smooth on the scale of the lattice spacing, quantum interference effects *increase* the conductivity through weak antilocalization. We note that the presence of only smooth disorder (an assumption corroborated by graphene experimental STM studies [9, 37, 59, 60, 70] and TEM studies [71]) is necessary to ensure that the two graphene valleys are decoupled. Intervalley transitions break the pseudospin

[11] The Landauer approach gives the universal value only for $W \gg L$, where the transport is primarily through evanescent modes. In the opposite limit, the conductivity depends strongly on the boundary conditions and is not universal. When comparing the quantum and semiclassical models, we will assume that $W \gg L$. For further discussion, see [15].

conservation resulting in the usual case of weak localization that decreases the conductivity signaling the transition to an insulating state [72].

The second approach was the semiclassical Boltzmann one described here. As discussed above, the minimum conductivity depends on the delicate balance between the carrier density induced by the screened disorder potential and the carriers scattering off the same screened impurities. For Coulomb impurities, the scattering term always wins out, albeit only weakly at large disorder. As a result, for increased disorder, the minimum conductivity always *decreases*. This is in stark contrast to the predictions of the fully quantum approach.

Reference [41] attempted to reconcile these two approaches. The first step was to ensure that one was making a fair comparison. Since most of the quantum transport work in the literature was done with the Gaussian correlated impurity potential, the self-consistent approach first had to be generalized to this potential. In this chapter, the results for the Gaussian impurity model were already discussed alongside the Coulomb results in the preceding sections.

As can be observed in Fig. 12.9, the minimum conductivity for the Gaussian correlated potential makes a "U"-shape with a minimum at around $K_0 \approx 10$. The main findings of [41] were the following: (1) The numerical quantum results are consistent with weak-antilocalization theory (i.e., $d\sigma/d\ln L = 4e^2/\pi h$) at all carrier densities for $\sigma \geq 4e^2/h$. (2) Away from the Dirac point, the full quantum solution and the semiclassical Boltzmann theory agree to leading order $\sigma \sim n^{3/2}$. Taken together with (1), this implies that outside the puddle regime, as one might expect, the graphene conductivity is determined by the semiclassical transport theory with small antilocalization corrections. (3) At the Dirac point, the theories are incompatible at weak disorder ($K_0 \lesssim 10$) when quantum fluctuations spread the carriers over many puddles and the concept of a local carrier density becomes problematic. This is consistent with the discussion in Sect. 12.3.2 above, where we argued that the local density approach obviously fails when there are fewer than a couple of electrons per puddle. The number of electrons per puddle corresponds roughly to $\pi n^* \xi^2 = K_0/2\pi$, so this transition to the quantum regime occurs when there are fewer than 2 electrons per puddle. The experimental signature of the quantum regime is a sharp cusp-like dip at the Dirac point as opposed to the smooth plateau of the effective medium semiclassical theory (see Fig. 12.11). (4) Most important, for the conductivity at the Dirac point, for $K_0 \gtrsim 10$ the quantum and the self-consistent theory agree (see Fig. 12.12, where in the right panel we subtract the antilocalization correction).

In the context of the results presented in this chapter, the consequence of [41] is that so long as the disorder is sufficiently large so that it induces more than a couple of electrons per puddle, the semiclassical transport theory effectively captures the transport properties of graphene and that additional physics that we have not considered such as the role of p-n junctions, are small corrections to our mean-field results.

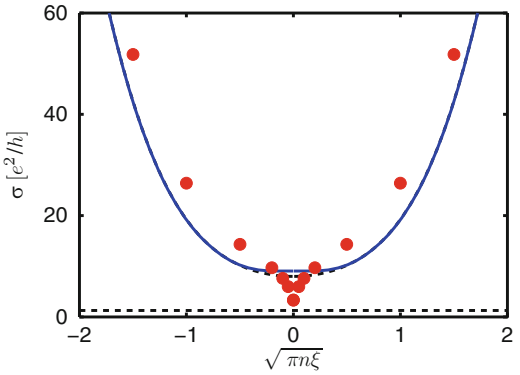

Fig. 12.11 Contrasting the quantum and semiclassical predictions for graphene Dirac point conductivity. Solid blue line is the semiclassical effective medium theory result, which shows a smooth plateau close to the Dirac point. The dashed black curve is the Boltzmann result. The red data points represent the fully quantum transport result, which shows a sharp dip at the Dirac point approaching the universal minimum value of $4e^2/\pi h$

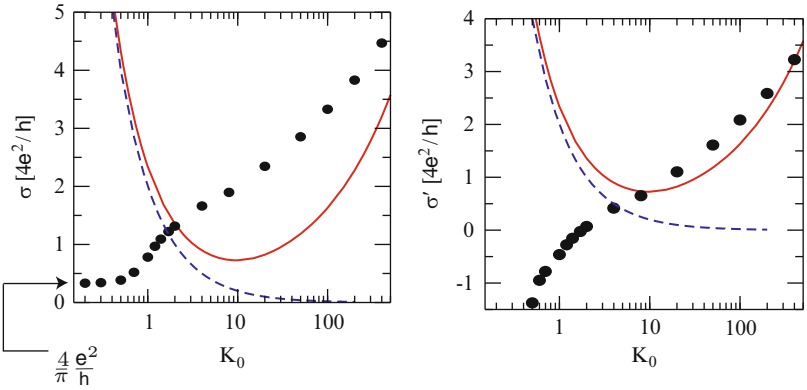

Fig. 12.12 Comparison of graphene conductivity calculated using the fully quantum theory and the semiclassical self-consistent approximation. The data points are the Landauer result (see [41]), while the solid red line is the SCA result (12.30). The dashed blue line is the Boltzmann result which for this model has a minimum conductivity that scales as K_0^{-1} (see (12.18)). For vanishing disorder, the quantum results give the universal value $\sigma_{\min} = 4e^2/\pi h$. With increasing disorder, the quantum results first increase sharply at $K_0 \approx 1$ followed by a more gradual increase for $K_0 \gtrsim 10$ (*left panel*). To test whether this gradual increase is compatible with the self-consistent approximation, in the right panel we plot the classical component of the Landauer conductivity $\sigma' = \lim_{L\to\infty}[\sigma(L) - \pi^{-1}\ln(L/\xi)]$, where we have verified that for $\sigma \gtrsim 4e^2/h$ the L dependence is consistent with weak antilocalization. The fully quantum result agrees with the self-consistent approach when the number of electrons per puddle $N_e \approx \pi n^* \xi^2 = K_0/2\pi \gtrsim 1.6$

12.3.5 Summary of Theoretical Predictions for Coulomb Impurities

The material in this chapter has covered several different transport regimes including the full crossover from quantum transport to semiclassical transport, and several different impurity models from Coulomb scatterers to Gaussian correlated impurities. In this last section, we narrow our focus to consider the framework necessary to understand the initial graphene transport experiments. To this end, we specialize to the case of semiclassical transport in graphene with long-range Coulomb impurities. The impurity potential is fully specified by two parameters: The impurity concentration $n_{\rm imp}$ and the typical distance d between the impurities and the 2D graphene sheet. We use $n_{\rm imp}$ as the single parameter to distinguish various graphene experiments by fixing $d = 1$ nm, which is the correct order-of-magnitude for impurities either in the interfacial layer of the substrate or on top of the graphene sheet, and also fixing $r_s = 0.8$, which corresponds to the most common case of graphene on top of a SiO_2 substrate. We use two additional results (that due to space constraints were not discussed elsewhere in this chapter): First, for $d \lesssim 1$ nm, the high-density conductivity is only weakly dependent on d, and it is sufficient to use the analytic $d = 0$ result (12.12). Second, as discussed in Sect. 12.3.1, once n^* is known, one can compute any moment of the disorder potential (see (12.22)). In particular, the first moment $\langle V_D \rangle = n_{\rm imp}\tilde{\phi}(q = 0)$ gives the shift of the Dirac point assuming that the disorder potential comprises only negatively charged impurities. Using the approximation of (12.30), we can summarize our results for graphene in a very compact analytical form [14]

$$\sigma(n-\bar{n}) = \begin{cases} \dfrac{20e^2}{h}\dfrac{n^*}{n_{\rm imp}} & \text{if } n-\bar{n} < n^*, \\ \dfrac{20e^2}{h}\dfrac{n}{n_{\rm imp}} & \text{if } n-\bar{n} > n^*, \end{cases} \tag{12.37}$$

$$\bar{n} = \frac{n_{\rm imp}^2}{4n^*},$$

$$\frac{n^*}{n_{\rm imp}} = 2r_s^2 C_0\left(r_s = 0.8,\ d = 1\ \text{nm},\ a = 4d\sqrt{\pi n^*}\right), \tag{12.38}$$

$$C_0(r_s, a) = -1 + \frac{4E_1(a)}{(2+\pi r_s)^2} + \frac{2e^{-a}r_s}{1+2r_s} + (1+2r_s a)\, e^{2r_s a}\left(E_1[2r_s a] - E_1[a(1+2r_s)]\right). \tag{12.39}$$

These theoretical predictions are shown in Fig. 12.13.

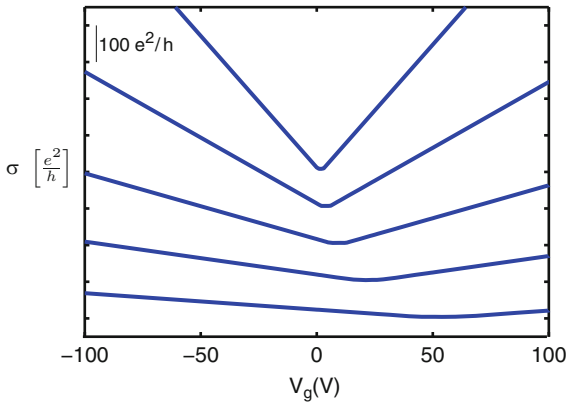

Fig. 12.13 Summary of theoretical predictions of the self-consistent approximation. Curves (*from top to bottom*) are for impurity density $n_{\text{imp}} = [20, 40, 80, 160, 320] \times 10^{10}\ \text{cm}^{-2}$ and are offset by $100\ e^2/h$ for clarity. The self-consistent theory [14] predicts that for charged impurity scattering, cleaner samples have (1) higher mobility, (2) narrower minimum conductivity plateaus, (3) smaller Dirac point offsets, and (4) larger values for the minimum conductivity

12.4 Comparison with Experiments

In this brief section, we discuss only three experimental tests of the predictions made by the theory. In the literature, one can find several other examples (some of which are discussed in the review article [15]). These three were picked as representative examples and are presented in chronological order. The important feature of all three experiments is that they span the full range of carrier density, thereby demonstrating that the physics at the Dirac plateau is governed by the same impurities that scatter carriers at high density, where the semi-classical Boltzmann transport theory is expected to be a good approximation.

12.4.1 Magnetotransport: Dependence of σ_{xx} and σ_{xy} on Carrier Density

The first test of the self-consistent theory was done in [43] by comparing with experimental data from the Manchester group [42]. The zero-magnetic-field experimental data were compared to the theory (12.37) and determined $n_{\text{imp}} \approx 1.75 \times 10^{12}\ \text{cm}^{-2}$. This fit and the experimental data are shown in the inset of Fig. 12.14. The experimental data for the longitudinal resistivity ρ_{xx} and Hall resistivity ρ_{xy} at $B = 1$ T was compared to the theoretical predictions given by (12.34) without introducing any additional fitting parameters. Since the experimentalists

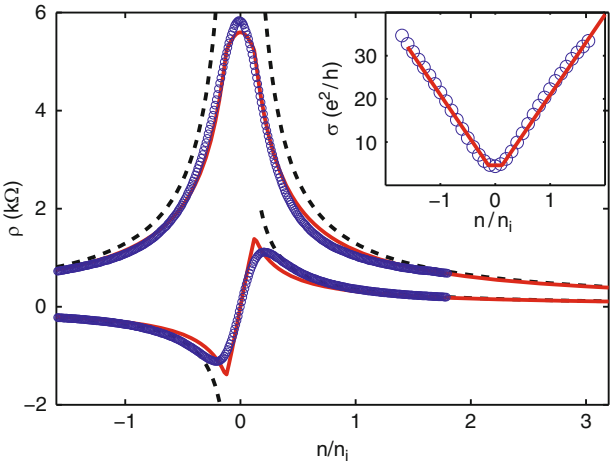

Fig. 12.14 Comparison of theoretical predictions for magneto-transport with experimental results. Red curves are (12.34) and (12.37) using the single fit parameter $n_{\rm imp} \approx 1.75 \times 10^{12}\,{\rm cm}^{-2}$. Blue circles are experimental data at $B = 1T$. Dashed lines show the Boltzmann transport result without the self-consistent correction that diverges at low carrier density. Inset: Conductivity data for the same sample at $B = 0$ T

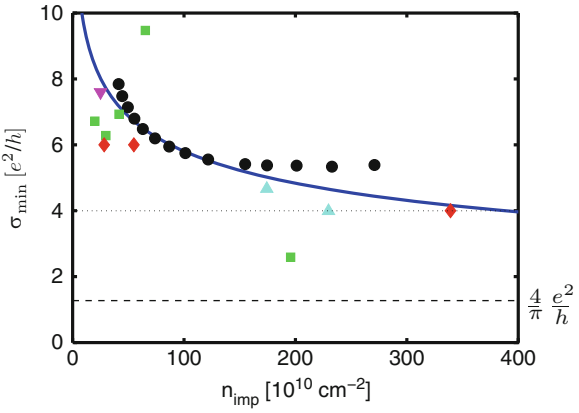

Fig. 12.15 Dependence of graphene minimum conductivity on charged impurity density. Experimental data is taken from Columbia (squares), Exeter (downward triangle), Manchester (upward triangles), and Maryland (diamonds and circles) groups (see text for details). The solid blue theoretical curve is the same as in the left panel of Fig. 12.9. The dashed horizontal line shows the universal quantum limited value of $\sigma_{\rm min} = (4/\pi)e^2/h$ and the dotted horizontal line shows $\sigma = 4e^2/h$ that was observed in the earlier experiments on dirtier samples

subtracted the Dirac point offset when taking the measurements, we could not test the additional prediction in (12.37) for the impurity-induced Dirac point shift. Nonetheless, the agreement for the full magneto-transport data with a single fit parameter is quite remarkable.

12.4.2 Dependence of σ_{min} and Mobility on Impurity Concentration

The theory presented here makes very specific predictions for the dependence of the minimum conductivity on impurity density. In the right panel of Fig. 12.15, we compare the theoretical results for $\sigma_{min}(n_{imp})$ with several different experimental data sets from various groups. We emphasize that there has been no arbitrary selection of data for this figure, it represents *all* the four-probe data sets for graphene on a SiO_2 substrate for which we have done a detailed comparison between theory and experiment.

The data from the Columbia group are the same samples that were analyzed in [13], where the values of n_{imp} were obtained from fitting the high-density data and the shift of the Dirac point. The upward triangles are data from the Manchester group [10,42], diamonds from the Maryland group [73] and the downward triangle taken from [74]. In all these samples, the value of n_{imp} is determined by fitting the high-density transport data. The black circles show the potassium doping experiments of [44], where charged impurities were intentionally added to graphene. The data shown here are for the initial deposition of the charged impurities on graphene. After annealing the sample, the subsequent runs showed different behavior suggesting the correlation between the impurity atoms. Our treatment here has been for uncorrelated impurities (see (12.21)), although it is worth mentioning that it is relatively straightforward to generalize our formalism to the case of correlated impurities if the distribution of the impurity positions is known. Subsequent experiments [75] using transition metal impurities instead of potassium also showed agreement with the theory before annealing, followed by an increase in conductivity after annealing, suggestive of impurity correlations. If the resultant potential fluctuations can be characterized by the Gaussian model (see (12.23)), we speculate that the results shown in Fig. 12.9 should apply, and in particular, that the minimum conductivity would be a nonmonotonic function of the impurity density. In any case, the agreement between theory and experiment shown in Fig. 12.15 is strong evidence both for the dominant role of Coulomb impurities and that the physics of the minimum conductivity is captured by the self-consistent approximation.

12.4.3 Dependence of σ_{min} and Mobility on Dielectric Environment

Perhaps, the most precise test of the theory presented here was done in [28]. In this experiment, the graphene conductivity was first measured in ultra-high vacuum (UHV) and fit to the Boltzmann theory discussed here for short-range and Coulomb impurities. Unlike the experiments discussed in Sect. 12.2.6, this combination of weak impurities provides a better description than the strong impurity model.

Several monolayers of ice were then introduced to the sample until there were no further changes in the transport properties. Since the dielectric constant for

vacuum, SiO_2 and ice are all known, the theory makes predictions for the changes in conductivity with *no free parameters*. In particular, it predicts that the low-density mobility should *increase* by 26 % (Fig. 12.2) and the high-density conductivity should *decrease* by 38 % (Fig. 12.2) and that the minimum conductivity (Fig. 12.9) should *decrease* by 0.01 % (i.e., stay unchanged). The experiments found the mobility increased by (31 ± 1) %, the high-density conductivity decreased by (38 ± 1) %, and the minimum changed by (0 ± 0.1) %, in excellent agreement with the theory. This experiment demonstrated that the theory presented in this chapter works to within a 5 % accuracy for large 4-probe samples in UHV. Reports using liquid dielectrics at room temperature and pressure are more ambiguous [76]. While these experiments qualitatively show the predicted trends for Coulomb and short-range impurities [77], quantitative comparisons are more difficult for several reasons. For example, one is often at high enough carrier densities that the opposing effects of long-range and short-range impurities result in only small changes to the conductivity. Also, the ions in solution could themselves act as additional charged impurities.

Focusing on the UHV results, in Fig. 12.16 we compare the theoretical predictions against the experimental data. Again, the theory has no fitting parameters, and captures not only the high-and low-density behavior (discussed above), but also the crossover from when Coulomb scatterers dominate to when short-range scatterers dominate (as reflected in the non-monotonicity of the curve). We point out that both the theoretical and experimental curves cross the x-axis at particular carrier densities. If one were to perform the same experiment sitting close to that point, then theory predicts that one would observe no changes in the conductivity when changing the dielectric constant, as discussed above in the context of liquid dielectrics.

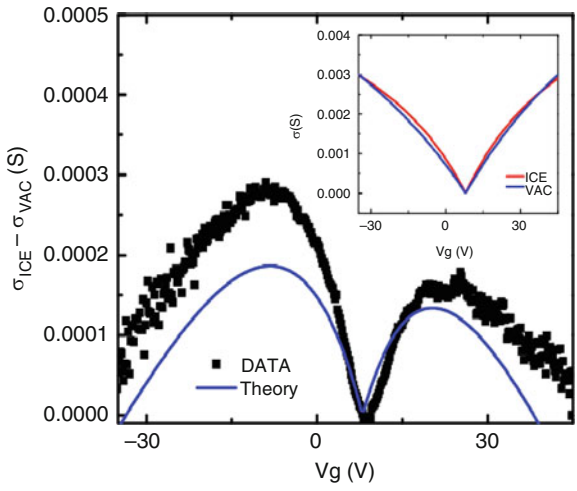

Fig. 12.16 Comparison of experimental data and theoretical predictions for $\sigma_{ice} - \sigma_{vac}$. Since the dielectric constants of vacuum, ice and SiO_2 are known, the theory has no adjustable parameters. Inset shows the experimental data. This figure was adapted from [28]

12.5 Conclusion

In this chapter, we have tried to provide a concise description of the different physical mechanisms at play in a typical graphene transport experiment. On the one hand, since the carrier transport involves quantum mechanical tunneling and scattering, many-body interaction effects, and strong disorder-induced spatial inhomogeneities, as well as the absence of a natural perturbation parameter, the problem could have been completely intractable. However, it seems that for this first practical realization of Dirac fermions in a condensed matter system, nature was rather kind. Exfoliated graphene sits at a particular sweet-spot, where although each of the mechanisms is important, and none can be neglected, they are very weak and can be treated to high accuracy within their simplest models. What matters then is not exploring any one constituent part to higher accuracy, but rather to understand the interplay between these mechanisms and the various competitions that give rise to the unusual transport properties in graphene.

For example, we have seen that graphene's minimum conductivity is a balance between how many carriers are induced by the disorder and how the disorder then scatters these carriers. The number of carriers induced by the disorder is in turn a feedback loop, where a strong disorder potential induces more carriers, which makes graphene better able to screen external potentials thereby weakening the effective disorder potential. And it is the highly efficient quantum tunneling between the electron and hole puddles that allows one to ignore the quantum transport and use the semiclassical effective medium theory.

It is primarily because graphene is perched at the intersection of these different influences that the minimum conductivity seems so insensitive to perturbations. In Fig. 12.9, we show that changing the disorder concentration by more than two orders of magnitude changes the value of $\sigma_{\min}$ by a factor of less than 3. In the same figure, we see that for typical disorder concentrations, changing the dielectric constant from 1 (vacuum) to 8 hardly changes $\sigma_{\min}$. But the theory also contains its limits. When the disorder is reduced such that the mean-free-path becomes longer than the distance between the contacts, then the quantum-limited (and universal) minimum conductivity of $\sigma_{\min} = 4e^2/\pi h$ should emerge. Achieving this is simpler than one might imagine – rather than looking for cleaner samples, one just needs to make closer contacts. Similarly, for graphene, we have $r_s \leq 2$ so that interaction effects are weak. But strained graphene or graphene in a large magnetic field, or some of the new Dirac fermion systems found on the surface of topological insulators have stronger interactions. There will certainly continue to be exciting new directions and ever-more exotic mechanisms to be discovered in graphene transport experiments in the future; however, we remain convinced that these will be observed as strong deviations from the weak coupling theory presented here.

Acknowledgements Most of the research leading up to the material covered in this chapter was done while I was a postdoctoral research associate with the Condensed Matter Theory Center at the University of Maryland under the mentorship of Sankar Das Sarma, where it was supported by U.S. ONR, and the NSF-NRI-SWAN. During this time, I also benefited enormously from collaborations

with Michael Fuhrer, Euyheon Hwang, Enrico Rossi, Victor Galitski and Ellen Williams. Some of the more recent work was done with Piet Brouwer, Mark Stiles and Parakh Jain. I am also grateful to Mark Stiles, Michael Fuhrer, Jabez McClelland, Joseph Stroscio, Hongki Min, Hassan Raza, and Nikolai Zhitenev for their valuable comments.

References

1. C. Lee, X. Wei, J.W. Kysar, J. Hone, Science **321**, 385 (2008)
2. Y.M. Lin, C. Dimitrakopoulos, K.A. Jenkins, D.B.. Farmer, H.Y. Chiu, A. Grill, P. Avouris, Science **327**(5966), 662 (2010)
3. J.H. Chen, C. Jang, S. Xiao, M. Ishigami, M.S. Fuhrer, Nature Nanotechnology **3**, 206 (2008)
4. S. Bae, H. Kim, Y. Lee, X. Xu, J.S. Park, Y. Zheng, J. Balakrishnan, T. Lei, H.R. Kim, Y.I. Song, Y.J. Kim, K.S. Kim, B. Ozyilmaz, J.H. Ahn, B.H. Hong, S. Iijima, Nature Nanotechnology **5**(8), 574 (2010)
5. D.E. Sheehy, J. Schmalian, Phys. Rev. Lett. **99**(22), 226803 (2007)
6. M.S. Fuhrer, S. Adam, Nature **458**(7234), 38 (2009)
7. J.H. Bardarson, J. Tworzydlo, P.W. Brouwer, C.W.J. Beenakker, Phys. Rev. Lett. **99**, 106801 (2007)
8. C.L. Kane, E.J. Mele, Phys. Rev. Lett. **95**(14), 146802 (2005)
9. Y.J. Song, A.F. Otte, Y. Kuk, Y. Hu, D.B. Torrance, P.N. First, W.A. de Heer, H. Min, S. Adam, M.D. Stiles, A.H. MacDonald, J.A. Stroscio, Nature **467**, 185 (2010)
10. K.S. Novoselov, A.K. Geim, S.V. Morozov, D. Jiang, Y. Zhang, S.V. Dubonos, I.V. Grigorieva, A.A. Firsov, Science **306**, 666 (2004)
11. K.S. Novoselov, A.K. Geim, S.V. Morozov, D. Jiang, Y. Zhang, M.I. Katsnelson, I.V. Grigorieva, S.V. Dubonos, A.A. Firsov, Nature **438**, 197 (2005)
12. Y. Zhang, Y.W. Tan, H.L. Stormer, P. Kim, Nature **438**, 201 (2005)
13. Y.W. Tan, Y. Zhang, K. Bolotin, Y. Zhao, S. Adam, E.H. Hwang, S. Das Sarma, H.L. Stormer, P. Kim, Phys. Rev. Lett. **99**(24), 246803 (2007)
14. S. Adam, E.H. Hwang, V.M. Galitski, S. Das Sarma, Proc. Natl. Acad. Sci. USA **104**, 18392 (2007)
15. S. Das Sarma, S. Adam, E. H. Hwang, and E. Rossi, Rev. Mod. Phys. **83**, 407 (2011)
16. E.R. Mucciolo, C.H. Lewenkopf, Journal of Physics: Condensed Matter **22**(27), 273201 (2010)
17. N.M.R. Peres, Rev. Mod. Phys. **82**(3), 2673 (2010)
18. S. Adam, E.H. Hwang, E. Rossi, S. Das Sarma, Solid State Commun. **149**, 1072 (2009)
19. A.W.W. Ludwig, M.P.A. Fisher, R. Shankar, G. Grinstein, Phys. Rev. B **50**(11), 7526 (1994)
20. N. Shon, T. Ando, J. Phys. Soc. Jpn. **67**, 2421 (1998)
21. T. Ando, J. Phys. Soc. Jpn. **75**, 074716 (2006)
22. E.H. Hwang, S. Das Sarma, Phys. Rev. B **75**, 205418 (2007)
23. B. Wunsch, T. Stauber, F. Sols, F. Guinea, New J. Phys. **8**, 318 (2006)
24. M. Polini, R. Asgari, Y. Barlas, T. Pereg-Barnea, A. MacDonald, Solid State Commun. **143**, 58 (2007)
25. K. Nomura, A.H. MacDonald, Phys. Rev. Lett. **98**, 076602 (2007)
26. E.H. Hwang, S. Adam, S. Das Sarma, Phys. Rev. Lett. **98**, 186806 (2007)
27. M. Trushin, J. Schliemann, Phys. Rev. Lett. **99**, 216602 (2007)
28. C. Jang, S. Adam, J.H. Chen, E.D. Williams, S. Das Sarma, M.S. Fuhrer, Phys. Rev. Lett. **101**(14), 146805 (2008)
29. S. Adam, E. Hwang, S. Das Sarma, Physica E **40**, 1022 (2008)
30. T. Stauber, N.M.R. Peres, F. Guinea, Phys. Rev. B **76**(20), 205423 (2007)
31. S. Adam, S. Cho, M.S. Fuhrer, S. Das Sarma, Phys. Rev. Lett. **101**, 046404 (2008)
32. E. Rossi, S. Das Sarma, Phys. Rev. Lett. **101**(16), 166803 (2008)
33. M. Polini, A. Tomadin, R. Asgari, A.H. MacDonald, Phys. Rev. B **78**(11), 115426 (2008)

34. J. Martin, N. Akerman, G. Ulbricht, T. Lohmann, J.H. Smet, K. von Klitzing, A. Yacobi, Nature Physics **4**, 144 (2008)
35. A. Deshpande, W. Bao, F. Miao, C.N. Lau, B.J. LeRoy, Phys. Rev. B **79**(20), 205411 (2009)
36. Y. Zhang, V. Brar, C. Girit, A. Zettl, M. Crommie, Nature Physics **5**, 722 (2009)
37. D. Miller, K. Kubista, G. Rutter, M. Ruan, W. de Heer, P. First, J. Stroscio, Science **324**, 924 (2009)
38. E. Rossi, S. Adam, S. Das Sarma, Phys. Rev. B **79**(24), 245423 (2009)
39. M.M. Fogler, Phys. Rev. Lett. **103**, 236801 (2009)
40. S. Adam, M.D. Stiles, Phys. Rev. B **82**(7), 075423 (2010)
41. S. Adam, P.W. Brouwer, S. Das Sarma, Phys. Rev. B **79**(20), 201404 (2009)
42. F. Schedin, A.K. Geim, S.V. Morozov, D. Jiang, E.H. Hill, P. Blake, K.S. Novoselov, Nature Materials **6**, 652 (2007)
43. E.H. Hwang, S. Adam, S. Das Sarma, Phys. Rev. B **76**(19), 195421 (2007)
44. J.H. Chen, C. Jang, S. Adam, M.S. Fuhrer, E.D. Williams, M. Ishigami, Nature Physics **4**, 377 (2008)
45. N.W. Ashcroft, N.D. Mermin, *Solid State Physics* (Saunders, 1976)
46. H. Bruus, K. Flensberg, *Many-Body Quantum Theory in Condensed Matter Physics: An Introduction* (Oxford University Press, Oxford, 2004)
47. A. Ferreira, J. Viana-Gomes, J. Nilsson, E.R. Mucciolo, N.M.R. Peres, A.H. Castro Neto, Phys. Rev. B **83**, 165402 (2011)
48. J. Gonzalez, F. Guinea, V.A.M. Vozmediano, Nucl. Phys. B **424**, 595 (1994)
49. T. Ando, A.B. Fowler, F. Stern, Rev. Mod. Phys. **54**, 437 (1982)
50. K. Bolotin, K. Sikes, Z. Jiang, G. Fudenberg, J. Hone, P. Kim, H. Stormer, Solid State Commun. **146**, 351 (2008)
51. S. Adam, S. Das Sarma, Solid State Commun. **146**, 356 (2008)
52. C.H. Lewenkopf, E.R. Mucciolo, A.H. Castro Neto, Phys. Rev. B **77**, 081410 (2008)
53. J. Katoch, J. Chen, R. Tsuchikawa, C. Smith, E.R. Mucciolo, M. Ishigami, Phys. Rev. B **82**(8), 081417 (2010)
54. T.O. Wehling, S. Yuan, A.I. Lichtenstein, A.K. Geim, M.I. Katsnelson, Phys. Rev. Lett. **105**(5), 056802 (2010)
55. Z.H. Ni, L.A. Ponomarenko, R.R. Nair, R. Yang, S. Anissimova, I.V. Grigorieva, F. Schedin, P. Blake, Z.X. Shen, E.H. Hill, K.S. Novoselov, A.K. Geim, Nano Lett. **10**, 3868 (2010)
56. M. Hentschel, F. Guinea, Phys. Rev. B **76**, 115407 (2007)
57. J.H. Chen, W.G. Cullen, C. Jang, M.S. Fuhrer, E.D. Williams, Phys. Rev. Lett. **102**, 236805 (2009)
58. V. Ugarte, V. Aji, C.M. Varma, arXiv:1007.3533 (2010)
59. S. Jung, G.M. Rutter, N.N. Klimov, D.B. Newell, I. Calizo, A.R. Hight-Walker, N.B. Zhitenev, J.A. Stroscio, Nat. Phys. **7**, 245 (2011)
60. M. Ishigami, J.H. Chen, W.G. Cullen, M.S. Fuhrer, E.D. Williams, Nano Lett. **7**, 1643 (2007)
61. S. Das Sarma, M.P. Lilly, E.H. Hwang, L.N. Pfeiffer, K.W. West, J.L. Reno, Phys. Rev. Lett. **94**(13), 136401 (2005)
62. V. Galitski, S. Adam, S. Das Sarma, Phys. Rev. B **76**(24), 245405 (2007)
63. E. Rossi, private communication (2008)
64. R. Landauer, J. Appl. Phys. **23**, 779 (1952)
65. I.S. Gradshteyn, I.M. Ryzhik, *Table of integrals, series, and products*, 5th edn. (Academic Press, 1994)
66. M.I. Katsnelson, Eur. Phys. J. B **51**, 157 (2006)
67. J. Tworzydło, B. Trauzettel, M. Titov, A. Rycerz, C.W.J. Beenakker, Phys. Rev. Lett. **96**(24), 246802 (2006)
68. K. Nomura, M. Koshino, S. Ryu, Phys. Rev. Lett. **99**, 146806 (2007)
69. P. San-Jose, E. Prada, D.S. Golubev, Phys. Rev. B **76**, 195445 (2007)
70. A. Luican, G. Li, E.Y. Andrei, Solid State Commun. **149**, 1151 (2009)
71. J.C. Meyer, C. Kisielowski, R. Erni, M.D. Rossell, M.F. Crommie, A. Zettl, Nano Lett. **8**, 3582 (2008)

72. H. Suzuura, T. Ando, Phys. Rev. Lett. **89**(26), 266603 (2002)
73. J.H. Chen, C. Jang, M. Ishigami, S. Xiao, W. Cullen, E. Williams, M. Fuhrer, Solid State Commun. **149**(27-28), 1080 (2009)
74. F.V. Tikhonenko, A.A. Kozikov, A.K. Savchenko, R.V. Gorbachev, Phys. Rev. Lett. **103**, 226801 (2009)
75. K. Pi, K.M. McCreary, W. Bao, W. Han, Y.F. Chiang, Y. Li, S.W. Tsai, C.N. Lau, R.K. Kawakami, Phys. Rev. B **80**(7), 075406 (2009)
76. L.A. Ponomarenko, R. Yang, T.M. Mohiuddin, M.I. Katsnelson, K.S. Novoselov, S.V. Morozov, A.A. Zhukov, F. Schedin, E.W. Hill, A.K. Geim, Phys. Rev. Lett. **102**, 206603 (2009)
77. K. Novoselov, private communication (2009)

Chapter 13
Exploring Quantum Transport in Graphene Ribbons with Lattice Defects and Adsorbates

George Kirczenow and Siarhei Ihnatsenka

Abstract The reader is introduced to the Landauer theory of quantum transport in the context of graphene nanoribbons as well as to the geometries and electronic structures of and ballistic quantum transport in ideal ribbons. Imperfections present in ribbons that are realized in the laboratory, including carbon atom vacancies, edge disorder, long-ranged defect potentials and covalently bonded adsorbates including H, F, O, and OH and their roles in quantum transport in the ribbons are then considered. Quantum transport simulations for ribbons with these defects show that carbon atom vacancies and adsorbates can give rise to quantized conductance steps such as those observed experimentally in samples with conductances much smaller than the conductance quantum $2e^2/h$. Adsorbate-induced scattering resonances in graphene are discussed from the perspective of extended Hückel-based tight binding models and T-matrix theory and the effects of the adsorbate-induced rehybridization of the graphene from sp^2 to sp^3 bonding on these resonances are examined. Transport gaps are shown to open in the conductances of graphene ribbons with adsorbed H, F, O, and OH for electron Fermi energies in the vicinities of these resonances.

Graphene nanoribbons are strips of graphene typically 20–100 nm wide but of arbitrary length. In recent years, they have been attracting increasing experimental [1–18] and theoretical [19–64] interest. Perfect graphene ribbons that are uniform in width and are free from defects, adsorbates, edge roughness and other disorder should at low temperatures be ideal quantum wires that transmit electrons ballistically (without scattering) and exhibit conductances that are quantized in multiples of $2e^2/h$. However, most ribbons realized experimentally to date have been far from this ideal and electronic transport in them has been dominated by the effects of

G. Kirczenow (✉) · S. Ihnatsenka
Department of Physics, Simon Fraser University, Burnaby, BC, Canada
e-mail: kirczeno@sfu.ca; siarhei.ihnatsenka@gmail.com

H. Raza (ed.), *Graphene Nanoelectronics*, NanoScience and Technology,
DOI 10.1007/978-3-642-22984-8_13, © Springer-Verlag Berlin Heidelberg 2012

disorder. However, some recent experiments [3, 17] have begun to show evidence of quantum transport phenomena that are indicative of a degree of order emerging in the samples being studied. In this Chapter, we discuss electronic transport in such ribbons where there is considerable disorder present but some quasi-ballistic quantum transport phenomena can never the less be discerned.

The Chapter is organized as follows. We begin in Sect. 13.1 with an introduction to the basic concepts of the Landauer theory of electronic transport in quasi-one dimensional conductors that can be used to describe electrical conduction in such ribbons. In Sect. 13.2 we discuss the geometry, and electronic structure of ideal ribbons. Conductance quantization in ballistic nanostructures is then briefly reviewed in Sect. 13.3. The basic concepts of electron transport in realistic graphene nanoribbon devices are introduced in Sect. 13.4. The experimental discovery of conductance quantization in strongly disordered ribbons is discussed in Sect. 13.5. The different kinds of defects present in graphene nanoribbon devices are discussed in Sect. 13.6 and a tight binding model that can be used to model the effects of some of them is presented in Sect. 13.7. The results of numerical simulations of electron quantum transport in graphene ribbons with carbon atom vacancies, edge disorder and long ranged defect potentials within the framework of the tight binding model described in Sect. 13.7 are discussed in Sect. 13.8. In Sect. 13.8.1, we discuss how disorder-induced scattering suppresses ballistic conductance quantization in graphene ribbons, as well as the specific ways in which the presence of carbon atom vacancies, edge disorder and long ranged defect potentials affects the quantum transport characteristics of the ribbons. In Sect. 13.8.2, we discuss the origin of the enhanced electron backscattering at graphene ribbon subband edges that plays a key role in the conductance quantization that has been observed in strongly disordered ribbons. In Sect. 13.8.3, we discuss how the ribbon quantum transport characteristics depend on the temperature. In Sect. 13.8.4, we discuss the transition with increasing disorder from ballistic transport to the regime of strongly localized electronic states. The results of the quantum transport calculations are compared with the experiments in the linear and non-linear transport regimes in Sect. 13.8.5. We next turn to the role of adsorbates in electrical conduction in graphene ribbons. In Sect. 13.9, we study the scattering properties of H, F, OH and O adsorbed on graphene: In Sect. 13.9.1, we explain how a tight binding Hamiltonian that incorporates the essential physics of graphene with covalently bound adsorbates may be constructed on the basis of extended Hückel theory. In Sect. 13.9.2, we show how this Hamiltonian can be transformed into an equivalent effective Hamiltonian for graphene alone but with modified site energies and hopping matrix elements. In Sect. 13.9.3, we explain how T-matrix theory and Green's functions describing the π-band electrons in graphene can be used to study scattering of graphene electrons by adsorbed atoms and molecules. In Sect. 13.9.4, we apply the results of the preceding Sections to study the electronic scattering resonances that arise near the Dirac point energy of graphene due to of H, F, OH, and O adsorbed on the graphene. Then in Sect. 13.10, we apply what was learned in Sect. 13.9 to the problem of quantum transport in ribbons with adsorbates: In Sect. 13.10.1, we construct minimal Hamiltonians of graphene ribbons with adsorbates that make possible efficient and accurate quantum

transport calculations for these systems, including the effects of the rehybridization of the graphene from sp^2 to sp^3 bonding that occurs due to covalent bonding of atoms and molecules to the graphene. The results of transport calculations for graphene ribbons with adsorbed H, F, OH, and O are then discussed in Sect. 13.10.2. Our conclusions are presented in Sect. 13.11.

13.1 Landauer Theory of Transport

In 1957, Landauer proposed [65] that conduction in one-dimensional systems could be viewed as quantum transmission problem and this idea eventually evolved into the Landauer transport formula [66–68] that is widely used to describe nanoscale quantum transport today, [69] and will be applied to graphene nanoribbons in this Chapter.

The graphene ribbons that we will consider are narrow wires made of a single atomic layer of graphene with electrons allowed to move along the ribbon but meeting impenetrable boundaries in transverse direction. To derive the relevant Landauer formulae, let us assume that the electron phase-relaxation length is large and the de Broglie wavelength of an electron is comparable to the width of the ribbon.

Consider a ribbon of length L bridging two macroscopic electrodes or electron reservoirs. In the ribbon, the electron states are quantized in the direction transverse to the length of the ribbon. Thus, they are characterized by their longitudinal momenta k along the ribbon and an index l associated with their quantized transverse nature that distinguishes between different states with the same longitudinal momentum k. For each value of the index l, the energies $E_l(k)$ of these ribbon states form a band called a *subband*. The electron density $n_l(k)$ per unit length corresponding to a given subband l in the range of longitudinal momentum between k and $k + \mathrm{d}k$ is given by

$$n_l(k)\,\mathrm{d}k = \frac{2}{L}\frac{L}{2\pi} f(E_l(k))\mathrm{d}k = \frac{1}{\pi} f(E_l(k))\mathrm{d}k, \tag{13.1}$$

where $f(E_l(k))$ is the Fermi distribution function. Spin degeneracy is included here and in the following. Let us assume for the moment ideal transmission of electrons between the electrodes and the ribbon and that the electrons travel through the ribbon ballistically, i.e., without scattering. Then for small bias voltages applied between the electrodes the electrons injected into the nanoribbon from each electrode can be regarded as being approximately in equilibrium and having quasi Fermi levels (or more precisely electrochemical potentials) and associated distribution functions $f_{\mathrm{R}}(E_l(k))$ and $f_{\mathrm{L}}(E_l(k))$ for electrons originating from the right and left lead, respectively. Then the longitudinal electron current carried by subband l (also referred to as "conducting mode l") of the ribbon is given by

$$I_l = -2\int_{-\infty}^{\infty} e v_l(k) n_l(k)\mathrm{d}k = -2e\int_0^{\infty} |v_l(k)| \left(\frac{f_{\mathrm{R}}(E_l(k))}{2\pi} - \frac{f_{\mathrm{L}}(E_l(k))}{2\pi}\right)\mathrm{d}k. \tag{13.2}$$

Here $v_l(k) = \partial E_l(k)/\partial(\hbar k)$ is the electron velocity along the ribbon in mode l. In the zero temperature limit, the Fermi distributions are step functions. Then, changing the variable of integration from k to $E_l(k)$, (13.2) takes the form

$$I_l = -\frac{2e}{2\pi}\int_{\mu_L}^{\mu_R}\frac{\partial E_l}{\partial(\hbar k)}\frac{\partial k}{\partial E_l}\mathrm{d}E_l = -\frac{2e^2}{h}\frac{\mu_R-\mu_L}{e} = \frac{2e^2}{h}V_{\mathrm{bias}}, \tag{13.3}$$

where $\mu_{R/L}$ are the electrochemical potentials of the leads and their relative values depend on the bias voltage V_{bias} so that $\mu_R - \mu_L = -eV_{\mathrm{bias}}$. From (13.3), we see that the conductance $G \equiv \partial I/\partial V_{\mathrm{bias}}$ for a single conducting mode, the so-called conductance quantum, is

$$G_0 = \frac{2e^2}{h}. \tag{13.4}$$

This is the maximum conductance of a single conducting mode with two spin states. In practice, a mode is not necessarily fully conducting, because electrons can backscatter within the nanodevice and at its connections to the electrodes. If this occurs, the current is lower than that given by (13.2) and (13.3). Let the probability for an electron with energy E to pass through the device from conducting mode j in the left lead into conducting mode i in the right lead be denoted $T_{ij}(E)$. Then the total zero temperature conductance of the ribbon in the limit of low-applied bias voltage has the form

$$G = \frac{2e^2}{h}\sum_{ij}T_{ij}(E_{\mathrm{F}}), \tag{13.5}$$

where the sum is over the conducting modes i of the right electrode and j of the left electrode at the electrode Fermi level and E_{F} is the Fermi energy. This equation is the so-called Landauer formula for the conductance. Equation (13.5) was generalized later by Büttiker [70] to systems with arbitrary numbers of leads and that generalization is now widely referred to as the Landauer–Büttiker formalism. The Landauer–Büttiker formalism is applicable to the coherent transport regime where it yields results equivalent to those obtained using the non-equilibrium Green's function techniques discussed in Chaps. 15–18.

Generalizing the above derivation to the case of non-zero temperatures yields

$$G = -\frac{2e^2}{h}\int_{-\infty}^{\infty}\mathrm{d}E\ T(E)\frac{\partial f(E)}{\partial E} \tag{13.6}$$

for the finite temperature conductance in the limit of low bias where $T(E) = \sum_{ij}T_{ij}(E)$ is the total transmission coefficient and $f(E)$ is the Fermi distribution function.

Based on the above discussion it is evident that the properties of the electronic subbands of graphene nanoribbons play a key role in electronic transport in these systems. We will discuss these properties in the next Section.

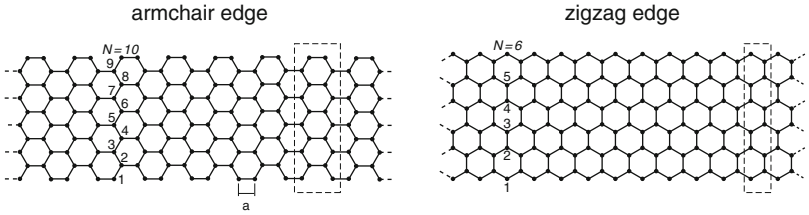

Fig. 13.1 Graphene ribbons with armchair and zigzag edges. N is the number of carbon atoms in a cross section of the ribbon. The *dashed rectangles* mark a unit cell of the ribbon. $a = 0.142\,\text{nm}$ is carbon–carbon distance

13.2 Subband Structure and Transport in Ideal Ribbons

In general, the subband structure of the graphene ribbons may be predicted from the band structure of two-dimensional (2D) graphene [19]; see Chap. 9 for an introduction to and detailed discussion of this topic. However, there are two principal topologies of ordered graphene ribbon edges, armchair and zigzag, that are shown in Fig. 13.1. They largely determine electron behavior in ideal ribbons. It turns out that while the densities of states and conductances of armchair and zigzag ribbons have many features in common, there are significant differences between their subband structures that give rise to important differences in their transport properties, as can be seen in Fig. 13.2.

A distinguishing feature of the band structure of graphene is the existence of electron and hole branches that touch each other at two inequivalent points in the first Brillouin zone [71, 72] that are referred to as the "Dirac points". The electron dispersion of 2D graphene at those points is approximately linear. The Dirac points in the graphene ribbons are defined by projecting the Dirac points of 2D graphene onto the longitudinal axes of the ribbons. They are located at $k = 0$ and $k = \pm 2\pi/3$ for armchair and zigzag ribbons, respectively [19] and are indicated by the dashed vertical lines in Fig. 13.2.

In Fig. 13.2, the electronic states at negative energies are filled while those at positive energies are empty for pristine ribbons not subjected to external fields. Thus, the armchair ribbon in Fig. 13.2a has an energy gap at the Fermi level and is therefore semiconducting, while the armchair ribbon in Fig. 13.2b and the zigzag ribbon in Fig. 13.2c have no such gap and are metallic. In general, an armchair ribbon is semiconducting or metallic depending on its width. It is metallic when the number of carbon atoms in the transverse direction equals to $N = 3M - 1$, where M is an integer. For the semiconducting ribbons, the size of the direct gap decreases with increasing ribbon width and tends to zero in the limit of very large N. Ribbon energy gaps can also be influenced by many-body electron interaction effects [23, 27, 32, 40] by periodic modulation of the ribbon's edge geometries [43] and by edge reconstruction [8, 52].

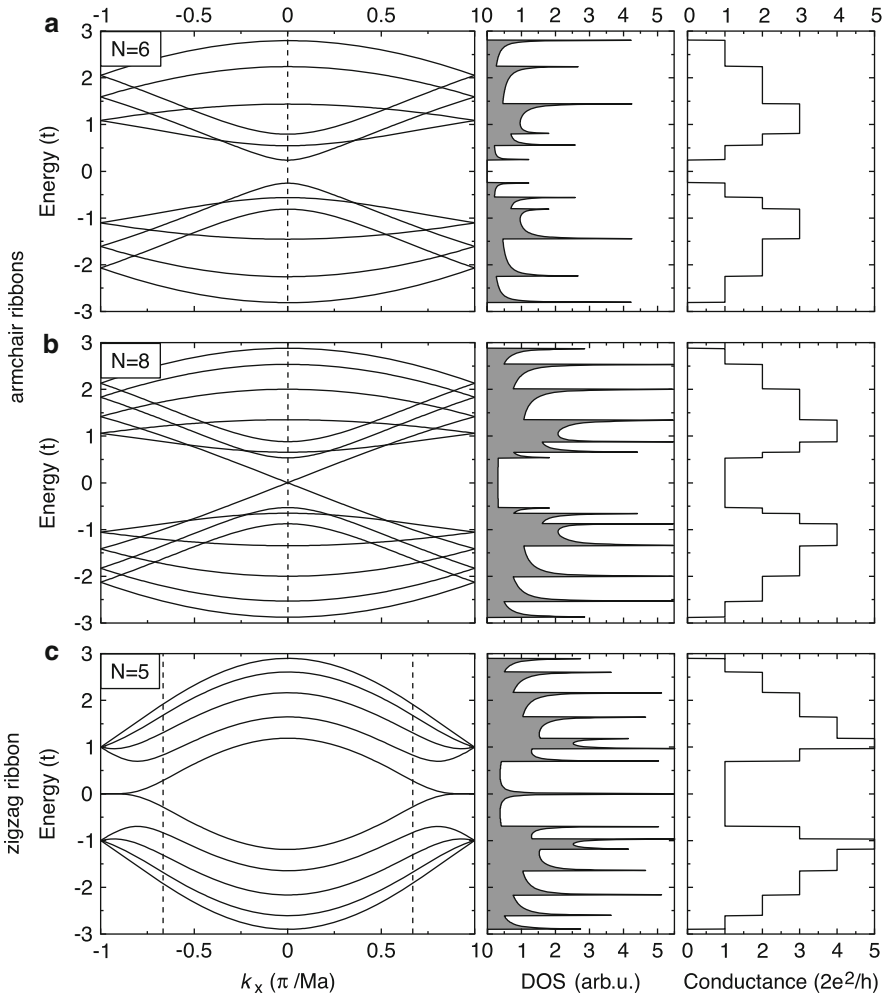

Fig. 13.2 The dispersion relation (*left column*), DOS (*middle column*), and conductance (*right column*) for ideal armchair (**a**), (**b**), and zigzag (**c**) graphene ribbons. The *dashed vertical lines* in the dispersion plots show the Dirac point location of 2D graphene projected onto the longitudinal axis of the ribbon. Ma is the unit cell size of the ribbon: $M = 3$ for armchair and $M = \sqrt{3}$ for zigzag ribbons; $a = 0.142$ nm. The Dirac point corresponds to zero energy

For zigzag ribbons, a unique and remarkable feature is present in the band structure, as is shown in Fig. 13.2c: The highest valence band state and the lowest conduction band state for the zigzag ribbons are always degenerate at $k = \pi$ (at zero energy in Fig. 13.2c) and the corresponding wave functions are completely localized on the edge sites of the ribbon [19, 20, 25]. These two bands are almost flat and lie very close to the Fermi level in a range of k within the region $2\pi/3 \leq |k| \leq \pi$. It has been suggested theoretically [21, 22, 24, 31, 39–41, 49–51, 54, 64, 73–78] that this

flat dispersion at the Fermi level may give rise to magnetism; however, we shall not discuss this further here.

As is also seen in Fig. 13.2c, the second lowest conduction band shows a dip not far from $|k| = 2\pi/3$ where the second highest valence band shows a rise. These bands approach each other as the width N of the ribbon increases, ultimately reproducing the electronic structure around the Dirac K point in 2D graphene.

The densities of states (DOS) and the zero temperature conductances for the representative ideal ribbons are also shown in Fig. 13.2. The conductances of the ideal ribbons are given by [20, 26, 28, 29, 35, 38, 42, 44–46, 55]

$$G_{\text{ideal}} = 2ne^2/h \tag{13.7}$$

where n is the number of ribbon subbands that are present at the electron Fermi energy that is taken to be equal to the electron energy plotted on the vertical axes in Fig. 13.2. Here it is assumed that the electron Fermi level in the ribbon can be swept through the energy range shown in Fig. 13.2, for example, by varying the voltage on a gate that is close to the ribbon (see Fig. 13.3) as is commonly done in nanoribbon transport experiments. [1–7, 9, 10, 12–15, 17] (13.7) follows from the Landauer formula (13.5) with $T_{ij}(E_{\text{F}}) = \delta_{ij}$ for the subbands i, j that are present at the Fermi energy E_{F}. The DOS in Fig. 13.2 exhibit sharp peaks at the band edges, and the associated conductance changes there by one conductance quantum $2e^2/h$.

Here we should note that the graphene ribbons are not strictly one-dimensional systems. They are rather two-dimensional structures having a finite width in a way similar to semiconductor quantum wires patterned in a two-dimensional electron gas [79]. There are two components of the total electron energy: transverse and longitudinal. The transverse energy is related to quantization of electron momentum in the transverse direction, while the longitudinal energy is associated with free electron motion along the ribbon. When a new transverse energy level (subband) becomes populated at a given energy, a continuous energy spectrum of subband states opens

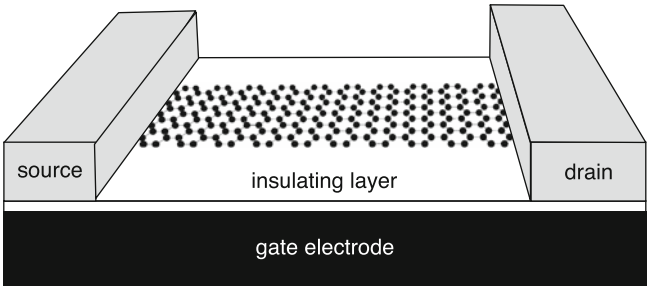

Fig. 13.3 Schematic depiction of a graphene ribbon device, not drawn to scale. The ribbon is contacted by metal source and drain electrodes and is separated by a thin insulating layer from a back gate electrode that acts as a capacitor plate and can thus be used to control the electron density in the ribbon, or equivalently the location of the electron Fermi level relative to the Dirac point energy of the ribbon

up to longitudinal electron propagation, as is seen from dispersion relation and DOS in Fig. 13.2. Note that close to the subband edges, the dispersion relation is well approximated by parabola as in conventional semiconductor quantum wires. Thus, the DOS diverges as $(E - E_i)^{-1}$ in that case, where E_i is the edge of the i-th subband. For wide ribbons, the dispersion (not too close to the band edges) gradually recovers the linear character of 2D graphene around the Dirac points at $k = 0$ and $k = \pm 2\pi/3$ for armchair and zigzag ribbons, respectively.

13.3 Quantized Ballistic Conductance

Conductance quantization in units of $2e^2/h$ similar to that predicted for ideal graphene nanoribbons [26, 28, 29, 35, 38, 42, 44–46, 55] as has been discussed in Sects. 13.1 and 13.2 (and is depicted in the right column of Fig. 13.2) has been observed experimentally in many mesoscopic systems, although not as yet in graphene ribbons. Examples of systems in which this phenomenon has been reported experimentally include semiconductor quantum point contacts [80, 81], gold nanowires [82,83], carbon nanotubes [84] and, most recently, ballistic graphene constrictions whose lengths are similar to or shorter than their widths [85].[1]

The seminal experiments of van Wees et al. [80] and Wharam et al. [81] on quantum point contacts revealed conductance quantization staircases with up to 16 clearly visible steps. Their experimental samples were formed in the two-dimensional electron gas at GaAs–AlGaAs interfaces. By applying a voltage to the top gates, electrons were repelled beneath the gates and a constriction ∼200 nm wide was formed, separating two large electron reservoirs. The width of the constriction was controlled by the gate voltage thus allowing varying numbers of electron subbands to be occupied. Each subband (or channel) contributed $2e^2/h$ to the conductance in accord with the Landauer formula (13.5). The measured conductance staircase was immediately attributed to quantized transverse momentum in the constriction. The experimentally measured value $2e^2/h$ of the individual steps, $2e^2/h$, pointed to ballistic electron transport with no inter-channel mixing. To observe the conductance steps, it was necessary for the constriction width to be comparable to the electron Fermi wavelength and for the temperature to be lower than subband energy separation. For constrictions of ∼200 nm, the latter means operating temperatures of a few Kelvins or less.

Conductance quantization is observable at much higher temperatures, even room temperature, in atomic constrictions as was shown in the experiments of Pascual et al. [82, 83]. They fabricated a short gold nanowire that was progressively elongated by pulling its two ends apart. Mechanical elongation is accompanied by

[1] Very recently S. Ihnatsenka and G. Kirczenow have demonstrated similar ballistic conductance quantization theoretically in a tight binding model of graphene constrictions with mesoscopically smooth but atomically stepped boundaries by means of million-atom quantum transport calculations.

shrinkage of the wire diameter until the wire consists at its narrowest of a single atom or chain of atoms, followed by rupture of the wire. The conductance measured across the nanowire showed clear quantization steps when distinct electron channels formed at particular atomic configurations in the constriction cross-section. Gold nanowires displaying conductance quantization at room temperature generally have lengths up to only several nanometers.

By contrast, carbon nanotubes with lengths up to 4 μm display ballistic electron transport [84]. Carbon nanotubes can be regarded as rolled up sheets of graphene and are routinely produced by chemical synthesis. Their extraordinary ballistic properties are explained by their highly regular atomic structures that repeat along the nanotube. Their measured conductances were found to be $2e^2/h$ to high precision. The experimental samples remained stable at high currents that exceeded by many orders of magnitude of critical currents for superconductors of comparable sizes. Such stability can be explained by energy dissipation in the electron reservoirs, not in the ballistic channel itself, another feature of Landauer transport theory [69].

13.4 Electron Transport in Graphene Ribbons

The ballistic transport that is a necessary prerequisite for the conductance quantization that is observed in the systems discussed in Sect. 13.3 occurs in those systems for different reasons: The material of the semiconductor quantum point contacts is highly refined with very low concentrations of defects that can scatter electrons within the conducting channel. Furthermore, the electrostatic potentials that define the edges of the channel have smooth profiles and act as an electron waveguide so that electrons in individual modes are typically either almost fully transmitted through the point contact or fully reflected. For this reason, the value of $\sum_{ij} T_{ij}$ in (13.5) is typically close to an integer and conductance quantization is observed. The ballistic transport in carbon nanotubes is possible because very pure and well ordered carbon nanotubes form spontaneously by self-assembly and the same is true of the gold atomic chains and single gold atoms that are responsible for conductance quantization in gold atomic constrictions.

By contrast, the graphene nanoribbons used in transport experiments to date have been fabricated using top-down techniques:[2] A 2D graphene sheet is placed on a substrate that consists of a conducting gate electrode covered by a thin insulating layer that isolates the gate electrically from the graphene. Then, a ribbon is patterned out of the graphene in a series of steps that include protecting the region of graphene that is to become the ribbon with an etch mask and removing the surrounding graphene by etching [1–3, 6, 7, 10, 12–14, 17]. Alternatively, ribbons have been produced by chemomechanical breaking of graphene sheets suspended in solution

[2] A bottom-up method of fabricating very narrow graphene ribbons by self-assembly has been demonstrated [16] but transport measurements on the ribbons produced in this way have not as yet been reported.

[4, 5] or by etching [9] or unzipping [11, 15] carbon nanotubes. In each case metal contacts were placed on the ends of the ribbon. The objective has been to produce a structure that, in its simplest form, is shown schematically in Fig. 13.3. However the procedures used result in imperfections (not shown in Fig. 13.3) that scatter electrons passing through the ribbon. The scattering mechanisms include: Scattering at the edges of the ribbon that need not be atomically smooth, scattering by graphene lattice defects such as carbon atom vacancies that may be introduced in the fabrication process, scattering due to adsorbates on the graphene ribbon that modify its electronic structure and scattering due to electrostatic interaction of electrons in the ribbon with charged centers in the substrate, among others.

These scattering mechanisms result in low electron transmission probabilities through the ribbons so that $T_{ij} \ll 1$ in (13.5). Thus instead of conductances quantized in integer multiples of $2e^2/h$ transport experiments on graphene ribbons to date have found transport gaps with low conductances for electron Fermi energies near the Dirac point, and at low temperatures thermally activated electron transport and conductances dominated by dense arrays of weak and narrow resonant peaks as a function of gate voltage. These resonances are due in some cases to quantum interference in the wave functions of electrons multiply scattered by defects [44] and in others to Coulomb blockade that arises from the electrostatic fields due to electrons trapped by irregularities in the ribbon geometry at various locations in the ribbon [10, 30].

There have been many theoretical studies of electron quantum transport in nanoribbons with disorder, and it has been concluded that ballistic conductance quantization is destroyed and the conductances of ribbons are strongly suppressed by the kinds of disorder discussed above, [28, 29, 35, 42, 44–46, 55] consistent with the experimental findings.

13.5 Discovery of Quantized Conductance in Strongly Disordered Graphene Ribbons

In view of the discussion in the preceding Section the recent experimental observation of quantized conductance steps in graphene nanoribbons by Lin et al. [3] was unexpected and surprising. Some aspects of their data were particularly puzzling:

1. The heights of the conductance steps were two orders of magnitude lower than conductance quantum $2e^2/h$.
2. The heights of the conductance steps decreased with increasing ribbon length.
3. The conductance steps were observed in a limited temperature range $15\text{K} < T < 80\text{K}$.

Graphene ribbons, while having some unique electronic properties, do not differ fundamentally from other mesoscopic systems and, therefore, under appropriate conditions should exhibit $2e^2/h$ quantization steps according to Landauer theory, Sect. 13.1. However, the conductance quantization observed by Lin et al. [3] (and subsequently also reported by Lian et al. [17]) was clearly a different phenomenon.

To uncover possible reasons for the above puzzling behavior let us consider closely the fabrication process [3]. The experimental devices (see Fig. 13.3) were fabricated from a mechanically exfoliated graphene sheet. This was mounted on a conducting p-doped Si substrate covered with a 300 nm-thick insulating SiO_2 layer. Pd metal contacts served as the source and drain electrodes while the Si substrate acted as the back gate. Narrow ribbons of graphene were formed by oxygen plasma reactive ion etching using a patterned hydrogen silsesquioxane (HSQ) layer as the protective mask. The HSQ layer was finally removed in a hydrofluoric acid solution. Removing the HSQ layer was found to be crucial in order to obtain a high electron mobility and to observe conductance quantization in the graphene ribbon devices. Transport measurements were performed in vacuum after annealing at 135°C to remove physisorbed residues. An indirect indication of the high quality of the fabricated samples was that the conductance minimum of the ribbon was found at to be near zero gate voltage $V_g \sim 0$ in agreement with the Dirac point position of graphene.

13.6 The Roles of Different Classes of Defects

While the experimental samples of Lin et al. [3] were of high quality, they were clearly not totally free from disorder. Possible candidates for the imperfections responsible for the measured conductances of these ribbons being much smaller than $2e^2/h$ include: Adsorbed atoms and molecules residing on the graphene surface, carbon atom vacancies in the interior of the ribbon, i.e., carbon atoms missing from the honeycomb lattice, disorder in the ribbon boundaries, i.e., deviations from the ideal armchair or zigzag edge geometries, and charged impurities in the substrate.

The influence of different kinds of imperfections on graphene nanoribbon transport and their possible role in the phenomenon observed by Lin et al. [3] will be considered below. It will be seen that quantized conductance steps with heights *much smaller* than $2e^2/h$ can occur in graphene nanoribbons with such defects in a range of temperatures due to enhanced backscattering of electrons by the imperfections whenever the edge of a subband of the ribbon crosses the Fermi level [44, 55]. It will also be seen that if carbon atom vacancies in the interior of the ribbon (we will also refer to these as "bulk vacancies") or certain atoms or molecules chemisorbed on the graphene ribbon are the primary defects responsible for backscattering the electrons then the quantized conductance steps are of equal height [44, 55] as was observed by Lin et al. [3] and Lian et al. [17].

We will focus initially on three disorder types, namely interior vacancies, edge imperfections, and long-range potentials due to charged impurities [44]. Other disorder types such as weak short-range potentials due to neutral impurities [86], and lattice distortions [8, 23], may be present, but the three disorder cases to be discussed here have a stronger impact on transport through nanoribbons and thus are more relevant to the strong conductance suppression reported in [3]. Adsorbates chemisorbed on the graphene ribbons can also have a strong effect on transport but require separate consideration [55] and will be discussed in Sects. 13.9 and 13.10.

13.7 Tight Binding Model of Ribbons with Edge Disorder, Interior Vacancies, and Long-Ranged Potentials

For the purpose of carrying out numerical quantum transport calculations on graphene nanoribbons with dimensions similar to those in current experiments it is necessary to use small sets of basis functions to describe the electronic states. In practice, this means working with tight-binding Hamiltonians such as

$$H = \sum_i \epsilon_i a_i^\dagger a_i - \sum_{\langle i,j \rangle} t_{ij} \left(a_i^\dagger a_j + h.c. \right) \tag{13.8}$$

that provide the simplest description of the π band electrons of graphene and graphene ribbons. Here, $a_i^\dagger$ creates and electron in the $2p_z$ orbital of carbon atom i of the graphene ribbon that is assumed to lie in the $x-y$ plane. ϵ_i is the energy of this atomic orbital. $t_{ij} = t = 2.7$ eV is the Hamiltonian matrix element between the $2p_z$ orbitals of nearest-neighbor carbon atoms i and j on the honeycomb lattice. This Hamiltonian is known to describe the π band dispersion of graphene well at low energies [71, 72, 87]. Interior vacancies and edge disorder are introduced by randomly removing carbon atoms and setting appropriate hopping elements t_{ij} to zero [44]. This model of interior vacancies is a simplified one. However it will be seen below that it is able to account very well [44] for the experimental data of Lin et al [3]. Also, in Sect. 13.10.2 we shall show that it yields ribbon conductances that are in quantitative agreement with those obtained from a sophisticated model of ribbons with adsorbed hydrogen atoms. It will be assumed here that atoms at the edges are always attached to two other carbon atoms and passivated by a neutral chemical ligand, such as hydrogen. In what follows, we shall disregard the effect of modification of the hopping integrals t_{ij} close to the ribbon edges due to any deviations in the atomic spacings at the edges from the bulk graphene geometry. The interior and edge disorder will be characterized by the probability of the relevant carbon atoms being removed, p^b and p^e, respectively. p^b is normalized relative to the whole sample, while p^e is defined relative to an edge only. The long-range potential due to charged impurities will be approximated by a Gaussian form [38,42] of range d: $\epsilon_i = \sum_{r_0} V_0 \exp(-|r_i - r_0|^2/d^2)$, where both the amplitude V_0 and coordinate r_0 are generated randomly.

13.8 Numerical Simulations of Quantum Transport

We will discuss conductances of graphene nanoribbons in the limit of low applied bias calculated [44] at zero and nonzero temperatures within the Landauer formalism described in Sect. 13.1 based on the tight-binding models outlined in the preceding Section.

While there have been many numerical studies of the effects of disorder on transport in graphene ribbons [28, 29, 35, 38, 42, 44–46, 55], we will focus here on identifying and studying mechanisms that can account for the conductance quantization observed by Lin et al. [3] and the specific properties of different defect types that may be relevant. Thus in the calculations [44] that we shall discuss geometries similar to those studied experimentally by Lin et al. [3] were chosen. The disorder was assumed to exist in a finite ribbon of width W and length L. This ribbon was assumed to be attached at its two ends to semi-infinite leads represented by ideal ribbons also of width W. In what follows the edge configuration (before disorder is introduced) will be taken to be of the armchair type. Representative disorder geometries are shown in the insets in Figs. 13.4a–13.6a.

The total electron transmission probability $T(E)$ through the ribbon that enters the Landauer formulae (13.5) and (13.6) was calculated [44] by the recursive Green's function method that is discussed in detail in [34]. Fluctuations of the

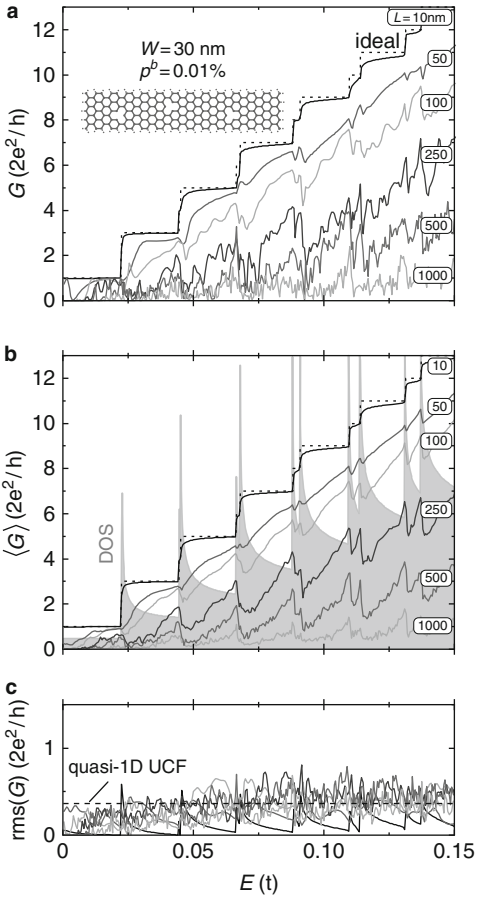

Fig. 13.4 From [44]. Electron transport in ribbons with interior carbon atom vacancies depicted in the inset. (**a**) conductance, (**b**) average conductance and (**c**) conductance fluctuations vs. electron Fermi energy. Ribbon width $W = 30$ nm and lengths $L = 10$ ... 1,000 nm. Vacancy concentration $p^b = 0.01\%$. *Dotted lines* in (**a**),(**b**) show the quantized conductance of the ideal ribbon. The *grey filled* area in (**b**) shows the density of states for the ideal ribbon. The *dashed horizontal line* in (**c**) marks the universal value of the conductance fluctuations for quasi-1D systems [88]. Temperature $T = 0$. $t = 2.7$ eV; $a = 0.142$ nm. The Dirac point is at $E = 0$

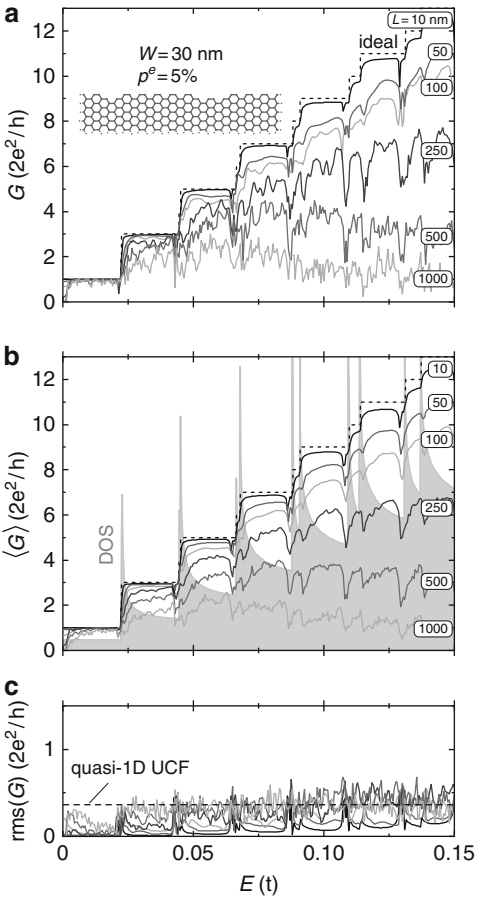

Fig. 13.5 From [44]. Electron transport in ribbons with edge disorder depicted in the inset. Defect concentration $p^e = 5\%$. The Dirac point is at $E = 0$. Notation and other parameters are as in Fig. 13.4

conductance defined by $\mathrm{rms}(G) = (\langle G^2 \rangle - \langle G \rangle^2)^{1/2}$ were also calculated [44]. Here, $\langle\rangle$ denotes averaging over an ensemble of samples with different realizations of disorder. For the results shown here, [44] averaging was carried out over ten realization for each disorder type.

13.8.1 Disorder-Induced Conductance Suppression, Fluctuations and Destruction of the Ballistic Quantized Conductance Plateaus

Figures 13.4–13.6 show the effect of the different kinds of disorder on conduction in the ribbons. For each disorder type, the defect concentration and strength and the ribbon width are kept fixed ($W = 30$ nm) and its length L is varied. The shortest

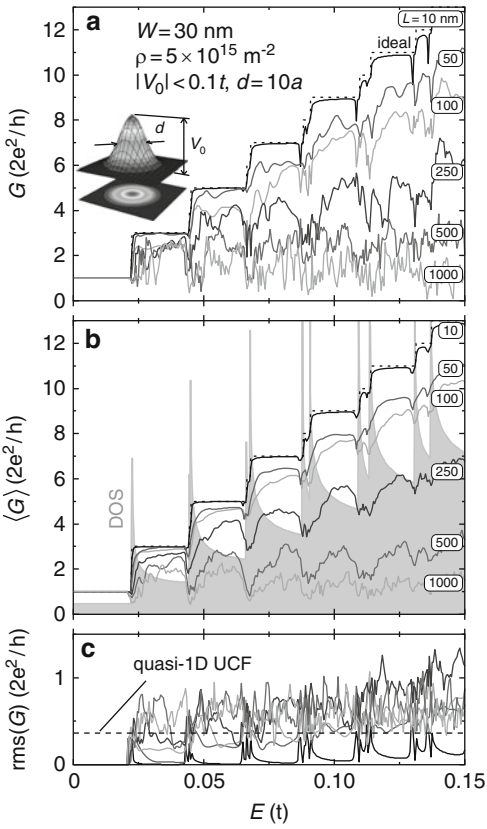

Fig. 13.6 From [44]. Electron transport in ribbons with disorder due to long-range impurity potentials depicted in the inset. Defect density $\rho = 5 \times 10^{15}\mathrm{m}^{-2}$. Potential parameters are indicated in (**a**). The Dirac point is at $E = 0$. Notation and other parameters are as in Fig. 13.4

ribbons are almost ballistic and display quantized ballistic conductance values close to those for ideal ribbons (the dotted lines in Figs. 13.4a,b–13.6a,b). As L increases, the number of scattering centers in the ribbon grows, the conductance decays and quantization steps are destroyed.

For interior vacancy disorder, even a small concentration of the defects affects the conductance strongly; see Fig. 13.4a, b. Apart from reduced conductances, the disorder results in sample-specific conductance fluctuations (see Fig. 13.4c) whose amplitude is of order e^2/h, independent of energy or ribbon length. This is a quantum interference effect similar to the universal conductance fluctuations (UCFs) of mesoscopic metals [88]. The particular value of the conductance depends sensitively on the electron energy, ribbon length and locations of the vacancies. Since the vacancies are distributed over the whole sample, intra-subband scattering predominates. Thus, the conductance in Fig. 13.4a, b (coarse grained in energy to smooth out UCF's) scales down *uniformly* as the ribbon length L increases, i.e., in a similar way for all subbands. This resembles bulk island scattering in conventional quantum wires [89].

By contrast, for edge disorder the conductance scales *non*-uniformly as is seen in Fig. 13.5a, b: Defects at the boundaries scatter electrons equally into all subbands resulting in stronger suppression of the conductance at higher energies E where more subbands are available; see, e.g., the $L = 1{,}000$ nm ribbon in Fig. 13.5a, b.

Potential inhomogeneities due to charged impurities lead to the appearance of electron and hole puddles in graphene nanoribbons [90]. Transmission through the puddles results in subband mixing that smears conductance steps as can be seen in Fig. 13.6a, b. As the subband number increases, intervalley scattering becomes more effective with stronger backscattering of higher subband states in long ribbons. The first subband, however, is not affected by the long-range potential because of internal phase structures of its wave function that make the scattering amplitude vanish [38]. The conductance fluctuations are roughly twice as strong for potential inhomogeneities due to charged impurities (Fig. 13.6c) as for interior vacancies and edge disorder (Figs. 13.4c and 13.5c). This may be due to weaker intervalley scattering for which electrons at the K and K' Dirac points contribute independently to the UCFs [28]. The fluctuation amplitudes agree reasonably well with the value for UCFs in quasi-1D systems [88], $0.729\frac{e^2}{h}$.

13.8.2 Conductance Dips at the Edges of Ribbon Subbands

A prominent effect for each type of disorder is the formation of a conductance dip when the Fermi level crosses a subband edge. This is most obvious in the averaged conductance $\langle G \rangle$, Figs. 13.4b–13.6b. The origin is the strong intersubband scattering caused by defects, where an electron in a state $|nk\rangle$ scatters into another state $|n'k'\rangle$. It can be understood physically by considering the Fermi Golden rule expression for the scattering time τ [79]:

$$\frac{1}{\tau} = \frac{2\pi}{\hbar} \sum_{n'} \left| \langle nk \left| H' \right| n'k' \rangle \right|^2 \rho_{n'}(E) \,. \tag{13.9}$$

Here, H' is the perturbation to the Hamiltonian that is due to defects and $\rho_{n'}(E)$ the density of states of the n'-th subband. Assuming that $|\langle nk\,|H'|\,n'k'\rangle|^2$ is independent of the band index n', the scattering rate $1/\tau$ in (13.9) is proportional to the total density of states of the ribbon, $\rho(E) = \sum_{n'} \rho_{n'}(E)$, i.e., to the density of final states available for the scattering process. For a perfect ribbon, the dispersion relation can be approximated by a parabolic function if k is small and $|n| > 1$ [33]. Therefore, $\rho(E)$ diverges at subband thresholds $E_{n'}$ as $(E - E_{n'})^{-1/2}$. This agrees with the numerically calculated density of states for the tight-binding Hamiltonian (13.8); see the grey areas in Figs. 13.4b–13.6b. Thus, the scattering time τ is strongly reduced when the Fermi energy crosses a subband threshold $E_{n'}$ and the transmission of electrons in the n-th subband is strongly suppressed due the

back-scattering of electrons into the n' subband. As a result, the conductance shows dips at the subband edges.

13.8.3 The Role of Temperature

In the finite temperature Landauer formula (13.6), the electron transmission probability $T(E)$ (that according to (13.5) is proportional to the zero temperature conductance) is convoluted with the energy derivative $\frac{\partial f(E)}{\partial E}$ of the Fermi function. $|\frac{\partial f(E)}{\partial E}|$ is strongly peaked around the electron chemical potential with a peak width proportional to the temperature. Thus as the temperature T increases, features in plots of the zero temperature conductance vs. the electron Fermi energy whose spacing is much smaller than $4\pi k_B T$ become smeared out.

Thus, as can be seen in Fig. 13.7, the conductance fluctuations that are very prominent at zero temperature have been completely smeared out thermally at temperatures ~80 K. The dips in the conductance associated with enhanced electron back scattering when the Fermi level crosses subband edges also broaden but remain very prominent in the conductance profile up to temperatures T not greatly exceeding the subband energy separation, i.e., for $4\pi k_B T \approx \Delta E = E_{n+1} - E_n$. For graphene ribbons 30 nm wide $\Delta E \approx 0.02t = 54$ meV (see Fig. 13.4a, b) which corresponds to $T \approx \frac{\Delta E}{4\pi k_B} = 50$ K. Above this temperature, the conductance dips are gradually smeared out, but well below it the conductance may be dominated by UCF's of the disordered ribbon. This estimate is in good agreement with the calculations presented in Fig. 13.7, where ribbons with different disorder types are

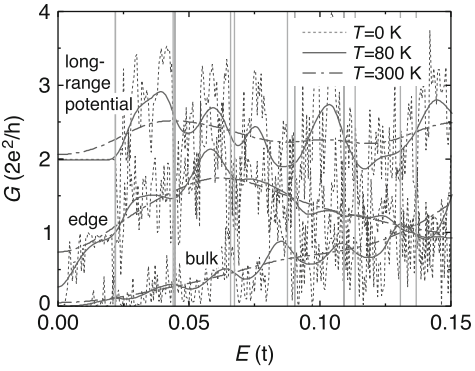

Fig. 13.7 From [44]. Conductances of disordered ribbons with interior (bulk) carbon atom vacancies, edge disorder, and long-range potential disorder vs. the electron Fermi energy for temperatures $T = 0, 80, 300$ K. The ribbons have width $W = 30$ nm and length $L = 1{,}000$ nm. The parameters of the disorder are listed in Figs. 13.4–13.6. The Dirac point is at $E = 0$. The *thin solid vertical lines* mark the energies at which the number of subbands changes by one. For the sake of clarity, the curves for the long-range potential are shifted upward by $2e^2/h$

subjected to temperatures $T = 0$ K, 80 K and 300 K: The conductance dips at subband edges manifest as the smooth conductance oscillations that are clearly visible for $T = 80$ K. They are very regular and are superimposed on a smoothly rising background for the case of the interior (bulk) vacancies, but become very distorted when edge disorder or long-range potentials are the dominant scatterers, except for the first two or three oscillations in the case of the edge disorder. As will be seen in Sect. 13.8.5 for appropriate defect concentrations and temperatures, this phenomenon manifests as quantized conductance steps of equal height in quantitative agreement with those observed by Lin et al. [3].

13.8.4 From Ballistic Transport to Anderson Localization

It was first pointed out by Anderson [91] that the presence of disorder can result in electronic states of conductors becoming spatially localized. Because of this, if random defects are introduced even at low concentrations into a quasi-one dimensional conductor of infinite length the system becomes an insulator at zero temperature. For quasi-one dimensional systems of finite length an important quantity characterizing the disorder is the localization length λ that is a measure of the typical spatial extent of the electronic wave functions in an infinite system with the same concentration of disorder.

The nature of the transport regime in a particular system is controlled largely by the relationship between the localization length λ and the length L of the quasi-one-dimensional system: If $\lambda \gtrsim L$, the regime is quasi-ballistic. If $\lambda \ll L$ the system is in the strong localization regime. The latter is also referred to as the hopping regime and can be characterized by two properties: Firstly, the decrease of the average zero temperature conductance with increasing L is exponential and mainly determined by λ and, secondly, the conductance depends exponentially on the temperature. An intermediate regime of diffusive transport was studied in [92, 93] for the ribbons with long-range scattering potentials. Ribbons with this kind of disorder were found to undergo a transition from ballistic to diffusive transport when the ribbon length or disorder strength increases. The diffusive transport was characterized by a $\sigma \sim E^2$ power law dependence of the conductivity σ on the energy E and by the mobility μ being independent of the electron density n [92]. The conductivity follows universal scaling curves as the density varies and depends solely on the disorder strength and the ratio of sample length to disorder correlation length [93]. In contrast, the ballistic transport regime follows $\sigma \sim E$ and $\mu \sim n^{0.5}$ dependences [92]. These different dependences may be relevant when experimental data are analyzed and interpreted.

Electron localization due to different kinds of disorder in graphene ribbons has been discussed in [35, 42, 44, 53, 59], among others. In Fig. 13.8, we present numerical results for the average conductances of graphene ribbons as a function of ribbon length L for different cases of disorder. The energies are chosen at the third and seventh plateaus, $E \sim 0.34t$ and $E \sim 0.78t$, respectively, see Fig. 13.4a, b. The value for the localization length can be estimated from Fig. 13.8, where $\langle G \rangle$ is fitted

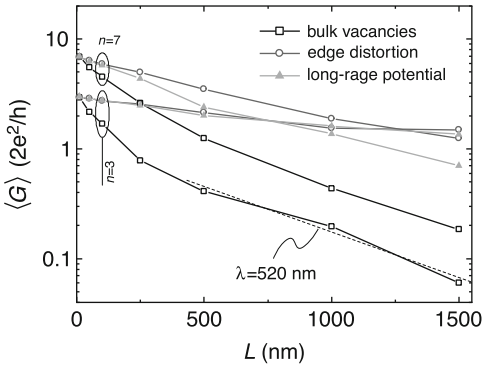

Fig. 13.8 Average conductance as a function of ribbon length calculated for different types of disorder. Averaging is performed over different realizations of disorder and Fermi energies at third ($n = 3$) and seventh ($n = 7$) conductance plateau, see Figs. 13.4–13.6. The values of the parameters characterizing the disorder are as in Figs. 13.4–13.6. The localization length λ is determined by the slope of the $\langle G \rangle = \langle G(L) \rangle$ plot in accordance with (13.10)

Table 13.1 Localization length λ for disordered graphene ribbons with concentrations p^b, p^e, and ρ of interior (bulk) carbon atom vacancies, edge disorder and defects with long ranged potentials, respectively

	λ (nm)	
	$n = 3$ ($E \sim 0.34t$)	$n = 7$ ($E \sim 0.78t$)
$p^b = 10^{-4}$	520	523
$p^b = 4 \times 10^{-4}$	190	481
$p^b = 8 \times 10^{-4}$	96	418
$p^e = 0.05$	2,109	1,428
$p^e = 1$	105	752
$p^e = 2$	91	623
$\rho = 5 \times 10^{15}$ m^{-2}, $\lvert V_0 \rvert \leq 0.1t$, $d = 10a$	2,500	1,782
$\rho = 10^{16}$ m^{-2}, $\lvert V_0 \rvert \leq 0.1t$, $d = 10a$	1,354	854
$\rho = 5 \times 10^{15}$ m^{-2}, $\lvert V_0 \rvert \leq 0.2t$, $d = 10a$	661	585
$\rho = 5 \times 10^{15}$ m^{-2}, $\lvert V_0 \rvert \leq 0.1t$, $d = 20a$	1,535	1,116

See the insets in Fig. 13.8a–c. The electron energies are those at which the ribbons with *no* disorder exhibit the $n = 3$ and 7 conductance plateaus in Fig. 13.4

with a straight line and λ is determined from its slope [42],

$$\frac{1}{\lambda} = -\frac{\partial \ln \langle G \rangle}{\partial L} \tag{13.10}$$

for ribbons of length $L \gg \lambda$. Exponential decay signals that transport is governed by the Anderson localization. Strong scattering by disorder can result in severe quantum interference that completely halts the electron waves inside the random medium. As the disorder concentration increases, the localization length λ decreases, see Table 13.1. It drops especially strongly for low energies, and

$\lambda \ll L$ for the highest concentrations of carbon atom vacancies or edge disorder in the ribbon. However, for all other cases in Table 13.1 the disordered ribbons are not in the strong localization regimes. The disorder concentrations that result in conductances similar to those of the experimental samples of Lin et al. [3] are relatively small and their samples, therefore, were not in the strong localization regime. That is, the localization lengths were merely comparable to the ribbon lengths, $\lambda \sim L$, in their experiment [3]. This conclusion is also supported by the temperature dependence of their measured conductances which was clearly not in an exponential regime [3]. Thermally activated transport including variable range hopping has, however, been reported experimentally in other graphene nanoribbons [12, 14].

13.8.5 The Quantized Conductance in Disordered Ribbons: Theory vs. Experiment

The conductances of the graphene ribbons measured by Lin et al. [3] were 65–260 times smaller than the conductance quantum and also much smaller than the conductances of the model systems studied above in Figs. 13.4–13.7. However, the ideas developed above apply equally well to the lower conductance regime in which the experiments were carried out and are able to account quantitatively for the conductance quantization that Lin et al. [3] observed. We demonstrate this next [44] by presenting simulations for ribbons with the same sizes as in the experiments [3] and with defect concentrations chosen to yield low conductances similar to those measured by Lin et al. [3].

Figure 13.9 shows the calculated conductances $\langle G \rangle$ of the disordered ribbons together with the experimental results from [3]. The features in the theoretical plots that match the experimental conductance plateaus are the conductance dips that are due to enhanced electron back scattering at the energies of the subband edges of the nanoribbon that we have already discussed in Sects. 13.8.2 and 13.8.3 in connection with Figs. 13.4–13.7. The agreement between theory and experiment is remarkable, especially for the heights of the conductance plateaus. Based on these results, it is clear that the conductance quantization observed by Lin et al. [3] can be accounted for very well if the dominant scattering mechanism in their ribbons is due either to interior carbon atom vacancies alone or to a combination of rough edges with a lower concentration of interior vacancies. The presence of the latter is crucial because they equalize the differences between the conductances of the different plateaus making them equidistant. In particular, we found [44] that $p^b = 4 \times 10^{-4}$ interior vacancies are enough to reduce the conductances of the quantized plateaus by a factor of 65 relative to the conductance quantum $\frac{2e^2}{h}$, in accord with the experiment [3]; see the solid line in Fig. 13.9a. This means that one in 2,500 carbon atoms has been removed, which seems possible. The other scenario consists of distorted edges with two rows of carbon atoms removed on average along

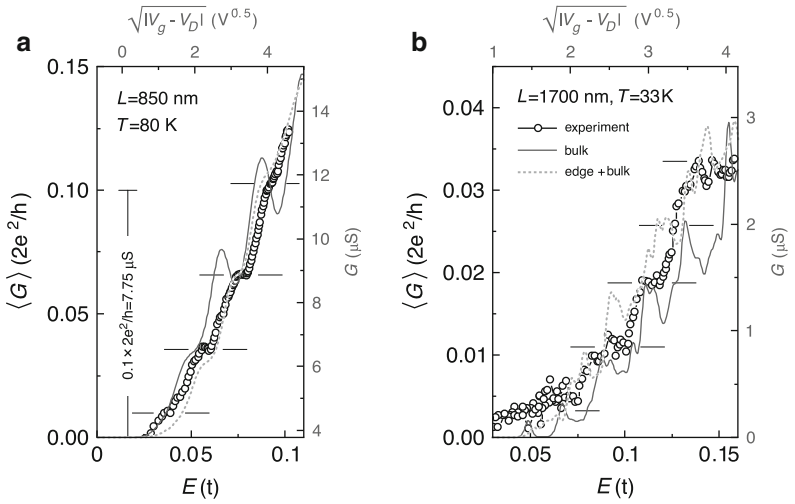

Fig. 13.9 From [44]. Comparison of theoretical and experimental data for ribbons of width $W = 30$ nm and length $L = 850$, and 1,700 nm. The experimental data is from [3]. Theoretical calculations are performed for two disorder cases: (**a**) Only interior (bulk) vacancies with $p^b = 4 \times 10^{-4}$ (*solid curve*), and a combination of edge disorder $p^e = 2$ and interior vacancies $p^b = 10^{-4}$ (*dotted curve*); (**b**) $p^b = 8 \times 10^{-4}$, and combination of $p^e = 3.5$ and $p^b = 2 \times 10^{-4}$. E is the electron Fermi energy measured from the Dirac point where $E = 0$. The gate voltage V_g is scaled to produce better fit; note that $E \sim \sqrt{V_g - V_D}$ where V_D is the gate voltage at which the Fermi level crosses the Dirac point, as is discussed in [94]

the boundaries and also one in 10,000 interior carbon atoms removed, $p^e = 2$ and $p^b = 10^{-4}$, see the dotted line in Fig. 13.9a. For the longer $L = 1,700$ nm ribbon, the height of conductance steps drops to a factor 260 lower than the conductance quantum, Fig. 13.9b. This implies defect concentrations twice those of the shorter $L = 850$ nm experimental ribbon. The lower temperature in Fig. 13.9b results in stronger conductance fluctuations than in Fig. 13.9a; the fourth plateau being not discernible in the experimental data [3] in Fig. 13.9b may also be due in part to a particular disorder configuration. However, all visible conductance plateaus are due to subband formation associated with particle motion quantized in the transverse direction. At much lower temperatures in our simulations these conductance plateaus are not discernible due to UCF's and they also disappear completely at room temperature, behavior similar to that in Fig. 13.7, and completely consistent with the data of Lin et al. [3].

Another interesting aspect of the conductance quantization in disordered ribbons was observed by Lin et al. [3] in the *nonlinear* transport regime: With increasing bias voltage applied between the source and drain electrodes, the quantized conductance plateaus were found by Lin et al. [3] to shift upward for both electron and hole conduction. It was suggested [3] that this effect was due to the increase with increasing bias of the number of subbands that are present in the energy window between the source and drain electrochemical potentials and therefore contribute to

transport. By contrast, recent quantum transport simulations [56] showed that in *ballistic* ribbons increasing the source-drain bias results in narrowing of the quantized conductance plateaus and a corresponding broadening of the transitions between them, and not increasing quantized conductance values. However, the simulations also showed [56] increasing quantized conductance values with increasing source-drain bias (similar to the nonlinear transport phenomenon reported by Lin et al. [3]) in *disordered* ribbons provided that the electrostatic potential in the ribbon is pinned to that of the (electron) drain for electron transport and to the source for hole transport in the ribbon. Consistent with this finding, calculations of potential profiles in gated ribbons under source-drain bias have indeed shown [57, 58] that the potentials in such ribbons can be nearly flat except near the ends and it has been suggested [56] that most of the potential drop along the ribbons of Lin et al. [3] may occur near the end of the ribbon at which the carriers enter due to the strong disorder-induced electron backscattering in those ribbons.

13.9 Adsorbates on Graphene and Dirac Point Resonances

In the preceding Section, we have demonstrated [44,56] that it is possible to account quantitatively for the conductance quantization phenomena observed by Lin et al. [3] in disordered graphene ribbons if it is assumed that carbon atom vacancies are present in the interior of the ribbons and are responsible for much of the electron scattering in these systems, even when other defects such as edge disorder contribute significantly to electron scattering in the ribbons as well. However, whether carbon atom vacancies were actually present in the samples of Lin et al. [3] in the required concentrations was not determined experimentally [3]. On the other hand, many chemical species are known to adsorb readily to graphene [55, 59, 62, 63, 95–101] (see Chap. 4) and it is reasonable to expect atomic and molecular species to be adsorbed on ribbons prepared using presently available fabrication techniques. For example, adsorbed H, F, and O atoms and OH molecules may have been present on the ribbons of Lin et al. [3] that were made by oxygen plasma reactive ion etching using a hydrogen silsesquioxane etch mask that was later removed in a

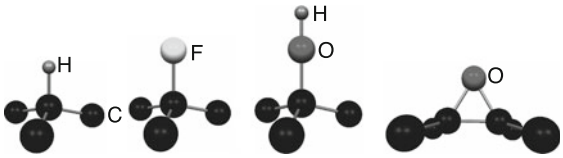

Fig. 13.10 Relaxed geometries of H, F, OH, and O on graphene. The H, F, and OH bond over a single carbon atom of the graphene [108]. The O bonds over a bridge site between two carbon atoms. The carbon atoms to which the H, F, OH, and O bond are pulled out of the graphene plane by the adsorbed moiety by 0.35, 0.36, 0.41, and 0.27Å. This is associated with partial rehybridization of the graphene occurring locally from sp^2 to sp^3 bonding. Adapted from [55]

hydrofluoric acid solution. These adsorbed species bond covalently to graphene and strongly affect its electronic structure: As is shown in Fig. 13.10, the graphene carbon atoms to which the atoms or molecules bond move out of the graphene plane toward the adsorbed moiety by substantial fractions of an Angstrom and thus partial rehybridization of the graphene electronic structure occurs locally from the sp^2 bonding of the planar graphene to the sp^3 bonding characteristic of carbon atoms in tetrahedral geometries. As a result, it is reasonable to expect these adsorbed species to strongly scatter electrons in graphene ribbons.

The scattering of the electrons in graphene by covalently bonded adsorbates and other impurities and defects that couple *strongly* to the graphene has been predicted theoretically [55, 101–107] to have an unusual property: Instead of scattering resonances occurring near the energies of atomic or molecular orbitals of the adsorbate or impurity as would be the case for a *weakly* couple adsorbate, the strongly coupled moieties gives rise to strong scattering resonances at energies close to the Dirac point energy of graphene. We will describe a theoretical methodology [55] for studying these "Dirac point resonances" in Sects. 13.9.1–13.9.3. Then we will discuss their properties [55] for adsorbates on infinite two-dimensional graphene in Sect. 13.9.4 and their role in electron transport in graphene ribbons with adsorbed H, F, and O atoms and OH molecules [55] in Sect. 13.10.

In our discussion of the Dirac point scattering resonances due to adsorbates on graphene, we will adopt an approach [55] based on a tight-binding Hamiltonian H_a that is a generalization of the Hamiltonian H given by (13.8) since such tight binding models are suitable for transport calculations on ribbons that have dimensions similar to those being studied experimentally at the present time and therefore contain large numbers of carbon atoms.

13.9.1 Tight Binding Hamiltonian for Adsorbates on Graphene

The tight binding Hamiltonian H_a that we consider has the form [55]

$$H_a = H_0 + \sum_{\alpha} \epsilon_\alpha d_\alpha^\dagger d_\alpha + \sum_{\alpha,j} \gamma_{\alpha j} \left(d_\alpha^\dagger a_j + h.c. \right), \tag{13.11}$$

where

$$H_0 = -\sum_{\langle i,j \rangle} t_{ij} \left(a_i^\dagger a_j + h.c. \right) \tag{13.12}$$

describes the graphene π band electrons as in (13.8) with the energy scale chosen so that the energy of the $2p_z$ orbitals of the graphene carbon atoms (ϵ_i in (13.8)) is set to zero. a_j is the destruction operator for an electron in the $2p_z$ orbital ϕ_j of carbon atom j. $d_\alpha^\dagger$ is the creation operator for an electron in an extended molecular orbital (EMO) ψ_α that is associated with an adsorbed atom or molecule and ϵ_α is the energy of that orbital. We define [55] an EMO associated with an adsorbed atom

or molecule as a linear combination of the valence orbitals of the adsorbed moiety and of certain valence orbitals of the graphene carbon atom(s) to which that moiety bonds and of nearby graphene carbon atoms. The carbon valence orbitals included in the EMOs are those *other* than the $2p_z$ orbitals of the graphene π band that are already included in the theory through the term H_0 in (13.11).

Inclusion of the graphene carbon orbitals other than the $2p_z$ orbitals (i.e., the carbon $2s$, $2p_x$, and $2p_y$ orbitals of the carbon atom(s) to which the adsorbed atom or molecule bonds and of its nearest carbon atom neighbors) in the theory in this way turns out to be important as these orbitals take part in the rehybridization of the graphene from sp^2 to sp^3 bonding induced by the adsorbate that strongly affects the electronic structure of the system and its transport properties.

The last term on the right in (13.11) describes the coupling between the graphene π band and the EMOs associated with the adsorbate. We estimate the relaxed geometry of the graphene and adsorbate from first principles using density functional theory-based calculations [109] and then use the semi-empirical extended Hückel electronic structure model [69], the version of extended Hückel theory that we use here is that of [110], to estimate the values of the tight-binding parameters ϵ_α and $\gamma_{\alpha j}$ that enter the model Hamiltonian (13.11) as will be explained next.

Extended Hückel theory (see also Chaps. 17 and 18) is formulated in terms of small basis sets of Slater-type atomic orbitals $\{|\phi_i\rangle\}$, their overlaps $S_{ij} = \langle\phi_i|\phi_j\rangle$, and a Hamiltonian matrix $\mathcal{H}_{ij} = \langle\phi_i|\mathcal{H}|\phi_j\rangle$. The diagonal Hamiltonian elements $\mathcal{H}_{ii} = \mathcal{E}_i$ are the experimentally determined atomic orbital ionization energies $\mathcal{E}_i$. We approximate the nondiagonal Hamiltonian matrix elements by $\mathcal{H}_{ij} = (1.75 + \Delta_{ij}^2 - 0.75\Delta_{ij}^4)S_{ij}\left(\mathcal{E}_i + \mathcal{E}_j\right)/2$, where $\Delta_{ij} = (\mathcal{E}_i - \mathcal{E}_j)/(\mathcal{E}_i + \mathcal{E}_j)$, a form chosen by Ammeter et al. [110] for consistency with experimental molecular electronic structure data.

In recent years, transport calculations based on electronic structures derived from extended Hückel theory have yielded elastic tunneling conductances [111–114] as well as inelastic tunneling spectra [115] in agreement with experiment for molecules bonded to metal electrodes and have accounted for transport phenomena observed in molecular arrays on silicon [116, 117, 128] as well as electroluminescence data [118], current-voltage characteristics [118] and STM images [119] of molecules on complex substrates.

In the version of extended Hückel theory that we use here [110], the carbon $2p_z$ orbital energy is the ionization energy $\mathcal{E}_{C_{p_z}} = -11.4$ eV. Accordingly, for consistency with (13.12) where the carbon $2p_z$ orbital energy is chosen to be zero, we make the replacement $\mathcal{H}_{ij} \rightarrow \mathcal{H}_{ij} - S_{ij}\mathcal{E}_{C_{p_z}}$ in the extended Hückel Hamiltonian matrix, adjusting the nondiagonal as well as the diagonal Hamiltonian matrix elements as is discussed in [120].

Now let $\mathcal{H}_{ij}^{\mathrm{R}}$ and S_{ij}^{R} be the extended Hückel Hamiltonian and overlap matrices defined as above but restricted to the Hilbert subspace R spanned by the valence orbitals of the adsorbate and valence orbitals of the graphene included in the EMOs associated with the adsorbed atom or molecule. $\mathcal{H}_{ij}^{\mathrm{R}}$ and S_{ij}^{R} are calculated [55] for the relaxed geometries shown in Fig. 13.10. Then the extended Hückel Schrödinger equation $\mathcal{H}^{\mathrm{R}}\psi_\alpha = \epsilon_\alpha S^{\mathrm{R}}\psi_\alpha$ is solved for the energy eigenvalues ϵ_α of the EMOs

that enter (13.11) and for the corresponding eigenvectors ψ_α. Finally, the matrix elements $\gamma_{\alpha j} = \langle \psi_\alpha | \mathcal{H} | \phi_j \rangle$ of the extended Hückel Hamiltonian between the $2p_z$ orbital ϕ_j of carbon atom j and EMO ψ_α are calculated.

13.9.2 Effective Hamiltonian for Adsorbates on Graphene

In the simplest possible model of an adsorbate represented by just one atomic orbital α that couples only to the $2p_z$ orbital of only one carbon atom j of the graphene, the tight-binding Hamiltonian of the graphene and adsorbate is $H_1 = H_0 + \epsilon_\alpha d_\alpha^\dagger d_\alpha + \gamma_{\alpha j} \left(d_\alpha^\dagger a_j + h.c. \right)$ where the notation is as in (13.11). The eigenstate $|\Psi\rangle$ of H_1 with energy eigenvalue ϵ can be written as $|\Psi\rangle = |\Psi_g\rangle + |\Psi_a\rangle$ where $|\Psi_g\rangle$ and $|\Psi_a\rangle$ are the projections of $|\Psi\rangle$ onto the space spanned by the $2p_z$ orbitals of graphene and onto the orbital of adsorbed atom, respectively. With these definitions, it has been shown [105] that $|\Psi_g\rangle$ is an exact eigenstate of an effective Hamiltonian $H_{\text{eff}} = H_0 + V_j a_j^\dagger a_j$ with the same energy eigenvalue ϵ as $|\Psi\rangle$. Here, $V_j = \gamma_{\alpha j}^2 / (\epsilon - \epsilon_\alpha)$. Thus for the purpose of calculating the transport coefficients of graphene with such an adsorbed atom, the Hamiltonian H_1 can be replaced with H_{eff}, i.e., the Hamiltonian of graphene without the adsorbed atom but with an energy dependent potential $\gamma_{\alpha j}^2 / (\epsilon - \epsilon_\alpha)$ on carbon atom j of the graphene sheet.

We have generalized this argument to the case of an adsorbed atom or molecule with more than one EMO and/or bonding to more than one graphene atom [55]. The result is an effective Hamiltonian

$$H_{\text{eff}} = H_0 + \sum_{i,j} V_{ij} a_i^\dagger a_j \tag{13.13}$$

with

$$V_{ij} = \sum_\alpha \gamma_{\alpha i} \gamma_{\alpha j}^* / (\epsilon - \epsilon_\alpha) \tag{13.14}$$

where i and j label the graphene carbon atoms to which the adsorbate bonds and α labels the EMOs associated with the adsorbate that are described in Sect. 13.9.1. With this generalization, the effective Hamiltonian applies to the H, F, OH, and O adsorbates that we consider and to many others. The generalization is required even for the case of H which has only one valence orbital since in order to properly treat the very important effects of the rehybridization of the graphene from sp^2 to sp^3 bonding induced by the adsorption of a H atom, it is necessary to include several graphene carbon atom valence orbitals as well as the H valence orbital in the EMOs of this system.

13.9.3 The T-matrix Formalism

The T-matrix formalism of scattering theory (not to be confused with the transmission probability matrix $T_{ij}(E)$ of the Landauer transport formalism discussed in Sect. 13.1) has yielded valuable insights into the resonant scattering of electrons in graphene by impurities and adsorbates [55, 102, 104, 105, 107]. As will be seen below, it can also be very helpful in both facilitating numerical studies of electron transport in graphene ribbons and in interpreting the results [55]. The T-matrix is defined [121] by

$$G = G^0 + G^0 T G^0 \tag{13.15}$$

where $G = (\epsilon + i\eta - H_{\text{eff}})^{-1}$ is the full Green's function based on the effective Hamiltonians H_{eff} discussed in Sect. 13.9.2 for a single adsorbed atom or molecule and $G^0 = (\epsilon + i\eta - H_0)^{-1}$ is the unperturbed Green's function for π band electrons in clean graphene with H_0 given by (13.12). T characterizes the strength of the scattering of electrons at energy ϵ due to the presence of the adsorbate. It can be written in the standard form [121]

$$T = \mathcal{V} + \mathcal{V}G^0\mathcal{V} + \mathcal{V}G^0\mathcal{V}G^0\mathcal{V} + \cdots \tag{13.16}$$

where, according to (13.13) and (13.14), $\mathcal{V} = a_j^\dagger a_j \sum_\alpha |\gamma_{\alpha j}|^2/(\epsilon - \epsilon_\alpha)$ for a H, F, OH atom or molecule with EMOs α bound to carbon atom j. For an O atom with EMOs α bound to two neighboring graphene C atoms 1 and 2, $\mathcal{V} = V_{11}a_1^\dagger a_1 + V_{22}a_2^\dagger a_2 + V_{12}a_1^\dagger a_2 + V_{21}a_2^\dagger a_1$ where $V_{nm} = \sum_\alpha \gamma_{\alpha n}\gamma_{\alpha m}^*/(\epsilon - \epsilon_\alpha)$.

Taking matrix elements of (13.16) between the graphene $2p_z$ orbitals of the carbon atom(s) to which the adsorbed atom or molecule binds and summing the resulting series yields

$$\tilde{T} = \left(1 - \tilde{\mathcal{V}}\tilde{G}^0\right)^{-1}\tilde{\mathcal{V}} \tag{13.17}$$

where for the O atom adsorbate $\tilde{T}$, $\tilde{\mathcal{V}}$, $\tilde{G}^0$, and 1 are the 2×2 matrices $\langle m|T|n\rangle$, $\langle m|\mathcal{V}|n\rangle$, $\langle m|G^0|n\rangle$, and δ_{mn} with $|m\rangle$ and $|n\rangle$ being the $2p_z$ orbitals of the carbon atoms m and n to which the O atom bonds. Here, $m = 1, 2$ and $n = 1, 2$. For H, F, and OH that bond to one C atom (labeled 1) $\tilde{T}$, $\tilde{\mathcal{V}}$, $\tilde{G}^0$ and 1 are the scalars $\langle 1|T|1\rangle$, $\langle 1|\mathcal{V}|1\rangle$, $\langle 1|G^0|1\rangle$, and 1 respectively.

Approximate analytic expressions for $\langle 1|G^0|1\rangle$ have been presented in [102, 122–125] and refined and also extended to $\langle 2|G^0|1\rangle$ (which is required for the case of O adsorbed on graphene) in [55], the resulting expression being

$$\langle 1|G^0(\epsilon)|1\rangle = \frac{\epsilon\alpha(\epsilon)}{\sqrt{3}\pi t^2}\ln\left(\frac{\epsilon^2}{\sqrt{3}\pi t^2 - \epsilon^2}\right) - i\frac{|\epsilon|\beta(\epsilon)}{\sqrt{3}t^2} \tag{13.18}$$

where $\alpha(\epsilon) = 1.07(1 + 0.66\epsilon^2/t^2)$ and $\beta(\epsilon) = 1 + 0.31\epsilon^2/t^2 + 0.33\epsilon^4/t^4$. Comparison of (13.18) with the results of an exact numerical calculation showed it to be accurate in the range $|\epsilon|/t \leq 0.8$ [55]. Here, $t = 2.7$ eV is the modulus of

the Hamiltonian matrix element between the $2p_z$ orbitals of nearest-neighbor carbon atoms i and j of the pristine graphene lattice. $\langle 2|G^0|1\rangle$ can be obtained from (13.18) using the identity [55]

$$\langle 2|G^0(\epsilon)|1\rangle \equiv \frac{1}{3t} - \frac{\epsilon}{3t}\langle 1|G^0(\epsilon)|1\rangle \tag{13.19}$$

13.9.4 Dirac Point Scattering Resonances due to H, F, and O Atoms and OH Molecules Adsorbed on Graphene

Estimating the values of the tight-binding parameters ϵ_α and $\gamma_{\alpha j}$ for the EMOs associated with a particular adsorbed atom or molecule as is described in Sect. 13.9.1, and using the analytic expressions (13.18) and (13.19) for the required Green's function matrix elements we have evaluated the matrix elements of the T-matrix given by (13.17) as a function of the electron energy for a H, F, and O atom and OH molecule adsorbed on graphene in the geometries shown in Fig. 13.10 [55]. The square moduli of the matrix elements of the T-matrix calculated in this way are shown vs. the electron energy ϵ in Fig. 13.11. The effects of the adsorbate-induced rehybridization of the graphene from sp^2 to sp^3 bonding are included since the EMOs in this calculation are linear combinations of the atomic valence orbitals of the adsorbed species and the $2s$, $2p_x$, and $2p_y$ valence orbitals of each of the carbon atoms shown in Fig. 13.11 for the respective adsorbed species.[3]

The strength of scattering associated with a defect is in general proportional to the square modulus of appropriate matrix elements of the T-matrix [121]. Thus, the energies ϵ at which resonant scattering by H, F, OH and O adsorbates should occur are those at which $|\langle m|T|n\rangle|^2$ have maxima. As can be seen in Fig. 13.11, strong scattering resonances are predicted to occur in the vicinity of the Dirac point energy $\epsilon = 0$ for all four adsorbed species. The electron energy $\epsilon_{\rm DR}$ at which the resonance is centered depends on the adsorbed species. $\epsilon_{\rm DR} = -0.136t, -0.089t, -0.0026t$ for F, OH, and H, respectively. For O, there is a narrow peak near $0.112t$ that overlaps a broader peak centered near $0.090t$. In addition to these Dirac point resonance for O there is an antiresonance (i.e., deep minimum in the scattering strength) near $0.55t$.

By far the strongest resonance (and the closest one to the Dirac point) is found for hydrogen. As will be seen in Sect. 13.10.2, electron scattering associated with this resonance is so strong that in electron transport in nanoribbons the adsorbed H atom scatters electrons in a way almost identical to a carbon atom vacancy, i.e., as if the carbon atom to which the H atom binds is missing entirely from the graphene

[3] In general the EMOs ψ_α are not orthogonal to the $2p_z$ orbitals ϕ_j of carbon atom(s) to which the adsorbate bonds. We allow for this in our T-matrix calculations [55] by making the substitution $\gamma_{\alpha j} \rightarrow \gamma_{\alpha j} - \epsilon\sigma_{\alpha j}$ where $\sigma_{\alpha j} = \langle \psi_\alpha | \phi_j \rangle$ as is discussed in [126, 127].

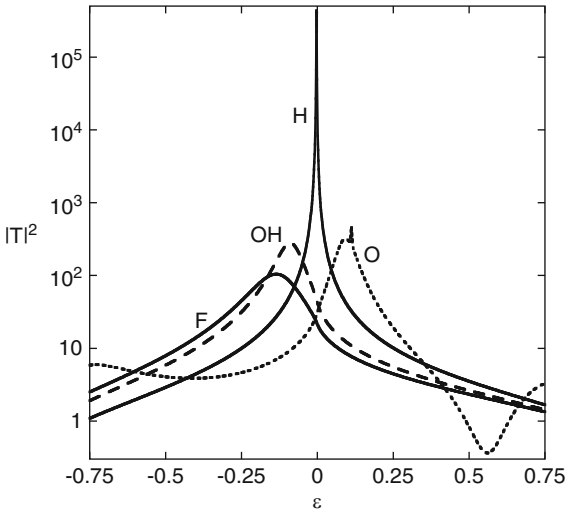

Fig. 13.11 Calculated square modulus of the T-matrix vs. electron energy ϵ for an H, F or O atom or OH group adsorbed on graphene. T and ϵ are in units of $t = 2.7\,\text{eV}$. The *solid curves* are for H and F, OH is *dashed*, O is *dotted*. The Dirac point of graphene is at $\epsilon = 0$. For H, F and OH, $T = \langle 1|T|1\rangle$. For O the square of the Frobenius norm of the matrix $\langle m|T|n\rangle$ is plotted. The effects of the adsorbate-induced rehybridization of the graphene from sp^2 to sp^3 bonding are included in the model. Adapted from [55]

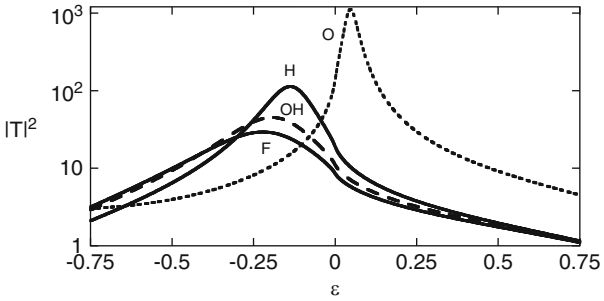

Fig. 13.12 Calculated square modulus of the T-matrix vs. electron energy ϵ for an H, F or O atom or OH group adsorbed on graphene, *omitting* the effects of the adsorbate-induced rehybridization of the graphene from sp^2 to sp^3 bonding from the model. The Dirac point is at $\epsilon = 0$. Notation as in Fig. 13.11. Adapted from [55]

lattice. The Dirac point resonances associated with the F, OH, and O adsorbates are not as strong but, as will be seen below, never the less have a strong effect in electron transport in graphene ribbons with those adsorbates.

In order to elucidate the role of the adsorbate-induced rehybridization of the graphene from sp^2 to sp^3 bonding in the Dirac point scattering resonances we show in Fig. 13.12 the results of a similar calculation to that for Fig. 13.11 but *omitting* the carbon $2s$, $2p_x$, and $2p_y$ valence orbitals from the EMOs so that the effects of the sp^2 to sp^3 rehybridization are omitted from the model used in Fig. 13.12. In Fig. 13.12, the scattering resonances associated with the adsorbates are centered at $-0.222t$, $-0.194t$, $-0.138t$, and $0.046t$ for F, OH, H, and O, respectively. Clearly the sp^2 to sp^3 rehybridization is directly responsible for the H Dirac point resonance being orders of magnitude stronger than the resonances of F, OH, and O in Fig. 13.11

since there is no such striking difference between the H resonance and the others in Fig. 13.12. The strengths of the resonances for the other adsorbates are not affected as drastically by the rehybridization although there are large quantitative differences in both the heights and positions of their peaks between Figs. 13.11 and 13.12. In the case of O, there are qualitative differences as well: There are two overlapping resonant peaks near the Dirac point in Fig. 13.11 where rehybridization is included but only one peak in Fig. 13.12 where it is not. The antiresonance at $0.55t$ in Fig. 13.11 is also absent in Fig. 13.12. As will be seen in Sect. 13.10.2, this scattering antiresonance that occurs due to the rehybridization is associated with a strong peak in the conductances of graphene nanoribbons that should be observable in transport experiments.

Interestingly, the Dirac point resonances for O occur at energies above the Dirac point in both models while those for H, F and OH occur below the Dirac point. This difference is related to the fact that O bonds to two carbon atoms while H, F, and OH bond only to one, although in general the signs of the energies at which the resonances occur are influenced not only by the number of C atoms to which the adsorbed species bonds but also by the values of the tight binding parameters ϵ_α and $\gamma_{\alpha j}$.

13.10 Electron Quantum Transport in Graphene Ribbons with Adsorbates

Recursive Green's function-based quantum transport calculations [34] similar to those presented in Sect. 13.8 for graphene ribbons with carbon atom vacancies, edge disorder, and long-ranged potentials can be carried out [55] for graphene ribbons with covalently bound adsorbates described by the tight binding model Hamiltonian (13.11) developed in Sect. 13.9.1. However, the computing resources required for such calculations (both memory and compute time) grow very rapidly as the number of extended molecular orbitals ψ_α per adsorbed atom or molecule increases. Thus, it is necessary to construct tight-binding models that capture the important physics accurately while minimizing the number of EMOs included in the Hamiltonian.

13.10.1 Building Efficient Tight-Binding Models

The adsorbate-induced rehybridization of the graphene from sp^2 to sp^3 bonding has been shown in Sect. 13.9.4 to have a strong effect on electron scattering by the adsorbates. Taking the rehybridization into account as in Sect. 13.9.4 by including in the model the $2s$, $2p_x$, and $2p_y$ valence orbitals of all of the carbon atoms shown in Fig. 13.10 as well as the valence orbitals of each of the adsorbed species means including in the model Hamiltonian (13.11) 13, 16, 17, and 22 EMOs per

Table 13.2 Minimal set of tight-binding parameters ϵ_α and $\gamma_{\alpha j}$ in units of $t = 2.7$ eV for the tight-binding Hamiltonian (13.11) describing the scattering of graphene π band electrons due to adsorbed H, F and O and OH on graphene

Adsorbate	ϵ_α	$\gamma_{\alpha j}$
H	−0.0383	2.219
F	−10.862	4.363
	−2.460	1.645
	−0.914	1.180
OH	−8.536	3.203
	−1.820	1.779
	−0.709	1.540
O	−5.356	3.240
	−1.448	±1.000
	−0.373	1.095
	0.130	±0.176
	1.463	1.650

This parameter set incorporates into the model the effects of adsorbate-induced local rehybridization of the graphene from sp^2 to sp^3 bonding and is valid for electron energies ϵ in the range $-0.75t < \epsilon < 0.75t$. $\gamma_{\alpha j}$ are matrix elements $\langle \psi_\alpha | H_a | \phi_j \rangle$ of the Hamiltonian between the $2p_z$ orbital(s) ϕ_j of carbon atom(s) j to which the adsorbed moiety bonds and the EMO ψ_α. The ϵ_α are measured from the Dirac point energy of graphene. $\pm$ means that $\gamma_{\alpha j}$ has opposite signs for the two carbon atoms to which the O atom bonds. Adapted from [55]

adsorbed atom or molecule for H, F, OH and O adsorbates, respectively. These EMOs were all included in the calculations [55] used to obtain the results shown in Fig. 13.11. However, some of these EMOs couple much more weakly than others to the graphene π system and have little effect on the scattering strength profile of the adsorbed moiety calculated with T-matrix theory that is shown in Fig. 13.11. This suggests that tight binding Hamiltonians with reduced sets of effective EMOs can adequately describe scattering of graphene electrons due to the adsorbates, including the effects of rehybridization. The energy and coupling strength parameters ϵ_α and $\gamma_{\alpha j}$ for a minimal set of effective EMOs for each adsorbate that accurately reproduce the scattering strength profiles shown in Fig. 13.11 in the range $-0.75t < \epsilon < 0.75t$ are given in Table 13.2. The ϵ_α values in Table 13.2 are actual EMO energy parameter values calculated as described in Sect. 13.9.1 however, the $\gamma_{\alpha j}$ values have in some cases been adjusted to obtain a better fit to the exact profiles shown in Fig. 13.11 from calculations that omit the nonorthogonality correction described in footnote 4. Although the tight-binding parameter set in Table 13.2 was developed for atoms and molecules adsorbed on an infinite graphene sheet, because of the very local character of the tight-binding Hamiltonian given by (13.11) it is reasonable to expect these tight-binding parameters to be applicable to graphene ribbons as well.

Table 13.3 Tight-binding parameters for adsorbed H, F, O, and OH for a model that does not include rehybridization of the graphene

Adsorbate	ψ_α	ϵ_α	$\gamma_{\alpha,j}$	$\gamma_{C_{2p_z},C_{2p_z}}$
H	$1s$	−0.81	1.89	0.79
F	2s	−10.59	4.70	0.79
	$2p_z$	−2.48	1.45	
OH	$2s^O$	−7.74	4.10	0.73
	$2p_z^O$	−1.26	1.24	
	$1s^H$	−0.81	0.36	
OH	ψ_1	−8.17	3.75	0.73
	ψ_2	−1.64	1.81	
	ψ_3	7.39	1.69	
O	2s	−7.74	3.47	0.92
	$2p_z$	−1.26	0.76	0.89
	$2p_x$	−1.26	±0.80	

Notation as in Table 13.2. For OH the parameters are given for both the O and H atomic valence orbitals and the molecular orbitals ψ_α of OH. $\gamma_{C_{2p_z},C_{2p_z}}$ is the Hamiltonian matrix element between the $2p_z$ orbital of the graphene C atom to which the adsorbed moiety bonds and the $2p_z$ orbital of a neighboring C atom in the relaxed geometry. For O, the first $\gamma_{C_{2p_z},C_{2p_z}}$ is for the two C atoms to which the O bonds while the second is for a C atom to which the O bonds and another nearest C neighbor of that C atom. Adapted from [55]

For comparison, we give in Table 13.3 the tight binding parameters ϵ_α and $\gamma_{\alpha j}$ for EMOs that include only the valence orbitals of the adsorbed species, i.e., the effects of graphene rehybridization are *not* included in Table 13.3. Notice that although there is only one EMO for H in both models the effect of rehybridization (Table 13.2) is to shift the EMO energy ϵ_α much closer to the Dirac point and also to increase the coupling $\gamma_{\alpha j}$ to the graphene π band somewhat, resulting in the huge difference between the scattering strength profiles for H shown in Figs. 13.11 and 13.12.

Tight-binding models of Dirac point resonances for use in transport calculations in graphene have also been constructed by fitting the tight-binding parameters to the results of ab initio density functional theory-based electronic structure calculations [101, 105]. In those models, the adsorbed atom or molecule was described by just a *single* effective orbital energy parameter and a *single* coupling parameter. However, very different values of these parameters have been obtained from the density functional theory-based calculations by different groups [101, 105], even for the case of atomic hydrogen, the simplest possible adsorbate. The reasons for these differences are unclear at present, but they may be related to the fundamental limitations of density functional theory [69] as a tool for calculating the energies of electronic quasiparticles.

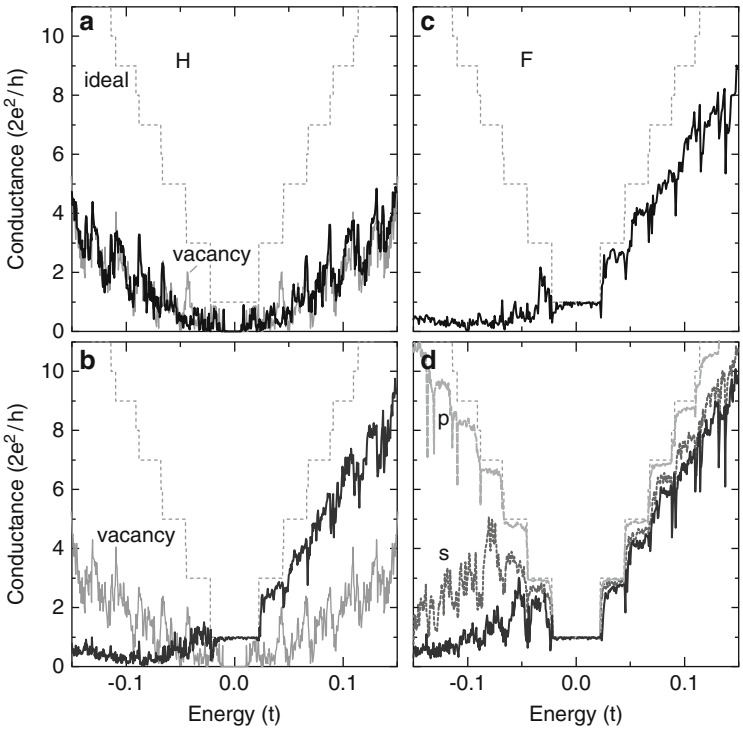

Fig. 13.13 Conductances (*solid black lines*) vs. Fermi energy for ribbons with adsorbed H ((**a**), (**b**)) and F ((**c**), (**d**)) at concentrations $p = 10^{-4}$. Geometries of the adsorbates and graphene are as in Fig. 13.10. (**a**) and (**c**) include the effects of local rehybridization of the graphene from sp^2 to sp^3 bonding embodied in Table 13.2. (**b**) and (**d**) do not include rehybridization and are based on Table 13.3. *Thin dotted pale grey lines* show the conductance of the ideal ribbon with no defects. *Grey solid lines* in (**a**), (**b**) show the conductance of a ribbon with interior carbon atom vacancies at $p_{\text{vac}} = 10^{-4}$. *Grey dashed and darker grey dotted lines* in (**d**) show the effects on the conductance of individual valence orbitals of the adsorbed species. Ribbon width $W = 30$ nm; length $L = 500$ nm. Temperature $T = 0$. $t = 2.7$ eV. Dirac point is at zero energy. Adapted from [55]

13.10.2 Results of Numerical Simulations of Quantum Transport in Ribbons with Adsorbates

The results of our conductance calculations [55] for ribbons with H, F, OH, and O adsorbates for electron Fermi energies close to the Dirac point energy are shown in Figs. 13.13 and 13.14.[4] The geometry of the ribbons is again similar to that in the experiment of Lin et al., i.e., the ribbon width $W = 30$ nm and the length $L = 500$ nm. The adsorbate concentration is $p = 10^{-4}$ per carbon atom. The

[4]For the relationship between the Fermi energy and experimental gate voltages see Fig. 13.9.

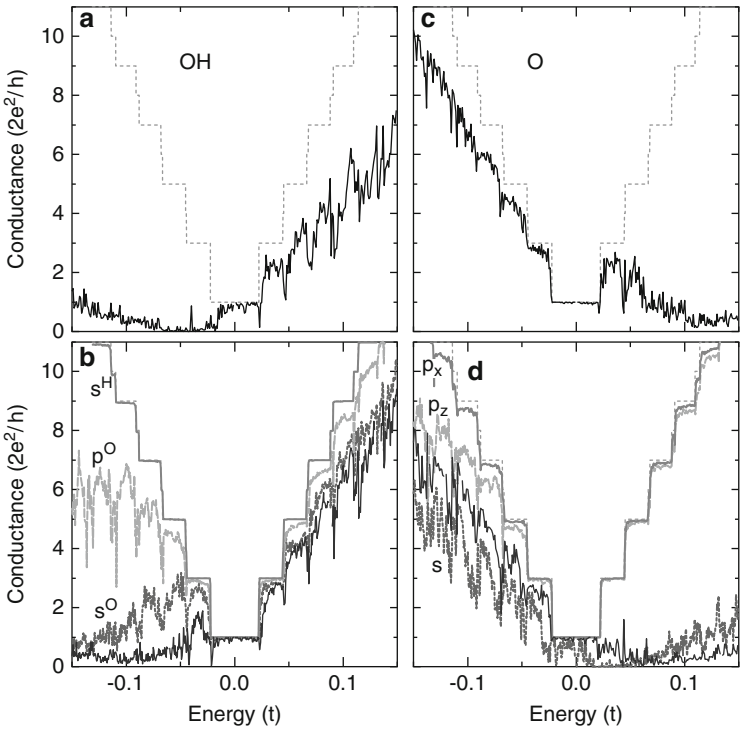

Fig. 13.14 The conductances (*solid black lines*) vs. Fermi energy for ribbons with adsorbed OH ((**a**), (**b**)) and O ((**c**), (**d**)) at concentrations $p = 10^{-4}$. The geometries of the adsorbates and graphene are shown in Fig. 13.10. (**a**) and (**c**) include the effects of the local rehybridization of the graphene from sp^2 to sp^3 bonding embodied in Table 13.2. (**b**) and (**d**) do not include rehybridization and are based on Table 13.3. *Thin dotted pale grey lines* show the conductance of the ideal ribbon with no defects. *The other grey lines* in (**b**) and (**d**) show the effects on the conductance of individual valence orbitals of the adsorbed species. Ribbon width $W = 30$ nm; length $L = 500$ nm. Temperature $T = 0$. $t = 2.7$ eV. The Dirac point is at zero energy. Adapted from [55]

results in the top pair of panels (a) and (c) in each figure include the effect of graphene rehybridization while those in the bottom pair (b) and (d) do not. The model parameters in the rehybridized and unrehybridized cases are those in Tables 13.2 and 13.3, respectively. In all of the calculations, the changes in the Hamiltonian matrix elements t_{ij} between carbon $2p_z$ orbitals in (13.12) that occur due to the change in graphene geometry induced by the adsorbate are taken into account. The relevant values of t_{ij} are listed in Table 13.3 under $\gamma_{C_{2p_z},C_{2p_z}}$. In each panel, the conductance of the ribbon with the adsorbate is indicated by the solid black line. The thin pale grey dotted line shows the conductance of the ideal ribbon without any defects. The grey solid lines in Fig. 13.13a, b show the conductance of a ribbon with interior carbon atom vacancies at the same concentration $p_{\text{vac}} = 10^{-4}$.

A striking aspect of Fig. 13.13a is the qualitative and quantitative agreement between the conductance of the ribbon with the adsorbed H atoms (calculated taking into account the local rehybridization of the graphene from sp^2 to sp^3 bonding) and that of the same ribbon but with an equal concentration of carbon atom vacancies instead of the adsorbed hydrogen. The agreement is almost perfect (apart from the fine sample-specific details of the mesoscopic conductance fluctuations) at low energies (throughout Fig. 13.13a) while at higher energies (Fig. 13.15) the conductance for the ribbon with the H adsorbate is $\sim 10\%$ higher on average.

It is possible to rationalize this similarity in terms of a simple picture of the rehybridization [107] in which a σ bond forms between the H atom and the C atom to which it bonds and the π bonds between that C atom and its neighbors break. Thus, the carbon atom is considered to decouple from the graphene π system and therefore to behave in some ways like a vacancy. However, this picture does not account for the differences between graphene with an H adsorbate and graphene with a F or OH adsorbate: The Dirac point resonances (Figs. 13.11 and 13.12) and conductance characteristics (Figs. 13.13 and 13.14) for F and OH adsorbates change much less drastically than those for H when rehybridization is included in the model, although the changes in the graphene geometry due to the adsorption of F and OH are very similar to and even slightly larger than for H adsorption.

Apart from the overall resemblance between the conductance plots, there are important *detailed* similarities in Figs. 13.13a and 13.15 between the conductance of the ribbon with the H (in the model that includes the local graphene rehybridization) and that of the ribbon with interior carbon atom vacancies.

1. In both cases, there are pronounced sample-specific conductance fluctuations that are a manifestation of quantum interference [44].
2. If the conductance fluctuations are ignored, the conductances are seen to scale down uniformly overall due to scattering by the adsorbate, i.e., in a similar way for all subbands.
3. The conductances show dips each time a new subband becomes available for propagation in the leads. This is because of enhanced electron backscattering by the defects at subband edges [44].

Because of these three similarities, we expect graphene nanoribbons with adsorbed H to exhibit equally spaced conductance steps similar to those observed experimentally by Lin et al. [3] for the same reasons and under the similar conditions (discussed in Sect. 13.8) as do graphene nanoribbons with carbon atom vacancies in the simple model of carbon atom vacancies that we have considered. That is, conductance steps of equal height should be observed even in samples with sufficiently high adsorbate concentrations for the ribbons to have conductances much smaller than $2e^2/h$, the conductance steps should break up into random conductance fluctuations as the temperature approaches zero Kelvin, and the conductance steps should become completely smeared out by thermal broadening at temperatures substantially larger than the subband spacing of the ribbons.

In short, electron scattering due to a low concentration of H atoms adsorbed on the graphene nanoribbons in our model that takes into account the

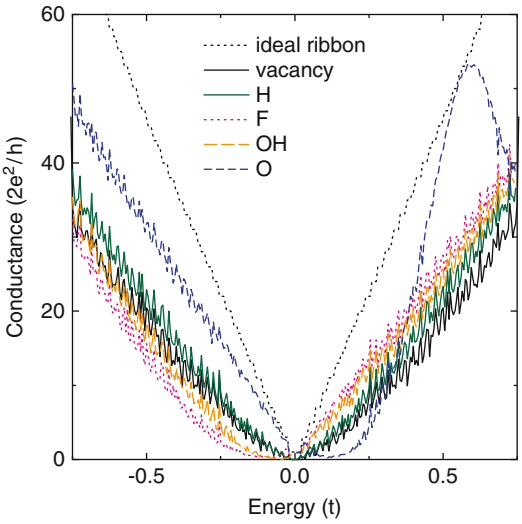

Fig. 13.15 Comparison of the conductances of graphene ribbons with different adsorbates and interior carbon atom vacancies at a concentration $p = 10^{-4}$ averaged over different positions of the defects. The effects of adsorbate-induced rehybridization of the graphene are included. The *grey dotted line* shows the conductance of the ideal ribbon without any defects. Dirac point is at zero energy. Adapted from [55]

adsorbate-induced rehybridization of the graphene provides an alternative and equally satisfactory explanation [55] of the experimental data of Lin et al. [3] to that [44] provided by electron scattering by carbon atom vacancies in the interior of the ribbon.

The three above similarities (1), (2), and (3) are also shared by ribbons with F, OH and O adsorbates for positive, positive and negative energies respectively, as can be seen in Figs. 13.13c and 13.14a, b. Therefore, conductance quantization of the kind observed by Lin et al. [3] should also occur under appropriate conditions in graphene ribbons with adsorbed F, OH and O.

If the rehybridization of the graphene is omitted from the model of the adsorbed hydrogen, the results of the transport calculations change as can be seen by comparing Fig. 13.13b (no rehybridization) with Fig. 13.13a (rehybridization included): If rehybridization is omitted, the conductance ceases to be approximately symmetric about the Dirac point (zero energy in Fig. 13.13) and its minimum shifts to lower energies $\sim -0.1t$ in Fig. 13.13b.

This is *not* due to a shift of the Dirac point itself to lower energies since the conductance dips that signal the electron Fermi-level crossing a subband edge (as is discussed in Sect. 13.8.2) still occur at almost the same energies in Fig. 13.13b as the subband edges of the *ideal* ribbon indicated by the discontinuities of the dotted line in Fig. 13.13b. Furthermore, the nearly ideal conductance of the first subband (similar to that for long-range potential scattering in Sect. 13.8.1 [38]) occurs in the solid black curve in Fig. 13.13b in the same energy range around zero energy as for the ideal ribbon. All of this shows that the subband energies of the ribbon (and, hence, also the Dirac point energy) have not shifted significantly in Fig. 13.13b from their ideal values. Thus, the low conductance at negative energies in Fig. 13.13b can only be due to particularly strong electron scattering at those energies suppressing

the conductance there. Since the Dirac point scattering resonance for adsorbed hydrogen in the model without rehybridization is centered nearby at $-0.138t$ (see Sect. 13.9.4 and Fig. 13.12) it is reasonable to suppose that the low conductance at negative energies in Fig. 13.13b is due to this scattering resonance.

This explanation is consistent with the fact that for the model that *includes* rehybridization, the H Dirac point resonance is centered *much* closer to the Dirac point (at $-0.0026t$ in Fig. 13.11) and the conductance minimum for that model (the solid black curve in Fig. 13.13a) is located extremely close to the Dirac point, as it is for carbon atom vacancy scattering.

The Dirac point scattering resonances for OH and F adsorbates are qualitatively similar to each other and are qualitatively similar in the models that do and do not include rehybridization of the graphene, as can be seen in Figs. 13.11 and 13.12. All of these resonances occur at negative energies, the resonances for F being at somewhat lower energies than for OH, and the resonances in the model without rehybridization are at lower energies than in the model with rehybridization included. This is all reflected in the locations of the respective conductance minima for these adsorbates in the two models: The conductance minima in Figs. 13.13–13.15 for both adsorbates in both models are located at negative energies that are very similar to those at which the respective Dirac point resonances occur in Figs. 13.11, and 13.12. Also the conductance minima for F occur at lower energies than for OH and those for the model without rehybridization of the graphene occur at lower energies than those in the model with rehybridization.

For the O adsorbate, the Dirac point resonances occur at positive energies relative to the Dirac point in Figs. 13.11 and 13.12 as do the conductance minima in Figs. 13.14c, d and 13.15. In this case, the Dirac point resonance in the model without rehybridization occurs at a lower energy than the resonances in the model with rehybrdization and the same is true of the conductance minima for O in Figs. 13.14 and 13.15. Also, the antiresonance (minimum) in the scattering strength profile for O that occurs at energies near $\epsilon = 0.55t$ in the model that includes rehybridization (Fig. 13.11) is associated with a local conductance maximum close to the same energy in the plot for O in Fig. 13.15. This is as one might expect as weak electron scattering is normally associated with high conductance.

We conclude that the properties of the adsorbate-induced Dirac point resonances associated with H, F, OH, and O adsorbates play a crucial role in electronic transport in graphene ribbons with these adsorbates, at least in ribbons in the quasiballistic regime where the localization length is comparable to or larger than the length of the ribbon. In particular, enhanced electron scattering due to these resonances results in strongly depressed conductances and transport gaps at electron Fermi energies in the vicinities of these resonances. Furthermore, electron scattering by all of these adsorbates for appropriate concentrations, temperatures, and gate voltages is expected to result in quantized conductance steps of equal height of the kind observed in graphene ribbons by Lin et al. [3].

13.11 Summary

As has been explained in Sect. 13.8.4, recent efforts to fabricate clean graphene nanoribbons for transport experiments have succeeded [3, 17] in making ribbons with Anderson localization lengths similar to the lengths of the ribbons. The disorder in such ribbons is still strong enough to depress the ribbon conductances by orders of magnitude below the ballistic conductance quantum $2e^2/h$. However, it is not strong enough to suppress all traces of quasi-ballistic behavior in these systems. In particular, as has been discussed in Sect. 13.8 it is plausible that the conductance steps observed experimentally in these samples [3, 17] constitute evidence that the ribbons are uniform enough to have discernible peaks in their density of states due to the formation of electronic subbands associated with quantized transverse electronic states in the ribbons. The equal heights of the experimentally observed conductance steps can be understood if electron scattering from carbon atom vacancies contributes in an important way to the electrical resistance of the ribbons. However, as is discussed in Sect. 13.10.2 the electronic scattering properties of H atoms adsorbed on graphene are very similar to those of carbon atom vacancies in the simple model of carbon atom vacancies that we have considered. Thus, hydrogen and other atoms or molecules chemisorbed at low concentrations on the graphene ribbons can account for the properties of the experimentally observed conductance steps as well. As has been discussed in Sect. 13.9.4, adsorbed atoms and molecules covalently bound to graphene give rise to strong electronic scattering resonances in the vicinity of the Dirac point energy of graphene. The properties of these Dirac point resonances are strongly influenced, especially in the case of hydrogen, by the partial rehybridization of graphene from sp^2 to sp^3 bonding that is induced by the chemisorption of the adsorbate. As is demonstrated in Sect. 13.10.2, the Dirac point resonances give rise to transport gaps in the conductances of graphene ribbons at electron Fermi energies in the vicinities of these resonances. Systematic experimental studies probing these resonances for different adsorbates on graphene and graphene ribbons by means of transport measurements and scanning tunneling spectroscopy would be of interest.

This work was supported by a Fellowship of the Canadian Institute for Advanced Research Nanoelectronics Program, by NSERC and by Westgrid.

References

1. M.Y. Han, B. Özyilmaz, Y. Zhang, P. Kim, Phys. Rev. Lett. **98**, 206805 (2007)
2. Z. Chen, Y.-M. Lin, M.J. Rooks, Ph. Avouris, Physica E **40**, 228 (2007)
3. Yu-Ming Lin, V. Perebeinos, Z. Chen, Ph. Avouris, Phys. Rev. B **78**, 161409(R) (2008)
4. X. Li, X. Wang, L. Zhang, S. Lee, H. Dai, Science **319**, 1229 (2008)
5. X. Wang, Y. Ouyang, X. Li, H. Wang, J. Guo, H. Dai, Phys. Rev. Lett. **100**, 206803 (2008)
6. F. Molitor, A. Jacobsen, C. Stampfer, J. Güttinger, T. Ihn, K. Ensslin, Phys. Rev. B **79**, 075426 (2009)
7. C. Stampfer, J. Güttinger, S. Hellmüller, F. Molitor, K. Ensslin, T. Ihn, Phys. Rev. Lett. **102**, 056403 (2009)

8. P. Koskinen, S. Malola, H. Häkkinen, Phys. Rev. B **80**, 073401 (2009)
9. L. Jiao, L. Zhang, X. Wang, G. Diankov, H. Dai, Nature **458**, 87 (2009)
10. K. Todd, H.-T. Chou, S. Amasha, D. Goldhaber-Gordon, Nano Lett. **9**, 416 (2009)
11. D.V. Kosynkin, A.L. Higginbotham, A. Sinitskii, J.R. Lomeda, A. Dimiev, B.K. Price, J.M. Tour, Nature **458**, 872 (2009)
12. M.Y. Han, J.C. Brant, P. Kim, Phys. Rev. Lett. **104**, 056801 (2010)
13. P. Gallagher, K. Todd, D. Goldhaber-Gordon, Phys. Rev. B **81**, 115409 (2010)
14. J.B. Oostinga, B. Sacépé, M.F. Craciun, A.F. Morpurgo, Phys. Rev. B **81**, 193408 (2010)
15. L. Jiao, X. Wang, G. Diankov, H. Wang, H. Dai, Nat. Nanotechnol. **5**, 321 (2010)
16. J. Cai, P. Ruffieux, R. Jaafar, M. Bieri, T. Braun, S. Blankenburg, M. Muoth, A.P. Seitsonen, M. Saleh, X. Feng, K. Müllen, R. Fasel, Nature **466**, 470 (2010)
17. C. Lian, K. Tahy, T. Fang, G. Li, H.G. Xing, D. Jena, Appl. Phys. Lett. **96**, 103109 (2010)
18. J.-M. Poumirol, A. Cresti, S. Roche, W. Escoffier, M. Goiran, X. Wang, X. Li, H. Dai, B. Raquet, Phys. Rev. B **82**, 041413(R) (2010)
19. K. Nakada, M. Fujita, G. Dresselhaus, M.S. Dresselhaus, Phys. Rev. B **54**, 17954 (1996)
20. K. Wakabayashi, Phys. Rev. B **64**, 125428 (2001)
21. T. Hikihara, X. Hu, H.-H. Lin, C.-Y. Mou, Phys. Rev. B **68**, 035432 (2003)
22. H. Lee, Y.-W. Son, N. Park, S. Han, J. Yu, Phys. Rev. B **72**, 174431 (2005)
23. Y.-W. Son, M.L. Cohen, S.G. Louie, Phys. Rev. Lett. **97**, 216803 (2006)
24. Y.-W. Son, M.L. Cohen, S.G. Louie, Nature **444**, 347 (2006)
25. L. Brey, H.A. Fertig, Phys. Rev. B **73**, 235411 (2006)
26. N.M.R. Peres, A.H. Castro Neto, F. Guinea, Phys. Rev. B **73**, 195411 (2006); Phys. Rev. B **73**, 239902 (2006)
27. V. Barone, O. Hod, G.E. Scuseria, Nano Lett. **6**, 2748 (2006)
28. D. Areshkin, D. Gunlycke, C.T. White, Nano Lett. **7**, 204 (2007)
29. D. Gunlyckea, D.A. Areshkin, C.T. Whiteb, Appl. Phys. Lett. **90**, 142104 (2007)
30. F. Sols, F. Guinea, A.H. Castro Neto, Phys. Rev. Lett. 99, 166803 (2007)
31. L. Pisani, J.A. Chan, B. Montanari, N.M. Harrison, Phys. Rev. B **75**, 064418 (2007)
32. L. Yang, C.-H. Park, Y.-W. Son, M.L. Cohen, S.G. Louie, Phys. Rev. Lett. **99**, 186801 (2007)
33. A. Onipko, Phys. Rev. B **78**, 245412 (2008)
34. H. Xu, T. Heinzel, M. Evaldsson, I.V. Zozoulenko, Phys. Rev. B **77**, 245401 (2008)
35. M. Evaldsson, I.V. Zozoulenko, H. Xu, T. Heinzel, Phys. Rev. B **78**, 161407(R) (2008)
36. A. Cresti, G. Grosso, G.P. Parravicini, Phys. Rev. B **77**, 233402 (2008)
37. Z.F. Wang, Q. Li, Q.W. Shi, X. Wang, J. Yang, J.G. Hou, J. Chen, Appl. Phys. Lett. **92**, 133114 (2008)
38. M. Yamamoto, Y. Takane, K. Wakabayashi, Phys. Rev. B **79**, 125421 (2009)
39. M. Zarea, C. Büsser, N. Sandler, Phys. Rev. Lett. **101**, 196804 (2008)
40. J. Jiang, W. Lu, J. Bernholc, Phys. Rev. Lett. **101**, 246803 (2008)
41. J. Fernández-Rossier, Phys. Rev. B 77, 075430 (2008)
42. E.R. Mucciolo, A.H. Castro Neto, C.H. Lewenkopf, Phys. Rev. B **79**, 075407 (2009)
43. S. Ihnatsenka, I.V. Zozoulenko, G. Kirczenow, Phys. Rev. B **80**, 155415 (2009)
44. S. Ihnatsenka, G. Kirczenow, Phys. Rev. B **80**, 201407(R) (2009)
45. A. López-Bezanilla, F. Triozon, S. Roche, Nano Lett. **9**, 2537 (2009)
46. A. La Magna, I. Deretzis, G. Forte, R. Pucci, Phys. Rev. B**80**, 195413 (2009)
47. P. San-Jose, E. Prada, E. McCann, H. Schomerus, Phys. Rev. Lett. **102**, 247204 (2009)
48. Q. Ran, M. Gao, X. Guan, Y. Wang, Z. Yu, Appl. Phys. Lett. **94**, 103511 (2009)
49. H.-H. Lin, T. Hikihara, H.-T. Jeng, B.-L. Huang, Ch.-Y. Mou, Phys. Rev. B**79**, 035405 (2009)
50. J. Jung, T. Pereg-Barnea, A.H. MacDonald, Phys. Rev. Lett. **102**, 227205 (2009)
51. J. Jung, A.H. MacDonald, Phys. Rev. B**80**, 235417 (2009)
52. A.V. Rozhkov, S. Savelev, F. Nori Phys. Rev. B **79**, 125420 (2009)
53. A. Cresti, S. Roche, New J. Phys. **11**, 095004 (2009)
54. J. Jung, A.H. MacDonald, Phys. Rev. B**81**, 195408 (2010)
55. S. Ihnatsenka, G. Kirczenow, Phys. Rev. B **83**, 245442 (2011)
56. S. Ihnatsenka, G. Kirczenow, Phys. Rev. B **83**, 245431 (2011)

57. H. Cheraghchi, H. Esmailzade, Nanotechnology **21**, 205306 (2010)
58. Q. Zhang, T. Fang, H. Xing, A. Seabaugh, D. Jena, IEEE Electron Device Lett., **29**, 1344 (2008)
59. D.H. Choe, J. Bang, K.J. Chang, New J. Phys. **12**, 125005 (2010)
60. I. Deretzis, G. Fiori, G. Iannaccone, A. La Magna, Phys. Rev. B **81**, 085427 (2010)
61. I. Deretzis, G. Fiori, G. Iannaccone, A. La Magna, Phys. Rev. B **82**, 161413(R) (2010)
62. A. Ramasubramaniam, Phys. Rev. B **81**, 245413 (2010)
63. M. Vanin, J. Gath, K.S. Thygesen, K.W. Jacobsen, Phys. Rev. B **82**, 195411 (2010)
64. A. Saffarzadeh, R. Farghadan, Appl. Phys. Lett. **98**, 023106 (2011)
65. R. Landauer, IBM J. Res. Dev. **1**, 223 (1957)
66. R. Landauer, Philos. Mag. **21**, 863 (1970)
67. E.N. Economou, C.M. Soukoulis, Phys. Rev. Lett. **46**, 618 (1981)
68. D.S. Fisher, P.A. Lee, Phys. Rev. B **23**, 6851 (1981)
69. For a recent review see G. Kirczenow, *The Oxford Handbook of Nanoscience and Technology*, vol. 1, ed. by A.V. Narlikar, Y.Y. Fu (Oxford University Press, Oxford New York, 2010), pp. 62–116
70. M. Büttiker, Phys. Rev. Lett. **57**, 1761 (1986)
71. P.R. Wallace, Phys. Rev. **71**, 622 (1947)
72. A.H. Castro Neto, F. Guinea, N.M.R. Peres, K.S. Novoselov, A.K. Geim, Rev. Mod. Phys. **81**, 109 (2009)
73. M. Fujita, K. Wakabayashi, K. Nakada, K. Kusakabe, J. Phys. Soc. Jpn. **65**, 1920 (1996)
74. K.-I. Sasaki, R. Saito, J. Phys. Soc. Jpn. **77**, 054703 (2008)
75. O.V. Yazyev, M.I. Katsnelson, Phys. Rev. Lett. **100**, 047209 (2008)
76. S. Dutta, S. Lakshmi, S.K. Pati, Phys. Rev. B **7**7, 073412 (2008)
77. S. Dutta, S.K. Pati, J. Phys. Chem. B **1**12, 1333 (2008)
78. S. Dutta, A.K. Manna, S.K. Pati, Phys. Rev. Lett. **1**02, 096601 (2009)
79. J. Davies, *The Physics of Low-Dimensional Semiconductors* (Cambridge University Press, Cambridge, 1998)
80. B.J. van Wees, H. van Houten, C.W.J. Beenakker, J.G. Williamson, L.P. Kouwenhoven, D. van der Marel, C.T. Foxon, Phys. Rev. Lett. **60**, 848 (1988)
81. D.A. Wharam, T.J. Thornton, R. Newbury, M. Pepper, H. Ahmed, J.E.F. Frost, D.G. Hasko, D.C. Peacock, D.A. Ritchie, G.A.C. Jones, J. Phys. **C21**, L209 (1988)
82. J.I. Pascual, J. Méndez, J. Gómez-Herrero, A.M. Baró, N. Garcia, Uzi Landman, W.D. Luedtke, E.N. Bogachek, H.-P. Cheng, Science **267**, 1793 (1995)
83. J.I. Pascual, J. Méndez, J. Gómez-Herrero, A.M. Baró, N. Garcia, Vu Thien Binh, Phys. Rev. Lett. **71**, 1852 (1993)
84. S. Frank, P. Poncharal, Z.L. Wang, W.A. deHeer, Science **280**, 1744 (1998)
85. N. Tombros, A. Veligura, J. Junesch, M.H.D. Guimarães, I.J. Vera-Marun, H.T. Jonkman, B.J. van Wees, Nat. Phys. **7**, 697 (2011)
86. M. Endo, T. Hayashi, Seong-Hwa Hong, T. Enoki, M.S. Dresselhaus, J. Appl. Phys. **90**, 5670 (2001)
87. S. Reich, J. Maultzsch, C. Thomsen, P. Ordejón, Phys. Rev. B **66**, 035412 (2002)
88. P.A. Lee, A.D. Stone, Phys. Rev. Lett. **55**, 1622 (1985)
89. K. Nikolić, A. MacKinnon, Phys. Rev. B **50**, 11008 (1994)
90. J. Martin, N. Akerman, G. Ulbricht, T. Lohmann, J.H. Smet, K. von Klitzing, A. Yacoby, Nature Phys. **4**, 144 (2008)
91. P.W. Anderson, Phys. Rev. **109**, 1492 (1958)
92. J.W. Klos, A.A. Shylau, I.V. Zozoulenko, H. Xu, T. Heinzel, Phys. Rev. B **80**, 245432 (2009)
93. C.H. Lewenkopf, E.R. Mucciolo, A.H. Castro Neto, Phys. Rev. B **77**, 081410(R) (2008)
94. Y.-J. Yu, Yue Zhao, S. Ryu, L.E. Brus, K.S. Kim, P. Kim, Nano Lett. **9**, 3430 (2009)
95. D. Stojkovic, P. Zhang, P.E. Lammert, V.H. Crespi, Phys. Rev. B **68**, 195406 (2003)
96. O. Leenaerts, B. Partoens, F.M. Peeters, Appl. Phys. Lett. **9**2, 243125 (2008)
97. O. Leenaerts, B. Partoens, F.M. Peeters, Phys. Rev. B **8**0, 245422 (2009a)
98. O. Leenaerts, B. Partoens, F.M. Peeters, Phys. Rev. B **7**9, 235440 (2009b)

99. Z.M. Ao, F.M. Peeters, J. Phys. Chem. C**1**14, 14503 (2010a)
100. Z.M. Ao, F.M. Peeters, Phys. Rev. B **8**1, 205406 (2010b)
101. T.O. Wehling, S. Yuan, A.I. Lichtenstein, A.K. Geim, M.I. Katsnelson, Phys. Rev. Lett. **105**, 056802 (2010)
102. Yu. V. Skrypnyk, V.M. Loktev, Phys. Rev. B **73**, 241402 (2006)
103. V.M. Pereira, F. Guinea, J.M.B. Lopes dos Santos, N.M.R. Peres, A.H. Castro Neto, Phys. Rev. Lett. **9**6, 036801 (2006)
104. T.O. Wehling, A.V. Balatsky, M.I. Katsnelson, A.I. Lichtenstein, K. Scharnberg, R. Weisendanger, Phys. Rev. B **75**, 125425 (2007)
105. J.P. Robinson, H. Schomerus, L. Oroszlány, V.I. Fal'ko, Phys. Rev. Lett. **101**, 196803 (2008)
106. V.M. Pereira, J.M.B. Lopes dos Santos, A.H. Castro Neto, Phys. Rev.B **7**7, 115109 (2008)
107. T.O. Wehling, M.I. Katsnelson, A.I. Lichtenstein, Chem. Phys. Lett. **476**, 125 (2009)
108. Image made with MacMolPlot program of B.M. Bode, M.S. Gordon, J. Mol. Graphics Modeling **16**, 133 (1998)
109. M.J. Frisch et al., computer code GAUSSIAN 03, revision A.02 (Gaussian Inc., Pittsburgh, PA, 2009) The HSEh1PBE hybrid functional and 6-311G(d) basis set were used to calculate the geometries in Fig. 13.10
110. J.H. Ammeter, H.-B. Bürgi, J.C. Thibeault, R. Hoffman, J. Am. Chem. Soc. **100**, 3686 (1978) as implemented in the YAEHMOP numerical package by G.A. Landrum, W.V. Glassey (Source-Forge, Fremont, California, 2001)
111. S. Datta, W. Tian, S. Hong, R. Reifenberger, J.I. Henderson, C.P. Kubiak, Phys. Rev. Lett. **79**, 2530 (1997)
112. E.G. Emberly, G. Kirczenow, Phys. Rev. Lett. **87**, 269701 (2001); Phys. Rev. B **64**, 235412 (2001)
113. J.G. Kushmerick, D.B. Holt, J.C. Yang, J. Naciri, M.H. Moore, R. Shashidhar, Phys. Rev. Lett. **89**, 086802 (2002)
114. D.M. Cardamone, G. Kirczenow, Phys. Rev. B **77**, 165403 (2008)
115. F. Demir, G. Kirczenow, J. Chem. Phys. **134**, 121103 (2011)
116. G. Kirczenow, P.G. Piva, R.A. Wolkow, Phys. Rev. B **72**, 245306 (2005)
117. P.G. Piva, R.A. Wolkow, G. Kirczenow, Phys. Rev. Lett. **101**, 106801 (2008)
118. J. Buker, G. Kirczenow, Phys. Rev. B **78**, 125107 (2008)
119. J. Buker, G. Kirczenow, Phys. Rev. B **72**, 205338 (2005)
120. E.G. Emberly, G. Kirczenow, Chem. Phys. **2**81, 311 (2002), Appendix A.
121. L.E. Ballentine, *Quantum Mechanics* (Prentice Hall, Englewood Cliffs, New Jersey, 1990) Ch. 16-5.
122. Yu. V. Skrypnyk, V.M. Loktev, Low Temp. Phys. **33**, 9 (2007)
123. D.M. Basko, Phys. Rev. B **78**, 115432 (2008)
124. S.S. Pershoguba, Yu. V. Skrypnyk, V.M. Loktev, Phys. Rev. B **80**, 214201 (2009)
125. Yu. V. Skrypnyk, V.M. Loktev, Phys. Rev. B **82**, 085436 (2010)
126. E. Emberly, G. Kirczenow, Phys. Rev. Lett. **81**, 5205 (1998)
127. E.G. Emberly, G. Kirczenow, J. Phys.: Condens. Matter **11**, 6911 (1999)
128. G. Kirczenow, P.G. Piva, R.A. Wolkow, Phys. Rev. B **80**, 035309 (2009)

Chapter 14
Graphene Oxide: Synthesis, Characterization, Electronic Structure, and Applications

Derek A. Stewart and K. Andre Mkhoyan

Abstract While graphite oxide was first identified in 1855 [1, 2], the recent discovery of stable graphene sheets has led to renewed interest in the chemical structure and potential applications of graphene oxide sheets. These structures have several physical properties that could aid in the large scale development of a graphene electronics industry. Depending on the degree of oxidization, graphene oxide layers can be either semiconducting or insulating and provide an important complement to metallic graphene layers. In addition, the electronic and optical properties of these films can be controlled by the selective removal or addition of oxygen. For example, selective oxidation of graphene sheets could lead to electronic circuit fabrication on the scale of a single atomic layer. Graphene oxide is also dispersible in water and other solvents and this provides a facile route for graphene deposition on a wide range of substrates for macroelectronics applications. Although graphite oxide has been known for roughly 150 years, key questions remain in regards to its chemical structure, electronic properties, and fabrication. Answering these issues has taken on special urgency with the development of graphene electronics. In this chapter, we will provide an overview of the field with special focus on synthesis, characterization, and first principles analysis of bonding and electronic structures. Finally, we will also address some of the most promising applications for graphene oxide in electronics and other industries.

D.A. Stewart (✉)
Cornell Nanoscale Facility, Cornell University, Ithaca, NY 14853, USA
e-mail: stewart@cnf.cornell.edu

K.A. Mkhoyan (✉)
Department of Chemical Engineering and Materials Science, University of Minnesota, Minneapolis, MN 55455, USA
e-mail: mkhoyan@umn.edu

H. Raza (ed.), *Graphene Nanoelectronics*, NanoScience and Technology,
DOI 10.1007/978-3-642-22984-8_14, © Springer-Verlag Berlin Heidelberg 2012

14.1 Introduction

The recent discovery that individual honeycomb atomic sheets of carbon or graphene could be easily isolated from bulk graphite with a bit of Scotch tape and persistence [3] has led to a flurry of research that has revealed unique electrical, thermal, and structural properties. While historically there are several instances where graphene was observed prior to 2004 [4], the recent synergy of nanoscale fabrication approaches with atomic scale characterization tools has provided the necessary environment to fully explore the potential of this material. In particular, for potential future electronic devices, graphene could provide a route to make truly atomic-scale electronic circuits by simply patterning an atomic layer of carbon into nanoribbons of various sizes and configurations. While the high electrical conductivity of graphene makes it a strong candidate for nanoscale electronics, graphene does not have the normal semiconducting properties that are usually required for key electronic devices such as field effect transistors and resonant tunneling diodes. Therefore, a considerable amount of work has focused on inducing a band gap in graphene nanoribbons [5], functionalized graphene, graphene bilayers [6] or else by integrating graphene with insulating atomic sheets such as hexagonal boron nitride [7].

In recent years, significant effort has also been devoted to finding cost-effective ways to mass produce graphene. While the original micromechanical cleavage technique [3] (aka Scotch tape) isolated the first single layer graphene flakes, the approach is labor intensive and there is little control on the size and shape of the flakes and their position on a wafer. Other possible routes for the development of graphene have been demonstrated, including growth on SiC [8], Cu [9], Ni [10], and other surfaces.

Oxidized graphene sheets, also known as graphene oxide, may help solve critical issues related to both the mass production of graphene and development of graphene devices. For example, sonication of graphite oxide in water leads to a stable colloidal suspension of graphene oxide platelets that can be further chemically reduced to graphene sheets. Graphene oxide also possesses a band gap and has the potential to serve as a key component in graphene-based electronics such as transistors and Schottky diodes. By selectively oxidizing portions of a graphene sheet, it may be possible to isolate conductive regions and develop barrier layers for electronic devices.

In this chapter, we will explore graphene oxide, the disordered cousin of pristine graphene. The level of oxidation and the specific type and locations of carbon–oxygen bonds that occur make graphene oxide chemically more complex than graphene and difficult to characterize accurately. However, it also provides a crucial example of how both the introduction and removal of surface modifications can affect the structural and electronic properties of graphene. It is important to note that this field is moving rapidly and at best, this chapter will serve as a reasonable and slightly blurry snapshot of current progress. It should provide new researchers

with guidance on key issues of interest and highlight mysteries that still remain for a material discovered over 150 years ago.

14.2 Understanding Bulk Graphite Oxide and Graphene Oxide Monolayers

Since its discovery by Brodie in 1855 [1, 2], several structural models have been developed for graphite oxide (GO). In this section, we will provide a brief overview of the structures that have developed over the years, with a particular focus on how proposed structural elements can help enhance our understanding of the two dimensional analog, graphene oxide (G-O). Given the long history of this material, there have been several excellent reviews of the structural models considered for graphite oxide and graphene oxide [11–13].

The initial studies focused on crystalline models with periodic additions of functional groups to the graphene surface. Diagrams for several common functional groups based on oxygen, carbon, and hydrogen are listed in Fig. 14.1 for the benefit of nonchemists. Hofmann and Holst in 1939 proposed a regular array of epoxy groups (C–O–C) on the graphene surface with a C_2O molecular weight [14]. Given experimental evidence for the presence of hydrogen in graphite oxide, Ruess developed a crystalline model for graphite oxide that included both epoxy groups as well as hydroxyl (OH) groups [15]. An important aspect of this model is that each graphene layer is distorted by the presence of the functional groups and the carbon atoms interact through sp^3 bonds. Since graphite oxide consists of multiple graphene sheets, bonding of oxygen both above and below an individual graphene sheet is to be expected. Based on experimental evidence that water molecules can be trapped between layers, Nakajima et al. proposed a model that emphasized the interaction of hydroxyl and carbonyl functional groups trapped between distorted graphene sheets [16]. They argued that the experimentally observed changes in the interlayer spacing in graphene oxide with humidity can be directly related to the ratio of hydroxyl to carbonyl groups, ranging from a completely dehydrated structure, C_8O_2, to a structure dominated by hydroxyl groups, $C_8(OH)_4$. While this model provides a possible range of structures based on water content, it is important to note that it still relies on a crystalline vision of graphite oxide with a periodic arrangement of functional groups. The wide variety of early structure models developed for graphite oxide is a result of two important issues. The first

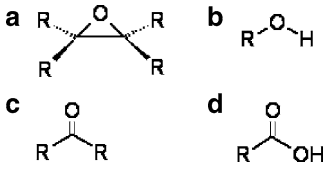

Fig. 14.1 Common functional groups found in graphene oxide (**a**) epoxy group (**b**) hydroxyl group (**c**) carbonyl group (**d**) carboxyl group

is due to the fact that the degree of oxidation depends on the fabrication technique used. The other is due to a sparsity of experimental data that allows for accurate characterization of the material at the atomic scale. While it was relatively easy to resolve the average interlayer spacing between graphene oxide layers using x-rays, it has been difficult to resolve whether the sheets are distorted and which specific functional groups are present.

Unlike the simple honeycomb structure of graphene, the term graphene oxide is best viewed as a concept representing a broad range of disordered oxidized graphene structures where the ratio of functional groups (epoxy, hydroxyl, and carboxyl groups) depends strongly on both the parent material and the processing approach used. Compton and Nguygen recently highlighted this aspect by noting that the carbon to oxygen ratio (C:O) measured in graphite oxide samples ranged from 1.3 to 2.25 depending on the approach used and oxidation time [13]. Lerf et al. were the first group to strongly advocate a structural model based on a nearly amorphous material with a random distribution of regions with unoxidized benzene rings and regions functionalized by epoxy and hydroxyl groups [11]. They also found NMR evidence that the epoxy and hydroxyl groups were usually located fairly close to each other on the graphene sheet. In addition to the presence of both epoxy and hydroxyl groups, they also noted evidence that water molecules could become trapped on the graphite oxide surface. Other groups have also noted that due to its hydrophilic nature, graphite oxide absorbs water under ambient conditions and this may also make characterization difficult. Although there has been one report of graphene oxide with a periodic arrangements of oxygen atoms on portions of the surface [17] (Fig. 14.2), most modern models and experimental measurements of graphene oxide indicate a random distribution of functional groups similar to Lerf et al.'s structure (Fig. 14.3). It is still unclear to what degree the graphene backbone is distorted by the presence of the oxygen functional groups and also whether functional group bonding occurs on one or both sides of graphene.

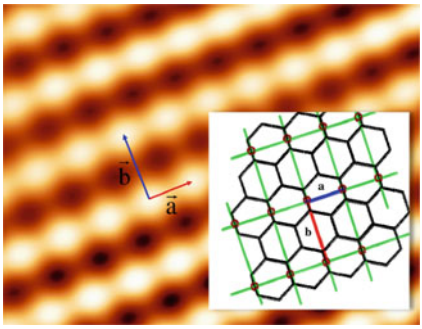

Fig. 14.2 Graphene oxide is typically characterized by a disordered arrangement of oxygen functional groups. This high resolution UHV STM image of oxidized graphene reveals a *rare* rectangular lattice with $a = 2.73$ Å and $b = 4.06$ Å. The inset shows a proposed graphene oxide crystal structure based on a rectangular lattice of epoxy groups. Adapted from [17] with permission from Elsevier, copyright 2008

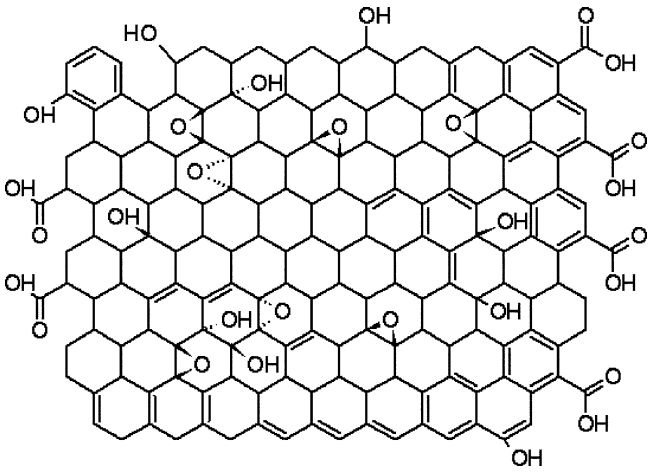

Fig. 14.3 Chemical structure of a graphene oxide sheet with randomly distributed epoxy and hydroxyl groups as well as carboxyl groups along the edges

Szab*ó* et al. argued that the carbon backbone would be corrugated with regions of linked cyclohexane chairs and flat carbon hexagons with double bonds [18]. Several groups have found evidence for carboxyl (–COOH) groups that bond on the edges of the graphene sheets. Based on ^{13}C NMR analysis, Gao et al. have presented a modified version of the Lerf model for Hummers fabricated graphite oxide which also includes five- and six-member-ring lactols along the edge of the graphene sheet [19]. They obtain highly conductive reduced graphene oxide by using a three-stage process where graphene oxide is first treated with $NaBH_4$ to remove most of the epoxy and hydroxyl groups and break down lactol rings, followed by concentrated sulfuric acid to remove remaining hydroxyl groups, and finally an annealing to eliminate carbonyl edge groups.

This variety of structures due to processing procedure can be beneficial for device applications, because it may provide a way to adjust the band gap of graphene oxide for specific device applications. To help understand the electronic and structure properties of graphene oxide, it is important to consider the key oxygen functional groups that form during the oxidation process and how they interact. A careful study of the energetics of oxygen on a graphene surface should also provide us with knowledge on how to potentially tailor the formation of graphene oxide for specific applications.

14.3 Fabrication of Graphite Oxide and Graphene Oxide

Several different approaches exist for fabricating graphite oxide and its two-dimensional analog, graphene oxide. In this section, we will discuss three traditional approaches used to fabricate graphite oxide, and we will also address some recent

techniques for the production of graphene oxide. It is important to stress that the exact chemical composition of graphite oxide is process dependent and that the different approaches outlined below can lead to different C:O ratios as well as the presence of different functional groups. Chemical and thermal techniques for producing reduced graphite and graphene from graphite oxide will also be discussed.

14.3.1 Traditional Approaches to Fabricate Graphite Oxide

The first production of graphite oxide was done by Benjamin C. Brodie in 1855 who added potassium chlorate ($KClO_3$) to a thick suspension of graphite in fuming nitric acid, HNO_3 [1, 2]. He found that the modified graphite crystals consisted of carbon, oxygen, and hydrogen and that the degree of oxidation could be increased by additional treatments of potassium chlorate to the solution, with a final molecular formula of $C_{2.19}H_{0.80}O_{1.00}$. Brodie also noted that graphite oxide was dispersible in water, one of the appealing aspects of this material for industrial applications. Later, Staudenmaier improved Brodie's technique by adding sulfuric acid to boost the acidity of the mixture as well as adding potassium chlorate at intervals during the reaction [12, 20]. However, this process was time consuming (taking roughly a week) and in early chemical labs, it also presented hazards due to the formation of toxic ClO_2 gas which can combust in air. In the 1950s, Hummers developed an alternative process for graphite oxide production that could be done in roughly 2 h and at lower temperatures [21, 22]. In this approach, a mixture of potassium permanganate ($KMnO_4$), sodium nitride ($NaNO_3$), and sulfuric acid (H_2SO_4) is used to oxidize graphite. Today, Hummers approach with minor modifications is widely used in the field to produce graphite oxide [23, 24]. Excess permanganate ions from the Hummers process can act as contaminants and it is important to remove these with a H_2O_2 water solution [13, 25]. There is also some evidence that graphite oxide produced using the Hummers approach contains sulfur impurities due to the use of sulfuric acid [26]. Other groups have advocated the use of the Brodie technique, arguing that graphite oxide produced using either Hummers or Staudenheimer can have a high degree of contaminants and can be susceptible to degradation [27, 28].

A recently published paper [29] by Marcano et al. describes an alternative approach to fabricating graphene oxide that increases the amount of potassium permanganate used and excludes the use of sodium nitride. They find that performing the reaction in a 9:1 mixture of H_2SO_4/H_3PO_4 improves overall oxidation, but that the subsequent chemically reduced graphene films have similar electronic properties to sheets generated by other techniques. A key advantage of this new approach is that toxic gases are not produced during the chemical reactions. Luo et al. found that pre-exfoliation of graphite via microwave heating helped to remove intercalated species and improved oxygen absorption in subsequent Hummers

processing [30]. This technique was able to generate large graphene oxide flakes ($\leq$ 2,000 μm^2) with a 90% yield, although the large flake size could also be due to the fact that they do not apply sonication to the samples.

The final molecular composition of graphite oxide depends strongly on the initial graphite sample (i.e., whether the sample has impurities or defects), the oxidizing process used, reaction time, and even humidity. The C:O ratio in graphite oxide can vary from 1.3 (Modified Hummer technique) to 2.28 (Brodie technique) and the intersheet spacing has also been found to range from 5.95 Å to 8.3 Å. The recent review by Compton and Nguyen [13] provides an excellent table summarizing the oxidants, reaction time, and chemical compositions of graphite oxide formed using the different techniques.

14.3.2 New Fabrication Techniques for Graphite Oxide and Graphene Oxide

The possibility of using graphite oxide as an efficient approach for developing graphene sheets has led to renewed interest in graphite oxide fabrication techniques and approaches to isolate single graphene oxide sheets. Graphite oxide exfoliates in a sonicated water solution into graphene oxide platelets which can then be deposited on surfaces [31]. The formation of thin graphite oxide sheets in solution was first noted in the original work by Brodie [2] and much later the presence of atomic layers of graphene oxide in solution was confirmed by Boehm et al. in 1962 [32]. These deposited thin films of graphene oxide are composed of stacked and overlapping graphene oxide platelets and it is important to keep this structural model in mind when graphene oxide and reduced graphene oxide thin films are discussed later in the text.

Graphene oxide sheets are generally viewed as being hydrophilic due to the presence of edge carboxyl (–COOH) groups that can ionize [11], making the sheets easy to disperse in water. However, recent research indicates that graphene oxide sheets may actually be amphiphilic with hydrophilic edge groups and a hydrophobic surface and could behave as a surfactant [33]. Due to the large molecular weight of the graphene oxide flakes, it can take several hours for these flakes to equilibrate at the air–water interface. However, this process can be sped up through the use of carbonated water. As CO_2 bubbles rise up through the water, amphiphilic graphene oxide platelets become trapped at the water–gas bubble interface and are carried to the water surface via flotation.

The growth of single graphene sheets on several different substrates in recent years has been demonstrated and these films can also be subsequently oxidized [34]. Carbon nanotubes can also be unzipped using potassium permangate to create graphene oxide nanoribbons [35, 36].

14.3.2.1 Fabricating Reduced Graphene Oxide

The ability to fabricate single sheets of graphene oxide via chemical means in solution provides an important base material for the production of reduced or chemically derived graphene (rG-O). With chemical reduction techniques and thermal annealing, it is not possible to completely eradicate oxygen functional groups or structural defects, so reduced graphene has a lower mobility than graphene produced via direct growth techniques or mechanical exfoliation. However, the mobility of these reduced graphene is still comparable to that of doped conductive polymers [37] and could provide a cheap approach for fabricating graphene based electronics.

There are currently several different approaches available to produce reduced graphene oxide. Schniepp et al. showed that rapid heating (> 2,000°C/min) of graphite oxide would lead to the release of CO_2 and split the remaining material into individual graphene sheets [38]. However, this technique required complete oxidation of graphite to be successful. Stankovich et al. developed a simple approach using hydrazine hydrate to reduce a colloidal suspension of graphene oxide sheets and form reduced graphene oxide sheets [39]. Since graphene oxide is negatively charged in solution, it can also be selectively deposited on predefined positively charged regions on a silicon surface [40]. It has also been shown that reduced graphene oxide films can be fabricated using a combination of hydrazine hydrate and a low temperature annealing session [41]. Electrochemical reduction of graphene oxide can also occur in a deaerated aqueous 0.1 M potassium nitrate (KNO_3) solution [42].

Decorating graphene oxide with TiO_2 particles provides an interesting photochemical route to reduce graphene oxide. When TiO_2-graphene oxide nanocomposites are suspended in ethanol and illuminated with ultraviolet (UV) radiation for over 15 min, the solution changes color from light brown to black [43]. This indicates increased light absorption similar to what would be found in graphene solutions. In this case, UV radiation leads to charge separation in the TiO_2 particles and the free electrons can reduce epoxy and carboxylate functional groups on graphene oxide. The presence of the TiO_2 particles also ensures that the reduced graphene sheets do not agglomerate in solution. Recently, Cote et al. showed that the Xenon flash lamp from a common digital camera could be used to flash irradiate graphite oxide in air and generate patterned regions of reduced graphite oxide [44]. For high power flashes, they also found that rapid degassing and air expansion can lead to complete ablation of the exposed regions and provide a chemical free etching technique.

In 2010, Wei et al. demonstrated that a heated atomic force microscope (AFM) tip (estimated temperature of 1,060°C) can pattern conductive regions of reduced graphene oxide with widths as small as 12 nm (Fig. 14.4) on a graphene oxide film through local annealing [37]. This opens an interesting route for patterning nanoscale graphene devices in graphene oxide sheets. In addition, a recent study has shown the reduction of graphene oxide can occur via bacterial respiration using

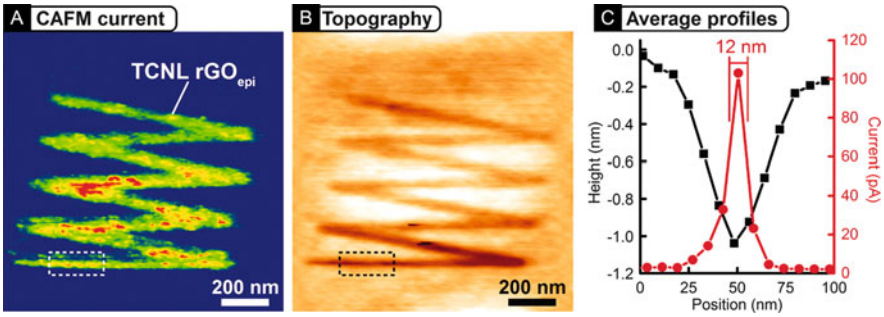

Fig. 14.4 (**a**) Room-temperature AFM current image of a zigzag-shaped nanoribbon fabricated by thermochemical nanolithography on epitaxial graphene oxide. (**b**) Corresponding topography image take simultaneously with (**a**). (**c**) Averaged profiles of current and height of the cross sections that are indicated as *dashed lines* in (**a**) and (**b**). From [37]. Reprinted with permission from AAAS

microbes (genus *Shewenella*) that are heterotrophic, facultative anaerobes [45]. This could provide an unique chemical free and *green* route to reduced graphene oxide.

Chemically derived graphene has a much lower electrical conductivity than pristine graphene which indicates that defects or scattered functional groups remain after the reduction process. The exact mechanisms for the removal of oxygen functional groups by chemical means [i.e., hydrazine (N_2H_4)] or by annealing has been unclear. Recently, Gao, Jang, and Nagase examined different reaction pathways for hydrazine and thermal reduction of graphene oxide using density functional theory [46]. They found that hydrazine is effective at removing epoxy groups in aromatic regions of graphene oxide via three different mechanisms, but converts edge epoxide groups to stable hydrazino alcohols that are difficult to remove. The presence of stable hydrazino alcohols on the edges of chemically reduced graphene sheets is supported by several experimental studies that find a significant amount of nitrogen in hydrazine reduced graphene oxides [39, 47, 48]. Gao, Jang, and Nagase find that hydrazine has no effect on hydroxyl, carboxyl, and carbonyl groups which must be removed using a high temperature thermal treatment. Reaction energetics indicate that the efficiency of hydrazine removal of epoxy groups *decreases* as temperature increases. Therefore, they suggest a two-stage reduction process with a low temperature chemical reduction for epoxy groups followed by a >700°C thermal annealing treatment. They propose the use of PPh_3 as the reducing agent catalyzed by $MeReO_3$ in 55°C toluene. Recent studies have shown that catalyzed PPh_3 can effectively remove epoxides both on graphite surfaces and edges [49,50], which could make it a superior graphene oxide reducing agent to hydrazine.

Molecular dynamics studies also help to provide insight into the local bonding structure in thermally reduced graphene oxide [51, 52]. Bagri et al. examined a graphene oxide sheet with an initial random configuration of epoxy and hydroxyl groups on the carbon backbone [51]. Using molecular dynamics simulations with the ReaxFF potential [53], the model graphene oxide sheet was annealed at 1,500 K.

They found that the reduced graphene oxide films were characterized by a large number of stable holes which form when C–C bonds break in the basal plane. These holes are decorated with a carbonyl and hydroxyl group or else two carbonyl groups. First principle simulations indicate that these holes form to relieve the stress in the carbon backbone induced by epoxy groups. The analysis of the molecular dynamics simulations also appears to be supported by additional transmission infrared and XPS spectra of reduced graphene oxide [52]. Based on these molecular dynamics simulations, they suggest that the primary culprit for poor reduced graphene oxide film quality (presence of holes, carbonyl groups) is due to the epoxy functional groups that strain the carbon backbone and promote C–C bond breaking and emission of CO and CO_2 from the film. To help ameliorate this issue, Bagri et al. propose a subsequent reheating of reduced graphene oxide in a hydrogen atmosphere to help heal the graphene lattice [52].

14.4 Characterization Approaches

14.4.1 Optical Microscopy

For general assessment of graphene and graphene oxide sheets for possible device fabrication, optical microscopy remains the leading high throughput and low-cost imaging approach in the field. Although graphene absorbs a relatively high percentage of visible light (2.3%) for a single atomic layer [54], it is difficult to obtain high contrast images of graphene based on transmitted light. Reflective illumination techniques can provide high-contrast optical images of graphene and graphene oxide. The addition of a single atomic layer (like graphene) to a dielectric layer grown on a reflective substrate alters the optical path of reflected light enough to change the reflected color [55]. This allows researchers to rapidly scan through large sections of deposited graphene sheets and measure graphene flake sizes, layer thickness, and wrinkles. In their seminal work on graphene [3], Novoselov et al. used this technique to resolve graphene layers deposited on oxidized silicon. Later works have focused on optimizing the dielectric material and layer thickness to provide high-contrast optical imaging for graphene oxide [56] and graphene [57]. However, it should be noted that reflective illumination requires that graphene is deposited on a dielectric coated silicon wafer with an optimized oxide thickness. Recently a group has developed a new technique for large scale imaging of graphene and graphene oxide that is based on fluorescence quenching [58]. Graphene-based materials have a strong quenching effect on fluorescence dyes. Upon excitation, graphene platelets, on a surface that has been coated with fluorescence dyes, appear as dark shapes in a bright background. Since this approach does not rely on interference effects, it can be used to characterize graphene and graphene oxide deposited on a range of substrates, including plastics and glass.

14.4.2 Scanning Transmission Electron Microscopy

Many graphene oxide research articles include conventional phase-contrast TEM images of the sheets. While these relatively low-magnification TEM images are quite useful to visualize the sheets, they contain very little information about the internal atomic structure of the sheets. For structural characterization, diffraction patterns are often obtained from the individual sheets [59, 60]. These diffraction patterns are the result of electron beam scattering from wide $\geq$100 nm areas of the specimen and can only describe the underlying long-range periodic arrangement of the atoms. They cannot be used to identify unique defects or short-range structural alterations in the sheets. However, when the operational conditions of the electron microscope are optimized to minimize possible electron beam-induced damage of the sheets [61], recorded atomic-resolution images can reveal many interesting structural features in the sheets. The recent report by Gomez-Navarro et al. [62] is a good example of using high resolution phase-contrast TEM imaging to detect and characterize defects in a single layer reduced graphene oxide sheet. As can be seen in Fig. 14.5, the atomic-resolution TEM image clearly reveals that the sheets are composed of intact 3 nm and 6 nm graphene islands along with various topological defects and deformations. Using TEM images, defects such as carbon pentagons, hexagons, and heptagons, dislocation dipoles, defect clusters, distortions in the hexagonal lattice can be identified.

Scanning transmission electron microscopy (STEM) is often the preferred approach for quantitative analysis of the local atomic structure and composition of graphene oxide. STEM with a high-brightness field emission electron source,

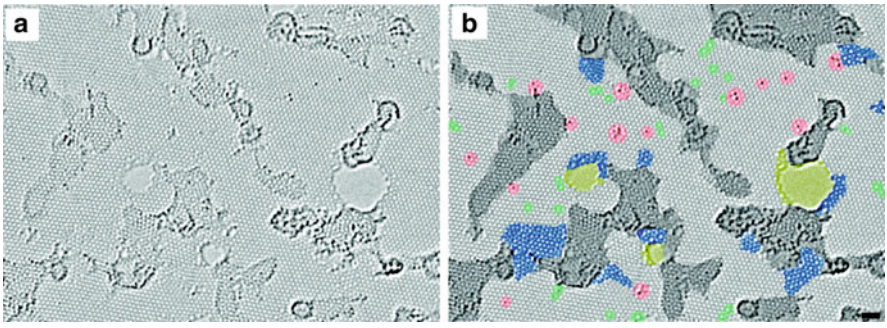

Fig. 14.5 TEM image of a single layer reduced-graphene oxide membrane. (**a**) Original image and (**b**) with color added to highlight the different features. The defect free crystalline graphene area is displayed in the original *light-gray color*. Contaminated regions are shaded in *dark gray*. *Blue* regions are the disordered single-layer carbon networks, or extended topological defects. *Red* areas highlight individual ad-atoms or substitutions. *Green* areas indicate isolated topological defects, that is, single bond rotations or dislocation cores. Holes and their edge reconstructions are colored in *yellow*. Scale bar 1 nm. Reprinted with permission from [62]. Copyright 2010 American Chemical Society

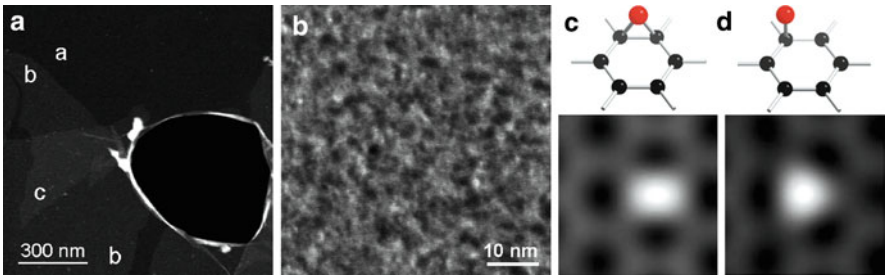

Fig. 14.6 (**a, b**) ADF-STEM image of the graphene oxide films where mono-, bi- and trilayers are labeled as **a**, **b**, and **c**, respectively. Round opening in the middle is a hole through the single film. (**c, d**) Simulated ADF-STEM images of graphene with oxygen bonded to the honeycomb of the graphene. The ball-stick models at the top illustrate the structures. Reprinted with permission from [71]. Copyright 2009 American Chemical Society

scanning with a focused electron probe, and the annular dark field (ADF) detector is an alternative approach for atomic-resolution imaging to conventional TEM with additional analytical capabilities [63]. The success of the STEM for quantitative imaging at high-resolution is governed by the ability to record images of the specimens by collecting elastically scattered probe electrons using a high-angle ADF detector. This allows visualization of specimens at resolutions smaller than 1Å with simplicity of interpretation: the heavier the atoms, the stronger the scattering and, as a result, the brighter the signal [64–66]. The simplicity of the method and the relatively weak dependence of ADF imaging on microscope-focusing conditions and specimen thickness allows very little room for error. For example, an ADF–STEM approach can image individual dopant atoms inside a silicon crystal [67] and reveal anomalies in the local thermal vibration of atoms in a quasicrystal [68].

Several ADF–STEM studies of graphene and graphene oxide sheets have been reported [69–71]. An ADF image of several layers of graphene oxide suspended over a hole is shown in Fig. 14.6a. The mono, bi-, and trilayered films can be clearly imaged, even though the signal from the single layer appears to be weak and barely distinguishable from the hole. A high-magnification ADF image taken from the single sheet with O:C = 1:5, shown in Fig. 14.6b, reveals not only the sheet but also the variation of intensities within the image, indicating that the oxidation of the graphene is uniformly random throughout the sheet.

For a better realization of the possibilities with ADF–STEM imaging in characterization of the graphene oxide films, several ADF–STEM images were simulated and two of them are presented in Fig. 14.6b, c. These ADF images were simulated using the *Multislice* method [72]. The results suggest that the ADF detector can be used to not only directly image single oxygen atoms on the graphene substrate but also identify the actual oxygen bonding sites on the carbon honeycomb structure.

14.4.3 Electron Energy Loss Spectroscopy

STEM combined with electron energy loss spectroscopy (EELS) is a very effective method for measuring electronic and optical properties of nanoscale materials [73]. When core-level electronic transitions are recorded with EELS, it is possible to carry out an analysis of the local chemistry and electronic structure. The Fermi golden rule describes the physics of these transitions and shows the element- and site-specific nature of these localized core-level transitions. A simple and intimate connection between the local density of unoccupied electronic states and the core-level excitations allows EELS to directly measure both the energy distribution and density of states for levels above the Fermi energy [74, 75].

Mkhoyan et al. [71] reported core-level EELS measurements from a single graphene oxide sheet. Spectra of C and O K-edges (Fig. 14.7), which are the result of $1s$ to $2p$ electronic transitions in carbon and oxygen atoms, represent the respective $2p$ partial density of states of the conduction band of graphene oxide. As can be seen from Fig. 14.7a, the fine structure of the C K-edge in graphene oxide shows considerable differences in fine structure relative to those in graphite and amorphous carbon (a-C). Removal of the STEM probe function from the measured C K-edge enhances the fine structure as shown in Fig. 14.7c. The analysis of the positions of identifiable peaks in a C K-edge in all three materials suggests that both sp^2 and sp^3 bonds are present in the graphene oxide. Additionally, for quantitative analysis, the EELS spectrum of the C K-edge can be fitted to a linear superposition of two spectra, C K-edge from graphite and amorphous carbon (a-C). For a O:C ratio of 1:5, as much as 40% of the carbon

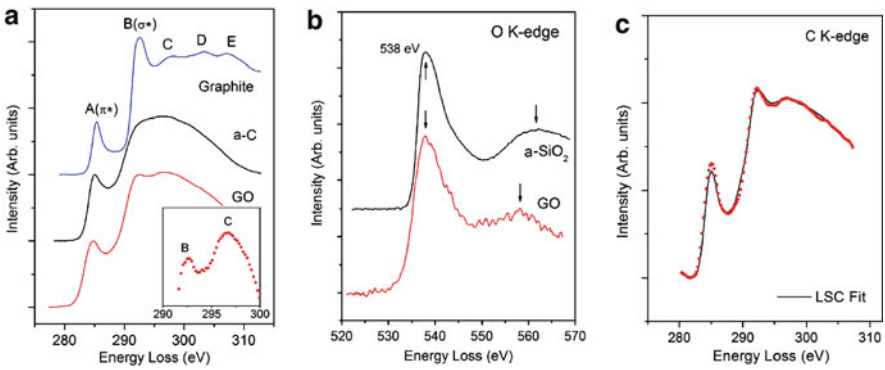

Fig. 14.7 Core-loss EELS spectra of (**a**) C K-edge and (**b**) O K-edge from the graphene oxide film. The spectrum of C K-edge is presented in comparison with C K-edges measured in graphite and a-C. The peaks of the fine structure are labeled A to E. The inset shows the section of the spectrum from graphene oxide for better visibility of the positions of the peaks B (or σ^*) and C. The O K-edge is presented in comparison with O K-edge in a-SiO_2. (**c**) The spectrum of the C K-edge in graphene oxide film and its best fit after removal of STEM probe function. Reprinted with permission from [71]. Copyright 2009 American Chemical Society

bonds are transformed into sp^3 bonds. The fine structure of the O K-edge, which lacks distinct features, presented in Fig. 14.7b, indicates the absence of periodicity for the oxygen atoms in the film and shows strong similarities with the O K-edge of amorphous SiO_2.

The low-loss region of EELS, on the other hand, measures optical properties of the specimens by recording electronic transitions between critical points of conduction and valence bands as well as characteristic plasmon excitations, which leads to the real and imaginary parts of dielectric function of the material [73]. The low-loss EELS spectrum was recorded from a single graphene oxide sheet [71]. The low-energy plasma excitations of the π^* electrons in graphene oxide occurs at 5 eV, similar to that in a-C. While the peaks of bulk plasma-loss (combination of π^* and σ^* electronic excitations) for graphite and a-C occur are at 27 eV and 24 eV, respectively, in graphene oxide films, it appears to be at 19 eV. Since the thickness of the film is only $\sim$1 nm thick, a full quantum mechanical description is needed to understand this 19 eV plasmon peak. A recent study by Eberlein et al. that combined EELS measurements with first principle calculations indicates that the plasmon modes of pure graphene are expected to have a significant red-shift from those found in graphite. They measured the main $\pi^* + \sigma^*$ plasma peak at 14.6 eV and a π^* peak at 4.7 eV [69, 70].

14.4.4 Atomic Force Microscopy

The atomic force microscope (AFM) was invented and introduced by Binning, Quate and Gerber in the mid-1980s [76]. It was based on the scanning tunneling microscope (STM) and took advantage of the existence of strong interatomic forces between atoms at the specimen surface and the scanning tip. For a good overview of STM and its use in characterizing graphene, please see Chap. 3 in this book. AFMs, which can operate in contact and noncontact mode, are extensively used in surface sciences and can even determine the structure of solid surfaces with atomic-resolution. A benchmark atomic-resolution AFM image of the Si(111)-(7x7) surface was recorded by Giessible [77] in 1995. In-depth discussion on the principals of operation and achievements of atomic-resolution AFM can be found in a recent book by Morita et al. [78] and in review by Giessible [79].

While atomic-resolution imaging of pristine solid surfaces using AFM can be challenging experimentally, measuring the atomic steps present on surfaces is relatively easy. This ability of AFM to determine z-heights of specimens with atomic precision makes it exceptionally suitable for measuring the thickness of graphene oxide sheets. Two examples of AFM images of graphene oxide sheets are presented in Fig. 14.8 [59]. The thickness of single or multiple sheets can be obtained either by taking a simple line scan going across the sheets and substrate as shown in Fig. 14.8a or by obtaining the histogram of the area of interest in the image as shown in Fig. 14.8b, c [71].

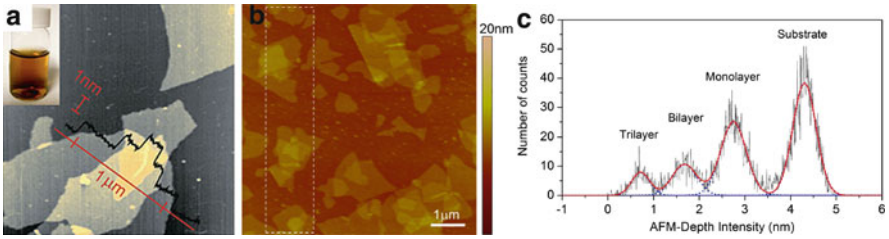

Fig. 14.8 (**a**) AFM image of graphene oxide sheets deposited onto a mica substrate obtained using the non contact mode from an aqueous dispersion (inset) with superimposed cross-section measurements taken along the *red line* indicating a sheet thickness of ∼1 nm. [59]; (**b**) AFM image of the graphene oxide sheets where mono-, bi-, and trilayers can be identified; (**c**) histogram of the AFM-depth intensities obtained from *dotted area* of the image (**b**). The histogram is fitted with a linear combination of four Gaussian functions representing each peak. Reprinted with permission from [71]. Copyright 2009 American Chemical Society

The typical thickness of a single graphene oxide sheet is within the range of 1–1.6 nm and it is thicker than a pristine graphene sheet, which is only 0.34 nm [39, 71, 80]. This is most likely due to the presence of different functional groups at either surfaces of the graphene oxide as well as some adsorbed molecules. It is also expected that some water molecules might be trapped between the sheet and substrate or between the sheets, since these functional groups make graphene oxide strongly hydrophilic [11, 80, 81]. When a large-scale AFM scan is performed with many graphene oxide sheets, statistical analysis can be carried out to quantify the size distribution of the sheets [82, 83].

14.4.5 X-ray Photoelectron Spectroscopy

When overall compositional analysis of the graphene oxide sheets is needed and atomic-scale structural details are not critical, X-Ray Photoelectron Spectroscopy (XPS) is an excellent alternative technique. Keeping in mind that the results of the XPS reflect the average X-ray response of the specimen, the measured spectra can reveal the presence of elements in the sheets (carbon, oxygen, hydrogen etc.), their relative fractions, and the nature of the bonds [84, 85]. However, to carry out compositional and structural analysis of graphene oxide with XPS, several precautions should be taken. For reliable measurement of the XPS spectra from a single sheet of graphene oxide, it is essential to develop a routine that will allow for controllable and systematic deposition of a single sheet of graphene oxide on the substrate. Since single sheets of graphene oxide are ∼1 nm thick, the presence of peaks from substrate elements in the measured XPS spectrum is unavoidable. Additional measurements from substrate-only regions might be needed. To minimize the effects of the substrate, a careful selection of the substrate

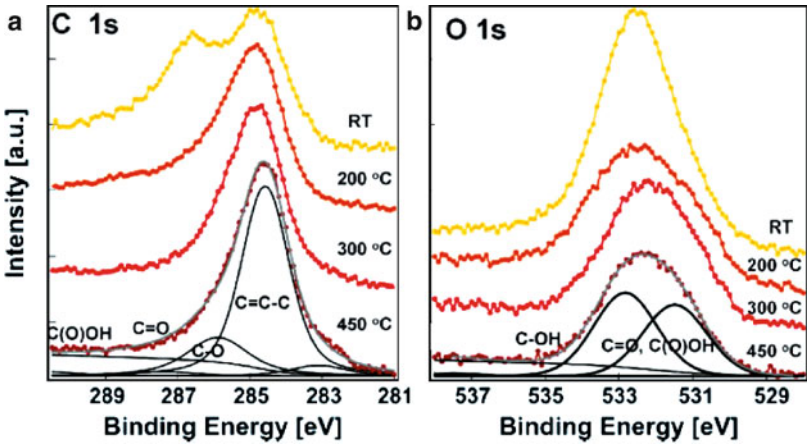

Fig. 14.9 (**a**) C 1s XPS spectra ($h\nu = 1{,}253.6$ eV) collected from a single atomic layer of graphene oxide deposited on Au(10 nm)/SiO_2(300 nm)/Si and annealed in UHV at the indicated temperatures for 15 min. The different components related to various chemical shifts of carbon bonds are indicated; (**b**) corresponding O 1s XPS spectra. Reprinted with permission from [86] courtesy of Wiley-VCH Verlag GmbH and Co. KGaA, Copyright 2009

can be instrumental. For XPS study of graphene oxide sheets, a preferable substrate should not contain elements such as carbon or oxygen or hydrogen. However, additional care must be taken even with those substrates, since most of the practical surfaces exposed to air easily experience oxidation.

Figure 14.9 shows XPS data recorded from a single layer graphene oxide film deposited on Au-coated SiO_2/Si substrate, which was later annealed at different temperatures in ultra-high-vacuum (UHV) for oxygen reduction [86]. The C 1s signal typically consists of five different chemically shifted components: C=C/C–C in aromatic rings (284.6 eV); C-O (286.1 eV); C=O (287.5 eV); C(=O)–(OH) (289.2 eV); and $\pi - \pi^*$ satellite peak (290.6 eV) [86–89]. For quantitative analysis, the spectrum of C 1s can be decomposed into individual components by fitting the entire spectrum to a linear superposition of all components present. This decomposition allows determination of the fractions of each component. Additionally, the fraction of sp^2 and sp^3 C–C bonds can be estimated by evaluating the intensities of the corresponding components.

The C-O bonds in graphene oxide is thought to come predominantly from epoxy and hydroxyl groups in the basal plane. The XPS measurements of O 1s, which includes typical contributions from C=O (531.2 eV), C–O (533 eV), and C(=O)–(OH) (533 eV) bonds, can be used to estimate the fraction of these groups present on sheets [87, 89]. An example of the O 1s XPS spectra from single-layer graphene oxide and reduced graphene oxide is presented in Fig. 14.9b.

14.4.6 Raman Spectroscopy of Graphene Oxide and Reduced Graphene

Raman spectroscopy can provide important information regarding the bonding configurations of atoms in carbon structures. This technique relies on illuminating a material with a laser and observing how inelastic scattering with lattice vibrations or phonons affects the photon energy. Conjugated carbon atoms and carbon atoms with double bonds give particularly strong Raman signals. A full discussion of the Raman spectroscopy of graphene can be found in Chap. 2 of this book. In this section, we will briefly highlight those aspects relevant to graphene oxide research.

The Raman spectra of graphite has a dominant peak (G band) at roughly 1,580 cm^{-1} that is due to an E_{2g} optical phonon mode that involves in-plane sp^2 bond stretching of the graphite lattice. A much smaller peak known as the D band is located at a lower frequency 1,355 cm^{-1} and is due to a breathing mode of the hexagonal carbon rings. It is Raman inactive in pristine graphite and the observed D band peak can be related to disorder along the edges of the graphite sample. The overtone of the D band, known as 2D, however, is Raman active even in pristine graphene and is due to double resonance transitions that generate two phonons with opposite momentums. The 2D peak can be used to determine the number of layers in pristine graphene multilayers [90–92], but it can be difficult to observe in graphene oxide samples.

During oxidation, the intensity of the D band increases significantly, indicating increased disorder and symmetry breaking in the graphene layers. The D band peak becomes broader and also experiences a blue shift to roughly 1,593 cm^{-1}. Upon transforming graphite oxide to reduced graphite, the G band peak returns to the original graphite frequency, indicating that the presence of oxygen could be related to the observed blue shift.

Using the Tuinstra–Koenig relation [93], the area ratio of the D and G peaks can be used to determine the size of sp^2 clusters in a sp^2 and sp^2 carbon network. Analysis of Raman spectra indicates that graphene oxide films can possess graphitic domains with sizes ranging from 2.5 nm to 6 nm. Above a critical defect density (< 2 nm sp^2 cluster size), the Tuinstra–Koenig relation fails and can not be used to interpret the Raman spectra. There has also been some difficult in interpreting the D/G ratio during graphene oxide reduction, since contradictory trends have been observed. A recent study [94] has shown that the ratio of 2D/G may provide a better measure of the extent of graphitic sp^2 region as demonstrated by a linear dependence of the 2D/G ratio with electron mobility for graphene oxide films (Fig. 14.10).

Using Raman spectra calculated with density functional perturbation theory [95], Kudin et al. found that a modified form of Scholz–Boehm-proposed GO structure provided the best spectral match and reasonable agreement with elemental composition [96]. This structure consists of wide ribbons of sp^2 bond carbon separated by parallel hydroxyl chains. A small concentration of epoxy groups are also located within the sp^2 regions. The wide sp^2 ribbons are necessary to produce

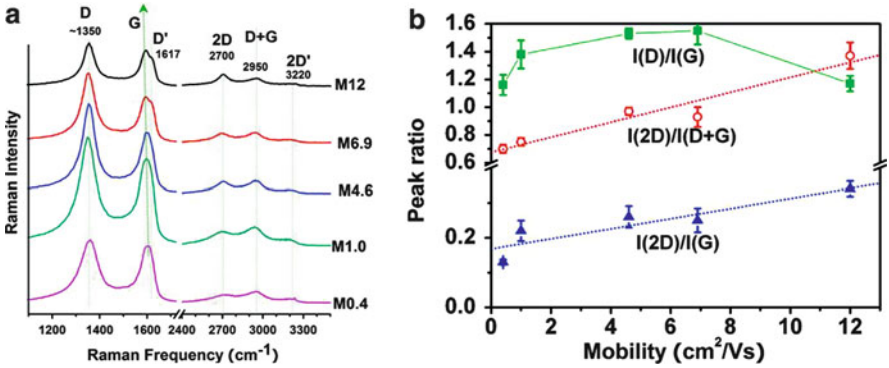

Fig. 14.10 (**a**) Raman spectra for five selected transistor devices with various values of effective mobility. The labels M0.4, M1.0, M4.6, M6.9, and M12 represent the devices with mobility 0.4, 1.0, 4.6, 6.9, and 12 $cm^2/(V\,s)$, respectively. (**b**) Various ratios for the integrated peak area for D, G, 2D, and D+G bands. Reprinted with permission from [94]. Copyright 2009 American Chemical Society

delocalized π electrons and the presence of the random epoxy groups are necessary to block additional Raman spectral peaks in the modified Scholz–Boehm structure that are not observed in experiment. However, despite the good match with the Raman spectra, the graphene oxide structure proposed by Kudin et al. has not been observed experimentally, indicating that another explanation for the Raman shift may exist.

14.5 Insight from Simulations

Nanoscale simulations can provide important insights into the structural, electronic, and chemical properties of graphene oxide. Empirical tight binding calculations coupled with results from detailed density functional approaches can provide a window into physical and chemical bonding. In recent years, these tools have also been brought to bear on the question of graphene oxide formation, structure, and reduction to graphene.

14.5.1 Using Epoxy Groups to Unzip Graphene

Numerous experimental studies of graphene oxide have indicated the presence of single oxygen atoms bonded to two carbons, otherwise known as epoxy groups (C–O–C). Electronic structure studies have also shown that oxygen atoms situated above a C–C bond provide one of the most stable bonding locations for oxygen on

a graphene sheet [71]. The presence of the oxygen atom acts to locally distort the graphene sheet, with the C–C distance of the nearest neighbor C atoms increasing from a sp^2 bond length to a bond length much closer to a sp^3 configuration.

In many graphite oxide samples, cracks and fault lines are noticeable under inspection using optical and force microscopy techniques [97, 98]. These boundary regions play an important role in the evolution of graphite during oxidation and may be central to the controlled formation of small reduced graphene oxide flakes. As such, a clear picture of the local atomic structure is crucial for understanding the oxidation process.

This issue was first addressed in 2006 by Li et al. [97] who used density functional theory to help resolve the formation of these cracks in small graphene platelets, $C_{12}H_{24}$ and $C_{54}H_{12}$. They focused in particular on the bonding of individual oxygen atoms (epoxy groups) on a single side of the graphene surface and how these functional groups strain the surface. The distance between the carbon atoms participating in the oxygen bond is transformed from sp^2 to sp^3 character and their energetic analysis indicates that epoxy groups prefer to form line structures (grain boundaries) on the graphene surface. It is important to note that the predicted hopping barrier for epoxy groups moving on a graphene surface is fairly large (0.9 eV) and this may prevent the formation of long epoxy chains in some cases. Li et al. argue that this barrier may be lower in solution, but this calculation has not been performed.

A later theoretical study [99] of an epoxy grain boundary noted that while the epoxy functional groups do increase the local C–C bond length, the structure is still stable and the presence of epoxy groups is not sufficient to fully unzip the graphene sheet. They find that the formation of carbonyl (C=O) groups along the chain is necessary to rip the sheets apart. They also examine the possibility of graphene tearing from carbonyl groups at the graphene sheet edge and found this to be energetically unfavorable. It is interesting to note a recent study [98] where graphene nanoribbons are sonochemically cut from chemically derived graphene sheets along fault lines possibly made up of epoxy functional grain boundaries.

The formation of epoxy chains on one side of the graphene sheet may be energetically favorable for the oxidation of graphene sheets resting on a substrate. However, in the case of the oxidation of graphite, the relatively large distance between graphene sheets allows oxygen to bond on either side of a given graphene sheet. In this scenario, other oxygen bonding configurations may be more energetically favorable. In the case where neighboring epoxy group in the chain are on opposite sides of the graphene sheets, the local strain on the carbon atoms is significantly reduced and the carbon bond preserves more of its sp^2 character. A recent density functional study found that fault lines that include a combination of both epoxy and hydroxyl groups (2O+2OH) are more energetically favorable than an epoxy chain on one side of the graphene sheet [100]. This corresponds well with experimental evidence that indicates epoxy and hydroxyl groups are usually located near each other on the carbon backbone. *Whether oxidation can occur on both sides of a graphene sheet rather than a single side could have important consequences on the degree of local strain placed on carbon bonds*. A greater portion of sp^3 bonds

should occur in graphene oxide with single sided growth due to epoxy groups. In cases where oxidation occurs on both sides, several atomistic studies show that stress fields can effectively cancel each other out and help maintain the hexagonal carbon network, leading to a smaller number of sp^3 bonds [100–102].

While the original work of Li et al. focused on the development of epoxy chains in small graphene platelets, it would be helpful to examine the energetics of long epoxy chain growth on large graphene sheets to insure that edge effects do not play a role. A recent paper [103] examined the distribution of functional groups on a graphene surface using a combination of density functional theory and Monte Carlo techniques. They found that an epoxy chain with four atoms would be stable, but they did not find evidence that chain growth beyond this length would be encouraged.

14.5.2 Graphene Oxide Electronic Structure

Due to the random distribution of epoxy and hydroxyl groups on the surface of graphene oxide, it is difficult to discuss the electronic structure in terms of a crystalline band structure model. A number of groups have used density functional theory to examine the energetics of possible crystalline configurations of graphene oxide, but these ordered structures appear to be difficult to fabricate with current chemical techniques, given that only one paper [17] reports an ordered graphene oxide region. Several experimental studies have shown that graphene oxide can be viewed in terms of fairly large insulating sp^3 regions surrounding small sp^2 islands [71]. In such a scenario, we would expect electrical transport to be primarily based on hopping between localized states in a percolation framework.

First principle calculations can provide insight into how functional groups affect the local electronic structure in graphene oxide. As an example, we can examine the local density of states near a single epoxy group on a graphene sheet (Fig. 14.11). The relaxed structure for the epoxy group is determined using a density functional calculation as outlined in Mkhoyan et al. [71]. The density of states for pristine graphene is shown in comparison with both the local density of states of a carbon atom in the epoxy group and one far away from it. For the carbon bond participating in the epoxy group, the π^* peak is no longer present and the local density of states near the Fermi energy is significantly reduced. The π^* peak is stable for a carbon atom located far from the stress field created by the epoxy bond.

Fully oxidized graphene has a light brownish color and is fully insulating with a direct optical band gap of 2.4 eV [104]. Optical studies indicate that the band gap of graphene oxide can be increased (decreased) through oxidation (reduction) [104, 105]. Jeong et al. found that the graphene oxide optical band gap could be adjusted from 1.7 eV (semiconducting) to 2.4 eV (insulating) in strong correlation to the oxygen to carbon ratio. The graphene oxide in this case was prepared using a simplified Brodie technique [28]. Blue photoluminescence from graphene oxide has also been found to depend on the degree of chemical reduction [105, 106].

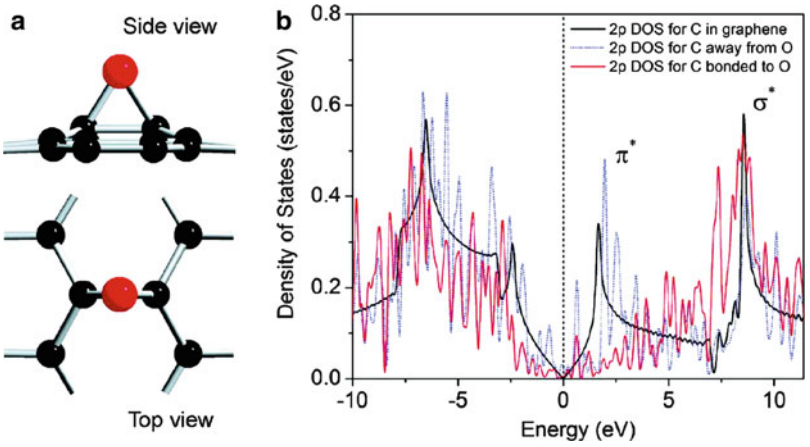

Fig. 14.11 (a) Ab-initio calculated electronic structure of a graphene sheet with a single oxygen atom (epoxy group) bonded to two adjacent carbon atoms. (**b**) Carbon 2p partial density of states for graphene and for C atom of graphene bonded to O and one that is far away from O. Reprinted with permission from [71]. Copyright 2009 American Chemical Society

For graphene structures with ordered or crystalline oxygen functional groups, density functional calculations indicates that the band gap also increases with the oxygen-carbon ratio [102, 107]. Yan, Xian, and Chou considered graphene oxide as an effective alloy consisting of three components, sp^2 C, epoxide groups (C_2O), and 1,2-hydroxyl pairs ($C_2(OH)_2$, with relative proportion based on the degree of oxidation [100]. Based on density functional calculations of ordered structures in the ternary diagram, they also found that the band gap increased with the oxygen to carbon ratio.

14.5.3 Electron Mobility and Transport

Since a great deal of research has been focused on mass production of graphene sheets from graphene oxide, the electron mobility of the reduced graphene oxide sheets has been an area of considerable interest and investigations. As we have seen throughout this chapter, the parent graphene oxide material can be thought of as a graphite backbone with a random distribution of oxygen functional groups (primarily epoxy and hydroxyl groups) on the surface. The presence of the functional groups leads to local strains and distortions of the honeycomb lattice and the subsequent transformation of sp^2 bonds into sp^3 bonds. In this sense, graphene oxide can be thought of as a material consisting of small sp^2 or conductive graphene islands surrounded by a sea of disordered, insulating sp^3 regions. By reducing a graphene oxide sample, a large number of sp^2 bonds can hopefully be restored to provide a conductive path across the film.

Discussions about transport in graphene oxide [108, 109] have focused on variable range hopping regimes where electrons hop between localized sp^2 states. In this model, the conductivity can be expressed as:

$$\sigma = \sigma_0 \exp\left(-\frac{B}{T^{1/3}}\right) \tag{14.1}$$

where T is the temperature and the hopping parameter B can be related to the wavefunction decay constant and the density of states at the Fermi energy. For graphene oxide samples that have not undergone a full reduction process, the $\ln(\sigma)$ does show a linear trend when plotted against $T^{-1/3}$, supporting the variable hopping model [108, 109]. Through analysis of different graphene oxide samples at various degrees of reduction, Eda et al. found that the change in the B parameter could be related to an increased number of localized states near the Fermi energy, but that the decay parameter or localization length for electrons still remained roughly constant [109, 110]. This indicates that while reduction may result in additional sp^2 islands, boosting the number of localized states, they are still, for the most part, not connected and this prevents the electrons from becoming itinerant. A transition from the variable hopping regime to a semimetal reduced graphene oxide with band-like transport was observed when the samples were well reduced. This is most likely due to the formation of a percolation regime with greater connectivity between sp^2 islands, electron delocalization, and the formation of efficient electrical paths through the sample. Mattevi et al. found that this transition to a percolation regime occurred at a sp^2 fraction of $\approx$0.6 [86].

Since the transport mechanism depends strongly on the degree of oxidation and oxidation procedure, it is not surprising that the measured mobilities vary widely between different groups. Eda, Fanchini, and Chhowalla grew graphene oxide using a modified Hummers approach and then used a combined hydrazine and thermal annealing method to reduce their samples [41]. They found this technique worked better than separate chemical or thermal annealing. Hole mobilities of the flakes ranged from 2 to 200 cm^2/Vs and the mobility for a thin film transistor with a long channel length (400 μm) was much smaller 1 cm^2/Vs and this reduction could be due to scattering at junctions between flakes [41].

Gomez-Navarro et al. used Hummers graphene oxide that was chemically reduced with hydrazine and found conductivity ranges from 0.05 to 2 S/cm and field effect mobilities of 2–200 cm^2/Vs at room temperature [111]. Several additional groups [112, 113] have fabricated graphene FETS with hole mobilities ranging from 0.25 cm^2/Vs to 4 cm^2/Vs and max electron mobilities of 1 cm^2/Vs. Recently Shin et al. found that reducing graphene oxide with sodium borohydride ($NaBH_4$) leads to a much smaller sheet resistance than graphene oxide reduced using hydrazine (N_2H_4) [114]. Wang et al. observed that electron mobility was higher than hole mobility in contrast to other experimental studies. They found a maximum transistor mobility of 10 cm^2/Vs [115].

14.6 Applications for Graphene Oxide

14.6.1 Graphene Oxide Electronics

Optical studies of graphene oxide have shown that the band gap of the material can be adjusted by the relative amount of oxidation [105]. This also leads to a measurable drop in the transparency of graphene oxide films during reduction. This ability to control the electronic properties of G-O makes it an appealing component for graphene based electronics. In 2008, Wu et al. examined the transport properties of graphene/graphene oxide junctions using both chemically derived graphene oxide flakes and graphene oxide formed from epitaxial graphene [34]. Transport measurements indicate the presence of Schottky barriers at the G/G-O interfaces with a height of 0.7 eV. The barrier height reduces with annealing (0.5 eV), which indicates that the degree of oxidation directly affects the band gap of graphene oxide.

Transparent conducting films based on graphene oxide were first demonstrated in 2007 [116]. The graphene oxide sheets were mixed with silica in solution and could be easily spin coated onto glass. Through careful processing, nanometer graphene oxide films can be reduced sufficiently to have both high conductivity and high optical transparency. Films with sheet resistances of $\approx$1 kΩ/sq and 90% transparency have been achieved with high temperature pyrolysis (1,000°C). Reduced graphene oxide electrodes could provide a cheap alternative to indium tin oxide (ITO) electrodes. Graphene also has a very similar work function to that of ITO, which should allow for easy integration into existing photovoltaic and LED device designs. However, the development of fabrication techniques that do not rely on high temperature pyrolysis will be essential for these devices to be competitive [110].

Typically for electronic applications of graphene oxide, the in-plane electrical conductivity is of primary importance. A recent work by Li et al., however, presents an interesting application of graphene oxide for solar cells where the conductivity perpendicular to the plane is the key metric for device performance [117]. In composite organic photovoltaics, the active region consists of acceptor nanostructures embedded in a donor polymer matrix which provides a large acceptor/donor interface surface area for effective charge separation. The efficiency of these devices can be limited by charge recombination when the anode and cathode contact both donor and acceptor regions in the photovoltaic. To block electrons and prevent charge recombination, thin p-doped layers or hole transport layers are often deposited on the anode [118, 119]. However, the need to vacuum deposit inorganic hole transport layers makes fabrication much more costly and removes any advantage in comparison to traditional solar cell technology. Hole transport layers that can be deposited in solution are known (i.e., PEDOT:PSS), but the deposition process required can degrade device performance. Li et al. found that a 2 nm graphene oxide layer can serve as an effective hole transport layer with an estimated band gap of 3.6 eV. They view graphene oxide as a graphene sheet covered primarily by wide band semiconducting regions due to sp^3 bonds with scattered conductive regions of sp^2 bonds. The large band gap regions effectively

blocks electron transport into the anode and the efficiency may be further improved by reducing the size of the sp^2 regions.

A group has recently demonstrated that graphene oxide can be used an effective charge trapping layer dielectric in memory storage devices where the threshold voltage is dictated by the charge trapped in the graphene oxide sheet [120]. These devices demonstrate a large memory window (7.5V) which is essential for nonvolatile memory applications. The memory window is also significantly larger than previous devices based on carbon nanotubes [121] (0.4V) and it can be adjusted over a range of (1.4–7.5 V) with chemical reduction. Due to the fact that graphene oxide can be processed in solution, it may provide an important memory component for flexible organic electronics.

The ability to store charges is also extremely important for capacitor applications. Electrochemical double layer capacitors (EDLCs) store charge by reversibly absorbing electrolyte ions on electrodes. In order to store a significant amount of charge, a large surface area is crucial. Typical high surface area electrode materials for EDLCs are based on a combination of activated carbon and carbon black filler and provide capacitances ranging from 120 F/g (organic electrolyte) to 300 F/g (aqueous electrolyte) [122]. Reduced graphene oxide films have a large surface area (400–700 m^2/g) and also exhibit very encouraging capacitances with 120 F/g (organic) [123] and 190 F/g (aqueous) [124]. Work is currently underway to enhance the surface area of graphene oxide layers through the use of spacers to prevent agglomeration. A more detailed discussion of the use of graphene oxide materials in capacitors can be found in [125].

14.6.2 Sensors

While the functional groups in graphene oxide are often used to adjust the electronic structure of the graphene sheet [105], they also offer important functional sites for biological and chemical applications. A research group has recently demonstrated a glucose biosensor based on a graphene oxide electrode [126]. The graphene oxide is functionalized by covalently bonding glucose oxidase amines to carboxyl acid groups on the surface. The functional modified graphene oxide sensor demonstrates a reproducible linear response over a wide range of glucose concentrations and initial studies indicate it could be biocompatible with human cells. Another group has also found that reduced graphene oxide sheets can serve as effective chemical sensors with parts per billion detection levels for chemical warfare agents and explosives [127].

14.6.3 Carbon-Based Magnetism

The development of nanoscale magnetic structures for memory applications and possibly spin-based electronics such as magnetic tunnel junctions has been one

of the main drivers for top down nanoscale fabrication. Magnetic materials used in industry rely on elements with d or f orbital electrons. The possibility of developing magnetic materials based on light elements with no d orbitals, such as carbon nanotubes and graphene, has been an active and controversial field [128]. Ferromagnetism in high pressure rhombohedral C_{60} was reported with a T_C of 500K in 2001 [129], but the work was later retracted when the results could be explained with the measured amount of magnetic (Fe) impurities in the sample [130]. However, more recent experiments using proton irradiated highly orientated pyrolytic graphite (HOPG) [131] and pristine graphite [132] have shown evidence of room temperature ferromagnetism. In addition, density functional calculations of graphene nanoribbons provide evidence of localized magnetic moments on surface or edge states. The review by Yazyev [128] is an excellent source for additional information of the numerous experimental and theoretical studies of magnetism in carbon nanostructures that have come out recently. In this work, we will only highlight recent works in the past year that have considered magnetism in graphene oxide structures.

A recent theoretical work based on density functional theory has indicated that graphene nanoribbons functionalized with an epoxy chain could be magnetic [133]. Based on energetic analysis, they find that graphene nanoribbons with a central epoxy chain should be energetically favorable. Similar to previous studies [134, 135], they find that zigzag graphene nanoribbons have an antiferromagnetic ground state. With the addition of a central epoxy chain, the nanoribbon ground state becomes ferromagnetic with magnetic moments situated primarily on the nanoribbon edges and along the epoxy chain. This model, however, does not explain a recent experimental study of magnetism in graphene oxide nanoribbons prepared by chemically unzipping carbon nanotubes [136] that found evidence of paramagnetism. In this case, placement of functional groups on the surface is disordered, and it is suggested that the paramagnetic behavior could be due to the presence of carbonyl functional groups at the edge of the graphene nanoribbons. The lack of agreement between theory and experiment could be due to this disorder. Wang and Li do note that calculations based on random epoxy groups do not lead to a magnetic state. Another explanation could be that the oxidized nanoribbons formed from carbon nanotubes do not possess a large number of epoxy groups or also include hydroxyl groups that prevent the formation of epoxy chains.

14.7 Future Perspectives

In this chapter, we have examined the atomic structure, electronic properties, and fabrication of graphene oxide, as well as some of its possible applications. Of all the functional forms of carbon that are currently under consideration, a clear understanding of the chemistry and physics of graphene oxide is perhaps the most critical for the birth of a graphene-based electronics industry. It is important to remember that the phrase *graphene oxide* actually encompasses a fairly wide range

of oxidized graphene structures that possess a range of C:O ratios and that can be fabricated using a variety of techniques. Current research strongly indicates that functional groups on the graphene oxide surface are for the most part randomly distributed and that the insulating properties of these materials depends strongly on the amount of oxidation. While there is limited evidence of ordered oxygen functional groups on a graphene surface, it remains to be seen whether careful growth conditions could lead to crystalline forms of graphene oxide. For the use of graphene oxide as a precursor for graphene sheets in industrial settings, the critical issue remains of how to effectively reduce graphene oxide to enhance mobility. Clear evidence exists that oxygen functional groups and defects remain after reduction. The development of processing steps that help the graphene lattice heal during this process will be crucial for the development of viable large scale manufacturing processes.

However, even without the motivation of graphene electronics, graphene oxide shows great promise for a number of industrial applications in its own right. As we have highlighted earlier in this chapter, graphene oxide has shown encouraging results as an charge trapping layer for memory storage devices. Due to its large surface area, reduced graphene oxide can also be used to make competitive capacitors. Transparent reduced graphene oxide sheets could also provide a cheap alternative to the expensive indium tin oxide used in panel displays. Finally, the ability to tune the electronic properties of graphene oxide from insulator to semiconductor to semimetal provides an important way to chemically define devices and circuits. It is clear that graphene oxide is an unique and promising material that requires further understanding and that should benefit progress in a number of fields.

Acknowledgements D.A.S. gratefully acknowledges support through the National Science Foundation for the National Nanostructure Infrastructure Network (NNIN) and the Cornell Nanoscale Science and Technology Facility. A portion of the density functional calculations discussed in this chapter were calculated using the Intel Cluster at the Cornell Nanoscale Facility. K. A. M. acknowledges partial financial support from the Abu Dhabi-Minnesota Institute for Research Excellence (AD-MIRE); a partnership between the Petroleum Institute of Abu Dhabi and the Department of Chemical Engineering and Materials Science of the University of Minnesota. The authors also thank collaborators Prof. M. Chhowalla, Dr. C. Mattevi at Rutgers University and Prof. J. Silcox, Prof. S. Tiwari at Cornell University for many fruitful discussions.

References

1. B.C. Brodie, Ann. Chim. Phys. **45**, 351 (1855)
2. B.C. Brodie, Phil. Trans. R. Soc. Lond. **149**, 249 (1859)
3. K.S. Novoselov, A.K. Geim, S.V. Morozov, D. Jiang, Y. Zhang, S.V. Dubonos, I.V. Grigorieva, A.A. Firsov, Science **306**, 666 (2004)
4. A.K. Geim, K.S. Novoselov, Nat. Mater. **6**, 183 (2007)
5. M.Y. Han, B. Ozyilmaz, Y. Zhang, P. Kim, Phys. Rev. Lett. **98**, 206805 (2007)
6. Y. Zhang, T.T. Tang, C. Girit, Z. Hao, M.C. Martin, A. Zettl, M.F. Crommie, Y.R. Shen, F. Wang, Nature **459**, 820 (2009)

7. L. Ci, L. Song, C. Jin, D. Jariwala, D. Wu, Y. Li, A. Srivastava, Z.F. Wang, K. Storr, L. Balicas, F. Liu, P.M. Ajayan, Nat. Mater. **9**, 430 (2010)
8. C. Berger, Z. Song, X. Li, X. Wu, N. Brown, C. Naud, D. Mayou, T. Li, J. Hass, A.N. Marchenkov, E.H. Conrad, P.N. First, W.A. de Heer, Science **312**, 1191 (2006)
9. X. Li, W. Cai, J. An, S. Kim, J. Nah, D. Yang, R. Piner, A. Velamakanni, I. Jung, E. Tutuc, S.K. Banerjee, L. Colombo, R.S. Ruoff, Science **324**, 1312 (2009)
10. K.S. Kim, Y. Zhao, H. Jang, S.Y. Lee, J.M. Kim, K.S. Kim, J.H. Ahn, P. Kim, J.Y. Choi, B.H. Hong, Nature **457**, 706 (2009)
11. A. Lerf, H. He, M. Forster, J. Klinowski, J. Phys. Chem. B **102**, 4477 (1998)
12. D.R. Dreyer, S. Park, C.W. Bielawski, R.S. Ruoff, Chem. Soc. Rev. **39**, 228 (2010)
13. O.C. Compton, S.T. Nguyen, Small **6**, 711 (2010)
14. U. Hofmann, R. Holst, Ber. Dtsch. Chem. Ges. B **72**, 754 (1939)
15. G. Ruess, Monatsh. Chem **76**, 381 (1946)
16. T. Nakajima, A. Mabuchi, R. Hagiwara, Carbon **26**, 357 (1988)
17. D. Pandey, R. Reifenberger, R. Piner, Surf. Sci. **602**, 1607 (2008)
18. T. Szabo, O. Berkesi, P. Forgo, K. Josepovits, Y. Sanakis, D. Petridis, I. Dekany, Chem. Mater. **18**, 2740 (2006)
19. W. Gao, L.B. Alemany, L. Ci, P.M. Ajayan, Nature Chem. **1**, 403 (2009)
20. L. Staudenmaier, Ber. Dtsch. Chem. Ges. **31**, 1481 (1898)
21. W.S. Hummers, U.S. Patent 2,798,878, 1957
22. W.S. Hummers, R.E. Offeman, J. Am. Chem. Soc. **80**, 1339 (1958)
23. N.I. Kovtyukhova, P.J. Ollivier, B.R. Martin, T.E. Mallouk, S.A. Chizhik, E.V. Buzaneva, A.D. Gorchinsky, Chem. Mater. **11**, 771 (1999)
24. M. Hirata, T. Gotou, S. Horiuchi, M. Fujiwara, M. Ohba, Carbon **42**, 2929 (2004)
25. J.A. Johnson, C.J. Benmore, S. Stankovich, R.S. Ruoff, Carbon **47**, 2239 (2009)
26. C. Petit, M. Seredych, T.J. Bandosz, J. Mater. Chem. **19**, 9176 (2009)
27. H.P. Boehm, W. Scholz, Justus Liebigs Ann. Chem. **691**, 1 (1965)
28. H.K. Jeong, Y.P. Lee, R.J.W.E. Lahaye, M.H. Park, K.H. An, I.J. Kim, C.W. Yang, C.Y. Park, R.S. Ruoff, Y.H. Lee, J. Am. Chem. Soc. **130**, 1362 (2008)
29. D.C. Marcano, D.V. Kosynkin, J.M. Berlin, A. Sinitskii, Z. Sun, A. Slesarev, L.B. Alemany, W. Lu, J.M. Tour, ACS Nano **4**, 4806 (2010)
30. Z. Luo, Y. Lu, L.A. Somers, A.T.C. Johnson, J. Am. Chem. Soc. **131**, 898 (2009)
31. S. Stankovich, R.D. Piner, S.T. Nguyen, R.S. Ruoff, Carbon **44**, 3342 (2006)
32. H.P. Boehm, A. Clauss, G.O. Fischer, U. Hofmann, Z. Naturforschung **17b**, 150 (1962)
33. J. Kim, L.J. Cote, F. Kim, W. Yuan, K.R. Shull, J. Huang, J. Am Chem. Soc. **132**, 8180 (2010)
34. X. Wu, M. Sprinkle, X. Li, F. Ming, C. Berger, W.A. de Heer, Phys. Rev. Lett. **101**, 026801 (2008)
35. D.V. Kosynkin, A.L. Higginbotham, A. Sinitskii, J.R. Lomeda, A. Dimiev, B.K. Price, J.M. Tour, Nature **458**, 872 (2009)
36. A.L. Higginbotham, D.V. Kosynkin, A. Sinitskii, Z. Sun, J.M. Tour, ACS Nano **4**, 2059 (2010)
37. Z. Wei, D. Wang, S. Kim, S.Y. Kim, Y. Hu, M.K. Yakes, A.R. Laracuente, Z. Dai, S.R. Marder, C. Berger, W.P. King, W.A. de Heer, P.E. Sheenan, E. Riedo, Science **328**, 1373 (2010)
38. H.C. Schnieep, J.L. Li, M.J. McAllister, H. Sai, M. Herrera-Alonso, D.H. Adamson, R.K. Prud'homme, R. Car, D.A. Saville, I.A. Aksay, J. Phys. Chem. B **110**, 8535 (2006)
39. S. Stankovich, D.A. Dikin, R.D. Piner, K.A. Kohlhaas, A. Kleinhammes, Y. Jia, Y. Wu, S.T. Nguygen, R.S. Ruoff, Carbon **45**, 1558 (2007)
40. R. Ishikawa, M. Bando, Y. Morimoto, S.Y. Park, A. Sandhu, Jpn. J. Appl. Phys. **49**, 06GC02 (2010)
41. G. Eda, G. Fanchini, M. Chhowalla, Nat. Nanotechnol. **3**, 270 (2008)
42. G.K. Ramesha, S. Sampath, J. Phys. Chem. C **113**, 7985 (2009)
43. G. Williams, B. Seger, P.V. Kamat, ACS Nano **2**, 1487 (2008)
44. L.J. Cote, R. Cruz-Silva, J. Huang, J. Am. Chem. Soc. **131**, 11027 (2009)
45. E.C. Salas, Z. Sun, A. Luttge, J.M. Tour, ACS Nano **4**, 4852 (2010)
46. X. Gao, J. Jang, S. Nagase, J. Phys. Chem. C **114**, 832 (2010)

47. V.C. Tung, M.J. Allen, Y. Yang, R.B. Kaner, Nat. Nanotech. **4**, 29 (2009)
48. D. Yang, A. Velamakanni, G. Bozoklu, S. Park, M. Stoller, R.D. Piner, S. Stankovich, I. Jung, D.A. Field, C.A. Ventrice, R.S. Ruoff, Carbon **47**, 145 (2009)
49. D. Ogrin, J. Chattopadhyay, A.K. Sadana, W.E. Billups, A.R. Barron, J. Am. Chem. Soc. **128**, 11322 (2006)
50. J. Chattopadhyay, A. Mukherjee, C.E. Hamilton, J. Kang, S. Chakraborty, W. Guo, K.F. Kelly, A.R. Barron, W.E. Billups, J. Am. Chem. Soc. **130**, 5414 (2008)
51. A. Bagri, R. Grantab, N.V. Medhekar, V.B. Shenoy, J. Phys. Chem. C **114**, 12053 (2010)
52. A. Bagri, C. Mattevi, M. Acik, Y.J. Chabal, M. Chhowalla, V.B. Shenoy, Nat. Chem. **2**, 581 (2010)
53. A.C.T. van Duin, S. Dasgupta, F. Lorant, W.A. Goddard, J. Phys. Chem. A **105**, 9396 (2001)
54. R.R. Nair, P. Blake, A.N. Grigorenko, K.S. Novoselov, T.J. Booth, T. Stauber, N.M.R. Peres, A.K. Geim, Science **320**, 1308 (2008)
55. K.S. Novoselov, D. Jiang, F. Schedin, T.J. Booth, V.V. Khotkevich, S.V. Morozov, A.K. Geim, Proc. Natl. Acad. Sci. U.S.A. **102**, 10451 (2005)
56. I. Jung, M. Pelton, R. Piner, D.A. Dikin, S. Stankovich, S. Watcharotone, M. Hausner, R.S. Ruoff, Nano Lett. **7**, 3569 (2007)
57. S. Roddaro, P. Pingue, V. Piazza, V. Pellegrini, F. Beltram, Nano Lett. **7**, 2707 (2007)
58. J. Kim, F. Kim, J. Huang, Mater. Today **13**, 28 (2010)
59. S. Stankovich, D.A. Dikin, G.H.B. Dommett, K.M. Kohlhaas, E.J. Zimney, E.A. Stach, R.D. Piner, S.T. Nguyen, R.S. Ruoff, Nature **442**, 282 (2006)
60. N.R. Wilson, P.A. Pandey, R. Beanland, R.J. Young, I.A. Kinloch, L. Gong, Z. Liu, K. Suenaga, J.P. Rourke, S.J. York, J. Sloan, ACS Nano **3**, 2547 (2009)
61. L. Reimer, H. Kohl, *Transmission Electron Microscope: Physics of Image Formation*, 5th edn. (Springer, Berlin, Heidelberg, New York, 2008)
62. C. Gomez-Navarro, J.C. Meyer, R.S. Sundaram, A. Chuvilin, S. Kurasch, M. Burghard, K. Kern, U. Kaiser, Nano Lett. **10**, 1144 (2010)
63. A.V. Crewe, J. Wall, J. Langmore, Science **168**, 1338 (1970)
64. P.E. Batson, N. Dellby, O.L. Krivanek, Nature **418**, 617 (2002)
65. P.D. Nellist, M.F. Chisholm, N. Dellby, O.L. Krivanek, M.F. Murfitt, Z.S. Szilagyi, A.R. Lupini, A. Borisevich, J.W.H. Sides, S.J. Pennycook, Science **305**, 1741 (2004)
66. K.A. Mkhoyan, P.E. Batson, J. Cha, W.J. Schaff, J. Silcox, Science **312**, 1354 (2006)
67. P.M. Voyles, D.A. Muller, J.L. Grazul, P.H. Citrin, H.J.L. Gossmann, Nature **416**, 826 (2002)
68. E. Abe, S.J. Pennycook, A.P. Tsai, Nature **421**, 347 (2003)
69. M.H. Gass, U. Bangert, A.L. Bleloch, P. Wang, R.R. Nair, A.K. Geim, Nat. Nanotechnol. **3**, 676 (2008)
70. T. Eberlein, U. Bangert, R.R. Nair, R. Jones, M. Gass, A.L. Bleloch, K.S. Novoselov, A. Geim, P.R. Briddon, Phys. Rev. B **77**, 233406 (2008)
71. K.A. Mkhoyan, A.W. Contryman, J. Silcox, D.A. Stewart, G. Eda, C. Mattevi, S. Miller, M. Chhowalla, Nano Lett. **9**, 1058 (2009)
72. E.J. Kirkland, *Advanced Computing in Electron Microscopy* (Plenum Press, NY, USA, 1998)
73. R.F. Egerton, *Electron Energy Loss Spectroscopy in the Electron Microscope*, 2nd edn. (Plenum Press, NY, USA, 1996)
74. D.A. Muller, D.J. Singh, J. Silcox, Phys. Rev. B **57**, 8181 (1998)
75. K.A. Mkhoyan, J. Silcox, E.S. Alldredge, N.W. Ashcroft, H. Lu, W.J. Schaff, L.F. Eastman, Appl. Phys. Lett. **82**, 1407 (2003)
76. G. Binnig, C.F. Quate, C. Gerber, Phys. Rev. Lett. **56**, 930 (1986)
77. F.J. Giessibl, Science **267**, 68 (1995)
78. S. Morita, R. Wiesendanger, E. Meyer, *Noncontact Atomic Force Microscopy*, 1st edn. (Springer, Berlin, Heidelberg, New York, 2002)
79. F.J. Giessibl, Rev. Mod. Phys. **75**, 949 (2003)
80. I. Jung, M. Vaupel, M. Pelton, R. Piner, D.A. Dikin, S. Stankovich, J. An, R.S. Ruoff, J. Phys. Chem. C **112**, 8499 (2008)
81. A. Buchsteiner, A. Lerf, J. Pieper, J. Phys. Chem. B **110**, 22328 (2006)

82. G. Eda, M. Chhowalla, Nano Lett. **9**, 814 (2009)
83. S. Pang, H.N. Tsao, X. Feng, K. Mullen, Adv. Mater. **21**, 3488 (2009)
84. D. Briggs, M.P. Seah, *Practical Surface Analysis, Auger and X-ray Photoelectron Spectroscopy*, 2nd edn. (Wiley, NY, USA, 1996)
85. B.V. Crist, *Handbook of Monochromatic XPS Spectra*, 1st edn. (Wiley, NY, USA, 2000)
86. C. Mattevi, G. Eda, S. Agnoli, S. Miller, K.A. Mkhoyan, O. Celik, D. Mastrogiovanni, G. Granozzi, E. Garfunkel, M. Chhowalla, Adv. Funct. Mater. **19**, 2577 (2009)
87. C. Hontoria-Lucas, A.J.L. Peinando, J.D.D. Lopez-Gonzalez, M.L. Rojas-Cervantes, R.M. Martin-Aranda, Carbon **33**, 1585 (1995)
88. D.Q. Yang, E. Sacher, Langmuir **22**, 860 (2006)
89. D. Yang, A. Velamakanni, G. Bozoklu, S. Park, M. Stoller, R.D. Piner, S. Stankovich, I. Jung, D.A. Field, C.A. Ventrice Jr., R.S. Ruoff, Carbon **47**, 145 (2008)
90. A.C. Ferrari, J.C. Meyer, V. Scardaci, C. Casiraghi, M. Lazzeri, F. Mauri, S. Piscanec, D. Jiang, K.S. Novoselov, S. Roth, A.K. Geim, Phys. Rev. Lett. **97**, 187401 (2006)
91. A. Gupta, G. Chen, P. Joshi, S. Tadigada, P.C. Eklund, Nano Lett. **6**, 2667 (2006)
92. Z. Ni, Y. Wang, T. Yu, Z. Shen, Nano Res. **1**, 273 (2008)
93. F. Tuinstra, J.L. Koenig, J. Chem. Phys. **53**, 1126 (1970)
94. C.Y. Su, Y. Xu, W. Zhang, J. Zhao, X. Tang, C.H. Tsai, L.J. Li, Chem. Mater. **21**, 5674 (2009)
95. S. Baroni, S. de Gironcoli, A.D. Corso, P. Giannozzi, Rev. Mod. Phys. **73**, 515 (2001)
96. K.N. Kudin, B. Ozbas, H.C. Schniepp, R.K. Prud'homme, I.A. Aksay, R. Car, Nano Lett. **8**, 36 (2008)
97. J.L. Li, K.N. Kudin, M.J. McAllister, R.K. Prud'homme, I.A. Aksay, R. Car, Phys. Rev. Lett. **96**, 176101 (2006)
98. Z.S. Wu, W. Ren, L. Gao, B. Liu, J. Zhao, H.M. Cheng, Nano Res. **3**, 16 (2010)
99. Z. Li, W. Zhang, Y. Luo, J. Yang, J.G. Hou, J. Am. Chem. Soc. **131**, 6320 (2009)
100. J.A. Yan, L. Xian, M.Y. Chou, Phys. Rev. Lett. **103**, 086802 (2009)
101. Z. Xu, K. Xue, Nanotechnology **21**, 045704 (2010)
102. D.W. Boukhvalov, M.I. Katsnelson, J. Am. Chem. Soc. **130**, 10697 (2008)
103. J.T. Paci, T. Belytschko, G.C. Schatz, J. Phys. Chem. **111**, 18099 (2007)
104. H.K. Jeong, M.H. Jin, K.P. So, S.C. Lim, Y.H. Lee, J. Phys. D: Appl. Phys. **42**, 065418 (2009)
105. Z. Luo, P.M. Vora, E.J. Mele, A.T.C. Johnson, J.M. Kikkawa, Appl. Phys. Lett. **94**, 111909 (2009)
106. G. Eda, Y.Y. Lin, C. Mattevi, H. Yamaguchi, H.A. Chen, I.S. Chen, C.W. Chen, M. Chhowalla, Adv. Mater. **22**, 505 (2010)
107. J. Ito, J. Nakamura, A. Natori, J. Appl. Phys. **103**, 113712 (2008)
108. A.B. Kaiser, C. Gomez-Navarro, R.S. Sundaram, M. Burghard, K. Kern, Nano Lett. **9**, 1787 (2009)
109. G. Eda, C. Mattevi, H. Yamaguchi, H.K. Kim, M. Chhowalla, J. Phys. Chem. C **113**, 15768 (2009)
110. G. Eda, M. Chhowalla, Adv. Mater. **22**, 2392 (2010)
111. C. Gomez-Navarro, R.T. Weitz, A.M. Bittner, M. Scolari, A. Mews, M. Burghard, K. Kern, Nano Lett. **7**, 3499 (2007)
112. T. Kobayashi, N. Kimura, J. Chi, S. Hirata, D. Hobara, Small **6**, 1210 (2010)
113. D. Joung, A. Chunder, L. Zhai, S.I. Khondaker, Nanotechnology **21**, 165202 (2010)
114. H.J. Shin, K.K. Kim, A. Benayad, S.M. Yoon, H.K. Park, I.S. Jung, M.H. Jin, H.K. Jeong, J.M. Kim, J.Y. Choi, Y.H. Lee, Adv. Funct. Mater. **19**, 1987 (2009)
115. S. Wang, P.J. Chia, L.L. Chua, L.H. Zhao, R.Q. Png, S. Sivaramakrishnan, M. Zhou, R.G.S. Goh, R.H. Friend, A.T.S. Wee, P.K.H. Ho, Adv. Mater. **20**, 3440 (2008)
116. S. Watcharotone, D.A. Dikin, S. Stankovich, R. Piner, I. Jung, G.H.B. Dommett, G. Evmenenko, S.E. Wu, S.F. Chen, C.P. Liu, S.T. Nguygen, R.S. Ruoff, Nano Lett. **7**, 1888 (2007)
117. S.S. Li, K.H. Tu, C.C. Lin, C.W. Chen, M. Chhowalla, ACS Nano **4**, 3169 (2010)
118. V. Shrotriya, G. Li, Y. Yao, C.W. Chu, Y. Yang, Appl. Phys. Lett. **88**, 073508 (2006)
119. M.D. Irwin, D.B. Buchholz, A.W. Bains, R.P.H. Chang, T.J. Marks, Proc. Natl. Acad. Sci. USA **105**, 2783 (2008)

120. S. Wang, J. Pu, D.S.H. Chan, B.J. Cho, K.P. Loh, Appl. Phys. Lett. **96**, 143109 (2010)
121. X.B. Lu, J.Y. Dai, Appl. Phys. Lett. **88**, 113104 (2006)
122. P. Simon, Y. Gogotsi, Nat. Mater. **7**, 845 (2008)
123. Y. Zhu, M.D. Stoller, W. Cai, A. Velamakanni, R.D. Piner, D. Chen, R.S. Ruoff, ACS Nano **4**, 1227 (2010)
124. Y. Zhu, S. Murali, M.D. Stoller, A. Velamakanni, R.D. Piner, R.S. Ruoff, Carbon **48**, 2118 (2010)
125. Y. Zhu, S. Murali, W. Cai, X. Li, J.W. Suk, J.R. Potts, R.S. Ruoff, Adv. Mater. (2010)
126. Y. Liu, D. Yu, C. Zeng, Z. Miao, L. Dai, Langmuir **26**, 6158 (2010)
127. J.T. Robinson, F.K. Perkins, E.S. Snow, Z. Wei, P.E. Sheenan, Nano Lett. **8**, 3137 (2008)
128. O.V. Yazyev, Rep. Prog. Phys. **73**, 056501 (2010)
129. T.L. Makarova, B. Sundqvist, R. Hohne, P. Esquinazi, Y. Kopelevich, P. Schaff, V. Dadydov, L.S. Kashevarova, A.V. Rakhmanina, Nature **413**, 716 (2001)
130. T.L. Makarova, B. Sundqvist, R. Hohne, P. Esquinazi, Y. Kopelevich, P. Schaff, V. Dadydov, L.S. Kashevarova, A.V. Rakhmanina, Nature **440**, 707 (2006)
131. P. Esquinazi, D. Spemann, R. Hohne, A. Setzer, K.H. Han, T. Butz, Phys. Rev. Lett. **91**, 227201 (2003)
132. Y. Kopelevich, P. Esquinazi, J.H.S. Torres, S. Moehlecke, J. Low Temp. Phys. **119**, 691 (2000)
133. M. Wang, C.M. Li, New J. of Phys. **12**, 083040 (2010)
134. Y.W. Son, M.L. Cohen, S.G. Louie, Phys. Rev. Lett. **97**, 216803 (2006a)
135. Y.W. Son, M.L. Cohen, S. Louie, Nature **444**, 347 (2006b)
136. S.S. Rao, A. Stesmans, D.V. Kosynkin, A. Higginbotham, J.M. Tour, Arxiv **1006.4942**, v1 (2010)

Part III
From Physics and Chemistry of Graphene to Device Applications

Chapter 15
Graphene *pn* Junction: Electronic Transport and Devices

Tony Low

Abstract This chapter provides a tutorial style review on the physics of electronic transport through a graphene *pn* junction in the absence and presence of a magnetic field, including the case of a strain-induced pseudo-magnetic field. We review the basic transport theories for the graphene *pn* junction and complement this understanding with numerical studies and key experimental findings. Novel devices, such as electron optics and strain-induced pseudo-magnetic devices, that exploit the physics of the graphene *pn* junction discussed in here, will be presented.

15.1 Introduction

The discovery of the modern semiconductor *pn* junction dates back to 1940 [1]. This discovery set the stage for the later discovery of the junction transistor. Ever since, the semiconductor *pn* junction has been a ubiquitous building block for many solid-state electronic devices such as transistors, rectifiers, bipolars, solar cells, and light-emitting devices [2,3]. One of the key technological reasons for the success of the *pn* junction lies in its ability to locally modulate the energy bands via an applied bias. By reducing or increasing the energy barrier that the majority carriers at the chemical potential see, one controls the electrical conduction across the device. This basic principle underlies the rectification effect in a *pn* diode [3] and even the ballistic transistor [4]. The presence of a bandgap much larger than kT is crucial for above-mentioned applications.

T. Low (✉)
Network for Computational Nanoelectronics, Hall for Discovery Learning Research, Purdue University, West Lafayette, IN 47907, USA

Nanometer Scale Science and Technology, IBM Research Division, IBM T.J. Watson Research Center, Yorktown Heights, NY 10598, USA
e-mail: tonyaslow@gmail.com

H. Raza (ed.), *Graphene Nanoelectronics*, NanoScience and Technology,
DOI 10.1007/978-3-642-22984-8_15,

Pristine graphene [5–7], a two-dimensional carbon sheet arranged in a honeycomb lattice with an unusual linear energy dispersion [6, 8–12], does not have a bandgap. There are currently various approaches to induce bandgaps in graphene. The most obvious solution is through size quantization by the formation of nanoribbons [13–16] or more novel approaches such as nanomesh [17]. However, edge disorder and coulomb effects reduces it into a "mobility gap" [18, 19]. Other known approaches include breaking of the sublattice symmetry by interactions with underlying substrates [20–23] and bilayers [24–28]. Currently, these methods can produce a bandgap of up to 300 meV. Forming chemical derivatives, e.g. graphane by hydrogenating graphene, might lead to formation of large bandgap [29]. Recent experiments [30, 31], however, show that graphene-on-substrate tends to form a disordered hydrogenated graphene instead. This leads to a "mobility gap," common for most adsorbates [32]. All these methods involved a modification or reconstruction of the graphene's electronic bandstructure in order to produce a bandgap. This raises the following question "Are there alternative electronic devices that can exploit the very unique property of graphene, namely its gapless Dirac electronic spectrum?" In this chapter, we shall address this question in the context of graphene pn junction.

The initial experiments on graphene [5–7] clearly demonstrate the linear dependence of density-of-states as function of energy, a consequence of its Dirac energy spectrum. Devices for high frequency radio applications [33] exploits this simple phenomenon. Graphene pn junctions, the basic building block of most devices, had recently been demonstrated using a combination of top and bottom electrostatic gates to create "doped" p and n regions [34–36]. The conductance asymmetry, between nn and pn counterparts, observed in experiments is due to angular selective transmission across a pn junction [37, 38]. In particular, carrier incident normal to the pn interface would transmit perfectly, a phenomenon known as Klein tunneling [39], whose signatures are also observed experimentally [40, 41]. This unique property allows spatial manipulation of electron flow, through devices such as an electron collimator (through electronic superlattices using pn junctions) [42] and multiplexer [43] (via a tilted pn junction). Drawing analogy to optics, where one manipulates the spatial flow of light through mediums of different refractive index, one envisions electron-optics devices [44–48]. Such devices include the Veselago lens for electron focusing [49], and the electron-optical fiber [50–53], for guiding of electrons. The latter was experimentally demonstrated very recently [54].

On another related front, graphene pn junction in the presence of magnetic field had also been studied rigorously, both in the weak magnetic field [40, 41] and quantum Hall regimes [34, 35]. An interesting phenomenon related to the latter effect is the appearance of new anamolous integer quantum Hall plateaus [55, 56]. This is related to the presence of snake states, which emerged in the presence of crossed uniform electric and magnetic fields [57, 58]. When the current flow is aligned parallel to the pn interface, these snake states can be probed directly in experiments [59]. An intriguing idea is to employ strain to generate a pseudo-magnetic field [60, 61] in replacement of the real magnetic field. Recently, Landau levels as a consequence of such pseudo-magnetic field (of up to 300 T) were probed

using a scanning tunneling microsope [62]. This opens up new opportunities for novel quantum Hall transport physics, such as snake states and valley polarized currents, to be realizable in electronic devices [63–69].

Establishing a basic understanding of the transport physics in graphene pn junction is therefore pertinent, since it is the most basic building block of most devices, including that of electron optics and pseudo-magnetic field devices. This chapter focuses on the physics of electronic transport through a graphene pn junction in the absence and presence of a magnetic field, including the case of a strain-induced pseudo-magnetic field. We divide this chapter into several main sections. Section 15.2 surveys the electronic transport physics in a graphene pn junction in the absence of a magnetic field. This includes the concept of pseudospin [70], the phenomenon of Klein tunneling [39], analogies with optics such as electron focusing [49] and total internal reflection, quantum tunneling [37] and the basics of conductance modulation [38]. Section 15.3 reviews the novel transport physics of a graphene pn junction in the presence of a magnetic field. Such transport phenomena include the concept of valley isospins [71], snake orbits [11], conductance modulation in a weak magnetic field [72], transport in quantum Hall regime, [34] and various types of disorder [56]. The anamolous quantum Hall plateaus will be discussed. Section 15.4.1 discusses the transport physics of a graphene pn junction in the presence of a strain-induced pseudo-magnetic field. The origin of strain-induced pseudo-magnetic field is explained. Edge states, transport gap, magnetic and electric snake states are also discussed. Lastly, Sect. 15.5 provides an update on current experimental effort in realizing these novel phenomena and devices. Broadly speaking, this chapter addresses the key physics, derives and presents the relevant physical models, most importantly, theories are corroborated with existing experiments. Numerical approaches to solving quantum transport are employed to elucidate on the physics, where the modeling methodology are discussed in Sects. 15.2 and 15.4.1. At various junctures of the discussion, device concepts stemming from these unique transport physics of the graphene pn junction are also introduced.[1]

15.2 Transport in the Absence of a Magnetic Field

Recently, the local control of the energy bands in graphene has been demonstrated using a combination of top and bottom electrostatic gates to create p and n regions [34–36]. In this section, our aim is to develop an understanding of the conductance modulation of the graphene pn junction. We begin by laying out the conventions and definitions in Sect. 15.2.1, which we will need for subsequent discussions, especially regarding the concept of pseudospin. Then we consider

[1] See also relevant chapters of this book, e.g. Sect. 15.2.1 should complements with Chaps. 8, 9 and 17 provides other aspects of electronic transport properties.

the simple scattering problem of a step potential in Sect. 15.2.2. Here, we see that conductance modulation can be understood as pseudospin mismatch. We also introduce a possible analogy to optics at this juncture. In Sect. 15.2.3, we consider the scattering problem under a linear electric potential using the Wentzel-Kramers-Brillouin (WKB) approximation. We also compare the difference between the tunneling of Dirac and Schrödinger Fermions. Armed with the simple theoretical models for conductance modulation, we tackle the problem of realistic modeling of experimental devices in Sect. 15.2.5. Section 15.2.4 introduces the general numerical quantum transport model. We will also attempt to explain the experimental observation in [36] using the understanding developed in this chapter.

15.2.1 Dirac Equation, Pseudospin, and Chirality

The lattice structure of graphene is shown in Fig. 15.1a. It is convenient to define two coordinate systems for armchair and zigzag edge ribbon as shown in Fig. 15.1b. Within the nearest neighbor tight-binding approach, the problem can be written as follows [73]:

$$t\begin{pmatrix} 0 & f(\mathbf{k}) \\ f(\mathbf{k})^\dagger & 0 \end{pmatrix}\begin{pmatrix} \psi_A \\ \psi_B \end{pmatrix} = \epsilon\begin{pmatrix} \psi_A \\ \psi_B \end{pmatrix} \tag{15.1}$$

where $t \approx 3\,\text{eV}$ is the nearest neighbor hopping energy and

$$f(\mathbf{k}) = \sum_j \exp\left(\mathrm{i}\mathbf{k}\cdot\mathbf{r}_j\right) \tag{15.2}$$

where $\mathbf{r}_1 = (-b, 0)$, $\mathbf{r}_2 = \frac{1}{2}(b, a)$ and $\mathbf{r}_3 = \frac{1}{2}(b, -a)$. The eigen-energies are given by $\epsilon(\mathbf{k}) = \pm t|f(\mathbf{k})|$. The zero energies are located at the corners of the Brillouin zone, known as the Dirac point (see Fig. 15.1c). Expanding $f(\mathbf{k})$ to the first order

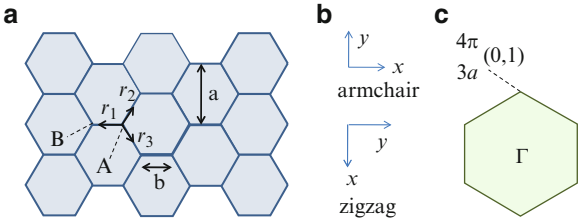

Fig. 15.1 (**a**) Honeycomb lattice of carbon where the primitive cell consists of two atoms, i.e., A/B. The carbon–carbon bond is $b \approx 1.44$Å, and the lattice constant is $a = \sqrt{3}b$. (**b**) The two coordinate systems used for armchair and zigzag cases. (**c**) The Brillouin zone corresponding to the lattice in (**a**). A Dirac point in the armchair coordinates is indicated

in $\mathbf{k}$ about the Dirac point at $\frac{4\pi}{3a}(0,1)$, we arrive at (using the armchair coordinate system)

$$f(\mathbf{k}) \approx -\frac{3b}{2}\left(\mathrm{i}k_x + k_y\right) \tag{15.3}$$

The Hamiltonian in (15.1) then becomes

$$\mathcal{H} \approx \hbar v_f \begin{pmatrix} 0 & -\mathrm{i}k_x - k_y \\ \mathrm{i}k_x - k_y & 0 \end{pmatrix} = v_f \left(P_x\sigma_y - P_y\sigma_x\right) \tag{15.4}$$

where $v_f = 3bt/2\hbar \approx 1 \times 10^6$ m/s is known as the Fermi velocity, and $\mathbf{P} \equiv -\mathrm{i}\hbar\nabla$ is the momentum operator. Using instead the coordinate system for the zigzag case, we arrive at a more familiar form,

$$\mathcal{H} = v_f \left(P_x\sigma_x + P_y\sigma_y\right) = v_f \mathbf{P}\cdot\boldsymbol{\sigma} \tag{15.5}$$

which is known as the Dirac equation of relativistic quantum mechanics. The corresponding eigen-states are given by

$$|\Psi_s(\mathbf{k})\rangle = \frac{1}{\sqrt{2}} \begin{pmatrix} \mathrm{e}^{-\mathrm{i}\theta/2} \\ s\mathrm{e}^{\mathrm{i}\theta/2} \end{pmatrix} \exp(\mathrm{i}\mathbf{k}\cdot\mathbf{r}) \tag{15.6}$$

where $s = +1/-1$ for electron/hole states, respectively, and $\theta = \tan^{-1}(k_y/k_x)$. This two-component wavefunction is known as pseudospin in the literature due to its transformation properties, which are similar to those of real spins. The corresponding eigen-energies are $\epsilon(\mathbf{k}) = s\hbar v_f|\mathbf{k}|$.

Next, we make the observation that the group velocity operator $\mathbf{v}$ is parallel to the pseudospin,

$$\mathbf{v} = \nabla_P \mathcal{H} = v_f\boldsymbol{\sigma} \tag{15.7}$$

Therefore, we have $\langle\mathbf{v}\rangle = v_f\langle\boldsymbol{\sigma}\rangle$, where

$$\langle\boldsymbol{\sigma}\rangle \equiv \langle\Psi_s|\,\boldsymbol{\sigma}\,|\Psi_s\rangle = s\frac{\mathbf{k}}{|\mathbf{k}|} \tag{15.8}$$

Equation (15.8) tells us that for a given $\mathbf{k}$ state, the velocity and pseudospin are parallel/antiparallel to $\mathbf{k}$ for the electron/hole states, respectively. The fact that the pseudospin (i.e. the wavefunction) is tied to the propagation direction has important consequences in transport. An example being the absence of backscattering [70], since $\pm\mathbf{k}$ states have opposite pseudospin.

In formal language, s is referred to as the state's chirality. This is because s could be written as $\langle\boldsymbol{\sigma}\rangle\cdot\mathbf{k}/|\mathbf{k}|$ like the definition of chirality in particle physics [74], except

that $\langle \boldsymbol{\sigma} \rangle$ is not the real spin. In a usual semiconductor such as Si, the complicated multi orbital environment prevents a similar pseudospin concept from being invoked for the wavefunction description. Hence, (15.8) does not apply to Si, although the statement about group and phase velocity is applicable in the vicinity of band edges.

15.2.2 Abrupt pn Junction and Analogy with Optics

In this section, we solve the quantum scattering problem of an abrupt potential step junction as shown in Fig. 15.2a, where the arrows in Fig. 15.2b indicate the directions of the pseudospin (or group velocity) for some representative forward $(+x)$ propagating states. Note the difference in chirality of electron/hole states as according to (15.8).

We consider an incoming wave with unity amplitude incident on the pn interface, which results in a reflected and transmitted wave. We denote the wavevectors as $\mathbf{k_i}$, $\mathbf{k_r}$ and $\mathbf{k_t}$, respectively. By requiring the conservation of transverse momentum (k_y), we can make the following statement:

$$|\mathbf{k_i}|\sin(\theta_i) = |\mathbf{k_r}|\sin(\theta_r) = |\mathbf{k_t}|\sin(\theta_t) \tag{15.9}$$

where $\theta = \tan^{-1}(k_y/k_x)$. Because $k_i = k_r$, this leads to $\theta_r = \pi - \theta_i$ (specular reflection), or what is commonly known as the second Snell law in ray optics. Similarly, we can also rewrite (15.9) as

$$\frac{\sin(\theta_i)}{\sin(\theta_t)} = \frac{k_t}{k_i} = \frac{\epsilon_{ft}}{\epsilon_{fi}} \tag{15.10}$$

This is analogous to the third Snell law in optics, where energy plays the role of the refractive index here. When the signs of ϵ_{ft} and ϵ_{fi} are opposite, a situation is obtained that is analogous to the Veselago lens [49], a negative refractive index medium.

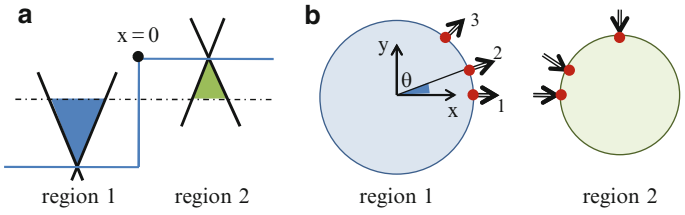

Fig. 15.2 (**a**) Energy band of an abrupt pn junction, where the *solid blue line* is the local position of the Dirac point and the *dashed black line* indicates the Fermi energy. (**b**) Illustration of the constant energy contour in the respective n/p regions of an abrupt graphene pn junction. The directions of group velocity (or equivalently pseudospin) for some representative transverse states are illustrated. State "1" undergoes perfect transmission, state "2" undergoes partial transmission and state "3" has complete reflection

When $|\epsilon_{ft}| < |\epsilon_{fi}|$, the situation of total internal reflection occurs. In a fashion similar to optics, we could define the critical angle as $\theta_c = \sin^{-1}(\epsilon_{ft}/\epsilon_{fi})$. Modes incident on the pn interface at angle larger than θ_c would be totally reflected (see Fig. 15.2b and caption). Technically speaking, this property could be used to create an electron analogue of an optical fiber for guiding electron flow [54]. This also translate to a "modes bottleneck effect" in the pn junction conductance, where the conductance is being limited by the junction with a smaller number of modes [38]. This is a classical effect due to momentum conservation. For modes incident at angle smaller than θ_c, one have to consider its quantum transmission.

To solve the scattering problem for the abrupt pn junction, we denote the solutions in each region and require them to be continuous at the interface $x = 0$, i.e.,

$$\begin{pmatrix} 1 \\ s_i e^{i\theta i} \end{pmatrix} + r \begin{pmatrix} 1 \\ s_r e^{i\theta r} \end{pmatrix} = t \begin{pmatrix} 1 \\ s_t e^{i\theta t} \end{pmatrix} \tag{15.11}$$

where r and t are the reflection and transmission coefficients, respectively. Using the fact that $s_r = s_i$ and $\theta_r = \pi - \theta_i$, we obtain the solution for r:

$$r = \frac{s_i e^{i\theta_i} - s_t e^{i\theta_t}}{s_i e^{-i\theta_i} + s_t e^{i\theta_t}} \tag{15.12}$$

The transmission probability can then be computed from $1 - |r|^2$. For the case of a symmetrically biased pn junction ($\epsilon_{fi} = -\epsilon_{ft}$), $|r|^2 = \sin^2(\theta_i)$ or a transmission probability of $\cos^2(\theta_i)$ would be obtained. From (15.12), it can be observed that $r = 0$ when $\theta_i = 0$, leading to the condition of perfect transmission. This phenomenon is also known as Klein tunneling [2] in the graphene literature [39]. The perfect transmission at normal incidence persists regardless of the energy barrier and the length of the transition region!

It is instructive to note the clear departure from optics in this regard. The transmission and reflection probabilities of an electromagnetic wave at the interface of two linear media (for the case of polarization in the plane of incidence) are described by Fresnel's equation [75]:

$$R = \left(\frac{\alpha - \beta}{\alpha + \beta}\right)^2, \; T = \alpha\beta \left(\frac{2}{\alpha + \beta}\right)^2 \tag{15.13}$$

α and β are defined as

$$\alpha = \frac{\cos\theta_t}{\cos\theta_i}, \; \beta = \frac{\mu_1 v_1}{\mu_2 v_2} \tag{15.14}$$

[2] Klein tunneling is to be distinguished from Klein paradox, see [130] for an interesting historical account of the related Klein paradox.

where μ is the permeability of the medium, and v is the group velocity. From (15.13) and (15.14), we see that perfect transmission occurs when the condition $\alpha = \beta$ is satisfied. The corresponding θ_i when this occurs is not necessarily zero and is called the Brewster angle, i.e., $\theta_B \approx n_2/n_1$. This fact is used in lasers for the construction of Brewster windows to enhance laser intensity by tilting the interface so that the laser incident at θ_B. For graphene, $\theta_B = 0$ due to Klein tunneling. A tilted graphene pn interface could also similarly enhance transmission of the modes coming at its θ_B [43].

Lastly, we shall compute the conductance of a symmetric pn junction. The transmission probability as a function of the incident angle is given by $\cos^2(\theta_i)$ or is alternatively written as $1 - k_y^2/k_f^2$. The junction conductance is then [38]

$$\begin{aligned} \mathcal{G}_{np} &= \frac{2q^2}{h} \sum_{ky} 1 - \frac{k_y^2}{k_f^2} = \frac{4q^2}{h} \frac{W}{2\pi} \int_{-kf}^{kf} 1 - \frac{k_y^2}{k_f^2} \mathrm{d}k_y \\ &= \frac{2q^2}{h} \frac{2M}{3} = \frac{2}{3} \mathcal{G}_{nn} \end{aligned} \tag{15.15}$$

where $M \equiv \frac{1}{\pi} 2Wk_f$ is the number of transverse modes (not including spin degeneracy) in the unbiased graphene nn counterpart. Now, consider the limit where the p side (see Fig. 15.2a) is electrically doped heavily, then the pseudospin direction could be approximated to be along x. In this case, it could be shown that the transmission probability as a function of the incident angle is given by $\cos^2(\theta_i/2)$. The junction conductance is then [38]

$$\mathcal{G}_{np} = \frac{2q^2}{h} \sum_{ky} \frac{1}{2} + \frac{\sqrt{k_f^2 - k_y^2}}{2k_f} = \left(\frac{1}{2} + \frac{\pi}{8} \right) \mathcal{G}_{nn} \tag{15.16}$$

Therefore, the conductance of an abrupt np junction would always be less than that of its unbiased counterpart, i.e., $\mathcal{G}_{np} < \mathcal{G}_{nn}$.

15.2.3 Tunneling for Dirac and Schrödinger Fermions

In experimental graphene pn junction devices, the pn transition length is finite and is dictated by the charge screening in the vicinity of the junction [76]. Here, we shall consider a simplified case where the potential is linear, instead of a step, as shown in Fig. 15.3a. In this limit, the semiclassical results for the tunneling probability could then be derived across such a junction based on the Wentzel–Kramers–Brillouin (WKB) approximation. In fact, it is known that the WKB approximation is exact if the potential is perfectly linear. However, in reality, the actual potential profile resembles more of a graded step potential. For example, Fig. 15.3b shows the

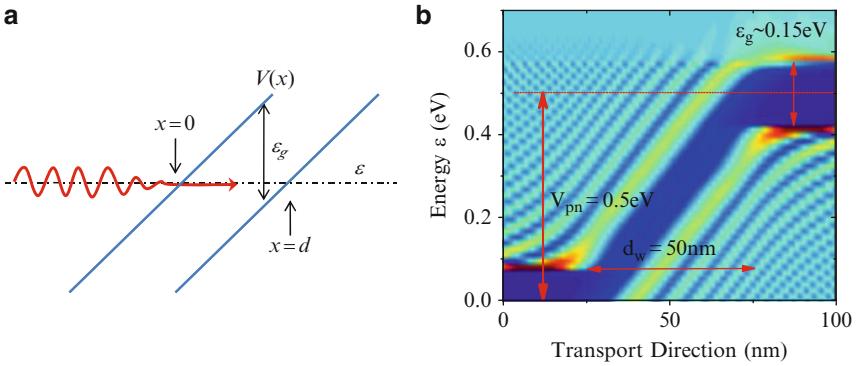

Fig. 15.3 (**a**) Illustration of electron transport through a linearly graded *pn* junction. ϵ_g is the apparent energy gap due to the finite transverse momentum k_y. d is the tunneling distance. (**b**) Energy-resolved local density of states (LDOS) for a graded step junction in graphene. Color scheme: *Blue (red) color* denotes low (high) intensity. (Fig. (b) adapted from [38])

energy-resolved local density of states (LDOS) of such a graded step potential. We defer the study of conductance through such a junction to Sect. 15.2.5.

Figure 15.3a illustrates the energy band as seen by a Dirac particle at some nonzero transverse momentum k_y that is undergoing the tunneling process. The finite k_y leads to an apparent energy gap of $\epsilon_g = 2\epsilon_y = 2\hbar v_f k_y$. By simple conservation of energy, a semiclassical equation could be generated that relates the total, kinetic and potential parts as follows:

$$\epsilon - V(x) = \hbar v_f \sqrt{k_x^2 + k_y^2} \tag{15.17}$$

$$V(x) = q\xi x + \epsilon - \epsilon_y/2 \tag{15.18}$$

where ξ is the electric field. From (15.17), the x component of the momentum $\mathbf{p} \equiv \hbar\mathbf{k}$ can be written as

$$p_x = \sqrt{\left(p_y - q\xi x/v_f\right)^2 - p_y^2} \tag{15.19}$$

where, at the classical turning point $x = 0$, $p_x = 0$ is obtained. The second occurs at $x = d$, as shown in Fig. 15.3a, where $d = \epsilon_g/\xi$. The WKB tunneling probability can be computed from $T = \exp(-2S)$, where S is the action integral defined as

$$S \equiv \frac{1}{\hbar}\int_0^d p_x \mathrm{d}x = \frac{\epsilon_g^2}{4\hbar v_f q\xi}\int_{-1}^{1}\sqrt{1-y^2}\mathrm{d}x = \frac{\epsilon_y^2\pi}{2\hbar v_f q\xi} \tag{15.20}$$

This result had been obtained for massive Dirac Fermions, studied in the context of semiconductor tunneling diodes [77] and recently in the graphene *pn* junction [37]. We note that $T = 1$ for carriers incident normally at the *pn* interface, i.e., $k_y = 0$,

which is an obvious result from WKB because the normally incident mode has no apparent bandgap (i.e., no classically forbidden region).

It would be interesting to compare the result obtained for Dirac Fermions with that of the Schrödinger Fermions counterpart. The result for a zero bandgap material with an effective mass m gives the following action integral:

$$S = \frac{2\sqrt{2m}}{3\hbar q\xi}\left(\epsilon_0 + \epsilon_g\right)^{\frac{3}{2}} \tag{15.21}$$

where ϵ_0 is the bandgap of the material, and ϵ_g is defined similarly as above. To make a comparison with graphene, we assume that $\epsilon_0 = 0$. Interestingly, Dirac Fermions exhibit a stronger angular dependence than their Schrödinger Fermions counterpart, with $S \propto (k_y)^2$ versus $S \propto (k_y)^{1.5}$. This implies that the pn junction would lead to stronger conductance modulation for Dirac Fermions. However, to be competitive with conventional semiconductor materials, it should still be complemented with a finite ϵ_0 in graphene through methods such as sublattice asymmetry through an underlying substrate [21] or bilayer [78]. The effects of band parameters are embodied in v and m for the Dirac and Schrödinger cases. Apart from these differences, both cases depend inversely on the strength of the electric field.

It would be instructive to make a connection between (15.20) and the Landau Zener formula [79, 80]. We begin by writing the Hamiltonian for the problem,

$$\mathcal{H}\Psi = \left(v_f\sigma_x P_x + v_f\sigma_y P_y + V(x)\right)\Psi = \epsilon\Psi \tag{15.22}$$

Performing a unitary transformation on (15.22) using $\frac{1}{\sqrt{2}}\left(I + i\sigma_y\right)$ and multiplying by σ_z, one obtains

$$v_f P_x \Psi = \left[\left(\epsilon - V(x)\right)\sigma_z + i v_f P_y \sigma_x\right]\Psi \tag{15.23}$$

By making the change in the variable $x \to t$, one arrives at

$$\mathrm{i}\hbar\frac{\partial}{\partial t}\Psi = \begin{bmatrix} \left(V(t) - \epsilon\right)/v_f & -\mathrm{i}\hbar k_y \\ -\mathrm{i}\hbar k_y & \left(\epsilon - V(t)\right)/v_f \end{bmatrix}\Psi \tag{15.24}$$

To make the connection to (15.20), we let $V(t) = q\xi t$. Then based on the Landau Zener model, the probability for transition is

$$P = \exp\left[-\frac{2\pi\left(\hbar k_y\right)^2}{\hbar\left(2\partial_t V/v_f\right)}\right] = \exp\left(-\frac{\epsilon_y^2\pi}{\hbar v_f q\xi}\right) \tag{15.25}$$

which is exactly the result obtained in (15.20). In the Landau Zener transition, ξ represents the rate at which the electron/hole energies ($\pm\epsilon$) cross each other. A larger ξ would therefore translate to a higher probability of transition P.

Lastly, we would like to compute the pn junction conductance. Let us consider again a symmetric pn junction and that the Fermi energy on the far left/right of the junction is well defined, say ϵ_F. This translates to a built-in potential of $V_{pn} = 2|\epsilon_F|$, as shown in Fig. 15.3b. The substitution of $q\xi = 2\epsilon_F/d_w$ can be made, where d_w is known as the pn transition length (see Fig. 15.3b). This allows us to rewrite the tunneling probability as

$$T = \exp(-\gamma d_w k_y^2/k_f) \tag{15.26}$$

where $\gamma = \pi/2$. The junction conductance is then

$$\begin{aligned}\mathcal{G}_{np} &= \frac{4q^2}{h}\frac{W}{2\pi}\int_{-kf}^{kf}\exp(-\gamma d_w k_y^2/k_f)\mathrm{d}k_y \\ &= \mathcal{G}_{nn}\left(2k_f d_w\right)^{-\frac{1}{2}} erf\left(\sqrt{\gamma d_w k_f}\right)\end{aligned} \tag{15.27}$$

For typical electrostatic doping of say $\epsilon_F = 0.2\,\mathrm{eV}$, we get $k_f \approx 3\times 10^8\,\mathrm{m}^{-1}$. A pn transition length of $10-100\,\mathrm{nm}$ would easily satisfy the inequality $d_w k_f \gg 1$. Thus, $\mathcal{G}_{np}$ is just inversely proportional to $\sqrt{k_f d_w}$ [37]. Assuming some typical experimental numbers, $\epsilon_F = 0.2\,\mathrm{eV}$ and $d_w = 100\,\mathrm{nm}$, we obtain $\mathcal{G}_{np} \approx 0.13\mathcal{G}_{nn}$. Therefore, the conductance modulation with the pn junction is typically an order of magnitude.

15.2.4 Quantum Transport Modeling

In the last two sections, we discussed the quantum transport problem across a step potential and a linear potential. In realistic experimental devices, the potential profile resembles more of a graded potential step, as shown in Fig. 15.3b. Supposing that the potential profile $V(x)$ is known a priori, there is a general scheme to compute the quantum conductance of the pn junction [38]. The objective of this section is to provide an outline of such a method, based on the nonequilibrium Green function approach, see [81–84] and references therein. Hence, we constrain ourselves to a concise description of the method.

The Hamiltonian is formulated by treating only the nearest neighbor interaction between p_z orbitals [73]. By taking the width to be large so that we can impose a periodic boundary condition along the width, the Hamiltonian is then written as ($2N_x \times 2N_x$ matrix)

$$\mathcal{H} = \begin{bmatrix} \alpha & \beta_1 & & \\ \beta_1^\dagger & \alpha & \beta_2 & \\ & \beta_2^\dagger & \alpha & \ddots \\ & & \ddots & \ddots \end{bmatrix} + \mathcal{V} \tag{15.28}$$

where $\mathcal{V}$ is just the lattice representation of $V(x)$, while α, β_1 and β_2 are all 2×2 matrices given by

$$\alpha = \begin{bmatrix} 0 & t \\ t & 0 \end{bmatrix} \beta_1 = \begin{bmatrix} 0 & 0 \\ t_y^\dagger & 0 \end{bmatrix} \beta_2 = \begin{bmatrix} 0 & 0 \\ t_y & 0 \end{bmatrix} \tag{15.29}$$

where $t \approx 3\,\mathrm{eV}$, and $t_y{=}t + t\mathrm{e}^{\mathrm{i}k_y a}$. The lattice parameter is $a{=}\sqrt{3}b$, where $b{=}1.44\text{Å}$ is the c–c bond distance. k_y is a quantum number for the quantized transverse momentum. To account for the semiinfinite boundary condition of $\mathcal{H}$, we need to compute the left/right surface Green's function, i.e., $g_{\mathrm{L/R}}$. For the left side, we have

$$\begin{aligned} g_L &= \left[(\epsilon_f + \mathrm{i}\eta)\mathcal{I} - \mathcal{V}_L - \alpha - \beta_2^\dagger \tilde{g} \beta_2\right]^{-1} \\ \tilde{g} &= \left[(\epsilon_f + \mathrm{i}\eta)\mathcal{I} - \mathcal{V}_L - \alpha - \beta_1^\dagger g_L \beta_1\right]^{-1} \end{aligned} \tag{15.30}$$

where η is a small real number. Equation (15.30) can be solved iteratively using a procedure outlined in [85]. g_R can be obtained in a similar fashion.

The central quantity of the quantum transport theory, the retarded Green function, is written as

$$G_{ky} = \left[(\epsilon_f + \mathrm{i}\eta)\mathcal{I} - \mathcal{H} - \mathcal{V} - \Sigma_{\mathrm{L}} - \Sigma_{\mathrm{R}}\right]^{-1} \tag{15.31}$$

where $\Sigma_{\mathrm{L/R}}$ is commonly known as the contact's self energy [81]. For example, Σ_{L} is defined as follows:

$$\Sigma_{\mathrm{L}} = \begin{bmatrix} \beta_2^\dagger g_L \beta_2 & & & \\ & 0 & & \\ & & 0 & \\ & & & \ddots \end{bmatrix} \tag{15.32}$$

and in a similar fashion for Σ_{R}. Finally, the current through contact i can then be computed using

$$I_i(\epsilon) = \frac{2q}{h} \sum_{k_y} \mathrm{Tr}\left[\Sigma_i^{in}(\epsilon)\mathcal{A}(\epsilon) - \Gamma_i(\epsilon) G^n(\epsilon)\right] \tag{15.33}$$

where $\mathcal{A}{=}i\,(G - G^\dagger)$ is the local density-of-states, $\Sigma_i^{in}{=}f_0(\epsilon)\Gamma_i(\epsilon)$ is the filling function (analogous to the in-scattering function for the incoherent case), $f_0(\epsilon)$ is the Fermi function of the contacts and $\Gamma_i{=}i\,(\Sigma_i - \Sigma_i^\dagger)$ is the contact broadening factor. In (15.33), $G^n(\epsilon)$ is the electron correlation function given by $G(\Sigma_l^{in} + \Sigma_r^{in})G^\dagger$. Note that $G^n \equiv -i\,G^<$ [81–84]. Usually, the sizes of the G matrices are computationally prohibitive for their inverses to be sought directly. Hence, G and

G^n are usually computed using a technique known as the "recursive Green function algorithm." This technique exploits the special properties of the tridiagonal nature of $\mathcal{H}$ through the use of Dyson's equation. See, for example, [86] for a nice tutorial-style discussion of this numerical technique.

Finally, before we conclude this section, we make some remarks about the choice of k_y. Usually, the widths of the experimental devices are large, such that k_y are just multiples of π/W. However, a more accurate choice of k_y that reflects the actual hard-wall boundary condition of a nanoribbon can be sought. By assuming an armchair edge and imposing a box-boundary condition, the Dirac equation yields the following [87]:

$$k_y = \left(\frac{2\pi}{3a} + \frac{2\pi n}{2W + a}\right) \pm \frac{2\pi}{3a} \tag{15.34}$$

for all integers n and with W as the width of the device. The last term accounts for the momentum of the Dirac points, **K** and **K**′, where the upper/lower sign is used when n is even/odd, respectively. With this choice of k_y, the method outlined in this section matches excellently with the exact real-space approach [38], even for ribbons of very narrow width.

15.2.5 Experiments: Asymmetry and odd Resistances

Several research groups have recently fabricated graphene pnp devices by using electrostatic gates to create p and n regions [34–36]. The typical setup consists of a back gate and a top gate, which are used to control the amounts of charge density in different regions of the graphene. Figure 15.4a illustrates the experimental

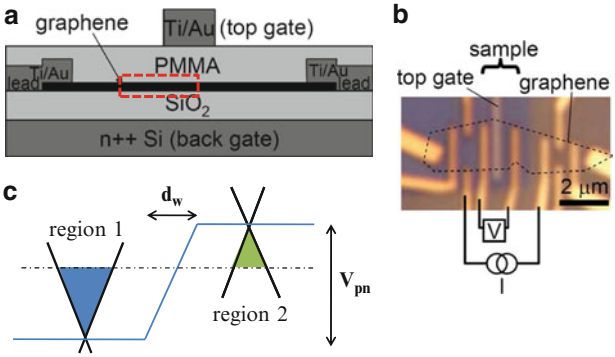

Fig. 15.4 (**a**) A typical experimental layout of the graphene *pn* junction device, where graphene is sandwiched between two insulator–metal structures, i.e., top/bottom gates. (**b**) An optical image of the fabricated device. (**c**) Illustration of the energy band in graphene for the region highlighted in (**a**). The Fermi energy is set by the chemical potential of the metal contacts. (Figs. (**a**) and (**b**) are adapted from [36])

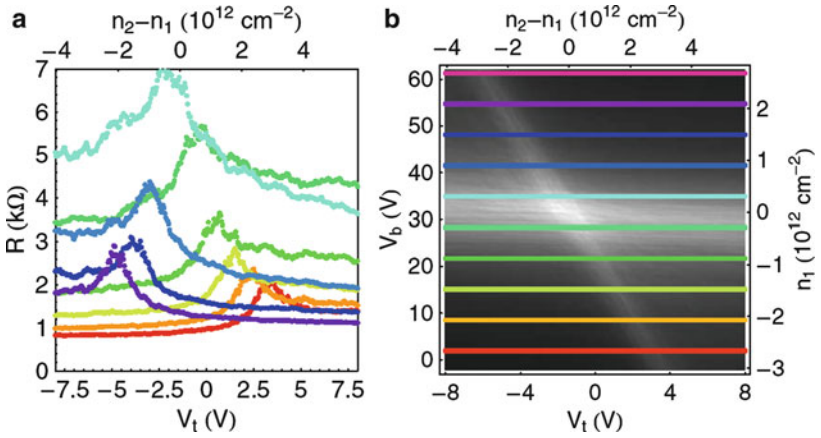

Fig. 15.5 (**a**) Measured resistance of the graphene sample at $4K$ as a function of the top-gate voltage for different values of back-gate voltages. (**b**) Two-dimensional plot of the same resistance as a function of both gate voltages, where the various colored cuts correspond to the respective traces in (**a**). (Figs. are adapted from [36])

structure employed in [36]. We define region 2 to be underneath the top-gate, and region 1 for the remaining part of graphene (see Fig. 15.4c). Electrostatic of region 1 is controlled by both top/bottom gates, while region 2 by back gate only. An asymmetry in the device's source to drain resistance as a function of the top-gate voltage has been experimentally observed [36], as shown in Fig. 15.5. The amount of this resistance asymmetry is a measure of the difference in resistance between the pn junction and its pp counterpart. For recent experiments [36], typical transition lengths for the pn junction are less than 100 nm. Recent experiments indicate that the carrier's mean free path is about 100 nm under low temperatures and moderate carrier density conditions of $10^{12}\,\mathrm{cm}^{-2}$ [88]. Therefore, a ballistic transport model should suffice for the study of the experimental pn junction devices reported in [36]. The objective of this section is to understand this experiment using the methods we have developed in the previous sections.

Following [36], we can divide the resistance of the device into odd and even parts as follows:

$$\begin{aligned} R_{n1}(n_2) &= R_{n1}^{\mathrm{even}}(n_2) + R_{n1}^{\mathrm{odd}}(n_2) \\ R_{n1}^{\mathrm{even}}(n_2) &= \tfrac{1}{2}\left(R_{n1}(n_2) + R_{n1}(-n_2)\right) \\ R_{n1}^{\mathrm{odd}}(n_2) &= \tfrac{1}{2}\left(R_{n1}(n_2) - R_{n1}(-n_2)\right) \end{aligned} \tag{15.35}$$

where n_1/n_2 refers to the electron densities in regions $1/2$ of the device, as shown in Fig. 15.4. The electron densities are related to the top-/bottom-gate voltages (V_{tg}/V_{bg}) through simple electrostatics, i.e., $qn_1 = C_b V_{bg} + n_1^0$ and $qn_2 = qn_1 + C_t V_{tg} + n_2^0$, as the chemical potential of the device is ≈ 0 in this setup. In the

experiment, region 2 is long enough such that we can regard $R_{n1}(n_2)$ as the sum of two pn junction resistances and the channel resistance. The channel resistance only contains the R_{n1}^{even} contribution, provided that the scattering processes and electronic bandstructure retain the electron/hole symmetry. The pn junction resistance instead has both R_{n1}^{even} and R_{n1}^{odd} contributions. Theoretically, the resistance of a pn junction could be computed and its R_{n1}^{odd} contribution extracted. By doing so, we would be able to connect the theory to experiments.

An important quantity is the pn transition length d_w, which has to be determined prior to our calculations. The determination of d_w is an electrostatics problem that is sensitive to the specific device geometry. In this work, we used a screening model presented in [76], which expresses d_w in terms of n_1 and n_2 as follows:

$$d_w \approx 0.196 \times \frac{V_{pn}}{\hbar v_f \alpha^{1/3}} \left(1 - \frac{n_2}{n_1}\right)^{\frac{4}{3}} \left|\frac{T_{ox}}{n_2}\right|^{\frac{2}{3}} \tag{15.36}$$

where $\alpha = \mathrm{e}^2/(\kappa\hbar v_f)$. κ and T_{ox} are the effective dielectric constant and thickness of the top gate oxide, respectively. V_{pn} is the built-in potential of the pn junction, which can be easily calculated from n_1 and n_2.

Figure 15.6a plots the R_{n1}^{odd} of the resistances of Fig. 15.5. Figure 15.6b shows a comparison between the theory and the experiments, using the quantum transport model described in Sect. 15.2.4. Besides the quantitative agreement, a general interesting trend of increasing R_{n1}^{odd} as n_1 decreases can also be observed. This is

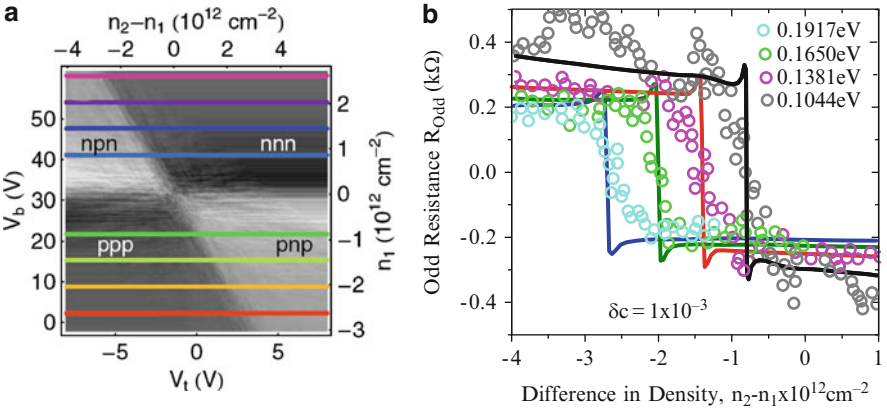

Fig. 15.6 (**a**) The extracted odd resistance R_{odd} from Fig. 15.5 [36]. (**b**) Comparison of the numerically calculated R_{odd} with the experimental results in [36] at different carrier densities of n_1, expressed in $E_f = (\pi\hbar^2 v_f^2 n_1)^{0.5}$, as shown in the inset. The device width is 1.7μm, and the operating temperature is 4 K. In the simulations, the contacts are assumed to have an energy broadening of $\delta_c = 1$ meV, which is included in the model through the parameter η. The calculations assumed $\alpha = 0.78$ due to a κ of 4.5 [36] and an oxide thickness of $T_{ox} \approx 80$ nm as a fitting parameter. The experimental data used here corresponds to the 4 traces in the npn and nnn regimes. (Figs. (**a**) and (**b**) adapted from [36] and [38] respectively)

explained as an increase in d_w as n_1 is reduced, indicating that proper treatment of d_w is the key to quantitative modeling of the graphene pn junction. If we make a gross assumption that $d_w \approx 0$, the back-of-the-envelope calculations would yield $R_{n1}^{\text{odd}} = \frac{1}{2} R_{n1}(n_2 = n_1)$, where $R_{n1}(n_2 = n_1)$ is the resistance of an unbiased graphene. This would only account for $\approx 10\%$ of the observed values as seen in the experiments.

Lastly, it is important to note that the quantity R_{n1}^{odd} in this experiment does not include the asymmetry due to the possible pn junction at the contacts, as recently observed in experiments [72]. This is because the top gate in this experiment only modulates n_2 and does not modulate the pn junction at the contacts, which are located a few electron mean free paths away.

15.3 Transport in the Presence of Magnetic Fields

In this section, we extend our previous discussion to include the effects of a magnetic field. We consider first the case of a graphene pn junction in a weak magnetic field in Sect. 15.3.1, comparing the positive magnetoresistance observed in experiments [40,41,89] with that of theory. Section 15.3.2 introduces the concepts of edge states, snake states, and valley isospins in preparation for the discussion of transport in the quantum Hall regime. In the absence of disorder, we show that the transport across a graphene pn junction is dictated by its valley isospin number in Sect. 15.3.3. Description of the experimental situation, however, requires the inclusion of various types of disorders. In Sect. 15.3.4, we study the experiments on the graphene pn junction in the quantum Hall regime [34]. Here we explain why edge disorder, in addition to pn interface disorder, is necessary to explain the experiments' new plateaus. In several instances, quantum simulations are employed (see 15.4.2 for description of the method).

15.3.1 Weak Magnetic Field Regime

Here, we seek the pn junction's conductance in the presence of a weak magnetic field, i.e., a nonquantum Hall regime. The Dirac equation for our transport problem is

$$\begin{aligned} \mathcal{H}\Psi &= \left(v_f \sigma_x P_x + v_f \sigma_y P_y + V(x)\right) \Psi = \epsilon \Psi \\ \Rightarrow v_f P_x \Psi &= \left[(\epsilon - V(x))\, \sigma_z + i v_f P_y \sigma_x\right] \Psi \end{aligned} \tag{15.37}$$

The second equation of (15.37) was obtained in the same way as (15.23). In the presence of magnetic field B, we make the replacement of $P_y \Rightarrow P_y - qBx$. Again, we describe the pn junction by a linear potential profile given by $V(x) = q\xi x$. Then from (15.37), the momentum operator P_x can be expressed as follows:

$$P_x = \begin{bmatrix} \hbar k_f - \alpha x & \mathrm{i}(\hbar k_y - \beta x) \\ \mathrm{i}(\hbar k_y - \beta x) & \alpha x - \hbar k_f \end{bmatrix} \tag{15.38}$$

where $\alpha = q\xi / v_f$, and $\beta = qB$. After diagonalizing P_x, the eigenvalues are found to be

$$p_x(x) = \pm \sqrt{(\hbar k_f - \alpha x)^2 - (\hbar k_y - \beta x)^2} \tag{15.39}$$

The classical turning point, i.e., $p_x = 0$, occurs at

$$x_{\mp} = \frac{\hbar(k_f \mp k_y)}{\alpha \mp \beta} \tag{15.40}$$

The WKB tunneling probability is then computed from $\exp(-2S)$, where

$$S = \frac{1}{\hbar} \int_{x_-}^{x^+} p_x(x) \mathrm{d}x = \pi \hbar \frac{(k_y \alpha - k_f \beta)^2}{2(\alpha^2 - \beta^2)^{3/2}} \tag{15.41}$$

One could easily check that (15.41) yields (15.20) when $B = 0$ ($\beta = 0$). The junction conductance is given by

$$\begin{aligned} \mathcal{G}_{np} &= \frac{4q^2}{h} \frac{W}{2\pi} \int_{-kf}^{kf} \exp\left(-\pi \hbar \frac{(k_y \alpha - k_f \beta)^2}{(\alpha^2 - \beta^2)^{3/2}} \right) \mathrm{d}k_y \\ &\approx \frac{4q^2}{h} \frac{W}{2\pi} \left[\frac{\sqrt{\pi}(\alpha^2 - \beta^2)^{3/4}}{\alpha \sqrt{\pi \hbar}} \right] \\ &= \frac{4q^2}{h} \frac{W}{2\pi} \sqrt{\frac{q\xi}{v_f \hbar}} \left[1 - \left(\frac{B v_f}{\xi} \right)^2 \right]^{3/4} \\ &= \mathcal{G}_{nn} (2k_f d_w)^{-\frac{1}{2}} \left[1 - \left(\frac{B v_f}{\xi} \right)^2 \right]^{3/4} \\ &\equiv \mathcal{G}_{np}^0 \left[1 - \left(\frac{B v_f}{\xi} \right)^2 \right]^{3/4} \end{aligned} \tag{15.42}$$

where $\mathcal{G}_{np}^0$ is the junction's conductance when $B = 0$, as depicted in (15.27). The approximation in the second line of (15.42) involves identifying that the inputs to the error functions are $\gg 1$. The fourth line of (15.42) involves making the substitution of $q\xi = 2\epsilon_{\mathrm{F}} / d_w$, which is done in a similar spirit as the derivations of (15.27), i.e., for the symmetric pn junction case. These results are as obtained in [90].

Experiments on pn junctions in the presence of a weak magnetic field are reported in [41, 89]. Here we again study the odd resistance $R_{n1}^{\text{odd}}(n_2)$, as previously done in Sect. 15.2.5 (using the same notations as before). To make contact with the experiments, we consider only the symmetric pn junction case, i.e., $R_{n1}^{\text{odd}} \equiv R_{n1}^{\text{odd}}(n_2 = n_1)$. It is reasonable to assume that $\mathcal{G}_{nn} \gg \mathcal{G}_{pn}$, at least for the experiments in [89]. This then leads to the following:

$$(2R_{n1}^{\text{odd}})^{-1} = \left(\mathcal{G}_{np}^{-1} - \mathcal{G}_{nn}^{-1}\right)^{-1} \approx \mathcal{G}_{np} \tag{15.43}$$

The quantity $(2R_{n1}^{\text{odd}})^{-1}$ was measured experimentally [89] and compared to $\mathcal{G}_{np}$ of (15.42), as shown in Fig. 15.7a. The electric field ξ of (15.42) is related to n_1 via $q\xi = 2\hbar v_f \sqrt{\pi n_1}/d_w$. A comparison between the WKB theory and the experiments shows that the effect of $\mathcal{G}_{np}$ modulation due to B corroborates with the experiment at a low magnetic field. In the WKB theory, $\mathcal{G}_{np} = 0$ when $B = \xi/v_f$, which clearly is the regime in which the theory breaks down (edge conduction is not included in the WKB theory). Therefore, (15.42) is only rigorously valid when $B \ll \xi/v_f$, beyond which the edge conduction of the device starts to play an important role. Figure 15.7b shows a numerical calculation (quantum transport using the tight binding model; see [56]) for a $W = 100$ nm device under somewhat similar electrostatic conditions (the value of d_w used is different from that of Fig. 15.7a). The edge conduction contribution is automatically included in the numerical calculations. Clearly, $\mathcal{G}_{np}$ is not zero as B increases beyond ξ/v_f, and its value depends on many physical factors. We will explore these factors in the next section.

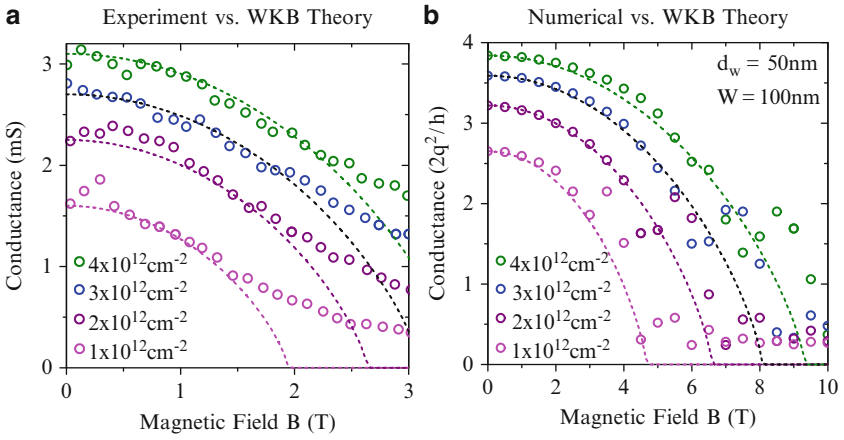

Fig. 15.7 (a) Experimentally measured $(2R_{n1}^{\text{odd}})^{-1}$ of a symmetric pn junction, i.e., $n_1 = -n_2$, at various concentrations n_1, shown in symbols. The dashed lines are the results computed from (15.42), where $\mathcal{G}_{np}^0$ is used as a fitting parameter for each case (see text). The pn transition widths for each curve are assumed to be 120 nm, 125 nm, 130 nm and 135 nm for increasing values of n_1. (b) Numerically simulated $\mathcal{G}_{np}$ at various concentrations n_1, shown in symbols. The dashed lines are again the results computed from (15.42)

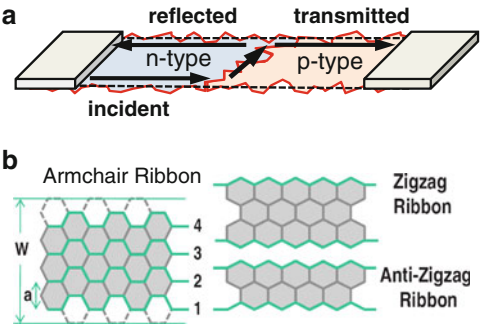

Fig. 15.8 (**a**) Illustration of a graphene *pn* junction with edge and interface disorder The edge and snake currents are also indicated. (**b**) Illustration of armchair, zigzag and anti-zigzag edge ribbons. The carbon layer numbering convention for an armchair edge ribbon used in this work is also depicted

15.3.2 Edge States, Snake States, and Valley Isospin

In the presence of a uniform normal magnetic field, the energy dispersion $\epsilon(k)$ develops plateau structures around the $\mathbf{K}/\mathbf{K}'$ valleys. These energy plateaus are known as Landau levels and are given by $\epsilon_n^{LL} = \text{sign}(n)\hbar\omega\sqrt{|n|}$ (where n is an integer), which is obtained by diagonalizing $\mathcal{H} = v_f\boldsymbol{\sigma}\cdot(\mathbf{P} + e\mathbf{A})$ [91], where $\mathbf{A} = (0, Bx)$. ω is the cyclotron frequency given by $\omega = \sqrt{2}v_f/\ell_B$, where $\ell_B = \sqrt{\hbar/(Bq)}$ is the magnetic length. When $\hbar\omega$ is greater than other energy scales of the system, the quantization described by the Landau levels translates into quantum Hall conductance plateaus given by $\mathcal{G} = 2q^2/h|2n + 1|$, as seen experimentally [6, 7]. It is convenient to define a quantity called the "filling factor" denoted by ν, which is the number of edge states participating in transport along each edge. Including spin degeneracy, it is given by $\nu = 2|2n + 1|$. In the quantum Hall regime, the current conduction is mediated by edge states, and their wavefunctions reside along the two edges of the system. How does current flow across the *pn* junction in this regime?

Figure 15.8a illustrates the current flow in a graphene *pn* junction in the quantum Hall regime. The edge current is incident on the *pn* interface and then transverses along it before splitting both ways (towards the source/drain) at the other edge. The state along the *pn* interface is usually known as the "snake state" in the literature, as its classical orbit resembles a snake [11]. Therefore, this is in contrast to the weak magnetic regime, where current is allowed to transmit across the *pn* interface. What determines the amounts of the reflected and transmitted components? In the remainder of this section, we will show how the amounts of the reflected and transmitted components can be calculated for a graphene ribbon with no disorder. To obtain such results, we have to introduce the concept of valley isospin [3]. Here, the basis are the $\vec{K}(\vec{K}')$ valleys in contrast to the A/B sublattice for pseudospin case.

[3] "isospin" used in this context has nothing to do with "isospin" in particle physics.

We write the Dirac equation for graphene as

$$H\Psi = \begin{bmatrix} v_f \vec{p}\cdot\vec{\sigma} & 0 \\ 0 & v_f \vec{p}\cdot\vec{\sigma} \end{bmatrix} \Psi \tag{15.44}$$

where $\Psi = (\psi_A, \psi_B, -\tilde{\psi}_B, \tilde{\psi}_A)$ and $\psi(\tilde{\psi})$ for the $\vec{K}(\vec{K}')$ valley wavefunction. We are interested in Ψ along the ribbon's edges. It is a convenient convention to write Ψ along the edges in the following form:

$$\Psi = \left(\vec{v}\cdot\vec{\tau}\right) \otimes \left(\vec{n}\cdot\vec{\sigma}\right) \Psi \tag{15.45}$$

where $\vec{v}$ is the "edge's valley isospin" (for Ψ along the edges), and $\vec{\tau}$ and $\vec{\sigma}$ are just the Pauli matrices for the isospin and pseudospin part respectively. $\vec{n}$ depends on the edge type, i.e., $\vec{n} = (0, 0, 1)$ for the zigzag and $\vec{n} = (\pm 1, 0, 0)$ for the bottom/top edges of armchair ribbons [11]. Equation (15.45) effectively expresses the boundary conditions of the edges.

We consider an armchair ribbon where the two edges are at $y = y_{\mathrm{T}}$ (top) and $y = y_{\mathrm{B}}$ (bottom). Along $y = y_{\mathrm{T}}$, the wavefunction $\Psi = (\psi_A, \psi_B, -\tilde{\psi}_B, \tilde{\psi}_A)$ must satisfy the boundary conditions [87],

$$\psi_A + \tilde{\psi}_A \mathrm{e}^{-\mathrm{i}\Delta y_{\mathrm{T}}} = 0 \tag{15.46}$$

$$\psi_B + \tilde{\psi}_B \mathrm{e}^{-\mathrm{i}\Delta y_{\mathrm{T}}} = 0 \tag{15.47}$$

where $\Delta = 4\pi/3a$, and a is the lattice constant of graphene. We can rewrite (15.47) in the form of $\Psi = M\Psi$, where

$$M = \begin{bmatrix} 0 & -\mathrm{e}^{-\mathrm{i}\Delta y_{\mathrm{T}}} \\ -\mathrm{e}^{\mathrm{i}\Delta y_{\mathrm{T}}} & 0 \end{bmatrix} \otimes \begin{bmatrix} 0 & 1 \\ 1 & 0 \end{bmatrix} \tag{15.48}$$

With some matrix algebra, we can show that

$$M = \left(\vec{v}_{\mathrm{T}}\cdot\vec{\tau}\right) \otimes \left(\vec{n}_{\mathrm{T}}\cdot\vec{\sigma}\right) \tag{15.49}$$

by defining $\vec{v}_{\mathrm{T}}$=$(\cos(\Delta y_{\mathrm{T}}), \sin(\Delta y_{\mathrm{T}}), 0)$ and $\vec{n}_{\mathrm{T}}$=$(-1, 0, 0)$. Repeating this procedure for y_{B}, we require $\vec{v}_{\mathrm{B}}$=$(-\cos(\Delta y_{\mathrm{B}}), -\sin(\Delta y_{\mathrm{B}}), 0)$ and $\vec{n}_{\mathrm{B}}$=$(1, 0, 0)$. It is straightforward to see that

$$\vec{v}_{\mathrm{T}}\cdot\vec{v}_{\mathrm{B}} = \cos\left(\Delta W + \pi\right) \equiv \cos(\theta) \tag{15.50}$$

where $W = y_{\mathrm{T}} - y_{\mathrm{B}}$=$a(l + \frac{1}{2})$, and l is the number of carbon layers.

Next, the assumption is made that the ground state LL's wavefunction, denoted by $|0\rangle$, could be approximated by the edge wavefunctions [71]. This allows the wavefunction overlap between the ground state LL's wavefunction along the top/bottom edges to be written as

$$\begin{aligned}\langle 0_{\mathrm{T}}|\ 0_{\mathrm{B}}\rangle &\approx \langle \Psi_T|\ \Psi_B\rangle \\ &= \left(|a|^2+|b|^2\right)\left(1+\vec{v}_{\mathrm{T}}\cdot\vec{v}_{\mathrm{B}}+\vec{v}_{\mathrm{T}}\times\vec{v}_{\mathrm{B}}\right)\end{aligned} \tag{15.51}$$

where we denote $(\psi_A, \psi_B) = (a, b)$, and $(\tilde{\psi}_A, \tilde{\psi}_B)$ is obtained through (15.45). By using the fact that $|a|^2 = |b|^2 = \frac{1}{4}$, we finally arrive at

$$|\langle 0_{\mathrm{T}}|\ 0_{\mathrm{B}}\rangle|^2 \approx \tfrac{1}{2}\left(1+\cos\theta\right) \tag{15.52}$$

The conductance plateau for filling factor $(\nu_n, \nu_p) = (2, 2)$ for the armchair ribbon is then given by [71]

$$\mathcal{G}_{np} = 2(1-|\langle 0_{\mathrm{T}}|\ 0_{\mathrm{B}}\rangle|^2) = \begin{cases} 2 & \ell = 3m+1 \\ \frac{1}{2} & \text{otherwise} \end{cases} \tag{15.53}$$

in units of q^2/h, where m is an integer. Note that $\ell = 3m + 1$ is also the same criterion for obtaining a metallic armchair ribbon ($\ell \neq 3m + 1$ yields semiconducting).

For zigzag-type edges, zigzag- and anti-zigzag-type ribbons can be distinguished (see Fig. 15.8a). Although similar width-dependent effects can be observed [71], they cannot be explained by similar valley isospin arguments, which were used for the armchair case. We shall elaborate on this in the next section. The conductance for zigzag-type ribbons is found to be [92]

$$\mathcal{G}_{np} = \begin{cases} 0 & \text{zigzag} \\ 2 & \text{anti-zigzag} \end{cases}. \tag{15.54}$$

Again, (15.54) is only for the filling factor of $(\nu_n, \nu_p) = (2, 2)$.

15.3.3 Quantum Hall Regime: The Ballistic Case

Here, we discuss the *pn* junction conductance in the quantum Hall regime, assuming zero disorder, i.e., perfect edges and *pn* interface. The results presented in this section are obtained from quantum transport numerical calculations (see [56] for the model description). We divide the discussion into armchair and zigzag devices, and connections to the theory presented in previous sections will be made.

Figure 15.9 shows the ballistic conductance of armchair edge-type ribbons as a function of depletion width. The n/p regions are biased at $\epsilon_{fn/fp}$, respectively, and the built-in potential (assumed to be linearly graded across the junction) is given by $\epsilon_{fn} + \epsilon_{fp}$. Figure 15.9a plots the conductance for biasing conditions corresponding to the Landau filling combinations of $(\nu_n, \nu_p) = (2, 2)$. Ribbons with different numbers of carbon layers along the width are considered. These ribbons exhibit

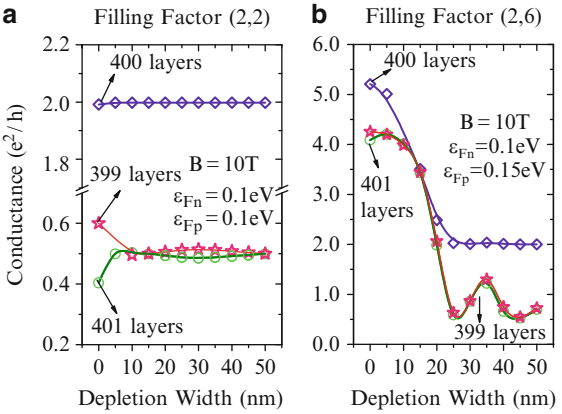

Fig. 15.9 (**a**) Junction conductance as a function of depletion width in the clean limit (i.e., no disorder) for armchair ribbons of different widths for the case of a filling factor of $(2, 2)$. (**b**) Same as (**a**), except for a filling factor of $(6, 2)$. (Figs. adapted from [56])

conductance plateaus of $\frac{1}{2}$ and 2 at sufficiently large depletion widths of > 25 nm. Indeed, these plateaus follow that of (15.53), a consequence of valley isospins. The typical length scales of depletion widths in experiments employing top/bottom gating schemes are usually several times larger than 25 nm [38]. These plateaus will emerge as long as the depletion widths are sufficiently large, regardless of the filling factor combinations. To illustrate this point, Fig. 15.9b plots the case when $(\nu_n, \nu_p) = (6, 2)$; we also checked that these ballistic plateaus remain intact when $(\nu_n, \nu_p) = (6, 6)$. It is observed that an increasing depletion width filters out the higher Landau levels such that only the zeroth-mode Landau edge states conduct through the junction. This is reminiscent of the more well-known filtering action of off-normal transverse modes by a pn junction in the zero magnetic field case [37, 38]. However, the physics in this context is completely different; the former is due to isospin, while the latter is due to pseudospin. Such a phenomenon might find applications in devices that use the Landau levels as information bits [93]. However, pn interface disorder would negate such filtering action.

For zigzag ribbons, a width-dependent effect similar to that described by (15.54) [71] can also be observed. Figure 15.10 shows the intensity plot for the nonequilibrium electron density. In particular, Fig. 15.10b shows the case of a perfect zigzag ribbon, where clearly $\mathcal{G}_{np} = 0$, as predicted by (15.54). However, these ballistic plateaus cannot be explained by the valley isospin argument used for the armchair case [92]. The breakdown of the isospin model occurs because the reflected and transmitted edge states both reside on valleys different from that of the incident state, i.e., $\vec{v}_{n\mathrm{T}} \cdot \vec{v}_{p\mathrm{T}} = \vec{v}_{n\mathrm{B}} \cdot \vec{v}_{p\mathrm{B}} = 1$ [92]. Therefore, current conservation must entail an inherent intervalley scattering process. Hence, another effect stemming from the parity of the wavefunction was invoked to explain these anomalous plateaus. We refer the reader to [92] for a more detailed discussion. We also note the presence of local peaks in the electron density at locations where the pn interface and the ribbon edge meet (see Fig. 15.10b). These are signatures of the intervalley scattering processes that have taken place. Note that these signatures are absent for the armchair ribbon (see Fig. 15.10a). Heuristically speaking, the

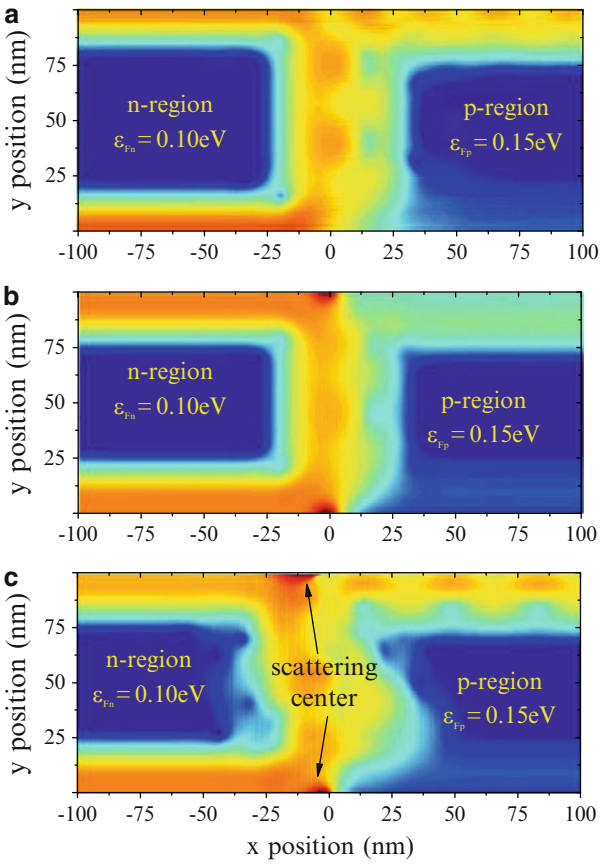

Fig. 15.10 Intensity plot of the nonequilibrium electron density, $log_{10}(n)$, for various ribbons with width $\approx$ 100 nm. We plotted several cases: (**a**) armchair ribbon (no disorder) with 401 carbon layers along the width; (**b**) zigzag ribbon with no disorder; and (**c**) zigzag ribbon with interface disorder. The magnetic field is assumed to be 10 T, while the depletion width is 25 nm. Color scheme: *Blue (red)* denotes low (high) intensity. (Figs. adapted from [56])

propagating states along the *pn* interface can be viewed as similar to that of an armchair edge, where the valley isospin is an equal-weight superposition of the two valleys. The two-times scattering process takes the Landau state from one valley to a superposition and then finally to the other valley. In other words, the valley isospin information of the incident Landau edge state is intrinsically diluted after the first scattering process.

As a concluding remark, we reiterate that the *pn* junction conductances of perfect armchair and zigzag ribbons can be understood in terms of the analytical models described in Sect. 15.3.2, where the concept of valley isospins plays an important role. However, disorder plays an important role in the transport physics in the quantum Hall regime. As depicted in Fig. 15.10c, the introduction of *pn*

interface disorder admits current, while the zero disorder case suppresses current (see Fig. 15.10b). In the next section, we will relax the constraint of a "perfect ribbon" and introduce disorders to the system, i.e., edge and pn interface roughness.

15.3.4 Experiments: Ballistic to Ohmic Transition

To explain the experiments on the pn junction in the quantum Hall regime [34], disorder is key. Several studies on the effect of disorder in this transport regime have been published recently [16, 56, 94, 95]. Figure 15.11 plots the measured junction conductance as a function of the top-/bottom-gate voltages V_{tg}/V_{bg} at $B = 4\,\mathrm{T}$ and $T = 250\,\mathrm{mK}$. Conductance plateaus were observed that registered values other than $2q^2/h|2n+1|$. Depending on whether the device is operating in the unipolar (nn or pp) or bipolar regime (np), these plateaus were found to follow some simple relationships given by [55]:

$$\begin{aligned} \mathcal{G}_{nn} &= \frac{q^2}{h}\min(\nu_1, \nu_2) \\ \mathcal{G}_{np} &= \frac{q^2}{h}\left(\frac{1}{\nu_1}+\frac{1}{\nu_2}\right)^{-1} \end{aligned} \tag{15.55}$$

where $\nu_{1,2}$ refers to the filling factor on the left/right side of the junction. In the experiments, deviations from (15.55) were found, and we will address these deviations later. The relationship for $\mathcal{G}_{nn}$ is rather intuitive and simply states that the unipolar junction's conductance is limited by the junction with the smaller number of modes, i.e., the mode bottleneck effect as previously discussed in Sect. 15.2.2. On the other hand, the relationship for $\mathcal{G}_{np}$ suggests the process of mode-mixing. An intuitive picture of this mode-mixing process can be understood as follows. The total number of modes transversing along the pn interface is $\nu_1+\nu_2$. For each mode injected from the source, the fraction going to the drain would be $\nu_2/(\nu_1+\nu_2)$, as there are ν_2 modes on the drain side. Multiplying by the number of injected modes ν_1, one arrives at (15.55). The purpose of this section is to explore the possible mechanisms for (15.55) to be true.

First, let us consider only pn interface disorder and assume perfect armchair edges. Let us assume the following filling factors $(\nu_n, \nu_p) = (2, 6)$. Here we shall make use of a Chalker–Coddington- [96] type analysis to argue that pn interface disorder alone is not sufficient. This model considers the following facts: (a) in the absence of time reversal symmetry, the electronic states exhibit only unidirectional transmission; (b) the scattering wavefunction follows approximately the equipotential lines of the random potential. The scattering state for a particular spin along the pn interface can be expressed as

$$|\Psi_i\rangle = c_0\,|0_{n\mathrm{B}}\rangle + c_1\,|0_p\rangle + c_2\,|1_p\rangle + c_3\,\left|1'_p\right\rangle \tag{15.56}$$

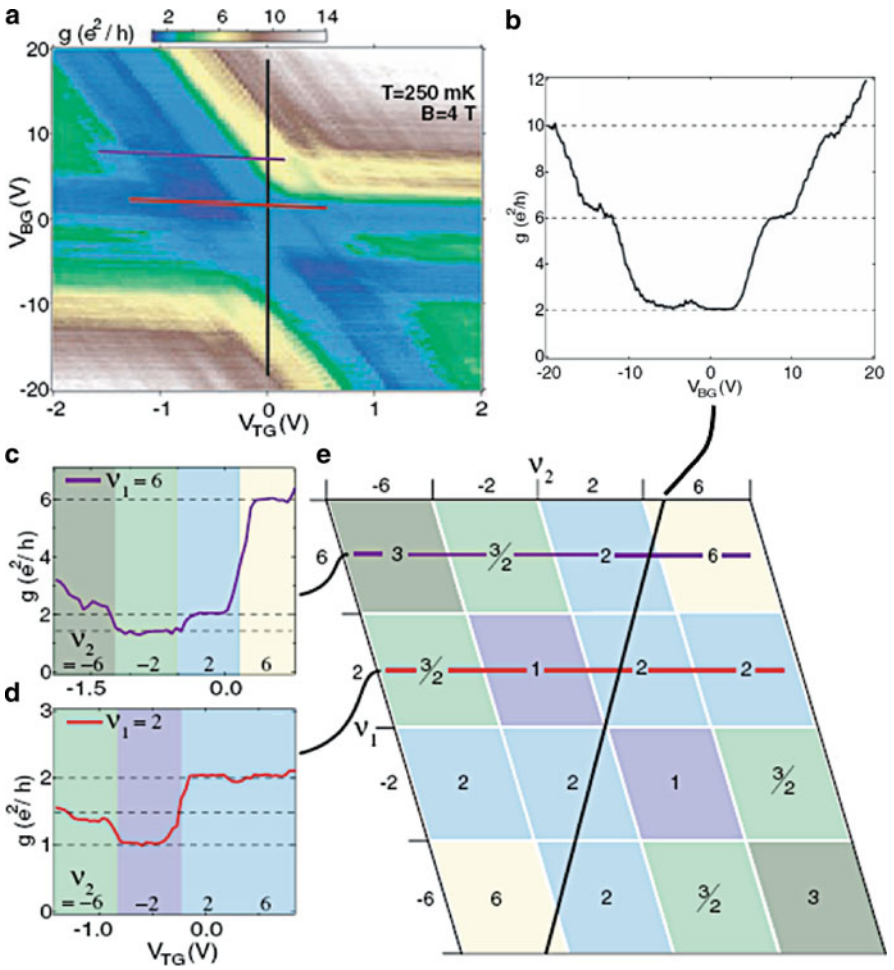

Fig. 15.11 (**a**) Measured conductance as a function of top-/bottom-gate voltages V_{tg}/V_{bg} at $B = 4\,\mathrm{T}$ and $T = 250\,\mathrm{mK}$. Three line plots corresponding to the three cuts in the figure are shown in (**b–d**). (**e**) Schematic of the theoretical conductance according to (15.55), where $\nu_{1,2}$ refers to the filling factor on the left/right sides of the junction. The line cuts for (**b–d**) are also indicated. (Figs. adapted from [34])

where $|0_p\rangle$, $|1_p\rangle$ and $|1'_p\rangle$ are the ground and first excited states of the LL in the p medium, respectively. $|0_{n\mathrm{B}}\rangle$ is the incident Landau mode from the n-side, where B denotes bottom edge (see also Sect. 15.3.2). We have $\vec{c}_i = (1, 0, 0, 0)$ at the beginning of the pn interface. We can define a "saddle point" to be where two Landau modes i and j undergo mode-mixing, which is characterized by a scattering matrix that evolves the scattering state $|\Psi\rangle$ in a unitary manner. The effective unitary matrix for the scattering of four modes can be parameterized as

$$S = \begin{bmatrix} c^2 & sc & s^2 & -sc \\ -sc & c^2 & sc & s^2 \\ s^2 & -sc & c^2 & sc \\ sc & s^2 & -sc & c^2 \end{bmatrix} \tag{15.57}$$

where $s \equiv \sin(\beta)$ and $c \equiv \cos(\beta)$. As usual, the accompanied phase factors are implicit [96]. The parameter β characterizes the degree of mode-mixing, i.e., $\beta = 0, \frac{\pi}{4}$ denotes minimum/maximum mixing. Undergoing a sufficient amount of mode-mixing processes S, the wavefunction at the end of the pn interface is then

$$\begin{aligned} \left|\Psi_f\right\rangle &= S\left(\beta_1\right) S\left(\beta_2\right) S\left(\beta_3\right) \ldots \left|\Psi_i\right\rangle \\ &\approx \tfrac{1}{2} \mathrm{e}^{\phi_0} \left|0_{n\mathrm{B}}\right\rangle + \tfrac{1}{2} \mathrm{e}^{\phi_1} \left|0_p\right\rangle + \tfrac{1}{2} \mathrm{e}^{\phi_2} \left|1_p\right\rangle + \tfrac{1}{2} \mathrm{e}^{\phi_3} \left|1'_p\right\rangle \end{aligned} \tag{15.58}$$

The final state is then said to have completely mixed – it is equally weighted over the available Landau modes. The reflection probability can then be computed as

$$|r|^2 = \left|\left\langle 0_{n\mathrm{T}} \middle| \Psi_f \right\rangle\right|^2 = \tfrac{1}{4} \left|\left\langle 0_{n\mathrm{T}} \middle| 0_{n\mathrm{B}} \right\rangle\right|^2 \left|\mathrm{e}^{\phi_0} + \mathrm{e}^{\phi_1}\right|^2 \tag{15.59}$$

In arriving at the above result, we had to make use of the orthogonality relationship $\left\langle 0_{n\mathrm{T}} \middle| 1_p \right\rangle = 0$. We also assumed that $\left|0_p\right\rangle$ retains the isospin information of the incident scattering state, therefore yielding $\left\langle 0_{n\mathrm{T}} \middle| 0_p \right\rangle = \left\langle 0_{n\mathrm{T}} \middle| 0_{n\mathrm{B}} \right\rangle$. By making use of the fact that the phase term averaged over a sufficiently large ensemble yields

$$\left\langle \left|\mathrm{e}^{\phi_0} + \mathrm{e}^{\phi_1} + \cdots + \mathrm{e}^{\phi_n}\right|^2 \right\rangle_{\text{ensemble}} \approx n + 1 \tag{15.60}$$

the junction conductance (including spin) at filling factor $(2, 6)$ could then be expressed as

$$\sigma_{pn}(2, 6) \approx 2\left(1 - \tfrac{1}{2} \left|\left\langle 0_{n\mathrm{T}} \middle| 0_{n\mathrm{B}} \right\rangle\right|^2\right) \tag{15.61}$$

For the case where the number of carbon layers of the armchair ribbon $\neq 3M + 1$, (15.61) yields $\mathcal{G}_{np} = \frac{5}{4}$ at $(\nu_n, \nu_p) = (2, 6)$. On the other hand, if the number of carbon layers of the armchair ribbon $= 3M + 1$, it will remain perfectly conducting, i.e., $\mathcal{G}_{np} = 2$. The results from a simple Chalker–Coddington analysis are in excellent corroboration with what we obtained from numerical calculations [56]. This finding unequivocally demonstrates that electron and hole Landau mode-mixing via pn interface disorder alone are not sufficient to arrive at the result of $\mathcal{G}_{np} = \frac{3}{2}$ predicted by (15.55). This result is only possible if the isospin information on the top/bottom edges is completely diluted, e.g., via edge disorder. It is shown numerically [56] that by including edge disorder, the results predicted by (15.55) can be obtained.

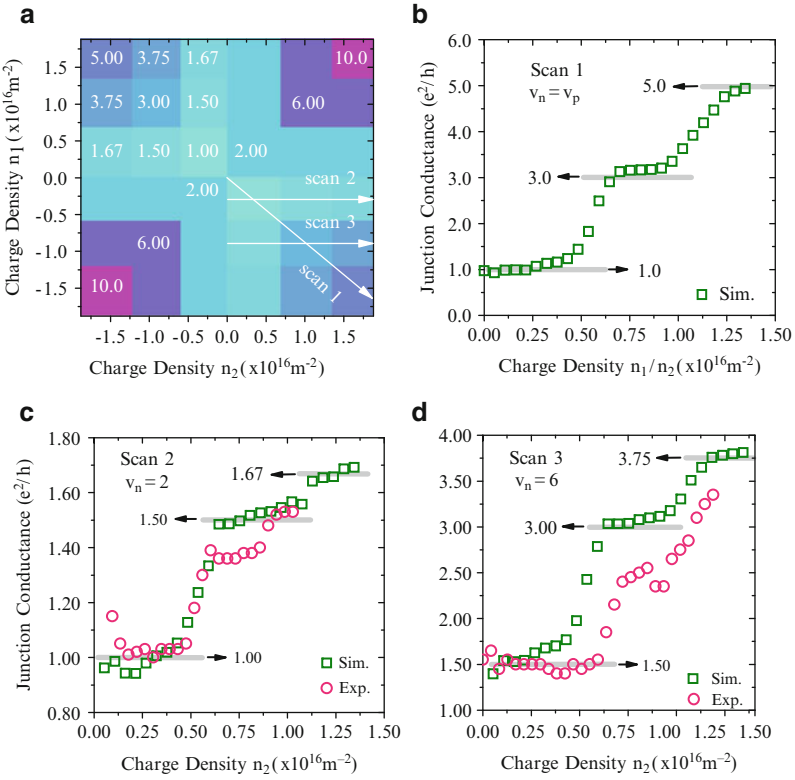

Fig. 15.12 (**a**) Depiction of the theoretical Ohmic plateaus $\hat{\sigma}_{pn}(\nu_n, \nu_p)$ [55] as a function of n_1/n_2, where the different colors represent the filling factors. (**b**)–(**d**) plots the linescan for the following cases: (1) $\nu_n = \nu_p$; (2) $\nu_n = 2$; and (3) $\nu_n = 6$, respectively; it also compares the simulation results with the experimental data. The experimental data are taken from [34] for a two-terminal pn junction quantum Hall measurement at $B = 4\,\mathrm{T}$. The simulations are done at $B = 10\,\mathrm{T}$. In the experimental data, the gate oxide capacitance is used as a fitting parameter. (Fig. is adapted from [56])

Figure 15.12 compares the numerically calculated junction conductance (with edge and pn interface disorder) against that of experiments [34]. Figure 15.12a depicts the theoretical plateaus of (15.55) as a function of the electron density n_1/n_2 (the different colors denote the different filling factors). In the numerical calculations, the electron density is obtained by taking the trace of the electron correlation function $G^n(\epsilon_f)$, which is an energy-resolved quantity. This quantity is defined to be $G^n = G\Sigma_{in}G^\dagger$, where $\Sigma_{in} = -2\mathrm{Im}(\Sigma_l + \Sigma_r)$ for $T = 0\,\mathrm{K}$. Electron density in the n/p medium can then be computed via the integral $n = \int \langle G^n \rangle \, d\epsilon$, where the averaging $\langle \ldots \rangle$ is performed over the spatial dimension. Figure 15.12b–d plots the linescan for the following cases: (1) $\nu_n = \nu_p$; (2) $\nu_n = 2$; and (3) $\nu_n = 6$, respectively. In general, the numerical results show satisfactory agreement with the experiments. As previously addressed [34], the junction conductance with

lower filling factors such as $\mathcal{G}_{np}(2,2)$ and $\mathcal{G}_{np}(2,6)$ plateaus at the expected Ohmic values of 1 and $\frac{3}{2}$, respectively. However, higher plateaus such as $(6,6)$ and $(6,10)$ could not be observed experimentally. This suggests that the interface disorder in the experiment is smaller than that necessary for complete Landau mode-mixing of the higher plateaus. We refer the readers to [56] for more elaborate discussions.

In summary, we have shown that the mixing of electron/hole Landau modes along the interface alone does not guarantee the recovery of the Ohmic-type plateaus predicted by [55]. Valley isospin dilution through edge disorder is necessary. In fact, the valley isospin [71] plays an important role in dictating the junction conductance in the ballistic limit. It is demonstrated numerically and theoretically that both interface and edge roughness (or intervalley scattering) are generally necessary for the crossover between the two theoretical limits.

15.4 Transport in the Presence of Strain-Induced Pseudo-Magnetic Fields

From an application point of view, one might legitimately challenge the usage of a magnetic field for practical device applications due to the difficulty in creating large local magnetic fields. In this chapter, we review an interesting notion, i.e., the creation of pseudo-magnetic fields through strain engineering. Strains in graphene is a ubiquitous phenomenon that had been observed through scanning tunneling microscopy in various experimental setup [97–102]. The pseudo gauge field generated with strains [10, 60, 61, 103] was recently demonstrated in scanning tunneling microscopy experiments [62, 104]. This phenomenon could lead to a new class of devices based on pseudo-magnetic field effects without the application of a real magnetic field. In Sect. 15.4.1, we explain how a pseudo-magnetic field can be generated through elastic deformation of graphene membranes [10, 61]. This is followed by Sect. 15.4.2 with a numerical study of electron transport in presence of pseudo-magnetic fields. Analogous quantum Hall effect, dissipative edge states, and formation of transport gap are discussed. Lastly, we examine snake states transport in Sect. 15.4.3.

15.4.1 Strain-Induced Pseudo-Magnetic Field

Recently, it has been shown that elastic deformation of graphene membranes could also lead to a pseudo-magnetic field (see [10, 61] for a review on this topic). Of particular technological importance are recent proposals to generate uniform pseudo-magnetic fields through particular strain geometries [60, 65, 66], where a strain of $\approx 10\%$ could lead to a pseudo-magnetic field of up to 10 T. Here, we provide a theoretical viewpoint regarding the origin of this pseudo-magnetic field through Dirac equations.

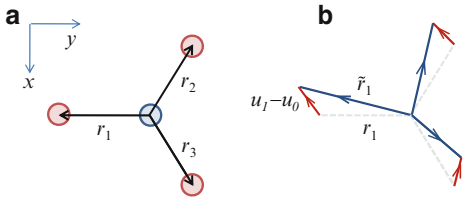

Fig. 15.13 (**a**) Illustration of a carbon atom with its nearest neighbor atoms and their bond vectors $\mathbf{r}_j$. (**b**) Distorted bond vectors $\tilde{\mathbf{r}}_j$ and atom displacement vectors $\mathbf{u}_j - \mathbf{u}_0$

Figure 15.13 shows the effect of strain on the local deformations of carbon–carbon bonds. In the unstrained case as depicted in Fig. 15.13a, the bond vectors are $\mathbf{r}_1 = (0, -b)$, $\mathbf{r}_2 = \frac{1}{2}(-a, b)$ and $\mathbf{r}_3 = \frac{1}{2}(a, b)$ (using the zigzag conventions described in Sect. 15.2.1). The effect of strain is to deform the lattice in such a way that the lattices acquire a new set of bond vectors $\tilde{\mathbf{r}}_j$, as depicted in Fig. 15.13b. In the spirit of nearest-neighbor interactions, the change in bond length, i.e., $|\tilde{\mathbf{r}}_j| - |\mathbf{r}_j|$, would result in a perturbation of the bond energy such that t_j is different from the unperturbed case of $t \approx 3\,\text{eV}$. Suppose that the strain is spatially smooth; then, a "local" effective Hamiltonian could be sought by assuming that the set of bond energies $\{t_1, t_2, t_3\}$ is relatively unchanged in the vicinity of that locality. With this in mind, we denote the following "local" Hamiltonian:

$$t \begin{pmatrix} 0 & \tilde{f}(\mathbf{k}) \\ \tilde{f}(\mathbf{k})^\dagger & 0 \end{pmatrix} \begin{pmatrix} \psi_A \\ \psi_B \end{pmatrix} = \epsilon \begin{pmatrix} \psi_A \\ \psi_B \end{pmatrix} \tag{15.62}$$

where

$$\tilde{f}(\mathbf{k}) = \sum_j (1 + \delta_j) \exp\left(\mathrm{i}\mathbf{k} \cdot \mathbf{r}_j\right) \tag{15.63}$$

and where $\delta_j \equiv (t_j - t)/t$ is the fractional change in the bond energy. Expanding $\tilde{f}(\mathbf{k})$ to the first order in $\mathbf{k}$ about the Dirac point at $\frac{4\pi}{3a}(-1, 0)$, we arrive at

$$\tilde{f}(\mathbf{k}) \approx \frac{3b}{2}\left(k_x - \mathrm{i}k_y\right) + \frac{1}{2}\left(2\delta_1 - \delta_2 - \delta_3\right) - i\frac{\sqrt{3}}{2}\left(\delta_3 - \delta_2\right) \tag{15.64}$$

The Hamiltonian in (15.62) then becomes

$$\begin{aligned} \mathcal{H} &\approx v_f \boldsymbol{\sigma} \left(\mathbf{P} + e\tilde{\mathbf{A}}\right) \\ \tilde{\mathbf{A}} &= \frac{1}{2v_f}\left(2\delta_1 - \delta_2 - \delta_3, \sqrt{3}\delta_3 - \sqrt{3}\delta_2\right) \end{aligned} \tag{15.65}$$

where $v_f = 3bt/2\hbar \approx 1 \times 10^6\,\text{m/s}$, and $\mathbf{P} \equiv -\mathrm{i}\hbar\nabla$ is the momentum operator. $\tilde{\mathbf{A}}$ is the local pseudo-gauge field induced by the strain. These results had previously

been derived in the context of carbon nanotubes [103, 105]. Our next step is to show that by employing a particular strain geometry, $\tilde{\mathbf{A}}$ could be rendered spatially independent, hence achieving a spatially uniform pseudo-magnetic field.

The deformation of graphene is described by the displacement vector $\mathbf{u}_j$ on each atomic position j. However, it is the difference of $\mathbf{u}_j$ from its nearest neighbor that characterizes the amount of strain on the bonds. For example, the change in the bond vector $\mathbf{r}_j$ can be written in the following manner:

$$\left|\tilde{\mathbf{r}}_j\right| - \left|\mathbf{r}_j\right| \approx \left(\mathbf{u}_j - \mathbf{u}_0\right) \cdot \frac{\mathbf{r_j}}{b} \tag{15.66}$$

In the continuum limit, the displacement vector is written as $\mathbf{u}(\mathbf{s})$, where $\mathbf{s} = (x, y)$ is the position vector. In the theory of elasticity, it is conventional to define the strain tensor as $u_{mn} = \frac{1}{2}\left(\partial_n u_m + \partial_m u_n\right)$, where m, n denotes the two spatial coordinates x, y. Then $\mathbf{u}(\mathbf{s}')$ can be approximated as follows:

$$\begin{pmatrix} u_x(\mathbf{s}') \\ u_y(\mathbf{s}') \end{pmatrix} \approx \begin{pmatrix} u_x(\mathbf{s}) \\ u_y(\mathbf{s}) \end{pmatrix} + \begin{bmatrix} u_{xx}(\mathbf{s}) & u_{xy}(\mathbf{s}) \\ u_{yx}(\mathbf{s}) & u_{yy}(\mathbf{s}) \end{bmatrix} \times \left(\mathbf{s}' - \mathbf{s}\right) \tag{15.67}$$

Equations (15.67) and (15.66) then imply the following:

$$\left|\tilde{\mathbf{r}}_j\right| - \left|\mathbf{r}_j\right| \approx \left(\begin{bmatrix} u_{xx} & u_{xy} \\ u_{yx} & u_{yy} \end{bmatrix} \times \mathbf{r}_j \right) \cdot \frac{\mathbf{r_j}}{b} \tag{15.68}$$

Assuming that the strain is small, one could make the approximation that the perturbation in t is directly proportional to the perturbation in bond length,

$$\delta_j \approx \beta \frac{\left|\tilde{\mathbf{r}}_j\right| - \left|\mathbf{r}_j\right|}{b} \tag{15.69}$$

where $\beta \approx 2\,\text{eV}$ is known as the Grüneisen parameter. Substituting (15.68) and (15.69) into the expression for $\tilde{\mathbf{A}}$, one then obtains

$$\tilde{\mathbf{A}} = c \frac{3\beta}{8 v_f} \left(u_{yy} - u_{xx}, 2u_{xy}\right) \tag{15.70}$$

where c is an extra factor (of order unity) introduced to account for the modification of the energy dispersion due to strain, which was previously ignored in the derivation of (15.65). From (15.70), it can be seen that a strain geometry of the following form [66],

$$\mathbf{u}(x, y) = \frac{1}{R}\left(xy, -\frac{x^2}{2}\right) \tag{15.71}$$

would result in $\tilde{\mathbf{A}} \propto (-y/R, 0)$, where R is the radius of curvature. This would then translate to a uniform pseudo-magnetic field because $\mathbf{B}_s = \nabla \times \tilde{\mathbf{A}}$. We note that an alternative form of $\mathbf{u}$ can also be sought, as described in [60, 66].

15.4.2 Edge States and Transport Gap

Here, we study the electronic transport in presence of strain-induced pseudo-magnetic field through numerical simulations. We first provide a brief description of the numerical approach. The Hamiltonian accounting for nearest neighbor interactions between p_z orbitals is given by [8],

$$\mathcal{H} = \sum_i V_i a_i^\dagger a_i + \sum_{ij} t_{ij} a_i^\dagger a_j \tag{15.72}$$

where V_i is the on-site energy due to the scalar potential $V(\vec{r})$ and $t_{ij} = t(1+\frac{\beta}{b}(b_{ij}-b))$ is the hopping energy. b_{ij} is the new bond length after strain. To facilitate the application of various numerical techniques, the problem is partitioned into block slices as shown in Fig. 15.14. The retarded Green's function in Ω_0, the device region of interest, can then be written as (see [81, 82, 84] for general theory),

$$\mathcal{G} = \left(\epsilon_f \mathcal{I} - \mathcal{H}_0 - \Sigma_{\mathrm{L}} - \Sigma_{\mathrm{R}}\right)^{-1} \equiv A^{-1} \tag{15.73}$$

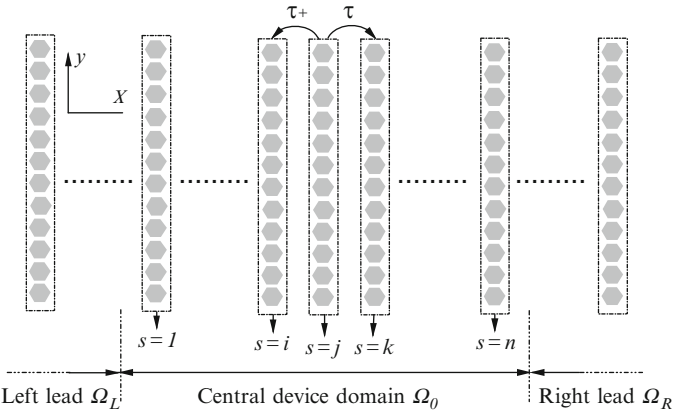

Fig. 15.14 The graphene ribbon is partitioned into block slices along the x-direction (transport) as indicated. Lattice interactions within each block is described by α. Nearest neighbor blocks interactions are represented by τ. Device domain Ω_0 will include the strains. Left/right leads regions ($\Omega_{\mathrm{L/R}}$) are assumed unstrained and electrically doped, due to charge transfer from contacts

where ϵ_f is the Fermi energy, and $\Sigma_{\mathrm{L/R}}$ are defined as $\Sigma_{\mathrm{L}} = \tau^\dagger g_L \tau$ and $\Sigma_{\mathrm{R}} = \tau g_R \tau^\dagger$, respectively. $g_{\mathrm{L/R}}$ are the surface Green's function, which can be obtained numerically through an iterative scheme [85] based on the decimation technique (see e.g. [106]). It is also useful to define the quantity, broadening function, $\Gamma_{\mathrm{L/R}} \equiv i(\Sigma_{\mathrm{L/R}} - \Sigma^\dagger_{\mathrm{L/R}})$. Physical quantities of interest such as the transmission $\mathcal{T}$ is given by,

$$\mathcal{T} = \mathrm{Tr}\left([\Gamma_L]^1_1 [\mathcal{G}]^1_n [\Gamma_R]^n_n [\mathcal{G}^\dagger]^n_1\right) \tag{15.74}$$

The electron density $n(\vec{r})$ at slice j is obtained from the diagonals elements of $\mathcal{G}^n$, given by,

$$[\mathcal{G}^n]^j_j = f_{\mathrm{L}} [\mathcal{G}]^j_1 [\Gamma_L]^1_1 [\mathcal{G}^\dagger]^1_j + f_{\mathrm{R}} [\mathcal{G}]^j_n [\Gamma_R]^n_n [\mathcal{G}^\dagger]^n_j \tag{15.75}$$

Local density-of-states is obtained from (15.75) by simply setting $f_{\mathrm{L}} = f_{\mathrm{R}} = 1$. Current density $j(\vec{r})$, flowing from slice j to $j+1$ is given by the diagonal of J, is given by,

$$[J]^j_{j+1} = \tfrac{2q}{h}\left([A]^j_{j+1}[\mathcal{G}^n]^{j+1}_j - [A]^{j+1}_j [\mathcal{G}^n]^j_{j+1}\right) \tag{15.76}$$

where,

$$\begin{aligned}
[\mathcal{G}^n]^{j+1}_j &= f_{\mathrm{L}} [\mathcal{G}]^{j+1}_1 [\Gamma_L]^1_1 [\mathcal{G}^\dagger]^1_j + f_{\mathrm{R}} [\mathcal{G}]^{j+1}_n [\Gamma_R]^n_n [\mathcal{G}^\dagger]^n_j \\
[\mathcal{G}^n]^j_{j+1} &= f_{\mathrm{L}} [\mathcal{G}]^j_1 [\Gamma_L]^1_1 [\mathcal{G}^\dagger]^1_{j+1} + f_{\mathrm{R}} [\mathcal{G}]^j_n [\Gamma_R]^n_n [\mathcal{G}^\dagger]^n_{j+1}
\end{aligned} \tag{15.77}$$

As apparent from (15.74)–(15.77), it is not necessary to obtain the full matrix $\mathcal{G}$. Through commonly used recursive formula of the Green's function derived from the Dyson equation and the decimation technique, one could obtain these block elements of the Green's function, $[\mathcal{G}]^i_j$, in a computationally/memory efficient manner. Further details of the numerical recipe are described elsewhere [43].

Figure 15.15a depicts a typical strain geometry described by (15.71). Its deformation has an arc geometry that can be characterized by a radius R, which is measured from the center of the unstrained graphene flake (also the origin for (15.71)). The maximum strain exerted on the flake would then be along the two edges, which is given by $\max(u_{xx}) \approx W/2R$. Figure 15.15b shows the numerically calculated zero-temperature quantum conductance as a function of strain geometry and Fermi energy, where the unstrained graphene has a dimension of $L = W = 100\,\mathrm{nm}$. Note that the source/drain contacts are placed at the left/right boundaries. Clean quantum Hall plateaus are observed with filling factors given by $v = 2, 6, 10, \ldots = 4n + 2$, exactly mimicking the conventional quantum Hall case. Knowing that the first excited Landau energy $\epsilon_1 = v_f\sqrt{2\hbar Bq}$ in the conventional quantum Hall case, we can numerically estimate the effective magnetic field induced by a deformation characterized by the ratio W/R, as for $B_s = \Omega W/R$ with $\Omega \approx 45$ T. For example,

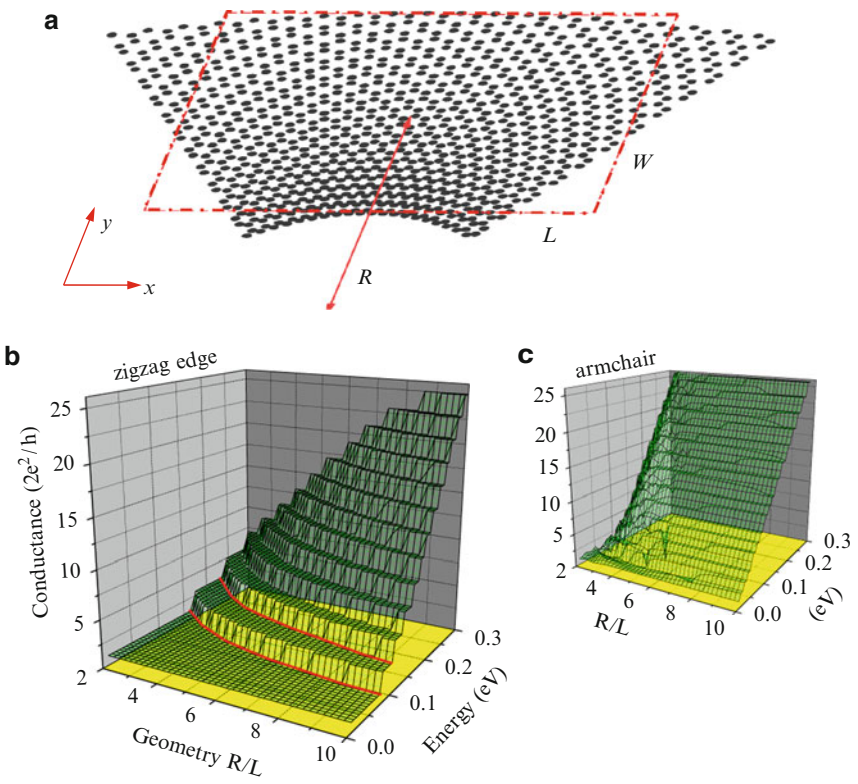

Fig. 15.15 (**a**) Sketch of a sample strain geometry with a maximum strain of 50%. Note that the actual size of the flake used in this paper is much larger, i.e., $L = W = 100\,\text{nm}$. Conductance is shown as a function of Fermi energy and strained geometry characterized by R/W for (**b**) zigzag and (**c**) armchair edge ribbons in the absence of real magnetic fields and edge disorder. The dimension of the graphene flake is $L = W = 100\,\text{nm}$. (Figs. adapted from [65])

$R/W = 5$ would correspond to a maximum strain of $\approx 10\%$ along the edges and a pseudo-magnetic field of $\approx 10\,\text{T}$.

However, when the same strain geometry is exerted on an armchair edge ribbon instead, no quantum Hall plateau is evident in the quantum conductance, as shown in Fig. 15.15c. The reason is that the strain geometry of (15.71) was derived for a zigzag ribbon case, such that it yields a uniform pseudo-magnetic field only for the zigzag ribbon. To be more specific, (15.71) leads to a gauge field along the x direction, $\tilde{A}_x(y)$, for a zigzag ribbon, but it instead results in a gauge field of $\tilde{A}_y(y)$ for an armchair ribbon. At the lowest order, this gauge field does not induce an effective magnetic field and leaves the electronic spectrum unchanged, as evident in Fig. 15.15c. Therefore, when employing the strain geometry prescribed by (15.71), a zigzag edge ribbon should be employed for a maximal pseudomagnetic effect.

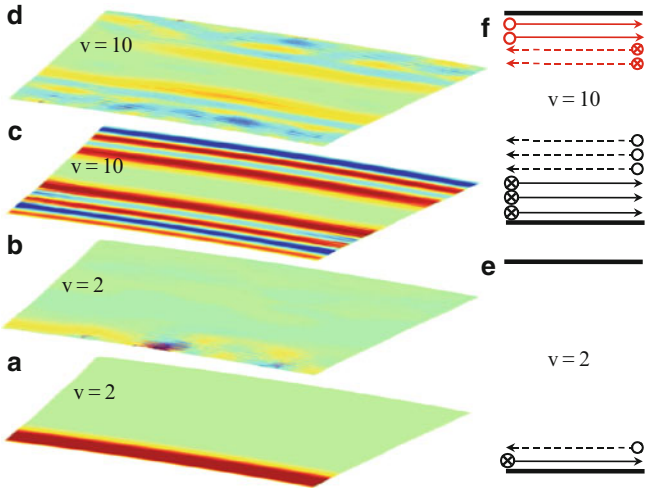

Fig. 15.16 The non-equilibrium current density $\text{sign}(j_x) \times |\mathbf{j}(x, y)|$ intensity plot for a 100 × 100 nm graphene flake under a strain of $R/W = 5$ (equivalent to $B_s \approx 9$ T) at ϵ_F corresponding to filling factor $\nu = 2$, (**a**) with edge disorder and (**b**) without. Similar plots are shown in (**c–d**), but for filling factor $\nu = 10$ instead. (**e**) and (**f**) illustrate the counter-propagating edge states at $\nu = 2$ and $\nu = 10$, respectively. (Figs. adapted from [65])

Lastly, we should point out the clear distinction between the strain-induced pseudo-magnetic effect and the Quantum Hall effect. Unlike situation in the Quantum Hall effect, the edge states are not protected by time-reversal symmetry, which means that they can be affected by elastic backscattering. Figure 15.16a and c plots the nonequilibrium current densities at Fermi energies corresponding to $\nu = 2$ and $\nu = 10$ for the case of a strain-induced pseudo-magnetic effect. For $\nu = 2$, strains induce two edge modes that propagate in opposite directions. Time-reversal symmetry implies that these two modes are localized at the same edge, in agreement with the numerical results. In general, the compressive strained edge would acquire two more modes than the other edge. The zigzag boundary condition used here does not mix the K and K' valleys, which leads to a clear distinction of the edge modes. It can be observed that for a given current direction, the edge states on the two edges are valley-polarized, i.e., showing a quantum valley Hall effect. This effect is analogous to the quantum spin Hall effect [107]. In both cases, the net pseudo-gauge field of the system is zero, but it is finite and opposite for each spin/valley. However, in this case, short-range scattering couples the valleys. Because the counter-propagating edge states residing along a particular edge belong to different valleys, inter-valley processes lead to backscattering. In the presence of edge disorder, substantial backscattering can occur, and Anderson localization spots can be observed (see Fig. 15.16b). A more quantitative evaluation of the impact of edge roughness is discussed in [65].

15.4.3 Magnetic and Electric Snake States

Would the electronic transport across a pn junction under strain-induced pseudo-magnetic field behaves similarly to its real magnetic field counterpart? The short answer is "no." Their main difference resides in the fact that one involves time reversal symmetry breaking while the other does not. For example, for filling factor $\nu = 2$, the two edge modes would reside on opposite edges for the real magnetic field case, while on the same edges for pseudo-field case as discussed in previous section. This would result in a drastically different transport behavior in pn junction, which remains an interesting problem for future investigation. In this section, we shall concern ourselves with instead transport along a pn junction. In this context, we are interested in the phenomenon of snake states.

There are myriad known ways to induce snake states. In high mobility two-dimensional electron gas system, such states are known to exists in nonuniform magnetic field and had been studied experimentally [108] and theoretically [109–111]. It has been shown theoretically that graphene also accommodates such magnetic snake states (MSS) [112, 113]. Controlled engineering of the magnetic field profile could possibly be achieved through precise lithographic patterning of ferromagnetic or superconducting films to create magnetic barriers [114], which however remains to be demonstrated experimentally. In addition to this, Dirac fermions in graphene also exhibits unique zero energy snake states (CSS) in the presence of crossed uniform electric and magnetic fields [57, 58]. These states present themselves in the magneto-transport of a two-terminal graphene pn junction [56], giving rise to new quantum Hall plateaus as observed experimentally [34] as discussed in Sect. 15.3.4. In this case, only a uniform quantizing magnetic field is required. The possibility of using strain to create a uniform pseudo gauge field in combination with an electric field is an attractive option, since it makes possible an electrically controlled snake state (ESS) for the first time, which might leads to novel electronic devices [115]. To facilitate following discussions, we plotted the electronic bandstructure of a 50 nm zigzag ribbon as shown in Fig. 15.17a–c, under different electric and magnetic potentials conditions.

Magnetic snake states (MSS): Fig. 15.17a plots the electronic bandstructure and its associated current density for the indicated states labeled **1**–**4**. Since there is no electric field in this case, the bandstructure retains its electron–hole symmetry. The Dirac equation describing low energy excitations is written as,

$$\mathcal{H}_{\text{MSS}} = -\mathrm{i}\hbar v_f \left(\partial_x \sigma_x \tau_z + \partial_y \sigma_y \tau_0\right) + eA_x \sigma_x \tau_z \tag{15.78}$$

where σ and τ are the Pauli matrices acting on the A/B sublattices (pseudospin) and $\mathbf{K}/\mathbf{K}'$ valleys (isospin) degree of freedom, respectively. A convenient gauge is employed such that $A_x = B\,|y|$, which yields a magnetic field of $\mathbf{B} = B(0, 0, \pm 1)$ for $\pm y$. $\mathcal{H}_{\text{MSS}}$ satisfies the following symmetry, $[\mathcal{H}_{\text{MSS}}, \sigma_x \tau_0 \mathcal{R}_y] = 0$, where $\mathcal{R}_y$ is the reflection operator i.e. $\mathcal{R}_y f(y) = f(-y)$. Similarly, the eigenfunctions Ψ would respect the symmetry $\sigma_x \tau_0 \mathcal{R}_y \Psi_i(\mathbf{r}) = \Psi_j(\mathbf{r})$. The edge states are

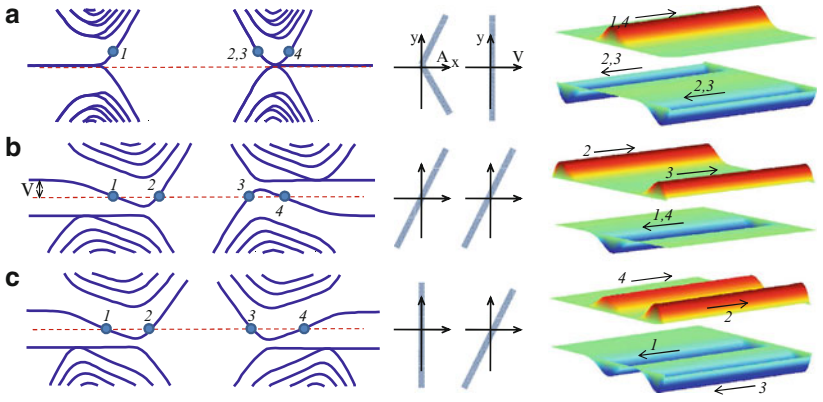

Fig. 15.17 (*Left*) Energy dispersion of a 50 nm graphene zigzag ribbon as a function of k_x, where x is along the length direction. They are plotted for the following cases: (**a**) a non-uniform magnetic field which changes abruptly from $+20$ T to -20 T halfway along the width of the ribbon, (**b**) a combination of uniform magnetic field of ≈ 10 T and a constant transverse electric field of V/W where $0.2V$ is the potential drop across the ribbon's width, (**c**) same as (**b**) except that the real magnetic field is replaced by a pseudo-magnetic field of equal strength generated by particular strain geometry. For clarity the associated vector/scalar potential are also depicted on the right of the bandstructure diagrams. (*Right*) Plots of current densities for the states as indicated on left

represented by **2** and **3** in Fig. 15.17a. Note that they resides within the same valley and are energetically degenerate. The snake states are represented by **1** and **4**, which flows in the direction $\nabla B_z \times \mathbf{z}$. Current conservation requires that the snake states flow in the opposite direction to the edge states. Spatial separation of these counter-propagating states renders them relatively robust against backscattering.

Crossed-field snake states (CSS). The Dirac equation in this case is given by,

$$\mathcal{H}_{\text{CSS}} = -\text{i}\hbar v_f \left(\partial_x \sigma_x \tau_z + \partial_y \sigma_y \tau_0\right) + eA_x \sigma_x \tau_z + eU(y)\sigma_0 \tau_0$$

where the vector and electrostatic potentials are $A_x = By$ and $U(y) = \xi y$, respectively. They correspond to a uniform crossed magnetic and electric fields. The electric field breaks the electron–hole symmetry and results in the mixing of electron and hole Landau wavefunctions at zero energy [57] i.e. snake states. They are represented by **1** and **4** in Fig. 15.17b, and they flow along the direction $\mathbf{B} \times \boldsymbol{\xi}$. Again, spatial separation of these counter-propagating states renders them relatively robust against backscattering.

Electrical snake states (ESS). As discussed in [60, 66], an effective constant magnetic field arises from strains varying at a constant rate. The Dirac equation describing low energy excitations in this case is written as [103, 116],

$$\mathcal{H}_{\text{ESS}} = -\text{i}\hbar v_f \left(\partial_x \sigma_x \tau_z + \partial_y \sigma_y \tau_0\right) + e\tilde{A}_x \sigma_x \tau_0 + eU(y)\sigma_0 \tau_0$$

Immediately, one makes the observation that $\mathcal{H}_{\rm ESS}$ is invariant under the time reversal operation $\mathcal{T} = \sigma_0\tau_x\mathcal{C}$ in the presence of $\tilde{\mathbf{A}}$, i.e. $\mathcal{T}^\dagger\mathcal{H}_{\rm ESS}(\tilde{\mathbf{A}})\mathcal{T} = \mathcal{H}_{\rm ESS}(\tilde{\mathbf{A}})$. This property is in contrary to the conventional quantum Hall effect. Graphene also accommodates another symmetry given by $\mathcal{S} = i\sigma_y\tau_0\mathcal{C}$ [117]. It does not couple valleys and it acts as a time reversal operator for each valley. Its action yields $\mathcal{S}^\dagger\mathcal{H}_{\rm ESS}(\tilde{\mathbf{A}})\mathcal{S} = \mathcal{H}_{\rm ESS}(-\tilde{\mathbf{A}})$ whose symmetry breaking under $\tilde{\mathbf{A}}$ gives rise to a possible quantum Hall effect [60]. The tight-binding result as shown in Fig. 15.17c yields the expected physical picture, where both the snake and edge states are accompanied by its counter-propagating counterpart. As a result, valley coupling perturbations could interfere with the above-mentioned process. An obvious example is short-range scattering process, i.e., $\propto \sigma_z\tau_z$ [70] mediated by edge disorder, leading to localization of the edge states [65]. However, since one could electrically tune the position of these snake states to be far away from the edges, one should be able to minimize the $\sigma_z\tau_z$-type processes.

15.5 Discussions

Previous sections focuses on the transport physics in graphene *pn* junction under various situations. Here, we discuss current status, effort, and challenges in realizing novel devices that exploits these effects.

15.5.1 Devices: Current Status and Outlook

We shall discuss two classes of devices which exploits the physics of graphene *pn* junction discussed in previous sections, namely electron-optics and pseudo-magnetic field devices. The former exploits the analogy with optics, since both electrons and photons exhibit analogous wave-like phenomena, a result of their similar Helmholtz type equation governing their dynamics [118, 119]. The latter exploits analogy with quantum Hall physics, where particular strain geometry [60,62] mimics a pseudo gauge field on top of the Dirac spectrum [10,61,103]. Here, we discuss experimental efforts, challenges, and outlook for these novel devices.

Electron-optics effects has been observed in conventional two-dimensional electron gas systems more than a decade ago [44–48], which includes a broad class of phenomena such as magnetic focusing, beam collimation and electron lens focusing. Interest in graphene electron-optics mainly stems from the following considerations. Zero bandgap, and consequently the low *pn* interface resistance, leads to possibility for negative refractive index applications [49]. Perfect isotropy of the energy dispersion and single p_z orbital environment in graphene makes it a "cleaner" system for electron optics devices. Electrostatics considerations also favor graphene-based electron optics. In both cases, one could view k_f as analogous to

the refractive index of the medium. At a given k_f, which also translate to the same density [4], the graphene case would yield a higher Fermi energy (if effective mass $m > \hbar k/2v_f$) due to its unique linear dispersion. The higher Fermi energy at a given density would renders graphene more immune to a characteristic potential disorder.

Recently, graphene-based electron-optic fiber [50–53] was demonstrated experimentally [54]. Depending on the top/bottom gating, the fiber could operates in the pp^+p (optical guiding), pnp (pn guiding) or pn^+p (mixture of optical and pn guiding) regimes, where middle denotes doping of the fiber. Clear signatures of enhanced guiding for pp^+p by tuning the acceptance cone of the fiber was observed, in accordance with the principle of total internal reflection (see Sect. 15.2.2). Poorer guiding observed in the pn guiding regimes was attributed to the larger amount of interface roughness along the fiber, apparently a result of bulk impurities disorder [120]. Improvements to guiding efficiency will result from reducing interface disorder. Recent development on high quality boron nitride substrates, with excellent mobilities and suppressed carrier inhomogeneities, presents a promising approach [121]. Engineering of a collimated source [42] would also improves guiding. Other device of interest includes the Veselago lens [49] and multiplexer [43], and experimental efforts are currently underway [122]. It is also encouraging to note the recent efforts in an attempt to formulate novel device architecture [123] for electron-optics based devices. Another interesting platform for electron-optics devices is that of bilayer graphene. Unlike its monolayer graphene counterpart, the pseudospins in the n and p regions are antiparallel to each other at $k_y = 0$ [39]. This leads to the suppression of transmission for electrons incident normal to the pn step interface.

Recent demonstration of a quantizing pseudo-magnetic field of up to 300 T generated by applying appropriate strain to graphene [62] opens up new opportunities for novel quantum Hall transport physics (see also [102, 104]). Sections 15.4.2 and 15.4.3 discuss the transport physics for the case where the strain geometry provides a uniform pseudo-magnetic field. A transport gap is induced, since the edge states would be strongly localized along the edges [65]. The conducting state could then be realized by inducing snake states as discussed in Sect. 15.4.3. One expects these snake states to be highly conductive since they can be made far away from the edges. In high mobility two-dimensional electron gas system, snake states had been studied experimentally [108] and theoretically [109–111], in the presence of a magnetic field. It has been shown theoretically that graphene also accommodates such magnetic snake states [112, 113]. There had been recent experimental reports on such observations in graphene [59, 124]. The former was detected by driving current along a pn junction interface, while the latter was observed through Aharonov–Bohm signatures in an array of $Ni_{0.8}Fe_{0.2}$ nanodots. Detecting this phenomenon in strained graphene counterpart is still yet to be demonstrated.

However, it should be emphasized that strains is a ubiquitous phenomenon that had been observed through scanning tunneling microscopy in various experimental

[4] Except when different valley degeneracies are accounted.

setup. They present themselves naturally through superlattice-type ripples on epitaxial substrates [97, 98], corrugation on SiO_2 substrates [99–101], in suspended graphene membranes [125, 126] or under deliberate strain [127]. Controlled engineering of strain in suspended graphene was also demonstrated, leading to formation of one-dimensional wrinkled graphene [126] or bubble graphene [125]. Graphene was also shown to admit large strains, with record mechanical strength [128]. Hence, one could envision all kinds of strain geometry to realized graphene "strain-tronics." For example, there are proposals on suspendend graphene [63], patterned substrates [64], wrinkles and superlattices [115], valleytronics [65, 67–69], nano-electromechanical device [129].

15.5.2 Conclusions

In this chapter, we discussed the electronic transport properties of a graphene *pn* junction. We had considered its transport properties in the absence and presence of a real magnetic field, and also that of a strain-induced pseudo-magnetic field. We discussed novel electronic devices based on concepts of electron optics and strain-induced pseudo-magnetic field, where *pn* junction plays a critical role. These devices are interesting because their operating principles are fundamentally different from those of conventional *pn* junctions. Electron-optics and strain-tronics might be a promising route to realizing all-graphene electronics; however, the field is just beginning.

Acknowledgements This work is supported by the Institute of Nanoelectronics EXploration (INDEX), a National Science Foundation (NSF) research center focusing on new computing devices beyond Moore's law, which forms the motivation for this review. This work had benefitted from useful collaborations/discussions with J. R. Williams, C. M. Marcus, J. U. Lee, P. Kim, C. Y. Sung, W. Wang, M. Lundstrom, J. Appenzeller, S. Datta, P. D. Ye, A. Neal, Y. Sui, D. Nikonov, M. Katsnelson, F. Guinea, K. Novoselov, A. Geim, D. Berdebes, R. Grassi. Generous computing resources from Network for Computational Nanoelectronics are gratefully acknowledge.

References

1. M. Riordan, L. Hoddeson, *Crystal Fire: The Invention of the Transistor and the Birth of the Information Age* (W. W. Norton and Company, New York, 1998)
2. S.M. Sze, K.K. Ng, *Physics of Semiconductor Devices* (Wiley-Interscience, New York, 2006)
3. R.F. Pierret, *Semiconductor Device Fundamentals* (Addison Wesley, Reading, Mass, 1996)
4. M. Lundstrom, *Fundamentals of Carrier Transport* (Cambridge University Press, Cambridge, 2000)
5. K.S. Novoselov, A.K. Geim, S.V. Morozov, D. Jiang, Y. Zhang, S.V. Dubonos, I.V. Grigorieva, A.A. Firsov, Science **306**, 666 (2004)
6. K.S. Novoselov, A.K. Geim, S.V. Morozov, D. Jiang, M.I. Katsnelson, I.V. Grigorieva, S.V. Dubonos, A.A. Firsov, Nature **438**, 197 (2005)

7. Y. Zhang, Y.W. Tan, P. Kim, Nature **438**, 201 (2005)
8. P.R. Wallace, Phys. Rev. **71**, 622 (1947)
9. T. Ohta, A. Bostwick, J.L. McChesney, T. Seyller, K. Horn, E. Rotenbarg, Phys. Rev. Lett. **98**, 206802 (2007)
10. A.H.C. Neto, F. Guinea, N.M.R. Peres, K.S. Novoselov, A.K. Geim, Rev. Mod. Phys. **81**, 109 (2009)
11. C.W.J. Beenakker, Rev. Mod. Phys. **80**, 1337 (2008)
12. S.D. Sarma, S. Adam, E.H. Hwang, E. Rossi, http://arxiv.org/abs/1003.4731 (2010)
13. M.Y. Han, B. Ozyilmaz, Y. Zhang, P. Kim, Phys. Rev. Lett. **98**, 206805 (2007)
14. D.V. Kosynkin, A.L. Higginbotham, A. Sinitskii, J.R. Lomeda, A. Dimiev, B.K. Price, J.M. Tour, Nature **458**, 872 (2009)
15. L. Jiao, L. Zhang, X. Wang, G. Diankov, H. Dai, Nature **458**, 877 (2009)
16. J. Li, S.Q. Shen, Phys. Rev. B **78**, 205308 (2008)
17. J. Bai, X. Zhong, S. Jiang, Y. Huang, X. Duan, Nature Nano. **5**, 190 (2010)
18. M.Y. Han, J.C. Brant, P. Kim, Phys. Rev. Lett. **104**, 056801 (2010)
19. P. Gallagher, K. Todd, D. Goldhaber-Gordon, Phys. Rev. B **81**, 115409 (2010)
20. F. Varcon, R. Feng, J. Hass, X. Li, B.N. Nguyen, C. Naud, P. Mallet, J.Y. Veuillen, C. Berger, E.H. Conrad, L. Magaud, Phys. Rev. Lett. **99**, 126805 (2007)
21. S.Y. Zhou, G.H. Gweon, A.V. Fedorov, P.N. First, W.A. de Heer, D.H. Lee, F. Guinea, A.H.C. Neto, A. Lanzara, Nat. Mat. **6**, 770 (2007)
22. G. Giovannetti, P.A. Khomyakov, G. Brocks, P.J. Kelly, J. Brink, Phys. Rev. B **76**, 073103 (2007)
23. S. Kim, J. Ihm, H.J. Choi, Y.W. Son, Phys. Rev. Lett. **100**, 176802 (2008)
24. T. Ohta, A. Bostwick, T. Seyller, K. Horn, E. Rotenberg, Science **313**, 5789 (2006)
25. E. McCann, Phys. Rev. B **74**, 161403(R) (2006)
26. F. Xia, D.B. Farmer, Y.M. Lin, P. Avouris, Nano Lett. **10**, 715 (2010)
27. T. Thiti, J.H. Pablo, Phys. Rev. Lett. **105**, 166601 (2010)
28. L. Jing, J. Velasco Jr., G. Liu, W. Bao, M. Bockrath, C.N. Lau, Nano Lett. **10**, 4000 (2010)
29. J.O. Sofo, A.S. Chaudhari, G.D. Barber, Phys. Rev. B **75**, 153401 (2007)
30. D.C. Elias, R.R. Nair, T.M.G. Mohiuddin, S.V. Morozov, P. Blake, M.P. Halsall, A.C. Ferrari, D.W. Boukhvalov, M.I. Katsnelson, A.K. Geim, K.S. Novoselov, Science **323**, 610 (2009)
31. R. Balog, B. Jorgensen, L. Nilsson, M. Andersen, E. Rienks, M. Bianchi, M. Fanetti, E. Lagsgaard, A. Baraldi, S. Lizzit, Z. Sljivancanin, F. Besenbacher, B. Hammer, T.G. Pedersen, P. Hofmann, L. Hornekar, Nat. Mat. **9**, 315 (2010)
32. J.P. Robinson, H. Schomerus, L. Oroszlany, V.I. Fal'ko, Phys. Rev. Lett. **101**, 196803 (2008)
33. Y.M. Lin, C. Dimitrakopoulos, K.A. Jenkins, D.B. Farmer, H.Y. Chiu, A. Grill, P. Avouris, Science **327**, 662 (2010)
34. J.R. Williams, L. DiCarlo, C.M. Marcus, Science **317**, 638 (2007)
35. B. Ozyilmaz, P. Jarillo-Herrero, D. Efetov, D.A. Abanin, L.S. Levitov, P. Kim, Phys. Rev. Lett. **99**, 166804 (2007)
36. B. Huard, J.A. Sulpizio, N. Stander, K. Todd, B. Yang, D. Goldhaber-Gordon, Phys. Rev. Lett. **98**, 236803 (2007)
37. V.V. Cheianov, V.I. Fal'ko, Phys. Rev. B **74**, 041403 (2006)
38. T. Low, S. Hong, J. Appenzeller, S. Datta, M. Lundstrom, IEEE Trans. Elec. Dev. **56**, 1292 (2009)
39. M.I. Katsnelson, K.S. Novoselov, A.K. Geim, Nat. Phys. **2**, 620 (2006)
40. A.F. Young, P. Kim, Nat. Phys. **5**, 222 (2009)
41. N. Stander, B. Huard, D. Goldhaber-Gordon, Phys. Rev. Lett. **102**, 026807 (2009)
42. C.H. Park, Y.W. Son, L. Yang, M.L. Cohen, S.G. Louie, Nano Lett. **8**, 2920 (2008)
43. T. Low, J. Appenzeller, Phys. Rev. B **80**, 155406 (2009)
44. N.D. Lang, A. Yacoby, Y. Imry, Phys. Rev. Lett. **63**, 1499 (1989)
45. L.W. Molenkamp, A.A.M. Staring, C.W.J. Beenakker, R. Eppenga, C.E. Timmering, J.G. Williamson, C.J.P.M. Harmans, C.T. Foxon, Phys. Rev. B **41**, 1274 (1990)
46. U. Sivan, M. Heiblum, C.P. Umbach, H. Shtrikman, Phys. Rev. B **41**, 7937 (1990)

47. H. van Houten, B.J. van Wees, J.E. Mooij, C.W.J. Beenakker, J.G. Williamson, C.T. Foxon, Europhys. Lett. **5**, 721 (1988)
48. J. Spector, J.S. Weiner, H.L. Stormer, K.W. Baldwin, L.N. Pfeiffer, K.W. West, Surf. Sci. **263**, 240 (1992)
49. V.V. Cheianov, V. Fal'ko, B.L. Altshuler, Science **315**, 1252 (2007)
50. J.M. Pereira, V. Mlinar, F.M. Peeters, P. Vasilopoulos, Phys. Rev. B **74**, 045424 (2006)
51. C.W.J. Beenakker, R.A. Sepkhanov, A.R. Akhmerov, J. Tworzydlo, Phys. Rev. Lett. **102**, 146804 (2009)
52. F.M. Zhang, Y. He, X. Chen, Appl. Phys. Lett. **94**, 212105 (2010)
53. Z. Wu, arXiv:1008.2495 (unpublished) (2010)
54. J.R. Williams, T. Low, M. Lundstrom, C.M. Marcus, Nature Nano. **6**, 222 (2011)
55. D.A. Abanin, L.S. Levitov, Science **317**, 641 (2007)
56. T. Low, Phys. Rev. B **80**, 205423 (2009)
57. V. Lukose, R. Shankar, G. Baskaran, Phys. Rev. Lett. **98**, 116802 (2007)
58. J.M. Pereira, F.M. Peeters, P. Vasilopoulos, Phys. Rev. B **75**, 125433 (2007)
59. J.R. Williams, Electronic Transport in Graphene: p-n Junctions, Shot Noise, and Nanoribbons, Harvard University, PhD thesis (2009)
60. F. Guinea, M.I. Katsnelson, A.K. Geim, Nat. Phys. **6**, 30 (2010)
61. M.A.H. Vozmediano, M.I. Katsnelson, F. Guinea, Phys. Rep. **496**, 109 (2010)
62. N. Levy, S.A. Burke, K.L. Meaker, M. Panlasigui, A. Zettl, F. Guinea, A.H.C. Neto, M.F. Crommie, Science **329**, 544 (2010)
63. M.M. Fogler, F. Guinea, M.I. Katsnelson, Phys. Rev. Lett. **101**, 226804 (2008)
64. V.M. Pereira, A.H.C. Neto, Phys. Rev. Lett. **103**, 046801 (2009)
65. T. Low, F. Guinea, Nano Lett. **10**, 3551 (2010)
66. F. Guinea, A.K. Geim, M.I. Katsnelson, K.S. Novoselov, Phys. Rev. B **81**, 035408 (2010)
67. T. Fujita, M.B.A. Jalil, S.G. Tan, Appl. Phys. Lett. **97**, 043508 (2010)
68. F. Zhai, X. Zhao, K. Chang, H.Q. Xu, Phys. Rev. B **82**, 115442 (2010)
69. A. Chaves, L. Covaci, K.Y. Rakhimov, G.A. Farias, F.M. Peeters, Phys. Rev. B **82**, 205430 (2010)
70. T. Ando, T. Nakanishi, R. Saito, J. Phys. Soc. Jpn. **67**, 2857 (1998)
71. J. Tworzydlo, I. Snyman, A.R. Akhmerov, C.W.J. Beenakker, Phys. Rev. B **76**, 035411 (2007)
72. B. Huard, N. Stander, J.A. Sulpizio, D. Goldhaber-Gordon, Phys. Rev. B **78**, 121402(R) (2008)
73. R. Saito, *Physical Properties of Carbon Nanotubes* (World Scientific Publishing, 1998)
74. G.L. Kane, *Modern Elementary Particle Physics* (Addison-Wesley, New York, 1987)
75. D.J. Griffiths, *Introduction to Electrodynamics* (Prentice Hall, Upper Saddle River, NJ, 1999)
76. L.M. Zhang, M.M. Fogler, Phys. Rev. Lett. **100**, 116804 (2008)
77. E.O. Kane, E.I. Blount, in *Tunneling Phenomena in Solids*, ed. by E. Burstein, S. Lundqvist (Plenum Press, New York, 1969), p. 79
78. Y. Zhang, T.T. Tang, C. Girit, Z. Hao, M.C. Martin, A. Zettl, M.F. Crommie, Y.R. Shen, F. Wang, Nature **459**, 820 (2009)
79. L. Landau, Phys. Sov. Union **2**, 46 (1932)
80. C. Zener, Proc. Roy. Soc. London A **137**, 696 (1932)
81. S. Datta, *Electronic Transport in Mesoscopic System* (Cambridge University Press, Cambridge, 1995)
82. M.D. Ventra, *Electrical Transport in Nanoscale Systems* (Cambridge University Press, Cambridge, 2008)
83. G.D. Mahan,(Plenum Press, 1990)
84. H. Haug, A.P. Jauho, Springer Series in Solid State Sci. 123 (1996)
85. M.P.L. Sancho, J.M.L. Sancho, J. Phys. F Met. Phys. **14**, 1205 (1984)
86. M.P. Anantram, M.S. Lundstrom, D.E. Nikonov, Proc. IEEE **96**, 1511 (2008)
87. L. Brey, H.A. Fertig, Phys. Rev. B **73**, 235411 (2006)
88. X. Du, I. Skachko, A. Barker, E.Y. Andrei, Nat. Nano. Lett. **3**, 491 (2008)
89. N. Stander, B. Huard, D. Goldhaber-Gordon, arxiv:0806.2319v1 (2008)

90. A. Shytov, M. Rudner, N. Gu, M. Katsnelson, L. Levitov, Sol. State Comm. **149**, 1087 (2009)
91. Y. Zheng, T. Ando, Phys. Rev. B **65**, 245420 (2002)
92. A.R. Akhmerov, J.H. Bardarson, A. Rycerz, C.W.J. Beenakker, Phys. Rev. B **77**, 205416 (2008)
93. C.W.J. Beenakker, Proc. Int. School Phys. E. Fermi **162** (2006)
94. W. Long, Q.F. Sun, J. Wang, Phys. Rev. Lett. **101**, 166806 (2008)
95. P. Carmier, C. Lewenkopf, D. Ullmo, Phys. Rev. B **81**, 241406(R) (2010)
96. J.T. Chalker, P.D. Coddington, J. Phys. C **21**, 2665 (1988)
97. G.M. Rutter, J.N. Crain, N.P. Guisinger, T. Li, P.N. First, J.A. Stroscio, Science **317**, 220 (2007)
98. A.L.V. de Parga, F. Calleja, M.C.G. Passeggi, J.J. Hinarejos, F. Guinea, R. Miranda, Phys. Rev. Lett. **100**, 056807 (2008)
99. M. Ishigami, J.H. Chen, W.G. Cullen, M.S. Fuhrer, E.D. Williams, Nano Lett. **7**, 1643 (2007)
100. E. Stolyarova, K.T. Rim, S. Ryu, J. Maultzsch, P. Kim, L.E. Brus, T.F. Heinz, M.S. Hybertsen, G.W. Flynn, Pro. Nat. Aca. Sci. **104**, 9209 (2007)
101. V. Geringer, M. Liebmann, T. Echtermeyer, S. Runte, M. Schmidt, R. Ruckamp, M.C. Lemme, M. Morgenstern, Phys. Rev. Lett. **102**, 076102 (2009)
102. M.L. Teague, A.P. Lai, J. Velasco, C.R. Hughes, A.D. Beyer, M.W. Bockrath, C.N. Lau, N.C. Yeh, Nano Lett. **9**, 2542 (2009)
103. H. Suzuura, T. Ando, Phys. Rev. B **65**, 235412 (2002)
104. N.C. Yeh, M.L. Teague, S. Yeom, B.L. Standley, R.T.P. Wu, D.A. Boyd, M.W. Bockrath, Surf. Sci. **605**, 1649 (2010)
105. K. Sasaki, Y. Kawazoe, R. Saito, Prog. Theor. Phys. **113**, 463 (2005)
106. F. Guinea, C. Tejedor, F. Flores, E. Louis, Phys. Rev. B **28**, 4397 (1983)
107. C.L. Kane, E.J. Mele, Phys. Rev. Lett. **95**, 226801 (2005)
108. A. Nogaret, S.J. Bending, Phys. Rev. Lett. **84**, 2231 (2000)
109. J.E. Muller, Phys. Rev. Lett. **68**, 385 (1992)
110. J. Reijniers, F.M. Peeters, J. Phys. Cond. Mat. **12**, 9771 (2000)
111. H.S. Sim, K.H. Ahn, K.J. Chang, G. Ihm, N. Kim, S.J. Lee, Phys. Rev. Lett. **80**, 1501 (1998)
112. A.D. Martino, L. Dell'Anna, R. Egger, Phys. Rev. Lett. **98**, 066802 (2007)
113. L. Oroszlany, P. Rakyta, A. Kormanyos, C.J. Lambert, J. Cserti, Phys. Rev. B **77**, 081403 (2008)
114. A. Matulis, F.M. Peeters, P. Vasilopoulos, Phys. Rev. Lett. **72**, 1518 (1994)
115. T. Low, F. Guinea, M.I. Katsnelson, Phys. Rev. B **83**, 195436 (2011)
116. J.L. Manes, Phys. Rev. B **76**, 045430 (2007)
117. H. Suzuura, T. Ando, Phys. Rev. Lett. **89**, 266603 (2002)
118. D.W. Wilson, E.N. Glytsis, T.K. Gaylord, IEEE J. Quan. Elec. **29**, 1364 (1993)
119. D. Dragoman, M. Dragoman, *Quantum-Classical Analogies* (Springer, Heidelberg, 2004)
120. E. Rossi, J.H. Bardarson, P.W. Brouwer, S.D. Sarma, Phys. Rev. B (R) **81**, 121408 (2010)
121. C.R. Dean, A.F. Young, I. Meric, C. Lee, L. Wang, S. Sorgenfrei, K. Watanabe, T. Taniguchi, P. Kim, K.L. Shepard, J. Hone, Nature Nano. **5**, 722 (2010)
122. P. Kim, J.U. Lee, Private communication (2010)
123. S. Tanachutiwat, J.U. Lee, W. Wang, C.Y. Sung, Proc. 47th Design Automation Conf. p. 883 (2010)
124. A.T. Neal, J.J. Gu, T. Low, P.D. Ye, APS March meeting (2011)
125. J.S. Bunch, S.S. Verbridge, J.S. Alden, A.M. van der Zande, J.M. Parpia, H.G. Craighead, P.L. McEuen, Nano Lett. **8**, 2458 (2008)
126. W. Bao, F. Miao, Z. Chen, H. Zhang, W. Jang, C. Dames, C.N. Lau, Nat. Nano. **4**, 562 (2009)
127. Z.H. Ni, T. Yu, Y.H. Lu, Y.Y. Wang, Y.P. Feng, Z.X. Shen, ACS Nano **2**, 2301 (2008)
128. C. Lee, X. Wei, J.W. Kysar, J. Hone, Science **321**, 385 (2008)
129. M. Poetschke, C.G. Rocha, L.E.F.F. Torres, S. Roche, G. Cuniberti, Phys. Rev. B **81**, 193404 (2010)
130. A. Calogeracos, N. Dombey, Contemp. Phys. **40**, 313 (1999)

Chapter 16
Electronic Structure of Bilayer Graphene Nanoribbon and Its Device Application: A Computational Study

Kai-Tak Lam and Gengchiau Liang

Abstract Two-dimensional monolayer graphene has the unique electrical and physical properties which can be exploited in new device structures. However, its application in field-effect device structure is limited due to its semi-metal nature. Therefore, a lot of research efforts have been focussed on introducing an energy bandgap in the electronic structure. For example, a commonly studied method involves cutting two-dimensional graphene into one-dimensional narrow ribbons (graphene nanoribbons), where the spatial quantum confinement introduced by the physical edges generates an energy bandgap that is closely related to the width and edge configurations of the ribbon. Similarly for a bilayer graphene, an energy bandgap can also be obtained like the monolayer graphene nanoribbons, and be further controlled by varying its interlayer distance. In this chapter, a review of the electronic structure of monolayer graphene nanoribbon is presented and the study on the bilayer counterpart is subsequently discussed. Furthermore, based on the electrical properties of the bilayer graphene nanoribbon, the device performance of the Schottky barrier diode is investigated. Lastly, a nanoelectromechanical (NEM) switch based on the floating gate design is presented and discussed.

16.1 Introduction

For the past few decades, miniaturization of silicon-based devices has been the main driving force in device performance enhancement, and it has been predicted that the channel length of a silicon transistor will reach sub-10 nm regime in 2015 with a combination of strained silicon, thin-body structure and innovative gate designs [1]. However, continual scaling down of silicon device is not attainable as the

K.-T. Lam · G. Liang (✉)
Department of Electrical and Computer Engineering, National University of Singapore, Singapore 117576, Republic of Singapore,
e-mail: elelg@nus.edu.sg

H. Raza (ed.), *Graphene Nanoelectronics*, NanoScience and Technology,
DOI 10.1007/978-3-642-22984-8_16, © Springer-Verlag Berlin Heidelberg 2012

devices approach the physical limits of silicon, and it can be foreseen that new materials are required for future device performance enhancement. Coincidentally, research on graphene electronics has been intensified in the recent years by the physical realization of thermal dynamically stable planar graphene since 2004 via physical exfoliation method [2–4] or chemical growth processes [5, 6]. Two-dimensional monolayer graphenes have unique electrical and physical properties which can be exploited in new device structures. The most interesting electrical property is the presence of massless, chiral, Dirac fermions which travel at very high speed [7], which manifest as high carrier mobility of 4,800 cm^2/Vs in experimental measurement [8] and a theoretical mobility of 27,000 cm^2/Vs [2,5]. Frequently used technique in the lab fabrication of graphene transistors is mechanical exfoliation [2], while growth methods, such as epitaxial graphene on top of SiC wafers [5, 9], are suitable for mass-production of graphene devices. Common semiconductor processing techniques such as lithography and etching can then be used for device fabrication. Recent fabrications of graphene transistors have reported a cut-off frequency of 100 GHz [10] and channel mobilities of 20,000 cm^2/Vs in top-gated device structures [11].

However, due to its semi-metal nature, application of graphene in present device structure is limited. Graphene transistors have excellent performance in radio-frequency applications, where OFF-state current is not a major requirement but they fared poorly in digital logic applications [12, 16]. This is due to the high standby power as a result of the absence of sufficient energy bandgap. Therefore, much research effort has been focussed on converting graphene-based materials into semi-conducting material, i.e. introducing an energy bandgap in the electronic structure. While applying an external electric field perpendicular to the plane of monolayer graphene only lead to electrostatic doping effect, in bilayer graphene, an energy bandgap can be induced, which can be tuned by both electric field and interlayer distance [13–19]. Although the experimental results have also demonstrated that this is achievable [20–23], a relatively large electric field is required to produce a sufficiently large energy bandgap that can be practically used for device applications.

On the other hand, a more commonly studied method involves cutting two-dimensional graphene into one-dimensional narrow ribbons (graphene nanoribbons), where the quantum confinement introduced by the physical edges generates an energy bandgap that is closely related to the width and edge configurations of the ribbon [24–28]. Such semi-conducting graphene nanoribbons can be relatively easy to integrate into existing device structures and the unique electronic properties can be used in new device applications. Therefore, it drives extensively both experimental and theoretical studies to focus on integrating graphene nanoribbons into existing device technologies such as metal-oxide-semiconductor field-effect transistors [2, 8, 29–32], resonant tunnelling diode (RTD) [33] and quantum dot devices [34].

Additionally, recent theoretical [35–38] and experimental [39] studies on bilayer graphene nanoribbon, which combines the unique electrical properties of graphene nanoribbon and bilayer graphene, show that it is a versatile material which can

enable new device designs that take advantage of tunable energy bandgap. Studies on the effect of electric field on bilayer graphene nanoribbon reveal hat materials with energy bandgap larger than 0.2 eV are not affected significantly by the perpendicular electric field while for materials with lower energy bandgap, effects similar to bilayer graphene is observed [40, 41]. Recent development in the fabrication of graphene nanoribbons involves the “unzipping" of multi-walled carbon nanotubes via oxidation [42, 43], plasma etching [44] and mechanical sonication in an organic solvent [45], with the latter resulting in high-quality narrow nanoribbons with smooth edges. Such advances in fabrication techniques indicate an imminent realization of mass-produced graphene nanoribbon devices and an understanding of the electronic structure is important in the design and optimization of such devices.

Therefore, in this chapter, a review of the electronic structure of monolayer graphene nanoribbon is firstly presented and our study on the bilayer counterpart is subsequently discussed. Next, based on the electrical properties of the bilayer graphene nanoribbon, the device performance of a Schottky barrier diode is discussed and a nanoelectromechanical (NEM) logic device based on this diode is presented. Lastly, this article will conclude with some suggestions on other possible novel devices based on the unique electrical properties of graphene nanoribbons. Reader are encouraged to peruse further discussions in this Book on graphene monolayers (Chap. 8), bilayers (Chaps. 8, 11 and 17) and nanoribbons (Chaps. 9 and 13).

16.2 Methodology

All simulation results presented in this chapter are calculated based on the first principle density functional theory (DFT) method implemented in ATOMISTIX TOOLKIT 2008.10 [46–48]. The local density approximation (LDA), coupled with the appropriate pseudo-potential, is chosen as the exchange-correlation functional to handle the many-body interaction of the system. Note that the energy bandgap is underestimated in LDA and an overall increase in the energy bandgap shown here is expected if the calculations are repeated using the *GW* approximation [49] as discussed in previous studies [50–52].

All graphene nanoribbons studied are assumed to be fully hydrogen-passivated, with an initial carbon–carbon bond length of 1.42 Å. The carbon–hydrogen bond length of 1.09 Å is assumed before the structures are relaxed to a maximum planar force of 0.05 eV/Å. The bilayer structures are obtained by combining two relaxed monolayer and calculating the total energy of the system as the interlayer distance varies from 2.8 to 6.0 Å. It is found that the total energy of the bilayer structure is minimized at an interlayer distance of 3.2 Å, $\pm$0.1 Å dependent on the ribbon widths. This is smaller than the simulated interlayer distance of bilayer graphene at 3.4 Å, [13] and it could be due to the strong interactions at the edges which contribute to the decrease in the energetically favourable interlayer distance [53].

The mesh cutoff for the real-space Poisson solver is set to 100 Ry for computational efficiency and the electron transport for the device simulations is calculated

based on the non-equilibrium Green's function (NEGF) implemented in the same software package with all other options kept at default values. The NEGF formulism is well described in [54] and only the main equations are presented here. The Green's function in the coherent regime, $G(E)$, is obtained by:

$$G(E) = [E - H_D - \Sigma_L - \Sigma_R]^{-1}, \tag{16.1}$$

where E represents the energy, H_D is the device Hamiltonian obtained by the *ab initio* self-consistent calculations, and the term Σ_L and Σ_R represent the self-energies between the channel and the left and right contacts which can be obtained via the recursive surface green function method described in [54].

From the Green's function, the carrier transmission, $\mathrm{T_c}(E)$, of the device can be calculated by:

$$\mathrm{T_c}(E) = \mathrm{Trace}(\Gamma_L G \Gamma_R G^{\dagger}), \tag{16.2}$$

and

$$\Gamma_n = i(\Sigma_n - \Sigma_n^{\dagger}), \tag{16.3}$$

with $n = L, R$.

After obtaining the transmission of the device, the current of the device can be found using the Landauer formula,

$$I = \frac{q}{h} \int_{-\infty}^{\infty} \mathrm{T_c}(E) \times [f_L(E) - f_R(E)]\, dE, \tag{16.4}$$

where q is the electron charge, h is the Planck constant and f_L, f_R are the Fermi-Dirac distributions of carriers at the left and right contacts and are defined as:

$$f_n(E) = \frac{1}{1 + e^{\frac{E-\mu_n}{k_B T}}}, \tag{16.5}$$

with μ_n being the chemical potential at the contacts which is related to the bias applied across the device, k_B is the Boltzmann constant, T is the operating temperature of the device in Kelvin and $n = L, R$. Readers can also refer to Chapters 15, 17 and 18 for further discussions on the implementations of NEGF formalism.

16.3 Electronic Structure of Monolayer Graphene Nanoribbon

16.3.1 Armchair Edges

The atomic structure of an armchair-edged graphene nanoribbon (AGNR) with width of 1.11 nm is shown in Fig. 16.1a. The white atoms at the left and right edges

of the ribbon are hydrogen and the ribbon is assumed to extend infinitely in the vertical direction. Due to the spatial quantum confinement of the edges, an energy bandgap can be induced as shown in the electronic band diagram in Fig. 16.1e (blue dashed line). From an example of the infinite quantum well, it is shown that as the width of the well increases, the discretized energy level decreases. Similarly, it is easy to follow that as the ribbon width increases, the energy bandgap will decrease. An interesting observation, however, is the presence of the three distinct family types, namely the $3p$, $3p+1$ and $3p+2$, which correspond to the number of carbon atoms along the width (N_A) with p being an integer. This is due to unique hexagonal lattice of graphene systems and the different edge configurations at various widths. As the carbons at the edges are passivated with hydrogen atoms (or any other functional groups), the bond energies and bond lengths at the edges are different to those in the middle of the AGNR and this gives rise to the difference in the quantum confinement effects at the edges [28].

The electronic structures for $N_A = 9$ ($3p$), 10 ($3p+1$) and 11 ($3p+2$), which correspond to ribbon width of 0.98, 1.11, and 1.23 nm are shown in Fig. 16.1e, and it is noted that 1.11 nm exhibits the largest energy bandgap, with 1.23 nm having the smallest. This is consistent for all ribbon widths, i.e. the $3p+1$ family has the largest energy bandgap, and the $3p+2$ family has the smallest, forming three distinct trends as the energy bandgap is plotted as a function of ribbon widths as shown in Fig. 16.2a. While this is an interesting property for AGNR, the fluctuation in energy bandgap, shown as dotted line in Fig. 16.2a, may become a problem during device application and innovative design may be necessary as suggested by [55].

16.3.2 Zigzag Edges

An atomic representation of zigzag-edged graphene nanoribbon (ZGNR) with width of 0.92 nm is shown in Fig. 16.1b with hydrogen (white) atoms passivating the edges at the left and right, and the ribbon extends infinitely in the vertical direction. The electronic structure of ZGNR with widths of 0.92, 1.14 and 1.35 nm are shown in Fig. 16.1f, and in contrast to the AGNR counterpart, there is no energy bandgap induced in ZGNR due to the presence of localized edge states [56]. This introduces a large density of states at the Fermi level (E_F) which is unstable in a non-magnetic configuration due to the strong electron–electron interactions [57]. The magnetic orders at the edges, anti-ferromagnetic or ferromagnetic, will determine the semiconductor or metallic states, respectively [28]. However, when the electron-hole symmetry is broken, either by electric fields [58], magnetic fields [40] or by the presence of dopants [59], these states become dispersive and an energy bandgap can be induced [60].

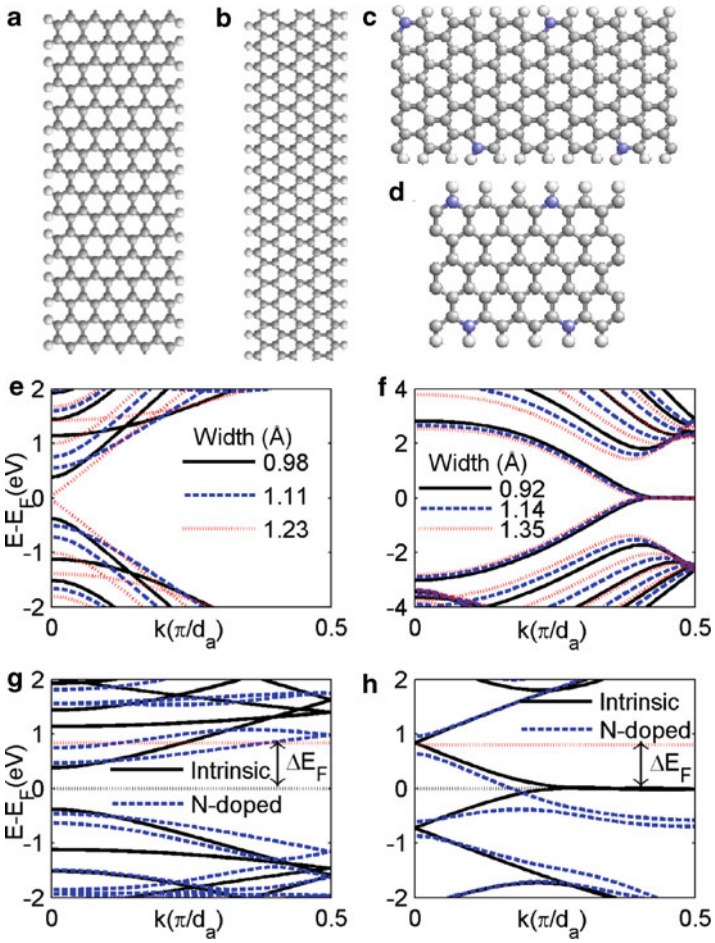

Fig. 16.1 Atomic structure of intrinsic (**a**) armchair-edged graphene nanoribbon (AGNR) and (**b**) zigzag-edged graphene nanoribbon (ZGNR). Nitrogen-doped AGNR (width = 0.98 nm) and ZGNR (width = 0.92 nm) are shown in (**c**) and (**d**), with a doping concentration of 0.47 and 0.27 dopants/Å, respectively. Their corresponding electronic structures are summarized in (**e**)–(**h**)

16.3.3 Dopant Effect

One of the advantages of the presence of edges for graphene nanoribbons is the possibility of changing the E_F of the material by substitution of carbon atoms at the edges with dopants such as boron and nitrogen [61]. An example of nitrogen (blue atoms) doped AGNR and ZGNR are shown in Fig. 16.1c and 16.1d, respectively, with a corresponding doping concentration of 0.47 and 0.27 dopants/Å. Note that

the doping concentration is expressed as the number of dopant atoms per unit length here. Figure 16.1g and 16.1h show an example of the change in the electronic structure due to the presence of the dopants for AGNR and ZGNR, respectively, with the corresponding E_F represented by the black and red dotted lines for intrinsic and doped ribbons.

It is noted that while there is a great difference in the concentration value, the change in E_F (ΔE_F) between the two different graphene nanoribbons are similar, with $\Delta E_F = 0.83\,\text{eV}$ for AGNR and $\Delta E_F = 0.79\,\text{eV}$ for ZGNR. Another important observation is that at such a doping concentration, the AGNR changed from semi-conducting to metallic, which is usual for highly doped semiconductor. On the other hand, for ZGNR, the presence of dopants removes the degeneracy of the eigenvalues and hence induced an energy bandgap near the new E_F, changing the semi-metallic ZGNR to a small energy bandgap semi-conductor. This observation is in agreement with previous study and similar results can be obtained with boron as the dopant [62].

In addition, the dopant-induced energy bandgap of ZGNR is found to be dependent on the width of the ribbon and the doping concentration, presented in Fig. 16.2b and its inset. In contrast to AGNR, semi-conducting ZGNR exhibits an energy bandgap that decreases monotonously with ribbon width. Furthermore, there is an optimal doping concentration where the energy bandgap can reach up to 0.5 eV and this is in agreement with [62]. Lastly, the ΔE_F is plotted against the varying doping concentration to show that it is still monotonously increasing despite the drop in energy bandgap as the doping concentration increases.

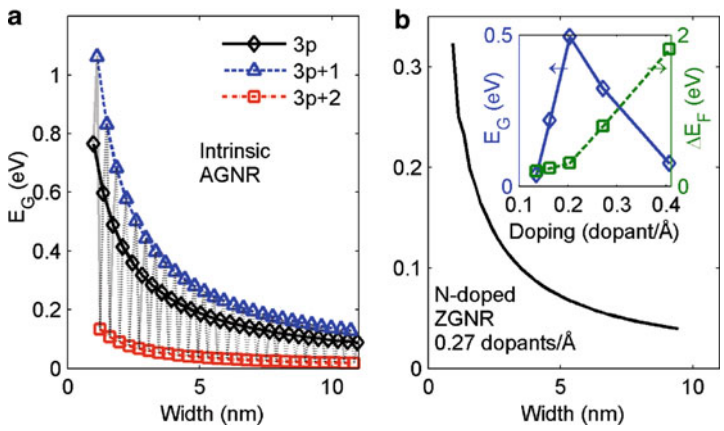

Fig. 16.2 Variation in energy bandgap with respect to the ribbon widths for (**a**) intrinsic AGNR and (**b**) Nitrogen-doped ZGNR. The change in energy bandgap and Fermi energy as doping concentration increases is shown in the inset for ribbon width of 0.92 nm

16.4 Electronic Structure of Bilayer Graphene Nanoribbon

Next, we investigate the electronic structure of bilayer graphene nanoribbon with armchair (bilayer AGNR) and zigzag edges (bilayer ZGNR). For simplicity, it is assumed that the monolayers are A-B stacked, also known as the Bernal stacking, and an example is shown in Fig. 16.3a. The red and blue carbon atoms are the top and bottom layers respectively, with the green carbon atoms stacking directly on top of each other. A side view of the Bernal stacking is shown in Fig. 16.3b. Since we are considering semi-conducting material, only intrinsic bilayer AGNR

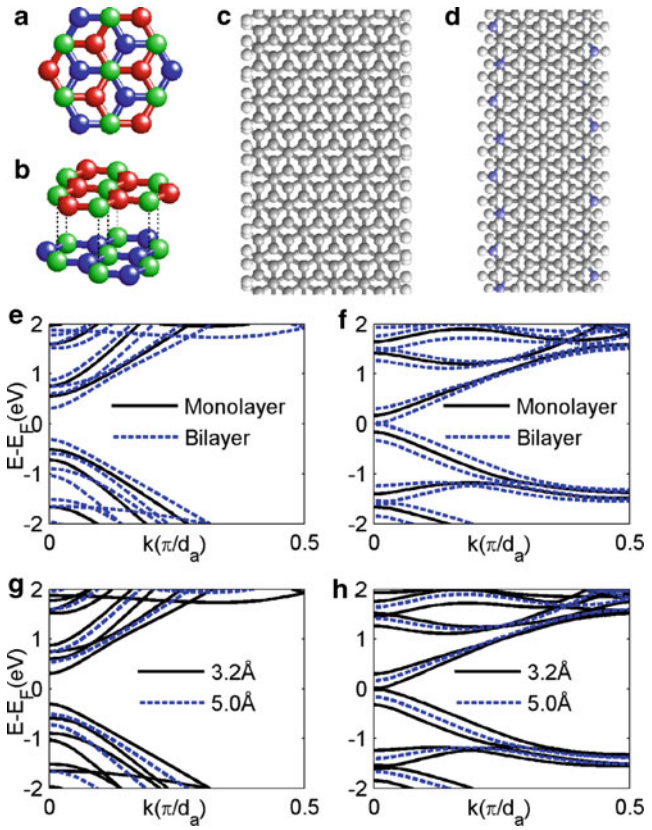

Fig. 16.3 The top and side views of bilayer structures are shown in (**a**) and (**b**) respectively to demonstrate the A-B Bernal stacking. Atomic structures of semi-conducting bilayer graphene nanoribbons are shown in (**c**) and (**d**) for intrinsic bilayer AGNR (width = 1.11 nm) and N-doped bilayer ZGNR (width = 0.99 nm, doping concentration = 0.54 dopants/Å) with their optimal interlayer distance of 3.2 Å, respectively. The corresponding electronic structures are shown in (**e**)–(**f**) in dash lines, with that of the monolayer counterparts plotted in solid for comparison. (**g**)–(**h**) show the band structures of intrinsic bilayer AGNR and N-doped bilayer ZGNR, respectively, with different interlayer distances

and nitrogen-doped bilayer ZGNR are discussed in this article. In addition, the issue of misalignment between the layers are ignored here and interested readers can refer to [63] for a general discussion on misaligned bilayer graphene. As discussed previously in Sect. 16.2, the energetically favourable interlayer distance is at 3.2 Å and this is discussed first, followed by the effect of varying the interlayer distance.

16.4.1 Armchair Edges

An atomic structure of an bilayer AGNR of width 1.11 nm is shown in Fig. 16.3c and the corresponding electronic structure is shown in Fig. 16.3e, superimposed onto that of the monolayer counterpart. Each of the monolayer energy bands (black solid line) is split into two bands (blue dashed lines) for bilayer AGNR and as a result, the energy bandgap of bilayer AGNR is much smaller than the monolayer counterpart. This is even more pronounced for the $3p + 2$ family, which is already a small energy bandgap material in monolayer structure. The reduction in energy bandgap in bilayer structure renders the $3p+2$ family semi-metallic, with an energy bandgap ranging from 7 to 4 meV. In addition, the effect of the energy bandgap reduction is more severe for the $3p + 1$ family than the $3p$ family and hence these two families merge into one as the ribbon width increases to more than 2.0 nm. A more in-depth discussion on the width dependency of the bilayer AGNR energy bandgap can be found in [53]. Next, the energy bandgap dependency on the width of bilayer AGNR is investigated [53], as shown in Fig. 16.4. We first examine the case where the interlayer distance is 5.0 Å (hollow points) where the interaction between the layers is not significant. The energy bandgap of this system shows the three families trends exactly matching the monolayer trends (dot-dashed lines). It indicates that an bilayer AGNR with large interlayer distance can be treated as two non-interacting AGNR in terms of electronic structure. On the other hand, at their respective optimum interlayer distance, which is different for various widths, the

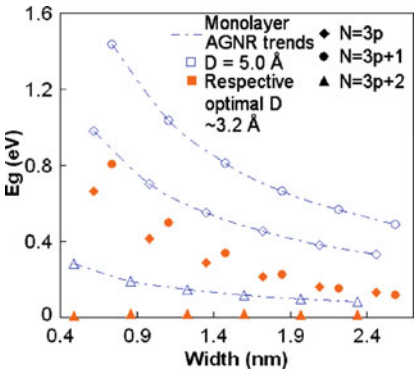

Fig. 16.4 energy bandgap variation with ribbon width for bilayer AGNR with interlayer distance (D) of 5.0 Å (empty markers) and respective optimal distance (solid markers) at approximately 3.2 Å

energy gaps of bilayer AGNR (solid markers) is reduced by 32–96% as compared to that of AGNR for all ribbon widths, similar to the observation above. This reduction in energy bandgap is possibly due to the electron–electron interaction between the layers at the edges and hence the edge effect diminishes as compared to AGNR.

16.4.2 Zigzag Edges with Dopants

The atomic representation of a bilayer ZGNR consisting of two 0.92 nm wide, 0.27 dopants/Å, nitrogen-doped ZGNR is shown in Fig. 16.3d. The resultant width of the bilayer ZGNR is 0.99 nm due to the Bernal stacking and due to the bilayer structure. The dopant concentration is doubled to 0.54 dopants/Å. From the corresponding electronic structure shown in Fig. 16.3f, the splitting of each monolayer energy bands leads to the closing of energy bandgap in the material and the doped bilayer ZGNR is semi-metallic. This is similar to the observation made for the bilayer AGNR $3p + 2$ family. Note that due to the high reactivity of the edge states in ZGNR, the edges of intrinsic bilayer ZGNR tend to be distorted as the width of ribbon increases as reported in [35] where the weak van der Waals forces are included in the DFT model. This edge distortion causes the dispersion of the edge states and hence there exists a finite energy bandgap in the energetically favourable non-magnetic configuration.

16.4.3 Interlayer Distance

After the observation of the closing and decreasing of the energy bandgaps of the bilayer graphene nanoribbons, we were interested to find out what happened when the interlayer distance is increased. An interlayer distance of 5.0 Å is used, and the corresponding electronic structures of bilayer AGNR and bilayer ZGNR are plotted in Fig. 16.3g and 16.3h, respectively, with their 3.2 Å counterparts. It is found that at 5.0 Å, the energy bandgaps of both bilayer ribbons increase back to that of the monolayer counterparts. In fact, the electronic structures of the monolayer and bilayer ribbons are identical at large interlayer distance. It indicates that the decrease of energy bandgap is related to the interactions between the layers and as the interlayer distance increases from the energetically favourable distance of 3.2 Å, the interlayer interaction becomes weaker and the energy bandgap is “restored” to that of the individual monolayers.

To validate this point, the energy bandgap dependency on the interlayer distance is calculated and presented in Fig. 16.5a and 16.5b for bilayer AGNR and nitrogen-doped bilayer ZGNR, respectively. The progressive increase of energy bandgap coincides with the weakening of interlayer interactions as the monolayers move further apart from 3.2 to 5.0 Å. Beyond 5.0 Å, the energy bandgap reaches the same value as the monolayer ribbon and then remain constant. Different widths of

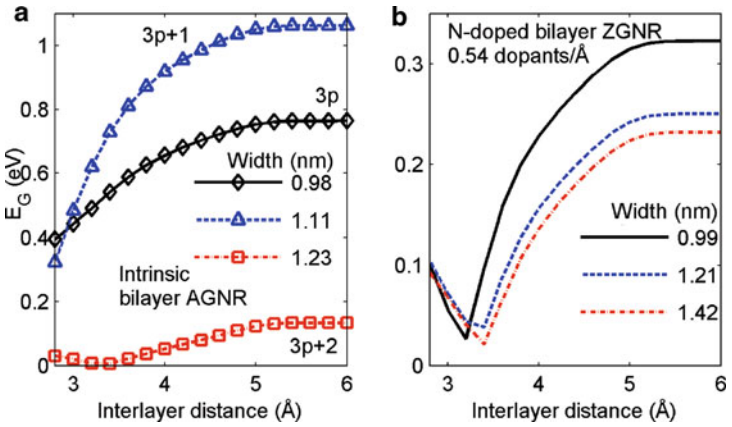

Fig. 16.5 Variation in energy bandgap of semi-conducting bilayer graphene nanoribbons as a function of the interlayer distance for (**a**) intrinsic bilayer AGNR and (**b**) N-doped bilayer ZGNR

bilayer AGNR corresponding to the three families are investigated and the $3p + 1$ family shows the steepest increase in the energy bandgap. More interestingly, as the interlayer distance decreases below 3.2 Å, the energy bandgap of the $3p$ and $3p + 1$ families of bilayer AGNR continue to decrease while that of the $3p + 2$ family and the bilayer ZGNR increases. This indicates that interlayer interaction is not the only reason for the change in the energy bandgap and further studies are required to discover what other mechanisms are involved.

Nevertheless, the unique feature of changing electronic property via interlayer distance brings about new device designs. In the following section, we propose a two-terminal Schottky barrier diode based on bilayer ZGNR whose current output can be varied by changing the interlayer distance.

16.5 Bilayer Graphene Nanoribbon Device

The studied bilayer ZGNR Schottky barrier diode consists of two monolayer device made up of semi-metallic intrinsic ZGNR as the contacts and semi-conducting nitrogen-doped ZGNR as the channel material, shown in Fig. 16.6a (not drawn to scale). The width of the ribbon is 0.92 nm and the channel length is 17.68 nm. The doping concentration of the channel is 0.27 dopants/Å. The top and side views of the proposed device are shown in Fig. 16.6b and 16.6c. The arrows in Fig. 16.6c indicate a vertically aligned force used to change interlayer distance of the bilayer ZGNR.

The current characteristics of the bilayer ZGNR Schottky barrier diode with interlayer distance (D) of 3.2 and 5.0 Å is calculated. For comparison, the current characteristic of the monolayer device is also calculated. The various

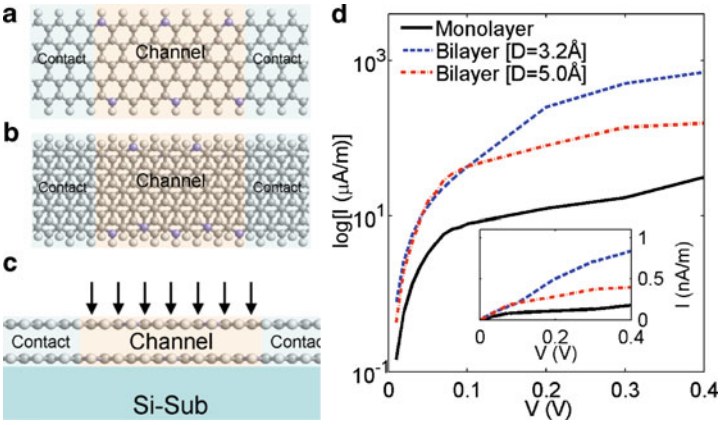

Fig. 16.6 Atomic schematic of the proposed N-doped ZGNR Schottky barrier diode: (**a**) monolayer and (**b**) bilayer. (**c**) Side view device schematic of the bilayer ZGNR diode. (**d**) The current characteristics of the device in semi-log plot with linear scale in the inset.

current-bias plots are summarized in Fig. 16.6d and the bilayer ZGNR device with $D = 3.2$ Å (blue dashed line) has the highest drive current as compared to the other two diodes. In addition, the current characteristics of bilayer ZGNR device with $D = 5.0$ Å (red dot-dashed line) are very similar to those of the monolayer device (black solid line), albeit with an almost doubled current.

To further understand the device operating mechanism, the transmission spectra at equilibrium of the three devices are plotted in Fig. 16.7a. The zero-transmission region corresponds to the Schottky barrier of the semi-metallic intrinsic AGNR and the semi-conducting nitrogen-doped ZGNR. The Schottky barrier height is related to the energy bandgap of the channel material and the band alignment between the intrinsic contacts and the doped channel. The monolayer device (black solid line) with the largest energy bandgap having the highest Schottky barrier of 0.62 eV. On the other hand, the Schottky barriers of the bilayer devices are 0.45 and 0.59 eV for an interlayer distance of 3.2 and 5.0 Å respectively. Another interesting observation is that for bilayer ZGNR Schottky barrier diode with interlayer distance of 3.2 Å, the transmission increases step-wise from 0 to 2, whereas the step is missing for the transmission of $D = 5.0$ Å. This is due to the merging of bands as the monolayers get further apart as shown in Fig. 16.3h.

From Fig. 16.6d, considering the bilayer ZGNR device with an initial interlayer distance of 3.2 Å and a bias of 0.4 V is applied, if one can change the interlayer distance to 5.0 Å, a two-state logic device with an ON–OFF ratio of about an order can be obtained. A simplified spatially resolved band diagram under a bias of 0.4 V is plotted in Fig. 16.7b to illustrate the operating mechanism of such a logic device. The bulk of the current obtained is due to the thermionic emission current above the Schottky barrier as indicated by the arrow. At an interlayer distance of 3.2 Å, the barrier is 0.45 eV (blue dashed line) and as the interlayer distance increases,

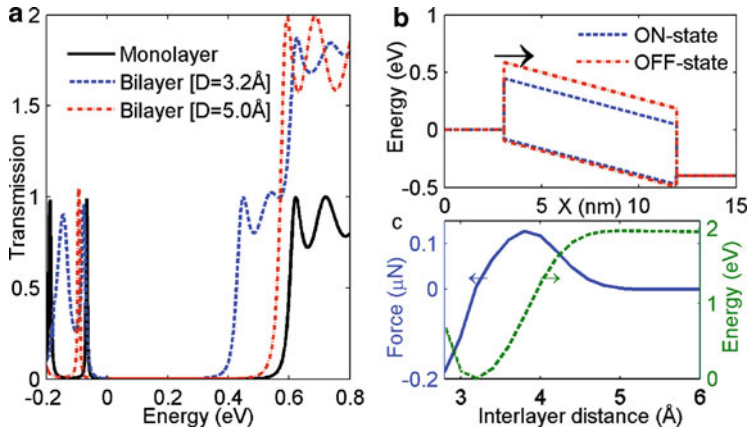

Fig. 16.7 (**a**) Transmission spectra, (**b**) band diagrams and (**c**) the switching force of the proposed device

the barrier increases to 0.58 eV (read dot-dashed line). Due to the Fermi-Dirac distribution of the carrier, there are fewer carriers present at higher energy level, and hence the current decreases for such device with larger interlayer distance. Similarly, the tunnelling current just below the Schottky barrier is larger for the smaller interlayer distance device due to the availability of more carriers for transport.

In addition, the feasibility of such a logic device is explored by estimating the force required to switch the proposed device. The total energy of the bilayer ZGNR device at various interlayer distances is calculated, and the results are summarized in Fig. 16.7c (green dashed line). The energy scale is normalized to the lowest total energy of the bilayer ZGNR device. After which, the force between the layer is calculated by taking the derivative of the total energy and it is presented as a blue solid line in Fig. 16.7c. It is clearly seen that there are two stable states for the bilayer ZGNR device, where the forces are zero when the interlayer distance is at 3.2 Å and beyond 5.0 Å. The switching force between the two states for the proposed device is found to be 0.14 μN for a channel area of 8.13 nm^2. This force can be supplied by direct application, rendering the device a force sensor or by using a floating gate design with a capacitive actuator [64] which can control the interlayer distance via electrostatic means.

16.6 Bilayer ZGNR NEM Switch

An analytic model for a bilayer ZGNR NEM switch based on the floating gate parallel plate capacitive actuator described in [64] is developed to provide the physical insights into the device characteristics of the switch, shown in Fig. 16.8. The switch is initially set to be at ON-state (Fig. 16.8a) with a fixed bias of 0.4 V.

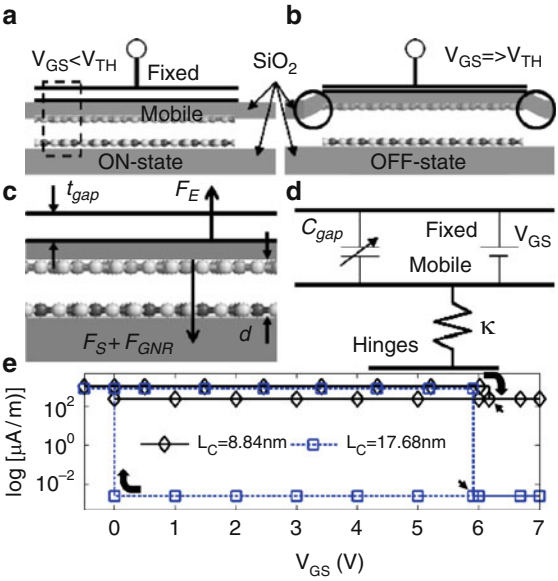

Fig. 16.8 The side-view schematics of the bilayer ZGNR NEM switch at (**a**) ON-state and (**b**) OFF-state. A free-body diagram of the dashed box region in (**a**) is shown in (**c**) and the equivalent circuit used to analysis the device is shown in (**d**). The device characteristics of the switch with different channel lengths are shown in (**e**)

The gate bias (V_{GS}) is applied across the floating gate to increase the interlayer distance of the bilayer ZGNR, thereby increasing the energy bandgap of the channel in order to decrease the conductance of the switch, leading to a distinct OFF-state (Fig. 16.8b). The free-body diagram indicating the forces involved in the boxed region in Fig. 16.8a is shown in Fig. 16.8c. Based on this operation principle, the system can be analysed using an equivalent circuit shown in Fig. 16.8d with a gap capacitor C_{gap} and the deformed oxide represented by the spring hinge.

In this model, the electrostatic attractive force (F_E) formed between the fixed and mobile electrodes is dependent on the electrode separation (t_{gap}) and the V_{GS}. The electrostatic attractive force has to overcome the combination of the restorative elastic force (F_S) and the interlayer force of the bilayer ZGNR (F_{GNR}). The restorative elastic force arises from the deformation of the oxide layer as the interlayer distance increases (indicated by the circles in Fig. 16.8b) and the interlayer force of the bilayer ZGNR is calculated from DFT simulations similar to Fig. 16.7c. The governing equations for the bilayer ZGNR NEM switch are as follows:

$$F_E = -\frac{V_{GS}^2}{2}\frac{d}{dx}\left(\frac{\epsilon_{\text{gap}} A}{t_{\text{gap}}}\right) = \frac{V_{GS}^2 \epsilon_{\text{gap}} A}{2t_{\text{gap}}^2}, \tag{16.6}$$

$$F_E = F_S + F_{\text{GNR}} = \kappa \Delta x + F_{\text{GNR}}, \tag{16.7}$$

$$V_{GS} = \sqrt{\frac{2t_{\text{gap}}^2(\kappa \Delta x + F_{\text{GNR}})}{\epsilon_{\text{gap}} A}}, \tag{16.8}$$

where ϵ_{gap} is the dielectric constant of the air gap between the electrodes, A is the surface area of the electrode, κ is the linear spring constant of deformed oxide and $\Delta x = t_{gap0} - t_{gap}$ where t_{gap0} is the initial electrode separation. Setting the $t_{gap0} = 0.5\,\text{nm}$, $\kappa = 50\,\text{N/m}$ and an electrode area of 5 times the channel area, the device characteristics for the NEM switch as V_{GS} varies are shown in Fig. 16.8e. A similar device with longer channel length (L_C) of 17.68 nm is also considered, which provides a much smaller OFF-state current due to the exponential decrease of direct tunnelling as L_C increases. The threshold gate biasses (V_{TH}), indicated by the arrows, are 6.17 and 5.90 V for the 8.84 and 17.68 nm device, respectively. As V_{GS} increases, the switch is at ON-state until V_{TH} where an abrupt change in the interlayer distance is achieved due to the snapping together of the electrode. V_{TH} is hence also known as the pull-in bias. Once the electrode are in contact, they do not separate until $V_{GS} = 0\,\text{V}$, also known as the pull-out bias. As a result, the hysteresis loop is observed in Fig. 16.8e. An I_{ON}/I_{OFF} ratio of 6 orders is achieved for the longer channel switch under the drain bias of 0.4 V, which has a great potential for low power memory applications.

While the V_{TH} can be controlled by varying the parameters such as the gate area and elastic spring constant of the hinge structure according to (16.8), the pull-out bias is always at 0 V for the first design due to the extremely strong electrostatic forces when the two electrodes is in contact. In order to control the pull-out bias, an additional oxide layer can be placed between the electrodes as shown in Fig. 16.9a to avoid the direct contact between the metal planes. The resultant capacitance can be considered as a serial combination of the oxide capacitance (C_{ox}) and C_{gap} shown

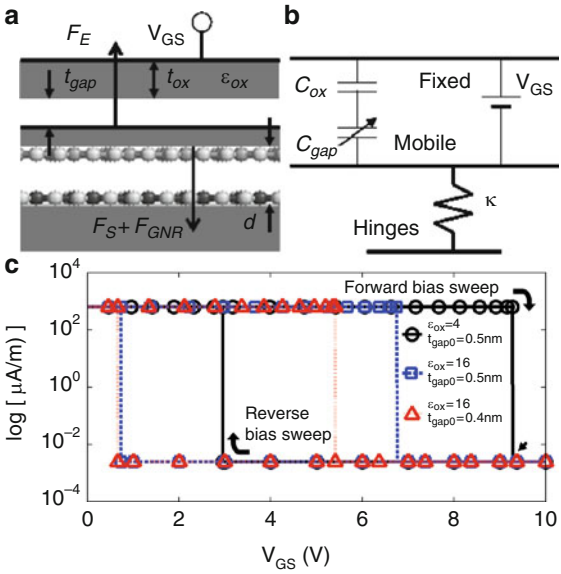

Fig. 16.9 (**a**) The side-view schematics of the NEM switch with an additional oxide layer between the floating gate electrodes and (**b**) the modified equivalent circuit. (**c**) The switching characteristics of the modified NEM with different oxide dielectrics (ϵ_{ox}) and initial electrode separation (t_{gap0})

in Fig. 16.9b. The modified governing equations are shown below:

$$F_E = \frac{V_{GS}^2 \epsilon_{\text{ox}}^2 \epsilon_{\text{gap}} A}{2(t_{\text{ox}} \epsilon_{\text{gap}} + t_{\text{gap}} \epsilon_{\text{ox}})^2}, \tag{16.9}$$

$$V_{GS} = \sqrt{\frac{2(t_{\text{ox}} \epsilon_{\text{gap}} + t_{\text{gap}} \epsilon_{\text{ox}})^2 (\kappa \Delta x + F_{\text{GNR}})}{\epsilon_{\text{ox}}^2 \epsilon_{\text{gap}} A}}, \tag{16.10}$$

It can be seen in Fig. 16.9c that the pull-out bias has shifted away from 0 V to 2.94 V, with a silicon dioxide layer (ϵ_{ox} assumed to be 4) of thickness (t_{ox}) 1 nm and the rest of the parameter same as previous design with channel length of 17.68 nm. However, V_{TH} increases from 5.90 to 9.71 V (arrow in Fig. 16.9c). It is because this additional C_{ox} serves as an additional configurable parameter in (16.10) to increase V_{TH}. Therefore, in order to reduce the V_{TH} in this design, high-k material can be used. As shown in Fig. 16.9c, the V_{TH} can be adjusted to a smaller value of 6.75 V using an oxide with $\epsilon_{\text{ox}} = 16$. Note that the basic operating principle is still predominated by the parameters described in the previous design and there is a limitation in adjusting the V_{TH} using this approach. It can be shown that a small t_{ox} or a very large ϵ_{ox} would convert (16.10) to (16.8), which shows that the V_{TH} of the second design will always be larger than that of the first one if all other parameters are kept constant. Additionally, the size of the hysteresis loop, i.e. difference between V_{TH} and pull-out bias, can be controlled by adjusting the initial air gap between the floating gate electrodes. More specifically by reducing the t_{gap0}, the size of the hysteresis loop reduces significantly. Further optimization of various parameters can eliminate the hysteresis loop for other application purposes.

16.7 Conclusion

In summary, we have reviewed the electronic structure of monolayer graphene nanoribbons and presented our study on the bilayer counterparts. The doping effect on the monolayer graphene nanoribbons are examined and it is found that not only the presences of dopants vary the E_F of ZGNR but also a metal-to-semi-conductor transition also occurs. We have shown that as the ribbon width increases, the energy bandgap of intrinsic AGNR and nitrogen-doped ZGNR decreases.

Furthermore, the electronic structures of intrinsic bilayer AGNR and nitrogen-doped bilayer ZGNR are examined and it is observed that the energy bandgap of the bilayer material is smaller than that of the monolayer counterpart. This reduction in energy bandgap is due to the interaction between the layers and as the interlayer distance increases, this interaction decreases and the energy bandgap increases back to that of the monolayer. The energy bandgap dependency on the interlayer distance is plotted for both bilayer AGNR and bilayer ZGNR. It is observed that the different

families of bilayer AGNR response in different degree to the change in the interlayer distance, with the $3p + 1$ family most affected.

Based on these observations, a Schottky barrier diode based on ZGNR is proposed, with the intrinsic ZGNR as the metal contact and the nitrogen-doped semi-conducting ZGNR as the channel material. A similar structure based on the bilayer ZGNR is also examined and the current characteristics are simulated for the monolayer device and bilayer device at different interlayer distance. Due to the difference in E_F and the band alignment between the contact and channel material, a Schottky barrier is formed and it is found that as the interlayer distance of the bilayer device increases, the Schottky barrier also increases. Exploiting this unique feature, a simple logic element which changes its state via a change in the interlayer distance is proposed and a force of 0.14 μN is required for a change of an order in the output current. Other than direct application of force, the interlayer distance can also be changed via electrostatic means such as via the implementation of a floating gate capacitive actuator design.

While the discussion here focussed on the implementation of bilayer ZGNR for device application, bilayer AGNR can also be used for devices such as RTDs [33], where the larger varying energy bandgap lends itself to the role of creating a variable barrier for the control of the quantum tunnelling currents. While further research in the fabrication and precise control of the edges is still required for the mass-production of graphene-based electronic devices, the progress in the recent years has been encouraging and due to its unique metallic/semi-conducting properties, all-graphene electronics may provide a huge contribution towards the advancement of device performance in the near future.

Acknowledgements The authors would like to acknowledge the financial supports of the Science and Engineering Research Council of the Agency for Science, Technology and Research, Singapore, under the fund No. 082-101-0023.

References

1. Process Integration, Devices, and Structures, in *International Technology Roadmap for Semiconductors (ITRS)*, 2009 edition. Link: http://www.itrs.net/Links/2009ITRS/2009Chapters_2009Tables/2009_PIDS.pdf. (Online)
2. K.S. Novoselov, A.K. Geim, S.V. Morozov, D. Jiang, Y. Zhang, S.V. Dubonos, I.V. Grigorieva, A.A. Firsov, Science **306**, 666 (2004)
3. K.S. Novoselov, A.K. Geim, S.V. Morozov, D. Jiang, M.I. Katsnelson, I.V. Grigorieva, S.V. Dubonos, A.A. Firsov, Nature **438**, 197 (2005)
4. Y. Zhang, Y.-W. Tan, H.L. Stormer, P. Kim, Nature **438**, 201 (2005)
5. C. Berger, Z. Song, X. Li, X. Wu, N. Brown, C. Naud, D. Mayou, T. Li, J. Hass, A.N. Marchenkov, E.H. Conrad, P.N. First, W.A. de Heer, Science **312**, 1191 (2006)
6. C. Berger, Z. Song, T. Li, X. Li, A.Y. Ogbazghi, R. Feng, Z. Dai, A.N. Marchenkov, E.H. Conrad, P.N. First, W.A. de Heer, J. Phys. Chem. B **108**, 11912 (2004)
7. A.H. Castro Neto, F. Guinea, N.M.R. Peres, K.S. Novoselov, A.K. Geim, Rev. Mod. Phys. **81**, 109 (2009)

8. M.C. Lemme, T.J. Echtermeyer, M. Baus, H. Kurz, IEEE Elec. Dev. Lett. **28**, 282 (2007)
9. J. Kedzierski, P.-L. Hsu, P. Healey, P.W. Wyatt, C.L. Keast, M. Sprinkle, C. Berger, W.A. de Heer, IEEE Trans. Elec. Dev. **55**, 2078 (2008)
10. Y.-M. Lin, C. Dimitrakopoulos, K.A. Jenkins, D.B. Farmer, H.-Y. Chiu, A. Grill, Ph. Avouris, Science **327**, 662 (2010)
11. L. Liao, J. Bai, Y. Qu, Y.-C. Lin, Y. Li, Y. Huang, X. Duan, Proc. Natl. Acad. Sci. USA **107**, 6711 (2010)
12. F. Schwierz, Nat. Nanotechnol. **5**, 487 (2010)
13. S.B. Trickey, F. Müller-Plathe, G.H.F. Diercksen, Phys. Rev. B **45**, 4460 (1992)
14. E. McCann, V.I. Fal'ko, Phys. Rev. Lett. **96**, 086805 (2006)
15. E. McCann, Phys. Rev. B. **74**, 161403 (2006)
16. Y. Ouyang, P. Campbell, J. Guo, Appl. Phys. Lett. **92**, 063120 (2008)
17. J. Nilsson, A.H. Castro Neto, F. Guinea, N.M.R. Peres, Phys. Rev. B **76**, 165416 (2007)
18. G. Fiori, G. Iannaccone, IEEE Elec. Dev. Lett. **30**, 1096 (2009)
19. M. Cheli, G. Fiori, G. Iannaccone, IEEE Trans. Elec. Dev. **56**, 2979 (2010)
20. E.V. Castro, K.S. Novoselov, S.V. Morozov, N.M.R. Peres, J.M.B. Lopes dos Santos, J. Nilsson, F. Guinea, A.K. Geim, A.H. Castro Neto, Phys. Rev. Lett. **99**, 216802 (2007)
21. L.M. Zhang, Z.Q. Li, D.N. Basov, M.M. Fogler, Z. Hao, M.C. Martin, Phys. Rev. B **78**, 235408 (2008)
22. Z.Q. Li, E.A. Henriksen, Z. Jiang, Z. Hao, M.C. Martin, P. Kim, H.L. Stormer, D.N. Basov, Phys. Rev. Lett. **102**, 037403 (2009)
23. Y. Zhang, T.-T. Tang, C. Girit, Z. Hao, M.C. Martin, A. Zettl, M.F. Crommie, Y.R. Shen, F. Wang, Nature **459**, 820 (2009)
24. M. Fujita, K. Wakabayashi, K. Nakada, K. Kusakabe, J. Phys. Soc. Jpn. **65**, 1920 (1996)
25. K. Nakada, M. Fujita, G. Dresselhaus, M.S. Dresselhaus, Phys. Rev. B **54**, 17954 (1996)
26. K. Wakabayashi, M. Fujita, H. Ajiki, M. Sigrist, Phys. Rev. B **59**, 8271 (1999)
27. M. Ezawa, Phys. Rev. B **73**, 045432 (2006)
28. Y.-W. Son, M.L. Cohen, S.G. Louie, Phys. Rev. Lett. **97**, 216803 (2006)
29. B. Obradovic, R. Kotlyar, F. Heinz, P. Matagne, T. Rakshit, M.D. Giles, M.A. Stettler, D.E. Nikonov, Appl. Phys. Lett. **88**, 142102 (2006)
30. G. Liang, N. Neophytou, M.S. Lundstrom, D.E. Nikonov, J. Appl. Phys. **102**, 054307 (2007)
31. G. Liang, N. Neophytou, M.S. Lundstrom, D.E. Nikonov, Nano Lett. **8**, 1819 (2008)
32. X. Li, X. Wang, L. Zhang, S. Lee, H. Dai, Science **319**, 1229 (2008)
33. H. Teong, K.-T. Lam, S.B. Khalid, G. Liang, J. Appl. Phys. **105**, 084317 (2009)
34. Z.F. Wang, Q.W. Shi, Q. Li, X. Wang, J.G. Hou, H. Zheng, Y. Yao, J. Chen, Appl. Phys. Lett. **91**, 053109 (2007)
35. M.P. Lima, A. Fazzio, A.J.R. da Silva, Phys. Rev. B **79**, 153401 (2009)
36. J.-W. Rhim, K. Moon, J. Phys.: Condens. Matter **20**, 365202 (2008)
37. N. Xu, J.W. Ding, J. Phys.: Condens. Matter **20**, 485213 (2008)
38. H. Xu, T. Heinzel, Phys. Rev. B **80**, 045308 (2009)
39. B.N. Szafranek, D. Schall, M. Otto, D. Neumaier, H. Kurz, Appl. Phys. Lett. **96**, 112103 (2010)
40. B. Sahu, H. Min, A.H. MacDonald, S.K. Banerjee, Phys. Rev. B **78**, 045404 (2008)
41. T.S. Lin, Y.C. Huang, S.C. Chang, Y.C. Chuang, M.F. Lin, Eur. Phys. J. B **64**, 73 (2008)
42. D.V. Kosynkin, A.L. Higginbotham, A. Sinitskii, J.R. Lomeda, A. Dimiev, B.K. Price, J.M. Tour, Nature **458**, 872 (2009)
43. N.L. Rangel, J.C. Sotelo, J.M. Seminario, J. Chem. Phys. **131**, 031105 (2009)
44. L. Jiao, L. Zhang, X. Wang, G. Diankov, H. Dai, Nature **458**, 877 (2009)
45. L. Jiao, X. Wang, G. Diankov, H. Wang, H. Dai, Nat. Nanotechnol. **5**, 321 (2010)
46. J. Taylor, H. Guo, J. Wang, Phys. Rev. B **63**, 245407 (2001)
47. M. Brandbyge, J.-L. Mozos, P. Ordejón, J. Taylor, K. Stokbro, Phys. Rev. B **65**, 165401 (2002)
48. J.M. Soler, E. Artacho, J.D. Gale, A. Gracia, J. Junquera, P. Ordejón, D. Sánchez-Portal, J. Phys: Cond. Matt. **14**, 2745 (2002)
49. M.S. Hybertsen, S.G. Louie, Phys. Rev. B **34**, 5390 (1986)
50. T. Miyake, S. Saito, Phys. Rev. B **68**, 155424 (2003)

51. T. Miyake, S. Saito, Phys. Rev. B **72**, 073404 (2005)
52. L. Yang, C.-H. Park, Y.-W. Son, M.L. Cohen, S.G. Louie, Phys. Rev. Lett. **99**, 186801 (2007)
53. K.-T. Lam, G. Liang, Appl. Phys. Lett. **92**, 223106 (2008)
54. S. Datta, in *Quantum Transport: Atom to Transistor* (Cambridge University Press, New York, 2005)
55. X. Guan, M. Zhang, Z. Yu, IEEE Elec. Dev. Lett. **29**, 759 (2008)
56. L. Brey, H. A. Fertig, Phys. Rev. B **73**, 195408 (2006)
57. M. Fujita, K. Wakabayashi, K. Nakada, K. Kusakabe, J. Phys. Soc. Jpn. **65**, 1920 (1996)
58. S.D. Dalosto, Z.H. Levine, J. Phys. Chem. C, **112**, 8196 (2008)
59. R. Peköz, Ş. Erkoç, Phys. E: Low Dimens. Syst. Nanostruct. **42**, 110 (2009)
60. A.H. Castro Neto, F. Guinea, N.M.R. Peres, Phys. Rev. B **73**, 205408 (2006)
61. X. Wang, X. Li, L. Zhang, Y. Yoon, P.K. Weber, H. Wang, J. Guo, H. Dai, Science **324**, 768 (2009)
62. B. Huang, Q. Yan, G. Zhou, J. Wu, B.-L. Gu, W. Duan, F. Liu, Appl. Phys. Lett. **91**, 253122 (2007)
63. S. Latil, V. Meunier, L. Henrard, Phys. Rev. B **76**, 201402 (2007)
64. M.-H. Bao, in *Micro Mechanical Transducers: Pressure Sensors, Accelerometers and Gyroscopes* (Elsevier, Amsterdam, 2000)

Chapter 17
Field-Modulation Devices in Graphene Nanostructures

Hassan Raza

Abstract In this chapter, we discuss the futuristic device applications of electronic-structure modulation due to an external electric field in a tutorial fashion. Such an electric field can be applied in the stacking direction for a bilayer graphene and in the width direction for armchair graphene nanoribbons (acGNR) and zigzag graphene nanoribbons (zzGNR). We first present a tutorial on the electronic-structure of various forms of graphene. After discussing the relevant theoretical models, we discuss the electric field modulation of bilayer graphene in the presence of strain and misalignment. Then we present the electric field modulation results of acGNRs with pristine and rough edges. We further discuss the modulation in zzGNRs with periodic edge roughness. Finally, we discuss the potential applications of such an electronic-structure modulation in electronics, photonics, plasmonics, etc.

17.1 Introduction

Unconstrained graphene is a two-dimensional (2D) semi-metallic material. The most important property that distinguishes it from other 2D materials/quasi-crystals is its linear instead of parabolic dispersion and excellent transport properties [1–7]. However, it has a severe bottleneck for nanoelectronics applications, namely, it has a zero band gap. When two graphene membranes are stacked in a Bernal ($\tilde{A}-B$) configuration, the dispersion becomes quadratic [8], although the band gap still remains zero. By engineering a band gap in the graphene nanostructure, one can make this material a competitor of silicon technology to extend Moore's law in this century.

H. Raza (✉)
Department of Electrical and Computer Engineering, University of Iowa, Iowa City, IA 52242, USA
e-mail: hraza@engineering.uiowa.edu

H. Raza (ed.), *Graphene Nanoelectronics*, NanoScience and Technology,
DOI 10.1007/978-3-642-22984-8_17, © Springer-Verlag Berlin Heidelberg 2012

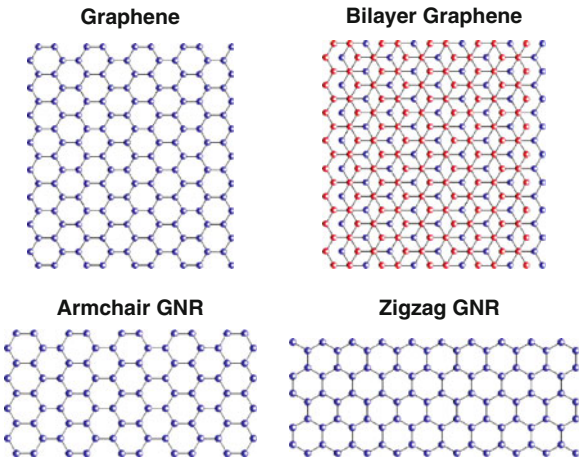

Fig. 17.1 Visualization of graphene, bilayer graphene, N = 9 armchair nanoribbon (acGNR), and N = 10 zigzag graphene nanoribbon (zzGNR). A uniform electric field E can be applied in the width direction for GNRs and in the bilayer direction. The atomic visualization is done using Hückel-NV [15]

Notably, when graphene is patterned into a nanoribbon by reducing one dimension, the quantization effects dictated by the fixed boundary conditions can result in a bandgap opening depending on the chirality and the width [2, 9–14]. The most simplistic graphene nanoribbons (GNRs) are zigzag GNR (zzGNR) and armchair GNR (acGNR) with zigzag and armchair edges, respectively, as shown in Fig. 17.1. Conventionally, when a zzGNR is rolled into a carbon nanotube (CNT), it forms an armchair CNT and vice versa. In CNT, the quantization follows the periodic boundary conditions and in such a case, by constraining one dimension of GNR, the dispersion no longer remains linear and the inherent advantages associated with the linear dispersion of graphene are thus lost.

Once the band gap is achieved, another important degree of freedom in devices that is essential to be explored is the effect of electrical field on various electronic structure features. Notably, using an electric-field (E) in the stacking direction for the bilayer graphene and in the width direction for the nanoribbons, one can modulate the band gap very effectively. This band gap modulation may lead to various applications. Similar studies can be performed on various graphene nanostrcutures and will form a significant part of this chapter. Novel devices based on the unique electronic structure features of graphene and its nanostructures and their modulation will be further discussed. Our objective is to discuss these topics on a tutorial-level.

17.2 Electronic Structure

As an example, Fig. 17.2 shows the electronic structure of a bilayer graphene and monolayer graphene using extended Hückel theory (EHT) [whose atomic structure is shown in Fig. 17.1]. The detailed theoretical model is discussed in the next section. The bilayer graphene has twice the number of bands as compared to

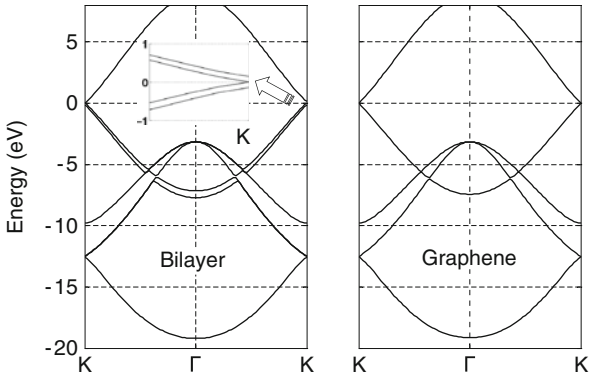

Fig. 17.2 Comparison of electronic structure of bilayer graphene and monolayer graphene calculated using EHT. The degeneracy is lifted in the graphene bilayer due to overlapping p_z orbitals of the two sheets. In the inset, a zoomed portion of E(k) diagram is shown around K-point to emphasize the lifting of degeneracy

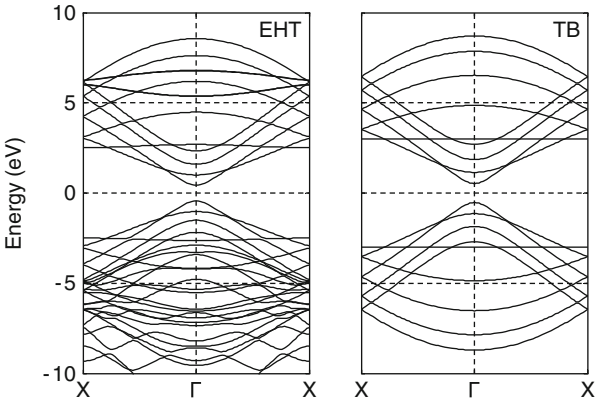

Fig. 17.3 Electronic structure of N = 9 passivated acGNR by spin-restricted EHT and TB Hamiltonians. Around the Fermi energy, the dispersions look similar. However, in general, the E(k) diagrams are quite different, in particular, for the valence band states

graphene with the degeneracy lifted (as shown in the inset) due to the finite coupling between the bands in the two graphene sheets.

Figure 17.3 compares the electronic structure methods, namely, EHT and p_z-orbital TB (tight binding), for N = 9 acGNR [see Fig. 17.1] with hydrogen passivated edges. The p_z-orbital TB parameter of 3 eV is used. In acGNRs, the wavefunctions associated with bands around Fermi energy are distributed throughout the width of the nanoribbon. These differ the most in the valence band. Since the sp^2 bands are not present in the p_z-orbital TB calculations, the bandgap is overestimated by 0.2 eV. Further differences in dispersion appear at high energies. If the bandgap is thus corrected in the p_z-orbital TB models (as discussed in Sect. 17.4), they may be accurate for the device modeling at the usual operating voltages. Moreover, p_z-orbital TB includes the nearest neighbor coupling only and any wavefunction effects, in the form of second-nearest interaction will be missing.

For N = 10 zzGNR shown in Fig. 17.1, the band structures using EHT and p_z-orbital TB schemes are shown in Fig. 17.4. Although there is much commonality between the two, the occupied bands deviate significantly and hence would lead to a different transmission response in this energy range. The deviation is however

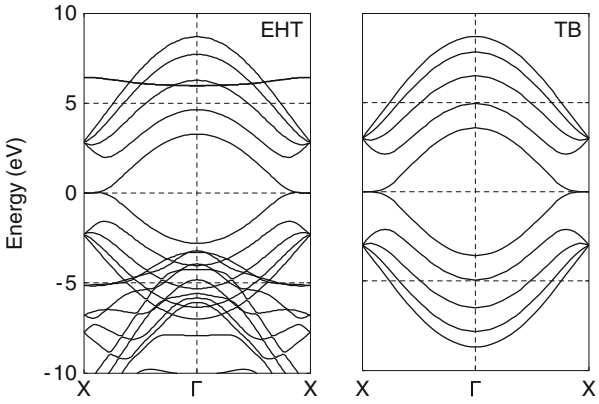

Fig. 17.4 Electronic structures of N = 10 passivated zzGNR calculated using spin-restricted EHT and TB Hamiltonians. The differences are similar to those of zzGNR as in Fig. 3

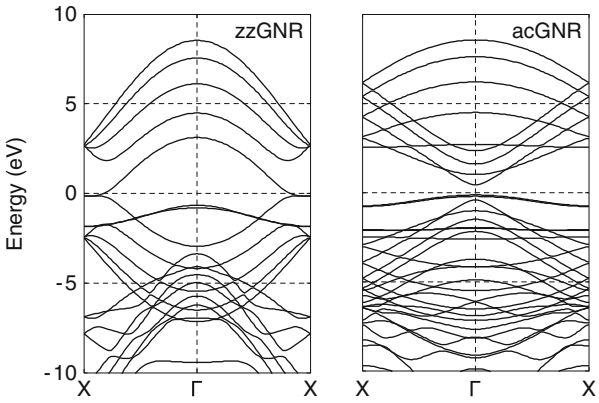

Fig. 17.5 Edge states for unpassivated zzGNR and acGNR, i.e., edges without H atoms. The dangling bonds introduce states below the Fermi energy for both configurations

less severe than in the case of acGNR. Furthermore, compared to the acGNRs, a dispersion-less state is observed at the Brillouin zone edge due to the edge belonging to one of the sublattices, whereas in acGNRs, the edges belong to both the sublattices. In zzGNRs, the wavefunctions for conduction and valence bands are localized at the edges [9, 10]. In addition, the small dispersion around the Fermi energy may lead to Stoner magnetism [9, 10]. It has also been proposed that the ground state may have spin-polarized edges, which may be modulated resulting in half metallicity [16].

An accurate description of the electronic structure thus becomes really important to accurately capture the electronic structure effects. Usually, one seeks for a trade off between the desired accuracy and available computational resources for the problem at hand.

Another electronic structure aspect is shown in Fig. 17.5. The surface states due to dangling bonds for unpassivated zzGNR and acGNR [13,17] are calculated using EHT. Such effects cannot be accounted for by a p_z-orbital TB method. For both GNRs, the dispersions in these bands are small as expected since these are localized on the unpassivated edges of GNRs. In acGNR, there is a finite density of edge states at the Fermi level, whereas for zzGNR, the surface states are below the Fermi level.

17.3 Theoretical Framework: Extended Hückel Theory

Accurate device prediction thus demands an efficient model that can simulate realistic structures under different conditions of applied fields and boundary conditions like attached molecules or multiple graphene layers or different substrates and hybrid structures with surrounding dielectric. A simple p_z orbital TB model [2], although very efficient and useful for specific problems, cannot account for many necessary physical effects or the chemical nature of bonding. On the other hand, density-function-theory (DFT) based models are computationally prohibitive for systems having more than about 200 atoms.

A semi-empirical method such as the EHT thus seems to be a good trade off, since it is computationally inexpensive and captures most of the electronic and atomic-structure effects present in the more rigorous methods. Usually with the EHT approach, systems with up to 1,000 atoms can be simulated relatively easily [18]. In the past, this model has been successfully applied to various nanostructures [19–22]. For graphene, since EHT has been benchmarked with generalized gradient approximation (GGA) in DFT, it can provide accurate results that less sophisticated methods like local density approximation (LDA) may not be able to capture due to an underestimation of the bandgap.

We use spin-restricted EHT for the electronic structure calculations. The nonorthogonal basis set consists of a double-ζ Slater Type Orbitals (STO). The STO is given as

$$\psi_{STO} = R(n)Y(l,m) \tag{17.1}$$

where Y represents spherical harmonics depending on the quantum numbers l and m. R is the spherical part, which depends on the principle quantum number n only (in comparison with its dependence on n and l in hydrogenic wavefunctions) and is given as

$$R(n) = N r^{n-1} \mathrm{e}^{-\zeta r} \tag{17.2}$$

where N is the normalization constant and ζ is the exponential decay constant.

Starting from the basis set, wavefunctions can be calculated using two STOs as follows:

$$\Psi_{EHT} = c_1\, \psi_{STO_1} + c_1\, \psi_{STO_2} \tag{17.3}$$

Here, two important EHT parameters are (c_1, ζ_1) for STO_1 and (c_2, ζ_2) for STO_2. These are generally obtained by benchmarking with various sophisticated methods and/or experiments. Table 17.1 shows these parameter set for valence carbon orbitals. For carbon, these parameters are benchmarked against GGA [23].

The overlap matrix S is calculated as follows:

$$S_{mn} = \langle m|n\rangle \tag{17.4}$$

Table 17.1 EHT parameter for carbon atom. $K = 2.80$

Orbital	E_{onsite} (eV)	c_1	c_2	ζ_1 (Å^{-1})	ζ_2 (Å^{-1})
2s	−20.315	0.740		2.037	
2p	−13.689	0.640	0.412	1.777	3.249

which is further used in calculating the Hamiltonian (H) as follows:

$$H_{mn} = \frac{1}{2} K S_{mn} (E_{\text{onsite},m} + E_{\text{onsite},n}) \tag{17.5}$$

Here K is a constant and E_{onsite}'s are the on-site energies, given in Table 17.1 for the carbon atom [23].

For the electronic band structure calculations, the H and S matrices of the infinite GNR, graphene sheet, and graphene bilayer are transformed to the reciprocal k-space as

$$H(\overrightarrow{k}) = \sum_{m=1}^{N} H_{mn} e^{i \overrightarrow{k} \cdot (\overrightarrow{d_m} - \overrightarrow{d_n})} \tag{17.6}$$

$$S(\overrightarrow{k}) = \sum_{m=1}^{N} S_{mn} e^{i \overrightarrow{k} \cdot (\overrightarrow{d_m} - \overrightarrow{d_n})} \tag{17.7}$$

where $\overrightarrow{k}$ is the reciprocal lattice vector of the Brillouin zone and has 1D characteristics for GNRs and 2D for single and bilayer graphene sheets. The index m represents the center unit cell and n represents the neighboring unit cells, whereas $\overrightarrow{d_m} - \overrightarrow{d_n}$ is the relative displacement. The energy eigenvalue spectrum at a specific K-point is then computed. In order to calculate the band structure under the influence of an electric field (E) in the width direction (y) for the nanoribbons and the stacking direction (y) for the bilayer graphene, the Laplace potential $U_L(y)$ is included in the Hamiltonian:

$$U_L(y) = -eEy \tag{17.8}$$

where e is the electronic charge. Within the EHT scheme, U_L is included as

$$U_L(m,n) = \frac{1}{2} S_{mn} [U_L(m) + U_L(n)] \tag{17.9}$$

We also use an orthogonal tight-binding scheme with hopping parameter t = 3eV (see [2] and Chap. 8) for p_z orbitals as a comparison. For an overview of doing calculations using the p_z-orbital TB methods, one can refer to Chap. 8 and [24].

We can further couple EHT or p_z-orbital TB with NEGF (nonequilibrium Green's function formalism) as discussed in [13] and Chaps. 13, 15, 17 and 18. NEGF has become a standard method of choice for calculating mean-field quantum transport [25].

17.4 Bilayer Graphene

When two graphene layers are stacked in Bernal ($\tilde{A} - B$) configuration, the monolayer feature of linear dispersion is lost and the dispersion becomes quadratic [8]. The bilayer configuration is very interesting for various applications, since the band gap can be modulated from zero to few tens of an electron volt by using an external out-of-plane electric field in the stacking direction [8, 13, 27–32]. Readers are encouraged to consult chaps. 8 and 11 for complementary discussion on bilayer graphene.

This electric field breaks the $A - \tilde{B}$ symmetry in the stacked bilayers and hence lifts the degeneracy, resulting in a band gap opening. The band gap depends on the coupling between the two graphene layers [8, 27]. Therefore, one should be able to tune this band gap by straining the bilayer [see Fig. 17.6]. This could be very useful in pressure sensors and other applications involving strain. In addition, we

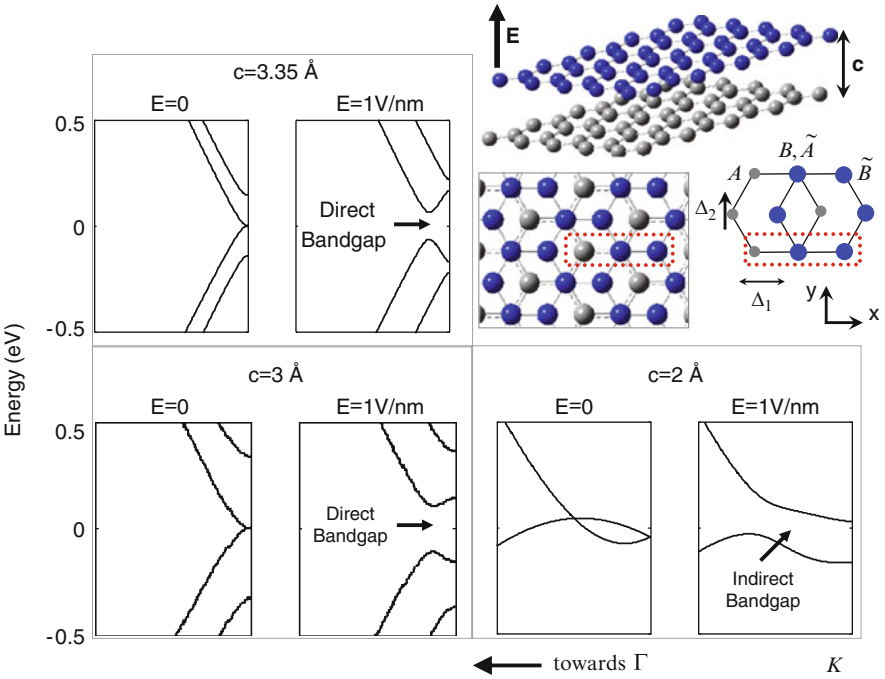

Fig. 17.6 Electronic structure of bilayer graphene. E(k) diagrams are shown around the Dirac point with and without electric fields. Δ_1 is the stacking misalignment in x-direction and Δ_2 is the misalignment in y-direction. For equilibrium stacking distance $c = 3.35$ Å, the dispersion is quadratic. With an external electric field, a direct band gap appears. For $c = 3$ Å, band gap modulation is larger due to increased hopping between the two layers and remains direct. For $c = 2$ Å, the bilayer becomes metallic with $E = 0$ and has an indirect band gap for a finite electric field. The atomic visualization is done using GaussView [26]

find that by straining bilayer graphene, conduction and valence band dispersions also change. The electronic structure and electric-field modulation of bilayers with stacking misalignments in Δ_1 and Δ_2 is shown in Fig. 17.6. We report that these misalignments may give rise to various characteristics of electronic-structure and electric-field modulation, and hence eventually influence the device applications and performance.

17.4.1 $\tilde{A}$–B stacking

The equilibrium C–C atomic distance is about 1.44 Å within the graphene plane. Out-of-plane equilibrium stacking distance (c) is 3.35 Å as shown in Fig. 17.6. The gray atoms belong to lower layer and the blue atoms represent the upper layer. The unit cell consists of four atoms – two atoms in each layer shown by red dotted line in Fig. 17.6. The two gray atoms in the lower layer are referred to as A and B, respectively. The two blue atoms in the upper layer are referred to as $\tilde{A}$ and $\tilde{B}$, respectively. For $\tilde{A} - B$ stacking, $\Delta_1 = 1.44$ Å and $\Delta_2 = 0$.

17.4.2 Strain Engineering

The electronic structure calculations for a bilayer graphene with equilibrium stacking distance $c = 3.35$ Å is shown in Fig. 17.6. Without any electric field, the dispersion is quadratic with a zero band gap at the Dirac (K) point. With an electric field of 1 V/nm, a direct band gap opens up due to $A - \tilde{B}$ symmetry breaking and the conduction/valence band minimum/maximum shifts away from the Dirac point. By decreasing c to 3 Å, without an electric field, the band gap is still zero with quadratic dispersion. However, the dispersion changes with an increase in the effective mass and the high lying bands move farther away from the Dirac point. With $E = 1$ V/nm, again a direct band gap is observed with the same features as the one for $c = 3.35$ Å. Apart from this, the band gap modulation is higher for $c = 3$ Å, although the Laplace's potential is smaller for the same electric field due to the reduced spacing. This is due to the increased wave function overlap between the two layers, which varies exponentially with the distance as compared to the Laplace's potential which is linearly dependent on the distance. Further reducing the stacking distance results in a metallic state for $c = 2$ Å. By applying 1 V/nm electric field, an indirect band gap is created.

Below about 2.5 Å, the distance between the atoms in the bottom layer and the next-nearest neighbors in the top layer is about 3.35 Å, which is the equilibrium stacking distance for bilayer graphene. Therefore, the hopping integral between $A - \tilde{B}$ sites becomes comparable to the equilibrium one of the $\tilde{A} - B$ sites. This results in the reported electronic structure modifications in Fig. 17.6 for $c = 2$ Å. This electronic structure change is also evident in the color plots of the valence band

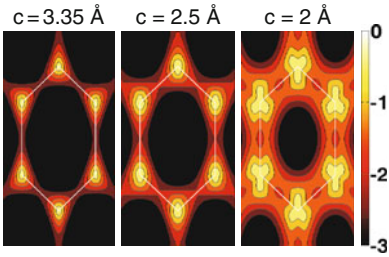

Fig. 17.7 Electronic structure of the valence band of the bilayer graphene. With decreasing the stacking distance (c), new features appear in the electronic structure due to increased coupling between the two layers. The color bar is in eV

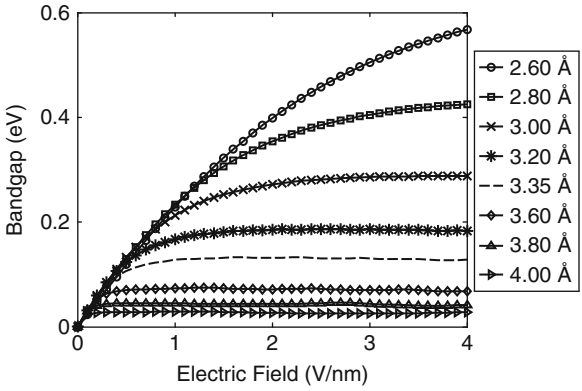

Fig. 17.8 Band gap modulation of strained bilayer with an external electric field. The dashed line is for equilibrium $c = 3.35$ Å, for which band gap saturates at about 0.13 eV. A convex relation is observed as a function of electric field above $c \approx 2.5$ Å. By decreasing c, band gap modulation increases due to increased interlayer hopping

states over the 2D Brillouin zone in Fig. 17.7. With decreasing stacking distance from $c = 3.35$ Å to $c = 2.5$ Å in the absence of an electric field, the features become broad indicating an increase in the effective mass. Further decreasing c to 2 Å results in a directional change of the features, which signifies that the additional bonding happens in different directions as compared to that for $c = 3.35$ Å.

We also find that smaller the stacking distance, higher the band gap modulation by the electric field as shown in Fig. 17.8. This is a desirable trait for practical applications. The band gap increases with increasing electric field and then saturates. For the equilibrium $c = 3.35$ Å, the band gap saturates at about 0.13 eV. Above about 2.5 Å, the trend of field modulation is convex and in the absence of electric field, a zero band gap is observed as shown in Fig. 17.8. Calculations for such a high field are reported to show the band gap saturation and the threshold trends for the strained bilayer. However, these high fields may not be feasible in devices due to the dielectric reliability concerns and physical constraints. High-K dielectrics may be used as an alternative to enhance field inside the graphene bilayer, while keeping the dielectric within the breakdown regime.

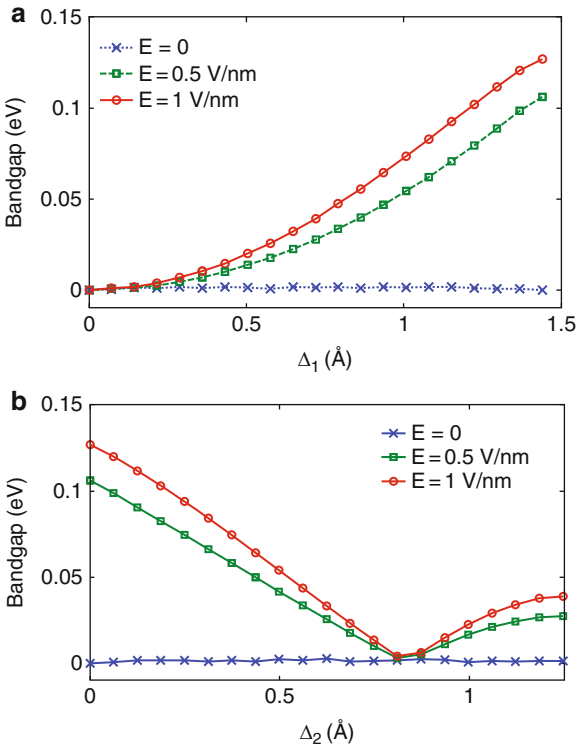

Fig. 17.9 Effects of Δ_1 and Δ_2 variation on the band gap with and without out-of-plane electric field. An increasing Δ_1 or Δ_2 results in an increasing, followed by a decreasing band gap for $E = 0$. (**a**) Electric-field modulation is absent for smaller Δ_1 and is higher for larger Δ_1. (**b**) Electric field modulation is higher for smaller Δ_2. Δ_1 and Δ_2 results are invariant under inversion, i.e., a negative Δ_1/Δ_2 shift results in the same effects as reported for the positive Δ_1/Δ_2 shift. Furthermore, the trends are repeated after a shift of ± 1.44 Å in Δ_1 or ± 1.24 Å in Δ_2

17.4.3 Misalignment

Next, we consider the effect of variation in Δ_1 and Δ_2. Fig. 17.17a,b summarizing the band gap opening due to Δ_1 and Δ_2 stacking misalignments and electric-field modulation. With increasing Δ_1 for E = 0, the band gap first increases and then decreases as shown in Fig. 17.9a. The same trend is observed for Δ_2 misalignment as shown in Fig. 17.9b. Electric-field modulation is small for $\Delta_1 \leq 0.25$ Å and becomes significant only beyond 0.5 Å. Similarly, the electric-field modulation is large for smaller Δ_2. The band gap decreases with increasing Δ_2, becomes a few millielectron volt and then starts increasing.

17.5 Armchair Graphene Nanoribbons

On a p_z level of the tight-binding theory, two thirds of acGNRs are semiconducting with a bandgap inversely proportional to their widths and the other has zero bandgap depending on the chirality [9]. However, one can obtain a different result using a more sophisticated theory [14, 33] such as EHT and DFT. First, the zero bandgap

acGNRs also have a small bandgap that is inversely proportional to the width. Second, the remaining semicondcuting acGNRs only follow an inverse relation within its own category. For convenience, we propose to categorize them into α-, β-, and γ-acGNRs. α-acGNRs are N = 8,11,14, ... and have very small bandgap. β-acGNRs are N = 9,12,15, ... and γ acGNRs are N = 10,13,16, ... acGNRs have also been classified into three subclasses in the context of the orbital diamagnetism [11]. Readers are encouraged to consult chaps. 9, 10, 13, 16, and 18 for complementary discussion on nanoribbons.

17.5.1 Pristine Edges

An electronic structure calculation using EHT for each type of acGNR is shown in Fig. 17.10. As can be seen that N = 8 α-acGNR has a small bandgap and has a nonlinear dispersion around the Γ-point. N = 9 β-acGNR has a large bandgap with a parabolic dispersion around the Γ-point. Interestingly, N = 10 γ-acGNR has a slightly larger bandgap with larger effective mass dispersion around the Γ-point and smaller velocity in the linear region away from the the Γ-point as compared to N = 9 β-acGNR. We extract the bandgaps and effective masses within a few tens

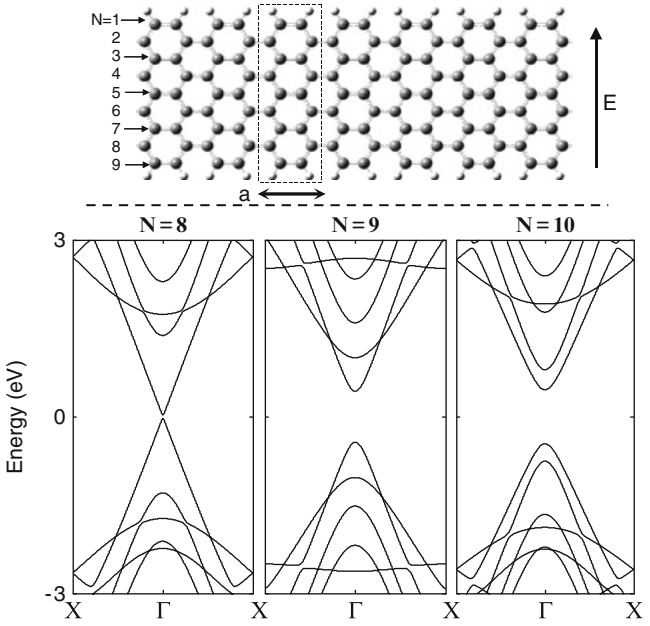

Fig. 17.10 Electronic structure of acGNRs. The ball and stick model of a graphene nanoribbon with N = 9 is shown with the unit cell. E-k diagrams are shown for three different types of acGNRs using EHT

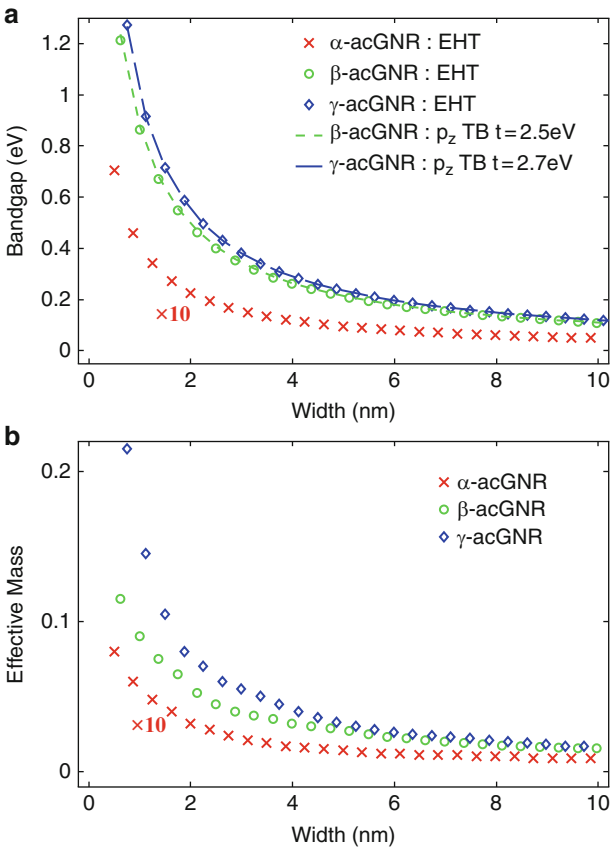

Fig. 17.11 Band gaps and effective masses of acGNR. (**a**) Variation of band gap with nanoribbon widths of different types of acGNRs. Using a p_z-orbital tight-binding method, $t = 2.5$ and 2.7 eV match the band gaps obtained by EHT for β-acGNRs and γ-acGNRs, respectively. (**b**) Variation of effective mass with nanoribbon widths of different types of acGNRs

of millielectron volt around the band edges of these three types of acGNRs and plot them in Fig. 17.11a,b, respectively. We find that incremental change in the bandgap of γ-acGNRs with respect to β-acGNRs is smaller in EHT [14] than LDA of density functional theory [33].

For each type of acGNR, bandgaps and effective masses are inversely proportional to the width with a different proportionality constant. The bandgap *versus* width (W) relations are given as [14]:

$$E_{gap} = \begin{cases} 0.04\,\text{eV}/\,W\,(\text{nm}) & \text{for } \alpha\text{-acGNR} \\ 0.86\,\text{eV}/\,W\,(\text{nm}) & \text{for } \beta\text{-acGNR} \\ 1.04\,\text{eV}/\,W\,(\text{nm}) & \text{for } \gamma\text{-acGNR} \end{cases}$$

We find that Fig. 17.11b is important because some approaches toward graphene structures involve effective mass description [34]. Each type of acGNRs follow an inverse relation of effective mass with the width given below:

$$\frac{m}{m_o} = \begin{cases} 0.005/W(\text{nm}) & \text{for } \alpha\text{-acGNR} \\ 0.091/W(\text{nm}) & \text{for } \beta\text{-acGNR} \\ 0.160/W(\text{nm}) & \text{for } \gamma\text{-acGNR} \end{cases}$$

where m_o is the free electron mass. It should be noted that using a p_z-orbital TB model, the effective mass follows the same inverse relation *versus* width for all three types of acGNRs [34]. Furthermore, we determine the p_z-orbital TB parameters that reproduce the bandgaps as shown in Fig. 17.11a. These parameters are 2.5 eV and 2.7 eV for β- and γ-acGNRs, respectively.

Fig. 17.12a shows electric-field modulation of the band structure for an N = 10 γ-acGNR. The effective mass around the Γ-point increases with the increasing electric field (E) and eventually changes sign, similar to [35]. Furthermore, for $E = 0$, the band dispersion in the linear regime away from the Γ-point shows

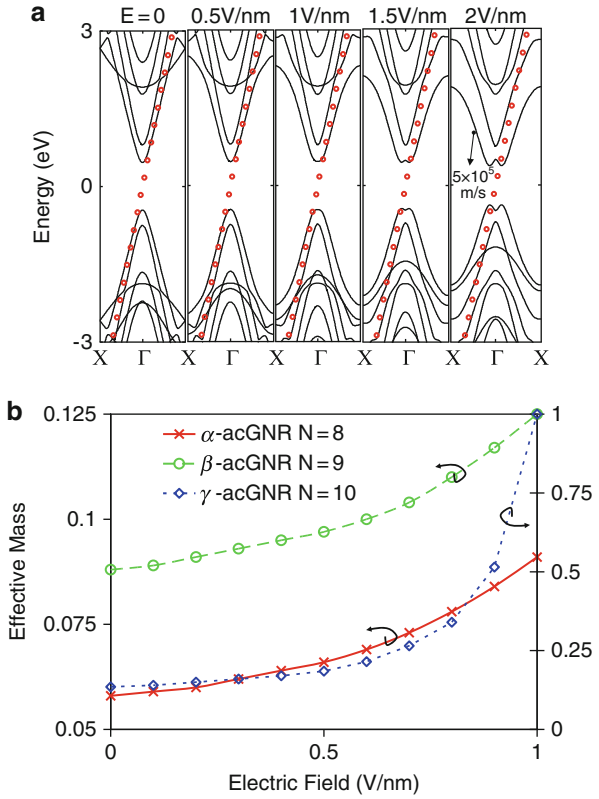

Fig. 17.12 Electric-field modulation of band dispersions. (**a**) Variation of velocity in the width direction for N = 10 γ-acGNR. The linear dispersion shown by red circles represents a value of 8.8×10^5 m/s velocity around the Dirac point for graphene calculated using EHT. (**b**) Variation of effective masses. Effective masses are obtained by parabolic fits to the conduction bands within a few $k_B T$ of band edge for β-acGNRs and γ-acGNRs and within a fraction of $k_B T$ for α-acGNRs

velocity very close to the unconstrained graphene velocity ($= 8.8 \times 10^5$ m/s) indicated by red (grey) circles. With increasing E, velocity in this linear regime away from the Γ-point decreases to about 5×10^5 m/s. In addition, the bandwidths of the valence and conduction bands are also decreasing and a *Mexican hat* structure is observable that has also been seen in acGNR [35], CNTs [36], and graphene bilayers [13, 27–29]. These features are in qualitative agreement with the electric field effects reported in semiconducting acGNRs elsewhere using a continuum model [35]. We show the extracted effective masses around the Γ-point for N = 8, 9, and 10, which are α-, β-, and γ-acGNRs, respectively, in Fig. 17.12b. These effective masses are valid for tenths of $k_B T$ for α-acGNRs and for a few $k_B T$ for β- and γ-acGNRs. After this energy scale, the band dispersions become linear again and remain so for about a few electron volts when they become nonlinear and hence saturate [as shown in Fig. 17.12a].

Apart from this, the bandgap is modulated with the increasing electric field. In Fig. 17.13, we show bandgap modulation as a function of width and electric field. A threshold behavior is observed, similar to [35], where bandgap starts

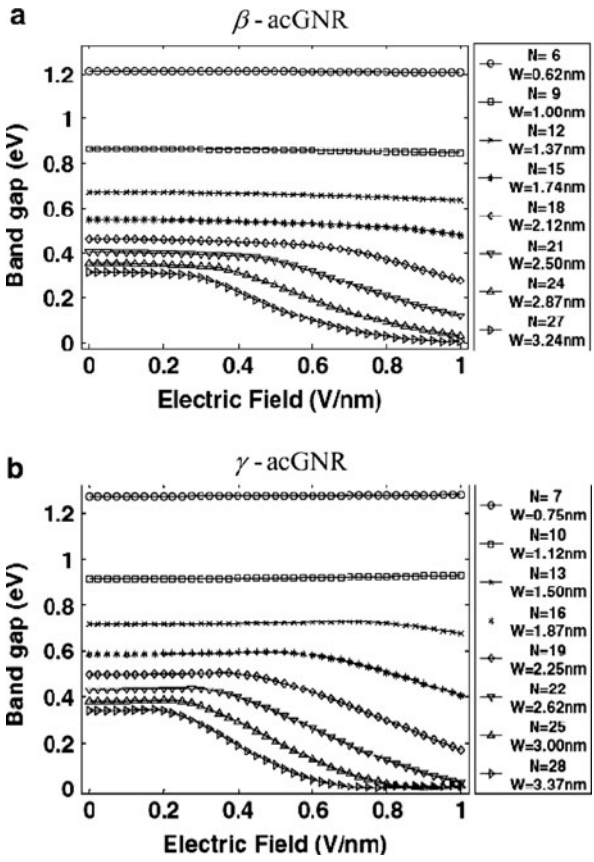

Fig. 17.13 Band gap modulation. Band gap as a function of width and electric field for (**a**) β-acGNRs and (**b**) γ-acGNRs. γ-acGNRs have larger band gap modulation as compared to β-acGNRs

decreasing appreciably above a threshold electric field E_t. Moreover, for γ-acGNRs, bandgap decreases at a faster rate compared to β-acGNRs and thus γ-acGNRs have larger bandgap modulation. This is consistent because wavefunctions are more hybridized in γ-acGNRs and hence any perturbation affects the band structure more as compared to the β-acGNRs.

The bandgap for β-acGNRs decreases monotonically with the electric field. However, the bandgap decreases appreciably only after a threshold electric field. This is different from [35], where below the threshold electric field, the bandgap is constant and it decreases only after the threshold electric field. Furthermore, for γ-acGNRs, the bandgap first increases a little and then decreases – a feature although small, but not present in continuum calculations [35].

With an appropriate electric field applied, one can reduce the bandgap of a semiconducting acGNR to a few meV. We find that bandgap never becomes zero, whereas using a continuum model [35], one can find zero bandgap. The physics behind this bandgap narrowing is the spectral shift of the conduction and valence band states on the two edges. This leads to downward and upward shifts for conduction and valence bands, respectively.

17.5.2 Periodic edge roughness effects

The experimentally fabricated graphene structure have inherently rough edges. Consider N = 8 acGNR in Fig. 17.14, which has semimetallic band structure,

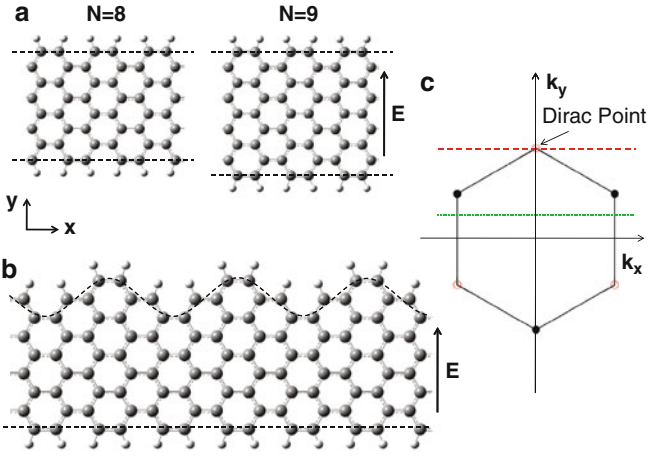

Fig. 17.14 Schematics of unit cell with mixed boundary conditions. (**a,b**) acGNRs with pristine edges are shown with N = 8 and N = 9 layers. (**b**) acGNR with N = 8,9 layers within a unit cell leads to a rough edge. (**c**) For every one-third acGNR with pristine edges, transverse quantized wavevector crosses the vicinity of one of the two Dirac points resulting in close to zero band gap. By mixing boundary conditions within a unit cell, such crossings can be avoided

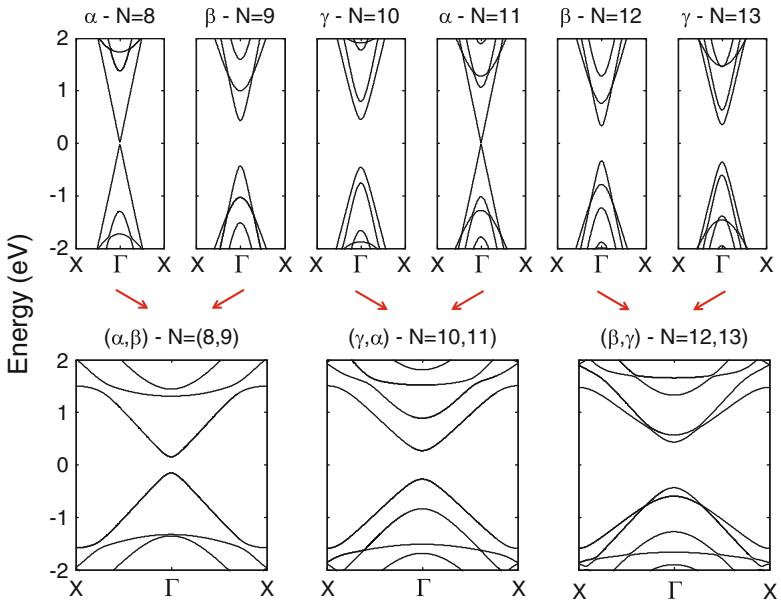

Fig. 17.15 Electronic structure of passivated acGNR with rough edges. The combination of an N and N+1 acGNR always leads to a band gap opening

whereas N = 9 acGNR is semiconducting. Conceptually, one can imagine the acGNR in Fig. 17.14b with one rough edge to be composed of N = 8 and N = 9 acGNRs. For N = 8 acGNR, the quantized wavevector crosses a Dirac point, schematically shown in Fig. 17.14c by a red dashed line, whereas for N = 9 acGNR, the quantized wavevector is away from the Dirac point, schematically shown by a green dotted line, giving rise to a band gap. For the acGNR with rough edges, the resulting boundary conditions are different from the ones for pristine (N = 8 and 9) acGNRs. For such boundary, it becomes less probable to cross a Dirac point [37].

As discussed in the last section, α-acGNRs have a very small band gap and are essentially semimetallic within the p_z-orbital tight-binding theory. β-acGNRs are semiconducting with an appreciable band gap. γ-acGNRs are also semiconducting but with even higher incremental band gap than β-acGNRs. Fig. 17.15 summarizes the band structure of α-, β-, and γ-acGNRs with pristine passivated edges, showing that every third has a very small band gap. With the mixing of the nanoribbons with pristine edges within the same unit cell, one can obtain rough edges as shown in Fig. 17.14b. We report the band structures of three different mixing, namely, (α,β), (γ,α), and (β,γ), in Fig. 17.15 – all of which show a significant band gap opening [38].

The extracted band gaps from the band structure calculations are summarized in Fig. 17.16a for the passivated acGNRs with rough edges. We report that the three combinations of acGNRs, namely, (α,β), (γ,α), and (β,γ) follow distinct band gap

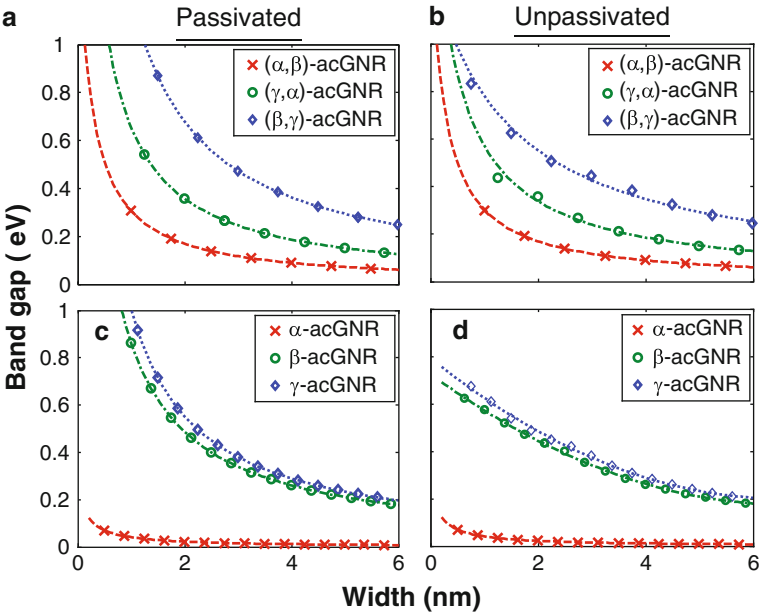

Fig. 17.16 Band gap opening. (**a**) Band gap is always observed for passivated nanoribbons with rough edges and hence mixed boundary conditions. Band gap inversely decreases with width of the ribbon. (**b**) Band gap is present for unpassivated nanoribbons. However, the trend is not hyperbolic due to dangling bond states within the band gap. (**c,d**) Band gap plots for passivated and unpassivated ribbons, respectively, as a reference for (**a,b**).

trends – an extension of the trends for pristine acGNRs. The band gaps are inversely proportional to the width and are given as

$$E_g = \begin{cases} 0.35\,(\text{eV})/\,W\,(\text{nm}) & \text{for } (\alpha,\beta)\text{-acGNR} \\ 0.70\,(\text{eV})/\,W\,(\text{nm}) & \text{for } (\gamma,\alpha)\text{-acGNR} \\ 1.37\,(\text{eV})/\,W\,(\text{nm}) & \text{for } (\beta,\gamma)\text{-acGNR} \end{cases}$$

where width (W) is defined for the widest section of the nanoribbon.

For the unpassivated acGNRs, the variation of the band gap with the nanoribbon width is summarized in Fig. 17.16b. Owing to a complex dependence of the position of the dangling bond states on the width, the trend is nonhyperbolic. However, a higher-order fit is shown to guide the eye. Clearly, three different band gap opening trends are observed for unpassivated (α,β)-, (γ,α)-, and (β,γ)-acGNRs, similar to those of the passivated acGNRs.

For passivated edges and unpassivated acGNRs, a gap of at least 0.1 eV can be opened for 5 nm wide nanoribbons. As a reference, we also show the band gap variation as a function of the width for acGNRs with passivated and unpassivated pristine edges in Figs. 17.16c,d, respectively. It is evident that one-third acGNRs

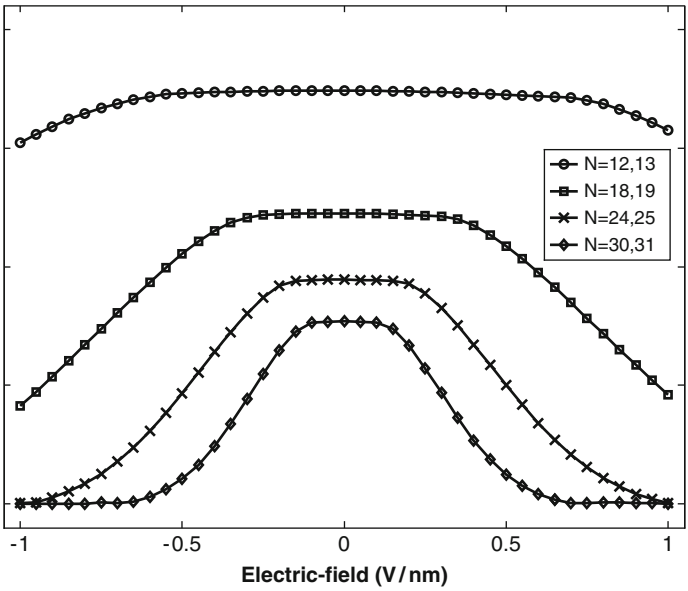

Fig. 17.17 Band gap modulation. For one kind of acGNRs, band gap modulation with electric field is shown. In general, the band gap decreases with increasing magnitude of the electric field. Furthermore, asymmetry in band gap modulation is due to asymmetry in the edge structure of the acGNRs

in both the cases have very small band gap, which are not very useful for nanoelectronics applications.

The band gap modulation of the passivated acGNRs with rough edges as a function of external electric field is summarized in Fig. 17.17 for (β,γ)-acGNRs. Similar to the acGNRs with pristine edges discussed in the previous section, a threshold behavior appears [14, 35], where the band gap starts to decrease appreciably above a threshold electric field E_t. As reported in Sect. 17.5.1, for the acGNRs with pristine edges, gap modulation behavior is polarity-symmetric due to the edge symmetry. However, the nonideal acGNRs considered in this paper do not posses the edge symmetry. This results in an asymmetric band gap modulation with opposite polarity of the electricfields.

17.6 Zigzag Graphene Nanoribbons with Periodic Edge Roughness

zzGNRs with pristine edges have zero band gap and localized states around the equilibrium chemical potential as discussed in Sect. 17.1 [9, 10]. In experiments, however, such pristine edges may not be feasible and the edge structure may develop

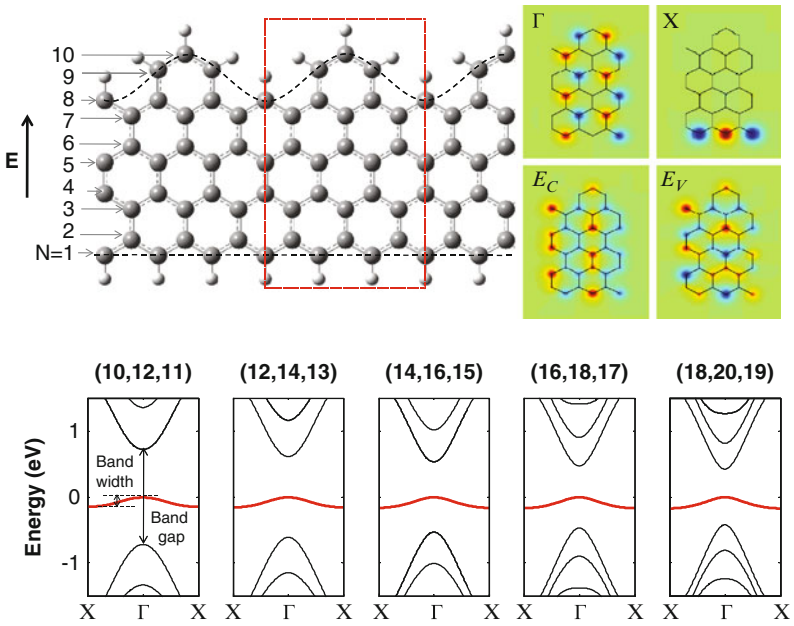

Fig. 17.18 Electronic-structure of passivated zigzag graphene nanoribbons with rough edges. The ball and stick model of a graphene nanoribbon with N = 8, N = 10, and N = 9 is shown. The combination of an even N, N+2, and N+1 zzGNR always leads to thermodynamically stable closed benzene rings. E(k) diagrams, calculated using EHT, are shown for five zzGNRs with different widths. A near-midgap state with a small band width is observed, whereas the nanoribbons have a significant band gap opening. The wavefunction at X-point for the midgap state shows edge localization, whereas the wavefunctions at Γ-point for the midgap states and conduction/valence band edges (E_C / E_V) are distributed throughout the width of the ribbon.

some roughness [39–42]. In this chapter, we study one such kind of roughness. One finds that for a zzGNR with even N layers of C atoms, there are no open benzene rings. This is a thermodynamically stable configuration with pristine edges, unlike a zzGNR with odd N layers, which always has open benzene rings at one end. Readers are encouraged to consult chaps. 9, 10, 13, 16, and 18 for complementary discussion on nanoribbons.

We find that for even N layers, two extra layers within a unit cell give rise to a rough edge but with closed benzene rings as shown in Fig. 17.18. In this configuration, the unit cell consists of zzGNRs with an even N, N+2, and N+1 layers. In addition, one edge is pristine with atoms belonging to one graphene sublattice only, whereas the other edge has an oscillatory corrugation leading to edge roughness with atoms from both sublattices [43]. An electronic-structure calculation for this class of zzGNRs is shown in Fig. 17.18.

Most importantly, one always finds a significant band gap opening. As expected, the band gap decreases with the increasing width, due to a smaller value of the quantized wavevector in the transverse direction. *Interestingly, we find a*

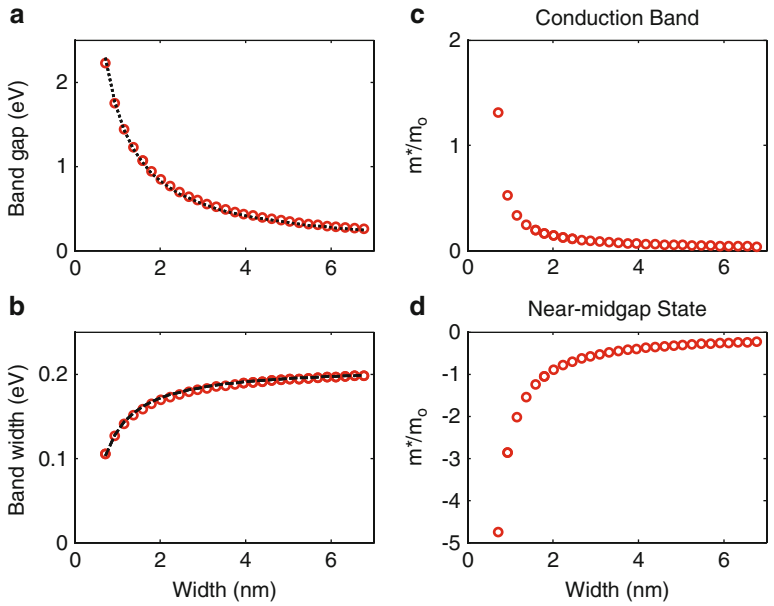

Fig. 17.19 Electronic-structure features of the zzGNRs. (**a**) The band gap decreases inversely with the width. (**b**) The band width of the near-midgap state monotonically increases with the width. (**c**) Effective mass for the conduction band state monotonically decreases with the width. (**d**) The effective mass for the near-midgap state is hole-like (i.e., negative) and it increases with the width (i.e., becomes less negative). Effective masses are obtained by parabolic fits to the bands within a few $k_B T$ of the band edge at the Γ-point

near-midgap state, which has a very small band width. Unlike the band gap, the band width of the near-midgap state tends to increase with the increasing width. The near-midgap state has a hole-like dispersion, i.e., the effective mass is negative around the Γ-point.

The variation of the band gap with the nanoribbon width is summarized in Fig. 17.19a. Similar to acGNRs [21], these zzGNRs follow an inverse band gap relation with the width. As compared to the acGNRs in Sect. 17.4, the band gap opening is larger for the same width. The important point however is that one always observes a band gap, which is desirable for nanoelectronics applications. In this case, a band gap of about 0.5 eV can be opened with a 4 nm wide zzGNR. For the midgap states, the band width monotonically increases with the increasing width, finally saturating to about 0.21 eV as shown in Fig. 17.19b.

In Fig. 17.19c,d, the effective masses are reported around the Γ-point for the conduction band and the near-midgap state, respectively. For the conduction and the valence bands, the effective masses around the band edges are nearly equal in the magnitude, although with opposite signs. We thus report only the conduction band effective masses. With the increasing width, these effective masses decrease in a nonhyperbolic fashion. The effective mass of the near-midgap state is negative,

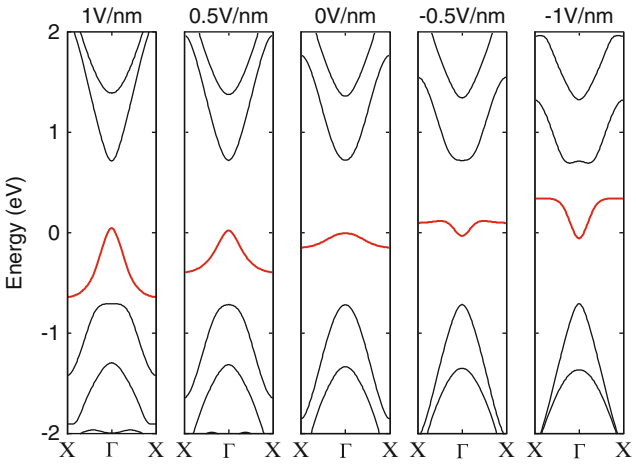

Fig. 17.20 Electric-field modulation of the band dispersions for (8,10,9)-zzGNR. The band gap almost remains constant, however, the dispersions of the conduction/valence band and the midgap states change asymmetrically with the polarity of the field

i.e., hole-like, which monotonically increases with the width. It is interesting to note that due to smaller band width, the magnitude of the effective mass of near-midgap state is almost five times that of the conduction/valence band effective mass.

The electronic-structure modulation of the zzGNRs due to an electric field in the width direction also reveals some interesting electronic structure features. As shown in Fig. 17.20, the electric field modulates the band dispersions of the conduction and the valence bands very effectively. The trends in the field modulation are clearly polarity dependent due to the edge asymmetry in the zzGNR under study. The band gap decreases slightly, but remains close to the equilibrium value. Since wavefunctions at the conduction/valence band edges are distributed throughout the width of zzGNR with periodic edge roughness, the effect of electric field effectively gets balanced out for these states. This has important implications for the manipulation of the near-midgap state due to its isolation from the conduction/valence bands even in the presence of an electric-field.

The modulation of the near-midgap state is the most interesting, where the band width can be modulated with both polarities of the electric-field. For these states, the effective mass around the Γ-point remains negative (hole-like) for positive electric fields. Beyond a threshold electric field, the mass becomes positive (electron-like) for negative electric fields. This polarity reversal and the band width modulation requires a detailed analysis of the wavefunction localization, which we discuss further.

At the X-point, the wavefunction of the near-midgap state is localized toward pristine edge and at the Γ-point, the wavefucntion is distributed throughout the ribbon width (see Fig. 17.18). When a voltage is applied to create an electric field in the width direction, the energy values at the Γ-point do not shift much due to

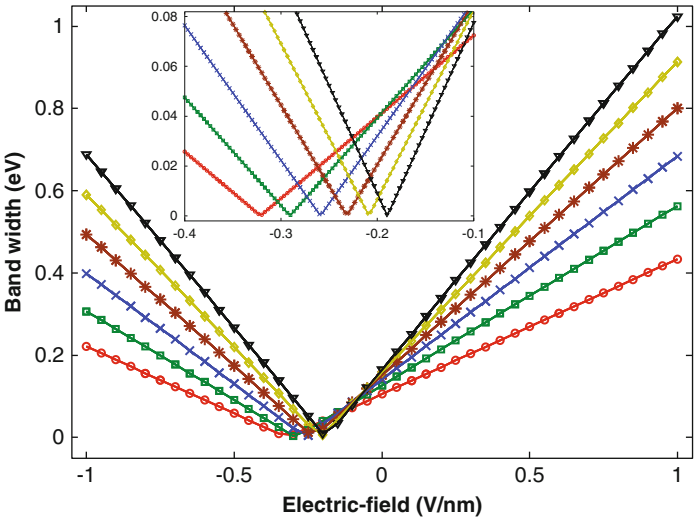

Fig. 17.21 Electronic-structure modulation. The band width of the midgap state can be modulated over a wide range. The inset shows an expanded view near the transition points

distribution of the wavefunction throughout zzGNR. However, for the X-point, the energy values shift depending on the polarity of the bias. Positive electric field leads to negative potential energy change at the pristine edge and shifts the energy values down at the X-point resulting in an increased band width. Negative electric field shifts the energy values at the X-point upwards, resulting in a decreasing and then an increasing band width, which also switches the dispersion to behave as electron-like with a positive effective mass.

The results of the electric-field modulation of the electronic-structure are quantitatively summarized in Fig. 17.21. The band width of the near-midgap state can be modulated from 0 to almost 1 eV, depending on the electric field and the width of zzGNR. The inset shows an expanded view of the band width modulation trends around the inflexion points. We have yet to see how the field modulation of these near-midgap states can lead to interesting applications in electronics, photonics, spintronics, and even plasmonics. However, their manipulation and formation of a band due to delocalization is quite intriguing compared to the nonconducting recombination-generation centers and dopant states in the nondegenerately doped semiconductors.

17.7 Novel Applications

In this section, we discuss some of the novel applications, which can be enabled by gate voltage (external electric-field) induced electronic-structure modulation, e.g.,

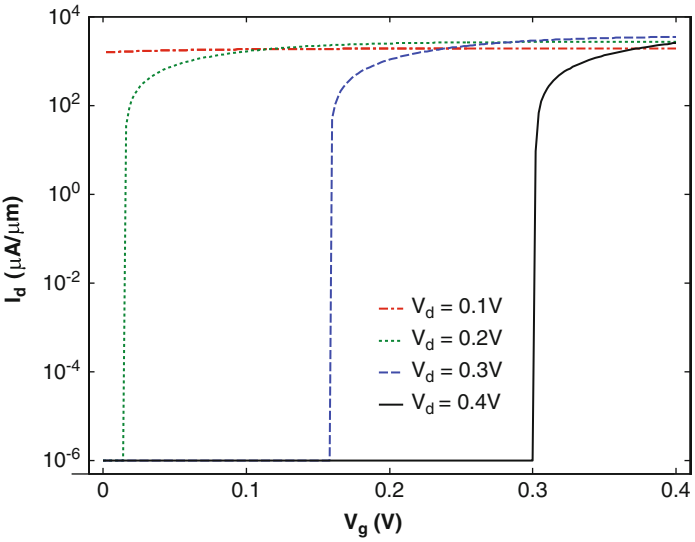

Fig. 17.22 Transport Characteristics of EMT. Transfer characteristics show steep subthreshold characteristics under low gate voltage

band gap modulation and band width modulation discussed in this chapter. The use of band gap modulation can result in low-power transistors, electric-field sensors, emission wavelength tunable light emitters, electrically tunable tinted windows, etc. We project that this list will continue to increase with more progress made in this area.

One example of the bandwidth modulation could be that of the proposed electronic-structure modulation transistor (EMT). The working principle is based on the band width modulation of a midgap or near-midgap state due to an electric field by applying a gate voltage [44, 45], enabling very steep subthreshold inverse slope as shown in Fig. 17.22. The proposed transistor, namely, EMT, has been studied as a possible replacement for CMOS (complementary metal oxide semiconductor) technology [46]. We envision that transistors based on the electronic-structure modulation of the channel material can open up a new class of post-CMOS logic devices.

17.8 Conclusions

We have discussed the electronic-structure modulation due to an external electric field in graphene nanostructures. In bilayer graphene, a direct band gap can be opened by breaking the $A - \tilde{B}$ symmetry. This band gap modulation depends on the strain and misalignment in the bilayers. For the acGNRs with and without pristine edges, the intrinsic band gap can be reduced to few millielectron volt by applying

an external electric field in the width direction. For the zzGNRs with rough edges, a near-midgap state is observed, whose bandwidth can be modulated by the external electric field. Such a bandgap is essential for numerous potential device applications. Many other electronic-structure modulation effects due to external electric field may also open up many device configurations. We anticipate that novel devices can be engineered using these effects, e.g., low-power transistors, tunable light emitters, etc. Notably, a possible low-power EMT may become CMOS replacement.

Acknowledgements We thank T.Z. Raza for a critical review of this chapter. This work was supported by the University of Iowa Presidential Faculty Fellowship.

References

1. P.R. Wallace, Phys. Rev. **71**, 622 (1947)
2. R. Saito, G. Dresselhaus, M.S. Dresselhaus, *Physical Properties of Carbon Nanotubes*, (Imperial College Press, London, 1998)
3. K.S. Novoselov, A.K. Geim, S.V. Morozov, D. Jiang, Y. Zhang, S.V. Dubonos, I.V. Grigorieva, A.A. Firsov, Science **306**, 666 (2004)
4. Y. Zhang, Y.-W. Tan, H.L. Stormer, P. Kim, Nature **438**, 201 (2005)
5. C. Berger, Z. Song, X. Li, X. Wu, N. Brown, C. Naud, D. Mayou, T. Li, J. Hass, A.N. Marchenkov, E.H. Conrad, P.N. First, W.A. de Heer, Science **312**, 1191 (2006)
6. A.K. Geim, K.S. Novoselov, Nat. Mater. **6**, 183 (2007)
7. A.H.C. Neto, F. Guinea, N.M.R. Peres, K.S. Novoselov, A.K. Geim, Rev. Mod. Phys. **81**, 109 (2009)
8. E. McCann, V.I. Fal'ko, Phys. Rev. Lett. **96**, 086805 (2006)
9. K. Nakada, M. Fujita, G. Dresselhaus, M.S. Dresselhaus, Phys. Rev. B **54**, 17954 (1996)
10. M. Fujita, K. Wakabayashi, K. Nakada, K. Kusakabe, J. Phys. Soc. Jpn. **65**, 1920 (1996)
11. K. Wakabayashi, M. Fujita, H. Ajiki, M. Sigrist, Phys. Rev. B. **59**, 8271 (1999)
12. L. Brey, H.A. Fertig, Phys. Rev. B **73**, 235411 (2006)
13. H. Raza, E.C. Kan, J. Comput. Electron. **7**, 372 (2008)
14. H. Raza, E.C. Kan, Phys. Rev. B **77**, 245434 (2008)
15. L. Oetting, T.Z. Raza, H. Raza, in preparation
16. Y.-W. Son, M.L. Cohen, S.G. Louie, Nature **444**, 347 (2006)
17. T. Kawai, Y. Miyamoto, O. Sugino, Y. Koga, Phys. Rev. B **62**, R16349 (2000)
18. H. Raza, Phys. Rev. B **76**, 045308 (2007)
19. H.Raza, K.H. Bevan, D. Kienle, Phys. Rev. B **77**, 035432 (2008)
20. H. Raza, J. Phys.: Condens. Matter **20**, 445004 (2008)
21. H. Raza, T.Z. Raza, E.C. Kan, Phys. Rev. B **78**, 193401 (2008)
22. T.Z. Raza, J.I. Cerda, H. Raza, J. Appl. Phys. **109**, 023705 (2011)
23. D. Kienle, J. Appl. Phys. **100**, 043714 (2006)
24. Please see, http://www.engineering.uiowa.edu/∼hraza/QTT_3.html
25. S. Datta, *Quantum Transport: Atom to Transistor* (Cambridge University Press, Cambridge, 2005)
26. R. Dennington II, T. Keith, J. Millam, K. Eppinnett, W.L. Hovell, R. Gilliland, *GaussView, Version 3.0* (Semichem, Inc., Shawnee Mission, KS, 2003)
27. E. McCann, Phys. Rev. B **74**, R161403 (2006)
28. H. Min, B. Sahu, S.K. Banerjee, A.H. MacDonald, Phys. Rev. B **75**, 155115 (2007)
29. E.V. Castro, K.S. Novoselov, S.V. Morozov, N.M.R. Peres, J.M.B. Lopes dos Santos, J. Nilsson, F. Guinea, A.K. Geim, A.H. Castro Neto, Phys. Rev. Lett. **99**, 216802 (2007)

30. T. Ohta, A. Bostwick, T. Seyller, K. Horn, E. Rotenberg, Science **313**, 951 (2006)
31. J.B. Oostinga, H.B. Heersche, X. Liu, A.F. Morpurgo, L.M.K. Vandersypen, Nat. Mater. **7**, 151 (2007)
32. H. Raza, E.C. Kan, J. Phys.: Condens. Matter **21**, 102202 (2009)
33. Y.-W. Son, M.L. Cohen, S.G. Louie, Phys. Rev. Lett. **97**, 216803 (2006)
34. G. Liang, N. Neophytou, D.E. Nikonov, M.S. Lundstrom, IEEE Trans. Electron Dev. **54**, 677 (2007)
35. D.S. Novikov, Phys. Rev. Lett. **99**, 056802 (2007)
36. D.S. Novikov, L.S. Levitov, Phys. Rev. Lett. **96**, 036402 (2006)
37. H. Raza, E.C. Kan, All-semiconducting armchair graphene nanoribbons: a band structure study, in *MRS Fall Meeting*, 2008
38. H. Raza, Phys. Rev. B 84, 165425 (2011)
39. Z. Chen, Y.-M. Lina, M.J. Rooksa, P. Avouris, Phys. E: Low-dimensional Syst. Nanostruct. **40**, 228 (2007)
40. M.Y. Han, B. Ozyilmaz, Y. Zhang, P. Kim, Phys. Rev. Lett. **98**, 206805 (2007)
41. T. Enoki, Y. Kobayashi, K.-I. Fukui, Int. Rev. Phys. Chem. **26**, 609 (2007)
42. X. Li, X. Wang, L. Zhang, S. Lee, H. Dai, Science **319**, 1229 (2008)
43. H. Raza, J. Phys.: Condens. Matter, **23**, 382203 (2011)
44. H. Raza, Electronic-structure modulation transistor. Patent pending (number: 12/711,007)
45. H. Raza, T.Z. Raza, T.-H. Hou, E.C. Kan, arXiv:0812.0123v2 (unpulished)
46. K. Bernstein, R.K. Cavin, W. Porod, A. Seabaugh, J. Welser, Proc. IEEE **98**, 2169 (2010)

Chapter 18
Graphene Nanoribbons: From Chemistry to Circuits

F. Tseng, D. Unluer, M.R. Stan, and A.W. Ghosh

Abstract The Y-chart is a powerful tool for understanding the relationship between various views (behavioral, structural, and physical) of a system, at different levels of abstraction, from high-level, architecture and circuits, to low-level, devices and materials. We thus use the Y-chart adapted for graphene to guide the chapter and explore the relationship among the various views and levels of abstraction. We start with the innermost level, namely, the structural and chemical view. The edge chemistry of patterned graphene nanoribbons (GNRs) lies intermediate between graphene and benzene, and the corresponding strain lifts the degeneracy that otherwise promotes metallicity in bulk graphene. At the same time, roughness at the edges washes out chiral signatures, making the nanoribbon width the principal arbiter of metallicity. The width-dependent conductivity allows the design of a monolithically patterned Wide–Narrow–Wide (WNW) all graphene interconnect-channel heterostructure. In a three-terminal incarnation, this geometry exhibits superior electrostatics, a correspondingly benign short-channel effect and a reduction in the contact Schottky barrier through covalent bonding. However, the small bandgaps make the devices transparent to band-to-band tunneling. Increasing the gap with width confinement (or other ways to break the sublattice symmetry) is projected to reduce the mobility even for very pure samples, through a fundamental *asymptotic* constraint on the bandstructure. An analogous trade-off, ultimately between error rate (reliability) and delay (switching speed) can be projected to persist for all graphitic derivatives. Proceeding thus to a higher level, a compact model is presented to capture the complex nanoribbon circuits, culminating in inverter characteristics, design metrics, and layout diagrams.

F. Tseng (✉) · D. Unluer (✉) · M.R. Stan · A.W. Ghosh
Charles L Brown School of Electrical and Computer Engineering, University of Virginia, Charlottesville, VA 22901, USA
e-mail: ft8e@virginia.edu; du7x@virginia.edu

H. Raza (ed.), *Graphene Nanoelectronics*, NanoScience and Technology,
DOI 10.1007/978-3-642-22984-8_18,

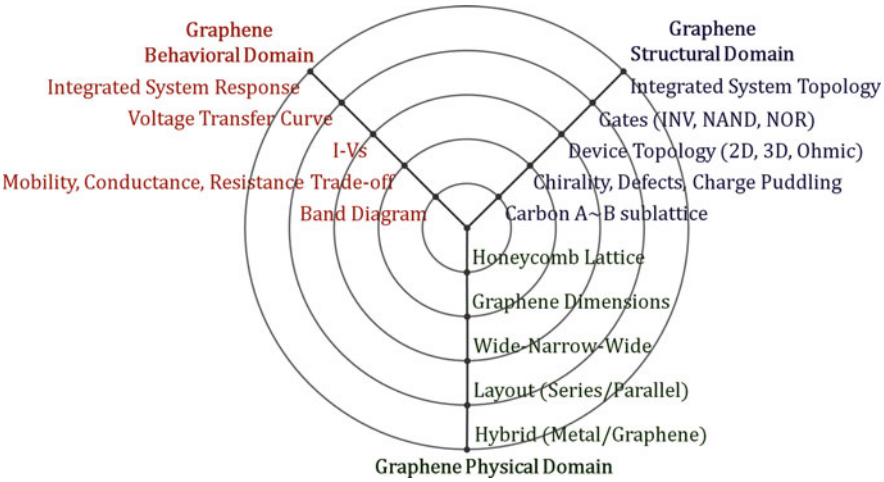

Fig. 18.1 Gajski–Kuhn Y-chart adapted for graphene

The Gajski–Kuhn Y-chart (Fig. 18.1) is a model which captures, in a snapshot view, the essential considerations in designing semiconductor devices [1]. The three domains of the Gajski–Kuhn Y-chart are on radial axes. Each of the domains can be divided into levels of abstraction, using concentric rings. At the top level (outer ring), we consider the architecture of the chip; at the lower levels (inner rings), we successively refine the design into finer detailed implementation:

- Creating a structural description from a behavioral one is achieved through the processes of high-level synthesis or logical synthesis.
- Creating a physical description from structural one is achieved through layout synthesis.

Building up such a multilevel view of graphene, a material of undoubted interest, is an ongoing process. The aim of this chapter is to touch upon just a few of the concentric circles to create such a viewing platform.

18.1 The Innermost Circle: The Atomistic View

Although there has been a lot of effort at this end from physicists and chemists, our aim here is more object-oriented – we wish to touch upon the graphene nanoribbons (GNRs), specifically, the edge chemistry that leads to the observed lack of chirality and metallicity, then progressively outward along the Y-chart toward their two and then three terminal properties, and finally to an overall compact model describing its circuit level potential.

18.1.1 Flatland: A Romance in Two Dimensions

Among elements on the periodic table, carbon is unique in that its sp^2 planar and sp^3 tetragonal bond energies are comparable, carbon allotrope making it geometrically vary all the way from 3-d diamond to 0-d buckyballs [2]. Of this entire set carbon allotropes, a candidate that combines impressive material properties (e.g., ultra-low effective mass), structural versatility, and amenability to industry-standard planar fabrication techniques is undoubtedly graphene and its multiple derivatives, including carbon nanotubes (CNTs), bilayer graphene (BLG), epitaxial graphene (epi-G), strained graphene (sG), and GNR.

The impressive electronic properties of CNTs and GNRs stem from their parent graphitic bandstructure [3]. Without delving into the mathematics, it is important to rehash some of the salient features relating the bandstructure to the underlying chemistry. The hybridization of one s and two carbon $p_{x,y}$-orbitals creates a planar honeycomb structure in a single graphene sheet, loosely resembling self-assembled benzene molecules minus the hydrogen atoms. The crystal structure can be described as a triangular network with a two-atom dimer basis, whose π electrons hybridize to create bonding–antibonding pairs that delocalize over the entire crystal to generate conduction and valence bands. However, since the two basis atoms and the orbitals involved are identical, we get a zero-band gap metal with a dispersion resembling photons, albeit with a much lower speed. The resulting low-energy linear dispersion corresponds to a constant slope and thus a constant velocity $v = \partial E/\hbar\partial k$.

The unique bandstructure of graphene contributes to its amazing electronic properties [2]. Because the Fermi velocity is energy independent, the cyclotron effective mass of graphene electrons, $m^* = \hbar k_F/v_F$ is vanishingly small at low energy ($k_F \to 0$, v_F being constant at roughly 10^8 cm/s). Furthermore, the two bands are derived out of symmetric and antisymmetric (bonding and antibonding) combinations of the two identical dimer atoms, creating a two-component pseudospinor out of the two Bloch wavevectors, with their ratio being just a phase factor $e^{i\theta}$, where $\tan\theta = k_y/k_x$ relates electron quasi-momentum components in the graphene x–y plane. The reversal of phase between the forward and backward velocity vectors suppresses 1D acoustic phonon back-scattering, allowing only Umklapp processes in confined graphitic structures such as CNTs and GNRs. The combination of low mass m^* and long scattering lengths λ_{sc} ultimately leads to very high mobilities $\mu = q\lambda_{sc}/m^*v_F$, with a record room temperature value at 230,000 cm^2/Vs [4] for suspended graphene sheets.

In the following sections, we discuss two bandstructure related issues that arise when we attempt to pattern or modify graphene to generate gapped or confined planar structures:

- The absence of metallicity- and chirality-dependent bandgaps in multiple experiments (Sects. 18.1.2–18.1.4).
- The increase in effective mass as a bandgap is progressively opened, arising from fundamental asymptotic constraint on graphene's high bandstructure (Sect. 18.1.4) that are expected to persist even for very pure samples.

18.1.2 Whither Metallicity?

The bandstructure of CNTs is by now, a textbook homework problem. Since the conduction and valence bands of its parent graphene structure touch precisely at the vertices of its hexagonal Brillouin zone, the Fermi wavelength of undoped graphene corresponds to a *unique electron wavelength* $\lambda_F = 3\sqrt{3}R/2$, where R is the C–C bond distance. The imposition of periodic boundary conditions along the circumference of a CNT filters out many allowed electron wavelengths and allows only modes that have integer ratios of $\pi D/\lambda_F$ (D being the tube diameter), so that a particular chirality (i.e., a wrapping topology) may or may not support λ_F needed to sustain metallicity. Accordingly, one can derive selection rules on paper, or using simple 1-orbital orthogonal nearest neighbor tight binding, that match experiments quite well. In any random array of CNTs, roughly a third are expected to be metallic, and impressive progress has been achieved in sorting them out from their semiconducting counterparts. Even in extremely narrow CNTs with strong curvature-induced out-of-plane hybridizations, the anomalous bandgaps are well captured by non-orthogonal tight-binding formulations such as extended Hückel theory (EHT) [5]. The bandgaps of CNTs bear relatively few surprises, at the end of the day.

Life is more complicated when dealing with GNRs. Indeed, it seems reasonable to expect a chirality dependence to arise for GNRs, simply replacing the periodic circumferential boundary conditions across CNTs with hard-wall boundary conditions across the GNR width. A few details may change, for instance, we now fit half-wavelengths rather than whole wavelengths, and the edges are not completely opaque to electrons tunneling outward so that the boundary conditions are more "diffuse". The quantization condition will roughly correspond now to integer ratios of $(W + R\sqrt{3})/\lambda_F$ (accounting for two unit cells the armchair edge outside for the wavefunction to vanish). However, one-orbital tight binding would still predict three chiral classes in GNRs, one of which is strictly metallic as in CNTs. Experimentally, however, no chirality dependence is observed for GNRs, nor are any GNRs observed to be strictly metallic at low temperature (Fig. 18.2). Regardless of wrapping vector,

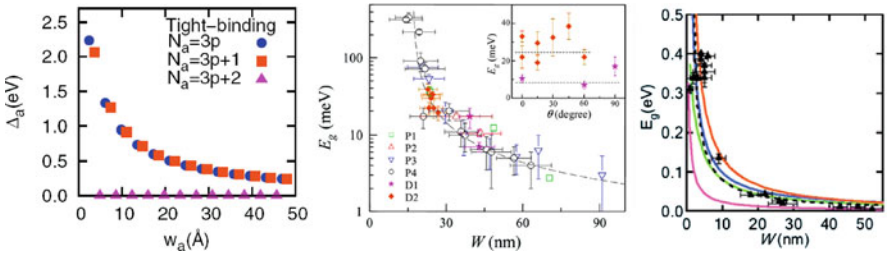

Fig. 18.2 (*Left*) Tight-binding 1-orbital calculations show three chiral curves, one of which is metallic [6]. By contrast, data from (*center*) Philip Kim's group [7] and (*right*) Hongjie Dai's group [8] show a single chirality free curve with no metallic signatures

GNRs wider than 10 nm are quasi-metallic while narrow ones semiconducting. We thus have a startling disconnect between simple theories and experiments [8].

18.1.3 Edge Chemistry: Benzene or Graphene?

The disconnect between naive expectations and observations arises from the boundaries, which ultimately impact the quantization rules behind patterned GNRs. Specifically, we argue that edge strain and roughness are the main factors behind the disconnect. Doing justice to such effects requires a proper bandstructure that can capture atomistic chemistry and distortion. While density functional theory (DFT) within the LDA-GGA approximation captures these effects well, we used DFT primarily for structure evaluation, and resorted to EHT fitted to bulk graphene to explore the low-energy bandstructures. We relaxed the hydrogenated edges of armchair GNRs using LDA-GGA and found a bonding environment distinct from bulk graphene. While the inner carbon atoms have a bond length of 1.42 Å, the edges tend to dimerize and see a 3.5% [6, 9] strain associated with a reduction in bond length to 1.37 Å. Thereafter, we employ non-orthogonal basis sets in EHT to capture the effect of the edge chemistry on the low-energy electronic structure.

There is an appealingly simple explanation for the observed bonding chemistry. Since the edge carbon atoms are connected to hydrogen on one side and carbon on the other, the difference in electronegativity tends to strain the armchair-edge C–C atoms closer to a benzene structure (Fig. 18.3). The unequal bonding environment at strained armchair-edge disallows any resonant hybridization that evens out the double-single bond distribution in aromatic rings. Therefore, the edge rings in armchair GNRs break into "domains" with nearly intact double bonds at the edges and slightly expanded single bonds toward the bulk end. Since benzene is semiconducting, the 3.5% strain at the dimerized edges increases intradimer overlap but reduces interdimer overlap, effectively opening a bandgap by 5%. The obvious consequence is that *all armchair GNRs become strictly semiconducting*, in sharp contrast to their CNT counterparts. Meanwhile the lateral symmetry along the

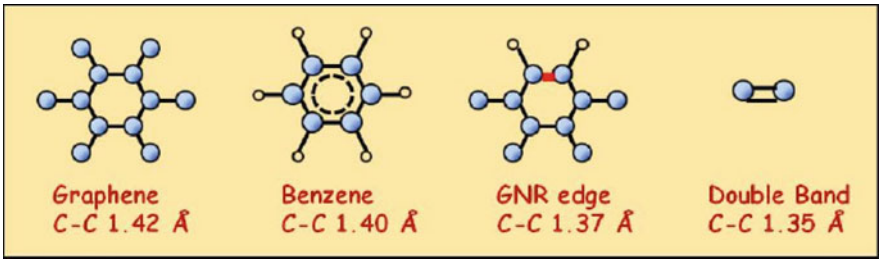

Fig. 18.3 C–C bond length comparisons show that strained armchair GNR edges lie between benzene and double bonds, enjoying only a partial resonant hybridization

zigzag edge is resistant to dimerization. In fact, the inward motion of the C–C edges away from the hydrogen atoms shrink both bond lengths equally, making zigzag edges more conducting.

To confirm our simple explanation on the impact of strained edge bonds on the electronic structure, we calculated the density of states (DOS) of a uniformly wide armchair GNR with edge strain using EHT. While EHT has been used widely to study molecular properties, it has also been extended to describe bulk semiconducting bandstructures using localized Wannier like non-orthogonal basis sets that still retain their individual orbital properties. Through extensive tests on both graphene and silicon, we have found that EHT accurately captures both bulk bandstructures as well as surface and edge distorted bandstructures [10]. The result of our simulation is shown in Fig. 18.4. The role of edge passivation is shown at the top, where we can see the explicit removal of edge-induced midgap states by hydrogenation. The bottom panels show the role of edge strain. In contrast to p_z

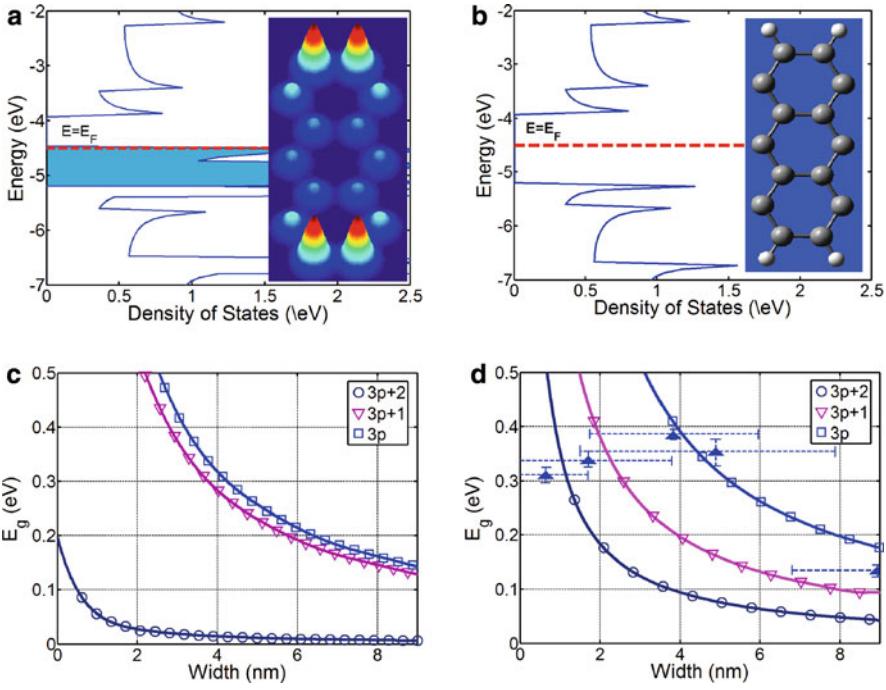

Fig. 18.4 (**a**) Open carbon bonds at the edges introduce edge-states (*shaded*) in the DOS. Spatial resolution of those eigenstates around the Fermi energy confirms the electron wavefunction localized at the armchair edges. (**b**) When open carbon bonds are hydrogen terminated, those edge-states are removed. (**c**) Applying EHT to GNR dispersion relation across a range of sub-10nm armchair edge widths finds an oscillating bandgap. (**d**) Strain of edge bonds that are hydrogen terminated widens the energy bandgap for $3p$ and reduces the gap for $3p + 1$ GNRs. E_g vs. width results are within the range of experimental data points [8] and also in agreement with DFT predictions

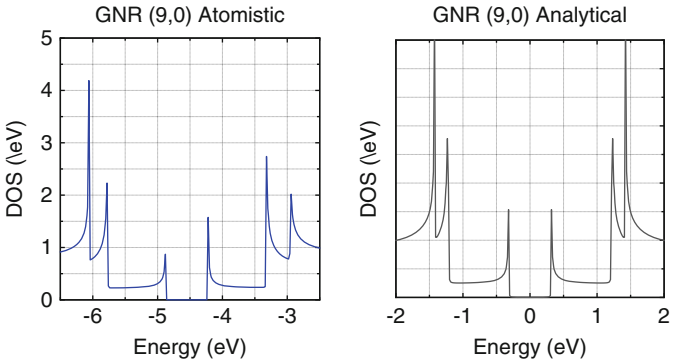

Fig. 18.5 Atomistic EHT plot (*left*) of the DOS of a (9,0) relaxed armchair GNR, compared with a next-nearest neighbor tight-binding fit (*right*) from C.T. White at NRL. From the p_z sector of the EHT Hamiltonian, we estimate the nearest neighbor coupling, third nearest neighbor coupling, and the shift in coupling at the 3.5% strained edges as $t_1 = -3.31$ eV, $t_3 = -0.106$ eV, and $\Delta t_1 = -0.38$ eV. These extracted parameters compare quite favorably with C.T. White's tight binding parameters, $t_1 = -3.2$ eV, $t_3 = -0.3$ eV and $\Delta t_1 = -0.2$ eV [9]

based nearest neighbor one orbital tight-binding theory, a small bandgap opens [5]. While CNTs have precise periodic boundary conditions along their circumference, the edge atoms do not provide an exact hard wall boundary condition, as the electrons tend to tunnel out into the surrounding region. In the presence of edge strain, the bandgap increases because of the aforementioned dimerization, removing any semblance of metallicity from the bandgap vs. width plots.

While EHT explains the removal of metallicity, compact models prefer a suitably calibrated orthogonal tight-binding model, with the edge chemistry captured through beyond nearest neighbor interactions. It is not clear if this reproduces the Bloch wavefunctions, but they do seem to capture the overall DOS. Figure 18.5 shows a comparison between a (9,0) EHT DOS and a (9,0) tight-binding DOS (parametrized independently by White) [11]. We will use this formulation for our simpler compact models described later.

18.1.4 Whither Chirality?

While we can explain away the lack of metallicity through the preponderance of edge strain, why do we not see the three chiral curves in a plot of experimentally measured bandgaps vs. ribbon widths? The primary reason, we believe, is roughness at the edges, which tends to wash away such chiral signatures. Currently, line edge roughness along a GNR edge is an unavoidable consequence of lithographic and chemical fabrication techniques [12, 13]. Unzipping CNTs via ion bombardment produces the smoothest GNR edges to date [14]. However, edge fluctuations even on the scale of a single atom can degrade transmission probability of modes near band edges or cut-off modes [10]

We have studied a wide spectrum of line edge roughnesses that can ultimately be classified as either a *width modulation* or *width dislocation*. Modulation in width along the armchair edge has a corresponding modulation in bandgap that follows an oscillating inverse square law relation between bandgap and width, spanning the three chiral curves. Meanwhile a width dislocation is an in-plane displacement in the GNR that energetically sees the same bandgap at interface of the slip dislocation, albeit with localized interfacial states. We introduced edge roughness in our geometries using a Gaussian white noise that adds or removes an integer number of dimer pairs with a correlation length L_m [11]. The results of our EHT simulations with statistics for rough edges explain why measured data are seen to cluster around one of the $3p + 1$ chirality curves.

An E–k relation cannot be rigorously defined for a structure without periodicity, so we focus instead on the transmission bandgap of the entire structure, calculated using the nonequilibrium Green's function (NEGF) formalism in its simplest, Landauer level implementation. The plotted transmission of the rough segment (Fig. 18.6), sandwiched between two bulk metallic contacts, is shown for a random mixture of (7,0) and (9,0) chiralities [10]. The rough GNR can be viewed as a random mixture of individual GNR segments with well-defined chiralities and bandgaps, as long as the correlation length L_m is larger than the electron wavelengths. In the large majority of our simulations, we find that the transmission bandgap for the rough GNR follows the largest bandgap of the individual segments

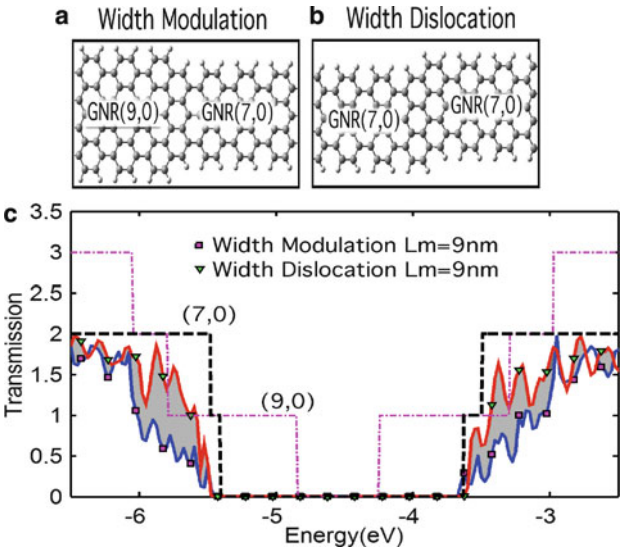

Fig. 18.6 (*Top*) Two kinds of roughness include variation in GNR width and a width dislocation across a slip line, maintaining the same width. (*Bottom*) Transmission plots show that for either case, segments with the larger bandgap filter out the rest of the segments, thereby promoting the chiral curve with the highest bandgap, in agreement with experiments and EHT calculations [10] (L_m represents the correlation length for edge roughness)

(in this case, the (7,0) segment). The larger bandgapped segments effectively filter out the incoming currents from the rest of the crystal, explaining the observed predilection toward the $3p+1$ chiralities. However, there are outliers corresponding to accidental situations where the length scales of large bandgap segments are narrow enough to become transparent to tunneling. As we increase the frequency of roughness by bringing the correlation length below the electron wavelength, we expect to see more tunneling events. Such high-frequency roughnesses, as well as inelastic scattering, will mix chiralities more thoroughly and are predicted to spread out the data more evenly over the three chiral curves rather than clustering them around the dominant $(3p+1)$ segment.

The upshot of this analysis is that for reasonably smooth GNRs with $L_m > \lambda_F$, we expect the GNR width to be the sole arbiter of metallicity, so that wide GNRs are metallic while narrow (< 10 nm) GNRs are semiconducting [8]. While the analyses leading to this conclusion assumed some simplifications (e.g., ignoring structural modifications due to back-bonding with substrates), experiments seem to support this conclusion.

18.2 The Next Circle: Two Terminal Mobilities and I–Vs

Our next circle would move on from the material parameters to electronic properties such as carrier density, mobility, conductivity, and ultimately current–voltage (I–V) characteristics.

18.2.1 Current–Voltage Characteristics (I–Vs)

The Landauer expression gives us a convenient starting point for the current through any material,

$$I = \frac{2q}{h} \int T(E)\, M(E)[f_1(E) - f_2(E)]\mathrm{d}E \tag{18.1}$$

where $T \approx \lambda_{sc}/(\lambda_{sc} + L)$ is the quantum mechanical transmission per mode, that relates its scattering length λ_{sc} with its geometrical length L. The number of modes $M = \gamma_{\text{eff}} D(E)$, $D(E)$ being the DOS, and the effective injection rate is given by $1/\gamma_{\text{eff}} = 1/\gamma_1 + 1/\gamma_2 + 1/\gamma_{\text{ch}}$, where $\gamma_{1,2}$ are the broadenings from the contacts, and $\gamma_{\text{ch}} = \hbar v(E)/L$ is the intrinsic transport rate in the channel. Assuming the contact broadenings are large so that the rate limiting step is γ_{ch}, we can replace $\gamma_{\text{eff}} \approx \gamma_{\text{ch}}$.

The band dispersion of graphitic materials, ranging from epi-G to sG, BLG, CNTs, and GNRs are all described by a universal formula [15]

$$E = \pm\sqrt{E_{C,V}^2 + \hbar^2 v_0^2 k^2} \tag{18.2}$$

where the band-edges are at $E_{C,V}$, while the high-energy velocity in the linear regime is $v_0 \approx 10^8$ cm/s. From the dispersion, we can readily extract the 2D DOS and band velocities

$$D(E) = \left(\frac{2WL}{\pi\hbar^2 v_0^2}\right)|E|\left[\theta(E - E_C) + \theta(-E_V - E)\right]$$
$$v(E) = v_0\sqrt{1 - E_{C,V}^2/E^2} \tag{18.3}$$

There is an additional energy dependence in the scattering length λ_{sc}. For ballistic channels, this is energy independent, while for charge impurity and edge roughness scattering, $\lambda_{sc} \propto E$, while for acoustic phonon scattering, $\lambda_{sc} \propto 1/E$. The actual dependences are a bit more complicated, but these are reasonable approximations to adopt.

The algebra becomes particularly simple if we ignore the energy dependence of λ_{sc}. We can then do the Landauer integral, leading to

$$I = \frac{8q}{h}\left(\frac{\lambda_{sc}W}{\pi\hbar v_0 L}\right)I_0 \tag{18.4}$$

where the shape function I_0 depends on the current flow regime. Assuming we start with an n-doped graphene with a bandgap, we get

$$I_0 = \begin{cases} \dfrac{1}{2}\left[\mu_1\sqrt{\mu_1^2 - E_C^2} - E_C^2\cosh^{-1}\left(\dfrac{\mu_1}{E_C}\right) - \mu_2\sqrt{\mu_2^2 - E_C^2} + E_C^2\cosh^{-1}\left(\dfrac{\mu_2}{E_C}\right)\right] \\ \qquad\qquad \text{if } qV_D < E_F - E_C, \\ \dfrac{1}{2}\left[\mu_1\sqrt{\mu_1^2 - E_C^2} - E_C^2\cosh^{-1}\left(\dfrac{\mu_1}{E_C}\right)\right] \\ \qquad\qquad \text{if } E_F - E_C < qV_D < E_F + E_V, \\ \dfrac{1}{2}\left[\mu_1\sqrt{\mu_1^2 - E_C^2} - E_C^2\cosh^{-1}\left(\dfrac{\mu_1}{E_C}\right) - \mu_2\sqrt{\mu_2^2 - E_V^2} - E_V^2\cosh^{-1}\left(\dfrac{\mu_2}{E_V}\right)\right] \\ \qquad\qquad \text{if } qV_D > E_F + E_V. \end{cases} \tag{18.5}$$

where $\mu_1 = E_F$ and $\mu_2 = E_F - qV_D$. The expressions can be further simplified. In the linear regime, the current looks like

$$I_{\text{linear}} \approx 2G_0 M\left(\frac{v_0}{v_F}\right)^2 V_D \tag{18.6}$$

where $G_0 = q^2/h$, the number of modes $M \approx 2W/(\lambda_F/2)$, and the Fermi velocity $v_F = v_0\sqrt{1 - E_C^2/E_F^2}$. The saturation current

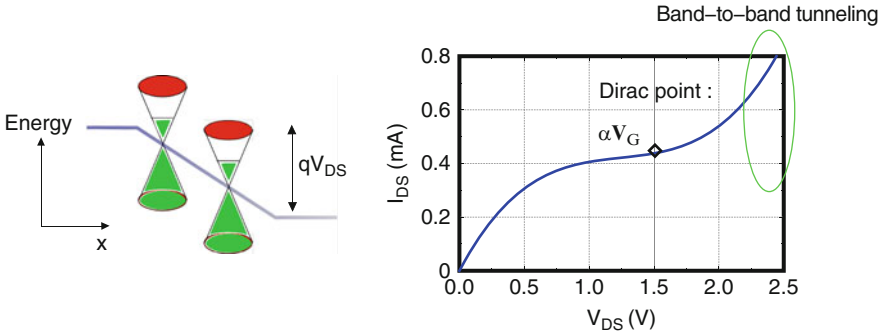

Fig. 18.7 A typical I–V output shows how the I–V tends to saturate at the Dirac point even without a bandgap. The shift in the Dirac point indicates the Laplace potential drop along the channel, eventually leading to band-to-band tunneling

$$I_{\text{sat}} \approx 4G_0M\left(\frac{E_F}{2q}\right) \tag{18.7}$$

while the band-to-band tunneling current at high bias varies quadratically as

$$I_{\text{BTB}} \approx 4G_0M\left(\frac{v_0}{v_F}\right)V_D\left(\frac{qV_D}{2E_F}\right) \tag{18.8}$$

Figure 18.7 shows typical I–Vs based on the above formula. These results agree with more involved, atomistic models for EHT coupled with NEGF based simulations [16]. The current shows a point of inflection at the Dirac point, which is shifted by the gate bias (a bandgap would provide an extended saturation region, as we will see for our three terminal I–Vs later on). The subsequent rise in current is indicative of band-to-band tunneling. Furthermore, a prominent I–V asymmetry, consistent with experiments on SiC, can be engineered into our I–Vs (Fig. 18.8) readily by shifting the Fermi energy to simulate a charge transfer "doping" [17] of 470 meV through substrate impurities, back-bonding, and/or charge puddle formation with SiC substrates. A scattering length (λ_{sc}) that varied inversely with gate voltage was implemented in the left figure in Fig. 18.8. For n-type conduction, λ_{sc} ranged between 18–40 nm and 20–31 nm for p-type. Typically we would expect at least 100 nm for low bias conductance and down to 10 nm as the biasing approaches the saturation and band-to-band tunneling regions. Chosen λ_{sc} represents an average scattering length for the different regions. A more accurate model for scattering is necessary and will be developed in future works. By contrast, SiO_2 seems to dope the sheets minimally and the measured I–Vs show the expected symmetry between the electron and hole conducting sectors.

From the low-bias I–Vs, we can now extract the conductance $G = I_{\text{linear}}/V_D$, thence the sheet conductance σ_s using $G = \sigma_s W/L$, and finally the mobility μ_s

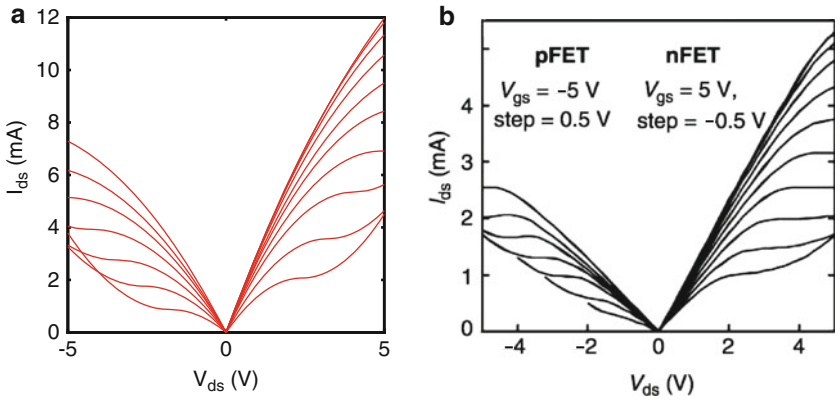

Fig. 18.8 (*Left*) Theoretical and (*Right*) experimental I–Vs for graphene. The calculations on the left assume a "doping" of the sheet by a charge density that shifts the K-point relative to neutrality. We also assume an inverse relation between the scattering length λ_{sc} and the applied voltage on the n-side, consistent with scattering by charge puddles associated with the above doping charge. The data on the right are for graphene on SiC, where charge puddles and/or back-bonding are expected to transfer a net charge density to the sheet [18]. Note that V_{gs} is the gate source voltage and step is the voltage step between each I-V curve

using $\sigma_s = q n_s \mu_s$, where n_s is the sheet charge density related to the Fermi wavevector as $k_F = \sqrt{\pi n_s}$. Let us focus on the mobility first, keeping in mind that the effective mass m^* in GNRs is *energy-dependent*.

18.2.2 *Low Bias Mobility-Bandgap Tradeoffs: Asymptotic Band Constraints*

Graphene's linear dispersion is known for contributing to an ultra-high mobility, but often overlooked is its origin in the low bandgap that ultimately hampers its ON–OFF ratio as an electronic switch. The carrier velocity ($v = 1/\hbar \mathrm{d}E/\mathrm{d}k$) fundamentally saturates to $v_0 = 3a_0 t/2\hbar \sim 10^8$ cm/s, which forces its high-energy bandstructure to a linear form regardless of bandgap size. Irrespective of the mechanism for opening bandgaps, or the particular progeny of graphene that we are looking at (epi-G, sG, CNT, GNR or BLG), the bandstructures are always writable as $E(k) \approx \pm\sqrt{(E_G/2)^2 + (\hbar v_0 k)^2}$ [2]. Such an intimate relation between bandgap and dispersion connecting ultimately to its conduction/valence band effective masses (as opposed to midgap tunneling effective mass) is unique in materials science.

An extended bandgap constrained by the high-energy velocity saturation localizes carriers, which shows up as a decrease in curvature at the band edges. It is easy to show from the above dispersion that the effective mass at each band-edge satisfies

$$m_0^* = E_G/v_0^2 \tag{18.9}$$

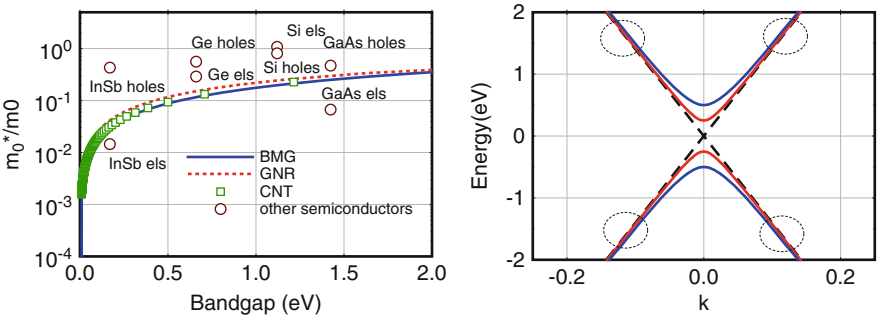

Fig. 18.9 Scaling of graphite effective masses shows that increasing the bandgap increases the mass $m^* = p_F/v_F$ due to the decrease in average curvature arising from a pinning of the E–k at high-energy values [19]

indicating that the kinetic energy gained by the electrons and holes upon bandgap opening is taken ultimately from the corresponding crystal potential (Fig. 18.9).

For transport considerations corresponding to high bias electrons and holes, we need to generalize the concept of effective mass to energies away from the band-bottom, using $m^* = p/v = \hbar k/[1/\hbar(\partial E/\partial k)]$. This expression reduces to the usual dependence on curvature near the band-bottoms upon using L'Hospital's rule with $k \rightarrow 0$. In other words, effective mass and carrier velocity must be treated as energy-dependent variables instead of material specific constants. From here, we can then extract the mobility $\mu = q\lambda_{sc}/p$, where carrier momentum $p = \hbar k$ and λ_{sc} is the scattering length, related by $\lambda_{sc} = (v_F\tau)\pi/2$. From the band dispersion or E *vs.* k relation, we define the Fermi wavevector as:

$$k_F = \frac{\sqrt{E_F^2 - E_{gap}^2/4}}{\hbar v_0} \tag{18.10}$$

$$= \sqrt{\pi n_S}. \tag{18.11}$$

where $E_{gap}/2 + \alpha_G q V_G$ marks the position of the Fermi level (E_F) relative to the Dirac point and n_S is the electron density. Relating (18.10) and (18.11), we can express a voltage and bandgap-dependent electron density to determine the mobility

$$\mu = \frac{q\tau}{m^*} = \frac{q\lambda_{sc}}{m^* v} = \frac{q\lambda_{sc}}{\hbar k_F} \tag{18.12}$$

It is thus clear that the mobility depends on the value of k_F. As we vary the bandgap of graphitic systems (epi-G, BLG, s-G, or GNR), the variation in k_F (equivalently, E_F) depends on what parameters are being held constant in the process. To start, let us assume that the scattering length λ_{sc} is independent of energy, so that we are effectively working in the ballistic limit. At this point, we can assume the electron density n_s is constant while the bandgap is being opened,

so that k_F is constant and the mobility does not change. However, possibly a more suitable metric is the gate overdrive $V_G - V_T$, which ultimately determines the charge density too using $n_s = C_G(V_G - V_T)$, where $C_G^{-1} = C_{\text{ox}}^{-1} + C_Q^{-1}$ involves both oxide and quantum capacitances. In the limit of small DOS ($C_Q \ll C_{\text{ox}}$) at smaller bandgaps, the gate overdrive is the quantity that is controlled externally, and this changes n_s as the quantum capacitance proportional to density of states increases with energy. We then get

$$n_S = \frac{\alpha_G q V_G(\alpha_G q V_G + E_{\text{gap}})}{L\pi\hbar^2 v_0^2} \tag{18.13}$$

$$\mu = \frac{q}{\hbar\sqrt{\pi n_S(\alpha_G q V_G, E_{\text{gap}})}} \tag{18.14}$$

where the gate transfer factor is $\alpha_G = C_{\text{ox}}/C_\Sigma$ and C_Σ is the equivalent capacitance of a three-terminal device including its quantum capacitance. The fundamental mean-free-path (λ_{sc}) can be approximated semiclassically from the conductance $\sigma_s = q^2 D(E_F)\mathcal{D} \approx \frac{2q^2}{h}\{\lambda_{\text{sc}} k_F\}$ with k_F defined in (18.11) and $\mathcal{D}$ being the diffusion constant. Single layer graphene (SLG) can have λ_{sc} on the order of microns. A more complete form of λ_{sc} from (18.14) would include scattering due to charged impurities, roughness, and possible phonons from interfacial materials given that phonons native to graphene are inherently suppressed, ($1/\lambda_{\text{sc}} = 1/\lambda_{\text{impurities}} + 1/\lambda_{\text{rough}} + 1/\lambda_{\text{ph}}$).

For a fixed gate overdrive, the mobility even for a ballistic device decreases with bandgap, primarily due to the asymptotic constraint that pins the band structure to a high-energy linear dispersion. We emphasize that this trade-off arises *independent of any reduction in scattering length* λ_{sc} *through the bandgap opening process*. The low effective mass of graphene arose from its sharp conical bandstructure in the first place, so that opening a bandgap without removing the higher-energy conical dispersion invariably makes the carriers heavier.

With respect to digital switching applications, the importance of the above trade-off cannot be overstated. The mobility ultimately determines the switching speed through the ON current, while the bandgap relates to the ON–OFF ratio. For cascaded devices, it is also worth emphasizing that the ON–OFF ratio needs to be computed at high bias, as the drain and gate terminals in regular CMOS like cascaded geometries are connected to the same supply voltage. Increasing the ON–OFF ratio by increasing the bandgap is predicted thereby to reduce the switching speed. We must therefore evaluate GNRs on this *entire* $\mu - E_G$ *curve* rather than at an isolated point on this 2D plot. Equation (18.14) elegantly relates E_{gap} and μ for various λ_{sc}'s. Analyzing the three parameters $E_{\text{gap}} - \mu - \lambda_{\text{sc}}$ simultaneously allows us to project the performance of graphene derivatives and compare against other common semiconductors as seen in Fig. 18.10.

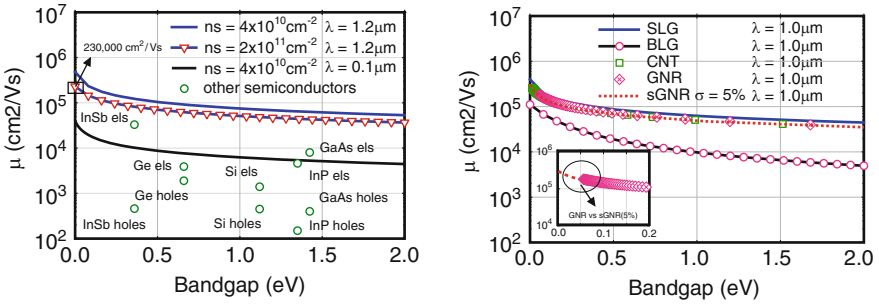

Fig. 18.10 Decrease in mobility (for fixed gate overdrive) between various graphitic materials as well as various electron densities. Note that $\lambda = \lambda_{sc}$

18.3 The Third Level: Active Three-Terminal Electronics

We now move outward to the next circle on the Y-chart, toward three terminal active electronic devices. Our main focus will be on a class of patterned device-interconnect hybrids, where we see certain notable advantages mainly on the electrostatics and the contact barriers, but challenges with the small bandgap show up as band-to-band tunneling and modest ON–OFF ratio.

18.3.1 Wide–Narrow–Wide: All Graphene Devices

The analysis from the previous sections set the platform for evaluating the I–V characteristics of GNR devices in the presence of a third gate terminal. Our lesson from Sect. 18.1 indicates that the GNR metallicity is primarily set by its ribbon width, showing that one might be able to monolithically pattern a wide–narrow–wide (WNW) all graphene device that flows seamlessly from semiconducting channels to metallic interconnects. Experiments have in fact shown the ability to carve out GNRs using either chemistry or nanoparticle mobilities that snip the sheets almost perfectly along their C–C bonds. GNRs as thin as 1 nm with perfect edges have been manufactured chemically [20]. It is thus interesting to query what the device level advantages of such a monolithically patterned GNR would be. We will later discuss the circuit level ramifications.

The structure of an imagined WNW graphene nanoribbon field-effect transistor (GNRFET) is shown in Fig. 18.11. The wide regions are metallic and the narrow ones semiconducting. A planar top metal gate modulates the channel conductance while a substrate acts as a back gate for electrostatic ‘channel doping’ (see figure later for inverters). Before we detail the advantages of such a structure, let us first discuss how we simulate the I–V of one of these WNW devices.

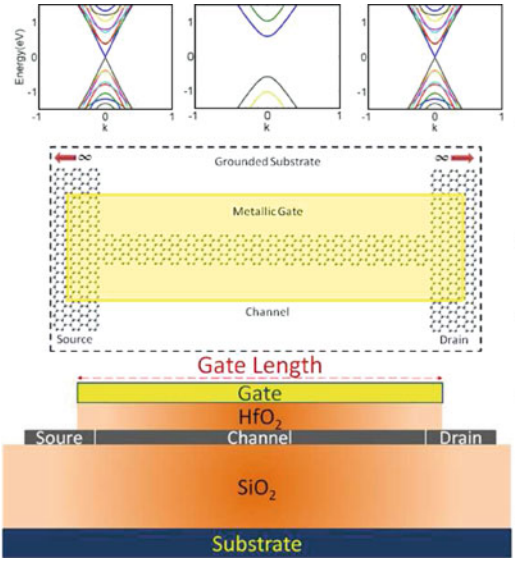

Device Dimensions and Parameters (nm)

Channel	*Structure*	(7,0)
	Width	0.74 nm
	Length	8.66 nm
Gate	*Width*	2.46 nm
	Length	10.51 nm
Source/ Drain	*Structure*	(35,0)
	Width	4.18 nm
HfO_2 Gate Dielectric	*Thickness*	1 nm
SiO_2 Substrate	*Thickness*	3 nm

Fig. 18.11 WNW dual gated all graphene device, showing local dispersion corresponding to the different regions of the device (*top*), top view (*center*), and side view (*bottom*) with the device parameters listed

18.3.2 Solving Quantum Transport and Electrostatic Equations

Our calculations couple a suitable bandstructure/DOS for the graphene channel with full 3D Poisson's equation for the electrostatics and the NEGF formulation for quantum transport [15]. The wider contact regions are captured recursively by computing their surface Green's functions $g_{1,2}(E)$. The corresponding energy-dependent self-energy matrices $\Sigma_{1,2}(E) = \tau_{1,2}\, g_{1,2}\, \tau_{1,2}^{\dagger}$ project the contact states onto the channel subspace, where τ is a matrix that describes the energetic coupling or bonding between the wide graphene source-drain contacts and the narrow graphene channel. An equivalent way to properly capture the interfacial chemistry between contact and channel would be to incorporate part of the wide graphene contact as the channel when defining the Hamiltonian matrix (H). The Coulomb matrix U is computed using the Method of Moments (MOM), described below [21].

From the above matrices, the retarded Green's function $G = (ES - H - U - \Sigma_1 - \Sigma_2)^{-1}$ is computed, and thence the charge density matrix $\rho = \int \mathrm{d}E\, G\Sigma^{\mathrm{in}} G^{\dagger}/2\pi$, whose trace gives us the total charge. $\Sigma^{\mathrm{in}} = (\Gamma_1 f_1 + \Gamma_2 f_2)$ in the simple limit where the only scattering arises at the contact channel interface. In the previous equation, $\Gamma_{1,2} = \mathrm{i}(\Sigma_{1,2} - \Sigma_{1,2}^{\dagger})$ give the contact broadenings (the matrix analog of the injection rates $\gamma_{1,2}$ introduced in Sect. 18.2.1), while $f_{1,2}(E) = 1/[1 + \mathrm{e}^{(E-\mu_{1,2})/k_{\mathrm{B}}T}]$ represent the contact Fermi–Dirac distributions, with $\mu_{1,2}$ being the bias-separated electrochemical potentials or quasi-Fermi energies in the contacts [16]. The charge

density matrix is then used to recompute the Coulomb matrix U self-consistently through Poisson's equation. Finally, the converged Green's function is used to compute the current $I = (2q/h)\int \mathrm{d}E\, T(E)[f_1(E) - f_2(E)]$, where the transmission $T(E) = trace(\Gamma_1 G \Gamma_2 G^{\dagger})$ [15].

Let us now get into a few details on the 3D Poisson equation we solve, using MOM numerically. MOM captures the channel potential by setting up grid points on the individual device atoms with a specific charge density δn_D and on the contact atoms with a specific applied voltage ϕ_C [21]. Using the notations "C" for Contact and "D" for Device, we get

$$\phi_d = \underbrace{(U_{\mathrm{dC}} U_{\mathrm{CC}}^{-1})\phi_C}_{\text{Laplace}} + \underbrace{(U_{\mathrm{dd}} - U_{\mathrm{dC}} U_{\mathrm{CC}}^{-1} U_{\mathrm{Cd}})}_{\text{Single Electron Charging Energy}} \Delta n_d \tag{18.15}$$

where we imply vector notations for the potentials ϕ and matrix notations for the Coulomb kernels U. Δn_d is calculated relative to its neutrality value N_0 by tracing over ρ above, while N_0 is calculated analogously, while grounding all the contact potentials (this would depend on the workfunction of the contacts, as in MOS electrostatics). The matrix elements in U need to be computed with the correct dielectric constants. Let us describe it in the simpler case with a dielectric constant κ for the top gate and a dielectric constant unity for the bottom (trivially generalized to multiple dielectrics). Using the method of images,

$$\begin{aligned} U(\boldsymbol{r}_1, \boldsymbol{r}_2) &= \frac{q}{4\pi\epsilon_0\epsilon_1}\left[\frac{1}{|\boldsymbol{r}_1 - \boldsymbol{r}_2|} - \left(\frac{\epsilon_2 - \epsilon_1}{\epsilon_2 + \epsilon_1}\right)\frac{1}{|\boldsymbol{r}_1 - \boldsymbol{r}_2'|}\right] \quad \text{(in the same medium)} \\ &= \frac{q}{2\pi\epsilon_0(\epsilon_1 + \epsilon_2)|\boldsymbol{r}_1 - \boldsymbol{r}_2|} \quad \text{(in different media)} \end{aligned} \tag{18.16}$$

where $\boldsymbol{r}_2'$ is the image of the charge at $\boldsymbol{r}_2$ [22, 23]. A tricky point is to avoid the infinities at the onsite locations, for instance, when $x_1 = x_2$ and $y_1 = y_2$. We can avoid these using the Mataga–Nishimoto approximation, where we replace terms like $1/|\boldsymbol{r}_1 - \boldsymbol{r}_2|$ with an atomistic correction $1/\sqrt{|\boldsymbol{r}_1 - \boldsymbol{r}_2|^2 + a^2}$, with the cut-off parameter a adjusted to represent the correct onsite Coulomb (Hubbard) charging energy given by the difference between the atomic ionization energy and the electron affinity [24].

Let us now discuss the observed electrostatic characteristics in the WNW device, which explains the geometric advantages of this particular structure.

18.3.3 Improved Electrostatics in 2-D

We simulate a device patterned monolithically from a two-dimensional sheet of graphene with a wide dilution of widths from the source and drain contacts to the active channel region. Simulated WNW (35-7-35) GNRFETs compose of (7,0) armchair GNR narrow regions for the channel and (35,0) armchair GNR regions for

the contact and interconnect regions. A metallic gate is placed above the channel region, while a wide grounded substrate is placed at the bottom of the channel. To calibrate with conventional CMOS technologies, the unique two-dimensional (2D) contacts of the GNRFET are replaced with (3D) bulk metal contacts (whose surfaces act as parallel plate capacitors) for the same channel, gate, and dielectric geometry.

A particular advantage of the WNW structure is the low capacitance of the 2D source–drain contacts [25]. In a conventional MOSFET, the gate electrode needs to compete electrostatically with the source and drain for control of the channel charge. Indeed, a majority of developments in transistor technology over the last few decades have concentrated on making the field lines gate controlled rather than source and drain controlled. This is becoming harder with aggressive size scaling. The 2D source and drain contacts with a top gate make the S/D capacitances lower, as they can only influence the channel through their fringing fields. Note that a 2D side gate geometry, as advocated in many device designs, would eliminate that electrostatic advantage, as the gate needs to compete with the S/D electrodes.

As the channel length gets shorter with the aggressively scaled technologies, the 3D contacts start to influence the channel potential as their surfaces act as parallel capacitor plates flanked by top and bottom insulators. In the case of monolithically patterned 2D GNR contacts, the charges on the contact surfaces are line charges so that the applied source–drain field decays into the channel, creating a *nonlinear channel potential even in the absence of a gate* (Fig. 18.12, left). Moving on to a three terminal, dually gated structure, Fig. 18.12 (right) shows that the gate contact holds the channel potential flat against the action of the drain, thereby reducing short-channel effects.

Figures 18.13 and 18.14 show that for the same channel geometry, the top gate with 2D side contacts has the largest capacitance, followed by the top gate with 3D side contacts, and finally the lowest gate to drain capacitance ratio is obtained when all electrodes are co-planar. The corresponding field line diagrams are also shown in these figures. Note also that in addition to the source, drain, and dual gate electrodes,

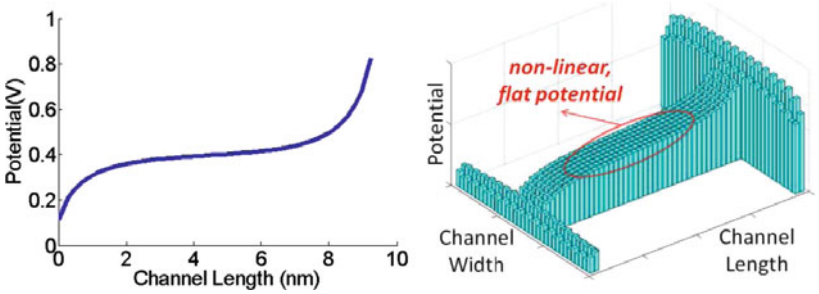

Fig. 18.12 (*Left*) The two-terminal potential shows the vanishing fields near the channel, implying the superior gate control and the improved short-channel effects with the 2D contacts. (*Right*) The 3D potential shows the non-linear flat potential in the middle of the channel

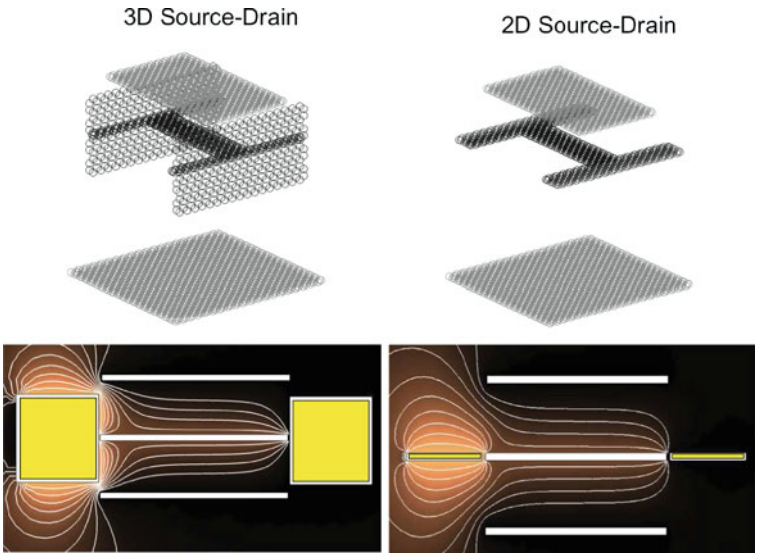

Fig. 18.13 Comparison of planar source–drain vs. 3D source–drain. Denser field lines on the channel from the 3D contacts correlate to stronger source coupling and DIBL. For the given material and geometrical parameters listed in Fig. 18.11, the C_g/C_d ratios are 4.95 and 5.80, respectively. Top and bottom gates were grounded while the source was simulated with a potential of 0.3 V and conducting channel had a potential of 0.1 V

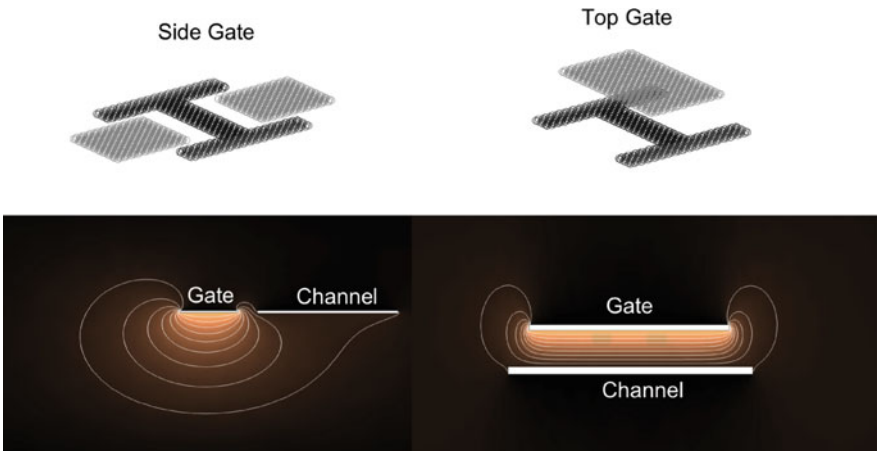

Fig. 18.14 Comparison of top vs. side gate. Denser field lines from the top gate ensure better gate control which is reflected by larger gate capacitance. For the given material and geometrical parameters listed in Fig. 18.11, the C_g/C_d ratios are 5.80 and 3.82, respectively. Gates were biased at 0.4 V, while the conducting channel had a potential of 0.1 V

one needs to worry about the quantum capacitance C_Q, which is automatically included from our density matrix calculations that enter Poisson's equation.

The gate to drain capacitance ratio (C_g/C_d) can be extracted by plotting the channel transmission (T) for two scenarios: maintaining a constant drain voltage (V_d) while sweeping gate voltage (V_g) , and analogously, maintaining a constant V_g while sweeping V_d. Sweeping the V_g creates a larger energy shift in the transmission of the GNRFET channel than the sweeping of the V_d. From the shifting rates of these transmissions and the charge density calculations from the MOM, we can extract the capacitance values of the contacts. With shifts in transmission plots, we once again find that 2D contacts indeed help the gate exercise superior control over the channel [25].

We will now explore the effect of the improved short-channel effect on the computed I–V characteristics.

18.3.4 Three-Terminal I–Vs

The computed three-terminal I–Vs (Fig. 18.15) show excellent short-channel effects, at least over a small voltage range given by the bandgap. Plotted vs. drain voltage, the current shows excellent saturation characteristics with a large output impedance. Plotted vs. gate voltage, the current shows little drain bias dependence (so-called drain-induced barrier lowering or DIBL). Taken together, the curves signify that the device electrostatics in the geometry is nearly ideal, making the outputs relatively robust with process variations. It is interesting to note that instead of enhancing the gate capacitance as in regular CMOS devices, the trick in WNW devices has been to reduce the source and drain capacitances in comparison.

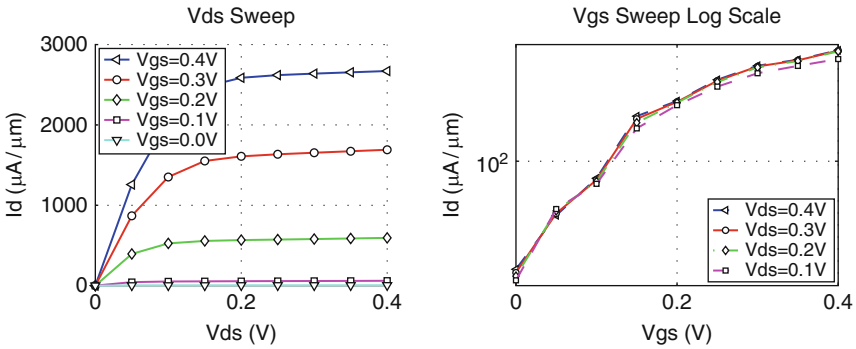

Fig. 18.15 I–V curves for a n-type GNRFET confined to create a large bandgap (in this case, a (7,0) armchair GNR with a bandgap nearly 1 eV). Such an extreme geometry postpones the onset of band-to-band tunneling. More importantly, the point of the I–V is to show the effect of better electrostatics which is independent of bandgap issues – resulting in a high current saturation, low DIBL, and SS

The simulation results of the model in Fig. 18.15 demonstrate a subthreshold swing (SS) of 84.3 mV/dec and a DIBL of 24 mV/V. We note that unless otherwise specified, all simulations refer to material and geometrical parameters shown in Fig. 18.11. The value of the DIBL and the SS can be further improved by increasing the length of the channel (currently 1:8.6 ratio of HfO_2 thickness to channel length). These values calculated are better (smaller) than the estimated values of DIBL = 122 mV/V and the SS = 90 mV/dec for the double gate, 10 nm scaled Si MOSFETs [26]. Also in addition to showing improved short-channel effects, the GNRFET structure with the 2D contacts also shows controlled switching behavior. The on-current (ON) of the system equals to 2670.62 μA/μm with the off-current (OFF) set at 4.07 μA/μm; thus giving a ON-OFF ratio of 656. The ON–OFF ratio, however, ends up being modest, and is a critical challenge in GNRFETs, especially in the light of its seemingly inverse relation with the charge mobility (Sect. 18.2.2).

With the scaling of the channel length, the short-channel effects started to have a huge influence on the device parameters such as the DIBL and SS. Shorter channel lengths allow the S/D electrodes to exact more control on the overall channel potential, which is reflected by the decrease in C_g/C_d ratio and increase in device DIBL and SS. The line charges with the 2D contacts endow the gate with more control over the channel and interface states compared to the 3D contacts by lowering the drain capacitance.

18.3.5 Pinning vs. Quasi-Ohmic Contacts

In today's semiconductors, Ohmic contacts are desired to help achieve linear and asymmetric I–V characteristics. The potential profile inside the channel can be influenced by increasing the drain–source voltage (V_{ds}) or the gate voltage (V_{gs}). For CNTs, this has been a particular challenge, as the metal-to-carbon bonds at the contact-channel interface tend to create Schottky barriers [27]. In our WNW geometries, since the bulk metal contacts are relegated to the ends of the device array, the bonding configuration near the wide–narrow interfaces are controlled by C–C covalent bonding. As our simulations show, this seems to promote a quasi-Ohmic behavior. The better bonding increases the decay lengths of the corresponding metal-induced gap states (MIGS) entering from the wide regions. The partial delocalization reduces the single-electron charging energy (that enters through our MOM treatment), thus making it harder for the contact regions to pin the Fermi energy and reducing the effectiveness of the Schottky barrier.

Schottky barrier FETs behave qualitatively different from MOSFETs. In the latter, an applied gate bias reduces the channel potential and controls the thermionic emission over the voltage-dependent interfacial barrier. In the former, the gate reduces the thickness of the Schottky barrier and controls the tunneling of electrons through a voltage-independent, pinned barrier height. The question is what the potential profile looks like in the channel, and whether the contact MIGS are effective in pinning this potential adequately.

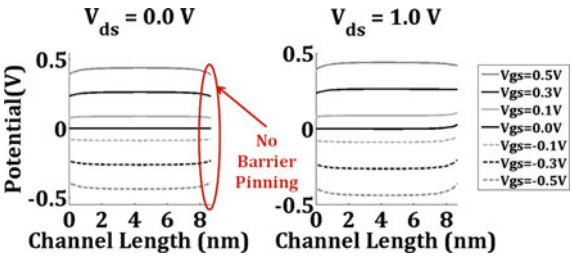

Fig. 18.16 At V_{ds} = 0.0 V and V_{ds} = 1.0 V, variation of channel potential with different gate voltages shows no barrier pinning at the contacts, implying Ohmic contacts

As seen in Fig. 18.16, the lowering of the potential throughout the entire graphene channel region with applied gate bias is a characteristic of the regular Ohmic contact FETs rather than the Schottky barrier FETs, whose potentials would otherwise be pinned to the midgap by charging of the interfacial states [28].

The MIGS due to the tail ends of the metal states in the contacts leak in the semiconductor. Even with this 2D contact geometry, the MIGS will be present because of the contact–channel interfaces [25]. Our WNW all-graphene structure can filter these quickly decaying states, resulting in no significant contribution to the electron transmission. In the case of our device with the channel length of 8.66 nm, the MIGS do not travel all the way from source to the drain, but only extend approximately 0.7 nm into the semiconducting channel (Note a typo in one of our earlier papers, where we wrongly quoted this as 0.07 nm) [25]. The decay length of these MIGS can be calculated by plotting the wavefunction of the channel electrons at specific energies, as well as by evaluating the complex E–k diagram. The intensity of these MIGS at a given distance x can be expressed as $I_0 * e^{(-x/2\lambda)}$, where I_0 is the intensity of MIGS at the interface and λ is the decay length.

Note that issues similar to those discussed here have been discussed in the context of pentacene molecules with CNT contacts. While CNTs would offer even better 1D electrostatic gains, a trade-off arises with the increasing series resistance in CNTs due to a paucity of modes. For GNR source–drain analogously, we will need to imagine wide blocks simultaneously contacting many GNR devices, so that the contact resistance is minimized by extending its width.

We now have all the tools to compute three-terminal I–Vs in graphitic structures, doing full justice to the complex electrostatics. Let us now see how this influences the circuit level performance metrics of GNRs.

18.4 The Penultimate Circle: GNR Circuits

Moving to the next level of abstraction and the last rung of our Gajski–Kuhn Y-chart, we focus on circuit level design issues when integrating GNR interconnects or devices. In the spirit of our WNW all graphene device, we start by exploring potential all graphene circuit topologies. Next, we focus on fundamental circuit response design issues revolving around a GNR-based inverter. The inverter is

the most basic logic circuit with the sole purpose of converting a logical 1 (ON) to a logical 0 (OFF). In the process of characterizing a GNR inverter, we touch on interconnects and finally discuss drivability between connected GNR logic elements.

18.4.1 Geometry of An All Graphene Circuit

An attractive feature of graphene is its atomic flatness, which makes it compatible to existing lithographic device fabrication techniques established for CMOS. By exploiting how chirality influences graphene's electronic properties, we present an array of potential circuit level building blocks (Fig. 18.17) that uses graphene for both active devices the interconnects. Having graphene device contacts and interconnects would help reduce extrinsic capacitance and circuit level delay. However circuit level enhancements start at the device level.

Two important device performance metrics for digital circuit performance are ON–OFF current ratio and intrinsic gate propagation delay. GNRFET ON current scales proportionally with width, while the OFF current goes as $e^{Eg/kT}$ or $e^{c/WkT}$, where W is the width. To achieve manageable OFF currents for digital applications, GNR widths must be scaled within the sub-10nm regime to avoid increased in static power dissipation and poor ON–OFF ratio. However, GNR scaling has little influence on propagation delay.

Propagation delay is defined as $C_{IN}V_{dd}/I_{ON}$, where C_{IN} is the intrinsic capacitance, V_{dd} is the supply voltage and I_{ON} is the saturating ON current at $V_{gs} = V_{dd}$.

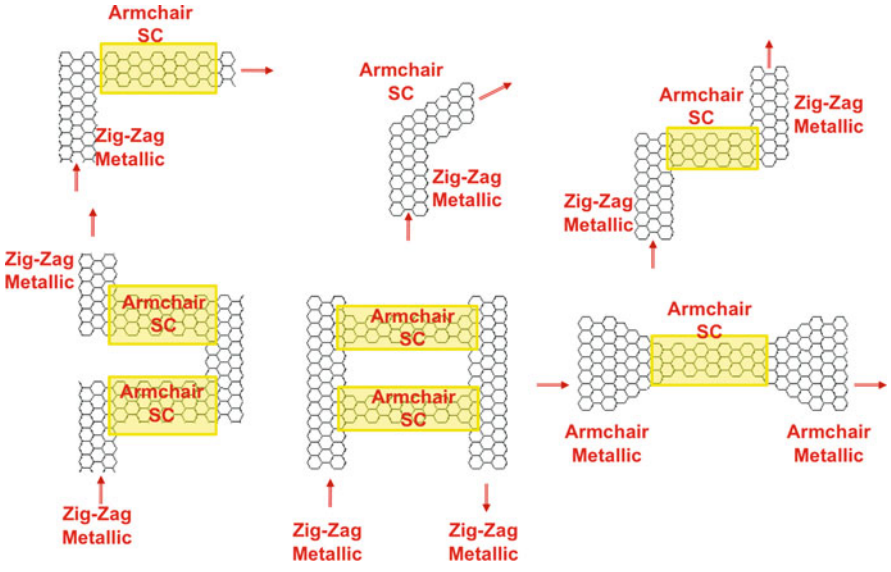

Fig. 18.17 The various building blocks for all graphene circuits

Increasing channel width increases I_{ON} by shifting the threshold voltage and would seemingly improve delay at the expense of an exponentially increasing OFF current. However, $C_{IN} = (1/C_{ox} + 1/C_Q)^{-1}$ also scales with width, thereby removing any improvement in propagation delay from simple scaling of graphene. From the perspective of a single GNR device, there are not many options to improving the propagation delay. However, a more useful context to address this issue would be on the circuit level where we have multiple logic elements.

On a circuit level, the complexity of propagation delay stems from a combined effect from the pull-up and pull-down network drain capacitances, interconnect capacitance ($C_{interconnect}$) and the next load gate capacitance or input of the next logic element. Using the building blocks in Fig. 18.17, we present an all graphene circuits shown in Fig. 18.18, with a cascade of parallel semiconducting GNRs over a semiconducting substrate and split gates to electrostatically dope different cascades n or p-type. The semiconducting GNRs and splits gates could be separated by a high-k dielectric or even boron nitride in hexagonal lattice. Boron Nitride has the advantage of being atomically flat and its absence of surface dangling bonds makes it less likely to carry adsorbents that could degrade the device. The advantage here is that ON–OFF ratio is held constant, while the increased ON current and capacitance, which scales with N number of parallel semiconducting GNRs, dilute the parasitic interconnect capacitance and improve propagation delay and circuit performance.

Good-quality graphene sheets have been made viable by current advancements in wafer-scale and pattern transfer techniques [18, 29]. However, full realization of an all graphene circuits with various GNR interconnects and devices rely on the ability to pattern GNRs to narrow enough widths to produce sizable bandgaps. Planar lithographic techniques are prone to edge roughness, while various chemical methods have had the most success in creating chemically precise GNR edges, but their applicability to scalable device level processes remain to be seen [7, 30–32]. While roughness helps to make GNRs insensitive to chirality, we need further simulations to see how atomic fluctuations in the widths influence the corresponding threshold voltages and ON/OFF currents, an issue critical for the overall reliability of GNR circuits.

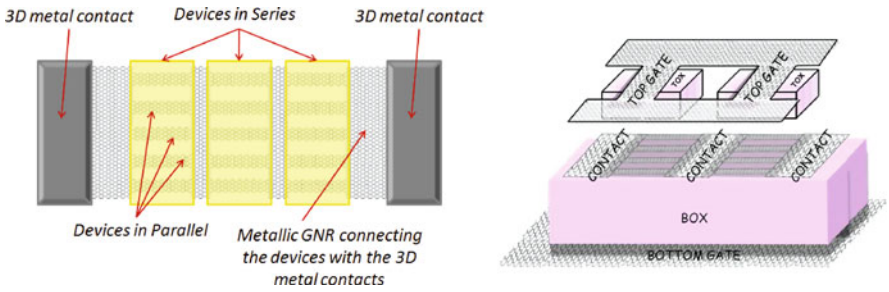

Fig. 18.18 Geometry of all graphene circuits

18.4.2 Compact Model Equations

To simulate the performance of such a circuit, let us first outline a compact model. This will require us to outline (a) an equation for the bandstructure that includes effects due to edge strain and roughness, (b) an equation for the scattering length that depends on the phonon spectrum and edge roughness, (c) equations for the 2D electrostatics due to the source and drain contacts, and (d) the resulting I–Vs obtained by integrating the transmission over the relevant energy window.

To recap, the bandstructure of GNRs, including edge strain, can be written in a tight-binding form as $E = \pm\sqrt{E_{C,V}^2 + \hbar^2 v_0^2 k^2}$. Specific expressions for $E_{C,V}$ and v_0 for variously strained graphitic materials exist in [9].

The next term is the scattering λ_{sc}, which is related to the scattering time through an angle averaged geometrical factor and the overall Fermi velocity. The scattering time is extracted from Fermi's golden rule. For short-range scattering by edge roughness and phonons, $\lambda_{sc} \propto 1/|E|$, while for long ranged unscreened Coulomb scattering, $\lambda_{sc} \propto |E|$. Explicit expressions exist in the literature [33, 34].

The tricky part that does not exist in the literature is the capacitances associated with the 2D electrostatics from the planar source and drain contacts, competing with the top and bottom gates through their individual dielectrics. We are in the process of extracting formulae based on knowledge of planar microstrip line electrostatics, with geometrical factors calibrated with our numerical MOM solutions for a variety of geometries [25].

Once we have the electrostatic, band and scattering parameters, we can then use (18.1) to extract the I–Vs. For energy-independent λ_{sc}, this was already shown (18.4) and (18.5). We will generalize it to various scattering configurations in our future work.

We thus have a comprehensive compact model that captures the chemistry and bandstructure, scattering, electrostatic, and transport parameters needed for our circuit simulations. We will report one example here and report further results in our subsequent publications.

18.4.3 Digital Circuits

Static complementary CMOS gates utilize pull-up (PUN) and pull-down (PDN) networks to achieve low-power dissipation and large noise margin in logic circuits such as the inverter, NAND, and NOR gates. CMOS logic circuits are composed of some series and parallel combinations of n and p-type FETs. An inverter illustrated in Fig. 18.19 is the simplest logic element and the focus of this section of the review.

When the input into the common gate is Vin = 0, the p-type FET (PUN) is active while the n-type FET (PDN) is cut-off, hence the circuit will pull the output voltage up toward the supply voltage (Vdd) or high, Vout = 1. Likewise when Vin = 1, n-type FET is active and p-type FET is cut-off pulling the circuit down toward

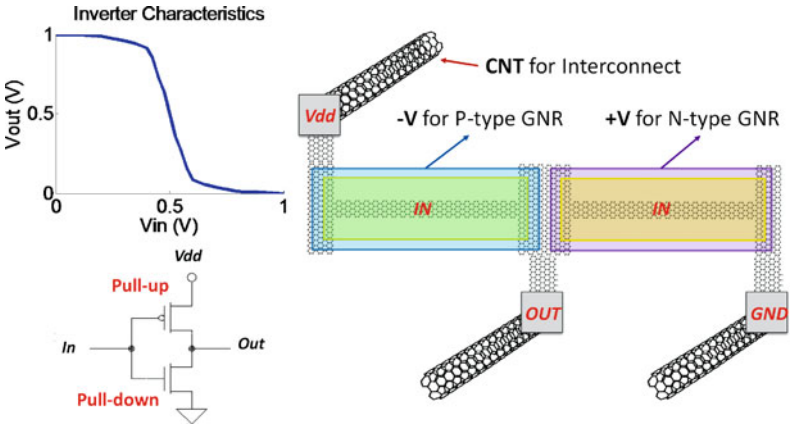

Fig. 18.19 GNR inverter geometry and voltage transfer curve. This inverter design uses the WNW (metal–semiconductor–metal) all graphene structure for pull-up and pull-down networks. In this design, CNT interconnects make direct contact with device level graphene. CNT–graphene interface has been experimentally demonstrated by Fujitsu Laboratories Ltd [35, 36]

ground, Vout = 0. Usually, it is impossible to pull-up or pull-down to exact values of 1 or 0, so threshold voltage and tolerance are designed for each circuit to help distinguish between these two logic levels. Circuit designers allow some tolerance in the voltage levels to avoid conditions that generate intermediate levels that are undefined. For example, 0–0.2 V on the output can represent logic (0) and 0.3–0.5 V can show (1), making the 0.2–0.3 V range invalid, not metastable, since the circuits cannot instantly change voltage levels.

The voltage-transfer curve (VTC) of an inverter circuit captures the DC or steady state of specific input vs. output voltages and provides a figure of merit for the static behavior of the inverter. VTCs for logic circuits provide information on operating logic levels at the output, noise margins, and gain. Ideally, we want the VTC to appear as an inverted step function, indicating precise switching between the ON and OFF states, but in real devices there is a continuous transition between ON and OFF. From the VTC, we can extract a noise margin (Fig. 18.20), which provides a measure of circuit reliability and predictability. Biasing outside the noise margin puts the logic circuit in an unpredictable state. Circuit designers want to maximize the noise margins.

18.4.4 How 'Good' is a Graphene-based Invertor?

A significant advantage of graphene is its intrinsic electron–hole effective mass symmetry. In the absence of extrinsic doping in a graphene-based FET, the I–V characteristics for n- and p-type conduction would be the symmetric. However, asymmetry can be introduced into the system through charge-transfer doping [17]

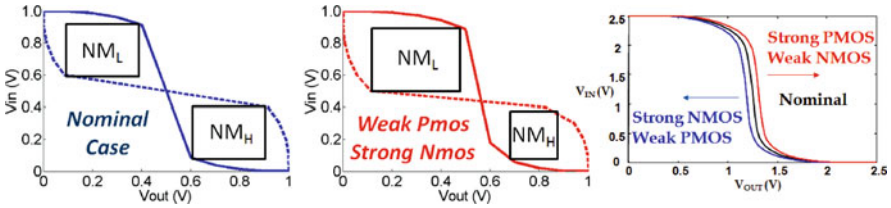

Fig. 18.20 Importance of balancing CMOS transistor sizes to achieve equal high and low-noise-margins (NM). The noise margin is graphically represented by the largest square that fits inside the enclosed space outlined by normal and rotated VTCs

(Fig. 18.8) or by contact-induced doping [37]. Significant screening of charge impurities in the substrate should bring Fermi level closer to its intrinsic value at the Dirac or K-point, therefore recovering symmetric n- and p-type I–V characteristics. *On a circuit level, this symmetry means the response of PUN and PDN would be equal and opposite, which is important for circuit reliability, and not to mention ease of circuit design.* In conventional Si-CMOS logic circuits, the asymmetry in the electron–hole effective mass is compensated by scaling the physical width of the p-type FETs in the PUN so the I–Vs are equal and opposite with the PDN. Graphene's natural electron–hole symmetry would allow circuit designers to bypass this design issue.

A major impediment to GNR–based logic circuits is its narrow bandgap ($\leqslant 200$ meV), as the device elements in the PUN and PDN are prone to subthreshold leakage from band-to-band tunneling. The two-fold effect on an GNRFET-based inverter where the channel has a narrow bandgap is demonstrated in Fig. 18.21. The first effect is a large voltage swing of approximately 0.4 V. The second effect is a significantly diminished noise margin. Band-to-band tunneling in narrow bandgap GNRFETs prevents either the PUN or the PDN from completely cutting off when its complement network is active.

Figure 18.19 shows the physical layout of a functional graphene inverter composed of WNW p-type and n-type GNR device arrays and the VTC. The inverter voltage-transfer curve and gain can be calculated readily from the current–voltage characteristics. As expected, the gain of the device determined by the electrostatics, geometrical parameters, and mobilities which ultimately determine the p and n-type GNR transconductances. The VTC above with gain of 4 is derived from the I–V shown in Fig. 18.19 for the 8.66 nm device by using the methodology described in detail in. [38]. These I–Vs generated in SPICE can be used to simulate other complex layouts such as NAND or NOR gates shown in Fig. 18.22 (The results of these logic gates will be reported in future publications).

Propagation delay can be measured by pulsing the input voltage between 0 and 1 and observing the output transient response. The transit time for a GNRFET is approximately L/v, where L is the length of the channel and v is an energy-dependent velocity defined in (18.3). Intrinsic and extrinsic device level scattering mechanics could also influence transit time. However, a cascade of inverters or some other logic elements in series, the load capacitance between each logic

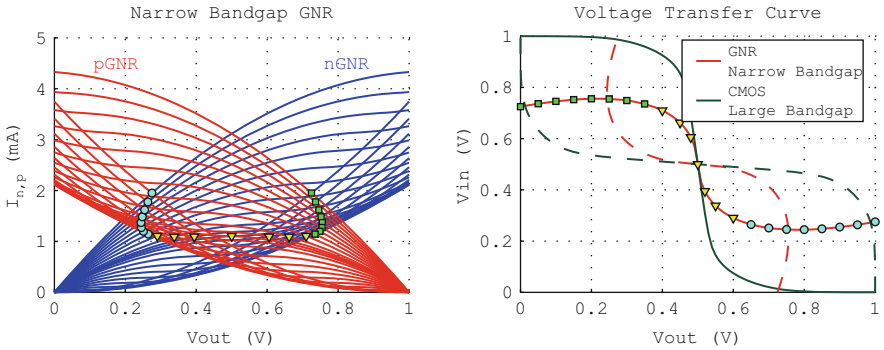

Fig. 18.21 Comparison of VTC curves for narrow bandgap GNR and 45 nm CMOS technology. Narrow bandgap GNRFETs will be more susceptible to noise than CMOS due to smaller noise margins. An possible design metric would be to limit the supply voltage to Vdd $< 0.8/W$, where W is the width of the semiconducting GNR channel

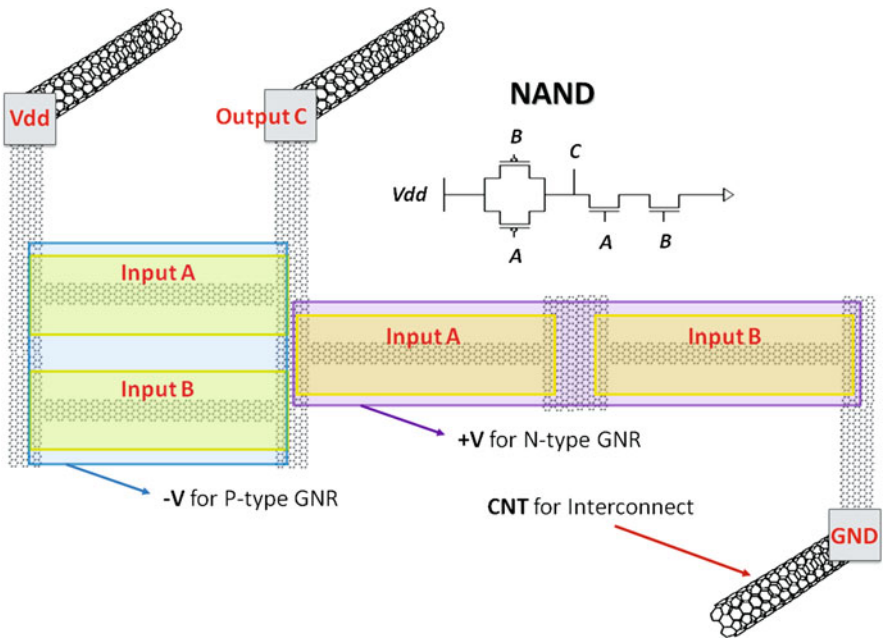

Fig. 18.22 GNR NAND layouts with electrostatic doped back-gates and interconnecting "vias" between multiple levels. CNT–graphene interface has been experimentally demonstrated by Fujitsu Laboratories Ltd [35, 36]

stage typically dominated by $C_{\text{interconnect}}$ would be responsible for the majority of the delay. The GNR circuit layout we presented earlier and shown in Fig. 18.18 addresses the parasitic capacitances by lowering delay and increasing performance.

Beyond individual logical elements (i.e., inverter, NAND, NOR), an important CMOS circuit design parameter is fan-out, which estimates the number of logic stages or CMOS gates that can be consecutively driven before signal attenuation is no longer tolerable. Past the maximum fan-out, a repeater or amplifier is necessary to drive subsequent logic stages in a circuit. The maximum fan-out scales proportionally with propagation delay; therefore, circuits designed for low-frequency applications have a larger maximum fan-out compared to circuits designed for higher-frequency applications. If graphene is to indeed follow the MOSFET and CMOS paradigm, fan-out would be an important circuit design trade-off to consider and a topic we will discuss in an upcoming work.

18.4.5 Physical Domain Issues: Monolithic Device-Interconnect Structures

The bane of many CNT-based circuit ideas is the degradation due to the dominant aspect of the Schottky contacts between the devices and interconnect. Luckily, GNR circuits can avoid this problem by using the same sheet of graphene for both active devices and interconnect, as seen in Fig. 18.22.

Using an all graphene device/interconnect circuit topology would benefit from Ohmic contacts; thus, largely preserving the ideal device characteristic we have predicted in our simulations (See Sec. 18.3). However, we cannot get rid of metal contacts completely for a few reasons. Firstly, the FET gates and S/D electrodes cannot share the same graphene sheet, because the larger resistivity of a 2D graphene sheet compared to a metal contact is enough to degrade the drivability of the next logic element. Secondly, topological requirements for connecting complex circuit elements are rarely mapped to a planar graph, while non-planar graphs would implicitly require more than one layer of interconnects. The number of additional interconnect layers would depend on the complexity of the circuit, which has ramifications in the form of interlayer parasitic capacitance. Potential cross-talk between various interconnects would compromise signal integrity and increase propagation delay. An interesting area we have not explored fully is whether or not using graphene electrodes and intra-layer interconnects can help reduce the number of interconnects layers for a circuit of similar complexity to a modern day CMOS circuit, which has approximately 10 interconnect layers.

18.5 Conclusions

The future of microelectronics relies on continually scaling the critical dimensions of bulk CMOS technologies. The semiconductor industry faces serious challenges in this respect, due to a host of technical and economic constraints. One way to

mitigate this is to use novel architectures, combining inherently scalable top-down techniques, such as lithography, with novel bottom-up fabrication approaches, such as self-assembly. An alternate way is to look for novel channel materials beyond silicon – a strong candidate being another group IV element, carbon, graphene being one of its distinguished allotropes.

Until recently, much attention has been focused on CNTs. CNTs have already demonstrated excellent intrinsic performance, high gain, high carrier mobility, high reliability, and are almost ideal devices in themselves [39–41]. Unfortunately, there seem to be no practical, scalable solutions for arranging multiple CNTs on a substrate uniformly with a small pitch, needed to deliver adequate current for fast switching [31, 42]. Neither are there clear approaches for contacting CNTs to interconnects or to each other at low impedance to realize complex circuits using large-scale fabrication schemes. In fact, CNTs frequently encounter Schottky barriers at the contacts that control the tunneling electrons, hampering their reliability [43].

In contrast, graphene's planar profile makes it amenable to well-established planar fabrication techniques for silicon CMOS devices. Its mobility can reach up to two orders of magnitude above silicon, and the ability to engineer its bandgap with width alone points to the feasibility of all-graphene devices that can exploit covalent bonding chemistry at the contact and better inherent electrostatics to allow more traditional, MOSFET, like gate control mechanisms. However, its bane seems to be its metallicity. As we saw earlier, graphene is naturally a zero-band gap semimetal, and attempts to open a bandgap, such as through strain, quantization, or field asymmetries have limited the bandgaps to < 200 mV [20]. In a regular field effect transistor application, such a bandgap translates to an ON–OFF ratio of ~ 70, inadequate for digital logic [44]. This seems consistent with experiments on high-speed graphene transistors, which show I–Vs that are essentially quasi-linear. There is a lot of activity also on opening bandgaps in graphene, although it seems that this may reduce the mobility that made graphene a promising electronic device in the first place.

Despite the significant challenges, graphene's high carrier mobility and fast switching speeds make it widely studied. This includes revolutionary applications such as based on charge focusing, graphene spintronics, and excitonic condensation of pseudospin states [45]. At the same time, there is wide activity on graphene-based conventional electronic devices, specifically, RF devices and CMOS switches. It is not clear what the prospects of GNRs are vis-a-vis switching, given its low bandgap and its seemingly fundamental mobility-bandgap tradeoff. However, as we have argued here, there still are a few notable advantages to using graphene geometries, namely, (a) *a natural electron–hole symmetry* that helps with inverter design; (b) *its convenient placement between 1D and 3D*, so that it offers distinct electrostatic advantages without picking up too much series resistance arising from a paucity of modes; (c) the *tunability of its electronic properties* primarily by controlling its width. Experiments are still emerging on these fronts, and it remains to be seen whether one can put these advantages to good use.

In this chapter, we made a first attempt to transverse the Gajski–Kuhn YZ chart adapted to graphene, spanning physical, structural, and behavioral domains for

graphene. We ended with monolithic all graphene circuits and device–interconnect geometries, ultimately stopping short of the outermost circle that covers a system level topology and behavior. A key tool developed along the way was a compact model for GNRs that capture chemical, geometric, electronic, electrostatic, and transport properties through a set of simple parameterized equations calibrated against a few emerging experiments. Such a Y-chart is the first step toward a holistic approach that we hope will catapult graphene from the domain of fascinating physics and chemistry to technologically relevant electronic applications.

Acknowledgements We would like to thank Keith Williams, Kurt Gaskill, Jeong-Sun Moon, and Mark Lundstrom for useful discussions. This work was supported by the NSF-NRI, NSF-NIRT, and the UVa-FEST grants.

References

1. T. Beierlein, O. Hagenbruch, *Taschenbuch Mikroprozessortechnik* (Fachbuchverlag Leipzig, Germany, 1999)
2. A.H. Castro Neto, F. Guinea, N.M.R. Peres, K.S. Novoselov, A.K. Geim, Rev. Mod. Phys. **81**(1), 109 (2009)
3. Z. Chen, Y.M. Lin, M.J. Rooks, P. Avouris, Physica E: Low-dimensional Systems and Nanostructures **40**(2), 228 (2007). International Symposium on Nanometer-Scale Quantum Physics
4. K. Bolotin, K. Sikes, Z. Jiang, M. Klima, G. Fudenberg, J. Hone, P. Kim, H. Stormer, Solid State Commun. **146**(9-10), 351 (2008)
5. D. Kienle, J.I. Cerda, A.W. Ghosh, J. Appl. Phys. **100**(4), 043714 (2006)
6. Y.W. Son, M.L. Cohen, S.G. Louie, Phys. Rev. Lett. **97**(21), 216803 (2006)
7. M.Y. Han, B. Ozyilmaz, Y. Zhang, P. Kim, Phys. Rev. Lett. **98**(20), 206805 (2007)
8. X. Li, X. Wang, L. Zhang, S. Lee, H. Dai, Science **319**(5867), 1229 (2008)
9. D. Gunlycke, C.T. White, Phys. Rev. B **77**(11), 115116 (2008)
10. F. Tseng, D. Unluer, K. Holcomb, M.R. Stan, A.W. Ghosh, Appl. Phys. Lett. **94**(22), 223112 (2009)
11. D. Areshkin, D. Gunlycke, C. White, Nano Lett. **7**(1), 204 (2007). PMID: 17212465
12. L. Tapaszto, G. Dobrik, P. Lambin, L.P. Biro, Nature Nanotechnology **3**(7), 397 (2008)
13. X. Wang, Y. Ouyang, X. Li, H. Wang, J. Guo, H. Dai, Phys. Rev. Lett. **100**(20), 206803 (2008)
14. D.V. Kosynkin, A.L. Higginbotham, A. Sinitskii, J.R. Lomeda, A. Dimiev, B.K. Price, J.M. Tour, Nature **458**, 872 (2009)
15. S. Datta, *Quantum Transport: Atom to Transistor* (Cambridge University Press, Cambridge, 2005)
16. S. Datta, in *Electron Devices Meeting, 2002. IEDM '02. Digest. International* (2002), pp. 703–706
17. S. Kopylov, A. Tzalenchuk, S. Kubatkin, V.I. Fal'ko, Appl. Phys. Lett. **97**(11), 112109 (2010)
18. P. First, W.A. deHeer, T. Seyller, C. Berger, J.A. Stroscio, J. Moon, MRS Bull. **35** (2010)
19. S.M. Sze, K.K. Ng, *Physics of Semiconductor Devices* (Wiley, New York, 2006)
20. J. Cai, P. Ruffieux, R. Jaafar, M. Bieri, T. Braun, S. Blankenburg, M. Muoth, A.P. Seitsonen, M. Saleh, X. Feng, K. Mullen, R. Fasel, Nature **466**, 470 (2010)
21. S. Ramo, J.R. Whinnery, T. Van Duzer, *Field and Wave in Communication Electronics* (Wiley, New York, 1993)
22. J. Jackson, *Classical Electrodynamics* (Wiley, New York, 1975)

23. N. Neophytou, J. Guo, M. Lundstorm, in *Computational Electronics, 2004. IWCE-10 2004. Abstracts. 10th International Workshop on* (2004), pp. 175–176
24. J.N. Murrell, A.J. Harger, *Semi-Empirical SCF MO Theory of Molecules* (Wiley, New York, 1972)
25. D. Unluer, F. Tseng, A.W. Ghosh, M.R. Stan, IEEE Trans. Nanotechnol. **10**(5), 931 (2011)
26. S. Hasan, J. Wang, M. Lundstrom, Solid State Electron. **48**(6), 867 (2004). Silicon On Insulator Technology and Devices
27. J. Guo, A. Javey, H. Dai, M. Lundstrom, in *Electron Devices Meeting, 2004. IEDM Technical Digest. IEEE International* (2004), pp. 703–706
28. F. Leonard, J. Tersoff, Phys. Rev. Lett. **84**(20), 4693 (2000)
29. Y.M. Lin, C. Dimitrakopoulos, K.A. Jenkins, D.B. Farmer, H.Y. Chiu, A. Grill, P. Avouris, Science **327**(5966), 662 (2010)
30. E. Stolyarova, K.T. Rim, S. Ryu, J. Maultzsch, P. Kim, L.E. Brus, T.F. Heinz, M.S. Hybertsen, G.W. Flynn, in *PNAS May 29, 2007* (2007)
31. Y. Zhang, A. Chang, J. Cao, Q. Wang, W. Kim, Y. Li, N. Morris, E. Yenilmez, J. Kong, H. Dai, Appl. Phys. Lett. **79**(19), 3155 (2001)
32. M.C. Lemme, T.J. Echtermeyer, M. Baus, H. Kurz, IEEE Electron Device Lett. **28**, 282 (2007)
33. R. Shah, T.M. Mohiuddin, Charge carrier mobility degradation in graphene sheetunder induced strain. ArXiv:1008.4425v3
34. T. Fang, A. Konar, H. Xing, D. Jena, Phys. Rev. B **78**(20), 205403 (2008)
35. M. Katagiri, Y. Yamazaki, N. Sakuma, M. Suzuki, T. Sakai, M. Wada, N. Nakamura, N. Matsunaga, S. Sato, M. Nihei, Y. Awano, in *Interconnect Technology Conference, 2009. IITC 2009. IEEE International* (2009), pp. 44 –46
36. Y. Awano, (The Fullerenes and Nanotubes Research Society, Japan, 2008)
37. D.B. Farmer, R. Golizadeh-Mojarad, V. Perebeinos, Y.M. Lin, G.S. Tulevski, J.C. Tsang, P. Avouris, Nano Lett. **9**(1), 388 (2009)
38. J.M. Rabaey, A. Chandrakasan, B. Nikolic, *Digital Integrated Circuits - A Design Perspective (2nd Ed)* (Prentice Hall, Upper Saddle River, NJ, 2003)
39. A. Bachtold, P. Hadley, T. Nakanishi, C. Dekker, Science **294**(5545), 1317 (2001)
40. R. Martel, H.S. Wong, K. Chan, P. Avouris, in *Electron Devices Meeting, 2001. IEDM Technical Digest. International* (2001), pp. 7.5.1–7.5.4
41. S.J. Tans, A.R.M. Verschueren, C. Dekker, Nature **393**, 49 (1998)
42. A.M. Cassell, N.R. Franklin, T.W. Tombler, E.M. Chan, J. Han, H. Dai, J. Am. Chem. Soc. **121**(34), 7975 (1999)
43. J. Guo, S. Datta, M. Lundstrom, IEEE Trans. Electron Dev. **51**(2), 172 (2004)
44. G.C. Liang, A.W. Ghosh, M. Paulsson, S. Datta, Phys. Rev. B **69**(11), 115302 (2004)
45. D. Reddy, L.F. Register, E. Tutuc, A. MacDonald, S.K. Banerjee, in *Device Research Conference, 2009. DRC 2009* (2009), pp. 67–68

Index

H. Raza (ed.), *Graphene Nanoelectronics*, NanoScience and Technology,
DOI 10.1007/978-3-642-22984-8, © Springer-Verlag Berlin Heidelberg 2012